Mathematical and Numerical Aspects of Dynamical System Analysis

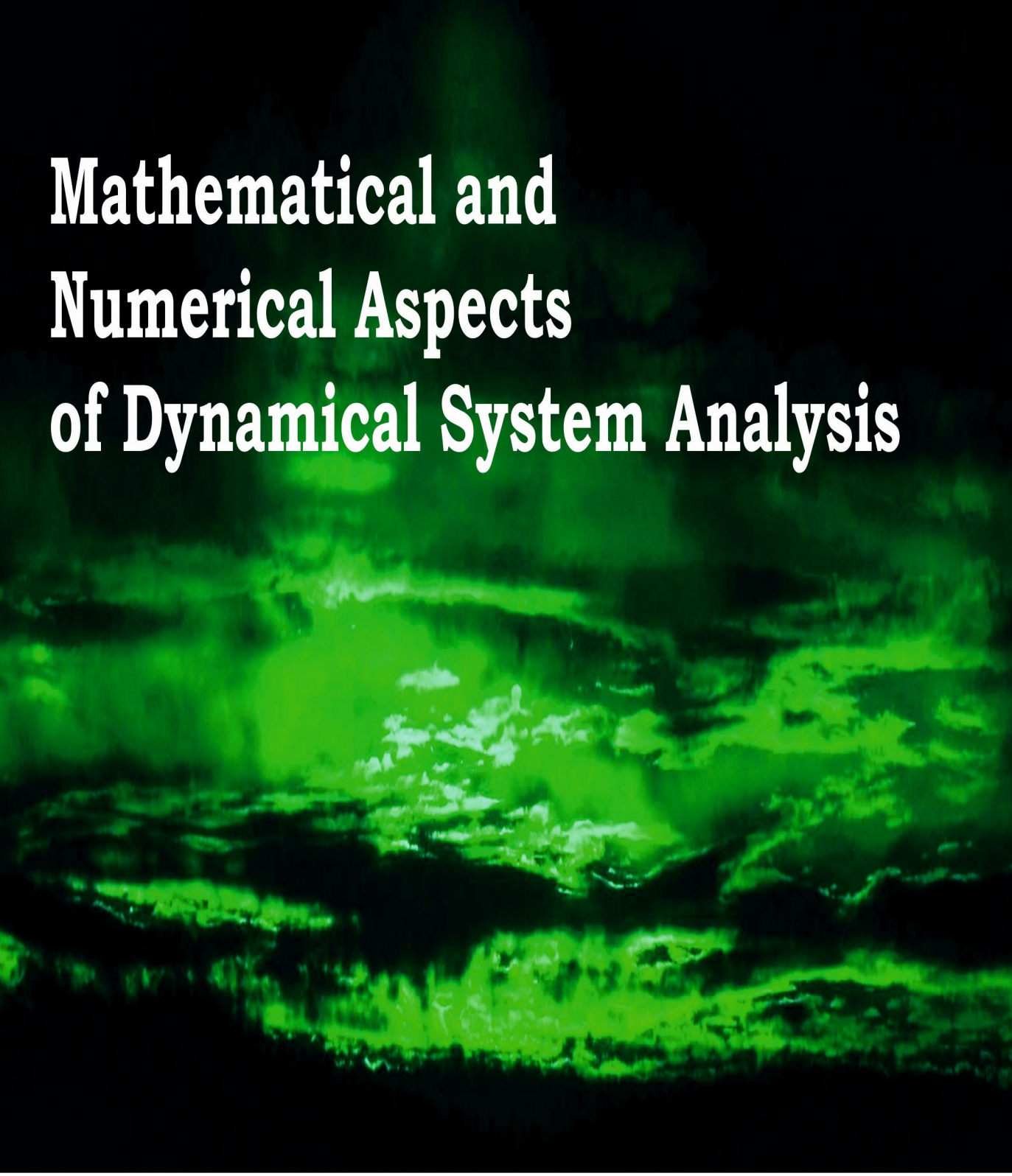

Editors
J. AWREJCEWICZ
M. KAŹMIERCZAK
J. MROZOWSKI
P. OLEJNIK

DSTA 2017

Mathematical and Numerical Aspects of Dynamical System Analysis

Editors

JAN AWREJCEWICZ, MAREK KAŹMIERCZAK
JERZY MROZOWSKI, PAWEŁ OLEJNIK

© Department of Automation, Biomechanics and Mechatronics
ISBN 978-83-935312-6-4
10.34658/9788393531264
https://doi.org/10.34658/9788393531264

Cover design: Marek Kaźmierczak
Technical editor: Marek Kaźmierczak

Printed by:
ARSA Druk i Reklama
90-270 Łódź, ul. Piotrkowska 4
tel./fax (042) 633 02 52
marta@arsa.net.pl
www.arsa.net.pl

PREFACE

This is the fourteenth time when the conference “Dynamical Systems: Theory and Applications” gathers a numerous group of outstanding scientists and engineers, who deal with widely understood problems of theoretical and applied dynamics.

Organization of the conference would not have been possible without a great effort of the staff of the Department of Automation, Biomechanics and Mechatronics. The patronage over the conference has been taken by the Committee of Mechanics of the Polish Academy of Sciences and Ministry of Science and Higher Education of Poland.

It is a great pleasure that our invitation has been accepted by recording in the history of our conference number of people, including good colleagues and friends as well as a large group of researchers and scientists, who decided to participate in the conference for the first time. With proud and satisfaction we welcomed over **180** persons from **31** countries all over the world. They decided to share the results of their research and many years experiences in a discipline of dynamical systems by submitting many very interesting papers.

This year, the DSTA Conference Proceedings were split into three volumes entitled “Dynamical Systems” with respective subtitles: *Vibration, Control and Stability of Dynamical Systems*; *Mathematical and Numerical Aspects of Dynamical System Analysis* and *Engineering Dynamics and Life Sciences*. Additionally, there will be also published two volumes of Springer Proceedings in Mathematics and Statistics entitled “*Dynamical Systems in Theoretical Perspective”* and *“Dynamical Systems in Applications”.*

These books include the invited and regular papers covering the following topics:

- asymptotic methods in nonlinear dynamics,
- bifurcation and chaos in dynamical systems,
- control in dynamical systems,
- dynamics in life sciences and bioengineering,
- engineering systems and differential equations,
- non-smooth systems
- mathematical approaches to dynamical systems
- original numerical methods of vibration analysis,
- stability of dynamical systems,
- vibrations of lumped and continuous systems,
- other problems.

Proceedings of the 14th Conference „Dynamical Systems - Theory and Applications" summarize **168** and the Springer Proceedings summarize **80** best papers of university teachers and students, researchers and engineers from all over the world. The papers were chosen by the International Scientific Committee from **370** papers submitted to the conference. The reader thus obtains an overview of the recent developments of dynamical systems and can study the most progressive tendencies in this field of science.

Our previous experience shows that an extensive thematic scope comprising dynamical systems stimulates a wide exchange of opinions among researchers dealing with different branches of dynamics. We think that vivid discussions will influence positively the creativity and will result in effective solutions of many problems of dynamical systems in mechanics and physics, both in terms of theory and applications.

We do hope that DSTA 2017 will contribute to the same extent as all the previous conferences to establishing a new and tightening the already existing relations and scientific and technological cooperation between both Polish and foreign institutions.

On behalf of both
Scientific and Organizing Committees

Chairman
Professor Jan Awrejcewicz

CONTENTS

Nicola Maria **Auciello**, Maria Anna **De Rosa**, Maria **Lippiello**, Stefania **Tomasiello**
Review on the Cell Discretitation Method (C.D.M.) **9**

Jan **Awrejcewicz**, Tatyana Y. **Yakovleva**, Ekaterina Y. **Krylova**, Anastasiya O. **Sinichkina**, Vadim A. **Krysko - jr.**
Theory of size-dependent physically nonlinear Euler-Bernoulli beams in an aggressive medium with account of coupling of temperature and deformation fields **19**

Jan **Awrejcewicz**, Tatyana V. **Yakovleva**, Vadim S. **Kruzhilin**, Svetlana A. **Mitskevich,** Vadim A. **Krysko**
Theory of coupled deformation and temperature fields for three-layer nano-mechanical structures **31**

Andrzej Bartoszewicz
Variable structure systems with sliding modes **39**

Peter B. **Beda**
Generic bifurcations in thermodynamics by fractional continuum mechanics **49**

Peter **Benner**, Andreas **Seidel-Morgenstern**, Alexander **Zuyev**
Computation of periodic switching strategies for the optimal control of chemical reactors **59**

Björn **Birnir**
Nonlinear quantum systems **67**

Alexey **Borisov**, Yury **Karavaev**
Selected problems of nonholonomic mechanics **87**

Thomas **Breunung**, George **Haller**
Time-varying spectral submanifolds: Analytic calculation of backbone curves and forced responses of nonlinear mechanical systems **101**

Stefan **Chwastek**
Parametric optimization in enumeration of alternative structures of mechanisms **109**

Ewa **Ciechanowicz**
Some value distribution and growth properties of solutions of Painleve and Riccati equations **119**

Eoin **Clerkin**, Rubens **Sampaio**
A bifurcation and symmetry discussion of the Sommerfeld effect **131**

Livija **Cveticanin**
On the acoustic metamaterial with negative effective mass **143**

Yulia **Danik**, Mikhail **Dmitriev**, Ekaterina **Komarova**, Dmitry **Makarov**
Application of Pade-approximations to the solution of nonlinear control problems **155**

Irina **Demiyanushko**, Ilya **Karpov**, Beka **Tavshavadze**
Developments of non-linear dynamics FEM simulation of the impact performance of road safety barriers with use of experimental validation of models **165**

Galina **Filipuk**
Nonlinear differential-difference equations related to the second Painleve equation **175**

Galina **Filipuk**, Thomas **Kecker**
Kahan discretisation of a cubic Hamiltonian system **185**

Peter **Giesl**
Computation of a Finsler-Lyapunov function using meshless collocation **193**

Alexander **Glushkov**, Yuliya **Dubrovskaya**, Vasily **Buyadzhi**, Eugeny **Ternovsky**
Chaos and strange attractors in environmental radioactivity dynamics of some geosystems: Atmospheric radon ^{222}Rn **205**

Sayan **Gupta,** Pankaj **Kumar,** Sadagopan **Narayanan**
Stochastic bifurcations of discontinuous and impacting nonlinear systems **215**

Sigurdur **Hafstein**, Asgeir **Valfells**
Study of dynamical systems by fast numerical computation of Lyapunov functions **229**

Katica **Hedrih (Stevanovic)**
Energy dissipation, free and forced modes in dynamics of two classes of fractional order systems **241**

Margarita **Kalashnikova**, Galina **Kurina**
Estimates of asymptotic solution of linear-quadratic optimal control problems with cheap controls of two different orders of smallness **253**

Ivana **Kovacic**
On some exact solutions for a forced response of nonlinear oscillators **265**

Alexander **Krot**
Derivation and investigation of the generalized nonlinear Schrödinger equation of cosmogonical body forming **277**

Vadim A. **Krysko - jr.**, Jan **Awrejcewicz**, Irina V. **Papkova**, Vadim A. **Krysko**
General theory of geometrically nonlinear size dependent shells taking into account contact interaction. Part 1: Chaotic dynamics of geometrically nonlinear axially symmetric one-layer shells **289**

Vadim A. **Krysko - jr.**, Jan **Awrejcewicz**, Irina V. **Papkova**, Vadim A. **Krysko**
General theory of geometrically nonlinear size dependent shells taking into account contact interaction. Part 2: Contact interaction of two-layer axially symmetric shells **301**

Lidiya **Kurpa**, Tetyana **Shmatko**, Jan **Awrejcewicz**
Free vibration analysis of laminated functionally graded shallow shells by the R-functions method **311**

Marcela **Machado**, Leila **Khalij**, Adriano **Fabro**
Spectral approach for dynamic analysis of a composite structure under random excitation **323**

Vasile **Marinca**, Nicolae **Herisanu**
Optimal auxiliary functions method for investigating a permanent magnet synchronous generator **335**

Adam **Martowicz**, Wieslaw J. **Staszewski**, Massimo **Ruzzene**, Tadeusz **Uhl**
Nonlocal elasticity theory for solving dynamic problems via peridynamics **345**

Adam **Martowicz**, Wieslaw J. **Staszewski**, Massimo **Ruzzene**, Tadeusz **Uhl**
Nonlocal numerical methods for solving second-order partial differential equations **357**

Hovik **Matevossian**, Mikhail **Nikabadze**, Armine **Ulukhanian**
On solutions of biharmonic problems **369**

Tomasz **Mirosław**
Computer model of ground under vehicle's wheels **381**

Cristina **Muresan**, Isabela **Birs**, Clara **Ionescu**, Robin **De Keyser**
Existence conditions for fractional order PI/PD controllers **395**

Dalma **Nagy**, László **Bencsik**, Tamás **Insperger**
Identification of the model of stick balancing using the cepstral analysis **405**

Mikhail **Nikabadze**
On decomposition of the initial boundary value problems in mechanics **413**

Paweł **Nowak**, Andrzej **Nowak**, Marek **Metelski**
Modelling of vibration and large deflections of lattice-boom structures of cranes by means of rigid finite element method **425**

Tomasz **Nowakowski**, Paweł **Komorski**, Grzegorz Marek **Szymański**, Franciszek **Tomaszewski**
Application of Hilbert transform in detection flat places on tram wheels **437**

Paweł **Olejnik**, Jan **Awrejcewicz**, Michal **Fečkan**
Mathematical models of two parametric pendulums with modulated length **449**

Irina V. **Papkova**, Olga A. **Saltykova**, Jan **Awrejcewicz**, Vadim A. **Krysko**
Chaotic dynamics of a two-layer beam set, described by mathematical models of the first and second approximation **459**

Laura **Ruzziconi**, Nizar **Jaber**, Lakshmoji **Kosuru**, Mohammed L. **Bellaredj**, Stefano **Lenci**, Mohammad **Younis**
Theoretical and experimental investigation of nonlinear dynamical features in a MEMS device electrically actuated **467**

Abhay Kumar **Sethi**, Arun Kumar **Tripathy**
Riccati transformation and oscillation of superlinear second order functional differential equations **479**

Maxim V. **Shamolin**
Mathematical modeling of the action of a medium on a conical body **491**

Aleksandr **Shvets**, Alexander **Makaseyev**
Deterministic chaos in some pendulum systems with delay **501**

Christos **Skiadas**, Charilaos **Skiadas**
The first exit time stochastic theory applied to estimate the life-time of a complicated machine. The case of cars **511**

Barbara **Tomczyk**, Anna **Litawska**
A new asymptotic-tolerance model of dynamics of thin uniperiodic cylindrical shells **519**

Duarte **Valério**, José **Tenreiro Machado**, António **Lopes**, Antonio **Santos**
A fractional perspective to the modelling of Lisbon's Public Transportation Network **533**

Aleksandra **Waszczuk-Młyńska**, Stanisław **Radkowski**
Analytical model of damaged circular membrane using a pseudo torus **545**

Krzysztof **Wilde**, Dawid **Bruski**, Stanisław **Burzyński**, Jacek **Chróścielewski**, Wojciech **Witkowski**
Numerical crash analysis of the cable barrier **555**

Tatyana Y. **Yaroshenko**, Jan **Awrejcewicz**, Igor I. **Shulga**, Maxim V. **Zhigalov**, Vadim A. **Krysko**
Application of non-linear dynamics to Poland's evolution **567**

Tatyana Y. **Yaroshenko**, Jan **Awrejcewicz**, Igor **Pelve**, Vadim A. **Krysko**
Understanding of origination, development and the sunset of the Ottoman Empire using wavelets and Lyapunov exponents **579**

Alena **Zarodnyuk**, Oleg **Cherkasov**
Optimal thrust programming along the brachistochronic trajectory with drag **591**

Ulrike **Zwiers**
A remark on point coordinates in multibody dynamics formulations **599**

Arkadiusz **Żak**, Marek **Krawczuk**, Grzegorz **Redlarski,** Wiktor **Waszkowiak**
Modelling of high frequency dynamic responses of engineering structures **611**

Review on the Cell Discretization Method

Nicola Maria Auciello, Maria Anna De Rosa, Maria Lippiello, Stefania Tomasiello

Abstract: In the last forty years, the Cell Discretization Method (CDM) has become a popular method for the statical and dynamical analysis of structures. According to this method, the structure is reduced to a set of rigid bars linked together by means of elastic constraints (cells). In this way, the structure is reduced to a rigid-elastic system with a finite number of Lagragian coordinates. The latter ones may be chosen in two alternative ways: the rotations of rigid bars or the displacements of the cells. This method found several applications, for instance: the dynamics and stability of arches; masonry arches; statical and dynamical analysis of Euler-Bernoulli beams under several load and boundary conditions; statical and dynamical analysis of Timoshenko and Rayleigh beams; statical analysis of plates; statical and dynamical analysis of carbon nanotubes, by taking into account nonlocal effects. Due to the renovated interest in this method, especially with regard to the application to the field of carbon nanotubes, it seems appropriate proposing a critical review on the method and its current and future applications.

1. Introduction

The Cell Discretization Method (CDM) has been becoming an important tool in the field of the structural engineering, thanks to its approximation abilities and easyness to be implemented.

The advent of sophisticated and totally generalized discretization tools, such as FEM, BEM, allowed to simulate the behaviour of structures taking into account several variables due to the removal of as many as simplified hypotheses, but on the other hand such procedures may induce to lose the physical sense of the real behaviour of the structures that should be always at the basis of engineering studies.

In this sense, the CDM may be regarded as a technique able to address such issues. It was developed by some of the present authors jointly with other co-workers in 80s. The idea behind the method, that is the discretization of structures by means of rigid bars linked through elastic constraints (cells), was in the literature since the beginning of the 20th century. Anyway, the first time it appeared as a formally theoretically supported method is in [1]. The method proposed in [1] was then developed to handle the problem of arches, by computing the conservative critical loads [2].

Raithel and Franciosi in [3] extend the discretization procedure to the dynamics problem by computing the vibration modes of arches without axial loads, while in [4] the presence of axial loads (applied to arches) is considered as a delay effect. In the last years, several proposals and calculation analyses were developed in the field of structural engineering, involving the behaviour of arches with different types of constraints, such as simply elastic supports or even rigid foundation blocks [5] – [15]. In all these works, the procedure is shown to be very versatile and able to work in any case on a finite number of Lagrangian parameters by bringing the solution into the alveo of the usual numerical analysis methods. With regard to the study of masonry arches, with a few numerical strategies and assuming the presence of non-reactive tensile units, a powerful investigation tool was proposed, for determining the collapse multipliers [16] – [19]. In addition, this method found several applications, even for the static and dynamical analysis of uniform and tapered Euler - Bernoulli beams, Timoshenko and Rayleigh beams and plates under several load and boundary conditions [20]–[39]. More recently, some of the present authors applied the method to the dynamical analysis of single- and double-walled carbon nanotubes, by taking into account non - local effects [40] – [42] and they obtained results showing that the method is able to describe the nanostructure behaviour satisfactorily with a little computational effort. At the moment, it seems proper writing a review note on the method and its former and coming applications. This work presents briefly the method and its application, as well as its potentialities.

2. The method

The discretization procedure of the CDM is intended to reduce the structure to a set of rigid bars, with equal length, linked by elastic cells. The choice of the Lagrangian coordinates can be done in two ways: the first one is choosing the rotations of the rigid bars while the second one is assuming the vertical displacements of the elastic cells. Consequently, based on the Lagrangian coordinates chosen, namely the set of rotations or the set of displacements, the method allows to derive all the possible configurations of the structure and writing the equations of motion. In the current literature, the difference between the two proposed procedures has not been emphasized yet, probably because the basic concept is the same, that is discretising the structure in rigid bars and elastic cells.

In this review work, we summarize the two discretization methods for the simple case of the dynamic analysis of an Euler–Bernoulli beam, leaving the reader looking for more complex cases in the cited works.

2.1. The discretization

By applying the Hamilton Principle for an Euler-Bernoulli beam, with span L, section of area A and inertia I, Young modulus E and mass density ρ, one has

$$\int_{t_1}^{t_2} [\delta \mathrm{T} - \delta \mathrm{E}_t] \mathrm{d}t = 0 \tag{1}$$

where t is the time variable and t_1, t_2 two arbitrarily fixed times.

The kinetic energy is

$$\mathrm{T} = \frac{1}{2} \int_0^{\mathrm{L}} \rho \mathrm{A} \left(\frac{\partial v(z,t)}{\partial t} \right)^2 \mathrm{d}z, \tag{2}$$

where z is the abscissa along the beam axis. The deformation energy is

$$\mathrm{E}_t = \frac{1}{2} \int_0^{\mathrm{L}} \mathrm{EI} \left(\frac{\partial^2 v(z,t)}{\partial z^2} \right)^2 \mathrm{d}z. \tag{3}$$

Subtracting Eq. 2 from Eq. 3, one has the Lagrangian

$$\mathrm{T} - \mathrm{E}_t = \frac{1}{2} \int_0^{\mathrm{L}} \rho \mathrm{A} \left(\frac{\partial v(z,t)}{\partial t} \right)^2 \mathrm{d}z - \frac{1}{2} \int_0^{\mathrm{L}} \mathrm{EI} \left(\frac{\partial^2 v(z,t)}{\partial z^2} \right)^2 \mathrm{d}z. \tag{4}$$

Performing the first variation of Eq. 4 we obtain the equation of motion and the corresponding boundary conditions:

$$\mathrm{EI} \frac{\partial^4 v(z,t)}{\partial z^4} + \rho \mathrm{A} \frac{\partial^2 v(z,t)}{\partial t^2} = 0 \tag{5}$$

If the structure is discretized, the Eq. 5 will be represented by the following Lagrange equation system:

$$\frac{d}{dt} \left(\frac{\partial \mathrm{T}}{\partial \dot{q}_i} \right) + \frac{\partial \mathrm{E}_t}{\partial q_i} = 0, \ i = 1, ...n, \tag{6}$$

with q_i Lagrangian coordinates.

2.2. First approach: rotations as Lagrangian coordinates

The structure is regarded as a set of n rigid bars linked by $n+1$ elastic constraints (Figure 1), representative of the flexural constraints. In this case, the structure configurations depend on a finite number of degree-of-freedoms (DOFs). The rigid rotations φ_i of the bars are assumed as Lagrangian parameters:

$$\mathbf{c} = [\varphi_1, \ldots, \varphi_i, \ldots, \varphi_n]^{\mathrm{T}} \tag{7}$$

and one can get the displacements of the beam by means of simple geometric considerations (Fig. 1). More precisely, let L/n be the length of the rigid bar, then by considering the

scheme in Fig. 1, the displacements v_i and the relative rotations in any elastic cell are given by

$$v_1 = 0, \qquad v_2 = -\varphi_1 \ \mathrm{L}/n, \qquad v_i = -\sum_{i=1}^{i-1} \varphi_i \mathrm{L}/n, \qquad v_{n+1} = -\sum_{i=1}^{n} \varphi_i \mathrm{L}/n, \tag{8}$$

$$\Delta\varphi_1 = \varphi_1, \qquad \Delta\varphi_2 = \varphi_2 - \varphi_1 \ , \qquad \Delta\varphi_i = \varphi_i - \varphi_{i-1}, \qquad \Delta\varphi_{n+1} = 0, \tag{9}$$

which in matrix form are

$$\mathbf{v} = \mathbf{A}\mathbf{c}, \qquad \boldsymbol{\Delta\varphi} = \mathbf{B}\mathbf{c}, \tag{10}$$

where the $(n+1) \times n$ matrices $\mathbf{A}$, $\mathbf{B}$ are written as follows

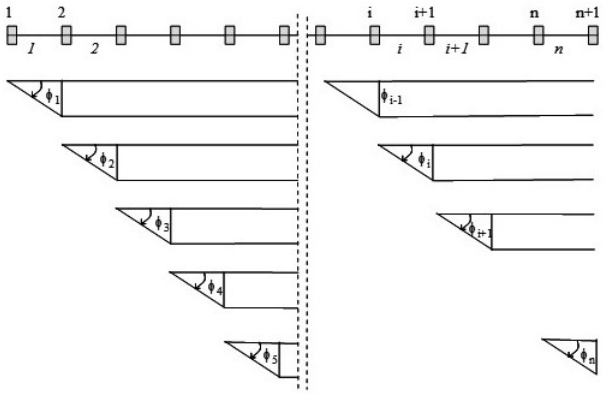

Figure 1. First method for chosing the Lagrangian parameters: rigid rotations

$$\mathbf{A} = \frac{\mathrm{L}}{n} \begin{pmatrix} 0 & 0 & 0 & \dots & 0 \\ -1 & 0 & 0 & \dots & 0 \\ -1 & -1 & 0 & \dots & 0 \\ \vdots & \vdots & \vdots & \vdots & \vdots \\ -1 & -1 & -1 & \dots & -1 \end{pmatrix}, \qquad \mathbf{B} = \begin{pmatrix} 1 & 0 & 0 & \dots & 0 \\ -1 & 1 & 0 & \dots & 0 \\ 0 & -1 & 1 & \dots & 0 \\ \vdots & \vdots & \vdots & \vdots & 0 \\ 0 & 0 & 0 & \dots & 0 \end{pmatrix}. \tag{11}$$

By considering Eq. 10, the kinetic energy can be written as follows

$$\mathrm{T} = \frac{1}{2} \int_0^{\mathrm{L}} \rho \mathrm{A} \dot{\mathbf{v}}^2 \mathrm{d}z = \frac{1}{2} \sum_{i=1}^{n+1} m_i \dot{v}_i^2. \tag{12}$$

The masses m_i are centred in the elastic cells and are given by

$$m_1 = \frac{\mathrm{L}}{2n} \rho \mathrm{A}_1, \quad m_i = \frac{\mathrm{L}}{2n} \rho \left(\mathrm{A}_i + \mathrm{A}_{i+1} \right), \quad m_{n+1} = \frac{\mathrm{L}}{2n} \rho \mathrm{A}_{n+1}, \qquad i = 2....n. \tag{13}$$

Then, the kinetic energy can be written as

$$\mathrm{T} = \frac{1}{2}\dot{\mathbf{c}}^{\mathrm{T}}\left[\mathbf{A}^{\mathrm{T}}\boldsymbol{m}\,\mathbf{A}\right]\dot{\mathbf{c}} = \frac{1}{2}\dot{\mathbf{c}}^{\mathrm{T}}\mathbf{M}\,\dot{\mathbf{c}}, \tag{14}$$

with $\mathbf{M}$ the mass matrix of order $(n, n+1)$.

The deformation energy is given by the work done by the bending moment because of the relative rotation in the generic elastic cell. By neglecting the shear effect, the bending moment is given by

$$\mathrm{M}_i = \frac{n}{\mathrm{L}}\mathrm{EI}\Delta\varphi_i = k_i\Delta\varphi_i, \tag{15}$$

with k_i being the stiffness of the rigid links, given by

$$k_1 = \frac{n}{2\mathrm{L}}\mathrm{EI}_1, \quad k_i = \frac{n}{\mathrm{L}}\mathrm{E}\left(\mathrm{I}_i + \mathrm{I}_{i+1}\right), \quad k_{n+1} = \frac{n}{2\mathrm{L}}\mathrm{EI}_{n+1}. \tag{16}$$

Then Eq. 3 becomes

$$\mathrm{E}_t = -\frac{1}{2}\int_0^{\mathrm{L}} \mathrm{EI}\left(\boldsymbol{v}''\right)^2 \mathrm{d}z = -\frac{1}{2}\sum_{i=1}^{n} M_i\Delta\varphi_i = -\frac{1}{2}\mathbf{c}^{\mathrm{T}}\,\mathbf{B}^{\mathrm{T}}\,\boldsymbol{k}\,\mathbf{B}\,\mathbf{c} = \frac{1}{2}\mathbf{c}^{\mathrm{T}}\boldsymbol{K}\,\mathbf{c}, \tag{17}$$

with $\boldsymbol{K} = \mathbf{B}^{\mathrm{T}}\boldsymbol{k}\,\mathbf{B}$.

Since the structure is reduced to an n DOFs system, the equation of motion will be given by the Lagrange equations (6) with $\dot{q}_i = \dot{\varphi}_i$ and $q_i = \varphi_i$ which can be written as follows, by replacing Eqs (13,16)

$$\mathbf{M}\ddot{\mathbf{c}} + \boldsymbol{K}\mathbf{c} = \mathbf{0}, \tag{18}$$

whose solutions can be found by

$$\det\left(\boldsymbol{K} - \omega^2\mathbf{M}\right) = 0, \tag{19}$$

2.3. Second approach: displacements as Lagrangian coordinates

As a second way for discretizing the structure, one can consider as Lagrangian coordinates the $n+1$ displacements v_i (Fig. 2), collected into a vector $\mathbf{v}$.

By means of the vector $\mathbf{v}$, one can easily get the vector of the n rotations of the rigid bars, defined as follows

$$\phi_i = n\frac{v_{i+1} - v_i}{\mathrm{L}}, \qquad i = 1, 2, ..., n, \tag{20}$$

that is in matrix form

$$\boldsymbol{\Phi} = \mathbf{V}\mathbf{v}, \tag{21}$$

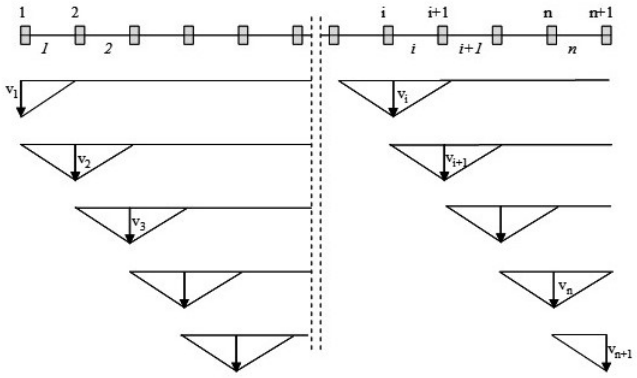

Figure 2. Second method for chosing the Lagrangian parameters: displacements

where $\mathbf{V}$ is the $(n, n+1)$ transfer matrix. The relative rotations between the two sides of any elastic cell are given by

$$\psi_1 = \phi_1, \qquad \psi_i = \phi_i - \phi_{i-1}, \qquad \psi_{n+1} = -\phi_n \tag{22}$$

or in matrix form

$$\boldsymbol{\psi} = \boldsymbol{\Delta\phi}, \tag{23}$$

where $\boldsymbol{\Delta}$ is the $(n+1 \times n)$ transfer matrix.

The deformation energy is centred into the cells and it will be given by

$$\mathrm{L}_e = \frac{1}{2}\sum_{i=1}^{n+1} k_{ii}\psi_i^2 = \frac{1}{2}\boldsymbol{\psi}^{\mathrm{T}}\boldsymbol{k}\,\boldsymbol{\psi} \tag{24}$$

In order to get a quadratic form, Eqs. 20-21 have to be used

$$\mathrm{L}_e = \frac{1}{2}\boldsymbol{\psi}^{\mathrm{T}}\boldsymbol{k}\,\boldsymbol{\psi} = \frac{1}{2}\boldsymbol{\phi}^{\mathrm{T}}\boldsymbol{\Delta}^{\mathrm{T}}\boldsymbol{k}\,\boldsymbol{\Delta}\,\boldsymbol{\phi} = \frac{1}{2}\mathbf{v}^{\mathrm{T}}(\mathbf{V}^{\mathrm{T}}\boldsymbol{\Delta}^{\mathrm{T}}\boldsymbol{k}\,\boldsymbol{\Delta}\mathbf{V})\mathbf{v} \tag{25}$$

By letting $\boldsymbol{K} = \mathbf{V}^{\mathrm{T}}\boldsymbol{\Delta}^{\mathrm{T}}\boldsymbol{k}\,\boldsymbol{\Delta}\mathbf{V}$, then

$$\mathrm{L}_e = \frac{1}{2}\mathbf{v}^{\mathrm{T}}\boldsymbol{K}\mathbf{v}. \tag{26}$$

The kinetic energy, similarly to the first approach, is written as

$$\mathrm{T} = \frac{1}{2}\sum_{i=1}^{n+1} m_i\dot{v}_i^2 \tag{27}$$

or in matrix form

$$\mathrm{T} = \frac{1}{2}\dot{\mathbf{v}}^{\mathrm{T}}\mathbf{M}\dot{\mathbf{v}}. \tag{28}$$

As mentioned in the previous section, Lagrange equations can be written as Eq. (6) setting $\dot{q}_i = \dot{\mathrm{v}}_i$ and $q_i = \mathrm{v}_i$.

3. Conclusions

In this note we analyzed the CDM, a method discretizing a structure in rigid bars and elastic cells. Thanks to the versatility of the procedure it is easy to understand that the method can be used for many structural types (beams, Timoshenko beams, higher order beams, single- and multiple-walled carbon nanotubes, plates, shells, arches, masonry arches, bridges, slightly curved beams etc.) and in the range of different theories (statical analysis, linear and nonlinear dynamics, stability analysis, in presence of conservative and non-conservative forces, nonlocal effects, in seismic analysis, etc.). It will be the task of researchers applying the method to new fields of investigation.

References

[1] FRANCIOSI, V. Scienza delle Costruzioni, 3 vol, Liguori editore, Napoli, 1984. (in Italian)

[2] FRANCIOSI, V. Problemi di Scienza delle Costruzioni, 3 vol, Liguori editore, Napoli, 1984. (in Italian)

[3] RAITHEL, A., FRANCIOSI, C. The stability of arches in the Langrangian approach, *J*ournal of Structural Engineering, 110(4) (1984) 847–856.

[4] RAITHEL, A., FRANCIOSI, C. Dynamic Analysis of arches using Langrangian approach. *I*nternational Journal of Solids Structures, 21 (1985) 427–438.

[5] FRANCIOSI, C. Free vibration of arches in presence of axial forces. *J*ournal of Sound snd Vibration, 120 (1988) 609–616.

[6] FRANCIOSI, V., AUCIELLO, N.M. Analisi modale degli archi su imposte comunque cedevoli. *I*ndustria Italiana del Cemento, 627 (1988) 706–711. (in Italian)

[7] AUCIELLO, N.M. Soil-structure interation problems in the presence of conservative soil. *P*roceedings of the Forth Rail Bridge Centenary Conference. Edinburgh, August (1990), 1157–1170.

[8] DE ROSA, M.A. The influence of the support flexibility on the vibration frequencies of arches. *J*ournal of Sound and Vibration, 146(1) (1991) 162–169.

[9] AUCIELLO, N.M., DE ROSA, M.A. Free vibrations of circular arches : a review. *J*ournal of Sound and Vibration 176 (1994) 433 – 458.

[10] AUCIELLO, N.M., DE ROSA, M.A. Free vibrations of circular arches: a review. *J*ournal of Sound and Vibration 187 (1995) 167 – 168.

[11] AUCIELLO, N.M. Effects of support flexibilities on arch-beam systems. *S*tructural Engineering Review, 3 (1991) 241–246.

[12] AUCIELLO, N.M. Stability of arch bridges on elastic soil., *P*roceedings of Tenth World Conference on Earthquake Engineering. Madrid, July (1992) 4785–4789.

[13] ERCOLANO, A., AUCIELLO, N.M. Seismic verification of foundation blocks in bridge structures. *P*roceedings of Tenth World Conference on Earthquake Engineering. Madrid, July (1992) 2205–2208.

[14] AUCIELLO, N.M. Stability and dynamics of arch bridges on elastic soil. *P*roceedings 10th European Conference on Earthquake Engineering, Vienna (1994) 2023–2027.

[15] MAURIZI, M.J., DE ROSA, M.A., BELLES, P.M., Frequencias naturales de vibracion del arco carpanel biarticulado, *X* Jornadas argentinas del hormigon presentado, Buenos Aires, October 1996, vol. II 186–199. (in Spanish)

[16] FRANCIOSI, C., FRANCIOSI, V., Il metodo delle celle nella verifica di un arco lapideo, *A*tti Accademia Pontaniana, 37 (1989) 5–32. (in Italian)

[17] DE ROSA, M.A., FRANCIOSI, C. Gli archi murari: analisi limite, elementi finiti, approcci elastici. *G*iornale del Genio Civile, 7–9 (1990) 179–206. (in Italian)

[18] FRANCIOSI, V., FRANCIOSI, C. The cells method in masonry arch analysis, *8*th International Brick/Block masonry conference, Dublin 19-21September (1988), Vol. III 1290–1301.

[19] FRANCIOSI, C., FRANCIOSI, V. Il metodo delle celle nella verifica di un arco lapideo. *A*tti Accademia Pontaniana, 37 (1989) 5–32. (in Italian)

[20] DE ROSA, M.A., Dynamic and seismic analysis of bridge gerders with elastic piers, *P*roceedings of the Third International Conferences on Civil and Structural Engineering Computing (Civil Comp 87), London September (1987) vol. 2,19–26.

[21] DE ROSA, M.A., Stability and dynamic of bridge girders under multiple axial loads. *C*omputers & Structures, 31(4) (1989) 473–486.

[22] DE ROSA, M.A., Stability and dynamic of beams on Winkler elastic foundations. *E*arthquake Engineering and Structural Dynamics, 18 (1989) 377–388.

[23] DE ROSA, M.A., A new Approach to the foundation beams analysis via the Cell Method. *M*echanics Research Communications, 16(5) (1989) 265–271.

[24] DE ROSA, M.A., FRANCIOSI, C. The influence of an intermediate support on the stability behaviour of cantilever beams subjected to follower forces. *J*ournal of Sound and Vibration, 137(1) (1990) 107–115.

[25] DE ROSA, M.A. Eigenvalues behaviour of continuous beams on elastic supports in the presence of damping and follower forces. *I*nternational Journal of Mechanics Science, 33(5) (1991) 325–337.

[26] DE ROSA, M.A., FRANCIOSI, C. Free vibrations of foundation beams on Green soil in the presence of conservative and nonconservative axial loads. *S*oil Dynamics and Earthquake Engineering, 10 (1991) 84–91.

[27] AUCIELLO, N.M., ERCOLANO, A. Nonlinear analysis of a beam subjected to axial and transverse loads. *C*omputers & Structures, 44 (1992) 863-868. England.

[28] AUCIELLO, N.M. On the transverse vibrations of non-uniform beams with axial loads and elastically restrained ends. *I*nternational Journal of Mechanical Sciences, 43 (2001) 193–208.

[29] DE ROSA, M.A., LIPPIELLO, M. Vibration frequencies of tapered beams. *E*ngineering Transactions, 57 (1) (2009) 45–66.

[30] DE ROSA, M.A. Stability analysis of Timoshenko beams on variable Winkler soil. *M*echanics Research Communications, 17(4) (1990) 255–261.

[31] DE ROSA, M.A., MAURIZI, M.J. Elishakoffs rod in the presence of shear deformation, *A*IMETA'92, Trento 28 Settembre-2 Ottobre 1992, vol. 1, 301–306.

[32] AUCIELLO, N.M. Free vibrations of Timoshenko beams on rigid blocks. *E*ngineering Transactions 41(2) (1993) 177–186.

[33] AUCIELLO, N.M. Free vibrations of Timoshenko beams with variable cross sections: a Lagrangian approach. *P*roceedings of Developments in Computational Engineering Mechanics. CIVIL-COMP 93 (1993) 237–241.

[34] AUCIELLO, N.M., DE ROSA M.A. Fundamental frequency of vibration of a Timoshenko beam of non-uniform cross-section on Winkler soil. *E*ngineering Mechanics Symposium, 1-4 June Winnipeg, Manitoba, Canada (1994) 1–4.

[35] AUCIELLO, N.M. Natural frequencies of a cantilever Timoshenko beam with tip mass. *E*ngineering Transactions, 43 (1995) 19–26.

[36] AUCIELLO, N.M. Free vibration of a estrained shear-deformable tapered beam with a tip mass at its free end. *J*ournal of Sound and Vibration, 237 (2000) 542–249.

[37] AUCIELLO, N.M., LIPPIELLO, M. Vibration analysis of rotating non-uniform Rayleigh beams using CDM method. *N*EWS IN ENGINEERING, 1(1) (2013) 30–37.

[38] AUCIELLO, N.M. A review of dynamic vibrations of shear-type immersed beam (CDM method). *P*roceeding 2nd Virtual Multidisciplinary Conference, December 2014, vol.1, 468–473.

[39] AUCIELLO, N.M. Nonconservative stability problems for cantilever column subjected to subtangential forces CDM discretization. *T*he 4th Global Virtual Conference, April 1 (4) (2016) ISBN: 978-80-554-1197-2.

[40] DE ROSA, M.A., LIPPIELLO, M. Free vibration analysis of DWCNTs using CDM and Rayleigh-Schimdt based on nonlocal Euler-Bernoulli beam theory, *T*he Scientific World Journal, Volume 2014 (2014), Article ID 194529, 13 pages.

[41] DE ROSA, M.A., LIPPIELLO, M. Free vibration analysis of SWCNT using CDM in the presence of nonlocal effect. *I*nternational Journal of Engineering and Innovative Technology, 4(4) (2014).

[42] DE ROSA, M.A., LIPPIELLO, M., AUCIELLO, N.M. Non-conservative instability of cantilevered nanotube via Cell Discretization Method (CDM). Submitted to (2017)

Nicola Maria Auciello, Professor: University of Basilicata, 85100 Potenza, ITALY (*nicola.auciello@unibas.it*)
Maria Anna De Rosa, Professor: University of Basilicata, 85100 Potenza, ITALY (*maria.derosa@unibas.it*)
Maria Lippiello, Ph.D.: University of Naples "Federico II", 80134 Naples,ITALY (*maria.lippiello@unina.it*)
Stefania Tomasiello, Ph.D.: CORISA - University of Salerno, 84084 Fisciano (SA), ITALY (*stomasiello@unisa.it*). The author gave a presentation of this paper during one of the conference sessions.

Theory of size-dependent physically nonlinear Euler-Bernoulli beams in an aggressive medium with taking into account the coupling of temperature and deformation fields

Jan Awrejcewicz, Tatyana Y. Yakovleva, Ekaterina Y. Krylova, Anastasiya O. Sinichkina, Vadim A. Krysko - jr.

Abstract: In this paper a size-dependent theory of physically nonlinear beams described by the kinematic theory of the first approximation is constructed. The basis of the developed theory is the moment theory of elasticity. The physical nonlinearity is taken into account following the Birger method of variable elasticity parameters, according to which the physical parameters of the beam material are not constant, but are functions of coordinates and a stress-strain state of the structure. The input partial differential equations of motion are obtained from the Hamilton variation principle. Equations take into account the relationship between deformation and temperature fields, material dependence on temperature and the aggressive medium properties in which the beam is located. The governing equations are nonlinear of the hyperbolic-parabolic type and exhibit different dimension. The equation of beam motion is one-dimensional, and the equation of thermal conductivity is two-dimensional. It means that no any restrictions for temperature distribution over beam thickness are employed. A calculation algorithm with nested iterations is developed in order to solve the problem in a reliable and validated way.

1. Introduction

The study of the effects associated with corrosion, wear and dynamic thermal force phenomena on the behavior of mechanical systems is an extremely complex but promising direction of the scientific research. The reorganization of the dynamic system modes may depend not only on the change in the parameters of the force (mechanical) loading, but also on the change in the thickness of the structure due to the action of the corrosive medium, as well as it is influenced by the temperature effects. Interest in such tasks is related to a need to develop mechanical structures capable of operating in corrosive environments under conditions of uneven non-stationary heating (for example, in aviation and rocketry industries, gyroscopes fabrication, nuclear reactor protection systems, micromechanical systems, etc.). Engineering practice constantly requires increasing the accuracy of mathematical models describing the vibrations of structural elements. Investigation of the effect of corrosion and wear on the vibrations of mechanical systems in the form of beams located in temperature fields is an actual and interesting problem.

Thin-walled and thick-walled spherical shells subjected to mechanical-chemical of corrosion under the action of external and internal pressure are considered in the series of papers Pronina and Sedova [1-4]. Analysis and comparison of the results obtained on the basis of analytical solutions is done in the works. A mathematical model of uniform corrosion of a thick-walled long flexible cylindrical tube subjected to the internal and external pressure at different temperatures has been constructed in reference [5]. The influence of corrosion is taken into account according to the Dolinsky model [7] with an exponential decay in time. The problems of calculating the tensile rod being inhomogeneous along its length, taking into account corrosion wear, and using geometric nonlinear theory, are considered in [6]. The necessity of taking into account the nonlinearity in the problems under consideration is justified in this paper. Fridman solved the problem of determining the dimensions of the cross-section of the truss elements of the ring section constructions (for a given period of their operation), subject to corrosion, using the Dolinsky model. The influence of two-sided and one-sided corrosion on the frequency of natural vibrations of freely supported plates has been studied in [8]. With the help of the finite element analysis, the influence of the corrosion degree on the value of the natural frequency and on the bending shape of a plate has been investigated. The papers [9, 10] are devoted to the study of the loss of stability of thin-walled cylindrical pipes (circular and non-circular cross section) of the Kirchhoff-Love model. The pipes are subjected simultaneously to the action of transverse compression forces and uniform unilateral corrosion on the outside or from the inside. The critical time of loss of stability of pipes has been found. Also, the authors considered the problems of stability loss of thin-walled spherical shells [11, 12] under the influence of external pressure and internal corrosion in temperature fields. It was shown that an increase in temperature leads to an increase in the corrosion rate. In the papers [13-17] it has been shown that to obtain more accurate results it is necessary to take into account the coupling of the temperature and deformation fields.

In recent decades, the interest in micro-dimensional mechanical structures has increased since in most cases they are the most important elements in MEMS [18, 19].

Many properties of the elastic bodies are associated with the characteristic dimensions, these properties are different [20-22]. Despite a large number of works on this subject, where linear models are used for numerical analysis, we note that it is necessary to take into account the influence of nonlinearity on the dynamics of micro and nano mechanical systems [23]. The resolving linear equations, initial and boundary conditions for the size-dependent Euler-Bernoulli model (the first-approximation model) have been obtained in [24, 25] using the modified moment theory of elasticity. The influence of the size parameter on the static deformation and the magnitude of the natural frequencies have been investigated.

For a static problem, a linear equation of the fourth order for longitudinal displacement is considered. The natural frequencies are investigated for small deflections using a linear equation of the

6th order for the function of deflection. To reduce the partial differential equations to the ordinary differential equations with respect to time, the Bubnov-Galerkin method has been empoyed in the first approximation. In reference [26], the equations for the geometrically nonlinear Euler-Bernoulli beam have been obtained on the basis of the Kármán relations has been used. To get a numerical solution, the Bubnov-Galerkin method in the first approximation. The effect of the size coefficient on the value of the natural frequency of nonlinear vibrations has been investigated.

The linear problems for the determination of natural frequencies and the static problems for investigating the influence of dimension-dependent parameters are considered in many papers. The effect of corrosion wear along with the temperature effect was considered for macro-dimensional mechanical systems. It is necessary to study in more detail the nonlinear deformations of size-dependent beams under the influence of static and dynamic loads, taking into account mechano-chemical corrosion and the related problem of thermodynamics. To study the dynamics of size-dependent beams, it is necessary to involve the apparatus of nonlinear dynamics on the basis of Fourier analysis and wavelet spectra, the phase portraits, the Poincaré sections, the change of the largest Lyapunov exponent (LLe) in time, the autocorrelation functions, amongst others [27-31]. The mentioned problems have been analysed with an account of three types of nonlinearity: physical, geometric and constructive (contact interaction in time). However, in these papers, the results have been obtained on the basis of the classical theory of elasticity, without considering the size-dependent behavior of structures [32-36].

At the moment, there are no mathematical models of vibrations of size-dependent beam structures including effects of corrosion wear, temperature and strain field connectivity, physical and geometric nonlinearity. In this paper we consider the interplay of all factors on the example of the Euler-Bernoulli beam.

2. Main hypotheses and assumptions

A mathematical model of non-linear vibrations of a beam of variable thickness under the influence of a normal distributed load is derived.

We make the following assumptions about the beam geometry, the material properties and the operating conditions for formulate the mathematical models: 1) the Euler-Bernoulli hypothesis [37]; 2) the inertia of rotation of beam elements is not taken into account; 3) external forces do not change their direction when the beam is deformed; 4) the longitudinal size of the beam considerably exceeds its lateral size; 5) to describe the size-dependent properties of the system, the modified momentum theory of elasticity is employed [38]; 6) the geometric nonlinearity is taken into account in the form of Kármán [39]; 7) the physical nonlinearity is taken into account on the basis of the Bierger's variable elasticity method [40,41]; 8) normal stresses in the direction of the normal to the middle surface can be neglected in comparison to the main stresses. Basic stresses mean normal and tangential stresses in the middle

surface itself and in layers parallel to it; 9) the influence of corrosion wear is taken into account according to the Dolinsky model; it is assumed that the corrosion rate depends linearly on the maximum stress and decays exponentially with time [42]; 10) there are no restrictions on the propagation of temperature over the thickness of the beams, that is, two-dimensional heat conduction equations are considered; 11) we consider isotropic homogeneous beams of variable thickness; 12) dissipative systems are considered.

3. Employment the moment theory of elasticity for a beam

In the modified couple stress based gradient theory [38], the potential deformation energy U in an elastic body occupying the domain $\Omega = \{0 \le x \le a; 0 \le y \le b;\ -h \le z \le h\}$, for infinitely small deformations is $U = \frac{1}{2}\int_{\Omega} (\sigma_{ij}\varepsilon_{ij} + m_{ij}\chi_{ij})dv$, where $i, j = \overline{x, y, z};\ \varepsilon_{ij} -$ the components of the deformation tensor and $\chi_{ij} -$ are the components of the symmetric tensor of the gradient of curvature $\varepsilon_{ij} = \frac{1}{2}\left(\frac{\partial u_i}{\partial x_j} + \frac{\partial u_j}{\partial x_i} + \sum_{m=1}^{3} \frac{\partial u_m}{\partial x_j}\frac{\partial u_m}{\partial x_j}\right),\ \chi_{ij} = \frac{1}{2}\left(\frac{\partial \theta_i}{\partial x_j} + \frac{\partial \theta_i}{\partial x_i}\right),\ \theta_i = \frac{1}{2}(rot(u))_i$. Here, u_i represent the components of the displacement vector u, θ is an infinitesimal rotation vector with the components. θ_i and δ_{ij} are the Kronecker symbols. For a linear isotropic elastic material, the stresses caused by the kinematic parameters included in the expression for the energy density of deformation are determined by the following state equations [38]: $\sigma_{ij} = \lambda\varepsilon_{mm}\delta_{ij} + 2\mu\varepsilon_{ij}, m_{ij} = 2\mu l^2\chi_{ij}$, where $\sigma_{ij},\ \varepsilon_{ij},\ m_{ij}$ and χ_{ij} denote the components of the classical stress tensor σ, the strain tensor ε, the deviator part of the symmetric moment tensor of higher order m and the symmetric part of the curvature tensor χ, respectively; $\lambda = \frac{Ev}{(1+v)(1-2v)}, \mu = \frac{E}{2(1+v)}$ are the Lamé parameters; $E(x, y, z), v(x, y, z)$ are the Young's modulus and Poisson's ratio, respectively; $\rho(x, y, z)$ is the density of the beam material; e_i is the intensity of deformation. The parameter l, appearing in the higher order moment m_{ij}, is an additional independent material length parameter associated with the symmetric rotational gradient tensor.

In this paper, the mathematical model of vibrations of a size-dependent geometrically and physically nonlinear beam exposed to unilateral corrosion wear will be constructed on the basis of the Euler-Bernoulli model (the hypothesis of the first approximation). The model reflects only the bending of the beam without turning and curving the cross section. The beam occupies the domain $\Omega = \{0 \le x \le a; 0 \le y \le 1;\ -h \le z \le h - \delta\}$, where $\delta = \delta(x, t)$ is the negative thickness increment function, due to corrosive wear. The displacement of an arbitrary point in a certain layer of a beam parallel to the median line away from it by a distance $z \ne 0$ will have the form: $u_x(x, t) = u(x, t) - z\frac{\partial w(x,t)}{\partial x}, u_y(x, t) = 0, u_z(x, t) = w(x, t)$, where $u(x, t)$ is the axial displacement of an arbitrary point of the middle line of the beam, and $w(x, t)$ is the transverse deviation.

We consider the inhomogeneous theory of elasticity. The physical constants are assumed to depend on the coordinates and the intensity of the deformations. We shall carry out the model studies, taking into account the physical nonlinearity with the dependence $E(x, y, z, e_i)$ on the coordinates, using the deformation theory of plasticity and employing the Bierger variable elasticity parameter [43], as is done for flexible physically nonlinear shells [44].

We consider an isotropic inhomogeneous rectilinear beam, under the action of the distributed transverse intensity force $q(x,t)$. The median line is located in the plane $z = 0$. Taking into account the Euler-Bernoulli hypothesis, we can write the expression for the deformation of the elongation in the x direction, taking into account the geometric nonlinearity according to the von Kármán model, the influence of the temperature field, the variable beam thickness and the corrosion wear:

$$\varepsilon_{xx} = \frac{\partial u}{\partial x} + \frac{1}{2}\left(\frac{\partial w}{\partial x}\right)^2 - \frac{1}{2}w\frac{\partial^2 h}{\partial x^2} - z\frac{\partial^2 w}{\partial x^2} - \alpha_t T(x,z,t). \quad (1)$$

The total deformation of an arbitrary point on a layer located from the median line by a distance *z*, where ε_{xx} is composed of the deformation of the median line $\frac{\partial u}{\partial x} + \frac{1}{2}\left(\frac{\partial w}{\partial x}\right)^2 - \frac{1}{2}w\frac{\partial^2 h}{\partial x^2}$, the deformation of the bend $-z\frac{\partial^2 w}{\partial x^2}$ and the temperature deformation $-\alpha_t T(x,z,t)$. Here $h = h(x)$ is the law of the beam thickness variation along its length, α_t is the coefficient of thermal expansion of the beam material, and $T(x,z,t)$ is the function of the temperature field.

We write the expressions for the nonzero components θ, the symmetric part of the curvature tensor χ, the normal stress σ_{xx} and the nonzero components of the higher order moments:

$$\theta_2 = -\frac{\partial w}{\partial x},\ \chi_{12} = \chi_{21} = -\frac{1}{2}\frac{\partial^2 w}{\partial x^2},$$

$$\sigma_{xx} = (\lambda + 2\mu)\left(\frac{\partial u}{\partial x} + \frac{1}{2}\left(\frac{\partial w}{\partial x}\right)^2 - \frac{1}{2}w\frac{\partial^2 h}{\partial x^2} - z\frac{\partial^2 w}{\partial x^2} - \alpha_t T(x,z,t)\right),\ m_{12} = m_{21} = \quad (2)$$

$$-\mu l^2\frac{\partial^2 w}{\partial x^2}.$$

4. Variational formulation of the problem: mathematical modelling of the flexible physically nonlinear and size-dependent Euler-Bernoulli beams

The potential energy *U*, obtained on the basis of the addition of higher-order forces, the kinetic energy *K*, the external work *W* associated with the distributed forces and energy dissipation will take the following form:

$$U = \frac{1}{2}\int_0^a \int_{-h}^{h-\delta} (\sigma_{11}\varepsilon_{11} + 2m_{12}\chi_{12})dzdx = \quad (3)$$

$$= \frac{1}{2}\int_0^a \int_{-h}^{h-\delta} \left((\lambda + 2\mu)\left(\frac{\partial u}{\partial x} + \frac{1}{2}\left(\frac{\partial w}{\partial x}\right)^2 - \frac{1}{2} w \frac{\partial^2 h}{\partial x^2} - z\frac{\partial^2 w}{\partial x^2} - \alpha_t T(x,z,t) + \right.\right.$$

$$\left.\left. \mu l^2 \left(\frac{\partial^2 w}{\partial x^2}\right)^2\right)^2 \right) dz dx,$$

$$K = \frac{1}{2}\rho \int_0^a \int_{-h}^{h-\delta} \left(\left(\frac{\partial u}{\partial t}\right)^2 + \left(\frac{\partial w}{\partial t}\right)^2 \right) dz dx \,,$$

$W = \int_0^a (q(x,t)w + \varepsilon \frac{\partial w}{\partial t} w) dx$, $\varepsilon -$ is the dissipation coefficient.

The equations of beams motion, as well as the boundary and initial conditions, are obtained from the Hamilton-Ostrogradskiy principle. According to this principle, a comparison is made of the close motions that lead the system of material points from the initial position at time t_0 to the final position at time t_1. For true motions, the condition: $\int_{t_0}^{t_1} (\delta K - \delta\Pi + \delta W) dt = 0$ should be satisfied. Varying over the variables u, w, integrating by parts, and equating the expressions for δu and δw to zero, we obtain the resolving equations of motion and add to the resulting system the equations for corrosive wear:

$$\left(\frac{\partial^2 u}{\partial x^2} + \frac{\partial u}{\partial x}\frac{\partial^2 u}{\partial x^2} + \frac{\partial w}{\partial x}\frac{\partial^2 w}{\partial x^2} - \frac{1}{2}\frac{\partial w}{\partial x}\frac{\partial^2 h}{\partial x^2} - \frac{1}{2} w \frac{\partial^3 h}{\partial x^3}\right) C_{00} + \left(\frac{\partial u}{\partial x} + \frac{1}{2}\left(\frac{\partial u}{\partial x}\right)^2 + \frac{1}{2}\left(\frac{\partial w}{\partial x}\right)^2 - \frac{1}{2} w \frac{\partial^2 h}{\partial x^2}\right) dC_{00} -$$

$$- \frac{\partial^3 w}{\partial x^3} C_{10} - \frac{\partial^2 w}{\partial x^2} dC_{10} + dN_t = \frac{\gamma(2h-\delta)}{2g p_1}\frac{\partial^2 u}{\partial t^2}; \quad (4)$$

$$\left(\frac{\partial^2 u}{\partial x^2} + \frac{\partial u}{\partial x}\frac{\partial^2 u}{\partial x^2} + \frac{\partial w}{\partial x}\frac{\partial^2 w}{\partial x^2} - \frac{1}{2}\frac{\partial w}{\partial x}\frac{\partial^2 h}{\partial x^2} - \frac{1}{2} w \frac{\partial^3 h}{\partial x^3}\right)\frac{\partial w}{\partial x} C_{00} + \left[\left(\frac{\partial u}{\partial x} + \frac{1}{2}\left(\frac{\partial u}{\partial x}\right)^2 + \frac{1}{2}\left(\frac{\partial w}{\partial x}\right)^2 - \frac{1}{2} w \frac{\partial^2 h}{\partial x^2}\right) C_{00} - \right.$$

$$\left. \frac{\partial^2 w}{\partial x^2} C_{10} - N_t \right]\frac{\partial^2 w}{\partial x^2} + \left[\left(\frac{\partial u}{\partial x} + \frac{1}{2}\left(\frac{\partial u}{\partial x}\right)^2 + \frac{1}{2}\left(\frac{\partial w}{\partial x}\right)^2 - \frac{1}{2} w \frac{\partial^2 h}{\partial x^2}\right) dC_{00} - \frac{\partial^3 w}{\partial x^3} C_{10} - \frac{\partial^2 w}{\partial x^2} dC_{10} + dN_t \right]\frac{\partial w}{\partial x} +$$

$$\left(\frac{\partial^3 u}{\partial x^3} + \left(\frac{\partial^2 u}{\partial x^2}\right)^2 + \frac{\partial u}{\partial x}\frac{\partial^3 u}{\partial x^3} + \left(\frac{\partial^2 w}{\partial x^2}\right)^2 + \frac{\partial w}{\partial x}\frac{\partial^3 w}{\partial x^3} - \frac{1}{2}\frac{\partial^2 w}{\partial x^2}\frac{\partial^2 h}{\partial x^2} - \frac{\partial w}{\partial x}\frac{\partial^3 h}{\partial x^3} - \frac{1}{2} w \frac{\partial^4 h}{\partial x^4}\right) C_{10} + 2\left(\frac{\partial^2 u}{\partial x^2} + \frac{\partial u}{\partial x}\frac{\partial^2 u}{\partial x^2} + \right.$$

$$\left. \frac{\partial w}{\partial x}\frac{\partial^2 w}{\partial x^2} - \frac{1}{2}\frac{\partial w}{\partial x}\frac{\partial^2 h}{\partial x^2} - \frac{1}{2} w \frac{\partial^3 h}{\partial x^3}\right) dC_{10} + \left(\frac{\partial u}{\partial x} + \frac{1}{2}\left(\frac{\partial u}{\partial x}\right)^2 + \frac{1}{2}\left(\frac{\partial w}{\partial x}\right)^2 - \frac{1}{2} w \frac{\partial^2 h}{\partial x^2}\right) d^2 C_{10} - \frac{\partial^4 w}{\partial x^4}\left(C_{20} + \right.$$

$$\left. \frac{p_2}{2p_1} l^2 C_{00}\right) - 2\frac{\partial^3 w}{\partial x^3} dC_{20} - \frac{\partial^2 w}{\partial x^2} d^2 C_{20} + d^2 M_t = \frac{1}{p_1}\left(\frac{\gamma(2h-\delta)}{2g}\frac{\partial^2 w}{\partial t^2} + \varepsilon\frac{\gamma(2h-\delta)}{2g}\frac{\partial w}{\partial t} - q\right); \quad (5)$$

$$\frac{\partial \delta}{\partial t} = \left(\delta_0 + K\left[(\lambda + 2\mu)\left(\frac{\partial u}{\partial x} + \frac{1}{2}\left(\frac{\partial w}{\partial x}\right)^2 - \frac{1}{2} w \frac{\partial^2 h}{\partial x^2} - z\frac{\partial^2 w}{\partial x^2} - \alpha_t T(x,z,t)\right)\right]\right) \exp(-bt); \quad (6)$$

where: $C_{00} = \int_{-h(x)}^{h(x)-\delta(x)} E(x,z,e_x) dz$, $C_{10} = \int_{-h(x)}^{h(x)-\delta(x)} E(x,z,e_x) z dz$,

$C_{20} = \int_{-h(x)}^{h(x)-\delta(x)} E(x,z,e_x) z^2 dz$, $N_t = \alpha_t \int_{-h(x)}^{h(x)-\delta(x)} E(x,z,e_x) T(x,z,t) dz$,

$M_t = \alpha_t \int_{-h(x)}^{h(x)-\delta(x)} E(x,z,e_x) T(x,z,t) z dz$, $p_1 = \frac{1-\nu}{(1+\nu)(1-2\nu)}$, $p_2 = \frac{1}{2(1+\nu)}$, where γ is the specific gravity of the beam material; g is the acceleration of free fall. The effect of corrosion wear is taken into account according to the Dolinsky model, and it is assumed that the corrosion rate linearly depends on

the maximum stress and decays exponentially with time [42]. The constants K and b are determined experimentally [45], and δ_0 is the initial corrosion rate.

No restrictions are imposed on the propagation of temperature over the thickness of the beam, and therefore a two-dimensional heat equation for a nonstationary field is considered, taking into account the coupling of deformation fields and temperatures:

$$\frac{C_0}{T_0}\frac{\partial T}{\partial t} - \frac{\lambda}{T_0}\left(\frac{\partial^2 T}{\partial x^2} + \frac{\partial^2 T}{\partial z^2}\right) = \frac{E\alpha_t}{1-\nu}\frac{\partial}{\partial t}\left(\frac{\partial u}{\partial x} + \frac{1}{2}\left(\frac{\partial w}{\partial x}\right)^2 - \frac{1}{2}w\frac{\partial^2 h}{\partial x^2} - z\frac{\partial^2 w}{\partial x^2} - \alpha_t T(x,z,t)\right), \tag{7}$$

where: C_0 is the specific heat of the beam material; T_0 is the beam temperature in the initial undeformed state.

We add initial conditions to the systems of differential equations (4)-(6):

$$\begin{aligned} &w(x,t) = \varphi_{30}(x);\ u(x,t) = \varphi_{10}(x);\ T(x,z,t) = \varphi_4(x,z);\ \delta(x,t) = \varphi_5(x);\ t = 0; \\ &\frac{\partial w(x,t)}{\partial t} = \psi_{30}(x);\ \frac{\partial u(x,t)}{\partial t} = \psi_{10}(x);\ t = 0. \end{aligned} \tag{8}$$

As well as one of the boundary conditions to the system of equations of motion (4)-(5) is taken, and to the heat conduction equation (7) one of the conditions I, II or III type are employed:

$$\begin{aligned} &w(x,t) = u(x,t) = \frac{\partial w(x,t)}{\partial x} = 0, x = 0, x = l; \\ &w(x,t) = u(x,t) = \frac{\partial^2 w(x,t)}{\partial x^2} = 0, x = 0, x = l; \\ &w(x,t) = u(x,t) = 0, x = 0, x = l, \frac{\partial w(0,t)}{\partial x} = \frac{\partial^2 w(l,t)}{\partial x^2} = 0; \\ &w(x,t) = u(x,t) = \frac{\partial w(x,t)}{\partial x} = 0, x = 0, x = l, M_x(x,t) = N_x(x,t) = 0. \end{aligned} \tag{9}$$

Here $\varphi_{10}(x), \varphi_{30}(x), \psi_{10}(x), \psi_{30}(x), \varphi_4(x,z), \varphi_5(x)$ are known functions that determine the initial state of the beam. The equation of motion of the beam element contains a fourth-order derivative, which is extremely important in proving the existence of a solution of the studied governing equations and the convergence of various methods for their solution.

The system of governing PDEs supplemented by boundary and initial conditions is reduced to the counterpart dimensionless form using the following variables:

$$\begin{aligned} &x = a\bar{x},\ \delta = h_0\bar{\delta},\ \delta_0 = \frac{\alpha}{h_0}\overline{\delta_0},\ b = b_0\bar{b},\ h = h_0\bar{h},\ l = h_0\bar{l},\ w = h_0\bar{w}, \\ &u = \frac{h_0^2}{a}\bar{u},\ q = \frac{h_0^4 E_0}{a^4}\bar{q},\ t = \frac{h_0^2}{\alpha}\bar{t},\ E = E_0\bar{E},\ \varepsilon = \frac{\alpha}{h_0^2}\bar{\varepsilon},\ \lambda = \frac{\alpha}{h_0},\ T = \frac{h_0^2}{a^2\alpha_{t0}}\bar{T},\ \alpha_t = \alpha_{t0}\overline{\alpha_t}, \\ &C_{00} = E_0 h_0\overline{C_{00}},\ C_{10} = E_0 h_0^2\overline{C_{10}},\ C_{20} = E_0 h_0^3\overline{C_{20}}. \end{aligned} \tag{10}$$

The system of equations of motion (4-5), corrosion wear (6), and the heat equation (7), with allowance for the dimensionless parameters, will have the following form (bars over the non-dimensional quantities are omitted):

$$\left(\frac{\partial^2 u}{\partial x^2} + \frac{\partial u}{\partial x}\frac{\partial^2 u}{\partial x^2} + \frac{\partial w}{\partial x}\frac{\partial^2 w}{\partial x^2} - \frac{1}{2}\frac{\partial w}{\partial x}\frac{\partial^2 h}{\partial x^2} - \frac{1}{2}w\frac{\partial^3 h}{\partial x^3}\right)C_{00} + \left(\frac{\partial u}{\partial x} + \frac{1}{2}\left(\frac{\partial u}{\partial x}\right)^2 + \frac{1}{2}\left(\frac{\partial w}{\partial x}\right)^2 - \frac{1}{2}w\frac{\partial^2 h}{\partial x^2}\right)dC_{00} -$$

$$-\frac{\partial^3 w}{\partial x^3}C_{10}-\frac{\partial^2 w}{\partial x^2}dC_{10}+dN_t=\frac{K}{\lambda^2}\frac{(2h-\delta)}{2p_1}\frac{\partial^2 u}{\partial t^2}; \quad (11)$$

$$\left(\frac{\partial^2 u}{\partial x^2}+\frac{\partial u}{\partial x}\frac{\partial^2 u}{\partial x^2}+\frac{\partial w}{\partial x}\frac{\partial^2 w}{\partial x^2}-\frac{1}{2}\frac{\partial w}{\partial x}\frac{\partial^2 h}{\partial x^2}-\frac{1}{2}w\frac{\partial^3 h}{\partial x^3}\right)\frac{\partial w}{\partial x}C_{00}+\left[\left(\frac{\partial u}{\partial x}+\frac{1}{2}\left(\frac{\partial u}{\partial x}\right)^2+\frac{1}{2}\left(\frac{\partial w}{\partial x}\right)^2-\frac{1}{2}w\frac{\partial^2 h}{\partial x^2}\right)C_{00}-\right.$$

$$\left.\frac{\partial^2 w}{\partial x^2}C_{10}-N_t\right]\frac{\partial^2 w}{\partial x^2}+\left[\left(\frac{\partial u}{\partial x}+\frac{1}{2}\left(\frac{\partial u}{\partial x}\right)^2+\frac{1}{2}\left(\frac{\partial w}{\partial x}\right)^2-\frac{1}{2}w\frac{\partial^2 h}{\partial x^2}\right)dC_{00}-\frac{\partial^3 w}{\partial x^3}C_{10}-\frac{\partial^2 w}{\partial x^2}dC_{10}+dN_t\right]\frac{\partial w}{\partial x}+$$

$$\left(\frac{\partial^3 u}{\partial x^3}+\left(\frac{\partial u}{\partial x}\right)^2+\frac{\partial u}{\partial x}\frac{\partial^3 u}{\partial x^3}+\left(\frac{\partial^2 w}{\partial x^2}\right)^2+\frac{\partial w}{\partial x}\frac{\partial^3 w}{\partial x^3}-\frac{1}{2}\frac{\partial^2 w}{\partial x^2}\frac{\partial^2 h}{\partial x^2}-\frac{\partial w}{\partial x}\frac{\partial^3 h}{\partial x^3}-\frac{1}{2}w\frac{\partial^4 h}{\partial x^4}\right)C_{10}+2\left(\frac{\partial^2 u}{\partial x^2}+\frac{\partial u}{\partial x}\frac{\partial^2 u}{\partial x^2}+\right.$$

$$\left.\frac{\partial w}{\partial x}\frac{\partial^2 w}{\partial x^2}-\frac{1}{2}\frac{\partial w}{\partial x}\frac{\partial^2 h}{\partial x^2}-\frac{1}{2}w\frac{\partial^3 h}{\partial x^3}\right)dC_{10}+\left(\frac{\partial u}{\partial x}+\frac{1}{2}\left(\frac{\partial u}{\partial x}\right)^2+\frac{1}{2}\left(\frac{\partial w}{\partial x}\right)^2-\frac{1}{2}w\frac{\partial^2 h}{\partial x^2}\right)d^2C_{10}-\left(C_{20}+\right.$$

$$\left.\frac{p_2}{2p_1}l^2\right)\frac{\partial^4 w}{\partial x^4}-2\frac{\partial^3 w}{\partial x^3}dC_{20}-\frac{\partial^2 w}{\partial x^2}d^2C_{20}+d^2M_t=\frac{1}{p_1}\left(\frac{K(2h-\delta)}{2}\frac{\partial^2 w}{\partial t^2}+\varepsilon\frac{K(2h-\delta)}{2}\frac{\partial w}{\partial t}-q\right); \quad (12)$$

$$\frac{\partial\delta}{\partial t}=\left(\delta_0+Pp_1\left(\frac{\partial u}{\partial x}+\frac{1}{2}\left(\frac{\partial w}{\partial x}\right)^2-\frac{1}{2}w\frac{\partial^2 h}{\partial x^2}-z\frac{\partial^2 w}{\partial x^2}-\alpha_t T(x,z,t)\right)\right)\exp(-Bt); \quad (13)$$

$$\frac{\partial T}{\partial t}-L\left(\frac{\partial^2 T}{\partial x^2}+\lambda^2\frac{\partial^2 T}{\partial z^2}\right)=D\alpha_t\frac{\partial}{\partial t}\left(\frac{\partial u}{\partial x}+\frac{1}{2}\left(\frac{\partial w}{\partial x}\right)^2-\frac{1}{2}w\frac{\partial^2 h}{\partial x^2}-z\frac{\partial^2 w}{\partial x^2}-\alpha_t T(x,z,t)\right). \quad (14)$$

Here $\frac{\lambda_g h_0^2}{a^2 C_0\alpha}=L$, $\frac{E_0\alpha_{t0}^2 T_0}{(1-v)C_0}=D$, $KE_0\frac{h_0^3}{a^2\alpha}=P$, $b_0\frac{h_0^2}{\alpha}=B$, $\frac{\gamma}{g}\frac{a^4\alpha^2}{h_0^2 E_0 h_0^4}=K$ are dimensionless physical and geometric parameters; λ_g is the coefficient of thermal conductivity of the beam material, and α is the thermal diffusivity of the beam material.

5. Methods of solution

The finite difference method is used for solving the resulting system of equations (5)-(8). When integrating the equations of motion with boundary and initial conditions, a uniform grid with the number of nodes n along the length and m along the thickness has been superimposed on the beam. Partial derivatives with respect to spatial coordinates, to improve the accuracy of the design scheme, have been replaced by central finite-difference approximations:

$$\Lambda_x(\square_i)=\frac{(\square)_{i+1}-(\square)_{i-1}}{2c},\ \Lambda_{x^2}(\quad_i)=\frac{(\square)_{i+1}-2(\square)_i-(\square)_{i-1}}{c^2},$$
$$\Lambda_{x^4}(\square_i)=\frac{(\square)_{i+2}-4(\square)_{i+1}-6(\square)_i-4(\square)_{i-1}+(\square)_{i-2}}{c^4},\ \Lambda_{x^2}\left(\square_{i,k}\right)=\frac{(\square)_{i+1,k}-2(\square)_{i,k}-(\square)_{i-1,k}}{c^2}, \quad (15)$$
$$\Lambda_{z^2}\left(\square_{i,k}\right)=\frac{(\square)_{i,k+1}-2(\square)_{i,k}-(\square)_{i,k-1}}{p^2},\ i=\overline{0,n},\ k=\overline{0,m},$$

where: $c-$ is step in the spatial coordinate x, $c=\frac{1}{(n-1)}$; step along the thickness of the beam is $p=\frac{1}{(m-1)}$.

The resulting system of the ordinary differential equations of the second order with the corresponding boundary and initial conditions reduces to a system of ordinary differential equations of the first order. The obtained system is solved by the Runge-Kutta method of the fourth order of accuracy. The choice of the method is due to the fact that the results obtained by the methods of the 4th

and 6th order of accuracy completely coincide, but the counting time for Runge-Kutta of the 4th order is half the size of the 6th order Runge-Kutta method [46].

At each step in time for the node x_i the value of the function $\delta(x_i)$, which corresponds to the change of the thickened beams due to corrosion, the values of the stiffnesses C_{00}, C_{10}, C_{20} and their derivatives, as well as the temperature moments and stresses, are calculated. After that, the obtained parameters are substituted into the equations of motion. The thickness of the beam $h(x_i)$ is recalculated taking into account the corrosive component from the previous layer. Based on the displacement and deflection of the beam obtained from the equations of motion, a total deformation is calculated for each points $\varepsilon_{11}(x_i, z_k)$. Substituting it into the expression for the corrosion function δ, we obtain its new value on the time layer under consideration. Substituting the values of the total deformation into the heat equation, we obtain the values of the temperature field function $T^j(x_i, z_k)$ at each point of the grid. Integrating over the thickness, we will have T_i in the middle line of the beam, which will allow us to obtain the values of the temperature moments and stresses.

6. Conclusions

In the presented work, the mathematical model of vibrations of the Euler-Bernoulli size-dependent beam with the taking into account the corrosive wear, temperature and strain field connectivity, physical and geometric nonlinearity has been worked out for the first time. The calculation algorithm is under development.

Acknowledgements

This work has been supported by the Grant RFBR 16-08-01108a, RFBR 16-01-00721a, as well as the Grant RFBR research project No 16-31-00092

References

[1] Pronina, Y.G., Sedova O.S., New benchmark for the life assessment of a thin-walled pipe subjected to stress assisted corrosion. ECCOMAS Congress 2016 - Proceedings of the 7th European Congress on Computational Methods in Applied Sciences and Engineering 4, pp. 6734-6740.

[2] Sedova, O.S., Pronina, Y.G., Calculation of the optimal initial thickness of a spherical vessel operating in mechanochemical corrosion conditions 2015 International Conference on "Stability and Control Processes" in Memory of V.I. Zubov, SCP 2015 – Proceedings 7342165, pp. 436-439.

[3] Pronina, Y.G., Mechanochemical corrosion: Modeling and analytical benchmarks for initial boundary value problems with unknown boundaries. 2016 Source of the Document Springer Proceedings in Mathematics and Statistics 171, pp. 301-309.

[4] Pronina, Y.G., Sedova, O.S., Kabrits, S.A., On the applicability of thin spherical shell model for the problems of mechanochemical corrosion. AIP Conference Proceedings 2015. C. 300008.

[5] Pronina, Y.G., Thermoelastic stress analysis for a tube under general mechanochemical corrosion conditions. Source of the Document Proceedings of the 4th International Conference on Computational Methods for Coupled Problems in Science and Engineering, COUPLED PROBLEMS 2011 pp. 1408-1415.

[6] Hasanov, M.A., Calculation of a stretched rod subjected to corrosion wear on the basis of a geometric nonlinear theory. Natural and Technical Sciences 4(49) (2010) 353-356.

[7] Fridman, M.M., Optimal design of tubular structures affected by corrosion, Problems of Mechanical Engineering 19(3) (2016) 37-42.

[8] Eslami-Majd, A., Rahbar-Ranji, A., Free vibration analysis of corroded steel plates, Journal of Mechanical Science and Technology 28(6) (2014) 2081–2088.

[9] Bergman, R.M., Levitsky, S.P., Haddad, J., Gutman, E.M., Stability loss of thin-walled cylindrical tubes, subjected to longitudinal compressive forces and external corrosion, Thin-Walled Structures 44 (7) (2006) 726-729

[10] Gutman, E.M., Haddad, J., Bergman, R., Stability of thin-walled high-pressure cylindrical pipes with non-circular cross-section and variable wall thickness subjected to non-homogeneous corrosion, Thin-Walled Structures 43 (1) (2005) 23-32.

[11] Gutman, E.M., Bergman, R.M., Levitsky, S.P., On stability loss of a thin-walled spherical shell subjected to external pressure and internal homogeneous corrosion, Proceedings of the 7th European Congress on Computational Methods in Applied Sciences and Engineering 1, 2016, pp. 254-260

[12] Gutman, E.M., Bergman, R.M., Levitsky, S.P., Influence of internal uniform corrosion on stability loss of a thin-walled spherical shell subjected to external pressure, Corrosion Science 111 (2016) 212-215.

[13] Krysko, V.A., Awrejcewicz, J., Kutepov, I.E., Zagniboroda, N.A., Papkova, I.V., Serebryakov, A.V., Krysko,A.V., Chaotic dynamics of flexible beams with piezoelectric and temperature phenomena, Physics Letters A 377 (2013) 2058-2061.

[14] Awrejcewicz, J., Krysko, V.A., Kutepov, I.E., Zagniboroda, N.A., Dobriyan, V., Papkova, I.V., Krysko, A.V., Chaotic vibrations of flexible curvilinear beams in temperature and electric fields, International Journal of Non-Linear Mechanics 76 (2015) 29-41.

[15] Krysko, A.V., Awrejcewicz, J., Kutepov, I.E., Krysko, V.A., On a contact problem of two-layer beams coupled by boundary conditins in a temperature field, Journal of Thermal Stresses 38 (2015) 468-484.

[16] Wang, J., Li, Y., Yang, E., Coupled thermoelastic vibration of the axially moving sandwich beam Applied Mechanics and Materials 312 (2013) 301-306.

[17] Jiang, S.Q., Liu, A.H., Wang, X.T., Wu, J.H., Li, B.K., Numerical study on bending behavior of copper alloy thin plate by single pulse laser, Advanced Materials Research 1003 (2014) 113-116.

[18] Saghir, S., Ilyas, S., Jaber, N., Younis, M.I., An experimental and theoretical investigation of the mechanical behavior of multilayer initially curved microplates under electrostatic actuation, Journal of Vibration and Acoustics 139(4) (2017) 040901-040911.

[19] Ilyas, S., Arevalo, A., Bayes, E., Foulds, I.G., Younis, M.I., Torsion based universal MEMS logic device, Sensors and Actuators A: Physical 236 (2015) 150-158.

[20] Fleck, N.A., Muller, G.M., Ashby, M.F., Hutchinson, J.W., Strain gradient plasticity: theory and experiments, Acta Metall. Mater. 42 (1994) 475–487.

[21] Lam, D.C.C., Yang, F., Chong, A.C.M., Wang, J., Tong, P., Experiments and theory in strain gradient elasticity, J. Mech. Phys. Solids 51 (2003) 1477–1508.

[22] Mazza, E., Abel, S., Dual, J., Experimental determination of mechanical properties of Ni and Ni-Fe microbars, Microsystem Technologies 2(4) (1996) 197-202.

[23] Scheible, D.V., Erbe, A., Blick, R.H., Evidence of a nanomechanical resonator being driven into chaotic response via the Ruelle–Takens route, Appl. Phys. Lett. 81 (2002) 1884–1886.

[24] Park, S.K., Gao, X.L., Bernoulli–Euler beam model based on a modified couple stress theory, Micromech Microeng 16(11) (2006) 2355–9.

[25] Kong Shengli, Zhou Shenjie, Nie Zhifeng, Wang Kai, The size-dependent natural frequency of Bernoulli–Euler micro-beams, Int. J. Eng. Sci. 46 (2008) 427–37.

[26] Rajabi, F., Ramezani, S., A nonlinear microbeam model based on strain gradient elasticity theory with surface energy, Arch. Appl. Mech. 82 (2012) 363–376.

[27] Krysko, V.A., Awrejcewicz, J., Chaos in Structural Mechanics, Springer, Berlin, 2008.

[28] Krysko, V.A., Awrejcewicz, J., Krysko, A.V., Thermodynamics of Plates and Shells, Springer, Berlin, 2007.

[29] Awrejcewicz, J.A., Krysko, V.A., Zhigalov, M.V., Saltykova, O.A., Krysko, A.V., Chaotic vibrations in flexible multilayered Bernoulli-Euler and Timoshenko type beams, Latin American Journal of Solids and Structures 5(4) (2008) 319-363.

[30] Krysko, A.V., Awrejcewicz, J., Saltykova, O.A., Zhigalov, M.V., Krysko, V.A., Investigations of chaotic dynamics of multi-layer beams using taking into account rotational inertial effects, Communications in Nonlinear Science and Numerical Simulation 19(8) (2014) 2568-2589.

[31] Awrejcewicz, J., Krysko, V.A., Papkova, I.V., Krysko, A.V., Deterministic Chaos in One Dimensional Continuous Systems, World Scientific, Singapore, 2016.

[32] Krylova, E.Y., Papkova, I.V., Erofeev, N.P., Zakharov, V.M., Krys'ko, V.A., Complex fluctuations of flexible plates under longitudinal loads with account for white noise, Journal of Applied Mechanics and Technical Physics 2 (2016) 0-84991661067.

[33] Awrejcewicz, J., Krysko, A.V., Papkova, I.V., Krylova, E.Y., Chaotic dynamics of flexible beams driven by external white noise Mechanical Systems and Signal Processing 2 (2016) 0-84962269243

[34] Krylova, E.Y., Yakovleva, T.V., Bazhenov, V.G., Chaotic dynamics of flexible rectangular panels in white noise field, PNRPU Mechanics Bulletin 2 (2016) 0-84978141669

[35] Yakovleva, T.V., Bazhenov, V.G., Krysko, V.A., Krylova, E.Y., Contact interaction plates, reinforced by ribs, with gaps under the influence of white noise, PNRPU Mechanics Bulletin 2 (2015) 0-84954200798

[36] Awrejcewicz, J., Krylova, E.Y., Papkova, I.V., Krysko, V.A., Regular and chaotic dynamics of flexible plates, Shock and Vibration 2014 (2014) ID 937967.

[37] Love, A.E.H., A Treatise on the Mathematical Theory of Elasticity, Dover Publications, New York, 1944.

[38] Yang, F., Chong, A.C.M., Lam, D.C.C., Tong, P., Couple stress based strain gradient theory for elasticity, Int. J. Solids Struct. 39 (2002) 2731–2743.

[39] Kármán, Th., Festigkeits probleme in Maschinenbau, Encykle. D . Math. Wiss. 47 (1910) 311-385.

[40] Birger, I.A., Some general methods for solving problems in the theory of plasticity, Applied Mathematics and Mechanics 15(6) (1951) 765-770.

[41] Birger, I.A., Some Mathematical Methods for Solving Engineering Problems, Oborongiz, Moscow, 1956.

[42] Dolinsky, V.M., Calculation of loaded pipes exposed to corrosion, Chemical and Petroleum Engineering 2 (1967) 9-10.

[43] Birger, I.A., Mavlyutov, R.R., The Resistance of Materials, Nauka, Moscow, 1986 (in Russian).

[44] Krysko, V.A., Nonlinear Statics and Dynamics of Non-Homogeneous Shells, Saratov University Press, Saratov, 1976 (in Russian).

[45] Pavlov, P.A., Kadyrbekov, B.A., Kolesnokov, V.A., Strength of steels in corrosive environments, Nauka, Alma-Ata, 1987 (in Russian).

[46] Krysko, A.V., Awrejcewicz, J., Kutepov, I.E., Zagniboroda, N.A., Dobriyan, V., Krysko, V.A., Chaotic dynamics of flexible Euler-Bernoulli beams, Chaos 34(4) (2014) 043130-1 - 043130-25.

_____

Jan Awrejcewicz, Professor: Lodz University of Technology, Faculty of Mechanical Engineering, Department of Automation, Biomechanics and Mechatronics, 1/15 Stefanowski Str., 90-924 Lodz, POLAND (awrejcew@p.lodz.pl), the author presented this contribution at the conference.

Tatyana Y. Yakovleva, Ph.D.: Department of Mathematics and Modeling, Saratov State Technical University, Politehnicheskaya 77, 410054 Saratov, RUSSIAN FEDERATION, and Cybernetic Institute, National Research Tomsk Polytechnic University, 634050 Tomsk, Lenin Avenue, 30, RUSSIAN FEDERATION (Yan-tan1987@mail.ru).

Ekaterina Y. Krylova, Associate Professor: Department of Mathematical and Computer Modeling, Saratov State University, Russian Federation, Astrakhanskaya, 83, 410012 Saratov, RUSSIAN FEDERATION (Kat.Krylova@bk.ru).

Anastasiya O. Sinichkina, M.Sc. (Ph.D. student): Department of Mathematics and Modeling, Saratov State Technical University, Politehnicheskaya 77, 410054 Saratov, RUSSIAN FEDERATION (andreevaanastasiaolegovna@gmail.com).

Vadim A. Krysko - jr., M.Sc. (Ph.D. student): Department of Mathematics and Modeling, Saratov State Technical University, Politehnicheskaya 77, 410054 Saratov, RUSSIAN FEDERATION (vadimakrysko@gmail.com).

Theory of coupled deformation and temperature fields for three-layer nano-mechanical structures

Jan Awrejcewicz, Tatyana V. Yakovleva, Vadim S. Kruzhilin,
Svetlana A. Mitskevich, Vadim A.Krysko

Abstract: In this work a mathematical model of a mechanical structure consisting of two nanoplates is developed, and between these nanoplates there is a nanobeam, and there are gaps between the elements. The resolving equations of this mathematical model are obtained using kinematic hypotheses of the first approximation (for the plates - Kirchhoff's conjecture, for beams - Bernoulli-Euler). The contact interaction is taken into account by the theory of Kantor. As a result, the obtained model takes into account the parabolic heat conduction equation. There are no restrictions on the temperature fields distribution in height for nanoplates and nanobeams (for nanoplates, the temperature field is three-dimensional, for a beam it is two-dimensional). The resulting system of partial differential equations is hyperbolic-parabolic and of different dimension. In addition, the equations are highly nonlinear and integro-differential, since the contact interaction between the elements of the structure is taken into account. To obtain reliable results, we reduce the resulting system to the Cauchy problem by two methods: the Faedo-Galerkin method in higher approximations and the finite difference method with the approximation $0(h^2)$ and $0(h^4)$ with respect to the spatial coordinates. Next, the Cauchy problem is solved by the Runge-Kutta methods of the 4th, 6th, 8th accuracy orders regarding time. Such a variety of methods of solution is necessary to obtain true results as a system with an infinite number of freedom degrees.

Keywords: mathematical model, temperature, strain field, contact interaction, plate-beam structures, Faedo-Galerkin method, Runge-Kutta type methods, nonlinear dynamics.

1. Introduction

At present, the production and application of miniature sensors of inertial and external information, micromotors and converters are in great demand. Modern micromechanical and microelectromechanical systems find their application for a wide range of mobile objects, i.e. in navigation equipment, automotive industry, military equipment, aircraft construction and rocket engineering [1-5]. Compound elements of micro- and nano electromechanical systems (MEMS, NEMS), such as vibration sensors [6], micro-drives [7], microswitches [8], are micro- and nanoscale beams and plates. Due to their nanosize and the presence of small gaps between the elements, an extremely important issue is the study of the contact interaction of nanoplates and nanobeams, taking into account the connectivity of the temperature and deformation fields. In references [9, 10], the

nonlinear dynamics of a three-layer microplate has been studied. On the basis of Kirchhoff plate theory and von Kármán nonlinear deformations, nonlinear size-dependent transverse and plane equations of motion have been derived. The model takes into account the nonconservative damping force of a viscous type, as well as the external exciting load. In references [11-13], according to the momentum theory of elasticity, mathematical models have been constructed and the layered beam nanostructures have been studied, but in these works the connection between the fields of temperature and deformation have not been taken into account.

2. Problem statement

In this paper we study the nonlinear dynamics of beam and plate nanostructures with allowance for their contact interaction and connection between the fields of temperature and deformation. The multilayer structure consists of two parallel nanoplates, and there is a nanobeam located centrally between them. There is a small gap h_k between all elements and they are connected only through the boundary conditions (Fig.1).

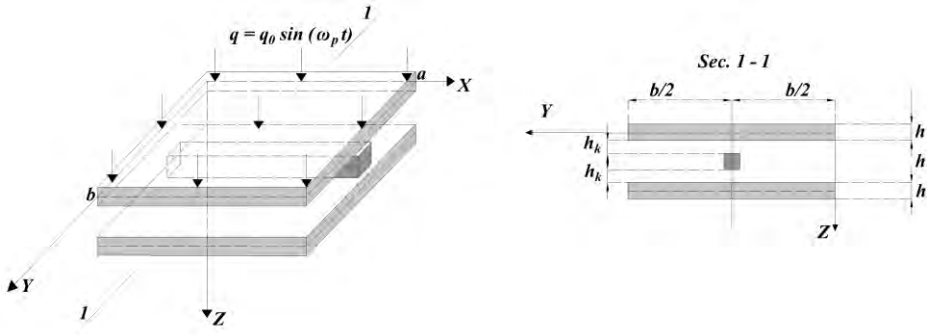

Figure 1. Scheme of the studied plate–beams structure.

For nanoplates the Kirchhoff kinematic model is employed, whereas for the nanobeam we use for the Euler-Bernoulli theory. The relationship between strain and deformations in the nanoplate ($\beta_1 = 1$) and nanobeam ($\beta_1 = 0$) can be represented in the following form [14]:

$$\varepsilon_1^z = \frac{1}{E}(\sigma_1 - \beta_1 \nu \sigma_2) + \alpha_T T_m \,, \overset{\leftrightarrow}{(1,2)} \,, \varepsilon_{12}^z = \beta_1 2 \frac{1+\nu}{E} \sigma_{12} \,, \overset{\leftrightarrow}{(1,2)} \qquad (1)$$

where: $E = E(x, \beta_1 y, z, \varepsilon_0, \varepsilon_i, \theta)$, $\nu = \nu(x, \beta_1 y, z, \varepsilon_0, \varepsilon_i, \theta)$. This representation is based on the variable elasticity method [15]. The following notation is employed: ε_0 - volume deformation, ε_i -

strain intensity, α_T - coefficient of linear thermal expansion, $\theta(x,\beta_1 y,z)$ – temperature increment for plate ($\beta_1=1$) and for beam ($\beta_1=0$). The resolving differential equations for nanoplates and nanobeam are yielded by the variation principle [16]:

$$\delta V+\delta D^*-\delta K^*=\iint\limits_A(\overline{F_0}\delta\overline{u_0}-\theta\bar{n}\delta\bar{S})dA, \tag{2}$$

where $\delta V,\delta D^*,\delta K^*$ stand for the variations of the generalized free energy, the dissipative function and the kinetic energy, respectively; $F_0,\overline{u_0}$ — the surface force and displacement; $\bar{n}$ — an outer normal; A – the bounding body surface.

After a few transformations according to the variational calculus, taking into account of (2) and according to the momentum theory of elasticity [17], the following differential equations for a three-layer nanostructure are obtained

$$\begin{cases}
\frac{\partial^2}{\partial x^2}[-\int\limits_{-h/2}^{h/2}(\gamma_1+\gamma_2)(\frac{\partial^2 w_1}{\partial x^2}+\nu\ \frac{\partial^2 w_1}{\partial y^2})dz-\alpha_1\int\limits_{-h/2}^{h/2}\theta\ z(1+\nu\ )dz]+\\
+\frac{\partial^2}{\partial y^2}[-\int\limits_{-h/2}^{h/2}(\gamma_1+\gamma_2)(\frac{\partial^2 w_1}{\partial y^2}+\nu\ \frac{\partial^2 w_1}{\partial x^2})dz-\alpha_1\int\limits_{-h/2}^{h/2}\theta z(1+\nu\ )dz]-\\
-2\frac{\partial^2}{\partial x\partial y}(\frac{\partial^2 w_1}{\partial x\partial y}\int\limits_{-h/2}^{h/2}(\gamma_1+\gamma_2)dz)+q_1-\frac{\gamma}{g}h\frac{\partial^2 w_1}{\partial t^2}-\varepsilon\frac{\gamma}{g}h\frac{\partial w_1}{\partial t}-q_{k1}=0,\\
\nabla^2(\theta\ )=\frac{T_0}{K_T}\frac{\partial}{\partial t}(\frac{c\theta}{T_0}+G^*\alpha_T e_1),\qquad(\beta_1=1),\\
-\frac{\partial^2}{\partial x^2}\left(\int\limits_{-h/2}^{h/2}(\gamma_3+\gamma_4)dz\frac{\partial^2 w_2}{\partial x^2}\right)-\frac{\partial^2 M_t}{\partial x^2}+q_2-\frac{\gamma}{g}h\frac{\partial^2 w_2}{\partial t^2}-\varepsilon\frac{\gamma}{g}h\frac{\partial w_2}{\partial t}+q_{k1}-q_{k2}=0,\\
\nabla^2(\theta\ )=\frac{T_0}{K_T}\frac{\partial}{\partial t}(\frac{c\theta}{T_0}+G^*\alpha_T e_2),\qquad(\beta_1=0),\\
\frac{\partial^2}{\partial x^2}[-\int\limits_{-h/2}^{h/2}(\gamma_1+\gamma_2)(\frac{\partial^2 w_3}{\partial x^2}+\nu\ \frac{\partial^2 w_3}{\partial y^2})dz-\alpha_3\int\limits_{-h/2}^{h/2}\theta\ z(1+\nu\ )dz]+\\
+\frac{\partial^2}{\partial y^2}[-\int\limits_{-h/2}^{h/2}(\gamma_1+\gamma_2)(\frac{\partial^2 w_3}{\partial y^2}+\nu\ \frac{\partial^2 w_3}{\partial x^2})dz-\alpha_3\int\limits_{-h/2}^{h/2}\theta z(1+\nu\ )dz]-\\
-2\frac{\partial^2}{\partial x\partial y}(\frac{\partial^2 w_3}{\partial x\partial y}\int\limits_{-h/2}^{h/2}(\gamma_1+\gamma_2)dz)+q_3-\frac{\gamma}{g}h\frac{\partial^2 w_3}{\partial t^2}-\varepsilon\frac{\gamma}{g}h\frac{\partial w_3}{\partial t}+q_{k2}=0,\\
\nabla^2(\theta\ )=\frac{T_0}{K_T}\frac{\partial}{\partial t}(\frac{c\theta}{T_0}+G^*\alpha_T e_3),\qquad(\beta_1=1),
\end{cases} \tag{3}$$

where: $M_t = \alpha_2 \int_{-h/2}^{h/2} E\theta_2 z dz$, $q_{k1} = K(w_1 - w_2 - h_k)\Psi_1$, $\Psi_1 = \frac{1}{2}[1 + sign(w_1 - h_k - w_2)]$, $q_{k2} = K(w_2 - w_3 - h_k)\Psi_2$, $\Psi_2 = \frac{1}{2}[1 + sign(w_2 - h_k - w_3)]$, $e_1 = \varepsilon_{11}^z + \beta_1 \varepsilon_{22}^z$, ($\nabla^2(\theta)$ — a three-dimensional ($\beta_1 = 1$) and $\nabla^2(\theta)$ — two-dimensional (β_1=0) Laplace operators). Furthermore, (γ_1, γ_3) and (γ_2, γ_4) are the coefficients of the general theory of elasticity and the coefficients of the moment theory of elasticity, respectively. The contact interaction is taken into account according to the Winkler model [18]. If there is a contact between the upper or lower nanoplate and nanobeam, then $\Psi_1 = 1$ and $\Psi_2 = 1$ if there is no contact, then $\Psi_1 = 0$ and $\Psi_2 = 0$, respectively. The expressions q_{k1} and q_{k2} represent Winkler connection between compression and contact pressure. The appearance of clutch zones is unlikely, since the contact pressure between layers is small. The conditions of contact between layers can depend on the coordinates and include all kinds of imperfect one-sided contact. In the system (3) w_1, w_3, w_2 denote the deflection functions of the upper, lower nanoplate and nanobeam, respectively; K is the stiffness factor of the transversal compression of the plate in the contact area; h_k – the gap between elements; g – the gravity acceleration; γ – the specific weight of material; c - the specific heat; G^* - bulk compression modulus. The nanoplates thickness h and beam height h are the same, the nanobeam width is 1; a denotes the nanobeam and nanoplate length, b stands for nanoplates width, whereas $q_i(x, \beta_1 y, t)$ is the transverse load acting on the nanoplates (β_1=1), and acting on the nanobeam (β_1=0).

As a result, the obtained model takes into account the parabolic heat conduction equations. There are no restrictions on the temperature fields distribution over the thickness for nanoplates and in height for nanobeams (for nanoplates, the temperature field is three-dimensional, for a nanobeam it is two-dimensional). The heat exchange between the elements is not taken into account. It is possible to consider different diagrams $\sigma_i(\varepsilon_i, \theta)$ describing the dependence of stress on deformation and temperature for several chosen materials. The boundary conditions of the first type and the initial conditions for the heat equations must be added to the system (3).

Boundary conditions of the first type. The temperature distribution is set on the body surface:

$$S: \quad (0 \le x \le a), (-h/2 \le z \le h/2),$$
$$\theta = \varphi(x, z, t) : (x, z) \in S. \tag{4}$$

As initial conditions, we take the distribution of deflections, deflection velocities, and temperature increment at the initial moment of time $t = 0$:

$$w(x,\beta_1 y,t)|_{t=0}=\varphi_1(x),,\ \dot{w}(z,t)|_{t=0}=\varphi_2(x)\,,\ \theta(x,\beta_1 y,z)|_{t=0}=\varphi_3(x,\beta_1 y,z). \tag{7}$$

Also, the boundary conditions for nanoplates (β_1=1) and nanobeam (β_1=0) are taken.

Hinged support on the contour for nanoplates and at the ends of the nanobeam:

$$w_{\bar{n}}=M_{\bar{n}}=0. \tag{8}$$

System (3) and boundary conditions create a system of integro-differential equations of different dimensions of hyperbolic-parabolic type, describing nonlinear oscillations and contact interaction of the related deformation and temperature fields for structure with physical nonlinearity, and also it exhibits the dependence of material properties on temperature. In addition, the equations are highly nonlinear and integro-differential, since the contact interaction between the elements of the structure is taken into account. To obtain reliable results, we reduce the resulting system to the Cauchy problem by two methods: the Faedo-Galerkin method in higher approximations and the finite difference method with the approximation $0(h^2)$ and $0(h^4)$ with respect to the spatial coordinate. In this case, an iterative procedure is constructed. The heat conductivity equations are solved by the finite differences method, the temperature moments are calculated, and the found values of the temperature field are substituted into the motion equations, and then we find deformations. For this aim, the Cauchy problem is solved by the methods of the Runge-Kutta type: the fourth-order Runge-Kutta-Felberg method (rkf45), and the eighth-order Runge-Kutta Prince-Dormand method (rk8pd) [19]. Such a variety of solution methods is necessary for obtaining true results for a system with an infinite number of freedom degrees, since the solution essentially depends on the method and the solution time step, i.e. of the initial conditions.

3. Concluding remarks

1. Mathematical model of a three-layer package of distributed mechanical structures, consisting of two parallel plates, and a beam has been derived. Between elements there are gaps. Each of the elements of the structure is described by kinematic models of the first approximation. Coupling of temperature and strain fields by Fourier theory has been taken into account. Equations from the Biot functional has been yielded. The mechanical structure is described by the modified couple stress theory.
2. The algorithm for nonlinear dynamics of a three-layer nanostructure, taking into account the contact interaction between the elements, is developed. The algorithm is based on the application of the Faedo-Galerkin method in higher approximations for reduction to the Cauchy problem, which is solved by the Runge-Kutta type methods. The developed software package allows to consider various options of heating the structure (preheated only the beam, or only one or another plate, or co-heating). The contact interaction between the elements yield a high nonlinearity effects of the studied system.

3. The proposed algorithm allows to solve constructively-nonlinear stationary problems.

4. Chaotic vibrations have been detected and studied.

Acknowledgement

This work has been supported by the Grant RFBR 16-08-01108a, RFBR 16-01-00721a, as well as the Grant President of the Russian Federation MK-5609.2016.8.

References:

[1] Haghighi H.S., Markazi A.H.D., Chaos prediction and control in MEMS resonators, Comm. Nonlin. Sci. Num. Simult. 15(10) (2010) 3091–3099.

[2] Khirallah K., Parametric excitation, amplification, and tuning of MEMS folded-beam comb drive oscillator, J. Microelectromech. Sys. 22(2) (2013) 318–330.

[3] Zhang W.M., Meng G., Wei K.X., Dynamics of nonlinear coupled electrostatic micromechanical resonators under two frequency parametric and external excitations, Shock Vib. 17(6) (2010) 759–770.

[4] Tocchio A., Comi C., Langfelder G., Corigliano A., Longoni A., Enhancing the linear range of MEMS resonators for sensing applications IEEE Sens. J. 11 (2011) 3202 –3210.

[5] Rhoads J., Shaw S.W., Turner K.L., Nonlinear Dynamics and Its A pplications in Micro and Nano Resonators. In Proceedings of DSCC 2008: The 2008 ASME Dynamic Systems and Control Conference, Ann Arbor, Michigan, USA, 20-22 October2008.

[6] Fu Y., Zhang J., Electromechanical dynamic buckling phenomenon in symmetric electric fields actuated microbeams considering material damping, Acta Mech. 212 (2010) 29–42.

[7] Moghimi Zand M., Ahmadian M.T., Static pull-in analysis of electrostatically actuated microbeams using homotopy perturbation method, Appl. Math. Model. 34 (2010) 1032–1041.

[8] Jia X.L., Yang J., Kitipornchai S., Pull-in instability of geometrically nonlinear micro-switches under electrostatic and Casimir forces. Acta Mech. 218 (2011) 161–174.

[9] Ghayesh M.H., Nonlinear dynamics of multi-layered microplates, J. Comput. Nonlin. Dyn. 20 (2017) doi:10.1115/1.4037596.

[10] Ghayesh M.H., Farokhi H., Nonlinear dynamics of microplates, Int. J. Eng. Sci. 86(0) (2015) 60-73.

[11] Awrejcewicz J., Pavlov S.P., Zhigalov M.V., Krysko-jr. V.A., Chaotic dynamics of the size-dependent non-linear micro-beam model, Comm. Nonlin. Sci. Num. Simulat. 50 (2017) 16–28.

[12] Krysko A.V., Awrejcewicz J., Zhigalov M.V., Pavlov S.P., Krysko V.A., Nonlinear behaviour of different flexible size-dependent beams models based on the modified couple stress theory. Part 1: Governing equations and static analysis of flexible beams, Int. J. Nonlin. Mech. 93 (2017) 96-105.

[13] Krysko A.V., Awrejcewicz J., Zhigalov M.V., Pavlov S.P., Krysko V.A., Nonlinear behaviour of different flexible size-dependent beams models based on the modified couple stress theory. Part 2. Chaotic dynamics of flexible beams, Int. J. Nonlin. Mech. 93 (2017) 106-121.

[14] Yakovleva T.V., Krysko-jr V.A., Contact interaction of a physically nonlinear three-layer plate-beam structure in a temperature field, Deform. Destruc. Mater. 6 (2017) 9–14.

[15] Birger I.A. Some general methods for solving problems in the theory of plasticity, J. Appl. Math. Mech. 15 (1951) 6-12.

[16] Biot M.A., Thermoelasticity and irreversible thermodynamics, J. Appl. Phys. 27(3) (1956) 240-253.

[17] Yang F., Chong A.C.M., Lam D.C.C., Tong P., Couple stress based strain gradient theory for elasticity, Int. J. Sol. Struct. 39 (2002) 2731–2743.

[18] Kantor B.Ya., Contact Problems of the Nonlinear Theory of Rotation Shells, Kiev, Science, 1990.

[19] Harder D.W., 4th -order Runge Kutta and the Dormand-Prince Methods. Ontario, University of Waterloo, 2012.

_____

Jan Awrejcewicz, Professor: Lodz University of Technology, Faculty of Mechanical Engineering, Department of Automation, Biomechanics and Mechatronics, 1/15 Stefanowskego Str., 90-924 Lodz, POLAND (jan.awrejcewicz@p.lodz.pl), the author presented this contribution at the conference.

Tatyana V. Yakovleva, Ph.D.: Department of Mathematics and Modeling, Saratov State Technical University, Politehnicheskaya 77, 410054 Saratov, and Cybernetic Institute, National Research Tomsk Polytechnic University, Lenin Avenue 30, 634050 Tomsk, RUSSIAN FEDERATION (Yan-tan1987@mail.ru).

Vadim S. Kruzhilin, B.A. (M.Sc. student): Department of Mathematics and Modeling, Saratov State Technical University, Politehnicheskaya 77, 410054 Saratov, RUSSIAN FEDERATION (mrkruzhilin@mail.ru).

Svetlana A. Mitskevich, Associate Professor: Department of Applied Mathematics and Systems Analysis, Saratov State Technical University, Politehnicheskaya 77, 410054 Saratov, RUSSIAN FEDERATION (svetlana.mitskevich@gmail.com).

Variable structure systems with sliding modes

Andrzej Bartoszewicz

Abstract: The main purpose of control engineering is to steer the regulated plant in such a way that it operates in a required manner. The desirable performance of the plant should be obtained despite the unpredictable influence of the environment on all parts of the control system, including the plant itself, and no matter if the system designer knows precisely all the parameters of the plant. Even though the parameters may change with time, load and external conditions, still the system should preserve its nominal properties and ensure the required behavior of the plant. In other words, the principal objective of control engineering is to design systems which are robust with respect to external disturbances and modelling uncertainty. This objective may be very well achieved using the sliding mode technique which is the main subject of this talk.
The theory of variable structure systems with sliding modes is currently one of the most significant research topics within the control engineering domain. Moreover, recently a number of important applications of the theory have also been reported. Therefore, this paper presents a tutorial introduction to the theory of sliding mode control. Some important results on the chattering attenuation, reaching phase elimination, finite time convergence and optimal sliding surface design are mentioned.

1. Introduction

First research papers on variable structure systems (VSS) and in particular on VSS with sliding modes were published in the former Soviet Union almost seven decades ago [8, 9, 10, 12, 18]. Initially, these systems were hardly applicable because electromechanical switches available at that time (relays) could not operate continuously at high frequencies. Therefore, only after the significant development of semiconductor technology took place at the end of the twentieth century, practical realization of sliding mode controllers became possible.

The principle of operation of VSS consists in the deliberate switching of different feedbacks (controllers) according to the evolution of the system representative point in the state space. Therefore, the dynamics of these systems are described by differential equations with a discontinuous right hand side. Thus, the traditional assertion of the existence and uniqueness of solutions to differential equations cannot be used directly for such systems. A. Filipov was among the first researchers to study this problem in his work [10]. The considerations presented therein go far beyond the scope of this tutorial presentation and therefore, only the idea of his work [10] will be given here.

2. Filipov's construction

Let us take into account a nonlinear and possibly time-varying, single input plant of the order *n* described as

$$\dot{\boldsymbol{x}} = \boldsymbol{f}(\boldsymbol{x}, t, u), \tag{1}$$

where $\boldsymbol{x}$ is the state vector, *t* denotes time and *u* is the control input defined by the following relation

$$u = \begin{cases} u^+ & \text{for } s(\boldsymbol{x}) > 0 \\ u^- & \text{for } s(\boldsymbol{x}) < 0 \end{cases}, \tag{2}$$

where $s(\boldsymbol{x})$ is a scalar function of the state $\boldsymbol{x}$, and $s(\boldsymbol{x}) = 0$ determines the sliding hypersurface. In the ideal case, on the hypersurface the system switches over infinitely fast between two vector fields $f(\boldsymbol{x}, t, u^+)$ and $f(\boldsymbol{x}, t, u^-)$. Let us denote appropriate limits of these fields by

$$\boldsymbol{f}^+ = \lim_{s \to 0^+} \boldsymbol{f}(\boldsymbol{x}, t, u^+), \tag{3}$$

and

$$\boldsymbol{f}^- = \lim_{s \to 0^-} \boldsymbol{f}(\boldsymbol{x}, t, u^-). \tag{4}$$

If the system remains in sliding mode, the following conditions are satisfied

$$\langle \boldsymbol{ds}, \boldsymbol{f}^+ \rangle \leq 0 \tag{5}$$

and

$$\langle \boldsymbol{ds}, \boldsymbol{f}^- \rangle \geq 0, \tag{6}$$

i.e. the scalar product of the vectors $\boldsymbol{ds}$ = grad $s(\boldsymbol{x})$ and $\boldsymbol{f}^+$ is non-positive, and the corresponding scalar product of the vectors $\boldsymbol{ds}$ and $\boldsymbol{f}^-$ is non-negative. It results from the above that on neither side of the sliding hypersurface the representative point of the object moves away from this hypersurface. Additionally, in the sliding mode the object behaves as if it was affected by the "averaged" field $\boldsymbol{f^0}$ constituting a convex combination of $\boldsymbol{f}^+$ and $\boldsymbol{f}^-$

$$\dot{\boldsymbol{x}} = \boldsymbol{f^0} = \alpha \boldsymbol{f}^+ + (1 - \alpha)\boldsymbol{f}^-, \tag{7}$$

where α is a non-negative real number smaller than or equal to one. For the representative point of the object to remain on the sliding hypersurface, the field must be tangent to it at every point, i.e. orthogonal to $\boldsymbol{ds}$, hence, the following condition must be satisfied

$$\langle \boldsymbol{ds}, \boldsymbol{f^0} \rangle = 0. \tag{8}$$

Assuming that the scalar product $\langle \boldsymbol{ds}, (\boldsymbol{f}^- - \boldsymbol{f}^+) \rangle$ is greater than zero and solving equation (8) for α, the following is obtained

$$\alpha = \frac{\langle \boldsymbol{ds}, \boldsymbol{f}^- \rangle}{\langle \boldsymbol{ds}, (\boldsymbol{f}^- - \boldsymbol{f}^+) \rangle}. \tag{9}$$

Then, substituting relation (9) into (7), one can formulate an equation which determines the object dynamics in the sliding mode

$$\dot{\boldsymbol{x}} = \alpha \boldsymbol{f}^+ + (1-\alpha)\boldsymbol{f}^- = \frac{\langle \boldsymbol{ds}, \boldsymbol{f}^- \rangle}{\langle \boldsymbol{ds}, (\boldsymbol{f}^- - \boldsymbol{f}^+) \rangle} \boldsymbol{f}^+ - \frac{\langle \boldsymbol{ds}, \boldsymbol{f}^+ \rangle}{\langle \boldsymbol{ds}, (\boldsymbol{f}^- - \boldsymbol{f}^+) \rangle} \boldsymbol{f}^-. \tag{10}$$

To sum up Filipov's reasoning presented here in a simplified form, one can state that the averaged solution to equation (1) with control (2), on the hypersurface $s(\boldsymbol{x}) = 0$ is uniquely determined by relation (10). Let us also note that the constant α determined by equation (9) can be interpreted as part of the time during which the representative point of the object remains on this side of the switching hypersurface on which the switching variable $s(\boldsymbol{x})$ assumes positive values.

Justification for introducing Filipov's construction was the fact that traditional methods in differential equation theories cannot directly be used for systems with ideal sliding motion. However, as noted in [19], ideal sliding motion does not occur in real variable structure systems due to hysteresis, inertia and the delay of switching elements. Therefore, these systems can be described by differential equations with a continuous right-hand side, and ideal sliding motion in such systems should be treated as a boundary case which occurs when the non-ideality of switching elements disappears. A detailed analysis of operation of control systems with sliding motion based on such an assumption – constituting an alternative approach to Filipov's method – is presented in [20].

3. Equivalent control

Filipov's reasoning discussed above allows, due to the averaging of the vector fields $\boldsymbol{f}^+$ and $\boldsymbol{f}^-$, determining the motion of the system on the switching hypersurface $s(\boldsymbol{x}) = 0$. Another method of determination of this motion is to introduce a concept of so called equivalent control, that is to say, such (fictitious, and in fact non-existing) continuous control under the effect of which the system would move in the same way as it moves due to the action of discontinuous variable structure control [19]. In other words, the equivalent control u_{eq} constitutes such a continuous control signal which ensures that the representative point remains on the sliding hypersurface. The fundamental difference between Filipov's method and the equivalent control method is that when the equivalent control method is used, the vector fields $\boldsymbol{f}^+$ and $\boldsymbol{f}^-$ are not averaged; instead, control itself $u^+(\boldsymbol{x}, t)$ and $u^-(\boldsymbol{x}, t)$ is averaged. In order to present this method, let us consider a single-input (generally nonlinear) dynamic object, which is linear with respect to control

$$\dot{\boldsymbol{x}} = \boldsymbol{f}(\boldsymbol{x}, t) + \boldsymbol{g}(\boldsymbol{x}, t)u, \tag{11}$$

where $\boldsymbol{f}$ and $\boldsymbol{g}$ are certain non-linear vector functions, $\boldsymbol{x}$ is the state vector, u is the control signal, and t denotes time. When the system is, and indeed remains in sliding mode, the following two relations are fulfilled

$$s(\boldsymbol{x}, t) = 0 \tag{12}$$

and

$$\dot{s}(\boldsymbol{x}, t) = 0. \tag{13}$$

From equation (13) it follows that

$$\dot{s} = \langle \boldsymbol{ds}, (\boldsymbol{f} + \boldsymbol{g}u) \rangle = \langle \boldsymbol{ds}, \boldsymbol{f} \rangle + \langle \boldsymbol{ds}, \boldsymbol{g}u \rangle = 0. \tag{14}$$

Assuming that the scalar product $\langle \boldsymbol{ds}, \boldsymbol{g} \rangle$ is not equal to zero, the expression determining the equivalent control is obtained

$$u_{eq} = -\frac{\langle \boldsymbol{ds}, \boldsymbol{f} \rangle}{\langle \boldsymbol{ds}, \boldsymbol{g} \rangle} \tag{15}$$

and substituting this expression into equation (11), one can, as in Filipov's method, establish the relation determining the object dynamics in sliding motion

$$\dot{\boldsymbol{x}} = \boldsymbol{f} - \boldsymbol{g}\frac{\langle \boldsymbol{ds}, \boldsymbol{f} \rangle}{\langle \boldsymbol{ds}, \boldsymbol{g} \rangle} \tag{16}$$

It is obvious that equations (10) and (16) are equivalent and constitute only a different form of description of the same motion which takes place on the switching hypersurface. An additional advantage of the equivalent control method is that it can be directly generalized for multiple-input systems.

As mentioned previously, one of the most important advantages of variable structure control systems with sliding modes is their insensitivity with respect to a considerably large class of model inaccuracy and external disturbances. To demonstrate this, let us consider a dynamic object whose model is not precisely known, subjected to the action of disturbances

$$\dot{\boldsymbol{x}} = \boldsymbol{f}(\boldsymbol{x}, t) + \boldsymbol{g}(\boldsymbol{x}, t)u + \boldsymbol{h}(\boldsymbol{x}, t), \tag{17}$$

The vector field $\boldsymbol{h}(\boldsymbol{x}, t)$ in equation (17) represents a combined effect of (independent of the vector $\boldsymbol{x}$) external disturbances and the modelling imperfections. If the system remains in sliding mode, relations (12) and (13) are satisfied. In turn, it results from relation (13) that

$$\dot{s} = \langle \boldsymbol{ds}, (\boldsymbol{f} + \boldsymbol{g}u + \boldsymbol{h}) \rangle = \langle \boldsymbol{ds}, \boldsymbol{f} \rangle + \langle \boldsymbol{ds}, \boldsymbol{g} \rangle u + \langle \boldsymbol{ds}, \boldsymbol{h} \rangle = 0\,. \tag{18}$$

Hence, assuming that the scalar product $\langle \boldsymbol{ds}, \boldsymbol{g} \rangle$ is different from zero, equivalent control can now be expressed in the following form

$$u_{eq} = -\frac{\langle \boldsymbol{ds}, \boldsymbol{f} \rangle + \langle \boldsymbol{ds}, \boldsymbol{h} \rangle}{\langle \boldsymbol{ds}, \boldsymbol{g} \rangle}. \tag{19}$$

Substituting relation (19) into equation (17), the following is obtained

$$\dot{\boldsymbol{x}} = \boldsymbol{f} - \boldsymbol{g}\frac{\langle \boldsymbol{ds}, \boldsymbol{f} \rangle + \langle \boldsymbol{ds}, \boldsymbol{h} \rangle}{\langle \boldsymbol{ds}, \boldsymbol{g} \rangle} + \boldsymbol{h}. \tag{20}$$

If the vector field $\boldsymbol{h}(\boldsymbol{x}, t)$ can be expressed in the form

$$\boldsymbol{h}(\boldsymbol{x}, t) = \boldsymbol{g}(\boldsymbol{x}, t)v(\boldsymbol{x}, t), \tag{21}$$

where $v(\boldsymbol{x}, t)$ is a certain scalar function, then equation (20) describing the dynamics of the object in sliding motion assumes the form

$$\dot{\boldsymbol{x}} = \boldsymbol{f} - \boldsymbol{g}\frac{\langle \boldsymbol{ds}, \boldsymbol{f} \rangle + \langle \boldsymbol{ds}, \boldsymbol{g} \rangle v}{\langle \boldsymbol{ds}, \boldsymbol{g} \rangle} + \boldsymbol{g}v = \boldsymbol{f} - \boldsymbol{g}\frac{\langle \boldsymbol{ds}, \boldsymbol{f} \rangle}{\langle \boldsymbol{ds}, \boldsymbol{g} \rangle}. \tag{22}$$

which does not depend on $\boldsymbol{h}(\boldsymbol{x}, t)$. Thus, the sliding motion considered is invariant with respect to disturbances and inaccuracy of the model satisfying equality (21), i.e. being in the range of input signals of the control object. The present considerations constitute theoretical justification for desirable properties of variable structure systems with sliding modes. These considerations are the generalization of the seminal results given first by Draženović in [7]. It should be added that constraints determined by relation (21) are often encountered in various robust control problems, and are usually called matching conditions. Let us stress at this point that sliding mode controllers ensure not only some degree of robustness, but complete insensitivity with respect to matched disturbances and inaccuracy of the model. This is an important property distinguishing them from other robust control methods, which do not offer insensitivity, but only some (sometimes quite satisfactory) degree of robustness. In other words – to the best of the author's knowledge – sliding mode control is the only technique which not only attenuates the effects of matched disturbance and modelling uncertainty on the plant, but totally rejects those undesirable effects.

The considerations presented hitherto have mainly dealt with single-input control objects. In multiple-input systems, however, it will be possible to select a larger number of switching hypersurfaces – equal to the number of independent control inputs of the object – and to design the control in such a way that sliding motion takes place at their intersection, i.e. at a certain manifold in the state space. In order to analyze the operation of such systems in more detail, let us consider an *n*-dimensional, linear with respect to control signals, object with *m* inputs

$$\dot{\boldsymbol{x}} = \boldsymbol{f}(\boldsymbol{x}, t) + \boldsymbol{B}(\boldsymbol{x}, t)\boldsymbol{u}, \tag{23}$$

where $\boldsymbol{x}$ is the state vector, $\boldsymbol{f}$ is a certain nonlinear vector function, $\boldsymbol{B}$ is the matrix of dimensions $n \times m$, $\boldsymbol{u}$ is the vector of m control signals, and t denotes time. Let us now select m sliding hypersurfaces $s_1(\boldsymbol{x}) = 0$, $s_2(\boldsymbol{x}) = 0$, $s_m(\boldsymbol{x}) = 0$, and let us form the vector

$$\boldsymbol{s}(\boldsymbol{x}) = [s_1(\boldsymbol{x}) \quad s_2(\boldsymbol{x}) \quad \ldots \quad s_m(\boldsymbol{x})]^{\mathrm{T}}, \tag{24}$$

which determines a multidimensional switching variable. By calculating a derivative of this vector with respect to time, comparing it to zero and assuming that the matrix $\frac{\partial \boldsymbol{s}}{\partial \boldsymbol{x}}\boldsymbol{B}(\boldsymbol{x}, t)$ is non-singular, it is possible to calculate the equivalent control

$$\boldsymbol{u}_{eq} = -\left[\frac{\partial \boldsymbol{s}}{\partial \boldsymbol{x}}\boldsymbol{B}(\boldsymbol{x}, t)\right]^{-1} \frac{\partial \boldsymbol{s}}{\partial \boldsymbol{x}}\boldsymbol{f}(\boldsymbol{x}, t), \tag{25}$$

and then, substituting equation (25) into relation (23), to determine the dynamics of the object in sliding mode

$$\dot{\boldsymbol{x}} = \left\{\boldsymbol{I}_n - \boldsymbol{B}(\boldsymbol{x}, t)\left[\frac{\partial \boldsymbol{s}}{\partial \boldsymbol{x}}\boldsymbol{B}(\boldsymbol{x}, t)\right]^{-1} \frac{\partial \boldsymbol{s}}{\partial \boldsymbol{x}}\right\}\boldsymbol{f}(\boldsymbol{x}, t), \tag{26}$$

where $\boldsymbol{I}_n$ is the identity matrix of the order n. Equation (26) defines such motion of the system in which the representative point of the object moves on a certain $(n - m)$-dimensional manifold, constituting the intersection of m sliding hypersurfaces $\boldsymbol{s}(\boldsymbol{x}) = [s_1(\boldsymbol{x}) \quad s_2(\boldsymbol{x}) \quad \ldots \quad s_m(\boldsymbol{x})]^{\mathrm{T}} = \boldsymbol{0}$ in the state space. Just as it has been done for a single-input system, one can also demonstrate that the sliding motion described by equality (26) is invariant with respect to disturbances and modeling uncertainty $\boldsymbol{h}(\boldsymbol{x}, t)$ satisfying the condition

$$\forall(\boldsymbol{x}, t), \exists \boldsymbol{v}(\boldsymbol{x}, t), \quad \boldsymbol{h}(\boldsymbol{x}, t) = \boldsymbol{B}(\boldsymbol{x}, t)\boldsymbol{v}(\boldsymbol{x}, t), \tag{27}$$

where $\boldsymbol{v}(\boldsymbol{x}, t)$ is a certain m-dimensional vector function. Let us add that in the case of multi-input objects – depending on how the controller has been designed – sliding motion can, but does not have to take place on each of the switching hypersurfaces separately. This is because a situation can occur when sliding motion will take place only at the intersection of these hypersurfaces and not on each of them independently. In paper [6] an extensive discussion and a number of methods for designing sliding mode control systems for multi-input dynamic objects are presented.

4. Conditions of the ideal sliding motion stability

In the foregoing considerations the most important properties of dynamic objects operating in sliding regime have been described. A separate important issue is determination of conditions for the existence of such regime, i.e. answering the question when – after representative point of the controlled object is (slightly) thrown off the sliding mode – it will return to the intersection of the switching hypersurfaces.

As can be seen, the issue considered here is, in its essence, the problem of sliding motion stability. Therefore, it can be fairly easily analyzed using Lyapunov methods [17]. On the basis of [18, 20], let us now quote a theorem concerning conditions for the existence (stability) of sliding motion.

Theorem: A sufficient condition for the ($n - m$)-dimensional domain D to be a domain of sliding motion is that in a certain n-dimensional area $\Omega \subset \Re^n$ where $D \subset \Omega$ there exists, a continuously differentiable with respect to all its arguments, scalar function V: $\Omega \times \Re_+ \times \Re^m \to \Re$ satisfying the following conditions:

i) $V(\boldsymbol{x}, t, \boldsymbol{s})$ is positive definite with respect to $\boldsymbol{s}$,

ii) The total derivative of the function $V(\boldsymbol{x}, t, \boldsymbol{s})$ has a negative upper limit on the spheres $\|\boldsymbol{s}\| = r$ except the points lying on the switching surface, where control may not be defined and the derivative of the function $V(\boldsymbol{x}, t, \boldsymbol{s})$ does not exist.

The proof of the theorem quoted herein can be found, among others, in [20]. The theorem can be directly applied to the design of control rules that will ensure stability, and hence will guarantee the actual occurrence of sliding motion in a variable structure system. However, this theorem is more frequently used in an indirect manner, formulating so called conditions for the existence of sliding motion and designing the control in such a way that one of these conditions is satisfied. One of the conditions for the existence of sliding motion quite often used in the literature is the following inequality [17]

$$\forall \boldsymbol{s} \neq \boldsymbol{0} \quad \boldsymbol{s}^{\mathrm{T}}\boldsymbol{s} \leq -\eta\|\boldsymbol{s}\| \tag{28}$$

where the constant η is greater than zero, and $\|\boldsymbol{s}\|$ denotes the Euclidean norm of the vector $\boldsymbol{s}$. It is easy to demonstrate that the validity of this inequality implies that the assumptions of the theorem quoted above are satisfied. To do so, let us take into account the positive definite function of the variable $\boldsymbol{s}$ in the form

$$V(\boldsymbol{s}) = \frac{1}{2}\boldsymbol{s}^{\mathrm{T}}\boldsymbol{s} \tag{29}$$

and calculate its derivative with respect to time

$$\dot{V}(\boldsymbol{s}) = \dot{\boldsymbol{s}}^{\mathrm{T}}\boldsymbol{s}\,. \tag{30}$$

If condition (28) is satisfied, then this derivative has everywhere – except those points in which $\boldsymbol{s} = \boldsymbol{0}$ – a negative upper limit equal to $-\eta\|\boldsymbol{s}\|$. Thus, the assumptions of the theorem are satisfied and the sliding motion in the system under consideration is stable. Let us also note that the fulfilment of relation (28) ensures not only the asymptotic stability of this motion, but also guarantees the convergence to the intersection of the switching hypersurfaces $\boldsymbol{s} = \boldsymbol{0}$ in finite time

$$t^* \leq \eta^{-1}\|\boldsymbol{s}(0)\|, \tag{31}$$

where $\boldsymbol{s}(0)$ denotes the value of the vector switching variable at the start of the control process. This inequality is of vital significance because it implies that for every time t greater than or equal to t^* the system under consideration is insensitive to external disturbances and modelling uncertainty. Of course, inequality (28) constitutes only one of many possible conditions for the existence of sliding mode and other similar relations facilitating the design of control systems are often used in the literature [11].

5. Selected problems in the field of sliding mode control

The previous sections illustrate important properties of VSS with ideal sliding modes. Unfortunately, in any real application there exist unavoidable differences between the ideal characteristics of switching devices and their actual performance. These include, but are not limited to, unmodelled inertia, inevitable hysteresis, non-negligible delays and limited gain of switches. Therefore, the application of the control method presented in the previous sections to any physical object causes high-frequency oscillations. This phenomenon typically referred to as chattering is undesirable because it causes wear and tear of the actuator components, and it can also be a reason of vibrations caused by the excitation of unmodelled part of the system dynamics. Hence, in practical systems the discontinuous variable structure control of the type

$$\boldsymbol{u}_n = \boldsymbol{\varphi}(\boldsymbol{x}, t)\frac{\boldsymbol{s}}{\|\boldsymbol{s}\|}, \tag{32}$$

where $\boldsymbol{\varphi}(\boldsymbol{x}, t)$ is a vector function of time, and the system state is replaced with its continuous approximation. In most cases, it consists in introducing a certain boundary layer [5, 15, 16, 17, 22]

$$\boldsymbol{u}_n = \boldsymbol{\varphi}(\boldsymbol{x}, t)\begin{cases}\frac{\boldsymbol{s}}{\|\boldsymbol{s}\|} & \text{for} \quad \|\boldsymbol{s}\| > \delta \\ \\ \frac{\boldsymbol{s}}{\delta} & \text{for} \quad \|\boldsymbol{s}\| \leq \delta\end{cases}, \tag{33}$$

where δ is a small positive constant. However, other approaches leading to the reduction of chattering [2] have also been proposed. Probably the most significant of them is the introduction of the second, and higher order sliding mode controllers [1, 13].

As it has already been demonstrated (see equality (22)), VSS in the sliding mode, ensure complete insensitivity of the controlled plant with respect to matched disturbances and modelling uncertainty. Therefore, much work has been performed to shorten or eliminate the reaching phase. For that purpose, on the one hand integral sliding mode control [21] has been proposed, and on the other, time-varying sliding surfaces were introduced [3, 4]. Both of these approaches attempt to select the sliding surface so that the representative point (state) of the controlled plant belongs to the sliding surface from the very beginning of the control process. When integral sliding mode technique is employed, this goal is achieved by introducing an extra state variable and extending the state space of the system. The initial

value of the extra state variable can be chosen arbitrarily, which makes it possible to place the extended state of the system on the sliding hypersurface at the start of the control action and keep it on the surface for any time greater than zero. On the other hand, when time-varying sliding surfaces are applied to eliminate the reaching phase, the surfaces are chosen to pass the representative point of the plant in the state space at the initial time, and then they smoothly move (usually they are either shifted or rotated) to their final location, which ensures desirable dynamical performance of the system and error convergence to zero.

Appropriate selection of the sliding surface is of utmost importance, since the system dynamics in the sliding mode is fully governed by the predefined surface. Therefore, the selection has to ensure stability, and the desired performance. Furthermore, smart choice of nonlinear surfaces can guarantee finite time error convergence to zero. VSS which actually make the error die out in finite time are usually called terminal sliding mode VSS [14]. Finally, let us mention that some researchers made an attempt to choose sliding surfaces in such a way that the closed loop system has become optimal in the sense of some control quality criterion [4], like integral of absolute error, integral of time multiplied absolute error, quadratic performance index, etc.

6. Conclusions

In this paper some basic properties of the sliding mode control systems have been briefly summarized. First, Filipov's construction has been presented, and the most important feature of continuous time VSS with sliding modes, i.e. their insensitivity with respect to matched model uncertainty and external disturbances, was demonstrated. Then the notion of equivalent control was presented and elaborated upon. Further in the paper conditions for the existence and stability of the sliding motion were presented. Finally, some research topics in the field were identified. These include, but are not limited to, the design of higher order sliding mode controllers, chattering attenuation, integral sliding mode control, design of terminal sliding mode control systems, and application of time-varying sliding hypersurfaces. Of course this list is not exhaustive and many other research problems in the field deserve attention and further studies.

References

[1] Bartolini G., Ferrara A. and Usai E. Chattering avoidance by second-order sliding mode control. *IEEE Transactions on Automatic Control*, 43 (1998), 241-246.

[2] Bartoszewicz A. Chattering attenuation in sliding mode control systems. *Control and Cybernetics*, 29 (2000), 585-594.

[3] Bartoszewicz A. and Nowacka A. Switching plane design for the sliding mode control of systems with elastic input constraints. *Proceedings of Institution of Mechanical Engineers, Part I, Journal of Systems & Control Engineering***,** 219 (2005), 393-403.

[4] Bartoszewicz A. and Nowacka-Leverton A. *Time-Varying Sliding Modes for Second and Third Order Systems*, Springer-Verlag, Berlin Heidelberg, 2009.

[5] Chung S. C. and Lin C. L. A general class of sliding surface for sliding mode control. *IEEE Transactions on Automatic Control*, 43 (1998), 115-119.

[6] DeCarlo R., Żak S. and Matthews G. Variable structure control of nonlinear multivariable systems: a tutorial. *Proceedings of IEEE*, 76 (1988), 212-232.

[7] Draženović B. The invariance conditions in variable structure systems. *Automatica*, 5 (1969), 287-295.

[8] Емельянов С. В. Применение нелинейных корректирующих устройств типа «ключ» для улучшения качества систем автоматического регулирования второго порядка. *Автоматика и Телемеханика*, 20 (1959), 868-883.

[9] Емельянов С. В. (editor): *Теория Систем с Переменной Структурой*. Издателство Наука, Москва, 1970.

[10] Filipov A. Differential equations with discontinuous right hand-sides. *American Mathematical Society Translations*, 42 (1964), 199-231.

[11] Gao W. and Hung J. C. Variable structure control of nonlinear systems: a new approach. *IEEE Transactions on Industrial Electronics*, 40 (1993), 45-55.

[12] Itkis U. *Control Systems of Variable Structure*. Wiley, New York, 1976.

[13] Levant A. Sliding order and sliding accuracy in sliding mode control. *International Journal of Control*. 58 (1993), 1247-1263.

[14] Man Z. and Yu X. H. Terminal sliding mode control of MIMO linear systems. *IEEE Transactions on Circuits and Systems – I: Fundamental Theory and Applications*, 44 (1997), 1065 – 1070.

[15] Rayan E. and Corless M. Ultimate boundedness and asymptotic stability of a class of uncertain dynamical systems via continuous and discontinuous control. *IMA Journal of Mathematical Control and Information*, 1 (1984), 223-242.

[16] Shtessel Y. and Lee Y. J. New approach to chattering analysis in systems with sliding modes. *Proceedings of the 35th Conference on Decision and Control*, Kobe, Japan (1996), 4014-4019.

[17] Slotine J. and Li W. *Applied Nonlinear Control*. Prentice-Hall International, Englewood Cliffs, 1991.

[18] Utkin V. Variable structure systems with sliding modes. *IEEE Transactions on Automatic Control*, 22 (1977), 212-222.

[19] Utkin V. *Sliding Modes in Control and Optimization*. Springer-Verlag, Berlin, 1992.

[20] Уткин В. И. *Скользящие Режимы и их Применения в Системах с Переменной Структурой*. Издателство Наука, Москва, 1974.

[21] Utkin V. and Shi J. Integral sliding mode in systems operating under uncertainty conditions. *Proceedings of the 35th Conference on Decision and Control*, Kobe, Japan (1996), 4591-4596.

[22] Young K., Utkin V. and Özgüner Ü. A control engineer's guide to sliding-mode control. *IEEE Transactions on Control Systems Technology*, 7 (1999), 328-342.

Andrzej Bartoszewicz, Professor: Institute of Automatic Control, Łódź University of Technology, postal address, 90-924 Łódź, Poland (*andrzej.bartoszewicz@p.lodz.pl*). The author gave a presentation of this paper during one of the conference sessions.

Generic bifurcations in thermodynamics by fractional continuum mechanics

Péter B. Béda

Abstract: In the last years non-integer differentiation became a popular tool for modeling complex behaviors of systems from diverse fields of mechanics. Especially, long-range temporal or spatial dependence phenomena inherent to fractional order systems present unique and intriguing peculiarities, not supported by their integer order version. In dynamic stability analysis mathematical aspects of non-locality were studied by using the theory of dynamical systems. Such approach results in conditions for cases, when the differential operators have critical eigenvalues of zero real-parts. When the critical eigenvalues have nontrivial eigenspace, the ways of loss of stability is classified as a typical (or generic) bifurcation. Our experiences show that material non-locality and the generic nature of bifurcation at instability are connected and the basic functions of the non-trivial eigenspace can be used to determine internal length quantities of non-local mechanics. Fractional calculus is already successfully used in thermo-elasticity. In the paper non-locality is introduced via fractional strain into the constitutive relations. Then by defining dynamical systems stability and bifurcation is studied for states of thermo-mechanic solids. Stability conditions and genericity conditions are presented for constitutive relations under consideration. Internal length effects are also studied by calculating critical non-trivial eigenspaces and the basic functions of them. Such functions are essential in bifurcation analysis in non-linear studies.

1. Introduction

The roots of fractional calculus, go back to Leibniz (1695) and Euler (1730) as a natural extension of calculus [1], and most definitions were already given in the golden age of analysis Liouville, Riemann and others. In recent years mechanics has brought back into the center of interest, because it is a useful tool to model non-locality. Such non-locality is an old problem of solid mechanics [2], and is usually treated by using integrals and second gradients [3], [4]. The first application was in visco-elasticity [5], as a kind of non-local time effect. In material instability problems spatial non-locality plays an important role in non-linear bifurcation (post-bifurcation) investigations, while in several cases local formulation of the basic equations of solid bodies may result an indeterminate behavior [6]. In numerical studies such behavior appears as mesh sensitivity, when the mesh used in finite element method, determines post-bifurcation behavior. Conventionally, such problem is avoided by introducing gradient terms into the constitutive equations. In physical interpretation: non-locality is used to cure indeterminate behavior. The aim of the paper is to describe non-locality by using fractional calculus,

and study a thermo-mechanical material instability problem. Here thermal stresses are added as usual [7] to a material instability investigation and heat propagation is described by the Vernotte-Cattaneo equation. Non-locality (in space) appears in a generalized fractional strain. Similar concept was used by [8] for non-local time in a visco-elastic problem. The focus of the study is on the existence of a set of regular basis for the non-trivial critical solutions in the post-bifurcation case.

The second part introduces the thermodynamic setting of a solid continuum taking into consideration thermal stresses. For the sake of simplicity small deformation theory is applied in a uniaxial problem. In the third part a stability and bifurcation analysis is performed. Two ways of loss of stabilities are treated, the static and the dynamic bifurcations. A dynamical system is defined from the basic equations presented in the previous part. The second subsection deals with the possibility of a static bifurcation. After then two subsections study dynamic bifurcation. The first of them is a general investigation, the second one present two special cases: a simplified version to show the possibility to get generic dynamic bifurcation and at last we show that with no fractional description no generic dynamic bifurcation is possible.

2. Fractional thermo-mechanics

This part describes the basic equations for a solid body with thermal stresses. In addition to the basic equations of continuum mechanics also heat propagation should be taken into account. To avoid non-generic behavior due to infinite propagation velocity Vernotte-Cattaneo equation is used instead of Fourier law.

The set of basic equations consists of the kinematic equation

$$\dot{\varepsilon} = \frac{\partial^{\alpha} v}{\partial x^{\alpha}}, \tag{1}$$

the equation of motion

$$\dot{v} = \frac{1}{\rho}\frac{\partial \sigma}{\partial x} \tag{2}$$

and the constitutive equation, which is in rate form reads

$$\dot{\sigma} = B\left(\dot{\varepsilon} - \theta\dot{\vartheta}\right) + \chi\dot{h}. \tag{3}$$

In equations (1), (2) and (3) the notations are: strain (for uniaxial small deformations) ε, velocity v, space coordinate x, mass density ρ, temperature θ. Overdot denotes derivative with respect to time t and B is tangent stiffness, while χ is a material constant. In (1) a generalized strain is used, where $0 < \alpha < 1$ denotes the order of the fractional derivative.

Heat conduction is given by the Vernotte-Cattaneo equation

$$\tau\dot{h} + a\frac{\partial}{\partial x}\vartheta + h = 0, \tag{4}$$

where the relaxation time of heat flux is denoted by τ, the heat flux by h, and heat conductivity by a. For the constitutive variables $\sigma, \varepsilon, \vartheta, h$ two types of constitutive equations are given. The one in form (3) could be referred as mechanical constitutive equation, while the other

$$\Theta_1\dot{\sigma} + \Theta_2\dot{\varepsilon} + \Theta_3\dot{h} = \dot{\vartheta} \tag{5}$$

may be called the thermodynamic constitutive equation [9], with material constants $\Theta_1, \Theta_2, \Theta_3$.
From (4)

$$\dot{h} = -\frac{a}{\tau}\frac{\partial}{\partial x}\vartheta - \frac{h}{\tau}. \tag{6}$$

By substituting (1) and (6) into the mechanical and thermodynamic constitutive equations, (3), (5) we have

$$\dot{\vartheta} = \Theta_1\dot{\sigma} + \Theta_2\frac{\partial^\alpha v}{\partial x^\alpha} - \Theta_3\frac{a}{\tau}\frac{\partial}{\partial x}\vartheta - \Theta_3\frac{h}{\tau}, \tag{7}$$

$$\dot{\sigma} = B\frac{\partial^\alpha v}{\partial x^\alpha} - B\theta\dot{\vartheta} - \chi\frac{a}{\tau}\frac{\partial}{\partial x}\vartheta - \chi\frac{h}{\tau}. \tag{8}$$

From (7), (8)

$$\dot{\sigma} = \left(B - B\theta\frac{\Theta_1 B + \Theta_2}{1+\Theta_1 B\theta}\right)\frac{\partial^\alpha v}{\partial x^\alpha} + \left(B\theta\frac{\Theta_1\chi+\Theta_3}{1+\Theta_1 B\theta} - \chi\right)\frac{a}{\tau}\frac{\partial}{\partial x}\vartheta + \left(B\theta\frac{\Theta_1\chi+\Theta_3}{1+\Theta_1 B\theta} - \chi\right)\frac{h}{\tau}, \tag{9}$$

$$\dot{\vartheta} = \frac{\Theta_1 B+\Theta_2}{1+\Theta_1 B\theta}\frac{\partial^\alpha v}{\partial x^\alpha} - \frac{\Theta_1\chi+\Theta_3}{1+\Theta_1 B\theta}\frac{a}{\tau}\frac{\partial}{\partial x}\vartheta - \frac{\Theta_1\chi+\Theta_3}{1+\Theta_1 B\theta}\frac{h}{\tau}. \tag{10}$$

By using simplifying notations (9) and (10) reads

$$\dot{\sigma} = c_1\frac{\partial^\alpha v}{\partial x^\alpha} + c_2\frac{a}{\tau}\frac{\partial}{\partial x}\vartheta + c_2\frac{h}{\tau}, \tag{11}$$

$$\dot{\vartheta} = d_1\frac{\partial^\alpha v}{\partial x^\alpha} - d_2\frac{a}{\tau}\frac{\partial}{\partial x}\vartheta - d_2\frac{h}{\tau}. \tag{12}$$

Now equations (2), (6), (11) and (12) for variables v, σ, ϑ, h can be used to describe the motion of the thermodynamic continuum.

3. Continuum as dynamical system and stability investigation

This part deals with stability analysis of a state of the thermo-mechanic continuum. A dynamical systems approach will be used. The investigation concentrates on the conditions of having a generic bifurcation. Generic type means the existence of non-trivial critical eigenspace at the loss of stability. The importance of it can be obvious in non-linear bifurcation and post-bifurcation analysis, while

nonlinearity is studied by projecting the expressions into the non-trivial critical eigenspace of a linear operator determined by the basic equations.

3.1. Stability and bifurcation conditions

In the previous part a set of equations was derived as the fundamental equation for a solid body taking into account the effect of thermal stresses and non-locality in form of fractional strain. This system is of first order in time and can be studied as a dynamical system. In vector form it reads

$$\begin{bmatrix} \dot{v} \\ \dot{\sigma} \\ \dot{\vartheta} \\ \dot{h} \end{bmatrix} = \begin{bmatrix} 0 & \frac{1}{\rho}\frac{\partial \sigma}{\partial x} & 0 & 0 \\ c_1 \frac{\partial^\alpha}{\partial x^\alpha} & 0 & c_2 \frac{a}{\tau}\frac{\partial}{\partial x} & c_2 \frac{1}{\tau} \\ d_1 \frac{\partial^\alpha}{\partial x^\alpha} & 0 & -d_2 \frac{a}{\tau}\frac{\partial}{\partial x} & -d_2 \frac{1}{\tau} \\ 0 & 0 & -\frac{a}{\tau}\frac{\partial}{\partial x} & \frac{1}{\tau} \end{bmatrix} \begin{bmatrix} v \\ \sigma \\ \vartheta \\ h \end{bmatrix}. \tag{13}$$

In (13) differential operator A is defined in a matrix form,

$$A(\, v, \sigma, \vartheta, h\,) = \begin{bmatrix} 0 & \frac{1}{\rho}\frac{\partial \sigma}{\partial x} & 0 & 0 \\ c_1 \frac{\partial^\alpha}{\partial x^\alpha} & 0 & c_2 \frac{a}{\tau}\frac{\partial}{\partial x} & c_2 \frac{1}{\tau} \\ d_1 \frac{\partial^\alpha}{\partial x^\alpha} & 0 & -d_2 \frac{a}{\tau}\frac{\partial}{\partial x} & -d_2 \frac{1}{\tau} \\ 0 & 0 & -\frac{a}{\tau}\frac{\partial}{\partial x} & \frac{1}{\tau} \end{bmatrix} \begin{bmatrix} v \\ \sigma \\ \vartheta \\ h \end{bmatrix}.$$

Assume that equations (2), (6), (11) and (12) has a stationary solution $v_0, \sigma_0, \vartheta_0, h_0$ satisfying all initial and boundary conditions. This solution represents a state of the thermo-mechanical continuum. Its stability can be studied as the Lyapunov stability of solution $v_0, \sigma_0, \vartheta_0, h_0$. By using perturbation technique:

$$v = v_0 + \tilde{v}, \;\; \sigma = \sigma_0 + \tilde{\sigma}, \;\; \vartheta = \vartheta_0 + \tilde{\vartheta}, \;\; h = h_0 + \tilde{h}, \tag{14}$$

where $\tilde{v}, \tilde{\sigma}, \tilde{\vartheta}, \tilde{h}$ are small perturbations satisfying homogeneous boundary conditions. While (13) is a linear equation, by substituting (14) into it a similar equation is obtained for the perturbations, and stability investigation is performed by the characteristic equation

$$\det(A - \lambda I) = 0. \tag{15}$$

When the real parts of all λ satisfying (15) are negative, the state of the material given by solution $v_0, \sigma_0, \vartheta_0, h_0$ is stable. On the stability boundary, there is at least one λ, which is zero (static bifurcation) or the real part of which is zero (dynamic bifurcation) [10].

Unfortunately (15) is an operator equation, which requires to solve a system of partial differential equations causing a lot of difficulties. In most cases such solutions are found by numerical analysis. Instead a generally used simplification can be done, when the study is restricted to periodic perturbations

$$v = \tilde{v}_0 \exp(i\omega x),\ \ \sigma = \tilde{\sigma}_0 \exp(i\omega x),\ \ \vartheta = \tilde{\vartheta}_0 \exp(i\omega x),\ \ h = \tilde{h}_0 \exp(i\omega x). \tag{16}$$

In the following subsections such simplification is used to remain at analytic approach.

3.2. Static bifurcation investigation

At static bifurcation 0 is an eigenvalue of the characteristic equation $(\lambda = 0)$, thus by substituting (16) into the matrix form of (15)

$$\det\begin{bmatrix} 0 & \frac{1}{\rho}\frac{\partial \sigma}{\partial x}\exp(i\omega x) & 0 & 0 \\ c_1 \frac{\partial^\alpha}{\partial x^\alpha}\exp(i\omega x) & 0 & c_2 \frac{a}{\tau}\frac{\partial}{\partial x}\exp(i\omega x) & c_2 \frac{1}{\tau} \\ d_1 \frac{\partial^\alpha}{\partial x^\alpha}\exp(i\omega x) & 0 & -d_2 \frac{a}{\tau}\frac{\partial}{\partial x}\exp(i\omega x) & -d_2 \frac{1}{\tau} \\ 0 & 0 & -\frac{a}{\tau}\frac{\partial}{\partial x}\exp(i\omega x) & \frac{1}{\tau} \end{bmatrix} = 0$$

is obtained. By calculating derivatives

$$\det\begin{bmatrix} 0 & \frac{1}{\rho}\omega\exp\left(i\frac{\pi}{2}\right) & 0 & 0 \\ c_1 \omega^\alpha \exp\left(i\frac{\pi}{2}\alpha\right) & 0 & c_2 \frac{a}{\tau}\omega\exp\left(i\frac{\pi}{2}\right) & c_2 \frac{1}{\tau} \\ d_1 \omega^\alpha \exp\left(i\frac{\pi}{2}\alpha\right) & 0 & -d_2 \frac{a}{\tau}\omega\exp\left(i\frac{\pi}{2}\right) & -d_2 \frac{1}{\tau} \\ 0 & 0 & -\frac{a}{\tau}\omega\exp\left(i\frac{\pi}{2}\right) & \frac{1}{\tau} \end{bmatrix} = 0. \tag{17}$$

Equation (17) should be solved for ω and a non-trivial solution is searched for. When we have such a solution (non-zero) ω_{int} , the basis of the critical non-trivial eigenspace is

$$\left[\tilde{v}_0 \exp(i\omega_{\text{int}} x),\ \ \tilde{\sigma}_0 \exp(i\omega_{\text{int}} x),\ \ \tilde{\vartheta}_0 \exp(i\omega_{\text{int}} x),\ \ \tilde{h}_0 \exp(i\omega_{\text{int}} x)\right] \tag{18}$$

and the non-trivial solutions for post-bifurcation investigations should be searched for a linear combination of it. In addition static internal length for this type of loss of stability can be defined as

$$\ell_{\text{int}} = \pi\omega_{\text{int}}. \tag{19}$$

From (17)

$$\omega^{\alpha+2}\frac{1}{\rho}e^{i\frac{\pi}{2}}\left(c_2\frac{a}{\tau^2}e^{i\frac{\pi}{2}}d_1 e^{i\frac{\pi}{2}\alpha} + d_2\frac{a}{\tau^2}e^{i\frac{\pi}{2}}c_1 e^{i\frac{\pi}{2}\alpha} + \frac{1}{\tau}\left(d_2\frac{a}{\tau}e^{i\frac{\pi}{2}}c_1 e^{i\frac{\pi}{2}\alpha} + d_1\frac{a}{\tau}e^{i\frac{\pi}{2}}c_2 e^{i\frac{\pi}{2}\alpha}\right)\right) = 0, \tag{20}$$

consequently, only the trivial solution exists. Thus, there is no regular non-trivial critical eigenspace for static bifurcation.

Let us study what happens, if damping is added to the mechanical constitutive equation. Then instead of (3)

$$\dot{\sigma} = B\left(\dot{\varepsilon} - \theta\dot{\vartheta}\right) + \chi\dot{h} + D\frac{1}{\rho}\frac{\partial^{\alpha}}{\partial x^{\alpha}}\frac{\partial}{\partial x}\sigma \tag{21}$$

should be used, where D is damping coefficient. After similar steps as before, the characteristic equation in case of a static bifurcation results

$$\det\begin{bmatrix} 0 & \frac{1}{\rho}\omega\exp\left(i\frac{\pi}{2}\right) & 0 & 0 \\ c_1\omega^{\alpha}\exp\left(i\frac{\pi}{2}\alpha\right) & c_3\omega^{\alpha+1}\exp\left(i\frac{\pi}{2}(\alpha+1)\right) & c_2\frac{a}{\tau}\omega\exp\left(i\frac{\pi}{2}\right) & c_2\frac{1}{\tau} \\ d_1\omega^{\alpha}\exp\left(i\frac{\pi}{2}\alpha\right) & d_3\omega^{\alpha+1}\exp\left(i\frac{\pi}{2}(\alpha+1)\right) & -d_2\frac{a}{\tau}\omega\exp\left(i\frac{\pi}{2}\right) & -d_2\frac{1}{\tau} \\ 0 & 0 & -\frac{a}{\tau}\omega\exp\left(i\frac{\pi}{2}\right) & \frac{1}{\tau} \end{bmatrix} = 0, \tag{22}$$

but (22) leads to the same result as (17), there is no regular non-trivial critical eigenspace for static bifurcation either.

3.3. Dynamic bifurcation investigation

The necessary condition for a dynamic bifurcation is to have pure imaginary solution $\lambda = \beta\exp\left(i\frac{\pi}{2}\right)$ of the characteristic equation (15). When the imaginary expression is substituted into (15)

$$\det\begin{bmatrix} -\beta e^{i\frac{\pi}{2}} & \frac{1}{\rho}\omega e^{i\frac{\pi}{2}} & 0 & 0 \\ c_1\omega^{\alpha}e^{i\frac{\pi}{2}\alpha} & -\beta e^{i\frac{\pi}{2}} & c_2\frac{a}{\tau}\omega e^{i\frac{\pi}{2}} & c_2\frac{1}{\tau} \\ d_1\omega^{\alpha}e^{i\frac{\pi}{2}\alpha} & 0 & \left(-d_2\frac{a}{\tau}\omega e^{i\frac{\pi}{2}} - \beta e^{i\frac{\pi}{2}}\right) & -d_2\frac{1}{\tau} \\ 0 & 0 & -\frac{a}{\tau}\omega e^{i\frac{\pi}{2}} & \left(\frac{1}{\tau} - \beta e^{i\frac{\pi}{2}}\right) \end{bmatrix} = 0 \tag{23}$$

is obtained. From (23)

$$-\frac{1}{\rho}\omega e^{i\frac{\pi}{2}}\left(-c_2\frac{a}{\tau^2}e^{i\frac{\pi}{2}}d_1\omega^{\alpha+1}e^{i\frac{\pi}{2}\alpha} - d_2\frac{a}{\tau^2}e^{i\frac{\pi}{2}}c_1\omega^{\alpha+1}e^{i\frac{\pi}{2}\alpha} + \left(\frac{1}{\tau} - \beta e^{i\frac{\pi}{2}}\right)\left(\left(-d_2\frac{a}{\tau}\omega - \beta\right)c_1\omega^{\alpha}e^{i\frac{\pi}{2}\alpha} - d_1\omega^{\alpha+1}\frac{a}{\tau}e^{i\frac{\pi}{2}}c_2e^{i\frac{\pi}{2}\alpha}\right)\right) + \beta^2e^{i\pi}\left(\left(-d_2\frac{a}{\tau}\omega - \beta\right)e^{i\frac{\pi}{2}}\left(\frac{1}{\tau} - \beta e^{i\frac{\pi}{2}}\right) - d_2\frac{a}{\tau^2}e^{i\frac{\pi}{2}}\omega\right) = 0. \tag{24}$$

Equation (24) is complex, its real and imaginary parts define a system of two equations

$$\left(\left(d_2c_1\beta\frac{a}{\rho\tau}-d_2c_1\frac{a}{\rho\tau^2}\right)\omega^{\alpha+2}+\frac{1}{\rho}\beta^2c_1\omega^{\alpha+1}\right)\cos\left(\frac{\alpha\pi}{2}\right)+\left(\left(-d_1c_2\beta\frac{a}{\rho\tau}+d_2c_1\frac{a}{\rho\tau^2}\right)\omega^{\alpha+2}+\right.$$

$$\left.\frac{1}{\rho\tau}\beta c_1\omega^{\alpha+1}\right)\left(-\sin\left(\frac{\alpha\pi}{2}\right)\right)-\beta^3\left(-d_2\frac{a}{\tau}\omega-\beta\right)=0, \tag{25}$$

$$\left(\left(d_2c_1\beta\frac{a}{\rho\tau}-d_2c_1\frac{a}{\rho\tau^2}\right)\omega^{\alpha+2}+\frac{1}{\rho}\beta^2c_1\omega^{\alpha+1}\right)\sin\left(\frac{\alpha\pi}{2}\right)+\left(\left(-d_1c_2\beta\frac{a}{\rho\tau}+d_2c_1\frac{a}{\rho\tau^2}\right)\omega^{\alpha+2}+\right.$$

$$\left.\frac{1}{\rho\tau}\beta c_1\omega^{\alpha+1}\right)\cos\left(\frac{\alpha\pi}{2}\right)=0, \tag{26}$$

and should be solved for variables $\beta\neq 0$ and $\omega\neq 0$. From (26) β can be expressed as a function of ω, then it can be substituted into (25), and now ω can be expressed.

If $c_1=0$, then

$$d_1c_2\beta\frac{a}{\rho\tau}\omega^{\alpha+2}\cos\left(\frac{\alpha\pi}{2}\right)=0, \tag{27}$$

that is, there is no solution with the necessary properties. Equation (27) is satisfied, when $\beta=0$, or $\omega=0$, but such solutions are excluded. The third possibility is $\cos\left(\frac{\alpha\pi}{2}\right)=0$. It happens when $\frac{\alpha\pi}{2}=\frac{\pi}{2},3\frac{\pi}{2},\dots$, but also these cases cannot be resent, because of condition $0<\alpha<1$. For material constants $c_1\neq 0$ implies

$$B\left(1-\theta\frac{\Theta_1B+\Theta_2}{1+\Theta_1B\theta}\right)\neq 0. \tag{28}$$

Now (26) could be divided by c_1 and simplified to

$$\beta^2-\left(1-\cot\left(\frac{\alpha\pi}{2}\right)\right)\frac{d_2a\omega}{\tau^2}+\beta\frac{1}{\tau}\left(d_2a\omega-d_1\frac{c_2}{c_1}a\omega\cot\left(\frac{\alpha\pi}{2}\right)+\cot\left(\frac{\alpha\pi}{2}\right)\right)=0. \tag{29}$$

To obtain $\beta=\beta(\omega)$ the second order equation (29) should be solved and the solution should be substituted into (25). Then the solvability of

$$\left(\left(d_2c_1\beta(\omega)\frac{a}{\rho\tau}-d_2c_1\frac{a}{\rho\tau^2}\right)\omega^{\alpha+2}+\frac{1}{\rho}\left(\beta(\omega)\right)^2c_1\omega^{\alpha+1}\right)\cos\left(\frac{\alpha\pi}{2}\right)+\left(\left(-d_1c_2\beta(\omega)\frac{a}{\rho\tau}+\right.\right.$$

$$\left.\left.d_2c_1\frac{a}{\rho\tau^2}\right)\omega^{\alpha+2}+\frac{1}{\rho\tau}\beta(\omega)\,c_1\omega^{\alpha+1}\right)\left(-\sin\left(\frac{\alpha\pi}{2}\right)\right)-\left(\beta(\omega)\right)^3\left(-d_2\frac{a}{\tau}\omega-\beta(\omega)\right)=0 \tag{30}$$

should be studied. If there exists regular non-zero ω satisfying (30), then the dynamic bifurcation is generic and a non-linear investigation is possible.

3.4. Dynamic bifurcation for two special cases

To show that (30) may have regular solution, this part will study simplified cases $\left(\alpha = \frac{1}{2} \text{ and } \alpha = 1\right)$, in which such solution can easily be derived. Then the case of the conventional strain will also be treated to demonstrate the need for fractional strain to have generic dynamic bifurcation.

Denote $A = \frac{d_2 a\omega}{\tau}$ and assume for the sake of simplicity that

$$c_2 = 0 \text{ and } \cot\left(\frac{\alpha\pi}{2}\right) = 0 \tag{31}$$

to study a simplified special case. Then (29) is

$$\beta^2 + A\beta - \frac{A}{\tau} = 0. \tag{32}$$

Equation (32) can be solved to

$$\beta_{1,2} = -\frac{A}{2} \pm \sqrt{A}\sqrt{\frac{A\tau+4}{4\tau}}. \tag{33}$$

Conditions (31) imply

$$\Theta_3 B\theta = \chi \text{ and } \alpha = \frac{1}{2}, \tag{34}$$

then the positive solution from (33) should be substituted into (25), and

$$\frac{\tau^2\sqrt{2}}{\rho} c_1 \omega^{\frac{3}{2}} - (d_2 a\omega)^3 - 3(d_2 a\omega)^2 - 3(d_2 a\omega) - 1 = 0 \tag{35}$$

is obtained. To have a generic dynamic bifurcation (35) should have a non-zero solution ω_{dyn}. In (35) coefficient $d_2 = \Theta_3$.

Instead of solving (35) we may assume, that dynamic material length $\ell_{\text{dyn}} \stackrel{\text{def}}{=} \omega_{\text{dyn}}\pi$ is determined by some measurement or physical experience. Then (35) presents a condition for the coefficients of the constitutive equations in form

$$\frac{\tau^2\sqrt{2}}{\rho}\left(B\left(1 - \theta\frac{\Theta_1 B + \Theta_2}{1 + \Theta_1 B\theta}\right)\right)\left(\frac{\ell_{\text{dyn}}}{\pi}\right)^{\frac{3}{2}} - \left(\Theta_3 a\frac{\ell_{\text{dyn}}}{\pi}\right)^3 - 3\left(\Theta_3 a\frac{\ell_{\text{dyn}}}{\pi}\right)^2 - 3\left(\Theta_3 a\frac{\ell_{\text{dyn}}}{\pi}\right) - 1 = 0. \tag{36}$$

Of course we should keep in mind all the previous assumptions (28), (34) and

$$\Theta_1 B + \Theta_2 \neq 0 \quad \text{and} \quad \Theta_3 \neq 0 \tag{37}$$

to set up conditions for the existence of a generic dynamic bifurcation as the way of loss of stability.

At last the case of conventional strain

$$\varepsilon = \frac{\partial u}{\partial x}$$

is studied. Then $\alpha = 1$ and (26) implies

$$\beta^2 + \frac{d_2 a\omega}{\tau}\beta - \frac{d_2 a\omega}{\tau^2} = 0. \tag{38}$$

its solution reads

$$\beta_{12} = -\frac{d_2 a\omega}{2\tau} \pm \frac{1}{2\tau}(d_2 a\omega)^{\frac{1}{2}}(d_2 a\omega + 4)^{\frac{1}{2}}. \tag{39}$$

When it is substituted into (25) at $\alpha = 1$, after some calculations

$$\left(-\frac{d_2 a\omega}{2\tau} + \frac{1}{2\tau}(d_2 a\omega)^{\frac{1}{2}}(d_2 a\omega + 4)^{\frac{1}{2}}\right)^3 \left(\frac{d_2 a\omega}{2\tau} + \frac{1}{2\tau}(d_2 a\omega)^{\frac{1}{2}}(d_2 a\omega + 4)^{\frac{1}{2}}\right) = 0 \tag{40}$$

is obtained. Unfortunately (40) cannot be satisfied, thus no ω solution exists, because (40) is valid either when

$$d_2 a\omega = (d_2 a\omega)^{\frac{1}{2}}(d_2 a\omega + 4)^{\frac{1}{2}}, \tag{41}$$

or

$$-d_2 a\omega = (d_2 a\omega)^{\frac{1}{2}}(d_2 a\omega + 4)^{\frac{1}{2}}, \tag{42}$$

Both (41) and (42) require

$$(d_2 a\omega)^2 = (d_2 a\omega)(d_2 a\omega + 4) \quad \Leftrightarrow \quad d_2 a\omega = d_2 a\omega + 4,$$

which is a contradiction. That is, no generic dynamic bifurcation is possible for conventional strain.

4. Conclusions

By using dynamical systems stability analysis of thermo-mechanical continua can easily be performed, even when fractional derivatives are used. Such case may be obtained, when non-locality is described by a generalized, fractional strain. In constitutive formulation two types of constitutive equations are used, thermodynamical constitutive equations should also be added to the classical "mechanical" constitutive equations. In such a way a closed systems of equations is obtained to determine the motion of the thermo-mechanical continuum. By using such system of equations a dynamical system can be defined and the requirements of generic static and dynamic bifurcations can be studied. When the investigation is restricted to homogeneous periodic perturbations, general necessary conditions are formulated for both static and dynamic bifurcations. For the conventional setting (small deformations, linearized constitutive equations, Vernotte-Cattaneo equation) no generic static bifurcations are found. For dynamic bifurcation there are possibilities to have generic behavior. A general formula is derived

for such case. Moreover, having done a few simplifying restrictions conditions are presented for the material constants of the constitutive equations to ensure generic dynamic bifurcation. The necessity of fractional strain is also presented, while at conventional strain no generic bifurcation is possible.

References

[1] Machado J.T., Kiryakova V., Mainardi F. Recent history of fractional calculus *Commun Nonlinear Sci Numer Simulat.,* 16 (2011) 1140–1153.

[2] Mindlin, R.D. Second gradient of strain and surface tension in linear elasticity, *Intl. Journal of Solids and Structures*, 1 (1965), 417–438.

[3] Eringen, A.C. *Nonlocal Continuum Field Theories*. Springer, New York, 2010.

[4] Aifantis. E.C. On the role of gradients in the localization of deformation and fracture. *International Journal of Engineering Science*, 30 (1992), 1279– 1299.

[5] Caputo. M. Linear model of dissipation whose Q is almost frequency independent – II. *Geophys. J. R. Astr. Soc.*, 13 (1967), 529–539.

[6] De Borst, R., Sluys, L.J., Mu¨hlhaus, H.-B., Pamin, J. Fundamental issues in finite element analyses of localization of deformation, *Engineering Computations*, 10 (1993) 99–121.

[7] Sumelka, W. Thermoelasticity in the Framework of the Fractional Continuum Mechanics, *Journal of Thermal Stresses*, 37 (2014), 678-706.

[8] Atanackovic, T. M., Stankovic, B. Generalized wave equation in nonlocal elasticity, *Acta Mech.* 208 (2009), 1–10.

[9] Béda, Gy. Second order thermodynamical wave in nonlocal continua, *Proc. 6th Intl. Congress on Thermal Stresses,* Vienna, 663-666, 2005.

[10] Béda, P.B. Dynamic systems, rate and gradient effects in material instability, *International Journal of Mechanical Sciences*, 42 (2000), 2101-2114.

Péter Balázs Béda, Professor: Budapest University of Technology and Economics, Műegyetem rkp. 1-3, H-1111 Budapest, Hungary (*bedap@kme.bme.hu*).

Computation of periodic switching strategies for the optimal control of chemical reactors

Peter Benner, Andreas Seidel-Morgenstern, Alexander Zuyev[1]

Abstract: In this paper an isoperimetric control problem for the optimization of the performance measure for a nonlinear chemical reaction model with periodic inputs is considered. For this problem, a family of bang-bang controls parametrized by switching times is introduced. The issue of defining these switching times is addressed for periodic boundary conditions by using the Fliess series expansion. Such a technique allows us to obtain analytical relations between the boundary conditions and control parameters for the case of small time periods. These theoretical results are illustrated by numerical simulations for a non-isothermal reaction model with two inputs.

1. Introduction

Problems of chemical engineering stimulate the development of nonlinear design techniques in mathematical control theory for distributed and lumped parameter systems. As an important reference, we cite the pioneering work by J.M. Douglas [1], where the performance measure of a nonlinear chemical reaction was estimated under sinusoidal modulations of the feed composition. Since then, problems of increasing the efficiency of periodic operations of chemical reactors have received considerable attention in theoretical and experimental studies (see, e.g., the recent papers [4, 5] and references therein).

A family of bang-bang extremal controls was proposed for an isoperimetric optimization problem in our previous work [8] in order to maximize the performance of a nonlinear chemical reaction with periodic inputs. It was noted that this control design methodology is based on solving an auxiliary system of equations with respect to the switching times. The properties of these switching strategies have not been fully analyzed so far, and we carry out a further study of this problem in the present work.

Our main theoretical contribution is summarized in Section 3. In Lemmas 1–3, we provide conditions for the switching times and the initial data of the considered isoperimetric problem. These analytic results allow to define bang-bang controls for the case of relatively small time periods (i.e., for relatively high frequencies of the input modulations). We also derive representations of the cost function along periodic trajectories for different switching

[1]Corresponding author.

scenarios. The novelty of this approach is underpinned by the use of essentially nonlinear techniques, based on the Fliess functional expansion, while the matrix exponentials of the linearized problem were previously used in [8]. The above theoretical results, linking switching parameters with the initial data, are illustrated with numerical simulations in Section 4 for a non-isothermal chemical reaction model.

2. Optimal control problem

This section contains a brief presentation of the necessary results related to the isoperimetric optimal control problem introduced in [8].

2.1. Mathematical model

Consider a mathematical model of a controlled non-isothermal chemical reaction of the type "$A \to$ product" governed by the following differential equations [8]:

$$\dot{x} = f_0(x) + u_1 f_1(x) + u_2 f_2(x), \quad x = \begin{pmatrix} x_1 \\ x_2 \end{pmatrix} \in \mathbb{R}^2, \; u = \begin{pmatrix} u_1 \\ u_2 \end{pmatrix} \in U \subset \mathbb{R}^2, \tag{1}$$

$$U = [u_1^{min}, u_1^{max}] \times [u_2^{min}, u_2^{max}].$$

We assume that the dimensionless components of $x(t)$ and $u(t)$ describe the deviation of basic physical quantities from their steady-state values under a suitable rescaling, so that $x_1(t)$ corresponds to the outlet concentration of A, $x_2(t)$ corresponds to the temperature of the reactor, $u_1(t)$ controls the inlet concentration of A, and $u_2(t)$ controls the temperature of the inlet stream. Here $t \geq 0$ is the dimensionless time. Thus, the nonlinear control system (1) describes the reactor dynamics in a neighborhood of some steady state, so that $f_0(0) = 0$, and the trivial solution $x = 0$ with $u = 0$ corresponds to the operation with a constant consumption of A at a constant temperature. More details concerning the derivation of equations (1) can be found in [4, 5, 8].

The problem of maximizing the mean conversion of A to the product (or, equivalently, minimizing the mean concentration of A at the output of the reactor) has been considered in [8] under periodic boundary conditions. To formulate this problem, we introduce the class of admissible controls $\mathcal{U}_{t_f}$ consisting of all measurable functions $u : [0, t_f] \to U \subset \mathbb{R}^2$.

2.2. Problem formulation

For given $t_f > 0$, $x^0 \in \mathbb{R}^2$, and $\bar{u}_1 \in \mathbb{R}$, the goal is to find a control $\hat{u}(\cdot) \in \mathcal{U}_{t_f}$ that minimizes the cost

$$J := \frac{1}{t_f} \int_0^{t_f} x_1(t)\, dt \tag{2}$$

along the solutions $x(t)$ *of system* (1) *corresponding to the admissible controls* $u(\cdot) \in \mathcal{U}_{t_f}$ *such that*

$$\frac{1}{t_f}\int_0^{t_f} u_1(t)\,dt = \bar{u}_1 \tag{3}$$

and

$$x(0) = x(t_f) = x^0. \tag{4}$$

The above isoperimetric problem formulation corresponds to an assumption that the process is controlled periodically and the mean consumption of the input reactant A is fixed to be $\bar{u}_1$ (in our dimensionless variables).

2.3. Parametrization of the switching times

If $\hat{u}(t)$ is an optimal control for the above problem then, as it was shown in [8], the Pontryagin maximum principle implies that

$$\begin{aligned}
\hat{u}_1(t) &= \frac{u_1^{max}+u_1^{min}}{2} + \frac{u_1^{max}-u_1^{min}}{2}\operatorname{sign}\left(p_1(t)+\eta_1\right),\\
\hat{u}_2(t) &= \frac{u_2^{max}+u_2^{min}}{2} + \frac{u_2^{max}-u_2^{min}}{2}\operatorname{sign} p_2(t), \quad t\in[0,t_f],
\end{aligned} \tag{5}$$

where $(p_1(t), p_2(t))$ satisfy the adjoint equations, and the constant η_1 plays the role of a Lagrange multiplier for problems with isoperimetric constraints (cf. [6]). For the case of a reaction of order n considered in [8], the vector fields of system (1) are

$$f_0(x) = \begin{pmatrix} k_1 e^{-\varkappa} - \phi_1 x_1 - k_1(x_1+1)^n e^{-\varkappa/(x_2+1)} \\ k_2 e^{-\varkappa} - \phi_2 x_2 - k_2(x_1+1)^n e^{-\varkappa/(x_2+1)} \end{pmatrix},\ f_1(x) = \begin{pmatrix} 1 \\ 0 \end{pmatrix},\ f_2(x) = \begin{pmatrix} 0 \\ 1 \end{pmatrix}, \tag{6}$$

and the adjoint differential equations for $(p_1(t), p_2(t))$ take the following form:

$$\begin{aligned}
\dot{p}_1 &= -p_0 + \phi_1 p_1 + n(k_1 p_1 + k_2 p_2)(x_1+1)^{n-1} e^{-\varkappa/(x_2+1)},\\
\dot{p}_2 &= \phi_2 p_2 + \frac{\varkappa(k_1 p_1 + k_2 p_2)(x_1+1)^n}{(x_2+1)^2} e^{-\varkappa/(x_2+1)}, \quad p_0 = \text{const} \le 0.
\end{aligned} \tag{7}$$

Here n, $\varkappa$, k_i, and ϕ_i are parameters of the reaction [8].

As there is no information about the initial values of the adjoint variables p_1 and p_2, the principal problem for implementing bang-bang controls of the form (5) is related to the computation of the switching times, when the functions $p_1(t)+\eta_1$ and $p_2(t)$ change their signs.

Remark 1. *The number of switchings has been estimated in our previous work [8] for the linearization of systems* (1) *and* (7)*, when* $n = 1$ *and the differential equations for* x *and* p *are decoupled. In this case, it was shown under an additional assumption on the parameters of the drift term* f_0 *(which holds for the reaction considered in [8]) that each control* $\hat{u}(\cdot) \in \mathcal{U}_{t_f}$ *satisfying the Pontryagin maximum principle has at maximum 4 switchings in the interval* $t \in [0, t_f]$.

Starting from this observation, we fix a natural number N and consider a finite sequence of boundary control values

$$u^j \in \left\{ \begin{pmatrix} u_1^{min} \\ u_2^{min} \end{pmatrix}, \begin{pmatrix} u_1^{min} \\ u_2^{max} \end{pmatrix}, \begin{pmatrix} u_1^{max} \\ u_2^{min} \end{pmatrix}, \begin{pmatrix} u_1^{max} \\ u_2^{max} \end{pmatrix} \right\} = U_b, \quad j = \overline{1, N}, \tag{8}$$

together with a partition

$$0 = t_0 < t_1 < ... < t_N = t_f, \quad (\tau_j := t_j - t_{j-1} > 0), \tag{9}$$

in order to define the following piecewise-constant control $u : [0, t_f) \to U_b$:

$$u(t) := u^j \quad \text{for } t \in [t_{j-1}, t_j), \quad j = \overline{1, N}. \tag{10}$$

Thus, the candidates for optimal controls may be obtained by checking all controls of the form (10) *corresponding to all possible choices of* N*, switching scenarios* (8)*, and partitions* (9) *such that the constraints* (3) *and* (4) *are satisfied.*

3. Equations for the switching times

In this section, we will propose analytic formulas for computing the switching times and corresponding asymptotic representations of the cost J for the case of small periods t_f. Our study is based on the Fliess functional expansion for solutions of system (1), which can be deduced from its Volterra representation [2]. Namely, for the analytic vector fields f_i, output function $y = h(x)$, initial data $x(0) = x^0 \in \mathbb{R}^2$, and piecewise-continuous input $u \in \mathcal{U}_{t_f}$, the value of $y(t) = h(x(t))$ for the corresponding solution $x(t)$ of system (1) can be represented as follows [2], [3, Chapter 4]:

$$y(t) = h(x^0) + \sum_{\nu=0}^{\infty} \sum_{i_0,\dots,i_\nu=0}^{2} L_{f_{i_0}} \cdots L_{f_{i_\nu}} h(x^0) \int_0^t d\xi_{i_\nu} \cdots d\xi_{i_0}, \quad t \in [0, t_f], \tag{11}$$

where $L_{f_i} h(x) = \frac{\partial h(x)}{\partial x} f_i(x)$ is the Lie derivative, $\frac{\partial h(x)}{\partial x}$ is the Jacobian matrix, $\int_0^t d\xi_0 = t$, $\int_0^t d\xi_i = \xi_i(t) = \int_0^t u_i(t)$ for $i = 1, 2$, and, by induction,

$$\int_0^t d\xi_{i_\nu} \cdots d\xi_{i_0} = \int_0^t d\xi_{i_\nu}(s) \int_0^s d\xi_{i_{\nu-1}} \cdots d\xi_{i_0}.$$

To simplify computations in the sequel, we assume that the mean consumption of the input reactant corresponds to the same amount that is used to achieve the steady-state $x = 0$, i.e. we assume that $\bar{u}_1 = 0$ in the isoperimetric constraint (3). We also assume that the set U_b is symmetric, i.e.

$$u_i^{max} = -u_i^{min} > 0, \quad i = 1, 2. \tag{12}$$

For a given number $N \geq 1$ and a switching scenario $u^1, u^2, ..., u^N \in U_b$, we introduce positive real variables τ_1, τ_2, ..., τ_N and denote $t_0 = 0$, $t_1 = \tau_1$, $t_2 = t_1 + \tau_2$, ..., $t_N = t_{N-1} + \tau_N = t_f$. Our goal is to define $(\tau_1,\ \tau_2,\ ...,\ \tau_N)$ from the conditions (3), (4) and to analyse their properties for small values of t_f. By assuming that Remark 1 remains valid for the nonlinear system (1) in a neighborhood of the origin, we will consider the cases with $N \leq 4$ only. It is clear that any constant control $u(t) \in U_b$ does not satisfy the isoperimetric constraint

$$\int_0^{t_f} u_1(t)\, dt = 0 \tag{13}$$

under the assumption (12). Thus, we will exclude the case $N = 1$ from consideration.

3.1. Case $N = 2$

For a given switching scenario $u^1, u^2 \in U_b$, the isoperimetric constraint (13) is satisfied for the control $u(t)$ of the type (10) only if

$$\tau_1 = \tau_2 = t_f/2 \quad \text{and} \quad u^2 = -u^1. \tag{14}$$

With this control $u(t)$, the Fliess functional expansion (11) with $h(x) \equiv x$ takes the form

$$x(t_f) = x^0 + 2\tau_1 f_0(x^0) + 2\tau_1^2 L_{f_0} f_0(x^0) + \tau_1^2 [g_1, f_0](x^0) + O(t_f^3) \quad \text{for small} \quad t_f > 0, \tag{15}$$

where $g_1 = u_1^1 f_1 + u_2^1 f_2$, and $[g_i, f_0] := L_{g_i} f_0 - L_{f_0} g_i$ is the Lie bracket of the vector fields g_i and f_0. Note that formula (15) is valid for any vector fields f_i of class C^2, and its remainder $O(t_f^3)$ can be estimated by Lemma 3.1 of [7]. We use the representation (15) to derive equations for the switching times from the periodic boundary conditions (4) in the following lemma.

Lemma 1. *Let $N = 2$, and let the parameters of the contol $u(t)$ given by* (10) *satisfy* (14)*. If the corresponding solution $x(t)$ of system* (1) *satisfies the boundary conditions* (4)*, then*

$$f_0 + \tau_1 \left\{ L_{f_0} f_0 + \frac{1}{2}[g_1, f_0] \right\} = O(t_f^2), \quad \textit{where} \ \ g_1 = u_1^1 f_1 + u_2^1 f_2, \tag{16}$$

and

$$\bar{x} := \frac{1}{t_f} \int_0^{t_f} x(t) dt = x^0 + \tau_1 \left\{ f_0 + \frac{1}{2} g_1 \right\} + \tau_1^2 \left\{ \frac{2}{3} L_{f_0} f_0 + \frac{1}{2} L_{g_1} f_0 \right\} + O(t_f^3) \tag{17}$$

for small $t_f > 0$.

Note that the vector fields in formulas (16), (17) and in the subsequent computations are evaluated at $x = x^0$.

3.2. Cases $N = 3$ and $N = 4$

If $N = 3$ and $u^1, u^2, u^3 \in U_b$, then the isoperimetric constraint (13) is satisfied for the control (10) if

$$\tau_1 = \tau_2 + \tau_3 = t_f/2 \quad \text{and} \quad u^2 = -u^1,\ u_1^3 = -u_1^1. \tag{18}$$

We summarize our analytic approach for the design of controls (10) with $N = 3$ as follows.

Lemma 2. *Let* $N = 3$*, and let the parameters of the contol* $u(t)$ *given by* (10) *satisfy* (18)*. If the corresponding solution* $x(t)$ *of system* (1) *satisfies* (4)*, then*

$$\begin{aligned} &2\tau_2 f_0 + \tau_3(2f_0 + g_1 + g_3) + \tau_2^2\{2L_{f_0}f_0 + [g_1, f_0]\} + 2\tau_2\tau_3\{2L_{f_0}f_0 + L_{f_0}g_3\} \\ &+ \frac{\tau_3^2}{2}\{4L_{f_0}f_0 + 3L_{g_1}f_0 + L_{g_3}f_0 + 3L_{f_0}g_3 + L_{f_0}g_1 \\ &+ L_{g_3}g_3 + 2L_{g_1}g_3 + L_{g_1}g_1\} = O(t_f^3), \quad \textit{where } g_i = u_1^i f_1 + u_2^i f_2. \end{aligned} \tag{19}$$

For the case $N = 4$, we observe that the control (10) with $u^1, u^2, u^3, u^4 \in U_b$ satisfies the isoperimetric constraint (13) if

$$\tau_3 = \tau_1,\ \tau_4 = \tau_2,\ 2(\tau_1 + \tau_2) = t_f \quad \text{and} \quad u^3 = -u^1,\ u^4 = -u^2. \tag{20}$$

In this case, we have:

Lemma 3. *Let* $N = 4$*, and let the parameters of the contol* $u(t)$ *given by* (10) *satisfy* (20)*. If the corresponding solution* $x(t)$ *of system* (1) *satisfies* (4)*, then*

$$\begin{aligned} &2(\tau_1 + \tau_2)f_0 + \tau_1^2\{2L_{f_0}f_0 + [g_1, f_0]\} + \tau_2^2\{2L_{f_0}f_0 + [g_2, f_0]\} \\ &+ \tau_1\tau_2\{4L_{f_0}f_0 + [g_1 + g_2, f_0] + [g_1, g_2]\} = O(t_f^3), \quad \textit{where } g_i = u_1^i f_1 + u_2^i f_2, \end{aligned} \tag{21}$$

and

$$\begin{aligned} \bar{x} :=& \frac{1}{t_f}\int_0^{t_f} x(t)dt = x^0 + (\tau_1 + \tau_2)f_0 + \frac{\tau_1 g_1 + \tau_2 g_2}{2} + \frac{2(\tau_1 + \tau_2)^2}{3}L_{f_0}f_0 \\ &+ \frac{\tau_1(2\tau_1 + 3\tau_2)}{4}L_{g_1}f_0 + \frac{\tau_2(\tau_1 + 2\tau_2)}{4}L_{g_2}f_0 + O(t_f^3) \ \textit{ for small } t_f > 0. \end{aligned} \tag{22}$$

The proof of Lemmas 1–3 is based on the Fliess functional expansion (11) and is omitted due to lack of space.

4. Numerical simulations

In this section, we will show how the above analytical results can be applied to control the hydrolysis reaction of the type $(CH_3CO)_2O + H_2O \to 2\,CH_3COOH$. We choose the same realistic parameters for the vector fields (6) of system (1) as in [8]: $n = 1$, $\phi_1 = \phi_2 = 1$, $\varkappa = 16.07$, $k_1 = 3.059 \cdot 10^7$, $k_2 = -1.058 \cdot 10^6$, $u_1^{max} = -u_1^{min} = 4.21$, $u_2^{max} = -u_2^{min} = 0.06$.

Let us first consider controls of the form (10) for $N = 2$, i.e. let

$$u(t) = \begin{cases} u^1, & t \in [0, \tau_1), \\ -u^1, & t \in [\tau_1, t_f], \end{cases} \tag{23}$$

with $\tau_1 > 0$, $t_f = 2\tau_2$, and $u^1 \in U_b$ (we take into account (14) to satisfy the isoperimetric constraint with $\bar{u}_1 = 0$). As, for an arbitrary initial condition $x(0) = x^0 \in \mathbb{R}^2$, the solution $x(t)$ of system (1) with control (23) does not necessary satisfy the periodic boundary condition $x(0) = x(t_f)$, we use Lemma 1 to satisfy the relation between x^0 and τ_1. Namely, if $t_f = 2\tau_1 = 0.4$, $u^1 = -u^2 = (u_1^{max}, u_2^{max})^T$, then condition (16) of Lemma 1 is satisfied with $x^0 \approx (-0.403, -0.006)^T$. We have truncated the term $O(t_f^2)$ in the right-hand side of (16) and solved the resulting equation numerically. The solution $x(t)$ of system (1), (6), (23) with the above choice of parameters is shown in Fig. 1. We observe that the solution $x(t)$ is t_f-periodic, and the cost is $J = \frac{1}{t_f}\int_0^{t_f} x_1(t)dt \approx -0.015$. As J is negative, the periodic control (23) ensures a better performance of the reactor in comparison to its steady-state operation with $x = u = 0$.

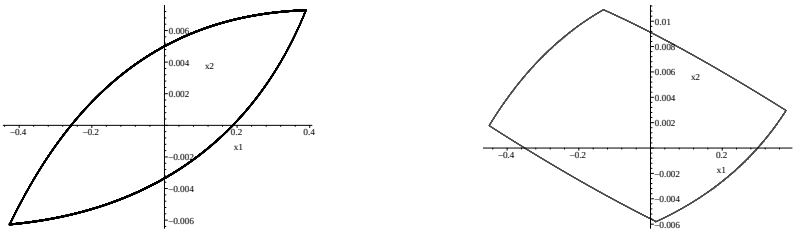

Figure 1. Trajectories of the control system (1), (6), (10): $N = 2$ (left) and $N = 4$ (right).

To illustrate the case $N = 4$, we choose control (10) with the same $t_f = 0.4$ and $u^1 = -u^3 = (u_1^{max}, u_2^{max})^T$, $u^2 = -u^4 = (u_1^{min}, u_2^{max})^T$. Then equation (21) (with higher order terms being truncated) is satisfied with $x^0 \approx (0.0152, -0.0058)^T$ and $\tau_j = 0.1$. The corresponding trajectory $x(t)$ of system (1), (6), (10) is presented in Fig. 1. The cost $J = \frac{1}{t_f}\int_0^{t_f} x_1(t)dt \approx -0.038$ is also negative in this case, which confirms the performance improvement with respect to the steady-state solution.

Note that the first coordinate of $\bar{x}$ in (22) provides a representation of the cost J for small values of τ_1 and τ_2. Hence, for future work, we plan to extend these analytical results for

estimating the optimal phase shift in the reactor model with two periodic inputs. Another direction for future development is related to the problems of stability and orbital stability of the proposed periodic trajectories for justifying possible implementations of our approach.

References

[1] Douglas, J. M. Periodic reactor operation. *I & EC Process Design and Development 6* (1967), 43–48.

[2] Lamnabhi-Lagarrigue, F. Volterra and Fliess series expansions for nonlinear systems. In *The Control Handbook, 2nd Ed.*, W. S. Levine, Ed. CRC Press, 2011, pp. 40–1 – 40–18.

[3] Nijmeijer, H., and van der Schaft, A. *Nonlinear Dynamical Control Systems*. Springer, New York, 1990.

[4] Nikolić, D., and Petkovska, M. Evaluation of performance of periodically operated reactors for single input modulations of general waveforms. *Chemie Ingenieur Technik 88* (2016), 1715–1722.

[5] Nikolić, D., Seidel-Morgenstern, A., and Petkovska, M. Nonlinear frequency response analysis of forced periodic operation of non-isothermal CSTR with simultaneous modulation of inlet concentration and inlet temperature. *Chemical Engineering Science 137* (2015), 40–58.

[6] Schmitendorf, W. E. Pontryagin's principle for problems with isoperimetric constraints and for problems with inequality terminal constraints. *Journal of Optimization Theory and Applications 18* (1976), 561–567.

[7] Zuyev, A. Exponential stabilization of nonholonomic systems by means of oscillating controls. *SIAM Journal on Control and Optimization 54* (2016), 1678–1696.

[8] Zuyev, A., Seidel-Morgenstern, A., and Benner, P. An isoperimetric optimal control problem for a non-isothermal chemical reactor with periodic inputs. *Chemical Engineering Science 161* (2017), 206–214.

Peter Benner, Prof. Dr.: Max Planck Institute for Dynamics of Complex Technical Systems, Computational Methods in Systems and Control Theory Group, Sandtorstraße 1, 39106 Magdeburg, Germany (*benner@mpi-magdeburg.mpg.de*).

Andreas Seidel-Morgenstern, Prof. Dr.: Max Planck Institute for Dynamics of Complex Technical Systems, Physical and Chemical Foundations of Process Engineering Group, Sandtorstraße 1, 39106 Magdeburg, Germany (*seidel@mpi-magdeburg.mpg.de*).

Alexander Zuyev, Prof. Dr.: Max Planck Institute for Dynamics of Complex Technical Systems, Computational Methods in Systems and Control Theory Group, Sandtorstraße 1, 39106 Magdeburg, Germany (*zuyev@mpi-magdeburg.mpg.de*). The author gave a presentation of this paper during one of the conference sessions.

Nonlinear quantum systems

Björn Birnir

Abstract: We model the dynamics of electrons in doped quantum wells driven by terahertz radiation and a superlattice biased by a dc voltage. We compute coherent, self-consistent electron states, density matrix equations of motion, and dipole absorption spectra. The model simultaneously accounts for intersubband transitions and many nonlinear phenomena that have been observed in these systems. We predict a bistable response for strong terahertz fields and bifurcations to coherent time-periodic quantum states. These bifurcation include, period-doubling bifurcations, producing a subharmonic response, Hopf bifurcations producing an incommensurate frequency response, and a cascade of period doubling bifurcations to a strange attractor. These bifurcation have been difficult to measure in single quantum wells. Therefore we design superlattice heterostructures of quantum wells where these bifurcations occur and are easier to measure.

1. Introduction

Quantum wells are fabricated (or 'grown') from semiconductors by depositing a thin layer of one material, such as gallium arsenide *GaAs*, onto a substrate of a different material, such as aluminum gallium arsenide *AlGaAs*, followed by another layer of substrate material, so that a type of 'sandwich' geometry called a heterostructure is formed. The defining property of quantum wells is that the middle layer has a significantly smaller band gap than the substrate layers, and has thickness of the same order as the de Broglie wavelength of the electron. This causes an electron occupying the conduction band of the middle layer to be confined to move freely in only two dimensions, while motion in the third dimension is only possible via transitions between quantized energy levels, called 'subbands', see Figure 1. These wells can be populated by a density of electrons by a process called doping and this makes them ideal quantum systems for the study of nonlinear effects.

The success of nonlinear dynamical systems theory in the late 20th century, see Guckenheimer and Holmes [23], and its application in the sciences and engineering, see for example Birnir [8], lead to the conjecture that similar phenomena could be found in quantum systems. In semi-classical systems nonlinear dynamics and bifurcations of coherent solutions (solitons) have been shown to exist [7, 9, 22, 30], so it is not unreasonable to expect nonlinearity in some quantum systems far from the semi-classical limit. In the late 1990s and early 2000s, Galdrikian, Batista, Birnir et al. [5, 6, 20] studied intersubband transitions of doped quantum wells. They developed computational methods for determining the coherent states of the electron gas in an oscillating external electric field. It was found that the density matrix

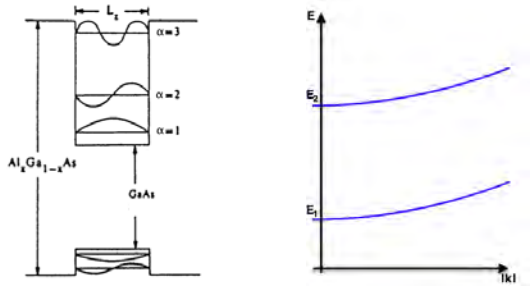

Figure 1. Left: The conduction and valance band for a semiconductor heterostructure, showing several 'bare' electron and hole subbands (states). Right: The parabolic subbands of the energies $E_{k_x k_y \alpha}$ of the envelope wavefunctions ξ_α.

equations of motion were nonlinear due to the interactions of the electron gas and that these nonlinearities could be enhanced by fabricating quantum wells with certain asymmetries, so that the lowest-lying subband levels were close to one another in energy. For sufficiently nonlinear wells, it was predicted that the wells would exhibit a bistable response as the terahertz power of the electric field (laser) was ramped up and then down. For strong enough terahertz fields, period-doubling bifurcations leading to a period-doubling cascade were predicted. Galdrikian, Batista, Birnir et al. [5, 6, 20] developed this nonlinear theory of semiconductor quantum wells, typically made out of $GaAs$ and $Al_z Ga_{1-z} As$ and populated by the technique of doping, where material providing electrons is deposited close to the well structure, see Heyman et al. [24, 25]. The nonlinearity was introduced through the Hartree and Hartree-Fock local density approximation where a system of n-interacting electrons is replaced by a system of n-noninteracting electrons in a different (Hartree) potential. This latter view leads to the quantum mechanical system of coherent electron states. These states satisfy a Schrödinger equation where the potential depends on several parameters and when these parameters change the coherent electron states can bifurcate.

2. The local density approximation

We now briefly describe the steps involved in obtaining the nonlinear quantum system describing the coherent electron states and their bifurcations. It is possible to add donor-type dopants at the interfaces of the middle layer with the substrate layers, so that a two-dimensional electron gas will occupy the well. In order to describe such a system theoretically, we take advantage of the fact that all the materials involved exhibit a periodic crystal lattice structure, which constrains the allowed electronic states and leads to a set of semiconductor Bloch equations. Assuming that the electron gas is not too dense, we make an effective mass approximation and work with a simplified model that will be discussed below.

The starting point is the Heisenberg equation for the electron operator

$$i\hbar\frac{\partial\psi}{\partial t} = [\psi, H].$$

Let the x- and z-coordinates parameterize the lateral and growth directions of the heterostructure, respectively. Here x is a two-dimensional coordinate parameterizing both the direction of lateral and the transverse direction. Since the wavelength of the laser drive is much longer than the width of the quantum well, the vertical field will be coupled to the electrons in the active region with the dipole approximation. In the effective mass approximation, the mean field Hamiltonian including the vertical field Fz (which falls off rapidly outside the active region) is

$$H(t) = \int \psi^\dagger(x,z,t)[\frac{\hbar^2}{2m}\nabla^2 + v(x,z) + w(x,z,t) - ezF(x,t)]\psi(x,z,t)\, d^2x dz,$$

where v and w are the time-independent and time-dependent parts of the electric potential, respectively, e is the electron charge and m is the effective mass. The electric potential is coupled to the electron density n by Poisson's equation

$$\nabla^2[v(x,z) + w(x,z,t)] = -\frac{e}{\varepsilon}n(x,z,t), \quad \text{where} \quad n(x,z,t) = \langle\psi^\dagger(x,z,t)\psi(x,z,t)\rangle,$$

is the electron density. The electron operator is expressed as

$$\psi(x,z,t) = \sum_\alpha \int e^{ik\cdot x}\xi_\alpha(z)a_{k\alpha}(t)\,\frac{d^2k}{2\pi} \tag{1}$$

where the envelope wavefunctions $\xi_\alpha(z)$ form a complete orthonormal basis. If the active region is filled and the bias voltage is zero (i.e. the electron density is uniform), then the self-consistent envelope wavefunctions may be calculated in the same manner as in Galdrikian, Batista and Birnir [5, 6, 20].

3. Homogeneous quantum wells

The theory of homogenous quantum wells with the local density approximation consists of the following steps. We discretize the integral in Equation (1) and write the electron operator as

$$\psi(x,y,z) = A^{-1/2}\sum_{k_x,k_y,\alpha} a_{k_xk_y\alpha}\, e^{ik\cdot x}\,\xi_\alpha(z),$$

where A is a constant. The envelope wavefunctions obey the time-independent Schrodinger equation

$$\left\{-\frac{\hbar^2}{2m}\frac{\partial^2}{\partial z^2} + v(z)\right\}\xi_\alpha(z) = E_\alpha\xi_\alpha(z), \quad E_{k_xk_y\alpha} = \frac{\hbar^2}{2m}(k_x^2+k_y^2) + E_\alpha, \tag{2}$$

with the energies lying in parabolic subbands see Figure 1. The envelope wave functions satisfy vanishing boundary conditions at the sides of the well, which is a good proxy for a vanishing boundary conditions at $z = \pm\infty$, see [6, 20]. The self-consistent potential is determined by Poisson equation

$$\frac{\partial^2}{\partial z^2}v(z) = -\frac{e^2}{\varepsilon}n(z). \tag{3}$$

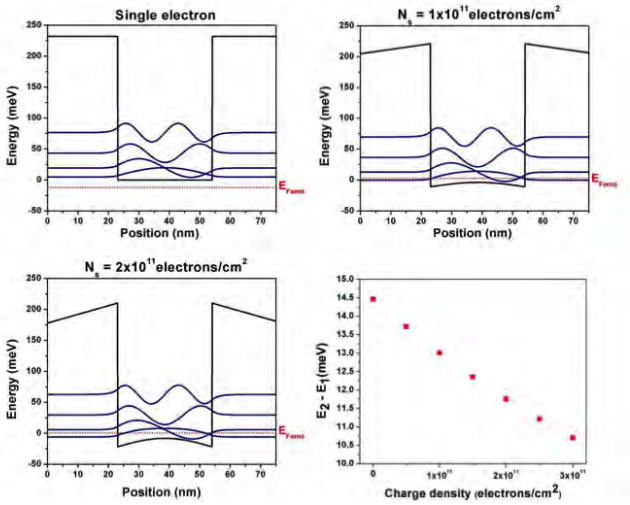

Figure 2. The first few energy states, the shape of the potential and the Fermi energy for different doping levels and the energy difference $E_2 - E_1$ between the first and second state as a function of the charge density.

The local density (or Hartree) approximation is implemented by use of the partition function that yields the relationship between the chemical potential μ, sheet density N_s and subband energies E_α, giving the thermal weights w_α

$$N_s = \frac{m}{\pi\hbar^2\beta}\sum_\alpha \log\left\{1 + e^{-\beta(E_\alpha - \mu)}\right\} \equiv \frac{m}{\pi\hbar^2\beta}\sum_\alpha w_\alpha,$$

where $\beta = 1/T$, T being temperature. Then the electron density can be expressed as

$$n(z) = \sum_\alpha w_\alpha |\xi_\alpha(z)|^2. \tag{4}$$

4. The Hartree iteration

The potential v is determined by a Hartree iteration:

1. Solve Schrödinger equation (2) for $\{\xi_\alpha(z), E_\alpha\}$. 2. Determine $\{\mu, w_\alpha\}$ from $\{N_s, E_\alpha\}$ and update $n(z)$ in (4). 3. Solve Poisson's equation and update $v(z)$ in (3). 4. Repeat until the iteration has converged.

Figure 2, shows the first few energy states, the shape of the potential and the Fermi energy for different doping levels and the energy difference between the first and second state as a function of the charge density.

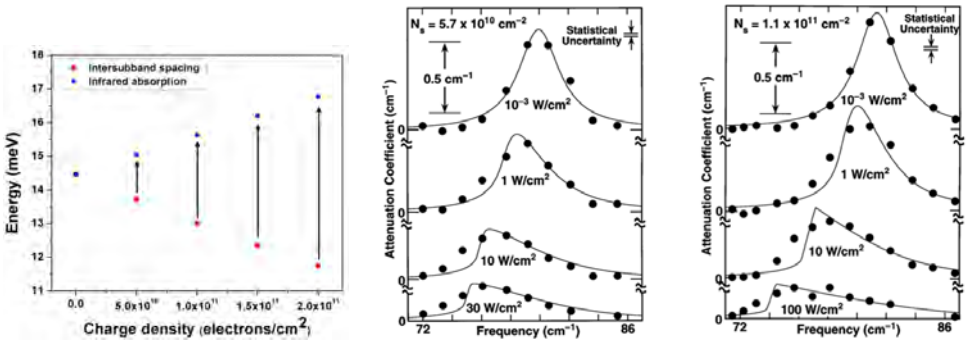

Figure 3. The absorption frequency. The leftmost picture shows the intersubband spacing (Stark shift) and infrared absorption due to the depolarization shift, as a function of the charge density. The second and third picture show that with fixed electron (doping) density the absorption peak shifts and changes form with the amplitude of the incoming radiation. The blue shift between the two leftmost figures is the depolarization shift.

5. Intersubband absorption

The nonlinear effects due to the electron density in the quantum wells have been understood and measured since the mid 1990s. The intersubband absorption when the quantum well is illuminated by an auxiliary laser, can be simulated and measured. The simulations were developed by Zalużny [40, 41] and the experiments were done by Craig et al. [16]. The incoming radiation first builds up a charge in the quantum well, this is a Stark effect and corresponds to a redshift of the absorption frequency. However, as the incoming radiation increases the electrons in the well shield against it, this is called the depolarization shift and is a blue shift. Eventually, the depolarization shift dominates, see Figure 3. One can also measure the relaxation times for the densities in the quantum well, namely Γ_1; the depopulation rate and Γ_2; the depolarization rate. This was also done by Craig et al. [16].

6. Time-dependent local density approximation

The driving of the quantum wells with time-periodic laser fields requires the development of the time dependent version of above theory. The laser field is added to the Hamiltonian in the electric dipole approximation, this works well since the wavelength of the laser is large compared to width of the well. The intersubband absorption now occurs by collective oscillations of electrons occupying the well and the resonance is broadened and shifted away from intersubband spacing (This is the depolarization shift discussed above). Using the time-dependent Hartree (local density) approximation, we calculate the self-consistent fluctuations due to time-periodic driving term. The time-dependent electric field $zF(t)$

now induces self-consistent fluctuations in potential $\delta v(z,t)$ and electron density $\delta n(z,t)$

$$\tilde{H}(t) = H - ezF(t) + \delta v(z,t); \qquad \frac{\partial^2}{\partial z^2}\delta v(z,t) = -\frac{e^2}{\varepsilon}\delta n(z,t).$$

These satisfy a Poisson equation with a self-consistency condition: $v(z,t) = v(z) + \delta v(z,t)$. $n(z,t) = n(z) + \delta n(z,t)$. Then we can find a Liouville-von Neumann equation

$$\frac{\partial \rho(z,z',t)}{\partial t} = -\frac{i}{\hbar}[\tilde{H}(t), \rho(z,z',t)] - R[\rho(z,z',t)],$$

for the density matrix ρ, where R is the relaxation operator. In the final quantum mechanical dynamical system, in 4 complex dimension, R is determined by the experimentally measured depolarization rate Γ_1 and decorrelation rate Γ_2, discussed above.

The time-dependent potential is determined by a time-dependent Hartree iteration:
1. Evolve $\rho(z,z',t)$ until a periodic response is reached. 2. Compute the electron density by the formula $n(z,t) = \rho(z,z',t)|_{z'=z}$. 3. Solve Poisson's equation and update $\delta v(z,t)$. 4. Repeat until converged.

7. Nonlinear phenomena in assymmetric quantum wells

Nonlinear bifurcation of the time-periodic coherent electron states were explored by the theory above. In 1996 Galdrikian and Birnir [20] found the period-doubling bifurcation of these states. In 2003 Batista and Birnir [5] found the Hopf bifurcation. These bifurcations were found in simulations of the above model and simulations showed the period-doubling cascade to the (Feigenbaum) strange attractor in first case [20] and the quasi-periodic cascade to another strange attractor in the second case [6]. We illustrate both of these in Figure 4, taken form Batista and Birnir [5]. We sample the normalized dipole momentum $< \mu > /\mu_{10}$, $\mu = zF$ above, onto the two pertinent complex valued states, in Figure 4, μ_{10} is a normalization. The first column in Figure 4 is the time series of this sample. It shows if there is a simple oscillation present or if there are more oscillations superimposed. The pattern in the third row is called beating. The second column is the phase portrait, the basic mode is plotted against its derivative. Both must be sampled at the same (spatial) point. The third column is the Poincaré map, again the mode and its derivative are sampled, but now only at each period T. This is also called the stroboscopic map. A circle on the second column turns into a point in the Poincaré map. Finally the fourth column is the power spectrum or the absolute value of the Fourier transform of the solution. The fundamental frequency $\omega = 2\pi/T$ shows up as the biggest peak. Superharmonics are smaller peaks at integer valued multiples $n\omega$ of the fundamental frequency. In the first row, we see a periodic orbit, with the fundamental frequency and one superharmonic on the power spectrum. The second row shows a period doubling, we see a periodic orbit with twice the period $2T$, this is now a simple periodic orbit (two dots) on the Poincaré map in the third column, and the power spectrum now has a peak at half

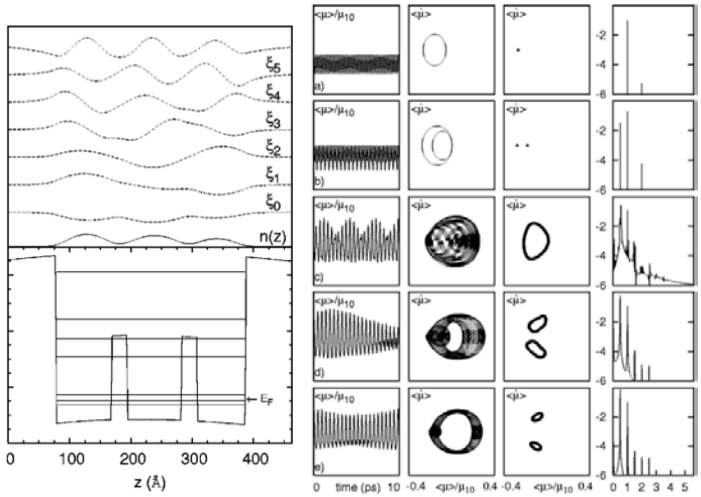

Figure 4. Left: The asymmetric quantum well with two barriers; bottom, the corresponding eigenstates, top. Right: Time series, phase portrait, Poincaré map and power spectrum.

the frequency $\omega/2$. On the third row, we see a Hopf bifurcation in the Poincaré map, that means that we now have a torus in the phase space. The Poincaré map is a cross section (cut) of this torus. The orbits are quasi-periodic and fill the surface of the torus. On the power spectrum we now see a new incommensurate frequency, smaller than the fundamental frequency. Then on the fourth row we see the torus period double. On the fifth row the doubled torus deforms.

8. Semiconductor Superlattices

The observation of Bloch oscillations in semiconductor superlattices (SSLs) [31] has led to many proposed applications of these heterostructures as sources and detectors at gigahertz and terahertz frequencies. More recently, nonlinear Gunn oscillations and chaotic dynamics have been observed in SSLs in the sequential tunneling regime. These nonlinear phenomena present the opportunity for development of new applications of SSLs, such as true random number generators and frequency mixers. Furthermore, recent advances in the design of SSLs have opened the possibility of realizing these applications at room temperature. In support of the development of applications of SSLs in the nonlinear regime, we theoretically characterize the nonlinear dynamical phenomena of the sequential resonant tunneling (SRT) model of weakly-coupled SSLs in this paper. We show the effects on the bifurcation diagram from variations of the number of periods making up superlattice, the sensitivity of the SRT model to time-dependent stochastic fluctuations in the bias voltage and local tunneling rates, and the effect of time-independent random perturbations of the widths of the wells and barriers. This and the next three sections follow [18].

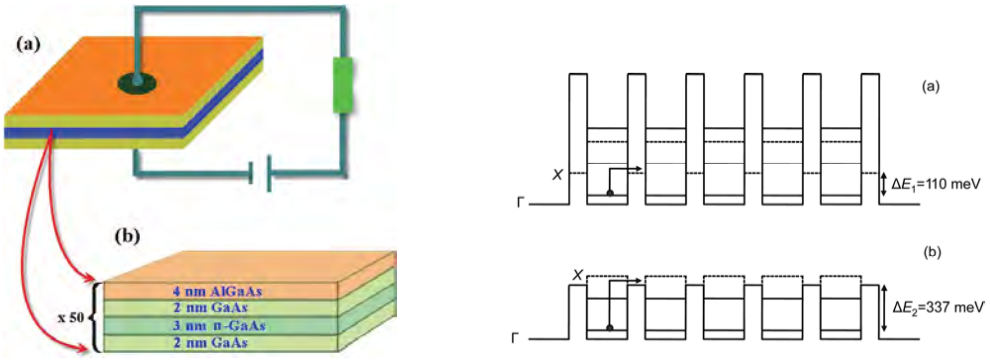

Figure 5. Left: Schematic diagram of a dc voltage-biased SSL, from Bonilla et al. [11]. Right: The band diagram of a GaAs/$Al_{0.7}Ga_{0.3}As$ SSL (a) and GaAs/$Al_{0.45}Ga_{0.55}As$ SSL (b), from Y. Huang et al. [32]. The conduction band and the bound states of the wells are indicated by the solid horizontal lines. The bottom of the X-valley is indicated by the dashed lines.

Spontaneous oscillations, quasiperiodic orbits, and chaos have already been observed experimentally at very low temperatures [29, 31, 39] and at room temperature [26–28, 32, 35] in 50-period SSLs with noisy voltage sources. Simulations by M. Alvaro, M. Carretero, and L. Bonilla [1] exhibited a strong chaotic signal. Experiments by Huang *et al.* [26, 27] show that heating supresses the nonlinear phenomena in SSLs, and we suspect this also occurs in single QWs. Huang *et al.* also describe a way of suppressing the effect of heating, enhancing the current oscillations: It was hypothesized that at warm temperatures, phonon-assisted transport though the X-valley of AlAs allowed a thermal distribution of carriers to diffuse through the SSL, overwhelming the nonlinear quantum dynamics. This effect was supressed by choosing the Aluminum concentration of GaAs/AlGaAs wells in order to maximize the lowest bandgap energy, i.e. make the X and Γ band gaps equal to one another (Figure 6). As a result, current oscillations were observed in SSLs at room temperature for the first time, see [26, 27].

We consider the SRT theory of Bonilla *et al.*, which describes the electronic dynamics of SSLs in the weakly-coupled, self-consistent regime [15]. Two different time scales are taken into account in this description of SSLs. The inter-site tunneling and inter-subband relaxation processes occur on much shorter timescales than the dielectric relaxation processes [11]. Therefore, the long timescale dynamics of semiconductor lasers [37] and superlattices [1, 14] are typically modeled using semiclassical equations, while the short timescale processes are treated separately as noise. In the case of the SRT model, the short-timescale processes are included through the addition of stochastic terms to the dynamical equations. Nonlinearities enter the model via the inter-site Coulomb interaction, which bends the conduction band of the SSL, modifying the inter-band tunneling rates by casting the energy levels of adjacent wells into or out of resonance [11]. The dynamical equations are discussed in detail in [18, 36].

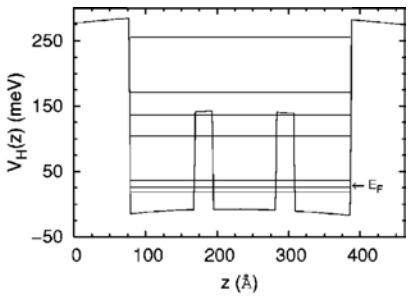

Figure 6. The stationary self-consistent potential resulting from the band structure and Coulomb potential of the assymetric GaAs/AlGaAs quantum well, taken from Batista et al. [6]. The energy levels of the bound states are indicated by the horizontal lines.

The bias voltage, V_{bias}, is treated as an external parameter of the model. Gunn-like oscillations in $J(t)$ are found to occur in the SRT model over several intervals of V_{bias} [10,17]. These oscillations undergo a series of bifurcations, which may cascade into chaotic behavior [1]. In [36], we characterized the route to chaos via analysis of the Poincaré map and power spectrum, and distinguished the effects of the noise terms from the deterministic chaos.

For sufficiently small bias voltages, the total current $J(t)$ through the SSL responds linearly to changes in the bias voltage. At higher bias voltages, $J(t)$ suddenly transitions to a time-dependent, oscillatory function, which passes through a further series of transitions leading to chaotic behavior. We summarize the behavior of $J(t)$ below:

Fixed-point: Over certain voltage intervals, $J(t)$ is attracted toward a stationary value.

Bistability: The first signal of the nonlinear dynamics is a bistable response of $J(t)$ to slow variations in V_{bias}. This behavior is observable only at sufficiently low temperatures [10,17]. Generically, bistable behavior is found at voltages near the Hopf bifurcation described below.

Supercritical Hopf Bifurcation: As the bias voltage is increased, we next observe a supercritical Hopf bifurcation. The fixed point becomes unstable, and $J(t)$ evolves to a periodic orbit. The periodic orbit is topologically equivalent to a circle in phase space, which corresponds to a one-cycle of the Poincaré map. In this regime, the SSL acts as a GHz oscillator with a discrete power spectrum involving the frequencies $f_n = n/T,\ n = 1,2,3,...$, where T is the period of the lowest-frequency oscillation present. The superharmonics $n > 1$ arise due to the nonlinearities present in the SRT model. In this dynamical phase, the fundamental period T varies smoothly with the bias voltage, therefore the oscillator is also *tunable*. By filtering out all but the desired harmonic and fine-tuning it via the bias voltage, a wide range of frequences may be selected.

Period Doubling Bifurcation: In this regime, one-cycles of the Poincaré map transition to two-cycles. The fundamental period of the oscillator is doubled, $T \to 2T$, and the fundamental frequency is cut in

half: $\omega \to \omega/2$. A new frequency peak will appear in the spectrum at half the fundamental frequency, and the number of superharmonics will double. Following a period doubling bifurcation, the reverse (period-halving) bifurcation may occur. We refer to the regions between these bifurcations as *period doubling bubbles*. An application of period doubling, due to the subharmonic peak, is that a signal may be read at lower frequency, where the noise may be reduced, and it can be used to make squeezed states [21].

Period Doubling Cascade: Period doubling may occur in succession over certain voltage intervals, and an infinite number of doublings is possible in a finite voltage range. The invariant phase space structures transition from compact manifolds (periodic orbits of high periods) to chaotic attractors. The Poincaré map takes on a fractal structure. Our simulations show that the SRT model does not support true quasiperiodic orbits, hence the chaotic attractor is the most complex structure in the bifurcation diagram. It is the result of a cascade of a period doubling sequence of periodic orbits. An application of the chaotic dynamics in this regime is ultrafast generation of random number sequences [32]. This has many applications in areas such as secure communication and data storage, stochastic modeling, and Monte Carlo simulations, see [4, 19, 34, 38]. Previously the generation of ultrafast random number sequences has been accomplished by fast semiconductor lasers but these require a mixture of optical and electronic components. SSLs on the other hand are entirely submicron devices that can be readily integrated into complex circuits.

In previous theoretical studies of optically-driven quantum wells, it was discovered that the introduction of one or more off-center "steps" in the confinement potential, see Figure 7, had a profound impact on the character of the nonlinear phenomena. In the presence of a single step, a period-doubling bifurcation in the electronic response was predicted to occur near the intersubband resonant frequency at high doping densities and strong driving fields. The presence of a second step unfolded the period-doubling bifurcation into a supercritical Hopf bifurcation which generated quasiperiodic behavior. Both single- and double-stepped assymetric quantum wells also exhibited period-doubling cascades to chaos. In analogy with these results, we consider the possibility of unfolding the period doubling bifurcation of the SRT model into a Hopf bifurcation, by breaking the periodic symmetry of the SSL, which we term "disordered superlattice."

The model for the superlattice is a quasi-one-dimensional resonant sequential tunneling model of nonlinear charge transport in SSLs [12, 14, 15]. We use the formulation in [18, 36].

9. Results

We simulate superlattices and characterize the dynamical instabilities that may be applied to create sources, period halvers and squeezers, random sequence generators and frequency mixers, even at room temperature. The dynamical equations in [18, 36] are evolved using the parameter values listed in Table 1 in [36] for a GaAs/$Al_{0.7}Ga_{0.3}$As SSL, with the quantized energy levels corresponding to $V_{barr} = 600$

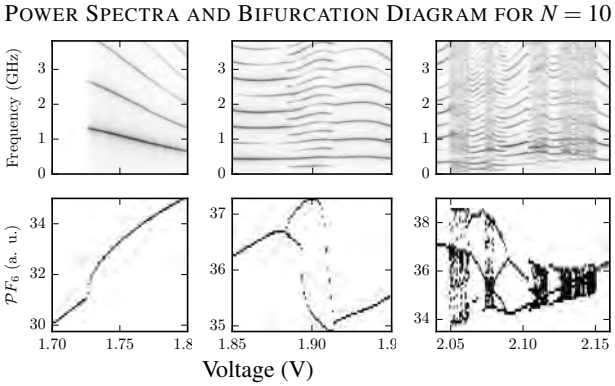

Figure 7. (Top row) The power spectrum of $J(t)$ plotted against the bias voltage, taken from [36]. (Bottom row) The bifurcation diagram, plotting the Poincaré map against the bias voltage. The Hopf bifurcation from the steady state is shown in the first column. A period doubling "bubble" is shown in the second column. A period-doubling cascade is shown in the third column

meV. The GaAs/$Al_{0.7}Ga_{0.3}$As SSL is treated here in order to illustrate bifurcations as clearly as possible, but the same phenomena and instabilities occur in $Al_{0.45}Ga_{0.55}$As SSLs [18]. Dynamical instabilities are found in two distinct *plateaus*, over which which the local electric fields of the SSL cease to increase monotonically as a function of V_{bias}. The *first plateau* occurs at very low voltages, with tunneling transport between the ground states of adjacent wells that are nearly aligned with one another in energy. The *second plateau* occurs in the region of V_{bias} where the the electric fields bend the potential of the SSL to align the ground state of well i with first excited state of well $i+1$. We do not observe a third plateau because the third excited state becomes unbound at bias voltages that align it with the first excited state of an adjacent well.

The leading edge, i.e. the lowest value of V_{bias} contained in a plateau, is identified by a supercritical Hopf bifurcation from fixed point to periodic orbit, as shown the leftmost column of Figure 8. At low temperatures, the Hopf bifurcation may be preceded by bistability, but at higher temperatures this phenomenon is supressed. Within a plateau, we may observe period-doubling, period-doubling cascades, and chaotic attractors whose locations depend upon on the values of the rest of the parameters, in particular N, the number of wells making up the superlattice. As a general rule, shorter superlattices exhibit a greater variety of dynamical behavior in the second plateau. In SSLs ($N \leq 10$), the Hopf bifurcation in the first plateau disappears and the first plateau is not present. As N increases, the dynamical instabilities appear to move from the second plateau into the first plateau: Near $N = 20$, the Hopf bifurcation appears in the first plateau. In longer SSLs ($N \geq 30$), the second plateau contains only a supercritical Hopf bifurcation to a periodic orbit without any further bifurcations, while the first plateau has gained a period-doubling bubble. In this section, we give a detailed description of the dynamical instabilities

of $N = 10$ SSLs, then we point out the effect of increasing N. We close with a discussion of the effects of stochastic terms and disorder on the dynamical instabilities.

9.1. N=10

As mentioned above, the first plateau does not exist for $N = 10$, and all oscillatory behavior takes place in the second plateau. Combining the bifurcation diagram, power spectra and phase portraits shown in Figures 8 and 9, we characterize the dynamical instabilities of the SRT model for $N = 10$:

Supercritical Hopf Bifurcation: In the leftmost column of Figure 8, we observe a transition from a stationary state to a periodic orbit. Subsequently, we observe a circle in the phase portrait, similar to the top row of Figure 9. The Poincaré map consists of a single point, or one-cycle, when visualized. The power spectrum contains peaks falling at integer multiples of a fundamental oscillation frequency as demonstrated in the top row of Figure 8. In this regime, the SSL acts as a GHz oscillator with a discrete power spectrum involving the frequencies $f_n = n/T,\ n = 1,2,3,...$, where T is the period of the lowest-frequency oscillation. The superharmonics $n > 1$ arise due to nonlinearities of the SRT model. We also observe that the fundamental frequency and resulting superharmonics can be continuously tuned by variation of V_{bias} as demonstrated in Figures 8.

Period Doubling Bifurcation: A period-doubling bifurcation is identified by a doubling of the orbits in phase space and consequent doubling of the number of points in the Poincaré map. We illustrate this phenomena in the transition between rows one and two of Figure 8 and in the second row of Figure 9. The power spectrum gains a *subharmonic* peak at half of the former fundamental frequency, and consequently we observe twice as many superharmonics in the power spectrum. A period-doubling bifurcation may be followed by a period-halving bifurcation forming a period-doubling bubble as shown in the second column of Figure 8.

Period Doubling Cascade: A period doubling cascade is identified when many period-doubling bifurcations occur in rapid succession over some interval of the bias voltage. In principle, an infinite number of doublings may occur over a finite voltage interval. This process terminates when the phase space orbits lose their periodicity altogether and the Poincaré map takes on the characteristics of a chaotic attractor. An example of a period-doubling cascade is illustrated in the last three rows of Figure 9. The rightmost column of Figure 8 also shows several period-doubling cascades connected by regions of orbits with very high periods. The broadening and merging of peaks in the power spectrum is characteristic of a chaotic attractor. We also compute the Feigenbaum constant of the cascade near 2.109 Volts, shown in Figures 8 and 9. We introduce the formula

$$\delta_n = \frac{V_{n-1} - V_{n-2}}{V_n - V_{n-1}}, \tag{5}$$

where V_n are the voltages corresponding to the nth doubling in the cascade. For a period-doubling cascade, $\delta_n \to 4.6692\ldots$ as $n \to \infty$. By taking sufficiently small steps (about 10^{-6} Volts) in the parameter

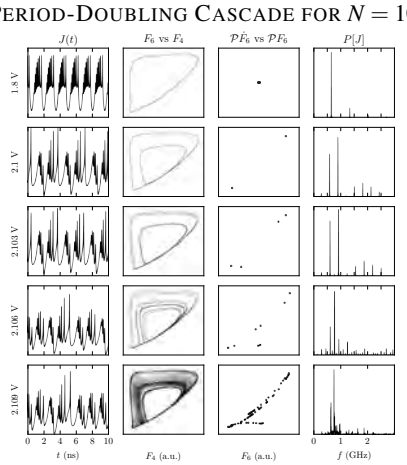

Figure 8. Representative phase portraits, taken from [36]. The first column shows the average current J plotted against time t. The second column shows the phase portrait $F_6(t)$ plotted against $F_4(t)$. The third column shows the Poincaré map $\mathscr{P}\dot{F}_6(t^*)$ plotted against $\mathscr{P}F_6(t^*)$. The last column shows the power spectrum of $J(t)$. A periodic oscillation is shown in the first row. A period-doubling bifurcation is observed in the second row. The period-doubling cascade to a chaotic attractor is shown in the bottom four rows.

V_{bias}, we have measured the first Feigenbaum constant with less than 1% error. We conclude that the route to chaos in the SRT model is a period-doubling cascade.

9.2. $N > 10$

We next describe the effects of increasing number of periods making up the SSL, keeping all other parameters fixed. In the case of $N = 20$, both the first and second plateaus are present. The supercritical Hopf bifurcation corresponding to the beginning of the first plateau is shown in the first column of Figure 10. No other bifurcations are observed in the first plateau. The onset of the second plateau is shown in the second column of Figure 10. In the second plateau, we again find period doubling cascades to chaotic attractors; this behavior is illustrated in the third column of Figure 10. Comparing the third columns of Figures 10 and 8, we observe that the period-doubling cascade and the chaotic attractor occur over narrower voltage intervals in the $N = 20$ case compared with the $N = 10$ case. For higher values of N, the voltage intervals containing the period doubling bifurcations become increasingly narrow, and eventually disappear entirely from the second plateau near $N = 30$.

As N is increased, we observe the appearance of more dynamical instabilities in the first plateau. A period-doubling bubble emerges in the first plateau near $N = 25$ and subsequently widens over a larger interval of V_{bias} with increasing N. This bubble is responsible for the period-two orbit illustrated in the

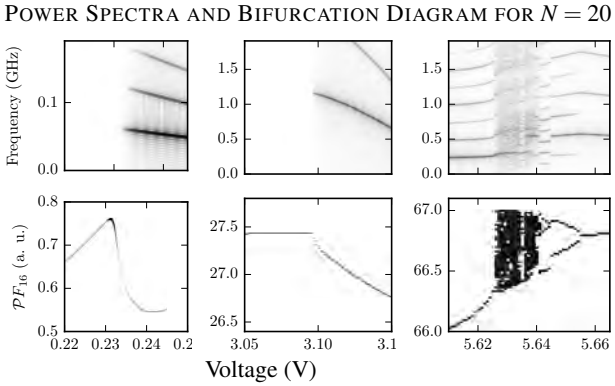

Figure 9. (Top row) The power spectrum of $J(t)$ plotted against the bias voltage. (Bottom row) The bifurcation diagram, plotting the Poincaré map against the bias voltage. The Hopf bifurcation from the steady state in the first plateau is shown in the first column. The Hopf bifurcation from the steady state in the second plateau is shown in the second column. A narrow region in the second plateau containing a chaotic attractor is shown in the third column.

top panel of Figure 12 for the case of $N = 50$. There are no further period-doubling bifurcations present in the first plateau for this value of N. For $N = 100$, simulations by Amann *et al.* showed chaotic dynamics occur in the first plateau [2]. This result fits with the trend of dynamical instabilities moving from the second plateau to the first plateau as N increases.

9.3. Noise

We next consider the effects of the stochastic terms in equations (8) and (9) in [18], which model the effects of a noisy voltage souce and intrinsically random tunneling processes. We observe that the dynamics become increasingly sensitive to noise with increasing N. For the case of $N = 10$, regions of interest in the bifurcation diagram are plotted in Figure 11. We have chosen these voltage intervals to be the same as in Figure 8 for clear comparison. We observe that the addition of noise stimulates the Hopf bifurcation to occur at lower voltages, which widens the second plateau. Noise also has the effect of broadening the peaks in the power spectrum as shown in the first row of Figure 11.

Upon perturbation by noise, period-doubling behavior may be enhanced and higher period orbits may occur over a particular window of V_{bias} than do in the noise-free case, see Figure 12. demonstrates the effect of very small perturbations by noise on the phase portrait over the window containing the period-doubling bubble, which occurs in the first plateau for the $N = 50$ case. For higher-period orbits, the broadening effect of perturbations on the power spectrum can cause the narrowly spaced peaks in the spectrum to merge, transforming high-period orbits to chaotic attractors as demonstrated in Figure 11. This effect may broaden the windows in which chaotic attractors occur, connecting chaotic attractors

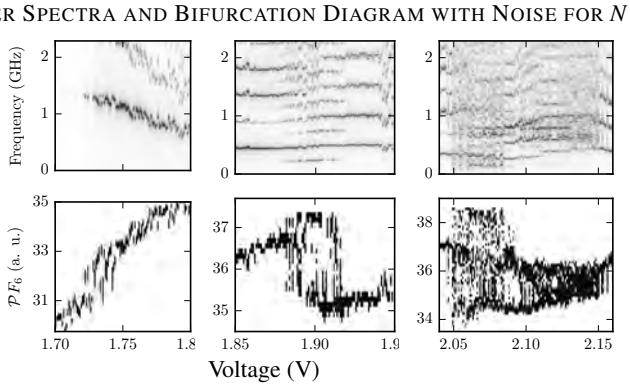

Figure 10. (Top row) The power spectrum of $J(t)$ plotted against the bias voltage. (Bottom row) The bifurcation diagram, plotting the Poincaré map against the bias voltage. The Hopf bifurcation from the steady state is shown in the first column. A period doubling bubble is shown in the second column. A period-doubling cascade is shown in the third column. $\sigma_\eta = 1.4 \times 10^{-5}$V.

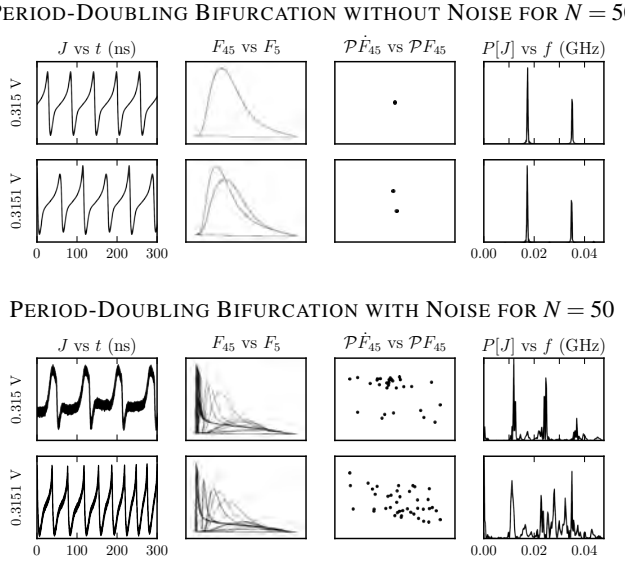

Figure 11. Period doubling with and without noise. $\sigma_\eta = 2.8 \times 10^{-6}$V

that are distinct in the noise-free limit as demonstrated by comparison of the chaotic regions in Figure 8 and Figure 11.

Periodic orbits in the first plateau for $N = 50$ are more sensitive to noise than those which occur in the second plateau for $N = 10$. This difference is evident upon comparison of Figure 11 with Figure 12, in particular the power spectra. We see similar results but have used much less noise to produce Figure 12 than Figure 11. The bottom panel of Figure 12 shows that the inclusion of noise terms may cause the Poincaré map and power spectrum to resemble those of a chaotic system. However, we simulate the same situation in the absence of noise in the top panel of Figure 12. While the SRT model is very sensitive to noise in this regime, the underlying dynamical structure is an orbit of period two, and hence our numerical methods are able discern between noise-sensitivity and true dynamical chaos.

10. Discussion

The connection that we are making between plasmon states in single quantum wells in the terahertz regime and density waves in superlattices in the gigahertz regime may seem to be a stretch. On the surface there are many differences between these systems. A superlattice of wells in the terahertz regime would be tightly coupled described by the equation in Section 3 with periodic boundary conditions, very different from the coupled equations in [18, 36] describing the sequential tunneling model in the gigahertz regime. The boundary conditions are obviously different but in both cases we have a qualitative description for a range of parameters involved. The striking similarity between these two system is that their qualitative behavior is in both cases governed by coherent electron states. In the former case these are the plasmons slushing back and forth in quantum well. In the latter case they are the density waves executing Gunn oscillations in the superlattice. In both cases these oscillations exhibit bifurcations with increase in parameters. In the first case with increase amplitude of the laser drive, in the second case the bifurcations take place with increased voltage bias. The bifurcating oscillations of the plasmons have been understood for a long time, but we have shown in [18,36] that the density wave form a coherent electron state extending through the superlattice and the oscillations of these states show the same bifurcations at the same values of the bias throughout the lattice. This is observed by taking different Poincaré sections for different lattice site. They turn out to be qualitatively the same for all the lattice sites. Thus we see coherent electron states exhibiting generic bifurcations in both cases. Both of these systems are genuine nonlinear quantum systems of coherent electron states and this makes them qualitatively similar in spite of the physical differences.

11. Conclusions

We have shown that the nonlinear bifurcations found by simulations in single quantum wells in the terahertz regime [5,6,20] also occur in semiconductor superlattices (SSLs) in the gigahertz range [2,3,13]. The only exception is the second Hopf bifurcation to quasi-periodic orbits on a torus, but this can pre-

sumably also be accomplished with the design of more structure in SSL. The advantage of experiments on SSLs in the gigahertz range is that the experiments can be conducted at room temperature and indeed a chaotic oscillator due to the random dressing of a period two-orbit has already been measured [26,27]. In [36] we have determined that the route to chaos for SSLs in the sequential tunneling regime is the period doubling cascade. Shorter (10-period) superlattices are observed to exhibit faster oscillations compared with longer (50-period) ones. Two plateaus are observed as functions of the voltage bias, and intrinsically chaotic dynamics on the second plateau are possible only for shorter SSLs, while the dynamics in the first plateau contain intrinsic chaos only for longer ($N > 50$) SSLs, see [18]. The robustness of these results to stochastic perturbations in the local tunneling currents and the bias voltage was tested in [18]. It was observed that shorter SSLs are much less sensitive to noise compared with longer SSLs. Therefore two modes of random number generation are possible: Faster, intrinsic chaos in the second plateau for shorter superlattices, and slower, noise-enhanced chaos in the first plateau for longer superlattices, see [18] for more details.

The effects of random variations in doping density and the width of the wells and the barriers was also examined in [18]. It was found that the period-doubling cascade is robust to these perturbations, but the detailed shape of the bifurcation diagram can change significantly. Then these perturbations cannot unfold the period-doubling bifurcation into a second Hopf bifurcation as we initially conjectured. They are simply not strong enough to break the reflection symmetry of the constituent wells. To observe the second Hopf bifurcation it is essential that this symmetry is broken analogous to the work of Batista and Birnir [5, 6], then two or more states would also exist below the Fermi level. We conjecture this greater number of active states will be successful at exposing the second Hopf bifurcation in a properly designed SSL. It remains an open question whether all of these bifurcations can be extended to SSLs in the terahertz regime. This would signify a nontrivial technological progress since terahertz devices are difficult to make and operate at room temperature. It these bifurcations are found in teraherz range the possibility of making all the devices discussed above opens up and such devices can be operated at signicantly faster time-scales.

Acknowledgments

This material is based upon work supported by, or in part by, the U. S. Army Research Laboratory and the U. S. Army Research Office under contract/grant number 444045-22682.

References

[1] ALVARO, M., CARRETERO, M., AND BONILLA, L. Noise-enhanced spontaneous chaos in semiconductor superlattices at room temperature. *EPL (Europhysics Letters) 107*, 3 (2014), 37002.

[2] AMANN, A., SCHLESNER, J., WACKER, A., AND SCHÖLL, E. Chaotic front dynamics in

semiconductor superlattices. *Phys. Rev. B 65* (2002), 193313.

[3] ANDO, T., FOWLER, A. B., AND STERN, F. Electronic properties of two-dimensional systems. *Reviews of Modern Physics 54*, 2 (1982), 437.

[4] ASMUSSEN, S., AND GLYNN, P. W. *Stochastic simulation: Algorithms and analysis*, vol. 57. Springer Science & Business Media, 2007.

[5] BATISTA, A. A., BIRNIR, B., TAMBORENEA, P., AND CITRIN, D. Period-doubling and hopf bifurcations in far-infrared driven quantum well intersubband transitions. *Physical Review B 68*, 3 (2003), 035307.

[6] BATISTA, A. A., TAMBORENEA, P. I., BIRNIR, B., SHERWIN, M., AND CITRIN, D. S. Nonlinear dynamics in far-infrared driven quantum-well intersubband transitions. *Physical Review B 66*, 3 (2002), 195325.

[7] BIRNIR, B. Chaotic perturbations of kdv equations: I. rational solutions. *Physica D: Nonlinear Phenomena 18*, 1 (1986), 464–466.

[8] BIRNIR, B. *Basic Attractors and Control*. To be published by Springer, New York, 2018.

[9] BIRNIR, B., AND GRAUER, R. An explicit description of the global attractor of the damped and driven sine-gordon equation. *Communications in mathematical physics 162*, 3 (1994), 539–590.

[10] BONILLA, L., ESCOBEDO, R., AND DELL'ACQUA, G. Voltage switching and domain relocation in semiconductor superlattices. *Physical Review B 73*, 11 (2006), 115341.

[11] BONILLA, L., PLATERO, G., AND SÁNCHEZ, D. Microscopic derivation of transport coefficients and boundary conditions in discrete drift-diffusion models of weakly coupled superlattices. *Physical Review B 62*, 4 (2000), 2786.

[12] BONILLA, L. L. Theory of nonlinear charge transport, wave propagation and self-oscillations in semiconductor superlattices. *Condensed Matter 14*, R341 (2002), 8644.

[13] BONILLA, L. L., GALÁN, J., CUESTA, J., MARTÍNEZ, F. C., AND MOLERA, J. M. Dynamics of electric field domains and oscillations of the photocurrent in a simple superlattice model. *Phys. Rev. B 50* (1994), 8644.

[14] BONILLA, L. L., AND GRAHN, H. T. Non-linear dynamics of semiconductor superlattices. *Reports on Progress in Physics 68*, 3 (2005), 577.

[15] BONILLA, L. L., AND TEITSWORTH, S. W. *Nonlinear wave methods for charge transport*. John Wiley & Sons, 2009.

[16] CRAIG, K., ET AL. Undressing a collective intersubband excitation in quantum well. *Phys. Rev. Lett. 76* (1996), 2382.

[17] DELL'ACQUA, G., BONILLA, L. L., AND ESCOBEDO, R. Hopf bifurcation in a superlattice model. *Proceedings of the International Conference on Computational and Mathematical Methods in Science and Engineering* (21–25 September 2006).

[18] ESSEN, J., RUIZ-GARCIA, M., JENKINS, I., CARRETERO, M., BONILLA, L., AND BIRNIR, B. Parameter dependence of high-frequency nonlinear oscillations and intrinsig chaos in short gaas/(al,ga)as superlattices. *(in submission)* (2017).

[19] G., G. R. *Principles of Digital Communication Cambridge*. University Press Cambridge, Cambridge, UK, 2008.

[20] GALDRIKIAN, B., AND BIRNIR, B. Period doubling and strange attractors in quantum wells. *Phys. Rev. Lett. 76* (1996), 3308.

[21] GRAHAM, R. Squeezing and frequency changes in harmonic oscillations. *Journal of Modern Optics 34*, 6-7 (1987), 873–879.

[22] GRAUER, R., AND BIRNIR, B. The center manifold and bifurcations of damped and driven sine-gordon breathers. *Physica D: Nonlinear Phenomena 56*, 2 (1992), 165–184.

[23] GUCKENHEIMER, J., AND HOLMES, P. *Nonlinear oscillations, dynamical systems, and bifurcations of vector fields*. Springer-Verlag, New York, 1983.

[24] HEYMAN, J. N., ET AL. Resonant harmonic generation and dynamics screening in a double quantum well. *Phys. Rev. Lett. 72* (1994), 2183.

[25] HEYMAN, J. N., ET AL. Temperature and intensity dependence of intersubband relaxation rates from photovolgate and absorption. *Phys. Rev. Lett. 74* (1995), 2682.

[26] HUANG, Y., LI, W., MA, W., QIN, H., GRAHN, H. T., AND ZHANG, Y. Spontaneous quasi-periodic current self-oscillations in a weakly coupled gaas/(al, ga) as superlattice at room temperature. *Applied Physics Letters 102*, 24 (2013), 242107.

[27] HUANG, Y., LI, W., MA, W., QIN, H., AND ZHANG, Y. Experimental observation of spontaneous chaotic current oscillations in gaas/al0. 45ga0. 55as superlattices at room temperature. *Chinese Science Bulletin 57*, 17 (2012), 2070–2072.

[28] KANTER, I., AVIAD, Y., REIDLER, I., COHEN, E., AND ROSENBLUH, M. An optical ultrafast random bit generator. *Nature Photonics 4*, 1 (2010), 58–61.

[29] KASTRUP, J., HEY, R., PLOOG, K., GRAHN, H., BONILLA, L., KINDELAN, M., MOSCOSO, M., WACKER, A., AND GALÁN, J. Electrically tunable ghz oscillations in doped gaas-alas superlattices. *Physical Review B 55*, 4 (1997), 2476.

[30] LAEDKE, E., AND SPATSCHEK, K. On localized solutions in nonlinear faraday resonance. *Journal of Fluid Mechanics 223* (1991), 589–601.

[31] LEO, K., BOLIVAR, P. H., BRÜGGEMANN, F., SCHWEDLER, R., AND KÖHLER., K. Observation of bloch oscillations in a semiconductor superlattice. *Solid State Communications* (1992), 943–946.

[32] LI, W., REIDLER, I., AVIAD, Y., HUANG, Y., SONG, H., ZHANG, Y., ROSENBLUH, M., AND KANTER, I. Fast physical random-number generation based on room-temperature chaotic oscillations in weakly coupled superlattices. *Physical review letters 111*, 4 (2013), 044102.

[33] MORRIS, C. M. *Interplay of quantum confinement, electron-electron interactions, and terahertz radiation in indium gallium arsenide quantum posts and gallium arsenide quantum wells*. PhD thesis, University of California, Santa Barbara, 2011.

[34] NIELSEN, M. A., AND CHUANG, I. L. *Quantum computation and quantum information*. Cambridge university press, 2010.

[35] REIDLER, I., AVIAD, Y., ROSENBLUH, M., AND KANTER, I. Ultrahigh-speed random number generation based on a chaotic semiconductor laser. *Physical review letters 103*, 2 (2009), 024102.

[36] RUIZ-GARCIA, M., ESSEN, J., CARRETERO, M., BONILLA, L., AND BIRNIR, B. Enhancing chaotic behavior at room temperature in gaas/(al, ga) as superlattices. *Physical Review B 95*, 8 (2017), 085204.

[37] SCIAMANNA, M., AND SHORE, K. A. Physics and applications of laser diode chaos. *Nature Photonics 9*, 3 (2015), 151–162.

[38] STINSON, D. R. *Cryptography: theory and practice*. CRC press, 2005.

[39] WU, J., JIANG, D., AND SUN, B. Room-temperature microwave oscillation in alas/gaas superlattices. *Physica E: Low-dimensional Systems and Nanostructures 4*, 2 (1999), 137–141.

[40] ZALUŻNY, M. Influence of the depolarization effect on the nonlinear intersubband absorption spectra of quantum wells. *Phys. Rev. B 47* (1993), 3995.

[41] ZALUŻNY, M. Saturation of intersubband absorption and optical rectification in asymmetric quantum wells. *J. Appl. Phys. 74* (1993), 4716.

Björn Birnir, Ph.D.: University of California Santa Barbara, Center of Complex and Nonlinear Science, Department of Mathematics, UC Santa Barbara CA 93106, USA (*birnir@math.ucsb.edu*). The author gave a presentation of this paper during one of the conference sessions.

Selected problems of nonholonomic mechanics

Alexey Borisov, Yury Karavaev

Abstract: The paper is concerned with some problems of nonholonomic mechanics. The results of their investigation can be useful in practice in developing various designs of mobile robotic devices. Special attention is given to the Chaplygin sleigh with time-varying mass distribution, which arises due to various movable mechanisms (rotors, flywheels etc.) and makes it possible to control the sleigh. From the physical point of view, the possibility of (constant) acceleration of the sleigh plays a key role. It is shown that all trajectories of the reduced system can be made unbounded by an appropriate choice of mass distribution. This, in turn, will allow one to observe the acceleration of the sleigh. Consideration is also given to the problem of controlling a combined spherical robot. This spherical robot is set in motion by means of an internal wheeled platform with a rotor placed inside. The results of theoretical and experimental research are presented for the above-mentioned prototype of the spherical robot.

1. Introduction

We consider two problems of nonholonomic mechanics, namely, the problem of the Chaplygin sleigh and the problem of controlling a combined spherical robot. The Chaplygin sleigh [10] is a rigid body moving on a horizontal plane in the presence of a nonholonomic constraint: the translational velocity at some point is orthogonal to the body-fixed direction. This constraint can be realized by means of a weightless knife edge (skate) fastened in the body or by means of a wheel pair [4]. A detailed qualitative analysis of the motion of the sleigh using explicit quadratures was carried out by C. Carathéodory [9]. It turned out that if the center of mass of the body is not displaced along the knife edge, the sleigh moves in a circle, otherwise the sleigh asymptotically tends to a straight-line motion. Various generalizations of the Chaplygin sleigh problem are considered in many papers [1, 8, 7, 6, 5]. It turned out that in this case the sleigh exhibits complicated intricate behavior, which, according to the author, resembles random walks of bacterial cells with some diffusion component. The sleigh exhibits similar behavior under the action of the torque, which depends on their orientation, and in the presence of viscous friction [5]. In this paper, we consider the Chaplygin sleigh with time-varying mass distribution, which arises due to various movable mechanisms (rotors, flywheels etc.). They enable the control of the sleigh.

Recently, there has been a large body of research devoted to different designs of spherical robots [11, 18, 13]. The most popular methods of executing the motion of the spherical robots are: to change the position of the center of mass [13, 12] and to change the internal gyrostatic momentum [3, 17]. Despite a large number of models of spherical robots and their technical implementation, the question remains open what type of propulsion device is the most optimal in terms of simplicity of control and efficiency of maneuver execution. Experimental investigations of the dynamics of the spherical robots with various internal propulsion devices (pendulum, rotors, omniwheeled platform) have shown that a mechanism combining the above-mentioned effects can become the most promising mechanism for controlled motion.

2. Investigation of the dynamics of motion of the Chaplygin sleigh

2.1. Equations of motion

We explore the dynamics of a multicomponent mechanical system with a nonholonomic constraint. The system consists of a platform that slides on a horizontal plane like the Chaplygin sleigh [10], that is, the point R given on the body (see Fig. 1) cannot slide in some direction $\boldsymbol{n}$ fixed relative to the platform:

$$(\boldsymbol{v}_R, \boldsymbol{n}) = 0. \tag{1}$$

According to a given law, n material points $P^{(i)}$, $i = 1, \dots n$, move on this platform.

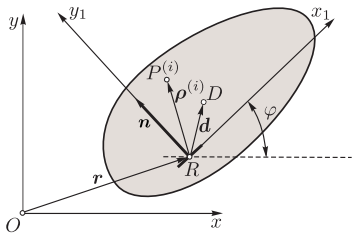

Figure 1. The Chaplygin sleigh

To describe the motion of the system, we define two coordinate systems: a fixed (inertial) coordinate system Oxy and a moving coordinate system Rx_1y_1 attached to the platform.

The position of each point relative to the platform is defined by the radius vector in the moving coordinate system:

$$\boldsymbol{\rho}^{(i)}(t) = \quad \rho_1^{(i)}(t), \rho_2^{(i)}(t) \quad , \quad i = 1, \dots n.$$

We will specify the position of the platform by the coordinates (x, y) of point R in the fixed coordinate system Oxy, and its orientation by the angle of rotation φ, see Fig. 1. Thus, the configuration space of the system $\mathcal{Q} = \{\boldsymbol{q} = (x, y, \varphi)\}$ coincides with the group of motions of the plane $SE(2)$.

Let $\boldsymbol{v} = (v_1, v_2)$ denote the projections onto the moving axes Rx_1x_2 of the velocity of the point R relative to the fixed coordinate system Oxy and let ω denote the angular velocity of the body. Then

$$\dot{x} = v_1 \cos\varphi - v_2 \sin\varphi, \quad \dot{y} = v_1 \sin\varphi + v_2 \cos\varphi, \quad \dot{\varphi} = \omega. \tag{2}$$

In this case, the constraint equation (1) has the form $v_2 = 0$. The equations of motion of the sleigh in the variables of momentum P and angular momentum M have the following form:

$$\begin{gathered} \dot{P} = m\omega \ c_1(t)\omega + \dot{c}_2(t) \ , \quad \dot{M} = -mv_1 \ c_1(t)\omega + \dot{c}_2(t) \ , \\ \dot{\varphi} = \omega, \quad \dot{x} = v_1 \cos\varphi, \quad \dot{y} = v_1 \sin\varphi, \end{gathered} \tag{3}$$

where the following expressions can be written for the velocities v_1 and ω:

$$\begin{aligned} v_1 &= \frac{I(t)P + mc_2(t)M - mI(t)\dot{c}_1(t) - mc_2(t)k(t)}{m \ I(t) - mc_2^2(t)}, \\ \omega &= \frac{c_2(t)P + M - mc_2(t)\dot{c}_1(t) - k(t)}{I(t) - mc_2^2(t)}, \end{aligned} \tag{4}$$

where the denominator is a positive definite function. Here, $m = m_{\mathrm{s}} + \sum\limits_{i=1}^{n} m_{\mathrm{p}}^{(i)}$ is the mass of the entire system, $I(t)$ is its moment of inertia, $\boldsymbol{c} = (c_1(t), c_2(t))$ is the position of the center of mass, and $k(t)$ is the gyrostatic momentum due to the motion of points. The last four quantities are given functions of time which are expressed in terms of the system parameters as follows:

$$\begin{gathered} k = \sum_{i=1}^{n} m_{\mathrm{p}} \ \ \rho_1^{(i)}\dot{\rho}_2^{(i)} - \rho_2^{(i)}\dot{\rho}_1^{(i)} \ \ , \quad I = I_{\mathrm{s}} + \sum_{i=1}^{n} m_{\mathrm{p}}^{(i)} \ \ \rho_1^{(i)\ 2} + \ \rho_2^{(i)\ 2} \ \ , \\ c_j = \frac{m_s}{m} d_j + \frac{1}{m} \sum_{i=1}^{n} m_{\mathrm{p}}^{(i)} \rho_j^{(i)}, \quad j = 1, 2. \end{gathered} \tag{5}$$

It can be seen that if the number of particles $n \geqslant 0$, the equations of motion contain four independent given functions of time: $c_1(t)$, $c_2(t)$, $I(t)$, $k(t)$. The resulting system is analogous to the well-known Liouville system describing the dynamics of a rigid body deformable according to a given law.

Equations (3) are invariant under the group of motions of the plane $SE(2)$. As a result, a closed (reduced) system of equations decouples which governs the evolution of P and M. It follows from (3) that the motion of the sleigh in the fixed coordinate system Oxy is defined by quadratures from the known solutions of the reduced system.

2.2. The motion of a point in the transverse direction

Consider the case of one point ($n = 1$) which executes periodic motions in the direction transverse to the plane of the knife edge

$$\boldsymbol{\rho}^{(1)} = \ a,\ b\sin(\Omega t)\ .$$

We also assume that the center of mass of the sleigh lies on the axis Rx_1, that is, $d_2 = 0$ (see Fig. 2). In this case, from (5) we obtain

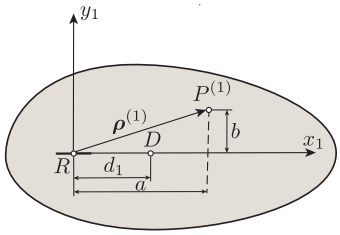

Figure 2. The Chaplygin sleigh

$$\begin{aligned} &I(t) = I_{\rm s} + m_{\rm p}^{(1)}(a^2 + b^2\sin^2(\Omega t)), \quad k(t) = m_{\rm p}^{(1)}ab\Omega\cos(\Omega t),\\ &c_1 = \frac{m_{\rm s}}{m}d_1 + \frac{m_{\rm p}^{(1)}}{m}a, \quad c_2(t) = \frac{m_{\rm p}^{(1)}}{m}b\sin(\Omega t), \ \ m = m_{\rm s} + m_{\rm p}^{(1)}. \end{aligned} \tag{6}$$

Let us define the dimensionless variables Z_1, Z_2, τ, X and Y

$$Z_1 = \frac{P}{mb\Omega}, \quad Z_2 = \frac{L}{mb^2\Omega}, \quad \tau = \Omega t, \ \ X = \frac{x}{b}, \ \ Y = \frac{y}{b},$$

where the angular momentum L is defined by the relation

$$L = c_2(t)P + M. \tag{7}$$

The reduced system of equations in these variables has the form

$$\begin{gathered} \frac{dZ_1}{d\tau} = \frac{Z_2 - \alpha\mu\cos\tau \quad \delta Z_2 - \mu\cos\tau(\alpha\delta - J - \mu(1-\mu)\sin^2\tau)}{(J + \mu(1-\mu)\sin^2\tau)^2},\\ \frac{dZ_2}{d\tau} = -\frac{\delta(Z_2 - \alpha\mu\cos\tau)Z_1}{J + \mu(1-\mu)\sin^2\tau} \end{gathered} \tag{8}$$

where the following dimensionless parameters have been introduced:

$$\alpha = \frac{a}{b}, \quad \delta = \frac{c_1}{b}, \quad \mu = \frac{m_{\rm p}^{(1)}}{m}, \quad J = \frac{I_{\rm s} + m_{\rm p}^{(1)}a^2}{mb^2}.$$

We note that in this case $0 \le \mu < 1$ and $J > 0$, and hence the denominator in the system (8) is always positive. Moreover, it follows from the condition $I_s - m_s d_1^2 > 0$ that the following inequality must be satisfied:

$$(1-\mu)(J-\delta^2) - \mu(\alpha-\delta)^2 > 0. \tag{9}$$

The equations of motion for the configuration variables are represented as

$$\begin{gathered} \frac{d\varphi}{d\tau} = \widetilde{\omega}, \quad \frac{dX}{d\tau} = \widetilde{v}_1 \cos\varphi, \quad \frac{dY}{d\tau} = \widetilde{v}_1 \sin\varphi, \\ \widetilde{\omega} = \frac{Z_2 - \alpha\mu\cos\tau}{J + \mu(1-\mu)\sin^2\tau}, \quad \widetilde{v}_1 = \frac{JZ_1 + \mu\sin\tau \;\; (1-\mu)Z_1\sin\tau + Z_2 - \alpha\mu\cos\tau}{J + \mu(1-\mu)\sin^2\tau}. \end{gathered} \tag{10}$$

Thus, the problem reduces to investigating the dynamics of the system (8), (10). Next, we consider in detail the possibility of constant *acceleration* of the sleigh depending on the mass distribution of the sleigh and the position of the oscillating point. By constant acceleration we mean an unlimited increase in the translational velocity of the sleigh which arises for unbounded trajectories of the reduced system. Consequently, this problem reduces to investigating the conditions under which the trajectories of the system (8) are bounded.

2.2.1. The case $\alpha \neq 0$ and $\delta = 0$

If $\alpha \neq 0$ and $\delta = 0$, then the value $Z_2 = C_2$ remains unchanged, and for Z_1 we obtain the following quadrature:

$$Z_1(\tau) = \int\limits_0^\tau \frac{\mu(C_2 - \alpha\mu\cos s)\cos s}{J + \mu(1-\mu)\sin^2 s} ds + C_1.$$

In this case, for $Z_1(\tau)$ (for the period of motion of the point) the following equation holds:

$$Z_1(\tau + 2\pi) = Z_1(\tau) + \frac{2\pi\alpha\mu}{1-\mu} \quad 1 - \sqrt{1 + \frac{\mu(1-\mu)}{J}}\Bigg).$$

Consequently, when $\alpha\mu \neq 0$, the function $Z_1(\tau)$ moves away with time (indefinitely) from its initial value C_1, and hence the translational velocity of the sleigh increases and acceleration is observed.

The equation for the angle specifying the orientation of the sleigh is represented as

$$\varphi' = \frac{C_2 - \alpha\mu\cos\tau}{J + \mu(1-\mu)\sin^2\tau}. \tag{11}$$

In the case $C_2 = 0$ the trajectories of equation (11) are periodic and have the form

$$\varphi(\tau) = -\frac{\alpha\sqrt{\mu}}{\sqrt{J(1-\mu)}} \arctan \quad \frac{\sqrt{\mu(1-\mu)}}{\sqrt{J}} \sin\tau\Bigg) + \varphi^{(0)}.$$

Possible motions of the point of contact are shown in Fig.3.

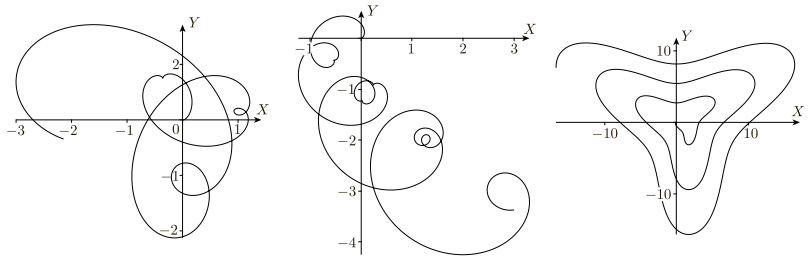

a) $C = \frac{\sqrt{3}}{8}$ $(\omega_\varphi = \sqrt{3})$ *b)* $C = \frac{3}{8}$ $(\omega_\varphi = 3)$ *c)* $C = \frac{1}{24}$ $\left(\omega_\varphi = \frac{1}{3}\right)$

Figure 3. Various trajectories of the point of contact of the sleigh for fixed parameters $\alpha = \frac{1}{3}$, $\delta = 0$, $J = \frac{1}{16}$, $\mu = \frac{1}{4}$ and for the initial conditions $Z_1 = 0$, $\tau = 0$ $\varphi = 0$, $X = 0$, $Y = 0$.

2.2.2. The general case

Consider qualitatively the issue of acceleration of the sleigh depending on the position of the oscillating point. For this purpose, we fix

$$\delta = 0.13,\ \mu = 0.43,\ J = 0.14,$$

and from inequality (9) we find $\alpha \in (-0.27, 0.53)$.

Let us represent the kinetic energy of the sleigh in the form

$$\widetilde{T} = \frac{1}{mb^2\Omega^2} T_{\mathrm{s}}|_{v_2=0} = \frac{1-\mu}{2} Z_1^2 + \frac{\mu(1-\mu)\sin\tau(Z_2 - \alpha\mu\cos\tau)Z_1}{J + \mu(1-\mu)\sin^2\tau} + \\ + \frac{(J - \alpha^2\mu + \mu^2(1-\mu)\sin^2\tau)(Z_2 - \alpha\mu\cos\tau)^2}{2(J + \mu(1-\mu)\sin^2\tau)^2}.$$

The dependence $\Delta\widetilde{T}(\alpha)$ is shown in Fig.4. It follows that when $\alpha < 0$, the kinetic energy always increases. Moreover, numerical experiments show that in this case the trajectories are unbounded and therefore a constant acceleration is observed.

Detailed numerical investigations show that the following hypothesis holds:

In the case where $\alpha\delta < 0$, all trajectories of the system are unbounded (8)*, that is, acceleration of the sleigh occurs under any initial conditions.*

In order to investigate the case $\alpha\delta > 0$, we consider on the plane (Z_1, Z_2) a point map for the period $\tau = 2\pi$ of the system (8). For the value $\alpha = 0.45$ this map is shown in Fig. 5.

The trajectory of the point of contact of the sleigh for the trajectory on a strange attractor is shown in Fig. 6.

The results of simulation show that the trajectory of the sleigh, with periodic oscillations of the material point in the transverse direction depending on parameters, can be both unbounded, accompanied by acceleration, and compact.

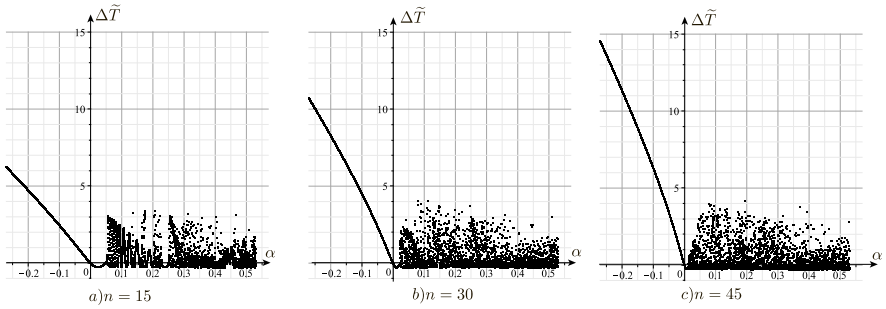

Figure 4. Dependence of the change in the kinetic energy $\Delta\widetilde{T} = \widetilde{T}|_{\tau=2\pi n} - \widetilde{T}|_{\tau=0}$ on α for a trajectory with the initial condition $Z_1 = 1$, $Z_2 = 0$, $\tau = 0$.

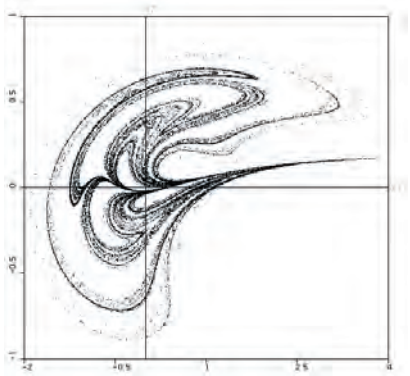

Figure 5. A Poincaré map of the system (8) for a period with $\alpha = 0.45$, $\delta = 0.13$, $\mu = 0.43$, $J = 0.14$.

3. Investigation of the dynamics of the motion of a spherical robot of combined type

3.1. Equations of motion

In this section, we consider the dynamics of a spherical robot of combined type that uses for its motion both the displacement of the center of mass and changes in the gyrostatic momentum. The results of theoretical research into the dynamics of such a model of the spherical robot rolling without slipping on a horizontal plane are presented in [15]. In this paper, we present the results of experimental investigation of the motion of the spherical robot of combined type.

Consider a spherical robot of combined type rolling without slipping on a horizontal

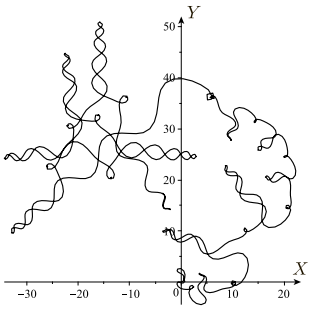

Figure 6. Trajectory of the point of contact for fixed $\alpha = 0.45$, $\delta = 0.13$, $\mu = 0.43$, $J = 0.14$ and the initial conditions $\tau = 0$, $Z_1 = 0.5$, $Z_2 = 0.5$, $\varphi = 0$, $X = 0$, $Y = 0$.

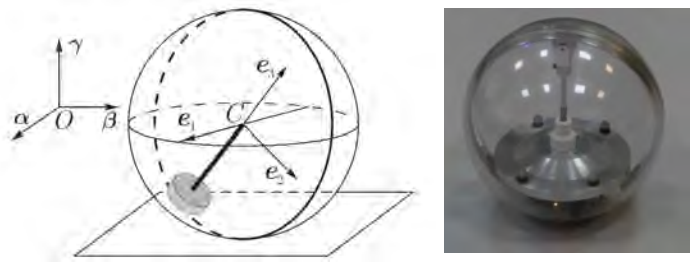

a) b)

Figure 7. a - a schematic model of a spherical robot of combined type, b - a picture of a full-scale specimen.

absolutely rough plane. The spherical robot is a spherical shell of radius R_s at the center of which an axisymmetric pendulum (Lagrange pendulum) is fastened. We will simulate the Lagrange pendulum by means of a weightless rod at the end of which a heavy rotor is installed. The rotor is an axisymmetric body (disk) rotating about a symmetry axis coinciding with the rod (see Fig. 7). The technical design of the spherical robot is such that the pendulum can execute oscillations only in a given plane attached to the shell, which we will call the plane of rotation of the pendulum.

To describe the dynamics of the spherical robot, we define two coordinate systems. The first,$O\boldsymbol{\alpha}\boldsymbol{\beta}\boldsymbol{\gamma}$, is a fixed (inertial) coordinate system with unit vectors $\boldsymbol{\alpha}$, $\boldsymbol{\beta}$, $\boldsymbol{\gamma}$. The second, $C\boldsymbol{e}_1\boldsymbol{e}_2\boldsymbol{e}_3$, is a moving coordinate system with unit vectors $\boldsymbol{e}_1$, $\boldsymbol{e}_2$, $\boldsymbol{e}_3$ and with axes attached to the pendulum so that the unit vector $\boldsymbol{e}_1$ is perpendicular to the plane of rotation of the pendulum and the unit vector $\boldsymbol{e}_3$ is directed along its symmetry axis. The origin of the moving coordinate system coincides with the geometric center of the shell C (see Fig. 7).

Further, we will refer all vectors to the axes of the moving coordinate system $Ce_1e_2e_3$.

The position of the system will be specified by the coordinates of the center of the sphere $\boldsymbol{r} = (x, y, 0)$, by the angles of rotation θ and φ of the pendulum about the axes $\boldsymbol{e}_1$ and $\boldsymbol{e}_3$, respectively, and by the matrix of transition from the fixed coordinate system to the moving coordinate system $\mathbf{Q}$, whose columns are the coordinates of the fixed vectors $\boldsymbol{\alpha}$, $\boldsymbol{\beta}, \boldsymbol{\gamma}$ referred to the axes of the moving coordinate system $Ce_1e_2e_3$.

Thus, the configuration space of the system is the product $\mathcal{N} = \{(\boldsymbol{r}, \theta, \varphi, \mathbf{Q})\} = \mathbb{R}^2 \times \mathbb{T}^2 \times SO(3)$.

The absence of slipping at the point of contact of the shell with the plane is described by the nonholonomic constraint

$$\boldsymbol{F} = \boldsymbol{v} - R_s \boldsymbol{\Omega} \times \boldsymbol{\gamma} = 0, \tag{12}$$

where $\boldsymbol{v}$ and $\boldsymbol{\Omega}$ are the velocity of the center and the angular velocity of rotation of the shell, respectively. This constraint does not exclude spinning of the spherical shell relative to the vertical, in contrast to the so-called rubber body model [16, 2].

The equations of the dynamics of the system can be written in the form of the d'Alembert – Lagrange equations of genus 2 in quasi-velocities with undetermined multipliers and forcing actions (for a detailed derivation, see [15]). As shown in [15], the equations of motion for the variables $\dot{\varphi}$, $\dot{\theta}$, $\boldsymbol{\Omega}$, $\boldsymbol{\gamma}$ decouple from the complete system and take the following form in the moving axes $Ce_1e_2e_3$:

$$\begin{aligned}
&(\boldsymbol{e}_3, I_{b3}(\dot{\boldsymbol{\Omega}} + \boldsymbol{e}_3\ddot{\varphi})) = K_\varphi,\\
&(\boldsymbol{e}_1, \mathbf{I}_b(\dot{\boldsymbol{\Omega}} + \boldsymbol{e}_1\ddot{\theta}) - m_b R_b R_s \boldsymbol{e}_3 \times (\dot{\boldsymbol{\Omega}} \times \boldsymbol{\gamma} + \boldsymbol{\Omega} \times \dot{\boldsymbol{\gamma}})) - (\boldsymbol{e}_1, m_b R_b R_s (\boldsymbol{\Omega} \times \boldsymbol{\gamma}) \times ((\boldsymbol{\Omega} + \dot{\theta}\, \boldsymbol{e}_1) \times \boldsymbol{e}_3)) +\\
&+(\boldsymbol{e}_1, \boldsymbol{\Omega} \times (m_b R_b R_s\, (\boldsymbol{\Omega} \times \boldsymbol{\gamma}) \times \boldsymbol{e}_3 + (\mathbf{I}_s + \mathbf{I}_b)\boldsymbol{\Omega} + \boldsymbol{e}_1 I_{b1}\dot{\theta} + \boldsymbol{e}_3 I_{b3}\dot{\varphi})) + m_b R_b g(\boldsymbol{e}_1, \boldsymbol{\gamma} \times \boldsymbol{e}_3) = K_\theta,\\
&m_b R_b R_s(\dot{\boldsymbol{\Omega}} \times \boldsymbol{\gamma} + \boldsymbol{\Omega} \times \dot{\boldsymbol{\gamma}}) \times \boldsymbol{e}_3 + (\mathbf{I}_s + \mathbf{I}_b)\dot{\boldsymbol{\Omega}} + \boldsymbol{e}_1 I_{b1}\ddot{\theta} + \boldsymbol{e}_3 I_{b3}\ddot{\varphi} - m_b R_b R_s(\boldsymbol{\Omega} \times \boldsymbol{\gamma}) \times ((\boldsymbol{\Omega} + \dot{\theta}\, \boldsymbol{e}_1) \times \boldsymbol{e}_3) +\\
&+(\boldsymbol{\Omega} + \boldsymbol{e}_1\dot{\theta}) \times (m_b R_b R_s\, (\boldsymbol{\Omega} \times \boldsymbol{\gamma}) \times \boldsymbol{e}_3 + (\mathbf{I}_s + \mathbf{I}_b)\boldsymbol{\Omega} + \boldsymbol{e}_1 I_{b1}\dot{\theta} + \boldsymbol{e}_3 I_{b3}\dot{\varphi}) + m_b R_b g\, \boldsymbol{\gamma} \times \boldsymbol{e}_3 =\\
&= R_s((m_s + m_b)R_s(\dot{\boldsymbol{\Omega}} \times \boldsymbol{\gamma} + \boldsymbol{\Omega} \times \dot{\boldsymbol{\gamma}}) - m_b R_b(\dot{\boldsymbol{\Omega}} + \ddot{\theta}\, \boldsymbol{e}_1) \times \boldsymbol{e}_3) \times \boldsymbol{\gamma} +\\
&+R_s((\boldsymbol{\Omega} + \boldsymbol{e}_1\dot{\theta}) \times ((m_s + m_b)R_s\boldsymbol{\Omega} \times \boldsymbol{\gamma} - m_b R_b(\boldsymbol{\Omega} + \dot{\theta}\, \boldsymbol{e}_1) \times \boldsymbol{e}_3)) \times \boldsymbol{\gamma},\\
&\dot{\boldsymbol{\gamma}} = \boldsymbol{\gamma} \times (\boldsymbol{\Omega} + \boldsymbol{e}_1\dot{\theta}).
\end{aligned} \tag{13}$$

where $\mathbf{I}_b = \operatorname{diag}(I_{b1}, I_{b1}, I_{b3}) = \operatorname{diag}(I_{bc1} + m_b R_b^2, I_{bc1} + m_b R_b^2, I_{bc3})$ is the tensor of inertia of the pendulum relative to the center of the sphere, m_s, I_s are, respectively, the mass and the moment of inertia of the spherical shell, m_b, $\mathbf{I}_{bc} = \operatorname{diag}(I_{bc1}, I_{bc1}, I_{bc3})$ are the mass and the central tensor of inertia of the pendulum, and the velocity of the center of mass of the pendulum $\boldsymbol{v}_b$ and its angular velocity $\boldsymbol{\omega}$ are given by the relations

$$\boldsymbol{v}_b = \boldsymbol{v} - R_b\boldsymbol{\omega} \times \boldsymbol{e}_3, \qquad \boldsymbol{\omega} = \boldsymbol{\Omega} + \boldsymbol{e}_1\dot{\theta} + \boldsymbol{e}_3\dot{\varphi}, \tag{14}$$

where R_b is the distance from the center of the sphere to the center of mass of the pendulum. K_φ, K_θ are the moments of external forces (control actions) that set the pendulum in motion relative to the ball and the rotor relative to the rod of the pendulum.

In [14], equations have been found to find controls implementing the motion along a given trajectory. However, these equations are not always solvable on a given time interval; this imposes some restrictions on possible trajectories and the maneuverability of the model under consideration. One of the methods for eliminating the disadvantage of constructing the control on the basis of a dynamical model is the development of a model of control using elementary basic maneuvers (gaits), as described in [15, 14]. Steady-state solutions of the free system and motions that transfer the system from one steady-state solution to another are considered as elementary maneuvers. In [15] it is shown that the dynamical system admits two types of steady-state solutions: motion in a straight line and motion in a circle. By combining these solutions one can implement the motion from any initial point to any end point. However, in practice, a moving spherical robot is acted upon by friction forces, which are not taken into account in the nonholonomic model. Therefore, in what follows we present experimental results that provide a better understanding of the process of motion of the spherical robot of combined type and the influence of rolling friction on this motion.

3.2. Experimental investigations of the trajectory of a spherical robot

The model of a combined spherical robot shown in Fig. 7a has been implemented by using a platform whose center of mass moves in the equatorial plane of a spherical shell. The platform has a rotor fastened in such a way that the axis of rotation of the rotor is directed along the radius of the spherical shell. A picture of a full-scale specimen is shown in Fig. 7b.

The spherical shell is made of a transparent polyethylene terephthalate material and has the following characteristics (here and in what follows, all numerical values have been brought in accordance with the SI system): $R_s = 0.150$ m, $m_s = 1.625$ kg, $\mathbf{I}_s = \mathrm{diag}(25.27 \cdot 10^{-3},\ 20.73 \cdot 10^{-3},\ 25.27 \cdot 10^{-3})$ kg·m^2. To ensure that there is no slipping, the platform's wheels, made of rubber, are synchronously actuated by two DC motors with a reduction gear. The rotor is a homogeneous aluminum disk of radius $R_r = 0.087$ m, mass $m_r = 2.46$ kg and axial moment of inertia $I_r = 5.64 \cdot 10^{-3}$ kg·m^2. The characteristics of the internal wheeled platform (with a rotor installed on it) are: $m_b = 3.25$ kg, $\mathbf{I}_b = \mathrm{diag}(31.88 \cdot 10^{-3},\ 30.59 \cdot 10^{-3},\ 8.76 \cdot 10^{-3})$ kg·m^2.

The controls for the spherical robot of combined type were given in the form of dependences of the angles $\dot\theta(t)$, $\dot\varphi(t)$.

Consider the most general case of controlled motion, which clearly demonstrates the contribution of each control to the character of the trajectory. An illustrative example in

this case is the impulse control, when at a constant value of control $\dot{\theta}(t)$ the control action $\dot{\varphi}(t)$ is switched on for some time and then it is switched off. In practice, this implies that, as the spherical robot is moving in a straight line with constant velocity, the rotor accelerates and after some time interval ceases to rotate, while the platform continues to move along the rim of the sphere. The dependence of controls on time will be given as follows:

$$\dot{\theta}(t) = \begin{cases} 0, \;\; t < t_1 = 0, \\ 1.57 \cdot \sin(\frac{\pi t}{3})^2, \;\; t_1 \le t \le t_1^* = 1.5, \\ 1.57, \;\; t > t_1^*, \end{cases} \tag{15}$$

$$\dot{\varphi}(t) = \begin{cases} 0, \;\; t < t_2 = 1.9, \\ 11.304 \cdot \sin(\frac{\pi}{3} t - \frac{19}{30}\pi)^2, \;\; t_2 \le t \le t_2^* = 3.4, \\ 11.304, \;\; t_2^* < t \le t_3 = 6.9, \\ 11.304 \cdot \sin(\frac{\pi}{3} t - \frac{23}{10}\pi)^2, \;\; t_3 \le t \le t_3^* = 8.4, \\ 0, \;\; t > t_3^*. \end{cases} \tag{16}$$

Graphs of the time dependence of control actions are presented in Fig. 8a. The trajectory along which the spherical robot moves with the control (15), (16) within the framework of the theoretical model considered is shown as an intermittent line in Fig. 8b. This trajectory can be divided into three segments: accelerated motion in a straight line $t \in [t_1,\ t_1^*]$; motion along a trajectory close to the circle $t \in [t_2^*,\ t_3]$; motion along a trajectory close to a straight line $t > t_3^*$. The angle between the straight lines along which the spherical robot moves on the first and the third segment depends on the duration of the impulse $\Delta t_\varphi = t_3 - t_2^*$.

The trajectory of the spherical robot with the control actions (15), (16), which has been retrieved from experimental data, is shown as a solid line in Fig. 8b. The markers in the figure indicate the positions of the spherical robot at instants corresponding to changes in the control actions. The numbers of the markers in Fig. 8b allow one to determine the position of the spherical robot at the instant of the corresponding change in the control action. As the rotor ceases to rotate ($t \in [t_3,\ t_3^*]$), the spherical robot turns in the reverse direction (relative to the original turn), and after some time the trajectory of the spherical robot becomes rectilinear.

Depending on the value of Δt_φ, there are three types of possible motions of the spherical robot with impulse control:

1. *"Long" impulse* — when the rotor rotates for a long time with constant velocity, the motion of the spherical robot becomes rectilinear. After that the stop of the rotor leads to a turn in the reverse direction. As a result, the final motion occurs in a straight line parallel

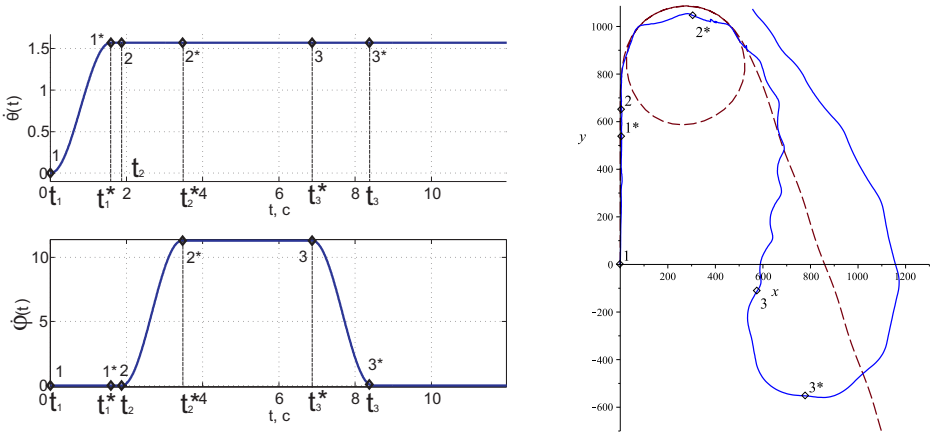

Figure 8. (a) - Control actions, (b) - the corresponding trajectory of the spherical robot.

to the initial motion. The motion of the spherical robot with controls in the form (15), (16) is close to this type. The trajectory of this motion is shown in Fig. 8b.

2. *"Medium" impulse* — after acceleration of the rotor, the motion of the spherical robot does not have time enough to become rectilinear. However, during the impulse Δt_φ the force of rolling friction affects considerably the trajectory of motion. As a result, after the maneuver the spherical robot turns through some angle. However, this angle depends strongly on the coefficient of friction, and the trajectory of the spherical robot differs considerably from the theoretical one.

3. *"Short" impulse* — during this impulse, the forces of rolling friction do not have time enough to considerably influence the trajectory of the spherical robot. As a result, the real trajectory is as close as possible to the theoretical trajectory. The angle of rotation can be adjusted by both the amplitude of the impulse (the maximal value of $\dot{\varphi}$) and its length (within certain limits).

The motion of the spherical robot can be executed by using the above-mentioned maneuvers, namely, by selecting appropriate characteristics of control actions and their combinations, but to compensate for the oscillations that accompany the motion, it is necessary to ensure a coordinated change in the controls taking into account the feedback about the current state of the dynamical system under consideration. The development of a motion model taking into account arising friction forces (especially spinning friction) is of the greatest importance to spherical robots of this type, since these forces influence considerably the trajectory and the pattern of motion.

Acknowledgments

The work of A. Borisov (chapters 1, 2) was carried out in MIPT in framework of Russian Academic Excellence Project 5-100, the work of Yu.Karavaev (chapter 3) was funded by RFBR according to the research project no. 15-08-09261-a.

References

[1] Bizyaev, I. A., Borisov, A. V., and Mamaev, I. S. Dynamics of the chaplygin sleigh on a cylinder. *Regular and Chaotic Dynamics 21*, 1 (2016), 136–146.

[2] Borisov, A., Mamaev, I., and Bizyaev, I. The hierarchy of dynamics of a rigid body rolling without slipping and spinning on a plane and a sphere. *Regular and Chaotic Dynamics 18*, 3 (2013), 277–328.

[3] Borisov, A. V., Kilin, A. A., and Mamaev, I. S. How to control the chaplygin ball using rotors. ii. *Regular and Chaotic Dynamics 18*, 1–2 (2013), 144–158.

[4] Borisov, A. V., Kilin, A. A., and Mamaev, I. S. On the hadamard-hamel problem and the dynamics of wheeled vehicles. *Regular and Chaotic Dynamics 20*, 6 (2015), 752–766.

[5] Borisov, A. V., and Kuznetsov, S. P. Regular and chaotic motions of a chaplygin sleigh under periodic pulsed torque impacts. *Regular and Chaotic Dynamics 21*, 7, 8 (2016), 792–803.

[6] Borisov, A. V., and Mamaev, I. S. The dynamics of a chaplygin sleigh. *Journal of Applied Mathematics and Mechanics 73*, 2 (2009), 156–161.

[7] Borisov, A. V., and Mamaev, I. S. An inhomogeneous chaplygin sleigh. *Regular and Chaotic Dynamics 22*, 4 (2017), 435–447.

[8] Borisov, A. V.and Mamaev, I. S., and Bizyaev, I. A. The jacobi integral in nonholonomic mechanics. *Regular and Chaotic Dynamics 20*, 3 (2015), 3836–400.

[9] Caratheodory, C. Der schlitten. *Z.Angew. Math. Mech., 13*, 2 (1933), 71–76.

[10] Chaplygin, S. A. On the theory of motion of nonholonomic systems. the reducing-multiplier theorem. *Regular and Chaotic Dynamics 13*, 4 (2008), 369–376.

[11] Chase, R., and Pandya, A. A review of active mechanical driving principles of spherical robots. *Robotics 1*, 1 (2012), 3–23.

[12] Gajbhiye, S., and Banavar, R. N. Geometric modeling and local controllability of a spherical mobile robot actuated by an internal pendulum. *Int. J. Robust Nonlinear Control* (2015).

[13] Karavaev, Y. L., and Kilin, A. A. Nonholonomic dynamics and control of a spherical robot with an internal omniwheel platform: Theory and experiments. *Proceedings of the Steklov Institute of Mathematics 295* (2016), 158–167.

[14] Kilin, A. A., and Karavaev, Y. L. Experimental research of dynamic of spherical robot of combined type. *Russian Journal of Nonlinear Dynamics 11*, 4 (2015), 721–734.

[15] Kilin, A. A., Pivovarova, E. N., and Ivanova, T. B. Spherical robot of combined type: Dynamics and control. *Regular and Chaotic Dynamics 20*, 6 (2015), 716–728.

[16] Koiller, J., and Ehlers, K. M. Rubber rolling over a sphere. *Regular and Chaotic Dynamics 12*, 2 (2007), 127–152.

[17] Morinaga, A., Svinin, M., and Yamamoto, M. A motion planning strategy for a spherical rolling robot driven by two internal rotors. *IEEE Trans. on Robotics 30*, 4 (2014), 993–1002.

[18] Ylikorpi, T., and Suomela, J. *Ball-Shaped Robots in Climbing and Walking Robots: Towards New Applications*. InTech, Vienna, 2007.

Borisov A. V., Professor: Moscow Institute of Physics and Technology, 141700, Institutskiper. 9, Dolgoprudnyi (*borisov@rcd.ru*). The author gave a presentation of this paper during one of the conference sessions.

Karavaev Yu. L., Ph.D.: Kalashnikov Izhevsk State Technical University, 426069, ul. Studencheskaya 7, Izhevsk (*karavaev_yury@istu.ru*). The author gave a presentation of this paper during one of the conference sessions.

Time-varying spectral submanifolds: Analytic calculation of backbone curves and forced responses of nonlinear mechanical systems

Thomas Breunung, George Haller

Abstract: Spectral submanifolds (SSMs) have recently been shown to provide exact and unique reduced-order models for nonlinear unforced mechanical vibrations. Here we extend these results to periodically or quasiperiodically forced mechanical systems, obtaining analytic expressions for forced responses and backbone curves on modal (i.e. two-dimensional) time dependent SSMs. A judicious choice of the parameterization of these SSMs allows us to simplify the reduced dynamics considerably. We demonstrate our analytical formulae on numerical examples and compare them to results obtained from available normal form methods.

1. Introduction

In drawing conclusions about a nonlinear mechanical system, an engineering analyst usually faces the challenge of high dimensionality and complex dynamic equations. To reduce simulation time and deduce general statements, it is desirable to reduce the dimension of the system and simplify the resulting reduced equations of motion.

For linear systems, decomposition into normal modes is a powerful tool to derive reduced-order models. While the lack of the superposition principle makes such a decomposition impossible for nonlinear systems, various definitions of nonlinear normal modes are also available in the literature (cf. [5, 16, 17]). Specifically, in [16] a nonlinear normal mode is defined as a synchronous periodic orbit of a conservative system. Later Shaw and Pierre [17] extended this definition to dissipative systems, by viewing a nonlinear normal mode as an invariant manifold tangent to a modal subspace of an equilibrium point.

While there are generally infinitely many Shaw-Pierre type surfaces for each modal subspace [12], Haller and Ponsioen [5] have shown that, under appropriate nonresonance conditions, there is a unique smoothest one, which they called a spectral submanifold (SSM). Due to their invariance, the SSMs are natural candidates for model order reduction, serving as nonlinear continuations of the invariant modal subspaces spanned by the eigenvectors of the linearized system. SSM-based moder-order reduction for unforced nonlinear mechanical systems appear in [8, 15, 19].

While most of the above work focuses on unforced (autonomous) mechanical systems, here we explore further the utility of SSMs for forced dissipative nonlinear mechanical systems. For this class of systems, the existence, uniqueness and regularity of SSMs has been clarified in [5], relying on the more abstract invariant manifold results of [6]. In this context, a nonlinear normal mode (NNM) is defined as the continuation of the trivial hyperbolic fixed point of the time-independent system under the addition of small time-dependent forcing with a finite number of frequencies. Depending on the frequency content of the time-varying terms, this continuation is a periodic or quasi-periodic orbit [5]. The SSM will be a time-dependent surface with the same frequency basis. This SSM is then tangent to the NNM along directions associated with a spectral subspace of the linearization.

The first attempts to construct such a non-autonomous SSM can be found in [3, 10, 18] who formally reduce an externally forced, dissipative mechanical system to a two-dimensional time-varying invariant manifold. In [10] the reduction is carried out numerically for fixed parameter values, aided by a Galerkin projection. This approach is extended to systems with time-periodic coefficients in their linear part in [3, 18]. There the assumed invariant manifold is expanded in a multivariate Taylor-Fourier series and the unknown coefficients are obtained from the invariance of the manifold. The studies are limited to specific examples and symbolic equations to derive general conclusions about the forced response are not obtained. Furthermore, the uniqueness, existence and smoothness of their assumed invariant manifold remains unclear from their procedure.

A generally applicable procedure for the simplification of the (formally) reduced dynamics is the method of normal forms (cf. e.g. [4]). The method applies a series of smooth transformations to obtain a Taylor series of the original dynamical equations, which contain only the terms essential for the dynamics. Jezequel and Lamarque [9] and Neild and Wagg [13] apply the method of normal forms to nonlinear mechanical systems. Since all state variables are transformed, the resulting dynamics have the same dimensionality as the original system and no model-order reduction is achieved. Furthermore, both of these normal form approaches start from conservative systems and treat damping as a small bifurcation parameter. Therefore, the unfolding from the conservative limit has to be discussed for every damping type separately.

Touzé and Amabili [20] seek to unite normal form theory with model-order reduction for the first time. After a normal form transformation, they restrict their calculations to heuristically chosen submanifolds. As pointed out by the authors, a strict time-varying normal form is not computed. Instead, the forcing is inserted directly into the normal form. This represents phenomenological forcing aligned with a curvilinear coordinates, rather than specific physical forcing applied to the system.

The model reduction methods surveyed so far are often used as tools to approximate backbone curves, which connect points of maximal response amplitude as a function of an external forcing frequency. As an alternative, [7, 11, 14] define the backbone curve as the frequency-amplitude relationship of a periodic solution family of the conservative unforced limit of the system. They observe that along each nonlinear normal mode (i.e. periodic orbit) of the conservative limit, weak viscos damping can be canceled by appropriately chosen external periodic forcing. For a general damped and forced nonlinear system however, the relevance of periodic orbits of the conservative limit for the forced response is not well understood. Since the backbone curve is obtained for the unforced conservative limit in these examples, another method is needed to actually calculate the maximum amplitude for a given forcing.

Parallel to theoretical considerations, backbone curves have been approximated in experiments through the *force appropriation method*. In this method, the nonlinear system is forced with a harmonic forcing such that the response has a 90-degree phase lag in a modal degree of freedom. While this force appropriation procedure is plausible for linear viscous damping (or nonlinear damping that is an odd function of the velocities), the approach has remained unjustified for general, nonlinear damping (cf. Peeters et al. [14]).

An experimental alternative to the force appropriation is the *resonance decay* method, in which the system is forced, such that its response is close to an envisioned invariant surface of the conservative limit. Then the forcing is turned off and the instantaneous amplitude-frequency relationship is identified by signal processing. Peeters et al. [14], however, relate this curve, which is essentially a feature of the damped system, to the orbits of the conservative system only phenomenologically.

We also note that force appropriation and the resonance decay aim to reconstruct nonlinear normal modes of the conservative limit. The set formed by these orbits is expected to deviate from the forced response of the actual dissipative system for lager amplitudes and larger damping. As a recent development, Szalai et al. [19] compute the backbone curves from the frequency-amplitude relationship of decaying vibrations on SSMs reconstructed from measured data. A connection with the backbone curve obtained from the forced response, however, is not immediate.

In summary, available approaches to compute forced response via model reduction for nonlinear mechanical systems suffer either from heuristic steps or omissions in the reduction procedure, or from a unclear relationship between backbone-curve definitions different from the one relevant for forced-damped vibrations in a practical setting. In the present work, we show how these shortcomings can be eliminated simultaneously. First, we employ a mathematically justified reduction process to time-dependent SSMs in the presence of general

damping and forcing. Second, with universal, system-independent formulas for the dynamics on the SSM at hand, we derive explicit, leading-order approximations to the actually observed backbone curve of the time-dependent, dissipative response.

2. Set-up

We consider a general, quasi-periodically forced, nonlinear, N-degree-of-freedom mechanical system of the form

$$\begin{aligned} \mathbf{M}\ddot{\mathbf{q}} + (\mathbf{C}+\mathbf{G})\dot{\mathbf{q}} + (\mathbf{K}+\mathbf{N})\mathbf{q} + \mathbf{f}_{nl}(\mathbf{q},\dot{\mathbf{q}}) = \varepsilon \mathbf{f}_{ext}(\Omega_1 t, ..., \Omega_k t), \quad \mathbf{q} \in \mathbb{R}^N, \\ \mathbf{f}_{nl}(\mathbf{q},\dot{\mathbf{q}}) = \mathcal{O}(|\mathbf{q}|^2, |\mathbf{q}||\dot{\mathbf{q}}|, |\dot{\mathbf{q}}|^2), \qquad 0 \leq \varepsilon \ll 1, \qquad k \geq 1, \end{aligned} \tag{1}$$

where the mass matrix $\mathbf{M}$ is positive definite and the nonlinear forcing vector $\mathbf{f}_{nl}(\mathbf{q},\dot{\mathbf{q}})$ is at least quadratic in its arguments. Observe, that $\mathbf{q} \equiv 0$ is an equilibrium of the unforced system ($\varepsilon = 0$). The external forcing $\varepsilon \mathbf{f}_{ext}$ does not depend on the generalized coordinates or velocities and has finitely many rationally incommensurate frequencies $(\Omega_1, ..., \Omega_k)$.

We denote the eigenvalues of the linearized system (1) by $\lambda_1, ..., \lambda_{2N}$, with multiplicities and conjugates included. We assume an underdamped configuration, i.e. complex eigenvalues with nonzero imaginary part and negative real part ordered as follows:

$$\lambda_j = \overline{\lambda}_{j+N} \qquad \mathrm{Im}(\lambda_j) > 0, \qquad \mathrm{Re}(\lambda_{min}) \leq \mathrm{Re}(\lambda_j) < 0, \qquad j = 1, ..., N. \tag{2}$$

By (2) the $\mathbf{q} = 0$ equilibrium of the unforced limit of (1) is asymptotically stable. This context is relevant for vibrations of lightly damped structures.

By letting $\mathbf{x} = (\mathbf{x}_1, \mathbf{x}_2) = (\mathbf{q}, \dot{\mathbf{q}})$ in (1), we obtain the first-order equivalent system of the form

$$\begin{aligned} &\dot{\mathbf{x}} = \mathbf{A}\mathbf{x} + \mathbf{G}_{nl}(\mathbf{x}) + \varepsilon \mathbf{G}_{ext}(\Omega_1 t, ..., \Omega_k t), \\ &\mathbf{A} = \begin{pmatrix} 0 & \mathbf{I} \\ -\mathbf{M}^{-1}(\mathbf{K}+\mathbf{N}) & -\mathbf{M}^{-1}(\mathbf{C}+\mathbf{G}) \end{pmatrix}, \qquad \mathbf{G}_{nl}(\mathbf{x}) = \begin{pmatrix} 0 \\ \mathbf{M}^{-1}\mathbf{f}_{nl}(\mathbf{x}) \end{pmatrix}. \end{aligned} \tag{3}$$

and denote the eigenvector corresponding to the eigenvalue λ_j of the linear part of system (3) with $\mathbf{v}_j$.

In [5] a $2q$-dimensional spectral submanifold (SSM) for the general mechanical system (1), or its equivalent first order form (3), is defined as the $2q$-dimensional invariant manifold $W(E)$ serving as the smoothest nonlinear continuation of an eigenspace of the form

$$E = \mathrm{span}\{\mathbf{v}_1, ..., \mathbf{v}_q, \mathbf{v}_{N+1}, ...\mathbf{v}_{N+q}\}. \tag{4}$$

If the nonresonance conditions

$$\sum_{j=1}^{q} m_j \mathrm{Re}(\lambda_j) \neq \mathrm{Re}(\lambda_n), \qquad n = q+1, ..., N, \qquad 2 \leq \sum_{j=1}^{q} m_j \leq \Sigma(E), \qquad m_j \in \mathbb{N}, \quad (5)$$

hold, with the absolute spectral quotient $\Sigma(E)$ defined as

$$\Sigma(E) = \mathrm{Int}\left(\frac{\mathrm{Re}(\lambda_{min})}{\max\limits_{j=1,...,q}(\mathrm{Re}(\lambda_j))} \right), \quad (6)$$

then a smoothest continuation $W(E)$ of the modal subspace (4) uniquely exists for the nonlinear system (1) in the class of $C^{\Sigma(E)+1}$ manifolds [5]. The operator Int( ) extracts the integer part of its argument. It follows from [1], that $W(E)$ can be constructed via a parameterization

$$\mathbf{x} = \mathbf{W}(\mathbf{z}, \Omega_1 t, ..., \Omega_k t), \qquad \mathbf{z} \in \mathbb{R}^{2q}, \quad (7)$$

where $\mathbf{z}$ is the parameterization variable. As shown in [6], the parameterization $\mathbf{W}$ can be approximated as a polynomial in $\mathbf{z}$, with time-dependent coefficients. The dynamics of system (3) along $W(E)$ is given by the reduced equation of motion

$$\dot{\mathbf{z}} = \mathbf{R}(\mathbf{z}, \Omega_1 t, ..., \Omega_k t), \quad (8)$$

which can also be approximated by a Taylor series in $\mathbf{z}$ near the $\mathbf{x}=0$ equilibrium of (3) .

Due to their robustness with respect to parameters (cf. [6]), the SSMs, as well as their reduced dynamics, can be expanded in ε for small $\varepsilon \geq 0$.

3. Spectral submanifolds for the forced system

In order to construct frequency-amplitude response curves, we now assume canonical single harmonic forcing ($k=1$) in the form of

$$\mathbf{f}_{ext} = \mathbf{f} \cos(\Omega t) \quad (9)$$

and focus on two-dimensional SSMs ($q = 1$). Szalai et al. [19] construct a parameterization for a two-dimensional SSM, continuing a modal subspace of (1) for the autonomous (unforced) limit of system (3). They give an explicit parameterization of the autonomous SSM ($\mathbf{W}(\mathbf{z})$) and its associated reduced dynamics ($\mathbf{R}(\mathbf{z})$).

With the existence, uniqueness and smoothness results from [5], we give strict conditions for the validity of the reduction of the system (1) to a two-dimensional non-autonomous SSM.

We continue a given autonomous parameterization of the SSM and the reduced dynamics under the addition of small forcing terms (cf. (1)). In case of near resonance forcing

$$\Omega \approx \mathrm{Im}(\lambda_l), \tag{10}$$

we eliminate arising small denominators by keeping terms in the reduced dynamics $\mathbf{R}(\mathbf{z}, \Omega t)$ that could otherwise be eliminated. Focusing on vibrations around the $\mathbf{q}=0$ equilibrium of system (1), we can give an explicit parameterization of the non-autonomous SSM and the reduced dynamics. Through judicious choice of the parameterization we simplify the reduced dynamics significantly, such that we can solve for $2\pi/\Omega$-periodic responses analytically.

Having derived condensed formulas for the forced response, we solve for the forcing frequency, at which the response amplitude is maximal. Such amplitude-frequency pairs form a one dimensional curve (i.e. the backbone curve) as the forcing amplitude is varied as a parameter. Furthermore we can analytically compute stability regions of the forced response.

4. Numerical examples

We show the application of our SSM-based analytic results on forced responses and backbone curves on two numerical examples. The first is a two-degree-of-freedom oscillator introduced in [17], modified and further studied in [5, 19]. The nonlinearity in this oscillator arises from a single cubic spring. Our second example, taken from [20], also has two degrees of freedom, but its nonlinearities are more complex, consisting of both quadratic and cubic terms.

On these examples, we compare our results with the second-order normal form approach of Neild and Wagg [13] and with a normal-form type method of Touzé and Amabili [20]. To compare the accuracy of these two methods to ours, we generate a benchmark solution via numerical continuation, where we use the MATCONT toolbox [2] of MATLAB to calculate the periodic responses in the two examples directly.

5. Conclusions

For backbone curve and forced response calculation we construct an approximation for the two-dimensional, non-autonomous spectral submanifolds (SSMs) that act as nonlinear continuations of modal subspaces of the linearized system. Under low-order nonresonance conditions on the eigenvalues of the linearization the existence, uniqueness and smoothness of the SSMs are guaranteed [5]. Through a judicious choice of the parameterization, the reduced dynamics are simplified significantly. Due to this simplification, we are able solve for the forced response analytically. We apply our results on two numerical examples and compare them with the results of the Neild-Wagg method [13], the Touzé-Amabili method [20] and

numerical continuation.

Ponsioen et al. [15] describe an automated computational algorithm to approximate two-dimensional SSMs of nonlinear mechanical systems up to arbitrary order. It is our ongoing effort to couple these algorithm with the results of this work.

We have limited our discussion to two-dimensional SSMs. For multi-frequency forcing and internally resonant structures a reduction to a higher-dimensional SSM is desirable. Since the theory developed in [1, 6] applies to higher-dimensional submanifolds, our calculations can be extended to the multi-frequency setting.

References

[1] Cabré, X., Fontich, E., and de la Llave, R. The parameterization method for invariant manifolds i: manifolds associated to non-resonant subspaces. Department of Mathematics Indiana University, pp. 283–328.

[2] Dhooge, A., Govaerts, W., and Kuznetsov, Y. Matcont: A matlab package for numerical bifurcation analysis of odes. *ACM Transactions on mathematical software 29*, 2 (2003), 141–164.

[3] Gabale, A., and Sinha, S. Model reduction of nonlinear systems with external periodic excitations via construction of invariant manifolds. *Journal of Sound Vibration 330* (May 2011), 2596–2607.

[4] Guckenheimer, J., and Holmes, P. *Nonlinear oscillations, dynamical systems, and bifurcations of vector fields*, corr. 7. printing ed., vol. 42 of *Applied mathematical sciences*. Springer, New York [u.a.], 2002.

[5] Haller, G., and Ponsioen, S. Nonlinear normal modes and spectral submanifolds: existence, uniqueness and use in model reduction. *Nonlinear Dynamics 86*, 3 (2016), 1493–1534.

[6] Haro, A., and de la Llave, R. A parameterization method for the computation of invariant tori and their whiskers in quasi-periodic maps: Rigorous results. *Journal of Differential Equations 228*, 2 (2006), 530 – 579.

[7] Hill, T., Cammarano, A., Neild, S., and Wagg, D. Interpreting the forced responses of a two-degree-of-freedom nonlinear oscillator using backbone curves. *Journal of Sound and Vibration 349* (2015), 276 – 288.

[8] Jain, S., Tiso, P., and Haller, G. Exact nonlinear model reduction for a von karman beam: Slow-fast decomposition and spectral submanifolds. *in preparation* (2017).

[9] Jezequel, L., and Lamarque, C. Analysis of non-linear dynamical systems by the normal form theory. *Journal of Sound and Vibration 149*, 3 (1991), 429 – 459.

[10] Jiang, D., Pierre, C., and Shaw, S. Nonlinear normal modes for vibratory systems under harmonic excitation. *Journal of Sound and Vibration 288*, 3-4 (2005), 791 – 812.

[11] Kerschen, G., Peeters, M., Golinval, J., and Vakakis, A. Nonlinear normal modes, part i: A useful framework for the structural dynamicist. *Mechanical Systems and Signal Processing 23*, 1 (2009), 170 – 194. Special Issue: Non-linear Structural Dynamics.

[12] Neild, S., Champneys, A., Wagg, D., Hill, T., and Cammarano, A. The use of normal forms for analysing nonlinear mechanical vibrations. *Philosophical Transactions of the Royal Society of London A: Mathematical, Physical and Engineering Sciences 373*, 2051 (2015).

[13] Neild, S., and Wagg, D. Applying the method of normal forms to second-order nonlinear vibration problems. *Proceedings: Mathematical, Physical and Engineering Sciences 467*, 2128 (2011), 1141–1163.

[14] Peeters, M., Kerschen, G., and Golinval, J.-C. Dynamic testing of nonlinear vibrating structures using nonlinear normal modes. *Journal of Sound and Vibration 330*, 3 (2011), 486–509.

[15] Ponioen, S., Pedergnana, T., and Haller, G. Automated computation of autonomous spectral submanifolds in nonlinear modal analysis. *in preparation* (2017).

[16] Rosenberg, R. On nonlinear vibrations of systems with many degrees of freedom. *Advances in Applied Mechanics 9* (1966), 155 – 242.

[17] Shaw, S., and Pierre, C. Normal modes for non-linear vibratory systems. *Journal of Sound and Vibration 164*, 1 (1993), 85 – 124.

[18] Sinha, S., Redkar, S., and Butcher, E. Order reduction of nonlinear systems with time periodic coefficients using invariant manifolds. *Journal of Sound and Vibration 284*, 3 (2005), 985–1002.

[19] Szalai, R., Ehrhardt, D., and Haller, G. Nonlinear model identification and spectral submanifolds for multi-degree-of-freedom mechanical vibrations. *Proceedings of the Royal Society of London A: Mathematical, Physical and Engineering Sciences 473*, 2202 (2017).

[20] Touzé, C., and Amabili, M. Nonlinear normal modes for damped geometrically nonlinear systems: application to reduced-order modelling of harmonically forced structures. *Journal of sound and vibration 298*, 4 (2006), 958–981.

Thomas Breunung, M.Sc.: Institute for Mechanical Systems, ETH Zürich, Leonhardstrasse 21 LEE M 228, 8092 Zürich, Switzerland (*brethoma@ethz.ch*). The author gave a presentation of this paper during one of the conference sessions.

George Haller, Prof. Dr.: Institute for Mechanical Systems, ETH Zürich, Leonhardstrasse 21 LEE M 210, 8092 Zürich, Switzerland (*georgehaller@ethz.ch*).

Parametric optimization in enumeration of alternative structures of mechanisms

Stefan Chwastek

Abstract: The Machine and Mechanism Theory [1, 6] provides a method of enumerating kinematic chains which involves identification of all possible alternatives of kinematic structures with respect to the required number of degrees of freedom and field of work. This article outlines a methodology of selecting optimal structure from a set of possible solutions. By introducing a certain quality criterion, such as the minimum force or minimum energy, most often in the form of quadratic functionals, a set of parameters optimized for the full range of motion is determined for each structure. Accordingly, each structure is assigned a value of the optimum quality index. The method was illustrated for a one-link crane with bilateral constraints (eg. lever mechanisms), and comparison was made with mechanisms in rope installations, optimized in previous works [3, 4]. For each of the optimized crane mechanisms, a separate optimization task was formulated by defining a specific objective function: 1) counterweight mechanism → minimum boom lifting force, 2) boom lifting mechanism → minimum boom pull force. Optimization tasks were formulated assuming the ideal stiffness of the structure in quasi-static conditions. Effectiveness was verified under dynamic impact conditions, taking into account rope flexibility.

1. Cranes with a pivoting jib as complex dynamic systems

During certain crane operations: hoisting/lowering the payload connected with a slewing jib, Euler and Coriolis forces are generated whose impacts should be minimized already at the stage of selection of the system parameters and mechanism structure. For each investigated crane mechanisms, the specific optimization task is formulated by defining the objective function, typically in the form of quadratic functionals. Thus, for the assumed lifting capacity and distance jaunt we get the structure of the crane mechanism that guarantees the minimal energy consumption. This study investigates the energy efficiency of the jib lift mechanism structures: that with unilateral constraints (rope mechanisms) and with bilateral constraints (eg. lever mechanisms), so that they can be optimized together with the jib-balancing mechanism. Thus obtained optimal sets of parameters for the mentioned mechanisms were optimized for the full range of the slewing motion. A crane with a pivoting boom is considered whose structure is shown in Figure 1. Major parameters include the length and weight of the boom l_{OW} = 30 m and G_W = 45 kN and the weight of the load Q = 50 kN.

Respective forces acting in ropes due to lifting load – S_Q, jib lifting – S_W, counterweight –S_P act at acute angles to the jib: $\alpha = \alpha(\varphi)$, $\beta = \beta(\varphi)$, $\gamma = \gamma(\varphi)$ - not indicated in Figure 1.

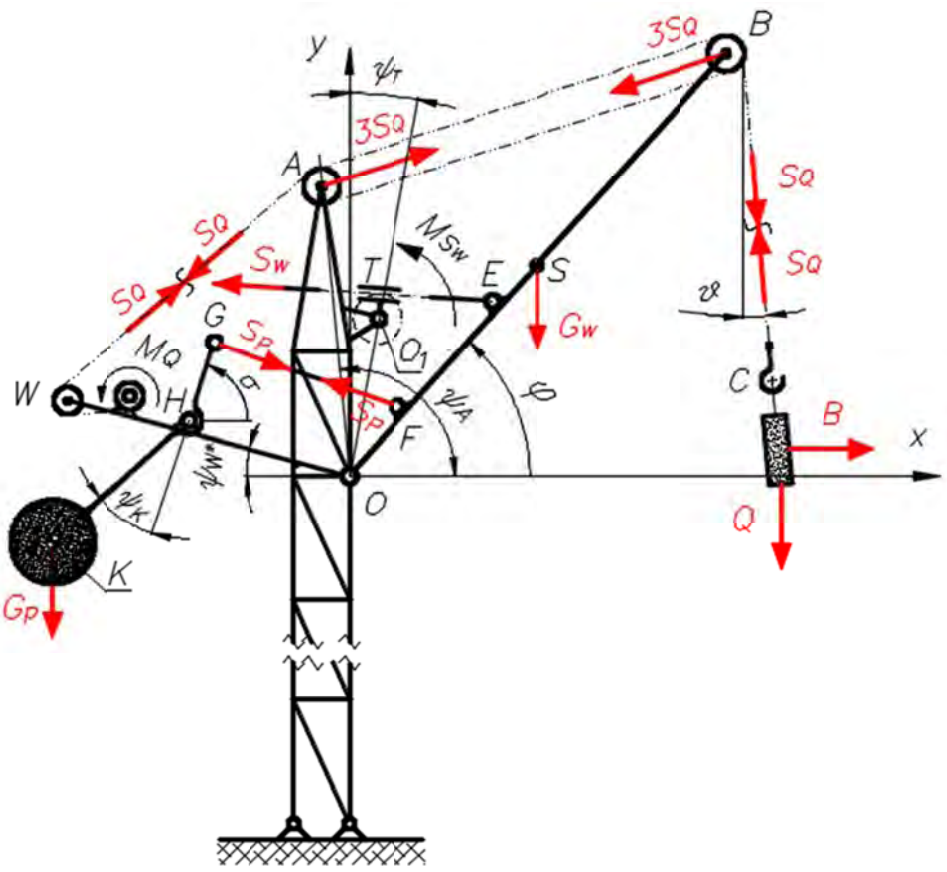

Figure 1. Physical model of a one-link crane

The physical model of a one-link crane is governed by the following equations of motion:

$$\begin{cases} J_{WO}\varepsilon_\varphi = L_{OB}\left[\beta\sin(\alpha)\cdot S_Q - \cos(\varphi-\upsilon)\cdot S_Q + \kappa_{OE}\sin(\beta)\cdot S_W + \kappa_{OF}\cdot\sin(\gamma)\cdot S_P - \kappa_{OS}\cos(\varphi)\cdot G_W\right] \\ m_Q\left[a_{BC} - L_{BC}\cdot\omega_\upsilon^2 - L_{OB}\sin(\varphi-\upsilon)\cdot\varepsilon_\varphi + L_{OB}\cos(\varphi-\upsilon)\cdot\omega_\varphi^2\right] = \cos(\upsilon)\cdot Q - S_Q \\ m_Q\left[L_{BC}\cdot\varepsilon_\upsilon + 2\cdot\omega_\upsilon\cdot v_{BC} - L_{OB}\cos(\varphi-\upsilon)\cdot\varepsilon_\varphi - L_{OB}\sin(\varphi-\upsilon)\cdot\omega_\varphi^2\right] = -\sin(\upsilon)\cdot Q \\ J_H\varepsilon_\sigma(\varphi) = G_P L_{KH}\cdot\cos\left[\sigma(\varphi)-\psi_K\right] - S_P L_{GH}\cdot\sin(\gamma) \end{cases} \quad (1)$$

The first three equations govern the motion of the boom and the load respectively. For a fixed structure of the slewing mechanism, these equations remain unchanged. Changing the structure of the boom lifting mechanism does not alter the form of these equations. The last of the equations (1), describes the specific counterbalance mechanism. Changing the structure of the counterweight

mechanism requires the alteration of the last of equation of motion. The structure and optimal parameters of the slewing mechanism were adopted on the basis of the work [3, 4]. Optimization of slewing mechanism discussed in [3, 4] in fact could be applied to the rope mechanism in a winch. The main objective was to ensure such roping configuration so as to minimize the horizontal hook trajectory error for the full variability range of the change in the jib's angle of horizontal inclination when the winch is blocked [7, 8]. A similar problem was investigated in more recent works such as [2, 5, 9] with respect to the luffing crane and to the two rocker port crane. The considerations focused on the search for the optimal position of blocks in a compensation mechanism such that the boom's unbalance moment should be minimized. In the work [5] a minimum deviation of the vertical load is sought for a finite number of boom positions, basing on the linearized form of the objective function.

2. Exploring the alternative structures of counterweight mechanisms

For the purpose of this study, two structures of counterbalance mechanisms are considered whose kinematic diagrams are shown in Table 1, together with the governing equations. Each structure was assigned a value of the optimum quality index - L_m. (index m – represents the number of the counterweight mechanism according to Table 1). The optimum quality index represents the value of the slewing work of the unloaded boom which will be performed by the mechanism with optimum parameters. Obviously, this will be the lowest value of work for a given structure, assuming the length and weight of the boom remain unchanged. The optimum index can be calculated from the following dependence:

$$L_m = \int_{\varphi_{min}}^{\varphi_{max}} M(\varphi)\, d\varphi \tag{2}$$

Where $M(\varphi)$ is the residual moment of the boom unbalance (for $Q = 0$):

$$M(\varphi) = G_W L_{OS} cos(\varphi) - S_P(\varphi) L_{OF} sin(\gamma). \tag{3}$$

The moment $M(\varphi) = M(\varphi, p_1, p_2, .., p_k)$ depends on the angular position of the boom and the p_i parameters (where $i = 1, 2, ..., k$) of the counterbalance mechanism. The set of optimal parameters is determined by the condition whereby the square function ought to be minimized:

$$J(p_1, p_2, ..., p_k) = \int_{\varphi_{min}}^{\varphi_{max}} [M(\varphi, p_1, p_2, ..., p_k)]^2 \, d\varphi \,. \tag{4}$$

In the optimization procedure, p_i – parameters become optimization variables belonging to a limited set of allowable solutions – Ω, where $\Omega \subset R^{k+r}$. Thus the limitations imposed on the parameters p_i, need to be taken into account, as explained in more detail in [3].

Table 1. Selected structures of counterweight mechanisms

Nr	Diagram of the counterbalance mechanism, equation of motion	Optimal parameters	L_m
1	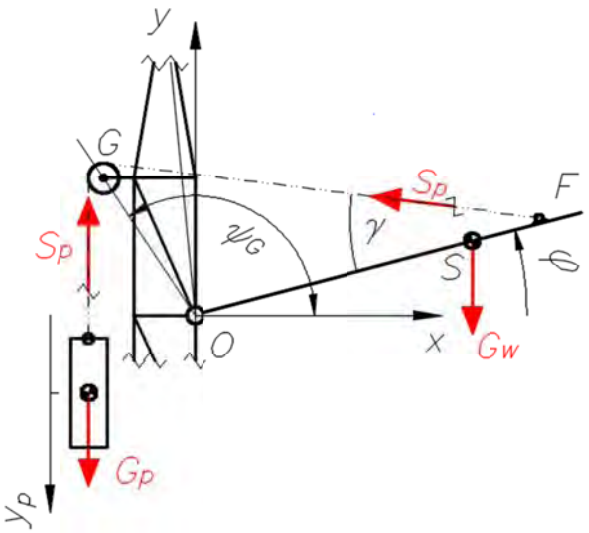 **Figure 2.** Rope counterbalance mechanism $m_P \cdot a_{y_P} = G_P - S_P$ (5)	$p_1 = L_{OG}$ = 7.065m $p_2 = L_{OF}$ = 30 m $p_3 = \psi_G$ = 85.489° $p_4 = G_P$ = 67 kN	L_{11} = 51.43 kJ
		$p_1 = L_{OG}$ = 7.065m $p_2 = L_{OF}$ = 30 m $p_3 = \psi_G$ = 85.489° $p_4 = G_P$ = 76.5 kN	L_{12} = 0.72 kJ
2	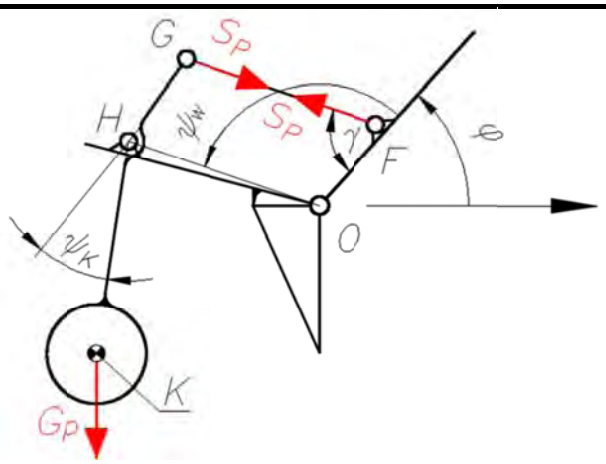 **Figure 3.** Counterbalance lever mechanism $J_P \varepsilon = G_P L_{HK} \cos(\varphi + \psi_K) + S_P L_{OF} \sin(\varphi - \psi_W)$ (6)	$p_1 = L_{OF}$ = 4 m $p_2 = L_{HK}$ = 5 m $p_3 = \psi_K$ = 0° $p_4 = G_P$ = 115.7 kN $L_{OH} = L_{GF}$ $L_{OF} = L_{GH}$	L_{21} = 44.95 kJ
		$p_1 = L_{OF}$ = 4 m $p_2 = L_{HK}$ = 5 m $p_3 = \psi_K$ = 0° $p_4 = G_P$ = 103 kN $L_{OH} = L_{GF}$ $L_{OF} = L_{GH}$	L_{22} = 0 kJ

Dimensions (G_W, L_{OS}) present in the dependence (3), as unrelated to the counterbalance mechanism – are considered as constant parameters in the optimization procedure. Rearranging the equation (5) or (6) (depending on the type of mechanism under consideration) we obtain a formula representing the force acting in the cable in equations (1) and (3). However, in the optimization procedure, the influence of the counterweight acceleration in equations (5) and (6) is neglected in order to determine its dependence on force - S_P. Comparing the quality index of the two optimized mechanisms shown in Table 1, the choice of the lever counterweight mechanism is obvious. It should be noted, however, that the optimization procedure takes into account only the mechanical properties of each solution, without considering the involved costs. The rope mechanism, due to unilateral constraints, excludes the occurrence of compressive forces in the line and therefore the optimum quality index has a relatively high value. When costs are considered in the optimization model, the function (6) can be transformed into a weight criterion.

3. Exploring the alternative options of the jib lifting mechanism

Exploration of alternative design solutions of the boom lifting mechanisms was confined to two structures. It is worthwhile to mention that optimization of the boom lifting mechanism is carried out for a particular counterbalance mechanism. Thus we get four variants of solutions and four optimization tasks are possible. When these are solved, the values of the optimum quality index – S_{Wmn} can be determined (index n - represents the number of the boom lifting mechanism according to Table 2). Table 2 shows the kinematic diagrams of boom lifting mechanisms: rope and rack mechanics, alongside the values of the optimum quality index - S_{Wmn}. The optimum quality index becomes the maximum value of the force acting in the lifting cable – S_W at the full slewing cycle of the boom under the nominal load – Q. The indices m, n identify the correlation: m – th counterbalance mechanism with the n – th boom lifting mechanism in the given crane structure variant. The set of optimal parameters is determined by the imposed condition that the square functional be minimized:

$$J\left(p_{k+1}, p_{k+2},..., p_{k+r}\right) = \int_{\varphi_{min}}^{\varphi_{max}} \left[S_w\left(\varphi, p_{k+1}, p_{k+2},..., p_{k+r}\right)\right]^2 d\varphi \,. \tag{7}$$

The formula expressing the force S_W in the optimization problem involving the boom lift mechanism is derived from equation (1) for zero angular acceleration, ie for $\varepsilon = 0$. The force $S_W(\varphi) = S_W(\varphi, p_{k+1}, p_{k+2}, ..., p_{k+r})$ depends on the boom angle and parameters p_j (where $j = k+1, k+2, .., k+r$) of the boom lifting mechanism. All parameters determined in previous sections remain constant throughout the entire optimization procedure.

Table 2. Selected structures of lifting mechanisms

<table>
<tr><th>n</th><th>Diagram of the boom lifting mechanism, optimal parameters</th></tr>
<tr><td>1</td><td>
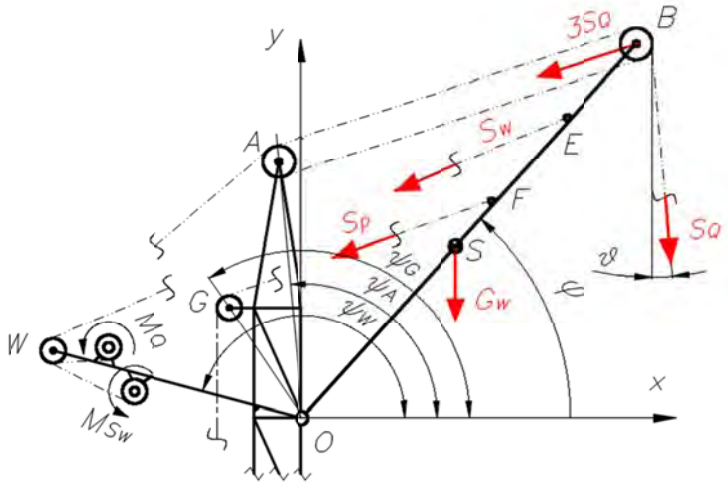

Figure 4. Boom-lifting rope mechanism
<table>
<tr><th>m</th><th>Optimal parameters for a given configuration (m 1)</th><th>S_{Wm1}</th></tr>
<tr><td>1</td><td>$p_4 = G_P$ = 67 kN $P_5 = L_{OE}$ = 30 m, $p_6 = L_{OW}$ = 10 m, $p_7 = \psi_W$ = 116.49°</td><td>17.67 kN</td></tr>
<tr><td>2</td><td>$p_4 = G_P$ = 103 kN $P_5 = L_{OE}$ = 30 m, $p_6 = L_{OW}$ = 10 m, $p_7 = \psi_W$ = 116.879°</td><td>14.64 kN</td></tr>
</table>
</td></tr>
<tr><td>2</td><td>
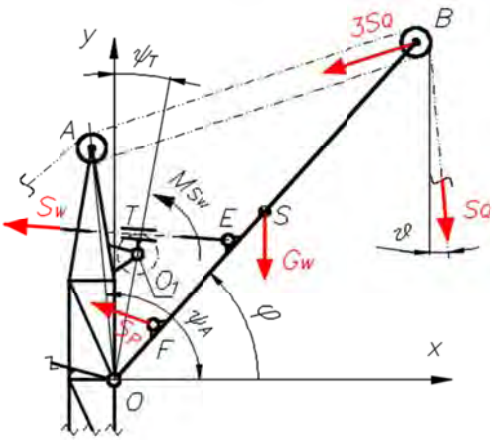

Figure 5. Boom lifting lever mechanism
<table>
<tr><th>m</th><th>Optimal parameters for a given configuration (m 2)</th><th>S_{Wm2}</th></tr>
<tr><td>1</td><td>$p_4 = G_P$ = 76.5 kN, $P_5 = L_{OE}$ = 3.75 m, $p_6 = L_{OT}$ = 3 m, $p_7 = \psi_T$ = 5°</td><td>60.55 kN</td></tr>
<tr><td>2</td><td>$p_4 = G_P$ = 115.71 kN , $P_5 = L_{OE}$ = 3.75 m, $p_6 = L_{OT}$ = 3.75m, $p_7 = \psi_T$ = 13.5°</td><td>27.33 kN</td></tr>
</table>
</td></tr>
</table>

The total value of the nominal lifting work - L_{Qmn} depends on the type and parameters of the counterbalance mechanism, and is independent on the type and parameters of the boom lifting mechanism. For the counterweight mechanisms with optimum parameters according to Table 1, we will get: $L_{Q11} = 58.7$ kJ, $L_{Q12} = 7.353$ kJ, $L_{Q21} = 44.9$ kJ, $L_{Q22} = 6.6$ kJ. The value $L_{Q21} = 44.9$ kJ is associated with the need to reduce the weight of the counterweight to 103 kN in the ropes mechanism lifting the boom combined with lever mechanism of counterweight.

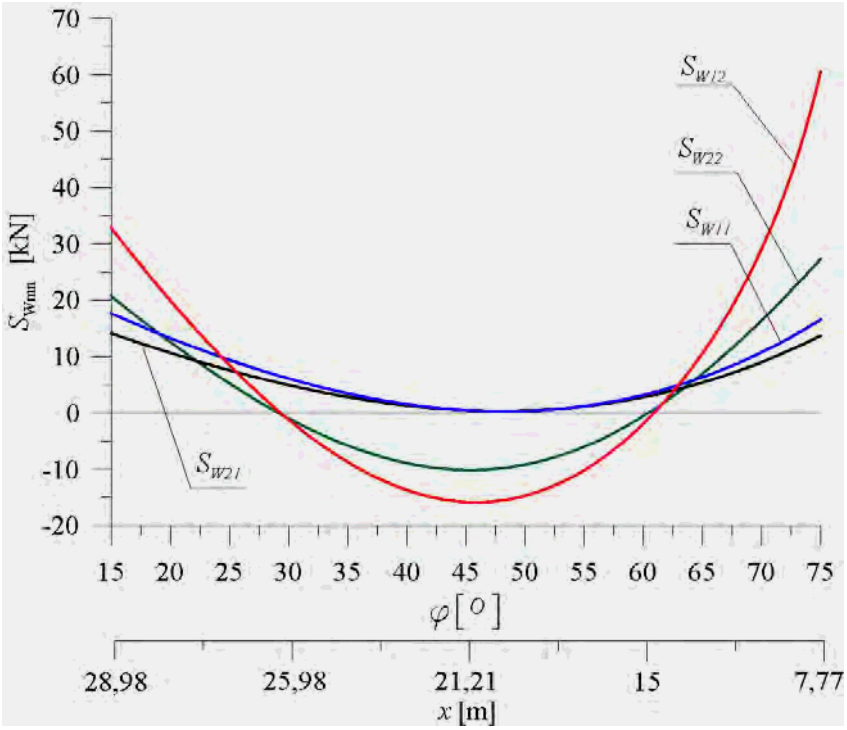

Figure 6. Forces acting in the cables of the jib-lifting mechanism during the slewing motion

Figure 6 confirms that in the task involving the synthesis of crane boom lifting mechanism, S_{Wmn} - is a better indicator of the optimality than the value of lifting work - L_{Qmn}.

Advantages of minimizing the force acting in the rope in the jib lifting mechanism are:

- Small rope diameter → small pulley → low resistance during rope winding,
- Low-power electric motors (approximately 8 kW) → reduced energy demand,
- Small force variations in ropes → less overloading of electric motors → little overheating of engines.

4. Verification of optimization results under dynamic conditions

To verify the optimization results in dynamic conditions it is required that flexibility in the system, including rope flexibility, should be taken into account. Rope flexibility is inversely proportional to its effective length (sag – l). Assuming the averaged value of the Young modulus E = 125 GPa for ropes with a non-metallic core, in accordance with [3, 4, 7, 8], the modulus of elasticity of the rope is obtained from the formula:

$$k(l) = i_k \frac{\mathrm{EA}}{l}, \tag{8}$$

where: A – effective cross-section area of the rope, i_k – multiplicity of the pulley block.

Rope cross-section areas in rope mechanisms are calculated basing on [10] and taken to be identical, ie. $A_P = A_{SW} = A_Q = 3.833$ cm^2. Damping in the ropes is assumed to be proportional to the modulus of elasticity through the dimensionless damping factor ζ_0 (in this paper been assumed: $\zeta_0 = 0$).

The effects of rope tension on its stiffness and damping are neglected.

The duty cycle of each mechanism involves the following stages: start, steady-state motion and braking, yielding a trapezoidal characteristics of drive velocity. Basing on the catalogue data, the universal model of kinematic excitations is adopted differing in the steady-state velocity values for specific mechanisms. For the winch in the luffing mechanism steady-state velocity values is $V_{Sw11} = V_{Sw21} = 24$ m/min, whilst for the rack-and-pinion lift mechanism combined with combined with lever mechanism of counterweight $V_{Sw22} = 9$ m/min, but combined with rope mechanism of counterweight $V_{Sw21} = 7.2$ m/min. The steady-state velocity for the load winch $V_Q = 27$ m/min. The start-up and braking times are taken to be identical $t_{s/b} = 3$ s. Solving the Matlab-Simulink system of differential equations (1) yields the vibration acceleration patterns and rope tension variations.

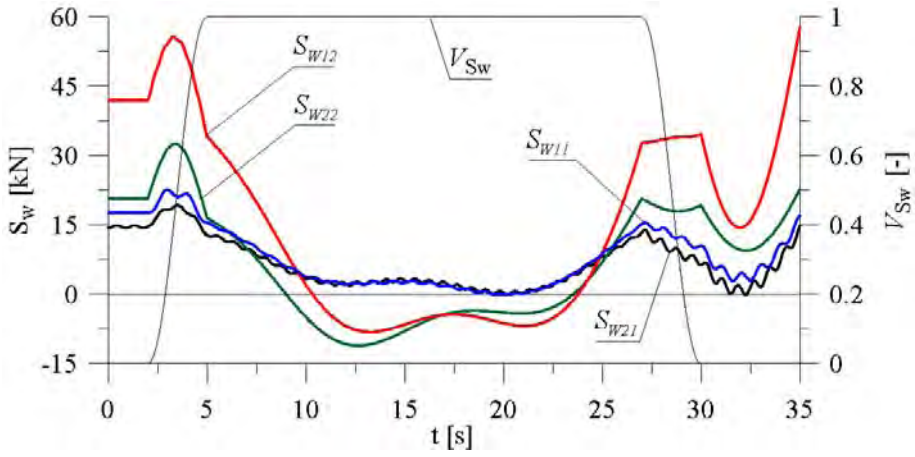

Figure 7. Comparison of dynamic forces acting in ropes of the hoisting boom

Of particular importance is comparison of forces acting in ropes and power consumption in the crane with the rope lifting mechanism and various counterbalance mechanisms under dynamic conditions. It appears (see Fig 7) that dynamic forces acting in ropes whilst lifting the boom in the entire motion range are smaller in the variant/ solution incorporating a counterweight lever mechanism, i.e. $S_{w21}(t) < S_{w11}(t)$ and $S_{w22}(t) < S_{w12}(t)$ for T = 30s. In the context of energy consumption, of particular importance are bilateral constraints in the boom-lifting mechanism. It is well demonstrated in Fig 8, indicating that that $P_{W22}(t) < P_{W12}(t) < P_{W21}(t) < P_{W11}(t)$ for $t \subset [0; T]$.

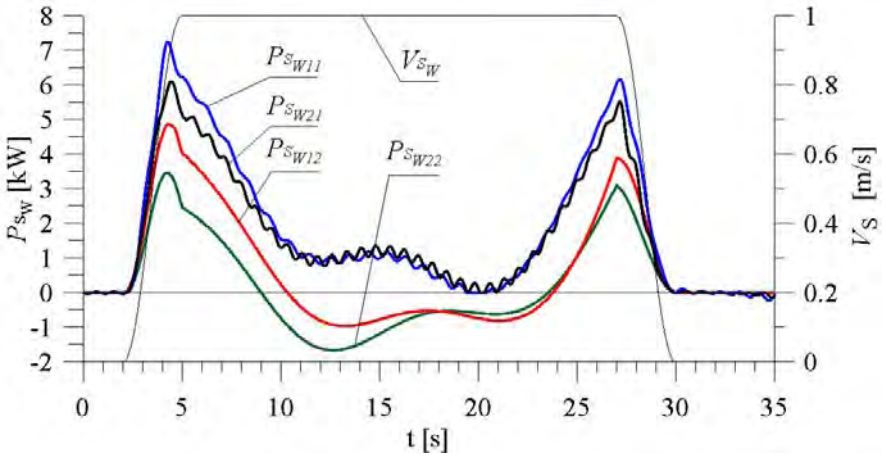

Figure 8. Comparison of power demand in boom lifting mechanisms

In this study the load characteristics of the drive motors are neglected, and for the purpose of comparison a more universal kinematic model governed by trapezoidal characteristics of velocity in normalized form – V_{Sw} is considered. Multiplying the normalized speed values by the specific steady-state velocity V_{Swmn}, we obtain the drive characteristic for the relevant boom lifting mechanism. As shown in Fig 6, forces acting in the toothed rack in cranes incorporating a rack-pinion lift mechanism are greater than forces acting in ropes. In terms of energy consumption, the optimal approach is to correlate the lever type counterbalance mechanism with the rack-pinion lifting mechanism, which is assumed to be self-locking.

5. Concluding remarks

Optimization tasks involving the two rope mechanisms and two lever mechanisms in a one-link jib crane lead us to the following conclusions:

Parametric optimization in the enumeration of alternative structures of mechanisms is aimed to yield the best combination of different mechanisms in a given structure from a previously selected set of structures with optimum parameters Ω_O. Where $\Omega_O \subset \Omega$. The procedure adopted to select the set of

solutions acceptable in the context of functional requirements is explained in more detail in [3, 4].

For the assumed lifting capacity and distance jaunt we get such combination of counterbalance mechanisms with the crane lifting mechanism that guarantees minimal dynamic force and minimal energy consumption. The extended method of exploring alternative structures of mechanisms for parametric optimization, outlined in this paper, allows for finding globally optimal design solution and the method is a universal. Effective optimization, confirmed by dynamic analysis, allows the dynamic overload values to be significantly reduced at the stage of design of the steel structure, resulting in a lighter and cheaper structure. Application of dedicated software (such as Mathcad) to solve variational problems such as finding a minimum of properly formulated quadratic functionals proves to be very effective and rapid solution to parametric optimization problems.

References

[1] Adamczyk E.: *Synteza strukturalna i geometryczna wieloczłonowych ustrojów nośnych maszyn roboczych*. Wydawnictwo Politechniki Wrocławskiej. Wrocław 1982, ISSN 0324 -962X.

[2] Cheng Wenming: *Optimization of cylindrical drum compensation luffing system for portal crane*; Hoisting and Conveying Machinery; International Conference of Electrical, Automation and Mechanical Engineering (EAME 2015).

[3] Chwastek S.: *Optymalizacja parametryczna mechanizmów wypadowych żurawi jedno-członowych*. Przegląd Mechaniczny, Zeszyt 9/12, str. 35–39. ISSN 0033-2259.

[4] Chwastek S.: *Optimisation of Crane Mechanisms – Selected Problems; Key Engineering Materials* Vol. 542 (2013) pp. 43-58, Trans Tech Publications, Switzerland, doi:10.4028/www.scientific.net/KEM.542.43.

[5] Dong Soo Kim Jongsoo Lee: *Structual Design of a Level-luffing Crane Through Trajectory Optimization and Strength-based Sized Optimization*. Structural and Multidisciplinary Optimization, pp. 515–531. Struct Multidisc. Optim. (2015), DOI 10.1007/s00158-014-1139-2.

[6] Gronowicz A., Miller S.: *Mechanizmy, Metody tworzenia rozwiązań alternatywnych, katalog schematów strukturalnych i kinematycznych.* Wydawnictwo Politechniki Wrocławskiej. Wrocław 1997, ISBN 83-7085-257-2.

[7] Piątkiewicz A., Sobolski R.: *Cranes*, WNT, Warsaw 1977, Symbol 78620/Tw. (in Polish).

[8] Scheffler M., Pajer G., Kurh F.: Fördertechnik. Unstetigförder, *Krane–mechanische Ausfürungen und Stahlverke*, VEB Verlag Berlin 1975.

[9] Xue Y. Xue, Wang, W., Ji M.S., Wu N.: *The Dimensionless-Parameter Robust Optimization Method Based on Geometric Approach of Pulley Block Compensation in luffing Mechanism*; International Conference of Electrical, Automation and Mechanical Engineering (EAME 2015).

[10] http://www.drumet.pl/pl,kat2,liny_specjalistyczne,8.html

Stefan Chwastek Ph.D: Cracow University of Technology, Faculty of Mechanical Engineering, al. Jana Pawła II 37, 31-864 Kraków, Poland *stefan.chwastek@mech.pk.edu.pl*).

Some value distribution and growth properties of solutions of Painlevé and Riccati equations

Ewa Ciechanowicz

Abstract: By Malmquist theorem, the first order non-linear algebraic differential equations with rational coefficients and admitting transcendental meromorphic solutions were recognised to be the Riccati equations. Classification of the second order ordinary differential equations without movable branch points, on the other hand, led to recognition of so-called Painlevé equations. Among them, six irreducible equations, usually denoted as $P_1 - P_6$, are best known. The equations P_1, P_2, P_4 and modified P_3, P_5 have only meromorphic solutions. Moreover, for certain parameters, equations $P_2 - P_6$ have particular solutions, which can be expressed in terms of Riccati equations with rational coefficients. Meromorphic solutions of both Riccati and Painlevé equations have been thoroughly studied by methods of value distribution theory since 1950's, with the topic gaining in popularity since 1990's, yet still leaving space for further research.

1. Introduction

In 1913 Malmquist proved that the differential equation $f' = R(z, f)$, where R is a rational function, admits a transcendental meromorphic solution if it is a Riccati equation or a linear equation [10] (see also: [8]). By the term Riccati equation we mean here the first order non-linear ordinary differential equation of the form

$$f' = a_0 + a_1 f + a_2 f^2, \tag{1}$$

where a_0, a_1, a_2 are meromorphic functions, $a_2(z) \not\equiv 0$. If the coefficients of the equation (1) are constant, all non-constant solutions are either transcendental meromorphic if $S := \frac{1}{2}(4a_0a_2 - a_1^2) \neq 0$ or rational (linear fractional transformations) if $S = 0$. Also in case of polynomial coefficients the solutions are meromorphic and their basic value distribution properties well known [21, Ch.5] (see also: [12, Ch.5]). More generally, if a_0, a_1, a_2 are entire then all local solutions of the equation can be extended to functions meromorphic in the whole complex plane [12]. In we admit meromorphic coefficients, even rational ones, the existence of meromorphic solutions is not guaranteed and depends on multiplicity of poles of the coefficients (for examples see: [12, Ch.9]).

By substitution $u = a_2 f + \frac{1}{2}a_1 + \frac{1}{2}\frac{a_2'}{a_2}$, the equation (1), preserving notation f for the solution, is transformed into

$$f' = Q + f^2, \tag{2}$$

where $Q(z) = a_0 a_2 - \frac{a_1^2}{4} + \frac{a_1'}{2} - \frac{3}{4}(\frac{a_2'}{a_2})^2 - \frac{a_1 a_2'}{2a_2} + \frac{a_2''}{2a_2}$ [12]. This substitution sets a one-to-one correspondence between solutions of (1) and (2). If a_0, a_1, a_2 are rational, then also Q is a rational function. Corresponding transcendental solutions of the equations differ by a rational component. In our further considerations concerning Riccati equations we discuss properties of solutions of (2), with additional assumption that $Q(z) \not\equiv const.$

Painlevé equations are nonlinear second order ordinary differential equations of the form $f'' = F(z, f, f')$, where F is rational in f, algebraic in f' and analytic in z, which possess the Painlevé property (solutions have no movable algebraic singularities). New functions appearing among solutions of these equations are called Painlevé transcendents. In this paper we concentrate on two equations out of original six irreducible ones on the list,

$$f'' = 2f^3 + zf + \alpha, \tag{P_2}$$

$$f'' = \frac{f'^2}{2f} + \frac{3f^3}{2} + 4zf^2 + 2(z^2 - \alpha)f + \frac{\beta}{f}, \tag{P_4}$$

where α, β, are fixed complex parameters and $f = f(z)$. We also discuss so-called equation P_{34}, given by

$$f'' = \frac{(f')^2}{2f} + 2Bf^2 - Bzf - \frac{A}{2f}, \tag{P_{34}}$$

where A, B are complex parameters. The equation is connected with P_2 via the Hamiltonian system. Hence all the local solutions not only of P_2 and P_4, but also of P_{34} can be extended to meromorphic functions in $\mathbb{C}$.

It is well-known that for special values of the parameters in the equation, Painlevé equations $P_2 - P_6$ possess special Riccati type solutions (the so-called classical solutions). In this context the associated Riccati equations have rational coefficients. Thus all meromorphic solutions of such an equation are of finite order of growth [12, Ch.9].

Painlevé second equation $P_2(\alpha)$ admits Riccati solutions iff $\alpha = n + \frac{1}{2}$, where $n \in \mathbb{Z}$ [7]. If, for instance, $\alpha = \varepsilon/2$, ($\varepsilon = \pm 1,$) then the Riccati equation associated with $P_2(\varepsilon/2)$ is

$$f' = \varepsilon f^2 + \frac{\varepsilon}{2} z.$$

As it is a Riccati equation with constant coefficients and $S \neq 0$, all solutions are transcendental meromorphic. It follows from the correspondence between P_2 and P_{34} that $P_{34}(1, B)$ also admits Riccati solutions [14].

When dealing with $P_4(\alpha, \beta)$ we meet with equations of the form

$$f' = a + bzf + cf^2, \tag{3}$$

where a, b, c are complex constants depending on parameters α, β. By the substitution $f = \frac{1}{c}(u - \frac{b}{2}z)$ the equation can be we transformed into

$$u' = P + u^2 \tag{4}$$

with $P(z) = ac + \frac{b}{2} - \frac{b^2}{4}z^2$. By Theorem 4.1 in [1], the equation (4) with the polynomial $P(z)$ of degree 2 admits at most one rational solution, the rest of them being transcendental meromorphic functions. Thus also the equation (3) admits at most one rational solution.

More accurately, the equation $P_4(\alpha, \beta)$ admits solutions expressible in terms of solutions of a Riccati equation iff $\beta = -2(2n + 1 + \varepsilon\alpha)^2$ or $\beta = -2n^2$, where $n \in \mathbb{Z}$, $\varepsilon = \pm 1$ [7]. For $\beta = 0$, the accompanying equation is

$$f' = \varepsilon(f^2 + 2zf) - 2(1 + \varepsilon\alpha).$$

Methods which were originally introduced to study Panlevé equations and thus also their Riccati solutions, as a sort of 'backshift', can be transferred to Riccati equations. Recently, such an approach was shown, for example, in [19] and [20].

2. Basic notions of Nevanlinna theory

In the paper we apply the standard notations of Nevanlinna Theory [13]. By the term 'meromorphic function' we always mean a function meromorphic in the whole complex plane. Thus, for a meromorphic f and $r > 0$, $m(r, f)$ denotes the mean proximity to infinity function and $N(r, f)$ the integrated function counting poles, $m(r, a, f)$ and $N(r, a, f)$ respective functions for a finite value a. Nevanlinna's characteristic function is defined by

$$T(r, f) := m(r, f) + N(r, f).$$

By the First Main Theorem of Nevanlinna, for any value $a \in \mathbb{C}$ the equality

$$m(r, a, f) + N(r, a, f) = T(r, f) + O(1) \qquad (r \to \infty) \tag{5}$$

holds. The Second Main Theorem of Nevanlinna states that for a meromorphic f and a finite number of distinct values $\{a_k\}_{k=1}^q \in \overline{\mathbb{C}}$ the inequality

$$\sum_{k=1}^{q} m(r, a_k, f) \leq 2T(r, f) + O(\log(rT(r, f))) \tag{6}$$

holds for $r \to \infty$, possibly outside a set $E \subset [0, \infty)$ of finite linear measure.

Inequality (6) in the Second Main Theorem can also be formulated in the following way:

$$(q-2)T(r,f) \leq \sum_{k=1}^{q} \overline{N}(r, a_k, f) + O(\log(rT(r,f))), \tag{7}$$

where $\overline{N}(r,a,f)$ is the integrated function counting each a-point once, regardless of its multiplicity. Let us also add the notation $N_1(r,a,f) := N(r,a,f) - \overline{N}(r,a,f)$.

The number a is *a Picard defective value* of a transcendental function f if f has only a finite number of $a-$points. *A Nevanlinna defective value*, on the other hand is a value for which the condition

$$\delta(a,f) := \liminf_{r\to\infty} \frac{m(r,a,f)}{T(r,f)} = 1 - \limsup_{r\to\infty} \frac{N(r,a,f)}{T(r,f)} > 0$$

holds. It follows from the Second Main Theorem, that $\sum\limits_{a\in\overline{\mathbb{C}}} \delta(a,f) \leq 2$.

Growth of a meromorphic function is measured with respect to the characteristic. Values

$$\varrho := \limsup_{r\to\infty} \frac{\log T(r,f)}{\log r} \qquad \text{and} \qquad \lambda := \liminf_{r\to\infty} \frac{\log T(r,f)}{\log r}$$

are called, respectively, *order* and *lower order* of a meromorphic function f.

In value distribution theory, if f is a meromorphic function, then any function $s : [0,\infty) \to \mathbb{R}$ with the property

$$s(r) = o(T(r,f)), \qquad r \to \infty,\ r \notin E,$$

for a set E of finite linear measure, is usually denoted by $S(r,f)$. If for a meromorphic function $a(z)$ we have

$$T(r,a) = S(r,f),$$

then we say that a is *a small function of* f or, sometimes *a small target of* f. The set of all functions small with respect to f is denoted by $\mathcal{S}(f)$.

Let us end this section with the following result on defective values of Riccati equations.

Theorem 2.1 [12] *Let f be a meromorphic solution of (1) with meromorphic coefficients small with respect to f. Then $\delta(a,f) = 0$ for $a = \infty$ and for all $a \in \mathbb{C}$ such that*

$$a_0(z) + a_1(z)a + a_2(z)a^2 \not\equiv 0.$$

If a fulfills the equality above, then it is a Picard defective value of f.

3. Special forms of the Second Main Theorem

Transcendental meromorphic solutions of Painlevé equations show extraordinary regularity. It is visible, in particular, in the fact that the Second Main Theorem in their cases reduces to the form of an asymptotic equality [9].

Theorem 3.1 *If f is an arbitrary transcendental solution of equation P_2 or P_4, then*

$$m(r,1/f)+N(r,1/f')+N_1(r,f)=2T(r,f)+O(\log r) \qquad (r\to\infty).$$

For transcendental solutions of P_{34} we have a similar form of the theorem [3].

Theorem 3.2 *Let f be an arbitrary transcendental meromorphic solution of $P_{34}(A,\ B)$, $A, B \in \mathbb{C}$. Then*

$$m(r,1/f)+N(r,1/f')+N_1(r,f)=2T(r,f)+O(\log r) \qquad (r\to\infty).$$

If, in addition, $A \neq 0$, then

$$N(r,1/f')+N_1(r,f)=2T(r,f)+O(\log r) \qquad (r\to\infty).$$

Let us now formulate a similar result concerning Riccati equations.

Theorem 3.3 *Let f be an arbitrary transcendental meromorphic solution of a Riccati equation with rational coefficients. Then the Second Main Theorem reduces to the asymptotic equality*

$$m(r,1/f)+N(r,1/f')+N_1(r,f)=2T(r,f)+O(\log r) \qquad (r\to\infty).$$

In the proof of Theorem 3.3 we shall apply the following lemma [9, Ch. 3].

Lemma 3.4 *Let f be an arbitrary transcendental meromorphic function satisfying*

$$m(r,f')=O(\log r) \quad (r\to\infty) \qquad \text{and} \qquad m(r,\frac{f}{f'})=O(\log r) \quad (r\to\infty).$$

Then

$$m(r,1/f)+N(r,1/f')=N(r,f')+O(\log r).$$

Proof of Theorem 3.3.

We consider the equation $f'=Q+f^2$ with $Q(z)$ rational and its transcendental meromorphic solution f. As f is a meromorphic function of finite order, by lemma on the

logarithmic derivative, we have $m(r, f'/f) = O(\log r)$. Applying the properties of $\log^+$, we get

$$m(r, f') \leq m(r, f'/f) + m(r, f).$$

Applying the Clunie lemma to (2), we get $m(r, f) = O(\log r)$ and thus $m(r, f') = O(\log r)$.

We now differentiate the Riccati equation and obtain

$$f'' = Q' + 2ff',$$

which leads to

$$\frac{f}{f'} = \frac{1}{Q'}\frac{f''}{f'}f - \frac{2}{Q'}f^2.$$

Applying the properties of the proximity function,

$$m(r, \frac{f}{f'}) \leq m(r, \frac{1}{Q'}) + m(r, \frac{f''}{f'}) + m(r, f) + m(r, \frac{2}{Q'}) + m(r, f^2) + O(1).$$

For a rational function q we have $m(r, q) = O(\log r)$, so $m(r, \frac{1}{Q'}) = O(\log r)$ and $m(r, \frac{2}{Q'}) = O(\log r)$. Also, by the lemma on the logarithmic derivative and the fact that f (as a solution of a Riccati equation with rational coefficients), and therefore also f', is of finite order we have $m(r, \frac{f''}{f'}) = O(\log r)$. Lastly, $m(r, f^2) \leq 2m(r, f) = O(\log r)$. The conclusion, that $m(r, \frac{f}{f'}) = O(\log r)$ follows. This way the conditions of Lemma 3.4 are fulfilled, so

$$m(r, 1/f) + N(r, 1/f') = N(r, f') + O(\log r).$$

Now, the number of poles of Q is finite. The poles of f, which are not the poles of Q must be simple. Thus $N(r, f') = 2N(r, f) + O(\log r)$ and $N_1(r, f) = O(\log r)$. It follows that

$$m(r, 1/f) + N(r, 1/f') + N_1(r, f) = N(r, f') + N_1(r, f) + O(\log r)$$

$$= 2N(r, f) + O(\log r) = 2T(r, f) + O(\log r).$$

4. Petrenko's defective values

Proximity of a meromorphic function to a value a may also be estimated by means of a different metric than in Nevanlinna theory. In 1969 Petrenko introduced the function

$$\mathcal{L}(r, a, f) := \begin{cases} \max\limits_{|z|=r} \log^+ |f(z)| & \text{for} \quad a = \infty, \\ \max\limits_{|z|=r} \log^+ |f(z) - a|^{-1} & \text{for} \quad a \neq \infty. \end{cases}$$

Hence $a \in \overline{\mathbb{C}}$ is *a defective value in the sense of Petrenko* if

$$\beta(a, f) := \liminf_{r\to\infty} \frac{\mathcal{L}(r, a, f)}{T(r, f)} > 0.$$

The quantity $\beta(a,f)$ is called *Petrenko's deviation*.

In 1969 in [15] Petrenko proved that if f is a meromorphic function of finite lower order, then for all $a \in \overline{\mathbb{C}}$ we have

$$\beta(a,f) \leq B(\lambda) := \begin{cases} \frac{\pi\lambda}{\sin \pi\lambda} & \text{if} \quad \lambda \leq 0.5\,, \\ \pi\lambda & \text{if} \quad \lambda > 0.5\,, \end{cases} \tag{8}$$

and in 1990 in [11] Marchenko and Shcherba proved the inequality

$$\sum_{a\in\overline{\mathbb{C}}} \beta(a,f) \leq 2B(\lambda). \tag{9}$$

The estimates of deviations of solutions of P_2, P_4 and P_{34} were shown in [2]. Here we present an estimate concerning Petrenko's deviations for solutions o Riccati equations.

Theorem 4.1 *Let f be a transcendental meromorphic solution of a Riccati equation (2) with the coefficient such that $T(r,Q) = S(r,f)$. Then, for all values $a \in \overline{\mathbb{C}}$ such that*

$$Q(z) + a^2 \not\equiv 0,$$

we have $\mathcal{L}(r,a,f) = S(r,f)$ and $\beta(a,f) = 0$. If $Q(z) + a^2 \equiv 0$, then $\beta(a,f) \geq 1$.

To prove the theorem we need the following results from [2]. They are, respectively, analogues of Clunie lemma and Mohon'ko-Mohon'ko lemma.

Lemma 4.2 *Let f be a transcendental meromorphic solution of $f^n P(z,f) = Q(z,f)$, where n is a positive integer, $P(z,f)$, $Q(z,f)$ are polynomials in f and its derivatives with meromorphic coefficients a_ν, b_ν, respectively, which are small with respect to f in the sense that*

$$\mathcal{L}(r,\infty,a_\nu) = S(r,f), \qquad \mathcal{L}(r,\infty,b_\nu) = S(r,f).$$

If the total degree d of $Q(z,f)$ as a polynomial in f and its derivatives is $d \leq n$, then

$$\mathcal{L}(r,\infty,P(z,f)) = S(r,f).$$

Lemma 4.3 *Let $P(z,f,f',...,f^{(n)}) = 0$ be an algebraic differential equation ($P(z,u_0,u_1,...,u_n)$ is a polynomial in all arguments) and let f be its transcendental meromorphic solution. If a constant a does not solve the equation, then $\mathcal{L}(r,a,f) = S(r,f)$ and $\beta(a,f) = 0$.*

Proof of Theorem 4.1. Equation (2) can be written as $f^2 = Q - f'$, so it fulfills conditions of Lemma 4.2 with $P(z, f) = f(z)$, $Q(z, f) = Q(z) - f'(z)$ and $n = 1$. It follows that

$$\mathcal{L}(r, f) = \mathcal{L}(r, P(z, f)) = S(r, f) \qquad (r \to \infty).$$

Next, we need to notice that if a constant a does not solve (2), by Lemma 4.3, we get $\mathcal{L}(r, \frac{1}{f-a}) = S(r, f)$. Finally, we observe that if a constant a solves the equation (2) then, by Theorem 2.1 it is a defective value of f in the sense of Picard. It means that this value is assumed by f at most a finite number of times, so $\delta(a, f) = 1$. Then the inequality $\delta(a, f) \leq \beta(a, f)$ completes the proof.

5. Small target functions

According to a conjecture of Nevanlinna, it is possible to replace in the Second Main Theorem constants a_k with meromorphic functions $a_k(z)$, provided that $a_k(z)$ are small functions of f. Let us then consider the notion of a defective function. If for a meromorphic a, we have $\delta(a_k, f) := \delta(0, \frac{1}{f-a_k}) > 0$, we say that a_k is *a defective function of f in the sense of Nevanlinna,* and if $\beta(a_k, f) := \beta(0, \frac{1}{f-a_k}) > 0$, we say that it is *a defective function in the sense of Petrenko.* Since 1920's Nevanlinna's conjecture was approached a number of times. Finally, in 1986 Steinmetz [18] proved the analogue of (6) for small functions in general and in 2004 Yamanoi in [22] obtained the analogue of inequality (7).

For defective functions in the sense of Petrenko the problem of obtaining the exact analogue of (9) has not been solved in generality. Ciechanowicz and Marchenko in 2007 [4] showed the analogue of (9) for entire f and rational a_k, and in 2011 [5] for rational a_k and f meromorphic with $N(r, f) = S(r, f)$. The most general result in this direction so far was given by the same authors in 2017 [6]. They showed that for f meromorphic and of finite lower order the quantity of small targets defective with respect to f in the sense of Petrenko is at most countable. However, the upper bound they received for the sum of deviations is not sharp.

Assessment of behavior towards small target functions of solutions of the second and fourth Painlevé equations was conducted by Shimomura [16, 17].

Theorem 5.1 *Let f be arbitrary transcendental meromorphic solution of P_2 and let a be a meromorphic function such that $T(r, a) = S(r, f)$. Then*

$$m(r, \frac{1}{f-a}) \leq \frac{1}{2}T(r, f) + O(\log r + T(r, a)) \qquad \textit{and} \qquad \delta(a, f) \leq \frac{1}{2}.$$

Theorem 5.2 *Let f be an arbitrary transcendental meromorphic solution of $P_4(\alpha, \beta)$*

and a be a transcendental meromorphic function such that $T(r,a) = S(r,f)$. If $\beta \neq 0$, then

$$m(r, \frac{1}{f-a}) \leq \frac{1}{2}T(r,f) + O(\log r + T(r,a)) \qquad \textit{and} \qquad \delta(a,f) \leq \frac{1}{2};$$

and if $\beta = 0$, then

$$m(r, \frac{1}{f-a}) \leq \frac{1}{4}T(r,f) + O(\log r + T(r,a)) \qquad \textit{and} \qquad \delta(a,f) \leq \frac{1}{4}.$$

The following result shows estimates of defects of a transcendental meromorphic solution of P_{34} with respect to small target functions [3].

Theorem 5.3 *Let a and f be arbitrary transcendental meromorphic solutions of $P_{34}(A,B)$, $A, B \in \mathbb{C}$, such that $T(r,a) = S(r,f)$. Then*

$$m(r, \frac{1}{f-a}) \leq \frac{1}{2}T(r,f) + O(\log r + T(r,a)) \qquad \textit{and} \qquad \delta(a,f) \leq \frac{1}{2}.$$

If a does not solve P_{34} and $T(r,a) = S(r,f)$, where f is an arbitrary transcendental meromorphic solutions of $P_{34}(A,B)$, then

$$m(r, \frac{1}{f-a}) = O(\log r + T(r,a)) \qquad \textit{and} \qquad \delta(a,f) = 0.$$

Let us now present a similar result concerning solutions of Riccati equations and small targets.

Theorem 5.4 *Let f be arbitrary transcendental meromorphic solution of (2) such that $T(r,Q) = S(r,f)$ and let a be a meromorphic function such that $T(r,a) = S(r,f)$. If a does not solve the equation, then*

$$m(r, \frac{1}{f-a}) = S(r,f) \qquad \textit{and} \qquad \delta(a,f) = 0.$$

If, on the other hand, $a(z)^2 - a(z)' + Q(z) \equiv 0$, then $\delta(a,f) = 1$.

Proof. Put $g(z) := f(z) - a(z)$. Then, inserting this in the equation (2) we get

$$(g+a)' = Q + (g+a)^2,$$

so

$$g^2 = g' - 2ag - (a^2 - a' + Q) := g' - 2ag - F(z,a). \tag{10}$$

As f is transcendental, g is also transcendental and the coefficients in the equation above are small with respect to f, hence also with respect to g. Thus, by Clunie lemma,

$$m(r, f-a) = m(r,g) = S(r,g) = S(r,f).$$

Next, we notice that zero solves the equation (10) only if $F(z,a) \equiv 0$. If not, by Mohon'ko-Mohon'ko lemma,

$$m(r, \frac{1}{f-a}) = m(r, \frac{1}{g}) = S(r,g) = S(r,f).$$

Assume now that $F(z,a) \equiv 0$. Then the equation (10) has the form

$$g' = g^2 + 2ag,$$

so it is a Riccati differential equation. By assumption, $T(r,a) = S(r,g)$ and zero fulfills the equation. Thus, by Theorem 2.1, zero is a Picard defective value of g, so

$$N(r, \frac{1}{f-a}) = N(r, \frac{1}{g}) = O(\log r),$$

and $\delta(a,f) = 1$.

Corollary 5.5 *If f and q are, respectively, a transcendental and a rational solution of* (3)*, then $\delta(q,f) = 1$. If f is a transcendental solution of* (3) *and q is a rational function which does not solve the equation, then $\delta(q,f) = 0$. Therefore*

$$\sum_{q \in \mathcal{Q}} \delta(q,f) = 1,$$

where $\mathcal{Q}$ denotes the set of all rational functions.

It is also possible to formulate the following theorem on Petrenko's deviations from small targets.

Theorem 5.6 *Let f be arbitrary transcendental meromorphic solution of* (2) *such that $T(r,Q) = S(r,f)$ and let a be a meromorphic function such that $T(r,a) = S(r,f)$. If a does not solve the equation, then*

$$\mathcal{L}(r, \frac{1}{f-a}) = S(r,f) \qquad \text{and} \qquad \beta(a,f) = 0.$$

If, on the other hand, $a(z)^2 - a(z)' + Q(z) \equiv 0$, then $\beta(a,f) \geq 1$.

Proof. As in the proof of Theorem 5.4 we put $g(z) := f(z) - a(z)$, insert this in the equation (2) and get

$$g^2 = g' - 2ag - F(z,a),$$

with $F(z,a) := a(z)^2 - a(z)' + Q(z)$. Assuming that $F(z,a) \not\equiv 0$, zero does not solve the equation. By Lemma 4.3, we obtain

$$\mathcal{L}(r, \frac{1}{f-a}) = \mathcal{L}(r,0,g) = S(r,g) = S(r,f)$$

and $\beta(a,f) = 0$. If, on the other hand, $F(z,a) \equiv 0$ then zero solves the equation (10) and, by Theorem 2.1, we get $\beta(a,f) = \beta(0,g) \geq \delta(0,g) = 1$.

References

[1] Bank, S., Gundersen, G., Laine, I. Meromorphic solutions of the Riccati differential equation. *Ann. Acad. Sci. Fenn. Mathematica,* 6 (1981), 369–398.

[2] Ciechanowicz, E., Filipuk, G. Meromorphic solutions of $P_{4,34}$ and their value distribution. *Ann. Acad. Sci. Fenn. Mathematica,* 41 (2016), 617–638.

[3] Ciechanowicz, E., Filipuk, G. Transcendental meromorphic solutions of P_{34} and small targets. In *Analytic, Algebraic and Geometric Aspects of Differential Equations*, pp. 307–323. Trends in Mathematics, Birkhauser, 2017.

[4] Ciechanowicz, E., Marchenko, I.I. On deviations from rational functions of entire functions of finite lower order. *Ann. Pol. Math.,* 91.2-3 (2007), 161–177.

[5] Ciechanowicz, E., Marchenko, I.I. On deviations and strong asymptotic functions of meromorphic functions of finite lower order. *Journal of Math. Anal. and Appl.,* 382 (2011), 383–398.

[6] Ciechanowicz, E., Marchenko, I.I. On deviations, small functions and strong asymptotic functions of meromorphic functions. *Kodai Math. J.*, 40 (2017), 379–404.

[7] Clarkson, P.A. Painlevé transcendents. *NIST Digital Library of Mathematical Functions,* http://dlmf.nist.gov/32.

[8] Eremenko, A.E. Meromorphic solutions of algebraic differential equations. *Uspekhi Mat. Nauk,* 37:4 (1982), 53–82. (Russian) Engl. transl. in *Russian Math Surveys,* 37:4 (1982), 61–95.

[9] Gromak, V., Laine, I., and Shimomura, S. *Painlevé Differential Equations in the Complex Plane.* De Gruyter Studies in Mathematics 28, Walter de Gruyter, Berlin, 2002.

[10] Malmquist, J. Sur les fonctions à un nombre fini des branches définies par les équations différentielles du premiere ordre. *Acta Math.,* 36 (1913), 297–343.

[11] Marchenko I.I., Shcherba A.I. On the magnitudes of deviations of meromorphic functions. *Mat. Sb.,* 181 (1990), 3–24. (Russian) Engl. transl. in *Math. USSR Sb.,* 69 (1991), 1–24.

[12] Laine,I. *Nevanlinna Theory and Complex Differential Equations.* Berlin, New York, De Gruyter, 1993.

[13] Nevanlinna, R. *Eindeutige analytische Funktionen*, Springer-Verlag, Berlin, 1970.

[14] Ohyama, Y. Rational transformations of cofluent hypergeometric equations and algebraic solutions of the Painlevé equations P_1 to P_5. In *Algebraic, analytic and geometric aspects of complex diffequations and their deformations. Painlevé hierarchies.* 137–150, RIMS Kokyuroku Bessatsu B2, Kyoto 2007.

[15] Petrenko V.P., The growth of meromorphic functions of finite lower order. *Izv. Akad. Nauk SSSR,* 33.2 (1969), 414–454. (Russian)

[16] Shimomura, S. Value distribution of Painlevé transcendents of the first and the second kind. *J. Anal. Math.,* 82 (2000), 333–346.

[17] Shimomura, S. On deficiencies of small functions for Painlevé transcendents of the fourth kind. *Ann. Acad. Sci. Fenn. Ser A I Math.,* 27 (2002), 109–120.

[18] Steinmetz, N. Eine Verallgemainerung des zweiten Nevanlinnaschen Hauptsatzes. *J. Reine Angew. Math.,* 368 (1986), 134–141.

[19] Steinmetz, N. Sub-normal solutions to Painlevé's second differential equation. *Bull. Lond. Math. Soc.,* 45 (2013), 225–235.

[20] Steinmetz, N. Complex Riccati differential equations revisited. *Ann.Acad.Sci.Fenn.Math.,* 39 (2014), 503–511.

[21] Wittich, H. *Neuere Untersuchunden über eindeutige analytische Funktionen.* Springer, Berlin, 1968.

[22] Yamanoi, K. The second main theorem for small functions and related problems. *Acta Math.,* 192 (2004), 225–294.

Ciechanowicz Ewa, Ph.D.: University of Szczecin, Faculty of Mathematics and Physics, Institute of Mathematics, Instytut Matematyki US, ul. Wielkopolska 15, 70-451 Szczecin, Poland (*ewa.ciechanowicz@usz.edu.pl*). The author gave a presentation of this paper during one of the conference sessions.

A bifurcation and symmetry discussion of the Sommerfeld effect

Eoin Clerkin, Rubens Sampaio

Abstract:

The Arnold Sommerfeld effect is an intriguing resonance capture and release series of events originally demonstrated in 1902. A single event is studied using a two degree of freedom mathematical model of a motor with imbalance mounted to laterally restricted spring connected cart. For a certain power supplied, in general the motor rotates at a speed consistent with a motor on a rigid base. However at speeds close to the natural frequency of the cart, it seemingly takes on extra oscillations where for a single rotation it both speeds up and then slows down. Therefore in a standard experimental demonstration of the effect, as the supplied torque force is increased or decreased, this may give the illusion that the stable operation of the motor is losing and gaining stability. This is not strictly the case, instead small oscillations always present in the system solution are amplified near the resonant frequency. The imbalance in the motor causes a single resonance curve to fold back on itself forming two fold bifurcations which leads to hysteresis and an asymmetry between increasing and decreasing the motor speed. Although the basic mechanism is due to the interplay between two stable and one unstable limit cycles, a more complication bifurcation scenario is observed for higher imbalances in the motor. The presence of a Z2 phase space symmetry tempers the dynamics and bifurcation picture.

1. Historical background of and introduction to the Sommerfeld effect

Arnold Sommerfeld's posthumous biography complied from his written correspondence [5], mentions an intriguing engineering problem proposed by Prof. Hermann Boost also of the Technical University of Aachen whereby a steam engine is to be installed in a building which is itself to be supported by beams. As a demonstration to the district association of German engineers (VDI), using a weighted motor with small imbalance screwed tightly to a table-top, he caused the motor to become enthralled to the frequency of the table which induced large vibrations highlighting to the audience the catastrophic potential of resonance. The phenomenon is justified with reference to linear resonance curves for harmonic forced linear differential equations in his seminal 1902 paper [16]. It was fifty years later with the work of Blekhman [1,7] that the phenomenon was named in his honour and more than fifty years still it has seen a renewed interest among the applied mechanics and mechanical engineering community, being a main discussion point at the 2015 IUTAM symposium in Frankfurt [2,8,10].

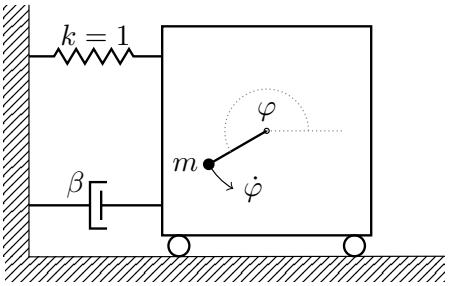

Figure 1. Schematic diagram of laterally restricted spring-connected and damped cart with a driven rotor with imbalance.

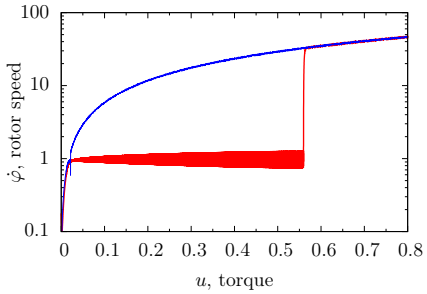

Figure 2. Sweep diagram showing the rotor speed as the torque force is slowly increased (red) and decreased (blue).

In order to study the Sommerfeld effect as a purely mechanical phenomenon, a translational oscillator rotational actuator, as schematically drawn in Fig. 1, has been investigated by a number of authors [2,8,9,11] as a minimal model that is believed to encompasses only its essential dynamical attributes. This paradigmatic example is made up of a rotor with a small imbalance (m) a certain distance from its centre which is mounted to a laterally-restricted spring-connected and damped cart. This drawing (Fig. 1) follows the normal applied mechanics convention whereby a single wall span implies restriction in two spatial directions. In addition, the rotor would normally be orientated in the horizontal plane, so as to remove any need to consider gravitational effects. Physical parameters expected to be important to model such a scenario would be mass inertia of the cart, imbalance and rotor, the spring and damping constants as well as a measure of the symmetry-brokenness in the rotor, i.e the distance between the imbalance and its centre of rotation. The supplied power or torque force to the rotor is varied to unveil the Sommerfeld effect.

As shown by the red curve in Fig. 2, as the power is monotony increased to the non-ideal [6] motor, its angular velocity increases until it approaches the natural frequency of the spring, which is normalised to one in this manuscript. After which, additional increases in power does not increase the motor speed, but instead leads to the growth of oscillations in the smooth operation of the motor and in the displacement of the cart (not seen). A log-scale diagram of rotor speed versus the supplied torque is shown in Fig. 2 where a linear response of the angular velocity to the torque appears as a logarithm function. Subsequently, as the torque force is increased further (red curve), there comes a point where the oscillations in the cart fall relatively silent and the rotor rapidly speeds up to match the expected speed of the rotor had it been on a rigid base. Characteristic of the Sommerfeld effect is an

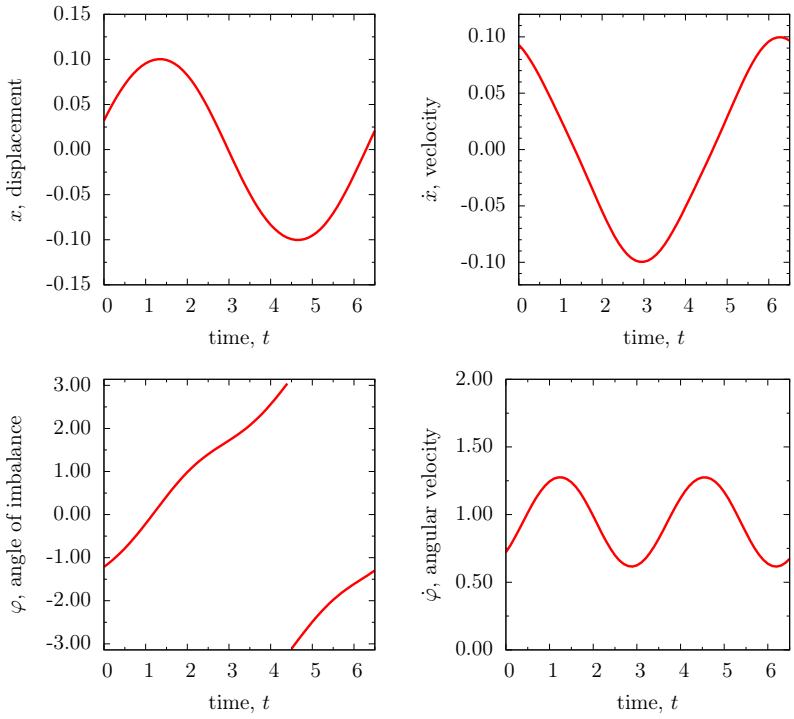

Figure 3. For $u = 0.1$, time-traces showing a symmetric, resonance captured S-type cycle (5). Period $\tau = \frac{2\pi}{avg(\dot{\varphi})} = \frac{6.28}{0.94} = 6.68$. x can be seen to precede $\dot{x}$ by $\frac{\tau}{4}$. $\epsilon = 0.0125$.

asymmetry between increasing (red curve) and decreasing (blue curve) the power to the motor, and significant hysteresis is seen, meaning that two distinct states for the system are concurrently stable. In fact, this was already alluded to in Sommerfeld's 1902 paper [16] where he discussed temporarily grasping the table legs to change the motors speed to a state operating at higher frequency. In our case, when the system is operating in the resonance captured zone, a temporarily restriction on cart's movement would allow the rotor to be released from resonance. The succeeding section to the next will explain the dynamics behind Fig.2, but first we introduce the equations of motion which were integrated to generate it.

2. Mathematical model of a translational oscillator rotational actuator

In order to investigate a single Sommerfeld resonance capture and release event, a model for a translational oscillator rotational actuator as schematically drawn in Fig. 1 is studied. The kinetic and potential energies of the cart and rotor are available from Appendix B of

Ref. [15] which can be used to derive the system of equations with dimensions such as those in Refs. [9, 11]. The following work uses the non-dimensionalised version of these equations from Ref. [7] as it significantly saves on the number of required parameters.

$$d_t^2 x + \beta d_t x + x = -\epsilon d_t^2 \left(\cos\left(\varphi\right)\right), \tag{1a}$$

$$d_t^2 \varphi + \nu d_t \varphi = u + \epsilon\kappa \sin(\varphi) d_t^2 x. \tag{1b}$$

The system has two degrees of freedom, the displacement of the cart x, defined positively to the right and negatively to the left from its equilibrium position, and φ as the angle of the imbalance in the rotor, defined by the normal mathematics convention from the right horizontal axis as shown in Fig. 1. In this paper d_t to the left of or a dot above a variable represents the operation of differentiating with respect to non-dimensionalised time t.

The non-dimensionalised parameter $\beta, \epsilon, \kappa, \nu$ encapsulates dependant dimensioned parameters such as the mass of the cart and imbalance, damping in the cart and rotor, level of symmetry-brokenness, and moment of inertia. Parameter values were chosen to compare with the work in Refs. [9, 11]. After transforming these parameter to their non-dimensionalised form, the parameter values become $\beta = 0.01983$, $\kappa = 0.017$, $\nu = 857.143$ and the natural frequency in the spring-cart is normalised to one (cf. Fig. 2). $\epsilon = \{0.005, 0.0125\}$ is one of the more important parameter as a measure of imbalance or symmetry-brokenness in the rotor which results in the coupling between relations (1a) and (1b) in Eq. (1). For this parameter, the following symmetry exists.

$$\begin{bmatrix} x \\ \epsilon \end{bmatrix} \longmapsto - \begin{bmatrix} x \\ \epsilon \end{bmatrix} \qquad \text{parameter symmetry} \tag{2}$$

Physically ϵ is proportional to the length between the imbalance and its centre of rotation and therefore the parameter symmetry (2) may be interpreted as a redefinition of orientation of x displacement as the imbalance is translated by 180^o after going to negative length. The torque u is the force supplied to the rotor, which is the parameter used to unveil the Sommerfeld effect and is the main sweep parameter in this study. A *parameter space symmetry* also exists, namely

$$\begin{bmatrix} \varphi \\ u \end{bmatrix} \longmapsto - \begin{bmatrix} \varphi \\ u \end{bmatrix} \qquad \text{parameter symmetry} \tag{3}$$

which allows one to obtain the dynamics due to clockwise driving of the rotor from the anti-clockwise driving by means of the additive inverse of the displacement and angle, thereby

velocity and angular velocity of the cart and rotor. Because of these two parameter symmetries, we may limit this study to positive torque and positive ϵ only and still obtain the full dynamical picture.

Unlike the two introduced parameter systems, a *phase space* symmetry such as the following involutionary (a.k.a reflection) symmetry influences the dynamics by itself.

$$\begin{bmatrix} x \\ \varphi \end{bmatrix} \longmapsto \begin{bmatrix} -x \\ \varphi + \pi \end{bmatrix} \qquad \mathbb{Z}_2 \text{ symmetry} \tag{4}$$

This means that if $y_1(t)$ is a solution to the Eq. (1) then so is $y_2(t) = \mathbf{R}y_1(t)$ where $\mathbf{R}$ is the action of the symmetry. As this study's primarily interest is in periodic orbits in the system as the resonance frequency of the cart is transversed by the rotor, it is of importance to consider how symmetry (4) may affect limit cycles. To this aim, we will use the results and language of Refs. [13, 14]. The phase space may be decomposed $\mathbb{R}^4 = X^+ \oplus X^-$ where the action of the symmetry (4) is $Rv = v$ for $v \in X^+$ and $Rv = -v$ for $v \in X^-$. Some care needs be exercised when doing this as φ is not strictly in $\mathbb{R}$, so we consider various coordinate transforms such as $\{\varphi, \dot{\varphi}\} = \{\dot{\varphi}\cos\varphi, \dot{\varphi}\sin\varphi\} \in \mathbb{R}^2$ which enforces this. It may be thus deduced that $X^+ = \emptyset$ and this has the immediate consequence to limit the types of limit cycles permitted in system (1), namely limit cycles of fixed or mixed fixed-symmetry type of Refs [13, 14] do not exist. The only cycles remaining which are *invariant* to $\mathbb{Z}_2$ symmetry (4) are of the following type

$$\begin{bmatrix} x \\ \varphi \end{bmatrix}(t) \longmapsto \begin{bmatrix} -x \\ \varphi + \pi \end{bmatrix}(t + \frac{\tau}{2}), \qquad \text{S- and M-type} \tag{5}$$

where τ is the minimal period of the limit cycle. In the nomenclature of Refs. [13, 14], these are called symmetric or S-type cycles. As can be seen after half the period of oscillation the displacement is exactly its negative. Likewise this rule applies for the velocity. Therefore, cycles invariant with respect to condition (5) must average to zero for these variables over one cycle. A typical limit cycle of system Eq. (1) is shown in Fig. (3) which can be seen to be invariant with respect to Eq. (5). It is known [12] that a period doubling bifurcation may not occur in limit cycles of S-type due to a multiplicity of two in their Floquet multipliers. In later sections, cycles which are symmetry-broken with respect to Eqs. (4) and (5) will be discussed.

3. Basic mechanism of the Sommerfeld effect

By direct integration of the equations of motion (1) with different initial angular velocities, Refs. [4, 11] highlight the existence of "hidden" bistable attractors. The 2D diagram Fig. 4

shows the ultimate limit cycles of these trajectories by the red and blue solid closed periodic orbits. The red curve shows large variance in the displacement and velocity, hence large potential and kinetic energy in the cart. Conversely, although the blue curve shows higher eccentricity thus a higher ratio of kinetic to potential energy in the cart, both energies are are substantially less than that of the red limit cycle, instead it has considerably greater total energy in the rotating rotor. This can be seen in Fig. 5 where the blue limit cycle has larger maximum angular velocity than the red limit cycle. In the case of the blue limit cycle, the rotor operates at the frequency consistent with a motor on a rigid base whilst in the case of the red limit cycle, the rotor rotates at an average frequency approximately consistent with the natural frequency of the cart. This oscillation frequency persists over an extensive change of torque as can be seen in Figs. 2 and 5 and the red limit cycle is captured by the resonance. In the resonance captured range of torque, there is therefore at least bistability of limit cycle states. which was, in fact, already alluded to in the seminal 1902 paper [16] where Sommerfeld discussed temporarily grasping the table legs to change the motors speed to a state operating at higher frequency. In our case, when the system is operating in the resonance captured zone, a temporarily restriction on cart's movement would allow the rotor to be released from resonance.

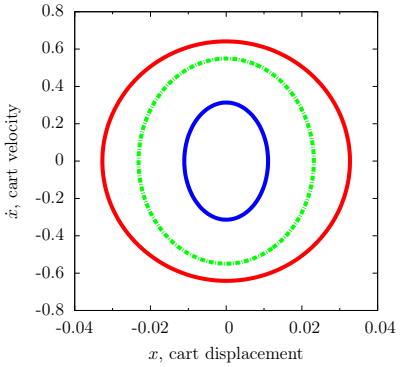

Figure 4. Two stable limit cycles (red and blue) separated by an unstable limit cycle (green - dashed). Generated for $u = 0.15$.

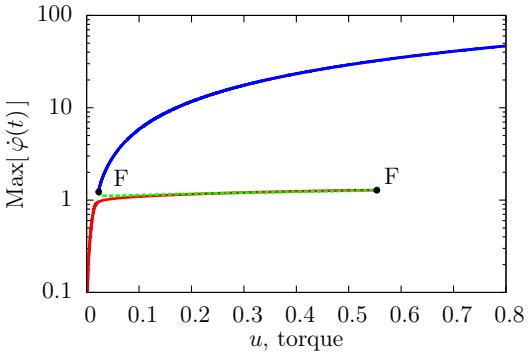

Figure 5. Continuation of the S-type cycle using AUTO [3] showing a loss and gain of stability at fold bifurcations of limit cycles (F). (cf. Fig 2)

In fact, a third limit cycle exists between the resonance captured and resonance released dynamics as shown in Figs 4 and 5 by the green dashed line. This limit cycle has intermediate energy in the cart and although it is unstable, it controls the limits of the stable dynamics. As the torque is increased from its value in Fig. 4, there comes a point, actually a fold bifurcation

of limit cycles, where the green unstable limit cycle collides with the red resonance captured limit cycle. They annihilate one another leaving the blue limit cycle as the only stable attractor. Consequently transience ensues as the dynamics is exponentially attracted to its new higher in terms of rotating speed but lower in terms of cart vibrations state. Physically this explains the resonance release event (cf. Fig 2) whereby the rotor is now free to rotate at a frequency approximately consistent with its supplied torque. Conversely, decreasing the supplied torque force from its value in Fig. 4, the blue resonance released limit cycle collides with the green unstable limit cycle. They annihilate one another in a fold bifurcation of limit cycles leaving only the red resonance captured limit cycle. This can also be seen in Figs 2 and 5 but the speed-down for the rotor is more modest as the blue and red limit cycles are much closer together at this bifurcation than the higher torque fold bifurcation. It should be noted that the red limit cycle follows the normal operation of the limit cycle on a rigid base for low torque force. We stress that the red limit cycle undergoes no change in its dynamical state, i.e. bifurcation, as it becomes captured by the resonance of the cart. Instead, small oscillations always present in the cart and rotating rotor are merely amplified in the resonance zone. As is often the case when a resonance curved is transversed, there is a phase difference of half the period between the red and blue limit cycles. This can been seen in Fig. 3 as the displacement proceeds the velocity by a quarter period, the opposite is the case for the resonance released cycle. Lastly we'd like to mention that the rate of change of the torque is important in the physical observation of the effect as the torque may be already significantly higher before the transient behaviour has had time to settle, this is emphasised well in Ref. [6].

4. Larger imbalance in the motor - Symmetry-broken limit cycles

As imbalance is needed in the motor to create the resonance capture and therefore the Sommerfeld effect, näively one may assume that an increase in the overall imbalance may lead to resonance capture to occur over a greater range of the supplied torque. In this section, it will be seen that this is not the case, but instead a different sequence of bifurcations than in Sec. 3 are possible whilst still maintaining the Sommerfeld effect phenomenon. The red points in Fig 6 are rastored data from an integration in time of the equations of motion (1) as the torque parameter is varied, but sufficiently slowly to allow the dynamics to settle to its steady state at each step. In order to concentrate on the resonance captured event, the resonance released dynamics, the blue curve in Figs. 2, 4 and 5 are not displayed in Fig. 6. As before, when the torque force is increased, the dynamics is captured into resonance. It can be seen that the rotor speed becomes enthralled to the resonance frequency of the cart but oscillates in $\dot{\varphi}$ with an amplitude that modestly grows as the torque increases. After

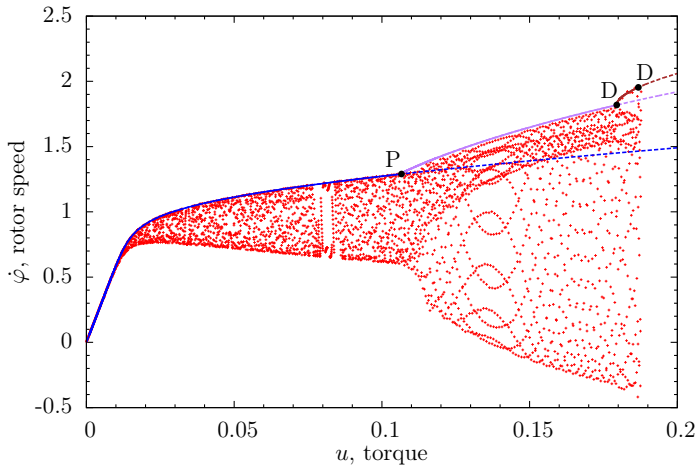

Figure 6. For $\epsilon = 0.0125$, the torque is slowly increased showing the resonance captured event. The dynamics undergo several bifurcations before at approximately $u = 0.19$ the resonance captured dynamics is released. Over plotted lines shows the maximum rotor speed of the limit cycles from continuation data. Blue line follows a S-type cycle (cf. Fig. 3), the purple line are M-type cycles (cf. Fig. 7, and brown line shows a M-type cycle of doubled period (cf. Fig 8). Solid lines are stable and dashed lines show unstable limit cycles. Bifurcations points are shown as solid black dots and labelled P to denote a supercritical pitchfork bifurcation of limit cycles and D to denote a period doubling bifurcation.

$u = 0.1$, there comes a point where the dynamics significantly changes. Continuation using software AUTO [3] reveals the S-type cycle (Fig. 5), crucial to the basic Sommerfeld effect mechanism outlined in Sec. 3, looses stability when a Floquet multiplier crosses the unit circle at real part one. This is a supercritical pitchfork bifurcation which is labelled P in diagram Fig. 5. After this point the S-type cycle although unstable continues in a similar bifurcation sequence discussed in the previous section.

At the supercritical pitchfork bifurcation, stability is transferred to a not-previously-discussed type of limit cycle, those that of course obeys the symmetry (5) but is no longer invariant to it but is symmetry broken. For these cycles applying the action of the symmetry (5) results in a different albeit congruent cycle. In the nomenclature of Ref. [14], these are called M-type cycles for "mirror" as they occur as a twin pair. If a change of stability or local dynamics happens to one of them, it must automatically happen to the other. However as the symmetry is now broken, the symmetry (4) no longer restricts the dynamics and the bifurcations that may occur individually. As the torque force is increased further, it can

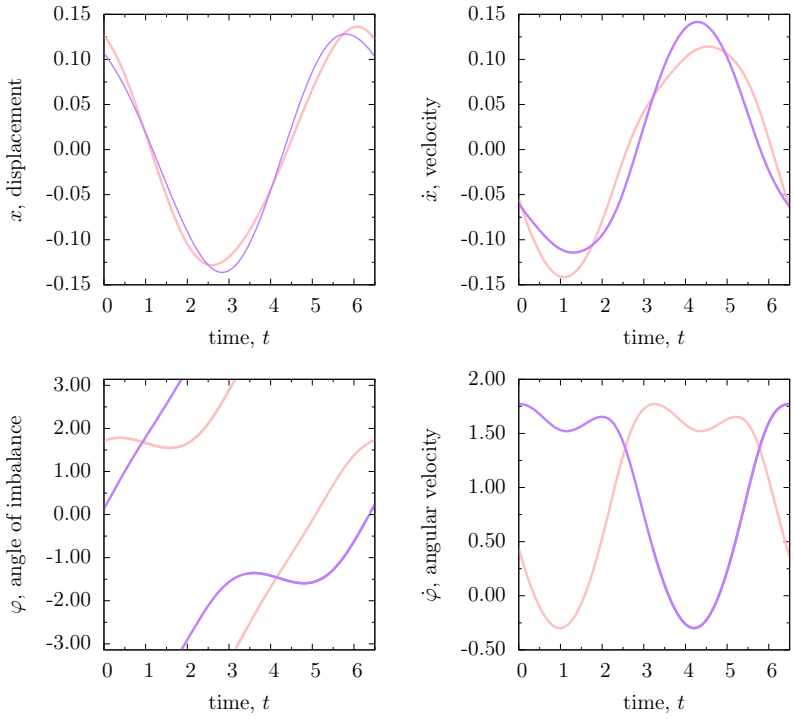

Figure 7. For $u = 0.17$, time-traces showing a symmetry-broken with respect to symmetry (4), resonance captured M-type cycle [14], which momentary rotor reversal. Period $\tau = \frac{2\pi}{avg(\dot{\varphi})} = \frac{6.28}{0.97} = 6.48$. x can be seen to preceed $\dot{x}$ by $\frac{\tau}{4}$. $\epsilon = 0.0125$.

be seen in Fig. 6 that eventually the rotor speed oscillations go through zero and become negative. Physically this would mean that the rotor, momentarily reverses to rotate in the clockwise direction before resuming its normal anti-clockwise revolutions. Dynamically the point at which this occurs is not special, however we caution that for some coordinate systems, continuation of the M-type cycles may be difficult. A typical M-type cycle, displaying this reversal of rotor direction is shown in Fig. 7. In these time-traces, applying the action of the symmetry (4) to the purple limit cycle results in the pink limit cycle and visa-versa. The two M-type cycles may now be distinguished by the purple limit cycle having lower maximum positive displacement but higher maximum velocity than the pink limit cycle. Both share the same angular velocity and therefore are difficult to distinguish in Fig. 6. The next significant change in dynamics seen in Fig. 6 is a period doubling bifurcation, labelled by the letter D. We note that although S-type weren't permitted to undergo a period doubling, no such restriction occurs for M-type cycles. At this point the twin cycles loose stability

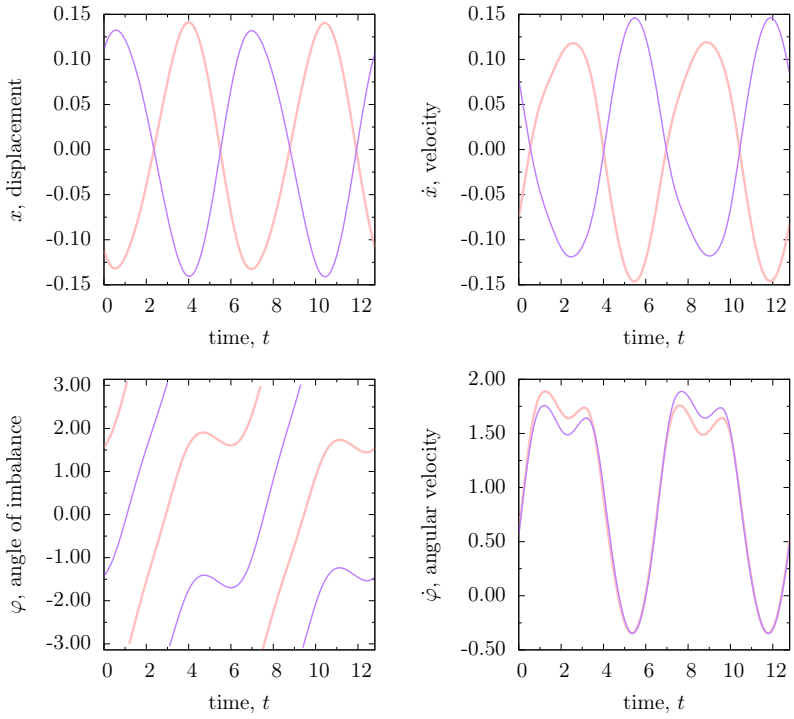

Figure 8. For $u = 0.18$, time-traces showing a symmetry-broken M-type limit cycle with respect to symmetry (4), with momentary rotor reversal. Period has doubled $\tau = \frac{2\pi}{avg(\dot{\varphi})} \times 2 = \frac{6.28}{0.98} \times 2 = 12.87$. x can be seen to preceed $\dot{x}$ by $\frac{\tau}{4}$. $\epsilon = 0.0125$.

and a new M-type cycle pair with double the original frequency is born. The displacement, velocity, angle of imbalance, and angular velocity of the rotor for this limit cycle is displayed in Fig. 8. The limit cycles are also symmetry-broken as can be seen from them having significantly different average displacement and velocity in the cart. Applying symmetry 4 converts between the congruent purple and pink limit cycle pair as before. Shortly after the torque force is increased further in Fig. 6 these period-doubled limit cycles in turn looses stability at another period doubling bifurcation creating stable limit cycles of even higher periods. Nevertheless, the stability of the resonance captured range is soon after lost and the dynamics is released from resonance to enter the higher rotor speed state. Comparing Figs. 2, 5 and 6, we note that this occurs at a significantly reduced torque strength than in Sec. 3, meaning that the resonance captured region was reduced by the extra imbalance.

5. Summary

In this manuscript we describe the basic Sommerfeld effect mechanism as a resonance curve folded back on itself creating two fold bifurcations of limit cycles. Although this basic mechanism has been known for some time, the authors are not aware of it being directly articulated in a fashion similar to this paper. The fold bifurcations explain the jump phenomena when the driving parameter is moved outside the domain of existance of a limit cycle solution creating fast transience to a neighbouring attractor. This naturally leads to an asymmetry between increasing and decreasing the driving parameter and a bistability of states. The symmetries present are discussed in order to categorise the observed limit cycles.

In Sec. 4 we examine the Sommerfeld effect at a larger imbalance in the motor. A different more complicated bifurcation sequence of pitchfork and period doubling bifurcations are witnessed allowing for multistabilities of limit cycles. Although the effect is considerable different than the lower imbalance in Sec. 3, both scenarios ought to fall under the general term of the Sommerfeld effect. The same resonance capture and release events occur but the general area of resonance captured has been significantly reduced by the symmetries in the system and the increase of imbalance. It may be therefore hoped that a further study of the bifurcation along with purposely added symmetries in the rotor and system may allow for a smooth passage through resonance.

Acknowledgements

It is our great pleasure to present a paper to a conference held in the honour of Prof. Peter Hagedorn. For the first author he is a postdoctoral advisor and for the second he is a dear friend of many decades. We thank him for his support of this research.

This work was conducted during a two month visit (Oct./Nov. 2016) of the first author to the beautiful Pontifical Catholic University campus in Rio de Janeiro sponsored by FAPERJ-DFG exchange (HA 1060/58-1). He especially acknowledges the great hospitality of Prof. Sampaio's team there. The lead author is funded by the DFG (HA 1060/56-1).

References

[1] Blekhman, I. Self-synchronization of vibrators for some vibration machines. *Ingenernyj sbornik 16* (1953), 49–72.

[2] Dantas, M. J. H., Sampaio, R., and Lima, R. Phase bifurcations in an electromechanical system. *Procedia IUTAM 19* (2016), 193–200.

[3] Doedel, E., Champneys, A., Dercole, F., Fairgrieve, T., Kuznetsov, Y. A., Oldeman, B., Paffenroth, R., Sandstede, B., Wang, X., and Zhang, C. Auto-07p. *Continuation and bifurcation software for ordinary differential equations* (2007).

[4] Dudkowski, D., Jafari, S., Kapitaniak, T., Kuznetsov, N. V., Leonov, G. A., and Prasad, A. Hidden attractors in dynamical systems. *Physics Reports 637* (2016), 1–50.

[5] Eckert, M., and Märker, K. Arnold Sommerfeld. *Wissenschaftlicher Briefwechsel 2* (2004), 1919–1951.

[6] Evan-Iwanowski, R. *Resonance oscillations in mechanical systems*. Elsevier Scientific Publishing Company, 1976.

[7] Fidlin, A. *Nonlinear oscillations in mechanical engineering*. Springer Science & Business Media, 2005.

[8] Fidlin, A., and Drozdetskaya, O. On the averaging in strongly damped systems: The general approach and its application to asymptotic analysis of the sommerfeld effect. *Procedia IUTAM 19* (2016), 43–52.

[9] Fradkov, A., Tomchina, O., and Tomchin, D. Controlled passage through resonance in mechanical systems. *Journal of Sound and Vibration 330*, 6 (2011), 1065–1073.

[10] Hagedorn, P., and Clerkin, E. Preface: IUTAM Symposium analytical methods in nonlinear dynamics. *Procedia IUTAM 19* (2016), 1–4.

[11] Kiseleva, M. A., Kuznetsov, N. V., and Leonov, G. A. Hidden attractors in electromechanical systems with and without equilibria. *IFAC-PapersOnLine 49*, 14 (2016), 51–55.

[12] Klíč, A. Bifurcations of the periodic solutions in symmetric systems. *Aplikace matematiky 31*, 1 (1986), 27–40.

[13] Nikolaev, E., and Shnol, E. Bifurcations of cycles in systems of differential equations with a finite symmetry group–I. *Journal of dynamical and control systems 4*, 3 (1998), 315–341.

[14] Nikolaev, E. V. Bifurcations of limit cycles of differential equations admitting an involutive symmetry. *Sbornik: Mathematics 186*, 4 (1995), 611–627.

[15] Rand, R. H., Kinsey, R., and Mingori, D. L. Dynamics of spinup through resonance. *International Journal of Non-Linear Mechanics 27*, 3 (1992), 489–502.

[16] Sommerfeld, A. Beiträge zum dynamischen Ausbau der Festigkeitslehe. *Phys. Z 3* (1902), 266–286.

Eoin J Clerkin, Ph.D.: Technische Universität Darmstadt, fnb, Dynamics & Vibrations Group, Dolivostr. 15, 64293 Darmstadt, Germany (*eoin@clerkin.biz*). The author gave a presentation of this paper during one of the conference sessions.

Rubins Sampaio, (professor): Pontifícia Universidade Católica do Rio de Janeiro, Departamento de Engenharia Mecânica, Mechanical Engineering Department, PUC-Rio, 22451-900 Rio de Janeiro, RJ, Brazil ().

On the acoustic metamaterial with negative effective mass

Livija Cveticanin

Abstract: Recently a significant attention is directed toward so called 'acoustic metamaterials' which have large similarity with already known 'electromagnetic metamaterials' which are applied for elimination of the electromagnetic waves. The stop of electromagnetic waves is realized with the negative refractive index, negative permittivity and negative permeability. Motivated by the mathematical analogy between acoustic and electromagnetic waves the acoustic metamaterials are introduced. It was asked the material to have negative effective mass. To obtain the negative effective mass the artificial material, usually composite, has to be designed. The basic unit is a vibration absorber which consists of a lumped mass attached with a spring to the basic mechanical system. The purpose of the unit is to give a band gap where some frequencies of acoustic wave are stopped. We investigated the nonlinear mass-in-mass unit excited with any periodic force. Mathematical model of the motion is a system of two coupled strong nonlinear and nonhomogeneous second order differential equations. The solution of equations is assumed in the form of the Ateb (inverse Beta) periodic function. The frequency of vibration is obtained as the function of the parameters of the excitation force. The effective mass of the system is also determined. Regions of negative effective mass are calculated. For these values the motion of the forced mass stops. It is concluded that the stop frequency gaps are much wider for the nonlinear than for the linear system. Based on the obtained parameter values the acoustic metamaterial could be designed.

1. Introduction

Metamaterials represent a novel type of engineered materials characterized by exceptional properties which are not commonly found in natural materials. Properties of these materials are not the result of their chemical composition. Materials are man-made designed composites with special structures for energy absorption or elimination. Originally metamaterials started in the field of electromagnetic waves where researchers found that the negative electrical permittivity, negative magnetic permeability and negative refractive index available absorption of electromagnetic waves [1]. Recently, using the mathematical analogy between acoustic and electromagnetic waves, acoustic, also known as mechanical or elastic, metamaterials for mechanical sound and vibration attenuation are designed [2], [3]. The purpose of these materials is to absorb acoustic waves and vibrations at certain excitation frequency. To fulfill this task and due to analogy with electromagnetic metamaterials it is required that mechanical metamaterials have a negative mass property. It is well

known that there are no materials with negative mass, but a concept of 'negative effective mass' is introduced into consideration. The effective mass is a mathematically calculated parameter whose value may be negative. Milton [4] introduced the dynamics of metamaterials with such non-conventional behaviour. It was seen that the negative effective nass density of metamaterial is obtained due to local resonators included as basic, units of material [5]. For the negative effective mass a stopband frequency area exists. The single mass-in-mass resonator offers negative effective mass property over a specific frequency range [6] – [8] and by connecting them into a system we obtain an acoustic metamaterial which exhibits negative effective mass density [9] – [11]. Based on the theoretical conclusion about negative effective mass systems the new acoustic metamaterials with local resonator units are designed [12] – [15]. The experimental investigation on these metamaterials give results which differ from those which would be predicted using the theoretical analysis. Because of that the modification of the model is necessary.

Our aim is to improve the model by introducing of the nonlinear property of the resonator unit and to investigate the influence of the nonlinearity on the resonance frequency bandgap. The resonator is assumed to be a two-degree-of-freedom mass-in-mass system with nonlinear elastic property. Already some investigation are done for the mass-in-mass unit where the spring is with cubic nonlinearity [16]. In this paper the generalization of the nonlinearity in the mass-in-mass system is done. The nonlinearity is assumed in the polynomial form of displacement with integer or noninteger order. The motion for the general periodic excitation is analyzed. The concept of effective mass is for the nonlinear system is newly defined and the negative effective mass is calculated. The bandgap for vibration at resonant case is determined and applied for explaining the property of the acoustic metamaterial in the chiral form.

2. Concept of effective mass in linear mass-in-mass unit

The single mass-in-mass unit is plotted in Fig.1. The unit contains the outer mass m_1 and the inner mass m_2. The inner mass is coupled to the outer by a linear spring of stiffness k_2 (Fig.1a).

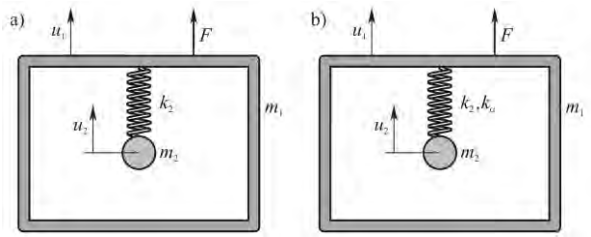

Figure 1. Mass-in-mass system: a) linear model, b) nonlinear model.

The system has two degrees-of-freedom and two generalized coordinates: the displacement u_1 of the mass m_1 and u_2 of the mass m_2. If the subsystem is excited with a harmonic force or harmonic wave, the differential equations of motion are [17]:

$$m_1\ddot{u}_1 + k_2^2(u_1 - u_2) = F\cos(\Omega t), \tag{1}$$

$$m_2\ddot{u}_2 + k_2^2(u_2 - u_1) = 0, \tag{2}$$

where F and Ω are the amplitude and the frequency of the excitation force. This system of coupled and linear second order differential equations has the exact closed form solution in the form:

$$u_1 = A\cos\Omega t, \quad u_2 = B\cos\Omega t, \tag{3}$$

where amplitudes of vibration are:

$$A = \frac{F(k_2^2 - \Omega^2 m_2)}{(k_2^2 - \Omega^2 m_1)(k_2^2 - \Omega^2 m_2) - k_2^4}, \tag{4}$$

$$B = \frac{Fk_2^2}{(k_2^2 - \Omega^2 m_1)(k_2^2 - \Omega^2 m_2) - k_2^4}, \tag{5}$$

Analyzing the obtained results it is obvious that the inertial force of the subsystem under resonance works against the excitation and attenuates the vibration. Using this conclusion the concept of effective mass is introduced [18].

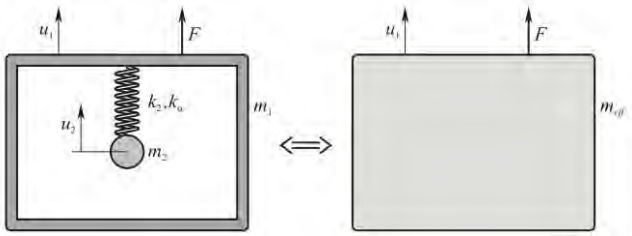

Figure 2. Mass-in-mass unit and its effective mass m_{eff}.

The concept is based on the physical condition that the motion of the outer mass m_1 has to be equal to that of an equivalent effective mass m_{eff} depicted in Fig.2, i.e., $m_{eff}\ddot{u}_1 = F\cos\Omega t$ and $-m_{eff}\Omega^2 A = F$. Thus, the effective mass is:

$$m_{eff} = (m_1 + m_2) + \frac{\Omega^2}{\omega_2^2 - \Omega^2} m_2, \tag{6}$$

where $\omega_2 = \sqrt{k_2^2 / m_2}$. Analyzing (6) it is seen that the effective mass is negative for excitation frequency which satisfies the relation:

$$1 < \frac{\Omega}{\omega_2} < \sqrt{\frac{m_1 + m_2}{m_1}}. \tag{7}$$

According to (7) it is evident that for the negative effective mass a narrow band gap region exists which is near to the local resonance frequency (Ω/ω_2=1) of the internal mass m_2. In [6] it is shown that the negative effective mass region corresponds to the band gap region of the dispersion curve when wave propagation is considered. Namely, if the mass becomes negative the acceleration is in the opposite direction to the applied force according to the Newton's second law of motion and the response amplitude reduces. This effect is greatly increased for the resonant case when the excitation frequency Ω approaches the frequency of the system ω_2. From (7) it is clear that the band gap region can be broadened if mass m_2 is increased and m_1 decreased. So, maximizing of the band gap region can be reached by increasing of the mass ration m_2/m_1. Unfortunately, the effect of negative mass is significant only close to Ω/ω_2=1, while in the broadened region the amplitude of negative mass is small and little reduction during wave propagation occurs.

3. Nonlinear vibration of the mass-in-mass unit

In Fig.1b a nonlinear mass-in-mass nonlinear subunit is plotted. Masses m_1 and m_2 are connected with a spring with nonlinear properties. Let us assume that the elastic force in the spring is a nonlinear displacement function:

$$F_e = k_\alpha^2 u_2 |u_2|^{\alpha-1},. \tag{8}$$

where k_α^2 is the coefficient of nonlinearity and $\alpha \geq 1 \in \mathrm{Re}_+$ is the order of nonlinearity. For the nonlinear two degrees-of-freedom mass-in-mass subunit the mathematical model is:

$$m_1 \ddot{u}_1 + k_\alpha^2 (u_1 - u_2) |u_1 - u_2|^{\alpha-1} = f, \tag{9}$$

$$m_2 \ddot{u}_2 + k_2^2 (u_2 - u_1) |u_1 - u_2|^{\alpha-1} = 0, \tag{10}$$

where f is the excitation force and u_1 and u_2 are displacements of masses m_1 and m_2. Equations (9) and (10) are coupled and strong nonlinear.

Let us assume that the excitation force has the form of the cosine Ateb periodic function ca:

$$f = Fca(\alpha,1,\Omega t)|ca(\alpha,1,\Omega t)|^{\alpha-1}, \tag{11}$$

where F and Ω are amplitude and frequency of the force and $\alpha \geq 1$ is a positive constant of integer or non-integer type. (The Ateb function is the inverse Beta function [19]). The period of the force is:

$$T = 2\Pi_\alpha = 2\mathrm{B}\left(\frac{1}{\alpha+1}, \frac{1}{2}\right), \tag{12}$$

where B is the Beta function which depends on α. Introducing (11) into (9) and (10) equations of motion are:

$$m_1\ddot{u}_1 + k_\alpha^2(u_1 - u_2)\left|u_1 - u_2\right|^{\alpha-1} = Fca(\alpha,1,\Omega t)\left|ca(\alpha,1,\Omega t)\right|^{\alpha-1}, \tag{13}$$

$$m_2\ddot{u}_2 + k_2^2(u_2 - u_1)\left|u_1 - u_2\right|^{\alpha-1} = 0. \tag{14}$$

The procedure for solving of the system (13) and (14) is introduced. Let us transform equations (13) and (14) into a system:

$$m_1\ddot{u}_1 + m_2\ddot{u}_2 = Fca(\alpha,1,\Omega t)\left|ca(\alpha,1,\Omega t)\right|^{\alpha-1}, \tag{15}$$

$$m_2\ddot{u}_2 + k_2^2(u_2 - u_1)\left|u_1 - u_2\right|^{\alpha-1} = 0, \tag{16}$$

which is suitable to be solved. The first equation is linear and nonhomogeneous, while the second is a homogenous strong nonlinear differential equation. For the forced vibrations the solution is assumed in the form [19]:

$$u_1 = Aca(\alpha,1,\Omega t), \quad u_2 = Bca(\alpha,1,\Omega t), \tag{17}$$

where A and B are unknown constants. Using the second time derivative of the Ateb function [20] and substituting (17) into (15) and (16) we obtain a system of a linear and a nonlinear algebraic equation:

$$m_1A + m_2B = -F\frac{\alpha+1}{2\Omega^2}, \tag{18}$$

$$-m_2\Omega^2\frac{2}{\alpha+1}B + k_\alpha^2(B - A)\left|A - B\right|^{\alpha-1} = 0. \tag{19}$$

Substituting

$$A = -\frac{m_2}{m_1}B - F\frac{\alpha+1}{2\Omega^2 m_1}, \tag{20}$$

into (19) the unknown parameter B is the solution of:

$$m_2 \frac{2\Omega^2}{\alpha+1} B - k_\alpha^2 \left(\frac{m_1+m_2}{m_1} B + F \frac{\alpha+1}{2\Omega^2 m_1} \right) \left| \frac{m_1+m_2}{m_1} B + F \frac{\alpha+1}{2\Omega^2 m_1} \right|^{\alpha-1} = 0. \tag{21}$$

Otherwise, for:

$$B = -\frac{m_1}{m_2} A - F \frac{\alpha+1}{2\Omega^2 m_2}, \tag{22}$$

the relation for A is:

$$m_1 \frac{2\Omega^2}{\alpha+1} A - k_\alpha^2 \left(\frac{m_1+m_2}{m_2} A + F \frac{\alpha+1}{2\Omega^2 m_2} \right) \left| \frac{m_1+m_2}{m_2} A + F \frac{\alpha+1}{2\Omega^2 m_2} \right|^{\alpha-1} = -F. \tag{23}$$

For simplification let us introduce the amplitude ratio C:

$$C = \frac{A}{B}. \tag{24}$$

Introducing (24) into (18) it is:

$$(m_1 C + m_2) B = -\frac{F(\alpha+1)}{2\Omega^2}. \tag{25}$$

For (25) the equation (21) transforms into:

$$m_2 + k_\alpha^2 (C-1) \frac{\alpha+1}{2\Omega^2} \left| \frac{F(\alpha+1)}{2\Omega^2} \frac{C-1}{m_1 C + m_2} \right|^{\alpha-1} = 0. \tag{26}$$

Let us rewrite (26) into the form:

$$(2\Omega^2)^\alpha m_2 + k_\alpha^2 (C-1)(\alpha+1)^\alpha \left| \frac{F(C-1)}{m_1 C + m_2} \right|^{\alpha-1} = 0. \tag{27}$$

It is obtained that the motion of the outer mass 1 stops for C=0.

4. Concept of effective mass in linear mass-in-mass unit

Usually, it is suggested to transform the mass-in-mass model into a single effective mass whose motion corresponds to the motion of m_1. Namely, the linear momentum of effective mass with velocity u_1 is equal to the sum of the linear momentums of masses m_1 and m_2:

$$m_{eff} \dot{u}_1 = m_1 \dot{u}_1 + m_2 \dot{u}_2. \tag{28}$$

Using the relations (17) the effective mass is:

$$m_{eff} = m_1 + \frac{m_2}{C}.$$

Substituting (27) we obtain:

$$m_{eff} = m_1 + m_2 + \frac{m_2\left(\frac{2\Omega^2}{\alpha+1}\frac{m_2}{k_\alpha^2 B^{\alpha-1}}\right)^{1/\alpha}}{1-\left(\frac{2\Omega^2}{\alpha+1}\frac{m_2}{k_\alpha^2 B^{\alpha-1}}\right)^{1/\alpha}}, \tag{29}$$

where the amplitude of vibration B is the solution of the relation (21). The effective mass depends not only on the masses of the unit and rigidity properties of the spring, but also the parameters of excitation (amplitude and frequency). The relation (29) is negative for:

$$1 < \left(\frac{2\Omega^2}{\alpha+1}\frac{m_2}{k_\alpha^2 B^{\alpha-1}}\right)^{1/\alpha} < 1 + \frac{m_2}{m_1}. \tag{30}$$

Introducing the notation for the eigenfrequency of the system:

$$\Omega_1^2 = \frac{k_\alpha^2 B^{\alpha-1}}{2m_2}(1+\alpha), \tag{31}$$

We transform the relation (30) into:

$$1 < \frac{\Omega}{\Omega_1} < \left(1 + \frac{m_2}{m_1}\right)^{\alpha/2}. \tag{32}$$

It is evident that the band gap is broadened with increasing the nonlinear property of the spring. Besides, the position of the resonant regime varies dependently on the parameter α. For the linear case, when α=1, the width of the band gap frequency (7) is smaller than for any nonlinear case and the position is fixed for Ω/Ω_1=1.

5. Acoustic metamaterial: Subunits connected in one dimensional lattice

Let us consider the case when the mass-in-mass subunits are connected in lattice [21] (see Fig.3).

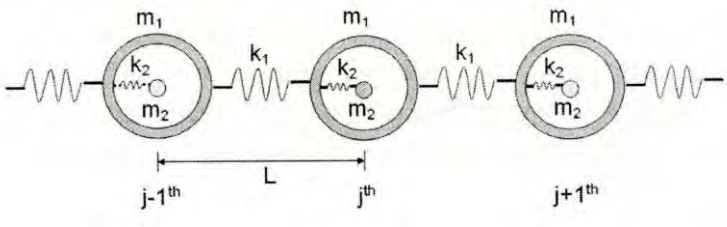

Figure 3. Mass-in-mass subunits connected in a 1D lattice [21].

For the case when the elastic property of the connection is nonlinear, equations of motion for the unit cell follow as:

$$m_1^{(j)}\ddot{u}_1^{(j)} + k_\alpha^2(u_1^{(j)} - u_2^{(j)})\left|u_1^{(j)} - u_2^{(j)}\right|^{\alpha-1} + k(u_1^{(j)} - u_1^{(j-1)})\left|u_1^{(j)} - u_1^{(j-1)}\right|^{\gamma-1}$$
$$+ k(u_1^{(j)} - u_1^{(j+1)})\left|u_1^{(j)} - u_1^{(j+1)}\right|^{\gamma+1} = 0,$$
$$m_2^{(j)}\ddot{u}_2^{(j)} + k_\alpha^2(u_2^{(j)} - u_1^{(j)})\left|u_2^{(j)} - u_1^{(j)}\right|^{\alpha-1} = 0, \tag{33}$$

where $\gamma \in \mathrm{Re}_+$ (integer or noninteger positive real number) is the order of nonlinearity and k is the rigidity constant.

Using the method of normal modes, suggested in the previous section, the relation between modes of vibration is:

$$u_1^{(j)} = Ku_2^{(j)}, \quad u_1^{(j-1)} = Ku_2^{(j-1)}, \quad u_1^{(j+1)} = Ku_2^{(j+1)}, \tag{34}$$

where K is an unknown constant. Applying (34), equations (33) transform into:

$$Km_1^{(j)}\ddot{u}_2^{(j)} + k_\alpha^2(K-1)\left|K-1\right|^{\alpha-1}u_2^{(j)}\left|u_2^{(j)}\right|^{\alpha-1} + kK\left|K\right|^{\gamma-1}(u_2^{(j)} - u_2^{(j-1)})\left|u_2^{(j)} - u_2^{(j-1)}\right|^{\gamma-1}$$
$$+ kK\left|K\right|^{\gamma+1}(u_2^{(j)} - u_2^{(j-1)})\left|u_2^{(j)} - u_2^{(j-1)}\right|^{\gamma+1} = 0, \tag{35}$$
$$m_2^{(j)}\ddot{u}_2^{(j)} + k_\alpha^2(1-K)\left|K-1\right|^{\alpha-1}u_2^{(j)}\left|u_2^{(j)}\right|^{\alpha-1} = 0. \tag{36}$$

The wave form solution is:

$$u_2^{(j+1)} = u_2^{(j)}\exp(i\beta L), \quad u_2^{(j-1)} = u_2^{(j)}\exp(-i\beta L), \tag{37}$$

where L is the length, β is the wave number and $i=\sqrt{(-1)}$ is the imaginary unit. Substituting (37) into (35) the equation transforms into:

$$Km_1^{(j)}\ddot{u}_2^{(j)} + u_2^{(j)}\left|u_2^{(j)}\right|^{\alpha-1}(k_\alpha^2(K-1)\left|K-1\right|^{\alpha-1} + kK\left|K\right|^{\gamma-1}(1-\exp(-i\beta L))\left|1-\exp(-i\beta L)\right|^{\gamma-1}$$
$$+ kK\left|K\right|^{\gamma+1}(1-\exp(i\beta L))\left|1-\exp(i\beta L)\right|^{\gamma+1} = 0. \tag{38}$$

Comparison of equations (36) and (38) yields:

$$\frac{1}{Km_1^{(j)}}k_\alpha^2(K-1)\left|K-1\right|^{\alpha-1}$$
$$+\frac{1}{Km_1^{(j)}}kK\left|K\right|^{\gamma-1}(1-\exp(-i\beta L))\left|1-\exp(-i\beta L)\right|^{\gamma-1} \tag{39}$$
$$+\frac{1}{Km_1^{(j)}}kK\left|K\right|^{\gamma+1}(1-\exp(i\beta L))\left|1-\exp(i\beta L)\right|^{\gamma+1} = \frac{1}{Km_2^{(j)}}k_\alpha^2(K-1)\left|K-1\right|^{\alpha-1}.$$

The equation (36) is a second order strong nonlinear differential equation with general solution:

$$u_2^{(j)} = Bca(\alpha,1,\Omega t), \tag{40}$$

where the frequency of ca Ateb function is:

$$\Omega = \sqrt{\frac{\alpha+1}{2}}\sqrt{\frac{k_\alpha^2}{m_2}}\sqrt{1-C}\left|C-1\right|^{\frac{\alpha-1}{2}}B^{\frac{\alpha+1}{2}}, \tag{41}$$

and B is the amplitude of vibration. According to 41) the constant C follows:

$$K = 1-\left(\frac{2\Omega^2}{\alpha+1}\frac{m_2^{(j)}}{k_\alpha^2 B^{\alpha-1}}\right)^{1/\alpha}. \tag{42}$$

Substituting 42) into 39) the dispersion equation is obtained:

$$k\left[1-\left(\frac{2\Omega^2}{\alpha+1}\frac{m_2^{(j)}}{k_\alpha^2 B^{\alpha-1}}\right)^{1/\alpha}\right]^\gamma[(1-\exp(-i\beta L))\left|1-\exp(-i\beta L)\right|^{\gamma-1}$$
$$+(1-\exp(i\beta L))\left|1-\exp(i\beta L)\right|^{\gamma+1}] = \frac{2\Omega^2}{\alpha+1}\frac{m_2^{(j)}}{B^{\alpha-1}}\left[\frac{m_1^{(j)}}{m_2^{(j)}} - \frac{m_1^{(j)}}{m_2^{(j)}}\left(\frac{2\Omega^2}{\alpha+1}\frac{m_2^{(j)}}{k_\alpha^2 B^{\alpha-1}}\right)^{1/\alpha}+1\right]. \tag{43}$$

If the lattice system is reduced to a homogenous monoatom lattice system, where only effective masses m_{eff} are connected by springs with rigidity k, the homogenous lattice system is obtained. The dispersion equation of the system is:

$$\Omega^2 = kB^{\alpha-1}\frac{\alpha+1}{2m_{eff}}[(1-\exp(-i\beta L))\left|1-\exp(-i\beta L)\right|^{\gamma-1} + (1-\exp(i\beta L))\left|1-\exp(i\beta L)\right|^{\gamma+1}. \quad (44)$$

Rewriting (44) into:

$$\Omega^2 \frac{2m_{eff}}{kB^{\alpha-1}(\alpha+1)} = (1-\exp(-i\beta L))\left|1-\exp(-i\beta L)\right|^{\gamma-1} + (1-\exp(i\beta L))\left|1-\exp(i\beta L)\right|^{\gamma+1}, \quad (45)$$

And substituting (45) into (43) we obtain:

$$m_{eff} = m_1^{(j)} + m_2^{(j)} + \frac{1}{\left[1-\left(\frac{2\Omega^2}{\alpha+1}\frac{m_2^{(j)}}{k_\alpha^2 B^{\alpha-1}}\right)^{1/\alpha}\right]^{\gamma}}(m_1^{(j)}(1-\left(\frac{2\Omega^2}{\alpha+1}\frac{m_2^{(j)}}{k_\alpha^2 B^{\alpha-1}}\right)^{1/\alpha}$$
$$-\left[1-\left(\frac{2\Omega^2}{\alpha+1}\frac{m_2^{(j)}}{k_\alpha^2 B^{\alpha-1}}\right)^{1/\alpha}\right]^{\gamma}) + m_1^{(j)}(1-\left[1-\left(\frac{2\Omega^2}{\alpha+1}\frac{m_2^{(j)}}{k_\alpha^2 B^{\alpha-1}}\right)^{1/\alpha}\right]^{\gamma})). \quad (46)$$

For the case when the order of nonlinearity of the connecting elements of the absorber are equal, i.e., $\alpha=\gamma$, it is:

$$m_{eff} = m_1^{(j)} + m_2^{(j)} + \frac{1}{\left[1-\left(\frac{2\Omega^2}{\alpha+1}\frac{m_2^{(j)}}{k_\alpha^2 B^{\alpha-1}}\right)^{1/\alpha}\right]^{\alpha}}(m_1^{(j)}(1-\left(\frac{2\Omega^2}{\alpha+1}\frac{m_2^{(j)}}{k_\alpha^2 B^{\alpha-1}}\right)^{1/\alpha}$$
$$-\left[1-\left(\frac{2\Omega^2}{\alpha+1}\frac{m_2^{(j)}}{k_\alpha^2 B^{\alpha-1}}\right)^{1/\alpha}\right]^{\alpha}) + m_1^{(j)}(1-\left[1-\left(\frac{2\Omega^2}{\alpha+1}\frac{m_2^{(j)}}{k_\alpha^2 B^{\alpha-1}}\right)^{1/\alpha}\right]^{\alpha})). \quad (47)$$

The monoatom lattice system is equivalent to the original mass-in-mass system if their dispersion systems (43) and (47) are identical.

5.1. Linear connection

If the connection between subunits is linear the order of nonlinearity is γ=1. Then, reducing the lattice system to a homogenous monoatom one, we obtain that only effective masses m_{eff} are connected by springs with rigidity k and the dispersion equation is

$$1-\cos(\beta L) = \frac{m_{eff}}{k}\frac{2\Omega^2}{\alpha+1}\frac{1}{B^{\alpha-1}}. \quad (48)$$

Eliminating the wave number β and using the relation (46) the effective mass is:

$$m_{eff} = m_1^{(j)} + m_2^{(j)} + \frac{m_2^{(j)}\left(\frac{2\Omega^2}{\alpha+1}\frac{m_2^{(j)}}{k_\alpha^2 B^{\alpha-1}}\right)^{1/\alpha}}{1-\left(\frac{2\Omega^2}{\alpha+1}\frac{m_2^{(j)}}{k_\alpha^2 B^{\alpha-1}}\right)^{1/\alpha}}. \quad (49)$$

Comparing (49) with the previous result for only one subunit (29) it is obtained that the monoatom lattice is equivalent to the original mass-in-mass system if the dispersion equations are identical.

6. Conclusions

Theory of acoustic metamaterial with resonators modelled as two-degree-or-freedom nonlinear mass-in-mass systems is considered. Concept of the effective mass for the nonlinear unit is developed. The regions of negative effective mass are calculated. The theory is extended on the nomoatom lattice system which is often used in acoustic metamaterials.Based on the investigation the following is concluded that resonators, which are basic units of acoustic metamaterial, eliminate the wave propagation at certain vibration frequencies. The concept of effective mass, introduced in the paper, gives the possibility to obtain the region of negative values for which wave propagation band gaps exist. For the case when the mass-in-mass subunits are connected into an one-dimensional lattice, the effective mass of the monoatom lattice system is equivalent to the original mass-in-mass system if their dispersion equations and the mass ratio are identical.

Acknowledgments

This article is based upon work from COST Action DENORMS - CA15125, supported by COST (European Cooperation in Science and Technology. The investigation has been supported by the Proj. No. 054 of the Faculty of Technical Sciences of Novi Sad.

References

[1] Veselago, V.G. The electrodynamics of substances with simultaneously negative values of permittivity and permeability. *Soc Phys Usp.* 10, (1968), 509-514

[2] Li, J., and Chan, C.T. Double-negative acoustic metamaterial. *Phys Rev E* 70, 055602 (2004), 1-4.

[3] Ding, Y., Liu, Z., Qiu, C., Shi, J. Metamaterial with simultaneously negative bulk modulus and mass density. *Phys Rev Lett.* 99, 9 (2007), 093904.

[4] Milton, G.W. New metamaterials with macroscopic behavior outside that of continuum elastodynamics. *New Journal of Physics* 9, 359 (2007), 1-13.

[5] Liu, Z., Zhang, X., Mao, Y., Zhu, Y.Y., Yang, Z., Chan, C.T. Locally resonant sonic materials. *Science* 289, 5485 (2000), 1734-1736.

[6] Huang, H.H., Sun, C.T., Huang, G.I On the negative effective mass density in acoustic metamaterials. *International Journal of Engineering Science* 47, (2009), 610-617.

[7] Cveticanin, L., Mester, Gy. Theory of acoustic metamaterials and metamaterial beams: An overview. *Acta Polytechnica Hungarica* 13, 7 (2016), 43-62.

[8] Wang, T., Sheng, M.P., Qin, Q.H. Multi-flexural band gaps in an Euler-Bernoulli beam with lateral local resonators. *Physics Letters A* 380, (2016), 525-529.

[9] Yao, SW., Zhou, X., Hu, G. Experimental study on negative effective mass in a 1D mass-spring system. *New Journal of Physics*, 043020 (2008), 1-10.

[10] Calius, E.P., Bremaud, X., Smith, B., Hall, A. Negative mass sound shielding structures: Early results. *Physica Status Solidi B* 246, 9 (2009), 2089-2097.

[11] Tan, K.T., Huang, H.H., Sun, C.T. Optimizing the band gap of effective mass negativity in acoustic metamaterials. *Appl Phys Lett*. 101, (2012), 241902.

[12] Liu, Z., Chan, C.T., Sheng, P. Analytic model of phononic crystals with local resonances. *Physical Review B* 71, 1 (2005) 014103.

[13] Zhao, H.G., Liu, Y.Z., Wen, J.H., Yu, D,L., Wang, G., Wen, X.S. Sound absorption of locally resonant sonic materials. *Chinese Physics Letters* 23, 8 (2006), 2132.

[14] Sheng, P., Zhang, X., Liu, Z., Chan, C.T. Locally resonant sonic materials. *Physica B* 338, (2003), 201--205.

[15] Pai, P.F., Peng, H., Jiang, S. Acoustic metamaterial beams based on multi-frequency vibration absorbers. *International Journal of Mechanical Sciences* 79, (2014), 195-205.

[16] Cveticanin, L., and Zukovic, M. Negative effective mass in acoustic metamaterial with nonlinear mass-in-mass subsystems. *Communications in Nonlinear Science and Numerical Simulation* 51, (2017), 89-104.

[17] Peng, H., and Pai, P.F. Acoustic metamaterial plates for elastic wave absorption and structural vibration suppression. *International Journal of Mechanical Sciences* 89, (2014), 350-361.

[18] Milton, G.W., and Willis, J.R. On modifications of Newton's second law and linear continuum elastodynamics. *Proceedings of the Royal Society A* 463, (2007), 855-880

[19] Cveticanin, L. Pure nonlinear oscillator, in *Strong Nonlinear Oscillators*. Mathematical Engineering, Springer, 9783319588254, 17-49, 2018.

[20] Cveticanin, L., and Kovacic, I. Exact solutions for the response of purely nonlinear oscillators: Overview. *Journal of the Serbian Society for Computational Mechanics* 10, 1 (2016), 116-134

[21] Zhang, S., Park, Y.S., Li, J., Lu, X., Zhang, E., Zhang, X. Negative refractive index in chiral metamaterial. *Phys Rev Lett.* 102, 2, 023901 (2009).

Livija Cveticanin, Professor: Faculty of Technical Sciences, University of Novi Sad, Trg D. Obradovica 6, 21000 Novi Sad, Serbia (*cveticanin@uns.ac.rs*). The author gave a presentation of this paper during one of the conference sessions.

Application of Pade approximations to the solution of nonlinear control problems

Yulia Danik, Mikhail Dmitriev, Ekaterina Komarova, Dmitry Makarov

Abstract: In this paper the Pade method of approximate solutions construction for various continuous control problems with a parameter, where it is possible to construct the control function asymptotics for small and large values of the parameter, is developed. As a result of constructing the asymptotic Pade interpolation (API), we obtain a control interpolation surface, where asymptotic approximations of the control are used as interpolation nodes. Such a dependence on parameters exists in numerous applications, where the large parameter value corresponds to large control gain coefficients, and small parameter values appear in case of weakly controlled systems, that is a family of controls with the varying gain is generated. For the case of a two-point API the constructed surface serves as a "bridge" that is asymptotically close to the exact control surface for the parameter domains for which the asymptotics are constructed. The properties of stability and optimality of the resulting feedback controls are studied for linear quadratic optimal control problems with a parameter perturbations. The results of numerical experiments are discussed.

1. Introduction

The Pade approximation (PA) [1,2] is one of the asymptotic approaches that allows to approximate a function expanded in a Taylor series by a rational function of a given order – a ratio of two polynomials of degree m in the numerator and a power of n in the denominator. To construct the PA, it is necessary to solve a system of linear algebraic equations.

One of the possible applications of this technique is the solution of control problems, namely the approximation of the optimal control law [3-4]. In papers [3-4], for example, the transfer function of a closed-loop control system is expanded into a series and is replaced by a Pade approximation. The unknown controller parameters are found from the equations and constraints obtained for the simplified transfer function of the second order.

Here we will consider the matrix Pade approximation of the solution of a state dependent Riccati equation (SDRE) for a particular class of nonlinear control problems, namely, a control problem with a parameter that can take both small and large values, thereby determining either a weakly controlled system or a system with a large gain. For the corresponding SDRE we construct the asymptotic expansions of its solution for large and small values of the parameter. The well-known review [5] is devoted to the SDRE technique of suboptimal nonlinear control synthesis. The methods for

constructing approximate solutions of continuous and discrete matrix algebraic Riccati equations with state-dependent coefficients on the basis of asymptotics by a formally small parameter are presented in [6-10]. Each of the two mentioned asymptotic expansions is applicable in its local domain. It is possible to extend the results obtained by asymptotic methods and to get one single solution that has better quality (better approximation of the exact solution) than each of the asymptotics in the «middle» of the parameter values interval by the construction of the Pade approximation.

This method allows to construct a solution for all possible values of the parameter by the combination of two asymptotics. The asymptotics splicing for the initial value problem solution of a singularly perturbed system of ordinary differential equations with the help of a two-point Pade approximation, or the so-called Pade-bridge, was carried out in [11] and also in [12]. In [11], a procedure for constructing approximations of the solutions of initial value problems with a parameter is proposed. In [12], an algorithm for constructing a parametric Pade-bridge for the solution of an optimal control problem with the free right end and two groups of motions is demonstrated. A singularly perturbed problem with left and right boundary layers is solved for small values of the parameter, and a regularly perturbed optimal control problem for large values of the parameter. The scalar Pade approximation constructed for this problem contains three series (with coefficients depending on t, fast and slow time, respectively) for each component of the solution vector, as in the Vasil'eva`s boundary functions method [13]. A system of equations for the coefficients of the Pade approximation was constructed, and a theorem on its solvability was presented.

In this paper a procedure for constructing a matrix Pade-bridge for the feedback control gain matrix on the basis of two asymptotic approximations of matrix Riccati equation solutions obtained for small and large values of the parameter is proposed. Matrix Riccati equation is used in the SDRE approach (State Dependent Riccatti Equation) which is applied here to a particular class of SDC (State Dependent Coefficients [5]) control systems with a parameter which defines either the weakly controlled system, or a system with a large gain. The conditions of the closed-loop system stability for all positive values of the parameter in the case of a stationary linear system are given here, i.e. the conditions under which the Pade regulator ensures robust asymptotic stability properties of the closed-loop system with respect to the parameter value. Another advantage of the proposed approach is that there is no need to recalculate the solution once the parameter value changes, as in the traditional SDRE method.

2. The control problem statement and the construction of asymptotic expansions of the Riccati equation solutions

Let us consider the following optimal control problem for nonlinear continuous systems with a parameter

$$\dot{x} = A(x)x + \varepsilon B(x)u,\ x(0) = x^0, \tag{1}$$

$$\int_0^\infty \left(x^T Q(x)x + u^T Ru \right) dt \to \inf_u, \tag{2}$$

where $x(t) \in X \subset R^n$, $u(t) \in R^r$, $t \in (0, \infty)$, $X \subset R^n$ - is a certain fixed bounded state space subset, $A(x) \in R^{n \times n}$, $B(x) \in R^{n \times r}$, $rank\, B(x) = r$, $\forall x \in X$, $Q(x) > 0$, $R > 0$, $\varepsilon \in (0, \infty)$ is a parameter which can take either small or large values. In the first case, system (1) is a weakly controllable system, in the second case, (1) is a system with a large control gain. All matrices` elements in (1) are rather smooth functions of their arguments. It should be noted that weight matrices $Q(x)$ and R are defined subjectively. Our aim is to find an approximate solution of problem (1) as a function of parameter ε. The question is whether it is possible to construct a parametric synthesis in (1) for all values of ε from a certain domain, including "middle" values, which provides good performance in comparison with the corresponding feedback control asymptotic approximations constructed in the specific domains of the parameter values.

The system (1) has state-dependent coefficients. So we will use the SDRE approach scheme [5] to find a feedback control. Such a control is sought with the help of the solution scheme of the standard linear-quadratic optimal control problem with the infinite-time-horizon, i.e.

$$u = -\varepsilon R^{-1} B^T(x) P(x, \varepsilon) x,\ \forall x \in X,\ \varepsilon \in (0, \infty), \tag{3}$$

where $P(x, \varepsilon)$ is a symmetric, positive-defined solution of the next matrix SDRE

$$-A^T(x)P(x,\varepsilon) - P(x,\varepsilon)A(x) + \varepsilon^2 P(x,\varepsilon)B(x)R^{-1}B^T(x)P(x,\varepsilon) - Q(x) = 0, \tag{4}$$

which follows from sufficient optimality conditions. Regulator (3), (4) is often quite close to the corresponding optimal control. But the computational difficulties associated with the solution of (4) give rise to various approximate constructions, in particular, created on the basis of matrices representation in a weakly nonlinear form [9]. In this paper, taking into account the parameter variation domain, we will use the Pade approximation (PA) formalism to obtain an approximate solution of (4). The Pade approximation can be constructed both on the basis of individual asymptotic approximations in the regions of small and large parameter values, and on the basis of their combination, for example, two-point PA or Pade-bridges.

At first, we construct the next formal second-order asymptotic approximation of $P(x, \varepsilon)$ for small values of ε

$$\tilde{P}_2(x,\varepsilon) = \tilde{P}_0(x) + \varepsilon\tilde{P}_1(x) + \varepsilon^2\tilde{P}_2(x), \tag{5}$$

representing matrix $Q(x)$ as

$$Q(x,\varepsilon) = Q_0(x) + \varepsilon Q_1(x) + \varepsilon^2 Q_2(x), \tag{6}$$

Substituting (5) into (4), and then equating the terms with the same powers of ε , we obtain the following tree matrix relations

$$\begin{aligned} &-A^T(x)\tilde{P}_0(x) - \tilde{P}_0(x)A(x) - Q_0(x) = 0, \; -A^T(x)\tilde{P}_1(x) - \tilde{P}_1(x)A(x) - Q_1(x) = 0, \\ &-A^T(x)\tilde{P}_2(x) - \tilde{P}_2(x)A(x) + \tilde{P}_0(x)B(x)R^{-1}B^T(x)\tilde{P}_0(x) - Q_2(x) = 0, \end{aligned} \tag{7}$$

which are the Lyapunov matrix equations for $\tilde{P}_0(x), \tilde{P}_1(x), \tilde{P}_2(x)$.

Next, we construct a second order formal asymptotic approximation of the solution of (4) for the case when ε is rather large. Let's make a substitution $\varepsilon = \frac{1}{\mu}$ and seek the solution of (4) as

$$\hat{P}_2(x,\mu) = \hat{P}_0(x) + \mu\hat{P}_1(x) + \mu^2\hat{P}_2(x) \tag{8}$$

Thus, we have

$$\begin{aligned} &-A^T(x)(\hat{P}_0 + \mu\hat{P}_1(x) + \mu^2\hat{P}_2(x)) - (\hat{P}_0 + \mu\hat{P}_1(x) + \mu^2\hat{P}_2(x))A(x) + \\ &+(\frac{1}{\mu}\hat{P}_0 + \hat{P}_1(x) + \mu\hat{P}_2(x))S(x)(\frac{1}{\mu}\hat{P}_0 + \hat{P}_1(x) + \mu\hat{P}_2(x)) - Q_0 - \frac{1}{\mu}Q_1(x) - \frac{1}{\mu^2}Q_2(x) = 0, \end{aligned}$$

where $S(x) = B(x)R^{-1}B^T(x)$. After equating the terms with the same powers of ε, we obtain the following system of equations for terms of (8)

$$\begin{aligned} &\hat{P}_0(x)S(x)\hat{P}_0(x) - Q_2(x) = 0, \\ &\hat{P}_0(x)S(x)\hat{P}_1(x) + \hat{P}_1(x)S(x)\hat{P}_0(x) - Q_1(x) = 0, \\ &-A^T(x)\hat{P}_0(x) - \hat{P}_0(x)A(x) + \hat{P}_0(x)S(x)\hat{P}_2(x) + \\ &+\hat{P}_2(x)S(x)\hat{P}_0(x) + \hat{P}_1(x)S(x)\hat{P}_1(x) - Q_0(x) = 0 \end{aligned} \tag{9}$$

The next statement follows from the Lyapunov`s linear matrix equations solvability

Theorem 1. If matrices $A(x), B(x)$ and the introduced positive definite matrices $Q_0(x), Q_1(x), Q_2(x)$ satisfy the next conditions for each $x \in X$

I. $\mathrm{Re}\,\lambda(A(x)) < 0, \; \forall x \in X$,

II. $Q_2(x) - \tilde{P}_0(x)B(x)R^{-1}B^T(x)\tilde{P}_0(x) > 0, \;\; \forall x \in X$,

III. $rank\, B(x) = n,\ \forall x \in X$,

IV. $Q_0 + A^T(x)\hat{P}_0(x) + \hat{P}_0(x)A(x) - \hat{P}_1(x)S(x)\hat{P}_1(x) > 0,\ \forall x \in X,$

then the following is true

1. The Riccati equation (9) has a positive definite solution $\hat{P}_0(x)$ for all $x \in X$.

2. The Lyapunov equations in (7) and (9) have unique positive definite solutions $\tilde{P}_0(x),\ \tilde{P}_1(x),$ $\tilde{P}_2(x),\ \hat{P}_1(x)\ \hat{P}_2(x)$ for each $x \in X$.

3. Asymptotic approximations $\tilde{P}_2(x,\varepsilon),\ \hat{P}_2\left(x,\mu\right)$ from (5) and (8) are positive definite matrices for all $x \in X,\ \varepsilon > 0$.

When the terms of representations (7), (9) are defined it is possible to establish the existence of a positive definite solution $P(x,\varepsilon)$ of (4) in some domains of large and small parameter values with the help of successive approximations method and it is also possible to obtain some asymptotic estimates. Thus we have

Theorem 2. Let us suppose that all the conditions from Theorem 1 are satisfied, then there exist a sufficiently small constant $\varepsilon_0^1 > 0$ and a sufficiently large constant $\varepsilon_0^2 > 0$ such that equation (4) has a positive definite solution $P(x,\varepsilon)$ for all $x \in X$ and $0 \le \varepsilon \le \varepsilon_0^1,\ \varepsilon \ge \varepsilon_0^2$, and the following is true

$$\begin{aligned} &\left\| P(x,\varepsilon) - \tilde{P}_2(x,\varepsilon) \right\| = O(\varepsilon^3),\ 0 \le \varepsilon \le \varepsilon_0^1,\ x \in X \\ &\left\| P(x,\varepsilon) - \hat{P}_2\left(x, \frac{1}{\varepsilon}\right) \right\| = O\left(\frac{1}{\varepsilon^3}\right),\ \varepsilon \ge \varepsilon_0^2,\ x \in X \end{aligned} \tag{10}$$

3. Pade bridge or a two-point PA.

By splicing of the two asymptotic expansions (5) and (8), we can now obtain an approximate solution of (4) for the entire interval of ε variation with the help of (10). That is, it is possible to construct a PA which will be close to (5) for small values of ε and will be close to (8) for large values. For "middle" values of ε it may be expected that such PA will be closer to an exact solution than any of these two asymptotics.

Definition. A two-point matrix Pade approximation (PA) will be referred to as a matrix Pade-bridge on the half-line for the solution of Riccati equation (4) if it exists for all $0 \le \varepsilon < \infty$ and estimates in (10) hold.

Obviously, different PAs can be constructed, but here we restrict ourselves to constructing only the right-hand PA of [1/2] order (see [1]), which we seek in the form

$$PA_{[1/2]}(x,\varepsilon)=\left(M_0(x)+\varepsilon M_1(x)\right)\left(I+\varepsilon N_1(x)+\varepsilon^2 N_2(x)\right)^{-1}, \tag{11}$$

where I is a $n\times n$ identity matrix.

Note that if (11) exists for any $x\in X$, $\varepsilon>0$, then such a Pade-bridge is an interpolation surface that approximates the surface $P(x,\varepsilon)$ by splicing the asymptotic approximations obtained in the neighborhoods of small and large values of ε.

Thus, taking into account (5) and (8) we have

$$\left(M_0(x)+\varepsilon M_1(x)\right)\left(I+\varepsilon N_1(x)+\varepsilon^2 N_2(x)\right)^{-1}=\tilde{P}_0(x)+\varepsilon\tilde{P}_1(x)+\varepsilon^2\tilde{P}_2(x)+O(\varepsilon^3),$$

$$\left(M_0(x)+\varepsilon M_1(x)\right)\left(I+\varepsilon N_1(x)+\varepsilon^2 N_2(x)\right)^{-1}=\hat{P}_0(x)+\frac{1}{\varepsilon}\hat{P}_1(x)+\frac{1}{\varepsilon^2}\hat{P}_2(x)+O\left(\frac{1}{\varepsilon^3}\right).$$

Multiplying both equalities on the right by $\left(I+\varepsilon N_1(x)+\varepsilon^2 N_2(x)\right)$ and equating the terms for the same powers of ε we get the next systems for determination of matrices in (11)

$$\varepsilon^0: M_0(x)=\tilde{P}_0(x),\ M_0(x)=\hat{P}_0(x)+\hat{P}_1(x)N_1(x)+\hat{P}_2(x)N_2(x)$$

$$\varepsilon^1: M_1(x)-\tilde{P}_0(x)N_1(x)-\tilde{P}_1(x)=0,\ M_1(x)=\hat{P}_0(x)N_1(x)+\hat{P}_1(x)N_2(x)$$

or $M_0(x)=\tilde{P}_0(x)$ and

$$\begin{pmatrix} I & -\tilde{P}_0(x) & 0\\ 0 & \hat{P}_1(x) & \hat{P}_2(x)\\ -I & \hat{P}_0(x) & \hat{P}_1(x)\end{pmatrix}\begin{pmatrix} M_1(x)\\ N_1(x)\\ N_2(x)\end{pmatrix}=\begin{pmatrix} \tilde{P}_1(x)\\ \tilde{P}_0(x)-\hat{P}_0(x)\\ 0\end{pmatrix}. \tag{12}$$

Let us introduce the condition

V. The system (12) is uniquely solvable, the matrix $\left(I+\varepsilon N_1(x)+\varepsilon^2 N_2(x)\right)$ is nonsingular, and the real parts of the $PA_{[1/2]}(x,\varepsilon)$ eigenvalues are positive for $\forall x\in X,\ \varepsilon>0$.

The condition V actually determines the existence of the Pade-bridge (11) for the Riccati equation (4) solution for all $\varepsilon\in(0,\infty)$ based on the asymptotic approximations (5), (8).

Now we can introduce the next regulator for all $x\in X,\ \varepsilon>0$

$$u(x,\varepsilon)=-\varepsilon R^{-1}B^T(x)K(x,\varepsilon)x, \tag{13}$$

where the symmetric matrix $K(x,\varepsilon)=\dfrac{\left(PA_{[1/2]}(x,\varepsilon)+PA^T{}_{[1/2]}(x,\varepsilon)\right)}{2}>0$ for all $x\in X,\ \varepsilon>0$.

Theorem 3. Under conditions I, III-V, there exist the Pade-bridge $PA_{[1/2]}(x,\varepsilon)$ (11), constructed for the solution of Riccati equation (4) on the basis of the asymptotic approximations (5), (8), for $\forall \varepsilon \in [0,\infty)$.

Remark 1. The condition II is not required in Theorem 3, since it is not used for the construction of the Pade-bridge (11).

4. The Pade regulator and stabilization

Let us consider the case of the stationary problem (1),(2), where all matrices do not depend on time. Accordingly, a positive definite matrix $K(\varepsilon)$ can be used to construct the Lyapunov function $V(x,\varepsilon) = x^T K(\varepsilon) x$ for such problem.

Now let's calculate the total time derivative along the trajectories of the closed-loop system (1),(13). We have

$$\frac{dV(x,\varepsilon)}{dt} = (\frac{dx}{dt})^T K(\varepsilon) x + x^T K(\varepsilon) \frac{dx}{dt} = (Ax + \varepsilon Bu)^T K(\varepsilon) x + x^T K(\varepsilon)(Ax + \varepsilon Bu) =$$
$$= (Ax - \varepsilon^2 SK(\varepsilon)x)^T P_{PA} x + x^T P_{PA}(Ax - \varepsilon^2 SK(\varepsilon)x) =$$
$$= x^T A^T K(\varepsilon) x - \varepsilon^2 x^T K(\varepsilon) SK(\varepsilon) x + x^T K(\varepsilon) Ax - \varepsilon^2 x^T K(\varepsilon) SK(\varepsilon) x =$$
$$= x^T [A^T K(\varepsilon) + K(\varepsilon) A] x - \varepsilon^2 x^T (K(\varepsilon) SK(\varepsilon) + K(\varepsilon) SK(\varepsilon)) x$$

By the Lyapunov lemma (see, for example, [14]), there exist such matrix $D_1 > 0$, that $D_1 = -A^T K(\varepsilon) - K(\varepsilon) A$. So we get $\frac{dV(x,\varepsilon)}{dt} = -x^T D_1 x - \varepsilon^2 x^T D_2 x < 0,\ \forall \varepsilon > 0,\ x \neq 0,$ where $D_2 = 2K(\varepsilon) SK(\varepsilon) > 0$. Thus the next theorem is true

Theorem 4. If all matrices in (1),(2) are constant, then under conditions I, III-V, the regulator (13), based on the Pade-bridge (11), stabilizes the system (1) for any $\varepsilon \in (0,\infty)$.

Remark 2. Examples show that due to the positive definiteness of the matrix terms of asymptotic approximations (5),(8), and the special choice of matrices $Q_0(x), Q_1(x), Q_2(x)$, the condition V can be satisfied.

Remark 3. The assertion of Theorem 4 can be generalized to weakly nonlinear systems by the scheme presented in [9], where the regulator (13) will be used in the zero order approximation.

So, the stabilizing regulator (13) is robust by ε for (1) in the stationary case, because the asymptotic stability of a closed-loop system along this regulator is preserved for any perturbations of parameter ε in the admissible domain of its variation.

Remark 4. Stabilizing Pade regulators can be constructed not only for continuous, but also for discrete time control systems with a smooth dependence on a parameter, for which the results on the stabilizing regulators asymptotic approximation can be found in [7, 10].

5. Numerical experiments.

Let us consider the following example with a vector control, where $A=\begin{pmatrix} -2 & -0.5 \\ -1 & -0.7 \end{pmatrix}$, $B=\begin{pmatrix} 2 & 0.4 \\ 0.5 & 1.4 \end{pmatrix}$, $Q_0=\begin{pmatrix} 5 & 0.5 \\ 0.5 & 5 \end{pmatrix}$, $Q_1=\begin{pmatrix} 1 & 0 \\ 0 & 1 \end{pmatrix}$, $Q_2=\begin{pmatrix} 1 & 0 \\ 0 & 1 \end{pmatrix}$, $R=\begin{pmatrix} 1 & 0 \\ 0 & 1 \end{pmatrix}$, $x_0=\begin{pmatrix} -1 & 1 \end{pmatrix}^T$. It clearly follows that here matrices $\tilde{P}_0, \tilde{P}_1, \hat{P}_0, \hat{P}_1, \hat{P}_2, M_0$ are symmetric and positive definite, $M_0=\begin{pmatrix} 2.315 & -2.130 \\ -2.130 & 5.093 \end{pmatrix}$, and matrices M_1, N_1, N_2 have positive eigenvalues but are not symmetric $M_1=\begin{pmatrix} 0.602 & -0.635 \\ -0.509 & 1.130 \end{pmatrix}$, $N_1=\begin{pmatrix} 0.070 & -0.086 \\ 0.024 & -0.022 \end{pmatrix}$, $N_2=\begin{pmatrix} 1.786 & -1.317 \\ -0.936 & 2.656 \end{pmatrix}$. A series of experiments were performed with different ε for the Pade regulator (13) and the SDRE regulator (3). The results of these regulators comparison by the quality criterion are presented in Table 1, and the trajectories of the corresponding closed systems are shown in Fig. 1.

Table 1. A comparison of two control algorithms by criterion values

	ε	**0.01**	**0.3**	**1**	**6**	**15**
I(u)	SDRE regulator (SDRE)	9,109	7,385	3,697	1,870	1,728
	Pade regulator (PA)	9,109	7,592	3,720	7,186	20,143
	Asymptotics by large ε *(second order)*	$1.253 \cdot 10^4$	17,702	3,947	1,870	1,728
	Asymptotics by small ε *(first order)*	9,109	8,180	7,425	13,433	24,700

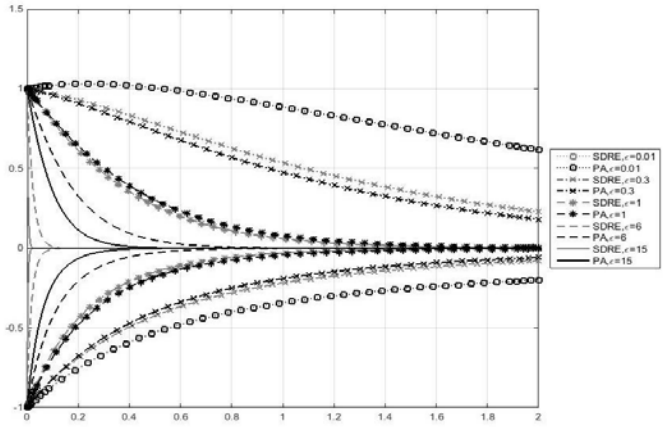

Figure 1. System stabilization for different values of ε in the stationary case

It can be seen from Table 1 that the Pade regulator demonstrates good performance almost for all values of ε except large values and Fig. 1 shows that it stabilizes the closed-loop system for the specified values of ε.

6. Conclusion

One of the possible stabilizing regulators for nonlinear control systems with a positive parameter $\varepsilon \in (0, \infty)$ is presented, which is based on the matrix Pade [1/2] approximation. The Pade approximation is constructed on the basis of two asymptotic approximations of the state-dependent matrix Riccati equation solution. For stationary control systems it was established that the constructed family of regulators is an approximate symbolic description of the parametric set of stabilizing controls. Numerical experiments show that two-point Pade regulators by using two asymptotic approximations can be more effective than regulators based on individual asymptotic expansions. For certain domains of parameter values the Pade regulator is close to the SDRE control, which is in some cases close to the optimal solution. The stabilizing Pade regulator is robust by the parameter in the stationary case, because the asymptotic stability of a closed-loop system along this regulator is preserved for any perturbations of parameter in the admissible domain of its variation.

Acknowledgments

Research supported by the Russian Science Foundation (project № 17-11-01220).

References

[1] Baker G.A. and Graves-Morris P. *Pade approximation: Foundations of the theory. Generalizations and applications*. Mir, Moscow, 1986 (in Russian).

[2] Andrianov I. V., and Awrejcewicz J. New trends in asymptotic approaches: summation and interpolation methods. *Applied Mechanics Reviews* 1, 2001, 69-91.

[3] Pal, J. Suboptimal control using Pade approximation techniques. *IEEE Transactions on Automatic Control* 5, 1980, 1007-1008.

[4] Halawa, J. Determination of PI and PID controllers settings using Pade approximation. *PrzeglądElektrotechniczny* vol. 85*,* 2009, 54-56.

[5] Cimen, T. Survey of state-dependent Riccati equation in nonlinear optimal feedback control synthesis". *AIAA Journal of Guidance, Control, and Dynamics* 4, 2012, 1025-1047.

[6] Chernous'ko F.L., Kolmanovskii V.B. Computational and approximate methods of optimal control. *J. Soviet Math* 3, 1979, 310-353.

[7] Naidu D. S. Singular perturbations and time scales in control theory and applications: an overview. *Dynamics of continuous, discrete and impulsive systems. Series B: Application & Algorithms* 9, 2002, 233-278.

[8] Dmitriev, M.G., and Kurina, G.A. Singular perturbations in control problems. *Automation and remote control* 1, 2006, 1-43.

[9] Dmitriev, M.G., and Makarov, D.A. The near optimality of the stabilizing control in a weakly nonlinear system with state-dependent coefficients. *AIP Conference Proceedings*, vol. 1759, 20016, 2016, 020016-1 – 020016-6.

[10] Danik, Yu.E., and Dmitriev, M. G. The robustness of the stabilizing regulator for quasilinear discrete systems with state dependent coefficients. *International Siberian Conference on Control and Communications (SIBCON–2016),* 2016.

[11] Belyaeva, N.P., Dmitriev, M.G. Construction of approximate solutions to initial value problems with a parameter based on pade approximants and asymptoticexpansions. *Computational mathematics and mathematical physics* 1, 2004, 112-124.

[12] Belyaeva, N. P., Dmitriev, M. G., Komarova, E. V. Pade-Approximation as a" Bridge" Between Two Parametric Boundary Asymptotics. *IFAC Proceedings Volumes* 6, 2001, 605-609.

[13] Vasil'eva, A.B. Asymptotic behavior of solutions to certain problems involving non-linear differential equations containing a small parameter multiplying the highest derivatives. *Russian mathematics surveys* 3*,*1963, 13-84.

[14] Balandin D.V., and Kogan M. M. *Controllers synthesis on the basis of linear matrix inequalities.* Litres, 2017 (in Russian).

Danik Yulia Eduardovna, M.Sc. (Ph. D. student): Federal Research Center "Computer Science and Control" of Russian Academy of Sciences (FRC CSC RAS), Moscow, Russia (yuliadanik@gmail.com).

Dmitriev Mikhail Gennadievich, D.Sc. (Professor): Federal Research Center "Computer Science and Control" of Russian Academy of Sciences (FRC CSC RAS), Moscow, Russia (mdmitriev@mail.ru). The author gave a presentation of this paper during one of the conference sessions.

Komarova Ekaterina Vladimirovna, D.Sc.: Russian State Social University, Moscow, Russia (evkomarova@mail.ru).

Makarov Dmitry Aleksandrovich, Ph.D.: Federal Research Center "Computer Science and Control" of Russian Academy of Sciences (FRC CSC RAS), Moscow, Russia (makarov@isa.ru).

Developments of non-linear dynamics FEM simulation of the impact performance of road safety barriers with use of experimental validation of models

Irina Demiyanushko, Ilya Karpov, Beka Tavshavadze

Abstract: A computer simulation with application use of the non-linear finite element programs developed to computational research of vehicle (cars, buses) collisions with road barriers having various original designs. It is demonstrated that for obtainment of adequate results of vehicle impact action on complex barrier structures an experimental validation of models is needed which allows obtain the main characteristics of the structures by calculation. Simulation calculations performed using approach virtually substitute field tests of the structures. Features of wave processes at single and repeated impacts, and corresponding power interactions in elements of designs investigate.

Road barrier is a device designed for traffic arrangement: reducing the number of cross-median crashes, collision with oncoming vehicle, hitting on roadside structures. In Russia, traditionally installed–concrete barriers (Fig. 1a) and metal guardrail (Fig. 1b), that prevent penetration of a vehicle to the oncoming lane or accidental exit from the road.

a) b)

Figure 1. Types of road barriers: a) concrete barriers; b) –guardrail barrier

Due to the increase vehicle mass and size, traffic load on the main routes, increase in driving speed, for retention of vehicles it is necessary to enhance the impact energy of road barriers, which is the main characteristic of barrier structure. The lateral impact energy – U corresponds to kinetic impact energy – E kJ, occurring at vehicle impact on the barrier, which the barrier must withstand without

considerable destruction and at the same time provide for a variety called consumer-oriented characteristics [1].

The impact energy calculated by

$$E = \frac{m(v * sin\alpha)^2}{2} \quad (1)$$

α – impact angle, degrees, m – vehicle mass, t; v– impact speed, m/s

Normally, the U value of the most barriers is within 90 –700 kJ [1].

Figure 2 shows the scheme of vehicle run into lateral barrier installed on the road center line and specifies some typical parameters, the target impact angles 20 degrees (average statistical value), value of barrier maximum dynamic deflection at the moment of impact.

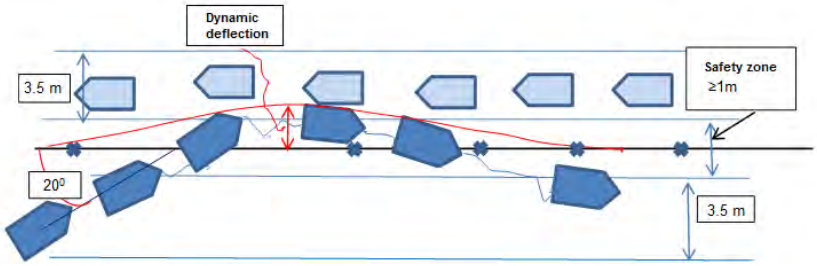

Figure 2. The scheme of vehicle running into the central line barrier

Enhancement of the lateral impact energy of classic barriers provided with increase of their height and material volume. The barriers become increasingly bulky, they occupy a substantial part of road space and block the road perspective for the drivers, disturb the architectural look of the roads. Some years ago developed new barrier structures– roadside and median versions of the cable barrier (Fig. 3) and "front barriers" that designed for damping of direct impact and installed on V-junctions and in front of lateral barriers [3].

a) b)

Figure 3. Cable median and roadside barrier (a) and front barriers (b) in front of the bridge footing

Evaluation of compliance with the requirements of basic barrier parameters is carried out by field testing of the barriers where vehicles run into a barrier. The tests carried out on special purpose testing grounds. However, in the design of the structures, benchmarking analysis, minor changes of the parameters and analysis of accident situations they currently widely use the computer simulation methods – so called "simulation analysis".

At Moscow Technical University MADI researches are conducted with design of barrier systems, laboratory tests of the elements and development of the computational simulation analysis. Use of mathematical simulation analysis based on modern computer products and modern computing technology made it possible in a short span of time to address the issues related to rational choice such structures, as of cable barriers, demonstrate their operating peculiarities, efficiency in holding / retaining of different type vehicles, and consequences of running into. The impact process when a vehicle runs into a barrier represents a highly nonlinear and fast process, so average value of vehicle interaction from the moment the vehicle touches the structure to the exit normally lasts for 200-300 ms. A barrier structure normally consists of thin-walled elements (beams) and cables – in cable structures; vehicle body parts are thin-walled as well, thus during the impact, considerable mutual deformations and displacements, contact interactions, plastic deformations take place, therefore the run into tasks is highly nonlinear. The structural complexity dictates use of the finite element method (FEM) for the computations. In this context, for solution of impact simulation task when a vehicle runs into a barrier, the multi-purpose FEM program complex LS-Dyna DYNA (Livermore Software Technology Corp., California, USA) (licensed version) was used [2]. Our experience in numerical analysis of different barrier structures and comparison with field and experimental study results made it possible to lay down requirements to computations, which formed in appropriate specifications and guidelines. The basic principle for construction of FE-analysis models is the necessity to verify the built individual FE-models of the structures and the full-size structure of colliding bodies system.

Thus, when selecting FE models for cables, required for simulation of cable barriers, they studied the statics and dynamics (Fig. 4) of currently used steel cables, developed appropriate testing methods [3,4] resulting in selection of an adequate model consisting of beam-shell elements considered in [5]. Those studies showed that the propagation of deformation waves in the cable in case of impact is a complex process, and the impact energy absorption is mainly due to friction of cable wires and depends heavily on cable pre-tension.

A similar verification study of impact on a barrier posts, mounted in a shell and concrete foundation or directly in the road top carried out both by experiment and simulation computation method (Fig.5) [6].

a) b)

Figure 4. Test for cable dynamic model validation: (a) experiment, (b) FE model

a) b)

Figure 5. Cable barrier post's test: a) experiment b) FE simulation

The studies show, that the simulation FE computation of impact on the posts reasonable accurately replicates the experiment results both qualitatively and quantitatively that afforded grounds for selection of appropriate FE models. Essential points in development of adequate simulation models are issues of selection and simulation of friction surfaces and work of connection elements in barrier structures under consideration.

The simulation analysis determines all characteristics of impact interaction of a vehicle with a barrier. Thus, the injury severity index ***I,*** which actually represents an average value of inertial accelerations in the center of vehicle mass, is one of the most important characteristics of the barrier.

The injury severity index determined by a formula [1]

$$I = \left[\left(\frac{N_x}{12}\right)^2 + \left(\frac{N_y}{9}\right)^2 + \left(\frac{N_z}{10}\right)^2\right]^{0,5}, \quad (2)$$

where N_x, N_y, N_z are average values of inertial accelerations along vehicle axes in m/s^2 are determined and analyzed in the simulation computation. Equally, important characteristics determined by the computational analysis are dimensions of so called "corridor", i.e. capabilities of impacted vehicle run beyond tolerable limits, as well as the coefficient of vehicle internal dimensions integrity determined by relative deformations of the vehicle body in the intended directions for each vehicle type.

Following are the results of simulation analysis of cable barrier behavior run into and impacted by a bus (Fig.6). This is a typical analysis carried out in accordance with safety standards.

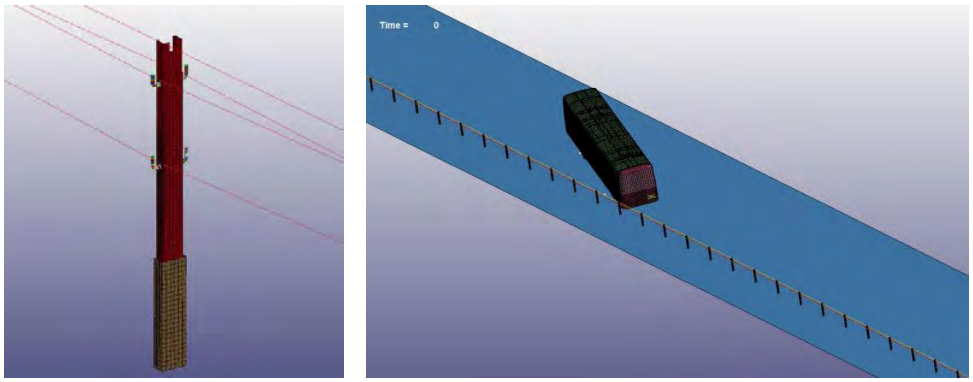

a) b)

Figure 6 – Simulation of cable barrier elements, a) – solid model, b) – FE model

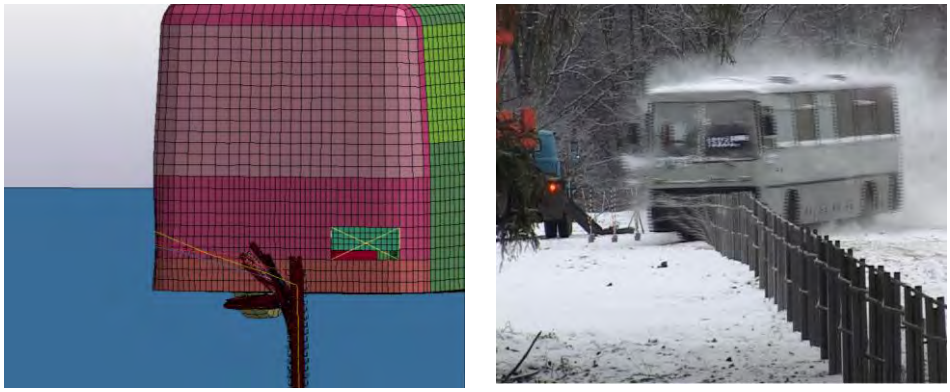

a) b)

Figure 7. Initial moment of bus impact on the cable barrier a) FE model b) Test

Tracking of bus runway identity in field tests and simulation computation (Fig. 7), as well as comparison of all parameters (Fig. 7- 9) makes it possible to establish adequacy of the computational model.

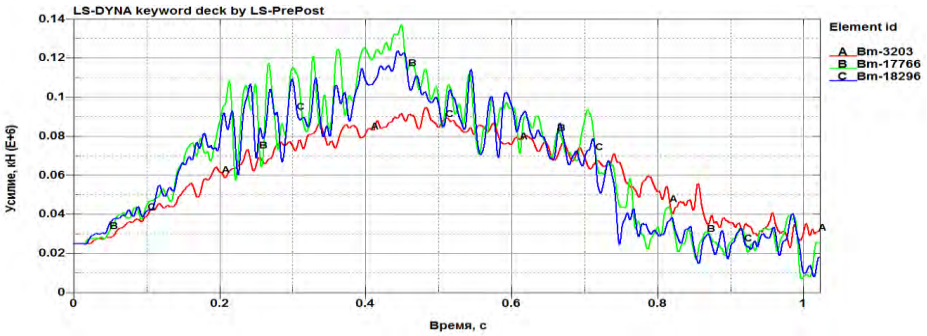

Figure 8. Change of cable forces in cables during the impact

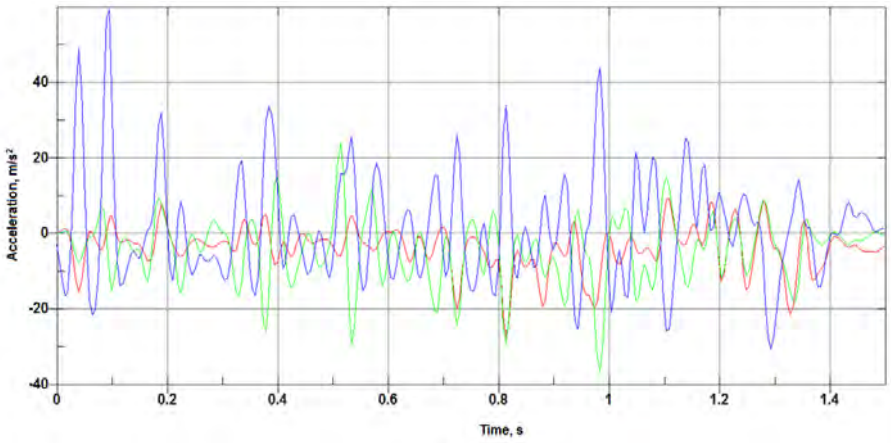

Figure 9. Accelerations in the center of bus masses when running into a barrier, $I = 0.56$, variation from the experiment equals to 7.5%.

Operating principle of different barrier structures is, certainly, different. If a cable barrier absorbs the impact energy due to the high friction and, consequently, damping in the system though the main forces in the cables are stretching forces then the barrier works as a beam system loaded with dynamic transverse forces. For these reasons, FE models of barrier railings differ from cable barriers. For simulation of a barrier beam, which is the main load-bearing element, they use shell elements; the appearance of FE models of the main barrier railing structural elements and their connections shown in Fig. 10 a, b. For connection of beam with a console-shock absorber are use a deformable destructible bolt connection. Connecting elements used for connection of the console-shock absorber with the poles are rigid and indestructible RBE-elements (Fig. 10b).

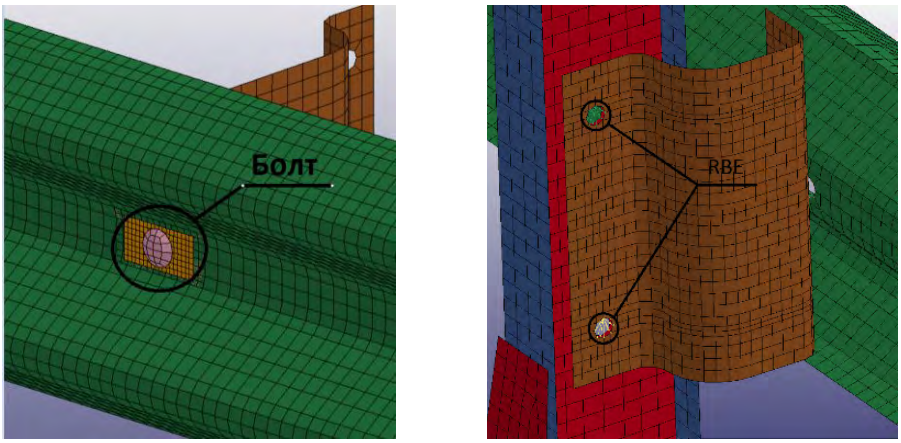

(a) (b)

Figure10. Appearance of barrier railing connection elements: (a) bolt connection of the beam with compensators, (b) connection of compensators with the pole using RBE-elements

Steel barrier beam is made of light-gauge sheet metal and FE model of the beam simulated with two-dimensional shell elements. Compensators, which along with the beam take the impact load, simulated with shell elements as well. The barrier post mounted (piled) in the soil body as well represents a beam of different section – a U-section for this example (Fig.11).

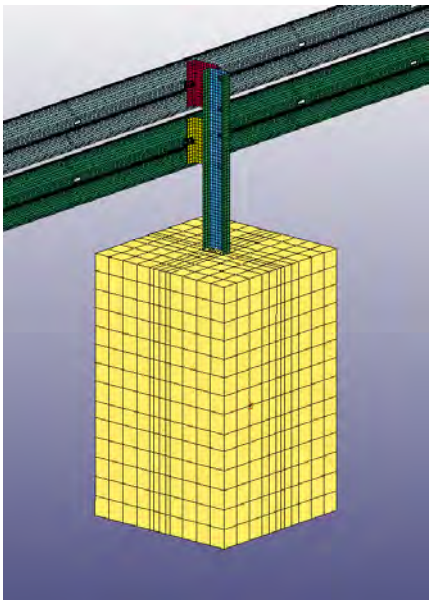

Figure 11. FE model of guardrail road barrier

Fig.12 illustrate an example of calculated model behavior at different time intervals in simulation of a bus running into a barrier at E=300 kJ, along with representation of not only the first impact but the bus turn and repeated impact on the barrier with its rear part.

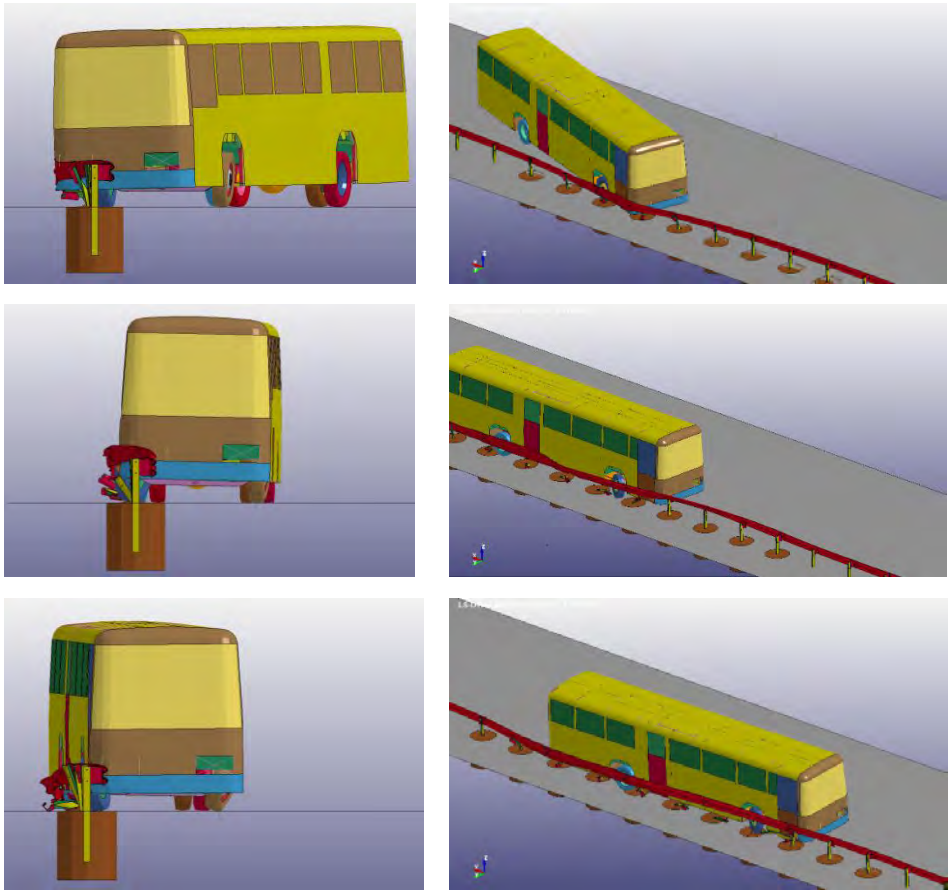

a) b)

Figure 12. Guardrail and bus interaction: a) side view b) top view

Accelerations in the center of mass making possible to assess the impact effect on the severity of consequences following computation results compared with the experimental results, Fig. 13, the computation results are coincides with the experiment.

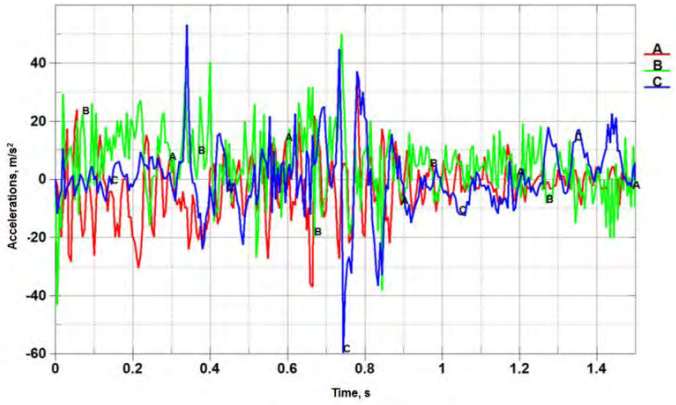

Figure 13. Acceleration in FE model in directions: X (red), Y (green), Z (blue)

In this article, we, naturally, were unable to demonstrate all study materials on simulation of run into processes and impact of various type vehicles on road barriers of different structures. However, even these limited results show, that application of modern numerical methods of nonlinear dynamic computation to complex tasks of vehicle impact collision with deformable safety barrier systems provide sample opportunities for analysis of these processes. It should be noted, that the costs of initial development of adequate FE models are, certainly, heavy; these procedures require the compulsory verification of the models by comparison with the experiment, however, in the future those costs reduce significantly due to use of the analogies, specifically, in models of materials and structures. For instance, we had no opportunity here to demonstrate extremely interesting solutions on analysis of vehicle running into rigid concrete barriers, where a concrete destruction simulation task occurs, and which is of great interest and which was resolved along with the use of nonlinear analysis complex MSC. Software / MARC [7]. Analysis of running into front barriers with account of variety of their structures and used materials is a challenge as well.

Acknowledgments

The authors thank students of MADI for their creative computation and analysis output – A.Rodionov, V. Lazarev and others.

References

[1] GOST33129-2014. Automobile Roads of General Use. Road Restraint Systems. Methods of Testing. M.: StandartInform,-2014. -19 p.

[2] LS-DYNA Keyword User's Manual. Version 971 Release 4. Livermore Software Technology Corporation. Livermore, California: 2009.

[3[Demyanushko I.V. Cable Road Barriers. Russian Experience.//Road Power,- 2014.-No. 52. -P. 22 – 24

[4] Karpov, I. A. Development of Finite-Element Models of Cable Road Barriers Using LS-DYNA software package / I. A. Karpov // Vehicle. Road. Infrastructure. - 2016. - No. 2.

[5] Reid, John, Paulsen, T.J., and Hiser, Nick. Simulation and Bogie Testing of a New Cable Barrier Terminal. //Crashworthiness, Occupant Protection and Biomechanics in Transportation Systems Conference.-2003.- Paper No. IMECE2003-55104.- 2003.

[6] Demyanushko I.V., Karpov I.A. Simulation of vehicle running into a road barrier pole // Transport Construction – No. 10 .-2013.- P.16-20

[7] Demyanushko I.V., Stain V.M., Stain A.V., Karpov I.A. Computation simulation of bus interaction with two-side concrete copestone barrier // Transport Construction No. 3.-2017.-.P.11-16.

[1)] Irina Demiyanushko, PhD, Prof., Moscow Automobile & Road State Technical University (MADI), Leningradskiy Prospect 64, 125319,Moscow/ Russia (demj-ir@mail.ru, irina.demiyanushko@gmail.com)., the author presents this work at the conference.

[2)] Ilya Karpov, M.Sc., Moscow Automobile & Road State Technical University (MADI), Leningradskiy Prospect 64, 125319, Moscow/ Russia (mymail169@gmail.com)

[3)] Beka Tavshavadze, M.Sc., Moscow Automobile & Road State Technical University (MADI), Leningradskiy Prospect 64, 125319, Moscow/ Russia (tavshavadze@niimech.ru)

Nonlinear differential-difference equations related to the second Painlevé equation

Galina Filipuk

Abstract: As a result of classification of second order ordinary differential equations without movable branch points,

$$f'' = F(z, f, f'), \quad f = f(z), \quad ' = d/dz,$$

where F is rational in f, algebraic in f' and analytic in z, a number of the so-called Painlevé equations was obtained. Among them, six irreducible equations are best known. They led to the recognition of new functions, called the Painlevé transcendents. The Painlevé equations have numerous applications in modern mathematics and mathematical physics. They can be obtained by similarity reductions from certain integrable partial differential equations (e.g., KdV, mKdV and others). They possess a number of other remarkable properties (e.g., Bäcklund transformations, classical solutions, the Hamiltonian structure). Via the Hamiltonian structure the Painlevé equations are related to their associated equations, the so-called $\sigma-$equations. In this paper we derive Bäcklund transformations for two $\sigma-$forms of the second Painlevé equation (with respect to two different Hamiltonians) and use these transformations to obtain nonlinear differential-difference and difference equations for the solutions.

1. Introduction

The sixth irreducible Painlevé equations are nonlinear second order ordinary differential equations of the form

$$f'' = F(z, f, f'), \quad f = f(z), \quad ' = d/dz, \tag{1}$$

where F is rational in f, algebraic in f' and analytic in z, which possess the Painlevé property (solutions have no movable algebraic singularities). They were obtained in the papers of Painlevé [5] and his student Gambier [1]. In general, solutions of nonlinear differential equations may have very complicated movable singularities, which depend on initial conditions [3], but the Painlevé property guarantees that solutions have at most movable poles. The Painlevé equations (and their associcated equations, including $\sigma-$forms and discrete equations) have numerous applications in modern mathematics and mathematical physics.

They can also be obtained by similarity reductions from certain integrable partial differential equations (e.g., KdV, mKdV and others). The Painlevé equations are irreducible in the sense that they cannot be linearised or their solutions cannot be expressed in terms of classical special functions for general values of the parameters in equations. However, for special values of the parameters, Painlevé equations may possess either rational or algebraic solutions, or solutions expressed in terms of classical special functions (e.g., Airy, Bessel, (confluent) hypergeometric functions).

In this paper we shall concentrate on the second Painlevé equation given by

$$f'' = 2f^3 + zf + \alpha, \tag{P_2}$$

where α is a fixed complex parameter and $f = f(z)$.

The Painlevé equations are known to possess the Hamiltonian structure [4]. Equation $P_2(\alpha)$ can be represented as a Hamiltonian system with the Hamiltonian

$$H_2(p, q, z) := \frac{1}{2}p^2 - (q^2 + \frac{1}{2}z)p - \left(\alpha + \frac{1}{2}\right) q,$$

such that

$$\begin{cases} \dfrac{dq}{dz} = \dfrac{\partial H_2}{\partial p} = p - q^2 - \dfrac{1}{2}z, \\ \dfrac{dp}{dz} = -\dfrac{\partial H_2}{\partial q} = 2qp + \alpha + \dfrac{1}{2}, \end{cases} \tag{2}$$

where q solves P_2 and p solves equation P_{34} given by

$$p'' = \frac{(p')^2}{2p} + 2p^2 - zp - \left(\alpha + \frac{1}{2}\right)^2 \frac{1}{2p}. \tag{P_{34}}$$

The so-called $\sigma-$form of the second Painlevé equation is obtained as follows. By putting

$$\sigma(z) := H_2(p, q, z),$$

it can be shown that the function σ solves the following second order second degree nonlinear differential equation:

$$(\sigma'')^2 + 4(\sigma')^3 + 2\sigma'(z\sigma' - \sigma) = \frac{1}{4}\left(\alpha + \frac{1}{2}\right)^2. \tag{S_2}$$

Conversely, if σ is a soluton of S_2, then

$$\begin{cases} q = \dfrac{4\sigma'' + 2\alpha + 1}{8\sigma'}, \\ p = -2\sigma' \end{cases} \tag{3}$$

solve P_2 and P_{34} respectively. Note that we have a constant solution to equation S_2 if $\alpha = -1/2$.

It is known [2] that the second Painlevé equation possesses the so-called Bäcklund transformations. They relate solutions with different values of the parameter α. In particular, if $q = q_\alpha(z)$ is a solution of $P_2(\alpha)$, then $q_{\alpha\pm1}$ given by

$$q_{\alpha\pm1} = -q - \frac{2\alpha \pm 1}{2q^2 \pm 2q' + z} \tag{4}$$

solve $P_2(\alpha \pm 1)$. Equations in (4) can be used to obtain a nonlinear difference equation for the solutions of P_2. Indeed, eliminating q' between two equations (4), we get

$$\frac{2\alpha + 1}{q_{\alpha+1} + q_\alpha} + \frac{2\alpha - 1}{q_\alpha + q_{\alpha-1}} + 4q^2 + 2z = 0. \tag{5}$$

The main objective of this paper is to obtain Bäcklund transformations for the $\sigma-$ form of the second Painlevé equation and use them to find the analogue of (5). Moreover, we shall also use another Hamiltonian system, derive the corresponding $\sigma-$form and examine various properties of its solutions.

2. Bäcklund transformations for the $\sigma-$ form of P_2 and nonlinear difference equations

From (2) we have

$$p = \frac{1}{2}(z + 2q^2 + 2q'),$$

and the Hamiltonian, which is also the function σ in our notation, becomes

$$\sigma = -\frac{1}{8}(z^2 + 4(2\alpha + 1)q + 4zq^2 + 4q^4 - 4q'^2). \tag{6}$$

Next, we write the Hamiltonian system (2) for $q_{\alpha+1}$ and $p_{\alpha+1}$. Using (4) we can find expression of $p_{\alpha+1}$ in terms of $q = q_\alpha$. Substituting this expression into $\sigma_{\alpha+1}$ and eliminating q'' and higher order derivatives by using P_2, we get

$$\sigma_{\alpha+1} = \frac{1}{8(z + 2q^2 + 2q')}(16\alpha + 8 - z^3 - 2qg_1 - 2q'g_2 + 4(z + 2q^2)q'^2 + 8q'^3), \tag{7}$$

where $g_1 = 2z(2\alpha - 1) + q(3z^2 + 2q(2q^3 + 3zq + 4\alpha - 2))$ and $g_2 = z^2 + 4q(2\alpha - 1 + zq + q^3)$.

Substituting (3) into (7), we get an expression of $\sigma_{\alpha+1}$ in terms of σ and its derivatives up to order 3. We can now use equation S_2 to get

$$\sigma_{\alpha+1} = \frac{4\sigma'' + 8\sigma\sigma' - 2\alpha - 1}{8\sigma'}. \tag{8}$$

Equation (8) is a (forward) Bäcklund transformation for the $\sigma-$ form of the second Painlevé equation. It relates solutions of equation S_2 with parameters α and $\alpha+1$.

To get a differential-difference equation for the solutions of S_2 we can take (7) and (6) and compute the resultant to eliminate q'. Next we can substitute (3) for q in terms of σ and its derivatives and use equation S_2 to eliminate the third and higher order derivatives of σ and powers of σ''. The resulting equation, which is quadratic in $\sigma_{\alpha+1}$ and contains σ, σ', σ'', is cumbersome and we shall not present it here.

Similar procedure yields

$$\sigma_{\alpha-1} = \frac{1}{8}(4q - z^2 - 8\alpha q - 4zq^2 - 4q^4 + 4q'^2) \tag{9}$$

and

$$\sigma_{\alpha-1} = \frac{4\sigma'' + 8\sigma\sigma' + 2\alpha + 1}{8\sigma'}. \tag{10}$$

Note that

$$\sigma_{\alpha-1} = \sigma + q. \tag{11}$$

Thus, we have the following theorem.

Theorem 2.1 *The Bäcklund transformations for equation S_2 are given by* (8) *and* (10)*. Moreover, using* (8) *and* (10)*, we get the following differential-difference equation:*

$$\sigma_{\alpha+1} - \sigma_{\alpha-1} + \frac{2\alpha+1}{4\sigma'} = 0.$$

We also remark that since $\sigma_{\alpha+1}$ can be expressed in terms of q and q', and since $q = \sigma_{\alpha-1} - \sigma$, $q' = \sigma'_{\alpha-1} - \sigma'$, we can find an expression of $\sigma_{\alpha+1}$ in terms of $\sigma_{\alpha-1}$, σ and their derivatives. This will give another differential-difference equation.

To get the analogue of (5) for solutions of equation S_2, we use expressions of σ and $\sigma_{\alpha+1}$ in terms of q and q', substitute there $q = \sigma_{\alpha-1} - \sigma$ and compute the resultant to eliminate q'. In the result, we get a nonlinear difference equation relating $\sigma_{\alpha\pm1}$ and σ.

Theorem 2.2 *Let $\sigma = \sigma_\alpha$ and $\sigma_{\pm1} = \sigma_{\alpha\pm1}$ be solutions of equation S_2 with parameter α and $\alpha \pm 1$ respectively. Then*

$$((2\alpha+1)\sigma - (2\alpha-1)\sigma_1)\sigma + ((2\alpha+1)\sigma_1 - (2\alpha+3)\sigma)\sigma_{-1} + \frac{(2\alpha+1)z}{2} = \frac{(2\alpha+1)^2}{4(\sigma_1 - \sigma_{-1})}. \tag{12}$$

3. Classical solutions of the $\sigma-$form of P_2

It is well-known that for special values of the parameter in the equation, P_2 possesses special Riccati type solutions (the so-called classical solutions). In particular, if $\alpha = 1/2$, then solutions of

$$q' = q^2 + z/2 \tag{13}$$

also solve P_2. For $\alpha = -1/2$ we have another one-parameter family of classical solutions:

$$q' = -q^2 - z/2. \tag{14}$$

Clearly, for family (13) we have $p = z + 2q^2$ and for family (14) $p = 0$ using the Hamiltonian system (2). For equation S_2 these two families of Riccati solutions correspond to $\sigma = -q$ and to $\sigma = 0$. Using (3) we have for $\alpha = 1/2$

$$\sigma'' = -\frac{1}{2}(4\sigma'\sigma + 1).$$

Substituting this expression into $S_2(1/2)$ we get an equation for Riccati solutions for the $\sigma-$form.

Theorem 3.1 *Solutions of*

$$\sigma' = -\frac{1}{2}(2\sigma^2 + z)$$

solve S_2 *with* $\alpha = 1/2$. *The Bäcklund transformations* (8) *and* (10) *for this family are*

$$\sigma_{3/2} = \frac{1}{z + 2\sigma^2}, \quad \sigma_{-1/2} = 0.$$

Therefore, we have Airy functions as special solutions of S_2.

4. Patterns for expansions

It is well-known that solutions of the second Painlevé equation are meromorphic functions in the complex plane. There are two types of expansions around movable poles:

$$q(z) = \frac{1}{z - z_0} - \frac{z_0}{6}(z - z_0) - \frac{\alpha + 1}{4}(z - z_0)^2 + a_3(z - z_0)^3 + O((z - z_0)^4) \tag{15}$$

or

$$q(z) = -\frac{1}{z - z_0} + \frac{z_0}{6}(z - z_0) - \frac{\alpha - 1}{4}(z - z_0)^2 + a_3(z - z_0)^3 + O((z - z_0)^4), \tag{16}$$

where a_3 is an arbitrary constant. The corresponding expansions for p in the Hamiltonian system are

$$p(z) = -\frac{2\alpha+1}{2}(z-z_0) + \frac{z_0^2+180a_3}{36}(z-z_0)^2 + \frac{(2\alpha+1)z_0}{6}(z-z_0)^3 + O((z-z_0)^4)$$

or

$$p(z) = \frac{2}{(z-z_0)^2} + \frac{z_0}{3} + \frac{1}{2}(z-z_0) + \frac{z_0^2+36a_3}{36}(z-z_0)^2 + \frac{z_0}{18}(z-z_0)^3 + O((z-z_0)^4).$$

Therefore, using the definition of σ we have the following expansions:

$$\sigma(z) = -\frac{z_0^2+180a_3}{35} + \frac{2\alpha+1}{8}(z-z_0)^2 + O((z-z_0)^3)$$

or

$$\sigma(z) = \frac{1}{z-z_0} - \frac{z_0^2-180a_3}{36} - \frac{z_0}{6}(z-z_0) - \frac{1}{8}(z-z_0)^2 + O((z-z_0)^3).$$

Next we shall study how corresponding expansions change after Bäcklund transformations. For the solutions of P_2 we have

$$q_{\alpha+1}(z) = \frac{z_0^2+180a_3}{18(2\alpha+1)} + O((z-z_0))$$

or

$$q_{\alpha+1}(z) = \frac{1}{z-z_0} - \frac{z_0}{6}(z-z_0) - \frac{\alpha+2}{4}(z-z_0)^2 + O((z-z_0)^3)$$

and

$$q_{\alpha-1}(z) = -\frac{1}{(z-z_0)} + \frac{1}{6}z_0(z-z_0) - \frac{\alpha-2}{4}(z-z_0)^2 + O((z-z_0)^3)$$

or

$$q_{\alpha-1}(z) = \frac{z_0^2-180a_3}{18(2\alpha-1)} + O(z-z_0).$$

Note that for the expansion of q with residue 1 at $z=z_0$ the forward Bäcklund transformation gives a regular expansion, whereas the backward Bäcklund transformation gives a polar expansion with residue -1. On the other hand, for the expansion of q with residue -1 at $z=z_0$ the forward Bäcklund transformation gives a polar expansion with residue 1 and the backward Bäcklund transformation gives a regular expansion at $z=z_0$.

For the solutions of S_2 we have

$$\sigma_{\alpha+1}(z) = -\frac{(3+2\alpha)(z_0^2+180a_3)}{36(2\alpha+1)} + O(z-z_0)$$

or

$$\sigma_{\alpha+1}(z) = -\frac{z_0^2 - 180a_3}{36} + \frac{2\alpha+3}{8}(z-z_0)^2 + O((z-z_0)^3),$$

and

$$\sigma_{\alpha-1}(z) = \frac{1}{(z-z_0)} - \frac{z_0^2 + 180a_3}{36} - \frac{z_0}{5}(z-z_0) - \frac{1}{8}(z-z_0)^2 + O((z-z_0)^3)$$

or

$$\sigma_{\alpha-1}(z) = -\frac{z_0^2 - 180a_3}{36} - \frac{2\alpha-1}{8}(z-z_0)^2 + O((z-z_0)^3).$$

Note that for the regular expansion of σ at $z = z_0$ the forward Bäcklund transformation gives a regular expansion, whereas the backward Bäcklund transformation gives a polar expansion with residue 1. On the other hand, for the expansion of q with residue 1 at $z = z_0$ both the forward and the backward Bäcklund transformation give a regular expansion at $z = z_0$.

Finally, we note that we can use equation (12) to get some information on the expansions of solutions of equation S_2. In particular, substituting the Ansatz

$$\sigma(z) = \sum_{n=0}^{\infty} b_n(z-z_0)^n, \quad \sigma_{\alpha-1}(z) = \sum_{n=-1}^{\infty} c_n(z-z_0)^n, \quad \sigma_{\alpha+1}(z) = \sum_{n=0}^{\infty} d_n(z-z_0)^n$$

with the assumption $c_{-1} = 1$ we can consecutively get a few relations between the unknown coefficients $b_n,\ c_n,\ d_n$. For instance, $(2\alpha+1)d_0 = (2\alpha+3)b_0$.

Similarly, substituting the Ansatz

$$\sigma(z) = \sum_{n=-1}^{\infty} b_n(z-z_0)^n, \quad \sigma_{\alpha-1}(z) = \sum_{n=0}^{\infty} c_n(z-z_0)^n, \quad \sigma_{\alpha+1}(z) = \sum_{n=0}^{\infty} d_n(z-z_0)^n$$

with the assumption $b_{-1} = 1$, we get $d_0 = c_0,\ d_1 = c_1,\ d_2 = c_2 + (2\alpha+1)/4$ and so on. This is similar to the results when we search for the expansions of (5) for instance in the form

$$q(z) = \sum_{n=-1}^{\infty} b_n(z-z_0)^n, \quad q_{\alpha-1}(z) = \sum_{n=-1}^{\infty} c_n(z-z_0)^n, \quad q_{\alpha+1}(z) = \sum_{n=0}^{\infty} d_n(z-z_0)^n$$

with $b_{-1} = 1$ and get $c_{-1} = -b_{-1},\ c_0 = -b_0,\ c_1 = -b_1,\ c_2 = -(b_2 + (2\alpha-1)/4)$ or in the form

$$q(z) = \sum_{n=-1}^{\infty} b_n(z-z_0)^n, \quad q_{\alpha-1}(z) = \sum_{n=0}^{\infty} c_n(z-z_0)^n, \quad q_{\alpha+1}(z) = \sum_{n=-1}^{\infty} d_n(z-z_0)^n$$

with $b_{-1} = -1$ and get $d_{-1} = 1,\ d_0 = -b_0,\ d_1 = -b_1,\ d_2 = -(b_2 + (2\alpha+1)/4)$.

5. Another Hamiltonian

Recently a new Hamiltonian for the second Painlevé equation was introduced in [6]. It has the form

$$\tilde{H}_2(z,p,q) = \frac{1}{2}p^2 - \frac{1}{2}q^4 - \frac{1}{2}zq^2 - \alpha q.$$

The corresponding Hamiltonian system is

$$q' = p, \quad p' = 2q^3 + zq + \alpha.$$

By introducing $s(z) := \tilde{H}_2(z,p,q)$, we get

$$s = \frac{1}{2}q'^2 - \frac{1}{2}q^4 - \frac{1}{2}zq^2 - \alpha q, \tag{17}$$

$$s' = -\frac{1}{2}q^2, \quad s'' = -qq'.$$

Next we derive the $\sigma-$form of P_2 with respect to this Hamiltonian and present Bäcklund transformations. We also briefly discuss differential-difference and difference equations, classical solutions and expansions of solutions around movable poles.

Theorem 5.1 *The function $s(z) := \tilde{H}_2(z,p,q)$ satisfies the following second order fourth degree differential equation:*

$$(s'')^4 + 8s'(s'')^2(s + s'(2s' - z)) + 16(s')^2(2\alpha s' + (s + s'(2s' - z))^2) = 0. \tag{18}$$

Moreover,

$$q = -\frac{(s'')^2 + 8(s')^3 - 4z(s')^2 + 4ss'}{4\alpha s'}, \quad q^2 + 2s' = 0.$$

The Bäcklund transformations are given (in terms if q and q') in the following theorem. Using expressions for q in the theorem above, we can get cumbersome expressions in terms of s and its derivatives up to second order, but we omit these expressions.

Theorem 5.2 *Let q be a solution of $P_2(\alpha)$. Then*

$$s_{\alpha+1} = \frac{1}{2}\left(q'^2 - q(q^3 + zq + 2\alpha) + \frac{2\alpha + 1}{2q' + 2q^2 + z}\right) \tag{19}$$

and

$$s_{\alpha-1} = \frac{1}{2}\left(q'^2 - q(q^3 + zq + 2\alpha) + \frac{2\alpha - 1}{2q' - 2q^2 - z}\right) \tag{20}$$

solve (18) *with parameters $\alpha+1$ and $\alpha-1$ respectively. If s is defined by* (17)*, then we have the following differential-difference equation:*

$$s_{\alpha+1} - s_{\alpha-1} = \frac{2(\alpha z + 2\alpha q^2 - q')}{z^2 - 8\alpha q - 8s}. \tag{21}$$

To get a nonlinear difference equation for s, $s_{\alpha+1}$ and $s_{\alpha-1}$ we use equation (21) to find q'. Substituting this expression into (17) and into either (19) or (20) we can eliminate q by computing the resultant. The resulting equation is very cumbersome.

As in the previous section, we can compute expansions of s, which correspond to expansions (15) or (16). We have

$$s(z) = \frac{1}{2(z-z_0)} + \frac{7z_0^2 - 360a_3}{72} + \frac{z_0}{6}(z-z_0) + \frac{1}{8}(\alpha+1)(z-z_0)^2 + O((z-z_0)^3)$$

or

$$s(z) = \frac{1}{2(z-z_0)} + \frac{7z_0^2 + 360a_3}{72} + \frac{z_0}{6}(z-z_0) - \frac{1}{8}(\alpha-1)(z-z_0)^2 + O((z-z_0)^3).$$

We also have

$$s_{\alpha-1} = \frac{1}{2(z-z_0)} + \frac{7z_0^2 - 360a_3}{72} + \frac{z_0}{6}(z-z_0) - \frac{\alpha-2}{8}(z-z_0)^2 + O((z-z_0)^3)$$

or

$$s_{\alpha-1} = \frac{720a_3(\alpha-1) + z_0^2(14\alpha-5)}{72(2\alpha-1)} + O(z-z_0)$$

and

$$s_{\alpha+1} = -\frac{720a_3(\alpha+1) - z_0^2(14\alpha+5)}{72(2\alpha+1)} + O(z-z_0)$$

or

$$s_{\alpha+1} = \frac{1}{2(z-z_0)} + \frac{7z_0^2 + 360a_3}{72} + \frac{z_0}{6}(z-z_0) + \frac{(\alpha+2)}{8}(z-z_0)^2 + O((z-z_0)^3).$$

Finally, for both (13) and (14) we have $z^2 = 8(\alpha q + s)$, which, using $q^2 = -2s'$, gives the following Riccati equation of (18) with $\alpha = \pm 1/2$:

$$128\alpha^2 s' + 64s^2 - 16z^2 s + z^4 = 0.$$

For the family (13) we have

$$s_{3/2} = \frac{2(2\alpha+1) + z^3 - 8z\alpha q + 2z^2q^2 - 16\alpha q^3}{8z + 16q^2}$$

and for the family (14) we have

$$s_{-3/2} = \frac{z^3 - 2(2\alpha-1) - 8z\alpha q + 2z^2q^2 - 16\alpha q^3}{8z + 16q^2}.$$

Acknowledgements

Support from the Alexander von Humboldt Foundation is greatefully acknowledged.

References

[1] Gambier, B. Sur les équations différentielles du second ordre et du premier degré dont l'intégrale générale est à points critiques fixés. *Acta Math.,* 33 (1909), 1–55.

[2] Gromak, V., Laine, I., and Shimomura, S. *Painlevé Differential Equations in the Complex Plane*. De Gruyter Studies in Mathematics 28, Walter de Gruyter, Berlin, 2002.

[3] Ince, E.L. *Ordinary Differential Equations*. London, Longmans Green, 1927.

[4] Okamoto, K. Studies on the Painlevé equations. III. Second and fourth Painlevé equations, P_{II} and P_{IV}. *Math. Ann.*, 275 (1986), 221–255.

[5] Painlevé, P. *Leçons sur la Théorie Analytique des Équations Différentielles, Profesées à Stockholm, 1895*. Hermann, Paris, 1897.

[6] Żołądek, H., and Filipuk, G. Painlevé equations, elliptic integrals and elementary functions. *J. Differential Equations*, 258 (2015), 1303–1355.

Galina Filipuk, Ph.D.: University of Warsaw, Faculty of Mathematics, Informatics and Mechanics, Banacha 2, Warsaw, 02-097, Poland (*filipuk@mimuw.edu.pl*). The author gave a presentation of this paper during one of the conference sessions.

Kahan discretisation of a cubic Hamiltonian system

Galina Filipuk, Thomas Kecker

Abstract: We apply Kahan's discretisation method, also known as the Hirota-Kimura method or Runge-Kutta method, to a cubic Hamiltonian system of Painlevé type. The system being non-autonomous it is not clear from the start whether discretisation will preserve integrability. Although the resulting discrete system is non-integrable, by introducing a parameter into the equations one obtains a system with reduced (though non-zero) algebraic entropy.

1. Introduction

It is a by now well-established fact that the integrability of differential and difference equations is closely linked to the singularity structure of their solutions in the complex plane. In the setting of (ordinary) differential equations the term 'integrability' is often synonymously denoted by the Painlevé property, meaning that all (movable) singularities of every solution of an equation are poles. The Painlevé test is a useful necessary criterion for an equation to have this property: At every point in the complex plane there must exist a sufficiently large family of Laurent series solutions with finite principle part (finitely many negative powers).

In the setting of discrete equations there is a known list of integrable difference equations, known as discrete Painlevé equations which possess continuum limits to the classical Painlevé equations [11]. There are several notions of discrete analogues for the Painlevé property, namely singularity confinement, zero algebraic entropy [5], and the existence of sufficiently many finite-order meromorphic solutions [4]. The method of singularity confinement has been a successful tool to detect integrable discrete (difference) equations, although it only provides a necessary criterion for the integrability of discrete systems, similar to the Painlevé test for differential equations providing a necessary criterion for an equation to have the Painlevé property. Within a given class of equations with a certain number of parameters or arbitrary functions it allows to single out those equations which are in some sense exactly solvable. A more refined criterion for the integrability of discrete systems is the degree growth of the iterates under the discrete mapping, measured by the algebraic entropy,

$$e_{\rm alg} = \lim_{n\to\infty} \frac{\log d_n}{n}, \tag{1}$$

where d_n, $n = 1, 2, \ldots$, denotes the degree of the nth iterate of a rational solution under the discrete mapping. For a generic (non-integrable) mapping ϕ with $\deg \phi = d$ one would assume

$\deg \phi^n \sim d^n$. When cancellations occur in the iterations the algebraic entropy will be less than $\log(d)$ but possibly greater 0, meaning that the degree growth is still exponential. When strong cancellations occur and the degrees only grow polynomially the algebraic entropy is zero which, in most cases, means that the dynamical system is integrable. Equations which have the singularity confinement property but which are not integrable as their the algebraic entropy is greater 0 were denoted *quasi-integrable* in [9]. There it was also noted that apart from second-order difference equations there are no known higher-order quasi-integrable difference equations or systems of order two or higher.

In this article we study the discrete version of a system of equations studied earlier by one of the authors in [10], given by a cubic Hamiltonian,

$$H = \frac{1}{3}\left(p^3 + q^3\right) + zpq + \alpha p + \beta q,$$

thus leading to a quadratic vector field given by

$$q' = \frac{\partial H}{\partial p} = p^2 + zq + \alpha, \quad p' = -\frac{\partial H}{\partial q} = -q^2 - zp - \beta. \tag{2}$$

This system is known to be related to the fourth Painlevé equation (P_{IV}), the combinations

$$w_j = \omega^j p + \bar{\omega}^j q - z, \quad j = 0, 1, 2, \quad \omega = \frac{-1 + i\sqrt{3}}{2},$$

satisfying the equation

$$2ww'' = w'^2 - w^4 - 4zw^3 - (2\alpha + 2\beta + 3z^2)w^2 - (1 - \alpha + \beta)^2,$$

which can be re-scaled to P_{IV}. In this way the solutions of (2) can be expressed by the transcendents of two copies of P_{IV}, with different sets of parameters. We remark that the Hamiltonian system retains the Painlevé property if z is replaced by a linear function $cz + d$, which can be achieved by a simple re-scaling of the independent variable.

The discretisation for the system (2) is performed using the Kahan method [8], which is also explained e.g. in [1], where it was applied to autonomous quadratic vector fields and also for instances of the Painlevé equations I, II and IV. Kahan's method was also applied to find integrable models for the discrete top [6, 7], and is thus also known as the Hirota-Kimura method. Incidentally, for quadratic vector fields this is also equivalent to the so-called Runge-Kutta method as was shown in [3]. We will apply the method to system (2), re-written as an autonomous system in three dependent variables. We will also rescale the variable z by introducing an additional parameter, c, into the equations. As we will see when discretising the system using Kahan's method, the resulting discrete system will in general be non-integrable. Only when c takes on a specific value do we at least obtain a *quasi-integrable* system.

2. Singularity confinement

We describe briefly the method of singularity confinement, which can be seen as a discrete analogue of the Painlevé test. Consider the second-order difference equation

$$x_{n+1} + x_{x-1} = x_n + \frac{a}{x_n^2}, \tag{3}$$

introduced by Hietarinta and Viallet [5]. When $x_n = 0$ we encounter a singularity, $x_{n+1} = \infty$ and $x_{n+2} = \infty$. The behaviour for x_{n+3} is indeterminate. To study the behaviour at the singularity an infinitesimally small parameter ϵ is introduced, letting $x_{n-1} = c$ (finite non-zero constant) and $x_n = \epsilon$. Letting $\epsilon \to 0$ this gives rise to a definite sequence of values, $\ldots, c, 0, \infty, \infty, c, c + a/c^2, \ldots$, the sequence returning to finite values meaning that the singularity is confined. However, the map (3) is known to be chaotic and singularity confinement is too insensitive to detect this. In particular, the system has non-zero algebraic entropy, which is a refined measure for integrability.

An example where singularity confinement successfully singles out integrable equations is provided by the class of difference equations

$$x_{n+1} + x_{n-1} = \frac{a_n x_n + b_n}{x_n^2}. \tag{4}$$

Here, the singularity confinement test leads to a sequence

$$\begin{aligned}
x_{n+1} &= \frac{b_n}{\epsilon^2} + \frac{a_n}{\epsilon} + O(1) \\
x_{n+2} &= -\epsilon + \frac{a_{n+1}}{b_n}\epsilon^2 + O(\epsilon^3) \\
x_{n+3} &= \frac{b_{n+2} - b_n}{\epsilon^2} - \frac{a_{n+2} - 2a_{n+1} + a_n}{\epsilon} + O(1),
\end{aligned}$$

showing that singularities will be confined if the conditions $a_{n+2} - 2a_{n+1} + a_n = 0$ and $b_{n+2} - b_n = 0$ are satisfied. Thus equation (4) becomes

$$x_{n+1} + x_{n-1} = \frac{(\alpha n + \beta)x_n + \gamma + (-1)^n \delta}{x_n^2},$$

where $\alpha, \beta, \gamma, \delta$ are constants. The iterates under this map have polynomial degree growth, i.e. the algebraic entropy is zero and the system is known to be integrable, being a discrete Painlevé equation with continuum limit to P_I.

3. Kahan discretisation

We are now going to study a discrete version of this system obtained by a method of Kahan, also known as the Hirota-Kimura method. Kahan first used this method in numerical calculations and found that the solutions of the discretised system are stable under small changes

of parameters. Independently, Hirota and Kimura applied the same method to discretise the equations of motion of a spinning top, namely for the integrable cases of the Euler top [6] and Lagrange top [7]. These are, of course, autonomous systems and they have shown that integrability is preserved under discretisation in these cases by finding a sufficient number of conserved quantities. In [1] the method was also applied to some non-autonomous Hamiltonian systems, namely those for the Painlevé equations I, II and IV. Here it was noticed that when discretising the system the integrability is only preserved in the case of the first Painlevé equation and in some special cases for the fourth Painlevé equation. The Kahan discretisation of systems of equations of the form

$$\mathbf{y}'(t) = f(\mathbf{y}), \quad \mathbf{y}(t_0) = \mathbf{y_0},$$

where f is a quadratic vector field, was shown to be equivalent to the Runge-Kutta method

$$\frac{\mathbf{y}-\tilde{\mathbf{y}}}{h} = \frac{1}{2}f(\mathbf{y}) - 2f\left(\frac{\mathbf{y}+\tilde{\mathbf{y}}}{2}\right) + \frac{1}{2}f(\tilde{\mathbf{y}}), \tag{5}$$

with step size h [3]. We introduce an additional parameter c into the system (2) and apply the method to the extended, autonomous system

$$\begin{aligned}
\dot{q} &= p^2 + czq + \alpha \\
\dot{p} &= -q^2 - czp - \beta \\
\dot{z} &= 1,
\end{aligned}$$

where $\dot{a} = \frac{da}{dt}$. Applying Kahan's method (5) to the above system yields

$$\begin{aligned}
\frac{x(n+1)-x(n)}{h} &= \alpha + \frac{1}{2}hc[(nx(n+1) + (n+1)x(n)] + y(n+1)y(n) \\
\frac{y(n+1)-y(n)}{h} &= -\beta - \frac{1}{2}hc[(ny(n+1) + (n+1)y(n)] - x(n+1)x(n),
\end{aligned} \tag{6}$$

where $x(n)$ and $y(n)$ correspond to $q(t)$, $p(t)$ and $z(t) = nh$. Solving the equations (6) for $x(n+1), y(n+1)$ yields the first order difference system

$$\begin{aligned}
x(n+1) =& \Big(-\left(h^2cn+2\right)\left(x(n)\left(h^2c(n+1)+2\right)+2\alpha h\right) + 2hy(n)^2\left(h^2c(n+1)-2\right) \\
&+ 4\beta h^2 y(n)\Big) \Big/ \Big(\left(h^2cn-2\right)\left(h^2cn+2\right) - 4h^2x(n)y(n)\Big) \\
y(n+1) =& \Big(-\left(h^2cn-2\right)\left(y(n)\left(h^2c(n+1)-2\right)+2\beta h\right) + 2hx(n)^2\left(h^2c(n+1)+2\right) \\
&+ 4\alpha h^2 x(n)\Big) \Big/ \Big(\left(h^2cn-2\right)\left(h^2cn+2\right) - 4h^2x(n)y(n)\Big).
\end{aligned} \tag{7}$$

We can interpret this system of difference equations as a rational map on complex projective space $\mathbb{CP}^2$ by letting $x(n) = u(n)/w(n)$, $y(n) = v(n)/w(n)$ and re-writing the dynamical system in the homogeneous variables $[u(n) : v(n) : w(n)]$,

$$\begin{aligned} u(n+1) =& -(cn+2)\left(u(n)w(n)\left(c(n+1)+2\right)+2\alpha w(n)^2\right)+2v(n)^2\left(c(n+1)-2\right) \\ &+4\beta v(n)w(n) \\ v(n+1) =& -(cn-2)\left(v(n)w(n)\left(c(n+1)-2\right)+2\beta w(n)^2\right)+2u(n)^2\left(c(n+1)+2\right) \\ &+4\alpha u(n)w(n) \\ w(n+1) =& (cn-2)(cn+2)\,w(n)^2-4u(n)v(n). \end{aligned} \tag{8}$$

The advantage of working in projective space is that singularities become just ordinary points which can be analysed accordingly.

4. Singularities of the discrete system

We are going to apply the singularity confinement test to the difference system (7) which, as we will see, fixes the parameter c. There are two major differences with this system compared to the examples above. Firstly, the denominator in the system (7) is n-dependent and so a singularity appearing in one step will *move on*. Secondly, there is a whole infinitude of singularities $(x(n), y(n))$ defined by the equation

$$\left(h^2cn-2\right)\left(h^2cn+2\right)-4h^2x(n)y(n)=0. \tag{9}$$

Starting with any pair $(x(n), y(n))$ satisfying equation (9) one obtains a singularity in the step, $(x(n+1), y(n+1)$. For the singularity confinement test we here choose the factorisation

$$x(n)=\frac{hcn}{2}-\frac{1}{h}+\epsilon, \quad y(n)=\frac{hcn}{2}+\frac{1}{h}+\epsilon,$$

where ε stands for an infinitesimally small quantity. In principle we should have put ε_1 and ε_2 here to express the fact that these small perturbations are independent, however, this makes no difference for the confinement test. In the next step we obtain the following singular behaviour,

$$\begin{aligned} x(n+1) &= \frac{\left(2+ch^2n\right)(\alpha-\beta-c)}{2h^2cn\epsilon}+O(1) \\ y(n+1) &= \frac{\left(2-ch^2n\right)(\alpha-\beta-c)}{2h^2cn\epsilon}+O(1) \end{aligned}$$

In the case $c \neq \alpha - \beta$, continuing this procedure we obtain

$$x(n+2)=\frac{hc(n+2)}{2}+\frac{1}{h}+\epsilon, \quad y(n+2)=\frac{hc(n+2)}{2}-\frac{1}{h}+\epsilon,$$

and in the next step the singularity prevails in the expressions for $x(n+3)$ and $y(n+3)$. However, in the case where $c = \alpha - \beta$, the singular behaviour in the expressions $x(n+1)$ and $y(n+1)$ is avoided. Strictly speaking in this case, there is no singularity confined, but rather the singularity doesn't arise in the first place! The situation becomes clearer if we perform the analysis in projective space. Starting from a point

$$[u(n) : v(n) : w(n)] = \left[\frac{cn}{2} - 1 + \epsilon : \frac{cn}{2} + 1 + \epsilon : 1\right], \tag{10}$$

leads to

$$\begin{aligned}\big[2(2+cn)(c-\alpha-\beta) + \left(c^2 n(n+1) + 2c(1-2n) + 4(\beta-3)\right)\epsilon + 2(c(n+1)-2)\epsilon^2 \ :\\ 2(2-cn)(c-\alpha-\beta) + \left(c^2 n(n+1) - 2c(1-2n) + 4(\alpha-3)\right)\epsilon + 2(c(n+1)-2)\epsilon^2 \ :\\ -4cn\epsilon - 4\epsilon^2\big].\end{aligned}$$

When we let the parameter $c = \alpha - \beta$ the $O(1)$ terms in the expansions vanish and, since we are in projective space, one can reduce the expressions by a common factor of ϵ, leaving us with

$$\begin{aligned}\big[(\alpha-\beta)^2 n(n+1) + 2(\alpha-\beta)(1-2n) + 4(\beta-3) + 2((\alpha-\beta)(n+1)-2)\epsilon \ :\\ (\alpha-\beta)^2 n(n+1) + 2(\alpha-\beta)(1-2n) + 4(\alpha-3) + 2((\alpha-\beta)(n+1)-2)\epsilon \ :\\ 4(\beta-\alpha)n - 4\epsilon\big].\end{aligned}$$

A consequence of this cancellation is a reduction in the degree growth of iterates under the rational map as explained in the next section. However, the cancellation are not strong enough to render the system integrable unless, of course, $\alpha = \beta$ which, however results in an autonomous system.

5. Algebraic entropy of the rational map

Algebraic entropy, defined in (1), is a measure for the degree growth of a family of rational functions obtained by iteration under the difference equation. In the generic case of the system (7), $c \neq \alpha - \beta$, starting from a rational functions of degree 1, we obtain the sequence of degrees $2, 4, 8, 16, 32, \ldots$, so the algebraic entropy is $\log(2)$. However in the case $c = \alpha - \beta$, where we observe singularity confinement, some cancellations in the rational expressions obtained by iterating the difference system take place, and the first numbers of the degree sequence obtained are

$$1, 2, 4, 8, 15, 28, 52, 96, 177, 326, 600, 1104, \ldots$$

Although the first few terms obey a 2^n rule, when cancellations take place the degrees of the subsequent iterates are lower. The sequence above is consistent with the recursive formula

$$d_n = 2d_{n-1} - d_{n-4},$$

if we define $d_n = 0$ for $n < 0$. This sequence still grows exponentially, $d_n \sim \lambda^n$, where $\lambda \approx 1.839\ldots$ is the largest root of the characteristic equation of the resursive formula. The algebraic entropy is $0 < e_{\mathrm{alg}} \approx 0.609\cdots < \log(2)$, meaning the system is quasi-integrable. Although Kahan's method did not preserve full integrability in this case, the example shows that integrability can be improved upon by introducing some parameters into the equations.

Acknowledgments

The results leading to this article were obtained during visits by TK to the Mathematical Institute of the Polish Academy of Science (IMPAN), Warsaw, hosted by GF. The visits were funded by the London Mathematical Society and IMPAN, for which we would like to acknowledge their generous support.

References

[1] E Celledoni, R I McLachlan, D I McLaren, B Owren and G R W Quispel, Integrability properties of Kahan's method, *J. Phys. A* 47 (2014), 365202 (20pp)

[2] E Celledoni, R I McLachlan, D I McLaren, B Owren and G R W Quispel, Geometric properties of Kahan's method, *J. Phys. A* 46 (2013), 025201 (12pp)

[3] E Celledoni, R I McLachlan, D I McLaren, B Owren, G R W Quispel and W Wright, Energy-preserving Runge-Kutta methods, *Math. Modelling Numer. Anal.* 43 (2009), 645–649

[4] R G Halburd and R J Korhonen, Finite-order meromorphic solutions and the discrete Painlevé equations, *Proc. London Math. Soc.* 94 (2007), 443–474

[5] J Hietarinta and C Viallet, Singularity confinement and chaos in discrete systems *Phys. Rev. Lett.* 82 (1998), 325–8

[6] R Hirota and K Kimura, Discretization of the Euler top, *J. Phys. Soc. Japan* 69 (2000), 627–630

[7] R Hirota and K Kimura, Discretization of the Lagrange top, *J. Phys. Soc. Japan* 69 (2000), 3193–3199

[8] W Kahan and R C Li, Unconventional schemes for a class of ordinary differential equations, *J. Comput. Phys.* 134 (1997), 316–331

[9] M Kanki, T Mase and T Tokihiro, Singularity confinement and chaos in two-dimensional descrete systems, *J. Phys. A* 49 (2016), 23LT01 (9pp)

[10] T Kecker, A cubic Hamiltonian system with meromorphic solutions, *Comput. Methods Funct. Theory* 16 (2016), 307 – 317

[11] A Ramani, B Grammaticos and J Hietarinta, Discrete versions of the Painlevé equations, *Phys. Rev. Lett.* 67 (1991), 1829 – 1832

Galina Filipuk, Dr hab.: Faculty of Mathematics, Informatics and Mechanics / University of Warsaw, Banacha 2, Warsaw, 02-097, Poland (*filipuk@mimuw.edu.pl*).

Thomas Kecker, Ph.D.: Department of Mathematics / University of Portsmouth, Lion Gate Building, Lion Terrace, Portsmouth, PO1 3HF, UK (*thomas.kecker@port.ac.uk*).

Computation of a Finsler-Lyapunov function using meshless collocation

Peter Giesl

Abstract: We study the stability of invariant sets such as equilibria or periodic orbits of a Dynamical System given by a general autonomous nonlinear ordinary differential equation (ODE). A classical tool to analyse the stability are Lyapunov functions, i.e. scalar-valued functions, which decrease along solutions of the ODE. An alternative to Lyapunov functions is contraction analysis. Here, stability is a consequence of the contraction property between two adjacent solutions (or incremental stability), formulated as the local property of a Finsler-Lyapunov function. This has the advantage that the invariant set plays no special role and does not need to be known a priori. In this talk, we numerically construct a Finsler-Lyapunov function by solving a first-order partial differential equation using meshless collocation. This method ensures that the partial differential equation holds at a set of given collocation points. If the equation is known to possess a smooth solution, error estimates are available. These error estimates provide bounds of the error between the true solution and the approximation in terms of the fill distance, measuring how dense the collocation points are. While meshless collocation has been used to compute classical Lyapunov functions, the computation of Finsler-Lyapunov functions is new and has the advantage that no information about equilibria or periodic orbits is required. In the talk we describe the method and present how it performs in examples.

1. Introduction

We study the stability of invariant sets such as equilibria or periodic orbits of a Dynamical System given by a general autonomous ordinary differential equation (ODE)

$$\dot{x} = f(x), x \in \mathbb{R}^n. \tag{1}$$

A classical tool to analyse the stability are Lyapunov functions. These are scalar-valued functions, which decrease along solutions of the ODE and measure in some way the distance of a point to the invariant set, thus being a global quantity. An alternative to Lyapunov functions is contraction analysis [7]. Here, stability is a consequence of the contraction property between two adjacent solutions, so formulated as a local property, e.g. of a Finsler-Lyapunov function [1]. This has the advantage that the invariant set plays no special role and does not need to be known a priori.

We search for a Finsler-Lyapunov function of the form[1] $V\colon \mathbb{R}^n \times \mathbb{R}^n \to \mathbb{R}_0^+$, defined on the tangential bundle of the manifold $\mathbb{R}^n$ for every $(x, v) \in \mathbb{R}^n \times \mathbb{R}^n$ which satisfies

$$LV(x,v) := \langle \nabla_x V(x,v), f(x)\rangle + (\nabla_v V(x,v))^T Df(x)v \leq 0, \tag{2}$$

where $\langle \cdot, \cdot \rangle$ denotes the Euclidean scalar product in $\mathbb{R}^n$, as well as the property $c_1\|v\|^p \leq V(x,v) \leq c_2\|v\|^p$ for a $p > 1$ and $0 < c_1 \leq c_2$. The inequality (2) describes the contraction between solutions through the point x and the point $x + v$.

For more details on Finsler-Lyapunov functions and the relation to contraction analysis see [1]. In particular, (2) implies that the system is incrementally stable, i.e. the evolution of the distance between any two solution is bounded for all positive times. If the inequality in (2) is replaced by sharper conditions, then the system can be shown to be incrementally asymptotically stable (distance converges to 0) or even incrementally exponentially stable (distance converges to zero exponentially fast).

While a Finsler-Lyapunov function satisfying (2) for all $v \in \mathbb{R}^n$ shows contraction in every direction v, we can modify the condition to capture only contraction in specific directions, e.g. to study problems with symmetry or to show the existence of periodic orbits as in this paper. To this end, a horizontal Finsler-Lyapunov function is defined in [1], where the tangent space at x is divided into a direct sum $\mathbb{R}^n = \mathcal{H}_x \bigoplus \mathcal{V}_x$ and (2) only is required for all $v \in \mathcal{H}_x$, i.e. the contraction is only guaranteed in horizontal direction.

Applied to periodic orbits, we choose $\mathcal{H}_x = \{v \in \mathbb{R}^n \mid v \perp f(x)\}$ and $\mathcal{V}_x = \operatorname{span}(f(x))$ for all x which are no equilibria, and assume that (2) holds for all $v \in \mathcal{H}_x$. If $V(x,v)$ is a quadratic form in v, then [6,8], see also [4, Section 2.10], have shown under some additional assumptions that this implies the existence, uniqueness and stability of a periodic orbit and gives information about its basin of attraction.

In this paper we numerically construct a Finsler-Lyapunov function by solving the PDE

$$\langle \nabla_x V(x,v), f(x)\rangle + (\nabla_v V(x,v))^T Df(x)v \quad = \quad -\|v\|^2 \tag{3}$$

using meshless collocation [10], which has been used to compute classical Lyapunov functions [2, 5]. One advantage of the proposed method is that the restrictions on the points v for which (3) is required, such as all v perpendicular to $f(x)$, can be easily implemented.

Let us give an overview of the contents: In Section 2 we introduce meshless collocation in general and then apply it to our specific problem. Section 3 presents the application of the method to three one- or two-dimensional with either an equilbrium or a periodic orbit. Section 4 discusses existence results and error estimates for the case of an equilibrium before we end with conclusions and an outlook in Section 5.

[1]Note that Finsler-Lyapunov functions as defined in [1] are more general than considered in our case.

2. Meshless collocation

In this section we introduce meshless collocation. We first introduce Reproducing Kernel Hilbert Spaces, and then formulate the generalised interpolation problem, which in our case is a linear PDE with fixed function values. We follow [5, Section 2], see also [10].

2.1. General method

We start with a short introduction to the general method of solving a generalized interpolation problem in a Reproducing Kernel Hilbert space of functions with domain in $\mathbb{R}^{2n}$, which is motivated by our application.

Let $O \subset \mathbb{R}^{2n}$ be a bounded set with Lipschitz continuous boundary. A Reproducing Kernel Hilbert Space (RKHS) is a Hilbert space H of functions $g\colon O \to \mathbb{R}$ with inner product $\langle \cdot, \cdot \rangle_H$ such that the following properties hold with a kernel $\Phi\colon O \times O \to \mathbb{R}$:

1. $\Phi(\cdot, \tilde{x}) \in H$ for all $\tilde{x} \in O$,
2. $g(\tilde{x}) = \langle g, \Phi(\cdot, \tilde{x}) \rangle_H$ for all $\tilde{x} \in O$ and $g \in H$.

We want to solve the following generalized interpolation problem:

Given $\tilde{N}$ linearly independent functionals $\lambda_1, \ldots, \lambda_{\tilde{N}} \in H^*$, where H^* denotes the dual of H, and $\tilde{N}$ numbers $\tilde{r}_i \in \mathbb{R}$, $i = 1, \ldots, \tilde{N}$, find the norm-minimal interpolant $s \in H$ satisfying

1. *$\lambda_i(s) = \tilde{r}_i$ for all $i = 1, \ldots, \tilde{N}$ (interpolant),*
2. *$\|s\|_H = \min\{\|\tilde{s}\|_H \mid \tilde{s} \in H, \lambda_i(\tilde{s}) = \tilde{r}_i$ for all $i = 1, \ldots, \tilde{N}\}$ (norm-minimal).*

It is well known that there is a unique norm-minimal interpolant, which is a linear combination of the Riesz representers of the functionals, and the coefficients can be determined by solving a system of $\tilde{N}$ linear equations. If H is a RKHS, then we have the following formula for the norm-minimal interpolant s:

$$s(\tilde{x}) \quad = \quad \sum_{j=1}^{\tilde{N}} \tilde{\alpha}_j \lambda_j^{\tilde{y}} \Phi(\tilde{x}, \tilde{y}), \tag{4}$$

where the superscript $\tilde{y}$ in $\lambda_j^{\tilde{y}}$ denotes the application of the functional with respect to $\tilde{y}$. Note that $\tilde{\alpha} \in \mathbb{R}^{\tilde{N}}$ is the solution of the linear system

$$\tilde{A}\tilde{\alpha} \quad = \quad \tilde{r}, \tag{5}$$

where $\tilde{r} = (\tilde{r}_i)_{i=1,\ldots,\tilde{N}} \in \mathbb{R}^{\tilde{N}}$ and $A = (a_{ij})_{i,j=1,\ldots,\tilde{N}} \in \mathbb{R}^{\tilde{N} \times \tilde{N}}$ is given by

$$\tilde{a}_{ij} \quad = \quad \lambda_i^{\tilde{x}} \lambda_j^{\tilde{y}} \Phi(\tilde{x}, \tilde{y}). \tag{6}$$

The matrix $\tilde{A}$ is positive definite, since the functionals are assumed to be linearly independent. In the following we consider the Sobolev space $W_2^\tau(\mathbb{R}^{2n})$ with $\tau > n$, which is a RKHS. While the reproducing kernel is rather complicated, there is a reproducing kernel, defined by a Wendland function, see Definition 2.1, which generates the same Hilbert space, but with a different, yet equivalent norm.

Definition 2.1 (see [9]) *Let $k \in \mathbb{N}_0$ and $l \in \mathbb{N}$. We define $x_+ = x$ for $x \geq 0$ and $x_+ = 0$ for $x < 0$. We define by recursion the Wendland function for $r \in \mathbb{R}_0^+$*

$$\phi_{l,0}(r) = (1-r)_+^l, \qquad \phi_{l,k+1}(r) = \int_r^1 t\phi_{l,k}(t)\,dt.$$

The following proposition follows from [5, Proposition 3.11] and the arguments in the proof; note that the space dimension in our case is $2n$.

Proposition 2.2 *Let $k \in \mathbb{N}$, $c \in \mathbb{R}^+$ and set $l = n + k + 1$. Define $\psi_0(r) = \phi_{l,k}(cr)$, where $\phi_{l,k}$ was defined in Definition 2.1, and $\Phi(\tilde{x}, \tilde{y}) = \psi_0(\|\tilde{x} - \tilde{y}\|)$, where $\|\cdot\|$ denotes the Euclidean norm in $\mathbb{R}^{2n}$. Then $\Phi \in C^{2k}$ is a reproducing kernel of $W_2^\tau(\mathbb{R}^{2n})$ with $\tau = k + n + \frac{1}{2}$ (and equivalent norm).*

From now on, we choose a Wendland function with smoothness degree $k \geq 2$ and choose Φ to be the kernel of the RKHS $H = W_2^\tau(\mathbb{R}^{2n})$ as above, with $\tau = k + n + \frac{1}{2}$.

Now let us apply the method to solve the problem

$$LV(\tilde{x}) = r(\tilde{x}) \text{ for } \tilde{x} \in O, \tag{7}$$

$$V(\tilde{x}) = r_0(\tilde{x}) \text{ for } \tilde{x} \in \Gamma, \tag{8}$$

where L is a first-order differential operator of the form

$$LV(\tilde{x}) = \sum_{|\beta| \leq 1} c_\beta(\tilde{x}) D^\beta V(\tilde{x}), \tag{9}$$

$c_\beta \colon O \to \mathbb{R}$, $r(\tilde{x})$ and $r_0(\tilde{x})$ are given functions and $O, \Gamma \subset \mathbb{R}^{2n}$. We call a point $\tilde{x} \in \mathbb{R}^{2n}$ a singular point of L if $c_\beta(\tilde{x}) = 0$ for all $|\beta| \leq 1$.

We choose collocation points $X_1 = \{\tilde{x}_1, \ldots, \tilde{x}_N\} \subset O$ and $X_2 = \{\tilde{\xi}_1, \ldots, \tilde{\xi}_M\} \subset \Gamma$ and define the functionals $\lambda_j = \delta_{\tilde{x}_j} \circ L$, $j = 1, \ldots, N$ and $\lambda_{N+j} = \delta_{\tilde{\xi}_j} \circ \mathrm{id}$, $j = 1, \ldots, M$ to find the norm-minimal interpolant.

These $\tilde{N} = N + M$ functionals are linearly independent if the collocation points x_j are no singular points of L, see [5, Proposition 3.3]; note that $\tau > 1 + n$.

We then have error estimates in terms of the mesh-norms $h_{X_1,O} = \sup_{\tilde{x} \in O} \min_{\tilde{x}_j \in X_1} \|\tilde{x} - \tilde{x}_j\|$ and $h_{X_2,\Gamma} = \sup_{\tilde{y} \in \Gamma} \min_{\tilde{\xi}_j \in X_2} \|\tilde{y} - \tilde{\xi}_j\|$, which measure how dense the collocation points X_1 lie in O or X_2 in Γ, respectively. Note that the error estimates in [5, Corollary 3.12] hold in the same way if Γ is not part of the boundary of O, but a smooth subset of O.

Theorem 2.3 *Let Γ be a smooth subset of O. Let $c_\beta \in W_\infty^{k+n}(O)$ and let the solution V of (7) and (8) satisfy $V \in W_2^{k+n+1/2}(O)$. Let $X_1 = \{\tilde{x}_1, \ldots, \tilde{x}_N\} \subset O$ be pairwise distinct points, which are not singular points of L, and $X_2 = \{\tilde{\xi}_1, \ldots, \tilde{\xi}_M\} \subset \Gamma$ be pairwise distinct points. We denote by s the norm-minimal interpolant of the data.*

Then, for sufficiently small mesh-norms, we have

$$\begin{aligned} \|LV - Ls\|_{L_\infty(O)} &\leq Ch_{X_1,O}^{k-1/2} \|V\|_{W_2^{k+n+1/2}(O)}, & (10) \\ \|V - s\|_{L_\infty(\Gamma)} &\leq Ch_{X_2,\Gamma}^{k+1/2} \|V\|_{W_2^{k+n+1/2}(O)}, & (11) \end{aligned}$$

where C is a constant independent of V.

2.2. Application to our specific problem

We denote $\tilde{x} = (x, v) \in \mathbb{R}^{2n}$. We define the differential operator L acting on a function $V(x, v)$, where $x, v \in \mathbb{R}^n$ by

$$LV(x,v) = \langle \nabla_x V(x,v), f(x) \rangle + (\nabla_v V(x,v))^T Df(x)v. \quad (12)$$

We wish to solve the problem

$$\begin{cases} LV(x,v) = -\|v\|^2, \\ V(x,0) = 0. \end{cases} \quad (13)$$

Note that the first equation in (13) is (3). The second equation in (13) fixes the values of $V(x, 0) = 0$ at $v = 0$, since otherwise the function V will in general not satisfy the requirement $c_1\|v\|^p \leq V(x, v)$.

Lemma 2.4 *$(x, v) \in \mathbb{R}^{2n}$ is a singular point of L as defined in (12) if and only if $f(x) = 0$ (x is equilibrium) and $Df(x)v = 0$.*

We fix a bounded set $K \subset \mathbb{R}^n$ with Lipschitz continuous boundary and define $B_r(0) := \{v \in \mathbb{R}^n \mid \|v\| \leq r\}$ with $r > 0$ small. We choose points $\tilde{x}_j \in K \times B_r(0)$ for $j = 1, \ldots, N$, which are no singular points of L, see Lemma 2.4, and denote this set of points by $X_1 := \{\tilde{x}_1, \tilde{x}_2, \ldots, \tilde{x}_N\}$. Moreover, we choose points for which we fix the values of $V(x, 0)$, namely $\tilde{\xi}_j = (\xi_j, 0) \in K \times \{0\} =: \Gamma$ for $j = 1, \ldots, M$; we denote this set of points by $X_2 := \{\tilde{\xi}_1, \ldots, \tilde{\xi}_M\}$.

The ansatz for the approximant v of the function V is given by (4), namely

$$s(\tilde{x}) = \sum_{k=1}^{N} \alpha_k (\delta_{\tilde{x}_k} \circ L)^{\tilde{y}} \psi_0(\|\tilde{x} - \tilde{y}\|) + \sum_{k=1}^{M} \beta_k \psi_0(\|\tilde{x} - \tilde{\xi}_k\|). \quad (14)$$

where ψ_0 was defined in Proposition 2.2. The coefficient vector is the solution of the following system of linear equations, see (5),

$$\widetilde{A}\begin{pmatrix}\alpha\\ \beta\end{pmatrix}=\begin{pmatrix}a\\ b\end{pmatrix}\text{ with }\widetilde{A}:=\begin{pmatrix}A & D\\ D^T & B\end{pmatrix}\in\mathbb{R}^{(N+M)\times(N+M)}. \tag{15}$$

The right-hand side of the linear system (15) is determined by $a_j=-\|v_j\|^2$ for $1\le j\le N$ and $b_j=0$ for $1\le j\le M$. The sub-matrices $A=(a_{jk})\in\mathbb{R}^{N\times N}$, $B=(b_{jk})\in\mathbb{R}^{M\times M}$ and $D=(d_{jk})\in\mathbb{R}^{N\times M}$ have the elements, see (6),

$$\begin{aligned}a_{jk} &= (\delta_{\tilde{x}_j}\circ L)^{\tilde{x}}(\delta_{\tilde{x}_k}\circ L)^{\tilde{y}}\psi_0(\|\tilde{x}-\tilde{y}\|),\\ b_{jk} &= \psi_0(\|\tilde{\xi}_j-\tilde{\xi}_k\|),\\ d_{jk} &= (\delta_{\tilde{x}_j}\circ L)^{\tilde{x}}\psi_0(\|\tilde{x}-\tilde{\xi}_k\|).\end{aligned}$$

To compute d_{jk} and a_{jk} explicitly, let us define recursively $\psi_{k+1}(r)=\frac{1}{r}\frac{\partial\psi_k(r)}{\partial r}$ for $k=0,1$ and $r>0$. Note that under our assumptions, these functions can be continued continuously up to $r=0$.

We have, denoting $\tilde{x}=(x,v)$, $\tilde{y}=(y,w)$, $\tilde{x}_k=(x_k,v_k)$ and $\tilde{\xi}_j=(\xi_j,\eta_j)$

$$d_{jk} = -\psi_1(\|\tilde{x}_j-\tilde{\xi}_k\|)\left[\langle\xi_k-x_j,f(x_j)\rangle+(\eta_k-v_j)^TDf(x_j)v_j\right].$$

Using the notation $x_{jk}=x_j-x_k$ and $v_{jk}=v_j-v_k$ we have

$$\begin{aligned}a_{jk} &= -\psi_2(\|\tilde{x}_j-\tilde{x}_k\|)\big[\langle x_{jk},f(x_j)\rangle\langle x_{jk},f(x_k)\rangle+\langle x_{jk},f(x_j)\rangle v_{jk}^TDf(x_k)v_k\\ &\qquad +\langle x_{jk},f(x_k)\rangle v_{jk}^TDf(x_j)v_j+v_{jk}^TDf(x_j)v_j\cdot v_{jk}^TDf(x_k)v_k\big]\\ &\quad -\psi_1(\|\tilde{x}_j-\tilde{x}_k\|)\left[\langle f(x_k),f(x_j)\rangle+v_j^TDf(x_j)^TDf(x_k)v_k\right].\end{aligned}$$

We have, similarly to the computation of a_{jk} the following formula, using the notation $x_{\cdot k}=x-x_k$ and $v_{\cdot k}=v-v_k$,

$$\begin{aligned}Ls(x,v) &= \sum_{k=1}^N\alpha_k(\delta_{\tilde{x}}\circ L)^{\tilde{x}}(\delta_{\tilde{x}_l}\circ L)^{\tilde{y}}\psi_0(\|\tilde{x}-\tilde{y}\|)+\sum_{k=1}^M\beta_k(\delta_{\tilde{x}}\circ L)^{\tilde{x}}\psi_0(\|\tilde{x}-\tilde{\xi}_k\|)\\ &= -\sum_{k=1}^N\alpha_k\Big\{\psi_2(\|\tilde{x}-\tilde{x}_k\|)\big[\langle x_{\cdot k},f(x)\rangle\langle x_{\cdot k},f(x_k)\rangle+\langle x_{\cdot k},f(x)\rangle v_{\cdot k}^TDf(x_k)v_k\\ &\qquad +\langle x_{\cdot k},f(x_k)\rangle v_{\cdot k}^TDf(x)v+v_{\cdot k}^TDf(x)v\cdot v_{\cdot k}^TDf(x_k)v_k\big]\\ &\qquad +\psi_1(\|\tilde{x}-\tilde{x}_k\|)\left[\langle f(x_k),f(x)\rangle+v^TDf(x)^TDf(x_k)v_k\right]\Big\}\\ &\quad -\sum_{k=1}^M\beta_k\psi_1(\|\tilde{x}-\tilde{\xi}_k\|)\left[\langle\xi_k-x,f(x)\rangle+(\eta_k-v)^TDf(x)v\right].\end{aligned}$$

3. Examples

3.1. One-dimensional example

We consider $n = 1$ and the dynamical system given by

$$\dot{x} \quad = \quad x - x^3 \tag{16}$$

which has one asymptotically stable equilibrium at 0 and two unstable equilibria at ± 1. We use the Wendland function $\psi_0(r) = \phi_{4,2}(r) = (1-r)_+^6(35r^2+18r+3)$ and the collocation grids $X_1 = \{(x, v) \mid x \in [-0.7, \ldots, -\rho, 0, \rho, \ldots, 0.7], v \in [-0.1, \ldots, -\tau, 0, \tau, \ldots, 0.1]\}$ and $X_2 = \{(x, 0) \mid x \in [-0.7, \ldots, -\rho, 0, \rho, \ldots, 0.7]\}$ with $\rho = 0.7/19 = 0.0368$ and $\tau = 0.1/3 = 0.0333$. The grids have $N = 272$ and $M = 39$ points, respectively, so together $\tilde{N} = N + M = 311$.

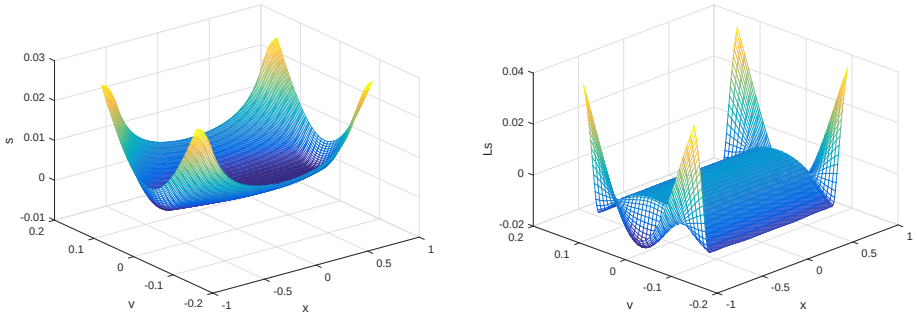

Figure 1. Example (16). Left: The function $s(x, v)$. Right: The function $Ls(x, v)$ which approximates $-\|v\|^2$ well.

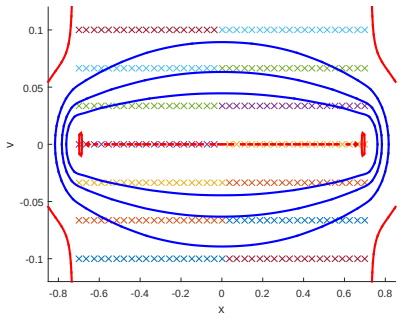

Figure 2. Example (16): The collocation points as well as the level set $Ls(x, v) = 0$ (red) and $s(x, v) = 0, 0.005, 0.01$ (blue). Note that $Ls(x, v) < 0$ holds in the area where the collocation points are placed, apart from a small area near $v = 0$.

Figure 1 (left) shows the computed function $s(x,v)$ which satisfies $c_1\|v\|^2 \leq s(x,v) \leq c_2\|v\|^2$ as well as $Ls(x,v)$ which approximates $-\|v\|^2$ well. Figure 2 shows the collocation points, the area where $Ls(x,v) = 0$ (red) as well as some level sets of $s(x,v)$ (blue) in the area where $s(x,v)$ satisfies the conditions.

3.2. Two-dimensional example – stable equilibrium

We consider $n = 2$ and the dynamical system given by

$$\begin{cases} \dot{x} &= -x(1-x^2-y^2)+y \\ \dot{y} &= -y(1-x^2-y^2)-x \end{cases} \tag{17}$$

which has one asymptotically stable equilibrium at the origin and an unstable periodic orbit at the unit sphere. We denote $\mathbf{x} = (x,y) \in \mathbb{R}^2$ and $\mathbf{v} = (v,w) \in \mathbb{R}^2$.

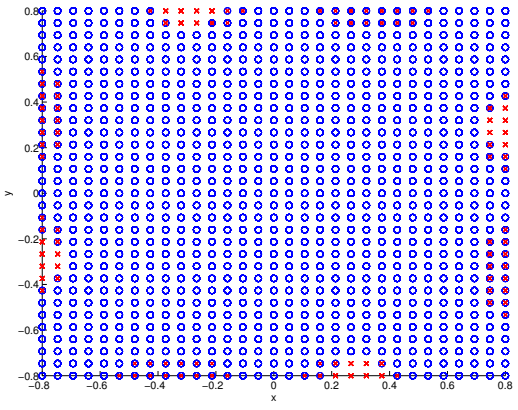

Figure 3. Example (17): Some points in the $\mathbf{x} = (x,y)$-plane, where the sign of $L(\mathbf{x},\mathbf{v})$ is calculated: if the sign of $L(\mathbf{x},\mathbf{v})$ is negative for a $\mathbf{v}$, then a blue circle is plotted, if the sign is non-positive for a $\mathbf{v}$, then a red cross is plotted. The points with the correct, negative sign are thus points with a blue circle only.

We use the Wendland function $\psi_{5,2}(r) = (1-r)_+^7(16r^2+7r+1)$ and the collocation grids defined below containing $N = 8580$ and $M = 441$ points, respectively; altogether we have $\tilde{N} = N + M = 9021$ points.

$$\begin{aligned} X_1 &= \big\{(\mathbf{x},\mathbf{v}) \in B_{0.9}(0,0) \times \mathbb{R}^2 \mid x,y \in \{-0.7,\ldots,-0.07,0,0.07,\ldots,0.7\}, \\ &\qquad \mathbf{v} \in \{r(\cos(a),\sin(a)), r \in \{0.05,0.1\}, a = 2k\pi/10, k = 1,\ldots,10\}\big\}, \text{ and} \\ X_2 &= \{(\mathbf{x},0) \in \mathbb{R}^2 \times \mathbb{R}^2 \mid x,y \in \{-0.7,\ldots,-0.07,0,0.07,\ldots,0.7\}\}, \end{aligned}$$

Figure 3 shows points $\mathbf{x}$ where $L(\mathbf{x}, \mathbf{v})$ was evaluated for many $\mathbf{v} \neq 0$. For each $\mathbf{v}$ where $L(\mathbf{x}, \mathbf{v}) < 0$, a blue circle was plotted at the position $\mathbf{x}$, while for each $\mathbf{v}$ where $L(\mathbf{x}, \mathbf{v}) \geq 0$ a red cross was drawn at position $\mathbf{x}$. Points $\mathbf{x}$ can thus have both a blue circle and a red cross, meaning that some directions $\mathbf{v}$ have the correct (negative) sign, while others have not. Points with only a blue circle are points where L has the correct sign, while points with any red cross are not. One can clearly see that the square $[-0.7, 0.7]^2$, where the collocation points where placed, contains only blue circles.

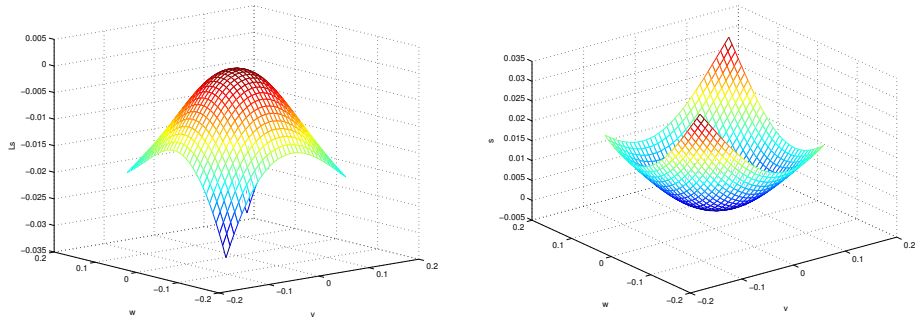

Figure 4. Example (17). Left: The function $Ls((0.5, 0.5), (v, w))$ which approximates $-\|(v, w)\|^2$ well. Right: The function $s((0.5, 0.5), (v, w))$ which has its minimum 0 at $(v, w) = (0, 0)$. Note that the point $\mathbf{x} = (0.5, 0.5)$ does not belong to the collocation grids.

Figure 4 shows the functions $s(\mathbf{x}, \mathbf{v})$ and $Ls(\mathbf{x}, \mathbf{v})$ for a fixed $\mathbf{x}_0 = (0.5, 0.5)$; note that there is no collocation point with this value. The function $Ls(\mathbf{x}_0, \mathbf{v})$ approximates $-\|\mathbf{v}\|^2$ well (left) and the function $s((0.5, 0.5), \mathbf{v})$ (right) satisfies $c_1\|\mathbf{v}\|^2 \leq s(\mathbf{x}_0, \mathbf{v}) \leq c_2\|\mathbf{v}\|^2$.

3.3. Two-dimensional example – stable periodic orbit

We consider the dynamical system given by

$$\begin{cases} \dot{x} &= x(1 - x^2 - y^2) + y \\ \dot{y} &= y(1 - x^2 - y^2) - x \end{cases} \tag{18}$$

which has one unstable equilibrium at the origin and an asymptotically stable periodic orbit at the unit sphere. This time we solve the problem

$$\begin{cases} LV(x, v) &= -\|v\|^2 \text{ for } v \perp f(x) \\ V(x, 0) &= 0. \end{cases} \tag{19}$$

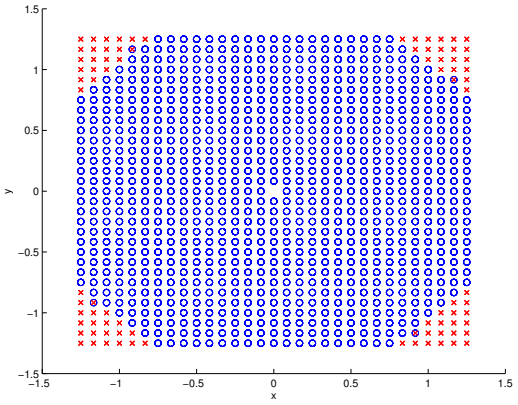

Figure 5. Example (18): Some points in the $\mathbf{x} = (x, y)$-plane, where the sign of $L(\mathbf{x}, \mathbf{v})$ is calculated: if the sign of $L(\mathbf{x}, \mathbf{v})$ is negative for all directions $\mathbf{v} \perp f(\mathbf{x})$, then a blue circle is plotted, if the sign is non-positive for all directions $\mathbf{v} \perp f(\mathbf{x})$, then a red cross is plotted, and if some directions $\mathbf{v}$ result in a negative and some in a non-negative sign, then both a red cross and a blue circle are plotted. The points with the correct, negative sign are thus points with a blue circle.

We use the Wendland function $\psi_{5,2}(r) = (1-r)_+^7(16r^2 + 7r + 1)$ and the points

$$\begin{aligned} X_1 &= \big\{(\mathbf{x}, \mathbf{v}) \in B_{1.2}(0,0) \setminus \{(0,0)\} \times \mathbb{R}^2 \mid x, y \in \{-1.2, \ldots, -\rho, 0, \rho, \ldots, 1.2\}, \\ &\qquad \mathbf{v} \in \{\pm 0.05\, f(\mathbf{x})/\|f(\mathbf{x})\|, \pm 0.1\, f(\mathbf{x})/\|f(\mathbf{x})\|\}\big\} \\ X_2 &= \{(\mathbf{x}, 0) \in B_{1.2}(0,0) \times \mathbb{R}^2 \mid x, y \in \{-1.2, \ldots, -\rho, 0, \rho, \ldots, 1.2\}\}, \end{aligned}$$

where $\rho = 1.2/9 = 0.1333$, with $N = 1168$ and $M = 293$ points, respectively, altogether $\tilde{N} = N + M = 1461$ points.

Figure 5 shows points $\mathbf{x}$ where $L(\mathbf{x}, \mathbf{v})$ was evaluated for several $\mathbf{v} \perp f(\mathbf{x})$. For each $\mathbf{v}$ where $L(\mathbf{x}, \mathbf{v}) < 0$, a blue circle was added, while for each $\mathbf{v}$ where $L(\mathbf{x}, \mathbf{v}) \geq 0$ a red cross was drawn. Points with only a blue circle are points where L has the correct (negative) sign, while points with any red cross are not. One can clearly see that the ball of radius 1.2, where the collocation points where placed, contains only blue circles.

4. Existence and error estimates

In certain dynamical situations we can prove the existence of a function satisfying (13), enabling us to obtain error estimates.

Proposition 4.1 *Assume that x_0 is an exponentially stable equilibrium of* (1)*, where $f \in C^\sigma(\mathbb{R}^n, \mathbb{R}^n)$, $\sigma \geq 2$, with basin of attraction $A(x_0)$.*

Then there is a function $V \in C^{\sigma-1}(A(x_0), \mathbb{R}^n)$ satisfying (13) *for all $(x, v) \in A(x_0) \times \mathbb{R}^n$.*

PROOF: Choose the positive definite matrix $C = I \in \mathbb{S}^n$, where $\mathbb{S}^n$ denotes the symmetric matrices in $\mathbb{R}^{n\times n}$. By [3, Theorem 4.4] there exists a matrix-valued function $M \in C^{\sigma-1}(A(x_0), \mathbb{S}^n)$ satisfying

$$Df(x)^T M(x) + M(x)Df(x) + M'(x) = -I \text{ for all } x \in A(x_0). \tag{20}$$

Here, $M'(x)$ denotes the matrix with entries $\langle \nabla_x M_{ij}(x), f(x)\rangle$, $i, j = 1, \ldots, n$, the orbital derivative of $M(x)$. Defining the $C^{\sigma-1}(A(x_0), \mathbb{R}^n)$ function $V(x, v) = v^T M(x)v$ we have $V(x, 0) = 0$ for all $x \in A(x_0)$ and

$$\begin{aligned} LV(x, v) &= \langle \nabla_x V(x, v), f(x)\rangle + (\nabla_v V(x, v))^T Df(x)v \\ &= v^T M'(x)v + v^T M(x)Df(x)v + v^T Df(x)^T M(x)v \\ &= -\|v\|^2 \text{ by (20)} \end{aligned}$$

for all $x \in A(x_0)$ and $v \in \mathbb{R}^n$. □

In the situation as above, where we know that a solution V with a certain smoothness exists, we can use the error estimate Theorem 2.3.

Proposition 4.2 *Let $k \geq 2$ be the smoothness degree of the Wendland function. In the situation of Proposition 4.1 let $f \in C^\sigma(\mathbb{R}^n, \mathbb{R}^n)$ with $\sigma \geq k + n + 1$, $K \subset \overline{K} \subset A(x_0)$ be an open bounded set with Lipschitz boundary and $\Gamma = \{(x, 0) \mid x \in K\}$. Then, for the collocation points as described in Theorem 2.3 the estimates* (10) *and* (11) *hold.*

PROOF: Let $O = K \times B_R(0)$ with $R > 0$. We check that the assumptions of Theorem 2.3 are satisfied: we have $c_\beta \in C^{\sigma-1}(\mathbb{R}^n) \subset W_\infty^{k+n}(O)$ and by Proposition 4.1 we have for the solution $V \in C^{\sigma-1}(A(x_0), \mathbb{R}^n) \subset W_2^{k+n+1/2}(O)$. □

5. Conclusion and outlook

We have presented a method to numerically construct Finsler-Lyapunov functions, which show incremental stability of solutions of an ODE $\dot{x} = f(x)$, $x \in \mathbb{R}^n$. A Finsler-Lyapunov function is a scalar-valued function with domain $(x, v) \in \mathbb{R}^n \times \mathbb{R}^n$, where x denotes a point in the phase space and v a point in the tangent space at x. We have used meshless collocation with a Wendland function, and have solved a first-order PDE with prescribed values at $v = 0$.

Finsler-Lyapunov functions can be used to show existence, uniqueness and stability for different kinds of attractors, such as equilibria or periodic orbits, and give information about their basin of attraction. Depending on the set of v for which the contraction condition holds, we can distinguish between different types of attractors. This can be implemented easily in the proposed method by choosing collocation points in the respective set. Further work will explore this feature further, studying symmetric systems and higher dimensional-ones. We have shown existence results and error estimates in the case of equilibria and seek to extend these results to other attractors such as periodic orbits in the future.

References

[1] Forni, F., and Sepulchre, R. A differential Lyapunov framework for contraction analysis. *IEEE Trans. Autom. Control 59*, 3 (2014), 614–628.

[2] Giesl, P. *Construction of Global Lyapunov Functions Using Radial Basis Functions*. Lecture Notes in Math. 1904, Springer, 2007.

[3] Giesl, P. Converse theorems on contraction metrics for an equilibrium. *J. Math. Anal. Appl. 424*, 2 (2015), 1380–1403.

[4] Giesl, P., and Hafstein, S. Review on computational methods for Lyapunov functions. *Discrete Contin. Dyn. Syst. Ser. B 20*, 8 (2015), 2291–2331.

[5] Giesl, P., and Wendland, H. Meshless collocation: Error estimates with application to dynamical systems. *SIAM J. Numer. Anal. 45* (2007), 1723–1741.

[6] Hartman, P., and Olech, C. On global asymptotic stability of solutions of differential equations. *Trans. Amer. Math. Soc. 104* (1962), 154–178.

[7] Lohmiller, W., and Slotine, J. E. On contraction analysis for non-linear systems. *Automatica 34*, 6 (1998), 683–696.

[8] Stenström, B. Dynamical systems with a certain local contraction property. *Math. Scand. 11* (1962), 151–155.

[9] Wendland, H. Piecewise polynomial, positive definite and compactly supported radial functions of minimal degree. *Adv. Comput. Math. 4*, 4 (1995), 389–396.

[10] Wendland, H. *Scattered Data Approximation*, vol. 17 of *Cambridge Monographs on Applied and Computational Mathematics*. Cambridge University Press, Cambridge, 2005.

Peter Giesl, Ph.D.: University of Sussex, Department of Mathematics, Falmer, BN1 9QH, United Kingdom (*p.a.giesl@sussex.ac.uk*). The author gave a presentation of this paper during one of the conference sessions.

Chaos and strange attractors in environmental radioactivity dynamics of some geosystems: Atmospheric radon ^{222}Rn

Alexander V. Glushkov, Yuliya V. Dubrovskaya, Vasily V. Buyadzhi and Eugeny V. Ternovsky

Abstract: The work is devoted to the development of the theoretical foundations and further application of an effective universal complex chaos-dynamical approach to description of the deterministic chaos, bifurcations and strange attractors in dynamics of the environmental radioactivity systems. In particular, the atmospheric radon ^{222}Rn concentration temporal dynamics is studied and computed. The analysis methods include advanced versions of the correlation integral, fractal analysis, algorithms of average mutual information, false nearest neighbors, Lyapunov exponents, surrogate data, non-linear prediction schemes, predicted trajectories algorithms, spectral methods etc. to solve problems quantitatively complete modeling and analysis of temporal evolution of the atmospheric radon ^{222}Rn concentration. There are firstly received data on topological and dynamical invariants for the time series of the ^{222}Rn concentration, discovered a deterministic chaos phenomenon using detailed data of measurements of the radon concentrations at SMEAR II station of the Finnish Meteorological Institute in the Southern Finland (2000-2006).

1. Introduction

The importance of studying a phenomenon of stochasticity or chaos in dynamical systems is provided by a whole number of applications, including a necessity of understanding chaotic features in different geophysical (hydrometeorological, environmental etc) systems. New field of investigations of these systems has been provided by a great progress in a development of a chaos and dynamical systems theory methods [1-28]. In our previous papers [21-38] we have given a review of new methods and algorithms to analysis of different systems of environmental and Earth sciences, quantum physics, electronics and photonics and used the nonlinear method of chaos theory and the recurrence spectra formalism to study stochastic futures and chaotic elements in dynamics of hydrometeorological, environmental and physical (namely, atomic, molecular, nuclear systems in an free state and an external electromagnetic field) systems. The non-trivial manifestations of a chaos phenomenon have been discovered. The studies concerning non-linear behaviour in the time series of atmospheric constituent concentrations are sparse, and their outcomes are ambiguous. In ref. [12,21] there is an analysis of the NO_2, CO, O_3

concentrations time series and there is no evidence of chaos received. Also, it was shown that O_3 concentrations in Cincinnati (Ohio) and Istanbul are evidently chaotic, and non-linear approach provides satisfactory results. In Ref. [21,22,25,29] the detailed analysis of the NO_2, CO, CO_2 concentration time series has been fulfilled in the Odessa and industrial regions of the Ukraine and Poland) and the evidence of a chaos has been definitely obtained. Moreover, a short-range forecast of atmospheric pollutants time evolution using non-linear prediction method has been given. These studies show that chaos theory methodology can be applied and the short-range forecast by the non-linear prediction method can be satisfactory. Time series of concentrations are however not always chaotic, and chaotic behaviour must be examined for each time series.

The work is devoted to the development of the theoretical foundations and further application of an effective universal complex chaos-dynamical approach to the atmospheric radon ^{222}Rn concentration changing analysis and prediction from beta particles activity data on radon monitors. The approach presented consistently includes a number of new or improved methods of analysis (correlation integral, fractal analysis, algorithms, average mutual information, false nearest neighbors, Lyapunov exponents, surrogate data, non-linear prediction, spectral methods, etc.) to solve problems of quantitatively complete modeling and analysis of temporal evolution of the atmospheric radon ^{222}Rn concentration. Topological and dynamical invariants data for the time series of the ^{222}Rn concentration has been received. By means (or Using) of detailed data of radon concentrations measurements at SMEAR II station of the Finnish Meteorological Institute during 2003 a deterministic chaos phenomenon has been revealed that is agreed with the preliminary data [9].

2. Universal chaos-dynamical approach in analysis of dynamics of the complex geosystems

As many blocks of the used approach have been developed earlier and need only to be reformulated regarding the problem studied in this paper, here we are limited only by the key moments following to Refs. [1, 11-33]. Let us formally consider scalar measurements $s(n) = s(t_0 + n\Delta t) = s(n)$, where t_0 is the start time, Δt is the time step, and is n the number of the measurements. Further it is necessary to reconstruct phase space using as well as possible information contained in the $s(n)$. Such a reconstruction results in a certain set of d-dimensional vectors y(n) replacing the scalar measurements. Packard et al. [14] introduced the method of using time-delay coordinates to reconstruct the phase space of an observed dynamical system. The direct use of the lagged variables $s(n + \tau)$, where τ is some integer to

be determined, results in a coordinate system in which the structure of orbits in phase space can be captured. Then using a collection of time lags to create a vector in d dimensions,

$$y(n) = [s(n), s(n + \tau), s(n + 2\tau), \ldots, s(n + (d-1)\tau)], \quad (1)$$

the required coordinates are provided. In a nonlinear system, the $s(n + j\tau)$ are some unknown nonlinear combination of the actual physical variables that comprise the source of the measurements. The dimension d is called the embedding dimension, d_E. Any time lag will be acceptable, is not terribly useful for extracting physics from data. If τ is chosen too small, then the coordinates $s(n + j\tau)$ and $s(n + (j + 1)\tau)$ are so close to each other in numerical value that they cannot be distinguished from each other. Similarly, if τ is too large, then $s(n + j\tau)$ and $s(n + (j + 1)\tau)$ are completely independent of each other in a statistical sense. Also, if τ is too small or too large, then the correlation dimension of attractor can be under- or overestimated respectively [1]. Therefore it is necessary to choose some intermediate (and more appropriate) position between above cases. First approach is to compute the linear autocorrelation function

$$C_L(\delta) = \frac{\frac{1}{N}\sum_{m=1}^{N}[s(m+\delta) - \bar{s}][s(m) - \bar{s}]}{\frac{1}{N}\sum_{m=1}^{N}[s(m) - \bar{s}]^2} \quad (2)$$

$$\bar{s} = \frac{1}{N}\sum_{m=1}^{N} s(m)$$

and to look for that time lag where $C_L(\delta)$ first passes through zero. This gives a good hint of choice for τ at that $s(n + j\tau)$ and $s(n + (j + 1)\tau)$ are linearly independent. However, a linear independence of two variables does not mean that these variables are nonlinearly independent since a nonlinear relationship can differ from linear one. It is therefore preferably to utilize approach with a nonlinear concept of independence, e.g. the average mutual information. Briefly, the concept of mutual information can be described as follows. Let us assume there are two systems, A and B, with measurements a_i and b_k. The amount one learns in bits about a measurement of a_i from measurement of b_k is given by arguments of information theory [20,21]. The average mutual information between any value a_i from system A and b_k from B is the average over all possible measurements of $I_{AB}(a_i, b_k)$,

$$I_{AB}(\tau) = \sum_{a_i, b_k} P_{AB}(a_i, b_k) I_{AB}(a_i, b_k) \tag{3}$$

To place this definition to a context of observations from a certain physical system, let us think of the sets of measurements $s(n)$ as the A and of the measurements a time lag τ later, $s(n + \tau)$, as B set. The average mutual information between observations at n and $n + \tau$ is

$$I_{AB}(\tau) = \sum_{a_i, b_k} P_{AB}(a_i, b_k) I_{AB}(a_i, b_k) \tag{4}$$

Now we have to decide what property of $I(\tau)$ we should select, in order to establish which among the various values of τ we should use in making the data vectors $y(n)$. One could remind that the autocorrelation function and average mutual information can be considered as analogues of the linear redundancy and general redundancy, respectively, which was applied in the test for nonlinearity. The general redundancies detect all dependences in the time series, while the linear redundancies are sensitive only to linear structures. Further, a possible nonlinear nature of process resulting in the vibrations amplitude level variations can be concluded.

The goal of the embedding dimension determination is to reconstruct a Euclidean space R^d large enough so that the set of points d_A can be unfolded without ambiguity. In accordance with the embedding theorem, the embedding dimension, d_E, must be greater, or at least equal, than a dimension of attractor, d_A, i.e. $d_E > d_A$. However, two problems arise with working in dimensions larger than really required by the data and time-delay embedding [1, 14-16, 21-24]. Firstly, many of computations for extracting interesting properties from the data require searches and other operations in R^d whose computational cost rises exponentially with d. Secondly, but more significantly from the physical point of view, in the presence of noise or other high dimensional contamination of the observations, the extra dimensions are not populated by dynamics, already captured by a smaller dimension, but entirely by the contaminating signal. When an embedding space one is too large it is unnecessarily to spend time working around aspects of a bad representation of the observations which are solely filled with noise. It is therefore necessary to determine the dimension d_A. There are several standard approaches to reconstruct the attractor dimension (see, e.g., [11-24]), but let us consider only two methods in this study. The correlation integral analysis is one of the widely used techniques to investigate the signatures of chaos in a time series. The analysis uses the correlation integral, $C(r)$, to distinguish between chaotic and stochastic systems. The Grassberger-Procaccia algorithm [19] is the most

commonly used approach to compute the correlation integral.. If the time series is characterized by an attractor, then the integral $C(r)$ is related to the radius r given by

$$d = \lim_{\substack{r\to 0 \\ N\to\infty}} \frac{\log C(r)}{\log r}, \tag{6}$$

where d is correlation exponent that can be determined as the slop of line in the coordinates log $C(r)$ versus log r by a least-squares fit of a straight line over a certain range of r, called the scaling region. The saturation value of the correlation exponent is defined as the correlation dimension (d_2) of the attractor. The method of surrogate data [1,8,9] is an approach that makes the use of the substitute data generated in accordance to the probabilistic structure underlying the original data. Often, a significant difference in the estimates of the correlation exponents, between the original and surrogate data sets, can be observed. In the case of the original data, a saturation of the correlation exponent is observed after a certain embedding dimension value (i.e., 6), whereas the correlation exponents computed for the surrogate data sets continue to increase with the increasing embedding dimension. It is worth consider another method for determining d_E that comes from asking the basic question addressed in the embedding theorem: when has one eliminated false crossing of the orbit with itself which arose by virtue of having projected the attractor into a too low dimensional space? By examining this question in dimension one, then dimension two, etc. until there are no incorrect or false neighbours remaining, one should be able to establish, from geometrical consideration alone, a value for the necessary embedding dimension. Advanced version is presented in Refs. [21]. The Lyapunov's exponents (LE) are the dynamical invariants of the nonlinear system. In a general case, the orbits of chaotic attractors are unpredictable, but there is the limited predictability of chaotic physical system, which is defined by the global and local LE. A negative exponent indicates a local average rate of contraction while a positive value indicates a local average rate of expansion. In the chaos theory, the spectrum of LE is considered a measure of the effect of perturbing the initial conditions of a dynamical system. In fact, if one manages to derive the whole spectrum of the LE, other invariants of the system, i.e. Kolmogorov entropy (KE) and attractor's dimension can be found. The inverse of the KE is equal to an average predictability. Estimate of dimension of the attractor is provided by the Kaplan-Yorke conjecture:

$$d_L = j + \frac{\sum_{\alpha=1}^{j} \lambda_\alpha}{|\lambda_{j+1}|}, \tag{8}$$

where j is such that $\sum_{\alpha=1}^{j} \lambda_\alpha > 0$ and $\sum_{\alpha=1}^{j+1} \lambda_\alpha < 0$, and the LE λ_α are taken in descending order.

There are a few approaches to computing the LE. One of them computes the whole spectrum and is based on the Jacobi matrix of system. In the case where only observations are given and the system function is unknown, the matrix has to be estimated from the data. In this case, all the suggested methods approximate the matrix by fitting a local map to a sufficient number of nearby points. To calculate the spectrum of the LE from the amplitude level data, one could determine the time delay τ and embed the data in the four-dimensional space. In this point it is very important to determine the Kaplan-Yorke dimension and compare it with the correlation dimension, defined by the Grassberger-Procaccia algorithm. The estimations of the KE and average predictability can further show a limit, up to which the amplitude level data can be on average predicted. Other details can be found in Refs. [1,9,11-24].

3. Analysis of the SMEAR station atmospheric radon concentration time series (2003) and conclusion

The first application of the chaos-dynamical approach to analysis of chaotic time series of the environment radioactivity has been preliminarily presented in [9] on the example of analysis of the atmospheric radon concentration time series during 2001 year. Measurements of the radon concentrations at SMEAR II station (61 ° 51'N, 24 ° 17'E, 181 m above sea level; near the Hyytiälä, Southern Finland) has been performed by group of experts of the Finnish Meteorological Institute (FMI) and actually integrated into the system long-term measurements (see details in Ref. [5] and [8,9] too). Here we list the analysis of the corresponding data on the atmospheric radon for 2003. It is worth to note (look details in Refs. [9]) that the continuous measurement was performed during 2003 on the seventh heights (from 4.2 m to 127 m). Technologically, a device with a pair of the Geiger-Müller counters, arranged in the lead corymbs is used for the beta particles detection. Registration of the beta particles was cumulatively carried in 10-minutes intervals. Effectiveness of a detection was 0.96% and 4.3% for beta radiation from ^{214}Pb and ^{214}Bi respectively. Estimate of the 1-σ statistical counting is ± 20% for stable concentrations of ^{222}Rn (1 Bq/m^3). The mean-daily values of atmospheric ^{222}Rn concentrations were in the range from <0.1 to 11

Bq/m^3. In fact, the lower limit of this range was limited by a hardware detection limit of the radon monitors. The average geometric value for the daily average radon concentrations was amounted to 2.3 to 2.6 Bq· m^{-3} per year. In general during 2003 as hourly, as daily values of a parameter, which corresponds to the radon concentration, were ranged from about 1 to 5 Bq/m^3. In Figure 1 there is presented the typical time dependent curve of the radon concentration, received on the base of measurements at SMEAR II station (61° 51'N, 24° 17'E, 181 m above sea level; near the Hyytiälä, Southern Finland) [5]).

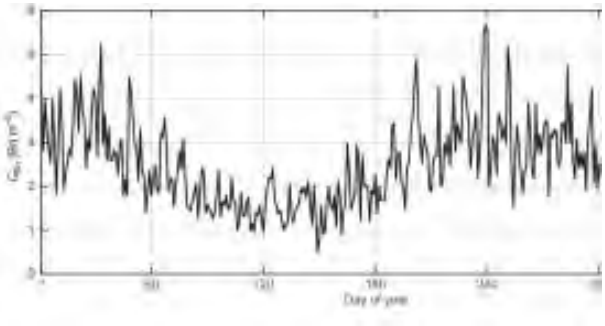

Figure 1. Time dependent curve of the radon concentration, received on the base of measurement (SMEAR II station)

In Table 1 we list the results of computing different dynamical and topological invariants (time delay τ,correlation dimension (d_2), embedding space dimension (d_E), Lyapunov exponent (λ_i), Kolmogorov entropy (K_{ent}), Kaplan-York dimension (d_L), and chaos indicator (K_{ch}) [13] for Rn concentration time series (2003). For comparison there also listed data of the analogous analysis of the Rn data during 2001 year [9].

Table 1. Time delay τ,correlation dimension (d_2), embedding space dimension (d_E), Lyapunov exponent (λ_i), Kolmogorov entropy (K_{ent}), Kaplan-York dimension (d_L), and chaos indicator (K_{ch}) for the radon concentration time series (2003)

Year	τ	d_2	d_E	λ_1	λ_2	K_{ent}	d_L	K
2001	12	5,48	6	0,0182	0,0058	0,024	5,36	0,80
2003	14	5,72	6	0,0198	0,0064	0,026	5,58	0,84

The analysis of the dynamical and topological invariants shows that, for example, the resulting Kaplan- York dimension is very close to the correlation dimension and is smaller than the dimension of attachment, which confirms the correctness of the choice of the latter.

This conclusions is fully analogous the conclusions [10]. To conclude, let us underline that the presented results of application of the chaos-dynamical approach to analysis of temporal evolution of the atmospheric radon ^{222}Rn concentration and received values of the topological and dynamical invariants for the time series of the ^{222}Rn concentration allows to reveal the deterministic chaos elements. It can be of a great theoretical and practical interest for the further studying environmental radioactivity time series for different radionuclides and by the way give the basis for the construction of the corresponding forecasting temporal and space distribution models (look in details [17, 1,21-24,28]).

References

[1] Glushkov, A.V. *Methods of a chaos theory.* Astroprint, Odessa, 2012.

[2] Glushkov, A.V. *Relativistic Quantum theory. Quantum Mechanics of Atomic Systems.* Astroprint, Odessa, 2008.

[3] Khetselius, O.Yu. *Hyperfine structure of atomic spectra.* Astroprint, Odessa, 2008.

[4] Glushkov, A.V., Khokhlov, V.N., and Tsenenko, I.A. Atmospheric teleconnection patterns: Wavelet analysis. *Nonlinear Processes in Geophysics*. 11, 3 (2004), 285-293.

[5] Chen, X., Paatero, J., Kerminen, V.-M., Riuttanen, L., et al. Responses of the atmospheric concentration of radon-222 to the vertical mixing and spatial transportation. *Boreal Environm. Res. (Helsinki)*. 21 (2016), 299–318.

[6] Parovik, R.I., Il'in, I.A., and Firstov, P.P., The mathematical diffusion model of mass transfer of radon (222Rn) in the ground and its exhalation into the surface layer of the atmosphere. *Vestnik Kraunts. Earth sciences* (in russian). 7, 1 (2006), 110-114.

[7] Khetselius, O.Yu. Hyperfine structure of radium. *Photoelectronics*. 14 (2005), 83-85.

[8] Glushkov, A.V., Safranov, T.A., Khetselius, O.Yu., Ignatenko, A.V., Buyadzhi, V.V., and Svinarenko A.A. Analysis and forecast of the environmental radioactivity dynamics based on methods of chaos theory: General conceptions. *Environmental Problems*. 1, 2 (2016), 115-120.

[9] Glushkov, A.V., Khetselius, O.Yu., Buyadzhi, V.V., Dubrovskaya, Yu.V., Serga, I.N., Agayar, E.V., and Ternovsky, V.B. Nonlinear chaos-dynamical approach to analysis of atmospheric radon ^{222}Rn concentration time series. Pramana–J. Phys. 123, (2017), in print.

[10] Jacob, D.J., and Prather, M.J. Radon-222 as a test of convective transport in a general circulation model. *Tellus*. 42b (1990), 118-134.

[11] Pinault, J.-L., and Baubron, J.C. Signal processing of diurnal and semidiurnal variations in radon and atmospheric pressure' A new tool for accurate in situ measurement of soil gas velocity, pressure gradient, and tortuosity. *Journal of Geophys.Res*. 102, 8 (1997), 101-120.

[12] Chelani, A.B. Predicting chaotic time series of PM10 concentration using artificial neural network. *Int. J. Environ. Stud*. 62 (2005), 181–191.

[13] Gottwald, G.A., and Melbourne, I., Testing for chaos in deterministic systems with noise. *Physica D*. 212 (2005), 100–110.

[14] Packard, N.H., Crutchfield, J.P., Farmer, J.D., and Shaw, R.S. Geometry from a time series. *Phys. Rev. Lett.* 45 (1980), 712–716.

[15] Kennel, M.B., Brown, R., and Abarbanel, H. Determining embedding dimension for phase-space reconstruction using a geometrical construction. *Phys. Rev.* A 45 (1992) 3403-3411.

[16] Abarbanel, H.D.I., Brown, R., Sidorowich, J.J., and Tsimring, L.Sh. The analysis of observed chaotic data in physical systems. *Rev. Mod. Phys.* 65 (1993), 1331–1392.

[17] Schreiber, T. Interdisciplinary application of nonlinear time series methods. Phys. Rep. 308 (1999), 1–64.

[18] Fraser, A.M., and Swinney, H.L. Independent coordinates for strange attractors from mutual information. *Phys. Rev. A*. 33 (1986), 1134–1140.

[19] Grassberger, P., and Procaccia, I. Measuring the strangeness of strange attractors. *Physica D*.9 (1983), 189–208.

[20] Gallager, R.G. *Information theory and reliable communication*. Wiley, N-Y., 1986.

[21] Bunyakova, Yu.Ya., and Glushkov, A.V. *Analysis and forecast of the impact of anthropogenic factors on air basein of an industrial city*. Ecology, Odessa, 2010.

[22] Bunyakova, Yu.Ya., and Khetselius, O.Yu. Non-linear prediction statistical method in forecast of atmospheric pollutants. *Proc. of 8th International Carbon Dioxide Conference*. T2-098 (2009).

[23] Glushkov, A.V., Khetselius, O.Y., Brusentseva, S.V., Zaichko, P.A., and Ternovsky, V.B. Studying interaction dynamics of chaotic systems within a non-linear prediction method: application to neurophysiology. *Advances in Neural Networks, Fuzzy Systems and Artificial Intelligence, Series: Recent Advances in Computer Engineering*, Ed. J.Balicki. WSEAS Pub., Gdansk. 21 (2014), 69-75.

[24] Glushkov, A.V., Svinarenko, A.A., Buyadzhi, V.V., Zaichko, P.A., and Ternovsky, V.B. Chaos-geometric attractor and quantum neural networks approach to simulation chaotic evolutionary dynamics during perception process. *Advances in Neural Networks, Fuzzy Systems and Artificial Intelligence, Series: Recent Advances in Computer Engineering*, Ed. J.Balicki. WSEAS Pub., Gdansk. 21 (2014), 143-150.

[25] Glushkov, A.V., Khetselius, O.Yu., Bunyakova, Yu.Ya., Grushevsky, O.N., and Solyanikova, E.P. Studying and forecasting the atmospheric and hydroecological systems dynamics by using chaos theory methods. *Dynamical Systems Theory*, ed. J. Awrejcewicz, M. Kazmierczak, P. Olejnik, J, Mrozowski. Wydawn. Politechniki Łódzkiej, Łódz. T1 (2013), 249-258.

[26] Glushkov, A.V., Prepelitsa, G.P., Svinarenko, A.A., and Zaichko, P.A. Studying interaction dynamics of the non-linear vibrational systems within non-linear prediction method (application to quantum autogenerators). *Dynamical Systems Theory*, ed. J. Awrejcewicz, M. Kazmierczak, P. Olejnik, J, Mrozowski. Wydawn. Politechniki Łódzkiej, Łódz. T1 (2013), 467-477.

[27] Glushkov, A.V., Kuzakon, V.M., Ternovsky, V.B., and Buyadzhi, V.V. Dynamics of laser systems with absorbing cell and backward-wave tubes with elements of a chaos. *Dynamical Systems Theory*, ed. J. Awrejcewicz, M. Kazmierczak, P. Olejnik, J, Mrozowski. Wydawn. Politechniki Łódzkiej, Łódz. T1 (2013), 461-466.

[28] Khetselius, O.Yu. Forecasting evolutionary dynamics of chaotic systems using advanced non-linear prediction method. *Dynamical Systems Applications*, ed. J. Awrejcewicz, M. Kazmierczak, P. Olejnik, J, Mrozowski. Wydawn. Politechniki Łódzkiej, Łódz. T2 (2013), 145-152.

[29] Glushkov, A.V., Vaschenko, V.N., Gerasimenko, G., and Bunyakova, Yu.Ya. Atmospheric pollutants concentrations temporal dynamics for the industrials ukrainian cities: Low-dimensional chaos. *Dynamical Systems Applications*, ed. J. Awrejcewicz, M. Kazmierczak, P. Olejnik, J, Mrozowski. Wydawn. Politechniki Łódzkiej, Łódz. T2 (2013), 241-250.

[30] Khetselius, O.Yu., Brusentseva, S.V., and Tkach, T.B. Studying interaction dynamics of chaotic systems within non-linear prediction method: Application to neurophysiology. *Dynamical Systems Applications*, ed. J. Awrejcewicz, M. Kazmierczak, P. Olejnik, J, Mrozowski. Wydawn. Politechniki Łódzkiej, Łódz. T2 (2013), 251-259.

[31] Glushkov, A.V., Buyadzhi, V.V., Kvasikova, A.S., Ignatenko, A.V., Kuznetsova, A.A., Prepelitsa, G.P., and Ternovsky, V.B. Nonlinear chaotic dynamics of Quantum systems: Molecules in an electromagnetic field and laser systems. *Quantum Systems in Physics, Chemistry, and Biology. Series: Progress in Theoretical Chemistry and Physics,* ed. A.Tadjer, R.Pavlov, J.Maruani, E.Brändas, G.Delgado-Barrio (Springer). 30 (2016), 71-84.

[32] Glushkov, A.V., Kuzakon', V.M., Khetselius, O.Yu., Bunyakova, Yu.Ya., and Zaichko P.A. Geometry of Chaos: Consistent combined approach to treating chaotic dynamics atmospheric pollutants and its forecasting. *Proc. International Geometry Center*. 6, 3 (2013), 6-13.

[33] Glushkov, A.V., Kuzakon, V.M., and Zaichko, P.A. Geometry of Chaos: Advanced approach to forecasting evolution of low-attractor chaotic systems. *Proc. International Geometry Center*. 7, 3 (2014), 67-72.

[34] Buyadzhi, V.V., Glushkov, A.V., Mansarliysky, V.F., Ignatenko, A.V., and Svinarenko A.A. Spectroscopy of atoms in a strong laser field: New method to sensing AC Stark effect, multiphoton resonances parameters and ionization cross-sections. *Sensor Electr. and Microsyst. Techn*. 12, 4 (2015), 27-36.

[35] Prepelitsa, G.P., Glushkov, A.V., Lepikh, Ya.I., Buyadzhi, V.V., Ternovsky,V.B., and Zaichko P.A. Chaotic dynamics of non-linear processes in atomic and molecular systems in electromagnetic field and semiconductor and fiber laser devices: new approaches, uniformity and charm of chaos. *Sensor Electr. and Microsyst.Techn*.11, 4 (2014), 43-57.

[36] Glushkov, A.V., Khetselius, O.Yu., Bunuakova, Yu.Ya., Buyadzhi, V.V, Brusentseva, S.V., and Zaichko P.A. Sensing interaction dynamics of chaotic systems within a chaos theory and microsystem technology Geomath with application to neurophysiological systems. *Sensor Electr. and Microsyst.Techn*. 11, 3 (2014), 62-69.

[37] Glushkov, A.V., Mansarliysky, V.F., Khetselius, O.Yu., Ignatenko, A.V., Smirnov, A., and Prepelitsa, G.P. Collisional shift of hyperfine line for thallium in an atmosphere of the buffer inert gas. J. Phys.: Conf. Ser. 810 (2017), 012034.

[38] Svinarenko, A.A., Glushkov, A.V., Khetselius, O.Yu., Ternovsky, V.B., Dubrovskaya, Yu.V., Kuznetsova, A.A., and Buyadzhi, V.V. Theoretical Spectroscopy of Rare-Earth Elements: Spectra and Autoionization Resonances. *Rare Earth Element*, ed. Jose E. A. Orjuela, InTech. (2017), 83-104.

[*]Alexander V. Glushkov, Professor: Odessa State Environmental University, Pure and Applied Mathematics Department, L'vovskaya str. 15, 65009 Odessa, Ukraine (*dirac13@mail.ru*). The author gave a presentation of this paper during one of the conference sessions.

[*]Vasily V. Buyadzhi, Ph.D.: Odessa State Environmental University, Pure and Applied Mathematics Department, L'vovskaya str. 15, 65009 Odessa, Ukraine (*vbuyad@mail.ru*)

[*]Yuliya V. Dubrovskaya, Ph.D.: Odessa State Environmental University, Pure and Applied Mathematics Department, L'vovskaya str. 15, 65009 Odessa, Ukraine (*dubrovskayayv@gmail.com*)

[*]Eugeny V. Ternovsky, Ph.D. student: Odessa State Environmental University, Pure and Applied Mathematics Department, L'vovskaya str. 15, 65009 Odessa, Ukraine (*ternovskyev@gmail.com*)

Stochastic bifurcations in discontinuous and impacting nonlinear systems

Sayan Gupta, Pankaj Kumar, Sadagopan Narayanan

Abstract: The non-smooth dynamics of Duffing van der Pol (DVDP) oscillator under additive Gaussian white noise excitation with unilateral or bilateral non-elastic constraints is numerically investigated. Applying the Zhuravlev-Ivanov non-smooth variable transformation, the discontinuous problem is first mapped into a continuous phase plane. A stochastic bifurcation analysis of the system is carried out using concepts of D- and P-bifurcations. P-bifurcations involve analysing the topological changes in the joint probability density function associated with the state variables. The joint pdf is obtained by solving the corresponding Fokker-Planck equation numerically using finite element method. D-bifurcation analysis is carried out by studying the behaviour of the largest Laypunov exponnet (LLE), computed using the Nordmark-Poincare map in conjunction with Wedig's algorithm. A measure based on Shannon entropy has been developed to quantitatively estimate the onset of P-bifurcations. A global parametric study carried out to identify the stochastic stability regimes using the concepts of D- and P-bifurcations reveal that the regimes could be slightly different. More studies on the interpretation of this phenomenon is currently being investigated.

1. Introduction

Nonlinear dynamical behaviours resulting due to impacts of elements of dynamical systems with rigid or elastic barriers exhibit many complex behaviour that cannot be explained using theory of smooth dynamical systems[4]. The fundamental nature of the non-smooth dynamics of the impacting systems, and the resulting qualitative changes in the dynamics is a matter of great interest[2]. Selection of appropriate mathematical model for impact is crucial for simulating accurately the behavior of the dynamical system. The simplest way of modeling impacts is based on the hypothesis of hard collision, which assumes infinitesimally small contact duration time and constant value of the coefficient of restitution. This model is based on the assumption that the impact is instantaneous, hence works well when impacting surfaces are hard. For many other practical applications, impact can be modeled more realistically by modelling it as soft impact described by using continuous functions of force-deformation relations during contacts. The Hertz impact law is such an example. A comprehensive survey for various impact models can be found in [4].

The presence of noise in the excitations for such non-smooth nonlinear systems leads to further complexities in the system behaviour of these systems. Noise has the potential to alter the stability boundaries and can play an important role in the design and life of non-smooth mechanical system. This has prompted investigations on the influence of noise on the dynamical behaviour and bifurcation characteristics for these non-smooth dynamical systems.

This study focusses on the development of a methodology for the stability and bifurcation analyses of a stochastically excited discontinuous Duffing-Van der Pol(DVDP) oscillator, with impacts modeled with hard as well as soft nonlinear elastic-damping structures (Hertz's damping contact model). The main objective is to analyze qualitatively and quantitatively the influence of Gaussian white noise on these two different models and to compare the resulting response. The analysis is carried out using two distinct approaches. Changes in the dynamical stability of the system is examined through the largest Lyapunov exponent (LLE) associated with the trajectories of the system. In computing the LLE, the discontinuities in the equation of motion on account of impact present difficulties which are bypassed by using the Nordmark-Poincare mapping [1] approach. Additionally, the bifurcation characteristics are examined using the topological structure of the joint probability density function(pdf) of the state variables. The difficulties in writing the Fokker-Planck (FP) equation associated with the vibro-impact system whose governing equations of motion are discontinuous, are addressed by using the Zhuravlev-Ivanov transformation [9, 5, 2]. A numerical solution to the FP equation in the transformed space is obtained using a recently developed finite element method [6]. Subsequently, a measure based on the Shannon entropy [7] is used to quantify the regimes where P-bifurcations take place. Parametric studies are carried out to examine the D- and P- bifurcation characteristics where the position of the barriers, the intensity of the excitation and the damping are taken as control parameters. The advantages and disadvantages of both models are discussed.

2. Mathematical model of the system

Discontinuous DVDP oscillator under stationary, zero-mean Gaussian process $W(t)$ as presented in Fig. 1 is considered. $\Delta/2$ represents the locations of the barriers on either side of the equilibrium position (taken to be at the origin). The barrier has been modeled as rigid Fig. 1(a) or elastic-damped (Hertz's damping contact) model Fig.1(b). The corresponding governing equations of motion for the oscillator with rigid barriers are

$$\ddot{X} - \alpha X - c\dot{X} + \beta_0 X^3 - \beta_1 X^2 \dot{X} + \beta_2 X^4 \dot{X} = \sigma W(t); \qquad -\frac{\Delta}{2} < X < \frac{\Delta}{2} \tag{1}$$

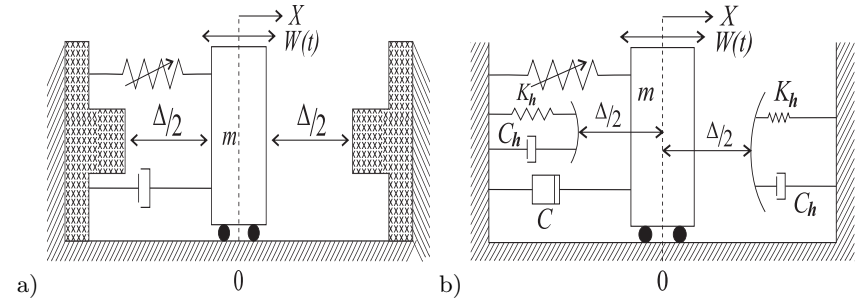

Figure 1. Schematic of the (a) impact based on restitutional model (b) Hertz contact impact model.

with the impact condition being mathematically expressed as

$$\dot{X}^{+} = -e\dot{X}^{-}, \quad X = \pm\frac{\Delta}{2} \quad 0 < e \leq 1, \tag{2}$$

where α and c denote the linear stiffness and damping coefficients, $\{\beta_i(t)\}_{i=0}^{2}$ are system parameter constants that define the nonlinear stiffness and damping and e is the coefficient of restitution. The corresponding governing equations of motion for the oscillator with impacts based on Hertz contact model is given by

$$\ddot{X} - \alpha X - c\dot{X} + \beta_0 X^3 - \beta_1 X^2\dot{X} + \beta_2 X^4\dot{X} + f(X,\dot{X}) = W(t), \tag{3}$$

where using Hertz's contact model of nonlinear damping the collision force $f(X,\dot{X})$ is mathematically expressed as

$$f(X,\dot{X}) \;\; = \begin{cases} k_h(X+\frac{\Delta}{2})^{3/2}(1+c_h\dot{X}) & \text{if } X < -\frac{\Delta}{2} \\ 0 & \text{if } -\frac{\Delta}{2} \leq X \leq \frac{\Delta}{2} \\ k_h(X-\frac{\Delta}{2})^{3/2}(1+c_h\dot{X}) & \text{if } X > \frac{\Delta}{2}, \end{cases} \tag{4}$$

here, k_h and c_h denote the stiffness and damping coefficients corresponding to the Hertz contact model.

3. Vibro impact oscillator

The non-smooth nature of the governing equations of motion for vibro-impact dynamical systems pose analytical and numerical challenges in their analysis. These difficulties can be overcome by invoking suitable non-smooth variable transformations that enable rewriting the governing equations of motion in a transformed variable space without any discontinuities. For oscillators with one sided rigid barrier a non-smooth variable transformation - known as the Zhuravlev transformation - has been proposed in [9]. Mathematically, Zhuravlev

transformation involves mapping the problem from the $(X, \dot{X})$ space to the $(Y, \dot{Y})$ space such that

$$X = |Y| = Y\text{sgn}(Y), \quad \dot{X} = \dot{Y}\text{sgn}Y, \tag{5}$$

where, sgn$(\cdot)$ is the signum function. While this transformation removes the discontinuity in the phase plane, the effect of impact and the consequent abrupt change in velocity is modelled into the governing equations of motion as an additional dissipative term $(1-e)\dot{Y}|\dot{Y}|\delta(Y)$. The presence of the discontinuous functions such as $|\cdot|$ and the $\delta(\cdot)$ presents numerical difficulties which can be bypassed by approximating using arc-tangent and Gaussian distribution of very low variance respectively.

The double sided impact changes the nature of the dynamics and the Zhuravlev-Ivanov transformation which is essentially a mirror image transformation cannot be applied. Instead, a piecewise differentiable periodic transformation proposed by Zhuravlev [9] for double sided barriers can be used to convert the equations of motion without any discontinuities. As a first step, a non-dimensional displacement variable $Y = X\pi/\Delta$ is defined. The equation of motion between impacts can now be expressed as

$$\ddot{Y} - \alpha Y - c\dot{Y} + \beta_0^{'}Y^3 - \beta_1^{'}Y^2\dot{Y} + \beta_2^{'}Y^4\dot{Y} = \sigma^{'}W(t), \quad -\frac{\pi}{2} < Y < \frac{\pi}{2}, \tag{6}$$

with the impact condition defined as

$$\dot{Y}^{+} = -e\dot{Y}^{-}, \quad Y = \pm\frac{\pi}{2}, \quad 0 < e \leq 1. \tag{7}$$

The superscript primes that appear in Eq.(6) refer to the corresponding non-dimensional parameters of the problem. Next, Eqs.(6-7) need to be transformed into the constraint free form. For case of elastic impacts $e = 1$, the following 2π periodic functions are first introduced [9]:

$$\Pi(Z) = \begin{cases} Z & \text{if } -\frac{\pi}{2} \leq Z \leq \frac{\pi}{2}, \\ -Z + \pi & \text{if } \frac{\pi}{2} \leq Z \leq \frac{3\pi}{2}, \end{cases} \tag{8}$$

$$M(Z) = \Pi^{'}(Z) = \begin{cases} 1 & \text{if } -\frac{\pi}{2} \leq Z \leq \frac{\pi}{2}, \\ -1 & \text{if } \frac{\pi}{2} \leq Z \leq \frac{3\pi}{2}. \end{cases} \tag{9}$$

The prime on $\Pi^{'}(Z)$ denotes differentiation with respect to Z. This enables expressing the displacement variable Y and its time derivatives in terms of $\Pi(Z)$ and $M(Z)$ as

$$Y = \Pi(Z), \quad \dot{Y} = M(Z)\dot{Z}, \quad \ddot{Y} = M(Z)\ddot{Z} + M'(Z)\dot{Z}^2. \tag{10}$$

Substituting Eq.(10) in Eq.(6), the equations of motion can be expressed as

$$\ddot{Z} - \alpha M(Z)\Pi(Z) - c\dot{Z} + \beta_0^{'} M(Z)\Pi^3(Z) - \beta_1^{'}\Pi^2(Z)\dot{Z} + \beta_2^{'}\Pi^4(Z)\dot{Z} = \sigma^{'} M(Z)W(t). \quad (11)$$

For inelastic impacts, when $(0 < e < 1)$, a modified smooth variable transformation has been suggested in [3] where

$$\begin{aligned} Y &= \Pi(Z + \lambda N(Z), \quad \dot{Y} = (M(Z) + \lambda\Pi(Z))\dot{Z}, \\ \ddot{Y} &= M^{'}(Z)\dot{Z}^2 + M(Z)\ddot{Z} + \lambda M(Z)\dot{Z}^2 + \lambda\Pi(Z)\ddot{Z}. \end{aligned} \quad (12)$$

Here, $N(Z)$ is 2π periodic *i.e.*, $N(Z + 2\pi) = N(Z)$ and is given by

$$N(Z) = \begin{cases} \frac{Z^2}{2} - \frac{\pi^2}{8} & \text{if } -\frac{\pi}{2} \le Z \le \frac{\pi}{2}; \\ \frac{-(Z-\pi)^2}{2} + \frac{\pi^2}{8} & \text{if } \frac{\pi}{2} \le Z \le \frac{3\pi}{2}, \end{cases} \quad , \qquad \lambda = \frac{2}{\pi}\left(\frac{1-e}{1+e}\right). \quad (13)$$

3.1. Stochastic bifurcation

Bifurcations in nonlinear dynamical systems are characterized by the birth or destruction of attractors at different parameter regimes, leading to dramatic and abrupt changes in its behaviour. Typically, it has been observed in the literature that systems subjected to noise could undergo bifurcations in two distinct modes: (a) dynamical or D-bifurcations occur when there are drastic topological changes associated with the phase space trajectories, and (b) phenomenological or P-bifurcations are observed when the underlying probabilistic structure of the long term behavior of the state variables undergo topological changes. More details on D- and P- bifurcations for the vibro-impact system being studied is discussed in the following sections.

3.1.1. P-bifurcation

P-bifurcation is characterized by changes in the probabilistic structure of the stationary joint pdf of the state variables at different parameter regimes. A parameter change leading to the changes in the attractor would lead to a corresponding change in the topology associated with the joint pdf; this is defined as a P-bifurcation. Under Gaussian white noise excitation, the state vector $\mathbf{Z} = [Z_1\ Z_2]^T$ corresponding to the equations of motion Eq.(11) will be Markovian, and hence, the time and space evolution of the joint pdf $p(\mathbf{Z}, t|\mathbf{Z}_0, t_0)$, is governed by the following FP equation.

$$\begin{aligned} \frac{\partial p}{\partial t} &= -Z_2\frac{\partial p}{\partial Z_1} - \frac{\partial}{\partial Z_2}\Big\{[\alpha M(Z_1)\Pi(Z_1) + cZ_2 - \beta_0^{'} M(Z_1)\Pi^3(Z_1) \\ &\quad + \beta_1^{'}\Pi^2(Z_1)Z_2 - \beta_2^{'}\Pi^4(Z_1)Z_2]p\Big\} + \frac{\sigma^{'2}}{2}\frac{\partial^2 p}{\partial Z_2^2}. \end{aligned} \quad (14)$$

The FP equation for the inelastic case corresponding to Eq.(12) is given by

$$\begin{aligned}\frac{\partial p}{\partial t} &= -Z_2\frac{\partial p}{\partial Z_1}+\frac{\sigma^{'2}}{2[A]^2}\frac{\partial^2 p}{\partial Z_2^2}\\ &\quad -\frac{\partial[cZ_2+[A]^{-1}[\alpha(B)-\beta_0^{'}(B)^3-\lambda M(Z_1)z_2^2]+\beta_1^{'}(B)^2Z_2-\beta_2^{'}(B)^4Z_2]p}{\partial Z_2},\end{aligned} \tag{15}$$

where, $A = M(Z_1) + \lambda\Pi(Z_1)$, $B = \Pi(Z_1) + \lambda N(Z_1)$. In this study, the recently developed finite element method [6] has been used to numerically estimate the stationary j-pdf of the response variables.

3.1.2. D-bifurcation

The dynamical stability characteristics of the attractors are estimated by investigating the long term behaviour of the trajectories and are best measured in terms of the LLE. Using the principle of Oseledec's multiplicative theorem, the LLE is mathematically defined as

$$\tilde{\lambda}_m = \max\left\{\lim_{t\to\infty}\mathrm{E}\left[\frac{1}{t}\log\frac{||\mathbf{u}(t)||}{||\mathbf{u}(0)||}\right]\right\}, \tag{16}$$

where $\{\mathbf{u}(t) : t > 0\}$ are the solution trajectories of the linearized differential equations when the governing equations of motion are linearized about a reference solution. However the presence of discontinuities through the signum functions lead to difficulties in the computation of the Jacobian essential for estimating the LLE. Instead one can use discontinuity mapping proposed in [1], which provides a local decomposition of a Poincare mapping into a sequence of four classes to distinguish between the contributions from the flow and those from the impact process. When the flow trajectory is continuous, a small perturbation $\mathbf{v}$ to the trajectory $X_0(t)$ - the solution of Eq.(1), is governed by the linearized equation

$$\dot{\mathbf{v}} = \mathbf{J(t)v}\quad\begin{cases} X > \Delta & \text{for one sided barrier;}\\ -\frac{\Delta}{2} < X < \frac{\Delta}{2} & \text{for both sided barriers,}\end{cases} \tag{17}$$

where, $\mathbf{J}$ is the Jacobian matrix obtained for the corresponding equations of motion. The approximate discrete map, for the perturbation $\mathbf{v}$ at the time of impact can be constructed using the Nordmark local map

$$\mathbf{v}_\mathbf{k}^+ = \left[\mathbf{D}_{\mathbf{P}c}\right]_{\mathbf{X}_0(t)}\mathbf{v}_\mathbf{k}^-,\quad\begin{cases} X_1 = \Delta & \text{for one sided impact,}\\ X_1 = \pm\frac{\Delta}{2} & \text{for both sided impacts,}\end{cases} \tag{18}$$

where, $\mathbf{D}_{\mathbf{P}c}$ is a compound map which describes the impact process through the Jacobian matrix

$$\mathbf{D}_{\mathbf{P}c} = \begin{Bmatrix} -e & 0\\ \frac{(1+e)(\alpha X_{1_k}+\beta_0 X_{1_k}^3+\sigma W(t_k))}{X_{2_k}} & -e\end{Bmatrix}. \tag{19}$$

3.2. Boundaries of stochastic bifurcation regimes

D-bifurcations are characterized by a sign change in the LLE and the locus in the parameter space where these sign changes occur indicates the boundaries for D-bifurcations. In contrast, P-bifurcation analysis is primarily a qualitative analysis, based on visual inspection of the structure of the pdf of the response. This makes it difficult to define the stability boundaries in terms of P-bifurcations. A quantitative measure based on the Shannon entropy has been recently proposed in [7] for identifying P-bifurcations quantitatively. The Shannon's entropy of $\mathbf{X}(t)$ at time t is defined as

$$H(a,t) = -\int_{-\infty}^{\infty} p(a,t)\log_b p(a,t)\mathrm{d}a, \tag{20}$$

where, b is an arbitrarily chosen logarithmic base, usually taken to be Euler's number. It has been shown in [8] that under stationary conditions, the entropy flux is proportional to the negative sum of the Lyapunov exponents implying that the entropy changes depend on the phase space contraction and a correction term that depends on the noise strength σ.

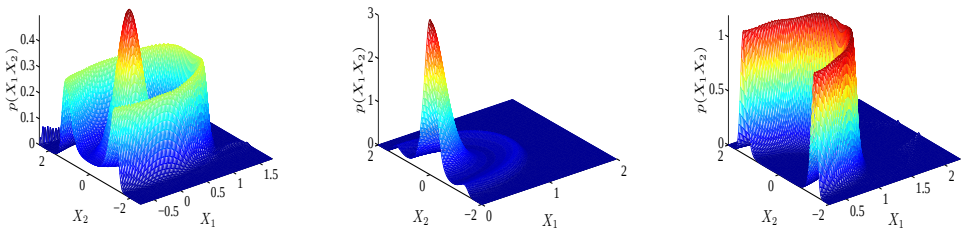

(a) (b) (c)

Figure 2. $p(X_1X_2)$ for $e = 0.98, \sigma = 0.1, c = -0.1$, (a) $\Delta = -0.75$, (b) $\Delta = 0$, (c) $\Delta = 0.25$.

3.3. Numerical results

For the numerical calculations, the parameters in Eq.(1) are taken to be $\beta_0 = 0.5$, $c = -0.1$, $\beta_1 = \beta_2 = 1$. The offset position Δ, coefficient of restitution e and the noise intensity σ are taken to be the control parameters which are varied. To investigate the effect of position of the barrier offset Δ, on the stability characteristics of the dynamical system, the stationary pdf are computed for the cases $\Delta = -0.75,\ 0$ and 0.25, when $\alpha = -1, \sigma = 0.1, e = 0.98$. Figure 2 shows the j-pdf for these three cases while Fig. 3 shows the corresponding contour plots. With barrier offset at relatively large distance $\Delta = -0.75$, Figures 2(a) and 3(a) clearly reveal the bistable character of the pdf; the two stochastic attractors - one representing small amplitude oscillations while the other represents large amplitude

oscillations - are clearly visible in the contour plot. This is indicative of the presence of two stable attractors. As Δ is decreased to $\Delta = 0$, one observes that the strength of attractor at origin increases while the large amplitude oscillations weakens and is significantly less pronounced; see Figs. 2(b) and 3(b). This can be attributed to the greater energy loss due to increasing damping effect upon impact, hence system has less energy for large amplitude oscillations.The corresponding contour plot in Fig. 3(b) shows that system exhibits small amplitude oscillations at this parameter regime. On further increasing $\Delta = 0.25$, the barrier

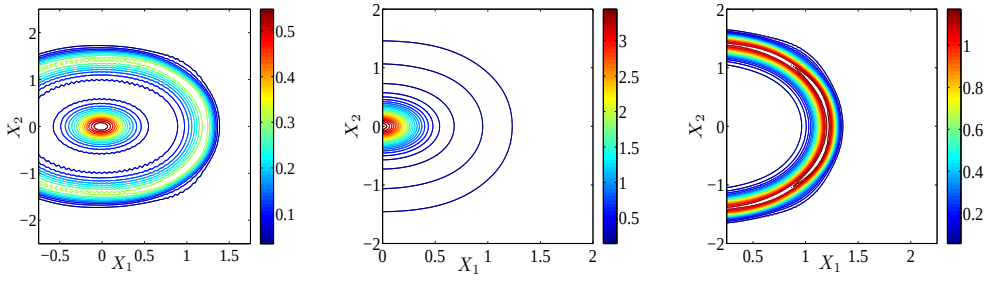

(a) (b) (c)

Figure 3. Contour plot of $p(X_1X_2)$ $e = 0.98, \sigma = 0.1, c = -0.1$, (a) $\Delta = -0.75$, (b) $\Delta = 0$, (c) $\Delta = 0.25$.

forces the system to move away from the attractor at the origin to the large amplitude oscillations. This is the reason why the attractor at the origin no longer exists and the system exhibits only large amplitude oscillations; see Figs. 2(c) and 3(c). These changes in the topological characteristics associated with the stochastic attractors is indicative of P-bifurcation.

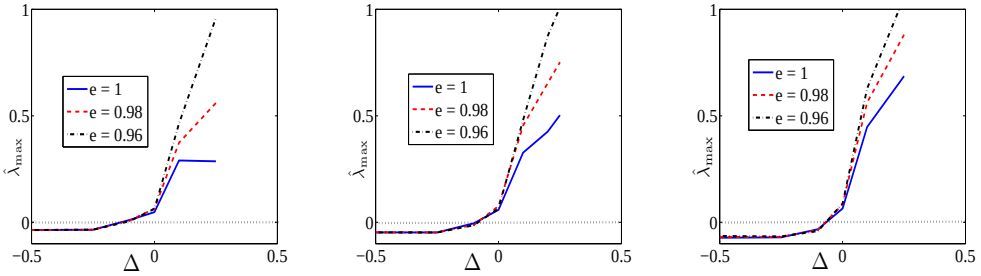

(a) (b) (c)

Figure 4. LLE for $\sigma = 0.1, \alpha = -1$ using Nordmark mapping (a) $c = -0.08$, (b) $c = -0.1$, (c) $c = -0.14$.

To investigate the dynamical bifurcation characteristics, the LLE are computed using

Nordmark mapping. Figure 4 shows the variation of the LLE as a function of the barrier offset for different values of c and e. An inspection of these figures clearly shows that in all cases, the LLE denoted by $\hat{\lambda}_{\max}$, is negative for $\Delta < 0$. However, as the barrier offset is varied, there is a dramatic change in $\hat{\lambda}_{\max}$ and at $\Delta = 0$, $\hat{\lambda}_{\max} > 0$ indicating loss of dynamical stability. Hence D-bifurcation occurs at $\Delta = 0$. This type of stochastic instability is referred to in the literature as discontinuity-induced instability. This can be explained by the fact that placing a barrier at the origin prevents the system from reaching the attractor causing the system to lose stability.

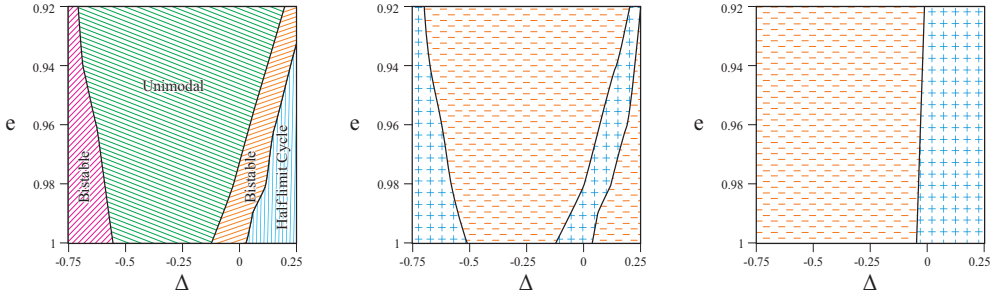

(a) (b) (c)

Figure 5. Identifying stochastic stability regimes for $c = -0.1, \sigma = 0.1$ based on (a) qualitative analysis of the joint pdf $p_{X_1 X_2}(x_1, x_2)$ (b) Shannon entropy measure estimated from the pdf of amplitude, $P_A(a)$ and (c) sign of the largest Lyapunov exponent.

Next, a global parametric study is undertaken for identifying the stability regimes in the $\Delta - e$ plane for the noisy DVDP vibro-impact oscillator. Figure 5(a) shows the different regimes identified based on visual inspection of the joint pdfs computed from the solution of the FP equation; this is the traditional P-bifurcation analysis based on qualitative changes in the structure of the joint pdf. Figure 5(b) shows the bifurcation diagram using the Shannon entropy definition $H(a)$ based on $p_A(a)$. Here, the regimes are demarcated based on the quantitative approach to P-bifurcation analysis. The bifurcation diagram shown in Fig. 5(c) is obtained based on D-bifurcation analysis from the computation of the LLE. The parameter space in Fig.5(a) is mainly subdivided into three different zones, the nomenclature of which is as follows: (i) half limit cycle − the only attractor is the limit cycle where one obtains large amplitude oscillations in the positive half space (due to impact) (ii) unimodal − only one attractor exists at the fixed point, characterzied by small amplitude oscillations, and (iii) bistable − both stochastic attractors - large amplitude as well as small amplitude oscillations exist simultaneously. It must be emphasised here that the boundaries of these zones do not have sharp demarcations and these are based on qualitative analysis based on

visual inspection of the joint pdf. On the other hand, Fig. 5(b) is divided into regimes based on the sign of $H(a)$; $H(a) > 0$ in the regions marked by the plus signs. It is observed that there are very close similarities between Figs.5(a) and (b). The parameter ranges where $H(a) > 0$ in Fig.5(b) correspond to regimes where the system exhibits bistability. This indicates the usefulness of the Shannon entropy approach in quantifying P-bifurcations. The demarcation of the regimes in Fig.5(c) is based on the sign of LLE. A comparison of the bifurcation diagrams in Fig. 5(c) with either Fig.5(a) or (b) clearly indicates that D- and P-bifurcations need not occur simultaneously for certain parameter ranges.

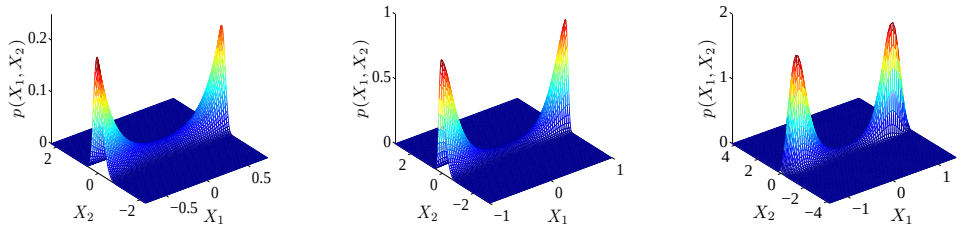

(a) (b) (c)

Figure 6. Stationary joint pdf $p_{X_1X_2}(x_1, x_2)$; $\sigma = 0.1$, $c = -0.1, e = 1$; (a) $\frac{\Delta}{2} = \pm 0.75$, (b) $\frac{\Delta}{2} = \pm 1$, (c) $\frac{\Delta}{2} = \pm 1.4$.

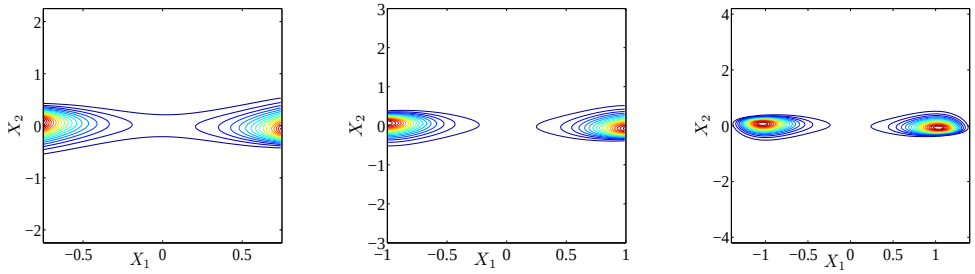

(a) (b) (c)

Figure 7. Contour plots for $p_{X_1X_2}(x_1, x_2)$; $\sigma = 0.1$, $c = -0.1, e = 1$; (a) $\frac{\Delta}{2} = \pm 0.75$, (b) $\frac{\Delta}{2} = \pm 1$, (c) $\frac{\Delta}{2} = \pm 1.4$.

Next, the numerical calculations are presented for the case when the barriers are placed symmetrically about the equilibrium position of the attractor and $\alpha = 1, \sigma = 0.1, e = 0.98$. Figures 6(a)-(c) show the j-pdf of the response variables when the distance between the barriers are 1.5, 2.0 and 2.8 respectively, while Figures 7(a)-(c) show the corresponding

contour plots. An inspection of these figures clearly indicate, that when barriers are closer to the system stable point, pdf has singular peak at both the barrier and system gains stability as barrier move away. When barrier is sufficiently apart such as case of $\frac{\Delta}{2} = \pm 1.4$, (see Figure 6(c)), the oscillator is free from any impact, and reveals the existence of two attractors. Figures 8-9 show the corresponding j-pdf of the state variables and the corresponding contour

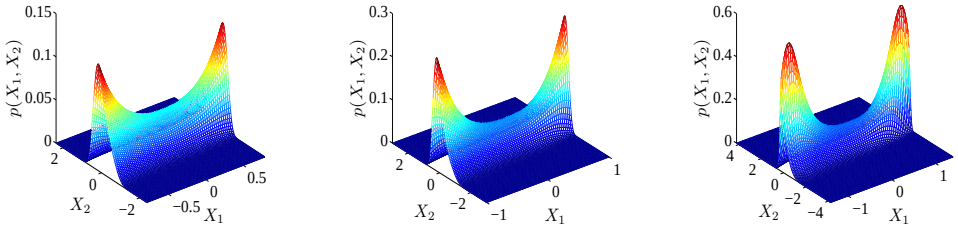

(a) (b) (c)

Figure 8. Stationary joint pdf $p_{X_1X_2}(x_1, x_2)$; $\sigma = 0.25$, $c = -0.1, e = 1$; (a) $\frac{\Delta}{2} = \pm 0.75$, (b) $\frac{\Delta}{2} = \pm 1$, (c) $\frac{\Delta}{2} = \pm 1.4$.

plots for the case $\sigma = 0.25$. A comparison of Fig. 6 with Fig. 8 reveal that as the intensity increases the two distinct attractors appear to merge together. This can be attributed to the fact that the higher energy available to the system enables it to move from the basin of attraction of one attractor to the other. Also as observed in Fig. 8 increase of noise intensity leads to decreasing its peak value while increasing the probability in the tail region significantly. Hence now even for the case of $\frac{\Delta}{2} = \pm 1.4$, system will have sufficient energy to touch both the barriers.

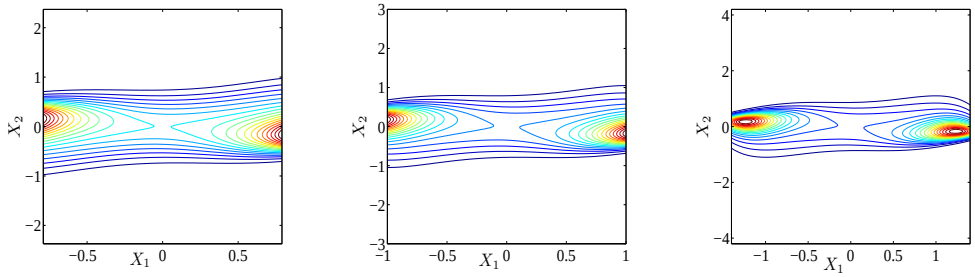

(a) (b) (c)

Figure 9. Contour plots for $p_{X_1X_2}(x_1, x_2)$; $\sigma = 0.25$, $c = -0.1, e = 1$; (a) $\frac{\Delta}{2} = \pm 0.75$, (b) $\frac{\Delta}{2} = \pm 1$, (c) $\frac{\Delta}{2} = \pm 1.4$.

4. Impact based on Hertz contact model

The DVDP oscillator with a barrier as presented by Eqs. (3) and (4) can be written equivalent to three stochastic system, which have a continuous and differential vector field defined as follows;

$$\begin{aligned}
\mathbf{f}_1: &\quad \ddot{X}-\alpha X-c\dot{X}+\beta_0 X^3-\beta_1 X^2\dot{X}+\beta_2 X^4\dot{X}+k_h(X+\frac{\Delta}{2})^{3/2}(1+c_h\dot{X})=W(t), \quad X<-\frac{\Delta}{2},\\
\mathbf{f}_2: &\quad \ddot{X}-\alpha X-c\dot{X}+\beta_0 X^3-\beta_1 X^2\dot{X}+\beta_2 X^4\dot{X}=W(t), \quad -\frac{\Delta}{2}\le X\le\frac{\Delta}{2}, \qquad (21)\\
\mathbf{f}_3: &\quad \ddot{X}-\alpha X-c\dot{X}+\beta_0 X^3-\beta_1 X^2\dot{X}+\beta_2 X^4\dot{X}+k_h(X-\frac{\Delta}{2})^{3/2}(1+c_h\dot{X})=W(t), \quad X>\frac{\Delta}{2}.
\end{aligned}$$

The response X_1, X_2 of Eqs. (21), is a Markov vector and the transitional joint pdf $p(\mathbf{X},t|\mathbf{X}_0,t_0)$, is governed by the following FP equation;

$$\begin{aligned}
\frac{\partial p}{\partial t} &= -X_2\frac{\partial p}{\partial X_1}-\frac{\partial(h(X_1,X_2)+f(X_1,X_2))p}{\partial X_2}+\frac{\sigma^2}{2}\frac{\partial^2 p}{\partial X_2^2}, \quad X<-\frac{\Delta}{2},\\
\frac{\partial p}{\partial t} &= -X_2\frac{\partial p}{\partial X_1}-\frac{\partial(h(X_1,X_2))p}{\partial X_2}+\frac{\sigma^2}{2}\frac{\partial^2 p}{\partial X_2^2}, \quad -\frac{\Delta}{2}\le X\le\frac{\Delta}{2}, \qquad (22)\\
\frac{\partial p}{\partial t} &= -X_2\frac{\partial p}{\partial X_1}-\frac{\partial(h(X_1,X_2)+f(X_1,X_2))p}{\partial X_2}+\frac{\sigma^2}{2}\frac{\partial^2 p}{\partial X_2^2}, \quad X>\frac{\Delta}{2},
\end{aligned}$$

where $h(X_1,X_2)=\alpha X_1+cX_2-\beta_0X_1^3+\beta_1X_1^2X_2-\beta_2X_1^4X_2$ and $p=p(\boldsymbol{X},t|\boldsymbol{X}^0,t_0)$, the joint transition pdf of the state variables is used for notational convenience.

4.1. Numerical Results

First, case of a single sided barrier fixed at equilibrium position at $X=0$ is considered and for $\alpha=-1,\sigma=0.1,c=-0.1$, barrier damping, c_h will be varied. Fig. 10 shows the j-pdf,for three different values of damping coefficient of damped-elastic barrier with $c_h=0.01,0.1$ and 0.5. With increasing the damping of barrier to 0.5 the LCO is completely destroyed and only one stable attractor - the fixed point at the origin, emerges, see Fig. 10(c). Hence similar to case of vibro impact, increasing the damping of barrier dissipates more energy and hence reduces the large amplitude oscillation. The topological changes in the nature of the stochastic attractor - from a stable limit cycle to a regime of bistability and subsequently the weakening and destruction of one attractor to the birth of another - is indicative of P-bifurcation.

Next, we consider bilateral impact, when $\alpha=1,\sigma=0.1,c=-0.1$. System dynamics of oscillator with bilateral barrier is completely different from that of single sided barrier. The barrier modeled on the Hertz contact model adds additional stiffness as well as damping to main oscillator. Hence depending on proximity of barrier position overall system behaviour

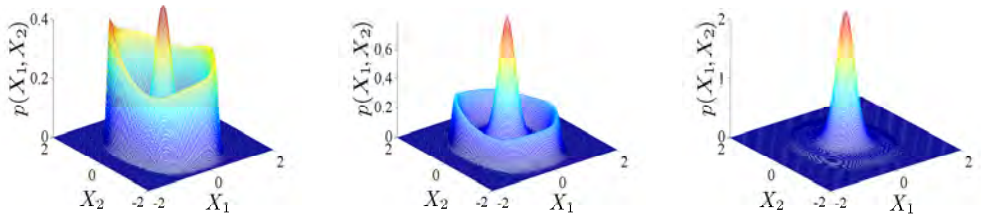

(a) $c_h = 0.1$ (b) $c_h = 0.75$ (c) $c_h = 2.5$

Figure 10. Stationary joint pdf of $p_{X_1X_2}(x_1, x_2)$ with $\Delta = 0$

is similar to barrier free DVDP oscillator of combined stiffness and damping. As shown in Fig. 11 for $\Delta = \pm 1.5$, when barrier is away from oscillator, system dynamics is similar to barrier free oscillator. For $\Delta = \pm 0.25$, when barrier is very close to oscillator, barrier stiffness and damping added with main oscillator and hence system dynamics is very much resemble to equivalent stiffness and damping of oscillator.

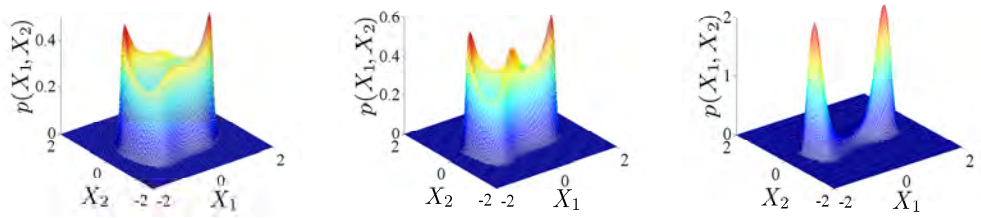

(a) $\Delta = \pm 0.25$ (b) $\Delta = \pm 0.5$ (c) $\Delta = \pm 1.5$

Figure 11. Stationary joint pdf of $p_{X_1X_2}(x_1, x_2)$ with bilateral offset.

5. Conclusions

Investigations on the stochastic bifurcations for a DVDP oscillator having hard or elastic-damped single or double sided barrier subjected to Gaussian white noise excitation has been carried out. Offset position, noise intensity, coefficient of restitution and stiffens of elastic barrier have been taken to be the control parameters. P-bifurcation analysis has been carried out by solving for the stationary probability density function of the state variables from the corresponding Fokker-Planck equation using a finite element based approach. The estimated largest Lyapunov exponents have been used for carrying out D-bifurcation analysis. The locus of the parameters at which the sign of the LLE changes indicates the dynamical stability boundaries. A newly developed quantitative measure based on the Shannon entropy associated with the amplitude process has been used to identify the onset of P-bifurcations. A global parametric study has been carried out to identify the stochastic stability regimes

based on visual inspection of the pdf of the state variables, the sign of the Shannon entropy measure and the sign of the largest Lyapunov exponent.

References

[1] Di Bernardo, M., Nordmark, A., and Olivar, G. Discontinuity-induced bifurcations of equilibria in piecewise smooth and impacting dynamical systems. *Physica D*, 119-136 (2008).

[2] Dimentberg, M., Naess, A., and Gaidai, O. Random vibrations with strongly inelastic impacts: Response pdf by pi method. *International Journal of Nonlinear Mechanics 44* (2009), 791–796.

[3] Dimentberg, M. F., and Menyailov, A. I. Response of a single mass vibro impact systems to white noise random excitation. *Journal of Applied Mathematics and Mechanics 59* (1979), 709 – 716.

[4] Ibrahim, R. A. *Vibro-Impact Dynamics Modeling, Mapping and Applications*. Springer, 2009.

[5] Ivanov, A. P. Impact oscillations: Linear theory of stability and bifurcations. *Journal of Sound and Vibrations 178*, 3 (1994), 361–378.

[6] Kumar, P., Narayanan, S., and Gupta, S. Finite element solution of fokker-planck equation of nonlinear oscillators subjected to colored non-gaussian noise. *Probabilistic Engineering Mechanics 38* (2014), 143–155.

[7] Kumar, P., Narayanan, S., and Gupta, S. Investigations on the bifurcation of a noisy duffing -van der pol oscillator. *Probabilistic Engineering Mechanics* (2015), under review.

[8] Phillis, Y. A. Entropy stability of continuous dynamic system. *International Journal of Control 35* (1982), 323 – 340.

[9] Zhuravlev, V. F. A method for analyzing vibro-impact systems by means of special functions. *Mechanics of Solids 11* (1976), 23–27.

Sayan Gupta, Ph.D.: Department of Applied Mechanics, Indian Institute of Technology Madras, Chennai 600036,India (*gupta.sayan@gmail.com*).

Pankaj Kumar, Ph.D.: Department of Mechanical Engineering, Indian Institute of Technology Madras, Chennai 600036,India (*pankajiit1@yahoo.co.in*).

Sadagopan Narayanan, Ph.D.: Indian Institute of Information Technology (Design and Manufacturing) Kancheepuram, Chennai 600127, India (*drs.narayanan@gmail.com*). The author gave a presentation of this paper during one of the conference sessions.

Study of dynamical systems by fast numerical computation of Lyapunov functions

Sigurdur Freyr Hafstein, Asgeir Valfells

Abstract: In this paper we discuss a computational method of numerically searching for Lyapunov functions for nonlinear systems and demonstrate its efficacy. The method is built upon applying various theoretical Lyapunov functions, given by integrating some specific positive functions along solution trajectories in the state space, to the vertices of a simplical complex. Then we assign the remaining values by convex interpolation over the simplices. The benefits of explicitly constructing the candidate functions in this manner are twofold. Firstly it is computationally inexpensive, growing linearly with the number of vertices we calculate a candidate function on, and secondly the freedom in choosing a positive function allows us flexibility to not be overly constrained by the shape of the attractor. Finally we will demonstrate the method on two planar examples. Most notably we will see that the constructed Lyapunov functions give us lower bounds on basins of attraction that are significantly larger than those found by other methods in the literature.

1. Introduction

Consider the dynamical system, whose dynamics are given by the ODE

$$\mathbf{x}' = \mathbf{f}(\mathbf{x}), \tag{1}$$

where $\mathbf{f} : \mathcal{D} \to \mathbb{R}^n$, $\mathcal{D} \subset \mathbb{R}^n$, is locally Lipschitz. We denote the (unique) solution to (1) with initial value $\boldsymbol{\xi} \in \mathcal{D}$ at $t = 0$ with $t \mapsto \boldsymbol{\phi}(t, \boldsymbol{\xi})$. If $\boldsymbol{\eta} \in \mathcal{D}$ is an equilibrium point for (1), i.e. $\mathbf{f}(\boldsymbol{\eta}) = \mathbf{0}$ and consequently $\boldsymbol{\phi}(t, \boldsymbol{\eta}) = \boldsymbol{\eta}$ for all $t \in \mathbb{R}$ a constant solution, its stability properties are of much practical interest. The equilibrium point $\boldsymbol{\eta}$ is said to be asymptotically stable if it is stable (in the sense of Lyapunov) and attractive. The former means that for all $\varepsilon > 0$ there exists $\delta > 0$ such that $\|\boldsymbol{\xi} - \boldsymbol{\eta}\| < \delta$ implies $\|\boldsymbol{\phi}(t, \boldsymbol{\xi}) - \boldsymbol{\eta}\| < \varepsilon$ for all $t \geq 0$ and the latter denotes that there exists a neighbourhood $\mathcal{N}_{\boldsymbol{\eta}}$ of $\boldsymbol{\eta}$ such that $\boldsymbol{\xi} \in \mathcal{N}_{\boldsymbol{\eta}}$ implies $\lim_{t\to\infty} \|\boldsymbol{\phi}(t, \boldsymbol{\xi}) - \boldsymbol{\eta}\| = 0$. The set of all points that are attracted to the asymptotically stable equilibrium $\boldsymbol{\eta}$ as $t \to \infty$, i.e. the largest possible $\mathcal{N}_{\boldsymbol{\eta}}$, is called its *basin of attraction* and its spatial extension is a measure of the robustness of the equilibrium's stability.

Stability of equilibrium points and basins of attraction are concepts of fundamental relevance in applications of dynamical systems. They are usually dealt with using the Lyapunov

stability theory. Some good references are [12, 16, 18]. The centerpiece of the Lyapunov stability theory is the so-called Lyapunov function, a scalar-valued function from the state-space of the dynamical system that is decreasing along all solutions of the system in a neighbourhood of the equilibrium in question. Lyapunov functions deliver lower bounds on basins of attraction through their sublevel sets and for linear systems $\mathbf{x}' = A\mathbf{x}$ they can be constructed explicitly using algebraic methods. For nonlinear systems there is no general method, but one can resort to linearization around the equilibrium in question and construct a Lyapunov function for the linearization. This Lyapunov function is also a Lyapunov function for the nonlinear system in a neighbourhood of the equilibrium, but it is not a good Lyapunov function in the sense that it does in general deliver very conservative lower bounds on the equilibrium's basin of attraction. For exact formulas see, e.g. [9].

2. Method to Compute Lyapunov Functions

For the reasons discussed in the last section there have been numerous methods proposed in the literature to generate Lyapunov functions for nonlinear systems [8]. One approach is to approximate numerically formulas for Lyapunov functions [1, 4, 5, 10] from classical converse theorems [11, 14, 19] in the Lyapunov stability theory. These converse theorems assert the existence of Lyapunov functions for systems with asymptotically stable equilibria and give formulas, in terms of the systems's solution, for these Lyapunov functions. Because these formulas include solutions to the systems, that are in general not obtainable for nonlinear systems, one resorts to approximate their values at a finite number of points. The Lyapunov function must be decreasing along solution trajectories in a whole neighbourhood of the equilibrium in question. If this cannot be asserted the constructed (Lyapunov) function is of little use, i.e. an approximation to a Lyapunov function is of little value. Therefore the computed values must be interpolated such that the resulting function is a Lyapunov function in a whole area. This can be achieved by using the linear programming (LP) problem from [7], but instead of using LP to compute the values of the Lyapunov function at the vertices of a simplicial complex, one uses a formula from a converse theorem to assign values at the vertices and then verifies if the linear constraints of the LP problem are fulfilled using these values. If the linear constraints are fulfilled for all vertices of a certain simplex, then the affine interpolation of these values over the simplex defines a function, whose orbital derivative is negative along all solution trajectories passing through this simplex. This was already shown in [1].

We improve this method in two ways. First, we incorporate sharper error estimates in the next section for the LP problem from [7], which leads to less conservative conditions in its linear constraints. Second, we tune the positive definite function in an integral formula

from [14] to enlarge the lower bound on the basin of attraction, i.e. we approximate the Lyapunov function

$$V(\mathbf{x}) = \int_0^T \frac{\|\boldsymbol{\phi}(\tau, \mathbf{x})\|^2}{\delta + \|\boldsymbol{\phi}(\tau, \mathbf{x})\|^p} d\tau \tag{2}$$

for some appropriately chosen $T, \delta, p > 0$ at the vertices, instead of using

$$V(\mathbf{x}) = \int_0^T \|\boldsymbol{\phi}(\tau, \mathbf{x})\|^2 d\tau. \tag{3}$$

3. Sharper Error Bounds

The error bounds in the LP problem form [7, Def. 6] that served as basis for the constructions in [1, 10] can be sharpened using more regular triangulations and results from [13]. Further, the statement of the essential part of the LP problem can be considerably simplified.

To achieve this the linear constraints LC4 from [13] must first be rewritten in the notation of [7]. Denote by Sym_n the set of the permutations of $\{1:n\} := \{1, 2, \ldots, n\}$, by $\mathfrak{P}(\{1:n\})$ the powerset of $\{1:n\}$, and set $\mathcal{Z} := \mathbb{N}_0^n \times \mathfrak{P}(\{1:n\})$. Let Γ and $\mathrm{PS_i}$, $i = 1:n$, be strictly increasing functions $\mathbb{R} \to \mathbb{R}$ that vanish at zero and define $\mathbf{PS} : \mathbb{R}^n \to \mathbb{R}^n$, $\mathbf{PS} = (\mathrm{PS}_1, \mathrm{PS}_1, \ldots, \mathrm{PS_n})^\top$. Define $\mathbf{R}^{\mathcal{J}}(\mathbf{x}) = \sum_{i=1}^n (-1)^{\chi(i)} x_i \mathbf{e}_i$ for every $\mathcal{J} \in \mathfrak{P}(\{1:n\})$,

$$\mathbf{x}_i^\sigma := \sum_{j=i}^n \mathbf{e}_{\sigma(j)} \quad \text{for every } \sigma \in \mathrm{Sym}_n \text{ and every } i = 1:n+1, \text{ and} \tag{4}$$

$$\mathbf{y}_{\sigma,i}^{(\mathbf{z},\mathcal{J})} := \mathbf{PS}(\mathbf{R}^{\mathcal{J}}(\mathbf{z} + \mathbf{x}_i^\sigma)) \quad \text{for every } (\mathbf{z}, \mathcal{J}) \in \mathcal{Z}, \text{ every } \sigma \in \mathrm{Sym}_n \text{ and every } i = 1:n+1.$$

Assume that the components of $\mathbf{f}$ in the system (1) are C^2 and let $B_{rs}^{(\mathbf{z},\mathcal{J})}$ for every $(\mathbf{z}, \mathcal{J}) \in \mathcal{Z}$ and $r, s = 1:n$ be a constant fulfilling

$$B_{rs}^{(\mathbf{z},\mathcal{J})} \geq \max_{\substack{\mathbf{x} \in \mathbf{PS}(\mathbf{R}^{\mathcal{J}}(\mathbf{z}+[0,1]^n)) \\ k=1:n}} \left| \frac{\partial^2 f_k(\mathbf{x})}{\partial x_r \partial x_s} \right| \tag{5}$$

For every $(\mathbf{z}, \mathcal{J}) \in \mathcal{Z}$, every $k, i = 1:n$, and every $\sigma \in \mathrm{Sym}_n$, define

$$A_{\sigma,k,i}^{(\mathbf{z},\mathcal{J})} := |\mathbf{e}_k \cdot (\mathbf{y}_{\sigma,i}^{(\mathbf{z},\mathcal{J})} - \mathbf{y}_{\sigma,n+1}^{(\mathbf{z},\mathcal{J})})|. \tag{6}$$

The constraints LC4 from [13] can now be written as: For every $(\mathbf{z}, \mathcal{J}) \in \mathcal{Z}$, every $\sigma \in \mathrm{Sym}_n$, and every $i = 1:n+1$:

$$\begin{aligned} -\Gamma[\|\mathbf{y}_{\sigma,i}^{(\mathbf{z},\mathcal{J})}\|] \geq \sum_{j=1}^n \frac{V[\mathbf{y}_{\sigma,j}^{(\mathbf{z},\mathcal{J})}] - V[\mathbf{y}_{\sigma,j+1}^{(\mathbf{z},\mathcal{J})}]}{\mathbf{e}_{\sigma(j)} \cdot (\mathbf{y}_{\sigma,j}^{(\mathbf{z},\mathcal{J})} - \mathbf{y}_{\sigma,j+1}^{(\mathbf{z},\mathcal{J})})} f_{\sigma(j)}(\mathbf{y}_{\sigma,i}^{(\mathbf{z},\mathcal{J})}) \\ + \frac{1}{2} \sum_{r,s=1}^n B_{rs}^{(\mathbf{z},\mathcal{J})} A_{\sigma,r,i}^{(\mathbf{z},\mathcal{J})} (A_{\sigma,s,i}^{(\mathbf{z},\mathcal{J})} + A_{\sigma,s,1}^{(\mathbf{z},\mathcal{J})}) \sum_{j=1}^n \left| \frac{V[\mathbf{y}_{\sigma,j}^{(\mathbf{z},\mathcal{J})}] - V[\mathbf{y}_{\sigma,j+1}^{(\mathbf{z},\mathcal{J})}]}{\mathbf{e}_{\sigma(j)} \cdot (\mathbf{y}_{\sigma,j}^{(\mathbf{z},\mathcal{J})} - \mathbf{y}_{\sigma,j+1}^{(\mathbf{z},\mathcal{J})})} \right| \end{aligned} \tag{7}$$

In [13] the vectors

$$\mathbf{x}_i^{\mathbf{z}\mathcal{J}\sigma} := \mathbf{R}^{\mathcal{J}}\left(\mathbf{z} + \sum_{j=1}^{i} \mathbf{e}_{\sigma(j)}\right) \quad \text{for } i = 0 : n \text{ are used.} \tag{8}$$

The relationship between the (4) and (8) is with $\mathbf{1} := \mathbf{e}_1 + \mathbf{e}_2 + \ldots + \mathbf{e}_n$ that

$$\mathbf{x}_{i-1}^{\mathbf{z}\mathcal{J}\sigma} + \mathbf{y}_{\sigma,i}^{(\mathbf{z},\mathcal{J})} = \mathbf{PS}(\mathbf{R}^{\mathcal{J}}(\mathbf{z})) + \mathbf{PS}(\mathbf{R}^{\mathcal{J}}(\mathbf{z}+\mathbf{1})) \tag{9}$$

for every $(\mathbf{z}, \mathcal{J}) \in \mathcal{Z}$, every $\sigma \in \mathrm{Sym}_n$, and every $i = 1 : n+1$. Thus with $\alpha \in \mathrm{Sym}_n$ defined through $\alpha(i) = \sigma(n+1-i)$ for $i = 1 : n$, we have $\sigma(i) = \alpha(n+1-i)$ and $\mathbf{y}_{\sigma,i}^{(\mathbf{z},\mathcal{J})} = \mathbf{x}_{n+1-i}^{\mathbf{z}\mathcal{J}\alpha}$. Hence, from (6)

$$A_{\sigma,k,i}^{(\mathbf{z},\mathcal{J})} = |\mathbf{e}_k \cdot (\mathbf{y}_{\sigma,i}^{(\mathbf{z},\mathcal{J})} - \mathbf{y}_{\sigma,n+1}^{(\mathbf{z},\mathcal{J})})| = |\mathbf{e}_k \cdot (\mathbf{x}_{n+1-i}^{\mathbf{z}\mathcal{J}\alpha} - \mathbf{x}_0^{\mathbf{z}\mathcal{J}\alpha})| =: A_{k,n+1-i}^{\mathbf{z}\mathcal{J}\alpha}$$

and (7) can be rewritten as

$$\begin{aligned} -\Gamma[\|\mathbf{x}_{n+1-i}^{\mathbf{z}\mathcal{J}\alpha}\|] \geq \sum_{j=1}^{n} \frac{V[\mathbf{x}_{n+1-j}^{\mathbf{z}\mathcal{J}\alpha}] - V[\mathbf{x}_{n-j}^{\mathbf{z}\mathcal{J}\alpha}]}{\mathbf{e}_{\alpha(n+1-j)} \cdot (\mathbf{x}_{n+1-j}^{\mathbf{z}\mathcal{J}\alpha} - \mathbf{x}_{n-j}^{\mathbf{z}\mathcal{J}\alpha})} f_{\alpha(n+1-j)}(\mathbf{x}_{n+1-i}^{\mathbf{z}\mathcal{J}\alpha}) \\ + \frac{1}{2} \sum_{r,s=1}^{n} B_{rs}^{(\mathbf{z},\mathcal{J})} A_{r,n+1-i}^{\mathbf{z}\mathcal{J}\alpha} (A_{s,n+1-i}^{\mathbf{z}\mathcal{J}\alpha} + A_{s,n}^{\mathbf{z}\mathcal{J}\alpha}) \sum_{j=1}^{n} \left| \frac{V[\mathbf{x}_{n+1-j}^{\mathbf{z}\mathcal{J}\alpha}] - V[\mathbf{x}_{n-j}^{\mathbf{z}\mathcal{J}\alpha}]}{\mathbf{e}_{\alpha(n+1-j)} \cdot (\mathbf{x}_{n+1-j}^{\mathbf{z}\mathcal{J}\alpha} - \mathbf{x}_{n-j}^{\mathbf{z}\mathcal{J}\alpha})} \right|. \end{aligned}$$

Thus by renaming $i \leftarrow n+1-i$ and $\sigma \leftarrow \alpha$, the linear constraints LC4 from [13] in (7) are fulfilled, if and only if for every $(\mathbf{z}, \mathcal{J}) \in \mathcal{Z}$, every $\sigma \in \mathrm{Sym}_n$, and every $i = 0 : n$, we have

$$\begin{aligned} -\Gamma[\|\mathbf{x}_i^{\mathbf{z}\mathcal{J}\sigma}\|] \geq \sum_{j=1}^{n} \frac{V[\mathbf{x}_j^{\mathbf{z}\mathcal{J}\sigma}] - V[\mathbf{x}_{j-1}^{\mathbf{z}\mathcal{J}\sigma}]}{\mathbf{e}_{\sigma(j)} \cdot (\mathbf{x}_j^{\mathbf{z}\mathcal{J}\sigma} - \mathbf{x}_{j-1}^{\mathbf{z}\mathcal{J}\sigma})} f_{\sigma(j)}(\mathbf{x}_i^{\mathbf{z}\mathcal{J}\sigma}) \\ + \frac{1}{2} \sum_{r,s=1}^{n} B_{rs}^{(\mathbf{z},\mathcal{J})} A_{r,i}^{\mathbf{z}\mathcal{J}\sigma} (A_{s,i}^{\mathbf{z}\mathcal{J}\sigma} + A_{s,n}^{\mathbf{z}\mathcal{J}\sigma}) \sum_{j=1}^{n} \left| \frac{V[\mathbf{x}_j^{\mathbf{z}\mathcal{J}\sigma}] - V[\mathbf{x}_{j-1}^{\mathbf{z}\mathcal{J}\sigma}]}{\mathbf{e}_{\sigma(j)} \cdot (\mathbf{x}_j^{\mathbf{z}\mathcal{J}\sigma} - \mathbf{x}_{j-1}^{\mathbf{z}\mathcal{J}\sigma})} \right|. \end{aligned} \tag{10}$$

We now show the connection between (10) and the statement of the constraints using the gradient of the Lyapunov function ∇V as in [7, Def. 6]. The so-called shape-matrix $X_{\mathbf{z}\mathcal{J}\sigma}$ of the simplex $\mathfrak{S}_{\mathbf{z}\mathcal{J}\sigma} := \mathrm{co}\left(\mathbf{x}_0^{\mathbf{z}\mathcal{J}\sigma}, \mathbf{x}_1^{\mathbf{z}\mathcal{J}\sigma}, \ldots, \mathbf{x}_n^{\mathbf{z}\mathcal{J}\sigma}\right)$ is defined by writing the vectors $\mathbf{x}_1^{\mathbf{z}\mathcal{J}\sigma} - \mathbf{x}_0^{\mathbf{z}\mathcal{J}\sigma}, \mathbf{x}_2^{\mathbf{z}\mathcal{J}\sigma} - \mathbf{x}_0^{\mathbf{z}\mathcal{J}\sigma}, \ldots, \mathbf{x}_n^{\mathbf{z}\mathcal{J}\sigma} - \mathbf{x}_0^{\mathbf{z}\mathcal{J}\sigma}$ consecutively in its rows. For the affine function $V_{\mathbf{z}\mathcal{J}\sigma} : \mathfrak{S}_{\mathbf{z}\mathcal{J}\sigma} \to \mathbb{R}$ defined through

$$V_{\mathbf{z}\mathcal{J}\sigma}\left(\sum_{j=0}^{n} \lambda_j \mathbf{x}_j^{\mathbf{z}\mathcal{J}\sigma}\right) = \sum_{j=0}^{n} \lambda_j V[\mathbf{x}_j^{\mathbf{z}\mathcal{J}\sigma}] \tag{11}$$

for all convex combinations of the vertices of $\mathfrak{S}_{\mathbf{z}\mathcal{J}\sigma}$, it is not difficult to see that with

$$\mathbf{v}_{\mathbf{z}\mathcal{J}\sigma} := \left(V[\mathbf{x}_1^{\mathbf{z}\mathcal{J}\sigma}] - V[\mathbf{x}_0^{\mathbf{z}\mathcal{J}\sigma}],\ V[\mathbf{x}_2^{\mathbf{z}\mathcal{J}\sigma}] - V[\mathbf{x}_0^{\mathbf{z}\mathcal{J}\sigma}], \ldots,\ V[\mathbf{x}_n^{\mathbf{z}\mathcal{J}\sigma}] - V[\mathbf{x}_0^{\mathbf{z}\mathcal{J}\sigma}]\right)^{\top}$$

we have

$$V_{\mathbf{z}\mathcal{J}\sigma}(\mathbf{x}) = (X^{-1}_{\mathbf{z}\mathcal{J}\sigma}\mathbf{v}_{\mathbf{z}\mathcal{J}\sigma})\cdot(\mathbf{x}-\mathbf{x}_0^{\mathbf{z}\mathcal{J}\sigma}) + V[\mathbf{x}_0^{\mathbf{z}\mathcal{J}\sigma}] = \mathbf{v}^\top_{\mathbf{z}\mathcal{J}\sigma}X^{-T}_{\mathbf{z}\mathcal{J}\sigma}(\mathbf{x}-\mathbf{x}_0^{\mathbf{z}\mathcal{J}\sigma}) + V[\mathbf{x}_0^{\mathbf{z}\mathcal{J}\sigma}] \quad (12)$$

for all $\mathbf{x} \in \mathfrak{S}_{\mathbf{z}\mathcal{J}\sigma}$. This is a simple consequence of the fact that (11) and (12) are affine functions with identical values at the vertices of $\mathfrak{S}_{\mathbf{z}\mathcal{J}\sigma}$. Thus the gradient of $V_{\mathbf{z}\mathcal{J}\sigma}$ is given by (the column vector) $\nabla V_{\mathbf{z}\mathcal{J}\sigma} := X^{-1}_{\mathbf{z}\mathcal{J}\sigma}\mathbf{v}_{\mathbf{z}\mathcal{J}\sigma}$. The linear constraints in [7, Def. 6] corresponding to (10), but for more general triangulations than discussed here, can be formulated as

$$-\Gamma[\|\mathbf{x}_i^{\mathbf{z}\mathcal{J}\sigma}\|] \geq \nabla V_{\mathbf{z}\mathcal{J}\sigma}\cdot\mathbf{f}(\mathbf{x}_i^{\mathbf{z}\mathcal{J}\sigma}) + E^{\mathbf{z}\mathcal{J}\sigma}\|\nabla V_{\mathbf{z}\mathcal{J}\sigma}\|_1, \quad (13)$$

where $E^{\mathbf{z}\mathcal{J}\sigma}$ is a simplex-dependent error bound.

To shorten formulas in the following computations we fix the simplex $\mathfrak{S}_{\mathbf{z}\mathcal{J}\sigma}$ and thus $\mathbf{z}$, $\mathcal{J}$, and σ and set $X := X_{\mathbf{z}\mathcal{J}\sigma}$. It is not difficult to see that $X = LSP$, where $S := \operatorname{diag}(s_1, s_2, \ldots, s_n)$ is a diagonal matrix with $s_i = \mathbf{PS}(\mathbf{R}^{\mathcal{J}}(\mathbf{z}+\mathbf{e}_i)) - \mathbf{PS}(\mathbf{R}^{\mathcal{J}}(\mathbf{z}))$,

$$L = \begin{pmatrix} 1 & 0 & \cdots & 0 \\ 1 & 1 & \cdots & 0 \\ \vdots & \vdots & \ddots & \vdots \\ 1 & 1 & \cdots & 1 \end{pmatrix} \quad \text{with} \quad L^{-1} = \begin{pmatrix} 1 & 0 & 0 & \cdots & 0 & 0 \\ -1 & 1 & 0 & \cdots & 0 & 0 \\ 0 & -1 & 1 & \cdots & 0 & 0 \\ \vdots & \vdots & \vdots & \ddots & \vdots & \vdots \\ 0 & 0 & 0 & \cdots & -1 & 1 \end{pmatrix}, \quad (14)$$

is a lower-triangular matrix $L_{ij} = 1$ if $i \geq j$, and P is a permutation matrix, $\mathbf{e}_i^\top P = \mathbf{e}^\top_{\sigma(i)}$ for $i = 1:n$. Especially $P^{-1} = P^\top$. Now set $\mathbf{x}_i := \mathbf{x}_i^{\mathbf{z}\mathcal{J}\sigma}$, $V_i := V[\mathbf{x}_i]$, $\nabla V := \nabla V_{\mathbf{z}\mathcal{J}\sigma}$, and $\mathbf{v} := (V_1 - V_0, V_2 - V_0, \ldots, V_n - V_0)^\top = \mathbf{v}_{\mathbf{z}\mathcal{J}\sigma}$ and note that

$$\begin{aligned}
\nabla V\cdot\mathbf{f}(\mathbf{x}_i) = \mathbf{v}^\top X^{-T}\mathbf{f}(\mathbf{x}_i) &= \left(\mathbf{v}^\top X^{-\top}\mathbf{f}(\mathbf{x}_i)\right)^\top = \mathbf{f}(\mathbf{x}_i)^\top X^{-1}\mathbf{v} = \mathbf{f}(\mathbf{x}_i)^\top P^\top S^{-1}L^{-1}\mathbf{v} \\
&= \mathbf{f}(\mathbf{x}_i)^\top P^\top S^{-1}L^{-1}\begin{pmatrix} V_1 - V_0 \\ V_2 - V_0 \\ \vdots \\ V_n - V_0 \end{pmatrix} = \mathbf{f}(\mathbf{x}_i)^\top P^\top S^{-1}\begin{pmatrix} V_1 - V_0 \\ V_2 - V_1 \\ \vdots \\ V_n - V_{n-1} \end{pmatrix} \\
&= \sum_{j=1}^n \frac{V_j - V_{j-1}}{s_j}\mathbf{f}(\mathbf{x}_i)^\top P^\top\mathbf{e}_j = \sum_{j=1}^n \frac{V_j - V_{j-1}}{s_j}\left(\mathbf{e}_j^\top P\mathbf{f}(\mathbf{x}_i)\right) \\
&= \sum_{j=1}^n \frac{V_j - V_{j-1}}{s_j}\mathbf{e}^\top_{\sigma(j)}\mathbf{f}(\mathbf{x}_i) = \sum_{j=1}^n \frac{V_j - V_{j-1}}{s_j}f_{\sigma(j)}(\mathbf{x}_i).
\end{aligned}$$

This implies that in our setting (10) is equivalent to (13) and we can replace the error bound $E^{\mathbf{z}\mathcal{J}\sigma}$ in [7, Def. 6] with the sharper estimate from (10):

$$\frac{1}{2}\sum_{r,s=1}^n B_{rs}^{(\mathbf{z},\mathcal{J})}A_{r,i}^{\mathbf{z}\mathcal{J}\sigma}(A_{s,i}^{\mathbf{z}\mathcal{J}\sigma} + A_{s,n}^{\mathbf{z}\mathcal{J}\sigma}), \quad \text{which is always} \leq E^{\mathbf{z}\mathcal{J}\sigma}. \quad (15)$$

Remark 1: Notionally it is often more convenient to suppress the dependance on $\mathbf{z}\mathcal{J}\sigma$ and just refer to a simplex $\mathfrak{S}_\nu$ rather than $\mathfrak{S}_{\mathbf{z}\mathcal{J}\sigma}$. When using this simplified notation one then refers to B^ν_{rs} and not $B^{(\mathbf{z},\mathcal{J})}_{rs}$ for all simplices $\mathfrak{S}_\nu$ such that $\mathfrak{S}_\nu \subset \mathbf{PS}(\mathbf{R}^{\mathcal{J}}(\mathbf{z}+[0,1]^n))$, and it is not difficult to see that one can use different estimates B^ν_{rs} for the different $\mathfrak{S}_\nu \subset \mathbf{PS}(\mathbf{R}^{\mathcal{J}}(\mathbf{z}+[0,1]^n))$, although this hardly justifies the effort.

Remark 2: From the decomposition $X = LSP$ one can easily derive concrete upper bounds on some matrix norms of $X^{-1} = X^{-1} = P^T S^{-1} L^{-1}$. For any matrix norm induced by a vector norm we have $\|X^{-1}\| \le \|P^T\|\,\|S^{-1}\|\,\|\mathrm{L}^{-1}\|$. For $\|\cdot\| = \|\cdot\|_1$ and $\|\cdot\| = \|\cdot\|_\infty$ one can easily see from (14) that for $n \ge 2$ we have

$$\|L^{-1}\|_1 = \|L^{-1}\|_\infty = 2,\ \|S^{-1}\|_1 = \|S^{-1}\|_\infty = \max_{i=1,2,\dots,n} |s_i|^{-1},\ \text{and}\ \|P^T\|_1 = \|P^T\|_\infty = 1.$$

It follows that $\|X^{-1}\|_1 \le 2s^*$ and $\|X^{-1}\|_\infty \le 2s^*$ with $s^* := \max_{i=1:n} |s_i|^{-1}$ and from the well known $\|X^{-1}\|_2^2 \le \|X^{-1}\|_1 \|X_\nu^{-1}\|_\infty$ it additionally follows that $\|X^{-1}\|_2 \le 2s^*$.

4. Examples

We present two examples for our method, where we approximate the Lyapunov function from (2) at the grid points with some appropriately chosen $T, \delta, p > 0$. Then we interpolate and verify the negativity of the orbital derivative of the interpolation as in [1], but use the sharper error estimate (15) in the LP program. Note that the orbital derivative of the Lyapunov functions computed by our method is not guarantied to be negative very close to the equilibrium. This is a known feature of the method, that can, however, be easily accounted for by using a local Lyapunov function for the linearized system at the equilibirum to assert its local stability.

We compare our results with the Massera construction from [1], i.e. where the Lyapunov function is approximated using (3) at the vertices, and to two other approaches suggested in the literature. The computations were programmed in C++ and run on a PC with an i9-7900X processor.

4.1. Example 1

The first example is a planar system from [6, Ex. 6],

$$\mathbf{x}' = \mathbf{f}(\mathbf{x}) \ \text{ with } \ \mathbf{f}(x,y) = \begin{pmatrix} -x+y \\ 0.1x - 2y - x^2 - 0.1x^3 \end{pmatrix}. \tag{16}$$

We assign in the LP problem (notation from Remark 1 in Section 3)

$$B^\nu_{1,1} = 2 + 0.6 \max_{(x,y)\in\mathfrak{S}_\nu} |x| \quad \text{and} \quad B^\nu_{1,2} = B^\nu_{2,1} = B^\nu_{2,2} = 0.$$

We set $T = 20$ for (3) and (2) and for the latter we set $\delta = 0.6$, and $p = 0.6$. The grid used for the vertices of the simplices was 2001×2001 with 4,004,001 points and 8,000,000 simplices/triangles. This corresponds to using the simplices $\mathfrak{S}_{\mathbf{z}\mathcal{J}\sigma}$ for $\mathbf{z} \in \{0 : 999\}^2$, $\mathcal{J} \in \{\emptyset, \{1\}, \{2\}, \{1, 2\}\}$, and $\sigma \in \{(1, 2), (2, 1)\}$ in the notation of Section 3. The computation of the Lyapunov function using (3) was done on the rectangle $[-20, 20]^2$, i.e. the mapping **PS** from Section 3 is given by $\mathbf{PS}(\mathbf{x}) = 0.02\mathbf{x}$ (because $0.02 \cdot 1000 = 20$). The computation took 43.6 s and the verification of the negativity of the orbital derivative took 0.45s. In 11.96% of the triangles/simplices the orbital derivative was not negative. For the computation using (2) on the rectangle $[-20, 20] \times [-40, 40]$, i.e. $\mathbf{PS}(x, y) = (0.02x, 0.04y)^\top$, the corresponding runtimes were 51.8 s and 0.45 s. In 10.05% of the triangles/simplices the orbital derivative was not negative. In Figure 1 the Lyapunov functions using formulas (3) and (2) respectively are plotted. In Figure 2 the level sets $\{\mathbf{x} \in \mathbb{R}^2 : V(\mathbf{x}) \leq 33\}$ and $\{\mathbf{x} \in \mathbb{R}^2 : V(\mathbf{x}) \leq 9\}$ for these functions respectively are plotted. These level sets are chosen such that they do not intersect with the areas where the orbital derivative is nonnegative and thus give lower bounds on the basin of attraction.

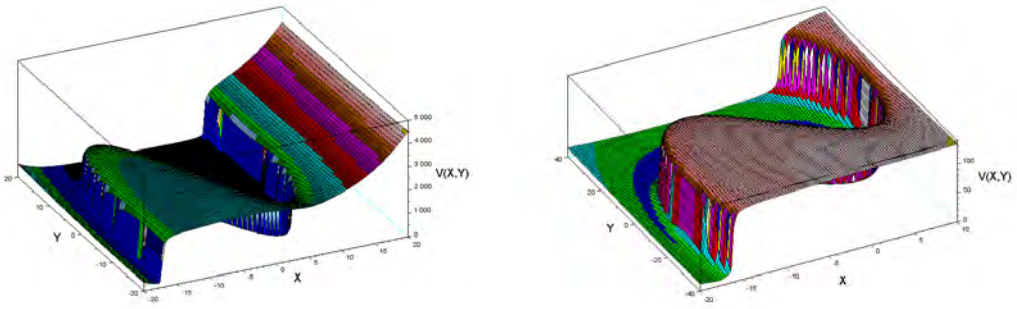

Figure 1. The Lyapunov functions computed for system (16) using formula (3) [left] and formula (2) [right].

In Figure 3 we compare our results with the approach from [17] as implemented in [15], where a rational Lyapunov function is computed for the same system, and to the method presented in [3], where Lyapunov functions that are sums of squared polynomials (SOS) are computed. The software SMRSOFT from [3] was downloaded and used for the computations. We computed 4th, 6th, and 8th order polynomial Lyapunov functions, but only draw the level set for the 4th order one, because it delivered the least conservative estimate. It is notable, that even though this method delivers a much smaller estimate of the basin of

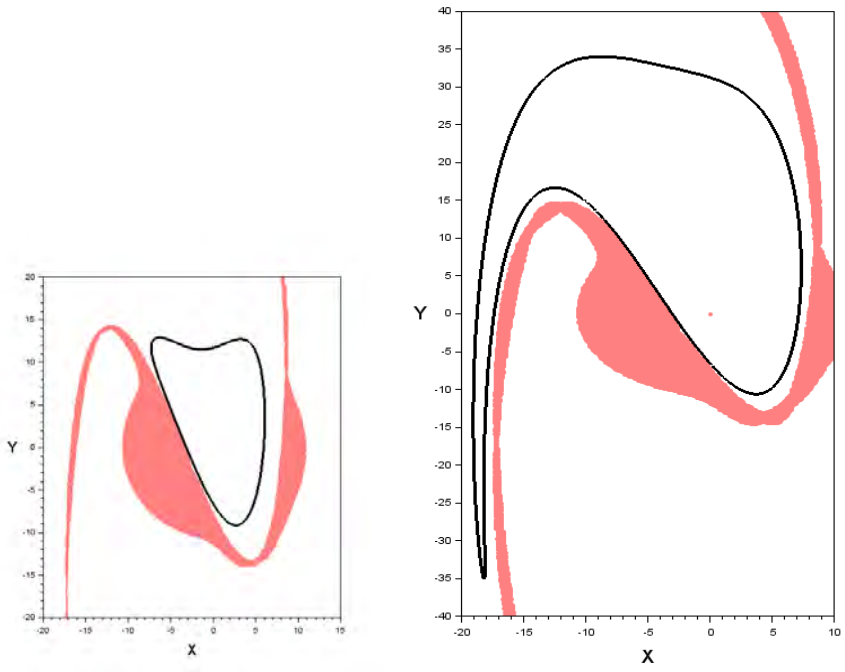

Figure 2. Level-sets of the Lyapunov functions computed for the system (16) using formula (3) [left] and (2) [right]. The area where the orbital derivative is not negative is drawn in red. Since the level-sets do not intersect the area where the orbital derivative is nonnegative they are lower bounds on the basin of attraction of the equilibrium at the origin.

attraction, it is not a proper subset of our estimates.

4.2. Example 2

The second example is a planar system from [2, Ex. 1],

$$\mathbf{x}' = \mathbf{f}(\mathbf{x}) \quad \text{with} \quad \mathbf{f}(x,y) = \begin{pmatrix} -x + y + \frac{1}{2}(e^x - 1) \\ -x - y + xy + x\cos(x) \end{pmatrix}. \tag{17}$$

We assign

$$B^{\nu}_{1,1} = \max_{(x,y)\in\mathbb{S}_\nu} \max(e^x/2, 2|\sin(x)| + |x\cos(x)|), \quad B^{\nu}_{1,2} = B^{\nu}_{2,1} = 1, \quad \text{and} \quad B^{\nu}_{2,2} = 0.$$

Further, we set $T = 20$ for (3) and (2) and for latter we set $\delta = 0.4$, and $p = 0.3$. As in Example 1 the grid was 2001×2001 with 4,004,001 points and 8,000,000 simplices/triangles. The computation of the Lyapunov function using (3) was done on the rectangle $[-8, 4] \times$

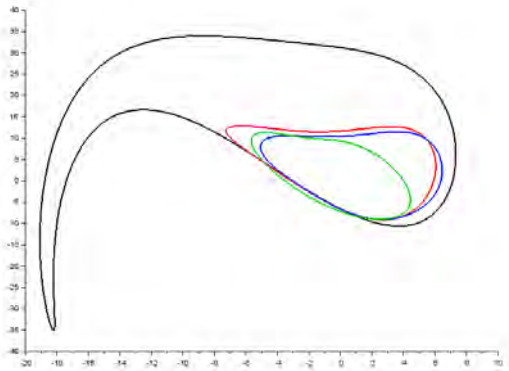

Figure 3. Level-sets of the Lyapunov functions computed for the system (16) using formula (2) (outermost, black), (3) (red), the method from [15, 17] (blue), and using the software SMRSOFT [3] (green).

$[-8, 8]$ and took 35.6 s and the verification of the negativity of the orbital derivative took 0.4 s. In 27.9% of the triangles/simplices the orbital derivative was not negative. In most of the area where the orbital derivative was not negative the Lyapunov function was not defined because the initial-value problems diverge too fast on the interval $[0, T]$ for the numerical solver.

For the computation using (2) on the rectangle $[-8, 3] \times [-10, 10]$ the corresponding numbers were 45.2 s and 0.4 s. In 23.4% of the triangles/simplices the orbital derivative was not negative, also mostly because the numerical solver was not able to assign values to the Lyapunov function at the grid points.

In Figure 4 the Lyapunov functions using formulas (3) and (2) respectively are plotted. In Figure 5 the level sets $\{\mathbf{x} \in \mathbb{R}^2 : V(\mathbf{x}) \leq 8\}$ and $\{\mathbf{x} \in \mathbb{R}^2 : V(\mathbf{x}) \leq 5.9\}$ for these functions are plotted. These level sets are chosen such that they do not intersect with the ares where the orbital derivative is nonnegative and thus give lower bounds on the basin of attraction.

In Figure 6 we compare our results with the approach from [17] as implemented in [15], where a rational Lyapunov function is computed for the same system. We also compared it with the method from [2], but the level sets obtained are very close to the ones from [15] and we omit drawing them.

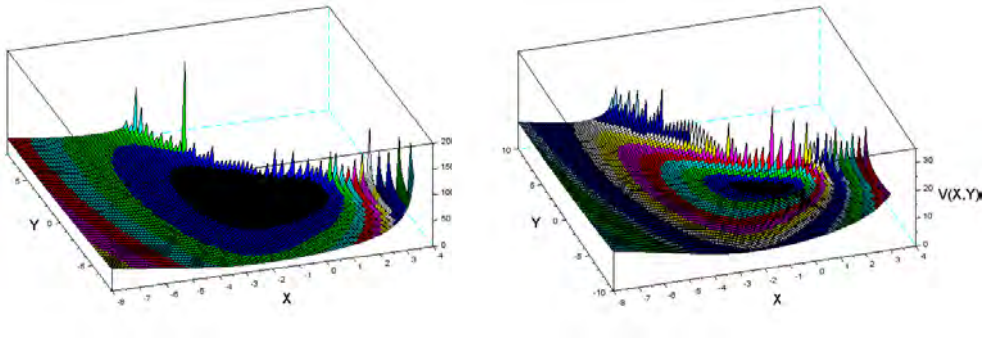

Figure 4. The Lyapunov functions computed for system (17) using formula (3) [left] and formula (2) [right].

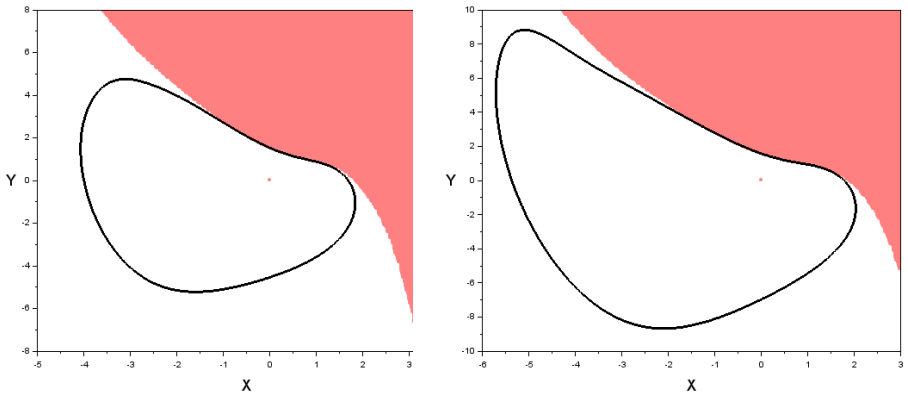

Figure 5. Level-sets of the Lyapunov functions computed for the system (17) using formula (3) [left] and (2) [right]. The area where the orbital derivative is not negative is drawn in red. Since the level-sets do not intersect the area where the orbital derivative is nonnegative they are lower bounds on the basin of attraction of the equilibrium at the origin.

5. Conclusions

We presented an improved method to estimate the basin of attraction for equilibria of dynamical systems. The method is based on approximating the values of Lyapunov functions from converse theorems and assign these values to the variables of a linear programming problem. The linear constraints of the problem are then verified and in simplices, of which they are fulfilled at all vertices, the function defined by interpolating these values over the simplex has a negative orbital derivative along the solutions of the system. Our method is an advancement of the method presented in [1], but with sharper error estimates and thus less

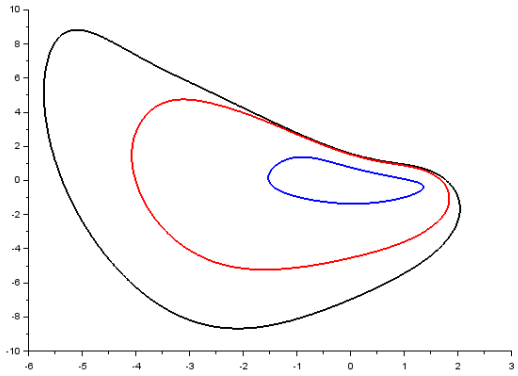

Figure 6. Level-sets of the Lyapunov functions computed for the system (17) using formula (2) (outermost, black), (3) (middle, red), and by using the method from [15, 17] (innermost, blue). In [2] results very close to the ones from [15,17] are obtained using SOS programming.

conservative linear constraints and a more general positive definite function of the solution under the integral in the Massera construction. We compared our novel method for two systems with the method from [1] and two other approaches from the literature; one using rational Lyapunov functions [15,17] and another using sum-of-squares programming [2,3]. In all cases our method delivered considerably larger inner estimates of the basins of attraction.

References

[1] Björnsson, J., Giesl, P., Hafstein, S., Kellett, C., and Li, H. Computation of continuous and piecewise affine Lyapunov functions by numerical approximations of the Massera construction. In *Proceedings of the CDC, 53rd IEEE Conference on Decision and Control* (Los Angeles (CA), USA, 2014).

[2] Chesi, G. Estimating the domain of attraction for non-polynomial systems via LMI optimizations. *Automatica 45* (2009), 1536–1541.

[3] Chesi, G. *Domain of Attraction: Analysis and Control via SOS Programming*. Springer, 2011.

[4] Doban, A. *Stability domains computation and stabilization of nonlinear systems: implications for biological systems*. PhD thesis: Eindhoven University of Technology, 2016.

[5] Doban, A., and Lazar, M. Computation of Lyapunov functions for nonlinear differential equations via a Yoshizawa-type construction. *IFAC-PapersOnLine 49*, 18 (2016), 29 – 34. 10th {IFAC} Symposium on Nonlinear Control Systems {NOLCOS} 2016.

[6] Genesio, R., Tartaglia, M., and Vicino, A. On the estimation of asymptotic stability regions: State of the art and new proposals. *IEEE Trans. Automat. Control 30*, 8 (1985), 747–755.

[7] Giesl, P., and Hafstein, S. Revised CPA method to compute Lyapunov functions for nonlinear systems. *J. Math. Anal. Appl. 410* (2014), 292–306.

[8] Giesl, P., and Hafstein, S. Review of computational methods for Lyapunov functions. *Discrete Contin. Dyn. Syst. Ser. B 20*, 8 (2015), 2291–2331.

[9] Hafstein, S. A constructive converse Lyapunov theorem on exponential stability. *Discrete Contin. Dyn. Syst. 10*, 3 (2004), 657–678.

[10] Hafstein, S., Kellett, C., and Li, H. Computing continuous and piecewise affine Lyapunov functions for nonlinear systems . *Journal of Computational Dynamics 2*, 2 (2015), 227 – 246.

[11] Kellett, C. Converse Theorems in Lyapunov's Second Method. *Discrete Contin. Dyn. Syst. Ser. B 20*, 8 (2015), 2333–2360.

[12] Khalil, H. *Nonlinear systems*, 3. ed. Pear, 2002.

[13] Marinósson, S. Lyapunov function construction for ordinary differential equations with linear programming. *Dynamical Systems: An International Journal 17* (2002), 137–150.

[14] Massera, J. Contributions to stability theory. *Annals of Mathematics 64* (1956), 182–206. (Erratum. Annals of Mathematics, 68:202, 1958).

[15] Matallana, L., Blanco, A., and Bandoni, J. Estimation of domains of attraction: A global optimization approach. *Math. Comput. Modelling 52*, 3-4 (2010), 574–585.

[16] Sastry, S. *Nonlinear Systems: Analysis, Stability, and Control*. Springer, 1999.

[17] Vannelli, A., and Vidyasagar, M. Maximal Lyapunov functions and domains of attraction for autonomous nonlinear systems. *Automatica 21*, 1 (1985), 69–80.

[18] Vidyasagar, M. *Nonlinear System Analysis*, 2. ed. Classics in applied mathematics. SIAM, 2002.

[19] Yoshizawa, T. *Stability theory by Liapunov's second method*. Publications of the Mathematical Society of Japan, No. 9. The Mathematical Society of Japan, Tokyo, 1966.

Sigurdur Hafstein, Ph.D.: Faculty of Physical Sciences, University of Iceland, Dunhagi 5, 107 Reykjavík, Iceland (*shafstein@hi.is*).

Asgeir Valfells, : Faculty of Physical Sciences, University of Iceland, Dunhagi 5, 107 Reykjavík, Iceland (*avalfells@gmail.com*).

Energy dissipation, free and forced modes in dynamics of two classes of fractional order systems

Katica R. (Stevanović) Hedrih

Abstract: Generalized functions of fractional order dissipation of energy in the discrete system and in multi-body system with interconnections by discrete continuum fractional order layers are defined. Energy dissipations in dynamics of two analogous classes of the fractional order systems are analyzed. Fractional order modes of the free and forced oscillations in dynamics of those two analogous classes of the fractional order systems are identified as eigen independent free as well as forced fractional order modes. Also, using formulas of transformation of a system of independent generalized coordinates and eigen main coordinates of considered classes of fractional order system dynamics relation between total mechanical energy (sum of kinetic and potential energies) and generalized function of fractional order energy dissipation on one eigen main fractional order mode is derived. On the basis of these relations, two theorems of energy fractional order dissipation of a class of the fractional order system with finite number of degrees of system are defined and proofed. A number of electrical fractional order oscillators and analogous mechanical fractional order oscillators with one, two or three degrees of freedom are described. For each of these analogous system expressions of kinetic and potential energies and generalized function of total system energy dissipation are formulated with corresponding analogies and corresponding physical explanations. Corresponding analogous energy analysis for each of analogous pairs is done. A number of energy change theorems are defined.

1. Introduction

The conception of this paper is to indicate an analogy between separately published different results of energy analysis and energy dissipation of two class of different mechanical systems, by identifications of structural, qualitative and mathematical analogies between models giving in result formally same vibration phenomena in different type of vibration of fractional order system dynamics as it is discrete system with finite number of degree of freedom and multi-body fractional order system containing same number of coupled deformable bodies with standard light discrete continuum fractional order layers. Also, it is possible an identification of analogies [14, 15, 17] with some electrical circuit chains.

For that reason, for first, let's to present a number of author's previous published research results in series of the papers.

In the Refs. [5] and [6] a generalized function of creep fractional order dissipation of fractional order system total mechanical energy and generalized forces of system no ideal visco-elastic creep fractional order dissipation of system energy for generalized coordinates are introduced and defined. A theory of generalized function of visco-elastic creep fractional order dissipation of system energy is defined. In the Ref. [5], extended Lagrange differential equations second kind for fractional order system dynamics in matrix formal form are introduced. By use presented matrix method, as special case, the fractional order chain system dynamics is considered. One example of the fractional order system with two degrees of freedom as an abstraction of the real part of geared planetary system dynamics is considered and solved for special case.

In the Ref. [2] a theory of free vibrations of discrete fractional order systems with a finite number of degrees of freedom is developed. A fractional order system with a finite number of degrees of freedom is defined by means of three matrices: mass inertia, system rigidity and fractional order elements. By adopting a matrix formulation, a mathematical description of a class of fractional order discrete system free vibrations is determined in the form of coupled fractional order differential equations. The corresponding solutions in analytical form, for the special case of the matrix of fractional order properties elements, are determined and expressed as a polynomial series along time. For the eigen characteristic numbers, the system eigen main coordinates and the independent eigen fractional order modes are determined. A generalized function of viso-elastic creep fractional order dissipation of energy and generalized forces of system with no ideal visco-elastic creep fractional order dissipation of energy for generalized coordinates are formulated. Extended Lagrange fractional order differential equations of second kind, for fractional order system dynamics, are also introduced. Two examples of fractional order chain systems are analyzed and the corresponding eigen characteristic numbers determined. It is shown that the oscillatory phenomena of a fractional order mechanical chain have analogies to electrical fractional order circuits. A fractional order electrical resistor is introduced and its constitutive voltage - currency is formulated. Also, a function of thermal energy fractional order dissipation of a fractional order electrical resistor is discussed.

In the Reference [7], dynamics of multi deformable, ideal linear elastic bodies (beams, plates, membranes, belts with corresponding same boundary conditions, see Fig.1) coupled by standard light fractional order discrete continuum layers is considered by using Petrović's theory of elements of mathematical phenomenology (see Refs. [15] and [16]). The sixth chapter of Petrović's theory contain phenomenological analogies and include the mathematical and structural analogies and qualitative analogy. Starting with coupled partial fractional order differential equations along transversal displacements of the linear elastic beams, same boundary conditions, and coupled by fractional order discrete continuum layers, system of coupled ordinary fractional order differential equations along eigen time functions in each eigen amplitude functions is obtained. Independent eigen main fractional

order modes and set of characteristic numbers of the corresponding eigen time function corresponding to eigen amplitude function are obtained. Using Petrović's theory of mathematical analogy and qualitative analogy properties of eigen main fractional order modes and characteristic numbers of time functions of transversal vibrations of multi-plates as well as multi-membranes coupled by fractional order discrete continuum layers are obtained. Energy analysis in fractional order discrete continuum layer is done. Generalized function of fractional order energy dissipation in fractional order discrete continuum layer is defined.

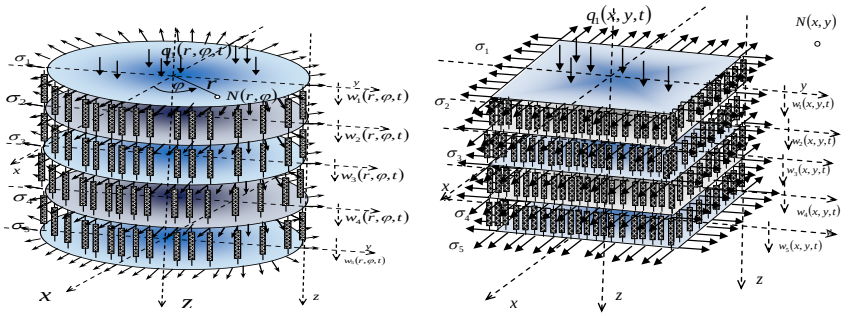

Figure 1. **Figure 1.** Models of multi membrane hybrid system: Five membranes, same contours and boundary conditions, coupled by discrete continuum fractional order layers with translator and rotator inertia properties: (a*) circular membranes; and (b*) rectangular membranes (from Reference [13]).

In the Reference [13], see Fig.1, a model of multi membrane fractional order oscillations is presented and corresponding partial fractional order differential equations are solved. A hybrid fractional order element with translator and rotator inertia properties is introduced by corresponding constitutive relations. Generalized function of fractional order energy dissipation is introduced. Generalized forces of two membrane and fractional order layer as well as of its constitutive element are expressed by energies and generalized function of fractional order energy dissipation. For obtaining solution of system of partial fractional order differential equations, it is used Euler-Bernoulli method of particular integral and transformation of the system of ordinary fractional order differential equations along eigen time functions introducing eigen main coordinates of fractional order system. In result it is obtained a system of independent ordinary fractional order differential equations each along one eigen fractional order main coordinates. Eigen fractional order main modes of an eigen tine function in each of infinite number of eigen amplitude shapes are defined. Energy analysis of the multi membrane system vibrations as well as energy analysis of eigen fractional order modes are presented.

In the Refs. [3] and [4] elements of mathematical phenomenology, and especially focused to mathematical, structural and qualitative analogies, are presented by numerous examples.

In the series of author's published References, starting from [1], and continued by [8-12] , serries of research results concerning vibrations and energy analysis in different mechanical conservative and no conservative discrete and/or discrete continuum systems, as well as in bio-dynamical systems are presented. Also, a series of theorems of mechanical energy change in dynamics of discrete fractional order system and of a multi-deformable body fractional order system are defined with corresponding proofs. Using structural, qualitative and mathematical analogies between mechanical chain system and electrical chain system the theorems of total mechanical energy change in mechanical fractional order system are presented as analogous with the theorems of total electrical energy change in electrical fractional order system. Also, see Ref. [16] by Rosikin Yuri and Maria Shitikova.

2. List of some selected earlier published theorems

Using previous published results and formulated theorems it possible to point out some of these for their use to obtain new conclusion of energy change, fractional order dissipation of energy in the system dynamics and point out some main mathematical, structural and qualitative analogies.

For that reason we made some list of selected energy change theorems:

Theorem 1: For a class of fractional order no conservative discrete system dynamics, with n degrees of freedom, determined by matrix column of independent generalized coordinates (x), and defined by: matrix of system inertia properties $\mathbf{A}=\left(a_{kj}\right)_{\rightarrow\ j=1,2,3,\ldots,n}^{\downarrow\ k=1,2,3,\ldots,n}$, matrix of system rigidity properties $\mathbf{C}=\left(c_{kj}\right)_{\rightarrow\ j=1,2,3,\ldots,n}^{\downarrow\ k=1,2,3,\ldots,n}$, matrix of system visco-elastic creep fractional order properties $\mathbf{C}_{\alpha}=\left(c_{\partial,kj}\right)_{\rightarrow\ j=1,2,3,\ldots,n}^{\downarrow\ k=1,2,3,\ldots,n}$ and matrix of system viscous-linear properties $\mathbf{B}=\left(b_{kj}\right)_{\rightarrow\ j=1,2,3,\ldots,n}^{\downarrow\ k=1,2,3,\ldots,n}$, the rate of fractional order degradation of system total mechanical energy $\mathbf{E}=\mathbf{E}_{\mathbf{k}}+\mathbf{E}_{p}$ is equal to negative sum of double classical Rayleigh function 2Φ and matrix product between velocity $(\dot{x})$ and first partial derivative $\frac{\partial\mathbf{P}_{\alpha}}{\partial\left(\mathrm{D}_{\mathrm{t}}^{\alpha}\{x\}\right)}$ of generalized function $\mathbf{P}_{\alpha}$ of fractional order energy dissipation with respect to fractional order derivative $\mathrm{D}_{t}^{\alpha}[x]$ and presented in the mathematical form:

$$\frac{d\mathbf{E}}{dt}=-2\Phi-\sum_{k=1}^{k=n}\sum_{j=1}^{j=n}\dot{x}_{k}\frac{\partial\mathbf{P}_{\alpha}}{\partial\left(\mathrm{D}_{\mathrm{t}}^{\alpha}\left[x_{j}\right]\right)},\quad for\quad \alpha\neq 0\ \text{ and }\ 0<\alpha\leq 1 \tag{1}$$

where $\mathsf{D}_t^{\alpha}[\bullet]$ is fractional order differential operator of the α^{th} derivative with respect to time t in the following form:

$$\mathsf{D}_t^{\alpha}[\bullet]=\frac{d^{\alpha}[\bullet]}{dt^{\alpha}}=\frac{1}{\Gamma(1-\alpha)}\frac{d}{dt}\int_0^t\frac{[\bullet]}{(t-\tau)^{\alpha}}d\tau \tag{2}$$

and $\Gamma(1-\alpha)$ is Euler Gama function; $\mathbf{P}_{\alpha}$ is generalized function of fractional order energy dissipation in the form:

$$\mathbf{P}_{\alpha}\left(\mathsf{D}_t^{\alpha}[x]\right)=\frac{1}{2}\left(\mathsf{D}_t^{\alpha}[x]\right)\mathbf{C}_{\alpha}\left\{\mathsf{D}_t^{\alpha}[x]\right\}=\frac{1}{2}\left(\mathsf{D}_t^{\alpha}[x]\right)\left(c_{\partial,kj}\right)_{\rightarrow\ j=1,2,3,...n}^{\downarrow\ k=1,2,3,...n}\left\{\mathsf{D}_t^{\alpha}[x]\right\} \tag{3}$$

Φ is classical Rayleigh function in the form: $\Phi(\dot{x})=\frac{1}{2}(\dot{x})\mathbf{B}\{\dot{x}\}$.

For proof of this theorem see References [2,5].

Theorem 2: For a class of fractional order no conservative discrete system dynamics, with n degrees of freedom, determined by matrix column of independent generalized coordinates (x), and defined by: matrix of inertia properties $\mathbf{A}=\left(a_{kj}\right)_{\rightarrow\ j=1,2,3,...n}^{\downarrow\ k=1,2,3,...n}$, matrix of rigidity properties $\mathbf{C}=\left(c_{kj}\right)_{\rightarrow\ j=1,2,3,...n}^{\downarrow\ k=1,2,3,...n}$, matrix of viscoelastic creep fractional order properties $\mathbf{C}_{\alpha}=\left(c_{\partial,kj}\right)_{\rightarrow\ j=1,2,3,...n}^{\downarrow\ k=1,2,3,...n}$ and matrix of viscous linear properties $\mathbf{B}=\left(b_{kj}\right)_{\rightarrow\ j=1,2,3,...n}^{\downarrow\ k=1,2,3,...n}$, with properties that both side product by modal matrix $\mathbf{R}=\left(\left\{K_{nk}^{s}\right\}\right)=\left(K_{nk}^{s}\right)_{\rightarrow\ s=1,2,3,...n}^{\downarrow\ k=1,2,3,...n}$ of corresponding linear system produce all system matrix in diagonal form: $\mathsf{A}=\mathbf{R}'\mathbf{A}\mathbf{R}=diag\left(\tilde{a}_{ss}\right)$, $\mathsf{C}=\mathbf{R}'\mathbf{C}\mathbf{R}=diag\left(\tilde{c}_{ss}\right)$, $\mathsf{B}=\mathbf{R}'\mathbf{B}\mathbf{R}=diag\left(\tilde{b}_{ss}\right)$, $\mathsf{C}_{\alpha}=\mathbf{R}'\mathbf{C}_{\alpha}\mathbf{R}=diag\left(\tilde{c}_{(\alpha)ss}\right)$, then rate of each system independent eigen main fractional order mode total mechanical energy $\mathbf{E}_s=\mathbf{E}_{kin,s}+\mathbf{E}_{pot,s}$ degradation is equal to negative sum of double Rayleigh function $2\Phi_s$ and matrix product between velocity $\dot{\xi}_s$ and first partial derivative $\frac{\partial\mathbf{P}_{\alpha}}{\partial\left(\mathsf{D}_{\mathrm{t}}^{\alpha}[\xi_s]\right)}$ of generalized function of fractional order energy dissipation with respect to fractional order derivative $\mathsf{D}_{\mathrm{t}}^{\alpha}[\xi_s]$:

$$\frac{d\mathbf{E}_s}{dt}=-2\Phi_s-\dot{\xi}_{ss}\frac{\partial\mathbf{P}_{\alpha}}{\partial\left(\mathsf{D}_{\mathrm{t}}^{\alpha}[\xi_s]\right)},\quad for\quad \alpha\neq 0,0<\alpha<1,s=1,2,3...,n, \tag{4}$$

or in the form:

$$\frac{d\mathbf{E}_s}{dt} = -2\Phi_s - \tilde{c}_{\alpha,ss}\dot{\xi}_s \mathsf{D}_t^{\alpha}[\xi_s], \quad for \quad \alpha \neq 0, 0 < \alpha \leq 1, \quad s = 1,2,3,...,n \tag{5}$$

where ξ_s, $s = 1,2,3,...,n$ eigen (main) fractional order system normal coosdinates.

Shaoes of independent eigen fractional order modes $\xi_s(t,\alpha)$, $s = 1,2,3,...,n$ for $0 \leq \alpha \leq 1$ in function of time and fractional order drivative α, graphycally are presented in References [2] and [5].

Theorem 3: For a class of fractional order no conservative discrete system dynamic, with n degrees of freedom, determined by matrux column of independent generalized coordinates (x), and defined by: matrix of inertia properties $\mathbf{A} = (a_{kj})_{\rightarrow\ j=1,2,3,...n}^{\downarrow\ k=1,2,3,...n}$, matrix of rigidity properties $\mathbf{C} = (c_{kj})_{\rightarrow\ j=1,2,3,...n}^{\downarrow\ k=1,2,3,...n}$, matrix of visco-elastic creep fractional order properties $\mathbf{C}_{\alpha} = (c_{\partial,kj})_{\rightarrow\ j=1,2,3,...n}^{\downarrow\ k=1,2,3,...n}$ and matrix of viscous linear properties $\mathbf{B} = (b_{kj})_{\rightarrow\ j=1,2,3,...n}^{\downarrow\ k=1,2,3,...n}$, with properties that both side product by modal matrix $\mathbf{R} = (\{K_{nk}^{s}\}) = (K_{nk}^{s})_{\rightarrow\ s=1,2,3,...n}^{\downarrow\ k=1,2,3,...n}$ of corresponding linear system produce all system matrix are not in no diagonal form: $\mathsf{A} = \mathbf{R}'\mathbf{A}\mathbf{R} = diag(\tilde{a}_{ss})$, $\mathsf{C} = \mathbf{R}'\mathbf{C}\mathbf{R} = diag(\tilde{c}_{ss})$, $\mathsf{B} = \mathbf{R}'\mathbf{B}\mathbf{R} \neq diag(\tilde{b}_{ss})$, $\mathsf{C}_{\alpha} \neq \mathbf{R}'\mathbf{C}_{\alpha}\mathbf{R} \neq diag(\tilde{c}_{(\alpha)ss})$,then each of the system eigen main fractional order mode, determined by coordinates ξ_s, $s = 1,2,3,...,n$ are coupled and no independent one to other.

For thise case, by use matrix formula of coordinate transformation $\{x\} = \mathbf{R}\{\xi_s\}$, following matrices $\mathsf{B} = \mathbf{R}'\mathbf{B}\mathbf{R} = (\tilde{b}_{rs})$ amd $\mathsf{C}_{\alpha} = \mathbf{R}'\mathbf{C}_{\alpha}\mathbf{R} = (\tilde{c}_{(\alpha)sk})_{\rightarrow\ s=1,2,3,...n}^{\downarrow\ k=1,2,3,...n}$ are not diagonal, and then expressions of kinetic energy, potential energy expressed by new coordinates ξ_s, $s = 1,2,...,n$ are same as in previous case defined in theorem 2. , but Rayleigh function of linear energy dissipation and generalized function of energy fractional order dissipationof energy take the following form:

$$2\Phi = (\dot{x})\mathbf{B}\{\dot{x}\} = (\dot{\xi})\mathsf{B}\{\dot{\xi}_s\} = \sum_{s=1}^{s=n}\sum_{r=1}^{s=n}\tilde{b}_{sr}\dot{\xi}_s\dot{\xi}_r = \sum_{s=1}^{s=n}\sum_{r=1}^{s=n}2\Phi_{sr} \tag{6}$$

$$2\mathbf{P}_{\alpha\neq 0} = (\mathsf{D}_t^{\alpha}\{x\})\mathbf{C}_{\alpha}\{\mathsf{D}_t^{\alpha}\{x\}\} = (\mathsf{D}_t^{\alpha}\{\xi_s\})\mathsf{C}_{\alpha}\{\mathsf{D}_t^{\alpha}\{\xi_s\}\} \tag{7}$$

$$2\mathbf{P}_{\alpha\neq 0} = \sum_{s=1}^{s=n}\sum_{r=1}^{s=n}\tilde{c}_{(\alpha)sr}\mathsf{D}_t^{\alpha}[\dot{\xi}_s]\mathsf{D}_t^{\alpha}[\dot{\xi}_r] = \sum_{s=1}^{s=n}\sum_{r=1}^{s=n}2\mathbf{P}_{\alpha\neq 0.sr}, \quad for \quad \alpha \neq 0, 0 < \alpha \leq 1 \tag{8}$$

where Φ_{sr} and $\mathbf{P}_{\alpha\neq 0.sr}$ are denotations of the term in the functions of linear and fractional order energy dissipation which are dependent of all coordinates ξ_s, $s=1,2,...,n$, and which express interactions between fractional order modes, which are not independent.

3. Main coordinates and main eigen normal fractional free and forced modes of eigen time functions of eigen amplitude shape of transversal vibrations of multi-deformable body system with discrete continuum fractional order layers

Transversal free and forced vibrations, of a hybrid multi membrane system, are analytically investigated in multi frequency vibration regimes on the basic of result obtained for corresponding structurally analogous with multi beam, as well as multi plate system transversal vibrations (for detail see Refs. [13] and [7]).

Using obtained conclusions for fractional order free as well as forced transversal vibrations of three deformable body (beam, plate or membrane) fractional order system with same contour and boundary conditions is possible on the basis analogies and generalization of these analogies between generalized coordinates of vibration of the discrete fractional order chain systems with finite number of degrees of freedom M and finite number of eigen time functions in each eigen amplitude shape function of transversal vibration of bodies in fractional order system and to write following analogies between kinetic parameters and eigen time functions in one eigen amplitude shape function describing fractional order free vibrations:

1* eigen amplitude shape functions for membrane $\mathbf{W}_{nm}(x,y)$, $n,m=1,2,3,4,....,\infty$ are analogous with eigen amplitude shape functions for plates $\mathbf{W}_{mn}(x,y)$, $n,m=1,2,3,4,....,\infty$, (as well as for beam with $\mathbf{W}_m(x)$, $m=1,2,3,4,....,\infty$;

2* Eigrn time functions in an eigen amplitude shape function for transversal vibrations of membranes and plates $T_{k(nm)}(t)$, $k=1,2,3,....,M$, $n,m=1,2,3,4,....,\infty$ are analogous with eigen time functions in an eigen amplitude shape function for transversal vibrations of beams $T_{k(m)}(t)$, $k=1,2,3,....,M$, $m=1,2,3,4,....,\infty$ in vorresponding eigen amplitude shape function;

3* Eigrn main normal coordinates (as well as eigen normal fractional order modes) of eigen time function in an eigen amplitude shape function for membranes and plates $\xi_{(nm)s}(t)$, $s=1,2,3,....,M$, $n,m=1,2,3,4,....,\infty$ are analogous with eigen normal coordinates (as well as eigen normal fractional order modes) of eigen time functions in an eigen amplitude shape function for beams $\xi_{(m)s}(t)$, $s=1,2,3,....,M$, $m=1,2,3,4,....,\infty$;

4* eigen square of circular frequencies $\tilde{\omega}^2_{nm(s)}$ and $\tilde{\omega}^2_{\alpha(nm)(s)}$, $s=1,2,3,....,M$, $n,m=1,2,3,....,\infty$ of eigen normal fractional order modes of an eigen time function in a eigen amplitude shape function of free transversal vibrations of plates and membranes are analogous with eigen square of circular frequencies $\tilde{\omega}^2_{m(s)}$ and $\tilde{\omega}^2_{\alpha(m)(s)}$, $s=1,2,3,....,M$, $m=1,2,3,4,....,\infty$ of eigen normal fractional order modes of correspodning eigen time fubctions in an eigen amplitude shape function of free transvesal vibrations of beams;

5* Eigen normal fractional order modes $\left[\xi_{(nm)s}(t)\right]_{Like\ \cos\left(\tilde{\omega}_{(nm)(s)}t+\alpha_{(nm)(s)}\right)}, s=1,2,3,....,M$, $n,m=1,2,3,....,\infty$, of corresponding eigen time function in an eigen amplitude shape function of free transversal vibrations of plates or membranes are analogous with eigen normal fractional order modes $\left[\xi_{(m)s}(t)\right]_{Like\ \cos\left(\tilde{\omega}_{(m)(s)}t+\alpha_{(m)(s)}\right)}$, $s=1,2,3,....,M$, $m=1,2,3,4,....,\infty$ of corresponding eigen time function in an eigen amplitude shape function of free transversal vibrations of beams;

6* Eigen normal fractional order modes $\left[\xi_{(nm)s}(t)\right]_{Like\ \sin\left(\tilde{\omega}_{(nm)(s)}t+\alpha_{(nm)(s)}\right)}, s=1,2,3,....,M$, $n,m=1,2,3,....,\infty$ of corresponding eigen time function in an eigen amplitude shape function of free transversal vibrations of plates or membranes are analogous with eigen normal fractional order modes $\left[\xi_{(m)s}(t)\right]_{Like\ \sin\left(\tilde{\omega}_{(m)(s)}t+\alpha_{(m)(s)}\right)}, s=1,2,3,....,M, m=1,2,3,4,....,\infty$ of corresponding eigen time function in an eigen amplitude shape function of free transversal vibrations of beams;

7*Ordinary fractional order differential equations of each independent fractional order oscillator of eigen time functions in an eigen amplitude shape function of plates or membranes along normal coordinates in the form $\ddot{\xi}_{(nm)s}(t)+\tilde{\omega}^2_{nm(s)}\xi_{(nm)s}(t)+\tilde{\omega}^2_{\alpha(nm)(s)}\mathrm{D}_t^{\alpha}\left[\xi_{(nm)s}(t)\right]=0$, $s=1,2,3,....,M$, $n,m=1,2,3,....,\infty$ are analogous with ordinary fractional order differential equations of each independent fractional order oscillator of eigen time functions in an eigen amplitude shape function of beams along normal coordinates in the form: $\ddot{\xi}_{(m)s}(t)+\tilde{\omega}^2_{m(s)}\xi_{(m)s}(t)+\tilde{\omega}^2_{\alpha(m)(s)}\mathrm{D}_t^{\alpha}\left[\xi_{(m)s}(t)\right]=0$, $s=1,2,3,....,M$, $m=1,2,3,4,....,\infty$ and present analogous eigen fractional order independent oscillatory modes of eigen time function in an eigen amplitude shape function in free vibrations regimes of multi body system dynamics.

7* Corresponding system of three independent ordinary fractional order differential equations along eigen main coordinates $\xi_{(nm)s}(t), s=1,2,3$, $n,m=1,2,3,4,....,\infty$.of eigen time function in an eigen amplitude shape function for forced transversal vibrations of three plate or three membrane

system excited by three surface single frequensy forces distributed along deformable bodies, and with different frequencies, are in the following forms:

$$\left\langle \ddot{\xi}_{(nm)1}(t)+\tilde{\omega}^2_{nm(1)}\xi_{(nm)1}(t)+\tilde{\omega}^2_{\alpha(nm)(1)}\mathrm{D}^{\alpha}_{t}\left[\xi_{(nm)1}(t)\right]\right\rangle=\frac{\begin{vmatrix} h_{01,nm}\sin\left(\Omega_{1,nm}t+\vartheta_{1,nm}\right) & \mathbf{K}^{(2)}_{(nm)31} & \mathbf{K}^{(3)}_{(nm)31} \\ h_{02,nm}\sin\left(\Omega_{2,nm}t+\vartheta_{2,nm}\right) & \mathbf{K}^{(2)}_{(nm)32} & \mathbf{K}^{(3)}_{(nm)32} \\ h_{03,nm}\sin\left(\Omega_{3,nm}t+\vartheta_{3,nm}\right) & \mathbf{K}^{(2)}_{(nm)33} & \mathbf{K}^{(3)}_{(nm)33} \end{vmatrix}}{\begin{vmatrix} \mathbf{K}^{(1)}_{(nm)31} & \mathbf{K}^{(2)}_{(nm)31} & \mathbf{K}^{(3)}_{(nm)31} \\ \mathbf{K}^{(1)}_{(nm)32} & \mathbf{K}^{(2)}_{(nm)32} & \mathbf{K}^{(3)}_{(nm)32} \\ \mathbf{K}^{(1)}_{(nm)33} & \mathbf{K}^{(2)}_{(nm)33} & \mathbf{K}^{(3)}_{(nm)33} \end{vmatrix}} \tag{9}$$

$$\left\langle \ddot{\xi}_{(nm)2}(t)+\tilde{\omega}^2_{nm(2)}\xi_{(nm)s}2(t)+\tilde{\omega}^2_{\alpha(nm)(2)}\mathrm{D}^{\alpha}_{t}\left[\xi_{(nm)2}(t)\right]\right\rangle=\frac{\begin{vmatrix} \mathbf{K}^{(1)}_{(nm)31} & h_{01,nm}\sin\left(\Omega_{1,nm}t+\vartheta_{1,nm}\right) & \mathbf{K}^{(3)}_{(nm)31} \\ \mathbf{K}^{(1)}_{(nm)32} & h_{02,nm}\sin\left(\Omega_{3,nm}t+\vartheta_{2,nm}\right) & \mathbf{K}^{(3)}_{(nm)32} \\ \mathbf{K}^{(1)}_{(nm)33} & h_{03,nm}\sin\left(\Omega_{3,nm}t+\vartheta_{3,nm}\right) & \mathbf{K}^{(3)}_{(nm)33} \end{vmatrix}}{\begin{vmatrix} \mathbf{K}^{(1)}_{(nm)31} & \mathbf{K}^{(2)}_{(nm)31} & \mathbf{K}^{(3)}_{(nm)31} \\ \mathbf{K}^{(1)}_{(nm)32} & \mathbf{K}^{(2)}_{(nm)32} & \mathbf{K}^{(3)}_{(nm)32} \\ \mathbf{K}^{(1)}_{(nm)33} & \mathbf{K}^{(2)}_{(nm)33} & \mathbf{K}^{(3)}_{(nm)33} \end{vmatrix}} \tag{10}$$

$$\left\langle \ddot{\xi}_{(nm)3}(t)+\tilde{\omega}^2_{nm(3)}\xi_{(nm)3}(t)+\tilde{\omega}^2_{\alpha(nm)(3)}\mathrm{D}^{\alpha}_{t}\left[\xi_{(nm)3}(t)\right]\right\rangle=\frac{\begin{vmatrix} \mathbf{K}^{(1)}_{(nm)31} & \mathbf{K}^{(2)}_{(nm)31} & h_{01,nm}\sin\left(\Omega_{1,nm}t+\vartheta_{1,nm}\right) \\ \mathbf{K}^{(1)}_{(nm)32} & \mathbf{K}^{(2)}_{(nm)32} & h_{02,nm}\sin\left(\Omega_{2,nm}t+\vartheta_{2,nm}\right) \\ \mathbf{K}^{(1)}_{(nm)33} & \mathbf{K}^{(2)}_{(nm)33} & h_{03,nm}\sin\left(\Omega_{3,nm}t+\vartheta_{3,nm}\right) \end{vmatrix}}{\begin{vmatrix} \mathbf{K}^{(1)}_{(nm)31} & \mathbf{K}^{(2)}_{(nm)31} & \mathbf{K}^{(3)}_{(nm)31} \\ \mathbf{K}^{(1)}_{(nm)32} & \mathbf{K}^{(2)}_{(nm)32} & \mathbf{K}^{(3)}_{(nm)32} \\ \mathbf{K}^{(1)}_{(nm)33} & \mathbf{K}^{(2)}_{(nm)33} & \mathbf{K}^{(3)}_{(nm)33} \end{vmatrix}} \tag{11}$$

$$s=1,2,3,\ n,m=1,2,3,4,....,\infty$$

Previous system (9)-(11) of ordinary fractional order differential equations of each independent fractional order forced oscillator of eigen time functions in one eigen amplitude shape of plates or membranes along eigen normal coordinates $\xi_{(nm)s}(t), s=1,2,3,....,M, n,m=1,2,3,....,\infty$ are analogous with corresponding system of ordinary fractional order differential equations of each independent fractional order oscillator of eigen time functions in one eigen amplitude shape of beams along eigen normal coordinates $\xi_{(m)s}(t), s=1,2,3,....,M,\ m=1,2,3,4,....,\infty$ and present analogous eigen fractional order independent forced oscillatory modes of eigen time function in one eigen amplituude sjape function in forced vibrations regimes of multi body system dynamics.

From previous, last, system of ordinary fractional order differential equations, three eigen main coordinates $\xi_{(nm)s}(t)$ of eigen fractional order time functions $T_{k(nm)}(t), k=1,2,3,$ $n,m=1,2,3,4,....,\infty$ in one eigen amplitude shape function $\mathbf{W}_{nm}(x,y),\ n,m=1,2,3,4,....,\infty$ of forced transversal vibrations of the three plate system is possible to obtain by use Laplace transform and developmement in time series, and result after inverse Laplace transforms. Also, this system is possible to solve by use the generalized Lagrange method of variation constants using obtained particular solutions. We can see that these vibrations will be like four frequency fractional order

vibrations, as a result of combinations of free fractional order like one frequency vibrations and additional three of three frequency external excitation three forces distributed along each of middle surfaces of the bodies (plates, membranes or beams). But, our aim is to present analogies and mathematical phenomenology in this paper, no to present solutions and analogies between changes of energies carried on the eigen main fractional modes. .

4. Conclusions in the form energy analysis

In part 3, from pointed results, we can conclude that eigen main coordinates of eigen time function in one eigen amplitude shape of transversal vibrations of a class of multi-body fractional order system correspond to eigen main coordinates of a chain fractional order system for free as well as for forced vibrations and that in considered class of the systems appear independent fractional order modes for free as well as for forced vibration regimess.

Previous conclusions directed us to the two previous theorems 1 and 2 from chapter 2. From these theorems mathematical formulation (1), (4) and (5) present change of total mechanical energy of fractional order system dynamics carried on vibration system dynamics, and also carried on each of eigen fractional order modes in a class of discrete fractional order oscillatory system dynamics in analogy applicable in full to a class of multi-deformable body (beams, plated and membranes) system with coupling discrete continuum fractional layers, but for free vibrations.

For forced vibration it is necessary to take into account power of active transversal forces distributed along middle surface of all deformable bodies along transversal displacements during transversal vibrations in the system and expression (1) from Theorem 1 take the following form:

$$\frac{d\mathbf{E}}{dt} = -2\Phi - \sum_{k=1}^{k=n}\sum_{j=1}^{j=n} \dot{x}_k \frac{\partial \mathbf{P}_{\alpha}}{\partial\left(\mathrm{D}_{\mathrm{t}}^{\alpha}\left[x_j\right]\right)} + \sum_{k=1}^{k=3}\iint_{A}\left(q_k(x,y,t),\dot{w}_k(x,y,t)\right)dA, \quad for \quad \alpha \neq 0 \text{ and } 0<\alpha\leq 1$$

Also, expressions (4) and (5) from theorem 2, for forced vibrations, need correction by an additional term presenting power of generalized force for eigen normal coordinate ξ_s, $s = 1,2,3,...,n$ along system motion along this coordinate.

Acknowledgments

Parts of this research were supported by the Ministry of Sciences of Republic Serbia trough Mathematical Institute SANU Belgrade Grants OI 174001" Dynamics of hybrid systems with complex structures. Mechanics of materials", and through Faculty of Mechanical Engineering University of Niš.

References

[1] O.A. Goroško and K.R. Hedrih (Stevanović), (2001), *Analitička dinamika (mehanika) diskretnih naslednih sistema, (*Analytical Dynamics (Mechanics) of Discrete Hereditary Systems), University of Niš, 2001, Monograph, p. 426, YU ISBN 86-7181-054-2.

[2] K.R. Hedrih (Stevanović), J. Tenreiro Machado, (2013), Discrete fractional order system vibrations, *International Journal Non-Linear Mechanics*, ISSN 0020-7462, *(January 6, 2014)*, , 73(2015)2–11, DOI: 10.1016/j.ijnonlinmec.2014.11.009. http://www.elsevier.com/locate/nlm http://authors.elsevier.com/authorforms/NLM2407/7c32b6b4f19f2471fb24556142da3cd1

[3] K.R. Hedrih (Stevanović), (2015), Elements of mathematical phenomenology: I. Mathematical and qualitative analogies, Труды МАИ. Выпуск №84, pp. 42 (1-42) www.mai.ru/science/trudy/ , http://www.mai.ru/upload/iblock/5f6/hedrih_eng_1.pdf, Эл № ФС77-58560, ISSN: 1727-6942

[4] K.R. Hedrih (Stevanović), (2015), Elements of mathematical phenomenology: II. Phenomenological approximate mappings, Труды МАИ. Выпуск №84, pp. 29 (1- 29) www.mai.ru/science/trudy/, http://www.mai.ru/upload/iblock/5c5/hedrih_eng_2.pdf, , Эл № ФС77-58560, ISSN: 1727-6942

[5] K.R. Hedrih (Stevanović), (2014), Generalized function of fractional order dissipation of system energy and extended Lagrange differential Lagrange equation in matrix form, *Dedicated to 86th Anniversary of Radu MIRON'S Birth.,* ***Tensor,*** Vol. 75, No. 1. pp. 35-51. Tensor Society (Tokyo), c/o Kawaguchi Inst. of Math. Soc. , Japan. ISSN 0040-3604..

[6] K.R. Hedrih (Stevanović), The Dissipation Function of a Nonconservative System of Mass Particles, **Tensor,** N.S.,Vol.63, No.2(2002), pp.176-186. Tensor Society , Japan .

[7] K.R. Hedrih (Stevanović), (2014), Elements of mathematical phenomenology in dynamics of multi-body system with fractional order discrete continuum layers, *Dedicated to the 100th Anniversary of the Russian Academician Yury Rabotnov,* Special issue of *International Journal of Mechanics*, 2014, Vol. 8, pp. 339-346, ISSN: 1998-4448 .(Paper submitted in January 2014), Journal indexed in SCOPUS (http://www.naun.org/cms.action?id=2828).

[8] K.R. Hedtrih (Stevanović), (2008), The fractional order hybrid system vibrations, Monograph, Chap in Monograph. Advances in Nonlinear Sciences, ANN, 2008, Vol. 2, pp. 226-326.

[9] K.R. Hedtrih (Stevanović), (2008), The fractional order hybrid system vibrations, Monograph, Chap in Monograph. Advances in Nonlinear Sciences, ANN, 2008, Vol. 2, pp. 226-326.

[10] K. R. Hedrih (Stevanović), (2011), Energy and Nonlinear Dynamics of Hybrid System, Chapter in Book Dynamical Systems and Methods, Edited by Albert Luo. 2011, Chapter oko 50 strana, Springer 2012, Part 1, 29-83, DOI: 10.1007/978-1-4614-0454-5_2, http://link.springer.com/chapter/10.1007%2F978-1-4614-0454-5_2

[11] K. R. Hedrih (Stevanović), (2008), Main chains and eigen modes of the fractional order hybrid multipendulum system dynamics, IOP PUBLISHING PHYSICA SCRIPTA, vol. T136, Phys. Scr. 78 (2008) 000000 (12pp) doi:10.1088/0031-8949/78/8/000000, http://www.iop.org/EJ/journal/1402-489, ISSN 0031-8949

[12] K. R. Hedrih (Stevanović), (2008), Energy analysis in a nonlinear hybrid system containing linear and nonlinear subsystems coupled by hereditary element (Article), NONLINEAR DYNAMICS , (2008) vol.51 br.1-2 str. 127 -140. DOI 10.1007/s11071-007-9197-2. ISSN 0924-090X (Print) 1573-269X , (Online), Volume 51, Numbers 1-2 / January, 2008, pp. 127-140. DOI 10.1007/s11071-007-9197-2, SpringerLink Date, Tuesday, January 30, 2007. http://www.springerlink.com.nainfo.nbs.bg.ac.yu:2048/content/rg2302474v1ru044/ž

[13] K. R. Hedrih (Stevanović), (214), Multi membrane fractional order system vibrations, Theoretical and Applied mechanics, Series: Special Issue – Dedicated to memory of Anton D. Bilimovič (1879-1970), Guest Editors: Katica R. (Stevanović) Hedrih and Dragoslav Šumarac, 2014, Vol. 41 (S1), pp. 43-61.

[14] M. Petrović, Elementi matematičke fenomenologije (Elements of mathematical phenomenology), Srpska kraljevska akademija, Beograd, 1911. str. 789. http://elibrary.matf.bg.ac.rs/handle/123456789/476?locale-attribute=sr

[15] M. Petrović, Fenomenološko preslikavanje (Phenomenological mapp), Srpska kraljevska akademija, Beograd, 1933. str. 33. http://elibrary.matf.bg.ac.rs/handle/123456789/475

[16] Rosikin Yuri and Maria Shitikova: (2010), Application of Fractional Calculus for Dynamic Problem of Solid Mechanics, Novel Trends and Resent Results, Applied Mechanics Reviews, American Society of Mechanical Enginewers –ASME, JANUAR 2010, Vol. 63/ pp. 010801-1 - 010801-52.

[17] Radu P. Voinea, On Some Analogies, Facta Universitatis, Series Mechanics, Automatic Control and Robotics, Nis, Vol 3, No 14, 1993, pp. 785-790.

Katica R. (Stevanović) Hedrih, University Professor, Doctor of technical Sciences, Department of Mechanics at Mathematical Institute of Serbian Academy of Science and Arts (SANU), Belgrade and Faculty of Mechanical Engineering University of Niš, Serbia, e-mail: khedrih@sbb.rs; Priv. address: 18000- Niš, Serbiam ul. Vojvode Tankosića 3/22.e-mail: khedrih@eunet.rs.

Estimates of asymptotic solution of linear-quadratic optimal control problems with cheap controls of two different orders of smallness

Margarita Kalashnikova, Galina Kurina

Abstract: This paper is devoted to a linear-quadratic optimal control problem with a performance index containing two different powers of a small parameter at quadratic forms with respect to controls. Problems of such type arise, for instance, as a result of applying the convolution method to problems with three performance indices, where the cost of one cheap control is negligible in comparing with another one. Estimates of the proximity of the solution of the original problem to an approximate asymptotic solution are obtained for the control, trajectory, and performance index. The used asymptotic solution has been constructed with the help of the so-called direct scheme method consisting of immediate substituting of a postulated asymptotic expansion of a solution into the transformed problem condition and determining optimal control problems for finding terms of the asymptotic expansion. The transformed problem is obtained from the original one as a result of variables change. It is a singularly perturbed optimal control problem with three-tempo state variables in a singular case. The constructed asymptotic solution contains regular and boundary functions of four types. It is also proved that a value of the performance index does not increase when higher order asymptotic approximations to the optimal control are used. The illustrative example is given.

1. Introduction

The motivation for a study of cheap control problems is justified in [4] by the pole assignment problem if eigenvalues that are "infinite" of different orders may be desired. Problems of such type also arise under research of models of multi-sector economics where control functions have different levels of "cheapness". If we apply the convolution method to problems with several performance indices, where the cost of one control is negligible in comparing with the other ones, we again obtain a problem with cheap controls.

Publications devoted to cheap control problems basically deal with the case where controls in a performance index have the same order of smallness (see surveys of such publications, for instance, in [2,5,8]). The papers [3–5,7,10] concerning cheap controls with different order costs are reviewed in [9].

The present paper deals with a problem, having controls of two different levels of "cheapness", of the form

$$J(\overset{(1)}{v}, \overset{(2)}{v}) = 1/2 \int_0^T (z'W(t,\varepsilon)z + \sum_{k=1}^{2} \varepsilon^{2k} \overset{(k)}{v}{}' \overset{(k)}{R}(t,\varepsilon) \overset{(k)}{v}) \, dt \to \min, \tag{1}$$

$$dz/dt = A(t,\varepsilon)z + C(t,\varepsilon)v, \ t \in [0,T], \ z(0,\varepsilon) = z^0, \tag{2}$$

where $T > 0$ is fixed, $\overset{(k)}{v}(t,\varepsilon) \in R^{n_k}$, $v(t,\varepsilon) = (\overset{(1)}{v}(t,\varepsilon)', \overset{(2)}{v}(t,\varepsilon)')'$, $z(t,\varepsilon) \in R^n$, the matrices $W(t,\varepsilon)$, $\overset{(k)}{R}(t,\varepsilon)$, $A(t,\varepsilon)$ and $C(t,\varepsilon)$ are assumed to be sufficiently smooth with respect to their arguments, $W(t,\varepsilon)$, $\overset{(k)}{R}(t,\varepsilon)$ are symmetric, $W(t,0)$, $\overset{(k)}{R}(t,0)$ are positive definite, $k = 1,2$, $n = n_1 + n_2$, the matrix $C(t,0)$ is invertible for all $t \in [0,T]$. Here and further in this paper $\varepsilon \geq 0$ is a small parameter and the prime denotes the transposition.

The formalism of constructing asymptotic solution of problem (1), (2) of the first and higher orders has been presented respectively in [5] and [9]. It is based on the so-called direct scheme method (see [1], [2]) and boundary function method (see [12]) applied to transformed problem obtained from (1), (2) with the help of variables change. This method consists of immediate substituting of a postulated asymptotic expansion of a solution of the boundary layer type into the problem condition and determining optimal control problems for finding terms of the asymptotic expansion.

In this paper, we will estimate the proximity of an approximate asymptotic solution constructed in [5] and [9] to the solution of original problem (1), (2) with respect to the control, the trajectory and the performance index. It is established that a value of the minimized functional does not increase when higher order asymptotic approximations to the optimal control are used. Moreover, we provide an example, which illustrates the paper's results.

2. Formalism of constructing asymptotic solution

In this section, we present some results from [5, 9] concerning the algorithm of constructing asymptotic solution of problem (1), (2).

At first, using the variables change $\overset{(k)}{u}(t,\varepsilon) = \varepsilon^k \overset{(k)}{v}(t,\varepsilon)$, $\overset{(k)}{y}(t,\varepsilon) = \int_0^t \overset{(k)}{v}(s,\varepsilon)\, ds$, $y(t,\varepsilon) = (\overset{(1)}{y}(t,\varepsilon)', \overset{(2)}{y}(t,\varepsilon)')'$, $x(t,\varepsilon) = z(t,\varepsilon) - C(t,\varepsilon)y(t,\varepsilon)$, $w(t,\varepsilon) = (x(t,\varepsilon)', y(t,\varepsilon)')'$, $u(t,\varepsilon) = (\overset{(1)}{u}(t,\varepsilon)', \overset{(2)}{u}(t,\varepsilon)')'$ original problem (1)-(2) is reduced to the following three-tempo optimal control problem

$$P_\varepsilon : \ J_\varepsilon(u) = 1/2 \int_0^T (w'\mathcal{W}(t,\varepsilon)w + u'\mathcal{R}(t,\varepsilon)u) \, dt \to \min, \tag{3}$$

$$dx/dt = A(t,\varepsilon)x + B(t,\varepsilon)y,\ \varepsilon^k d\overset{(k)}{y}/dt = \overset{(k)}{u},\ k = 1,2, \tag{4}$$

$$x(0,\varepsilon) = z^0,\ y(0,\varepsilon) = 0, \tag{5}$$

where $\mathcal{W}(t,\varepsilon) = \begin{bmatrix} W(t,\varepsilon) & W(t,\varepsilon)C(t,\varepsilon) \\ C(t,\varepsilon)'W(t,\varepsilon) & C(t,\varepsilon)'W(t,\varepsilon)C(t,\varepsilon) \end{bmatrix}$, $\mathcal{R}(t,\varepsilon) = diag(\overset{(1)}{R}(t,\varepsilon), \overset{(2)}{R}(t,\varepsilon))$, $B(t,\varepsilon) = A(t,\varepsilon)C(t,\varepsilon) - dC(t,\varepsilon)/dt$.

Since for sufficiently small $\varepsilon > 0$ the matrix $\mathcal{R}(t,\varepsilon)$ is positive definite and the matrix $\mathcal{W}(t,\varepsilon)$ is positive semi-definite then problem (3)-(5) is uniquely solvable and the optimal control can be found from the equality

$$\mathcal{B}'\xi - \mathcal{R}(t,\varepsilon)u = 0, \tag{6}$$

where the costate variable $\xi(t,\varepsilon) = (\zeta(t,\varepsilon)', \eta(t,\varepsilon)')'$, $\eta(t,\varepsilon) = (\overset{(1)}{\eta}(t,\varepsilon)', \overset{(2)}{\eta}(t,\varepsilon)')'$, is a solution of the problem

$$\mathcal{E}(\varepsilon)\frac{d\xi}{dt} = \mathcal{W}(t,\varepsilon)w - \mathcal{A}(t,\varepsilon)'\xi, \tag{7}$$

$$\xi(T,\varepsilon) = 0, \tag{8}$$

$\mathcal{A}(t,\varepsilon) = \begin{bmatrix} A(t,\varepsilon) & \overset{(1)}{B}(t,\varepsilon) & \overset{(2)}{B}(t,\varepsilon) \\ 0 & 0 & 0 \\ 0 & 0 & 0 \end{bmatrix}$, $B(t,\varepsilon) = \begin{bmatrix} \overset{(1)}{B}(t,\varepsilon) & \overset{(2)}{B}(t,\varepsilon) \end{bmatrix}$, $\mathcal{B} = \begin{bmatrix} 0 & 0 \\ I_{n_1} & 0 \\ 0 & I_{n_2} \end{bmatrix}$,

I_k denotes an identity matrix of the order k, $\mathcal{E}(\varepsilon) = diag(I_n, \varepsilon I_{n_1}, \varepsilon^2 I_{n_2})$.

According to [12], [13] a solution of problem (3)-(5) is sought in the following form

$$\mathrm{v}(t,\varepsilon) = \overline{\mathrm{v}}(t,\varepsilon) + \sum_{i=0}^{1}(\Pi_i\mathrm{v}(\tau_i,\varepsilon) + Q_i\mathrm{v}(\sigma_i,\varepsilon)), \tag{9}$$

where $\mathrm{v}(t,\varepsilon) = (w(t,\varepsilon)', u(t,\varepsilon)')'$, $\overline{\mathrm{v}}(t,\varepsilon) = \sum_{j\geq 0}\varepsilon^j\overline{\mathrm{v}}_j(t)$, $t \in [0,T]$, $\tau_i = t/\varepsilon^{i+1}$, $\sigma_i = (t-T)/\varepsilon^{i+1}$, $\Pi_i\mathrm{v}(\tau_i,\varepsilon) = \sum_{j\geq 0}\varepsilon^j\Pi_{ij}\mathrm{v}(\tau_i)$, $Q_i\mathrm{v}(\sigma_i,\varepsilon) = \sum_{j\geq 0}\varepsilon^j Q_{ij}\mathrm{v}(\sigma_i)$, $i = 0,1$, $\overline{\mathrm{v}}_j(t)$ are regular functions, $\Pi_{ij}\mathrm{v}(\tau_i)$ are boundary functions of the exponential type in a neighbourhood of $t = 0$, $Q_{ij}\mathrm{v}(\sigma_i)$ are boundary functions of the exponential type in a neighbourhood of $t = T$.

The algorithm of the direct scheme method consists of immediate substituting expansion (9) into problem condition (3)-(5) and determining the optimal control problems $\overline{P}_j$, $\Pi_{ij}P$, $Q_{ij}P$ for finding $\overline{\mathrm{v}}_j(t)$, $\Pi_{ij}\mathrm{v}(\tau_i)$, $Q_{ij}\mathrm{v}(\sigma_i)$, $i = 0,1$, respectively. The explicit expressions for these problems are given in [9].

3. Asymptotic estimates for control, trajectory and performance index

Suppose that optimal control problems $\overline{P}_j$, $\Pi_{ij}P$, $Q_{ij}P$, $i = 0,1$, $j = \overline{0,n}$, have been solved. Let us estimate the proximity between the asymptotic solution of problem (1)-(2): $\widetilde{\overset{(k)}{v}}_{n-k}(t,\varepsilon) = \widetilde{\overset{(k)}{u}}_n(t,\varepsilon)/\varepsilon^k$, $\widetilde{z}_n(t,\varepsilon) = \widetilde{x}_n(t,\varepsilon) + \sum_{j=0}^{n}[C(t,\varepsilon)]_j[\widetilde{\overset{(k)}{y}}_n(t,\varepsilon)]_{n-j}$, $k = 1,2$, constructed by the direct scheme method and the exact solution. Here for the expansion of a function $\omega = \omega(\varepsilon)$ with respect to ε: $\omega(\varepsilon) = \sum_{j\geq 0}\varepsilon^j\omega_j$ we use the following notation $[\omega]_n = \omega_n$, $\widetilde{\omega}_n = \sum_{j=0}^{n}\varepsilon^j\omega_j$.

We write down the costate variable in the form of expansion (9)

$$\xi(t,\varepsilon) = \overline{\xi}(t,\varepsilon) + \sum_{i=0}^{1}(\Pi_i\xi(\tau_i,\varepsilon) + Q_i\xi(\sigma_i,\varepsilon)), \tag{10}$$

where the each summand is represented as a series with respect to non-negative integer powers of ε with corresponding coefficients $\overline{\xi}_j(t)$, $\Pi_{ij}\xi(\tau_i)$, $Q_{ij}\xi(\sigma_i)$, $i = 0,1$.

Further we write the relations for the remainder terms of asymptotic solution of problem (4)-(8). Let us introduce the notation $r_n w = (r_n x', r_n y')' = w - \widetilde{w}_n$, $r_n\xi = (r_n\zeta', r_n\eta')' = \xi - \widetilde{\xi}_n$, $X = \begin{bmatrix} x \\ \zeta \end{bmatrix}$, $\overset{(k)}{Y} = \begin{bmatrix} \overset{(k)}{y} \\ \overset{(k)}{\eta} \end{bmatrix}$, $\widetilde{\mathrm{X}}_n = \begin{bmatrix} \widetilde{x}_n \\ \widetilde{\zeta}_n \end{bmatrix}$, $\widetilde{\overset{(k)}{\mathrm{Y}}}_n = \begin{bmatrix} \widetilde{\overset{(k)}{y}}_n \\ \widetilde{\overset{(k)}{\eta}}_n \end{bmatrix}$, $r_n X = \begin{bmatrix} r_n x \\ r_n\zeta \end{bmatrix}$, $r_n\overset{(k)}{Y} = \begin{bmatrix} r_n\overset{(k)}{y} \\ r_n\overset{(k)}{\eta} \end{bmatrix}$, $k = 1,2$. Taking into account that state equations and costate equations for constructed optimal control problems $\overline{P}_j$, $\Pi_{ij}P$, $Q_{ij}P$, $i = 0,1$, are obtained by substituting expansions for $\mathrm{v}(t,\varepsilon)$ and $\xi(t,\varepsilon)$ into (4), (6), (7) and equating coefficients of the same power of ε separately depending on t, τ_i, σ_i, $i = 0,1$, we get for sufficiently small $\varepsilon > 0$ from (4), (6), (7) the following system

$$\begin{aligned}
\frac{dr_n\mathrm{X}}{dt} &= \mathcal{A}(t,\varepsilon)r_n\mathrm{X} + \overset{(1)}{\mathcal{B}}(t,\varepsilon)r_n\overset{(1)}{\mathrm{Y}} + \overset{(2)}{\mathcal{B}}(t,\varepsilon)r_n\overset{(2)}{\mathrm{Y}} + \overset{(0)}{\mathrm{V}}(t,\varepsilon),\\
\varepsilon\frac{dr_n\overset{(1)}{\mathrm{Y}}}{dt} &= \overset{(1)}{\mathcal{A}}(t,\varepsilon)r_n\mathrm{X} + \overset{(1)}{\mathcal{B}}_1(t,\varepsilon)r_n\overset{(1)}{\mathrm{Y}} + \overset{(1)}{\mathcal{B}}_2(t,\varepsilon)r_n\overset{(2)}{\mathrm{Y}} + \overset{(1)}{\mathrm{V}}(t,\varepsilon),\\
\varepsilon^2\frac{dr_n\overset{(2)}{\mathrm{Y}}}{dt} &= \overset{(2)}{\mathcal{A}}(t,\varepsilon)r_n\mathrm{X} + \overset{(2)}{\mathcal{B}}_1(t,\varepsilon)r_n\overset{(1)}{\mathrm{Y}} + \overset{(2)}{\mathcal{B}}_2(t,\varepsilon)r_n\overset{(2)}{\mathrm{Y}} + \overset{(2)}{\mathrm{V}}(t,\varepsilon),
\end{aligned} \tag{11}$$

where $\mathcal{A} = \begin{bmatrix} A & 0 \\ W & -A' \end{bmatrix}$, $\overset{(i)}{\mathcal{B}} = \begin{bmatrix} \overset{(i)}{B} & 0 \\ \overset{(i)}{S} & 0 \end{bmatrix}$, $i = 1,2$, $\begin{bmatrix} \overset{(1)}{S} & \overset{(2)}{S} \end{bmatrix} = WC$, $\overset{(1)}{\mathcal{A}} = \begin{bmatrix} 0 & 0 \\ \overset{(1)}{S'} & \overset{(1)}{-B'} \end{bmatrix}$, $D = C'WC = \begin{bmatrix} D_{11} & D_{12} \\ D_{12}' & D_{22} \end{bmatrix}$, $\overset{(1)}{\mathcal{B}}_1 = \begin{bmatrix} 0 & \overset{(1)}{R^{-1}} \\ D_{11} & 0 \end{bmatrix}$, $\overset{(1)}{\mathcal{B}}_2 = \begin{bmatrix} 0 & 0 \\ D_{12} & 0 \end{bmatrix}$, $\overset{(2)}{\mathcal{A}} = \begin{bmatrix} 0 & 0 \\ \overset{(2)}{S'} & \overset{(2)}{-B'} \end{bmatrix}$,

$\overset{(2)}{\mathcal{B}}_1 = \begin{bmatrix} 0 & 0 \\ D_{12}' & 0 \end{bmatrix}$, $\overset{(2)}{\mathcal{B}}_2 = \begin{bmatrix} 0 & \overset{(2)}{R^{-1}} \\ D_{22} & 0 \end{bmatrix}$ (for brevity, the arguments t, ε in the notation of matrices are dropped), $\overset{(0)}{\mathrm{V}}(t,\varepsilon) = \mathcal{A}(t,\varepsilon)\widetilde{\mathrm{X}}_n + \overset{(1)}{\mathcal{B}}(t,\varepsilon)\widetilde{\overset{(1)}{\mathrm{Y}}}_n + \overset{(2)}{\mathcal{B}}(t,\varepsilon)\widetilde{\overset{(2)}{\mathrm{Y}}}_n - d\widetilde{X}_n/dt$, $\overset{(1)}{\mathrm{V}}(t,\varepsilon) = \overset{(1)}{\mathcal{A}}(t,\varepsilon)\widetilde{\mathrm{X}}_n + \overset{(1)}{\mathcal{B}}_1(t,\varepsilon)\widetilde{\overset{(1)}{\mathrm{Y}}}_n + \overset{(1)}{\mathcal{B}}_2(t,\varepsilon)\widetilde{\overset{(2)}{\mathrm{Y}}}_n - \varepsilon d\overset{(1)}{Y}_n/dt$, $\overset{(2)}{\mathrm{V}}(t,\varepsilon) = \overset{(2)}{\mathcal{A}}(t,\varepsilon)\widetilde{\mathrm{X}}_n + \overset{(2)}{\mathcal{B}}_1(t,\varepsilon)\widetilde{\overset{(1)}{\mathrm{Y}}}_n + \overset{(2)}{\mathcal{B}}_2(t,\varepsilon)\widetilde{\overset{(2)}{\mathrm{Y}}}_n - \varepsilon^2 d\overset{(2)}{Y}_n/dt$.

Taking into consideration conditions for terms of expansions (9), (10) and the equalities $\Pi_{00}x(\tau_0) = 0$, $\Pi_{10}x(\tau_1) = \Pi_{11}x(\tau_1) = 0$, $\Pi_{10}\overset{(1)}{y}(\tau_1) = 0$ we obtain from (5) and (8) the boundary conditions

$$\begin{aligned} r_n w(0,\varepsilon) &= -\widetilde{Q}_{0n}w(-T/\varepsilon,\varepsilon) - \widetilde{Q}_{1n}w(-T/\varepsilon^2,\varepsilon), \\ r_n\xi(T,\varepsilon) &= -\widetilde{\Pi}_{0n}\xi(T/\varepsilon,\varepsilon) - \widetilde{\Pi}_{1n}\xi(T/\varepsilon^2,\varepsilon). \end{aligned} \tag{12}$$

In view of the algorithm of constructing asymptotics (9), (10) the functions $\overset{(k)}{V}$, $k = \overline{0,2}$, satisfy for sufficiently small $\varepsilon > 0$ the following estimates:

$$\begin{aligned} \|\overset{(0)}{\mathrm{V}}(t,\varepsilon)\| \le c(\varepsilon^{n+1} + \varepsilon^n(\exp(-æt/\varepsilon) + \\ + \exp(æ(t-T)/\varepsilon)) + \varepsilon^{n-1}(\exp(-æt/\varepsilon^2) + \exp(æ(t-T)/\varepsilon^2))), \end{aligned} \tag{13}$$

$$\|\overset{(1)}{\mathrm{V}}(t,\varepsilon)\| \le c(\varepsilon^{n+1} + \varepsilon^n(\exp(-æt/\varepsilon^2) + \exp(æ(t-T)/\varepsilon^2))),\ \|\overset{(2)}{\mathrm{V}}(t,\varepsilon)\| \le c\varepsilon^{n+1},$$

where positive constants c, æ in this paper are independent of t, ε.

Using the variables change $\rho_n w(t,\varepsilon) = r_n w(t,\varepsilon) + \widetilde{Q}_{0n}w(-T/\varepsilon,\varepsilon) + \widetilde{Q}_{1n}w(-T/\varepsilon^2,\varepsilon)$, $\rho_n\xi(t,\varepsilon) = r_n\xi(t,\varepsilon) + \widetilde{\Pi}_{0n}\xi(T/\varepsilon,\varepsilon) + \widetilde{\Pi}_{1n}\xi(T/\varepsilon^2,\varepsilon)$ we get from (11), (12) the system

$$\frac{d\rho_n\mathrm{X}}{dt} = \mathcal{A}(t,\varepsilon)\rho_n\mathrm{X} + \overset{(1)}{\mathcal{B}}(t,\varepsilon)\rho_n\overset{(1)}{\mathrm{Y}} + \overset{(2)}{\mathcal{B}}(t,\varepsilon)\rho_n\overset{(2)}{\mathrm{Y}} + \overset{(0)}{\mathcal{V}}(t,\varepsilon), \tag{14}$$

$$\varepsilon\frac{d\rho_n\overset{(1)}{\mathrm{Y}}}{dt} = \overset{(1)}{\mathcal{A}}(t,\varepsilon)\rho_n\mathrm{X} + \overset{(1)}{\mathcal{B}}_1(t,\varepsilon)\rho_n\overset{(1)}{\mathrm{Y}} + \overset{(1)}{\mathcal{B}}_2(t,\varepsilon)\rho_n\overset{(2)}{\mathrm{Y}} + \overset{(1)}{\mathcal{V}}(t,\varepsilon), \tag{15}$$

$$\varepsilon^2\frac{d\rho_n\overset{(2)}{\mathrm{Y}}}{dt} = \overset{(2)}{\mathcal{A}}(t,\varepsilon)\rho_n\mathrm{X} + \overset{(2)}{\mathcal{B}}_1(t,\varepsilon)\rho_n\overset{(1)}{\mathrm{Y}} + \overset{(2)}{\mathcal{B}}_2(t,\varepsilon)\rho_n\overset{(2)}{\mathrm{Y}} + \overset{(2)}{\mathcal{V}}(t,\varepsilon), \tag{16}$$

$$\rho_n w(0,\varepsilon) = 0,\ \rho_n\xi(T,\varepsilon) = 0. \tag{17}$$

Expressions for $\overset{(k)}{\mathcal{V}}(t,\varepsilon)$, $k = \overline{0,2}$, can be easily written. They satisfy respectively estimates of form (13).

Since $D(t,0)$ is positive definite for all $t \in [0,T]$ then the matrices $D_{22}(t,0)$ and $\widetilde{D}_{11}(t,0) = D_{11}(t,0) - D_{12}(t,0)D_{22}(t,0)^{-1}D_{12}(t,0)$ are also positive definite. Therefore $\Lambda_1(t) = \overset{(1)}{\mathcal{B}}_1(t,0) -$

$\overset{(1)}{\mathcal{B}}_2(t,0)\overset{(2)}{\mathcal{B}}_2(t,0)^{-1}\overset{(2)}{\mathcal{B}}_1(t,0) = \begin{bmatrix} 0 & \overset{(1)}{R}(t,0)^{-1} \\ \widetilde{D}_{11}(t,0) & 0 \end{bmatrix}$ and $\Lambda_2(t) = \overset{(2)}{\mathcal{B}}_2(t,0) =$

$= \begin{bmatrix} 0 & \overset{(2)}{R}(t,0)^{-1} \\ D_{22}(t,0) & 0 \end{bmatrix}$ are positive Hamiltonian matrices. For each $t \in [0,T]$ they have non-zero real eigenvalues which are symmetric with respect to the origin.

Assume that the following condition takes place

(i) for all $t \in [0,T]$ eigenvalues of the matrices $\Lambda_k(t)$, $k = 1,2$, are different and arranged in the order of increasing.

In view of the forms of $\Lambda_k(t)$ the boundary value problems

$$\varepsilon^k d\overset{(k)}{\mathrm{Y}}/dt = \Lambda_k(t)\overset{(k)}{\mathrm{Y}},\ \overset{(k)}{y}(0) = 0,\ \overset{(k)}{\eta}(T) = 0,\ k = 1,2, \tag{18}$$

are uniquely solvable.

It is easy to see if $(\overset{(k)}{y_1},...,\overset{(k)}{y}_{n_k},\overset{(k)}{\eta_1},...,\overset{(k)}{\eta}_{n_k})'$ is an eigenvector of the matrix $\Lambda_k(t)$ for the eigenvalue λ, then $(-\overset{(k)}{y_1},...,-\overset{(k)}{y}_{n_k},\overset{(k)}{\eta_1},...,\overset{(k)}{\eta}_{n_k})'$ is the eigenvector of the same matrix for the eigenvalue $-\lambda$. It follows from the assumption (i) that eigenvectors of the matrix $\Lambda_k(t)$ are linearly independent. If we consider the matrix $\overset{(k)}{\mathrm{B}} = \begin{bmatrix} \overset{(k)}{\mathrm{B}}_{11} & \overset{(k)}{\mathrm{B}}_{12} \\ \overset{(k)}{\mathrm{B}}_{21} & \overset{(k)}{\mathrm{B}}_{22} \end{bmatrix}$ consisting of eigenvectors of the matrix $\Lambda_k(t)$ corresponding to eigenvalues arranged in the order of increasing then it is obvious that matrices $\overset{(k)}{\mathrm{B}}_{11}$, $\overset{(k)}{\mathrm{B}}_{22}$ of the order n_k are non-singular. Hence the conditions from [13, p.125] are fulfilled and following to [13] it is possible to construct for boundary value problems (18) the matrix Green functions $\overset{(k)}{G}(t,s,\varepsilon)$, which satisfy the inequalities $\|\overset{(k)}{G}(t,s,\varepsilon)\| \le c\exp(-æ|t-s|/\varepsilon^k),\ t,s \in [0,T],\ k = 1,2$.

Note that a limit passage of initial value problem solutions for systems of differential equations containing small parameters in front of the higher derivatives has been studied in [11] under small parameters tending to zero. Following to the terminology of [11], equations (18) are called as associated systems of the second (k=1) and first (k=2) orders. The limit passage of boundary value problem solutions for systems of such type has been researched in [6].

Further the following two lemmas are needed.

Lemma 1 *If $G(t,s)$ is a matrix Green function of the uniquely solvable on $[0,T]$ boundary value problem*

$$dx/dt = A(t)x + f(t),\ P_1x(0) = 0,\ (I - P_1)x(T) = 0$$

where the operator $A(t)$ is invertible for all $t \in [0,T]$ and P_1 is a projector then

$$\frac{\partial G(t,s)}{\partial t} = -A(t)\frac{\partial G(t,s)}{\partial s}A(s)^{-1},\ t \neq s.$$

Let $\mathcal{G}$ be a contractive mapping acting in a Banach space X, i.e. there exists a number $0 < q < 1$ such that for all $x_1,\ x_2 \in X$ the inequality $\|\mathcal{G}(x_1) - \mathcal{G}(x_2)\| \leq q\|x_1 - x_2\|$ is valid.

Lemma 2 *If $x_0 = 0$, $x_k = \mathcal{G}(x_{k-1})$, $k = 1,2,...$, and $\|x_1\| \leq a$, then $\|x_k\| \leq a/(1-q)$.*

Theorem 1 *Under sufficiently small $\varepsilon > 0$ for a solution $\overset{(k)}{v}{}_*(\cdot,\varepsilon)$, $k = 1,2$, $z_*(\cdot,\varepsilon)$ of problem (1), (2) the inequalities $\|\overset{(k)}{v}{}_*(t,\varepsilon) - \widetilde{\overset{(k)}{v}}{}_{n-k}(t,\varepsilon)\| \leq c\varepsilon^{n+1-k}$, $\|z_*(t,\varepsilon) - \widetilde{z}_n(t,\varepsilon)\| \leq c\varepsilon^{n+1}$, $t \in [0,T]$, are realized.*

For the proof of this theorem system of differential equations (14)-(16) with boundary conditions (17) is reduced with the help of Lemma 1 to a system of integral equations. Lemma 2 and the estimates for the matrix Green functions $\overset{(k)}{G}(t,s,\varepsilon)$, $k = 1,2$, allow us to apply the principle of contracting mappings.

Problem (4), (5) with some control $\overset{(k)}{u}(t)$, $k = 1,2$, belongs to the critical case in the singular perturbations theory. Such case has been studied in [14]. One of the approaches for finding asymptotic solution for controlled systems consists of searching a feedback control ensuring the system stability (see, for instance, [3], [10]). However according to specific structure of the considered problem for a special control the following lemma is valid.

Lemma 3 *Asymptotic solution of form (9) can be constructed for problem (4), (5) with the control $u = \widetilde{u}_n = (\widetilde{\overset{(1)}{u}}_n, \widetilde{\overset{(2)}{u}}_n)$. Moreover asymptotics terms $\Pi_{ij}x$, $Q_{ij}x$, $\Pi_{ij}\overset{(1)}{y}$, $Q_{ij}\overset{(1)}{y}$, $i = 0,1$, $\Pi_{1j}\overset{(2)}{y}$, $Q_{1j}\overset{(2)}{y}$ with $j = \overline{0,n}$, $\overset{(1)}{\overline{y}}_j$, $\Pi_{0j}\overset{(2)}{y}$, $Q_{0j}\overset{(2)}{y}$ with $j = \overline{0,n-1}$, and $\overline{x}_j$, $\overset{(2)}{\overline{y}}_j$ with $j = \overline{0,n-2}$ coincide with the corresponding terms in the expansion of the optimal trajectory x_*, $\overset{(1)}{y}{}_*$, $\overset{(2)}{y}{}_*$.*

Theorem 2 *For sufficiently small $\varepsilon > 0$ the inequality $J(\widetilde{\overset{(1)}{v}}_{n-1}, \widetilde{\overset{(2)}{v}}_{n-2}) - J(\overset{(1)}{v}{}_*, \overset{(2)}{v}{}_*) \leq c\varepsilon^{2n-2}$ takes place.*

Theorem 3 *For sufficiently small $\varepsilon > 0$ the values of the performance index do not increase if the next approximation to the optimal control is used, i.e. the inequalities $J(\widetilde{\overset{(1)}{v}}_{j-1}, \widetilde{\overset{(2)}{v}}_{j-2}) \leq J(\widetilde{\overset{(1)}{v}}_{j-2}, \widetilde{\overset{(2)}{v}}_{j-3})$, $j = \overline{1,n}$, are valid.*

The proof of the last two theorems is based on Lemma 3.

Unfortunately, in view of the limitation of the paper size we cannot present here proofs of the statements in details.

4. Example

Consider the following optimal control problem of form (1), (2)

$$J(\overset{(1)}{v},\overset{(2)}{v}) = 1/2\int_0^1 ((\overset{(1)}{z})^2 + (\overset{(2)}{z})^2 + \varepsilon^2(\overset{(1)}{v})^2 + \varepsilon^4(\overset{(2)}{v})^2)\,dt \to \min,$$

$$d\overset{(1)}{z}/dt = \overset{(1)}{z}/2 + (5-10\varepsilon)\overset{(1)}{v},\ d\overset{(2)}{z}/dt = \overset{(2)}{v},\ \overset{(1)}{z}(0,\varepsilon) = 10,\ \overset{(2)}{z}(0,\varepsilon) = 5.$$

Using the control optimality condition in the Pontryagin maximum principle form, it is not difficult to obtain the exact solution of this problem.

With the help of the variables change $\overset{(1)}{u} = \varepsilon\overset{(1)}{v}$, $\overset{(2)}{u} = \varepsilon^2\overset{(2)}{v}$, $\overset{(k)}{y}(t,\varepsilon) = \int_0^t \overset{(k)}{v}(s,\varepsilon)\,ds$, $\overset{(1)}{x} = \overset{(1)}{z} - (5-10\varepsilon)\overset{(1)}{y}$, $\overset{(2)}{x} = \overset{(2)}{z} - \overset{(2)}{y}$, we get the following three-tempo optimal control problem of form (3)-(5)

$$J_\varepsilon(u) = 1/2\int_0^1 (\langle w, \mathcal{W}w\rangle + \langle u, \mathcal{R}u\rangle)\,dt \to \min_u,$$

$$d\overset{(1)}{x}/dt = \overset{(1)}{x}/2 + (5-10\varepsilon)\overset{(1)}{y}/2,\ d\overset{(2)}{x}/dt = 0,\ \varepsilon d\overset{(1)}{y}/dt = \overset{(1)}{u},\ \varepsilon^2 d\overset{(2)}{y}/dt = \overset{(2)}{u},$$

$$\overset{(1)}{x}(0,\varepsilon) = 10,\ \overset{(2)}{x}(0,\varepsilon) = 5,\ \overset{(1)}{y}(0,\varepsilon) = 0,\ \overset{(2)}{y}(0,\varepsilon) = 0,$$

$$\mathcal{W} = \begin{bmatrix} 1 & 0 & 5-10\varepsilon & 0 \\ 0 & 1 & 0 & 1 \\ 5-10\varepsilon & 0 & (5-10\varepsilon)^2 & 0 \\ 0 & 1 & 0 & 1 \end{bmatrix},\ \mathcal{A} = \begin{bmatrix} 1/2 & 0 & (5-10\varepsilon)/2 & 0 \\ 0 & 0 & 0 & 0 \\ 0 & 0 & 0 & 0 \\ 0 & 0 & 0 & 0 \end{bmatrix},\ \mathcal{R} = \begin{bmatrix} 1 & 0 \\ 0 & 1 \end{bmatrix}.$$

The symbols $\mathcal{W}_i$, $\mathcal{A}_i$, $\mathcal{R}_i$ will denote coefficients with ε^i in expansions of three last matrices with respect to non-negative integer powers of ε.

Following to [9] we present here optimal control problems for finding asymptotics terms of the second order for the transformed problem solution. Symbol ψ denotes the costate variable in constructed optimal control problems.

$$\overline{P}_0:\ \overline{J}_0 = 1/2\int_0^1 (\langle \overline{w}_0, \mathcal{W}_0\overline{w}_0\rangle + \langle \overline{u}_0, \mathcal{R}_0\overline{u}_0\rangle)\,dt \to \min_{\overline{u}_0},$$

$$d\overset{(1)}{\overline{x}}_0/dt = \overset{(1)}{\overline{x}}_0/2 + 5\overset{(1)}{\overline{y}}_0/2,\ d\overset{(2)}{\overline{x}}_0/dt = 0,\ 0 = \overset{(k)}{\overline{u}}_0,\ k = 1,2,\ \overset{(1)}{\overline{x}}_0(0) = 10,\ \overset{(2)}{\overline{x}}_0(0) = 5.$$

$$\Pi_{00}P:\ \Pi_{00}J = 1/2\int_0^{+\infty} (\langle \Pi_{00}w, \mathcal{W}_0\Pi_{00}w\rangle + \langle \Pi_{00}u, \mathcal{R}_0\Pi_{00}u\rangle)\,d\tau_0 \to \min_{\Pi_{00}u},$$

$$d\Pi_{00}\overset{(k)}{x}/d\tau_0 = 0,\ k = 1,2,\ d\Pi_{00}\overset{(1)}{y}/d\tau_0 = \Pi_{00}\overset{(1)}{u},\ 0 = \Pi_{00}\overset{(2)}{u},\ \overset{(1)}{\overline{y}}_0(0) + \Pi_{00}\overset{(1)}{y}(0) = 0.$$

$$Q_{00}P:\ Q_{00}J = 1/2\int\limits_{-\infty}^{0}(\langle Q_{00}w, \mathcal{W}_0 Q_{00}w\rangle + \langle Q_{00}u, \mathcal{R}_0 Q_{00}u\rangle)\,d\sigma_0 \to \min\limits_{Q_{00}u},$$

$$d{Q_{00}}\overset{(k)}{x}/d\sigma_0 = 0,\ k = 1,2,\ \ d{Q_{00}}\overset{(1)}{y}/d\sigma_0 = {Q_{00}}\overset{(1)}{u},\ 0 = {Q_{00}}\overset{(2)}{u}.$$

$$\Pi_{10}P:\ \Pi_{10}J = 1/2\int\limits_{0}^{+\infty}(\langle \Pi_{10}w, \mathcal{W}_0 \Pi_{10}w\rangle + \langle \Pi_{10}u, \mathcal{R}_0 \Pi_{10}u\rangle)\,d\tau_1 \to \min\limits_{\Pi_{10}u},$$

$$d{\Pi_{10}}\overset{(k)}{x}/d\tau_1 = 0,\ k = 1,2,\ d{\Pi_{10}}\overset{(1)}{y}/d\tau_1 = 0,\ d{\Pi_{10}}\overset{(2)}{y}/d\tau_1 = {\Pi_{10}}\overset{(2)}{u},$$

$$\overset{(2)}{\overline{y}}_0(0) + {\Pi_{00}}\overset{(2)}{y}(0) + {\Pi_{10}}\overset{(2)}{y}(0) = 0.$$

$$Q_{10}P:\ Q_{10}J = 1/2\int\limits_{-\infty}^{0}(\langle Q_{10}w, \mathcal{W}_0 Q_{10}w\rangle + \langle Q_{10}u, \mathcal{R}_0 Q_{10}u\rangle)\,d\sigma_1 \to \min\limits_{Q_{10}u},$$

$$d{Q_{10}}\overset{(k)}{x}/d\sigma_1 = 0,\ k = 1,2,\ d{Q_{10}}\overset{(1)}{y}/d\sigma_1 = {Q_{10}}\overset{(1)}{u},\ 0 = {Q_{10}}\overset{(2)}{u}.$$

$$\overline{P}_1:\ \overline{J}_1 = \int\limits_{0}^{1}(\langle \overline{w}_1, 1/2\mathcal{W}_0\overline{w}_1 + (\mathcal{W}_1\overline{w}_0 - \mathcal{A}_1'\overline{\psi}_0)\rangle + \langle \overline{u}_1, 1/2\mathcal{R}_0\overline{u}_1\rangle)\,dt \to \min_{\overline{u}_1},$$

$$d\overset{(1)}{\overline{x}}_1/dt = \overset{(1)}{\overline{x}}_1/2 + 5\overset{(1)}{\overline{y}}_1/2 - 5\overset{(1)}{\overline{y}}_0,\ d\overset{(2)}{\overline{x}}_1/dt = 0,\ \ d\overset{(2)}{\overline{y}}_0/dt = \overset{(1)}{\overline{u}}_1,\ 0 = \overset{(2)}{\overline{u}}_1,$$

$$\overset{(k)}{\overline{x}}_1(0) + {\Pi_{01}}\overset{(k)}{x}(0) + {\Pi_{11}}\overset{(k)}{x}(0) = 0,\ k = 1,2.$$

$$\Pi_{01}P:\ \Pi_{01}J = \int\limits_{0}^{+\infty}(\langle \Pi_{01}w, 1/2\mathcal{W}_0\Pi_{01}w + (\mathcal{W}_1\Pi_{00}w - \mathcal{A}_1'\Pi_{00}\psi)\rangle +$$

$$+\langle \Pi_{01}u, 1/2\mathcal{R}_0\Pi_{01}u\rangle)\,d\tau_0 \to \min\limits_{\Pi_{01}u},$$

$$d{\Pi_{01}}\overset{(1)}{x}/d\tau_0 = {\Pi_{00}}\overset{(1)}{x}/2 + 5{\Pi_{00}}\overset{(1)}{y}/2,\ d{\Pi_{01}}\overset{(2)}{x}/d\tau_0 = 0,$$

$$d{\Pi_{01}}\overset{(1)}{y}/d\tau_0 = {\Pi_{01}}\overset{(1)}{u},\ \ d{\Pi_{00}}\overset{(2)}{y}/d\tau_0 = {\Pi_{01}}\overset{(2)}{u},\ \overset{(1)}{\overline{y}}_1(0) + {\Pi_{01}}\overset{(1)}{y}(0) + {\Pi_{11}}\overset{(1)}{y}(0) = 0.$$

$$Q_{01}P:\ Q_{01}J = 1/2\int\limits_{-\infty}^{0}(\langle Q_{01}w, \mathcal{W}_0 Q_{01}w\rangle + \langle Q_{01}u, \mathcal{R}_0 Q_{01}u\rangle)\,d\sigma_0 \to \min\limits_{Q_{01}u},$$

$$d{Q_{01}}\overset{(1)}{x}(\sigma_0)/d\sigma_0 = {Q_{00}}\overset{(1)}{x}/2 + 5{Q_{00}}\overset{(1)}{y}/2,\ d{Q_{01}}\overset{(2)}{x}/d\sigma_0 = 0,\ d{Q_{01}}\overset{(1)}{y}/d\sigma_0 = {Q_{01}}\overset{(1)}{u},$$

$$d{Q_{00}}\overset{(2)}{y}/d\sigma_0 = {Q_{01}}\overset{(2)}{u}.$$

$$\Pi_{11}P:\ \Pi_{11}J = 1/2\int\limits_{0}^{+\infty}(\langle \Pi_{11}w, \mathcal{W}_0 \Pi_{11}w\rangle + \langle \Pi_{11}u, \mathcal{R}_0 \Pi_{11}u\rangle)\,d\tau_1 \to \min\limits_{\Pi_{11}u},$$

$$d{\Pi_{11}}\overset{(k)}{x}/d\tau_1 = 0,\ k = 1,2,\ d{\Pi_{11}}\overset{(1)}{y}/d\tau_1 = {\Pi_{10}}\overset{(1)}{u},\ d{\Pi_{11}}\overset{(2)}{y}/d\tau_1 = {\Pi_{11}}\overset{(2)}{u},$$

$\overset{(2)}{\overline{y}}_1(0) + \Pi_{01}\overset{(2)}{y}(0) + \Pi_{11}\overset{(2)}{y}(0) = 0.$

$$Q_{11}P:\ Q_{11}J = 1/2\int\limits_{-\infty}^{0}\left(\langle Q_{11}w, \mathcal{W}_0 Q_{11}w\rangle + \langle Q_{11}u, \mathcal{R}_0 Q_{11}u\rangle\right)d\sigma_1 \to \min_{Q_{11}u},$$

$$d{Q_{11}}\overset{(k)}{x}/d\sigma_1 = 0,\ k = 1,2,\ \ d{Q_{11}}\overset{(1)}{y}/d\sigma_1 = {Q_{10}}\overset{(1)}{u},\ \ d{Q_{11}}\overset{(2)}{y}/d\sigma_1 = {Q_{11}}\overset{(2)}{u}.$$

$$\overline{P}_2:\ \overline{J}_2 = \int\limits_0^1\left(\langle\overline{w}_2, 1/2\mathcal{W}_0\overline{w}_2 + (\mathcal{W}_1\overline{w}_1 + \mathcal{W}_2\overline{w}_0 - \mathcal{A}_1'\overline{\psi}_1)\rangle + \langle\overline{u}_2, 1/2\mathcal{R}_0\overline{u}_2\rangle\right)dt \to \min_{\overline{u}_2},$$

$$d\overset{(1)}{\overline{x}}_2/dt = \overset{(1)}{\overline{x}}_2/2 + 5\overset{(1)}{\overline{y}}_2/2 - 5\overset{(1)}{\overline{y}}_1,\ d\overset{(2)}{\overline{x}}_2/dt = 0,\ d\overset{(1)}{\overline{y}}_1/dt = \overset{(1)}{\overline{u}}_2,\ d\overset{(2)}{\overline{y}}_0/dt = \overset{(2)}{\overline{u}}_2,$$

$$\overset{(k)}{\overline{x}}_2(0) + \Pi_{02}\overset{(k)}{x}(0) + \Pi_{12}\overset{(k)}{x}(0) = 0,\ k = 1,2.$$

$$\Pi_{02}P:\ \Pi_{02}J = \int\limits_0^{+\infty}\left(\langle\Pi_{02}w, 1/2\mathcal{W}_0\Pi_{02}w + (\mathcal{W}_1\Pi_{01}w + \mathcal{W}_2\Pi_{00}w - \mathcal{A}_1'\Pi_{01}\psi)\rangle + \right.$$

$$\left. + \langle\Pi_{02}u, 1/2\mathcal{R}_0\Pi_{02}u\rangle\right)d\tau_0 \to \min_{\Pi_{02}u},$$

$$d\Pi_{02}\overset{(1)}{x}/d\tau_0 = \Pi_{01}\overset{(1)}{x}/2 + 5\Pi_{01}\overset{(1)}{y}/2 - 5\Pi_{00}\overset{(1)}{y},\ d\Pi_{02}\overset{(2)}{x}/d\tau_0 = 0,\ d\Pi_{02}\overset{(1)}{y}/d\tau_0 = \Pi_{02}\overset{(1)}{u},$$

$$d\Pi_{01}\overset{(2)}{y}/d\tau_0 = \Pi_{02}\overset{(2)}{u},\ \overset{(1)}{\overline{y}}_2(0) + \Pi_{02}\overset{(1)}{y}(0) + \Pi_{12}\overset{(1)}{y}(0) = 0.$$

$$Q_{02}P:\ Q_{02}J = 1/2\int\limits_{-\infty}^{0}\left(\langle Q_{02}w, \mathcal{W}_0 Q_{02}w\rangle + \langle Q_{02}u, \mathcal{R}_0 Q_{02}u\rangle\right)d\sigma_0 \to \min_{Q_{02}u},$$

$$d{Q_{02}}\overset{(1)}{x}/d\sigma_0 = {Q_{01}}\overset{(1)}{x}/2 + 5{Q_{01}}\overset{(1)}{y}/2 - 5{Q_{00}}\overset{(1)}{y},\ d{Q_{02}}\overset{(2)}{x}/d\sigma_0 = 0,$$

$$d{Q_{02}}\overset{(1)}{y}/d\sigma_0 = {Q_{02}}\overset{(1)}{u},\ \ d{Q_{01}}\overset{(2)}{y}/d\sigma_0 = {Q_{02}}\overset{(2)}{u}.$$

$$\Pi_{12}P:\ \Pi_{12}J = 1/2\int\limits_0^{+\infty}\left(\langle\Pi_{12}w, \mathcal{W}_0\Pi_{12}w\rangle + \langle\Pi_{12}u, \mathcal{R}_0\Pi_{12}u\rangle\right)d\tau_1 \to \min_{\Pi_{12}u},$$

$$d\Pi_{12}\overset{(1)}{x}/d\tau_1 = \Pi_{10}\overset{(1)}{x}/2 + 5\Pi_{10}\overset{(1)}{y}/2,\ d\Pi_{12}\overset{(2)}{x}/d\tau_1 = 0,\ d\Pi_{12}\overset{(1)}{y}/d\tau_1 = \Pi_{11}\overset{(1)}{u},$$

$$d\Pi_{12}\overset{(2)}{y}/d\tau_1 = \Pi_{12}\overset{(2)}{u},\ \overset{(2)}{\overline{y}}_2(0) + \Pi_{02}\overset{(2)}{y}(0) + \Pi_{12}\overset{(2)}{y}(0) = 0.$$

$$Q_{12}P:\ Q_{12}J = 1/2\int\limits_{-\infty}^{0}\left(\langle Q_{12}w, \mathcal{W}_0 Q_{12}w\rangle + \langle Q_{12}u, \mathcal{R}_0 Q_{12}u\rangle\right)d\sigma_1 \to \min_{Q_{12}u},$$

$$d{Q_{12}}\overset{(1)}{x}/d\sigma_1 = {Q_{10}}\overset{(1)}{x}/2 + 5{Q_{10}}\overset{(1)}{y}/2,\ d{Q_{12}}\overset{(2)}{x}/d\sigma_1 = 0,$$

$$d{Q_{12}}\overset{(1)}{y}/d\sigma_1 = {Q_{11}}\overset{(1)}{u},\ d{Q_{12}}\overset{(2)}{y}/d\sigma_1 = {Q_{12}}\overset{(2)}{u}.$$

The results of calculations are given in Fig. 1, 2 and in the table.

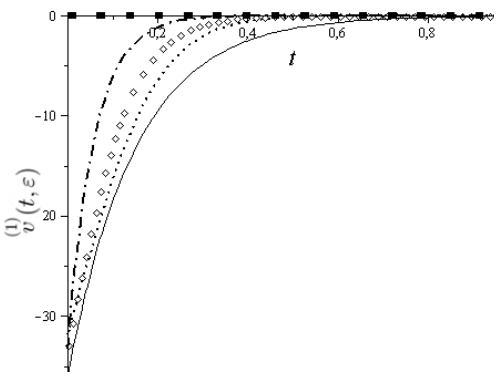

Figure 1. Control $\overset{(1)}{v}(t,\varepsilon)$ with $\varepsilon = 0.3$.

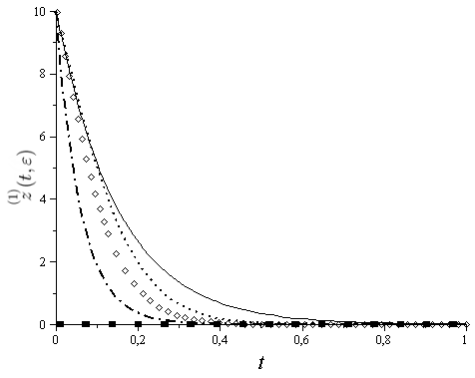

Figure 2. Trajectory $\overset{(1)}{z}(t,\varepsilon)$ with $\varepsilon = 0.3$.

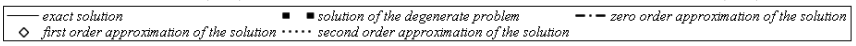

ε	$J(\overset{(1)}{\overline{v}}_{-1}, \overset{(2)}{\overline{v}}_{-2})$	$J(\overset{(1)}{\widetilde{v}}_{-1}, \overset{(2)}{\widetilde{v}}_{-2})$	$J(\overset{(1)}{\widetilde{v}}_{0}, \overset{(2)}{\widetilde{v}}_{-1})$	$J(\overset{(1)}{\widetilde{v}}_{1}, \overset{(2)}{\widetilde{v}}_{0})$	$J(\overset{(1)}{v}_{*}, \overset{(2)}{v}_{*})$
0.3	98.5	36.46	18.80	12.60	9.21
0.1	98.5	4.99	1.54	1.40	1.39
0.05	98.5	1.51	0.60	0.59	0.59

5. Conclusions

Estimates of the proximity of the asymptotic solution to the exact one, given in this paper, show that the direct scheme is an effective method for asymptotic solving the considered class of problems. Moreover, according to lack of growth of values of the performance index under using new asymptotics terms of the optimal control, we obtain for some ε the minimizing sequence of controls $\{\widetilde{u}_n(t,\varepsilon)\}$. The presented example demonstrates this property.

Acknowledgments

The work of the first author was supported by the Russian Science Foundation (Project No. 17-11-01220).

References

[1] Belokopytov, S. V., and Dmitriev, M. G. Direct scheme in optimal control problems with fast and slow motions. *Syst. Control Lett. 8*, 2 (1986), 129–135.

[2] Dmitriev, M. G., and Kurina, G. A. Singular perturbations in control problems. *Autom. Remote Control 67*, 1 (2006), 1–43.

[3] Dmitriev, M. G., Kurina, G. A., and Ovezov, K. A. The use of direct scheme for solution of linear-square problem of optimal control with singular perturbation. *J.*

Comput. Syst. Sci. Int. 35, 4 (1996), 559–565.

[4] Dragan, V. Cheap control with several scales. *Rev. Roumaine Math. Pures Appl. 33*, 8 (1988), 663–677.

[5] Kalashnikova, M. A., and Kurina, G. A. Asymptotic solution of linear-quadratic problems with cheap controls of different costs. *Trudy Instituta Matematiki i Mekhaniki UrO RAN 22*, 1 (2016), 124–139 (in Russian).

[6] Kozlovskaya, T. D. Boundary value problem for systems of conditionally stable type with different small parameters before higher derivatives. *Differentsial'nye Uravneniya 9*, 5 (1973), 832–845 (in Russian).

[7] Kurina, G. A. On a degenerate optimal control problem and singular perturbations. *Soviet Math. Dokl. 18*, 6 (1977), 1452–1455.

[8] Kurina, G. A. Singular perturbations of control problems with equation of state not solved for the derivative (a survey). *J. Comput. Syst. Sci. Int. 31*, 6 (1993), 17–45.

[9] Kurina, G. A., and Kalashnikova, M. A. High order asymptotic solution of linear-quadratic optimal control problems under cheap control with two different costs. *Proceeding of ICSTCC 2017, Romania, Sinaia, October 19-21 (to appear)*.

[10] Kurina, G. A., and Shchekunskikh, S. S. Asymptotics of the solution to a liner-quadratic periodic problem with a singular matrix perturbation in the performance index. *Comput. Math. Mathematic. Phys. 45*, 4 (2005), 579–592.

[11] Tikhonov, A. N. Systems of differential equations containing small parameters in front of the derivatives. *Matematicheskii Sbornik 31(73)*, 3 (1952), 575–586 (in Russian).

[12] Vasil'eva, A. B. Asymptotic methods in the theory of ordinary differential equations containing small parameters in front of the higher derivatives. *USSR Comput. Math. Mathematic. Phys. 3*, 4 (1963), 823–863.

[13] Vasil'eva, A. B., and Butuzov, V. F. *Asymptotic Expansion of Solutions of Singularly Perturbed Equations*. Nauka, Moscow, 1973 (in Russian).

[14] Vasil'eva, A. B., and Butuzov, V. F. *Singularly Perturbed Equations in the Critical Case*. Mathematics Research Center, University of Wisconsin-Madison, 1980.

Kalashnikova M. A., M.Sc. (Ph.D. student): ATOS IT Solutions and Services, Russia, 39400, Voronezh, prospekt Truda, 65 (*margarita.kalashnikova@mail.ru*).

Kurina G.A., Ph.D.: Federal Research Center "Computer Science and Control" of Russian Academy of Sciences; Voronezh State University, Faculty of Mathematics; Institute of Law and Economics, Russia, 119333, Moscow, Vavilova ul., 44/2; Russia, 394018, Voronezh, Universitetskaya pl., 1; Russia, 394000, Voronezh, Leninskii prospekt, 119-A (*kurina@math.vsu.ru*).
The author gave a presentation of this paper during one of the conference sessions.

On some exact solutions for a forced response of nonlinear oscillators

Ivana Kovacic

Abstract: This work presents a theoretical concept for obtaining exact solutions for a forced response of a wide class of externally excited nonlinear oscillators. This includes Duffing-type (hardening, softening, bistable, pure cubic) oscillators and purely nonlinear oscillators whose power of nonlinearity can be any positive real number higher than unity. For that purpose, the external excitation is designed in a special way as having the appropriate form related to the free response of these oscillators, i.e. it is modelled in terms of Jacobi elliptic and Ateb functions. The concept also enables one to design the external excitation of a nonlinear oscillator in such a way that it responds as a completely different type of nonlinear oscillator or as a linear one. In addition, certain known approximate solutions for harmonically excited oscillators in primary resonance can be derived from these exact solutions.

1. Introduction

Nonlinear oscillators with a single or multi-term power-form restoring force appear in many systems in science and engineering [1, 2]. Of interest for this study are those whose free response can be expressed in terms of an exact, closed-form solution. They are governed by the following equation of motion:

$$\ddot{x} + c_1 x + c_\alpha \mathrm{sgn}(x)|x|^\alpha = 0. \tag{1}$$

This model includes the following Duffing-type oscillators (DO) with cubic nonlinearity ($\alpha = 3$): hardening ($c_1 > 0, c_3 > 0$), softening ($c_1 > 0, c_3 < 0$), bistable ($c_1 < 0, c_3 > 0$), and pure cubic ($c_1 = 0, c_3 > 0$). This also includes purely nonlinear oscillator ($\alpha > 1,\ c_1 = 0,\ c_\alpha > 0$). The aim of this study is to show how to design a periodic external excitation $F(t)$ acting on them, so that the corresponding equation of motion

$$\ddot{x} + c_1 x + c_\alpha \mathrm{sgn}(x)|x|^\alpha = F(t), \tag{2}$$

has the steady-state response obtained as an exact solution as well. The motivating methodology is presented in Section 2. Section 3 contains its extension to Duffing-type oscillators, followed by an illustrative example. Section 4 is structured in the same way but it is concerned with purely nonlinear oscillators. Section 5 contains the derivation showing that the well-known approximate solution for

harmonically excited Duffing oscillator in primary resonance can be derived from the exact solution obtained for the system with an elliptic-type excitation.

Given the fact that the oscillators listed above have the exact solutions in terms of Jacobi elliptic and Ateb functions, the external excitation $F(t)$ will also be expressed in terms of these functions. Thus, the external excitation will be periodic, but not harmonic as in the case $F(t) = \cos(\Omega t)$, which has been widely studied in the literature (see, for example, [1] and [2] and the references cited therein). Dynamics of such harmonically excited nonlinear oscillators have been thoroughly investigated and associated with *approximate* solutions for their steady-state responses. However, the investigations presented herein are fundamentally different as they are associated with *exact solutions* for their steady-state responses. It has already been demonstrated that some of the already known approximated solutions can be derived from such exact solutions obtained for a specially designed periodic excitation [3, 4], which makes this approach very interesting and general. The idea of a special design of the external excitation to obtain the exact solution for the resulting steady-state response dates back to Hsu [3]. This idea has recently been extended to forced one-degree-of-freedom undamped nonlinear oscillators with cubic and quadratic nonlinearities [5], multi-degree-of-freedom purely nonlinear chains [6] as well as to pure cubic bars exhibiting longitudinal vibration [7]. The results presented subsequently are the continuation of these investigations, aiming to contribute to their further extensions.

2. On the motivating methodology

Let us start with a simple harmonic oscillator (SHO) governed by Eq. (1) with $c_\alpha = 0$, where $c_1 > 0$. Its free response corresponding to the following initial conditions $x(0) = A, \dot{x}(0) = 0$ has the form

$$x = A\cos(\sqrt{c_1}\, t). \tag{3}$$

Although the initial amplitude A and the coefficient c_1 in front of the linear term (the square of the natural frequency) can be both made equal to unity by an appropriate normalization, they are left in this form for the sake of clarity and clear generalizations.

If one takes the external excitation F as proportional to the displacement $F=B\,x$, where B stands for the coefficient of proportionality, the equation of motion is

$$\ddot{x} + (c_1 - B)x = 0. \tag{4}$$

The solution satisfying $c_1 > B$ is easily obtained based on Eqs. (3) and (4) in the form:

$$x = A\cos(\Omega\, t), \quad \Omega = \sqrt{c_1 - B}. \tag{5a,b}$$

Equations (5a,b) can now be used to transform Eq. (1) with $c_\alpha = 0$ into the equation of motion of the forced SHO

$$\ddot{x} + c_1 x = BA\cos\left(\sqrt{c_1 - B}\, t\right), \tag{6}$$

whose response has the form given by Eq. (5a,b). Note that since there is no damping in the system and the excitation acts from t=0, the resulting response does not have a transient part and a steady-state part, but it goes straight to the latter. It should be emphasized that there are three parameters involved in the solution A, B and Ω and only one relationship between two of them, Eq. (5b). This implies that A can be arbitrarily chosen, while one a priory decides whether to define B or Ω, and the other parameter should then be calculated based on Eq. (5b).

The external force is assumed here to be proportional to the displacement to yield the forced response in a straightforward way, but it can actually be interpreted as being proportional to the restoring force. This interpretation enables one to apply the same methodology to nonlinear oscillators, which will be demonstrated subsequently.

3. Application to Duffing-type oscillators

Let us consider now conservative Duffing-type oscillators listed after Eq. (1). Their free response can be expressed as in terms of different Jacobi elliptic functions [4, 5, 8] as follows

$$x = A\,\mathrm{ep}[\omega\, t|m], \tag{7}$$

where ep stands for the cn or sn Jacobi elliptic function, ω is their frequency and m is the corresponding elliptic parameter. Note that both the frequency of these elliptic functions and the elliptic parameter are amplitude-dependent. Only in the case of the pure cubic oscillator, the latter is constant and equal to ½. Note also that for $c_1 > 0, c_3 = 0$, the elliptic function turns into the trigonometric function [4] and the solution of motion for the SHO is obtained, Eq. (3).

Let us now focus on externally excited DOs, assuming that this excitation has the form of the Duffing-type restoring force $F = Bx + Dx^3$, where B and D are constants. With this substitution, Eq. (2) becomes

$$\ddot{x} + (c_1 - B)x + (c_3 - D)x^3 = 0. \tag{8}$$

By comparing Eq. (8) to Eq. (1) with $\alpha = 3,$ and using Eq. (7), the exact solution for the resulting response x_r is found to be

$$x_r = A\,\mathrm{ep}[\omega_r\, t|m_r], \tag{9}$$

where ω_r and m_r now differs from the one in Eq. (7) in the fact that the constant c_1 is replaced by $c_1 - B$, and the constant c_3 is replaced by $c_3 - D$. The external excitation is then

$$F = BA\,\mathrm{ep}[\omega_r\, t|m_r] + DA\,\mathrm{ep}^3[\omega_r\, t|m_r]. \tag{10}$$

Note that if the signs of the expressions $(c_1 - B)$ and $(c_3 - D)$ are the same as in the original unforced DO, then the type of ep and the expressions for its frequency and elliptic parameter stay the same, but if their signs change, resulting in another type of the DO, then one needs to use the appropriate forms of the solution for such type of the oscillator [4, 5, 8]. Thus, not only that this approach can be used for obtaining the exact solution for the steady-state forced response, but it enables one to design the external excitation to make DOs respond as free DOs of the same or different types. This approach is illustrated subsequently on an example.

3.1. Example 1

The methodology presented can be used for choosing the external force to change the type of the oscillators governed by Eq. (8) and there are several possibilities for doing so. The case D=0 when the external force is proportional to the displacement, i.e. to the linear part of the restoring force, is considered in [5]. The general case when B and D are different from zero, i.e. when the external force is related to the overall restoring force is analysed in [3]. Here, the case that is not covered in these publications is considered: $B = c_1$ and $c_3 > D$. With these conditions used, Eq. (8) turns into a pure cubic oscillator, with the exact solution for the response

$$x_r = A\,\mathrm{cn}\left[\omega_r\, t\middle|\frac{1}{2}\right],\ \omega_r = \sqrt{c_3 - D}\,A. \tag{11a,b}$$

By introducing this solution into the expression for the force and then into Eq. (2) with $B = c_1$, the following equation of motion is obtained

$$\ddot{x} + c_1 x + c_3 x^3 = c_1 A\,\mathrm{cn}\left[\sqrt{c_3 - D}\,A\,t\middle|\frac{1}{2}\right] + DA^3\mathrm{cn}^3\left[\sqrt{c_3 - D}\,A\,t\middle|\frac{1}{2}\right]. \tag{12}$$

There are three parameters A, D and ω_r here and one relationship between them, which is given by Eq. (11b). Thus, two of them are arbitrary. If the amplitude is to be calculated, the frequency-amplitude relationship (11b) needs to be used. Note that for c_3 close to D, the value of A can be very large, which might be undesirable and should be carefully dealt with.

In order to illustrate the results derived, let us make the requirement that the period of the response T is fixed. This period is related to the frequency of the cn function via the relationship $T = 4K(m_r)/\omega_r$, where $K(m_r) \equiv K$ is the elliptic integral of the first kind, which gives $\omega_r = 4K(m_r)/T$. By choosing D as well, the amplitude A can be calculated from Eq. (11b). The corresponding example with the period of 10s is shown in Figure 1a (the rest of the parameters c_1, c_3,

D are given in the figure caption, while the amplitude is calculated to be $A = 2\sqrt{2}K\left(\frac{1}{2}\right)/5 \approx 1.04882$. As another example, the additional requirement is introduced: let the period, the parameters c_1 and c_3 stay the same, but the amplitude is reduced for 50%. Equation (11b) leads $D = -1$, and the corresponding responses are presented in Figure 1b. Numerical solutions of the original equation of motion of the hardening DO, Eq. (1) are also plotted as the green dotted line, clearly illustrating the change caused.

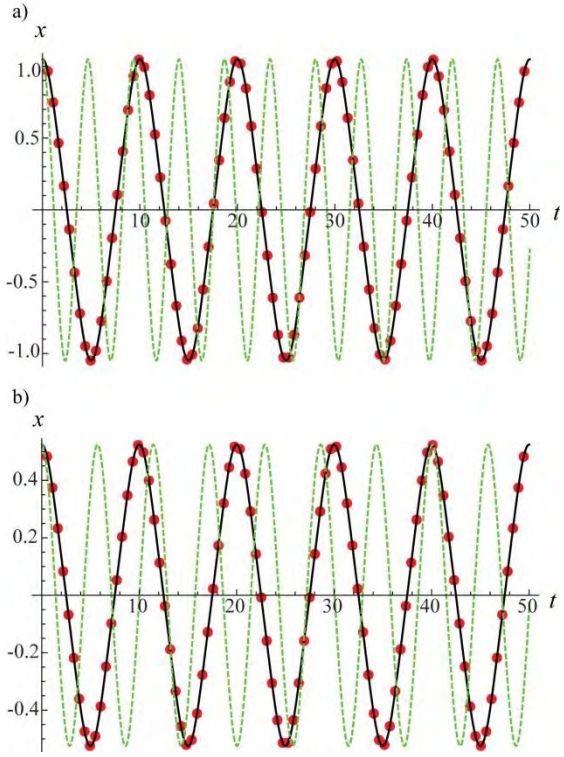

Figure 1. Time response corresponding to $c_1 = 1,\ c_3 = 1$ and: a) $D = 0.5\ \ A = 2\sqrt{2}K\left(\frac{1}{2}\right)/5$, b) $D = -1\ \ A = \sqrt{2}K\left(\frac{1}{2}\right)/5$. Numerical solutions of Eq. (12) - black solid line, the analytical response (11a,b) - red dots, the numerical solution of the original equation of motion of the hardening Duffing equation (1) - green dotted line.

To provide additional insights into the harmonic content of the response for the case shown in Figure 1b, the Fourier series expansion for the cn function with the elliptic parameter $m = 1/2$ is used. It gives:

$$\frac{x_r}{A} \approx 0.95501\cos(0.62832t) + 0.04305\cos(1.88496t) + \\ 0.00186\cos(3.14160t) + 0.00008\cos(4.39823t) + ..., \tag{13}$$

leading to the conclusion that the first harmonic takes 95,5% of the overall response, the third harmonic 4.3% and the rest of them all together contribute less than 0.2%. The corresponding force from the right-hand side of Eq. (12) can be developed into the following Fourier series

$$F_{app} \approx 0.401959\cos(0.62832t) - 0.0175306\cos(1.88496t) - 0.00481469\cos(3.14160t) + ... \tag{14}$$

The expression for the force given by Eq. (14) defines how this tuned excitation can be generated in a lab - as a multi-term harmonic excitation. Figure 2 is plotted based on it. It contains: i) the numerical solution of Eq. (12) (black thick solid line); ii) the numerical solution of Eq. (12) where the right-hand side is approximated by Eq. (13), labelled by the green dotted line; iii) the numerical solution of Eq. (12), where the right-hand side is approximated by first two terms from Eq. (14) and labelled by the blue dashed line; iv) the numerical solution of Eq. (12), where the right-hand side is approximated only by the first term from Eq. (14) and labelled by red solid line. It is seen that the approximations described under ii) and iii) are in good agreement with the exact one, while the last one described under iv) shows some discrepancy around the maximal displacement, as better seen in the enlarger part of the time-response plotted in Figure 2b.

4. Applications to purely nonlinear oscillators

Let us consider now purely nonlinear oscillators governed by Eq. (1) with $\alpha > 1,\ c_1 = 0,\ c_\alpha > 0$. Their free response can be expressed in terms of the Ateb function [9 - 11], as follows

$$x = A\ \mathrm{ca}(\alpha, 1, \omega\ t),\ \omega = A^{(\alpha-1)/2}\sqrt{\frac{c_\alpha(\alpha+1)}{2}}. \tag{15a,b}$$

When $\alpha = 1$, this Ateb-form solution transforms into the Cosine solution, Eq. (3).

Focusing now on the external excitation in Eq. (2) with $c_1 = 0$, it is assumed that $F(t) = B\mathrm{sgn}(x)|x|^\alpha$, so that the equation of motion becomes

$$\ddot{x} + (c_\alpha - B)\mathrm{sgn}(x)|x|^\alpha = 0. \tag{16}$$

Assuming that $c_\alpha > B$, the steady-state response has the form (15a) with c_α in (15b) replaced by $(c_\alpha - B)$. So, the equation of motion and its response x_r are

$$\ddot{x} + c_\alpha\mathrm{sgn}(x)|x|^\alpha = BA\ \mathrm{ca}\left(\alpha, 1, A^{(\alpha-1)/2}\sqrt{\frac{(c_\alpha-B)(\alpha+1)}{2}}\ t\right), \tag{17}$$

$$x_r = A\,\mathrm{ca}\left(\alpha, 1, A^{(\alpha-1)/2}\sqrt{\frac{(c_\alpha - B)(\alpha+1)}{2}}\,t\right). \tag{18}$$

Another possible modification is that one assumes the excitation force in the form

$$F(t) = c_\alpha \mathrm{sgn}(x)|x|^\alpha - E\mathrm{sgn}(x)|x|^\beta, \tag{19}$$

where E>0 and $\beta > 1$. The resulting response will have the form (15a,b) but with α replaced by β, and c_α replaced by E. So, the response will correspond to a free purely nonlinear oscilaltor with a different power of nonlinearity β. One example is given subsequently to illustate this methodology.

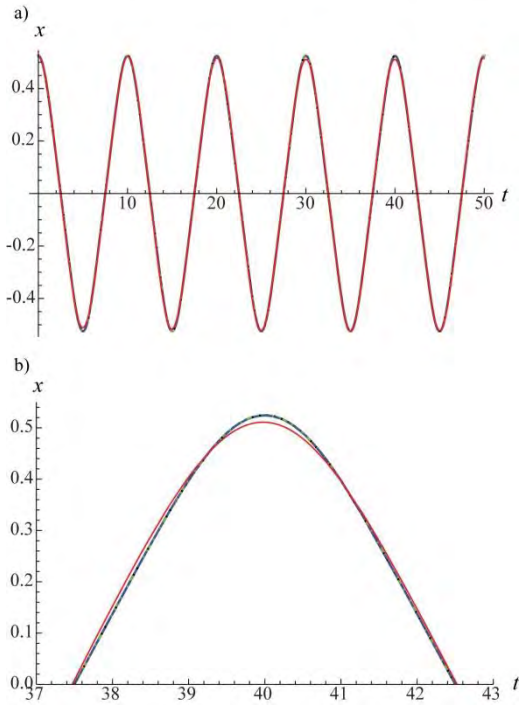

Figure 2. Time response corresponding to $c_1 = 1,\ c_3 = 1,\ D = 1,\ A = \frac{\sqrt{2}K\left(\frac{1}{2}\right)}{5}$: a) several periods; b) an enlarged part around the maximal displacement. The numerical solution of Eq. (12) - black thick solid lines, the numerical solution of Eq. (12) with the right-hand side approximated by Eq. (14) - green dotted lines, the numerical solution of Eq. (12) with the right-hand side approximated by first two terms from Eq. (14) - blue dashed lines, the numerical solution of Eq. (12) where the right-hand side is approximated by only the first term from Eq. (14) - blue solid lines.

4.1 Example 2

If $\beta = 1$, the resulting oscillator is the SHO. Its solution has the form of the Cosine function:

$$x_r = A\cos\left(\sqrt{E}t\right), \tag{20}$$

which should be substituted into Eqs. (1) and (19) to derive the equation of motion:

$$\ddot{x} + c_\alpha \operatorname{sgn}(x)|x|^\alpha = c_\alpha \operatorname{sgn}\left(A\cos\left(\sqrt{E}t\right)\right)\left|A\cos\left(\sqrt{E}t\right)\right|^\alpha - EA\cos\left(\sqrt{E}t\right) \tag{21}$$

If $\beta = 3$, the excitation in Eq. (19) would yield the equation of motion corresponding to a pure cubic DO. The corresponding response is given by

$$x_r = A\operatorname{cn}\left(\sqrt{E}At\middle|\frac{1}{2}\right). \tag{22}$$

After substituting it into Eqs. (1) and (19), the equation of motion of externally excited purely nonlinear oscillators that respond as a conservative pure cubic DO is derived:

$$\ddot{x} + c_\alpha \operatorname{sgn}(x)|x|^\alpha = c_\alpha \operatorname{sgn}\left(A\operatorname{cn}\left(\sqrt{E}At\middle|\frac{1}{2}\right)\right)\left|A\operatorname{cn}\left(\sqrt{E}At\middle|\frac{1}{2}\right)\right|^\alpha - EA^3\operatorname{cn}^3\left(\sqrt{E}At\middle|\frac{1}{2}\right). \tag{23}$$

It is believed that this can be a convenient way for modifying the stiffness characteristics without influencing internal elements, but by using the external excitation.

Figure 3 contains the time responses of the original oscillator with the power of nonlinearity $\alpha = 1/2$ as well as time responses for all the following cases: $\beta = 1$ (Figure 3a), $\beta = 3$ (Figure 3b). It is clearly seen that the change of the power of nonlinearity causes the extension of the period. The shape of vibrations also changes implying the modification of the harmonic content.

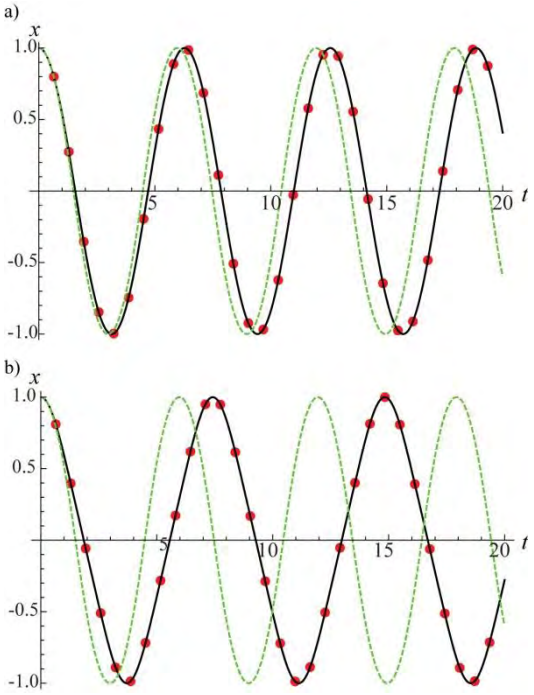

Figure 3. Time responses for purely nonlinear oscillators corresponding to $c_{1/2}$ =1, $\alpha = 1/2$, E=1, A=1 and a) $\beta = 1$; b) $\beta = 3$. Numerical solutions of the externally excited original oscillator with the force given by Eq. (20) - black solid line, the resulting analytical response - red dots, the numerical solution of the original conservative oscillator Eq. (1) - green dotted line.

5. On some approximations

Let us consider now the case when the external force is propotional only to the linear part of the restoring force, which is given by Eq. (8) with D=0 [3]. Using the well known exact solution for the Duffing conservative oscillator [4], its solution can be written down as:

$$x = A\,\mathrm{cn}\left[\omega_r t, m\right], \quad \omega_r = \sqrt{1 - B + c_3 A^2}\,, \quad m = \frac{c_3 A^2}{2\left(1 - B + c_3 A^2\right)}. \tag{24a-c}$$

Equations (24b,c) yield the following expressions for amplitude of the response A and the constant B :

$$A = \sqrt{\frac{2m}{c_3}}\,\omega_r\,, \quad B = 1 - \omega_r^2\left(1 - 2m\right). \tag{25a,b}$$

Thus, the excitation $F=Bx$ is given by

$$F = \sqrt{\frac{2m}{c_3}}\omega_r \,[1-\omega_r^2(1-2m)]\mathrm{cn}[\omega_r t, m]. \tag{26}$$

It will be demonstarted now that this case can be transformed into a harmonically excited Duffing oscillator and the exact solution (24a-c) can be simplified to the well-known approximation for its steady-state primary resonance response. The harmonic excitation with the amplitude F_0 and the angular frequency Ω is

$$F = F_0 \cos\Omega t. \tag{27}$$

Comparing it with Eq. (26) and using (25a), one finds that

$$F_0 = A[1-\omega_r^2(1-2m)], \tag{28}$$

while the equality of periods of the elliptic and harmonic function imposes $4K/\omega_r = 2\pi/\Omega$, where $K(m) \equiv K$. This yields $\Omega = \omega_r \pi/2K$. Using this expression, Eq. (25a) and the series expansion $K^2 \approx \frac{\pi^2}{4}\left(1+\frac{m}{2}\right)$, one can derive

$$c_3 A^2 - 2\Omega^2 \, m = 0. \tag{29}$$

Analogously, Eq. (28) transforms into

$$1-\Omega^2 + \frac{3}{2}m\Omega^2 = \frac{F_0}{A}. \tag{30}$$

Equations (29) and (30) give:

$$\Omega^2 = 1 + \frac{3}{4}c_3 A^2 - \frac{F_0}{A}, \tag{31}$$

which is the well-known frequency-amplitude equation of a conservative harmonicallz excited Duffing oscilaltor [1, 2]. Furthermore, the exact solution (24a) can be developed into the Fourier series, expanding also the first two coefficients into series with respect to m to derive

$$\begin{aligned} x = A\,\mathrm{cn}[\omega_r t, m] &\approx A\,C_1 \cos\left(\frac{\pi}{2K}\omega_r t\right) + A\,C_3 \cos\left(3\frac{\pi}{2K}\omega_r t\right) + \ldots = \\ &= A\left(1-\frac{m}{16}\right)\cos\Omega t + A\frac{m}{16}\cos(3\Omega t) = \left(A - \frac{1}{32}c_3 A^3\right)\cos\Omega t + \frac{1}{32}c_3 A^3 \cos(3\Omega t). \end{aligned} \tag{32}$$

This approximate solution has the form of the well-known solution obtained by the classical method of multiple scales [1, 2]. The fact that the exat steady-state response of the Dyffing oscillator with an elliptic-type forcing can be transformed into the well-known and widely used expressions for the harmonically forced Duffing oscillator speaks in favour of the presented methodology involving specially designed external excitation, despite the fact that it is given in terms of special functions.

6. Conclusions

This study has been concerned with a methodology related to the design of external excitation of conservative nonlinear oscillators that enables one to obtain the exact solution for the corresponding steady-state response. The nonlinear oscillators considered have included Duffing-type oscillators (hardening, softening, bistable, pure cubic) and also purely nonlinear oscillators. They have the exact solutions in terms of Jacobi elliptic functions and the Ateb function, respectively. These solutions have been used to express the external excitation in terms of these functions as well. It has also been demonstrated how one can design the external excitation of a nonlinear oscillator in such a way that it responds as a completely different type of nonlinear oscillator or as a linear one. Furthermore, it has been shown that certain known approximate solutions for harmonically excited Duffing oscillators in primary resonance can be derived from these exact solutions, which speaks in favor of their generality and requires further investigations of these approximations for other nonlinear oscillators.

Acknowledgments

This work has been financially supported by the Ministry of Education, Science and Technological Development, Republic of Serbia (Project No. ON174028).

References

[1] Kovacic, I. and Brennan, M.J. (Eds). *The Duffing equation: nonlinear oscillators and their behavior*. John Wiley and Sons, Chichester, 2011.

[2] Nayfeh, A.H. and Mook, D.T. *Nonlinear oscillations*. Wiley, NewYork, 1979.

[3] Hsu, C.S. On the application of elliptic functions in nonlinear forced oscillations. Quarterly of *Applied Mathematics* 17 (1960), 393-407.

[4] Kovacic, I., Cveticanin, L., Zukovic, M., Rakaric, Z. Jacobi elliptic functions: a review of nonlinear oscillatory application problems. *Journal of Sound and Vibration* 380 (2016), 1-36.

[5] Rakaric., Z., Kovacic, I., Cartmell, M. On the design of external excitations in order to make nonlinear oscillators respond as free oscillators of the same or different type. *International Journal of Non-Linear Mechanics*, in press, doi:10.1016/j.ijnonlinmec.2016.06.012.

[6] Kovacic, I., Zukovic, M. Coupled purely nonlinear oscillators: normal modes and exact solutions for free and forced responses. *Nonlinear Dynamics* 87 (2017), 713-726.

[7] Kovacic, I., Zukovic, M. On the response of some discrete and continuous oscillatory systems with pure cubic nonlinearity, *International Journal of Nonlinear Mechanics*, Under Review, 2017.

[8] Byrd, P., Friedman, M. *Handbook of elliptic integrals for engineers and scientists*. Springer, Berlin, 1954.

[9] Senik, P.M. On Ateb-functions, *DAN URSR* 1 (1968), 23-26.

[10] P.M. Senik, Inversions of the incomplete Beta function. *Ukrainian Mathematical Journal* 21 (1969), 271-278.

[11] Kovacic I., On the response of purely nonlinear oscillators: an Ateb-type solution for motion and an Ateb-type external excitation. *International Journal of Nonlinear Mechanics* 92 (2017), 15-24.

Ivana Kovacic, Professor: University of Novi Sad, Faculty of Technical Sciences, Centre of Excellence for Vibro-Acoustic Systems and Signal Processing, Trg. D. Obradovica 6, 21000, Novi Sad, Serbia (*ivanakov@uns.ac.rs*).

Derivation and investigation of the generalized nonlinear Schrödinger equation of cosmogonical body forming

Alexander M. Krot

*A*bstract: This work considers the statistical theory of gravitating spheroidal bodies to derive a new generalized nonlinear Schrödinger-like equation of a gravitating cosmogonical body formation. The statistical theory for a cosmogonical body forming (so-called spheroidal body with fuzzy boundaries) has been proposed in our previous works. This paper investigates different dynamical states of a gravitating spheroidal body and respective forms of the generalized nonlinear time-dependent Schrödinger equation. In particular, the derived time-dependent generalized nonlinear Schrödinger-like equation describes not only the state of virial mechanical equilibrium and the quasi-equilibrium gravitational condensation state, but the initial equilibrium gravitational condensation state taking place in a forming gas-dust protoplanetary cloud as well as the soliton disturbances state occurring in a spheroidal body under formation and also the gravitational instability states providing a formation of core of cosmogonical body.

1. Introduction

A statistical theory of a gravitating cosmogonical body formed by a numerous of interacted particles isolated from an influence of external fields and bodies has been proposed in our previous works [1–4]. Within framework of this theory, the forming cosmogonical bodies are shown to have fuzzy contours and are represented by spheroidal forms (unlike ordinary macroscopic bodies having distinct contours). It has been pointed out that a spheroidal body has a clearly outlined form if the potential energy of gravitational interaction of its particles is sufficiently great and the body's mass itself is relatively small.

A process of slow-flowing-in time initial gravitational condensation of a spheroidal body has been investigated in Ref. [1–3]. Within framework of this approach, the equations have been derived for description of a slow-flowing *gravitational condensation* of a spheroidal body in a vicinity of equilibrium and quasi-equilibrium state.

For the first time the problem of gravitational condensation was investigated by J. Jeans [5]. Let us note that the gravitational condensation problem of an infinitely distributed substance is directly connected with the gravitational instability problem, see for example Ref. [6]. The main difficulty of

Jeans' theory is connected with the *gravitational paradox* [6]: for an infinite homogeneous substance there exists no potential of gravitational field φ_g in accord with Poisson equation.

E. Nelson [7] and later on L. Nottale [8, 9] have developed their theories to describe both deterministic and stochastic behavior of a particle in gravitational field. The important point in Nelson's work [7] is that a diffusion process can be described in terms of a *Schrödinger-type equation*, with help of the hypothesis that any particle in the empty space, under the influence of any interaction field, is also subject to a universal Brownian motion.

In this work, we derive the generalized nonlinear Schrödinger equation of cosmogonical body forming within framework of the statistical theory [1–4]. With its help, we also investigate the dynamical states of a process of gravitational condensation of cosmogonical body.

2. The mass density and potentials in result of an initial gravitational condensation of a molecular cloud

To solve the mentioned problems of gravitational condensation of a molecular cloud we will use the statistical theory [1–4]. We consider the statistical theory beginning from the derivation of a distribution function of particles in a space filled in homogeneous and isotropic initially gaseous nebula. The statistical aspect of the problem results from the fact that the considered body consisting of gaseous matter is a system containing a large number of particles interacting among themselves by oscillations in a cosmic vacuum. In microphysics, the cosmic vacuum represents a ground energetic state of quantum fields, and its experimental manifestation is Casimir effect [10 p.1154]. The similar oscillations modifying forms of particle trajectories have been considered by Nelson [7] and Nottale [8, 9], so that we can say about the *initial oscillatory interactions* of particles. In macrophysics, it is alleged that the cosmological constant describes the cosmic vacuum [10, 11].

According to our previous work [1] the volume probability density function Φ describing a particle distribution into a rotating gaseous cloud (being in a *state of relative mechanical equilibrium*) can be expressed in spherical coordinates as follows:

$$\Phi(r,\theta) = (\alpha/2\pi)^{3/2}(1-\varepsilon_0^2)e^{-\alpha r^2(1-\varepsilon_0^2\sin^2\theta)/2}, \tag{1}$$

where r is a distance, θ and ε are polar and azimuth angles, α is a *parameter of gravitational condensation*, ε_0 is a constant of stabilization of the variable ε.

Obviously, when $\varepsilon_0^2 \to 0$ then the equation (1) goes to the describing volume probability density equilibrium function in the non-rotational case (or *slowly rotational* one) [1, 3]:

$$\Phi(r) = (\alpha/2\pi)^{3/2}e^{-\alpha r^2/2}, \tag{2}$$

If M is a mass of gaseous body then its mass density is $\rho = M\Phi$ simply. Therefore, the mass density for a rotating gaseous body can be written in spherical coordinate system [1, 3]:

$$\rho(r,\theta) = \rho_0(1-\varepsilon_0^2)e^{-\alpha r^2(1-\varepsilon_0^2\sin^2\theta)/2}, \tag{3}$$

where $\rho_0 = M(\alpha/2\pi)^{3/2}$. Obviously, the iso-surfaces (isostera) of the mass density (3) are flattened ellipsoidal ones, and ε_0^2 is a parameter of their flatness (ε_0 is the eccentricity of ellipse). As a rule $|\varepsilon_0| << 1$, so that these mass density iso-surfaces become *spheroidal surfaces.* Thus, under the influence of the initial oscillations of particles an isolated gaseous cloud can be transformed to the spheroid-like gaseous body or, simply say, *spheroidal body* [1–4].

Let us consider the important particular case of spheroidal body which is *sphere-like* gaseous body. Really, we can see that if $\varepsilon_0^2 \to 0$ then the equation (3) becomes the mass density function for a slowly rotating or *immovable* spheroidal body [1–4]:

$$\rho(r) = \rho_0 e^{-\alpha r^2/2}. \tag{4}$$

Calculating the derivatives of ρ (3) with respect to the spatial coordinates h and z as well as the parameters α and ε_0 (supposing them as slowly changing functions, i.e. $\alpha = \alpha(t)$ and $\varepsilon_0 = \varepsilon_0(t)$) we can obtain the following *general equation of antidiffusion* with regard to a deformation of spheroidal body as a result of its rotation [3]:

$$\frac{d\rho}{dt} = -\tilde{\mathrm{G}}(t)\nabla^2\rho, \tag{5}$$

where $\tilde{\mathrm{G}}(t)$ is the generalized *gravitational compression function* (GCF):

$$\tilde{\mathrm{G}}(t) = \frac{1}{2\alpha^2(t)}\cdot\frac{d\alpha}{dt} + \frac{1}{\alpha\varepsilon_0(1-\varepsilon_0^2)}\cdot\frac{d\varepsilon_0}{dt}. \tag{6}$$

In the particular case when $\varepsilon_0 = \mathrm{const}$ and $\varepsilon_0 \approx 0$, Eqs.(5) becomes the pure antidiffusion equation of initial gravitational condensation of immovable (or slowly rotating) spheroidal body [1–4]:

$$\frac{\partial\rho}{\partial t} = -\mathrm{G}(t)\nabla^2\rho, \tag{7}$$

where $\mathrm{G}(t) = \frac{1}{2\alpha^2(t)}\cdot\frac{d\alpha}{dt}$. (8)

Analogous equation of initial gravitational condensation of gaseous substance is true for the distribution function Φ of an immovable (slowly rotating) spheroidal body [1–3]:

$$\frac{\partial\Phi}{\partial t} = -\mathrm{G}(t)\nabla^2\Phi. \tag{9}$$

Thus, initial gravitational interactions of particles stipulated by their quantum oscillations in an isolated gaseous cloud form a spheroidal body and lead to gravitational field becoming. Namely, there is a *threshold* (*critical*) *value* α_c that if $\alpha \geq \alpha_c$ then gravitational field arises in the spheroidal body [1–3]. In the simplest case (4) we can seek a spherically symmetric solution of the Poisson equation:

$$\varphi_g(r) = -\frac{4\pi\gamma\rho_0}{\alpha r}\int_0^r e^{-\frac{\alpha}{2}x^2}\,dx. \tag{10}$$

In the general case of a *rotating* spheroidal body, the axial rotation creates a flattening of its core, therefore the gravitational potential of a uniformly rotating spheroidal body is described by the following expression:

$$\varphi_g(r,\theta) = -2\sqrt{2}\pi\gamma\rho_0(1-\varepsilon_0^2)\int_0^\infty e^{-\frac{\alpha(1-\varepsilon_0^2)r^2\sin^2\theta}{2+\alpha(1-\varepsilon_0^2)s}} e^{-\frac{\alpha r^2\cos^2\theta}{2+\alpha s}} \frac{ds}{\sqrt{2+\alpha s}\cdot[2+\alpha(1-\varepsilon_0^2)s]}. \tag{11}$$

3. The density of antidiffusion mass flow and the antidiffusion velocity into a slow-flowing gravitational compressible spheroidal body

Taking into account that GCF $G(t)$ as well as $\tilde{G}(t)$ does not depend on the spatial variable (see (6) and (8)) we can note therefore the both equations (5), (7) remind completely the continuity equation expressing the law of conservation of mass in a nonrelativistic system [12]:

$$\frac{\partial\rho}{\partial t} + \operatorname{div}\vec{j} = 0 \tag{12}$$

if $\vec{j}$ is a continuum flow density (like a conductive flow) arising at the slow-flowing gravitational condensation of both spheroidal bodies [1–3]:

$$\vec{j} = G(t)\operatorname{grad}\rho; \qquad \vec{j} = \tilde{G}(t)\operatorname{grad}\rho. \tag{13a, b}$$

The conductive (owing to diffusion or thermal conductivity) flows satisfying analogous Eq. (12) in dissipative systems were investigated by I. Prigogine and his co-workers (see, for example, [13, 14]). As it follows from Eq. (13a,b) directly, there exists an *antidiffusion mass flow density* in a slowly compressible gravitating spheroidal body [1–3]. Indeed, applying the equation of continuity (12) to this antidiffusion flow density (13a) (or (13b)) we obtain again the linear antidiffusion equation (7) (or (5)) of initial gravitational condensation. In this connection, let us introduce a conductive velocity for the antidiffusion mass flow density or, simply say, the *antidiffusion velocity* (unlike of the ordinary hydrodynamic velocity $\vec{v}$) for an immovable (or a slowly rotating) spheroidal body [2, 3]:

$$\vec{u} = G(t)\frac{\nabla\rho}{\rho} = G(t)\frac{\nabla(\rho/\rho_0)}{\rho/\rho_0} = G(t)\,\mathrm{grad}\ln(\rho/\rho_0). \tag{14}$$

Since the mass density of spheroidal body is directly proportional to the probability volume density function Φ, then antidiffusion velocity (14) can be defined by the probability volume density function:

$$\vec{u} = G(t)\frac{\nabla\Phi}{\Phi} = G(t)\,\mathrm{grad}\ln\Phi. \tag{15}$$

Now let us estimate the antidiffusion velocity (14) of particles into a spherically symmetric slow-flowing compressible spheroidal body taking account of its mass density function (4):

$$\vec{u}(\vec{r},t) = G(t)\nabla\ln(\rho/\rho_0) = G(t)\nabla\left(-\alpha(t)\vec{r}^{\,2}/2\right) = -G(t)\alpha(t)\vec{r}. \tag{16}$$

We can see that the antidiffusion velocity $\vec{u}$ is expressed by the very simple relation (16) in the case of a spherically symmetric cosmogonical body.

In the general case of *rotating* ellipsoid-like cloud when $\varepsilon_0 \neq 0$ we can also estimate the antidiffusion velocity of particles using the general equation (5) of antidiffusion mass transfer and the formula (3) of mass density [3]:

$$\vec{u} = \tilde{G}(t)\frac{\nabla\rho}{\rho} = \tilde{G}(t)\,\mathrm{grad}\ln\left(\rho(h,z)/\rho_0\right) = \tilde{G}(t)\,\mathrm{grad}\left\{\ln\left(1-\varepsilon_0^2\right) - \alpha\left[h^2\left(1-\varepsilon_0^2\right)+z^2\right]/2\right\} =$$
$$= -\tilde{G}(t)\alpha\left\{\left(1-\varepsilon_0^2\right)h\cdot\vec{e}_h + z\cdot\vec{e}_z\right\} = u_h\cdot\vec{e}_h + u_z\cdot\vec{e}_z \tag{17a}$$

where $\vec{e}_h$ and $\vec{e}_z$ are the basis vectors of cylindrical frame of reference, u_h and u_z are the radial h-projection and the axial z-projection of antidiffusion velocity respectively:

$$u_h = -\tilde{G}(t)\alpha\left(1-\varepsilon_0^2\right)h; \qquad u_z = -\tilde{G}(t)\alpha z. \tag{17b, c}$$

3.1. The derivation of the equations of substance movement into a slow-flowing gravitational compressible spheroidal body

Without loss of generality, we suppose $\varepsilon_0 \to 0$, so that we are going to use Eq. (7) of the slow-flowing gravitational compression of *sphere-like* cosmogonical body. Since the antidiffusion velocity $\vec{u}$ of antidiffusion mass flow satisfies the mentioned continuity equation (12):

$$\frac{\partial\rho}{\partial t} + \mathrm{div}(\rho\vec{u}) = 0 \tag{18}$$

then we can calculate the partial derivative of the antidiffusion velocity (14) with respect to the time:

$$\frac{\partial\vec{u}}{\partial t} = \frac{dG(t)}{dt}\,\mathrm{grad}\ln\rho + G(t)\,\mathrm{grad}\left[\frac{1}{\rho}\cdot\frac{\partial\rho}{\partial t}\right] = \frac{dG(t)}{dt}\left[\frac{1}{G(t)}\vec{u}\right] + G(t)\nabla\left[\frac{1}{\rho}(-\mathrm{div}(\rho\vec{u}))\right] = \tag{19}$$
$$= \frac{d\ln G(t)}{dt}\vec{u} - G(t)\nabla\left[\nabla\vec{u} + \vec{u}\frac{\nabla\rho}{\rho}\right] = -G(t)\,\mathrm{grad}(\mathrm{div}\,\vec{u}) - \mathrm{grad}(\vec{u}^{\,2}) + \frac{d\ln G(t)}{dt}\vec{u}.$$

Let us rewrite Eq. (19) based on the familiar formulas of vector analysis [12, 15]:

$$\frac{1}{2}\,\mathrm{grad}\vec{u}^{\,2} = (\vec{u}\cdot\nabla)\,\vec{u} + [\vec{u}\times \mathrm{rot}\vec{u}]; \qquad \nabla^2\vec{u} = \mathrm{grad}(\mathrm{div}\,\vec{u}) - \mathrm{rot}(\mathrm{rot}\vec{u}). \tag{20a, b}$$

Taking into account Eq. (14) we can see that $\mathrm{rot}\vec{u} = 0$, so that Eqs. (20a, b) become respectively:

$$\mathrm{grad}\vec{u}^{\,2} = 2(\vec{u}\cdot\nabla)\vec{u}; \qquad \nabla^2\vec{u} = \mathrm{grad}(\mathrm{div}\,\vec{u}). \tag{21a, b}$$

Substituting Eqs. (21a, b) in Eq. (19) we obtain:

$$\frac{\partial\vec{u}}{\partial t} = -\mathrm{G}(t)\nabla^2\vec{u} - 2(\vec{u}\cdot\nabla)\vec{u} + \frac{d\ln \mathrm{G}(t)}{dt}\,\vec{u}. \tag{22}$$

Substituting Eq. (21a) again, the equation (22) can be written as follows:

$$\frac{\partial\vec{u}}{\partial t} + (\vec{u}\cdot\nabla)\vec{u} = -\mathrm{grad}(\vec{u}^{\,2}/2) - \mathrm{G}(t)\nabla^2\vec{u} + \frac{d\ln \mathrm{G}(t)}{dt}\,\vec{u}. \tag{23}$$

The obtained equation (23) is similar to Navier–Stokes equation of motion of a viscous liquid [12, 15] under conditions that a gas-dust substance of spheroidal body is isolated from influence of external fields and $\mathrm{G}(t) = \mathrm{G}_s = \mathrm{const}$.

Along with the antidiffusion velocity $\vec{u}$ there exists an ordinary *hydrodynamic velocity* $\vec{v}$ (or a convective velocity [13, 14]). In principle, the hydrodynamic velocity $\vec{v}$ of mass flow arises as a result of powerful gravitational contraction of a spheroidal body on the next (field) stages of its evolution. The growing magnitude of gravitational field strength $\vec{a}$ induces the significant (i.e. observable) value of hydrodynamic velocity $\vec{v}$ of mass flows moving into spheroidal body. This means that the value of antidiffusion velocity (14) becomes much less than the value of hydrodynamic velocity, i.e. $|\vec{u}| << |\vec{v}|$. Under this condition, a common (hydrodynamic and antidiffusion) mass flow density inside a spheroidal body satisfies the hydrodynamic equation of continuity [12, 15]:

$$\frac{\partial\rho}{\partial t} + \mathrm{div}(\rho\vec{v}) = 0. \tag{24}$$

Taking into account Eq. (24) we can also calculate the partial derivative of the antidiffusion velocity (14) with respect to the time:

$$\frac{\partial\vec{u}}{\partial t} = \frac{d\mathrm{G}(t)}{dt}\,\mathrm{grad}\ln\rho + \mathrm{G}(t)\,\mathrm{grad}\left\{\frac{1}{\rho}\frac{\partial\rho}{\partial t}\right\} = \frac{d\mathrm{G}(t)}{dt}\left\{\frac{1}{\mathrm{G}(t)}\,\vec{u}\right\} + \mathrm{G}(t)\nabla\left\{\frac{1}{\rho}(-\mathrm{div}(\rho\vec{v}))\right\} = \tag{25}$$

$$= \frac{d\ln \mathrm{G}(t)}{dt}\,\vec{u} - \mathrm{G}(t)\nabla\left\{\nabla\vec{v} + \vec{v}\frac{\nabla\rho}{\rho}\right\} = -\mathrm{G}(t)\,\mathrm{grad}(\mathrm{div}\vec{v}) - \mathrm{grad}(\vec{v}\vec{u}) + \frac{d\ln \mathrm{G}(t)}{dt}\,\vec{u}.$$

As known from a fluid-like description [12, 15], the complete time-derivative of the common (hydrodynamic plus antidiffusion) velocity $\vec{\mathrm{v}}+\vec{\mathrm{u}}$ inside a spheroidal body defines the common acceleration (or *gravitational field strength* of spheroidal body) including the partial time-derivatives and convective derivatives [2, 3]:

$$\vec{a}=\frac{d(\vec{\mathrm{v}}+\vec{\mathrm{u}})}{dt}=\frac{\partial\vec{\mathrm{v}}}{\partial t}+(\vec{\mathrm{v}}\cdot\nabla)\vec{\mathrm{v}}+\frac{\partial\vec{\mathrm{u}}}{\partial t}+(\vec{\mathrm{u}}\cdot\nabla)\vec{\mathrm{u}}. \tag{26}$$

Taking into account Eq. (23) as well as Eq. (21a), the complete acceleration (26) can be represented in the form [2, 3]:

$$\vec{a}=\frac{d(\vec{\mathrm{v}}+\vec{\mathrm{u}})}{dt}=\frac{\partial\vec{\mathrm{v}}}{\partial t}+(\vec{\mathrm{v}}\cdot\nabla)\vec{\mathrm{v}}-(\vec{\mathrm{u}}\cdot\nabla)\vec{\mathrm{u}}-\mathrm{G}(t)\nabla^2\vec{\mathrm{u}}+\frac{d\ln\mathrm{G}(t)}{dt}\vec{\mathrm{u}}. \tag{27}$$

Let us note that $\mathrm{rot}\vec{\mathrm{u}}=0$ for the antidiffusion velocity (17a), too. So, we can see that Eqs. (21a,b) are also true. Thus, if we replace GCF $\mathrm{G}(t)$ on the generalized GCF $\widetilde{\mathrm{G}}(t)$ in the Eqs. (19), (23), (25)-(27) they remain valid in the general case of a rotating ellipsoid-like cosmogonical body. Obviously, the antidiffusion velocity (15) of probability volume flow density also satisfies the same equations.

3.2. The derivation of the dimensionless equations

Using Eqs. (25), (27) we can carry out an analysis of dynamical states of a spheroidal body by introducing the scales of physical values $T,L,V,U,F,\mathrm{G}_\mathrm{s}$ and the respective dimensionless variables $\tau,\vec{\xi},\vec{v},\vec{u},\vec{f},g$ as follows:

$$t=T\tau;\quad \vec{r}=L\vec{\xi};\quad \vec{\mathrm{v}}=V\vec{v};\quad \vec{\mathrm{u}}=U\vec{u};\quad \vec{a}=F\vec{f};\quad \mathrm{G}(t)=\mathrm{G}_\mathrm{s}g(t), \tag{28}$$

where $\mathrm{G}(t)=\mathrm{G}_\mathrm{s}=\mathrm{const}$ under the condition of *mechanical equilibrium* state.

By substituting Eqs. (28) in Eqs. (25), (27) we obtain:

$$\frac{U}{T}\frac{\partial\vec{u}}{\partial\tau}=-\mathrm{G}(t)\frac{V}{L^2}\mathrm{grad}(\mathrm{div}\vec{v})-\frac{VU}{L}\mathrm{grad}(\vec{v}\vec{u})+\frac{U}{T}\frac{d\ln\mathrm{G}(t)}{dt}\vec{u}; \tag{29a}$$

$$\frac{V}{T}\frac{\partial\vec{v}}{\partial\tau}=F\vec{f}-\frac{V^2}{L}(\vec{v}\cdot\nabla)\vec{v}+\frac{U^2}{L}\mathrm{grad}(\vec{u}^2/2)+\mathrm{G}(t)\frac{U}{L^2}\mathrm{grad}(\mathrm{div}\vec{u})-\frac{U}{T}\frac{d\ln\mathrm{G}(t)}{dt}\vec{u}. \tag{29b}$$

Similarly to [15], dividing Eq. (29b) by V^2/L and Eq. (29a) by VU/L we derive the following dimensionless equations:

$$\mathrm{Sh}\frac{\partial\vec{u}}{\partial\tau}=-\frac{\mathrm{G}_\mathrm{s}}{\nu}\cdot\frac{1}{\mathrm{K}\cdot\mathrm{Re}}\mathrm{grad}(\mathrm{div}\vec{v})-\mathrm{grad}(\vec{v}\vec{u})+\mathrm{Sh}\frac{d\ln g(t)}{dt}\vec{u}; \tag{30a}$$

$$\mathrm{Sh}\frac{\partial\vec{v}}{\partial\tau}=\frac{1}{\mathrm{Fr}}\vec{f}-(\vec{v}\cdot\nabla)\vec{v}+\mathrm{K}^2\mathrm{grad}(\vec{u}^{\,2}/2)+\frac{\mathrm{G_s}}{\nu}\cdot\frac{\mathrm{K}}{\mathrm{Re}}g(t)\,\mathrm{grad}(\mathrm{div}\vec{u})-\mathrm{Sh}\cdot\mathrm{K}\frac{d\ln g(t)}{dt}\vec{u}, \tag{30b}$$

where $\mathrm{Sh}=L/VT$ is the Strouhal number, $\mathrm{Fr}=V^2/FL$ is the Froude number, $\mathrm{Re}=VL/\nu$ is the Reynolds number (ν is a kinematic coefficient of viscosity of flow of particles [15]), $\mathrm{K}=U/V$ is a new number of similarity.

The new number of similarity is a measure of the values $|\vec{\mathrm{u}}|$ versus $|\vec{\mathrm{v}}|$ prevailing:

$$\mathrm{K}=|\vec{\mathrm{u}}|/|\vec{\mathrm{v}}|. \tag{31}$$

When this similarity number exceeds unity ($\mathrm{K}>>1$) the antidiffusion contraction of a spheroidal body occurs exclusively, so that the value of hydrodynamic velocity is negligible ($|\vec{\mathrm{v}}|\approx 0$) because a gravitational field is absent practically. If the similarity number becomes close to unity ($\mathrm{K}\approx 1$) then the hydrodynamic velocity $\vec{\mathrm{v}}$ of mass flow arises as a result of a gravitational contraction of a spheroidal body on the field stage of its evolution. As mentioned, the value of antidiffusion velocity (14) becomes much less than the value of hydrodynamic velocity $|\vec{\mathrm{u}}|<<|\vec{\mathrm{v}}|$ when $\mathrm{K}<<1$. This means that the growing magnitude of powerful gravitational field strength $\vec{a}$ induces the significant value of hydrodynamic velocity $\vec{\mathrm{v}}$ of mass flows moving into a spheroidal body. Thus, like the Mach number M [15] the new number of similarity K is a *control parameter* of dynamical states of a forming spheroidal body.

In particular, in the special case $\mathrm{K}>>1$ the dimensionless Eqs. (30a), (30b) can be reduced to the one dimensionless equation of the kind:

$$\mathrm{K}\,\mathrm{grad}(\vec{u}^{\,2}/2)+\frac{\mathrm{G_s}}{\nu}\cdot\frac{1}{\mathrm{Re}}g(t)\,\mathrm{grad}(\mathrm{div}\vec{u})=\mathrm{Sh}\cdot\frac{\partial\vec{u}}{\partial\tau}, \tag{32}$$

which corresponds the following equation:

$$\mathrm{grad}(\vec{\mathrm{u}}^{\,2}/2)+\mathrm{G}(t)\,\mathrm{grad}(\mathrm{div}\vec{\mathrm{u}})=\frac{\partial\vec{\mathrm{u}}}{\partial t}. \tag{33}$$

Excepting the antidiffusion solution, Eq. (33) has a *wave solution* when $\mathrm{G_s}=\mathrm{const}$ and $|\vec{\mathrm{u}}|<1$:

$$\vec{\mathrm{u}}=\vec{\mathrm{u}}_0\,e^{\pm\mathrm{i}\vec{k}\vec{r}-\vec{k}^2\mathrm{G_s}t}. \tag{34}$$

i.e. in the *quasi-equilibrium* gravitational condensation state (when $\overline{\mathrm{G}(t)}=\mathrm{G_s}=\mathrm{const}$) the wave solutions (34) are generated.

4. The derivation of the generalized nonlinear Schrödinger-like equation in the statistical theory of spheroidal bodies

The considerations in the previous sections point to an *initial quasi-equilibrium* gravitational condensation occurring in a forming spheroidal body. However, a sharp *increase* of the antidiffusion velocity of particles inside a spheroidal body can lead to the coherent displacement of particles and, as a consequence, a resonance increase of the parameter of gravitational condensation $\alpha(t)$ occurs [2]. This means that *nonlinear phenomena* arise owing to self-organization processes [14] into a spheroidal body under its formation. These nonlinear phenomena induce nonlinear soliton-type waves [16] satisfying a *nonlinear* undulatory Schrödinger-like equation.

To obtain a nonlinear generalized Schrödinger equation, let us consider again Eqs. (25), (27) with regard to the simple formulas (21a, b). We intend to investigate some special solution of these equations in the case that the acceleration (or gravitational field strength) comes from a gravitational field potential [17]:

$$\vec{a} = -\operatorname{grad}\varphi_{\mathrm{g}} \tag{35}$$

under the assumption that the hydrodynamic velocity $\vec{\mathrm{v}}$ is a gradient of a *statistical* action $\Im$ which reminds a potential of velocity [12, 15]:

$$\vec{\mathrm{v}} = 2\mathrm{G}(t)\operatorname{grad}\Im = \operatorname{grad}(2\mathrm{G}(t)\Im). \tag{36}$$

In the special case of $\mathrm{G}(t)$ as $\hbar/2m_0$ Eq. (36) becomes the Nelson' formula [7]: $\vec{\mathrm{v}} = (\hbar/m_0)\operatorname{grad}\Im$. In this connection, $\operatorname{rot}\vec{\mathrm{v}} = 0$, i.e. $(\vec{\mathrm{v}}\cdot\nabla)\vec{\mathrm{v}} = \operatorname{grad}(\vec{\mathrm{v}}^2/2)$. Since $\vec{\mathrm{u}}$ is also a gradient due to Eq. (15) as well as $\vec{a}$ and $\vec{\mathrm{v}}$ according to Eqs. (35), (36), so that Eqs. (25), (27) become the following:

$$\operatorname{grad}\frac{\partial(\mathrm{G}(t)\ln\Phi)}{\partial t} = -\mathrm{G}(t)\operatorname{grad}(\operatorname{div}\vec{\mathrm{v}}) - \operatorname{grad}(\vec{\mathrm{v}}\cdot\vec{\mathrm{u}}) + \{d\ln\mathrm{G}(t)/dt\}\mathrm{G}(t)\operatorname{grad}\ln\Phi; \tag{37a}$$

$$\operatorname{grad}\frac{\partial(2\mathrm{G}(t)\Im)}{\partial t} = -\operatorname{grad}\varphi_g - \operatorname{grad}(\vec{\mathrm{v}}^2/2) + \operatorname{grad}(\vec{\mathrm{u}}^2/2) + \mathrm{G}(t)\operatorname{grad}(\operatorname{div}\vec{\mathrm{u}}) - \{d\ln\mathrm{G}(t)/dt\}\mathrm{G}(t)\operatorname{grad}\ln\Phi. \tag{37b}$$

Integrating these Eqs. (37a, b) and taking into account a simplification $\{d\ln\mathrm{G}(t)/dt\}\cdot\mathrm{G}(t) = d\,\mathrm{G}(t)/dt$, we can find that

$$\frac{\partial(\mathrm{G}(t)\ln\Phi)}{\partial t} = -\mathrm{G}(t)\operatorname{div}\vec{\mathrm{v}} - \vec{\mathrm{v}}\cdot\vec{\mathrm{u}} + \frac{d\,\mathrm{G}(t)}{dt}\ln\Phi; \tag{38a}$$

$$\frac{\partial(2\mathrm{G}(t)\Im)}{\partial t} = -\varphi_g - \frac{\vec{\mathrm{v}}^2}{2} + \frac{\vec{\mathrm{u}}^2}{2} + \mathrm{G}(t)\operatorname{div}\vec{\mathrm{u}} - \frac{d\,\mathrm{G}(t)}{dt}\ln\Phi. \tag{38b}$$

Let us carry out a change of dependent variable:

$$\Re = \frac{1}{2}\ln\Phi; \qquad \Psi = \mathrm{e}^{\Re + \mathrm{i}\Im}, \tag{39a, b}$$

where $\Im$ is defined by Eq. (36), $\mathrm{i} = \sqrt{-1}$. Obviously, as follows from Eqs. (39a, b) directly

$$\Psi = \sqrt{\Phi}\cdot \mathrm{e}^{\mathrm{i}\Im}, \tag{40}$$

so that $\Phi = \Psi\Psi^* = |\Psi|^2$ as usually. According to the first change (39a) it is not difficult to see that

$$\frac{\partial(2\mathrm{G}(t)\,\Re)}{\partial t} = -2\mathrm{G}^2(t)\nabla^2\Im - 4\mathrm{G}^2(t)\nabla\Re\cdot\nabla\Im + 2\frac{d\,\mathrm{G}(t)}{dt}\Re; \tag{41a}$$

$$\frac{\partial(2\mathrm{G}(t)\Im)}{\partial t} = -\varphi_g + 2\mathrm{G}^2(t)(\nabla\Re)^2 - 2\mathrm{G}^2(t)(\nabla\Im)^2 + 2\mathrm{G}^2(t)\nabla^2\Re - 2\frac{d\,\mathrm{G}(t)}{dt}\Re. \tag{41b}$$

Let us rewrite these two Eqs. (41a, b) as one. To this end, after multiplication of the second Eq.(41b) on imaginary unit and then addition both of Eqs. (41a, b), we can obtain the following:

$$\frac{\partial}{\partial t}\left[2\mathrm{G}(t)(\Re + \mathrm{i}\,\Im)\right] = -\mathrm{i}\varphi_g + \mathrm{i}\,2\mathrm{G}^2(t)(\nabla^2\Re + \mathrm{i}\nabla^2\Im) + \mathrm{i}\left[\sqrt{2}\mathrm{G}(t)\nabla(\Re + \mathrm{i}\,\Im)\right]^2 + 2(1-\mathrm{i})\frac{d\,\mathrm{G}(t)}{dt}\Re. \tag{42}$$

Taking into account the second change (39b) we can see that $\Re + \mathrm{i}\,\Im = \ln\Psi$; $2\Re = \ln\Psi + \ln\Psi^* = \ln|\Psi|^2$; $\nabla(\Re + \mathrm{i}\,\Im) = \nabla\ln\Psi = \nabla\Psi/\Psi$; $\nabla^2(\Re + \mathrm{i}\,\Im) = \nabla^2\Psi/\Psi - (\nabla\Psi)^2/\Psi^2$, so that Eq. (42) takes the form:

$$\frac{\partial}{\partial t}\left[2\mathrm{G}(t)\ln\Psi\right] = -\mathrm{i}\varphi_g + \mathrm{i}\,2\mathrm{G}^2(t)\frac{\nabla^2\Psi}{\Psi} + (1-\mathrm{i})\frac{d\,\mathrm{G}(t)}{dt}\ln|\Psi|^2. \tag{43}$$

After some transformations and simplifications Eq. (43) can be represented as follows:

$$\mathrm{i}\,2\mathrm{G}(t)\frac{\partial\Psi}{\partial t} = \varphi_g\Psi - 2\mathrm{G}^2(t)\nabla^2\Psi + 2\mathrm{i}(1-\mathrm{i})\frac{d\,\mathrm{G}(t)}{dt}\Psi\ln|\Psi| - 2\,\mathrm{i}\frac{d\,\mathrm{G}(t)}{dt}\Psi\ln\Psi \tag{44}$$

whence we can obtain a nonlinear time-dependent generalized Schrödinger-like equation of the kind:

$$\mathrm{i}\,2\mathrm{G}(t)\frac{\partial\Psi}{\partial t} = \left[-2\mathrm{G}^2(t)\nabla^2 + \varphi_g\right]\Psi + 2\frac{d\,\mathrm{G}(t)}{dt}\left|\ln|\Psi| - \mathrm{i}\ln\frac{\Psi}{|\Psi|}\right|\Psi. \tag{45}$$

5. Concluding remarks on particular cases of the generalized nonlinear time-dependent Schrödinger-like equation

Let us consider different dynamical states of a gravitating spheroidal body as well as the respective forms of the generalized nonlinear time-dependent Schrödinger-like equation (45). Indeed, the derived Eq. (45) describes not only the mentioned state of *virial mechanical equilibrium* [1–3] when GCF $\mathrm{G}(t) = \mathrm{G}_s = \mathrm{const} \in \mathbf{R}$ and $\Psi \in \mathbf{R}$ or $\Psi \in \mathbf{C}$:

$$i\mathrm{G}_s\frac{\partial\Psi}{\partial t}=\left[-\mathrm{G}_s{}^2\nabla^2+\frac{1}{2}\varphi_g\right]\Psi \tag{46}$$

and the *quasi-equilibrium gravitational condensation state* $\overline{(\mathrm{G}(t)}=\mathrm{G}_s=\mathrm{const})$ when $\mathrm{G}(t)\in\mathbf{R}$ and $\Psi\in\mathbf{R}$ or $\Psi\in\mathbf{C}$:

$$i\mathrm{G}(t)\frac{\partial\Psi}{\partial t}=\left[-\mathrm{G}^2(t)\nabla^2+\frac{1}{2}\varphi_g\right]\Psi+\frac{d\,\mathrm{G}(t)}{dt}\ln|\Psi|\cdot\Psi \tag{47}$$

but the *initial equilibrium gravitational condensation state* occurring in a forming gas-dust protoplanetary cloud:

$$i\frac{\partial\Psi}{\partial t}=-\mathrm{G}_s\nabla^2\Psi \tag{48}$$

as well as the *soliton disturbances state* taking place in a spheroidal body under formation (see Fig.1):

$$i\frac{\partial\Psi}{\partial t}=\left[-\mathrm{G}(t)\nabla^2+\frac{1}{2}\frac{d\ln\mathrm{G}(t)}{dt}|\Psi|^2\right]\Psi \tag{49}$$

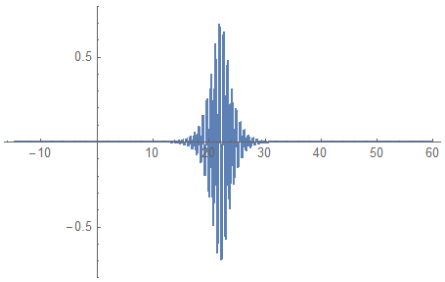

Figure 1. Soliton solution of the generalized cubic time-dependent Schrödinger-like equation

and finally the gravitational instability states when GCF $\mathrm{G}(t)\in\mathbf{C}$ and $\Psi=|\Psi|e^{i\arg\Psi}\in\mathbf{C}$:

$$i\mathrm{G}(t)\frac{\partial\Psi}{\partial t}=\left[-\mathrm{G}^2(t)\nabla^2+\frac{1}{2}\varphi_g\right]\Psi+\frac{d\,\mathrm{G}(t)}{dt}\left[\ln|\Psi|+\arg\Psi\right]\Psi \tag{50}$$

including the increase of gravitational compression of spheroidal body providing a formation of core of cosmogonical body if $0\le\arg\Psi<2\pi$ and the case of unlimited gravitational compression leading to a collapse if $\arg\Psi\to\arg\Psi\pm2\pi n,\ n\in\mathbf{Z}$ in Eq. (50).

References

[1] Krot, A.M. A statistical approach to investigate the formation of the Solar system. *Chaos, Solitons & Fractals* 41 (2009), 1481–1500.

[2] Krot, A.M. A quantum mechanical approach to description of initial gravitational interactions based on the statistical theory of spheroidal bodies. *Nonlinear Sci. Lett. A* 1 (2010), 329–369.

[3] Krot, A.M. *Statistical Theory of Formation of Gravitating Cosmogonical Bodies*. Bel. Navuka, Minsk, 2012. – 448 pp. [in Russian].

[4] Krot, A.M. On the universal stellar law for extrasolar systems. *Planet. Space Sci.* 101C (2014), 12–26.

[5] Jeans, J. *Astronomy and Cosmogony*. University Press, Cambridge, 1929.

[6] Safronov, V.S. *Evolution of Protoplanetary Cloud and Formation of Earth and Planets*. Nauka, Moscow, 1969 [reprinted by NASA Tech. Transl. F-677, Washington, D.C., 1972].

[7] Nelson, E. Derivation of the Schrödinger equation from Newtonian mechanics. *Phys. Rev*. 150 (1966), 1079–1085.

[8] Nottale, L. Scale relativity, fractal space-time, and quantum mechanics. *Chaos, Solitons & Fractals* 4 (1994), 361–388.

[9] Nottale, L. Scale-relativity and quantization of the universe: I. Theoretical framework. *Astron. Astrophys*. 327 (1997), 867–889.

[10] Chernin, A.D. Cosmic vacuum. *Usp. Fiz. Nauk* 171 (2001), 1153–1175.

[11] Weinberg, S. The cosmological constant problem. *Rev. Mod. Phys.* 61 (1989), 1–23.

[12] Landau, L.D., and Lifschitz, E.M. *Fluid Mechanics*. Pergamon, Oxford, 1959.

[13] Glansdorff, P., and Prigogine, I. *Thermodynamic Theory of Structure, Stability and Fluctuations*. London, 1971.

[14] Nicolis, G., and Prigogine, I. *Self-Organization in Nonequilibrium Systems: From Dissipative Structures to Order through Fluctuation*. John Willey and Sons, New York, 1977.

[15] Loytsyanskiy, L.G. *Mechanics of Fluid and Gas*. Nauka, Moscow, 1973 [in Russian].

[16] Dodd, R.K., Eilbeck, J.C., Gibbon, J.D., and Morris, H.C. *Solitons and Nonlinear Wave Equations*. Academic Press, London, 1984.

[17] Landau, L.D., and Lifschitz, E.M. *Classical Theory of Fields.* Addison–Wesley Publishing Co., Reading (MA), 1951.

Alexander M. Krot, Professor: United Institute of Informatics Problems of the National Academy of Science of Belarus, Surganov str. 6, 220012, Minsk, Belarus, BELARUS (*alxkrot@newman.basnet.by*).

General theory of geometrically nonlinear size dependent shells taking into account contact interaction.
Part 1. Chaotic dynamics of geometrically nonlinear axially symmetric one-layer shells

Vadim A. Krysko - jr., Jan Awrejcewicz, Irina V. Papkova, Vadim A. Krysko

Abstract: A mathematical model of flexible flat rectangular in plan shells is proposed. A special case for spherical axisymmetric shells taking into account nanoscale effects has been studied. Shell structure material is homogeneous and isotropic, and the nanoscale factors has been taken into account. Partial differential equations for axisymmetric spherical shallow shells were reduced to the Cauchy problem by the method of finite differences of the second order of accuracy. The Cauchy problem was solved by the Runge-Kutta method of the 4th order. Convergence of the obtained results in dependence of the number of partitions along the radius was investigated. The system was studied as a system with an infinite number of degrees of freedom. The effect of the size-dependent parameter, which significantly affects the nonlinear dynamics of the shell, was taken into account.

Keywords: Mathematical model, rectangular shell, spherical axisymmetric shell, moment theory of elasticity, loss of stability, chaos, numerical experiment, geometric nonlinearity, distributed mechanical structure.

1. Introduction

In experimental studies of metals, polymers and metallic glass, a size dependent effect was observed when the thickness of mechanical structures in the form of rods, plates, and full shells was compressed to a micron [1, 2]. This effect plays an important role when taking into account the mechanics of the mentioned structures [3].

Experimental studies of the real microstructures are extremely complex and expensive. Chong and Lam [4] observed that the flexural rigidity increases by about 2.4 times with a decrease in thickness from 115 to 20 μm when testing the micro-rod from epoxy polymers for bending. From the works of these interesting experiments can be concluded that the size-caused behavior is an inherent property of materials that can not be neglected when designing optimal dynamic devices using MEMS [5], [6].

Young et al. [7] developed couple stress based strain gradient theory for elasticity using the theory of higher order of continuous media. The behavior of the pairs of forces was determined by an additional symmetrical equilibrium relation, at which only one additional parameter of the scale of the length of the material took place.

Based on the modified theory of moment stresses, static mechanical properties [2], elastic bending [1], fluid transfer [8], dynamic characteristics [9-11], nonlinear vibration [12-13] of micro-rods were studied.

Modified couple stress theory of moment stresses for computation the size dependent plates was applied. The theory of moment stresses of microstructurally dependent pairs of forces applied to functionally graded rods and the Timoshenko rod was investigated by Reddy et al. [14-15]. Ciata [6] studied the static analysis of isotropic microplates using the Kirchhoff plate model. Iain et al. [16] analyzed the types of dynamic behavior of the Kirchhoff microplate, based on a modified theory of moment stresses. Lazopoulos [17], adopting the Kirchhoff model for plates, investigated the stress gradient in the bending of thin plates to determine the size effect. Ke et al. [5] performed studies using the moment theory for plates of Mindlin plates. Reddy et al. [18] applied the theory of the third approximation (model of Sheremetyev-Pelekh) [19] taking into account piezo effects. Stress-strain state size dependence microstructures: plates, rods and shells take into account temperature effects for homogeneous materials was studied in papers [19-32]. In conclusion, it is important to note that the study of nonlinear dynamics of the size effect for rods, plates and shells is not done. The main goal of this paper is the construction of a general theory and study of nonlinear dynamics of size dependent plates and shells in a temperature field with account for couple of deformation fields and temperature. Algorithms and software complexes for analysis of nonlinear dynamics of size dependent effects of the flat in plan axisymmetric shells under the action of a transverse periodic load were created.

2. Mathematical background

In the classical theory of elasticity, the work of deformation and the strain energy depend on the stress tensor and do not depend on the rotation vector due to material independence. However, the gradient of the rotation vector can be an important factor in the equations of state. Based on the modified couple stresses theory of moment stresses presented by Yang et al. [7], the strain energy density is a function of both the couple stress tensor (conjugate to the strain tensor) and the curvature tensor (conjugate to the tensor of moment stresses). In deformed isotropic linear elastic material, located in the region Ω, strain energy Π is expressed by the following equations

$$\Pi = \int_{\Omega} (\sigma_{ij}\,\varepsilon_{ij} + m_{ij}\eta_{ij})d\Omega \quad (i,j = 1,2,3) \tag{1}$$

Here σ_{ij} is the Cauchy stress tensor, ε_{ij} is the stress tensor, m_{ij} is a deviator component of the stress tensor, a η_{ij} - symmetric curvature tensor. The parameter of the material length scale related to the microstructures of the material was developed for the purpose of interpreting the dimensional effect in the non-classical Kirchhoff-Love model. These tensors are defined by formulas

$$\sigma_{ij} = \lambda tr(\varepsilon_{ij})I + 2\mu\varepsilon_{ij}, \quad (2)$$

$$\varepsilon_{ij} = \frac{1}{2}[\nabla u + (\nabla u)^T], \quad (3)$$

$$m_{ij} = 2l^2\mu\chi_{ij}, \quad (4)$$

$$\eta_{ij} = \frac{1}{2}\left[\nabla\varphi + \left(\nabla_{\varphi}\right)^T\right], \quad (5)$$

where: u - displacement vector; $\lambda = \frac{Ev}{(1+v)(1-2v)}$ and $\mu = \frac{E}{2(1+v)}$ - constants of Lamé; E, v represent the Young's modulus and Poisson's ratio for the shell material, respectively; l — this parameter is a scale of the length of the material, understood as a property of the material, characterizing the effect of the moment stress [15]. The latter parameter describes mathematically the square of the ratio of the curvature module to the shear modulus and it can be determined by experiments for thin torsion cylinders [33] or for thin rods for bending [34] on a micron scale; φ — this rotation vector, represented as $\varphi_{i=}\frac{1}{2}rot(u_i)$.

From the analysis of equations (3) and (5) it follows that the stress tensor ε_{ij} and the curvature tensor η_{ij} are symmetric, and, consequently, equations (2) and (4) yields the stress tensor σ_{ij} and deviator component of the stress tensor m_{ij} also symmetric. In deriving the equations of flexible, dimensionally dependent shallow shells, the following hypotheses are used:

- shell is homogeneous, isotropic, and elastic;
- shallow shells are defined by the Reissner [35] or by V.Z. Vlasov [36];
- shell is subjected to the hypothesis of Kirchhoff-Love;
- geometric nonlinearity is introduced by the Kármán model [37].

Let a shallow shell be considered in rectangular system of coordinates (see Fig.1) introduced in the following way: $\Omega = \{x, y, z | (x, y) \in [0; a] \times [0; b], z \in [-h; h]\}, 0 \leq t < \infty$.

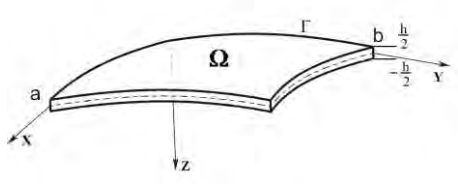

Fig. 1. Single-layer rectangular in plan shell

According to the principle of Hamilton-Ostrogradsky;

$$\int_{t_0}^{t_1} (\delta K - \delta\Pi + \delta' W)dt = 0, \tag{6}$$

where: K, Π – kinetic and potential energy, respectively; $\delta' W$ - work of external forces.

The system of nonlinear PDEs governing dynamics of the flexible rectangular shells on the basis of couple stress theory has the following form:

$$(D_0 + D_l)\nabla^4 w - \Delta_k^2 F - L(w,F) + ph\varepsilon\dot{w} - \frac{q}{h} + ph\ddot{w} = 0, \tag{7}$$

$$\nabla_k^2 w + \frac{1}{2}L(w,w) + \frac{1}{Eh}\nabla^4 F = 0, \text{ где } D_l = \frac{El^2 h}{2(1+\mu)}, D_0 = \frac{Eh^3}{12(1-\mu^2)},$$

$$L(w\ ,F\ ) = 2\left[\frac{\partial^2 w}{\partial x^2}\frac{\partial^2 F}{\partial y^2} + \frac{\partial^2 w}{\partial y^2}\frac{\partial^2 F}{\partial x^2} - 2\frac{\partial^2 w}{\partial x \partial y}\frac{\partial^2 F}{\partial x \partial y}\right],$$

$$\nabla_k^2(\cdot) = K_y\frac{\partial^2(\cdot)}{\partial x^2} + K_x\frac{\partial^2(\cdot)}{\partial y^2},$$

where $\nabla_k^2(\cdot) -$ 4th order Laplace operator; K_x and K_y - curvature of the shell or can be interpreted small initial irregularities; t- time; ε - coefficient of resistance of the medium in which the shell moves; F - stress function; w - deflection function; h - shell thickness; μ - Poisson's coefficient; q - external load parameter; l – size-dependent parameter.

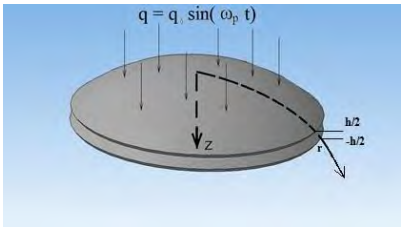

Fig. 2. Spherical axisymmetric shell.

To obtain the axial symmetric theory of size dependent shells, we employ the cylindrical coordinate system. The second equation of the system is multiplied by r, integrated and a new resolving function $\Phi\ = \frac{\partial F}{\partial r}$ is introduced [1].

Equations for nano axisymmetric shells have the following form

$$\frac{\partial^2 w}{\partial t^2} + \varepsilon\frac{\partial w}{\partial t} = -\left(1 + \frac{\gamma\eta}{2(1+\mu\ )}\right)\frac{\partial^4 w}{\partial r^4} - \frac{2}{r}\frac{\partial^3 w}{\partial r^3} + \frac{1}{r^2}\frac{\partial^2 w}{\partial r^2} - \frac{1}{r^3}\frac{\partial w}{\partial r} + \frac{\partial\Phi}{\partial r}\left(1 + \frac{1}{r}\frac{\partial w}{\partial r}\right) + \frac{\Phi}{r}\left(1 + \frac{\partial^2 w}{\partial r^2}\right) + 4q. \tag{8}$$

We introduce the following dimensionless quantities:

$$t = \omega_0 t;\ \bar{x} = b\frac{x}{c};\ \bar{y} = b\frac{y}{c};\ \omega_0 = \sqrt{\frac{Eg}{\gamma R^2}};\ \bar{\varepsilon} = \sqrt{\frac{g}{\gamma E}}\frac{R}{h}\varepsilon;\ \bar{F} = \eta\frac{F}{Eh^3};\ \bar{w} = \sqrt{\eta}\frac{w}{h};\ \bar{r} = b\frac{r}{c};$$

$$\bar{q} = \frac{\sqrt{\eta}}{4}\frac{q}{E}(\frac{R}{h})^2;\eta = 12(1-\mu^2);\ \gamma = \frac{l^2}{h^2};\ b = \sqrt{\eta\ \frac{c^2}{Rh}};$$

where: R, C - the main radius of curvature of the reference contour and the radius of the reference contour in the circumferential direction, respectively; b - parameter of flatness; r - distance from the axis of rotation to the point on the middle surface. In the given equations, the bars over dimensionless quantities are omitted for simplicity. For an axisymmetric problem, the boundary conditions are written in the following form.

1) Simple movable contour in the meridional direction:

$$\Phi = w = 0, \frac{\partial^2 w}{\partial r^2} + \frac{v}{b}w = 0, \qquad \text{for } r = \bar{r}. \tag{9}$$

2) Rigidly clamed contour

$$\frac{\partial \Phi}{\partial r} - v\frac{\Phi}{b} = 0, w = 0, \frac{\partial^2}{\partial r^2} + \frac{v}{r}\frac{\partial w}{\partial r} = 0, \quad \text{for } r = \bar{r}. \tag{10}$$

3) Sliding clamping of the contour:

$$\Phi = w = 0, \frac{\partial w}{\partial r} = 0, \ \text{for } r = \bar{r}. \tag{11}$$

4) Simple nonmovable contour:

$$\frac{\partial \Phi}{\partial r} - v\frac{\Phi}{b} = 0, w = 0, \frac{\partial w}{\partial r} = 0, \ \text{for } r = \bar{r}. \tag{12}$$

and the following initial conditions: $w = f_1(r,0) = 0, w' = f_2(r,0) = 0 \ \ 0 \le t < \infty$.

In addition, the following conditions in the vicinity of the shallow top are employed:

$\Phi \approx Ar;\ \Phi' \approx A; w \approx B + Cr^2; w' \approx 2Cr; w'' \approx 2C;\ w''' \approx 0.$

In order to reduce the problem (8) - (12) governing dynamics of the considered continuous system into a system with lumped parameters, the method of finite differences (FDM) with approximation $O(\Delta^2)$ is used. PDEs as well as the boundary and initial conditions (9) - (12) are recast to the following finite difference formulas with respect to the spatial coordinate *r* and time:

$$w'' + \varepsilon w' = -\frac{w_{i+1} - w_{i-1}}{2\Delta}\left(\frac{1}{r_i^3} - \frac{\Phi_{i+1} - \Phi_{i-1}}{2r_i\Delta}\right) + \frac{w_{i+1} - 2w_i + w_{i-1}}{r_i\Delta^2}\left(\Phi_i + \frac{1}{r_i}\right) +$$

$$+ \frac{\Phi_{i+1} - \Phi_{i-1}}{2\Delta} + \frac{\Phi_i}{r_i} - \left(1 + \frac{\gamma\eta}{2(1+\mu)}\right)\frac{w_{i+2} - 4w_{i+1} + 6w_i + 4w_{i-1} + w_{i-2}}{\Delta^2}$$

$$- \frac{w_{i+2} - 2w_{i+1} + 2w_{i-1} - w_{i-2}}{r_i\Delta^3} + 4q, \tag{13}$$

$$\Phi_{i+1}\left(-\frac{1}{\Delta^2}-\frac{1}{2r_i\Delta}\right)+\Phi_i\left(\frac{2}{\Delta^2}+\frac{1}{r_i^2}\right)+\Phi_{i-1}\left(-\frac{1}{\Delta^2}+\frac{1}{2r_i\Delta}\right)=\frac{w_{i+1}-w_{i-1}}{2\Delta}\left(1-\frac{w_{i+1}-w_{i-1}}{4r_i\Delta}\right),$$

where $\Delta = b/n$ and n denotes the number of modes of the shell radius.

The counterpart difference forms of the boundary conditions are as follows: If small terms are neglected and the differential operators are substituted by the central finite differences for $r = \Delta$, the following conditions are obtained in the shell top:

$$\Phi_0 = \Phi_2 - 2\Phi_1;\ w_0 = \frac{4}{3}w_1 - \frac{1}{3}w_2;\ w_{-1} = \frac{8}{3}w_1 - \frac{8}{3}w_2 + w_3 \quad (14)$$

The transverse load can be changed arbitrarily with respect to the spatial coordinate and time. In this work the harmonic transverse load of the form $q = q_0\sin(\omega_p t)$ where q_0 stands for an amplitude and $\omega_p = \frac{2\pi}{T}$ is a frequency of the excitation, is used.

After reduction of the problem (14) to the normal form, we solve the Cauchy problem by the Runge-Kutta method of the fourth order of accuracy. The time step is chosen from the stability condition of the solution ($\Delta t = 2.441 \cdot 10^{-4}$).

3. Results and discussions

Investigate complex vibrations shallow spherical shell with the boundary conditions: simple movable contour in the meridional direction (9), the parameter shallowness $b = 4$, $\gamma = 0;\ 0.3;\ 0.7$. When solving the problem by the method of finite differences $r \in [0; b]$ the interval of integration was divided into 120 parts. This number of partitions of the integration interval made it possible to treat the shell structure as with distributed parameters, rather than as a structure with lumped parameters, i.e. considered it as a system with an infinite number of degrees of freedom. Figures 3, 4, 5 show the dependence of the deflection at the center of the shell in dependence of the alternating transverse load q_0 (load on the shell uniformly distributed, changing according to law $q = q_0 sin(\omega_p t)$, where $\omega_p = 0.516$ is a frequency of the excitation, which is close to the fundamental frequency of linear vibration). Colored dots in Figures 3-5 denote the free vibrations (the dependence of the deflection at the top of the shell in time W(0), phase portraits W(W'), Fourier frequency power spectra, S(ω), and their characteristics are given in Table 1.

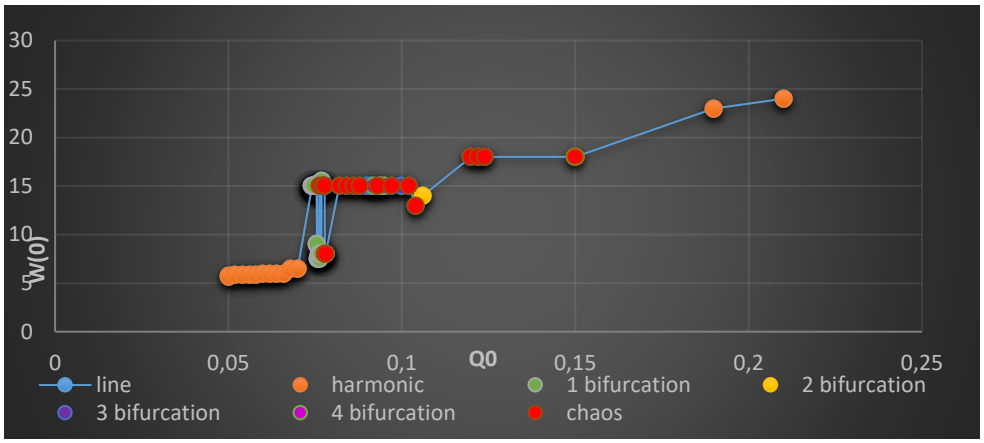

Fig. 3. Dependence W(q) for n=120, ϫ= 0.0

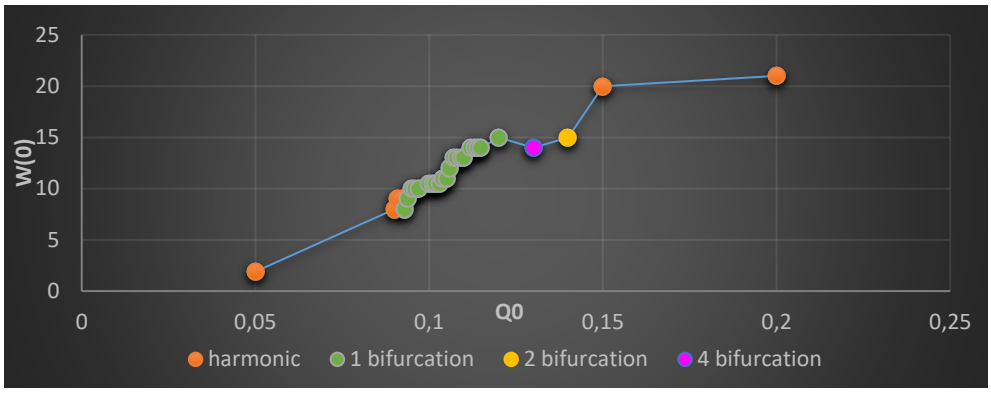

Fig. 4. Dependence W(q) for n=120, ϫ= 0.3

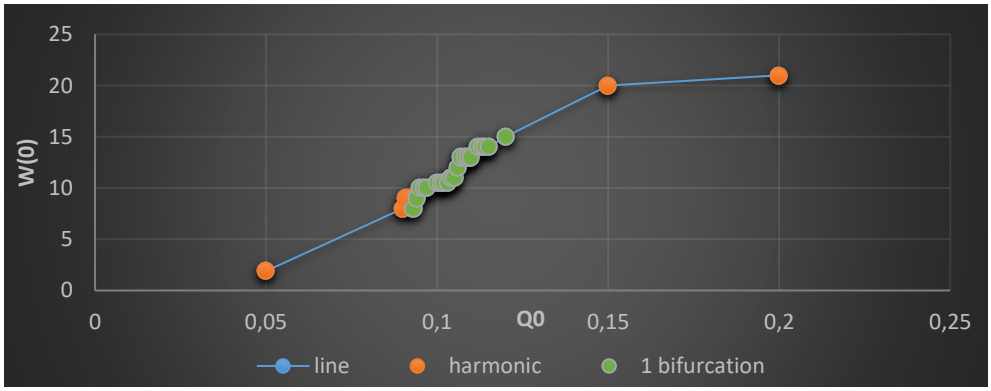

Fig. 5. Dependence W(q) for n=120, ϫ= 0.7

Table 1

	Type of vibrations		
	Time history	Phase portrait	Power spectrum
	$q_0 = 0.07$		
1	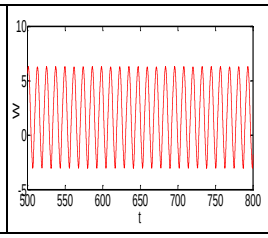	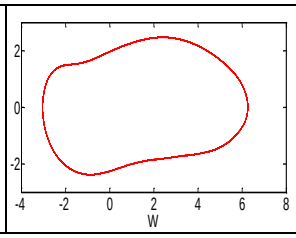	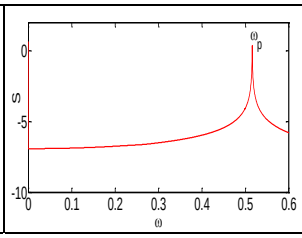
	$q_0 = 0.07351$		
2	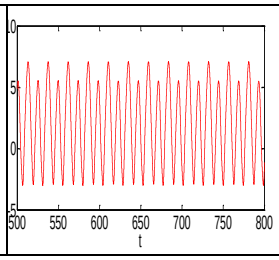	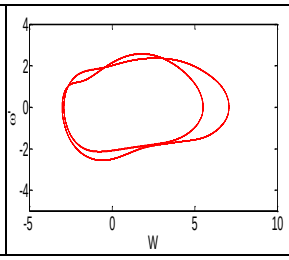	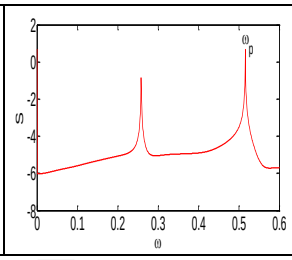
	$q_0 = 0.07822$		
3	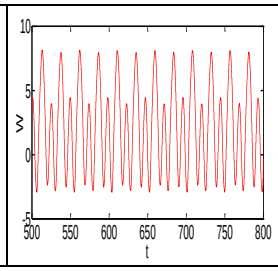	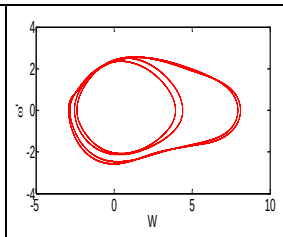	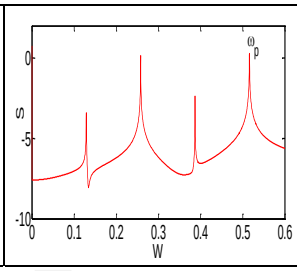
	$q_0 = 0.07933$		
4	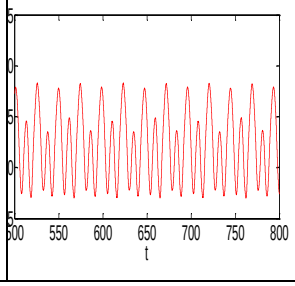	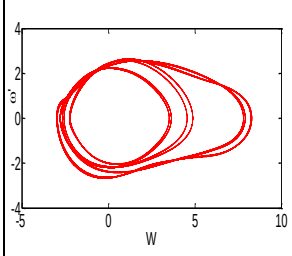	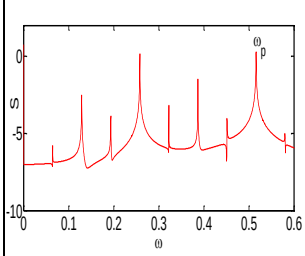

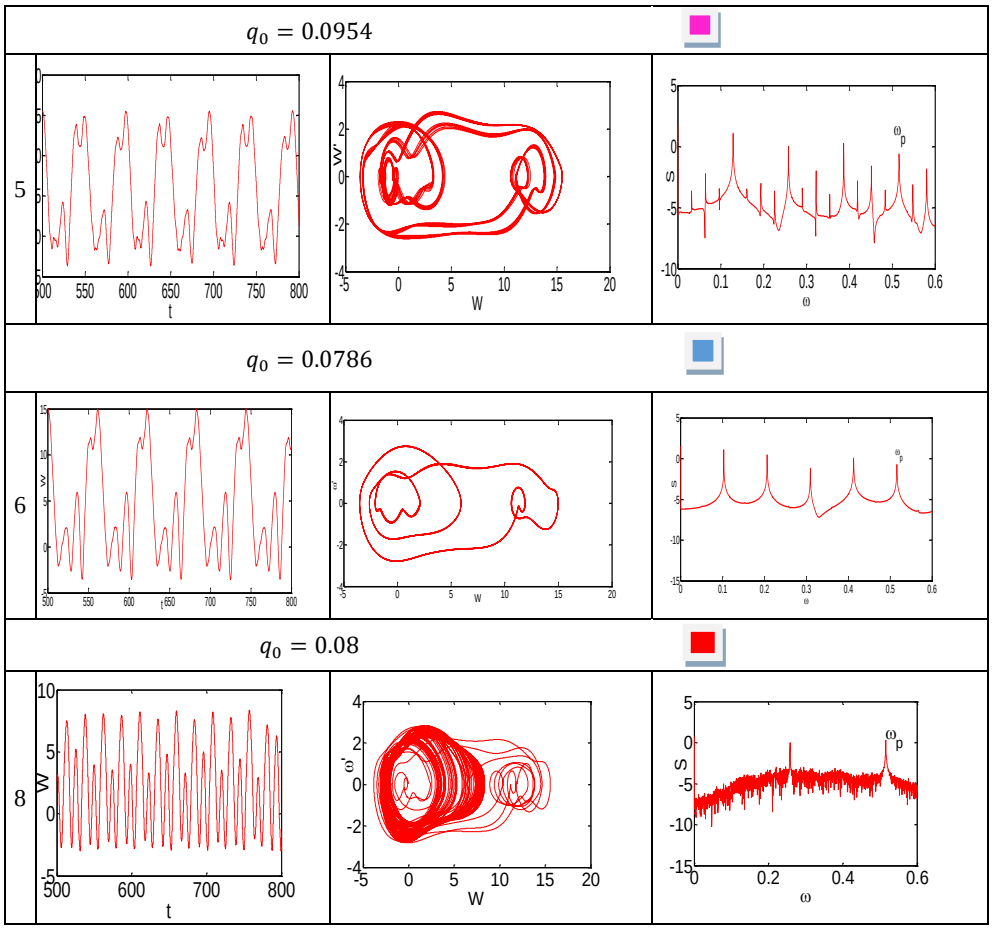

4. Conclusion

The analysis of the results shows that an increase in the value of the parameter γ is simplifies the shell vibrations and transition from chaotic vibrations to harmonic vibrations has been observed. Complex vibrations with the effect of loss of stability are characteristic for the shells with γ = 0. Increasing γ parameter does not yield loss of stability. In this case, the vibrations become periodic. The amplitude gradually increases together with increase of the load (γ = 0.7). For MEMS devices, this effect is of great importance, as no chaotic vibration MEMS devices results in greater system reliability and durability.

Acknowledgements

This work has been supported by the grants the Russian Science Foundation, RSF 16-19-10290.

REFERENCES

[1] Kong, S., Zhou, S., Nie, Z., Wang, K., The size-dependent natural frequency of Bernoulli–Euler micro-beams. Int. J. Eng. Sci. 46(5) (2008) 427–437.

[2] Ke, L.L,. Yang, J, Kitipornchai, S., Bradford, M.A., Wang, Y.S., Axisymmetric nonlinear free vibration of size-dependent functionally graded annular microplates, Compos. 53 (2013) 207–217.

[3] Zhu, H.X., Size-dependent elastic properties of micro- and nanohoneycombs, J. Mech. Phys. Solids 58(52) (2010) 696–709.

[4] Chong, A.C.M., Lam, D.C.C., Strain gradient plasticity effect in indentation hardness of polymers, J. Mater. Res. 14(10) (1999) 4103–4110.

[5] Ke, L.-L., Wang, Y.-S., Yang, J., Kitipornchai, S., Free vibration of size-dependent Mindlin microplates based on the modified couple stress theory, J. Sound Vib. 331(1) (2012) 94–106,

[6] Tsiatas, G.C., A new Kirchhoff plate model based on a modified couple stress theory, Int. J. Solids Struct. 46(13) (2009) 2757–2764.

[7] Yang, F., Chong, A.C.M., Lam, D.C.C., Tong, P, Couple stress based strain gradient theory for elasticity, Int. J. Solids Struct. 39(10) (2002) 2731–2743.

[8] Wang, L., Size-dependent vibration characteristics of fluid-conveying microtubes, J. Fluids Struct. 26(4) (2010) 675–684.

[9] Kahrobaiyan, M.H., Asghari, M., Rahaeifard, M., Ahmadian, M.T., Investigation of the size-dependent dynamic characteristics of atomic force microscope microcantilevers based on the modified couple stress theory, Int. J. Eng. Sci. 48(12) (2010) 1985–1994.

[10] Asghari, M., Ahmadian, M.T., Kahrobaiyan, M.H., Rahaeifard, M., On the size-dependent behavior of functionally graded micro-beams, Mater. Des. 31(5) (2010) 2324–2329.

[11] Nayfeh, A.H., Younis, M.I., Modeling and simulations of thermoelastic damping in microplates, J. Micromech. Microeng. 14(12) (2004) 1711–1717.

[12] Ke, L.-L., Yang, J., Kitipornchai, S., Dynamic stability of functionally graded carbon nanotube-reinforced composite beams, Mech. Adv. Mater. Struct. 20(1) (2013) 28–37.

[13] Lifshitz, R., Roukes, M.L., Thermoelastic, damping in micro-and nanomechanical systems, Phys. Rev. B 61(8) (2000) 5600–5609.

[14] Reddy J.N., Microstructure-dependent couple stress theories of functionally graded beams, J. Mech. Phys. Solids 59(11) (2011) 2382–2399.

[15] Ma, H., Gao, X., Reddy, J., A microstructure-dependent Timoshenko beam model based on a modified couple stress theory, J. Mech. Phys. Solids 56(12) (2008) 3379–3391.

[16] Yin, L., Qian, Q., Wang, L., Xia, W., Vibration analysis of microscale plates based on modified couple stress theory, Acta Mech. Solida Sinica, 23(5) (2010) 386–393.

[17] Lazopoulos, K.A., On bending of strain gradient elastic micro-plates, Mech. Res. Commun. 36(7) (2009) 777–783.

[18] Reddy, J.N., Kim, J., A nonlinear modified couple stress-based third-order theory of functionally graded plates, Compos. Struct., 94(3) (2012) 1128–1143.

[19] Sheremetev, M.P., Pelekh, V.F., On development of the improved theory of plates, Eng. J. 4(3) (1964) 34-41 (in Russian).

[20] Duwel, A., Candler, R. N., Kenny, T. W, Varghese, M., Engineering MEMS resonators with low thermoelastic damping, J. Microelectromech. Syst. 15(6) (2006) 1437–1445.

[21] Li, P., Fang, Y., Hu, R., Thermoelastic damping in rectangular and circular microplate resonators, J. Sound Vib. 331(3) (2012) 721–733.

[21] Rezazadeh, G., Tayefeh-rezaei, S., Vahdat, A.S., Nasirzadeh, V., Study of thermoelastic damping in an electrostatically deflected circular micro-plate using hyperbolic heat conduction model, J. Solid Mech. 3(3) (2011) 271–282.

[22] Salajeghe, S., Khadem, S.E., Rasekh, M., Nonlinear analysis of thermoelastic damping in axisymmetric vibration of micro circular thinplate resonators, Appl. Math. Model. 36(12) (2012) 5991–6000.

[23] Ali, N.A., Mohammadi, A.K., Thermoelastic damping in clampedclamped annular microplate, Appl. Mech. Mater. 110–116 (2011) 1870–1878.

[24] Zener, C., Internal friction in solids: I. Theory of internal friction in reeds, Phys. Rev. 52(3) (1937) 230.

[25] Prabhakar, S., Vengallatore, S., Thermoelastic, damping in bilayered micromechanical beam resonators, J. Micromech. Microeng. 17(3) (2007) 532–538.

[26]. Sun, Y, Fang, D., Soh, A.K., Thermoelastic damping in microbeam resonators, Int. J. Solids Struct. 43(10) (2006) 3213–3229.

[27] Srikar, V.T., Senturia, S.D., Thermoelastic damping in finegrained polysilicon flexural beam resonators, J. Microelectromech. Syst. 11(5) (2002) 499–504.

[28] Sun, Y., Tohmyoh, H., Thermoelastic damping of the axisymmetric vibration of circular plate resonators, J. Sound Vib. 319(1–2) (2009) 392–405.

[29] Sun, Y., Saka, M., Thermoelastic damping in micro-scale circular plate resonators, J. Sound Vibr. 329(3) (2010) 328–337.

[30] Prabhakar, S., Vengallatore, S., Thermoelastic damping in hollow and slotted microresonators, J. Microelectromech. Syst. 18(3) (2009) 725–735.

[31] Sosale, G., Prabhakar, S., Fréchette, L.G., Vengallatore, S., A microcantilever platform for measuring internal friction in thin films using thermoelastic damping for calibration, J. Microelectromech. Syst. 20(3) (2011) 764–773.

[32] Nourmohammadi, Z., Prabhakar, S., Vengallatore, S., Thermoelastic damping in layered microresonators: Critical frequencies, peak values, and rule of mixture, J. Microelectromech. Syst., 22(3) (2013) 747–754.

[33] Chong, A.C.M., Yang, F., Lam, D.C.C., Tong, P., Torsion and bending of micron-scaled structures, J. Mater. Res. 16(4) (2001) 1052–1058.

[34] Lam, D.C.C., Yang, F., Chong, A.C.M., Wang, J., Tong, P., Experiments and theory in strain gradient elasticity, J. Mech. Phys. Solids, 51(8) (2003) 1477–1508.

[35] Reissner, E. On the theory of bending of elastic plates, J. Math. Phys. 23 (1944).

[36] Vlasov, V.Z., General theory of shells and its application in engineering, NASA-TT-F-99, Washington, National Aeronautics and Space Administration, 1964.

[37] Kármán, Th. Festigkeitsprobleme in Maschinenbau, Encykle. D. Math. Wiss. 4(4) (1910) 311-385.

Vadim A. Krysko - jr., M.Sc. (Ph.D. student): Department of Mathematics and Modeling, Saratov State Technical University, Politehnicheskaya 77, 410054 Saratov, RUSSIAN FEDERATION (vadimakrysko@gmail.com).

Jan Awrejcewicz: Department of Automation, Biomechanics and Mechatronics, Lodz University of Technology, 1/15 Stefanowski St., 90-924 Lodz, POLAND; (*awrejcew@p.lodz.pl*). The author gave a presentation of this paper during one of the conference sessions

Irina V. Papkova, PhD.: Department of Mathematics and Modeling, Saratov State Technical University, Politehnicheskaya 77, 410054 Saratov, RUSSIAN FEDERATION (ikravzova@mail.ru).

Vadim A. Krysko: Department of Mathematics and Modeling, Saratov State Technical University, Politehniekhskaya 77, 410054, Saratov, RUSSIAN FEDERATION *(tak@san.ru)*

General theory of geometrically nonlinear size dependent shells taking into account contact interaction.
Part 2. Contact interaction of two-layer axially symmetric shells

Vadim A. Krysko – jr., Jan Awrejcewicz, Irina V. Papkova, Vadim A. Krysko

Abstract: In this paper a mathematical model of the nonlinear dynamics of flexible two-layer axisymmetric spherical shells of equal curvature is proposed. The geometric nonlinearity is taken into account by the model of Theodore von Karman. The shell material is isotropic and homogeneous. For each layer, the Kirchhoff-Love hypothesis is applied. The contact interaction between them is taken into account according to the Cantor model. The problems are considered as systems with an infinite number of degrees of freedom. The method of finite differences of the second order of accuracy, and the Runge-Kutta type methods are used. The impact of the size-dependent parameter, amplitude and frequency of the forcing load on the contact interaction of shells is studied.

Keywords: spherical shell, contact interaction, nonlinear dynamics, chaos, power spectra, phase portrait, Poincaré map, wavelet analysis, phase synchronization.

1. Introduction

The study of the nonlinear dynamics of mechanical systems with contact interaction is a necessary direction of research for many areas of life and human activity. Multi-layer systems are elements of structures in engineering construction, consumer equipment, medical equipment, military and aerospace engineering, and nuclear power engineering. Questions of studies of nonlinear vibrations of mechanical systems are discussed in [1-4]. Method of solving a differential equation with a nonlinear relationship between components, based on replacement of non-linear terms by integrals from their derivatives is proposed in these works. The obtained solutions allowed to improve the accuracy of a gyroscope by analytical error compensation. One-dimensional mathematical models of beams, panels of infinite length and shells are constructed into account geometric, physical, constructive kinematic nonlinearity and their different combinations. Many problems were solved by various methods: finite differences method, Bubnov-Galerkin method, Rayleigh-Ritz method. Scenarios of transition of mechanical systems from periodic vibrations to temporal and space-temporal chaos are obtained. By analogy with the phenomenon of the universality of the onset of chaos in simple systems, the existence of a certain universality of the turbulence transition in the spatial problems of the theory of one-

dimensional mechanical structures is shown. Studies of nonlinear dynamics of multilayer structures are devoted in references [5-10]. The features of analysis of complex vibrations of a two-layer mechanical structures in the form of beams, rectangular plates supported by beams, cylindrical shells are considered. An analysis of the modern literature shows that the problems considered in this paper have not been investigated previously.

2. Problem statement

Mathematical model of nonlinear dynamics of flexible two-layer spherical round in plan hinged-supported shells, taking into account their size properties has been built. The geometric nonlinearity is taken into account by the von Kármán model. Shells material is elastic, isotropic, and homogeneous with constant density. The contact interaction between them is taken into account according to the Cantor [11] model. For each layer the Kirchhoff-Love hypothesis is applied. Between the shells there is a gap, and hence the shells are connected via boundary conditions.

According the modified couple stress theory we consider the two-layer flexible spherical shell on a rectangular plane under the action of transverse dynamic loading. Load is evenly distributed on the surface of the first shell $q(t) = q_0 \sin(\omega_p t)$ (Fig. 1). Each layer system satisfies the Kirchhoff hypotheses.

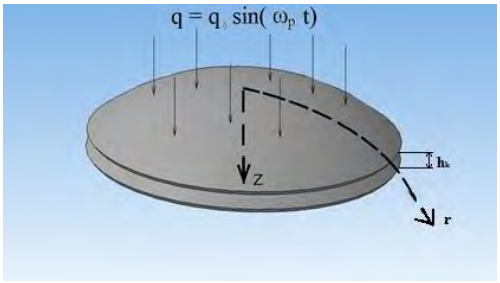

Fig. 1. The construction of two axisymmetric spherical shells of equal curvature connected through boundary conditions

The system of nonlinear PDEs control dynamics of a design from nano-axisymmetric shells has the following form

$$\frac{\partial^2 w_i}{\partial t^2} + \varepsilon \frac{\partial w_i}{\partial t} = -\left(1 + \frac{\gamma \eta_i}{2(1+\mu_i)}\right)\frac{\partial^4 w_i}{\partial r^4} - \frac{2}{r}\frac{\partial^3 w_i}{\partial r^3} + \frac{1}{r^2}\frac{\partial^2 w_i}{\partial r^2} - \frac{1}{r^3}\frac{\partial w_i}{\partial r} + \frac{\partial \Phi_i}{\partial r}\left(1 + \frac{1}{r}\frac{\partial w_i}{\partial r}\right) +$$
$$\frac{\Phi_i}{r}\left(1 + \frac{\partial^2 w_i}{\partial r^2}\right) + 4q + (-1)^i K_i (w_1 - w_2 - h_k)\Psi, \quad (1)$$

$$\frac{\partial^2\Phi_i}{\partial r^2}+\frac{1}{r}\frac{\partial^2\Phi_i}{\partial r^2}-\frac{1}{r^2}\Phi_i=-\frac{\partial w_i}{\partial r}\left(1+\frac{1}{2r}\frac{\partial w_i}{\partial r}\right),$$

$$D_0=\frac{Eh^3}{12(1-\mu^2)}, D_1=\frac{El^2h}{2(1+\mu)},\quad L(w_i,F_i)=2\left[\frac{\partial^2 w_i}{\partial x^2}\frac{\partial^2 F_i}{\partial y^2}+\frac{\partial^2 w_i}{\partial y^2}\frac{\partial^2 F_i}{\partial x^2}-2\frac{\partial^2 w_i}{\partial x\partial y}\frac{\partial^2 F_i}{\partial x\partial y}\right].$$

For the simple movable contour in the meridional direction we have:

$$\Phi=w=0,\frac{\partial^2 w}{\partial r^2}+\frac{v}{b}w=0,\ \text{for}\ r=\bar{r}, \tag{2}$$

the following initial conditions are taken

$$w=f_1(r,0)=0,w'=f_2(r,0)=0,0\le t<\infty, \tag{3}$$

and the following conditions in the vicinity of the shallow top are employed

$$\Phi\approx Ar,\Phi'\approx A; w\approx B+Cr^2; w'\approx 2Cr, w''\approx 2C;\ w'''\approx 0.$$

The following nondimensional quantities (with bars) are introduced:

$$\bar{t}=\omega_0 t;\ \bar{x}=b\frac{x}{c};\ \bar{y}=b\frac{y}{c};\ \omega_0=\sqrt{\frac{Eg}{\gamma R^2}};\ \bar{\varepsilon}=\sqrt{\frac{g}{\gamma R^2}}\frac{R}{h}\varepsilon,\bar{F}=\eta\frac{F}{Eh^3};\ \bar{w}=\sqrt{\eta}\frac{w}{h};$$

$$\bar{r}=b\frac{r}{c};\ \bar{q}=\frac{\sqrt{\eta}}{4}\frac{q}{E}\left(\frac{R}{h}\right)^2;\ \eta=12(1-\mu^2);\ \gamma=\frac{l^2}{h^2}; b=\sqrt{\eta}\frac{c^2}{Rh},\bar{K}=\frac{b^4K}{h^5},$$

where: t - time; ε- coefficient of viscous-type external damping in which the shell moves; F- stress function; w- displacement function; R, C - main radius of the shell curvature and the radius of the shell contour, respectively; h - shell thickness; b- parameter of flatness; μ- Poisson's ratio; r - distance from the axis of rotation to the point on the middle surface; q - external load parameter; l - size-dependent parameter; h_k - casing gap; K - bulk modulus of elasticity.

In order to reduce the problem (1)-(3) governing dynamics of the considered continuous system into a system with lumped parameters, the method of finite differences (FDM) with approximation $O(\Delta^2)$ is used. PDEs as well as the boundary and initial conditions (2)-(3) are recast to the following finite difference formulas with respect to the spatial coordinate r and time:

$$\begin{aligned}
&w''+\varepsilon w'=-\frac{w_{j+1,i}-w_{j-1,i}}{2\Delta}\left(\frac{1}{r_j^3}-\frac{\Phi_{j+1,i}-\Phi_{j-1,i}}{2r_j\Delta}\right)+\frac{w_{j+1,i}-2w_{j,i}+w_{j-1,i}}{r_j\Delta^2}\\
&\left(\Phi_j+\frac{1}{r_j}\right)+\frac{\Phi_{j+1,i}-\Phi_{j-1,i}}{2\Delta}+\frac{\Phi_{j,i}}{r_j}-\left(1+\frac{\gamma_i\eta}{2(1+\mu_i}\right),\\
&\frac{w_{j+2,i}-4w_{j+1,i}+6w_{j,i}-4w_{j-1,i}+w_{j-2,i}}{\Delta^4}-\frac{w_{j+2,i}-2w_{j+1,i}+2w_{j-1,i}-w_{i-2}}{r_j\Delta^3}+\\
&+4q_i+(-1)^iK\left(w_{i,1}-w_{i,2}-h_k\right)\psi,
\end{aligned} \tag{4}$$

$$\Phi_{j+1,i}\left(-\frac{1}{\Delta^2}-\frac{1}{2r_j\Delta}\right)+\Phi_{j,i}\left(\frac{2}{\Delta^2}+\frac{1}{r_j^2}\right)+\Phi_{j-1,i}\left(-\frac{1}{\Delta^2}+\frac{1}{2r_j\Delta}\right)$$
$$=-\frac{w_{j+1,i}-w_{j-1,i}}{2\Delta}\left(1-\frac{w_{j+1,i}-w_{j-1,i}}{4r_j\Delta}\right),$$

where: $\Delta = {}^{b}/_{n}$; n - denotes the number of modes of the shell radius.

Boundary conditions for the shell is pivotally-movable in the meridian direction supporting contour:

$$\Phi_n = 0; w_{i+1} = \frac{\nu\Delta-2b}{2b+\nu\Delta}w_{i-1}\; w_n = 0 \text{ for } r_n = b \tag{5}$$

and the following initial conditions are taken

$$w_n = f_1(r_k, 0), w'_n = f_2(r_k, 0), (0 \le k \le n), 0 \le t \le \infty. \tag{6}$$

If small terms are neglected and the differential operators are substituted by the central finite differences for $r = \Delta$, the conditions are obtained in the shell top. If we neglect the small terms and replace the central differential operators with finite-difference we obtain the conditions at the vertex:

$$\Phi_0 = \Phi_2 - 2\Phi_1;\; w_0 = \frac{4}{3}w_1 - \frac{1}{3}w_2;\; w_{-1} = \frac{8}{3}w_1 - \frac{8}{3}w_2 + w_3. \tag{7}$$

The transverse load can be changed arbitrarily with respect to the spatial coordinate and time. In this work the harmonic transverse load of the form $q = q_0\sin(\omega_p t)$, where q_0 stands for an amplitude and ω_p is a frequency of the excitation, is used.

After reducing the task (1) – (3) to the normal form, we solve the Cauchy problem by the Runge-Kutta method of the fourth order of accuracy. The time step is chosen from the stability condition of the solution($\Delta t = 1.2207 \cdot 10^{-4}$).

3. Numerical results

We study the vibrations of axisymmetric for the simple movable contour in the meridional direction (2) construction consists of two nano shells (b = 4) under the action of an alternating load on the upper shell. Signals, phase portraits, Poincaré section, autocorrelation function, Fourier spectrum, sign changes the highest Lyapunov exponent in time was analyzed for each of the shells. Impact magnitudes the size dependent parameter γ between the shells was studied. Change the contact area in time has also been studied.

The method of phase chaotic synchronization of mechanical dynamical systems on the basis of wavelet analysis is used. To describe and analyze phase chaotic synchronization, the phase of the chaotic signal is introduced. Phase chaotic synchronization means that the phase of chaotic signals is captured. Time as the amplitudes of these signals remain unrelated together and look chaotic. The

phase capture entails coincidence of frequencies signals. The dark zones of the wavelet spectrum correspond to phase synchronization of the beam vibrations.

The influence of magnitude the size-dependent parameter γ on the vibration character of a two-layer packet shells has been studied. Particular attention is drawn on initial joint vibrations, i.e. from the moment of contact of the shells. In Table 1 are given signals, phase portraits and power spectra for the construction from shells with a small gap $\delta = 0.01$ and $\gamma = 0;\ 0.7$. In both cases, before the contact, the first shell experiences harmonic vibrations, and the second shell is on rest. Increase parameter γ yield the system more rigid and resistant to loads, and deflection at depending on ascending loads increases slower. Contact for shells with the parameter γ = 0 comes at an amplitude of the sign of the variable load $q_0 = 0.0002$, and for shells with the parameter $\gamma = 0.7$, at the load amplitude $q_0 = 0.0005$. In Tables 2 and 3, the results are in the following way: a) the signal of joint vibrations of the two shells; b) the phase portrait for the first shell; c) the phase portrait for the second shell; d) the power spectrum based on the fast Fourier transform for the first shell; e) the power spectrum for the second shell; e) the phase difference.

Table 1.

$b = 4,\ h_k = 0.01\ , \gamma = 0.0$		
$q_0 = 2 \cdot 10^{-4}$		
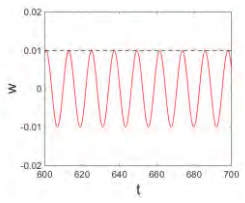	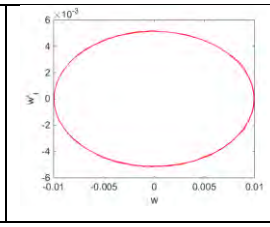	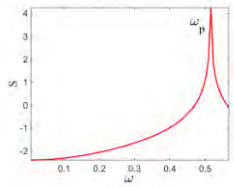
$b = 4,\ h_k = 0.01\ , \gamma = 0.7$		
$q_0 = 2 \cdot 10^{-4}$		
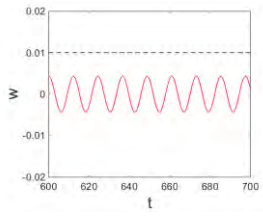	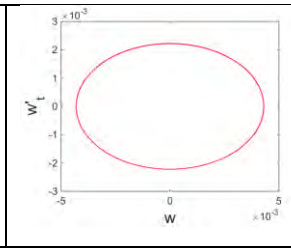	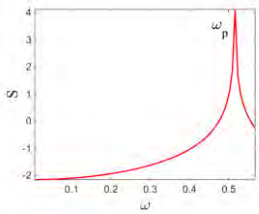

Table 2.

$b = 4,\ h_k = 0.01\ ,\gamma = 0.0$		
$q_0 = 5 \cdot 10^{-4}$		
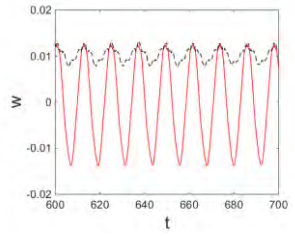	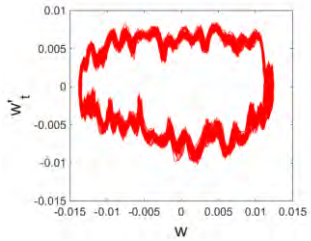	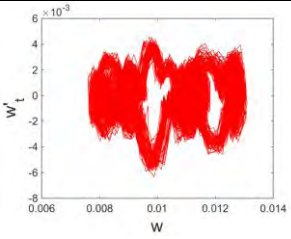
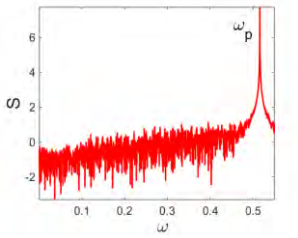	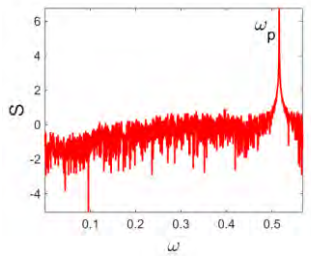	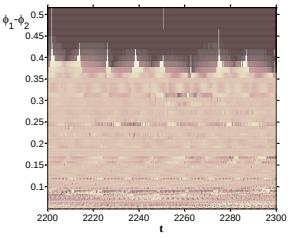
$q_0 = 5 \cdot 10^{-3}$		
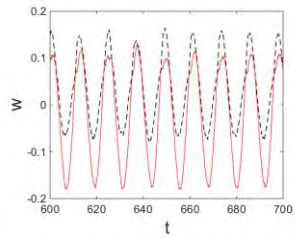	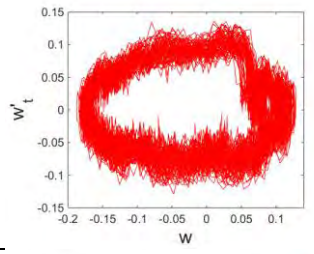	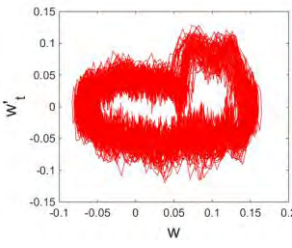
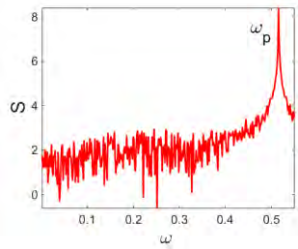	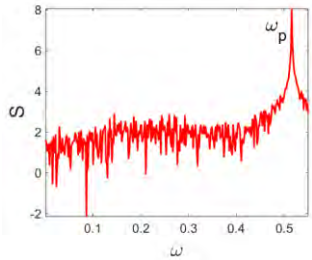	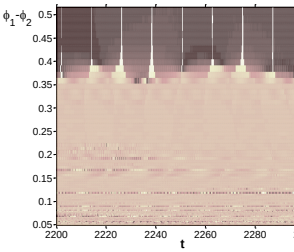

Table 3.

$b = 4,\ h_k = 0.01\ ,\gamma = 0.7$		
$q_0 = 5 \cdot 10^{-4}$		
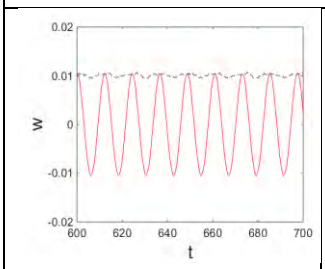	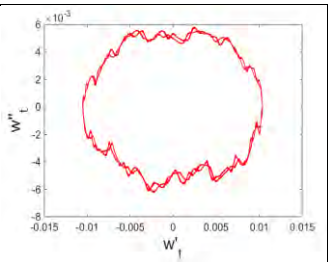	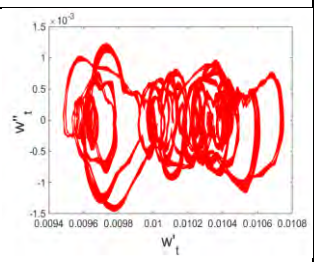
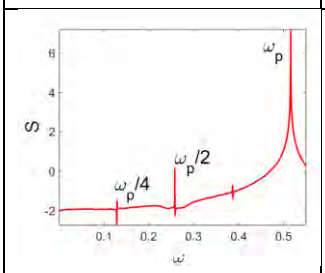	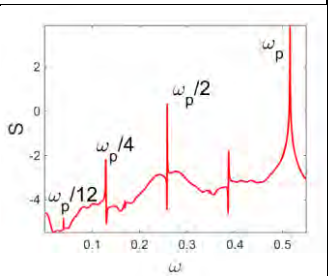	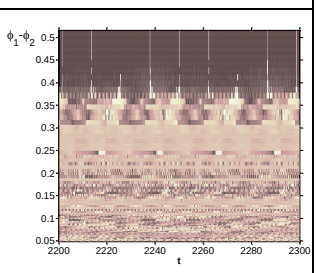
$q_0 = 5 \cdot 10^{-3}$		
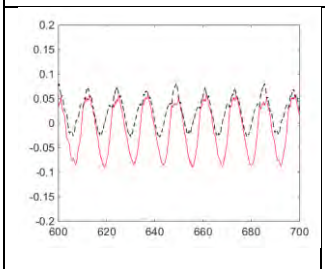	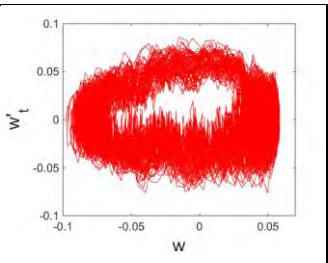	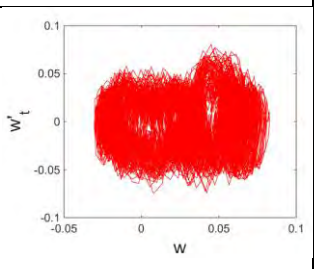
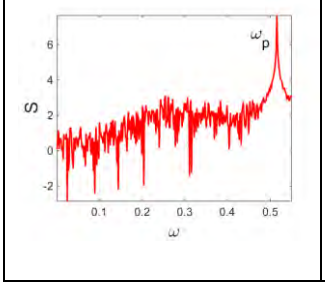	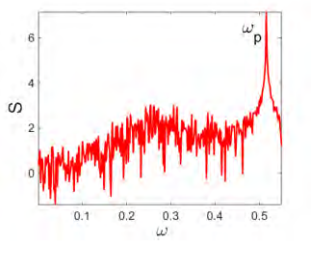	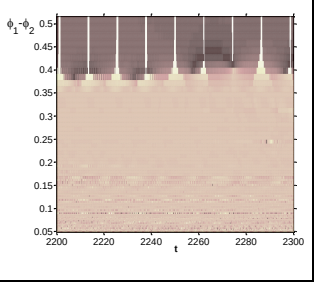

Consider the vibrations of a two-layer package with a gap $h_k = 0.01$ between the shells and with parameter $\gamma = 0$. At increase amplitude of the load there is a contact of the shells. Both shells vibrate chaotically. The phase portrait for the first envelope represents a thickened orbit. In the phase portrait of the second shell three centers of attraction of phase trajectories are visible. On the power spectrum of the first shell, chaos is observed at low frequencies, and for a second shell, on a solid pedestal. The phase difference indicates that the frequencies present in the signal are not synchronized. Further increase of the amplitudes of excitation also generates chaotic vibrations of the shells. Phase portraits of shells have a similar shape. Power spectra have noisy components. On the graph, the phase difference increased the number of dark spots, which means synchronization of some frequencies.

Now we will analyze the situation when the vibrations of a two-layered packet with a gap $h_k = 0.01$ and parameter $\gamma = 0.7$ between shells are studied. At initial joint vibrations of a two-layer package shells with an amplitude of the driving force $q_0 = 0.0005$ shell power spectrum of the first shell demonstrates frequencies ω_p, $\frac{\omega_p}{2}$, and $\frac{\omega_p}{4}$ and in the signal of the second shell there are frequencies: ω_p, $\frac{\omega_p}{2}$, $\frac{\omega_p}{4}$. $\frac{\omega_p}{12}$. In the phase portrait of the first shell two orbits are visible, and the second shell has 12 thickened orbits. When increasing the amplitude excitation to $q_0 = 0.005$, the vibrations become chaotic.

4. **Concluding remarks**

A mathematical model of the contact interaction of two spherical axisymmetric circular nano-shells has been constructed. The nonlinear dynamics of the contact interaction of two axisymmetric nano-shells has been investigated. Comparison vibrations depending on from increase the size-dependent parameter has been carried out. It is revealed that with the increase in the dimension-dependent parameter, the stability of the system increases. On the other hand, a contact between shells implies chaotic vibrations.

Acknowledgements

This work has been supported by the grants the Russian Science Foundation, RSF 16-19-10290.

References

[1] Awrejcewicz, J., Krysko A.V., Kutepov I.E., Chaotic dynamics of flexible Euler-Bernoulli beams, Chaos 5 (2013) 043130-1 -043130-25.

[2] Awrejcewicz, J., Krysko, V.A., Papkova, I.V., Krysko, A.V., Deterministic Chaos in One Dimensional Continuous Systems, Singapore, World Scientific, 2016.

[3] Kharlanov, V.L., Kharlanov, S.V., Numerical method of integration of nonlinear differential equations of the problems of structural mechanics, Construct. Mech. Calcul. Struct. 1(264) (2016) 62-65 (in Russian).

[4] Merkuriev, I.V., Pankratieva, G.V., Podalkov, V.V., Sbytova, Ye.S., Nonlinear vibrations of a micromechanical gyroscope with a resonator in the form of elastic plates, J. Moscow Power Eng. Instit. (2013) 013-018 (in Russian).

[5] Krysko, V.A., Krylova, E.Yu, Papkova, I.V., Nonlinear dynamics of parametric vibrations of two-layered distributed systems with allowance for the gap between layers, Bulletin of the Saratov State Technical University 11(69) (2013) 7-11 (in Russian).

[6] Yakovleva, T.V., Saltykova, O.A., Krysko, V.A., Contact interaction of a plate and a locally located beam, Actual Probl. Sci. XIII (2014) 7-14 (in Russian).

[7] Saltykova, O.A., Krysko, V.A., Contact interaction of two beams Timoshenko, Nonlin. Dyn. 13(1) (2017) 41-53 (in Russian).

[8] Awrejcewicz, J., Krysko-jr, V.A., Yakovleva, T.V., Krysko, V.A., Alternating chaos versus synchronized vibrations of interacting plate with beams, Int. J. Nonlin. Mech. 88 (2017) 21–30.

[9] Awrejcewicz, J., Krysko-jr., V.A., Yakovleva, T.V., Krysko, V.A., Noisy contact interactions of multi-layer mechanical structures coupled by boundary conditions, J. Sound Vib. 369 (2016) 77–86.

[10] Yakovleva, T.V., Krysko-jr., V.A., Contact interaction of a physically nonlinear three-layer plate-beam structure in a temperature field, Russian Metallurgy 7 (2017) (accepted).

[11] Kantor, B. Ya., Nonlinear Problems in the Theory of Inhomogeneous Shallow Shells, Naukova Dumka, Kiev, 1971 (in Russian).

[12] Volmir, A.S., Nonlinear Dynamics of Plates and Shells, Moscow, Nauka, 1972 (in Russian).

Vadim A. Krysko - jr., M.Sc. (Ph.D. student): Department of Mathematics and Modeling, Saratov State Technical University, Politehnicheskaya 77, 410054 Saratov, RUSSIAN FEDERATION (vadimakrysko@gmail.com).

Jan Awrejcewicz: Department of Automation, Biomechanics and Mechatronics, Lodz University of Technology, 1/15 Stefanowski St., 90-924 Lodz, POLAND; (*awrejcew@p.lodz.pl*). The author gave a presentation of this paper during one of the conference sessions

Irina V. Papkova, PhD.: Department of Mathematics and Modeling, Saratov State Technical University, Politehnicheskaya 77, 410054 Saratov, RUSSIAN FEDERATION (ikravzova@mail.ru).

Vadim A. Krysko: Department of Mathematics and Modeling, Saratov State Technical University, Politehniekhskaya 77, 410054, Saratov, RUSSIAN FEDERATION *(tak@san.ru)*

Free vibration analysis of laminated functionally graded shallow shells by the R-functions method

Lidiya Kurpa, Tetyana Shmatko, Jan Awrejcewicz

Abstract: The R-functions theory and Ritz approach are applied for analysis of free vibration laminated shallow shells with different types of curvatures and complex planform. Shallow shells are considered as sandwich ones of the different types: a) face sheets of the shallow shells are made of functionally graded material (FGM) and core is isotropic material; b) face sheets of the shallow shells are isotropic, but core is made of FGM. It is assumed that FGM layers are made of a mixture of metal and ceramics and effective material properties of layers are varied accordingly to Voight's rule. Formulation of the problem is carried out using the refined theory of shallow shells of the first order (Timoshenko's type). The different types of boundary conditions including clamped, simply supported, free edge and their combinations are studied. The proposed method and created computer code have been examined on test problems for shallow shells with rectangular planforms. In order to demonstrate the possibility of the developed approach, new results for laminated FGM shallow shells with complex planform are presented. Effects of the different material distributions, mechanical properties of the constituent materials, lamination scheme, boundary conditions and geometrical parameters on natural frequencies are shown and analyzed.

1. Introduction

Functionally graded materials (FGMs) can be considered as a new class of the composite materials used extensively for manufacture of shell structural elements. The main advantages of these materials in comparison with conventional composite materials are the smoothness and continuous change of material properties along the thickness of the object. This avoids the appearance of stress concentration that is found in laminated composites. Analysis of vibration of laminated and FGM shallow shells has been carried out by numerous investigators [1-3]. Last decade analysis of nonlinear free and force vibrations of the FG shells have been extensive studied in addition to the linear vibration (see [4-6]). Joint application of the FGM and pure metallic and ceramic is widely used for design of many elements of the modern constructions. However, the number of publications devoted to the study of multilayered FGM shallow shells is rather small [2, 3].

The main goal of this paper is to present efficient and enough universal approach to analyze the laminated functionally graded shallow shells with complex shape of their planforms and different

boundary conditions. The proposed method is based on matching both the R-functions theory and variational Ritz method [5-6]. Formulation of the problem is carried out using the refined theory of shallow shells of the first order (FSDT). In the present study this approach is applied to three-layered shallow shells like sandwich ones. Two types of lamination schemes are considered. Type 1-2 corresponds to sandwich shallow shells with FGM face sheets and isotropic core. Type 2-2 describes sandwich shallow shells with isotropic face sheets (pure ceramics or metal), and core made of FGM. It is assumed that FGM layers are made of a mixture of metal and ceramics and effective material properties of layers are varied according to Voight's rule. The proposed method is validated by investigation of test problems for shallow shells with rectangular plan-form and different boundary conditions. The current method is also employed to novel vibration problems for doubly- curved shallow shells with complex form of the cut.

2. Mathematical formulation

Consider three-layered functionally graded shallow shell with uniform thickness *h*. It is assumed that the FGM layers are made of a mixture of ceramics and metals. Double curved shallow shell can have an arbitrary planform. The effective material properties of layers vary continuously and smoothly in thickness direction and can be estimated by the Voight's law:

$$E^{(r)} = \left(E_u^{(r)} - E_l^{(r)}\right)V_c^{(r)} + E_l^{(r)}, \quad \nu^{(r)} = \left(\nu_u^{(r)} - \nu_l^{(r)}\right)V_c^{(r)} + \nu E_l^{(r)}, \quad \rho^{(r)} = \left(\rho_u^{(r)} - \rho_l^{(r)}\right)V_c^{(r)} + \rho_l^{(r)}, \qquad (1)$$

where $E_u^{(r)}, \nu_u^{(r)}, \rho_u^{(r)}$ and $E_l^{(r)}, \nu_l^{(r)}, \rho_l^{(r)}$ are Young modulus, Poisson's ratio and mass density of the upper and lower surfaces of the r-layer, respectively, and $V_c^{(r)}$ is the volume fraction of ceramic. As example the value $V_c^{(r)}$ is shown for the scheme lamination of types 1-2 and 2-2 in Table 1.

Shallow shells of type 1-2 correspond to sandwich shallow shells with FGM face sheets and isotropic (metal) core (Fig.1, Table 1). The shells of type 2-2 correspond to sandwich shallow shell with FGM core and ceramics on top face sheet and metal on bottom face sheet (Fig. 2, Table 1). Let us note that the values p_1, p_2, p_3 are the power-law FGM exponents of the corresponding layer. The thickness of the layers may be varied. The ratio of thickness of layers from bottom to top is denoted by the combination of three numbers. For example, "1-2-1" denotes that ratio of thickness of the layers is defined as $h^{(1)} : h^{(2)} : h^{(3)} = 1:2:1,$ where $h^{(1)} = h_1 + h/2, h^{(2)} = h_2 - h_1, \quad h^{(3)} = h/2 - h_2$ (see Fig.1, 2). According to the first order shear deformation theory of shallow shell (FSDT) , the displacements components u_1, u_2, u_3 at a point (x, y, z) are expressed as functions of the middle

surface displacements u, v and w in the Ox, Oy and Oz directions and the independent rotations ψ_x, ψ_y of the transverse normal to middle surface about the Oy and Ox axes, respectively [1-4]:

$$u_1 = u + z\psi_x, \quad u_2 = v + z\psi_y, \quad u_3 = w. \tag{2}$$

Table 1. Value of volume fraction $V_c^{(r)}$ for two types laminated FGM shallow shells

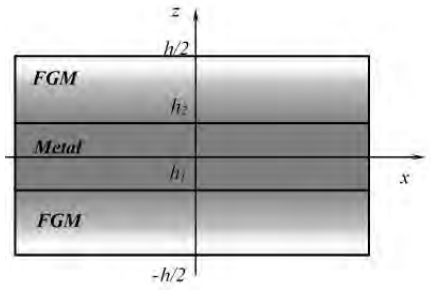

Figure 1. Type 1-2

$$\begin{cases} V_c^{(1)} = \left(\dfrac{z - h_1}{-h_1 - h/2}\right)^{p_1}, & z \in [-h/2, h_1], \\ V_c^{(2)} = 0, & z \in [h_1, h_2], \\ V_c^{(3)} = \left(\dfrac{z - h_2}{h/2 - h}\right)^{p_3}, & z \in [h_2, h/2] \end{cases}$$

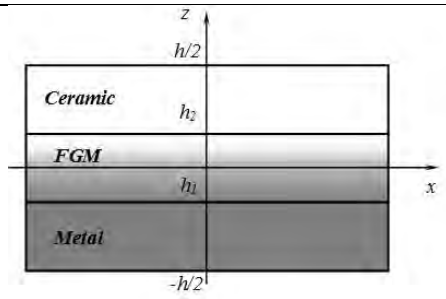

Figure 2. Type 2-2

$$\begin{cases} V_c^{(1)} = 0, & z \in [-h/2, h_1], \\ V_c^{(2)} = \left(\dfrac{z - h_2}{h/2 - h}\right)^{p_2}, & z \in [h_1, h_2], \\ V_c^{(3)} = 1, & z \in [h_2, h/2] \end{cases}$$

Strain components $\varepsilon = \{\varepsilon_{11}; \varepsilon_{22}; \varepsilon_{12}\}^T$, $\chi = \{\chi_{11}; \chi_{22}; \chi_{12}\}^T$ at an arbitrary point of the shallow shell are:

$$\varepsilon_{11} = u_{,x} + w/R_x \quad \varepsilon_{22} = v_{,y} + w/R_y \quad \varepsilon_{12} = u_{,y} + v_{,x}, \tag{3}$$

$$\varepsilon_{13} = w_{,x} + \psi_x, \quad \varepsilon_{23} = w_{,y} + \psi_y, \chi_{11} = \psi_{x,x}, \quad \chi_{22} = \psi_{y,y} \quad \chi_{12} = \psi_{x,y} + \psi_{y,x}. \tag{4}$$

In-plane force resultant vector $N = (N_{11}, N_{22}, N_{12})^T$, bending and twisting moments resultant vector $M = (M_{11}, M_{22}, M_{12})^T$ and transverse shear force resultant $Q = (Q_x, Q_y)^T$ are calculated by integration along Oz-axes and defined as:

$$[N] = [A]\{\varepsilon\} + [B]\{\chi\}, \quad [M] = [B]\{\varepsilon\} + [D]\{\chi\}. \tag{5}$$

Elements A_{ij}, B_{ij}, D_{ij} of the matrices *A, B* and *D* in relations (4) are calculated by formulas:

$$A_{ij}=\sum_{r=1}^{3}\int_{z_r}^{z_{r+1}}Q_{ij}^{(r)}dz\,,\qquad B_{ij}=\sum_{r=1}^{3}\int_{z_r}^{z_{r+1}}Q_{ij}^{(r)}zdz\,,\qquad D_{ij}=\sum_{r=1}^{3}\int_{z_r}^{z_{r+1}}Q_{ij}^{(r)}z^2dz\,. \tag{6}$$

Values $Q_{ij}^{(r)}\left(i,j=1,2,3\right)$ are defined by the following expressions

$$Q_{11}^{(r)}=Q_{22}^{(r)}=\frac{E^{(r)}}{1-\left(\nu^{(r)}\right)^2}\,,\qquad Q_{12}^{(r)}=\frac{\nu^{(r)}E^{(r)}}{1-\left(\nu^{(r)}\right)^2},\qquad Q_{66}^{(r)}=\frac{E^{(r)}}{2\left(1+\nu^{(r)}\right)} \tag{7}$$

Transverse shear force resultants Q_x, Q_y are defined as follows

$$Q_x=K_s^2A_{33}\varepsilon_{13},\quad Q_y=K_s^2A_{33}\varepsilon_{23}\,, \tag{8}$$

where K_s^2 denotes the shear correction factor. In this paper, it will be fixed to $5/6$.

Further, we consider materials with Poisson's ratio independent of temperature and with the same for ceramics and metal i.e. $\nu_m=\nu_c$. Then coefficients A_{ij}, B_{ij}, D_{ij} can be calculated directly. Analytical expressions of these coefficients for the shells of Types 1-2 and 2-2 are presented below provided that the following designations have been inserted:

$$as1=\left(\frac{h}{2}+h_1\right),\ as2=h_2-\frac{h}{2},\quad bs1=\frac{1}{2as1},\quad bs2=\frac{1}{2as2},\quad E_{cm}=E_c-E_m\,.$$

Type 1-2:

$$A_{11}=\frac{1}{1-\nu^2}\left(E_{cm}\left(\frac{as1}{p_1+1}-\frac{as2}{p_3+1}+\right)+E_mh\right),$$

$$\mathbf{B}_{11}=\frac{E_{cm}}{1-\nu^2}\left(as1\left(\frac{h_1}{p_1+1}-\frac{as1}{p_1+2}\right)-as2\left(\frac{h_2}{p_3+1}-\frac{as2}{p_3+2}\right)\right),$$

$$D_{11}=\frac{1}{1-\nu^2}\left(E_{cm}\left(as1\left(\frac{h_1^2}{p_1+1}-\frac{2as1}{p_1+2}h_1+\frac{as1^2}{p_1+3}\right)-\right.\right.$$

$$\left.\left.-as2\left(\frac{as2^2}{p_3+3}-2h_2\frac{as2}{p_3+2}h+\frac{h_2^2}{p_3+1}\right)\right)+\frac{E_m}{12}h^3\right).$$

Type 2-2:

$$A_{11}=\frac{1}{1-\nu^2}\left(E_{cm}\left(\frac{h_2-h_1}{p_2+1}-h_2\right)+\frac{h}{2}\left(E_c+E_m\right)\right),$$

$$\mathbf{B}_{11}=\frac{E_{cm}}{1-\nu^2}\left(\frac{as1}{p_2+2}\left(h_2+\frac{h_1}{p_2+1}\right)+\frac{1}{2}\left(\frac{h^2}{4}-h_2^2\right)\right),$$

$$D_{11}=\frac{1}{1-\nu^2}\left(E_{cm}\left(as1\left(\frac{h_1^2}{p_2+1}+\frac{2as1}{p_2+2}h_1+\frac{as1^2}{p_2+3}\right)-\frac{h_2^3}{3}\right)+\frac{\left(E_m+E_c\right)}{24}h^3\right).$$

Note that values $A_{12}, A_{66}, B_{12}, B_{66}, D_{12}, D_{66},$ for all types of the lamination schemes, are defined as follows

$$R_{12}=\nu R_{11},\quad R_{22}=R_{11},\quad R_{66}=\frac{1-\nu}{2}R_{11}.$$

3. Solution method

To solve the free vibration problem let us present the vector of unknown functions in the following way

$$\begin{aligned}&\vec{U}(\bar{u}(x,y,t),\bar{v}(x,y,t),\bar{w}(x,y,t),\overline{\psi_x}(x,y,t),\overline{\psi_y}(x,y,t))=\\&=\vec{U}(u(x,y),v(x,y),w(x,y),\psi_x(x,y),\psi_y(x,y))\sin\lambda t,\end{aligned}\tag{9}$$

where λ stands for vibration frequency. Applying the principle of Ostrogradskiy-Hamilton, we get the variational equation in the form

$$\partial\left(U_{\max}-\lambda^2 T_{\max}\right)=0\,,\tag{10}$$

Expressions for strain U and kinetic energy T are defined by relations:

$$U_{\max}=\frac{1}{2}\iint_{\Omega}\left(N_{11}\varepsilon_{11}+N_{22}\varepsilon_{22}+N_{12}\varepsilon_{12}+M_{11}\chi_{11}+M_{22}\chi_{22}+M_{12}\chi_{12}+Q_x\varepsilon_{13}+Q_y\varepsilon_{23}\right)dxdy,\tag{11}$$

$$T_{\max}=\frac{1}{2}\iint_{\Omega}I_0\left(u^2+v^2+w^2\right)+2I_1\left(u\psi_x+v\psi_y\right)+I_2\left({\psi_x}^2+{\psi_y}^2\right)dxdy,\tag{12}$$

where I_0, I_1, I_2 are defined by the following expressions:

Type 1-2:
$$I_0=\rho_{cm}\left(\frac{as1}{p_1+1}-\frac{as2}{p_3+1}+\right)+\rho_m h\frac{1}{1-\nu^2},\quad \rho_{cm}=\rho_c-\rho_m\,,$$

$$I_1=\rho_{cm}\left(as1\left(\frac{h_1}{p_1+1}-\frac{as1}{p_1+2}\right)-as2\left(\frac{h_2}{p_3+1}-\frac{as2}{p_3+2}\right)\right),$$

$$I_2=\left(\rho_{cm}\left(as1\left(\frac{h_1^2}{p_2+1}+\frac{2as1}{p_2+2}h_1+\frac{as1^2}{p_2+3}\right)-\frac{h_2^3}{3}\right)+\frac{\left(\rho_m+\rho_c\right)}{24}h^3\right)$$

Type 2-2:
$$I_0=\rho_{cm}\left(\frac{h_2-h_1}{p_2+1}-h_2\right)+\frac{h}{2}\left(\rho_c+\rho_m\right),$$

$$I_1 = \rho_{cm}\left(\frac{as1}{p_2+2}\left(h_2+\frac{h_1}{p_2+1}\right)+\frac{1}{2}\left(\frac{h^2}{4}-h_2^2\right)\right)$$

$$I_2 = \rho_{cm}\left(as1\left(\frac{h_1^2}{p_2+1}+\frac{2as1}{p_2+2}h_1+\frac{as1^2}{p_2+3}\right)-\frac{h_2^3}{3}\right)+\frac{(\rho_m+\rho_c)}{24}h^3.$$

Minimization of the functional (10) will be performed using the Ritz's method. Necessary sequence of coordinate functions we will build employing the R-functions theory [7].

4. Numerical results

4.1. Validation of the presented results

To verify the accuracy of the present results obtained by the proposed approach, we consider the solution of several test problems.

Case study 1. Natural frequencies of laminated FGM square shallow shells of Type 1-2 and 2-2 with various boundary conditions and geometrical parameters: $h/a=0.1$; $b/a=1$; $a/R_x=0.2$ are analyzed. The material constituents M_1 and M_2 are assumed to be aluminum and alumina [1-4]. The material properties of the FG mixture used in the present study are

$$Al: \quad E_c = 70\ GPA, \nu_c = 0.3, \quad \rho_c = 270 kg/m^3$$

$$Al_2O_3: \quad E_c = 380\ GPA, \nu_c = 0.3, \quad \rho_c = 3800 kg/m^3$$

The boundary conditions are defined as follows:

(i) CCCC- shell is clamped on sides $x=\pm\frac{a}{2}, y=\pm\frac{b}{2}$;

(ii) SSSS-shell is simply supported on sides $x=\pm\frac{a}{2}, y=\pm\frac{b}{2}$;

(iii) SFSF-shell is free on sides $x=\pm\frac{a}{2}$ and simply-supported on sides $y=\pm\frac{b}{2}$;

(iv) SCSC-shell is simply supported on sides $x=\pm\frac{a}{2}$ and clamped on sides $y=\pm\frac{b}{2}$.

Values of the fundamental linear frequency parameters $\Omega_L^{(1)}=\lambda_1 h\sqrt{\rho_c/E_c}$ of the cylindrical and spherical shells of Types 1-2 and 2-2 for thickness scheme 1-2-1 are presented in Table 2.

Table 2. Comparison of the fundamental frequency parameter $\Omega_L^{(1)} = \lambda_1 h\sqrt{\rho_c / E_c}$ of cylindrical and spherical shallow shells with square plan-form and various boundary conditions (Type of the shell 1-2, thickness scheme 1-2-1).

p	Methods	Cylindrical shell k_1=0.2,k_2=0				Spherical shell k_1=k_2=0.2			
		SFSF	SSSS	CCCC	SCSC	SFSF	SSSS	CCCC	SCSC
0.6	[3]	0.833	1.686	2.800	2.299	0.838	1.733	2.846	2.345
	RFM	0.834	1.692	2.829	2.319	0.840	1.738	2.874	2.365
5	[3]	0.627	1.274	2.132	1.746	0.632	1.313	2.170	1.784
	RFM	0.628	1.278	2.152	1.760	0.633	1.317	2.189	1.798
20	[3]	0.519	1.060	1.797	1.466	0.525	1.099	1.833	1.504
	RFM	0.520	1.063	1.811	1.476	0.525	1.101	1.847	1.513

These results were obtained using 28 admissible functions to approximate each of the functions u, v, ψ_x, ψ_y , and 36 admissible functions in order to approximate deflection *w*.

Due to the doubly-symmetric nature of the shell, at numerical implementation of the developed software the integration is performed above only on one-quarter domain. It can be observed that presented results are in excellent agreement with those reported in reference [3].

4.2. Free vibration of the functionally graded shells with complex form of a plan

In order to present new results and to illustrate the versatility and efficiency of the proposed method and the developed computer code let us consider the shallow shell with shape of the plan presented in the Fig. 3. Its geometrical parameters are fixed: $k_1 = R_x / 2a = 0.2, k_2 = R_y / 2a = (0,0.2,-0.2)$, $b / a = 1,\ r_1 / 2a = 0.125, r_2 / 2a = 0.25, h / 2a = 0.1.$

Suppose that shell is clamped at the internal border of the region. However, on the outer boundary of the region the shell can be either clamped or simply supported or may have the mixed boundary conditions like boundary conditions in Task 1 (CCCC, SSSS, SFSF and SCSC). Then the solution structure for shells with complete clamped on inside and outside borders can be taken as:

$$w = \omega\Phi_1, \quad u = \omega\Phi_2, \quad v = \omega\Phi_3, \quad , \quad \psi_x = \omega\Phi_4, \quad \psi_y = \omega\Phi_5 . \tag{13}$$

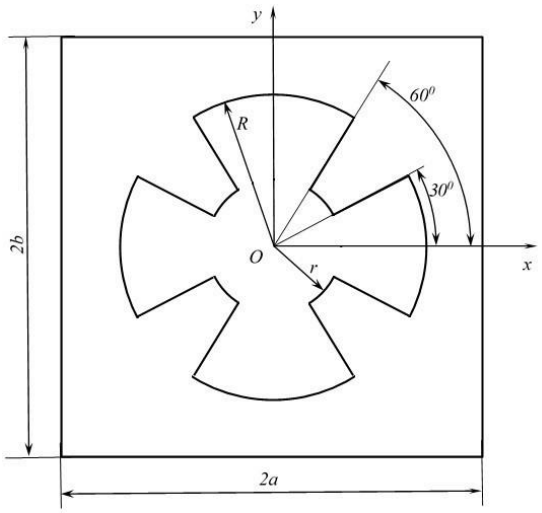

Figure. 3. Shape of the plan of the laminated FGM shallow shell

For another type of the boundary conditions we propose to take solution structure satisfying kinematic boundary conditions in the following form:

$$w = \omega^{(w)}\Phi_1, \quad u = \omega^{(u)}\Phi_2, \quad v = \omega^{(v)}\Phi_3, \quad , \quad \psi_x = \omega^{(\psi_x)}\Phi_4, \quad \psi_y = \omega^{\psi_y}\Phi_5, \quad (14)$$

where $\Phi_i, i = \overline{1,5}$ are indefinite components of the structure [6,7] presented as an expansion in a series of some complete system (power polynomials, trigonometric polynomials, splines etc.), $\omega = 0$ is equation of the whole border of the shell plan-form. The functions $\omega^{(u)}, \omega^{(v)}, \omega^{(w)}, \quad \omega^{(\psi_x)}, \omega^{(\psi_y)}$ are constructed by the R-functions theory in such a way that they vanish on those parts of the boundary where the functions u, v, w, ψ_x, ψ_y are zero. To realize the solution structure (13) and (14) we should construct the equation of whole border and functions $\omega^{(u)}, \omega^{(v)}, \omega^{(w)}, \quad \omega^{(\psi_x)}, \omega^{(\psi_y)}$. Using the R-operations [7], we build the equation of border in the form:

$$\omega = \omega_{inside} \wedge_0 \omega_{outside}, \quad (15)$$

where

$$\omega_{inside} = \left(-\left(\left(\left(f_1 \wedge_0 f_2\right) \vee_0 \left(\overline{f_1} \wedge_0 \overline{f_2}\right) \vee_0 \left(\left(f_3 \wedge_0 f_4\right) \vee_0 \left(\overline{f_3} \wedge_0 \overline{f_4}\right)\right)\right) \vee_0 f_5\right) \wedge_0 f_6\right),$$

$$\omega_{outside} = f_7 \wedge_0 f_8 .$$

Functions $f_i, i = \overline{1,8}$ are defined as follows:

$$f_1 = \left(y + \frac{1}{\sqrt{3}}x\right) \geq 0, \quad f_2 = \left(-y + \frac{1}{\sqrt{3}}x\right) \geq 0, \quad f_3 = \left(y - \sqrt{3}x\right) \geq 0, \quad f_4 = \left(y + \sqrt{3}x\right) \geq 0,$$

$$f_5 = \left(r_1^2 - x^2 - y^2\right) \geq 0, \quad f_6 = \left(r_2^2 - x^2 - y^2\right) \geq 0, \quad f_7 = \left(a^2 - x^2\right) \geq 0, \quad f_8 = \left(b^2 - y^2\right) \geq 0.$$

Below, we write down expressions for functions $\omega^{(u)}, \omega^{(v)}, \omega^{(w)}, \omega^{(\psi_x)}, \omega^{(\psi_y)}$ for different boundary conditions on outside part of the region border provided that cut of the shell is clamped. We have

CCCC: $$\omega^{(u)} = \omega^{(v)} = \omega^{(w)} = \omega^{(\psi_x)} = \omega^{(\psi_y)} = \omega, \tag{16}$$

SSSS: $$\omega^{(u)} = \omega^{(v)} = \omega^{(w)} = \omega^{(\psi_x)} = \omega^{(\psi_y)} = \omega, \tag{17}$$

SFSF: $$\omega^{(w)} = \omega^{(u)} = \omega^{(\psi_x)} = \omega_{inside} \wedge_0 f_8, \quad \omega^{(v)} = \omega^{(\psi_y)} = \omega_{inside}, \tag{18}$$

SCSC: $$\omega^{(w)} = \omega^{(u)} = \omega^{(\psi_x)} = \omega, \quad \omega^{(v)} = \omega^{(\psi_y)} = \omega_{inside} \wedge_0 = f_7. \tag{19}$$

Indefinite components Φ_i, $i = \overline{1,5}$ in solution structures (13)-(14) were approximated by a system of power polynomial taking into account the doubly–symmetric of the problem. As earlier, the integration procedure is performed over one-quarter domain.

Table 3. Fundamental frequency parameters $\Omega_L^{(1)} = \lambda_1 a^2 \sqrt{\rho_c / E_c} / h$ for shells of Type 2-2 with clamped cut and simply supported on outside contour of the domain (See Fig.1)

Thickness scheme	p	k_1=0.2,k_2=0	k_1=0.2,k_2=-0.2	k_1=0.2,k_2=0.2
2-1-2	0.5	23.66	23.68	23.65
	5	22.84	22.87	22.83
	10	22.76	22.79	22.74
2-2-1	0.5	23.37	23.40	23.37
	5	22.24	22.27	22.22
	10	22.09	22.12	27.07

In Table 3 the fundamental frequency parameters $\Omega_L^{(1)} = \lambda_1 a^2 \sqrt{\rho_c / E_c} / h$ for SSSS cylindrical, spherical and hyperbolic paraboloidal shells of Type 2-2 and two thickness schemes (2-1-2) and (2-2-1) are presented. Note that fundamental frequencies parameters for considered shells with general thickness h/2a=0.1 are close for cylindrical, spherical and hyperbolic paraboloidal shells. Effects of power – law exponent $p = p_1, p_2, p_3$ on fundamental frequency parameter $\Omega_L^{(1)} = \lambda_1 a^2 \sqrt{\rho_c / E_c} / h$ for cylindrical, spherical and hyperbolic paraboloidal shells of Type 1-2 and 2-2 with different boundary conditions are shown in Fig. 4, 5, 6.

The different thickness schemes are taken for shallow shells under consideration. The obtained results for cylindrical shells with thickness scheme (1-2-1) are presented in Fig.4.

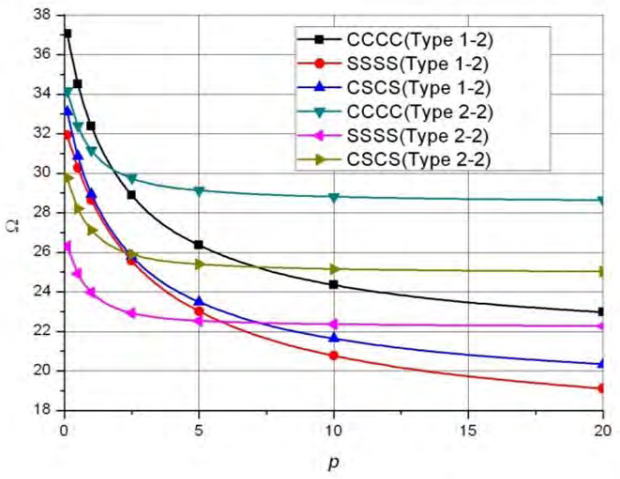

Figure. 4. Variation of the fundamental frequency parameter $\Omega_L^{(1)} = \lambda_1 a^2 \sqrt{\rho_c / E_c} / h$ of cylindrical shells with increasing power-law exponent *p (* thickness scheme 1-2-1).

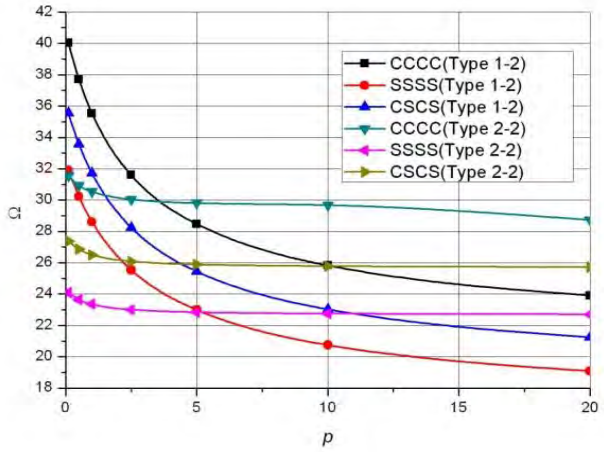

Figure. 5. Variation of the fundamental frequency parameter $\Omega_L^{(1)} = \lambda_1 a^2 \sqrt{\rho_c / E_c} / h$ of the spherical shells with increasing power-law exponent *p* (thickness scheme 2-1-2)

The effects of material types and power-law exponents on frequency parameter of spherical shells

with (2-1-2) thickness scheme are presented in Fig. 5. Similar results for hyperbolic paraboloid shells with (1-1-1) thickness scheme are shown in Fig. 6.

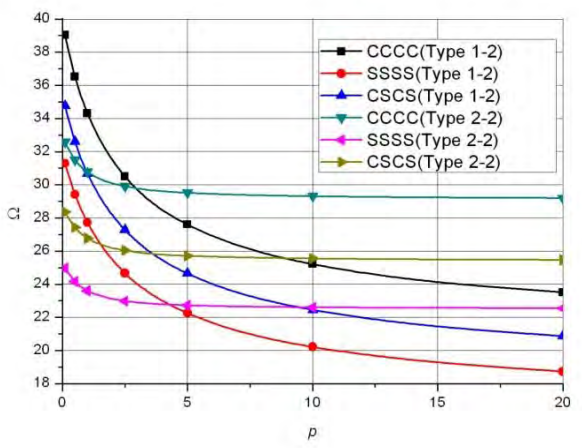

Figure. 6. Variation of the fundamental frequency parameter $\Omega_L^{(1)} = \lambda_1 a^2 \sqrt{\rho_c / E_c}\,/ h$ of Type 1-2 and 2-2 with thickness scheme (1-1-1) of hyperbolic paraboloidal shells with increasing *p*.

As follows from Fig. 4-6 the value of fundamental frequency parameters depends essentially on the material type, thickness schemes, and boundary conditions. Obvious that the fundamental frequencies parameters for all considered cases decrease with increasing power-law exponent. For shells of type 1-2 the decrease is more essential than for shells of Type 2-2.

5. Conclusions

This paper proposes a method of investigation of free vibration of laminated functionally graded shallow shells with complex shape of plan form. The method is based on the theory of R-functions and Ritz variational method. Comparison of the obtained results for shallow shells of the doubly-curved with square planform confirms the validation of the developed software. New solution structures are proposed for shallow shells with clamped hole of the different form. In addition, the novel results are obtained for cylindrical, spherical and hyperbolic paraboloidal shallow shells of FGM sandwich FGM type with cutout of the complex shape. Effects of material types, power-law exponents, thickness schemes and different boundary conditions are studied for shells with clamped hole of the complex shape.

References

[1] Loy C.T., Lam K.Y., Reddy J.N. Vibration of functionally graded cylindrical shells. Int J Mech Sci 41, (1999), 309–324.

[2] Neves AMA, Ferreira AJM, Carrera E, Cinefra M, Roque CMC, Jorge RMN, et al. Static, free vibration and buckling analysis of isotropic and sandwich functionally graded plates using a quasi-3D higher-order shear deformation theory and a meshless technique. Compos B: Eng 44 (1), (2013), 657 –674.

[3] Guoyong J., Shuangxia S., Zhu S., Shouzuo L., Zhigang L. A modified Fourier-Ritz approach for free vibration analysis of laminated functionally graded shallow shells with general boundary conditions. Int.J. of Mechanical Science 93, (2015), 263-269/

[4] Amabili M. Nonlinear Vibrations and Stability of Shells and Plates, Cambridge: Cambridge University Press, Cambridge, (2008).

[5] Awrejcewicz J., Kurpa L., Shmatko T., Investigating geometrically nonlinear vibrations of laminated shallow shells with layers of variable thickness via the R-functions theory. Composite Structures 125, (2015), 575–585.

[6] Kurpa L.V. Nonlinear free vibrations of multilayer shallow shells with a symmetric structure and with a complicated form of the plan. J. Math. Sciences 162 (1), (2009), 85-98.

[7] Rvachev V.L. The R-functions theory and its some application. Naukova Dumka, Kiev, (1982), (in Russian).

1. Lidiya Kurpa, Professor, National Technical University"KhPI", Department of Applied mathematics, 2 Kyrpychov Str., 61002 Kharkov,Ukraine (*kurpalidia@gmail.com*). The author gave a presentation of this paper during one of the conference sessions.

2. Tetyana Shmatko, Ph.D., National Technical University"KhPI", Department of Higher mathematics, 2 Kyrpychov Str., 61002 Kharkov,Ukraine *(ktv_ua@yahoo.com)*

3. Jan Awrejcewiczc, Professor, Lodz University of Technology, Department of Automation, Biomechanical and Mechatronics,1/15 Stefanowski str.,90-924 Lodz and Warsaw University of Technology, Department of Vehicles, 84 Narbutta Str., 02-524 Warsaw,Poland *(jan.awrejcewicz@p.lodz.pl)*

Spectral approach for dynamic analysis of a composite structure under random excitation

M.R. Machado, L. Khalij, A.T. Fabro

Abstract: The application of the composite materials in aeronautical and aerospace industries has been increasing on the last several decades. Compared to metallic material composites, they present better strength to weight and stiffness to weight ratio. However, the high level of uncertainty in composite materials is mainly associated with the manufacturing processes. The uncertainty in the composite material parameters is reflected in the variability of stiffness and strength descriptors affecting the overall performance, mainly on the structural dynamic response. Randomness can be present in geometry, mechanical properties, and external sources like random excitation. This paper treats the dynamic analysis of a composite plate under random excitation. The plate is modelled by the Spectral Finite Element method, a wave propagation technique. A numerical example is used to study the influence of random source on the dynamic composite structure behaviour.

1. Introduction

Wave based models at high-frequency analysis require a large number of elements to obtain an accurate solution. An alternative to Finite Element Method (FEM), which can become too expensive or even infeasible from a computational point of view is to use the Spectral Element Method (SEM). As the SEM assumes the exact frequency-domain solution, it implies high accuracy. Other advantages of the method are the reduction of the problem size and DOFs, low computational cost, effectiveness in dealing with frequency-domain problems and with the non-reflecting boundary conditions of the infinite or semi-infinite-domain problems [1, 2, 7]. SEM has been also applied to laminate composite (e.g. [13, 11, 5, 4]).

The main dynamic excitations are typically arising from natural phenomena such as impacts, gusty winds, earthquake ground motion, sea waves, etc. In some cases, harmonic excitation is considered; however, it is easy the situations where devices are operating under unknown or random excitations. For structural analysis purposes, random excitation is commonly modelled as a Gaussian stochastic processes[12]. Several approaches have been proposed to cope with the challenging problem of characterizing the random response of a structural system under stochastic excitation, it is addressed in [9, 8, 6]. The random excitation is usually specified in terms of its Power Spectral Density (PSD), which it is a function that describes the power content distribution of a quantity over a frequency range.

This paper presents a study of the dynamic response of a composite beam subjected to random excitation. For a given configuration of ply-angle, random excitation is taken into account to evaluate the affects of the randomness in the excitation into the structural response. Three different random excitations, described by typicall PSDs, are used in the analysis. Numerical tests show the influence of the random excitation on the dynamic composite beam behaviour.

2. Wave motion in laminated composite beam

Wave based methods have been applied during last decades in laminated and delaminated composites. It is a powerful tool to non-destructive damage detection. In order to obtain the wave parameters (wave number and group velocity), we need to perform a spectral analysis on the governing equation(s) of motion. In this paper, a multilayer composite beam, showed in fig. 1, is treated.

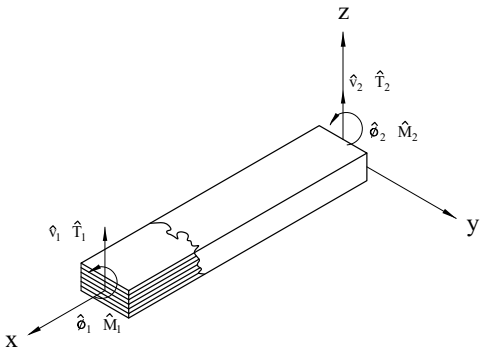

Figure 1. Model of a composite beam.

It is considered the first order shear (FSDT) axial and transverse motion displacement

field, given by

$$u(x,y,t) = -y\phi(x,t), \tag{1}$$
$$v(x,y,t) = v^0(x,t),$$

where, u and v are the axial and transverse displacements, ϕ and v^0 denotes independent rotation and transverse displacement along the $x-axis$, respectively. The constitutive relation for transversely orthotropic laminated composite is based on the laminated theory [3], which is given by

$$\left\{ \begin{array}{c} \sigma_{xx} \\ \tau_{xx} \end{array} \right\} = \left[\begin{array}{cc} \bar{Q}_{11} & 0 \\ 0 & \bar{Q}_{66} \end{array} \right] \left\{ \begin{array}{c} \varepsilon_{xx} \\ \gamma_{xx} \end{array} \right\}. \tag{2}$$

The Hamilton's principle along with eqs. 1 and 2 was used to derive the governing wave equation, expressed as

$$I_0\ddot{v}^0 - A_{66}(v^0_{xx} - \phi_x) = 0, \tag{3}$$
$$I_2\ddot{\phi} - A_{66}(v^0_x - \phi) - D_{11}\phi_{xx} = 0,$$

where $\langle\rangle_x$ $\langle\rangle_{xx}$ are derivatives of the field variables with respect to x. The stiffness coefficients, which are functions of the individual ply properties and orientation, and the coefficients associated with the inertial terms are integrated over the beam cross-section, i.e.

$$[A_{ls}, B_{ls}, D_{ls}] = \sum_s \int_{z_l}^{z_{l+1}} \bar{Q}_{ls}[1, z, z^2]bdz, \tag{4}$$
$$[I_0, I_1, I_2] = \sum_l \int_{z_l}^{z_{l+1}} \rho[1, z, z^2]bdz,$$

coefficients b is the width of the beam, ρ is the density of composite, and z_l and z_{l+1} denotes z-coordinate of the top and bottom surfaces of the lth layer. The spectral solution for the primary displacement field variables can be obtained by using the Discrete Fourier Transform (DFT) for the temporal field, it can be expressed as

$$\mathbf{u}(x,t) = \sum_{n=1}^{N} e^{-\omega_n t} = \sum_{n=1}^{N} \left(\sum_{j=1}^{4} \mathbf{u}_j e^{ik_j x} \right) e^{i\omega_n t}, \tag{5}$$

where $i = \sqrt{-1}$, ω_n is the circular frequency at nth sampling point, and N is the Nyquist point in DFT. Assuming the solution for the displacements as $\mathbf{u}_j$, it is suitable to calculate the wavenumbers k_j associated with the jth wave mode. Since there are only two independent variables v_j and ϕ_{xj} from the FSDT assumption, Eq. 1, the following solutions are assumed

$$v_j = v_{0,j}e^{-i(kx-\omega t)}, \tag{6}$$
$$\phi_j = \phi_{0,j}e^{-i(kx-\omega t)}, \qquad (j = 1, ..., 4)$$

Substituting eqs. 6 into 3, it gives the characteristic equation

$$\begin{bmatrix} -I_0\omega^2 + A_{66}k^2 & -ikA_{66} \\ ikA_{66} & -I_2\omega^2 + A_{66} + D_{11}k^2 \end{bmatrix} \begin{Bmatrix} v_{0,j} \\ \phi_{0,j} \end{Bmatrix} = \begin{Bmatrix} 0 \\ 0 \end{Bmatrix}. \tag{7}$$

A non-trivial solution of the displacement field, Eq. 7, yields a fourth order characteristic polynomial equation in k_j

$$A_{66}D_{11}k^4 - (A_{66}I_2\omega^2)k^2 + (I_2\omega^2 - A_{66})I_0\omega^2 = 0. \tag{8}$$

The characteristic equation is quadratic in k^2 and hence can be easily solved. There are four roots, representing two sets of wave mode pairs, in the form

$$k_1 = \pm \frac{\sqrt{\dfrac{(D_{11}I_0 + A_{66}I_2)\omega^2 - \sqrt{4A_{66}^2D_{11}I_0\omega^2 + (D_{11}I_0 - A_{66}I_2)^2\omega^4}}{A_{66}D_{11}}}}{\sqrt{2}},$$

$$k_2 = \pm \frac{\sqrt{\dfrac{(D_{11}I_0 + A_{66}I_2)\omega^2 + \sqrt{4A_{66}^2D_{11}I_0\omega^2 + (D_{11}I_0 - A_{66}I_2)^2\omega^4}}{A_{66}D_{11}}}}{\sqrt{2}}. \tag{9}$$

This solution gives the dispersion relation, i.e. the wavenumber as a function of the circular frequency and can be used to find the group velocity, by $c_{g1,2}(\omega) = \partial k_{1,2}/\partial\omega$. The next section presents the spectral element formulation for a laminated beam.

3. Laminated multilayer composite beam spectral element

The spectral element model for analysis of flexural-shear coupled wave propagation approached in this paper was proposed by Palacz et al. [10].

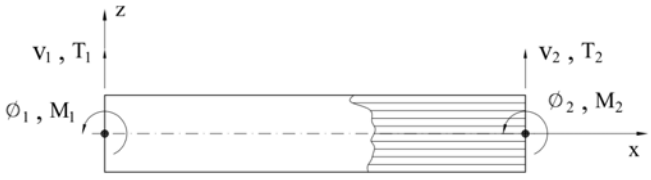

Figure 2. Multilayer composite beam spectral element.

Figure 2 shows a laminated multilayer composite beam spectral element of two nodes with transverse displacement and independent rotation per node. The beam is assumed to have total length L , width b, and height h. The spectral element nodes are given by the

displacement v and rotation ϕ, from the FSDT assumption, such that

$$v(x) = R_1 A_1 e^{-ik_1 x} + R_2 A_2 e^{-ik_2 x} - R_1 A_3 e^{-ik_1(L-x)} - R_2 A_4 e^{-ik_2(L-x)},$$

$$\phi(x) = A_1 e^{-ik_1 x} + A_2 e^{-ik_2 x} + A_3 e^{-ik_1(L-x)} + A_4 e^{-ik_2(L-x)}, \tag{10}$$

where $i = \sqrt{-1}$, k_1 and k_2 are roots of the characteristic equation given in Eq.9, and $R_n (n = 1, 2)$ is the amplitudes ratio as given by Doyle [2],

$$R_n = \frac{ik_n A_{66}}{A_{66} k_n^2 - I_0 \omega^2}, \quad \text{for} \quad (n = 1, 2). \tag{11}$$

The coefficients $A_j (j = 1 - 4)$ are calculated as a function of the nodal spectral displacements, using the boundary conditions, having the form at the left end of the element $(x = 0)$

$$v_1 = q_1, \tag{12}$$

$$\phi_1 = q_2, \tag{13}$$

and at the right end of the element $(x = L)$

$$v_2 = q_3, \tag{14}$$

$$\phi_2 = q_4. \tag{15}$$

The boundary conditions can then be used to write Eq. 10 in a matrix form as

$$\underbrace{\begin{bmatrix} R_1 & R_2 & -R_1 e^{-ik_1 L} & -R_2 e^{-ik_2 L} \\ 1 & 1 & e^{-ik_1 L} & e^{-ik_2 L} \\ R_1 e^{-ik_1 L} & R_2 e^{-ik_2 L} & -R_1 & -R_2 \\ e^{-ik_1 L} & e^{-ik_2 L} & 1 & 1 \end{bmatrix}}_{\Psi} \begin{Bmatrix} A_1 \\ A_2 \\ A_3 \\ A_4 \end{Bmatrix} = \begin{Bmatrix} q_1 \\ q_2 \\ q_3 \\ q_4 \end{Bmatrix}. \tag{16}$$

The element has two nodes and two degrees of freedom (DOF) per node, where the unknown coefficients $A_j (j = 1, 2, 3, 4)$ are calculated from Eq. 16 as a function of nodal spectral displacements. The nodal spectral forces (shear force and bending moment) for the left hand side of the beam $(x = 0)$ can be determined as

$$M_1 = D_{11} \frac{\partial^2 v_1(x)}{\partial x^2} \tag{17}$$

$$T_1 = -D_{11} \frac{\partial^3 v_1(x)}{\partial x^3} - I_2 \omega^2 \frac{\partial v_1(x)}{\partial x} \tag{18}$$

and the nodal spectral forces for the right hand side of the beam ($x = L$) as follows

$$M_2 = D_{11}\frac{\partial^2 v_2(x)}{\partial x^2} \tag{19}$$

$$T_2 = -D_{11}\frac{\partial^3 v_2(x)}{\partial x^3} - I_2\omega^2\frac{\partial v_2(x)}{\partial x} \tag{20}$$

Equation 11 can be applied to Eq. 16 leading to

$$\begin{Bmatrix} q_1 \\ q_2 \\ q_3 \\ q_4 \end{Bmatrix} = \underbrace{\begin{bmatrix} d_1^* & d_2^* & d_1^* z_1 & d_2^* z_2 \\ iD_{11}k_1 & iD_{11}k_2 & (iD_{11}k_1)z_1 & (iD_{11}k_2)z_2 \\ d_1 z_1 & d_2 e_2^z & d_1 & d_2 \\ (iD_{11}k_1)z_1 & (iD_{11}k_2)z_2 & -iD_{11}k_1 & -iD_{11}k_2 \end{bmatrix}}_{\Gamma} \begin{Bmatrix} A_1 \\ A_2 \\ A_3 \\ A_4 \end{Bmatrix}, \tag{21}$$

where $d_1^* = -D_{11}k_1^2 + I_2\omega^2$, $d_2^* = -D_{11}k_2^2 + I_2\omega^2$, $d_1 = D_{11}k_1^2 + I_2\omega^2$, $d_2 = D_{11}k_2^2 + I_2\omega^2$, $z_1 = e^{-ik_1L}$ and $z_2 = e^{-ik_2L}$. Taking into account relations of the Eqs. 16 and 21 the frequency dependent dynamic stiffness matrix, which relate the nodal spectral forces with the nodal spectral displacements, can be written as

$$\{\mathbf{P}\} = [\mathbf{K}(\omega)]\{\mathbf{q}\}, \tag{22}$$

where $\{\mathbf{P}\}$ is vector content the forces, $\{\mathbf{q}\}$ is the displacement vector, and the dynamic stiffness matrix are obtained as $[\mathbf{K}(\omega)] = \Psi^{-1}\Gamma$.

4. Random excitation

Composite structures are typically subjected to random dynamic loads, like earth-quakes and wind loads, in civil, aeronautic and aerospace industry. This loads are usually modelled as second order stationary Gaussian stochastic processes with a given autocorrelation funcion $R(\tau)$, describing the smoothness, ou roughness, of the time series. The WienerKhinchin theorem relates $R(\tau)$ to a frequency domain Power Spectral Density (PSD) $S(\omega)$ by a Fourier transform pair [9]. The time series can be numerically generated by a FFT-based algorithm, by taking the inverse discrete Fourier transform (IDFT) of the discretized target PSD, being its amplitude is estimated as the square root of the discretized PSD, $\sqrt{S_k}$, and a random phase is generated from a uniform distribution within the interval $[0, 2\pi]$.

A very common PSD model is the white noise, given by $S(\omega) = S_0$. It is a idealization in which the signal frequency content is equally distributed over the frequency band (band-limited white noise). This assumption is not physically sound and other PSD models can be

used, like a First Order Filter (FOF),

$$S(\omega) = \frac{S_0}{\nu^2 + (2 * \pi * \omega).^2} \tag{23}$$

or Kanai-Tajimi model, a second order type of filter given by

$$S(\omega) = \frac{1 + 4\xi_g^2(\omega/\omega_g)S_0}{(1 + (\omega/\omega_g)^2 + 4\xi_g^2(\omega/\omega_g)^2} \tag{24}$$

where the constant ν, ξ and ω_g are adjusted according to specific features of the random load. An important relations used in the analysis of the dynamic response of any system to random excitation is that the PSD of the response of a system $S_o(\omega)$ to an input PSD $S_i(\omega)$ is given by [9]

$$S_o(\omega) = |H(\omega)|^2 S_i(\omega), \tag{25}$$

where the function $H(\omega)$ is the frequency response function (FRF) between the input and the output.

5. Numerical simulations

For de numerical examples, a free-free multilayer composite beam modelled by a two nodes spectral element, as showed in fig. 2, is made out of glass-epoxy with 10 layers orientated of 0°. Each layer's thickness is 1 mm, the length of the beam is 2 m, and the width is 0.02 m. The physical properties Young's modulus, Poisson ration , Kirchhoff modulus and density of the matrix-epoxy are: $E_M = 3.43$ GPa, $\nu_M = 0.35$, $G_M = 1.27$ GPa, $\rho_M = 1250$ (km/m^3); for of the fibers-glass are: $E_F = 66.5$ GPa, $\nu_F = 0.23$, $G_F = 27.0$ GPa, $\rho_F = 2250$ (km/m^3). The calculated FRF simulates the transfer receptance with force excitation at node 1 and displacement response measured at node 1 and 2.

Random excitation includes a mixture of different levels of external forces or externally imposed displacements that contain components of many different frequencies, according to its corresponding PSD. It is verified the influence of three different random excitations and a sinusoidal harmonic force in the dynamic response of the composite beam. The random excitation signals were generated as specified in Section (4).

Figure 3 shows a sample of the time domain input for different PSD models which were used to excite the composite beam, i.e. the white noise excitation, FOF and the Kanai-Tajimi as well as the harmonic force. Additionally, The Power Spectral Density of tip excitation force for each signal is also shown in fig. 4.

The PSD of the beam displacement in the frequency and time domain are shown in figure 5 to figure 8. The dynamic response of the beam excited with a sinusoidal harmonic

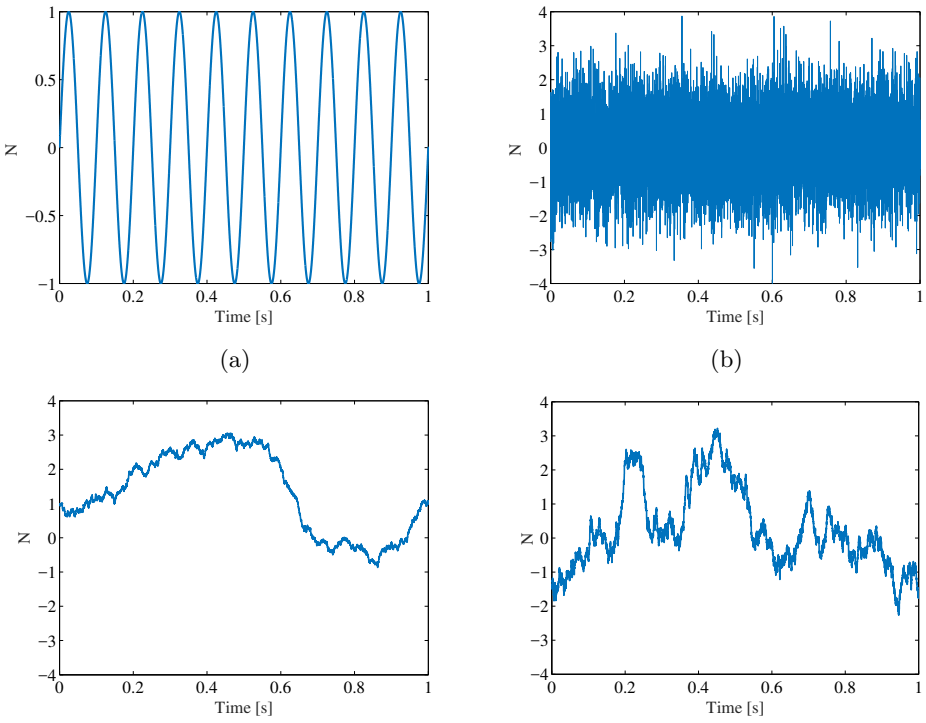

Figure 3. Time domain samples of excitation using (a) sine, (b) white noise, (c) FOF and (d) Kanai-Tajimi.

force also present a sinusoidal harmonic with same frequency in the time domain, such response was expected once it is a linear system. Note that the response in frequency domain presents a curve resembling the FRF. This is due to a windowing effect in the time domain excitation. Moreover, when the beam is excited by a random force the response will be also random, with PSD given by Eq. 25 behaviour.The knowledge about how the structure will behave under specific excitation is crucial for example for the vibration control, structure reliability, or fatigue analyses.

Note that the time domain displacement response is mainly due to the first mode in all cases under random excitation. This is because the contribution of the others modes on the response do not have great influence, as it can be observed from the frequency domain reponse where the higher order resonance peaks a much smaller in magnitude. The beam response in the frequency domain excited with a white Noise, FOF, and Kanai-Tajimi presented a closer behaviour and amplitudes in both measured nodes. However, in time domain a visible

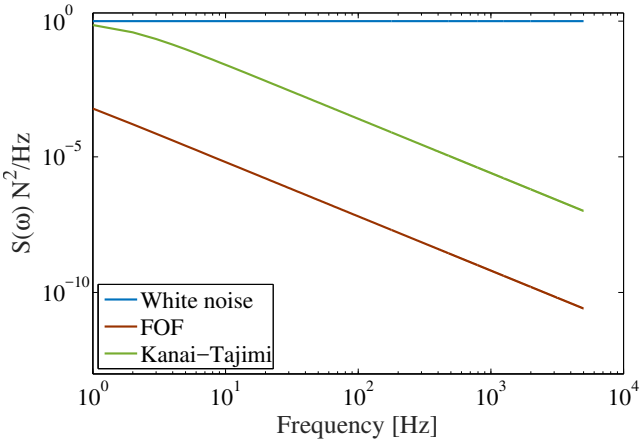

Figure 4. Power Spectral Density of tip excitation force for white noise (blue), First Order Filter (red) and Kanai-Tajimi (green).

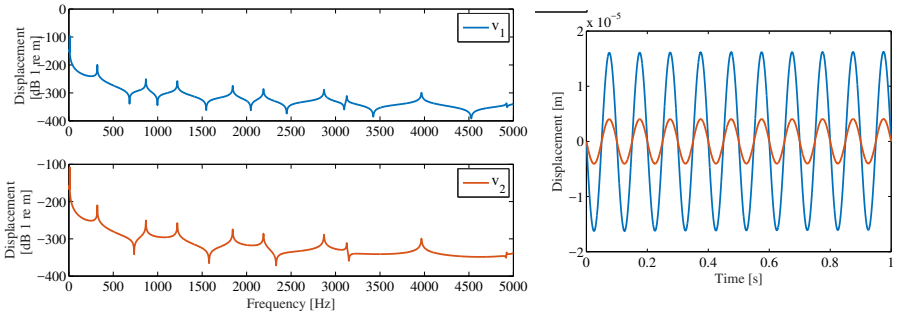

Figure 5. Frequency (left) and time (rigth) domain reponse of the composite beam at nodes 1 and 2, excited by harmonic force.

difference is observed among the simulated cases. The responses derived using First Order Filter (FOF) and Kanai-Tajimi excitation showed maximum displacement around 0.002 m, while that the maximum displacement obtained with the white noise excitation was around 0.0005 m. It demonstrated how the change in the input force can affect the outcomes. Next step of this work consists in add random properties in the beam and analyse how the randomness in the structure combined with the random excitation can impact in the dynamic response.

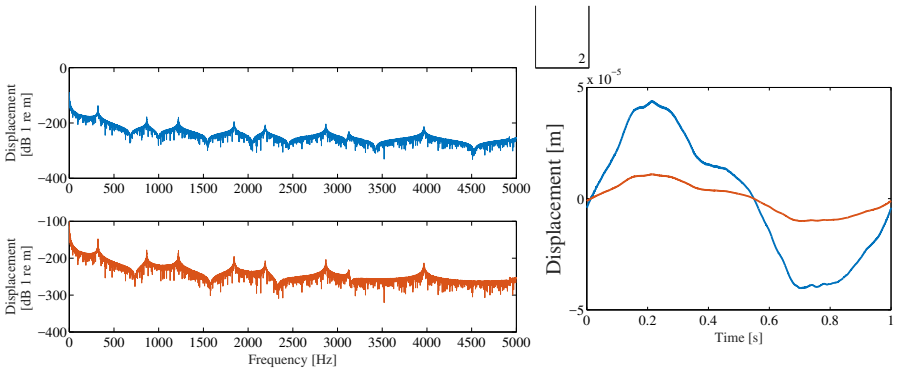

Figure 6. Frequency (left) and time (rigth) domain reponse of the composite beam at nodes 1 and 2, excited by white noise.

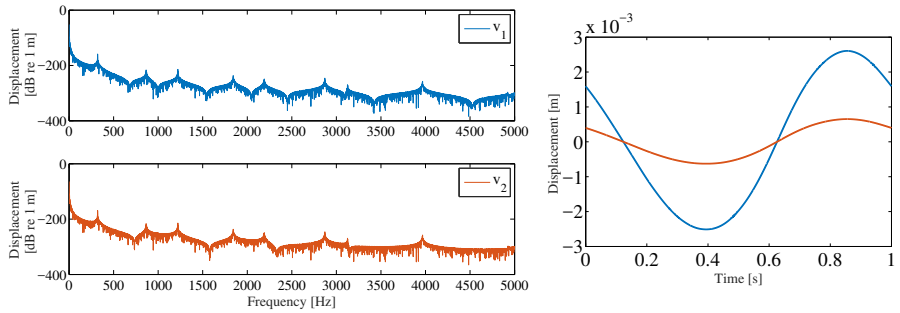

Figure 7. Frequency (left) and time (rigth) domain reponse of the composite beam at nodes 1 and 2, excited by FOF PSD.

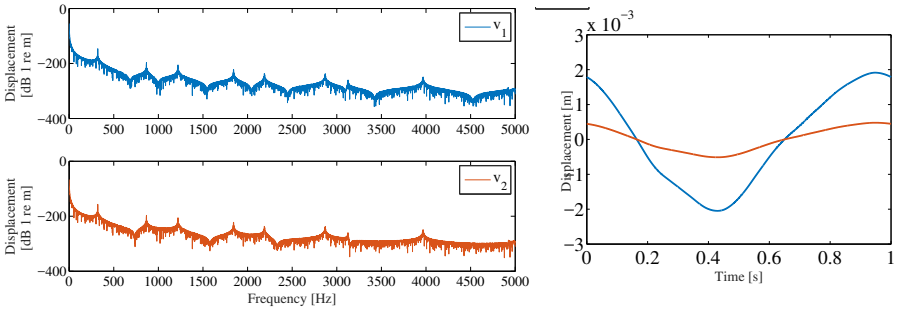

Figure 8. Frequency (left) and time (rigth) domain reponse of the composite beam at nodes 1 and 2, excited by Kanai-Tajimi PSD.

6. Conclusions

The dynamic response of a composite beam subjected to three different random excitation was addressed in this paper. The composite beam was excited with a deterministic harmonic

force and random excitation given by white noise, FOF and Kanai-Tajimi PSD model. A dynamic response of the beam excited with a harmonic force has a harmonic behaviour in the time domain, as expected. When the random PSD model were approached an random dynamic behaviour was expected. Evethough the FRFs obtained from the beam excited with the random PSD model had close amplitudes, the time domain reponse presented a visible difference during as well as different maximum displacement amplitude. It shows that corretly representing the random excitation model is very important. This is a crucial information in vibration control, structural reliability or fatigue analyses.

References

[1] Doyle, J. F. A spectrally formulated finite elements for longitudinal wave propagation. *Journal of Analytical and Experimental Modal Analysis 3* (1988), 1 – 5.

[2] Doyle, J. F. *Wave propagation in structures : spectral analysis using fast discrete Fourier transforms*, second ed. Mechanical engineering. Springer-Verlag New York, Inc., New York, 1997.

[3] Gay, D. *Materials design and Applications*. CRC Press Taylor & Francis Group, 2015.

[4] Gopalakrishnan, S. *Wave propagation in materials and structures*. CRC Press Taylor & Francis Group, New York, 2016.

[5] Gopalakrishnan, S., Chakraborty, A., and Mahapatra, D. R. *Spectral Finite Element Method*. Springer Verlag, New York, 2007.

[6] J.Li, and Chen, J. *Structural Dynamics and Probabilistic Analyses for Engineers*. John Wiley & Sons, 2009.

[7] Lee, U. *Spectral Element Method in Structural Dynamics*. Inha University Press, 2004.

[8] Maymon, G. *Stochastic dynamics of structures*. Elsevier Inc., 2008.

[9] Newland, D. E. *An introduction to random vibrations, spectral & wavelet analysis*. Courier Corporation, 2012.

[10] Palacz, M., Krawczuk, M., and Ostachowicz, W. The spectral finite element model for analysis of flexural-shear coupled wave propagation. part 2: Delaminated multilayer composite beam. *Composite Structures 68* (2005), 45–51.

[11] Palacz, M., Krawczuk, M., and Ostachowicz, W. The spectral finite element model for analysis of flexural?shear coupled wave propagation. part 1 laminated multilayer composite beam. *Computers and Structures 68* (2005), 37–44.

[12] Papoulis, A., and Pillai, S. U. *Probability, random variables and stochastic processes*. McGraw-Hill, Boston, 2002.

[13] SA, S. R., AND DOYLE, J. A spectral element approach to wave motion in layered solids. *Journal of Vibration and Acoustic 114* (1992), 569–77.

Marcela R. Machado, Ph.D.: University of Brasilia, Department of Mechanical Engineering, Campus Universitrio Darcy Ribeiro Asa Norte - Braslia / DF, 70910-900 (*marcelam@unb.br*). The author gave a presentation of this paper during one of the conference sessions.

Leila Khalij, Ph.D: Institut National des Sciences Appliques de Rouen, Rouen,FRANCE, - (-).

, Adriano T. Fabro: Ph.D, University of Brasilia, Department of Mechanical Engineering (*Campus Universitrio Darcy Ribeiro Asa Norte - Braslia / DF, 70910-900*). fabro@unb.br -

Optimal auxiliary functions method for investigating a permanent magnet synchronous generator

Vasile Marinca, Nicolae Herisanu

*Abstract:*In the present paper we investigate the transitory working regime of a permanent magnet synchronous generator that works in actual wind power station. For the nonlinear differential equations which describe this type of machines we apply the Optimal Auxiliary Functions Method (OAFM) and an explicit analytical solution is obtained.The governing equations are expressed in the non-dimensional form and are solved by means of OAFM. Two stages of the generator's dynamic behaviors are known: the beginning of the transitory regime and the ending of this regime. The first stage of the regime shows the electromagnetic fast transitory regime and the second one generally emphasize the mechanical slow transitory regime, caused by inertia. In each of these stages of the transitory regime, the solutions are built using different functions, for example trigonometric functions in combination with exponential functions for the first stage and polynomial functions in combination with exponential functions in the case of the second stage. On the other hand, these functions depend on several optimal-convergence-control parameters which ensure a fast convergence of the approximate solution to the exact ones. Numerical examples analyzed in this paper lead to the conclusion that the results obtained through the proposed procedure are very accurate and the method is very efficient in practice.

1. Introduction

The permanent magnet synchronous generators (PMSG) are rotating electrical machines having a classic three-phase stator like that of an induction motor, and the rotor has surface-mounted permanent magnets. They are widely used to convert the mechanical wind energy into electrical energy, which is a hot topic nowadays [1-6]. That is why various aspects of design and functioning of permanent magnet synchronous machines received an increased interest from scientists. Small signal stability of permanent magnet synchronous generator (PMSG)-based wind turbines connected to the power grid is properly studied in [7] in order to facilitate damping strategy design.Song et al. [8] applied the Taguchi method to optimal design of permanent magnet synchronous motors to optimize the thrust and thrust ripple, and using finite-element analysis, the relative importance of each design parameter was estimated in detail.Based on a linearized model, the relation between the PMSG electromagnetic torque and boost converter current is extracted, and then system's control-loops are developed by Rahimi in [9].

In this paper, the behavior of the PMSGis predicted using the classical d-q equivalent circuit models. Starting from the equations of the smooth-air-gap synchronous machine, the D-Q axis equations of PMSG in the rotor reference frame, lead to a system of three nonlinear differential equations with unknowns instantaneous values of stator current components and electrical angular speed. These equations are expressed in the non-dimensional form and the system is analyzed by means of a novel method, namely the Optimal Auxiliary Functions Method. Analytical approximate solutions which are obtained are of considerable importance for practical analysis of electrical power system dynamic behavior with problems caused by possible perturbations generated by some short circuits, sudden change of loads, disconnection of load and other switching transients in power station or stability problem of such systems.

The proposed approach has been applied on a low-power generator and this work should be continued with the case of high-power electrical generators, connected directly into a large electrical power system.

2. Governing equations of PMSG

Using the classical D-Q equivalent circuit models, the equation of the smooth-air-gap synchronous machine in the rotor reference frame are of the form:

$$\begin{aligned} u_D &= R_G i_D + \frac{d\psi_D}{dt} - \omega_E \psi_Q \\ u_Q &= R_G i_Q + \frac{d\psi_Q}{dt} + \omega_E \psi_D \\ \psi_D &= L_G i_D + \psi_{PM};\ \psi_Q = L_G i_Q \end{aligned} \tag{1}$$

where the instantaneous values of D and Q axis stator voltage components are u_D and u_Q; the stator components are i_D, i_Q; R_G and L_G are electrical resistance and synchronous inductance of the generator phase windings; ψ_D and ψ_Q are instantaneous values of D and Q axis stator flux components; ψ_{PM} is the permanent magnet flux and ω_E is the electrical angular such that $\Omega_M=\omega_E/P_1$, where P_1 is the number of pole pairs of the generator and Ω_M is the mechanical angular speed of the turbine-generator system. If R_L is the electrical resistance of the external load connected to the output of the generator, the PMSG output voltages are:

$$\begin{aligned} u_D &= -R_L i_D \\ u_Q &= -R_L i_Q \end{aligned} \tag{2}$$

The motion equation of the generator is described by [1]:

$$\frac{J_M}{P_1}\frac{d\omega_E}{dt} = T_M + \frac{3}{2}P_1 \psi_{PM} i_Q \tag{3}$$

where J_M is total axial moment of inertia and T_M is the mechanical torque of the wind turbine:

$$T_M = \frac{1}{2}\rho\pi r^3 v^2 C_t(\lambda_r) \quad , \quad \lambda_r = \frac{r\omega_E}{P_1 v} \tag{4}$$

Within Eq.(4) ρ is the air density, r is the turbine radius, v is the wind speed, λ_r is the tip-speed ratio and C_t is the torque coefficient provided by the turbine manufacturer:

$$C_t(\lambda_r) = 0.125 + 0.2092\lambda_r - 0.1209\lambda_r^{2.5} \tag{5}$$

For the values ρ=1.225 Kg/m^3, P_1=16, r=2.5 m, the torque becomes:

$$T_M = 3.758252931v^2 + 0.982783141v\omega_E - \frac{0.035079416}{\sqrt{v}}\omega_E^{2.5} \tag{6}$$

Concerning the wind speed, different from other works, we consider the analytical model of the speed as [6]:

$$v(t) = v_m + Asin\frac{\pi}{T_G}t + Bsin\frac{3\pi}{T_G}t \tag{7}$$

wherev_m is the mean wind speed of the base wind velocity that is a constant. The base wind velocity v_m is considered only in the case in which the generator is active and A and B are two different amplitudes and T_G is the gust period.

Considering a practical case of a real wind turbine PMSG, the characteristics of the steady-state regime are: R_G=0.9 Ω, L_G=0.03 H, ψ_{PM}=$\sqrt{2}$ Wb, P_1=16 pole pairs, J_M=4.75 Kgm^2. The nominal speed of rotation id n_N=70 rpm, which lead to Ω_N=7.330352856 rad/s or ω_N=117.2856457rad/s, where N denotes the nominal values (or rated values). Corresponding to these values, from Eq.(6) one retrieves T_{MN}=684.192163461 Nm and for the steady-state regime one can get i_{QN}=-20.158204693. It follows from Eqs. (1) and (2) that i_{DN}=-11.118492391 A, R_{LN}=5.479285888 Ω, u_{DN}=60.9213984503 V, u_{QN}=110.45256648 V, $\sqrt{2}I_N$=$\sqrt{i_{QN}^2 + i_{DN}^2}$=23.02116616 A, $\sqrt{2}u_N$=$\sqrt{u_{QN}^2 + u_{DN}^2}$=126.139550551 V.

In the nominal point of working, the wind turbine develops the mechanical power $P_{1N} = T_{MN} \approx$ $\approx 5015\ W$ and the electric generator develops the electrical power$P_{2N} = 3U_N I_N \approx$ 4355.82W.

It is often convenient to express the generator's parameters, variables and the governing equation in dimensionless quantities. For this aim these terms are divided by base quantities. Usually, the following set of base quantities is widely used: the base voltage U_B (peak stator phase nominal voltage U_B=$\sqrt{2}U_N$), the base current I_B (peak stator phase nominal current I_B=$\sqrt{2}I_N$), the base power S_B (nominal apparent power S_B=$3U_NI_N$), the base angular speed ω_B (nominal electrical angular speed ω_B=ω_N. The additional quantities are the base torque T_B=P_1S_B/ω_B, the base flux linkage ψ_B=U_B/ω_B, the base impedance Z_B=U_B/I_B; the base time t_B=$1\omega/_B$.

By means of the following transformations

$$u_D=\frac{U_D}{U_B};\ u_Q=\frac{U_Q}{U_B};\ i_D=\frac{I_D}{I_B};\ i_Q=\frac{i_Q}{i_B};\ \psi_D=\frac{\Psi_D}{\Psi_B};\psi_Q=\frac{\Psi_Q}{\Psi_B};\ \psi_{PM}=\frac{\Psi_{PM}}{\Psi_B}$$
$$\omega=\frac{\omega_E}{\omega_B};\ r_l=\frac{R_L}{Z_B};\ r_g=\frac{R_G}{Z_B};\ x_g=\frac{\omega_B L_G}{Z_B};\ T_m=\frac{T_M}{T_B};k=\frac{J_M\omega_B^2}{3P_1^2U_N I_N};\ \tau=\frac{t}{t_B}=\omega_B t \quad (8)$$

the governing Eqs.(1) can be written in dimensionless form as

$$\begin{aligned}&\frac{di_d}{d\tau}-\omega i_q+\frac{r_l+r_g}{x_E}i_d=0\\&\frac{di_q}{d\tau}+\omega i_d+\frac{r_l+r_g}{x_E}i_q+\omega\frac{\psi_{PM}}{x_E}=0\\&k\frac{d\omega}{d\tau}-T_m-\psi_{PM}i_q=0\end{aligned} \quad (9)$$

The initial conditions for Eqs.(9) are obtained considering the steady-state regime characterized by a constant angular speed at constant speed of the wind v_m=10 m/s and external electrical load r_l=0.4528. One gets the initial conditions:

$$i_d(0)=-438786995;\ \ i_q(0)=-0.843879596;\ \ \omega(0)=0.499239911 \quad (10)$$

The governing Eqs.(9) can be retrieved in the form:

$$\begin{aligned}\frac{di_d}{d\tau}+0.9601432255i_d-\omega i_q&=0\\\frac{di_q}{d\tau}+0.960143255i_q+\omega i_d+2.061756973\omega&=0\\\frac{d\omega}{d\tau}-0.168386689i_q-0.000808844v^2-0.024807429v\omega+\frac{1.124718044}{\sqrt{v}}\omega^{2.5}&=0\end{aligned} \quad (11)$$

where v is given by Eq.(7), considering A=10, B=4, v_m=10 m/s and T_G=20.5:

$$v(\tau)=10+10sin\frac{\pi}{\lambda}\tau+4sin\frac{3\pi}{\lambda}\tau \quad (12)$$

where λ=2407.

The dynamical system (11) with the initial conditions (10) and with the wind speed (12) will be investigated in what follows using a new solution approach, namely the Optimal Auxiliary Functions Method.

3. Basic ideas of the Optimal Auxiliary Functions Method

The most general form of a nonlinear differential equation is

$$L[F(\tau)]+N[F(\tau)]=0,\quad \tau\in D \quad (13)$$

in which L is a linear operator, F(τ) is an unknown function, N is a nonlinear operator and D is the domain of interest. The corresponding initial/boundary conditions are known as:

$$B(F(\tau),\frac{dF(\tau)}{dt})=0 \quad (14)$$

For Eqs.(13) and (14) we demand an approximate solution $\tilde{F}(\tau)$which contains only two components [10]

$$\tilde{F}(\tau) = F_0(\tau) + F_1(\tau, C_i), \quad i = 1,2,\dots,n \tag{15}$$

where C_i are unknown parameters at this moment.

Substituting Eq.(15) into (13) we obtain

$$L[F_0(\tau)] + L[F_1(\tau, C_i)] + N[F_0(\tau) + F_1(\tau, C_i)] = 0 \tag{16}$$

The initial approximation $F_0(\tau)$ can be determined from the linear equation

$$L[F_0(\tau)] = 0, \quad B(F_0(\tau), \frac{dF_0(\tau)}{dt}) = 0 \tag{17}$$

and the first approximation $F_1(\tau,C_i)$ from the remaining equation

$$L[F_1(\tau, C_i)] + N[F_0(\tau) + F_1(\tau, C_i)] = 0, \quad B(F_1(\tau), \frac{dF_1(\tau)}{dt}) = 0, \tag{18}$$

but in general Eq.(18) is a nonlinear differential equation which is often very difficult to solve. Now, the nonlinear term from Eq.(18) is expanded in the form:

$$N[F_0(\tau) + F_1(\tau, C_i)] = N[F_0(\tau)] + \sum_{k\geq 1} \frac{F_1^k(\tau, C_i)}{k!} N^{(k)}[F_0(\tau)] \tag{19}$$

where $N^{(k)} = \frac{d^k N}{d\tau^k}$. In order to avoid the difficulties that appear in solving the nonlinear differential equation (18) and to accelerate the convergenceof the first approximation and implicitly of the approximate solution $\tilde{F}(\tau, C_i)$, instead of the last term arising in Eq. (18) we propose another expression, such that Eq.(18) can be written in a new form

$$L\big[F_1(\tau, C_i)\big] + A(F_0(\tau), C_j)\big]P[N\big(F_0(\tau)\big)] + B(F_0(\tau), C_k) = 0, \quad B(F_1, \frac{dF_1}{d\tau}) = 0, \tag{20}$$

where A and B are two arbitrary auxiliary functions depending on the initial approximation$F_0(\tau)$ and several unknown parameters C_j and C_k, j=1,2,…,p, k=p+1, p+2,…,n; i=j+k. $P[N\big(F_0(\tau)\big)]$ means a part of the operator $N\big(F_0(\tau)\big)$. The auxiliary functions A and B called optimal auxiliary functions are not unique and are of the same form as $F_0(\tau)$ or of the form of $N\big(F_0(\tau)\big)$or combinations of $F_0(\tau)$ and $N\big(F_0(\tau)\big)$. The unknown parameters C_j and C_k (i=j+k) can be optimally identified by means of different methods, such as for example by minimizing the square residual error by considering the functional

$$J\big(C_j, C_k\big) = \int_{(D)} R^2\big(\tau, C_j, C_k\big) d\tau \tag{21}$$

where $R(\tau, C_j, C_k) = L[\tilde{F}(\tau, C_i)] + N[\tilde{F}(\tau, C_i)]$, i=j+k, j=1,2,…,p, k=p+1,p+2,…,n. The conditions of minimization of the residual are

$$\frac{\partial J}{\partial C_1} = \frac{\partial J}{\partial C_2} = \cdots = \frac{\partial J}{\partial C_n} = 0 \tag{22}$$

By this novel approach the approximate solution (15) is well determined. It is to remark that the optimal values of the parameters C_i called convergence-control parameters may be obtained by means of other procedures, such as the Ritz method, Galerkin method, collocation method, the Kantorovich method and so on [11].

Our novel approach proves to be a powerful tool for solving nonlinear problems not depending on small or large parameters. It should be emphasized that our method contains the optimalauxiliary functions A and B which provides us with a simple way to adjust and control the convergence of the approximate solution after only one iteration.

4. Approximate solution of Eqs. (11) and (10) using OAFM

In order to apply our procedure to obtain an approximate solution of Eqs.(11) and (10), we consider the linear operators for the system (11) in the following form:

$$\begin{aligned} L_1[i_d(\tau)] &= \frac{di_d}{d\tau} + 0.9601432255 i_d \\ L_2[i_q(\tau)] &= \frac{di_q}{d\tau} + 0.960143255 i_q \\ L_3[\omega(\tau)] &= \frac{d\omega}{d\tau} \end{aligned} \tag{23}$$

and the nonlinear operators

$$\begin{aligned} N_1[i_d(\tau), i_q(\tau), \omega(\tau)] &= -\omega i_q \\ N_2[i_d(\tau), i_q(\tau), \omega(\tau)] &= \omega i_d + 2.061756973\omega \\ N_3[i_d(\tau), i_q(\tau), \omega(\tau)] &= -0.168386689 i_q - 0.000808844 v^2 - \\ &\quad -0.024807429 v\omega + \frac{1.124718044}{\sqrt{v}}\omega^{2.5} \end{aligned} \tag{24}$$

where the wind velocity is given by Eq.(12).

The initial approximations id_0, iq_0, ω_0 are determined from Eqs.(17), which become

$$\frac{did_0(\tau)}{d\tau} + 0.9601432255 id_0(\tau) = 0 \qquad id_0(0) = -438786995 \tag{25}$$

$$\frac{diq_0(\tau)}{d\tau} + 0.960143255 iq_0(\tau) = 0 \qquad iq_0(0) = -0.843879596 \tag{26}$$

$$\frac{d\omega_0(\tau)}{d\tau} = 0 \qquad \omega_0(0) = 0.499239911 \tag{27}$$

The solutions of Eqs. (25)-(27) are

$$id_0(\tau) = -438786995\exp(-0.9601432255\tau) \tag{28}$$

$$iq_0(\tau) = -0.843879596\exp(-0.960143255\tau) \tag{29}$$

$$\omega_0(\tau) = 0.499239911 \tag{30}$$

The nonlinear operators (24)for the initial approximations (28)-(30) are:

$$N_1[id_0(\tau), iq_0(\tau), \omega_0(\tau)] = -0.421298371\exp(-0.9601432255\tau) \tag{31}$$

$$N_2[id_0(\tau), iq_0(\tau), \omega_0(\tau)] = 1.029311368 - 0.21905998\exp(-0.960143255\tau) \tag{32}$$

$$\begin{aligned} N_3[id_0(\tau), iq_0(\tau), \omega_0(\tau)] &= 0.14209809\exp(-0.9601432255\tau) - \\ &-0.000808844(10 + 10sin\frac{\pi}{\lambda}\tau + 4sin\frac{3\pi}{\lambda}\tau)^2 - \\ -0.012384789&\left(10 + 10sin\frac{\pi}{\lambda}\tau + 4sin\frac{3\pi}{\lambda}\tau\right) + \frac{0.1980091808}{\sqrt{10+10sin\frac{\pi}{\lambda}\tau+4sin\frac{3\pi}{\lambda}\tau}} \end{aligned} \tag{33}$$

Taking into account the expressions (31)-(33) and (20), in the following we consider

$$A_1(\tau, C_j) = A_2(\tau, C_k) = A_3(\tau, C_l) = 0$$

$$\begin{aligned} B_1(\tau, C_j) &= C_1 - \frac{\pi}{\lambda}\left(C_2cos\frac{\pi}{\lambda}\tau + 3C_3cos\frac{3\pi}{\lambda}\tau + 5C_4cos\frac{5\pi}{\lambda}\tau + 7C_5cos\frac{7\pi}{\lambda}\tau + 9C_6cos\frac{9\pi}{\lambda}\tau\right) - \\ &-0.960143255(C_2sin\frac{\pi}{\lambda}\tau + C_3sin\frac{3\pi}{\lambda}\tau + C_4sin\frac{5\pi}{\lambda}\tau + C_5sin\frac{7\pi}{\lambda}\tau + C_6sin\frac{9\pi}{\lambda}\tau) \\ B_2(\tau, C_j) &= C_7 - \frac{\pi}{\lambda}\left(C_8cos\frac{\pi}{\lambda}\tau + 3C_9cos\frac{3\pi}{\lambda}\tau + 5C_{10}cos\frac{5\pi}{\lambda}\tau + 7C_{11}cos\frac{7\pi}{\lambda}\tau + 9C_{12}cos\frac{9\pi}{\lambda}\tau\right) - \\ &-0.960143255(C_8sin\frac{\pi}{\lambda}\tau + C_9sin\frac{3\pi}{\lambda}\tau + C_{10}sin\frac{5\pi}{\lambda}\tau + C_{11}sin\frac{7\pi}{\lambda}\tau + C_{12}sin\frac{9\pi}{\lambda}\tau) \\ B_3(\tau, C_j) &= C_{13}cos\frac{\pi}{\lambda}\tau + C_{14}cos\frac{3\pi}{\lambda}\tau + C_{15}cos\frac{5\pi}{\lambda}\tau + C_{16}cos\frac{7\pi}{\lambda}\tau + C_{17}cos\frac{9\pi}{\lambda}\tau \end{aligned} \tag{34}$$

The linear differential equations for the first approximations are

$$\begin{aligned} &\frac{did_1(\tau)}{d\tau} + 0.9601432255id_1(\tau) + C_1 - \frac{\pi}{\lambda}(C_2cos\frac{\pi}{\lambda}\tau + 3C_3cos\frac{3\pi}{\lambda}\tau + 5C_4cos\frac{5\pi}{\lambda}\tau + \\ &+7C_5cos\frac{7\pi}{\lambda}\tau + 9C_6cos\frac{9\pi}{\lambda}\tau) - 0.960143255(C_2sin\frac{\pi}{\lambda}\tau + C_3sin\frac{3\pi}{\lambda}\tau + \\ &+C_4sin\frac{5\pi}{\lambda}\tau + C_5sin\frac{7\pi}{\lambda}\tau + C_6sin\frac{9\pi}{\lambda}\tau) = 0, \qquad id_1(0) = 0 \end{aligned} \tag{35}$$

$$\begin{aligned} &\frac{diq_1(\tau)}{d\tau} + 0.960143255iq_1(\tau) + C_7 - \frac{\pi}{\lambda}(C_8cos\frac{\pi}{\lambda}\tau + 3C_9cos\frac{3\pi}{\lambda}\tau + 5C_{10}cos\frac{5\pi}{\lambda}\tau + \\ &+7C_{11}cos\frac{7\pi}{\lambda}\tau + 9C_{12}cos\frac{9\pi}{\lambda}\tau + 11C_{13}cos\frac{11\pi}{\lambda}\tau + 13C_{14}cos\frac{13\pi}{\lambda}\tau + 15C_{15}cos\frac{15\pi}{\lambda}\tau + \\ &+17C_{16}cos\frac{17\pi}{\lambda}\tau) - 0.960143255(C_8sin\frac{\pi}{\lambda}\tau + C_9sin\frac{3\pi}{\lambda}\tau + C_{10}sin\frac{5\pi}{\lambda}\tau + C_{11}sin\frac{7\pi}{\lambda}\tau \\ &+C_{12}sin\frac{9\pi}{\lambda}\tau + C_{13}sin\frac{11\pi}{\lambda}\tau + C_{14}sin\frac{13\pi}{\lambda}\tau + C_{15}sin\frac{15\pi}{\lambda}\tau + C_{16}sin\frac{17\pi}{\lambda}\tau), iq_1(0) = 0 \end{aligned} \tag{36}$$

$$\frac{d\omega_1(\tau)}{d\tau} + \frac{\pi}{\lambda}(C_{17}cos\frac{\pi}{\lambda}\tau + 3C_{18}cos\frac{3\pi}{\lambda}\tau + 5C_{19}cos\frac{5\pi}{\lambda}\tau + 7C_{20}cos\frac{7\pi}{\lambda}\tau) = 0, \quad \omega_1(0) = 0 \tag{37}$$

and the solutions are

$$\begin{aligned} id_1(\tau) = 0.438786995[\exp(-0.9601432255) - 1] + C_2sin\frac{\pi}{\lambda}\tau + C_3sin\frac{3\pi}{\lambda}\tau + \\ +C_4sin\frac{5\pi}{\lambda}\tau + C_5sin\frac{7\pi}{\lambda}\tau + C_6sin\frac{9\pi}{\lambda}\tau \end{aligned} \tag{38}$$

$$iq_1(\tau) = 0.843879596[\exp(-0.960143255) - 1] + C_8 sin\frac{\pi}{\lambda}\tau + C_9 sin\frac{3\pi}{\lambda}\tau + C_{10} sin\frac{5\pi}{\lambda}\tau + \\ + C_{11} sin\frac{7\pi}{\lambda}\tau + C_{12} sin\frac{9\pi}{\lambda}\tau + C_{13} sin\frac{11\pi}{\lambda}\tau + C_{14} sin\frac{13\pi}{\lambda}\tau + C_{15} sin\frac{15\pi}{\lambda}\tau + C_{16} sin\frac{17\pi}{\lambda}\tau \quad (39)$$

$$\omega_1(\tau) = -C_{17} sin\frac{\pi}{\lambda}\tau - C_{18} sin\frac{3\pi}{\lambda}\tau - C_{19} sin\frac{5\pi}{\lambda}\tau - C_{20} sin\frac{7\pi}{\lambda}\tau \quad (40)$$

The approximate solutions of Eqs.(11) and (10) are

$$id(\tau) = id_0(\tau) + id_1(\tau) \quad (41)$$

$$iq(\tau) = iq_0(\tau) + iq_1(\tau) \quad (42)$$

$$\omega(\tau) = \omega_0(\tau) + \omega_1(\tau) \quad (43)$$

The optimal values of the convergence-control parameters C_i are obtained by means of a collocation approach as:

$$C_2 = -1.3089571472,\ C_3 = -0.4503649177, C_4 = -0.0961880721, \\ C_5 = -0.0529407913,\ C_6 = -0.0001149325, C_8 = -0.1013914279, \\ C_9 = -0.0111456049, C_{10} = -0.0738099321, C_{11} = -0.0471348271, \\ C_{12} = -0.0324127981, C_{13} = -0.0222245798, C_{14} = -0.0131280042, \\ C_{15} = -0.0077014973, C_{16} = -0.0034482411, C_{17} = -1.3204012731, \\ C_{18} = -0.5072910784, C_{19} = -0.0225673217, C_{20} = -0.0141314789 \quad (44)$$

Finally, the approximate solution of Eq.(11) and (10) can be written as:

$$id(\tau) = -0.438786995 - 1.3089571472 sin\frac{\pi}{2407}\tau - 0.4503649177 sin\frac{3\pi}{2407}\tau - \\ -0.0961880721 sin\frac{5\pi}{2407}\tau - 0.0529407913 sin\frac{7\pi}{2407}\tau - 0.0001149325 sin\frac{9\pi}{2407}\tau \quad (45)$$

$$iq(\tau) = -0.843879596 - 0.1013914279 sin\frac{\pi}{2407}\tau - 0.0111456049 sin\frac{3\pi}{2407}\tau - \\ -0.0738099321 sin\frac{5\pi}{2407}\tau - 0.047134827 sin\frac{7\pi}{2407}\tau - 0.0324127981 sin\frac{9\pi}{2407}\tau - \\ -0.0222245798 sin\frac{11\pi}{2407}\tau - 0.0131280042 sin\frac{13\pi}{2407}\tau - 0.0077014973 sin\frac{15\pi}{2407}\tau - \\ -0.0034482411 sin\frac{17\pi}{2407}\tau \quad (46)$$

$$\omega(\tau) = 0.499239911 + 1.3204012731 sin\frac{\pi}{2407}\tau + 0.5072910784 sin\frac{3\pi}{2407}\tau + \\ +0.0225673217 sin\frac{5\pi}{2407}\tau + 0.0141314789 sin\frac{7\pi}{2407}\tau \quad (47)$$

Figs.1-3 show the obtained approximate solutions of Eqs.(11) and (10), which, for validation purposes, are compared with numerical solutions obtained using a fourth-order Runge-Kutta method.

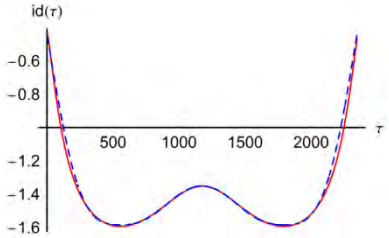

Figure 1. Comparison between the analytical and numerical results for id.

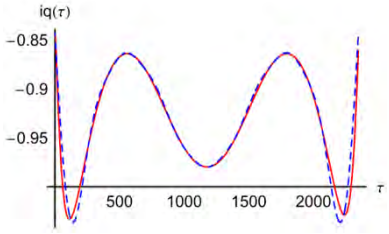

Figure 2. Comparison between the analytical and numerical results for iq.

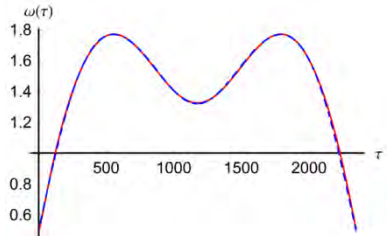

Figure 3. Comparison between the analytical and numerical results for ω.

5. Conclusions

A new technique is employed in this paper to obtain an analytic approximate solution for the dynamical model of a wind power system. The proposed dynamical model which describes the influence of a wind gust to a low-power PMSGallows analyzing both mechanical and electrical phenomena and determining the characteristics of the dynamic regime produced by wind turbine. The wind speed can be considered in the system of equations which describes the dynamic model to predict the system response to specific changes in speed. For this purpose it is necessary to know the wind profile as a function of time. The proposed procedure allows obtaining an analytical solution which is very advantageous and useful for automatic control systems and protection systems used in this kind of aero-elastic installations.

In the present paper we obtained an effective approximate solution to the governing equations. The proposed method is very accurate comparing our analytical results with numerical results, which

proves the validity of our approach. In the present construction of this simple iterative procedure are involved some distinct concepts such as the linear operator, the auxiliary functions A and B and several convergence-control parameters C_i, which ensure a fast convergence of the approximate solutions to the exact ones after only one iteration. The values of the convergence-control parameters are optimally determined using rigorous procedures. It is to remark that this new proposed approach is valid even if the nonlinear differential equation does not contain any small or large parameters.

References

[1] Herisanu, N., Marinca, V., Madescu, G. An analytical approach to nonlinear dynamical model of a permanent magnet synchronous generator, *Wind Energy* 18 (2015) 1657-1670

[2] Boldea, I. *Variable speed generators*. CRC Press, Boca Raton, 2006

[3] Vas, P. *Electrical machines and drives. A space-vector theory approach*, Claredon Press, Oxford, 1996

[4] Binder, A. *ElektrischeMaschinenundAntriebe*, Springer, Berlin-Heidelberg, 2012

[5] Krause, P.C., Wasynczuk, O., Sudhoff, S.D. *Analysis of electrical machinery*, IEEE Press, New York, 1995

[6] Herisanu, N., Marinca, V., Madescu G. Nonlinear dynamics of a wind turbine permanent magnet generator system in different wind profile conditions, *AIP Conference Proceedings*, 1863 (2017) 460002

[7] Xie, D., Lu, Y.P., Sun, J.B., Gu, C.H. Small signal stability analysis for different types of PMSGs connected to the grid, *Renewable Energy* 106 (2017) 149-164

[8] Song, J.C., Dong, F., Zhao, J.W., Lu S.L., Dou, S.K., Wang, H. Optimal design of permanent magnet linear synchronous motors based on Taguchi method, *IET Electric Power Applications* 11 (2017) 41-48

[9] Rahimi, M. Modeling, control and stability analysis of grid connected PMSG based wind turbine assisted with diode rectifier and boost converter, *International Journal of Electrical Power & Energy Systems* 93 (2017) 84-96

[10] Herisanu, N., Marinca, V. Approximate analytical solutions to jerk equations, *Springer Proceedings in Mathematics & Statistics*, 182 (2016) 169-176

[11] Marinca, V., Herisanu, N. *The optimal homotopy asymptotic method. Engineering applications*, Springer, Cham, 2015

Vasile Marinca, Professor: Centre for Advanced Technical Research, Romanian Academy – Timisoara Branch, Bd. Mihai Viteazu 24, 300222Timisoara, Romania (*vasile.marinca@upt.ro*).

Nicolae Herisanu, Professor: University Politehnica Timisoara, Department of Mechanics and Vibration, Bd. Mihai Viteazu 1, 300222 Timisoara, Romania (*nicolae.herisanu@upt.ro*).The author gave a presentation of this paper during one of the conference sessions.

Nonlocal elasticity theory for solving dynamic problems via peridynamics

Adam Martowicz, Wieslaw J. Staszewski, Massimo Ruzzene, Tadeusz Uhl

Abstract: The paper deals with the developed peridynamic numerical tools used for solving various types of dynamic problems. The peridynamics makes use of nonlocal formulation for computational mechanics and, therefore, offers unique properties in terms of more realistic modeling different types of physical phenomena. The authors briefly highlight the fundamentals of nonlocal elasticity theory to show capabilities of the elaborated numerical approach. The theoretical part of the work is complemented with the results obtained for various case studies taking into account elastic wave propagation and analysis of crack propagation. Practical aspects regarding efficiency, required computer resources and accuracy of the proposed numerical tools are addressed. Finally, an analogy between peridynamics and Finite Difference formulations is derived to show possibility of building equivalent model descriptions when solving dynamic problems.

1. Introduction

Nonlocal modeling in the field of computational mechanics is known for over fifty years, introduced in the early papers given by Kröner, Kunin, Eringen, Edelen, and others [1-3]. It is used as an alternative approach, providing very specific advantages, compared to the classical local formulations for statics and dynamics [4]. Following the mathematical description of physics present at nano and microscale – where granularity of matter plays an important role with its all related consequences – both local and long-range interactions between pieces of matter are taken into account. As a result, integral based equations of motion are introduced. Consequently, the total resultant reactions (derived from potential based formulations) are found by aggregating contributing interactions between locally and nonlocally linked particles. The resultant reaction forces are determined based on the properties of the connecting bonds established between modelled solid. The contributing reactions are summed up over some region to determine the total force. The radius of the region of local and nonlocal interactions can be found with a sensitivity analysis. The obtained data allows to decide on the number of considered long-range contributors, found to be the influential ones in calculations.

In fact, spatial partial derivatives – present in classical locally formulated equations of motion – aimed to be solved at geometric discontinuities, grain boundaries, interfaces exhibiting mechanical impedance mismatches, or interconnection layers, may lead to numerical inconveniences.

Discontinuities (i.e. step changes, discretizations, outliers) involved in the functions describing geometry, material properties, and boundary requirements may lead to ambiguity in calculation of derivatives. Nonlocality and integral based formulations aid to avoid this problem. Hence, due to the above mentioned property, nonlocality is well recognized in damage modeling [5]. However, it should be noted that a questionable issue arises, related to the computational costs of applied nonlocal approach. Even though, more convenient analytical and numerical tools are found, there is a necessity of introduction a significant number of additional interactions, which are required to determine kinematic characteristics for each degree of freedom. It results in more populated global matrices of the entire system, which are present in its equation of motion. Nowadays, however, this issue may be successfully addressed with multithreaded algorithms, also employing GPU calculations.

Recently, the peridynamics is one of the most popular nonlocal approach [6]. There are known its various applications addressing problems in many different physical domains [7-9]. Peridynamics makes use of nonlocal, integral based formulation for computational mechanics and, therefore, also offers unique properties in terms of more realistic modeling. The specificity of peridynamics, which is worth to be mentioned, is its capability of direct use of macroscale material properties (i.e. engineering properties, e.g. elastic moduli), irrespectively from what geometric scale is actually referred to. It also means that multiscale studies may be easily performed employing peridynamics [10]. Addressing the risk of possible higher computational effort, necessary to perform peridynamics, the reader may also find the results of convergence analyses carried out to determine the most efficient relationships between the particles distances and the radius of the region covering all nonlocal interactions [11]. Taking into account the above mentioned properties of peridynamics, the authors of the present paper provide the results of exemplary case studies devoted to the properties of a cracked aluminum plate model. The advantages of peridynamics, offering more physical modelling with respect to geometric discontinuities, are shown with numerical examples.

The paper covers the following: introductory Section 1 provides an overview on nonlocal modeling and, specifically, introduces peridynamics as potential tool for solving dynamics. Next, analytical fundamentals of peridynamics and characteristics of the elaborated numerical tools are addressed in Section 2 and 3. Section 4 describes a numerical model of a cracked aluminum plated and the obtained results. An analogy between peridynamics and Finite Difference (FD) Method is discussed in Section 5. Final Section 6 summarizes the paper and presents the authors' conclusions.

2. Peridynamics – analytical fundamentals

Integral based equation of motion for a peridynamic model of a solid body takes the following form

$$\rho\ddot{\mathbf{u}}(\mathbf{x},t) = \int_H \mathbf{f}(\mathbf{u}(\hat{\mathbf{x}},t) - \mathbf{u}(\mathbf{x},t), \hat{\mathbf{x}} - \mathbf{x}) dV_{\hat{\mathbf{x}}} + \boldsymbol{b}(\mathbf{x},t) \tag{1}$$

where: ρ - mass density, $\mathbf{u}$ – displacement vector of an actual central particle (localized at the position $\mathbf{x}$, as shown in Fig. 1; the term "particle" refers to a single piece of the modelled solid body), H - horizon, i.e. the region of local and nonlocal interactions, defined with respect to the central particle. The position of neighboring particle is defined as $\hat{\mathrm{x}}$. $\mathbf{f}$ is the pairwise function characterizing the properties of the links between central and neighboring particles. The external particle excitation is given as force volumetric density $\mathbf{b}$ vector. $dV_{\hat{\mathbf{x}}}$ is a portion of volume attached to the neighboring particle.

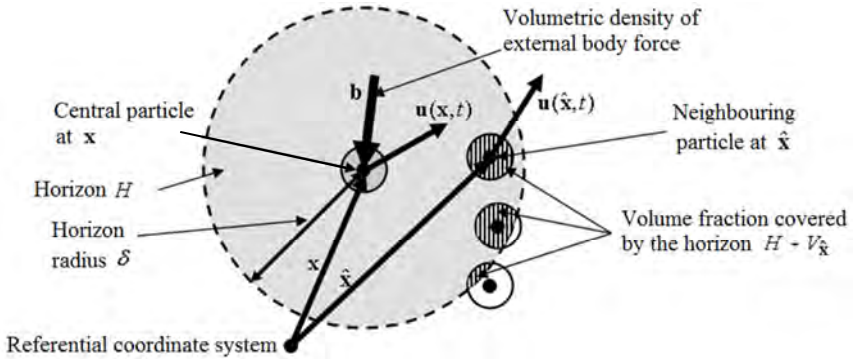

Figure 1. Nonlocality in peridynamics, definition of the area of horizon for nonlocal interactions between particles.

The function $\mathbf{f}$ introduces the material properties and is specified in terms of the expressions:

$$\mathbf{u}(\hat{\mathbf{x}},t)-\mathbf{u}(\mathbf{x},t)=\boldsymbol{\eta} \tag{2}$$

$$\hat{\mathbf{x}}-\mathbf{x}=\boldsymbol{\xi} \tag{3}$$

which stand for relative displacement $\boldsymbol{\eta}$ and relative particle position $\boldsymbol{\xi}$. For a two-dimensional (2-D) case, $\mathbf{f}$ is defined as

$$\mathbf{f}(\boldsymbol{\eta},\boldsymbol{\xi})=\begin{cases}\mathbf{e}(\boldsymbol{\eta},\boldsymbol{\xi})c(\boldsymbol{\xi})s \text{ if } \|\boldsymbol{\xi}\|\le\delta \\ 0, \text{otherwise}\end{cases} \tag{4}$$

where the micromodulus function c for isotropic and homogeneous material equals

$$c=\frac{6E}{\pi\delta^3(1-\nu)T} \tag{5}$$

δ, s and $\mathbf{e}$ denote the horizon radius, strain and the unit vector defining the direction of the reaction forces between particles, respectively. The material elastic properties are: E - Young's modulus, ν - Poisson's ratio. The thickness of the model is defined as T. As found in Eq. (4), $\mathbf{f}$ is

nonzero only for the neighboring particles, which are localized within the horizon *H*. The peridynamics, by its nature constitutes nonlocal interactions, however, when decreasing the horizon radius δ one can easily find a convergence to the local formulations for dynamics. In the following, a numerical formulation for a peridynamic 2-D model is briefly shown.

3. Peridynamics – numerical approach

Based on Eq. (1) and considering a 2-D case, a numerical formulation of the equation of motion may be derived for the *i*-the particle in the form

$$\begin{cases} \rho \dfrac{\partial^2 u_i(t)}{\partial t^2} = \displaystyle\sum_{j \in H_i} \left(\left(\xi_{X_{i,j}} + u_j(t) - u_i(t) \right) F_{i,j}(t) c A_{i,j} T \right) + b_{X_{i,j}} \\ \rho \dfrac{\partial^2 v_i(t)}{\partial t^2} = \displaystyle\sum_{j \in H_i} \left(\left(\xi_{Y_{i,j}} + v_j(t) - v_i(t) \right) F_{i,j}(t) c A_{i,j} T \right) + b_{Y_{i,j}} \end{cases} \tag{6}$$

where $u_{i(j)}(t)$ and $v_{i(j)}(t)$ are the in-plane particle displacements. The indexes *i* and *j* denote the actual central and neighboring particles (i.e. covered by the horizon H_i), respectively. The remaining indexed parameters have the meaning explained in Section 2, taking into account their horizontal and vertical components in the present numerical case. The auxiliary function $F_{i,j}$ takes the form

$$F_{i,j}(t) = \frac{1}{\sqrt{\xi_{X_{i,j}}^2 + \xi_{Y_{i,j}}^2}} - \frac{1}{\sqrt{\left(\xi_{X_{i,j}} + u_j(t) - u_i(t) \right)^2 + \left(\xi_{Y_{i,j}} + v_j(t) - v_i(t) \right)^2}} \tag{7}$$

$A_{i,j}$ defines the area the *j*-th (neighboring) particle covered by the horizon H_i. The general flowchart used to solve dynamic problems with peridynamics is shown in Fig. 2.

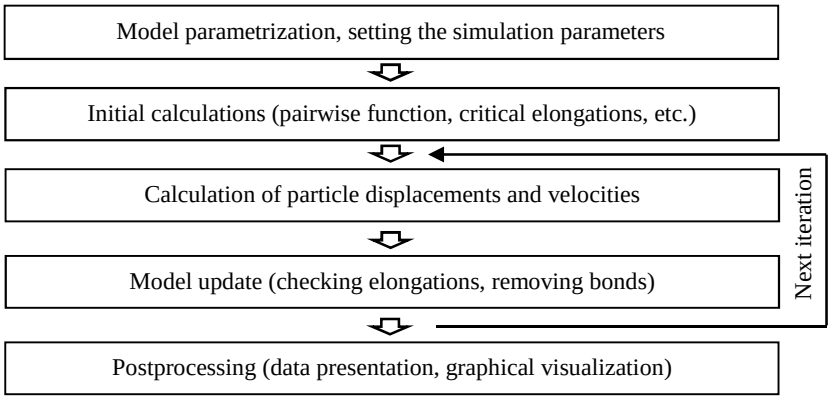

Figure 2. Flowchart for the numerical studies using a peridynamic model.

During the first stage of calculations, model parameterization is performed to set geometric and material properties. The boundary conditions (excitations and fixed displacement areas) are introduced to determine the governing equations for each particle of the model. Moreover, initial conditions regarding particle displacements and velocities are assumed. The simulation parameters provide data on the time step, total simulation time, distances between particles, the radius of the horizon and maximum displacement error (applied when an explicit formulation of the solver is chosen). Next, within the initial calculations, based on the ultimate stress, critical elongations for the bonds between particles are found. Micromodulus function and volumes of the neighboring particles within the horizon are determined. Notches are introduced by removal chosen bonds between particles. During iterative part of the numerical procedure, updated values of the particle displacements and velocities are determined. Based on these values, additional bonds are searched where critical elongations are exceeded. Moreover, already broken bonds between particles are temporarily sustained to let the model undergo external compressing excitation for its compressed regions. Final postprocessing and data presentation provide the results in a readable form.

Making use of the capabilities of the elaborated numerical tools for peridynamics, the results obtained for selected case studies, taking into account elastic wave propagation and analysis of crack propagation, are shown in the following.

4. Case studies for peridynamics

In the following, exemplary results for the application of the above introduced peridynamic numerical code are briefly shown. Based on the elaborated 2-D model, two cases are considered, namely: (i) longitudinal elastic wave propagation observed across the body of an aluminum plate due to the clapping phenomenon (study on wave propagation in the transversal direction with respect to the initial notch orientation), and (ii) the phenomenon of acoustic emission originated from growing crack.

4.1. Numerical model

In the present work a 2-D peridynamic model is considered, as shown in Fig. 3. The model of an aluminum plate with the overall dimensions: 4mm x 4.125mm x 1mm (length x width x thickness) constitutes the subject of the study. The following material properties are assumed: Young's modulus E=70GPa, Poisson's ratio ν=0.3, mass density ρ=2100kg/m^3, and ultimate stress σ_U=40MPa. The distance between particles Δx equals 0.125mm, whereas the horizon radius δ is 0.5mm. The total simulation time is 20μs, and the time step Δt equals 1ns. For both numerical cases a single notch is introduced as a 0.625mm-long centrally localized horizontal geometric discontinuity, where all crossing modelled physical links between particles - present within the horizon - are broken.

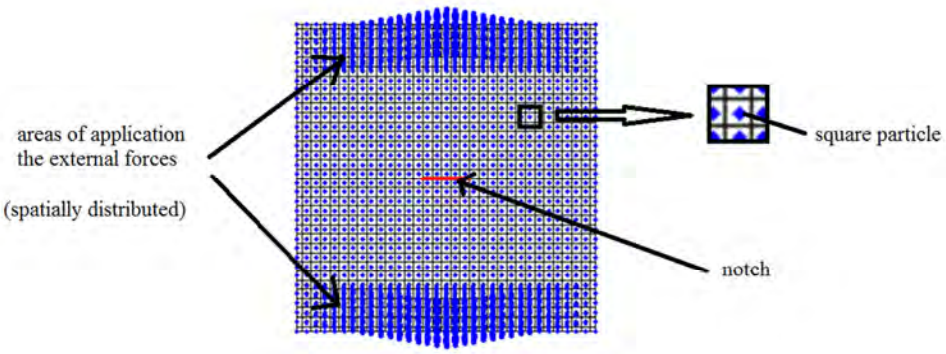

Figure 3. Peridynamic 2-D model of a rectangular aluminum plate used to study wave propagation resulting from clapping and to track the crack growth based on acoustic emission.

Boundary conditions are defined with two spatially distributed sinusoidal forces. Their frequency equals 200kHz. Due to different goals of the two executed simulations, various amplitudes of the external forces are considered [12]. In case of the clapping phenomenon, the resultant force amplitude equals 13.5N, which is achieved by a linear growth after the time period of 0.2μs. A limited value of the force amplitude prevents from further crack growth. Oppositely, the higher force amplitude is set, i.e. the resultant amplitude of 33.75N (also achieved after 0.2μs), for the study on acoustic emission to assure gradual evolution of the initial notch. Hence, in the second case, generation of additional waves is observed due to breaking the links between particles in the peridynamic model.

As regard to the boundary conditions, it should be noted, that a spatial distribution for the external force, over hypothetical clamping regions, must be taken into account to prevent from nonphysical (concentrated) force application and sudden unexpected model break [8]. The other solution to address the issue is locally increase the stiffness properties for the links between particles. However, spread of the force over some area seems more physical, and was chosen by the authors of the present work to set the boundary conditions.

4.2. Elastic wave propagation

In the literature, there are known studies on elastic waves (and stress waves) propagation using peridynamics, utilized for both macroscale models (e.g. metallic and composite structures) [9,12,13], and micro/nanoscale models (e.g. graphene) [14]. Irrespectively from the lengthscale used, a peridynamic model provides both a straightforward way of introduction the material properties (including reference to the commonly applied engineering characteristics, e.g. elastic moduli) and reliable assessment and interpretation of the physical phenomena present in the modelled materials and structures.

In the present study, the phenomenon of wave generation and propagation due to clapping mechanism is considered. As already mentioned, the amplitude of the external sinusoidal forces is limited to prevent from further crack growth. While clapping, cyclic behavior of the modelled plate is observed – when the opposite faces of the crack hit each other, a longitudinal wave is generated. It propagates through the model. As reported in [12], making use of a similar numerical model, 5-MHz transverse vibrations are identified at the crack's edges. Presently, the displacements for the particles lying perpendicularly the crack's orientation are under investigation, at the localizations shown in Fig. 4. The registered temporal plots for the vertical particle displacements are presented in Fig. 5.

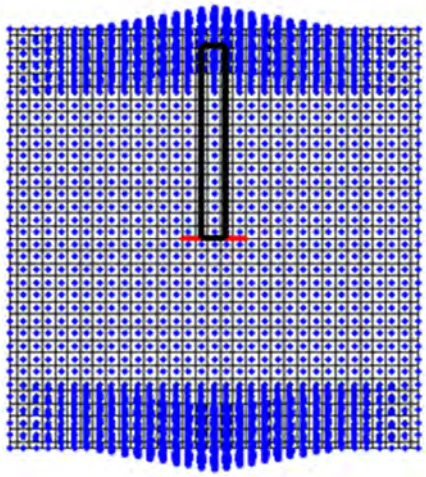

Figure 4. Investigated particles in a peridynamic 2-D model of an aluminum plate (covered by a black rectangular) used to track longitudinal elastic wave propagation originated from the phenomena of clapping. The initial notch is marked in red.

As identified in Fig. 5, the propagating vertical disturbance (assessed with respect to the particle positions) refers to the velocity of longitudinal elastic wave (bulk wave in aluminum) – c_L=6695m/s. The expected theoretical time for the wave to travel between the neighboring particles can be found as $\Delta x/c_L$=18,67ns, whereas the average propagation time between all fifteen investigated particles equals 19.9ns. Hence, the application of a peridynamic model effectively aids to study elastic wave propagation in a model with a notch.

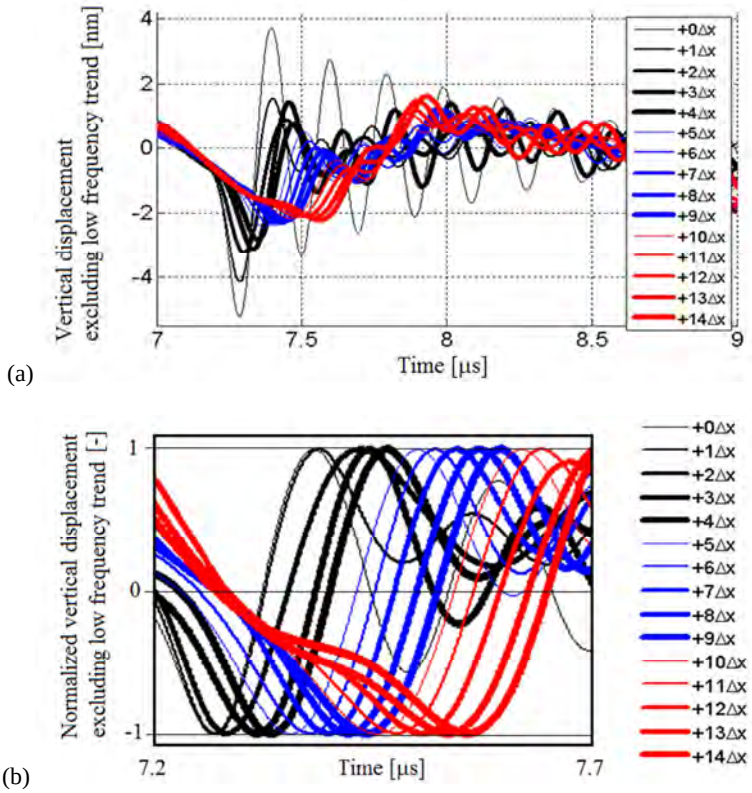

Figure 5. Vertical in-plane displacements of the investigated particles while propagation of the longitudinal wave, generated at the crack's upper edge: (a) plots registered for the longer time period when a series of vibration cycles are seen after the crack's edges hit each other, (b) normalized plots shown for the limited time domain to indicate propagating wave. Gradual increase of the particles vertical coordinates are marked with subsequent multiples of their distance – Δx.

4.3. Crack propagation identification based on acoustic emission

The second case study for peridynamics deals with the phenomenon of acoustic emission, which is present due to growing crack. Acoustic emission is observed in a model since its particles start disconnecting due to exceedance of the assumed ultimate stress. The links (bonds) between particles break, which, in turn, leads to its local vibrations. Finally, the generated disturbance travels through the model from the area where the moving crack's tip is localized. Fig. 6 shows the localization of a "virtual sensor" used to register the generated wave – at the center of the selected particle lying at the initial position of the crack's tip. Generally, three phases may be observed in the studied case, as shown in Fig 7.

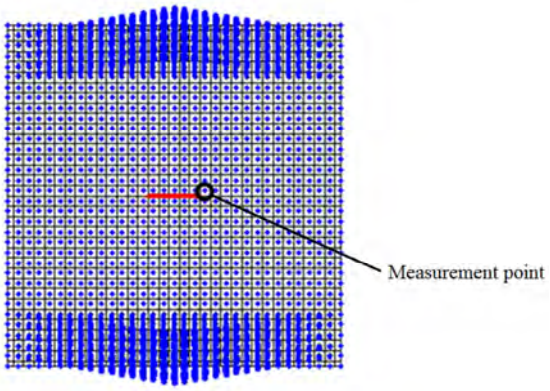

Figure 6. Localization of the measurement point ("virtual sensor") used to identify the wave generated due to acoustic emission.

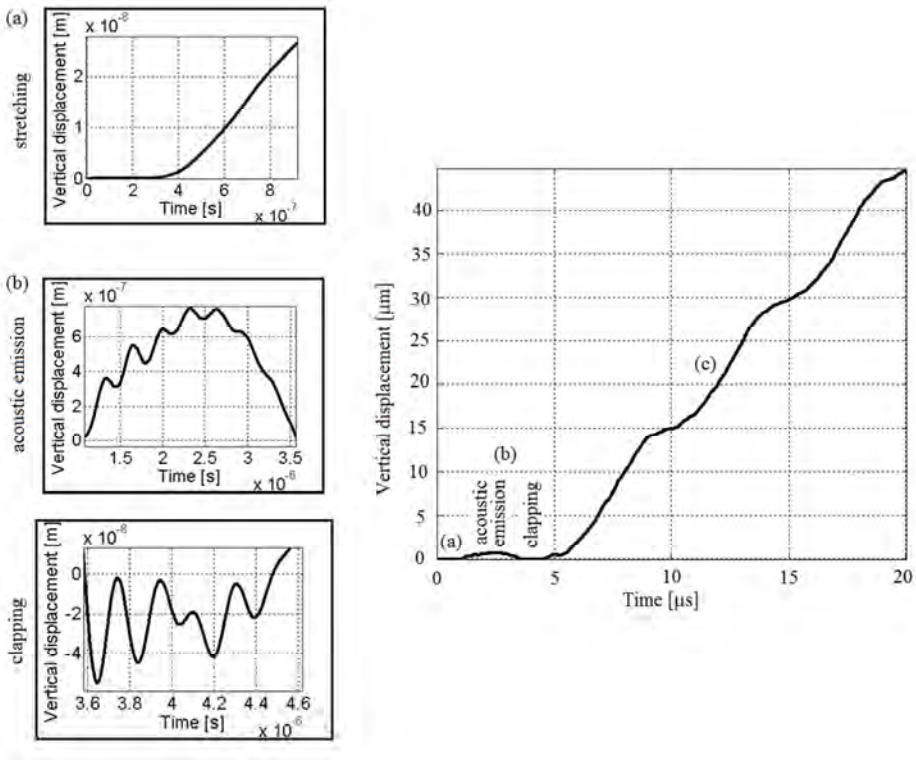

Figure 7. Phases identified in simulation – illustrated with the particle vertical displacements: (a) initial model stretching until ultimate stresses is exceeded, (b) wave generation due to acoustic emission (accompanied by additional wave originating from the clapping mechanism), (c) disconnected parts of the model move away.

First, a gradual vertical displacement of the particle is shown (Fig. 7 (a)), as the model undergoes deformation due to external forces. The crack does not evolve at this stage. After the ultimate stress is exceeded at the crack's tip, the phenomenon of acoustic emission is detected (Fig. 7 (b)). Critical relative elongations are exceeded in the connecting links, which leads to the crack growth. The connections between particles start to break and the path of growing crack may be tracked. Model degradation (i.e. its stiffness reduction) proceeds, followed by particle oscillations originating from their fast cyclic motion in vicinity of the moving crack's tip. The highest amplitudes of the generated wave measured in the model refer to the particles lying directly on the crack's edges, principally in the area of its tips. Since the model undergoes stretching and compression due to a sinusoidal excitation, clapping mechanism is also observed – the crack's faces touch while model cyclic compression. Clapping is identified based on additional wave generation (Section 4.2). Finally, when all connecting links between the two parts of the plate are broken, the simulation enters its last stage. The two pieces of the plate move away, which is characterized by the last part of the plot - marked in Fig. 7 (c). Hence, integral based model dynamics description conveniently handles the physical phenomena of acoustic emission, which is present at given geometric discontinuity (initial crack).

5. Analogy between peridynamics and nonlocal FD Method

This section shows an exemplary analogy between numerical codes for peridynamics and nonlocal formulation of FD Method. In case of a one-dimensional (1-D) model, Eq. (1) takes the form

$$\rho\frac{\partial^2 u_i(t)}{\partial t^2}=\sum_{j\in H_i}\left(\frac{u_j(t)-u_i(t)}{\xi_{i,j}}cnA\Delta x\right)+b_i(t);\ \text{where}\ \begin{cases} n=\dfrac{1}{2} & \text{for the two boundary paricles} \\ \text{n}=1 & \text{otherwise}\end{cases} \tag{8}$$

The micromodulus function c can be found as $c=2E/(\delta^2 A)$ [11]. The parameters A and Δx denote the cross-sectional area of the modelled rod and the distance between particles. On the other hand, a general form of the equation of motion based on a FD scheme (for spatial partial derivative) for 1-D case can be transformed to the following form [15]

$$\rho\frac{\partial^2 u_i(t)}{\partial t^2}=\sum_{j\in H_i}k_j\left(u_j(t)-u_i(t)\right)+b_i(t) \tag{9}$$

where k_j is the *j*-the coefficient of the nonlocal scheme. Hence, k_j may be found as

$$k_j=\frac{2nE}{j\delta^2},\quad j\in H_i,\ \text{where}\ \begin{cases} n=\dfrac{1}{2} & \text{for the two boundary degrees of freedom} \\ \text{n}=1 & \text{otherwise}\end{cases} \tag{10}$$

The analogy between peridynamics and nonlocal FD Method is derived to show possibility of building equivalent model descriptions when solving dynamic problems. Having introduced the

newly calculated coefficients of the FD schemes – which are in fact originally built based on derivative based formulations) – one may conveniently use the exiting solvers (either implicit or explicit) to apply the theory of peridynamics and check its capability in practice.

6. Summary and concluding remarks

The paper is devoted to practical aspects of applications of the nonlocal theory to solution of dynamic problems. The capabilities of nonlocal formulations of governing equations are briefly discussed, showing both advantages and drawbacks. The exemplary theory of peridynamics is presented, illustrated with two numerical case studies related to elastic wave propagation and crack tracking with the phenomenon of acoustic emission. Finally, an analogy between formulation of peridynamics and nonlocal FD Method for a 1-D case is introduced.

The applications of nonlocal theories are very fruitful. The advantages of peridynamics are of special concern. On one hand, lack of spatial partial derivatives allows to easily handle model discontinuities (related to geometry, functions describing the material properties, and boundary), which let the researcher analyze models of cracked structures, as well as helps to avoid numerical problems while differentiating. As shown in the presented numerical cases, peridynamics enables solving dynamic problems, especially those related to wave propagation in structures with introduced notches. More physical description also promises more reliable analyses of the crack growth direction, not governed by the structure of the model itself, as observed in locally formulated mesh based approaches. On the other hand, peridynamics considers the macroscale elastic moduli ready to be introduced irrespectively from the lengthscale used. Moreover long-range interactions allow van der Waals forces to be taken into account when dealing with nano and microscale computations.

Acknowledgments

This work has been supported by the AGH University of Science and Technology, WIMiR, research grant no. 11.11.130.560.

References

[1] Kröner, E. Elasticity theory of materials with long range cohesive forces. *International Journal of Solids and Structures* 3 (1967), 731-742.

[2] Kunin, I.A. Inhomogeneous elastic medium with non-local interactions. *Journal of Applied Mechanics and Technical Physics* 8, 3 (1967), 60-66.

[3] Eringen, A.C., and Edelen, D.G.B. On nonlocal elasticity. *International Journal of Engineering Science*, 10 (1972), 233-248.

[4] Martowicz, A. On nonlocal modeling in continuum mechanics. *Mechanics and Control* 34, 2 (2015), 41-46.

[5] Bazant, Z.P., and Jirasek, M. Nonlocal Integral Formulations of Plasticity and Damage: Survey of Progress. *Journal of Engineering Mechanics* 128, 11 (2002), 1119-1149.

[6] Silling, S.A. Reformulation of elasticity theory for discontinuities and long-range forces. *Journal of the Mechanics and Physics of Solids* 48 (2000), 175–209.

[7] Madenci, E., and Oterkus, E. *Peridynamic theory and its applications.* Springer, New York, (2014).

[8] Martowicz, A. Peridynamics for damage modelling and propagation via numerical simulations. *Diagnostyka* 18, 1 (2017), 73-78.

[9] Hu, W., Ha, Y.D., and Bobaru, F. Peridynamic model for dynamic fracture in unidirectional fiber-reinforced composites. *Computer Methods in Applied Mechanics and Engineering* 217-220 (2012), 247–261.

[10] Seleson, P., Parks, M.L., Gunzburger, M., and Lehoucq, R.B. Peridynamics as an upscaling of molecular dynamics. *Journal on Multiscale Modeling and Simulation* 8, 1 (2009), 204-227.

[11] Bobaru, F., Yang, M., Alves, L.F., Silling, S.A., Askari, E., and Xu, J. Convergence, adaptive refinement, and scaling in 1D peridynamics. *International Journal for Numerical Methods in Engineering* 77 (2009), 852–877.

[12] Martowicz, A., Ruzzene, M., Staszewski, W.J., and Uhl, T. Non-local modeling and simulation of wave propagation and crack growth. *AIP Conference Proceedings*, AIP Publishing 1581, 513 (2014), 513-520.

[13] Martowicz, A., Staszewski, W.J., Ruzzene, M., and Uhl, T. Vibro-acoustic wave interaction in cracked plate modeled with peridynamics. *Proc. of the Conference WCCM XI, ECCM V, ECFD VI*; Onate E., Oliver X., Huerta (eds.), International Center for Numerical Methods in Engineering, Barcelona, Spain, (2014), 4021-4027.

[14] Martowicz, A., Staszewski, W.J., Ruzzene, M., and Uhl, T. Peridynamics as an analysis tool for wave propagation in graphene nanoribbons. SPIE Smart Structures and Materials + Nondestructive Evaluation and Health Monitoring, San Diego, California, United States, *Proc. SPIE Vol. 9435, Sensors and Smart Structures Technologies for Civil, Mechanical, and Aerospace Systems*, (2015); 94350I; doi: 10.1117/12.2084312.

[15] Martowicz A., Ruzzene, M., Staszewski, W.J., Rimoli, J.J., and Uhl, T. Out-of-Plane Elastic Waves in 2D Models of Solids: A Case Study for a Nonlocal Discretization Scheme with Reduced Numerical Dispersion. *Mathematical Problems in Engineering* (2015), Article ID 584081.

Adam Martowicz, Ph.D.: AGH University of Science and Technology, Department of Robotics and Mechatronics, al. A. Mickiewicza 30, 30-059 Krakow, Poland (adam.martowicz@agh.edu.pl). The author gave a presentation of this paper during one of the conference sessions.

Wieslaw J. Staszewski, Professor: AGH University of Science and Technology, Department of Robotics and Mechatronics, al. A. Mickiewicza 30, 30-059 Krakow, Poland (staszews@agh.edu.pl).

Massimo Ruzzene, Professor: Georgia Institute of Technology, School of Aerospace Engineering, School of Mechanical Engineering, 270 Ferst Drive, GA 30332, Atlanta, USA (ruzzene@gatech.edu).

Tadeusz Uhl, Professor: AGH University of Science and Technology, Department of Robotics and Mechatronics, al. A. Mickiewicza 30, 30-059 Krakow, Poland (tuhl@agh.edu.pl).

Nonlocal numerical methods for solving second-order partial differential equations

Adam Martowicz, Wieslaw J. Staszewski, Massimo Ruzzene, Tadeusz Uhl

Abstract: The work presents efficient numerical schemes dedicated for solving dynamic problems governed by second-order partial differential equations. The proposed approach makes use of a nonlocal formulation of the Finite Difference method. Higher order components incorporated into the discretization schemes are found, using the Fourier series based decomposition, to assure desired reduction of numerical dispersion. Hence, the elaborated approach is primarily proposed to carry out both vibration and wave propagation based analyses. Stability conditions and mitigation rate of numerical dispersion for the proposed discretization schemes are verified. The authors discuss the influence of the order of components used in nonlocal formulations on performance of the proposed methods. Additionally, as confirmed with exemplary numerical results, the proposed nonlocal numerical schemes allow for more sparse spatial model discretization, keeping similar properties regarding numerical dispersion, compared to the most commonly used finite difference formulations. Effectively, less populated domain of spatially distributed model's degrees of freedom may be taken into account. This ability may be critical in terms of available computer resources (both processing speed and memory) when dealing with either complicated geometry, topology or long-term temporal analyses.

1. Introduction

Contrarily to the classical approaches, which are applied in the field of computational mechanics (or computational physics in general), the nonlocal methods introduce integral based components to substitute or develop the existing partial derivative based contributors of the equations of motion (governing equations) [1,2]. A general attribute of nonlocality in statics and dynamics stands for either (i) aggregation of some contributing quantities – which are used in governing equations – in the region of both local and nonlocal interactions between pieces of modelled body or (ii) introduction some nonlocally formulated operators into the existing partial derivatives. By doing so, the classical problem descriptions extend their capabilities dramatically. It should be however noted, that the nonlocal equations certainly converge to the local ones – by decreasing the radius of the region where all nonlocal interactions are considered, or simply by removal any lengthscale parameter originally taken into account. In such a case, a simplification (one may say degeneration or loss) of the initial functionalities is carried out.

The motivation for application of nonlocality in governing equations stems from physical observations. It turns out that there are some physical phenomena that cannot be accurately described employing classical locally formulated mathematical equations. Application of adequate lengthscales into the governing equations is also an issue to address the physics at various geometric scales [3,4]. The two known examples of the above mentioned type of somewhat problematic phenomena, in the field of mechanics, are wave dispersion are shear bands for stretching [4-6]. Hence, nonlocality helps to solve the problem of the inconsistency identified between physical observations and the exiting attempts at their descriptions.

Nonlocality, due to its extraordinary capabilities, has been applied to solve problems for various physical domains [7]. Nonlocal approaches are well recognized in the following analytical and numerical modeling fields: damage evolution [8], including a demand for its spontaneous growth not governed by a structure of the model mesh [9], vibro-acoustic wave interactions [10], reduction of numerical dispersion [11], boundary conditions [12], regularization of boundary value problems [13], piezoelectricity [14], thermoelasticity [15-17] shape memory alloys [18], and graphene [19,20].

The present paper is devoted to efficient nonlocal numerical schemes dedicated for solving specific dynamic problems – governed by second-order partial differential equations (PDE). The proposed approach makes use of a nonlocal formulation of the Finite Difference (FD) method. The idea of employing nonlocality to increase the quality of numerical models is not a new one. The nonlocal approaches may be used to avoid high mesh density keeping acceptable quality of the results [21,22]. Based on the previous authors' works carried for solving wave equation, the recently proposed numerical schemes, exhibiting reduced numerical dispersion, are now adapted to thermal diffusion equation (thermal conductivity equation).

The paper is organized as follows. Section 1 serves as an introduction to the nonlocal theory in the field of computational physics (computational mechanics in particular). Section 2 provides examples of mathematical formulations incorporating nonlocality, complemented with more detailed description on practical aspects of its applications. Next, the scope of potential applications of the present work is shown in Section 3 to provide motivation for studies on the nonlocal schemes. Section 4 presents the elaborated schemes, followed by examples of their applications and discussion on the results in Section 5. Final Section 6 summarizes the wok and draws the conclusions.

2. Nonlocality in computational mechanics

The specificity of the mathematical descriptions of nonlocal approaches originates from the nature of matter, which is basically gradual. This fundamental fact leads to the key question: is it possible to accurately model the physical behavior of a solid matter using spatial PDEs? The answer is: yes, it is, however, to some extent. Local theories operate based on PDEs, which is convenient at

macroscale, where, in general, we deal with continuum of matter. Hence, it is an acceptable approximation of the material and structure properties due their averaging. Similarly, one may note, that quantum effects are negligible as well, at the mentioned lengthscale. Engineering properties (macroscale properties, e.g. elastic moduli) may be freely used to build a material model. The resultant properties are found using homogenization techniques (averaging of the properties over a specific region) to be able to use continuous physical domain [5]. This approach is valid for sufficiently long waves propagating in a homogenized model with respect to the lengthscale at which inherent anisotropy of material manifests its presents.

Generally, necessity of introduction the nonlocality into governing equations emerges when: (i) computations directly concern the study of matter at nano and microscale, or (ii) a macroscale behavior of matter is strongly affected by the phenomena present at nano and microscale. In fact, if a macroscale model (e.g. with size of tens of centimeters) is built to track the growth path of a fatigue crack, the macroscale effects identified in the model, i.e. its break along some surface(s), originate from nano and microscale phenomena. Indeed, we may have some successful attempts at averaging the material properties, however, the macroscale effects may results from very chaotic and spatially distributed phenomena at nano and microscale. Physically, crack growth means subsequent and relatively fast breaks of the enormous number of links between atoms or grains. Potential based local and nonlocal reactions between fundamental pieces of matter influence the model behavior at larger geometric scales. Hence, the above-mentioned phenomena should be mathematical handled to properly infer on the model behavior at macroscale. Finally, the use of nonlocality in governing equations enables relatively easy determination of the dispersion properties of the applied material. This is important, as it preserves desired relationships between the length of propagating waves and their velocities, following the physical characteristics of the modelled medium.

Apart from pure physical reasons for using nonlocality, there are also numerical aspects. First of all, nonlocal numerical schemes, used to substitute partial derivatives in governing equations, allow to search and then apply very specific values of their coefficients to reduce numerical dispersion when solving a problem. The key issue is to derive schemes, which would lead to more accurate solutions without requirement of further increase of the number of degrees of freedom (DOF) used to cover the entire modelled domain. This aspect is within the scope of the authors' present work. New FD based schemes are proposed to efficiently solve PDEs based on a limited number of DOFs. Second, use of nonlocal region of interactions between pieces of the modelled solid also inherently leads to more physical behavior of a model as it seems to be more independent from its structure. The reactions are spread over some region, and, actually, there is no a single specific distance in the model, i.e. the distance between neighboring DOFs, which would imprint a peculiar stamp in the form of PDEs, as it happens in case of local formulations. It is so since nonlocality assures that both integer and real

numbered multiples (e.g. at diagonals) of the mentioned distance appear in the governing equation. Moreover higher diversity regarding directions of nonlocal interactions is observed, which favors more “spontaneous” behavior of the model, as in the case of a fatigue crack growth.

In the context of computational aspects of nonlocality, the following issues should be also briefly marked. On one hand, accuracy and efficiency of the used scheme rely on the relationships between distances between DOFs and the radius of the horizon of the region, where nonlocal interactions are determined. However, in the literature there are already reported the results on the convergence analysis carried out to find the proper dependencies [23]. On the other hand, nonlocality, by its nature, suits for parallel processing (e.g. based on GPU), which would partially compensate the increased computational effort necessary to consider all the required long-range interactions.

In the following, exemplary nonlocal formulations of equation of motion for dynamics are provided to give reference. For sake of clarity only spatial components are of concern. There are shown various nonlocal operators and integrals (the sum in case of numerical approach) to be used with kernel functions, which define constitutive dependencies. Classically formulated local Cauchy problem becomes a spatial integro-differential based relationship, e.g.:

- integro-differential-based expression for one-dimensional (1-D) case [24]

$$\frac{\partial^2 u(x,t)}{\partial t^2} = \frac{\partial^2}{\partial x^2}\int_{\Re} \beta(x-\hat{x}) g(u(\hat{x},t)) d\hat{x} \tag{1}$$

with an integrable kernel function $\beta(x-\hat{x})$. The quantity $g(u(\hat{x},t))$ denotes a nonlinear function of the displacement $u(x,t)$. x, $\hat{x}$ - actual central and neighboring localizations of DOFs;

- integro-differential expression for three-dimensional (3-D) case with nonlocal formulation of the Cauchy problem [25]

$$\rho(x)\frac{\partial^2 \mathbf{u}(\mathbf{x},t)}{\partial t^2} = \nabla \cdot \boldsymbol{\sigma}(\mathbf{u}(\mathbf{x},t)) + \mathbf{b}(\mathbf{x},t) \tag{2}$$

where: $\boldsymbol{\sigma}$ - nonlocal stress tensor, $\rho(x)$ - mass density and $\mathbf{b}(\mathbf{x},t)$ - external body force;

- integro-differential expression for a generic volume element, for 1-D case [26]

$$\rho(x)A(x)\frac{\partial^2 u(x,t)}{\partial t^2} - \frac{\partial}{\partial x}[E_{nl}(x)A(x)\frac{\partial u(x,t)}{\partial x}] + \int_a^b g(x,\xi)\eta(x,\xi,t)d\xi = A(x)f(x,t) \tag{3}$$

where $g(x,\xi)$ is the kernel function, which depends on the distance-decaying function, $\eta(x,\xi,t)$ is the relative displacement determined at coordinates x and ξ. $f(x,t)$ - field of external body force. $A(x)$, $E_{nl}(x)$ - the cross-sectional area and Young’s modulus;

- peridynamics based on integral formulation (3-D case) [16,27]

$$\rho \frac{\partial^2 \mathbf{u}(\mathbf{x},t)}{\partial t^2} = \int_H \mathbf{f}(\mathbf{u}(\hat{\mathbf{x}},t) - \mathbf{u}(\mathbf{x},t), \hat{\mathbf{x}} - \mathbf{x}) dV_{\hat{\mathbf{x}}} + \mathbf{b}(\mathbf{x},t) \tag{4}$$

where the pairwise force $\mathbf{f}$ is defined in the finite domain H (called as horizon). It depends on: relative displacement $\mathbf{u}(\hat{\mathbf{x}},t) - \mathbf{u}(\mathbf{x},t)$, the relative position $\hat{\mathbf{x}} - \mathbf{x}$;

- nonlocal FD based expression for discretized 1-D case, for the *i*-th DOF [21]

$$m \frac{\partial^2 u_i(t)}{\partial t^2} + \sum_{j=1}^{N} k_j \left[2u_i(t) - u_{i-j}(t) - u_{i+j}(t) \right] = 0 \tag{5}$$

where: m - discretized mass attached to a single DOF, k_j - the j-th coefficient of the FD based scheme (it actually represents – in the presented form of discretized wave equation – the resultant stiffness coefficients of the two hypothetical springs linking the *i*-the DOF with the $i-j$-th and $i+j$-th DOFs), N - number of nonlocal interactions;

- other discrete approaches [7]: cellular automata e.g. with a secondary von Neumann neighborhood, molecular dynamics, the approaches based on the micropolar and Cosserat theories, nonlocal Finite Element Method; and analytical ones based on: higher-order spatial partial derivatives, domain decomposition and variational calculus.

Amongst all the above-mentioned approaches peridynamics and nonlocal FD are worth to be mentioned because of their specific capabilities. Peridynamics is unique amongst analytical methods since it does not take into account spatial partial derivatives at all, which prevents from numerical errors at geometric discontinuities. On the other hand, the FD based method stands for a straightforward nonlocal description of the problem. Due to its clarity (detailed description is presented in [21]), it may be relatively easily applied to various case studies, which is confirmed in Section 4 and 5 of the paper. The intention of the authors is to adapt the elaborated FD scheme, already used in case of wave equation to be able to solve thermal problems, specifically with the application of thermal conductivity equation. In the following, group of exemplary specific types of PDEs is presented, which may be handled by the elaborated nonlocal FD scheme.

3. Scope of application - motivation

The present work deals with solving a specific class of PDEs, using numerical approaches based on nonlocal formulations of FD method. The case of second-order spatial PDFs is of special concern, as it refers to the mathematical descriptions of many various physical phenomena. Amongst others, the following equations take the desired form of PDFs (excluding physical constants for clarity) [28]:

- Laplace's equation – used to define source-free fields of scalar quantities (potentials), e.g. in case of gravitational (electrostatic) field in the space devoid of mass (charge)

$$\Delta u = 0 \quad \Rightarrow \quad \frac{\partial^2 u}{\partial x^2} + \frac{\partial^2 u}{\partial y^2} + \frac{\partial^2 u}{\partial z^2} = 0, \quad u = u(x, y, z) \tag{6}$$

- Poisson equation – applied to potential fields with considered sources

$$\Delta u = f \quad \Rightarrow \quad \frac{\partial^2 u}{\partial x^2} + \frac{\partial^2 u}{\partial y^2} + \frac{\partial^2 u}{\partial z^2} = f, \quad u = u(x, y, z), \quad f = f(x, y, z) \tag{7}$$

- Helmholtz equation – used e.g. in acoustics to determine field of pressure

$$\Delta u + \lambda u = 0 \quad \Rightarrow \quad \frac{\partial^2 u}{\partial x^2} + \frac{\partial^2 u}{\partial y^2} + \frac{\partial^2 u}{\partial z^2} + \lambda u = 0, \quad u = u(x, y, z) \tag{8}$$

- diffusion equation – applied to solve thermal conductivity related problems

$$u_{,t} - \Delta u = 0 \quad \Rightarrow \quad \frac{\partial u}{\partial t} = \frac{\partial^2 u}{\partial x^2} + \frac{\partial^2 u}{\partial y^2} + \frac{\partial^2 u}{\partial z^2}, \quad u = u(x, y, z, t) \tag{9}$$

- Schrödinger equation – used to describe quantum states of a physical system

$$iu_{,t} + \Delta u = 0 \quad \Rightarrow \quad i\frac{\partial u}{\partial t} + \frac{\partial^2 u}{\partial x^2} + \frac{\partial^2 u}{\partial y^2} + \frac{\partial^2 u}{\partial z^2} = 0, \quad u = u(x, y, z, t) \tag{10}$$

- wave equation – solved to analyze wave propagation

$$u_{,tt} - \Delta u = 0 \quad \Rightarrow \quad \frac{\partial^2 u}{\partial t^2} = \frac{\partial^2 u}{\partial x^2} + \frac{\partial^2 u}{\partial y^2} + \frac{\partial^2 u}{\partial z^2}, \quad u = u(x, y, z, t) \tag{11}$$

As already mentioned, the physical phenomena, which are described using Eq. (9) and (11) are of the authors' special concern. However, further applications of the theory presented in [21] are already scheduled as future work to show capabilities of the nonlocal FD based numerical scheme for solving static and dynamic problems. Hereinafter, the theory of the elaborated FD scheme is concisely introduced, followed by its adaptation to address the thermal conductivity equation (diffusion).

4. Nonlocal FD schemes with reduced numerical dispersion

The theory of numerical discretization, proposed in [21], was derived for wave equation. In case of 1-D, the wave equation takes the form

$$\frac{\partial^2 u(x,t)}{\partial t^2} = c^2 \frac{\partial^2 u(x,t)}{\partial x^2} \tag{12}$$

where $c=\sqrt{E/\rho}$ is the velocity of longitudinal wave propagation through modelled rod, calculated with Young's modulus E and mass density ρ. Introducing the plane wave solution

$$u(x,t)=u(x,0)e^{j(\kappa x-\omega t)} \quad \text{, j – imaginary unit} \tag{13}$$

into Eq. (12), the relation between wavenumber κ and angular velocity ω is found

$$\omega=c\kappa \tag{14}$$

Next, based on the theory of Fourier series, the following stiffness coefficients k_j (i.e. coefficients of the FD based numerical scheme) were found for Eq. (5) [21]

$$k_j=(-1)^{j-1}\frac{2}{j^2}\frac{EA}{a}, \text{ for } j<N \quad \wedge \quad k_j=(-1)^{j-1}\frac{1}{j^2}\frac{EA}{a}, \text{ for } j=N \tag{15}$$

where a is the distance between subsequent DOFs in the modelled rod, and N is the number of local and nonlocal interaction terms defined within the rod by each side with respect to an actual central DOF localized at the coordinate $x_i=ia$ (N - order of nonlocality). Increase of N leads to lower numerical dispersion in the final solution, maintaining spatial distribution of DOFs [21].

Based on the above presented theory, a similar FD based scheme for 1-D case is proposed for the following general form of the thermal conductivity equation

$$\frac{\partial T(x,t)}{\partial t}=\alpha\frac{\partial^2 T(x,t)}{\partial x^2}, \quad T \text{ - temperture along a rod} \tag{16}$$

where the coefficient $\alpha=k/(\rho c_p)$ is specified in terms of: $k=\dot{Q}a/(A\Delta T)$ - thermal conductivity coefficient, $\rho=m/(aA)$ - mass density, and $c_p=Q/(m\Delta T)$ - specific heat capacity. A discretized model for Eq. (16) consist of discretized masses m - uniformly distributed along the x axis, i.e. at each DOF of the model at coordinates $x_i=ia$, and the linking rods of the specified k and geometry (a - length, i.e. the distance between DOFs, A -cross-sectional area). The linking rods transfer heat whereas the masses are heated up or cooled down depending on the direction of heat energy flow between DOFs. Q and $\dot{Q}=\partial Q/\partial t$ respectively denote heat energy and its temporal rate (power). After parameter rearrangement, Eq. (16) may be rewritten to the respective semi-discretized local form for the *i*-th DOF

$$mc_p\frac{\partial T_i(t)}{\partial t}+\frac{kA}{a}\left(2T_i(t)-T_{i-j}(t)-T_{i+j}(t)\right)=0 \tag{17}$$

which may be extended to the general nonlocal expression

$$mc_p \frac{\partial T_i(t)}{\partial t} + \sum_{j=1}^{N} k_j \left[2T_i(t) - T_{i-j}(t) - T_{i+j}(t) \right] = 0 \tag{18}$$

Eq. (18) fits the structure of Eq. (5). Next, a general solution of Eq. (16) may be found as [28]

$$T(x,t) = \frac{T_0}{t^{n/2}} e^{\frac{-x^2}{4t}} \tag{19}$$

Hence, Eq. (19), at discrete localizations for both an actual central DOF ($x_i = ia$) and the neighboring DOFs ($x_{i\pm j} = (i \pm j)a$) equal:

$$T_i(t) = \frac{T_0}{t^{n/2}} e^{\frac{-i^2 a^2}{4t}} \tag{20}$$

$$T_{i\pm j}(t) = T_i(t) e^{\frac{-a^2 \left(j^2 \pm 2ij \right)}{4t}} \tag{21}$$

Based on the similarities between Eq. (5) and Eq. (18), and definition of the coefficients k_j given by Eq. (15), which are adapted to the case of diffusion equation, a convergence analysis for analytical and numerical solutions is carried out in the following. The calculations are performed for an exemplary explicit nonlocal FD scheme when $N = 2$ (with index q for discretized time domain)

$$\frac{T_i^{q+1} - T_i^q}{\Delta t} = \frac{\alpha}{a^2} \left(-\frac{1}{4} T^q_{i-2} + 2T^q_{i-1} - \frac{7}{2} T^q_{i} + 2T^q_{i+1} - \frac{1}{4} T^q_{i+2} \right) \tag{22}$$

First, a theoretical spatial partial derivative for the *i*-th DOF is calculated, which takes the form

$$\left. \frac{\partial^2 T(x,t)}{\partial x^2} \right|_{x = x_i = ia} = T_i(t) \frac{i^2 a^2 - 2t}{4t^2} \tag{23}$$

which, in turn, converges for $a \to 0$ to

$$\lim_{a \to 0} T_i(t) \frac{i^2 a^2 - 2t}{4t^2} = -\frac{T_0}{2t^{(n+2)/2}} \tag{24}$$

Then, the respective derivative for the numerical case may be found from the expression

$$\frac{\partial^2 T_i(t)}{\partial x^2} = \frac{1}{a^2} \left(-\frac{1}{4} T_{i-2}(t) + 2T_{i-1}(t) - \frac{7}{2} T_i(t) + 2T_{i+1}(t) - \frac{1}{4} T_{i+2}(t) \right) \tag{25}$$

After: (i) substitution the quantities $T_{i\pm j}(t)$ in Eq. (25) using Eq. (21) and (ii) application of the Taylor series theory to the derived exponential expressions, the derivative $\frac{\partial^2 T_i(t)}{\partial x^2}$ in Eq. (25)

reaches the limit calculated in Eq. (23). This confirms the convergence of the proposed spatial nonlocal FD scheme in diffusion equation. For the time domain a standard forward Euler method is used, as shown in Eq. (22).

Finally, von Neumann stability analysis is carried out to derive stability condition for the exemplary scheme (22), which considers $N = 2$. The condition is found to be

$$\left|1 + r\left(-\frac{1}{2}\cos(2\beta) + 4\cos(\beta) - \frac{7}{2}\right)\right| \le 1 \text{ with } r = \alpha\frac{\Delta t}{a^2} \text{ and } \beta = \kappa a \tag{26}$$

Condition (26) may by transformed to the final form

$$\alpha\Delta t / a^2 \le 1/4 \tag{27}$$

Hence, the scheme (22) is stable if the time step Δt does not exceed $a^2/(4\alpha)$.

5. Applications – numerical cases for diffusion equation

A straightforward 1-D model is taken into account to show capabilities of the proposed FD schemes for the diffusion equation – including the example defined by Eq. (23). Thermal conductivity mechanism in a 30cm-long aluminum rod is under study. The material properties are: k = 200W/(mK), ρ =2100kg/m^2, c_p =900J/(kgK). Arbitrarily chosen temperature initial condition is presented in Fig. 1(a). Fig. 1(b) shows temperature distributions captured in the model after t =1.4s.

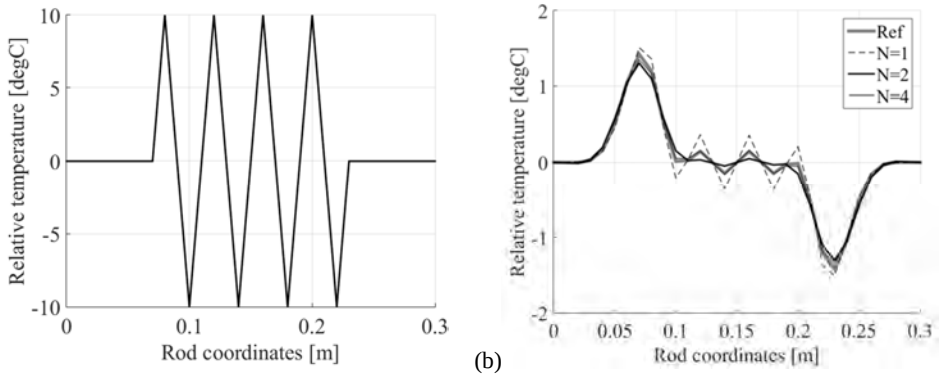

(a) (b)

Figure 1. Numerical simulations for thermal diffusion in a 1-D model of an aluminum rod: (a) initial temperature distribution, (b) temperature distribution for various order of nonlocality N including the referential plot.

The total errors (i.e. absolute errors summed for all DOFs) decrease as the order of nonlocality N increases. These errors equal: 2.22degC ($N = 1$), 1.56degC ($N = 2$) and 0.77degC ($N = 4$).

Various meshes are also used for transient analyses. As confirmed by the obtained results, as an example, a four-time denser mesh (i.e. with four times smaller a equaled to 0.0025m), which is applied with a local approach when $N=1$, may compete with a nonlocal scheme built for $N=4$ (considering the model exhibiting a crude mesh - with the distance between DOFs a =0.01m), i.e. it may provide more accurate results, i.e. of smaller total error - 0.0869degC. Similarly, the local case of a =0.005m with the total error 1.1617degC corresponds to the nonlocal case characterizing a =0.01m and $N=2$ (with total error - 1.56degC). This model behavior justifies the usage of rather crude mesh considering nonlocal interactions. One may take an advantage of less memory occupation and faster calculations due to considerable smaller number of DOFs in the model. Hence, less populated domains of spatially distributed model's DOFs may be also taken into account.

6. Summary and concluding remarks

The work presents efficient FD based nonlocal schemes dedicated for solving dynamic problems governed by second-order PDEs. Specifically, diffusion equation is of concern. The theory of the elaborated approach is illustrated with exemplary results showing its capabilities.

The following conclusions should be highlighted regarding applicability of the present work. First of all, as confirmed with the results, less dense meshes may be applied in numerical models - accompanied by the proposed nonlocal problem statements - without any noticeable loss of quality. This issue may be critical for the models with complicated geometry or topology, in case when computer resources are limited. Second, within the same spatial discretization used, more accurate results may be achieved by increasing the order of nonlocality. Mitigation rate for numerical dispersion increases while introduction more and more long-range interaction terms into the FD scheme.

The elaborated schemes present a general approach to the techniques of model discretization. In the authors' opinion, they are capable of solving other types of problems for various physical domains described by PDEs. In fact, based on the presented theory, it seems possible to increase the scope of possible applications for the investigated theory, which is considered by the authors as future work.

Acknowledgments

This work has been supported by the AGH University of Science and Technology, WIMiR, research grant no. 11.11.130.560.

References

[1] Kröner, E. Elasticity theory of materials with long range cohesive forces. *International Journal of Solids and Structures* 3 (1967), 731-742.

[2] Kunin, I.A. Inhomogeneous elastic medium with non-local interactions. *Journal of Applied Mechanics and Technical Physics* 8, 3 (1967), 60-66.

[3] Chen, Y., Lee, J.D., and Eskandarian, A. Atomistic viewpoint of the applicability of microcontinuum theories. *International Journal of Solids and Structures* 41 (2004), 2085-2097.

[4] Di Paola, M., Pirrotta, A., and Zingales, M. Mechanically-based approach to non-local elasticity: Variational principles. *International Journal of Solids and Structures* 47 (2010), 539-548.

[5] Eringen, A.C., and Edelen, D.G.B. On nonlocal elasticity. *International Journal of Engineering Science*, 10 (1972), 233-248.

[6] Kaliski, S., Rymarz, C., Sobczyk, K. and Włodarczyk, E. *Vibrations and waves, Part B: Waves. Studies in Applied Mechanics 30B*, Elsevier, Amsterdam – London – New York – Tokyo, PWN – Polish Scientific Publishers, Warsaw, (1992).

[7] Martowicz, A. On nonlocal modeling in continuum mechanics. *Mechanics and Control* 34, 2 (2015), 41-46.

[8] Rodrıguez-Ferran, A., Morata, I., and Huerta, A. Efficient and reliable nonlocal damage models. *Computer Methods in Applied Mechanics and Engineering* 193 (2004), 3431-3455.

[9] Martowicz, A., Ruzzene, M., Staszewski, W.J., and Uhl, T. Non-local modeling and simulation of wave propagation and crack growth. *AIP Conference Proceedings*, AIP Publishing 1581, 513 (2014), 513-520.

[10] Martowicz, A., Staszewski, W.J., Ruzzene, M., and Uhl, T. Vibro-acoustic wave interaction in cracked plate modeled with peridynamics. *Proc. of the Conference WCCM XI, ECCM V, ECFD VI*; Onate E., Oliver X., Huerta (eds.), International Center for Numerical Methods in Engineering, Barcelona, Spain, (2014), 4021-4027.

[11] Yang, D., Tong, P., and Deng, X. A central difference method with low numerical dispersion for solving the scalar wave equation. *Geophysical Prospecting* 60 (2012), 885-905.

[12] Martowicz, A. Peridynamics for damage modelling and propagation via numerical simulations. *Diagnostyka* 18, 1 (2017), 73-78.

[13] Bazant, Z.P., and Jirasek, M. Nonlocal Integral Formulations of Plasticity and Damage: Survey of Progress. *Journal of Engineering Mechanics* 128, 11 (2002), 1119-1149.

[14] Zhang, L.L., Liu, J.X., Fang, X.Q., and Nie G.Q. Effects of surface piezoelectricity and nonlocal scale on wave propagation in piezoelectric nanoplates. *European Journal of Mechanics – A/Solids* 46 (2014), 22-29.

[15] Chang, D.M., and Wang, B.L. Surface thermal shock cracking of a semi-infinite medium: a nonlocal analysis. *Acta Mechanica* 226 (2015), 4139-4147.

[16] Silling, S.A. Reformulation of elasticity theory for discontinuities and long-range forces. *Journal of the Mechanics and Physics of Solids* 48 (2000), 175–209.

[17] Martowicz, A., Kijanka, P., and Staszewski, W.J. A semi-nonlocal numerical approach for modeling of temperature-dependent crack-wave interaction. SPIE Smart Structures and Materials + Nondestructive Evaluation and Health Monitoring, Las Vegas, Nevada, United States, *Proc. SPIE Vol.* 9805, *Health Monitoring of Structural and Biological Systems* (2016), 980515; doi: 10.1117/12.2219148.

[18] Badnava, H., Kadkhodaei, M., and Mashayekhi, M. A non-local implicit gradient-enhanced model for unstable behaviors of pseudoelastic shape memory alloys in tensile loading. *International Journal of Solids and Structures* 51, 23-24 (2014), 4015-4025.

[19] Arash, B., Wang, Q., Liew, K.M. Wave propagation in graphene sheets with nonlocal elastic theory via finite element formulation. *Computer Methods Applied Mechanics and Engineering* 223–224 (2012), 1-9.

[20] Martowicz, A., Staszewski, W.J., Ruzzene, M., and Uhl, T. Peridynamics as an analysis tool for wave propagation in graphene nanoribbons. SPIE Smart Structures and Materials + Nondestructive Evaluation and Health Monitoring, San Diego, California, United States, *Proc. SPIE Vol. 9435, Sensors and Smart Structures Technologies for Civil, Mechanical, and Aerospace Systems*, (2015); 94350I; doi: 10.1117/12.2084312.

[21] Martowicz, A., Ruzzene, M., Staszewski, W.J., Rimoli, J.J., and Uhl, T. Out-of-Plane Elastic Waves in 2D Models of Solids: A Case Study for a Nonlocal Discretization Scheme with Reduced Numerical Dispersion. *Mathematical Problems in Engineering* (2015), Article ID 584081.

[22] Martowicz, A., Ruzzene, M., Staszewski, W.J., Rimoli, J.J., and Uhl, T., A nonlocal finite difference scheme for simulation of wave propagation in 2D models with reduced numerical dispersion. SPIE Smart Structures and Materials + Nondestructive Evaluation and Health Monitoring, San Diego, California, United States, *Proc. SPIE Vol. 9064, Health Monitoring of Structural and Biological Systems*, (2014); 90640F; doi: 10.1117/12.2045252.

[23] Bobaru, F., Yang, M., Alves, L.F., Silling, S.A., Askari, E., and Xu, J. Convergence, adaptive refinement, and scaling in 1D peridynamics. *International Journal for Numerical Methods in Engineering* 77 (2009), 852–877.

[24] Duruk, N., Erbay, H.A., and Erkip, A. Global existence and blow-up for a class of nonlocal nonlinear Cauchy problems arising in elasticity. *Nonlinearity* 23 (2010), 107-118.

[25] Eringen, A.C. Vistas of nonlocal continuum physics. *International Journal of Engineering Science* 30, 10 (1992), 1551-1565.

[26] Zingales, M. Wave propagation in 1D elastic solids in presence of long-range. *Journal of Sound and Vibration* 330 (2011), 3973-3989.

[27] Nishawala, V.V., Ostoja-Starzewski, M., Leamy, M.J., and Demmie, P.N. Simulation of elastic wave propagation using cellular automata and peridynamics, and comparison with experiments. *Wave Motion* 60 (2016), 73-83.

[28] Evans, L.C. *Partial Differential Equations.* American Mathematical Society, (1998).

Adam Martowicz, Ph.D.: AGH University of Science and Technology, Department of Robotics and Mechatronics, al. A. Mickiewicza 30, 30-059 Krakow, Poland (adam.martowicz@agh.edu.pl). The author gave a presentation of this paper during one of the conference sessions.

Wieslaw J. Staszewski, Professor: AGH University of Science and Technology, Department of Robotics and Mechatronics, al. A. Mickiewicza 30, 30-059 Krakow, Poland (staszews@agh.edu.pl).

Massimo Ruzzene, Professor: Georgia Institute of Technology, School of Aerospace Engineering, School of Mechanical Engineering, 270 Ferst Drive, GA 30332, Atlanta, USA (ruzzene@gatech.edu).

Tadeusz Uhl, Professor: AGH University of Science and Technology, Department of Robotics and Mechatronics, al. A. Mickiewicza 30, 30-059 Krakow, Poland (tuhl@agh.edu.pl).

On solutions of biharmonic problems

Hovik Matevossian, Michail Nikabadze, Armine Ulukhanian

Abstract: For solving biharmonic problems with application to radar imaging, we need to solve boundary value problems for the Poisson equation using the scattering model. In addition, no information about boundary values is available. In order to select suitable solutions, we solve the Poisson equation under the side condition that some criterion function, usually a Sobolev norm, should be minimized. Under appropriate smoothness assumptions these problems may be reformulated as boundary value problems for the biharmonic equation.

1. Introduction

Let $\Omega \subset \mathbb{R}^n$, $n \geq 2$, be a bounded Lipschitz domain with connected boundary $\partial\Omega$, and $\Omega \cup \partial\Omega = \overline{\Omega} =$ is the closure of Ω. We consider the following boundary value problems for the biharmonic equation in Lipschitz domains:

$$\Delta^2 u(x) = f(x), \qquad x \in \Omega \tag{1}$$

with the Navier boundary conditions

$$u = g, \quad Mu \equiv \sigma\Delta u + (1-\sigma)\frac{\partial^2 u}{\partial \nu^2} = h_1, \quad \text{on} \quad \partial\Omega, \tag{2}$$

or the Neumann boundary conditions

$$Mu \equiv \sigma\Delta u + (1-\sigma)\frac{\partial^2 u}{\partial \nu^2} = h_1,$$

$$Nu \equiv \frac{\partial \Delta u}{\partial \nu} + (1-\sigma)\,\mathrm{div}_{\partial\Omega}(\partial^2 u \cdot \nu)_{\partial\Omega} = h_2, \quad \text{on} \quad \partial\Omega, \tag{3}$$

where ν is the outward unit normal to $\partial\Omega$, and $\frac{1}{n-1} < \sigma < 1$, σ is a constant known as the Poisson ratio. A unique solution u (modulo linear functions) is obtained in the class of solutions with non-tangential maximal function of the second-order derivatives in $L^p(\partial\Omega)$. The corresponding Poisson problem is well-posed unless $\sigma = 1$.

Note that standard elliptic regularity results are available in [3]. This monograph covers higher order linear and nonlinear elliptic boundary value problems, mainly with the biharmonic or polyharmonic operator as leading principal part. Underlying models and, in particular, the role of different boundary conditions are explained in detail. As for linear problems, after a brief summary of the existence theory and L^p and Schauder estimates, the focus is on positivity. The required kernel estimates are also presented in detail.

Boundary value problems for a biharmonic (polyharmonic) equation in unbounded domains are studied in [7]– [12], in which the condition of the boundedness of the following weighted Dirichlet integral of solution is finite, namely

$$\int_\Omega |x|^a |\partial u|^2 \, dx < \infty, \quad a \in \mathbb{R},$$

where $a \in \mathbb{R}$ is a fixed number and $|\partial u|^2$ denotes the Frobenius norm of the Hessian matrix of u. The author in [7]– [12] investigates the dimension of the space of the solutions to the boundary value problems for a biharmonic (polyharmonic) equation, providing explicit formulas which depends on n and a.

Elliptic problems with parameters in the boundary conditions are called Steklov problems from their first appearance in [18]. In the case of the biharmonic operator, these conditions were first considered in [1], [6] and [16], who studied the isoperimetric properties of the first eigenvalue.

In [2] the boundary value problems for the biharmonic equation and the Stokes system are studied in a half space, and, using the Schwartz reflection principle in weighted L^q -space the uniqueness of solutions of the Stokes system or the biharmonic equation is proved.

Notation: $C_0^\infty(\Omega)$ is the space of infinitely differentiable functions in Ω with compact support in Ω; $H^m(\Omega)$ is the Sobolev space obtained by the completion of $C^\infty(\overline{\Omega})$ with respect to the norm

$$\|u(x); H^m(\Omega)\| = \left(\int_\Omega \sum_{|\alpha| \le m} |\partial^\alpha u(x)|^2 dx \right)^{1/2}, \; m = 1, 2,$$

where $\partial^\alpha \equiv \frac{\partial^{|\alpha|}}{\partial x_1^{\alpha_1} \ldots \partial x_n^{\alpha_n}}$, $\alpha = (\alpha_1, \ldots, \alpha_n)$ is a multi-index, $\alpha_i \ge 0$ are integers, and $|\alpha| = \alpha_1 + \cdots + \alpha_n$;

$\overset{\circ}{H}{}^m(\Omega)$ is the space obtained by the completion of $C_0^\infty(\Omega)$ with respect to the norm $||u(x); H^m(\Omega)||$;

Definition 1 *A solution of the homogenous biharmonic equation* (1) *in* Ω *is a function* $u \in H^2(\Omega)$ *such that for every function* $\varphi \in C_0^\infty(\Omega)$*, the following integral identity holds:*

$$\int_\Omega \Delta u \, \Delta\varphi \, dx = \int_\Omega f \, \varphi \, dx.$$

In Section 2 we will derive the mathematical model used for describing the radar process. In our parametrization the unknown is the height function H. As will be shown in Section 2 the height function is determined in two steps. In the first step $\mathfrak{L}(H)$, with $\mathfrak{L}$ a certain second-order differential operator, is determined. After retrieving H the equation $\mathfrak{L}(H) = f$ must be solved. To a good approximation the operator $\mathfrak{L}$ can be replaced by the Laplacian. So the second step simply consists of solving the Poisson equation over some smooth bounded domain, usually a rectangular region in the plane. The problem here is that no natural boundary conditions are available.

In Section 3 we discuss different possibilities of defining a unique height function. Essentially our approach consists in minimizing some norm of the solution provided that it also satisfies the Poisson equation. In particular we consider the L^2- and H^1-norms. We also show how these two optimization problems may be reformulated as boundary value problems for the biharmonic equation.

As applications, in [14], the eigenvalue problems of the symmetric tensor-block matrix of any even rank and sizes 2×2 is studied. Some definitions and theorems are formulated concerning the tensor-block matrix. Formulas expressing the classical invariants of the tensor-block matrix of any even rank and sizes 2×2 through the first invariants of the powers of this tensor-block matrix are given. As a special case, we consider the tensor-block matrix of the elastic modulus tensors. The canonical representation of the tensor-block matrix is given. Using this representation, we get the canonical forms of the elastic strain energy and the constitutive relations. Besides, a classification of the micropolar linear elastic anisotropic bodies that do not have a center of symmetry is given. In [15], some questions about the parametrization of three-dimensional thin body with one small size under an arbitrary base surface and the changing of transverse coordinate from 1 to 1 are considered. The vector parametric equation of the thin body domain is given. In particular, we have defined the various families of bases and geometric characteristics generated by them.

2. A scattering model

Here we will briefly discuss the mathematical inverse problem to be resolved in order to recover the ground topography height function from radar data. First cylindrical coordinates (r, φ, z) are introduced according to Fig. 1, where it is understood that the aircraft is flying at a constant speed along the z-axis. Further r denotes the distance from a point on the

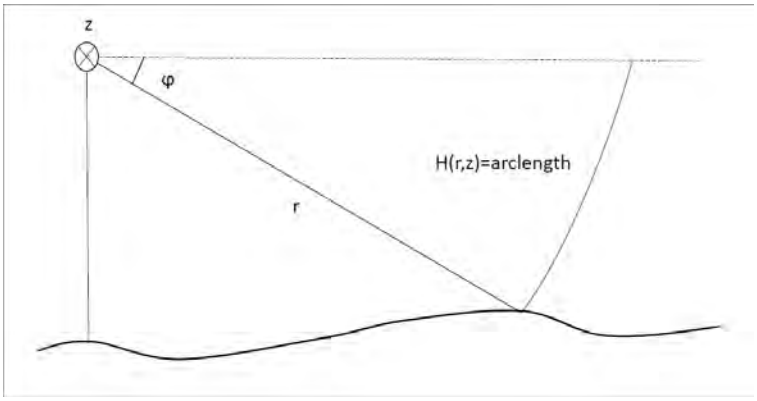

Figure 1. The ground surface measured at a fixed aircraft position.

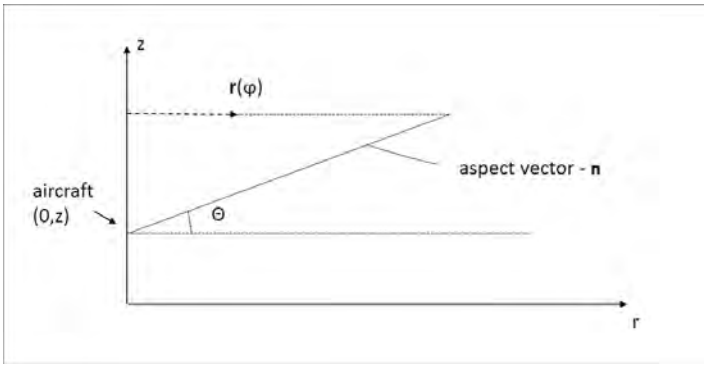

Figure 2. The measuring geometry as seen from above.

ground surface to the z-axis and φ is the angle between radius vector and a horizontal plane through the z-axis. Then the ground surface may be described by a function $H(r, z)$ through the equation

$$\frac{H(r,z)}{r} - \varphi = 0. \tag{4}$$

When r is large, $-H(r, z)$ is approximately a Cartesian height function. Fig. 2 shows a top view of the same scene. We have also indicated an aspect vector from the aircraft to some point on the ground, forming an angle θ with a vertical plane through the aircraft. Normalized to unit length, the aspect vector is denoted by $\hat{n}$.

Accordingly

$$\hat{n} = \cos\theta\,\hat{r}(\varphi) + \sin\theta\,\hat{z}. \tag{5}$$

Here $\hat{r}(\varphi)$ denotes the cylindrical unit basis vector corresponding to the r-coordinate for the ground point as shown in the Fig. 2. For a point on the ground surface with coordinates (r, φ, z) we obtain, from Eq. (4), the following expression for the ground surface normal $\bar{m}$,

$$\bar{m} = grad\left(\frac{H(r,z)}{r} - \varphi\right) = \frac{\partial(H/r)}{\partial r}\hat{r} + \frac{1}{r}\frac{\partial H}{\partial z}\hat{z} - \frac{1}{r}\hat{\varphi}. \tag{6}$$

Let $\hat{m}$ denote the normalized normal. Then

$$\hat{m} \circ \hat{n} = \left(r\cos\theta\frac{\partial(H/r)}{\partial r} + \sin\theta\frac{\partial H}{\partial z}\right) / \sqrt{1 + \left(\frac{\partial(H/r)}{\partial r}\right)^2 + \left(\frac{\partial H}{\partial z}\right)^2}. \tag{7}$$

Note that (r, φ, z) in Eq. (7) are related to the ground surface point and not to the position of the aircraft.

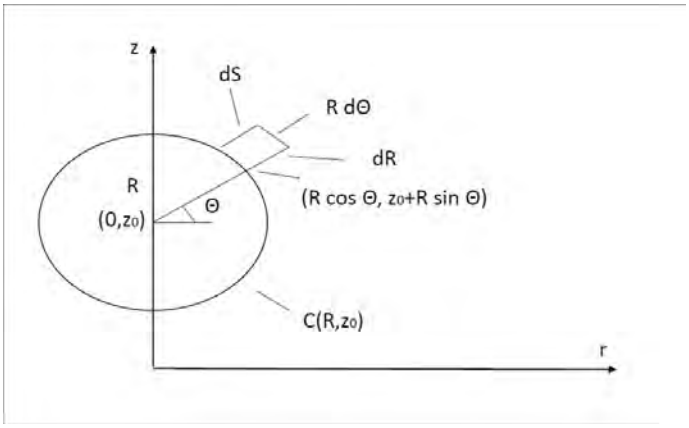

Figure 3. The coordinate system used to describe an infinitesimal surface element, dS.

Let $(z_0, 0)$ be a position of the aircraft and R the distance to some point on the surface. According to Fig. 3 the coordinates (r, z) are then equal to $(z_0 + R\sin\theta, R\cos\theta)$. Next, to obtain a scattering model we will assume that the reflectivity from a ground surface element (see Fig. 4) is

$$\approx \frac{\hat{m} \circ \hat{n}}{R} dR\, d\theta. \tag{8}$$

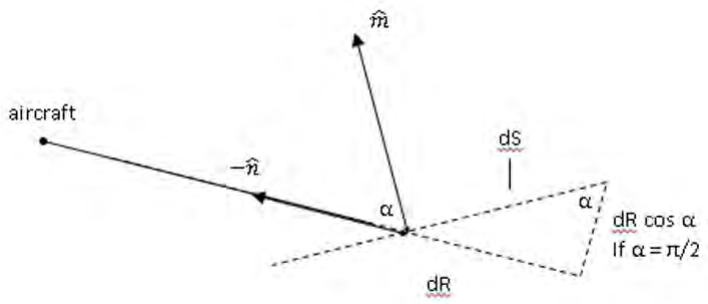

Figure 4. The infinitesimal surface element, dS, as it is seen from the aircraft.

From Fig. 4, where a vertical plane through $(z_0, 0)$ (the aircraft) and the ground point $(z_0 + R\sin\theta, R\cos\theta)$ is displayed, we conclude that the solid angle $d\Omega$ under which the surface element dS is seen from the antenna is approximately

$$\frac{dR\,\cos\alpha\, R d\,d\theta}{R^2} = -\frac{\hat{m}\circ\hat{n}}{R} dR\,d\theta.$$

In expression (8) we are consequently assuming that the local reflectivity is proportional to the solid angle occupied by the infinitesimal surface element dS. The total reflected signal $G(R, z_0)$

from all points at a distance R from the antenna may now be obtained by integration over the circle $C(R, z_0) = \{(r, z) : (z - z_0)^2 + r^2 = R^2\}$ in Fig. 3.

$$G(R, z_0)dR = c\int_{-\pi}^{\pi} \frac{\hat{m}\circ\hat{n}(z_0 + R\cos\theta, R\sin\theta)}{R} d\theta dR$$

i.e.

$$RG(R, z_0) = c\int_{-\pi}^{\pi} \hat{m}\circ\hat{n}(z_0 + R\cos\theta, R\sin\theta)d\theta. \tag{9}$$

Assuming that $\hat{m}\circ\hat{n}$ is small Eq. (7) may be replaced by

$$\hat{m}\circ\hat{n} = r\cos\theta\frac{\partial(H/r)}{\partial r} + \sin\theta\frac{\partial H}{\partial z}.$$

By inserting this into Eq. (9) we get, after multiplying by R,

$$R^2G(R, z_0) = c\int_{-\pi}^{\pi} \big(rR\cos\theta\frac{\partial(H/r)}{\partial r} + R\sin\theta\frac{\partial H}{\partial z}\big)d\theta.$$

Using the parametrization

$$z = z_0 + Rsin\theta, \quad r = Rcos\theta,$$

this may be rewritten as a curve integral over $C(R, z_0)$, with $dz = R\cos\theta d\theta$ and $dr = -R\sin\theta d\theta$,

$$R^2 G(R, z_0) = c \int_{C(R,z_0)} \big(r\frac{\partial(H/r)}{\partial r}dz - \frac{\partial H}{\partial z}dr\big). \tag{10}$$

By applying Green's formula we get

$$R^2 G(R, z_0) = c \iint_{D(R,z_0)} \mathfrak{L}(H)(r, z)dzdr, \tag{11}$$

where D is the disc, $D(R, z_0) = \{(r, z) : (z - z_0)^2 + r^2 \leq R^2\}$ and

$$\mathfrak{L}(H) = \frac{\partial}{\partial r}\big(r\frac{\partial}{\partial r}(H/r)\big) + \frac{\partial^2}{\partial z^2}(H). \tag{12}$$

The problem of finding the height function H from radar data $G(r, z)$ may now be divided into two parts.

(a) First solve the integral equation (11) for $\mathfrak{L}(H)(r, z) = f(r, z)$.

(b) Next solve the partial differential equation

$$\mathfrak{L}(H) = f \tag{13}$$

for H. We note that if r is large and if $\hat{m} \circ \hat{n}$ is small it is reasonable to make the approximation

$$\mathfrak{L}(H) \approx \frac{\partial^2 H}{\partial r^2} + \frac{\partial^2 H}{\partial z^2} = \Delta H$$

so that Eq. (13) becomes Poisson's equation. To consider the first problem (a), both members in Eq. (11) are differentiated with respect to R. Then we get

$$\frac{1}{R}\frac{d}{dR}(R^2 G(R, z_0)) = c \int_{-\pi}^{\pi} \mathfrak{L}(H)(z_0 + R\cos\nu, R\sin\nu)d\nu,$$

where the right-hand side is proportional to the average of $\mathfrak{L}(H)$ over the circle $C(R, z_0)$. In [2] an explicit solution is given for this problem of recovering the function $\mathfrak{L}(H)(r, z)$ when the average of $\mathfrak{L}(H)$ is known for all circles $C(R, z_0)$ with center on the z-axis and with arbitrary radius R. The solution formula is

$$\mathfrak{L}(H)^{(F,F)}(\sigma, \omega) \sim |\omega|\big[\frac{1}{R}\frac{d}{dR}\{R^2 G(r, z)\}\big]^{(F,H_0)}(\sigma, \sqrt{\omega^2 + \sigma^2}). \tag{14}$$

Here the notation (F, F) means that we have taken the Fourier transform with respect to both the variables and (F, H_0) means that we have taken Fourier transform with respect

to the first variable and the Hankel-zero transform with respect to the second. After some calculations Eq. (14) may be rewritten

$$\mathfrak{L}(H)^{(F,F)}(\sigma,\omega) \sim |\omega|\sqrt{\omega^2+\sigma^2}[RG(r,z)]^{(F,H_1)}(\sigma,\sqrt{\omega^2+\sigma^2}). \tag{15}$$

Formula (15) may now be used in order to recover the function $\mathfrak{L}(H)$ in spatial coordinates. Of course, approximating $\mathfrak{L}(H)$ by ΔH we could rewrite Eq. (15) as

$$H^{(F,F)}(\sigma,\omega) \sim |\omega|\frac{1}{\sqrt{\omega^2+\sigma^2}}[RG(r,z)]^{(F,H_1)}(\sigma,\sqrt{\omega^2+\sigma^2}), \tag{16}$$

where H_1 denotes that we have taken the Hankel-one transform with respect to the second variable. Then we could obtain H directly by a two timensional Fourier transform. However, our solution might be expected to have errors caused by, e.g. noisy radar data and errors caused by the particular numerical implementation of the inversion formula (14) (or Eq. (15)) and therefore we would rather prefer to divide the solution procedure into the two steps described above and to use the second step, the solution of Poisson's equation, so that we perform some kind of regularization of the final solution. Note also that by using Eq.(16) as our solution formula we have tacitly assumed periodic boundary conditions for the Poisson equation.

3. Solution concepts for the Poisson equation

In the domain Ω we consider the following boundary value problems for the Poisson equation

$$\Delta u = f(x), \quad x \in \Omega \tag{17}$$

with the boundary conditions

$$u = g \quad \text{on} \quad \partial\Omega, \tag{18}$$

and

$$u = g, \quad \nabla u \cdot \nu = h \quad \text{on} \quad \partial\Omega \tag{19}$$

Finally for Ω a rectangular region in, e.g., the plane

$$\Omega = \{(x,y) : a < x < b,\, c < y < d\}, \tag{20}$$

there may be the following boundary conditions

$$u(a,y) = u(b,y), \quad u(x,c) = u(x,d), \tag{21}$$

and

$$\begin{cases} u(a,y) = u(b,y), \quad u(x,c) = u(x,d), \\ u_x(a,y) = u_x(b,y), \quad u_y(x,c) = u_y(x,d) \end{cases} \tag{22}$$

Lemma 1 *Let u and w be solutions of Eq.* (17) *satisfying the Dirichlet boundary conditions* (18) *with $g = g_1$ abd $g = g_2$, respectively. Assume $f \in C(\Omega)$, g_1, $g_2 \in C(\partial\Omega)$ and that $\partial\Omega$ is Lipschitz. Then*

$$||u - w||_{\infty,\Omega} \leq ||g_1 - g_2||_{\infty,\partial\Omega}.$$

Hence the Dirichlet problem is well posed in the sence that small pertutbations in the boundary values result in small perturbations in the solution.

We now consider a different way to select a solution to Eq. (17). Here we use a criterion function and optimize this criterion over the set of solutions to the Poisson equation. As discussed in Section 2 the physical interpretation of $u(x, y)$ is a surface function. A possibility is to pick out the smoothest surface (in some sense) that fulfills Eq. (17). We propose to use Sobolev space norms as criterion functions. Denote by $V_{f,i}$ the following set:

$$V_{f,i} = \{u \in H^i(\Omega) : \quad \Delta u = f, \ f \in L^2(\Omega)\}, \quad i = 0, 1, 2, \tag{23}$$

where $H^0(\Omega) = L^2(\Omega)$.

The equality $\Delta u = f$ is to be interpreted in the sense of distributions. i.e.,

$$\int_\Omega u \, \Delta\varphi \, dx = \int_\Omega f\varphi \, dx, \quad \forall\varphi \in C_0^\infty(\Omega).$$

Lemma 2 *$V_{f,i}$ is a closed, convex and nonempty set of $H^i(\Omega)$.*

Let α be a multiindex and $\beta_1 > 0$ a given parameter. We consider the following optimization problems:

$$min_{u \in V_{f,0}} ||u||_2^2, \tag{24}$$

and

$$min_{u \in V_{f,1}} ||u||_2^2 + \beta_1 \sum_{|\alpha|=1} ||\partial^\alpha u||_2^2. \tag{25}$$

Theorem 1 *Problems* (24) *and* (25) *have unique solutions u_0 and u_1 respectively.*

We conclude this section by a theorem relating the solution of problems (24) and (25). First we recall the following definition.

Definition 2 *$\Omega \subset \mathbb{R}^n$ is called star-shapet if there exists $x_0 \in \Omega$ such that for all $x \in \Omega$ the set $\{t \in \mathbb{R} : \quad x_0 + t(x - x_0) \in \Omega\}$ is an interval.*

Remark 1 *All convex sets are star-shaped. Rectangles Ω appearing in our applications are thus star-shaped.*

Theorem 2 *Assume that $\Omega \subset \mathbb{R}^n$ is open, bounded and star-shaped. If $u_{1,\beta_1} \in H^1(\Omega)$ denotes the solution of problem (25) with the parameter $\beta_1 > 0$ and if $u_0 \in L^2(\Omega)$ denotes the solution of problem (24), then*

$$u_{1,\beta_1} \to u_0 \quad in \quad L^2(\Omega) \quad as \quad \beta_1 \to 0+ .$$

Acknowledgments

This work was supported by Shota Rustaveli National Science Foundation (project no. DI-2016-41) and the Russian Foundation for Basic Research (project no. 15-01-00848-a).

References

[1] Brock, F. An isoperimetric Inequality for Eigenvalues of the Stekloff Problem. *ZAMM Z. Angew. Math. Mech.*, 81(1) (2001), 69–71.

[2] Farwig, F. A note on the reflection principle for the biharmonic equation and the Stokes system. *Acta Appl. Math.*, 34(1–2) (1994), 41–51.

[3] Gazzola, F., Grunau, H.-Ch., and Sweers, G. *Polyharmonic Boundary Value Problems: Positivity Preserving and Nonlinear Higher Order Elliptic Equations in Bounded Domains*. Lecture Notes Math., **1991**, Springer, 2010.

[4] Kondratiev, V. A., and Oleinik, O. A. Boundary value problems for the system of elasticity theory in unbounded domains. Korn's inequalities. *Russ. Math. Surveys*, 43(5) (1988), 65–119.

[5] Kondratiev, V. A., and Oleinik, O. A. Hardy's and Korn's inequality and their application. *Rend. Mat. Appl., Serie* VII, 10(1990), 641–666.

[6] Kuttler, J. R., and Sigillito, V. G. Inequalities for membrane and Stekloff eigenvalues. *J. Math. Anal. Appl.*, 23(1) (1968), 148–160.

[7] Matevossian, O. A. The exterior Dirichlet problem for the biharmonic equation: solutions with bounded Dirichlet integral. *Math. Notes*, 70(3) (2001), 363–377.

[8] Matevossian, O. A. Solution of a mixed boundary value problem for the biharmonic equation with finite weighted Dirichlet integral. *Diff. Equations*, **51**(4) (2015), 487–501.

[9] Matevossian, O. A. On solutions of the Neumann problem for the biharmonic equation in unbounded domains. *Math. Notes*, 98(6) (2015), 990–994.

[10] Matevossian, O. A. On solutions of the mixed Dirichlet–Navier problem for the polyharmonic equation in exterior domains. *Russ. J. Math. Phys.*, 23(1) (2016), 135–138.

[11] Matevossian, O. A. On solutions of one boundary value problem for the biharmonic equation. *Differ. Equation*, 52:10 (2016), 1379–1383.

[12] Matevossian, O. A. On the biharmonic Steklov problem in weighted spaces. *Russ. J. Math. Phys.*, 24(1) (2017), 134–138.

[13] Morrey, C. B. *Multiple Integrals in the Calculus Variations.* Springer Verlag, 1966.

[14] Nikabadze, M. U. Eigenvalue problems of a tensor and a tensor-block matrix (TMB) of any even rank with some applications in mechanics. H. Altenbach and S. Forest (eds.), *Generalized continua as models for classical and advanced materials, advanced structured materials*. 42, 2016. 279-317. DOI 10.1007/978-3-319-31721-2_14

[15] Nikabadze, M. U., and Ulukhanyan, A. R. Analytical solutions in the theory of thin bodies. H. Altenbach and S. Forest (eds.), *Generalized continua as models for classical and advanced materials, advanced structured materials.* 42, 2016. 319-361. DOI 10.1007/978-3-319-31721-2_15

[16] Payne, L. E. Some isoperimetric inequalities for harmonic functions. *SIAM J. Math. Anal.*, 1(3) (1970), 354–359.

[17] Sobolev, S. L. *Some Applications of Functional Analysis in Mathematical Physics*, 3rd ed. Nauka, Moscow 1988; *Applications of Functional Analysis in Mathematical Physics*, AMS Providence 1991.

[18] Stekloff, W. Sur les problèmes fondamentaux de la physique mathématique, *Annales Sci. de l'E.N.S.*, 3^e *série*, 19 (1902), 191–259 et 455–490.

Hovik Matevossian, Ph.D.: Russian Academy of Sciences, Federal Research Center "Computer Science and Control", Vavilova str., 40, Moscow 119333, Russia, & Moscow Aviation Institute (National Research University), Volokolomskoe Shosse, 4, Moscow 125993, Russia.

(*hmatevossian@graduate.org*). The author gave a presentation of this paper during one of the conference sessions.

Mikhail Nikabadze, Ph.D.: Lomonosov Moscow State University, Department of Mechanics and Mathematics, Leninskie Gory, 1, Moscow 119992, Russia, & Bauman Moscow State Technical University, Baumanskaya 2-ya, str., 5, Moscow 105005 (*nikabadze@mail.ru*).

Armine Ulukhanian, Ph.D.: Bauman Moscow State Technical University, Baumanskaya 2-ya, str., 5, Moscow 105005, Russia (*armine_msu@mail.ru*).

Computer model of ground under vehicle's wheels

Tomasz Mirosław

Abstract: In this paper author presents new approach to modeling ground behavior under pressure of a vehicle's wheel. The ground under the wheel is deformed by compression and displacement in vertical and horizontal direction. Some layer direct under tire is abraded, torn and transported by the wheel. The pressure of the tire causes deformation which grows with increasing of rolling resistance. The model of ground behavior, especially for multi-axle off road vehicle, is very important for traction calculation. This model is nonlinear. The running process of ground transformation depends on forces, acceleration and time and frequencies repeating stresses. In the presented model the ground is divided into cubes/cells which are deformed and transform their density and features. Deformed cubic effects its neighbors and cause their deformation and forces inside them. The pressed cube in first stage is displaced, if it's movement is blocked cube is deformed and if it is still pressed it is transformed to another form of its substance changing its physical properties and features. The presented model can also be applied to crushing stones and calculating swimming resistance in the water.

1. Introduction

The biggest invention in transport – the wheel is known for more than 5000 years. But we still are looking for ideal model which can describe all cases of its behaviour on the road surface. These models are necessary for transport means designing. They concern the railways, road and off-road transportation or vehicles and mobile machineries. We all know how important wheel is for efficiency and safety of transport. We spend billions of Euro for tires, hard (asphalt or concrete) roads to make the human and goods transport faster and safer.

But the great part of human activity is off-road. It refers to the construction machinery working on the pristine ground or agriculture machinery passing fields. For terrain vehicles generally two kinds of propelling systems can be mentioned as the main types: wheeled and track.

Both have some advantages and disadvantages but for them both, the cooperation with ground is the most important thing. For both drives we need to know how to describe processes which are going between tire and ground.

Currently for propelling vehicles we use classical models. Most of these models reflect the empirical experiments and observations effects not the process.

Many authors of models for force calculation use slip "s" parameter defined as:

$$s = 1 - \frac{V}{V_t} \tag{1}$$

where: V – real velocity of a vehicle,

V_t – theoretical velocity (circumferential speed of wheel)

Slip does not have any physical representation – it is not possible to measure it and is defined as a result of a mathematical operation, and it is defined in different ways by various authors depending on wheel action if it is propelled (rotated) by vehicle engine, or it is a braked wheel pushed by the vehicle.

Generally the force between tire and road is calculated with (eq.2.*)* [1, 2, 3, 4, 6,7, 10, 12,13].

$$F(s) = N\mu(s) \qquad (2)$$

where: F – propelling force,

N – load (weight of a vehicle),

$\mu(s)$ – friction coefficient depending on slip

In literature we can find various relations $\mu(s)$ as well as the definitions of slip.

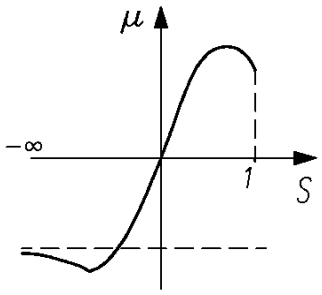

Figure 1. Diagram of the wheel's slip as a function of the propelling force coefficient [18].

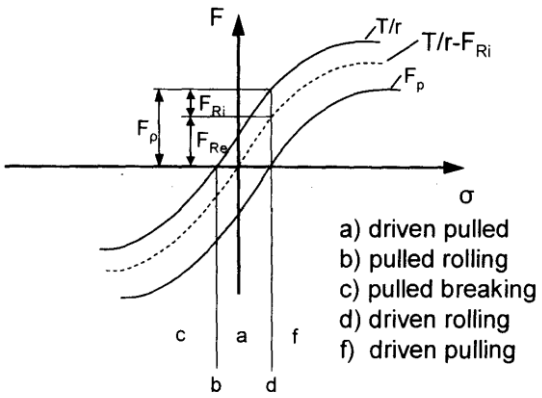

Figure 2. Gross traction T/r, circumferential force T/r-F_{Ri} and net traction Fp in dependence on the slip *σ*. [17]

On of commonly used model was developed by Schreiber, Kutzbac*h* [7] who based on other authors like Grecenko, Schuring and others. They noticed the difficulties with the slip definition and introduced different models for pulled and driven wheel like presented in the paper [16]. Different movement possibilities can be seen in diagram depicted in figure 2.

Such models are very difficult to use in a computer simulation. Referring to the Steinkamof's measurement data, Schreiber and Kutzbach proposed the standardization of tire characteristics [4].

The standardized curve was proposed in the form presented in figure 3. [5].

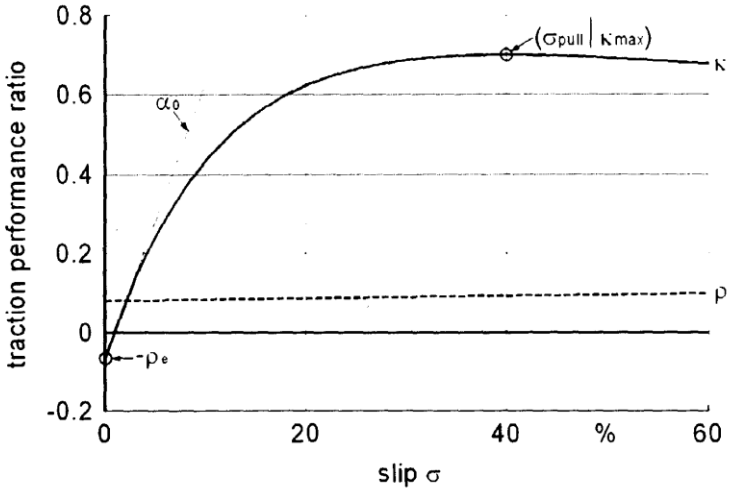

Figure 3. κ-curve with four characterizing values ρ_e, α_0, κ_{max} and σ_{pull}.

To find out the right curve some coefficients need to be calculated.

The most popular examples of propelling force relation to slip is the "Pacejka" magic formula commonly used for vehicle behaviour [11]

It is written in form:

$$F(s) = d \bullet sin\{c \bullet arctan[b \bullet (1-e) \bullet k + e \bullet arctan(b \bullet k)]\}. \quad (3)$$

Where*:* ***F(s)*** is the propelling force that depends on s (slip),

b, c, d and ***e*** that represent fitting parameters.

Each tire can be characterized by ten to twenty coefficients that are mostly determined in an experimental way. This formula does not have any logical explanation. It is an experimentally obtained engineering tool, but very easy to use especially in computer simulations and we can find it in computer games, simulators etc. But the force or slip is found not by physical phenomena analyses but by computer solver which suits the output value to equation. The main discomfort situation comes from the fact that we can get the same slip for different vehicle speed.

2. The model

In paper "*The Vehicle Tire Model based on energy flow*" [16] it was proved, that the eq. 2 can be derived based on energy (power) flow and propelling force depend on the difference between wheel circumferential speed and vehicle speed. Shortly if we take the power which is needed to propel the vehicle as the:

$$P = F \bullet V \quad (4)$$

Where: **F** – propelling force, (produced in the tire-ground contact area) speed of vehicle,.

The power which is going to the road as the effect of Viscous friction force depends on the mutual speed of the two rubbing against each other surfaces, in case of the wheel moving on a pavement, where V is the velocity of a vehicle and V_t is the velocity of the tire-ground contact area, it equals:

$$P = T \bullet (V - V_t) \quad (5)$$

After comparing both equations following is obtained:

$$F \bullet V = T \bullet (V - V_t) \quad (6)$$

Hence:

$$F = T \bullet \frac{V - V_t}{V} \quad ( )$$

Taking into account that for the zero slip value the static friction occurs with its maximum value (F_{max}) proportional to the weight:

$$F = F_{max} = N \bullet \mu \quad (8)$$

where: **N** – vehicle load,

μ - traction coefficient (determines grip between the tire and the ground).

Coherent notation of above mentioned relationships needs to be done:

$$F = N \bullet \frac{\mu(V - V_t)}{V} = N \bullet \mu(s) \qquad (9)$$

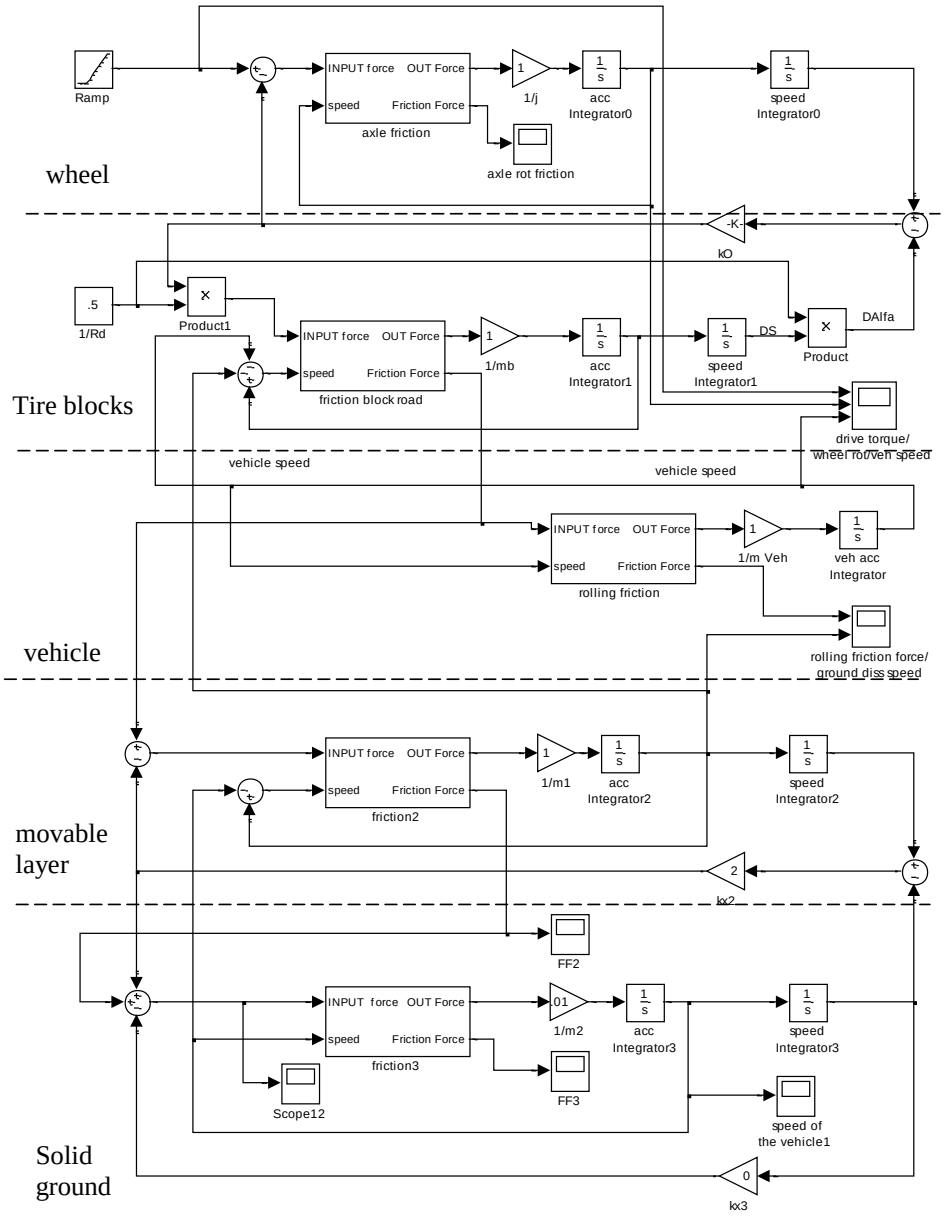

Figure 4. Model of a wheel-ground cooperation for a vehicle.

So the energy flow model can be used to vehicle propelling force evaluation. Normally we can expect that some additional layers between tire and solid ground are present and take part in this energy flow. So the multilayer (cascade) model of a wheel-ground cooperation was developed [11]. It is based on energy flow and forces acting between individual layers.

Model depicted in figure 4. consists of four similar layers: a wheel, thread blocks, a movable intermediate layer and an immovable (solid) ground. The vehicle is modelled by a mass and an acceleration integrating system that outputs the velocity. All the layers consist of "friction" block which inputs are: the force (from moment) propelling given layer and the mutual velocity of two cooperating layers. This block's outputs are: the resultant force that propels an element of a given layer, the amplifying system that represents inertia of a given element and the integrating elements that are connected in series.

Between a wheel and a thread block occurs a conversion of moments into forces by dividing moments by dynamic radius R_d. In the model multiplication by a reciprocal of a dynamic radius ($1/R_d$) was used.

Depending on a layer type the driving force is decreased by the motion resistance of the inner layer. Friction block is depicted in figure 5. Input signals are: the driving force and the velocity and output signals are: the friction force and the propelling force. Friction force acts between the adjacent layers and propelling force causes the acceleration of an element of the layer. Friction force value depends on the velocity.

Friction block has a maximum value limit. That corresponds to the force when wearing off of an element appears – once the grip loss (friction loss) appears. Presented friction model describes well the rolling resistance that appears in the part of the model describing the vehicle.

In the model depicted in figure 4. Mutually moving elements can act on each other with elastic forces likewise between a tire and thread blocks. Stopped thread blocks twist and act on the tire with the force dependent on the position difference between the block end and the block origin (base, that is joined with a tire).

Presented model shows basic types of interactions i.e. friction and elastic force of mutual deflection. This model can be extended with more layers.

Simulations tested behaviour of the system. Between the thread blocks and the pavement appears the moving layer and the limitation of the maximum friction value between layers influences the motion.

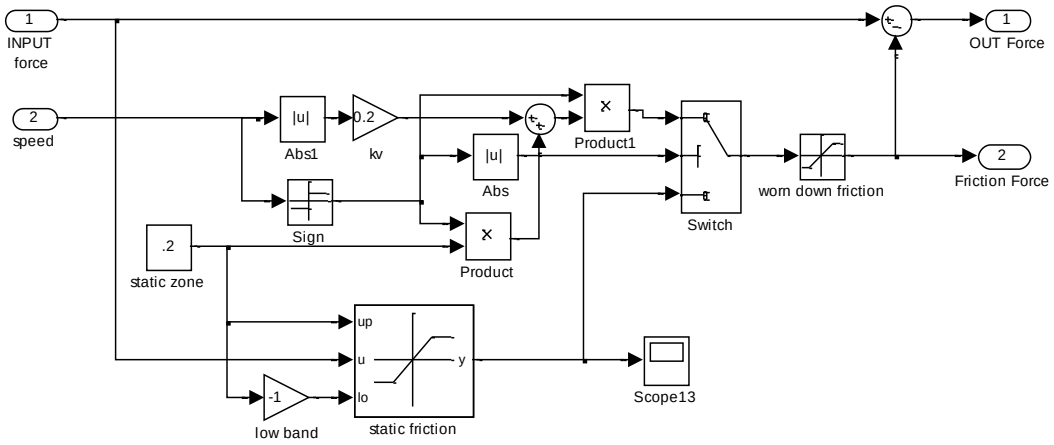

Figure 5. Friction model.

Testing the model showed a very good consistence of appearing phenomena during simulation with the observations of reality [19] for some types of thin layers like water or sand. This model does not work properly when we take account thicker and deformable layers of sand or mud.

3. Ground model problem

When we are talking about an off-road vehicle we are thinking about wading of sand, mud and rocky roads. The vehicle sinking in the wet sand etc. But the ground effects on vehicle. We all experienced that the ground reaction depends on the movement speed. We can pass a muddy ground if we start with high speed and we can stay in it if this speed is too low. When we move on the sand it is beeing deformed, replaced and changes the structure and its properties. So the rear wheel moving in the trace of tha front wheel is in fact riding on the different surface than the front one. This effect have great influence on vehicle's behaviour.

Figure 6. An example of wheel trace on the sand

The modeling of ground which can move, change the shape and structure, is a very attractive problem.

The assumption for the model is that it should reflect process of deformation and soil compacting.

Figure 7 presents taken model of ground behavior. Under increasing pressure the ground is deformed. For small pressure which doesn't overcome the solid bearing capacity, the ground comes back to previous shape after the load releases. If the pressure is bigger than critical load, the process of condensation is started, and the density of ground increases. So after the load releases ground comes back to other shape. The condensation of ground needs time and runs with inertia. The critical bearing of ground and the constant time of condensation inertia depends on density which is changing under load. The example of compaction process is presented on figure 7. In figure 7a load F is increasing from 0 to F_{kp1} . If the F doesn't reach F_{kp1} and it is realized , the ρ_k density comes back to the initial value ρ_0 on curve 1 if F overcomes the F_{kp1} the density comes back to value ρ_1 on curve 2. And so on. The process of compaction is running in time as it is presented in Figure 7b. Of course in normal ground there critical values of force and time are not so quantized. It is pointed out only for concept presentation.

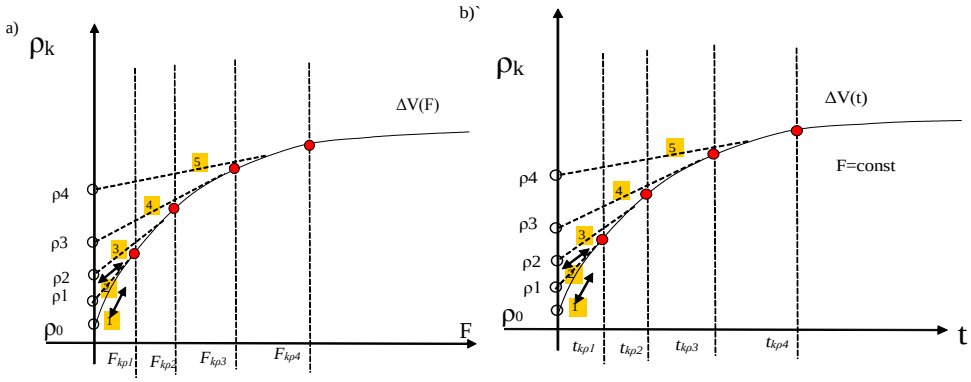

Figure 7. The ground characteristic a) density in relation to load b) density in time for constant load.

Ground under load is:

- moved in two dimensions
  - orthogonally in deep as effect of pressure and effects on layers bellow
  - vertically being pushed by rotating tire and effects on ground ahead and back of rotating
- deformed in 3 dimension: it is oblate under wheel and pushed on sides effecting on adjacent ground, causing its deformation, like uplift etc.

– compacting increases the density.

The ground is modeled as the net of cells with 3D elasticity and damping features. A concept of the ground model in 2D version is presented in figure 8a. It is a system of springs and dampers of varying parameters. When the cell is compressed the internal pressure Pp is balanced by force of springs and dampers in all dimensions.

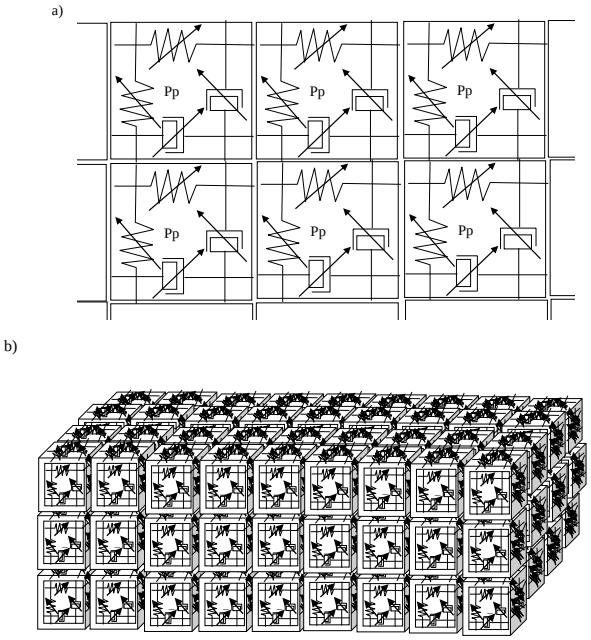

Figure 8. a) The 2D cellular model of ground. B) 3D cellular model of ground

If the ground is loaded the movement and deformation process starts. In figure 9 some cases of deformation are presented. Figure 9a presents the model when the wheel is put on the ground and the cell under it is compressed and the neighboring one is uplifted. I case on figure 9b wheel is pushed and effects on the cell ahead. When wheel starts to rotate under friction force, the cell pushes the cell ahead with lower force. If wheel is propelled with motor (moves slower than its circumferential speed) it pushes ground under itself to the back and compresses the cell ahead.

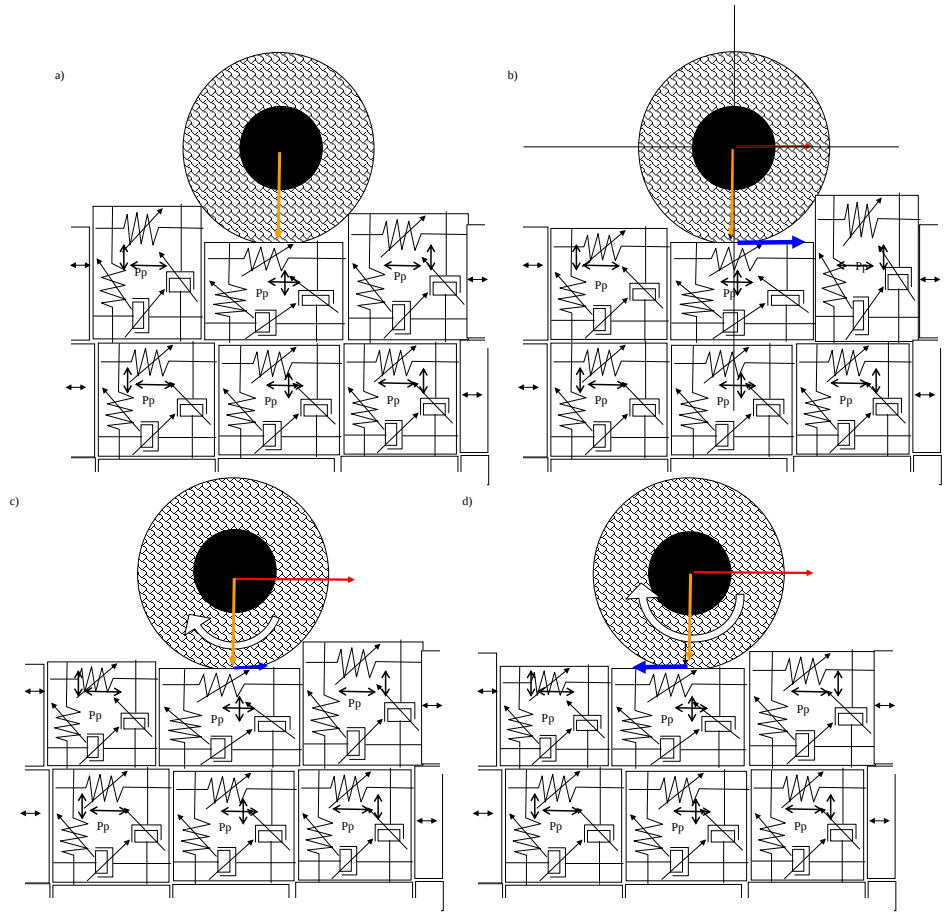

Figure 9. The model of wheel cellular ground cooperation

The model of 2D ground cell is presented in figure 10. The input is the speed of movement of the adjacent cell or the wheel. If the end of cell in moving with different speed the cell is being deformed in this dimension. It causes the resistance force proportional to speed of shape to change and the volume of the cell too. The internal pressure increases and gives the forces propelling the wall of cell in all directions and reaction force. This pressure changes the shape of the cell, for instance when X dimension is decreasing the Y dimension would increase. The coefficients of volume elasticity $\mathbf{K_v}$ and directional dampers k_{vx}, k_{vy} depend on density which is changing under internal pressure **pin**.

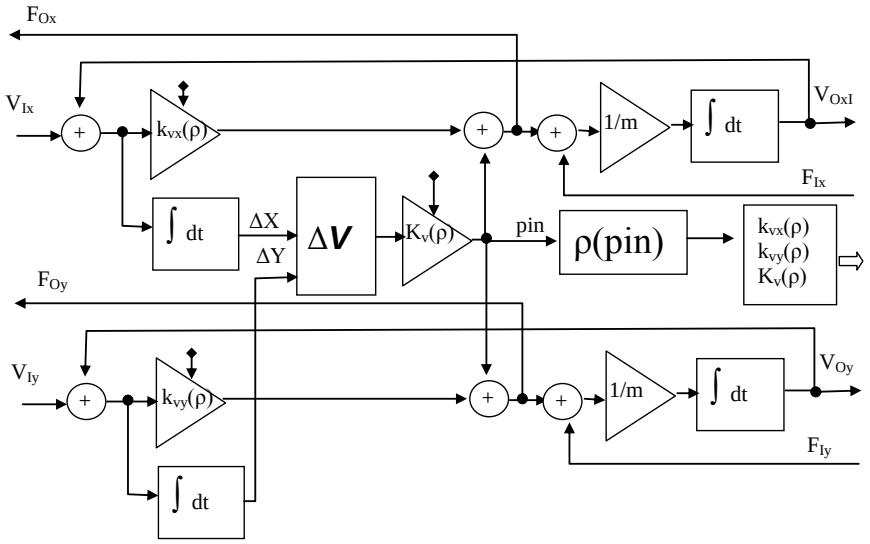

Figure 1. Model of 2D ground cell

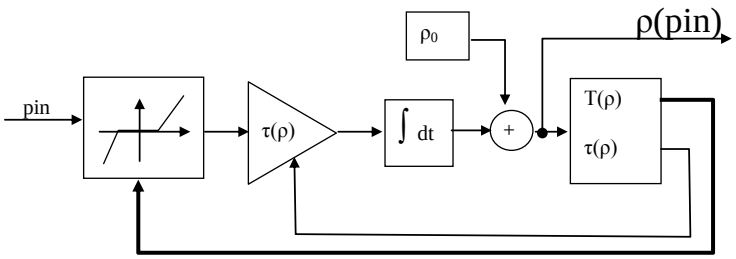

Figure 10. The model of ground compaction process ρ(t)

The pin is given to the dead zone block which limits depending on cell density. If pressure pin overcomes the limit which represents the limit of elasticity, the process of compaction starts as the inertial changing of density and the value of coefficients. The function coefficients value can be stored in matrix or written as the function. Normally with the rising pressure the density increases, but if it overcomes the limit value the ground can be broken (crashed) for instance when sample of ground is pressed without side supporting-reacting bodies.

When we resign from structure transformation and keep the elasticity in whole range we get such environment of movement like air or water. The model of water acting on vehicle is presented on figure 12. The water buoyant and dynamic resistance forces act on the vehicle.

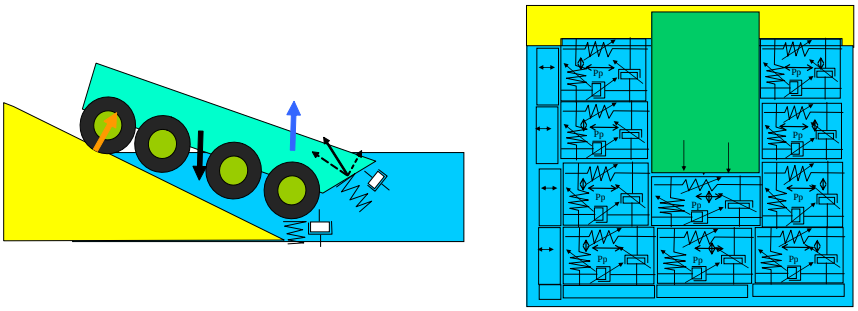

Figure 11. The model of water reaction based on cellular concept

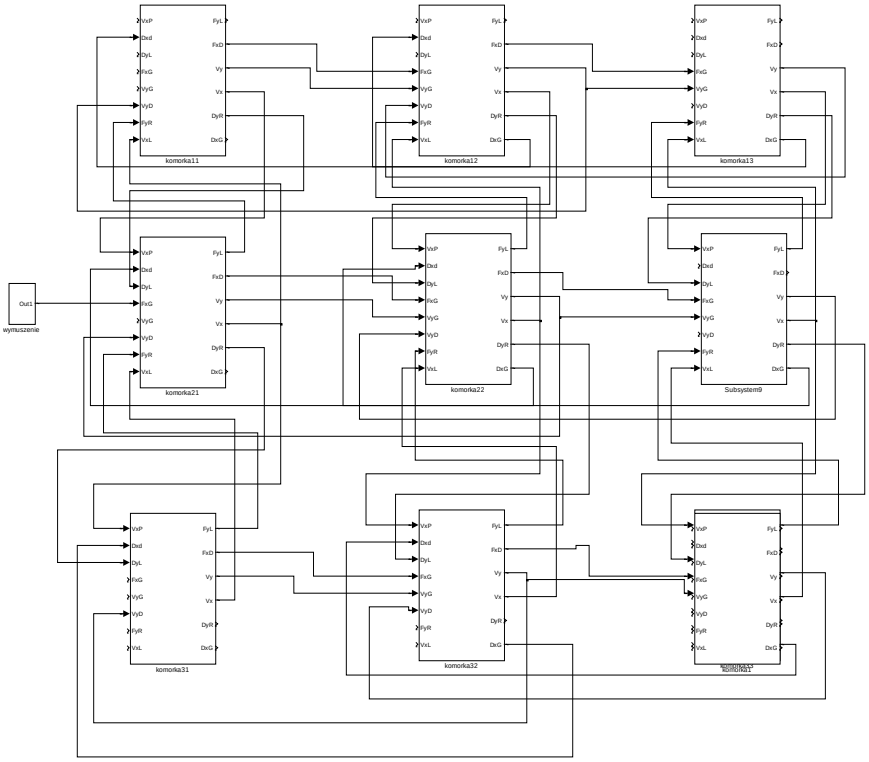

Figure 12. The example of cellular net model made in Matlab/Simulink

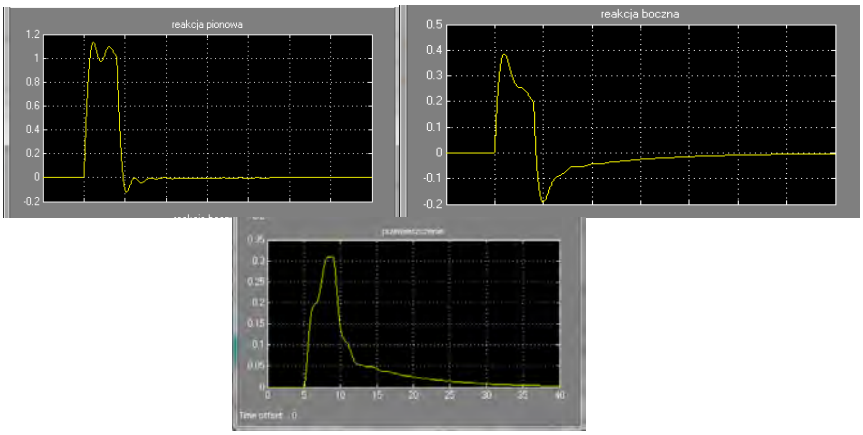

Figure 13. Examples of simulation results. The answer of ground for compactor hit. The direction of hit reaction is force direction and causes increase of internal pressure and density increase.

4. Conclusions

The presented modelling concept reflects quite good ground behaviour under wheel of moving vehicle. It shows the deformation, replacing and compaction of the ground. Simulation results are qualitatively consistent with the observations.

- This is a modular model, so it can be adjusted to various types of materials.
- This is a dynamic model therefore it cannot be used to determine the forces values or the slip values in a specific time moment without continuous analysis.
- This model can be used for environment resistance and bearing force calculation like ground, mud, water.
- This nonlinear method (relations between elasticity, damping and conversion limit forces) can be used for simulations of the rock crashing or other materials feature simulation.
- Together with layer model method can be used for vehicle behaviour simulations.
- This model can be easily readjusted to the dimensions what would allow modelling a tire-ground cooperation during making a turn.
- While changing model parameters of the individual layers behaviour of the system can by modified.

References

[1] Bekker M., 1969.: Introduction to terrain-vehicle systems. Michigan Press, An Arbor, USA

[2] Bakker, E. ; Nyborg, L. ; Hans B. Pacejka H. B.: Tyre modelling for use in vehicle dynamics studies 1987 Jan. Society of Automotive Engineers, Warrendale, PA.

[3] Goriaczkin B.P.: "Theory of Wheel…", Moscow 1937.

[4] Grečenko A.: Einflüsse auf die Kraftübertragung von Ackerschlepperreifen. Agrartechnische Kolloquium, Hohenheim, 1989.

[5] Gurkan Erdogan, Tire modelling Lateral and longitudinal Tire Forces Aprill 27, 2009.

[6] Jakliński L., 1999. „Models of pneumatic wheel effecting on the soil" the scientific work Warsaw University of Technology Mechanics edition 175.

[7] Kutzbach D., 1982. Ein Beitrag zur Fahrmechanik der Ackerschleppers-Reifenschlupf, Schleppermasse und Flächenleistung. Grundladen Landtechnik Bd. 32(2).

[8] Matlab 2004 – User Handbook. MathWorks, Natick, USA.

[9] Mirosław T., Żebrowski Z.: "Modelling and Simulation of Tractor Differential Mech-anism.; „Mechanical Review" 6'2013.

[10] Pacejka H. B.: The wheel shimmy phenomenon: A theoretical and experimental investigation with particular reference to the nonlinear problem (Analysis of shimmy in pneumatic tires due to lateral flexibility for stationary and no-stationary conditions), Ph.D. Thesis, Delft University of Technology, Delft, 1966.

[11] Pacejka H. B.: Tire and Vehicle Dynamics, Butterworth-Heinemann, Oxford, 2002.

[12] Pacejka H., 2004.: Tyre and Vehicle Dynamics. Elsevier Press

[13] Prochowski L., 2004. "Mechanics of movement" Care Vehicles edition, WKiŁ Warsaw

[14] Pytka J. "Theoretical experimental Study of drive on flexible surface" Lublin University of Technology Edition. Lublin 2011

[15] Schreiber M., Kutzbach H.D., 2007. Comparison of different zero-slip definitions and a proposal to standardize tire traction performance. J. Terramechanics 44.

[16] [16] Miroslaw T., Zebrowski Z., "The Vehicle Tire Model Based on Energy Flow" Springer Proceedings in Mathematics & Statistics 184 Volumes from 2012 – 2017

Tomasz Mirosław Ph.D. (Assistant Professor) Warsaw University of Technology Faculty of Automotive and construction Machinery. Institute of construction Machinery Engineering. 84 Narbutta str. 02-524 Warsaw POLAND (tmiroslaw@simr.pw.edu.pl)

Existence conditions for fractional order PI/PD controllers

Cristina I. Muresan, Isabela R. Birs, Clara M. Ionescu, Robin De Keyser

Abstract: Fractional order Proportional Integral (FO-PI) and Proportional Derivative (FO-PD) controllers are increasingly used in controlling various types of processes, with several papers demonstrating their advantage over the traditional PI/PD controllers. Quite frequently the design of these FO-PI/FO-PD controllers is based on a set of performance specifications that refer to the open loop gain crossover frequency, phase margin and the iso-damping property. These three performance specifications lead to a system of three nonlinear equations that need to be solved in order to determine the three tuning parameters of the controllers. However, it might occur that for a certain process and with some specific gain crossover frequency and phase margin values, the computed parameters of the FO-PI/FO-PD controllers do not fall into a range of values with correct physical meaning. In this paper, a study regarding this limitation, as well as the existence conditions for the FO-PI/FO-PD parameters are presented. The paper shows that given a specific process and open loop modulus and phase specifications, the gain crossover frequency (or in general, a certain test frequency used in the design) must be selected such that the process phase fulfills an important condition. Once this is met, the proposed approach ensures that the tuning parameters of the fractional order controller will have a physical meaning. Illustrative examples are included.

1. Introduction

Fractional calculus represents the generalization of the integration and differentiation to an arbitrary order. Its application to control theory has been postponed due to its inherent complexity [1]. However, recent advances in computation made possible its use in control engineering, with an increasing popularity in modeling and controller design [2-4].

The fractional order $PI^{\mu}D^{\lambda}$ controller, first described by Podlubny [5] is a generalization of the classical integer order PID controller. Several papers and researchers have shown that the fractional order controllers are generally able to meet more performance specifications and to behave more robustly than the traditional PID controller [6-7]. This is due to the supplementary tuning parameters, the fractional order of integration, μ, and of differentiation, λ. Special cases of this fractional order $PI^{\mu}D^{\lambda}$ controller include the fractional order PI^{μ} controller and the fractional order PD^{λ} controller.

Several approaches to tuning fractional order PI^{μ} (FO-PI) or PD^{λ} (FO-PD) controllers have been proposed so far [6], [8-9]. Quite frequently the design of these FO-PI/FO-PD controllers is based on a set of performance specifications. Since both the FO-PI and the FO-PD controller have three tuning

parameters, three performance specifications are usually considered in their design. Also, since frequency domain is more appealing to control engineers and the description of fractional order elements is more straightforward than in the time domain, these three performance specifications usually refer to the open loop gain crossover frequency, phase margin and the iso-damping property. To generalize this approach, the performance specifications refer to a certain modulus and phase of the loop transfer function at a specific frequency defined as the test frequency. To tune the FO-PI and FO-PD controllers based on these performance specifications, the resulting set of nonlinear equations needs to be solved. Several techniques to find the solution exist, ranging from simple optimization routines to more complex genetic algorithms or graphical methods [2], [6-7], [10-11].

Problems in finding a solution exist, since solving the system of nonlinear equations needs to be done by meeting design constraints that refer to a certain range for the fractional order of integration/differentiation, as well as for the proportional gain and the integral or derivative time constant. These problems, however, can be avoided with a proper choice of the performance specifications, namely of the test frequency used in the design. To the best of our knowledge, such a study regarding the adequate choice for the test frequency has not been reported so far. In this paper, a study regarding the existence conditions for FO-PI/FO-PD parameters is presented. The paper shows that given a certain open loop modulus and phase specification, the test frequency must be selected such that the process phase fulfills an important condition. Choosing the performance specifications such that this condition is met ensures that the tuning parameters of the fractional order controller will have a physical meaning. Also, the study shows that given a test frequency and the corresponding phase of the open loop transfer function, a minimum value for the fractional order of integration or differentiation exists. Illustrative examples are included for validation purposes.

The paper is structured as follows. Section 2 and 3 present the existence conditions for FO-PI and FO-PD controllers, respectively. The mathematical approach to derive the condition for a proper selection of the test frequency such that the parameters of these controllers have physical meaning is detailed. Section 4 presents numerical examples to validate the mathematical approach in both cases, for the FO-PI and the FO-PD controller, respectively. The last section presents the concluding remarks, as well as some insights regarding possibilities for future research on this topic.

Assume in what follows that the process transfer function is denoted as P(s), the controller transfer function is denoted by C(s) and the loop transfer function is L(s). The design is based on imposing a certain set of performance specifications on the loop transfer function. Frequently, these specifications refer to phase margin, gain crossover frequency and iso-damping [6], [12-13]. The result is a specific value for the modulus, $M_{PC,}$ and phase, φ_{PC}, of the loop transfer function, at a certain frequency, $\bar{\omega}$:

$$L(j\bar{\omega}) = P(j\bar{\omega})C(j\bar{\omega}) = M_{PC}e^{j\varphi_{PC}} \quad (1)$$

For example, if the phase margin, PM, is specified, then M_{PC}=1, φ_{PC}=-180º+PM and $\bar{\omega}$ is a user specified gain crossover frequency. In (1), $P(j\bar{\omega}) = M_P e^{j\varphi_P}$ is considered to be fully known and could be easily determined via a sine test with the frequency $\bar{\omega}$ [13].

In what follows, conditions regarding the choice for the frequency $\bar{\omega}$ are derived for fractional order PI and PD controllers, such that their parameters have physical meaning.

2. Design constraints for parameter ranges of fractional order PI controllers

The transfer function of a fractional order PI controller is defined as:

$$C(s) = K_p\left(1 + \frac{1}{T_i s^{\alpha}}\right), \tag{2}$$

with K_p>0 and T_i>0 the proportional gain and the integral time constant and $0 < \alpha < 2$ - the fractional order. Using (2), the frequency response for the loop transfer function at the test frequency $\bar{\omega}$ is defined as:

$$L(j\bar{\omega}) = P(j\bar{\omega}) \cdot K_p\left(1 + \frac{1}{T_i(j\bar{\omega})^{\alpha}}\right) \tag{3}$$

Expanding (3) and separating the unknown and known terms lead to:

$$K_p\left(1 + \frac{\cos\frac{\alpha\pi}{2} - j\sin\frac{\alpha\pi}{2}}{T_i\bar{\omega}^{\alpha}}\right) = \frac{L(j\bar{\omega})}{P(j\bar{\omega})} = \frac{M_{PC}}{M_P}e^{j(\varphi_{PC}-\varphi_P)} = a + jb \tag{4}$$

Relation (4) can also be written as:

$$K_p\left(1 + \frac{\cos\frac{\alpha\pi}{2}}{T_i\bar{\omega}^{\alpha}}\right)\left(1 - j\frac{\sin\frac{\alpha\pi}{2}}{T_i\bar{\omega}^{\alpha} + \cos\frac{\alpha\pi}{2}}\right) = a\left(1 + j\frac{b}{a}\right) \tag{5}$$

which leads to:

$$K_p\left(T_i\bar{\omega}^{\alpha} + \cos\frac{\alpha\pi}{2}\right) = aT_i\bar{\omega}^{\alpha} \text{ and } \sin\frac{\alpha\pi}{2} = -\frac{b}{a}\left(T_i\bar{\omega}^{\alpha} + \cos\frac{\alpha\pi}{2}\right) \tag{6}$$

Then, using (6) the proportional gain and the integral time constant are determined as:

$$T_i = -\frac{1}{\bar{\omega}^{\alpha}}\left(\frac{a}{b}\sin\frac{\alpha\pi}{2} + \cos\frac{\alpha\pi}{2}\right) \text{ and } K_p = -\frac{bT_i\bar{\omega}^{\alpha}}{\sin\frac{\alpha\pi}{2}} \tag{7}$$

A couple of conditions arise from (7). For $0 < \alpha < 2$, then $\sin\frac{\alpha\pi}{2} > 0$; but K_p>0 implies that $-\frac{bT_i\bar{\omega}^{\alpha}}{\sin\frac{\alpha\pi}{2}} > 0$, which leads to b<0. According to (4), the real and imaginary parts a and b, respectively can be computed as:

$$a = \frac{M_{PC}}{M_P}\cos(\varphi_{PC} - \varphi_P) \text{ and } b = \frac{M_{PC}}{M_P}\sin(\varphi_{PC} - \varphi_P) \tag{8}$$

Since b<0, it follows that $\frac{M_{PC}}{M_P}\sin(\varphi_{PC}-\varphi_P)<0$, leading to $\sin(\varphi_{PC}-\varphi_P)<0$, which ultimately results in $-180^o<\varphi_{PC}-\varphi_P<0^o$ or:

$$\varphi_{PC}<\varphi_P<\varphi_{PC}+180^o \tag{9}$$

Also, the condition for the integral time constant is $T_i>0$ or according to (7):

$$-\frac{1}{\bar{\omega}^\alpha}\left(\frac{a}{b}\sin\frac{\alpha\pi}{2}+\cos\frac{\alpha\pi}{2}\right)>0 \tag{10}$$

leading to:

$$a\sin\frac{\alpha\pi}{2}+b\cos\frac{\alpha\pi}{2}>0 \tag{11}$$

where the fact that $b<0$ has been used. Replacing a and b with the result in (8) leads to:

$$\cos(\varphi_{PC}-\varphi_P)\sin\frac{\alpha\pi}{2}+\sin(\varphi_{PC}-\varphi_P)\cos\frac{\alpha\pi}{2}>0 \tag{12}$$

and to its more compact form:

$$\sin\left(\varphi_{PC}-\varphi_P+\frac{\alpha\pi}{2}\right)>0 \tag{13}$$

In order for relation (13) to hold, the following must be valid $0^o<\varphi_{PC}-\varphi_P+\frac{\alpha\pi}{2}<180^o$ or:

$$\varphi_{PC}+90^o\alpha-180^o<\varphi_P<\varphi_{PC}+90^o\alpha \tag{14}$$

Finally, combining (9) and (14) yields the following conditions:

$$\varphi_{PC}<\varphi_P<\varphi_{PC}+90^o\alpha \text{ and } \alpha>\frac{\varphi_P-\varphi_{PC}}{90^o} \tag{15}$$

As a consequence, in order to determine a valid fractional order PI controller with $K_p>0$, $T_i>0$ and $0<\alpha<2$, if φ_{PC} is specified, the test frequency $\bar{\omega}$ must be chosen such that the process phase fulfills the condition $\varphi_P>\varphi_{PC}$. Also, the minimum possible value for the fractional order can be computed via the second condition in (15).

3. Design constraints for parameter ranges of fractional order PD controllers

The transfer function of a fractional order PD controller is defined as:

$$C(s)=K_p(1+T_d s^\alpha), \tag{16}$$

with $K_p>0$ and the derivative time constant, $T_d>0$. Using (16), the frequency response for the loop transfer function at the test frequency $\bar{\omega}$ is defined as:

$$L(j\bar{\omega})=P(j\bar{\omega})\cdot K_p(1+T_d(j\bar{\omega})^\alpha) \tag{17}$$

Expanding (17) and separating the unknown and known terms lead to:

$$K_p\left(1+T_d\bar{\omega}^{\alpha}\left(\cos\frac{\alpha\pi}{2}+j\sin\frac{\alpha\pi}{2}\right)\right)=\frac{L(j\bar{\omega})}{P(j\bar{\omega})}=\frac{M_{PC}}{M_P}e^{j(\varphi_{PC}-\varphi_P)}=a+jb \tag{18}$$

Relation (18) can also be written as:

$$K_p\left(1+T_d\bar{\omega}^{\alpha}\cos\frac{\alpha\pi}{2}\right)\left(1+j\frac{T_d\bar{\omega}^{\alpha}\sin\frac{\alpha\pi}{2}}{1+T_d\bar{\omega}^{\alpha}\cos\frac{\alpha\pi}{2}}\right)=a\left(1+j\frac{b}{a}\right) \tag{19}$$

which leads to:

$$K_p\left(1+T_d\bar{\omega}^{\alpha}\cos\frac{\alpha\pi}{2}\right)=a \text{ and } T_d\bar{\omega}^{\alpha}\sin\frac{\alpha\pi}{2}=\frac{b}{a}\left(1+T_d\bar{\omega}^{\alpha}\cos\frac{\alpha\pi}{2}\right) \tag{20}$$

Then, using (20) the proportional gain and the derivative time constant are determined as:

$$T_d=\frac{1}{\bar{\omega}^{\alpha}\left(\frac{a}{b}\sin\frac{\alpha\pi}{2}-\cos\frac{\alpha\pi}{2}\right)} \text{ and } K_p=\frac{b}{T_d\bar{\omega}^{\alpha}\sin\frac{\alpha\pi}{2}} \tag{21}$$

For $0<\alpha<2$, then $\sin\frac{\alpha\pi}{2}>0$; but $K_p>0$ and using (21), it follows that $\frac{b}{T_d\bar{\omega}^{\alpha}\sin\frac{\alpha\pi}{2}}>0$, which leads to $b>0$.

Since $b>0$ and using (8), it follows that $\frac{M_{PC}}{M_P}\sin(\varphi_{PC}-\varphi_P)>0$, leading to $\sin(\varphi_{PC}-\varphi_P)>0$, which ultimately results in $0^o<\varphi_{PC}-\varphi_P<180^o$ or:

$$\varphi_{PC}-180^o<\varphi_P<\varphi_{PC} \tag{22}$$

Also, the condition for the derivative time constant is $T_d>0$ or according to (21):

$$\frac{1}{\bar{\omega}^{\alpha}\left(\frac{a}{b}\sin\frac{\alpha\pi}{2}-\cos\frac{\alpha\pi}{2}\right)}>0 \tag{23}$$

leading to:

$$a\sin\frac{\alpha\pi}{2}-b\cos\frac{\alpha\pi}{2}>0 \tag{24}$$

where the fact that $b>0$ has been used. Replacing a and b with the result in (8) leads to:

$$\cos(\varphi_{PC}-\varphi_P)\sin\frac{\alpha\pi}{2}-\sin(\varphi_{PC}-\varphi_P)\cos\frac{\alpha\pi}{2}>0 \tag{25}$$

and to its more compact form:

$$\sin\left(\frac{\alpha\pi}{2}-\varphi_{PC}+\varphi_P\right)>0 \tag{26}$$

In order for relation (26) to hold, the following must be valid $0^o<\frac{\alpha\pi}{2}-\varphi_{PC}+\varphi_P<180^o$ or:

$$\varphi_{PC}-90^o\alpha<\varphi_P<\varphi_{PC}-90^o\alpha+180^o \tag{27}$$

Finally, combining (22) and (27) yields the following conditions:

$$\varphi_{PC} - 90^o\alpha \ < \varphi_P < \varphi_{PC} \text{ and } \alpha > \frac{\varphi_{PC}-\varphi_P}{90^o} \quad (28)$$

As a consequence, in order to determine a valid fractional order PD controller with $K_p>0$, $T_d>0$ and $0 < \alpha < 2$, if φ_{PC} is specified, the test frequency $\bar{\omega}$ must be chosen such that the process phase fulfills the condition $\varphi_P < \varphi_{PC}$. Also, the minimum possible value for the fractional order can be computed via the second condition in (28).

4. Numerical examples

Two numerical examples are considered: the first for the design of a FO-PI controller and the second one for the design of a FO-PD controller. We assume in what follows that the fractional order of integration or differentiation has been determined using some other tuning technique.

Consider the first order transfer function given as:

$$P(s) = \frac{10}{0.5s+1} \quad (29)$$

A fractional order PI controller needs to be designed, with the transfer function as indicated in (2), such that the phase margin of the loop frequency response (FR) is PM=60º. Then, the loop FR phase is determined as:

$$\varphi_{PC} = -180^o + PM = -120^o \quad (30)$$

Assume in this case that the fractional order of integration has been determined using some tuning technique to be α=0.3. Then, according to the first condition in (15), the following must hold:

$$-120^o < \varphi_P < -120^o + 90^o\alpha \text{ or } -120^o < \varphi_P < -93^o \quad (31)$$

It is clear from here that no test frequency $\bar{\omega}$ can be selected such that the condition in (31) holds. Assume that the fractional order of integration has now been determined to be α=0.7. Using the first condition in (31), the following must hold for the FO-PI parameters to have physical meaning:

$$-120^o < \varphi_P < -120^o + 90^o\alpha \text{ or } -120^o < \varphi_P < -57^o \quad (32)$$

In this case a test frequency $\bar{\omega}$ can be selected such that the process phase $\varphi_P \in (-120^o, -57^o)$. Using the Bode diagram of the process in (29), as indicated in Fig. 1, this test frequency is selected to be $\bar{\omega} = 10\ rad/s$, the gain crossover frequency for the loop FR. Hence, $M_{PC} = 1$. According to Fig. 1, the modulus and phase of the process FR at the test frequency are $M_P = 5.84dB = 1.96$ and $\varphi_P = -78.7^o$, value that meets the condition in (32). The parameters *a* and *b* are determined using (8):

$a = 0.3833$ and $b = -0.3367$ (33)

Notice that b<0, as determined in Section 2 above. The parameters of the FO-PI controller can now be computed based on (7):

$T_i = 0.1118$ and $K_p = 0.2117$ (34)

Notice that since condition (32) has been met, the parameters of the FO-PI controller have physical meaning, with T_i>0 and K_p>0. Notice that the second condition in (15) also holds:

$$\alpha > \frac{120^o - 78.7^o}{90^o} \Longrightarrow \alpha > 0.459 \quad (35)$$

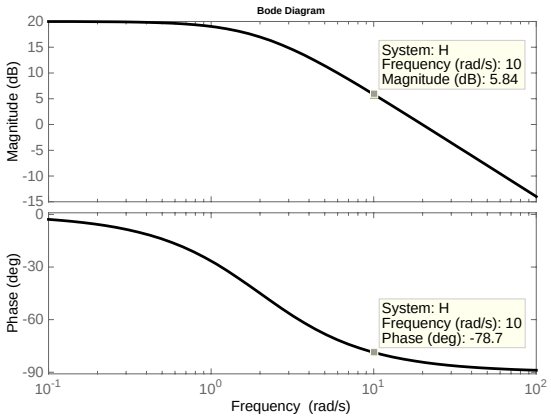

Figure 1. Bode diagram for the first numerical example

Consider the process transfer function given as:

$$P(s) = \frac{10}{s(0.5s+1)} \quad (36)$$

A fractional order PD controller needs to be designed, with the transfer function as indicated in (16), such that the phase margin of the loop FR is PM=45°. Then, the loop FR phase is determined as:

$$\varphi_{PC} = -180^o + PM = -135^o \quad (37)$$

Assume in this case that the fractional order of differentiation has been determined using some tuning technique to be α=0.3. Then, according to the first condition in (28), the following must hold:

$$-135^o - 90^o\alpha < \varphi_P < -135^o \text{ or } -162^o < \varphi_P < -135^o \quad (38)$$

In this case a test frequency, $\bar{\omega}$, can be selected such that the process phase $\varphi_P \in (-162^o, -135^o)$. Using the Bode diagram of the process in (36), as indicated in Fig. 2, this test frequency is selected to be $\bar{\omega} = 4\ rad/s$, the gain crossover frequency for the loop FR. Hence, $M_{PC} = 1$. According to Fig. 2, the modulus and phase of the process FR at the test frequency are $M_P = 0.976dB = 1.119$ and $\varphi_P = -153^o$, value that meets the condition in (38). The parameters a and b are determined using (8):

$$a = 0.85 \text{ and } b = 0.2762 \tag{39}$$

Notice that b>0, as determined in Section 3 above. The parameters of the FO-PD controller can now be computed based on (21):

$$T_d = 1.3033 \text{ and } K_p = 0.308 \tag{40}$$

Notice that since condition (38) has been met, the parameters of the FO-PD controller have physical meaning, with T_d>0 and K_p>0. Notice also that the second condition in (28) also holds:

$$\alpha > \frac{\varphi_{PC} - \varphi_P}{90^o} \Longrightarrow \alpha > 0.2 \tag{41}$$

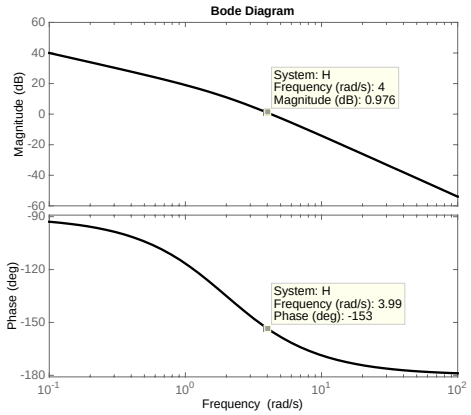

Figure 2. Bode diagram for the second numerical example

5. Conclusions

The design of fractional order PI/PD controllers can be a difficult task due to the nonlinear equations or system of equations that need to be solved. Occasionally, a solution for this system of equations might yield complex or negative values for the controller parameters, which poses problems in terms of control engineering. The existence of a solution with physical meaning is closely linked to

the process to be controlled as well as to the imposed performance specifications. So far, an attempt to analyze and give some guidelines regarding the choice of these performance specifications has not been considered. In this paper a mathematical approach to ensure that the parameters of the fractional order controller have physical meaning is presented. The approach considers the frequency domain with performance specifications that refer to a certain modulus and phase of the loop FR at a specific frequency, referred to as the test frequency. It is shown that given a certain process and a certain fractional order of differentiation or integration, the test frequency must be selected such that a condition regarding the process phase is achieved. Two numerical examples are presented which consider the phase margin and the gain crossover frequency as performance specifications. The numerical examples validate the results. The mathematical approach only requires knowledge of the process phase and modulus at the test frequency, and not a full mathematical model.

In this paper, the fractional order of integration/differentiation is assumed to be known apriori. Further research, however, includes a procedure to determine this fractional order.

Acknowledgments

This work was supported by a grant of the Romanian National Authority for Scientific Research and Innovation, CNCS/CCCDI-UEFISCDI, project number PN-II-P2-2.1-PED-2016-0101, with PNCDI III.

References

[1] Barbosa, R.S., Machado, J.T. Implementation of Discrete-Time Fractional-Order Controllers based on LS Approximations. *Acta Polytechnica Hungarica* 3, 4 (2006), pp. 5-22

[2] Muresan, C.I. Fractional Calculus: From Simple Control Solutions to Complex Implementation Issues. chapter in Machado, J.A.T., Baleanu, D., Luo, A. (eds). *Discontinuity and Complexity in Nonlinear Physical Systems*, Nonlinear Systems and Complexity Volume 6, pp. 113-134, DOI:10.1007/978-3-319-01411-1__7, Springer, Switzerland, 2014

[3] Shang, B., Liu, J., Zhao, T., Chen, Y.Q. Fractional order robust visual servoing control of a quadrotor UAV with larger sampling period. *International Conference on Unmanned Aircraft Systems (ICUAS)*. pp. 1228-1234, June 7-10, Arlington, USA, 2016

[4] Huang, J., Chen, Y.Q., Li, H., Sh, X. Fractional order modeling of human operator behavior with second order controlled plant and experiment research. *IEEE/CAA Journal of Automatica Sinica* 3, 3 (2016), pp. 271-280

[5] Podlubny, I. Fractional-order systems and $PI^{\lambda}D^{\mu}$-controllers. *IEEE Transactions on Automatic Control* 44, 1 (1999), pp. 208–214

[6] Monje, C.A., Chen, Y.Q., Vinagre, B.M., Xue, D., Feliu, V. *Fractional order Systems and Controls: Fundamentals and Applications*. Springer-Verlag, London, 2010

[7] Muresan, C.I., Folea, S., Mois, G., Dulf, E.H. Development and Implementation of an FPGA Based Fractional Order Controller for a DC Motor. *Elsevier Journal of Mechatronics* 23, 7 (2013), pp. 798-804

[8] Folea, S., Muresan, C.I., De Keyser, R., Ionescu, C. Theoretical Analysis and Experimental Validation of a Simplified Fractional Order Controller for a Magnetic Levitation System. *IEEE Transactions on Control Systems Technology* 24, 2 (2016), pp. 756 – 763

[9] Copot, C., Muresan, C.I., Ionescu, C.M., De Keyser, R. Fractional Order Control of a DC Motor with Load Changes. *14th International Conference on Optimization of Electrical and Electronic Equipment OPTIM*, pp. 956-961, May 22-24, Bran, Romania, 2014

[10] Muresan, C.I., Dulf, E.H., Both, R., Palfi, A., Caprioru, M. Microcontroller Implementation of a Multivariable Fractional Order PI Controller. *The 9th International Conference on Control Systems and Computer Science (CSCS19-2013)*, pp. 44-51, 29-31 May, Bucharest, Romania, 2013

[11] Jesus I.S., Barbosa R.S. Genetic optimization of fuzzy fractional PD+I controllers. *ISA Trans*actions 57 (2015), pp. 220–230

[12] Muresan, C.I., Dulf, E.H., Both, R. Vector Based Tuning and Experimental Validation of Fractional Order PI/PD Controllers. *Journal of Nonlinear Dynamics* 84, 1 (2016), pp. 179-188

[13] De Keyser, R., Muresan, C.I., Ionescu, C. A Novel Auto-tuning Method for Fractional Order PI/PD Controllers, *ISA Transactions* 62 (2016), pp. 268-275

Cristina I. Muresan, Associated Professor: Department of Automation, Technical University of Cluj-Napoca, Memorandumului St., No. 28, Cluj-Napoca, Romania (corresponding author C. I. Muresan, +40264401821; e-mail: Cristina.Muresan@aut.utcluj.ro)

Isabela R. Birs, Master student: Department of Automation, Technical University of Cluj-Napoca, Memorandumului St., No. 28, Cluj-Napoca, Romania (e-mail: Isabela.Birs@aut.utcluj.ro). The author gave a presentation of this paper during one of the conference sessions

Clara M. Ionescu, Professor: Department of Automation, Technical University of Cluj-Napoca, Memorandumului St., No. 28, Cluj-Napoca, Romania and with the Faculty of Engineering and Architecture, Research group on Dynamical Systems and Control, Technologiepark 914, 9052 Ghent, Belgium (e-mail: Claramihaela.Ionescu@Ugent.be)

Robin De Keyser, Professor: Faculty of Engineering and Architecture, Research group on Dynamical Systems and Control, Technologiepark 914, 9052 Ghent, Belgium (e-mail: Robain.DeKeyser@Ugent.be)

Identification of the model of stick balancing using the cepstral analysis

Dalma J. Nagy, László Bencsik, Tamás Insperger

Abstract: Stick balancing on the fingertip is one of the simplest human balancing tasks, still it represents the key features of more complex balancing tasks, namely, an unstable equilibrium should be stabilized in the presence of a reaction time delay. In order to understand the mechanism of human balancing, first we have to identify the control concept employed by the human brain during stick balancing. There are several possible concepts in the literature to model this neural control mechanism. Here, we assume a delayed proportional-derivative-acceleration (PDA) feedback. This concept assumes that, besides the inclination and the angular velocity, humans are able to estimate the angular acceleration of the stick from the pressure distribution perceived by mechanoreceptors at the fingertip. Because of the acceleration feedback, the mathematical model is a neutral delayed differential equation (NDDE). For systems governed by NDDEs, cepstral analysis can be used to identify the time delay, and to gain information about the neutral behaviour of the model. In a proposed experimental study, sticks with different weights have to be balanced. In case of sticks with larger masses the pressure at the fingertip during balancing is larger and it is supposed that the acceleration gains are also of higher value. In this work we verify this phenomenon using cepstral analysis of signals obtained by time-domain simulations.

1. Introduction

How humans balance themselves physically can be viewed as a complex feedback control system. The neurons transmit the information to and from the brain that controls muscle groups in a synchronized process that maintains balance and prevents falling. Although the exact mechanism of this complex control system is not known, there are some elements, which can easily be identified. One of the most important elements of the control mechanism is the reaction delay, which is the result of the finite-time information transmission and processing of the neurons. The simplest model for human balance control is the proportional-derivative (PD) controller [6, 9, 16], which accounts for the perception of the position and the velocity of the controlled object. Since mechanoreceptors are able to measure forces and pressure distributions, it is a straightforward idea that this information is used by the nervous system for motor control mechanisms. Since force is related to acceleration, control models which involves the feedback of the acceleration have been analyzed extensively in the

literature [7, 15]. In this study, we assume a proportional-derivative-acceleration feedback (PDA) controller to model stick balancing on the fingertip. Due to the reaction delay and the acceleration feedback, the mathematical model is a neutral delayed differential equation (NDDE). In case of a signal generated by a NDDE, the time delay can be estimated using cepstral analysis [4, 8]. The goal of this study is to show how the control gain for the acceleration feedback is related to the result of the cepstral analysis. Several nonlinear numerical simulations are presented with different acceleration gains and the corresponding cepstrum is analyzed with respect to the feedback delay.

The outline of this paper is the following. In Section 2, the dynamic model of stick balancing together with the assumed control concept and the corresponding equation of motion is introduced. In Section 3, the cepstral analysis is described briefly with some examples and a possible application to the stick balancing model identification process is demonstrated. Section 4 presents the detailed numerical study.

2. Dynamic model of stick balancing

The principles of general human balancing tasks is aimed to understand through stick balancing on the fingertip shown in Fig. 1. In this study, stick balancing in the anterior-posterior plane [10] is investigated. In order to simplify the problem, the vertical motion is neglected. Thus we have a two-degree-of-freedom mechanical model, which is illustrated on the right hand side of Fig. 1.

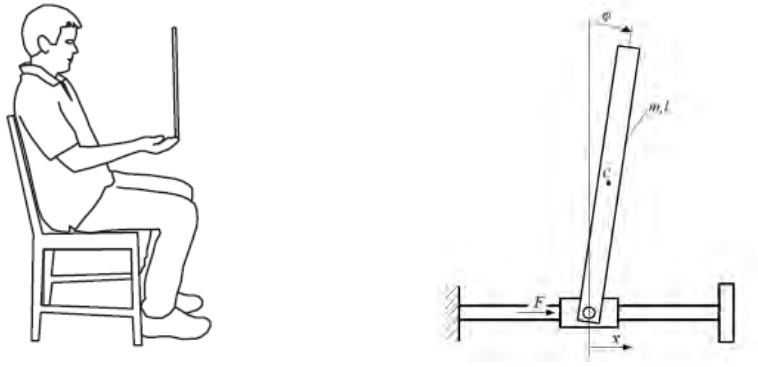

Figure 1. Stick balancing and the inverted pendulum as mechanical model.

In the mechanical model, the tilt angle of the stick is denoted with φ, and x represents the horizontal displacement of the massless cart, which represents the motion of the palm.

The equation of motion was derived using Lagrange's equation of the second kind as:

$$\begin{bmatrix} m & \frac{1}{2}ml\cos\varphi \\ \frac{1}{2}ml\cos\varphi & \frac{1}{3}ml^2 \end{bmatrix} \begin{bmatrix} \ddot{x} \\ \ddot{\varphi} \end{bmatrix} + \begin{bmatrix} -\frac{1}{2}ml\dot{\varphi}^2\sin\varphi \\ -\frac{1}{2}mgl\sin\varphi \end{bmatrix} = \begin{bmatrix} F \\ 0 \end{bmatrix}, \tag{1}$$

where m is the mass of the stick, l is the length of the stick, C refers to the center of gravity and the stick is assumed to be a homogeneous body. On the right hand side of the equation F represents the control force.

Since x is a cyclic coordinate [3], it can be eliminated from the equation. Thus the equation of the essential motion transforms to:

$$\ddot{\varphi} = -\frac{Fl\cos\varphi}{2(\frac{1}{3}ml^2 - \frac{1}{4}ml^2\cos^2\varphi)} - \frac{(\frac{1}{4}ml^2\dot{\varphi}^2\cos\varphi - \frac{1}{2}mgl)\sin\varphi}{(\frac{1}{3}ml^2 - \frac{1}{4}ml^2\cos^2\varphi)}. \tag{2}$$

2.1. Modelling the control mechanism

As it was mentioned in the Introduction, in this study a PDA type controller is assumed to model the control mechanism of the brain during stick balancing. Thus, the control force F has the following form:

$$\begin{aligned} F_{PDA}(\varphi,\dot{\varphi},\ddot{\varphi}) = K_p\varphi(t-\tau) + K_d\dot{\varphi}(t-\tau) + K_a\ddot{\varphi}(t-\tau) = \\ = K_p\varphi_D + K_d\dot{\varphi}_D + K_a\ddot{\varphi}_D, \end{aligned} \tag{3}$$

where K_p, K_d and K_a stand for the proportional, derivative and acceleration gains, respectively. Substituting F_{PDA} into Eq. (2) results a NDDE [5].

A delay differential equation (DDE) is a differential equation, in which the rate of change of state depends on present and past states of the system, too. If the DDE involves a time-delay in the derivative term of the highest order, then it is a neutral delay differential equation (NDDE). There exists several techniques to solve and to analyze DDEs [1], [2], [14]. An important property of NDDEs is the accumulation of the discontinuities which are introduced into the solution through the initial data. This property is utilized in the model identification process. The initial data in case of an NDDE is called the history function for the interval $t < 0$ [11].

2.2. Determination of the stability charts

For the further analysis of the described system stability analysis should be carried out in order to find the parameters of the stable operation. Stability charts are diagrams constructed in the plane of some system parameters, which present the stable and unstable parameter regions. Here, the stability charts are constructed using the D-subdivision method [7, 13]. In case of NDDEs, the so called strong stability is a necessary condition for stability.

The physical parameters in this study were set as follows. The length of the stick was $l = 1\,[\mathrm{m}]$, the delay parameter was $\tau = 0.2\,[\mathrm{s}]$, and the gravitational acceleration was $g = 9.81\,[\mathrm{m/s^2}]$. For the stability investigation the equation of the essential motion (2) was linearized and the dimensionless time was introduced as $t^* = t\,/\tau$. Thus, the dimensionless control gains are:

$$k_p = \frac{6\tau^2 K_p}{ml}, k_d = \frac{6\tau K_d}{ml}, k_a = \frac{6K_a}{ml}. \tag{4}$$

Fig. 2 shows the stability charts and the stable domains (shaded areas) with varying values of the dimensionless acceleration gain k_a. The strong stability condition is that $|k_a| < 1$. If $|k_a| > 1$, then the NDDE (2) has infinitely many characteristic roots with positive real parts, therefore the solution is unstable (see [13]). For the forthcoming numerical study the control parameters are selected as follows: the dimensionless proportional gain is $k_p = 2.4$ and the dimensionless derivative gain is $k_d = 2.5$.

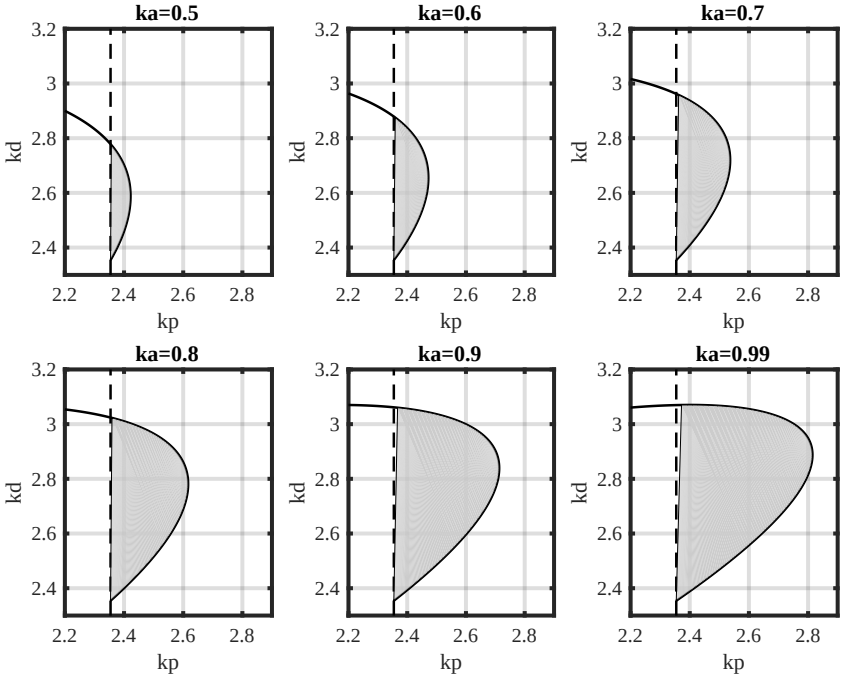

Figure 2. Stability charts for delayed PDA control. Stable regions are indicated by gray shading.

3. The cepstrum and its application in signal processing

The cepstrum was first defined as the power spectrum of the logarithm of the power spectrum [12]. Later, a new type of cepstrum was defined as the inverse Fourier Transform of the complex logarithm of the complex spectrum. Thus the formula for computing the cepstrum is:

$$\hat{f} = \frac{1}{2\pi} \int_{-\pi}^{\pi} \log[\phi(\omega)] \mathrm{e}^{(\mathrm{i}\omega n)} \mathrm{d}\omega. \tag{5}$$

where $\phi(\omega)$ is the Fourier Transform of the function f, and n is the independent variable of f. Therefore, the cepstrum is the spectrum of the spectrum, and transforms the spectrum back in the time domain. The independent variable of the cepstrum is quefrency, which is of time unit [s].

The original application of the cepstrum was the detection of echoes in seismic signals, and one of the other earliest applications was speech analysis. Cepstral analysis is also used in machinery fault identification: to detect gear eccentricity, general wear of gears and identifying local faults. [4]

If there is time-delay in a system described by a NDDE, then the cepstrum of the solution changes because of the accumulation of discontinuities. As a consequence of the time-delay a peak appears in every equal interval of the domain of the cepstrum. This interval is equal to the delay of the system [8]. This property of the cepstrum is used in this study in the case of stick balancing.

4. Numerical study

Instead of an built-in solver routine like ddeNsd in MatLab, for the nonlinear numerical simulations a self-developed solver was used. In order to consider the time delay the routine is based on the concept of semi-discretization, which was introduced for time-delay systems in [14]. However, instead of the exponential mapping for the integration a $4th$ order Runge-Kutta method was applied. The values of the proportional and derivative control gains were selected as it was discussed in Section 2.2, and the acceleration gain k_a was varied between 0.5 and 0.99. First, the NDDE was solved, and we checked, whether with the chosen control gains the solution is indeed stable. During the nonlinear simulations, the initial data were those specified in Section 2.2 (length, delay parameter, gravitational acceleration).

Since the mathematical model of the analysed problem (2) is an NDDE, we expect peaks to appear in the cepstrum in every 0.2 [s] of the quefrency domain. The proportional and derivative gains were hold constant, and the change in the cepstrum was examined if the acceleration gain was changed. Naturally, the position of the peaks should not alter, because the delay parameter τ is not changed.

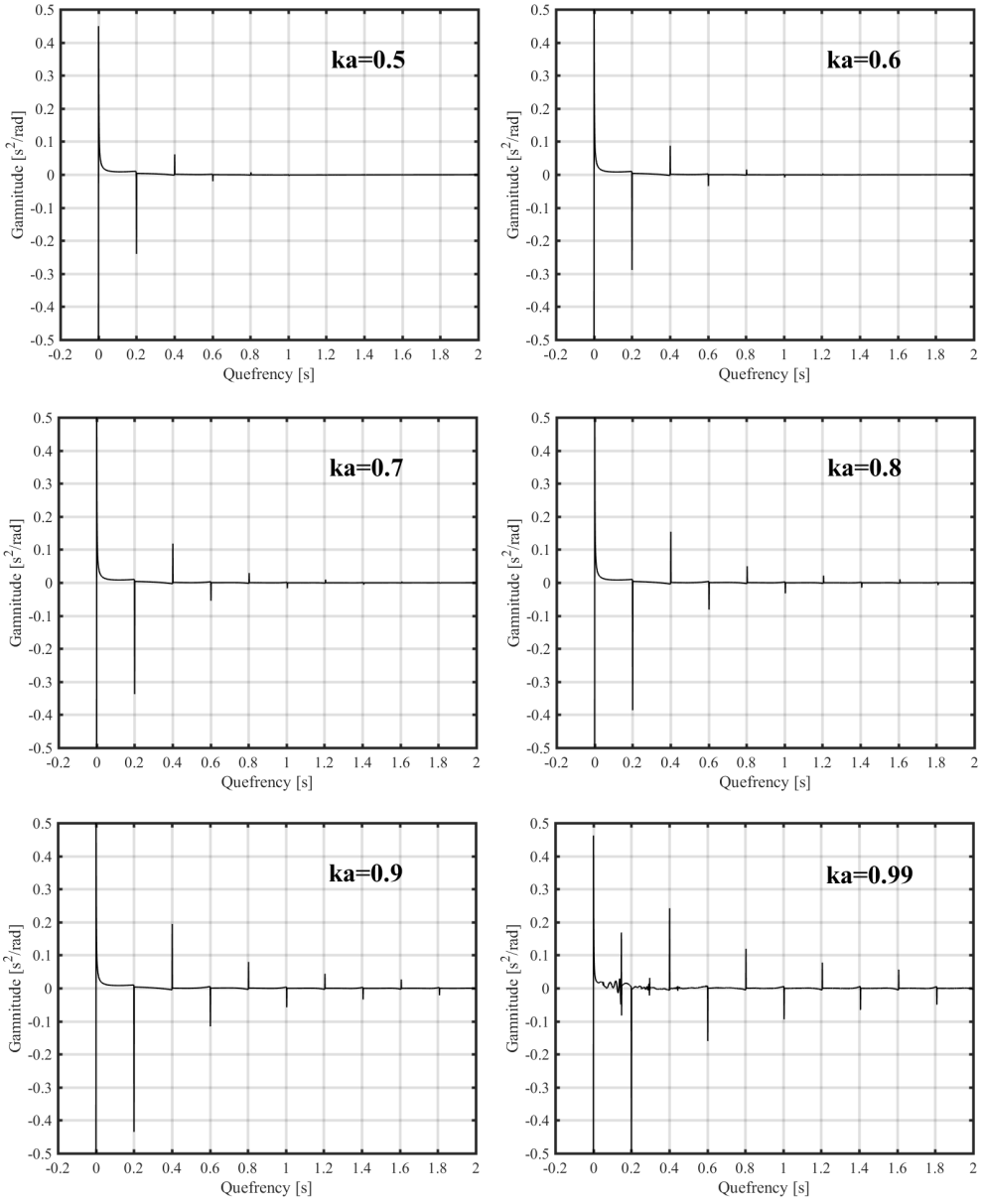

Figure 3. Results of the cepstral analysis.

The results of the cepstral analysis are shown in Fig. 3. The value of the dimensionless k_a acceleration gain is displayed in each diagram. It can be seen, that the peaks of the cepstrum

appear at every 0.2 [s] interval of the quefrency domain, as was expected. Furthermore, the peaks are getting larger (in absolute value) when the value of the acceleration gain is increased. In the last diagram, when $k_a = 0.99$, the solution contains several harmonics because it is a solution close to the stability boundary. This is why the cepstrum has peaks other than the peaks indicating the defined delay of the system.

5. Conclusions

In this study the problem of stick balancing was modelled as a planar cart-pole system. It is likely, that humans can measure forces and thus acceleration during stick balancing. Therefore, it is supposed that during the human stick balancing in addition to the proportional and derivative feedback the acceleration feedback is also used. This type of controller is known as a PDA type controller and the resulting mathematical model is a neutral delay differential equation.

In the numerical study cesptral analysis was applied to examine the effect of the changing of the acceleration gain. It was demonstrated, that from the cepstrum the delay parameter τ can be detected. Furthermore, as the value of the acceleration gain was increased the peaks of the cepstrum were larger in absolute value. This indicates that by increasing the mass of the stick, the role of the acceleration gain also increases in the neutral feedback.

In the future we intend to perform measurements with subjects balancing sticks of different masses in order to verify the results of the current study. In order to trigger the examined person to apply different acceleration gains the tests will be carried out with sticks with different masses.

References

[1] A. Balachandran, T. Kalmár-Nagy, D. E. G. *Delay Differential Equations, Recent Advances and New Directions*. Springer-Verlag New York, 2009.

[2] Erneux, T. *Applied Delay Differential Equations*. Springer-Verlag New York, 2009.

[3] Goldstein, H. *Classical Mechanics*. 2nd ed. Addison-Wesley, 1980.

[4] H. Konstantin-Hansen, H. H. Envelope and cepstrum analyes for machinery fault identification. *Sound and Vibration*, May (2010), 3pp.

[5] Hairer, E., and Wanner, G. *Solving Ordinary Differential Equations II: Stiff and Differential-Algebraic Problems*. Springer-Verlag, Berlin (2nd ed.), 1996.

[6] Insperger, T., and Milton, J. Sensory uncertainty and stick balancing at the fingertip. *Biological Cybernetics 108*, 1 (2014), 85–101.

[7] Insperger, T., Milton, J., and Stepan, G. Acceleration feedback improves balancing against reflex delay. *Journal of the Royal Society Interface 10*, 79 (2013), Article No. 20120763.

[8] J. Xu, Y. S. Parameter identification for linear controlled with multi time-delay. In *The 4th International Conference on Dynamics, Vibration and Control* (2014).

[9] Mehta, B., and Schaal, S. Forward models in visuomotor control. *Journal of Neurophysiology 88* (2002), 942953.

[10] Nordin, M., and Frankel, V. H. *Basic biomechanics of the musculoskeletal system.* Lea & Febiger, 1989.

[11] Paul, C. A. H. Treatment of derivative discontinuities in differential equations. In *Journal* (Year).

[12] Randall, R. Cepstrum analysis and gearbox fault diagnosis. Tech. rep., Bruel & Kjaer, Application notes, 1975.

[13] Stépán, G. *Retarded Dynamical Systems.* Longman, 1989.

[14] T. Insperger, G. S. *Semi-Discretization for Time-Delay Systems, Stability and Engineering Applications.* Springer-Verlag New York, 2011.

[15] Welch, T., and Ting, L. A feedback model reproduces muscle activity during human postural responses to support-surface translations. *Journal of Neurophysiology*, 99 (2008), 10321038.

[16] Yoshikawa, N., Suzuki, Y., Kiyono, K., and Nomura, T. Sensory uncertainty and stick balancing at the fingertip. *Frontiers in Computational Neuroscience 10* (2016), 34.

Dalma J. Nagy, BSc (MSc student): Department of Applied Mechanics, Budapest University of Technology and Economics and MTA-BME Lendület Human Balancing Research Group, H-1111, Budapest Muegyetem rkp 5., Hungary (*nagy.dalma22@gmail.com*).

László Bencsik, PhD: MTA-BME Lendület Human Balancing Research Group, H-1111, Budapest Muegyetem rkp 5., Hungary (*bencsik@mm.bme.hu*). The author gave a presentation of this paper during one of the conference sessions.

Tamás Insperger, PhD, DSc: Department of Applied Mechanics, Budapest University of Technology and Economics and MTA-BME Lendület Human Balancing Research Group, H-1111, Budapest Muegyetem rkp 5., Hungary (*insperger@mm.bme.hu*).

On decomposition of the initial boundary value problems in mechanics

Mikhail U. Nikabadze

Abstract: The canonical formulation of the initial boundary value problems of the classical (micropolar) theory of elasticity for any anisotropic material is given. In particular, the canonical formulations of initial boundary value problems are considered in the case of isotropic and transversely isotropic materials. Expressions for tensors-operators of classical (micropolar) equations in displacements (in displacements and rotations) are found. For these tensors-operators the tensors-operators of cofactors are found, on the basis of which the equations are split. It should be noted here that the equations are always split, and the boundary conditions only for bodies with a piecewise plane boundary. From three dimensional canonical equations the corresponding canonical equations for the theory of prismatic bodies are obtained. For prismatic bodies the canonical equations were obtained also in moments with respect to any system of orthogonal polynomials. For each moment of the unknown vector function the equation of elliptic type of high order is obtained, the characteristic roots of which are easily found. Using the Vekua method, we can obtain their analytical solution.

1. Equations of motion relative to the displacement and rotation vectors

The constitutive relations (CR) for a linearly elastic inhomogeneous anisotropic material without a center of symmetry for small displacements and rotations have the form

$$\underset{\sim}{\mathbf{P}} = \underset{\approx}{\mathbf{A}}\overset{2}{\otimes}\underset{\sim}{\boldsymbol{\gamma}} + \underset{\approx}{\mathbf{B}}\overset{2}{\otimes}\underset{\approx}{\boldsymbol{\varkappa}}, \quad \underset{\sim}{\boldsymbol{\mu}} = \underset{\approx}{\mathbf{C}}\overset{2}{\otimes}\underset{\sim}{\boldsymbol{\gamma}} + \underset{\approx}{\mathbf{D}}\overset{2}{\otimes}\underset{\approx}{\boldsymbol{\varkappa}} \quad (\underset{\sim}{\boldsymbol{\gamma}} = \nabla\mathbf{u} - \underset{\sim}{\mathbf{C}}\cdot\boldsymbol{\varphi}, \quad \underset{\approx}{\boldsymbol{\varkappa}} = \nabla\boldsymbol{\varphi}), \tag{1}$$

where $\underset{\sim}{\mathbf{P}}$ $\underset{\sim}{\boldsymbol{\mu}}$ — stress and couple-stress tensors, $\underset{\sim}{\boldsymbol{\gamma}}$ $\underset{\approx}{\boldsymbol{\varkappa}}$ — tensors of deformation and bending-torsion, $\mathbf{u}$ $\boldsymbol{\varphi}$ — displacement and rotation vectors, $\underset{\approx}{\mathbf{A}}$, $\underset{\approx}{\mathbf{C}} = \underset{\approx}{\mathbf{B}}^T$ $\underset{\approx}{\mathbf{D}}$ — material tensors of the fourth rank, $\underset{\simeq}{\mathbf{C}}_2$ — discriminant tensor of third rank, $\otimes$ — the inner 2-product [1, 2, 3, 4, 5, 6, 7, 8, 9, 10], the superscript T in the upper right corner of the quantities denotes transposition.

Introducing the tensor columns of the deformation and bending-torsion tensors and stress and couple-stress tensors, as well as the tensor-block matrix (TBM) of the elastic tensors

$$\underset{\approx}{\mathbb{X}} = \begin{pmatrix} \underset{\sim}{\boldsymbol{\gamma}} \\ \underset{\approx}{\boldsymbol{\varkappa}} \end{pmatrix} \quad \left(\underset{\approx}{\mathbb{X}}^T = \begin{pmatrix} \underset{\sim}{\boldsymbol{\gamma}}, \underset{\approx}{\boldsymbol{\varkappa}} \end{pmatrix}\right), \quad \underset{\approx}{\mathbb{Y}} = \begin{pmatrix} \underset{\sim}{\mathbf{P}} \\ \underset{\sim}{\boldsymbol{\mu}} \end{pmatrix} \quad \left(\underset{\approx}{\mathbb{Y}}^T = \begin{pmatrix} \underset{\sim}{\mathbf{P}}, \underset{\sim}{\boldsymbol{\mu}} \end{pmatrix}\right), \tag{2}$$

$$\underset{\approx}{\mathbb{M}} = \begin{pmatrix} \underset{\approx}{\mathbf{A}} & \underset{\approx}{\mathbf{B}} \\ \underset{\approx}{\mathbf{C}} & \underset{\approx}{\mathbf{D}} \end{pmatrix} \ \big(\underset{\approx}{\mathbb{M}}^T = \underset{\approx}{\mathbb{M}}\big), \tag{3}$$

the specific strain energy and the CR can be written in the form

$$2\Phi(\underset{\sim}{\boldsymbol{\gamma}}, \underset{\sim}{\boldsymbol{\varkappa}}) = \underset{\sim}{\boldsymbol{\gamma}} \overset{2}{\otimes} \underset{\approx}{\mathbf{A}} \overset{2}{\otimes} \underset{\sim}{\boldsymbol{\gamma}} + 2\underset{\sim}{\boldsymbol{\gamma}} \overset{2}{\otimes} \underset{\approx}{\mathbf{B}} \overset{2}{\otimes} \underset{\sim}{\boldsymbol{\varkappa}} + \underset{\sim}{\boldsymbol{\varkappa}} \overset{2}{\otimes} \underset{\approx}{\mathbf{D}} \overset{2}{\otimes} \underset{\sim}{\boldsymbol{\varkappa}} = \underset{\sim}{\mathbb{X}}^T \overset{2}{\otimes} \underset{\approx}{\mathbb{M}} \overset{2}{\otimes} \underset{\sim}{\mathbb{X}}, \quad \underset{\sim}{\mathbb{Y}} = \underset{\approx}{\mathbb{M}} \overset{2}{\otimes} \underset{\sim}{\mathbb{X}}. \tag{4}$$

If the material has a center of symmetry in the sense of elastic properties, then $\underset{\approx}{\mathbf{B}} = \underset{\approx}{\mathbf{0}}$, where $\underset{\approx}{\mathbf{0}}$ — zero tensor of the fourth rank and the TBM of the elastic modulus tensors (3) will take the form of a tensor-block-diagonal matrix.

Substituting (1) in the equations of motion for small displacements and rotations

$$\nabla \cdot \underset{\sim}{\mathbf{P}} + \rho\mathbf{F} = \rho\partial_t^2\mathbf{u}, \quad \nabla \cdot \underset{\sim}{\boldsymbol{\mu}} + \underset{\approx}{\mathbf{C}} \overset{2}{\otimes} \underset{\sim}{\mathbf{P}} + \rho\mathbf{m} = \underset{\sim}{\mathbf{J}}\partial_t^2\boldsymbol{\varphi},$$

and introducing the TBM operator of the equations of motion and the vector columns of the displacement and rotation vectors and vectors of volume forces and moments

$$\underset{\approx}{\mathbb{M}} = \begin{pmatrix} \underset{\approx}{\mathbf{A}} & \underset{\approx}{\mathbf{B}} \\ \underset{\approx}{\mathbf{C}} & \underset{\approx}{\mathbf{D}} \end{pmatrix}, \quad \mathbb{U} = \begin{pmatrix} \mathbf{u} \\ \boldsymbol{\varphi} \end{pmatrix}, \quad \mathbb{X} = \begin{pmatrix} \rho\mathbf{F} \\ \rho\mathbf{m} \end{pmatrix}, \tag{5}$$

we obtain the equations of motion in displacements and rotations in the form

$$\underset{\approx}{\mathbb{M}} \cdot \mathbb{U} + \mathbb{X} = 0, \tag{6}$$

where the differential tensors-operators $\underset{\approx}{\mathbf{A}}$, $\underset{\approx}{\mathbf{B}}$, $\underset{\approx}{\mathbf{C}}$ and $\underset{\approx}{\mathbf{D}}$ have expressions

$$\begin{aligned}
&\underset{\approx}{\mathbf{A}} = \underset{\approx}{\mathbf{A}}' - \underset{\approx}{\mathbf{E}}\rho\partial_t^2, \quad \underset{\approx}{\mathbf{A}}' = \mathbf{r}_j\mathbf{r}_l(A^{ijkl}\nabla_i + \nabla_i A^{ijkl})\nabla_k, \quad \underset{\approx}{\mathbf{D}} = \underset{\approx}{\mathbf{D}}' - \underset{\sim}{\mathbf{J}}\partial_t^2, \\
&\underset{\approx}{\mathbf{B}} = \mathbf{r}_j\mathbf{r}_l[(B^{ijkl}\nabla_i + \nabla_i B^{ijkl} - C^{l\,\cdot\,\cdot}_{\cdot\,mn}A^{mnkj})\nabla_k - C^{l\,\cdot\,\cdot}_{\cdot\,mn}\nabla_i A^{mnij}], \\
&\underset{\approx}{\mathbf{C}} = \mathbf{r}_j\mathbf{r}_l(B^{klij}\nabla_i + \nabla_i B^{klij} + C^{j\,\cdot\,\cdot}_{\cdot\,mn}A^{mnkl})\nabla_k, \quad \underset{\approx}{\mathbf{D}}' = \mathbf{r}_j\mathbf{r}_l\{[D^{ijkl}\nabla_i \\
&+\nabla_i D^{ijkl} + (g_s^j g_t^l - g_s^l g_t^j)C^{s\,\cdot\,\cdot}_{\cdot\,mn}B^{mnkt}]\nabla_k - C^{l\,\cdot\,\cdot}_{\cdot\,pq}(A^{pqmn}C^{\cdot\,\cdot\,j}_{mn\cdot} + \nabla_i B^{pqij})\}.
\end{aligned} \tag{7}$$

Here and below $\underset{\approx}{\mathbf{E}}$ is the unit tensor of the second rank, t is the time, and ∂_t is the partial derivative operator with respect to time.

2. On static boundary conditions. Tensor-operator of stress and couple-stress

Given (1), the static boundary conditions can be written as follows:

$$\mathbf{n} \cdot \underset{\sim}{\mathbf{P}} = \underset{\sim}{\mathbf{T}}^{(1)} \cdot \mathbf{u} + \underset{\sim}{\mathbf{T}}^{(2)} \cdot \boldsymbol{\varphi} = \mathbf{P}, \quad \mathbf{n} \cdot \underset{\sim}{\boldsymbol{\mu}} = \underset{\sim}{\mathbf{T}}^{(3)} \cdot \mathbf{u} + \underset{\sim}{\mathbf{T}}^{(4)} \cdot \boldsymbol{\varphi} = \boldsymbol{\mu}, \tag{8}$$

which is still equivalent to equalities

$$\mathbf{n} \cdot \underset{\sim}{\mathbb{Y}} = \begin{pmatrix} \underset{\sim}{\mathbf{T}}^{(1)} & \underset{\sim}{\mathbf{T}}^{(2)} \\ \underset{\sim}{\mathbf{T}}^{(3)} & \underset{\sim}{\mathbf{T}}^{(4)} \end{pmatrix} \cdot \begin{pmatrix} \mathbf{u} \\ \boldsymbol{\varphi} \end{pmatrix}. \tag{9}$$

Here $\mathbf{P}$ and $\boldsymbol{\mu}$ are the stress and couple-stress vectors given on the body surface and the following differential tensors-operators are introduced:

$$\begin{aligned} \underset{\sim}{\mathbf{T}}^{(1)} &= \mathbf{r}_j \mathbf{r}_l n_i A^{ijkl} \nabla_k, \quad \underset{\sim}{\mathbf{T}}^{(2)} = \mathbf{r}_j \mathbf{r}_l n_i B^{ijkl} \nabla_k - \mathbf{n} \cdot \underset{\approx}{\mathbf{A}} \overset{2}{\otimes} \underset{\simeq}{\mathbf{C}}, \\ \underset{\sim}{\mathbf{T}}^{(3)} &= \mathbf{r}_j \mathbf{r}_l n_i C^{ijkl} \nabla_k, \quad \underset{\sim}{\mathbf{T}}^{(4)} = \mathbf{r}_j \mathbf{r}_l n_i D^{ijkl} \nabla_k - \mathbf{n} \cdot \underset{\approx}{\mathbf{C}} \overset{2}{\otimes} \underset{\simeq}{\mathbf{C}}. \end{aligned} \tag{10}$$

Introducing the TBM operator stress and couple-stress and the vector column of stress and couple-stress vectors

$$\mathbb{T} = \begin{pmatrix} \underset{\sim}{\mathbf{T}}^{(1)} & \underset{\sim}{\mathbf{T}}^{(2)} \\ \underset{\sim}{\mathbf{T}}^{(3)} & \underset{\sim}{\mathbf{T}}^{(4)} \end{pmatrix}, \quad \mathbb{Q} = \begin{pmatrix} \mathbf{P} \\ \boldsymbol{\mu} \end{pmatrix}, \tag{11}$$

the static boundary conditions (8), taking into account the notation given by the second relation (5), can be written in the form

$$\mathbb{T} \cdot \mathbb{U}\big|_S = \mathbb{Q}. \tag{12}$$

We note that the kinematic boundary conditions are represented in the form

$$\mathbb{U}\big|_S = \mathbb{Z} \quad \left(\mathbb{Z} = \begin{pmatrix} \mathbf{f} \\ \boldsymbol{\psi} \end{pmatrix} \right), \tag{13}$$

mixed boundary conditions can be written as follows:

$$\mathbb{T} \cdot \mathbb{U}\big|_{S_1} = \mathbb{Q}; \quad \mathbb{U}\big|_{S_2} = \mathbb{Z}, \tag{14}$$

and the initial conditions have the form

$$\mathbb{U}|_{t=t_0} = \mathbb{U}_0 \quad \mathbb{V}|_{t=t_0} = \mathbb{V}_0, \tag{15}$$

$$\mathbb{U}_0 = \begin{pmatrix} \mathbf{u}_0 \\ \boldsymbol{\varphi}_0 \end{pmatrix}, \quad \mathbb{V}_0 = \frac{d\mathbb{U}}{dt}\Big|_{t=t_0} = \begin{pmatrix} \mathbf{v}_0 \\ \boldsymbol{\omega}_0 \end{pmatrix}, \quad \mathbf{v}_0 = \frac{d\mathbf{u}}{dt}\Big|_{t=t_0}, \quad \boldsymbol{\omega}_0 = \frac{d\boldsymbol{\varphi}}{dt}\Big|_{t=t_0}. \tag{16}$$

Here $\mathbf{f}$ and $\boldsymbol{\psi}$ are the displacement and rotation vectors given on the body surface, $\mathbf{u}_0$ and $\boldsymbol{\varphi}_0$ are the displacement and rotation vectors given at the initial instant of time (for $t = t_0$), $\mathbf{v}_0$ and $\boldsymbol{\omega}_0$ are the velocity and angular velocity vectors given at the initial instant of time, S is the body surface, $S_1 \cup S_2 = S$, $S_1 \cap S_2 = S$.

3. Formulation of initial-boundary value problems

Definition 1. If the displacement and rotation vectors (kinematic boundary conditions) are given on the body boundary S, then such conditions are called boundary conditions of the first kind, and the problem of the micropolar solids mechanics (SM), using these conditions, and also the initial conditions is called the first initial-boundary value problem.

In the case the first initial-boundary value problem includes: the equations of motion (6), the kinematic boundary conditions (13) and the initial conditions (15).

Definition 2. If static boundary conditions (stress and couple-stress vectors) are given on the body boundary S, then such boundary conditions are called boundary conditions of the second kind, and the problem of micropolar SM using them and initial conditions is called the second initial-boundary value problem.

In the case under consideration, the second initial-boundary value problem includes: the equations of motion (6), the static boundary conditions (12) and the initial conditions (15).

Definition 3. If kinematic boundary conditions are given on one part of the body boundary S_1, and on the remaining part of it S_2 are given the static boundary conditions, where $S_1 \cup S_2 = S$, $S_1 \cap S_2 = \emptyset$, then such boundary conditions are called mixed boundary conditions, and the problem of micropolar SM, using them and initial conditions is called the mixed initial-boundary value problem.

In this case, the mixed (third) initial-boundary value problem includes: the equations of motion (6), the kinematic boundary conditions (13) on one part of the body boundary and the static boundary conditions (12) on the rest of the body boundary and the initial conditions (15).

Note that, excluding the characteristics of the micropolar theory from the above definitions, we obtain the corresponding definitions for classical SM.

It should be noted that the kinematic boundary conditions and the initial conditions do not need to be split, since they are set in a split form. Hence, for the splitting of the first initial-boundary value problem, it is sufficient to split only the equations of motion, since, as already mentioned in the previous proposition, the kinematic boundary conditions and the initial conditions are split. In this connection, the splitting of the static boundary conditions is of great interest. If the equations of motion (6) and the static boundary conditions (12) can be split under some conditions, then under the same conditions all the initial-boundary value problems formulated above can be split. Hence, it is necessary to establish the conditions under which the equations of motion (6) and the static boundary conditions (12) are split.

4. Decomposition of the equation of motion for the isotropic micropolar medium

In this case, as many authors (see, for example, [11, 12]) consider $\underset{\approx}{\mathbf{B}} = 0$ and differential tensors-operators $\underset{\approx}{\mathbf{A}}$, $\underset{\approx}{\mathbf{B}}$, $\underset{\approx}{\mathbf{C}}$ and $\underset{\approx}{\mathbf{D}}$ (see (7)) have the form

$$\begin{aligned}
&\underset{\approx}{\mathbf{A}} = \underset{\approx}{\mathbf{E}} Q_2 + d\nabla\nabla, \;\; \underset{\approx}{\mathbf{B}} = \underset{\approx}{\mathbf{C}} = -2\alpha \underset{\approx}{\mathbf{C}} \cdot \nabla, \;\; \underset{\approx}{\mathbf{D}} = \underset{\approx}{\mathbf{E}} Q_4 + m\nabla\nabla, \\
&Q_2 = b\Delta - \rho\partial_t^2, \;\; Q_4 = g\Delta - l - J\partial_t^2, \;\; Q_1 = Q_2 + d\Delta, \;\; Q_3 = Q_4 + m\Delta, \;\; \underset{\sim}{\mathbf{J}} = J\underset{\approx}{\mathbf{E}}, \\
&d = \lambda + \mu - \alpha, \;\; l = 4\alpha, \quad b = \mu + \alpha, \quad g = \delta + \beta, \;\; m = \gamma + \delta - \beta,
\end{aligned} \tag{17}$$

where Q_1, Q_2, Q_3 Q_4 are wave operators, and the elasticity tensors have expressions

$$\underset{\approx}{\mathbf{A}} = a_1 \underset{\approx}{\mathbf{C}}_{(1)} + a_2 \underset{\approx}{\mathbf{C}}_{(2)} + a_3 \underset{\approx}{\mathbf{C}}_{(3)}, \quad \underset{\approx}{\mathbf{D}} = d_1 \underset{\approx}{\mathbf{C}}_{(1)} + d_2 \underset{\approx}{\mathbf{C}}_{(2)} + d_3 \underset{\approx}{\mathbf{C}}_{(3)}. \tag{18}$$

Here $\underset{\approx}{\mathbf{C}}_{(1)}$, $\underset{\approx}{\mathbf{C}}_{(2)}$ $\underset{\approx}{\mathbf{C}}_{(3)}$ are basic isotropic tensors of the fourth rank, and for material constants we use the notation $a_1 = \lambda$, $a_2 = \mu$, $a_3 = \alpha$, $b_1 = \gamma$, $b_2 = \delta$ $b_3 = \beta$. Denoting by

$$\underset{\approx}{\mathbb{M}}_* = \begin{pmatrix} \hat{\underset{\approx}{\mathbf{A}}} & \hat{\underset{\approx}{\mathbf{B}}}^{(1)} \\ \hat{\underset{\approx}{\mathbf{B}}}^{(2)} & \hat{\underset{\approx}{\mathbf{C}}} \end{pmatrix} \tag{19}$$

the TBM operator of the cofactors for the TBM operator $\underset{\approx}{\mathbb{M}}$ of the equation (6), after cumbersome calculations we obtain [5, 6, 7, 13]

$$\begin{aligned}
&\hat{\underset{\approx}{\mathbf{A}}} = Q_3 P \underset{\approx}{\mathbf{R}} \;\; (\hat{\underset{\approx}{\mathbf{A}}}^T = \hat{\underset{\approx}{\mathbf{A}}}), \;\; \hat{\underset{\approx}{\mathbf{B}}} = \hat{\underset{\approx}{\mathbf{B}}}^{(1)} = \hat{\underset{\approx}{\mathbf{B}}}^{(2)} = Q_1 Q_3 P \underset{\approx}{\mathbf{B}} \;\; (\hat{\underset{\approx}{\mathbf{B}}}^T = -\hat{\underset{\approx}{\mathbf{B}}}), \\
&\hat{\underset{\approx}{\mathbf{C}}} = Q_1 P \underset{\approx}{\mathbf{T}} \;\; (\hat{\underset{\approx}{\mathbf{C}}}^T = \hat{\underset{\approx}{\mathbf{C}}}); \;\; \underset{\approx}{\mathbf{R}} = \underset{\approx}{\mathbf{E}} Q_1 Q_4 - (dQ_4 - 4\alpha^2)\nabla\nabla, \;\; \underset{\approx}{\mathbf{B}} = -2\alpha \underset{\approx}{\mathbf{C}} \cdot \nabla, \\
&\underset{\approx}{\mathbf{T}} = \underset{\approx}{\mathbf{E}} Q_2 Q_3 - (mQ_2 - 4\alpha^2)\nabla\nabla, \;\; P = Q_2 Q_4 + 4\alpha^2 \Delta.
\end{aligned} \tag{20}$$

It is easy to see that by virtue of (20) the TBM operator of the cofactors (19) can be represented as follows:

$$\underset{\approx}{\mathbb{M}}_* = \begin{pmatrix} PQ_3 & 0 \\ 0 & PQ_1 \end{pmatrix} \underset{\approx}{\mathbb{N}}^{(1)} = \underset{\approx}{\mathbb{N}}^{(2)} \begin{pmatrix} PQ_3 & 0 \\ 0 & PQ_1 \end{pmatrix}, \tag{21}$$

where TBM operators are introduced

$$\underset{\approx}{\mathbb{N}}^{(1)} = \begin{pmatrix} \underset{\approx}{\mathbf{R}} & Q_1 \underset{\approx}{\mathbf{B}} \\ Q_3 \underset{\approx}{\mathbf{B}} & \underset{\approx}{\mathbf{T}} \end{pmatrix}, \quad \underset{\approx}{\mathbb{N}}^{(2)} = \begin{pmatrix} \underset{\approx}{\mathbf{R}} & Q_3 \underset{\approx}{\mathbf{B}} \\ Q_1 \underset{\approx}{\mathbf{B}} & \underset{\approx}{\mathbf{T}} \end{pmatrix}. \tag{22}$$

It is easy to prove the relations

$$\underset{\approx}{\mathbb{M}} \cdot \underset{\approx}{\mathbb{N}}^{(1)T} = \underset{\approx}{\mathbb{N}}^{(2)T} \cdot \underset{\approx}{\mathbb{M}} = \begin{pmatrix} \underset{\approx}{\mathbf{E}} Q_1 P & \underset{\approx}{\mathbf{O}} \\ \underset{\approx}{\mathbf{O}} & \underset{\approx}{\mathbf{E}} Q_3 P \end{pmatrix}, \;\; |\underset{\approx}{\mathbb{M}}| = \det(\underset{\approx}{\mathbb{M}}) = Q_1 Q_3 P^2. \tag{23}$$

Then if we shall seek the solution of the equation (6) in the form (similar to Galerkin)

$$\mathbb{U} = \underset{\approx}{\mathbb{N}}^{(1)T} \cdot \mathbb{V} \quad \left(\mathbb{U} = \begin{pmatrix} \mathbf{u} \\ \boldsymbol{\varphi} \end{pmatrix}, \quad \mathbb{V} = \begin{pmatrix} \mathbf{v} \\ \boldsymbol{\psi} \end{pmatrix} \right), \tag{24}$$

then, by virtue of the appropriate relation (23), we obtain the following split equations:

$$Q_1(Q_2Q_4 + 4\alpha^2\Delta)\mathbf{v} + \rho\mathbf{F} = 0, \quad Q_3(Q_2Q_4 + 4\alpha^2\Delta)\boldsymbol{\psi} + \rho\mathbf{m} = 0. \tag{25}$$

Applying the operator $\underset{\approx}{\mathbb{N}}^{(2)T}$ to the left of (6), by the first relation (23) we will have

$$\begin{aligned} &Q_1[(Q_2Q_4 + 4\alpha^2\Delta)\mathbf{u} + 2\alpha(\underset{\approx}{\mathbf{C}}\cdot\nabla)\cdot(\rho\mathbf{m})] + [\underset{\approx}{\mathbf{E}}Q_1Q_4 - (dQ_4 - 4\alpha^2)\nabla\nabla]\cdot(\rho\mathbf{F}) = 0, \\ &Q_3[(Q_2Q_4 + 4\alpha^2\Delta)\boldsymbol{\varphi} + 2\alpha(\underset{\approx}{\mathbf{C}}\cdot\nabla)\cdot(\rho\mathbf{F})] + [\underset{\approx}{\mathbf{E}}Q_2Q_3 - (mQ_2 - 4\alpha^2)\nabla\nabla]\cdot(\rho\mathbf{m}) = 0. \end{aligned} \tag{26}$$

For $\alpha = 0$ (the case of a reduced medium), the classical equation follows from the first equation (26), and the second equation has a similar form.

5. Decomposition of static boundary conditions

In the case of an isotropic micropolar material without a center of symmetry, by virtue of (18) and $\underset{\approx}{\mathbf{B}} = b_1\underset{\approx}{\mathbf{C}}_{(1)} + b_2\underset{\approx}{\mathbf{C}}_{(2)} + b_3\underset{\approx}{\mathbf{C}}_{(3)}$, from (10) we have

$$\begin{aligned} &\underset{\sim}{\mathbf{T}}^{(1)} = a_2\underset{\sim}{\mathbf{E}}\mathbf{n}\cdot\nabla + a_1\mathbf{n}\nabla + a_3(\mathbf{n}\nabla)^T, \ \underset{\sim}{\mathbf{T}}^{(2)} = b_2\underset{\sim}{\mathbf{E}}\mathbf{n}\cdot\nabla + b_1\mathbf{n}\nabla + b_3(\mathbf{n}\nabla)^T - (a_2 - a_3)\mathbf{n}\cdot\underset{\approx}{\mathbf{C}}, \\ &\underset{\sim}{\mathbf{T}}^{(3)} = b_2\underset{\sim}{\mathbf{E}}\mathbf{n}\cdot\nabla + b_1\mathbf{n}\nabla + b_3(\mathbf{n}\nabla)^T, \ \underset{\sim}{\mathbf{T}}^{(4)} = d_2\underset{\sim}{\mathbf{E}}\mathbf{n}\cdot\nabla + d_1\mathbf{n}\nabla + d_3(\mathbf{n}\nabla)^T - (b_2 - b_3)\mathbf{n}\cdot\underset{\approx}{\mathbf{C}}. \end{aligned} \tag{27}$$

We note that some authors (see, for ex., [11, 12]) consider $\underset{\approx}{\mathbf{B}}$ as an asymmetric tensor, so in the case of an isotropic medium it is zero, as above. However, some authors prove that $\underset{\approx}{\mathbf{B}}$ is a symmetric tensor and in the case of an isotropic medium, it is not equal to zero, and how any isotropic fourth-rank tensor is generally determined by three parameters (see, for ex., [14]), as is customary in this case. Further, it is easy to see

$$\underset{\sim}{\mathbf{T}}^{(2)} = \underset{\sim}{\mathbf{T}}^{(3)} - (a_2 - a_3)\mathbf{n}\cdot\underset{\approx}{\mathbf{C}}, \ \underset{\sim}{\mathbf{T}}^{(4)} = \underset{\sim}{\mathbf{T}}^{\prime(4)} - (b_2 - b_3)\mathbf{n}\cdot\underset{\approx}{\mathbf{C}}, \ \underset{\sim}{\mathbf{T}}^{\prime(4)} = d_2\underset{\sim}{\mathbf{E}}\mathbf{n}\cdot\nabla + d_1\mathbf{n}\nabla + d_3(\mathbf{n}\nabla)^T.$$

Assuming that the body has a piecewise-plane boundary and denoting by $\underset{\sim}{\mathbf{T}}^{(1)}_*$ and $|\underset{\sim}{\mathbf{T}}^{(1)}|$, $\underset{\sim}{\mathbf{T}}^{(3)}_*$ and $|\underset{\sim}{\mathbf{T}}^{(3)}|$, $\underset{\sim}{\mathbf{T}}^{\prime(4)}_*$ and $|\underset{\sim}{\mathbf{T}}^{\prime(4)}|$ the differential tensors-operators of the cofactors and determinants for the tensor operators $\underset{\sim}{\mathbf{T}}^{(1)}$, $\underset{\sim}{\mathbf{T}}^{(3)}$ and $\underset{\sim}{\mathbf{T}}^{\prime(4)}$ respectively, after cumbersome calculations, where $a_{12} = a_1 + a_2$, $a_{23} = a_2 + a_3$, $\Delta_{\mathbf{n}} = \nabla\nabla + (\mathbf{nn} - \underset{\sim}{\mathbf{E}})\Delta$), we obtain

$$\begin{aligned} &\underset{\sim}{\mathbf{T}}^{(1)}_* = [a_{12}a_{23}\underset{\sim}{\mathbf{E}}\mathbf{n}\cdot\nabla - a_3a_{12}\mathbf{n}\nabla - a_1a_{23}(\mathbf{n}\nabla)^T]\mathbf{n}\cdot\nabla + a_1a_3\Delta_{\mathbf{n}}, \\ &\underset{\sim}{\mathbf{T}}^{(3)}_* = [(b_1 + b_2)(b_2 + b_3)\underset{\sim}{\mathbf{E}}\mathbf{n}\cdot\nabla - b_3(b_1 + b_2)\mathbf{n}\nabla - b_1(b_2 + b_3)(\mathbf{n}\nabla)^T]\mathbf{n}\cdot\nabla + b_1b_3\Delta_{\mathbf{n}}, \\ &\underset{\sim}{\mathbf{T}}^{\prime(4)}_* = [(d_1 + d_2)(d_2 + d_3)\underset{\sim}{\mathbf{E}}\mathbf{n}\cdot\nabla - d_3(d_1 + d_2)\mathbf{n} - d_1(d_2 + d_3)(\mathbf{n}\nabla)^T]\mathbf{n}\cdot\nabla + d_1d_3\Delta_{\mathbf{n}}, \\ &|\underset{\sim}{\mathbf{T}}^{(1)}| = a_2[a_{12}a_{23}\mathbf{nn}\overset{2}{\otimes}\nabla\nabla - a_1a_3\Delta]\mathbf{n}\cdot\nabla, \ |\underset{\sim}{\mathbf{T}}^{(3)}| = b_2[(b_1 + b_2)(b_2 + b_3)\mathbf{nn}\overset{2}{\otimes}\nabla\nabla - b_1b_3\Delta]\mathbf{n}\cdot\nabla, \\ &|\underset{\sim}{\mathbf{T}}^{\prime(4)}| = d_2[(d_1 + d_2)(d_2 + d_3)\mathbf{nn}\overset{2}{\otimes}\nabla\nabla - d_1d_3\Delta]\mathbf{n}\cdot\nabla. \end{aligned}$$

Note that we want to obtain boundary conditions separately for $\mathbf{u}$ and $\boldsymbol{\varphi}$. In order to shorten the letter, we consider the case when $b_2 = b_3$, $a_2 = a_3$. Then $\underset{\sim}{\mathbf{T}}^{(2)} = \underset{\sim}{\mathbf{T}}^{(3)}$, $\underset{\sim}{\mathbf{T}}^{(4)} = \underset{\sim}{\mathbf{T}}^{'(4)}$ and the boundary conditions (12) can be written in the form

$$\underset{\sim}{\mathbf{T}}^{(1)}\cdot\mathbf{u}+\underset{\sim}{\mathbf{T}}^{(3)}\cdot\boldsymbol{\varphi} = \mathbf{P}, \quad \underset{\sim}{\mathbf{T}}^{(3)}\cdot\mathbf{u}+\underset{\sim}{\mathbf{T}}^{'(4)}\cdot\boldsymbol{\varphi} = \boldsymbol{\mu}. \tag{28}$$

In this case, it is easy to obtain the boundary conditions separately for $\mathbf{u}$ and $\boldsymbol{\varphi}$

$$\left(|\underset{\sim}{\mathbf{T}}^{'(4)}|\underset{\sim}{\mathbf{T}}^{(3)T}_{*}\cdot\underset{\sim}{\mathbf{T}}^{(1)} - |\underset{\sim}{\mathbf{T}}^{(3)}|\underset{\sim}{\mathbf{T}}^{'(4)T}_{*}\cdot\underset{\sim}{\mathbf{T}}^{(3)}\right)\cdot\mathbf{u} = |\underset{\sim}{\mathbf{T}}^{'(4)}|\underset{\sim}{\mathbf{T}}^{(3)T}_{*}\cdot\mathbf{P} - |\underset{\sim}{\mathbf{T}}^{(3)}|\underset{\sim}{\mathbf{T}}^{'(4)T}_{*}\cdot\boldsymbol{\mu},$$

$$\left(|\underset{\sim}{\mathbf{T}}^{(3)}|\underset{\sim}{\mathbf{T}}^{(1)T}_{*}\cdot\underset{\sim}{\mathbf{T}}^{(3)} - |\underset{\sim}{\mathbf{T}}^{(1)}|\underset{\sim}{\mathbf{T}}^{(3)T}_{*}\cdot\underset{\sim}{\mathbf{T}}^{'(4)}\right)\cdot\boldsymbol{\varphi} = |\underset{\sim}{\mathbf{T}}^{(3)}|\underset{\sim}{\mathbf{T}}^{(1)T}_{*}\cdot\mathbf{P} - |\underset{\sim}{\mathbf{T}}^{(1)}|\underset{\sim}{\mathbf{T}}^{(3)T}_{*}\cdot\boldsymbol{\mu}.$$

6. Decomposition of the canonical equations for the transversely isotropic body

Under the canonical equations we are understood equations that are obtained by the canonical representations of the material tensors. In a similar sense, the term canonical mechanics can also be used. Thus, in this case the elastic modulus tensor $\underset{\approx}{\mathbf{A}}$ is represented in the canonical form [8, 9, 10], that is $\underset{\approx}{\mathbf{A}} = \sum\limits_{k=1}^{6} \lambda_k \underset{\sim}{\mathbf{w}}_k \underset{\sim}{\mathbf{w}}_k$, where λ_k and $\underset{\sim}{\mathbf{w}}_k$, $k = 1, \ldots, 6$, are the eigenvalues and eigentensors for $\underset{\approx}{\mathbf{A}}$. Then the vector equation with respect to the displacement vector can be written in the form

$$\underset{\sim}{\mathbf{L}}\cdot\mathbf{u} + \rho\mathbf{F} = 0, \quad \underset{\sim}{\mathbf{L}} = \sum_{k=1}^{6} \lambda_k \underset{\sim}{\mathbf{w}}_k\cdot\nabla\underset{\sim}{\mathbf{w}}_k\cdot\nabla. \tag{29}$$

Further we introduce the definition.

Definition. The symbol $\{\alpha_1, \alpha_2, \ldots, \alpha_k\}$, where k is the number of different eigenvalues of the tensor, and α_i is the multiplicity of the eigenvalue λ_i $(i = 1, 2, \ldots, k)$, is called *the anisotropy symbol* (*structure symbol*) of the tensor.

We note that on the basis of this definition, the classification of classical and microcontinuum anisotropic materials is given in [8, 9, 10]. By virtue of this classification, classical (micropolar) isotropic materials are special cases of materials in which the anisotropy symbol consists of not more than two (three) elements. A similar situation occurs for other anisotropies [8, 9, 10]. In particular, classical transversely isotropic materials are special cases of anisotropic materials whose anisotropy symbols consist of four elements, and orthotropic materials are special cases of anisotropic media whose structure symbols consist of no more than 6 elements. The anisotropy symbol of an orthotropic micropolar material with a symmetry center consists of not more than 9 elements [8, 9, 10].

We now consider the canonical representation of the transversely isotropic elastic modulus tensor with the anisotropy symbol {1,1,2,2} [8, 9, 10]:

$$\underset{\approx}{\mathbf{A}} = \mu_1 \underset{\sim}{\mathbf{w}}_1 \underset{\sim}{\mathbf{w}}_1 + \mu_2 \underset{\sim}{\mathbf{w}}_2 \underset{\sim}{\mathbf{w}}_2 + \mu_3(\underset{\sim}{\mathbf{w}}_3 \underset{\sim}{\mathbf{w}}_3 + \underset{\sim}{\mathbf{w}}_4 \underset{\sim}{\mathbf{w}}_4) + \mu_5(\underset{\sim}{\mathbf{w}}_5 \underset{\sim}{\mathbf{w}}_5 + \underset{\sim}{\mathbf{w}}_6 \underset{\sim}{\mathbf{w}}_6). \tag{30}$$

(According to the classification of materials adopted in [8, 9, 10], transversely isotropic materials can be of the following types: {1,1,2,2}, {1,2,1,2}, {1,2,2,1}, {2,1,1,2}, {2,1,2,1}, {2,2,1,1}). For the material {1,1,2,2} the eigenvalues are determined by the formulas [8, 9, 10]

$$\begin{aligned}&\mu_1=1/2(A_{11}+A_{12}+A_{33}-\sqrt{(A_{11}+A_{12}-A_{33})^2+8A_{13}^2}),\ \mu_3=\mu_4=A_{11}-A_{12},\\&\mu_2=1/2(A_{11}+A_{12}+A_{33}+\sqrt{(A_{11}+A_{12}-A_{33})^2+8A_{13}^2}),\ \mu_5=\mu_6=A_{55},\end{aligned}\tag{31}$$

and the eigentensors are represented in the form

$$\begin{aligned}&\underset{\sim}{\mathbf{w}}_1=-\frac{\sqrt{2}}{2}\sin\alpha(\underset{\sim}{\mathbf{e}}_1+\underset{\sim}{\mathbf{e}}_2)+\cos\alpha\underset{\sim}{\mathbf{e}}_3=-\frac{\sqrt{2}}{2}\sin\alpha\underset{\sim}{\mathbf{I}}+\cos\alpha\underset{\sim}{\mathbf{e}}_3,\ \ \underset{\sim}{\mathbf{e}}_\alpha=\mathbf{e}_\alpha\mathbf{e}_\alpha,\ \ \alpha=1,2,3,\\&\underset{\sim}{\mathbf{w}}_2=\frac{\sqrt{2}}{2}\cos\alpha(\underset{\sim}{\mathbf{e}}_1+\underset{\sim}{\mathbf{e}}_2)+\sin\alpha\underset{\sim}{\mathbf{e}}_3=\frac{\sqrt{2}}{2}\cos\alpha\underset{\sim}{\mathbf{I}}+\sin\alpha\underset{\sim}{\mathbf{e}}_3,\ \ \underset{\sim}{\mathbf{e}}_4=(1/\sqrt{2})(\mathbf{e}_3\mathbf{e}_2+\mathbf{e}_2\mathbf{e}_3),\\&\underset{\sim}{\mathbf{w}}_3=\frac{\sqrt{2}}{2}(\underset{\sim}{\mathbf{e}}_1-\underset{\sim}{\mathbf{e}}_2),\quad \underset{\sim}{\mathbf{w}}_4=\underset{\sim}{\mathbf{e}}_4,\quad \underset{\sim}{\mathbf{w}}_5=\underset{\sim}{\mathbf{e}}_5,\quad \underset{\sim}{\mathbf{w}}_6=\underset{\sim}{\mathbf{e}}_6,\quad \mathrm{tg}2\alpha=\frac{2\sqrt{2}A_{13}}{A_{11}+A_{12}-A_{33}},\end{aligned}\tag{32}$$

$$\begin{aligned}&\underset{\sim}{\mathbf{e}}_5=(1/\sqrt{2})(\mathbf{e}_1\mathbf{e}_3+\mathbf{e}_3\mathbf{e}_1),\ \ \underset{\sim}{\mathbf{e}}_6=(1/\sqrt{2})(\mathbf{e}_2\mathbf{e}_1+\mathbf{e}_1\mathbf{e}_2),\ \ \mathbf{e}_i\cdot\mathbf{e}_j=\delta_{ij},\ \ i,j=1,2,3,\\&\underset{\sim}{\mathbf{e}}_m\overset{2}{\otimes}\underset{\sim}{\mathbf{e}}_n=\delta_{mn},\ \ m,n=\overline{1,6},\ \ \underset{\sim}{\mathbf{I}}=\mathbf{e}_1\mathbf{e}_1+\mathbf{e}_2\mathbf{e}_2=\underset{\sim}{\mathbf{e}}_1+\underset{\sim}{\mathbf{e}}_2.\end{aligned}$$

The canonical representations of the tensor-operator of the equations and its determinant and the tensor of cofactors, as well as the stress tensor-operator, its determinant and the components of the tensor-operator of cofactors by virtue of (30) – (32) have the form

$$\begin{aligned}&\underset{\sim}{\mathbf{L}}=(a_1\underset{\sim}{\mathbf{I}}+a_3\mathbf{e}_3\mathbf{e}_3)\Delta+a_2\nabla^0\nabla^0+a_5[\mathbf{e}_3\nabla^0+(\mathbf{e}_3\nabla^0)^T]\partial_3+(a_3\underset{\sim}{\mathbf{I}}+a_4\mathbf{e}_3\mathbf{e}_3)\partial_3^2;\\&|\underset{\sim}{\mathbf{L}}|=A\Delta^3+B\Delta^2\partial_3^2+C\Delta\partial_3^4+D\partial_3^6=k(\Delta+k_1\partial_3^2)(\Delta+k_2\partial_3^2)(\Delta+k_3\partial_3^2),\ k=A,\\&k_1+k_2+k_3=B/A,\ \ k_1k_2+k_1k_3+k_2k_3=C/A,\ \ k_1k_2k_3=D/A;\\&\underset{\sim}{\mathbf{L}}_*=a(a_3\underset{\sim}{\mathbf{I}}+a_1\mathbf{e}_3\mathbf{e}_3)\Delta^2-a_2a_3\Delta\nabla^0\nabla^0-a_1a_5[\mathbf{e}_3\nabla^0+(\mathbf{e}_3\nabla^0)^T]\partial_3\\&+\Big\{\Big[[(a_2+a_3)a_4+c(a_3+a_5)]\underset{\sim}{\mathbf{I}}+a_2(a+a_1)\mathbf{e}_3\mathbf{e}_3\Big]\Delta+(a_5^2-a_2a_4)\nabla^0\nabla^0\Big\}\partial_3^2\\&-a_3a_5[\mathbf{e}_3\nabla^0+(\mathbf{e}_3\nabla^0)^T]\partial_3^3-a_3(a_4\underset{\sim}{\mathbf{I}}-a_3\mathbf{e}_3\mathbf{e}_3)\partial_3^4,\ \underset{\sim}{\mathbf{T}}=(a_1\underset{\sim}{\mathbf{I}}+a_3\mathbf{e}_3\mathbf{e}_3)\mathbf{n}^{00}-b\mathbf{n}^0\nabla^0+\\&a_1(\mathbf{n}^0\nabla^0)^T+n_3[-c\mathbf{e}_3\nabla^0+a_3(\mathbf{e}_3\nabla^0)^T]+[n_3(a_3\underset{\sim}{\mathbf{I}}+a_4\mathbf{e}_3\mathbf{e}_3)-c\mathbf{n}^0\mathbf{e}_3+a_3\mathbf{e}_3\mathbf{n}^0]\partial_3,\\&|\underset{\sim}{\mathbf{T}}|=a_1a_3\{[b-(b+c)n_3^2]\Delta+2a_2\mathbf{n}^0\mathbf{n}^0\overset{2}{\otimes}\nabla^0\nabla^0\}\mathbf{n}^{00}+\{b(a_1a_4-a_3^2)+a_1c^2\\&-[(c-b)a_3^2+a(c^2+ba_4)]n_3^2\}n_3\Delta\partial_3+2a_1[(a_3+c)a_5+a_2a_4]n_3\mathbf{n}^0\mathbf{n}^0\overset{2}{\otimes}\nabla^0\nabla^0\partial_3\\&+a_3\{-a_1c+[a_1c+(a+a_1)a_4-c^2]n_3^2\}\mathbf{n}^{00}\partial_3^2-a_3^2[c-(c+a_4)n_3^2]n_3\partial_3^3,\\&T_{*11}=a_3(a_1n_1\partial_1+an_2\partial_2)\mathbf{n}^{00}-c_{33}+[(a_1a_4+a_3^2)n_1\partial_1+(aa_4-c^2)n_2\partial_2]n_3\partial_3+(a_4n_3^2-cn_2^2)a_3\partial_3^2,\\&T_{*12}=a_3(bn_1\partial_2-a_1n_2\partial_1)\mathbf{n}^{00}+[(c^2+ba_4)n_1\partial_2+(a_3^2-aa_4)n_2\partial_1]n_3\partial_3+ca_3(n_3^2\partial_1\partial_2+n_1n_2\partial_3^2),\\&T_{*13}=-(ba_3n_3\partial_2+a_1cn_2\partial_3)\underset{\sim}{\mathbf{C}}\overset{2}{\otimes}\mathbf{n}^0\nabla^0-a_1(a_3n_3\partial_1+cn_1\partial_3)\mathbf{n}^{00}-a_3^2n_3^2\partial_1\partial_3-ca_3n_1n_3\partial_3^2,\\&T_{*21}=a_3(bn_2\partial_1-a_1n_1\partial_2)\mathbf{n}^{00}+[(c^2+ba_4)n_2\partial_1+(a_3^2-a_1a_4)n_1\partial_2]n_3\partial_3+ca_3(n_3^2\partial_1\partial_2+n_1n_2\partial_3^2),\\&T_{*22}=a_3(a_1n_2\partial_2+an_1\partial_1)\mathbf{n}^{00}-c_{31}+[(a_1a_4+a_3^2)n_2\partial_2+(aa_4-c^2)n_1\partial_1]n_3\partial_3+(a_4n_3^2-cn_1^2)a_3\partial_3^2,\\&T_{*23}=(ba_3n_3\partial_1+a_1cn_1\partial_3)\underset{\sim}{\mathbf{C}}\overset{2}{\otimes}\mathbf{n}^0\nabla^0-a_1(a_3n_3\partial_2+cn_2\partial_3)\mathbf{n}^{00}-a_3^2n_3^2\partial_2\partial_3-ca_3n_2n_3\partial_3^2,\end{aligned}$$

$$T_{*31}=(ca_1n_3\partial_2+ba_3n_2\partial_3)\underset{\sim}{\mathbf{C}}\overset{2}{\otimes}\mathbf{n}^0\nabla^0-a_1(cn_3\partial_1+a_3n_1\partial_3)\mathbf{n}^{00}-ca_3n_3^2\partial_1\partial_3-a_3^2n_1n_3\partial_3^2,$$
$$T_{*32}=-(ca_1n_3\partial_1+ba_3n_1\partial_3)\underset{\sim}{\mathbf{C}}\overset{2}{\otimes}\mathbf{n}^0\nabla^0-a_1(cn_3\partial_2+a_3n_2\partial_3)\mathbf{n}^{00}-ca_3n_3^2\partial_2\partial_3-a_3^2n_2n_3\partial_3^2,$$
$$T_{*33}=ba_1(1-n_3^2)\Delta+a_1(a-b)\mathbf{n}^0\mathbf{n}^0\overset{2}{\otimes}\nabla^0\nabla^0+(aa_3+a_1c)n_3\mathbf{n}^{00}\partial_3+a_3^2n_3^2\partial_3^2,\ \ \underset{\sim}{\mathbf{T}}_*=T_{*ij}\mathbf{e}_i\mathbf{e}_j,$$

where the following notations are introduced:

$$A=aa_1a_3,\ B=a(a_3^2+a_1a_4)+ca_1(a_3+a_5),\ C=a_3[aa_4+c(a_3+a_5)];\ a=a_1+a_2,\ c=a_3-a_5$$
$$D=a_3^2a_4,\quad a_1=(1/2)\mu_3,\quad a_2=(1/2)(\mu_1\sin^2\alpha+\mu_2\cos^2\alpha),\quad a_3=(1/2)\mu_5,\ c_{33}=ca_3n_3^2\partial_2^2,$$
$$a_4=\mu_1\cos^2\alpha+\mu_2\sin^2\alpha, a_5=(1/2)[\sqrt{2}(\mu_2-\mu_1)\sin\alpha\cos\alpha+\mu_5],\ \Delta=\partial_1^2+\partial_2^2,\ \mathbf{n}^{00}=\mathbf{n}^0\cdot\nabla^0,$$
$$\mathbf{n}^0=n_I\mathbf{e}_I,\ \nabla^0=\mathbf{e}_I\partial_I,\ \mathbf{n}^0\mathbf{n}^0\overset{2}{\otimes}\nabla^0\nabla^0=n_In_J\partial_I\partial_J,\ \underset{\sim}{\mathbf{C}}=C_{IJ}\mathbf{e}_I\mathbf{e}_J,\ b=a_1-a_2,\ c_{31}=ca_3n_3^2\partial_1^2.$$

If we apply the operator $\underset{\sim}{\mathbf{L}}_*$ from the left with a single multiplication to the equation (the first relation (29)), and the operator $\underset{\sim}{\mathbf{T}}_*^T$ to the boundary conditions $\underset{\sim}{\mathbf{T}}\cdot\mathbf{u}=\mathbf{P}$, then we obtain the split equations and boundary conditions

$$|\underset{\sim}{\mathbf{L}}|\mathbf{u}+\underset{\sim}{\mathbf{L}}_*^T\cdot(\rho\mathbf{F})=0,\quad |\underset{\sim}{\mathbf{T}}|\mathbf{u}=\underset{\sim}{\mathbf{T}}_*^T\cdot\mathbf{P}, \tag{33}$$

and if we look for the solution $\mathbf{u}$ in the form $\mathbf{u}=\underset{\sim}{\mathbf{L}}_*\cdot\mathbf{v}$, then we have the split equations and boundary conditions

$$|\underset{\sim}{\mathbf{L}}|\mathbf{v}+\rho\mathbf{F}=0,\quad |\underset{\sim}{\mathbf{T}}|(\underset{\sim}{\mathbf{L}}_*\cdot\mathbf{v})=\underset{\sim}{\mathbf{T}}_*^T\cdot\mathbf{P}. \tag{34}$$

When obtaining (33) and (34), we took into account the relation $\underset{\sim}{\mathbf{F}}\cdot\underset{\sim}{\mathbf{F}}_*^T=\underset{\sim}{\mathbf{F}}_*^T\cdot\underset{\sim}{\mathbf{F}}=\underset{\sim}{\mathbf{E}}|\underset{\sim}{\mathbf{F}}|,\ \forall\underset{\sim}{\mathbf{F}}$.

Further, applying, for example, to the split equations from (34), the kth moment operator [4, 6, 7], the equations for prismatic bodies in moments with respect to any system of orthogonal polynomials can be represented in the form

$$A\Delta^3\overset{(k)}{\mathbf{v}}+B\Delta^2\overset{(k)}{\mathbf{v}}{}''+C\Delta\overset{(k)}{\mathbf{v}}{}^{IV}+D\overset{(k)}{\mathbf{v}}{}^{VI}+\rho\overset{(k)}{\mathbf{F}}=0,\ \ k=\overline{0,\infty}; \tag{35}$$

where in the application of the system of Legendre polynomials, the expressions for $\overset{(k)}{\mathbf{v}}{}''$, $\overset{(k)}{\mathbf{v}}{}^{IV}$ and $\overset{(k)}{\mathbf{v}}{}^{VI}$ are defined using the following relationship:

$$\overset{(n)(2m)}{\mathbf{v}}=(2n+1)\sum_{k=1}^{\infty}C_{k+2m-2}^{2m-1}\prod_{s=1}^{2m-1}(2n+2k+2s-1)\overset{(n+2k+2m-2)}{\mathbf{v}},\ n\in\mathbb{N}_0,\ m\in\mathbb{N}. \tag{36}$$

Note that analogous (35) equations can also be easily obtained from the equations (33).

7. The quasistatic canonical problem of the micropolar theory of elasticity in displacements and rotations

To reduce the letter, we consider an isotropic material with a center of symmetry. The mechanical properties of such a linear material are characterized by two fourth-rank tensors,

each of which in turn is determined by three essential components. These materials are special cases of materials whose anisotropy symbols consist of three elements and the number of which, according to the classification adopted above, is 28 [8, 9, 10], among which the materials $\{1,5,3\}$ and $\{5,1,3\}$ are. The first of them has a positive Poisson's ratio, and the second one has negative Poisson's ratio. Under the canonical problem we mean the problem, in the formulation of which the material tensors are written in the canonical form. We confine ourselves to the isotropic material $\{1,5,3\}$. In this case, the material tensors have the expressions

$$\begin{aligned}
&\underset{\approx}{\mathbf{A}} = \frac{1}{3}(\lambda_1-\lambda_2)\underset{\approx}{\mathbf{C}}_{(1)} + \frac{1}{2}(\lambda_2+\lambda_7)\underset{\approx}{\mathbf{C}}_{(2)} + \frac{1}{2}(\lambda_2-\lambda_7)\underset{\approx}{\mathbf{C}}_{(3)},\\
&\underset{\approx}{\mathbf{D}} = \frac{1}{3}(\mu_1-\mu_2)\underset{\approx}{\mathbf{C}}_{(1)} + \frac{1}{2}(\mu_2+\mu_7)\underset{\approx}{\mathbf{C}}_{(2)} + \frac{1}{2}(\mu_2-\mu_7)\underset{\approx}{\mathbf{C}}_{(3)}.
\end{aligned} \tag{37}$$

Then, by virtue of (37), it is not difficult to obtain equations analogous to (26), from which in the case of a quasistatic we have

$$\Delta^2(a_1\Delta+a_2)\mathbf{u} + \mathbf{S}^* = 0, \quad \Delta(\Delta^2+b_2\Delta+b_3)\boldsymbol{\varphi}+\mathbf{H}^*=0, \tag{38}$$

$$\begin{aligned}
&\mathbf{S}^* = \lambda_7 Q_1^*(\underset{\approx}{\mathbf{C}}\cdot\nabla)\cdot(\rho\mathbf{m}) + [\underset{\sim}{\mathbf{E}}Q_1^*Q_4^* - (dQ_4^*-\lambda_7^2)\nabla\nabla]\cdot(\rho\mathbf{F}), \quad Q_1^* = (b+d)\Delta,\\
&\mathbf{H}^* = \lambda_7 Q_3^*(\underset{\approx}{\mathbf{C}}\cdot\nabla)\cdot(\rho\mathbf{F}) + [\underset{\sim}{\mathbf{E}}Q_2^*Q_3^* - (mQ_2^*-\lambda_7^2)\nabla\nabla]\cdot(\rho\mathbf{m}), \quad Q_4^* = g\Delta - l,\\
&Q_2^* = b\Delta, \quad Q_3^* = (g+m)\Delta - l, \quad d = \frac{1}{6}(2\lambda_1+\lambda_2) - \frac{1}{2}\lambda_7, \ \ l = 2\lambda_7,\\
&b = \frac{1}{2}(\lambda_2+\lambda_7), \ \ m = \frac{1}{6}(2\mu_1+\mu_2) - \frac{1}{2}\mu_7, \ \ g = \frac{1}{2}(\mu_2+\mu_7),\\
&a_1 = \frac{1}{12}(\lambda_1+2\lambda_2)(\lambda_2+\lambda_7)(\mu_2+\mu_7), \ \ a_2 = -\frac{1}{3}\lambda_2\lambda_7(\lambda_1+2\lambda_2), \ \ b_3 = 2\lambda_2\lambda_7^2\\
&b_1 = \frac{1}{12}(\mu_1+2\mu_2)(\mu_2+\mu_7)(\lambda_2+\lambda_7), \ \ b_2 = -\lambda_7[\frac{1}{3}\lambda_2(\mu_1+2\mu_2) + \frac{1}{2}(\mu_2+\mu_7)(\lambda_2+\lambda_7)],
\end{aligned} \tag{39}$$

7.1. The quasistatic canonical problem of the micropolar theory of prismatic bodies in displacements and rotations and in their moments

Let's consider a prismatic body of constant thickness $2h$. As the base plane, we take the middle plane. In this case the Laplacian has the form

$$\hat{\Delta}\mathbb{F} = (\bar{\Delta} + h^{-2}\partial_3^2)\mathbb{F}, \quad \bar{\Delta} = g^{PQ}\nabla_P\nabla_Q, \tag{40}$$

and by (40) the equations (38) for the theory of prismatic bodies of constant thickness in displacements and rotations can be written in the form

$$\begin{aligned}
&[\bar{\Delta}^3 + A\bar{\Delta}^2 + h^{-2}(3\bar{\Delta}+2A)\bar{\Delta}\partial_3^2 + h^{-4}(3\bar{\Delta}+A)\partial_3^4 + h^{-6}\partial_3^6]\hat{\mathbf{u}} + \hat{\mathbf{S}}^{**} = 0,\\
&[\bar{\Delta}^3 + (B\bar{\Delta}+A)\bar{\Delta} + h^{-2}[(3\bar{\Delta}+2B)\bar{\Delta}+C]\partial_3^2 + h^{-4}(3\bar{\Delta}+B)\partial_3^4 + h^{-6}\partial_3^6]\hat{\boldsymbol{\varphi}} + \hat{\mathbf{H}}^{**} = 0;\\
&\hat{\mathbf{S}}^{**} = \frac{\hat{\mathbf{S}}^*}{a_1}, \quad \hat{\mathbf{H}}^{**} = \frac{\hat{\mathbf{H}}^*}{b_1}, \quad A = -\frac{4\lambda_2\lambda_7}{(\lambda_2+\lambda_7)(\mu_2+\mu_7)}, \quad B = \frac{b_2}{6b_1}, \quad C = \frac{2b_3}{b_1}.
\end{aligned} \tag{41}$$

Applying the kth moment operator of some system of orthogonal polynomials (Legendre, Tchebyshev) to the equations (41), we find the equations for the micropolar theory of prismatic bodies of constant thickness in the moments of the displacement and rotation vectors

$$\begin{aligned}&[\bar{\Delta}^3+(B\bar{\Delta}+A)\bar{\Delta}]\overset{(k)}{\boldsymbol{\varphi}}+h^{-2}[(3\bar{\Delta}+2B)\bar{\Delta}+C]\overset{(k)}{\boldsymbol{\varphi}}{}''+h^{-4}(3\bar{\Delta}+B)\overset{(k)}{\boldsymbol{\varphi}}{}^{IV}+h^{-6}\overset{(k)}{\boldsymbol{\varphi}}{}^{VI}+\overset{(k)}{\mathbf{H}}{}^{**}=0,\\&[\bar{\Delta}^3+A\bar{\Delta}^2]\overset{(k)}{\mathbf{u}}+h^{-2}(3\bar{\Delta}+2A)\bar{\Delta}\overset{(k)}{\mathbf{u}}{}''+h^{-4}(3\bar{\Delta}+A)\overset{(k)}{\mathbf{u}}{}^{IV}+h^{-6}\overset{(k)}{\mathbf{u}}{}^{VI}+\overset{(k)}{\mathbf{S}}{}^{**}=0,\ \ k\in\mathbb{N}_0.\end{aligned}\tag{42}$$

Having the equations (42), by the formula (36) it is easy to obtain systems of equations of any approximation in moments with respect to the system of Legendre polynomials. We note that the equations of the fifth (in the classical case) and the 8th (in the micropolar case) approximations in moments were obtained in the papers [5, 6, 7, 13] for isotropic material in the traditional form, as well as the similarly to (38), (41) and (42) equations in the traditional form are given in [5, 6, 7, 13]. Equations in moments for thin bodies with two small dimensions and thin multilayered structures are also given there.

Adding the corresponding canonical boundary conditions to the equations (42), we obtain a canonical statement of quasistatic boundary value problems for prismatic bodies. In order to shorten the letter, we shall not dwell on this in this paper, but refer to the interested reader in the papers [5, 6, 7], in which the formulations of boundary-value problems in the traditional form are given in detail, and they easily extend to canonical statements.

Note that for the theory of thin bodies, the split equations at equilibrium, depending on the order of approximation, are equations of elliptical type of high order [5, 6, 7, 13] and using the I.N. Vekua method [18], for them it is possible to get analytical solutions.

Acknowledgments

This work was supported by Shota Rustaveli National Science Foundation (project no. DI-2016-41) and the Russian Foundation for Basic Research (project no. 15-01-00848-a).

References

[1] Vekua, I. N. *Fundamentals of tensor analysis and covariant theory.* Nauka, Moscow, (in Russian), 1978, 296 p.

[2] Nikabadze, M. U. *Several Questions of Tensor Calculus with Applications to Mechanics.* Deposited in VINITI RAS, No. 231–V2013, 05.08.2013, (in Russian), Moscow, 2013, 242 p.

[3] Nikabadze, M. U. Construction of Eigentensor Columns in the Linear Micropolar Theory of Elasticity. *Moscow Univ. Mech. Bull.*, 69(1) (2014), 1–9.

[4] Nikabadze, M. U. *The method of orthogonal polynomials in the classical and micropolar mechanics of elastic thin bodies.* I. Deposited in VINITI RAS, No. 135-V2014, (in Russian), Moscow, 2014, 278 p.

[5] Nikabadze, M. U. *The method of orthogonal polynomials in the classical and micropolar mechanics of elastic thin bodies.* II. Deposited in VINITI RAS, No. 136-B2014, (in Russian), Moscow, 2014, 218 p.

[6] Nikabadze, M. U. *Development of the method of orthogonal polynomials in the classical and micropolar mechanics of elastic thin bodies* (in Russian), Moscow Univ. Press, Moscow, 2014, 515 p.

[7] Nikabadze, M. U. *The method of orthogonal polynomials in the classical and micropolar mechanics of elastic thin bodies.* Diss. Doctor Phys.–Math. Sci. (in Russian), Moscow, 2014, 384 p.

[8] Nikabadze, M. U. On several issues of tensor calculus with applications to mechanics. *Contemporary Math.*, (in Russian), 55 (2015), 3-194.

[9] Nikabadze, Mikhail U. Eigenvalue Problems of a Tensor and a Tensor-Block Matrix (TMB) of Any Even Rank with Some Applications in Mechanics. *H. Altenbach and S. Forest (eds.), Generalized Continua as Models for Classical and Advanced Materials, Advanced Structured Materials*, Springer International Publishing Switzerland, 42 (2016), 279-317.

[10] Nikabadze, M. U. Topics on tensor calculus with applications to mechanics. *J. Math. Sci.*, 225(1) (2017), 194.

[11] Eringen, A. C. *Microcontinuum field theories. 1. Foundation and solids.* N.Y.: Springer-Verlag, 1999.

[12] Novacky, V. *Theory of elasticity.* Mir, Moscow, 1975 (transl. in Russian).

[13] Nikabadze, Mikhail U. and Ulukhanyan, Armine R. Analytical Solutions in the Theory of Thin Bodies. *H. Altenbach and S. Forest (eds.), Generalized Continua as Models for Classical and Advanced Materials, Advanced Structured Materials*, Springer International Publishing Switzerland, 42 (2016), 319-361.

[14] Baskakov, V. A., Bestuzheva, N. P. and Konchakova N.A. *Linear Dynamic Theory of thermoelastic media with a microstructure.* Voronezh, Voronezh State Tech. Univ. Press, (in Russian), 2001. 162 p.

[15] Rykhlewsky, J. *"CEIIINOSSSTTUV" Mathematical structure of elastic solid1s. Preprint.* Moscow: Inst. Problem Mech. Acad. Sci. USSR, (in Russian), 217 (1983), 113 p.

[16] Ostrosablin, N. I. On the classification of anisotropic materials. *Dynamic Problems of an Inelastic Medium*, (in Russian), 71 (1985), 82–95.

[17] Ostrosablin, N. I. On the structure of the elastic modulus tensor and the classification of anisotropic materials. *J. Appl. Mech. Tech. Phys.*, (in Russian), 4 (1986), 127–135.

[18] Vekua, I. N. *New methods for solving elliptic equations.* OGIZ, Moscow, (in Russian), 1948, 296 p.

Mikhail Nikabadze, Ph.D.: Lomonosov Moscow State University, Department of Mechanics and Mathematics, Leninskie Gory, 1, Moscow 119992, Russia, & Bauman Moscow State Technical University, Baumanskaya 2-ya, str., 5, Moscow 105005 (*nikabadze@mail.ru*). The author gave a presentation of this paper during one of the conference sessions.

Modelling of vibration and large deflections of lattice-boom structures of cranes by means of rigid finite element method

Paweł Nowak, Andrzej Nowak, Marek Metelski

Abstract: The rigid finite element method (RFEM) is an original Polish method of slender system modelling. Structures with stable or changeable configuration are modelled by means of this method. The RFEM is most often used to discretise flexible units of mechanisms and machines, ropes and risers, and dynamics of machine tools, as well as plates and shells. The method can be also successfully used to analyse large lattice-boom structures for deformations. The aim of this paper is to present a 3D model of lattice-boom structure, in which the RFEM is used to discretise beam elements. The possibility of large deflections of the boom (within the range of several meters) was considered. The results of our own calculations (deflections, stresses, reaction forces), according to models of various degrees of complexity, were compared to results obtained using professional FEM package Abaqus/CAE software.

1. Introduction

This paper was written in cooperation between the Chair of Computer Modelling and PROTEA company, which is involved in the design and manufacture of offshore equipment – e.g. crane structures. One of the most important stages in the design of cranes mounted on drilling platforms and ships is computer verification of the construction assumption correctness. It is done by multiple calculations using commercial packages, or based on one's own modelling programs that have already been validated [1-3]. Custom programs [4] are generally better adapted to the needs of designers and the requirements of surveillance companies such as Norwegian DNV [5] or American API.

One of the most essential components of a crane are its booms. The paper presents the application of a rigid finite element method for lattice-work boom modelling. Linear and non-linear approach was validated by comparing the Chair's own results with those obtained using the Abaqus package.

The work presents the following models of the crane boom:

A. Beam type – all elements are beams of a longitudinal, transverse, flexural and torsional flexibility, rigidly connected in nodes.

B. Mixed type – where both beam-form elements connected in a rigid way and bar elements joined in an articulated way in nodes occur.

Analysing the construction of current latticework booms and design work on new structures, it is assumed that the latticework matrix consists of four supporting beams connected by bars (Fig. 1).

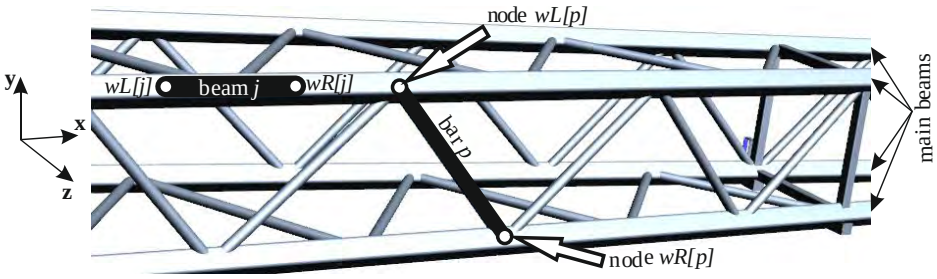

Figure 1. Supporting (main) beams and connecting elements.

In the work, the nodes are marked with w (w=1,...,n), while the connecting elements with the letter p (p=1,...,m). We assumed that the coordinates of all nodes are known prior to the deformation of the truss, i.e. $\boldsymbol{r}$ vectors in the global coordinate system:

$$\mathbf{r}_i^0 = \begin{bmatrix} x_i^0 & y_i^0 & z_i^0 \end{bmatrix}^T \text{ dla } i=1..n. \tag{1}$$

and their orientation in the space is defined by the angles of Euler ZYX [6-8]. We also assumed that for each bar the numbers of nodes that it connects, or is connected to, are known, namely:

$$\begin{cases} wR[p] \text{ - right node of bar } p, \\ wL[p] \text{ - left node of bar } p. \end{cases} \tag{2}$$

Geometric and material sizes characterizing bars (bar length before deformation l_p^0, density, Young's modulus, cross-sectional area, moment of inertia, etc.) are known, too.

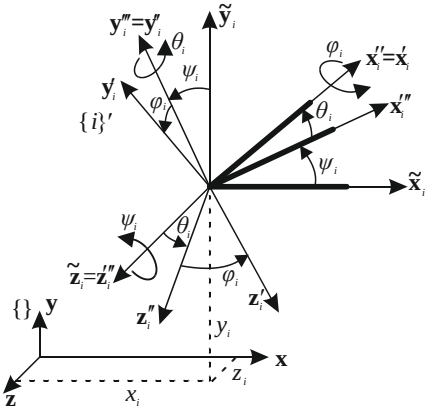

Figure 2. Node translation displacement and Euler ZYX angles.

The generalized coordinates of the nodes are the components of the following vectors:

$$\mathbf{q}_i = \left[\mathbf{r}_i \quad \mathbf{\Phi}_i\right]^{\mathrm{T}}, \tag{3}$$

where:

$$\mathbf{r}_i = \left[x_i \quad y_i \quad z_i\right]^{\mathrm{T}} \text{ - translation coordinates vector in the base system,} \tag{4}$$

$$\mathbf{\Phi}_i = \left[\varphi_i \quad \theta_i \quad \psi_i\right]^{\mathrm{T}} \text{ - Euler ZYX angles } \left(\text{Fig. 2.}\right). \tag{5}$$

Equations of the truss balance were derived from the Lagrange's equations (II kind), which in the statics task are presented as follows::

$$\frac{\partial V_s}{\partial \mathrm{q}_k} + \frac{\partial V_g}{\partial \mathrm{q}_k} = \mathrm{Q}_k \ , \tag{6}$$

where:

V_s— resilient deformation energy of the system,
V_g— energy of the gravity forces,
Q_k— generalized forces from external forces (loadings and node reactions),
q_k— *k*-th generalized coordinate.

In the analysed cases, the generalized coordinates were the relocations of the nodes.

2. SES models

The work presents models based on the rigid finite element method. The mixed model B is a combination of models, in which the main support beams are modelled as beams, and the connecting elements as bars. Computer programs based on them have been optimized to make computation time shorter than in the case of commercial packages.

2.1. Bar element model

In the work, we assumed that in the bar model the elements transfer only the axial forces and that the generalized coordinates are the translation relocations of the nodes. The potential energy of bar elastic deformation is determined by the equation:

$$V_s^{(p)} = \tfrac{1}{2} c_p \Delta_p^2 \ , \tag{7}$$

where:

$$\Delta_p = l_p - l_p^0 \ ; \ l_p = \left\{ \left[\mathbf{r}_{wR[p]} - \mathbf{r}_{wL[p]} \right]^{\mathrm{T}} \left[\mathbf{r}_{wR[p]} - \mathbf{r}_{wL[p]} \right] \right\}^{\frac{1}{2}} \ ; \ c_p = \frac{EF_p}{l_p^0},$$

E – material modulus of elasticity,

F_p – cross-sectional area of bar p, assuming its constant value.

Taking into account the form of vectors $\mathbf{q}_i$ (3) and (7) we obtained:

$$\left.\begin{aligned} \frac{\partial V_s^{(p)}}{\partial \mathbf{q}_{wR[p]}} &= c_p \frac{\Delta_p}{l_p} \left[\mathbf{q}_{wR[p]} - \mathbf{q}_{wL[p]} \right] \\ \frac{\partial V_s^{(p)}}{\partial \mathbf{q}_{wL[p]}} &= -c_p \frac{\Delta_p}{l_p} \left[\mathbf{q}_{wR[p]} - \mathbf{q}_{wL[p]} \right] \end{aligned}\right\} \tag{8}$$

We assumed that the mass of the bar p is reduced to nodes $wL[p]$ and $wR[p]$ in two equal parts. This leads to the following correlation:

$$V_g^{(p)} = g \frac{m_p}{2} \left[y_{wR[p]} + y_{wL[p]} \right]. \tag{9}$$

Therefore:

$$\left.\begin{aligned} \frac{\partial V_g^{(p)}}{\partial \mathbf{q}_{wR[p]}} &= \left[0 \quad \frac{m_p}{2} g \quad 0 \right]^{\mathrm{T}} \\ \frac{\partial V_g^{(p)}}{\partial \mathbf{q}_{wL[p]}} &= \left[0 \quad \frac{m_p}{2} g \quad 0 \right]^{\mathrm{T}} \end{aligned}\right\} \tag{10}$$

2.2. Beam element model

The transformation of coordinates from the node local system $\{i\}'$ to the base system $\{\}$ was made according to the equation below:

$$\mathbf{r}_i = \overline{\mathbf{r}}_i + \mathbf{R}_i \mathbf{r}_i', \tag{11}$$

where:

$$\overline{\mathbf{r}}_i = \begin{bmatrix} x_i \\ y_i \\ z_i \end{bmatrix} \ ; \ \mathbf{R}_i = \mathbf{R}_i^{\psi} \mathbf{R}_i^{\theta} \mathbf{R}_i^{\varphi} \ ; \ \mathbf{R}_i^{\psi} = \begin{bmatrix} c\psi_i & -s\psi_i & 0 \\ s\psi_i & c\psi_i & 0 \\ 0 & 0 & 1 \end{bmatrix} \ ; \ \mathbf{R}_i^{\theta} = \begin{bmatrix} c\theta_i & 0 & s\theta_i \\ 0 & 1 & 0 \\ -s\theta_i & 0 & c\theta_i \end{bmatrix} \ ; \ \mathbf{R}_i^{\varphi} = \begin{bmatrix} 1 & 0 & 0 \\ 0 & c\varphi_i & -s\varphi_i \\ 0 & s\varphi_i & c\varphi_i \end{bmatrix},$$

$c\alpha_i = \cos\alpha_i, \ s\alpha_i = \sin\alpha_i, \ \alpha_i \in \{\psi_i, \theta_i, \varphi_i\},$

$\mathbf{r}'_i$ – vector of point coordinates in the node $\{i\}'$ local system.

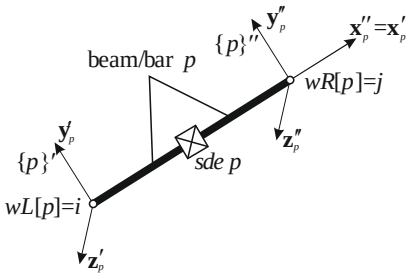

Figure 3. Bar *p* connecting nodes *wL*[*p*] and *wR*[*p*] and the spring-damping element (sde *p*).

We assumed that for the connecting bar *wL*[*p*] and *wR*[*p*] (Fig.3) the coordinates of the nodes are determined by the vectors $\mathbf{r}^0_{wL[p]}$ and $\mathbf{r}^0_{wR[p]}$ and angles $\varphi_i = \psi_i = \theta_i = 0.$ Hence, the coordinates defined in the local system of the bar *p* can be expressed in the base system according to the following equation:

$$\mathbf{r}_p = \bar{\mathbf{r}}_{wL[p]} + \mathbf{R}_{wL[p]} \cdot \mathbf{A}_p \cdot \mathbf{r}'_p \ , \tag{12}$$

where:

$$\mathbf{A}_p = \mathbf{A}^{\psi}_p \mathbf{A}^{\theta}_p \ ; \ \mathbf{A}^{\psi}_p = \begin{bmatrix} c\psi^0_p & -s\psi^0_p & 0 \\ s\psi^0_p & c\psi^0_p & 0 \\ 0 & 0 & 1 \end{bmatrix} ; \ \mathbf{A}^{\theta}_p = \begin{bmatrix} c\theta^0_p & 0 & s\theta^0_p \\ 0 & 1 & 0 \\ -s\theta^0_p & 0 & c\theta^0_p \end{bmatrix},$$

$\mathbf{r}'_p$ – point coordinates in the $\{p\}'$ system.

In the beam model, it is assumed that the elements connecting individual nodes are divided in a manner specific for the rigid finite element method (Fig. 3). Stiffness coefficients sde *p* are determined from the formulas:

— longitudinal stiffness coefficient:

$$c^x_p = \frac{EF_p}{l^0_p} \ , \tag{13.1}$$

—shear stiffness coefficients:

$$c^y_p = \begin{cases} \dfrac{12EI^y_p}{(l^0_p)^3} \text{ for Bernoulli beam model,} \\ \dfrac{GF_p}{l^0_p} \text{ for Timoschenko beam model,} \end{cases} \tag{13.2}$$

$$c_p^z = \begin{cases} \dfrac{12EI_p^z}{(l_p^0)^3} \text{ for Bernoulli beam model,} \\ \dfrac{GF_p}{l_p^0} \text{ for Timoschenko beam model.} \end{cases} \tag{13.3}$$

—bending stiffness coefficients:

$$c_p^\psi = \frac{EI_p^y}{l_p^0} \ , \tag{13.4}$$

$$c_p^\theta = \frac{EI_p^z}{l_p^0} \ , \tag{13.5}$$

—torsional stiffness coefficient:

$$c_p^\varphi = \frac{G(I_p^y + I_p^z)}{l_p^0} \ , \tag{13.6}$$

where:

I_p^y, I_p^z – moment of inertia of the cross-section area of the bar *p* in relation to the axes **y** and **z**,

E, G – Young and Kirchhoff modulus of elasticity.

3. Determination of the F_p' forces

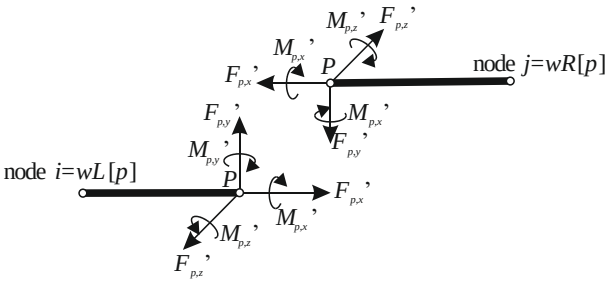

Figure 4. Forces and moments due to the deformation sde *p*

The elastic forces transmitted by sde *p* are shown in Fig. 4. Their value can be expressed by:

$$\mathbf{F}_p' = \mathbf{C}_p^t \cdot \mathbf{\Delta}_p', \tag{14}$$

where:

$$\mathbf{C}_p^t = \begin{bmatrix} c_p^x & 0 & 0 \\ 0 & c_p^y & 0 \\ 0 & 0 & c_p^z \end{bmatrix} \text{– stiffness matrix sde } p,$$

$\mathbf{\Delta}'_p$ – vector of the relative translation relocations at sde p.

In order to obtain the magnitudes of relative translational deformations in sde p, it was necessary to determine:

$$\mathbf{\Delta}'_p = \left[\mathbf{R}_i \cdot \mathbf{A}_p\right]^{\mathrm{T}} \cdot \mathbf{\Delta}_p = \left[\mathbf{R}_i \cdot \mathbf{A}_p\right]^{\mathrm{T}} \cdot (\mathbf{r}_p^R - \mathbf{r}_p^L) = \left[\mathbf{R}_i \cdot \mathbf{A}_p\right]^{\mathrm{T}} \cdot (\bar{\mathbf{r}}_j - \bar{\mathbf{r}}_i + \mathbf{R}_j \cdot \mathbf{A}_p \cdot \mathbf{r}''_p - \mathbf{R}_i \cdot \mathbf{A}_p \cdot \mathbf{r}'_p). \tag{15}$$

Forces $\mathbf{F}'_p$ and $-\mathbf{F}'_p$ can be expressed in the base system by the formula:

$$\mathbf{F}_p^L = \mathbf{B}_i \cdot \bar{\mathbf{F}}'_p \; ; \; \mathbf{F}_p^R = -\mathbf{B}_j \cdot \bar{\mathbf{F}}'_p \tag{16}$$

where: $\bar{\mathbf{F}}'_p = \begin{bmatrix} F'_x & F'_y & F'_z & 0 \end{bmatrix}$; $\mathbf{B}_i = \begin{bmatrix} \mathbf{R}_i \cdot \mathbf{A}_p & \bar{\mathbf{r}}_i \\ 0 & 1 \end{bmatrix}$; $\mathbf{B}_j = \begin{bmatrix} \mathbf{R}_j \cdot \mathbf{A}_p & \bar{\mathbf{r}}_j \\ 0 & 1 \end{bmatrix}$.

The generalized forces induced by the translational deformations sde p, included in the equations of the equilibrium of nodes i and j, have been derived from the following relation:

$$Q_{i,k} = \left(\mathbf{F}_p^L\right)^{\mathrm{T}} \cdot \mathbf{B}_{i,k} \cdot \mathbf{r}'_p \; ; \; Q_{j,k} = \left(\mathbf{F}_p^R\right)^{\mathrm{T}} \cdot \mathbf{B}_{j,k} \cdot \mathbf{r}''_p \; , \tag{17}$$

where: $\mathbf{B}_{i,k} = \dfrac{\partial \mathbf{B}_i}{\partial q_{i,k}}$, $\mathbf{B}_{j,k} = \dfrac{\partial \mathbf{B}_j}{\partial q_{j,k}}$, for k=1,...,6.

4. Determination of $\mathbf{M}_p'$ moments

$\mathbf{M}_p$' moments from Fig. 4 can be calculated from the following formula:

$$\mathbf{M}'_p = \mathbf{C}_p^r \cdot \mathbf{\Delta\Phi}'_p, \tag{18}$$

where:

$$\mathbf{C}_p^r = \begin{bmatrix} c_p^{\psi} & 0 & 0 \\ 0 & c_p^{\theta} & 0 \\ 0 & 0 & c_p^{\varphi} \end{bmatrix} \text{– rotational stiffness matrix sde } p,$$

$\mathbf{\Delta\Phi}'_p = \begin{bmatrix} \Delta\psi'_p \\ \Delta\theta'_p \\ \Delta\varphi'_p \end{bmatrix}$ – rotation angles of the right part of the *p* element in relation to its left part (Fig. 4).

Determined moments have been introduced into the equilibrium equations of nodes *i* and *j* as generalized forces. According to the formulas given in [9] the generalized forces at nodes *i* and *j* can be expressed by the formulas below:

$$\left.\begin{aligned} Q_{i,k} &= M'_{p,x} \cdot \sum_{i=1}^{3} \left(\mathbf{B}_i\right)_{l,3} \cdot \left(\mathbf{B}_{i,k}\right)_{l,2} + M'_{p,y} \cdot \sum_{i=1}^{3} \left(\mathbf{B}_i\right)_{l,1} \cdot \left(\mathbf{B}_{i,k}\right)_{l,3} + M'_{p,z} \cdot \sum_{i=1}^{3} \left(\mathbf{B}_i\right)_{l,2} \cdot \left(\mathbf{B}_{i,k}\right)_{l,1} \\ Q_{j,k} &= -M'_{p,x} \cdot \sum_{j=1}^{3} \left(\mathbf{B}_j\right)_{l,3} \cdot \left(\mathbf{B}_{j,k}\right)_{l,2} - M'_{p,y} \cdot \sum_{j=1}^{3} \left(\mathbf{B}_j\right)_{l,1} \cdot \left(\mathbf{B}_{j,k}\right)_{l,3} - M'_{p,z} \cdot \sum_{j=1}^{3} \left(\mathbf{B}_j\right)_{l,2} \cdot \left(\mathbf{B}_{j,k}\right)_{l,1} \end{aligned}\right\}, \tag{19}$$

for $k = 4, 5, 6$.

5. Lattice-boom – geometry, loading

In computer calculations, we assumed that the crane base is rigid and only the boom is deformed. In the work it was assumed that the crane arm consists of four supporting beams connected with one another by bars, and that the beams and bars have box cross sections (Fig. 5). Dimensions of these cross-sections are given in Table 1. Furthermore, we assumed that both support beams and bars are made of the same material (steel: E = 210 GPa, $\nu = 0.3$, $\rho = 7850$ kg/m^3). It is worth emphasizing that the material parameters of the 8 elements imitating the end of the E outrigger are equal to the parameters of the supporting beams. This implies, practically, the stiffening of this part of the structure.

Table 1. Parameters of the cross-sections for the crane arm beams and bars.

Dimension:	Supporting beams [m]	Bars [m]
W	0,350	0,160
H	0,350	0,160
t	0,010	0,005

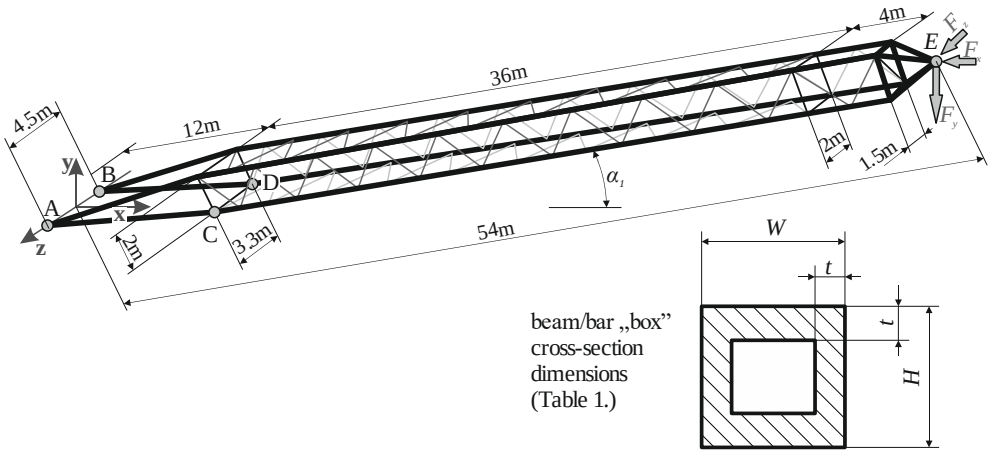

Figure 5. General geometry of the crane arm.

6. Calculation results

Calculations were made for one of the characteristic operating positions of the boom (α_1 = 0°, i.e. the maximum tilt), under load in the control node E with concentric forces F_x = -0.1 MN, F_y = -2,5 MN, F_z = 0,1 MN (Fig. 5). The values of the R_α reaction in the joints A and B, as well as supports C and D, the displacement u_k of the control node E and the values and location of maximum compressive/tensile stresses σ_{11} (stresses due to longitudinal forces in components) were recorded. The results of our own calculations were compared with the results of calculations obtained using the Abaqus package, where to model all the elements of the boom arm, two-node beam elements type B31 were used. In the model the nonlinear effects of large deformations and displacements were taken into account.

Table 2 presents the reaction values in boom supports for Abaqus, A (beam) and B (mixed) models, respectively. These data were used to calculate the relative differences in response values (δR_α) in the supports, with the Abaqus model reaction values being reference values. Differences are presented in Table 3. In addition, in the „A vs. B” column values from models A and B were compared.

Table 2. R_α reactions in joints A, B and supports C, D of the crane arm.

	Model		
	Abaqus	A	B
Reaction R_α	[MN]		
R_A	2,351	2,371	2,388
R_B	2,349	2,316	2,284
R_C	2,510	2,637	2,630
R_D	2,790	2,671	2,678

Table 3. Relative differences in the reaction values δR_α in crane arm articulations and supports.

	Model		
	A vs. B	A vs. Abaqus	B vs. Abaqus
	[%]		
δR_A	-0,7	-0,9	-1,6
δR_B	1,4	1,4	2,7
δR_C	0,2	4,9	4,6
δR_D	-0,3	4,2	4,0

Table 4 illustrates the values of the displacement components u_{Ek} of the control point E of the boom arm for the Abaqus, A (beam) and B (mixed) models, respectively.

Table 4. Displacements $u_{\alpha k}$ of the control point E of the crane arm..

	Model		
	Abaqus	A	B
Displacement u_{Ek}	[m]		
u_{Ex}	-0.1988	-0.1987	-0.1993
u_{Ey}	-3.9315	-3.9060	-3.9096
u_{Ez}	0.1646	0.1557	0.1557

Table 5 shows the relative (δu_{Ek}) differences in the values of these components; similarly as for δR_α, the displacement component values from the Abaqus model were the reference values (columns A and B); the "A vs. B" column lists the differences between A and B models.

Table 5. Relative differences of the component value δR_α of the control point E of the crane arm.

	Model		
	A vs. B	A vs. Abaqus	B vs. Abaqus
Reaction δu_α	[%]		
δu_{Ex}	-0,3	0,0	-0,2
δu_{Ey}	-0,1	0,6	0,6
δu_{Ez}	0,0	5,4	5,4

Table 6 gives the values σ_{11} for the maximum longitudinal stresses in the boom arm, the numbers of the elements, in which they occur, and their corresponding relative differences $\delta\sigma_{11}$ in the maximum stress values.

Table 6. σ_{11} values and their corresponding value differences $\delta\sigma_{11}$.

	Model		
	Abaqus	A	B
Element number	155		
σ_{11} [MPa]	907,4	898,1	897,7
$\delta\sigma_{11}$ [%]	-	1,03	1,07

The value differences do not exceed 1.1% of respective values of the maximum stresses obtained in the Abaqus model.

7. Conclusions

Carried out calculations and the comparative analysis of results demonstrate that both models yielded similar results, while errors were within acceptable limits for this type of analyses due to the fact that differences reflected in results did not exceed a few percent. We also obtained similar results as regards to reactions, important for engineers, in joints of the outrigger with the frame as well as the relocations and longitudinal stresses in beams and bars.

For both models the SES method was implemented in its geometrically non-linear version, i.e. trigonometric functions of angles describing the rotation of elements were not linearized. Moreover, this method has an unquestionable advantage based on the introduction of concentrated masses and loads at any point of beam elements (except nodes). This can play a pivotal role in imitating such a complex system as the crane.

References

[1] Wang G., Qi Z., Kong X., Geometrical nonlinear and stability analysis for slender frame structures of crawler cranes. *Engineering Structures*, 83 (2015), 209-222.

[2] Kong X., Qi Z., Wang G., Elastic instability analysis for slender lattice-boom structures of crawler cranes. *Journal of Constructional Steel Research*, 115 (2015), 206-222.

[3] Sun X., *Design of unconventional slender steel structures by stability analysis*, The Hong Kong Polytechnic University Publishing Office, Hong Kong, 2002 (http://hdl.handle.net/10397/3454).

[4] https://www.dnvgl.com/services/strength-assessment-of-offshore-structures-sesam-software-1068, 11.10.2017.

[5] DNV: *Standard for Certification No. 2.22. Lifting Appliances.* Det Norske Veritas, 2011.

[6] Adamiec-Wójcik I., *Modelling dynamics of multibody systems using homogenous transformations*, University of Bielsko-Biała Publishing Office, Bielsko-Biała, 2003.

[7] Szczotka M., *The Rigid Finite Element Method in Modelling of Nonlinear Offshore Systems*. Gdańsk University of Technology Publishing Office, Gdańsk, 2011 (in Polish).

[8] Drąg Ł., *Application of Rigid Finite Element Method in modeling of ropes, risers and cranes*, University of Bielsko-Biała Publishing Office, Bielsko-Biała, 2017 (in Polish).

[9] Adamiec-Wójcik I., Wojciech S., Wittbrodt E., *Dynamics of Flexible Multibody Systems - Rigid Finite Element Method*, Springer, 2006.

Andrzej Nowak, Professor: Department of Computer Modeling, University of Bielsko-Biała, Willowa 2, 43-309 Bielsko-Biała, Poland (*a.nowak@ath.bielsko.pl*).

Paweł Nowak, M.Sc.: Department of Computer Modeling, University of Bielsko-Biała, Willowa 2, 43-309 Bielsko-Biała, Poland (*pnowak@ath.bielsko.pl*).

Marek Metelski: Protea Sp. z o.o., Galaktyczna 30A, 80-299 Gdańsk, Poland (*marek.metelski@protea.pl*).

Application of Hilbert transform in detection flat places on tram wheels

Tomasz Nowakowski, Paweł Komorski, Grzegorz M. Szymański, Franciszek Tomaszewski

Abstract: The development of urban rail transport in Poland in recent years has been associated to the access of city dwellers to the modern rolling stock. These rolling stock has to meet the increasingly stringent requirements of it's owners regarding the reliable execution of the transport process, as well as residents' demands for vibroacoustic comfort observed both in the passenger space and track surroundings. All of these activities are related to the reduction of adverse vibrations which may: reduce the durability of the individual components and structural junctions of the tram and generate excessive noise. In this case it is important to maintain the quality of the cooperation of vehicles and track, which revolves around the wheel-rail contact area. One of the main causes for increased vehicle-dependent dynamic impacts at the wheel-rail contact area are irregularities on the rolling surface of the wheels, including flat places. The paper presents the problems of the phenomena which are generated during passing of a tram with flat places on the wheels. Experimental research on the phenomena carried out under real operating conditions is also presented. The purpose of the study was to verify the applicability of Hilbert transform method in the frequency domain on signals from rails for the purpose of identifying flat places in the vehicle. Finally, a universal algorithm for identifying these irregularities for light rail vehicles has been developed.

1. Introduction

The developement of urban railway transport in Poland is associated with numerous railway vehicle investments. An example of a polish city consequently realizing its orders for new railway vehicles is Poznań. Since the beginning of the year 2016 Poznań has ordered 80 new trams, which are consequently introduced into tram traffic. Requirements set by users of those new trams – owners, city dwellers and passengers alike – most of all demand a reliable realization of the transportation process, as well as vibroacoustic comfort. It has to do with reduction of undesirable vibrations that can reduce the durability of tram elements, as well as track elements. In this case, maintaining a high quality of cooperation between the vehicle and the track is crucial. One of the main factors of increased dynamic

impact dependent on the vehicle in the point of contact between the wheel and the track are irregularities on the rolling surface of wheels, and among them – flat places (also: flat spots).

A flat spots is a defect on the rolling surface in the form of a flat surface, due to laminating or flattening of its material. Causes of flat spot occurance are well known and described in numerous papers, eg. [1]. Flat spots are caused by absolute or temporary lock of the wheel axis as a result of incorrect break operativeness, or decreased traction in the wheel-rail area (moisture, contamination). In such cases, locked wheels are propelled along the rail, grinding the rolling surface material. The ground material is often relocated on the rolling surface behind the flat spot, creating spalling. This causes a sudden loss of primary features of the wheel during operation. The observed results are - loss of noiselessness during movement (high levels of noise), as well as increased dynamic impact on the rail. The impact is significant and different to those resulting from roughness in constant contact with running surfaces of the wheel and rail. A basic model of the phenomenon has been depicted on fig.X

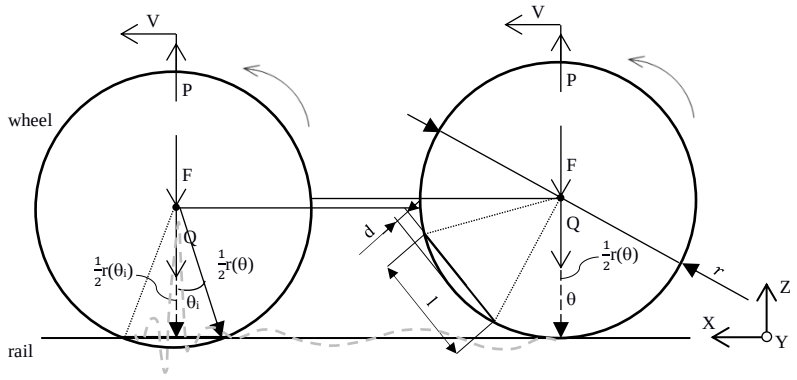

Figure 1. Wheel with flat spot basic model:

V - wheel linear velocity, θ – wheel rotational velocity, θ_i - wheel rotational velocity with flat spot, Q – weight of non-sprung elements per one wheel, F – total weight of sprung elements per one wheel, r – diameter of wheel, P – d'Alembert's reaction force, d – defect depth, l – defect length.

Results of such defects are considered on three surfaces: technical, economical and social. The technical aspect relates to the influence of the defects on stability of the wheelset and the influence of the generated vibrations on the construction's durability. The economical aspect considers all the costs associated with reprofiling the rolling surfaces as well as their shorter utility time. The social aspect considers complaints by the passengers and dwellers of buildings in close proximity to the tracks on increased vibrations and noise. Thus, considering these aspects, it is necessary to correctly recognize the technical state of the rolling surfaces by introducing flat spots detectors in a tram depot.

The first track system for detection of flat spots was introduced in a tram depot in Cracow. It is a WF system, and its basic function is to monitor the increase of vibrations from transducers located on two rails at the distance of 3 m. With velocities of 10÷20 km/h flat spots on the wheels are automatically detected [2]. The second used system is Revega, based on monitoring the pressure of wheels on rails at a distance of 3,6 m, with velocities no greater than 15km/h. Unfortunately, not all municipal transportation company in Poland are equipped with systems of detection of flat spots. In Poznań, only one of three tram depots is equipped with such a system.

There are many systems for detection of flat spots available. Among them, for example [3], where flat spot diagnostic tool via wavelet transform of signals from the rail registered by four transducers was developed. A similar, new approach, although with use of machine learning was introduced in [4]. Further on, article [5] introduced a method for detection of flat spots based on ultrasound and a transducer on the rail. It generates propagating waves in the rail, which, in contact with the wheel-rail point, produces an echo, which is then assessed.

The method of detecting flat spots described in this paper is unique and simplified, as shown further.

2. Method of research

2.1. Basic assumptions

Defects on rolling surfaces of wheels in the form of flat spots generate cyclical impulses in the wheel – rail area of contact. Thus, measurement points were located on the rail. These vibrations are characterized by low displacement amplitudes and high acceleration amplitudes [6]. And so acceleration was assumed as a basic physical quantity.

The suggested method for detection of flat spots is partially analogous to diagnostics of rolling elements in machines, eg. bearings, with the use of Hilbert's transform (envelope analysis). In both cases: defect of a bearing element, or defect in form of a flat spot is directly correlated to rotational frequencies. Envelope analysis allows for extraction of a signal envelope containing a low frequency modulation, which corresponds to cyclical impulses, indicating a flat spot on a wheel. The suggested method considers analysis of envelope in the time domain as well as the frequency domain.

Impulses events on rails coming from a flat spot are also characterized by low energy, when compared to the total energy in the vibration signal. The higher harmonics of repeating impulses will thus be amplified during resonance of the vibration-emitting structure, i.e. the rail. It is another argument for use of envelope analysis, which uses resonance vibrations carrying information about impulses (defects in the form of flat spots). Thus, analysis of signals from tram passes followed the analysis of rail structure dynamics.

In order to minimize financial expense, measurement points were located only on one rail (above the sleepers). The number of measurement points (P_m) was determined by considering the maximum circumference of the wheel ($c_{w,max}$) and distances between sleepers (l_s), as in the formula (1).

$$P_m = \text{int}\left(\frac{c_{w,max}}{l_s}\right) \mid P_m \in \mathbb{N} \tag{1}$$

Thusly determined measurement points designate the controlled length of the rail (C_{rea}) upon which contact with a flat spot is certain. The suggested method of flat spot detection assumes a divalent grading of technical state, considering the limit values of vibration acceleration as criteria for grading, statewise with a collection of states W:

$$W = \{w^1, w^2\} \tag{2}$$

where: w^1 – bad condition of tram, w^2 – good condition of tram.

2.2. Objects, localization and conditions of research

Research was conducted on a track of a tram depot S2 of MPK Poznań. The track upon which measurements were realized was constructed from a rail 60R2 on Moll sleepers, which are located at a distance of 750 mm (l_s). The greatest expected circumference of a wheel in MPK Poznań rail stock, assuming a nominal radius of 654 mm (r) is approx. 2054 mm ($c_{w,max}$). Applying those values to the formula, we receive the number 4, denoting a necessity for 4 measurement points on the rail. The real controlled distance was 2250 mm (C_{real}). Location of the measurement points has been shown on fig. 2.

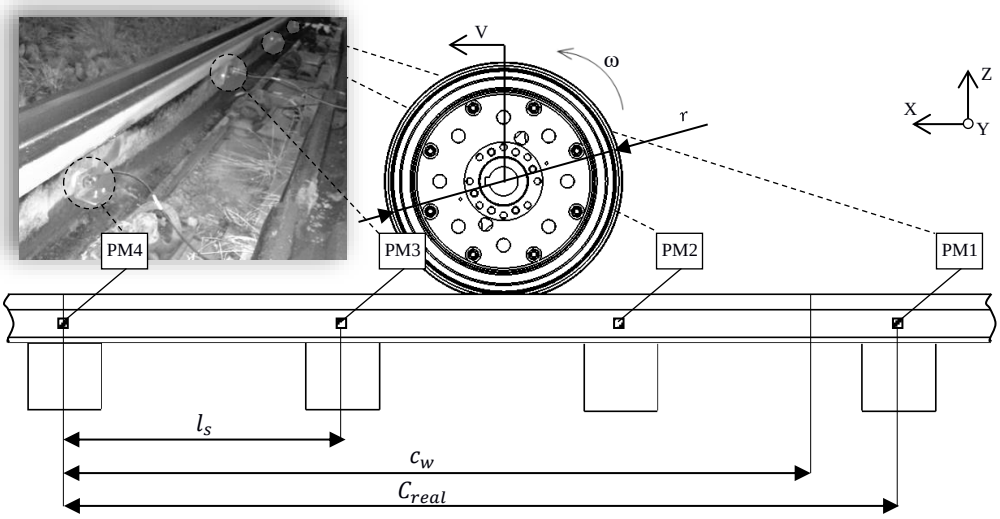

Figure 2. A view of the measurement points location with a basic designations of dimensions and measurement realization: ω – rotational velocity of the wheel, V – linear velocity of the wheel

Acquisition and archiving measurement's data was carried out using a multi-channel data acquisition module LAN-XI type 3050 (Brüel & Kjær). For registering of vibration signals piezoelectric transducer Brüel & Kjær type 4504 (PM1÷PM3) and type 4524 (PM4) was used.

Research was conducted on Moderus Beta MF 22 AC BD trams, which has been shown on fig. 3 with its chosen technical parameters.

Max. velocity:	70 km/h
Wieght:	40,65 t
Length:	28 250 mm
Width:	2 354 mm
Height:	3 350 mm

Figure 3. Moderus Beta MF 22 AC BD – the object of research [7]

Research was conducted on trams with rail stock numbering #920 and #916, realizing transportation processes for approx. a year. Tram #916 was free of rolling surface defects, whereas tram #920 was observed to have defects in the form of flats spots and spalling on the last, 8th wheelset (fig. 4).

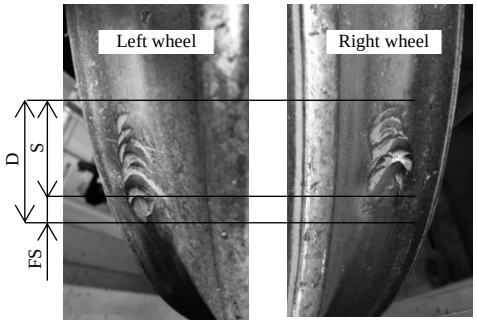

Figure 4. heel defect on wheel tread of tram #920 in the form of flat spots and spalling'

D – wheel defect on wheel tread, FS – flat spot, S – spalling.

Surface of the entire defect on the wheel tread of both wheels converted to coordinated of length and width of an approximated ellipse was equal to, correspondingly, 66 mm and 32 mm.

3. Analysis of research results

The rail material and state of strain cause a significant speed of wave spread, around 5000 m/s. Thus, a cross–correlation analysis of the signals registered during transit was conducted. The mutual correlation was determined based on the assumptions of the formula:

$$K_{a_1,a_2}(\tau) = \frac{1}{T}\int a_1(t)\, a_2(t+\tau)dt \tag{3}$$

where: a_1,a_2 – analysed signals of vibration acceleration, t – time, τ – time delay.

Whereas in analysis the correlation was determined numerically, according to the formula [8]:

$$\mathrm{K}_{a_1,a_2}(\mathrm{K}\Delta\tau)=\frac{1}{\mathrm{N}\Delta\mathrm{T}}\sum_{n=0}^{N-1} a_1(n\Delta t)a_2(n\Delta t + k\Delta t)\Delta t = \mathrm{K}_{a_1,a_2}(\mathrm{k})=\frac{1}{\mathrm{N}}\sum_{n=0}^{N-1} a_1(n)a_2(n+k) \tag{4}$$

Results of mutual corelation analysis between signals PM1 and PM2, PM3 and PM4 has been depicted on fig. 5.

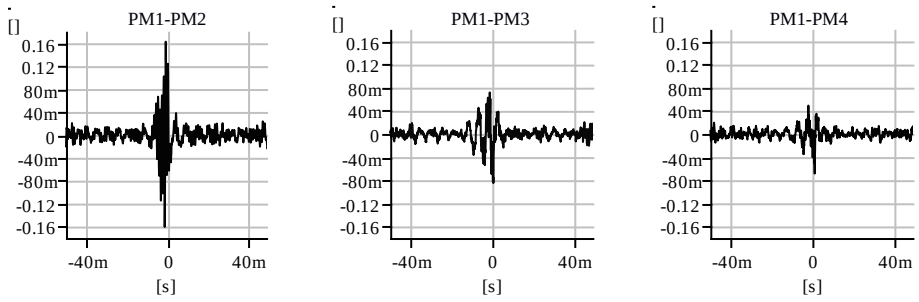

Figure 5. Charts of cross-correlation between vibration signals measured in all points of measurement

From the charts above one may extrapolate, that the registered vibration signals had a degree of timeliness for all measurement points. The apex of cross–correlation function, falling close to the zero of time parameter (variation from 656 μs to 1 ms) is the evidence of this.

In the next step, according to the research assumptions, analysis of rail structure dynamics was conducted. A tool for modal analysis, that is an impact test, was used. Force exaction were realized in the surface of rail's head, on the surface of measurement points. The response to the exaction was measured as acceleration of vibrations in the nearby measurement points. For each point a numerous exactions were conducted, which ultimately allowed for eliciting a frequency response function (FRF). For example, the fig. 6 presents the results of the frequency response function for the measuring point PM1.

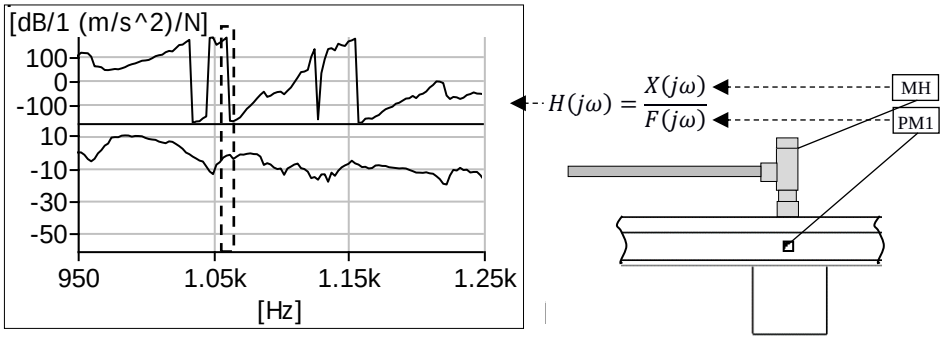

Figure 6. Amplitude-frequency characteristics (bottom part of the chart) and phase-frequency (upper part of the chart) from impact test carried out on the track; X(jω) is complex spectrum of an object response F(jω) is complex spectrum of a force stimulating the object vibration; H(jω) is complex function of a frequency response, MH – modal hammer, PM1 – first point of measurement.

The rail resonance in the PM1 point, which allows for observation of the impulse signals in tram passing, was at the frequency of 1,063 kHz. All vibration signals on the output of the transducers were filtered by band–pass filter with the center frequency equivalent to the frequency of the rail resonance. Filtered signals were subjected to demodulation in order to achieve signals's envelope. Those signals could have contained low-frequency modulations correspondent to the cyclically appearing impulsive events resulting from the eventual flat spot on the wheel.

Analysis in time domain

Hilbert Transform (HT) of the signal a(t) can be analitically defined based on the equation:

$$HT = \hat{a}(t) = \frac{1}{\pi}\int_{-\infty}^{\infty}\frac{a(\tau)}{t-\tau}d\tau \tag{5}$$

In this paper, Hilbert Transform was applied to the signals numericaly, as in the equation (6).

$$\overleftrightarrow{\boldsymbol{a}}(\boldsymbol{k}) = \sum_{\boldsymbol{n=0}}^{\boldsymbol{N-1}} \boldsymbol{h_{k-n}a(n)} \tag{6}$$

where:

$$h_n = \begin{cases} \frac{2}{N}sin^2(0{,}5\pi n)ctg\left(\frac{\pi n}{N}\right) & \underset{N\epsilon f(n)}{\forall} \; f(n) = 2n \\ \frac{2}{N}\left[1-\cos(\pi n)\,ctg\left(\frac{\pi n}{N}\right)/cos\left(\frac{\pi n}{N}\right)\right] & \underset{N\epsilon f(n)}{\forall} \; f(n) = 2n+1 \end{cases}$$

An exemplary time signals' envelopes for the passing of the #916 and #920 trams were presented on fig. 7 and 8. Envelope of the signal presented on fig. 7 for the #920 tram, was concerning the measurment's point PM1, extreme in case of the values of the acceleration of vibration.

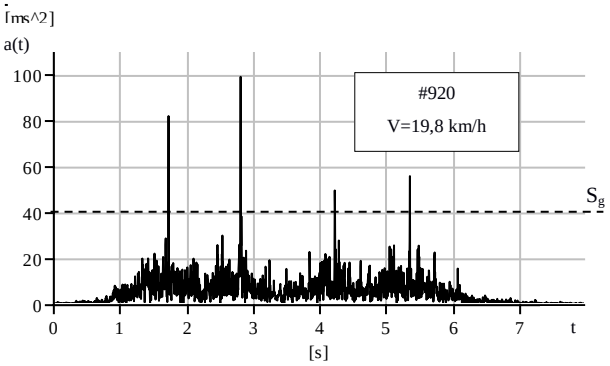

Figure 7. The time signal envelope for the tram #920 with the flat spot on the wheel

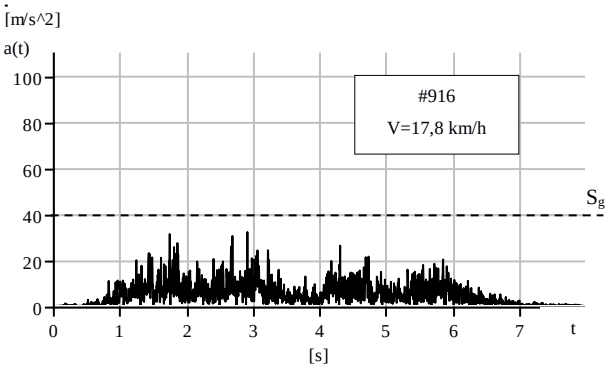

Figure 8. The time signal envelope for the tram #916 without the flat spot on the wheel

As seen on fig. 7 time signal envelope from the #920 tram is characterized by the appearance of the explicit, periodic peak of the amplitude higher than 30 m/s^2. Whereas, time signal envelope from #916 tram shows no such feature. The conclusion from this analysis imply that monitoring of the amplitude of the acceleration of vibration in the time signal envelope may be a successive method of detection of flat spots. In this case, acceleration of vibration must be treated as the diagnostic parameter a(t)=S, which, after achieving the set limit value S_g would show the occurrence of the flat spots on the wheel. In this case it is necessary to define the set limit value S_g of the observed diagnostic parameter S, individually for all operated tram types. On the fig 7. and 8. presented an exemplary set limit value „a priory" for the value of 40 m/s^2. This value should be appointed by the users of this method based on a large number of the observation of the signal a(t) parameter and structure D parameter (lack or the value of the flat spot). A base of relations, created in this way, between the technical state of the rolling surface of the wheel and the accompanying rail vibration will be the base for calculation of the set limit value, based on the statistic method or heuristic method.

Analysis in frequency domain

The analysis started from the calculation of the characteristic frequency for the discussed defect of the rolling surface of the wheel, based on the following formula:

$$f_{fp} = \frac{V \cdot 3{,}6^{-1}}{c_w} \tag{7}$$

where: c_w – circumference of the wheel, V – linear velocity of the tram.

Consideration of the circumference of a wheel requires the measurements of its actual diameter before the analysis can be done. To bypass this, it was decided to simplify the methods, introducing an algorithm to search for the rotation frequency, in the possible rotation frequency section (f_{wheel}) for the particular velocity. Those sections defined from the formula 7, considering the possible tram velocity up from 20 km/h to 15 km/h (step 1km/h), and the extreme value of the diameter of the wheel. The results were presented in table 1.

Table 1. The sections of the possible rotation frequencies of the wheel for the particular tram velocities

*the section for the passing of the #920 tram, ** the section for the passing of the #916

Tram velocity \ Wheel diameter	max: 654 mm	min: 600 mm	f_{wheel} [Hz]
20 km/h	2,71 Hz	2,95 Hz	<2,71, 2,95>*
19 km/h	2,57 Hz	2,80 Hz	<2,57, 2,80>
18 km/h	2,43 Hz	2,65 Hz	<2,43, 2,65>**
17 km/h	2,30 Hz	2,51 Hz	<2,30, 2,51>
16 km/h	2,16 Hz	2,36 Hz	<2,16, 2,36>
15 km/h	2,03 Hz	2,21 Hz	<2,03, 2,21>

The algorithm is set on finding a peak in the particular section of the frequencies f_{wheel}. Its location on the axis abscissa will testify the diameter of the wheel. As it results from the presented table 1, for the tram #920, the rotational velocity will be included in the section from 2,71 Hz up to 2,95 Hz. Whereas, for tram #916 the frequency will be set in the section from 2,43 Hz up to 2,65 Hz.

In case of the FFT spectrum from the signal envelope, the visible difference between the passes is observed in the values of the frequency amplitude f_p, corresponding to the rotation frequency of the wheels, presented on fig 9.

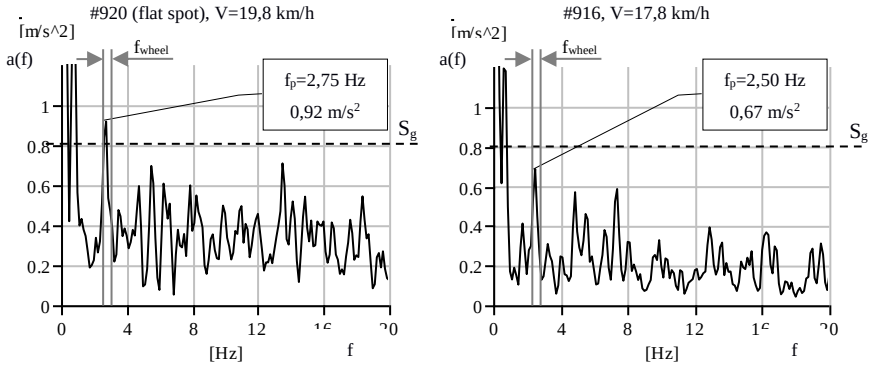

Figure 9. Spectrum from envelope vibration signals for tram #920 i #916

Finally, an universal algorithm for identifying the irregularities for the light rail vehicles was developed, presented on fig.10.

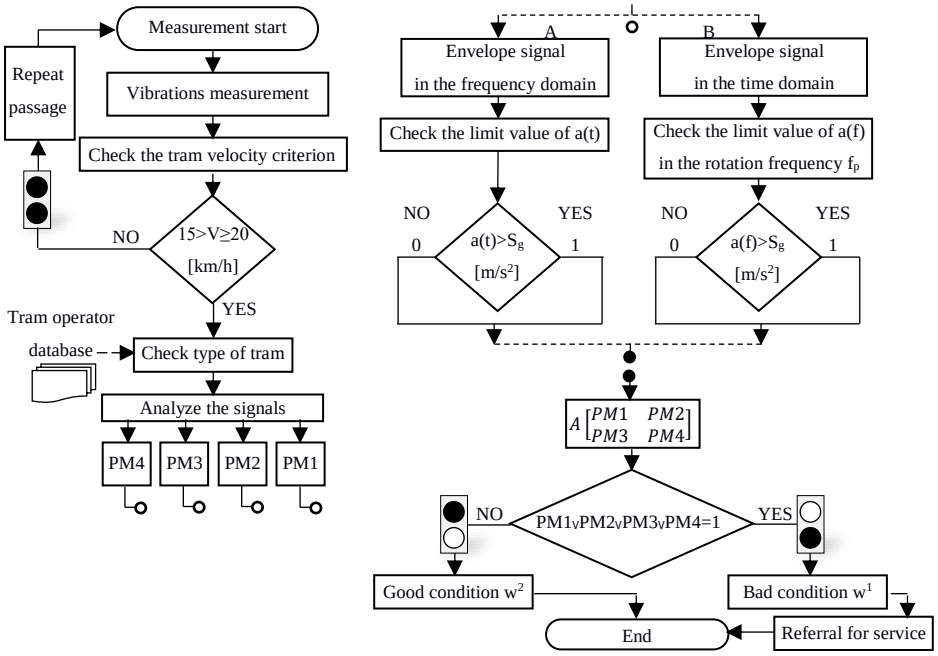

Figure 10. The universal algorithm for detection of the flat spots on the tram wheels

The signal of the start of the measurements can be made freely by the user, for example from the signal of the inductive sensor, which can detect the wheel set. When the velocity criterium will have been fullfiled, there comes the processing of the signals from all of the transducers, with the use of the

envelope analysis. Every signal undergoes the analysis, depending on the chosen variant of the algorithm's functionality in the time domain (variant A) or in the frequency domain (variant B). Independently from the variant, the extreme values individually established by the user of the system are checked on the base of numerous observations of the wheel's defect, as the flat spots and the accompanying vibration's signals. If, in whichever point of the measurement, the limit values will be exceeded, the technical state of the tram will be in a bad condition – w^1. It is equivalent to referral the tram for the service, otherwise the technical state of the tram will be in a good condition – w^2.

4. Summary

The study and the method of detecting the flat spots in this paper, can be introduced on the tram depot. Experimentally indicated the connection between the presence of the flat spots on the rolling wheel and generated vibrations of the rail. The indicated methods of the detection, same as in the time and frequency domain, show effectiveness, verified in conditions of the real operations occurring in the tram depot. The proposed method may be used on a larger scale of tram velocity. The inspection of both vehicles in the technical condition, confirmed the diagnosis considering both assumed methods. The possibility of stating the individual limit value of vibrations, will enable adjustment of the method to different conditions of the tram company.

The application of the proposed method will successively contribute to reducing the number of trams with flat spots on wheels, routing mainly in a urban area. The consequences of this will be observed in reduction of the external costs of the transport borne by the society

5. Acknowledgements

Thanks to the Municipal Communication Company in Poznań for the possibility of carrying out measurements at the Franowo tram depot. Special thanks go to Krzysztof Bromirski – deputy manager of the tram depot and Mikołaj Drozda – tram operation specialist.

All presented work is partly funded by Statutory Activities fund of the Institute of Combustion Engines and Transport, PUT (PL) 5/52/DSPB/0259.

6. References

[1] D. J. Thompson, "Railway Noise and Vibration. Mechanisms, Modelling and Means of Control," *J. Chem. Inf. Model.*, vol. 53, no. 9, p. 519, 2009.
[2] J. Madejski, "Automatic detection of flats on the rolling stock wheels," *J. Achiev. Mater. …*, vol. 16, no. 1, pp. 160–163, 2006.
[3] V. Belotti, F. Crenna, R. C. Michelini, and G. B. Rossi, "Wheel-flat diagnostic tool via wavelet transform," *Mech. Syst. Signal Process.*, vol. 20, no. 8, pp. 1953–1966, 2006.
[4] G. Krummenacher, C. S. Ong, S. Koller, S. Kobayashi, J. M. Buhmann, and S. Member, "Wheel Defect Detection With Machine Learning," pp. 1–12, 2017.

[5] J. Brizuela, C. Fritsch, and A. Ibáñez, “Railway wheel-flat detection and measurement by ultrasound,” *Transp. Res. Part C Emerg. Technol.*, vol. 19, no. 6, pp. 975–984, 2011.
[6] A. Chudzikiewicz, *Elementy diagnostyki pojazdów szynowych*. Oficyna Wydawnicza Politechniki Warszawskiej, 2002.
[7] http://www.modertrans.pl/product/moderus-beta/, Modertrans Poznań, “Product - Moderus Beta.”
[8] C. Cempel, *Wibroakustyka stosowana*. Warszawa: Państwowe Wydawnicwo Naukowe, 1978.

Tomasz Nowakowski, MSc Eng.: Poznan University of Technology, Institute of Combustion Engines and Transport, Division of Rail Vehicles, 60-965 Poznan, Poland (*tomasz.zb.nowakowski@doctorate.put.poznan.pl*).
Paweł Komorski, MSc Eng.: Poznan University of Technology, Institute of Combustion Engines and Transport, Division of Rail Vehicles, 60-965 Poznan, Poland (*pawel.r.komorski@doctorate.put.poznan.pl*).
Grzegorz M. Szymański, Ph.D.D.Sc.: Poznan University of Technology, Institute of Combustion Engines and Transport, Division of Rail Vehicles, 60-965 Poznan, Poland (*grzegorz.m.szymanski@put.poznan.pl*).
Franciszek Tomaszewski, Prof.Ph.D.D.Sc: Poznan University of Technology, Institute of Combustion Engines and Transport, Division of Rail Vehicles, 60-965 Poznan, Poland (*franciszek.tomaszewski@put.poznan.pl*).

Mathematical models of two parametric pendulums with modulated length

Paweł Olejnik, Jan Awrejcewicz, Michal Fečkan

Abstract: Dynamics of a parametric pendulum excited by a wave-modulated discrete function of its length is investigated both analytically and with the use of computer simulations. An existence results of almost periodic sequences of ordinary differential equations with linear boundary value conditions are observed. Behavior of an exemplary oscillator subjected to both an almost-periodic step elongation and forcing, analogously tends to almost-periodic motions. Finally, conditions for that synchronization as well as numerical trajectories on phase planes and Poincaré sections are presented.

1. Introduction

In this study two nonlinear dynamical system of one and three degrees of freedom with a wave-modulated length and a variable-length spring pendulum [3,4,7] and a vibrating suspension [1] are mathematically derived.

Parametric excitation of a rigid planar pendulum caused by a square-wave modulation of its length is investigated in [2] both analytically and with the use of computer simulations. The threshold and other characteristics of parametric resonance are found. The role of non-linear properties of the pendulum in restricting the resonant swinging is emphasized. The boundaries of parametric instability are determined as functions of the modulation depth and the quality factor. Stationary oscillations at these boundaries and at the threshold conditions are investigated. The feedback providing active optimal control of pumping and damping is analyzed. Phase locking between the drive and the pendulum at large amplitudes and the phenomenon of parametric autoresonance are discussed.

The existence of the resonance phenomena both external and internal occurs in vibrating structures as an increased amplitude of vibrations. In general, from the engineering point of view this type of grazing behavior is usually unwanted also in solid bodies. Appearance of resonance generate greater complexity of a mechanical system behavior. In this paper, the study is performed to create the simulation and investigation for better understating of resonance phenomena of a periodically forced slider-spring pendulum mechanical system of three degrees of freedom.

Pendulum can be excited parametrically by a given vertical motion of its suspension point. In the frame of reference associated with the pivot, such forcing of the pendulum is equivalent to periodic

modulation of the gravitational field [2]. This apparently simple physical system exhibits a surprisingly vast variety of possible regular and chaotic motions. Many contributions are devoted to investigation of the pendulum with vertically oscillating pivot: see, for instance [8]. A widely known curiosity in the behavior of an ordinary rigid planar pendulum whose pivot is forced to oscillate along the vertical line is the dynamic stabilization of its inverted position, occurring for the precise intervals of the driving amplitude and frequency.

The pendulum may be suspended to the flexible element. In this system the autoparametric excitation may occur as a result of inertial coupling. Analogous behavior happens when the mass is attached to the pendulum type elastic oscillator, and then, it is possible to observe autoparametric nonlinear coupling between the angle of the pendulum and elongation of the spring. All of such cases depend on the set of parameters for the investigating system. Examples are as follows: dumping, mass ratio of components, and specification of external excitation. As a result of system specification, the resonance phenomena transferring the energy between system components or their mutual excitation can appear differently.

2. Problem description

We analyze the three-degrees-of-freedom dynamical system presented in Fig. 1.

Our system consists of an elastic pendulum with the initial length l_0, the stiffness k and the damping c. The pendulum is attached to the moving slider with the point-focused mass M. The slider moves horizontally along the x-axis. The mass m hangs down from the end of the spring. The body of mass M (slider) is subjected to the harmonic vertical excitation force $F(t) = F_0\cos\omega t$. The planar mechanical system presented above has three degrees of freedom. The generalized coordinates are assumed for the angle θ between the pendulum spring and the vertical axis z (inclination angle), the incremental elongation of the spring Δs and the horizontal displacement x of the body of mass M.

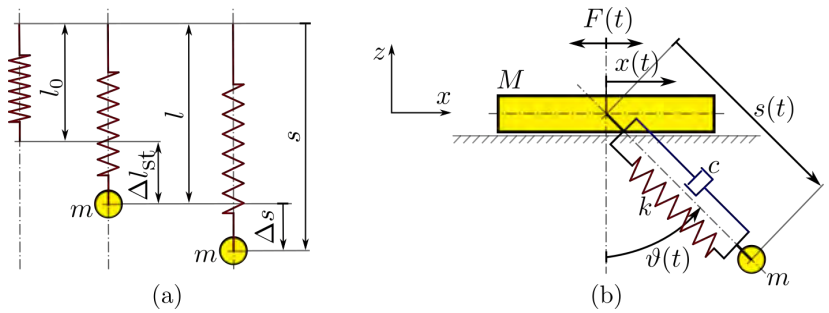

Figure 1. Dimensions of loaded (stretched or compressed) and unloaded (free) linear spring (a), a variable-length forced spring pendulum system of three degrees of freedom (b).

Any of the existing phenomena cannot be presented, examined and transferred to mathematical or engineering problem in the infinitely direct way [9]. According to this fact some assumptions allowing for a reduction of the complexity of the analyzed problem will be made. To weaken the system's complexity, but still maintaining its basic properties we have assumed:

- friction of the slider does not exists in the dynamical system;
- energy dissipated by the frictional contact of the base and the slider vibrating on it can be compensated from an external source of energy, for instance, determined by a control system;
- radial elongation of the spring pendulum exists;
- the spring is considered as massless, and its force of reaction described by Hooke's law appears when it is stretched or compressed from its free length;
- the slider has a point mass focused at the rotationally constrained end (upper) of the spring;
- excitation is caused by an external harmonic force, e.g., it can come from a magnetic field;
- mass of the spring pendulum is focused in a point at the second (lower) end of the spring;
- damping of motion is associated only with elongation of the spring of the pendulum.

We assume the almost ideal case in which the dissipation of energy by the frictional contact could be partially compensated by an external source.

3. Two mathematical models of pendulums with variable length

For the mathematical description of the dynamical system with a time-varying parameter, such as the variable length of the pendulum, the Hill or Mathieu equations are often used [10]. Nevertheless, in similar studies referring to the analyzed case, the Euler-Lagrange equation can be used.

3.1. A variable-length pendulum springily attached to the forced very weakly damped slider

The kinetic energy of the analyzed three-degrees-of-freedom system is calculated according to the sum of kinetic energies of both system bodies (see Fig. 1):

$$\begin{aligned} U(\vartheta, s, x, \dot{\vartheta}, \dot{s}, \dot{x}) &= \frac{1}{2} M\dot{x}^2 + \frac{1}{2} m\Big[\big(\dot{x} + \dot{s}\sin\vartheta + s\dot{\vartheta}\cos\vartheta\big)^2 + \big(s\dot{\vartheta}\sin\vartheta - \dot{s}\cos\vartheta\big)^2 \\ &= \frac{1}{2}\big(M+m\big)\dot{x}^2 + \frac{1}{2} m\Big[\dot{s}^2 + s^2\dot{\vartheta}^2 + 2\dot{x}\big(\dot{s}\sin\vartheta + s\dot{\vartheta}\cos\vartheta\big)\Big]. \end{aligned} \tag{1}$$

The potential energy of the analyzed mechanical system is a sum of a) the energy of the linear spring, that is accumulated after the incremental elongation Δs and the static elongation Δl_{st} (static stretching or compression by a hanging pendulum body of mass m) measured from the equilibrium free length l_0 of the spring; b) the gravitational potential energy of the body of mass m on the vertical distance $(\Delta s + l)\cos\theta$ between centers of the slider and the pendulum body, i.e.,

$$V(\vartheta,\Delta s,x)=\frac{1}{2}k(\Delta s+\Delta l_{st})^2-mg\big(\Delta s+l\big)\cos\vartheta. \tag{2}$$

Taking into account that

$$\Delta s+\Delta l_{st}=s-l_0,\quad l=l_0+\Delta l_{st}, \tag{3}$$

one finds

$$V(\vartheta,s,x)=\frac{1}{2}k(s-l_0)^2-mgs\cos\vartheta. \tag{4}$$

For each component of the vector of general coordinates y_k, at independence of the assumed general coordinates, the Lagrangian $L = U - V$ satisfies the following Euler-Lagrange equation as follows:

$$\begin{aligned}&\frac{d}{dt}\left(\frac{\partial L}{\partial\dot{y}_k}\right)-\frac{\partial L}{\partial y_k}+\frac{\partial R}{\partial\dot{y}_k}=Q_k,\quad k=1\ldots3,\\&y_k=\big[\vartheta(t),s(t),x(t)\big],\quad Q_k=\big[0,0,F_0\cos\omega t\big],\end{aligned} \tag{5}$$

where Q_k is understood to be the reminder of the k-th generalized force when viscous damping of motion of the pendulum body in direction s is accounted for with the Rayleigh dissipation function:

$$R(\dot{\vartheta},\dot{s},\dot{x})=\frac{1}{2}c\left[\frac{d\big(s-l_0\big)}{dt}\right]^2=\frac{c\dot{s}^2}{2}. \tag{6}$$

After applying the equations (1), (4) and (6) to the Euler-Lagrange equation (5), for each generalized coordinate y_k, we get the three coupled differential equations of motion for each degree of freedom.

For the generalized coordinate θ (pendulum angle):

$$s\ddot{\vartheta}+2\dot{s}\dot{\vartheta}+\ddot{x}\cos\vartheta+g\sin\vartheta=0. \tag{7}$$

For the generalized coordinate s (pendulum elongation):

$$m\big(\ddot{s}+\ddot{x}\sin\vartheta-s\dot{\vartheta}^2-g\cos\vartheta\big)+c\dot{s}+k\big(s-l_0\big)=0. \tag{8}$$

For the generalized coordinate x (slider displacement):

$$\big(M+m\big)\ddot{x}+m\cos\vartheta\big(s\ddot{\vartheta}+2\dot{s}\dot{\vartheta}\big)+m\sin\vartheta\big(\ddot{s}-s\dot{\vartheta}^2\big)=F_0\cos\omega t. \tag{9}$$

Equations (7)-(9) can be algebraically decoupled with respect to the second derivative, we have:

$$\begin{aligned}
\ddot{\vartheta} &= -\frac{1}{s}\left(2\dot{\vartheta}\dot{s} + \rho\cos\vartheta + g\sin\vartheta\right),\\
\ddot{s} &= -\frac{c}{m}\dot{s} - \frac{k}{m}\left(s - l_0\right) + s\dot{\vartheta}^2 - \rho\sin\vartheta + g\cos\vartheta,\\
\ddot{x} &= \rho,
\end{aligned} \tag{10}$$

where

$$\rho = M^{-1}\left(c\dot{s} + k\left(s - l_0\right)\right)\sin\vartheta + F_0 M^{-1}\cos\omega t \tag{11}$$

expresses acceleration of the slider.

The system (10) of three second order ordinary differential equations is highly non-linear due to multiplication of state variables and some trigonometric functions. It describes the continuous system dynamics that will be subject to an analysis of long term solutions that will occur far and near its resonance zones. Numerical solution of the system of equations has to be preceded by its transformation to a system of six first order differential equations, assumption of some initial conditions for the six-element state vector and also by the change of the variable $s = \Delta s + \Delta l_{st} + l_0$, so the numerical solution referred to the second degree of freedom (the state variable s) will represent an incremental elongation of the spring, i.e., Δs, about its equilibrium length l_0. The system dynamics will be investigated in the next section.

3.2. A damped mathematical pendulum with periodically modulated length

Let us consider the motion of the damped mathematical pendulum [5] with changing length $l = l(t)$ and external force $e = e(t)$ given by

$$l(t)\ddot{\phi} + c\dot{\phi} + \sin\phi = e(t). \tag{12}$$

We suppose that $l(t)$ and $e(t)$ are almost periodic step functions in the following sense: there are sequences

$$\begin{aligned}
&\{t_n\}_{n\in\mathbf{Z}} \subset \mathbf{R}, \quad \{l_k\}_{k\in\mathbf{Z}} \subset \mathbf{C}, \quad \{e_k\}_{k\in\mathbf{Z}} \subset \mathbf{C},\\
&\{T_k\}_{k\in\mathbf{Z}} \subset \mathbf{C}, \quad \{w_k\}_{k\in\mathbf{Z}} \subset \mathbf{R},
\end{aligned} \tag{13}$$

such that

$$t_n = nT + \sum_{k\in\mathbf{Z}} T_k e^{iw_k n}, \quad \forall n \in \mathbf{Z}, \quad T > 0, \quad \sum_{k\in\mathbf{Z}} \left|T_k\right| < \frac{T}{2}, \tag{14}$$

and for any $t_n < t < t_{n+1}$, we have:

$$e(t) = \sum_{k\in\mathbf{Z}} e_k e^{iw_k n}, \quad l(t) = \sum_{k\in\mathbf{Z}} l_k e^{iw_k n}, \tag{15}$$

where

$$\sum_{k\in\mathbf{Z}} \left|e_k\right| < \infty, \quad \sum_{k\in\mathbf{Z}} \left|l_k\right| < \infty. \tag{16}$$

Moreover, we suppose that $l(t)$ and $r(t)$ are step functions with almost periodic jumps. We are interested in finding conditions on $l(t)$, $e(t)$ and c that Eq. (12) has a bounded solution on **R** with the same almost periodic properties as $l(t)$ and $e(t)$. To solve this problem, a sequence of ordinary differential equations with linear boundary value conditions has to be studied. Being motivated by the approach presented in [6], considering continuous almost periodic ordinary differential equations, the boundary value problem can be solved with the use of Banach fixed point theorem together with a method of majorant functions. For a simplicity, taking into account a concrete form of Eq. (12) the solution will be found, as well as to visualize the pendulum's behavior, some numerical computations performed.

Let the difference equation be analyzed in the form:

$$x_{n+2} + ax_{n+1} + x_n = bx_n^3 + d_1 \cos n\sqrt{2} + d_2 \sin 3n, \quad n \in \mathbf{Z}, \tag{17}$$

where $a \in \mathbf{R}$, $|a| > 2$ and $b, d_1, d_2 \in \mathbf{R}$. It can be shown that if

$$27\left|b\right|\left(\left|d_1\right| + \left|d_2\right|\right)^2 < 4\left(\left|a\right| - 2\right)^3 \tag{18}$$

then Eq. (18) has a solution of the form:

$$x_n = \sum_{k,p\in\mathbf{Z}} z_{kp} e^{i(k\sqrt{2}+3p)n}, \quad \sum_{k,p\in\mathbf{Z}} \left|z_{kp}\right| \le \frac{3}{2}\frac{\left|d_1\right| + \left|d_2\right|}{\left|a\right| - 2}. \tag{19}$$

4. Numerical computations

At this stage of our study, the dynamics of the very weakly damped pendulum is discussed. In Fig. 7, we see an interesting example of quasi-periodic oscillations of the slider-pendulum system in each degree of freedom. It is confirmed in Fig. 7b by three closed color curves on Poincaré maps. The slider oscillates quasi-periodically with the frequency $f_2 \approx 0.9707$ being synchronized with the same frequency of angular oscillations of the pendulum. Additionally, with regard to the weakly damped case and in comparison to the previous case, the elongation of the spring pendulum is much greater as well as the remaining state variables take higher maximal amplitudes of oscillations.

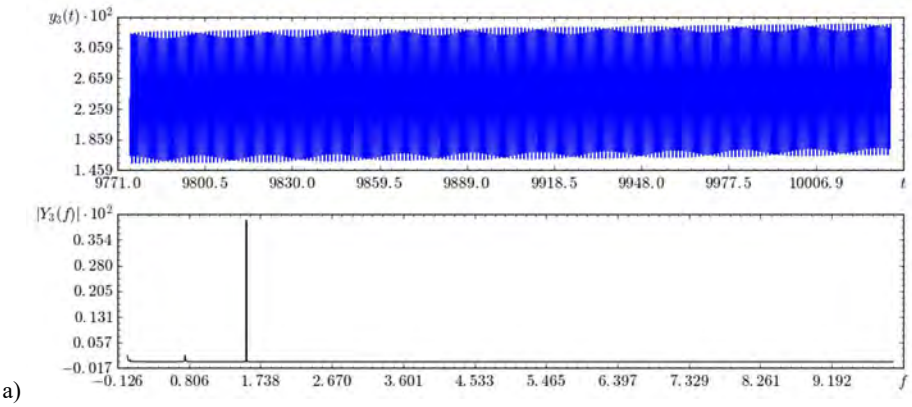

a)

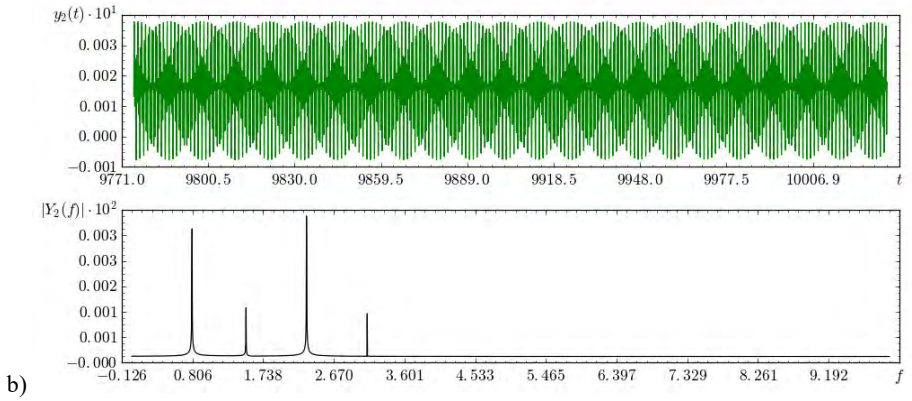

b)

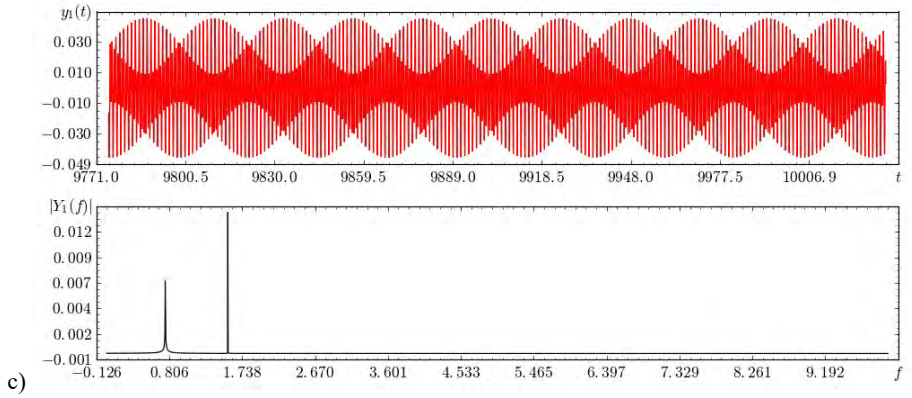

c)

Figure 2. Time histories with amplitude modulation of the length of the pendulum given by Eq. (10), phase planes (grey lines) and Poincaré maps (red, green and blue dots) for the case of weakly damped variable-length spring pendulum (see Sec. 3, $c = 0.01$ Ns/m). Parameters: $t_0 = 9775.12$, $t_k = 10032.36$, $t_{ob} = 257.24$, $T = 0.6431$ s, $n_T = 400$, $\omega = 9.77$ rad/s.

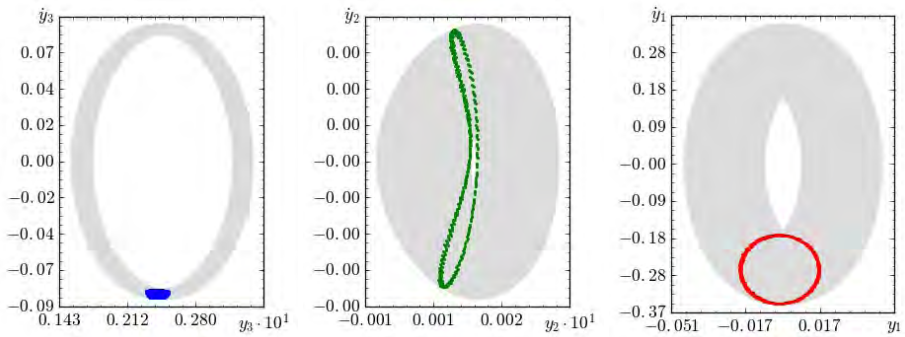

d)

Figure 2 (continued).

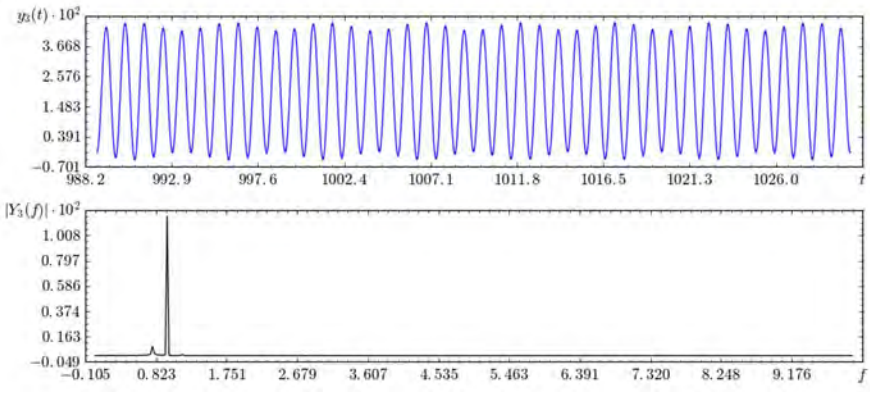

a)

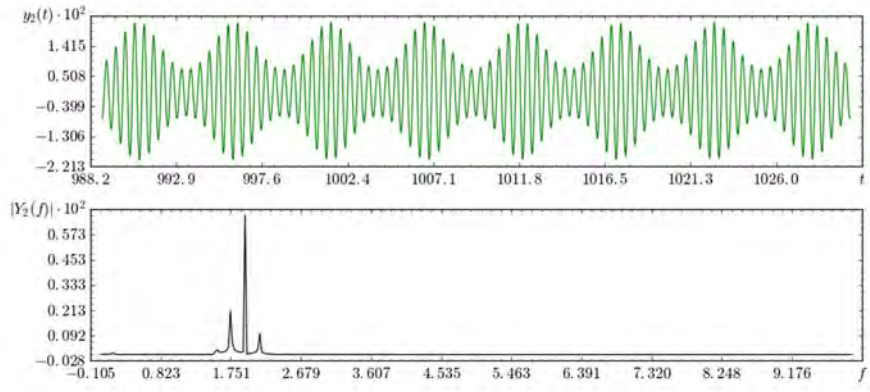

b)

Figure 3. Time histories with amplitude modulation of the length of the pendulum given by Eq. (10), phase planes (grey lines) and Poincaré maps (red, green and blue dots) for the case of weakly damped variable-length spring pendulum (see Sec. 3, c = 0.01 Ns/m). Parameters: t_0 = 988.848, t_k = 1030.05, t_{ob} = 30.9015, T = 1.03005 s, n_T = 40, ω = 6.1 rad/s.

c)

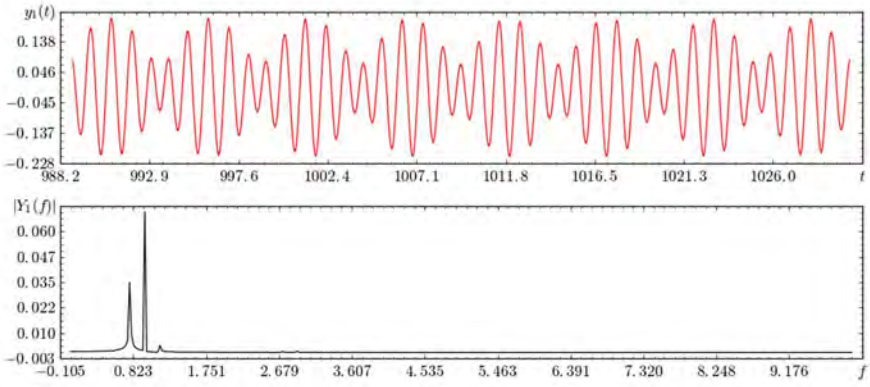

d)

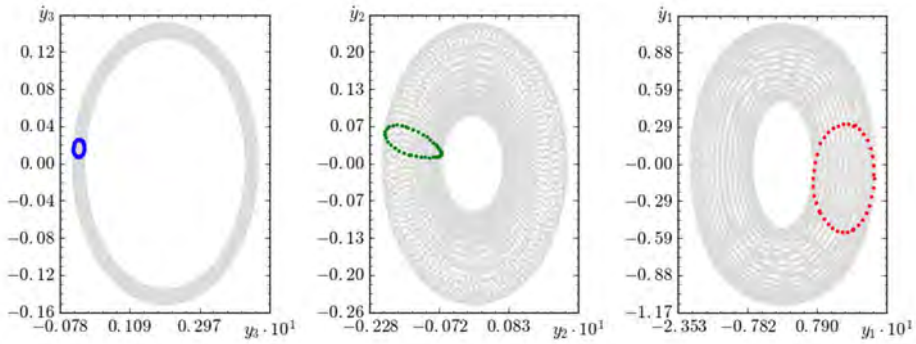

Figure 3 (continued).

Figures 2 and 3 represent quasi-periodic behaviour of all system bodies confirmed by closed curves on Poincaré maps. Inspecting the spectral power density plots in Fig. 2c and 3c, each mode of oscillations is associated with a slightly different frequency. It is a very characteristic dynamical behaviour since at least two different frequencies of oscillations are reported.

5. Conclusions

Two mechanical systems consisting of a variable-length pendulums were subject to a mathematical derivations and numerical computations. The two systems dynamics was investigated based on the derivation of mathematical model and the resonance plot obtained for the case of very weak damping of incremental elongation of the pendulum. The observations brought us interesting results, summarizing that the three-degrees-of-freedom mechanical system with partial dissipation of kinetic energy of motion oscillates mainly periodically and quasi-periodically. Nevertheless, the system dynamics can exhibit chaos in a close vicinity of resonance peaks of maximum amplitudes. The damped spring pendulum with a moving point of its attachment has two modes of oscillations, the pendulum

angle of rotation mode and the spring incremental elongation mode. Finally, the second model of a mathematical pendulum with jumping length has been defined for proving the existence of almost periodic solutions. A mathematical analysis supported with numerical computations of the jumping discontinuity system will be taken into a deeper consideration in further works.

References

[1] Aduyenko, A.A. and Amel'kin, N.I. Resonance rotations of a pendulum with a vibrating suspension, *Journal of Applied Mathematics and Mechanics*, 79(6), 2015, 531–538.

[2] Butikov, E.I. Pendulum with a square-wave modulated length. *International Journal of Non-Linear Mechanics,* 55, 2013, 25–34.

[3] Zhang, P., Ren, L., Li, H. and Jiang, T. Control of wind-induced vibration of transmission tower-line system by using a spring pendulum, *Mathematical Problems in Engineering,* 10, 2015, 1–10.

[4] Plaksiy, K.Yu. and Mikhlin, Yu.V. Interaction of free and forced nonlinear normal modes in two-DOF dissipative systems under resonance conditions, *International Journal of Non-Linear Mechanics*, 94, 2017, 281–291.

[5] Hatvani, L. and Stachó, L. On small solutions of second order differential equations with random coefficients. *Arch. Math. EQUADIFF 9* (Brno, 1997) 34, 1998, 119–126.

[6] Stoker, J.J. *Nonlinear Vibrations in Mechanical and Engineering Systems*, New York, 1950.

[7] Belyakova A.O., Seyranian, A.P. and Luongo, A. Dynamics of the pendulum with periodically varying length, *Physica D: Nonlinear Phenomena,* 238(16), 2009, 1589–1597.

[8] Broer, H.W., Hoveijn, I., Noort, M. van, Simo, C., and Vegter, G. The parametrically forced pendulum: a case study in 1 1/2 degree of freedom, *Journal of Dynamics and Differential Equations*, 18, 2004, 897–947.

[9] Olejnik, P. and Awrejcewicz, J. Coupled oscillators in identification of nonlinear damping of a real para-metric pendulum, *Mechanical Systems and Signal Processing*, 98, 2018, 91–107.

[10] Nayfeh, A.H. and Mook, D.T. *Nonlinear Oscillations*, Wiley, New York, 1979.

Paweł Olejnik, Associate Professor: Department of Automation, Biomechanics and Mechatronics, Lodz University of Technology, 1/15 Stefanowski Str., 90-924 Lodz, Poland (*pawel.olejnik@p.lodz.pl*). The author gave a presentation of this paper during one of the conference sessions.

Jan Awrejcewicz, Professor: Department of Automation, Biomechanics and Mechatronics, Lodz University of Technology, 1/15 Stefanowski Str., 90-924 Lodz, Poland (*jan.awrejcewicz@p.lodz.pl*).

Michal Fečkan, Professor: Department of Mathematical Analysis and Numerical Mathematics, Faculty of Mathematics, Physics and Informatics, Comenius University in Bratislava, Mlynská Dolina, 842 48 Bratislava, Slovakia (*Michal.Feckan*@fmph.*uniba*.sk).

Chaotic dynamics of a two-layer beam set, described by mathematical models of the first and second approximation

Irina V. Papkova, Olga A. Saltykova, Jan Awrejcewicz, Vadim A. Krysko

Abstract: Chaotic dynamics of a two beams set with a small clearance between them is investigated. Such a clearance is adopted for problems where geometric nonlinearity can be ignored. In the studied case each of the beams may exhibit vibrations with an amplitude of no more than 0.25 of the beam height. The transverse uniformly distributed harmonic load acts on the outer beam (beam 1). The contact interaction is accounted through the Kantor model. Two cases are considered: (i) beam 1 is described by the first approximation model, and beam 2 is governed by the second approximation model; (ii) beam 1 is described by a second approximation model, whereas beam 2 by a first approximation model. The problem is solved as a system with an infinite number of degrees of freedom. The finite difference method and Runge-Kutta type methods are used. The analysis of the obtained results is carried out by the methods of nonlinear dynamics and the qualitative theory of differential equations. The problems were solved both in geometrically linear and nonlinear formulations. The solution takes into account the constructive nonlinearity. To obtain reliable results, we calculated the values of the largest Lyapunov exponent using three different algorithms, and hence our results can be treated as true ones.

1. Introduction

The aim of the paper is to study the influence of the kinematic model on the nonlinear dynamics of the contact interaction of beams. It is impossible to obtain an analytical solution for the problems under investigation, because the differential equations that describe the dynamics of a beam structure are complex and nonlinear.

It is necessary to use several numerical methods to solve nonlinear problems. Among the methods of reducing the system of nonlinear partial differential equations to the Cauchy problem, we use methods such as: the finite differences method (FDM), the Bubnov-Galerkin method in higher approximations, and the finite elements method (FEM) and the finite boundary elements method. To solve the Cauchy problem, one can use the FDM, the Adams method, the Runge-Kutta type methods, and so on.

The application of numerical methods can lead to an accumulation of the error of the solution. The question arises about the reliability of the obtained solutions. This question is posed in his work by Ren'e Lozi [1]. To ensure the numerical reliability of the obtained results, we propose an approach

for verifying the truth of the results. This approach is connected in the transition of the original problem from a finite number of degrees of freedom to an infinite one.

A significant dependence on the initial conditions is a fundamental feature of chaos. Gulik [2] considers that chaos exists when either there is an essential dependence on the initial conditions or the function has a positive Lyapunov exponent at each point of the domain of its definition and therefore is not ultimately periodic. In our studies we follow the definition of chaos according to the Gulik's work [2].

The solutions obtained depend on the chosen kinematic hypothesis in the construction of the mathematical model, the boundary and initial conditions, the number of integration intervals in the FDM, the method for solving the Cauchy problem in the form of methods of the Runge-Kutta class, the time step in solving dynamics problems and the method for determining the Lyapunov exponent .

The geometric dimensions of the beams are the same. The material of the beams is isotropic and homogeneous. Between the beams there is a small gap, the value of which is less than 0.2h, where h is the height of the beam, i.e. consider small clearance between the beams.

2. Statement of the problem and the mathematical model

The considered structure composed of two beams occupies a 2D space within the R^2 space with the rectangular system of coordinates given in the following way: a reference line, further called the middle line , is fixed in the beam 1, the axis OX is directed z=0 from the left to the right of the middle line, and the axis OZ is directed downwards. In the given system of coordinates, the space Ω is defined in the following way (see Fig. 1): $\Omega = \{x \in [0, a]; -h \leq z \leq h_k + 3h\}, 0 \leq t \leq \infty$.

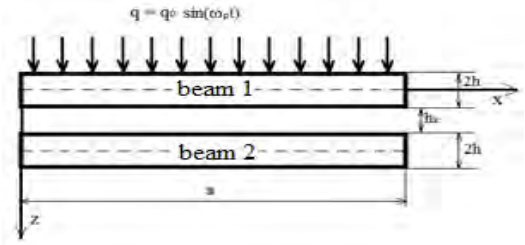

Figure 1. The investigated beams

The hypothesis of the second approximation [3] - the hypothesis of Tymoshenko, lies in the fact that the tangential displacements u^z are distributed along the beam thickness according to a linear law. To obtain the Euler-Bernoulli equations [4], we assume that the tangential displacement u^z is distributed along the thickness of the stack of layers according to a linear law.

In order to model the contact interaction of the beam within the Kantor model, we introduce the term $(-1)^i K(w_1 - w_2 - h_k)\Psi$, $i = 1, 2$ into the equation governing the beams, i – is stands for the

beam number. The function is Ψ defined by the formula $\Psi=\frac{1}{2}[1+sign(w_1-h_k-w_2)]$, i.e. if Ψ=1 the beams are in contact $w_1 > w_2 + h_k$, otherwise there is no contact between [5] (see Fig. 1). There is a gap between the beams - h_k. К - stands for the coefficient of transverse stiffness of the contact zone. By "beam 1" we understand the externally beam loaded, whereas "beam 2" stands for the unloaded beam.

Equations of beams motion, as well as the boundary and initial conditions, are obtained from the Hamilton-Ostrogradskiy principle [6-7].

A wide class of papers on the nonlinear dynamics of Euler-Bernoulli beams [8-9], Timoshenko [10-11], and also on the contact interaction of mechanical structures [12-13] is presented in the modern scientific literature. But to the present time, there is no work on the study of beam structures with a gap, where each beam is described by kinematic hypotheses of different approximations.

Equations of motion of a structure consisting of an Euler-Bernoulli beam and a Timoshenko beam in the displacements taking into account the energy dissipation will be written in the following form

$$\begin{cases} \frac{1}{\lambda^2}\left[L_2(w_i,w_i)+L_1(u_i,w_i)-\frac{1}{12}\frac{\partial^4 w_i}{\partial x^4}\right]- \\ -(-1)^i K(w_1-w_2-h_k)\Psi+q_i(t)-\frac{\partial^2 w_i}{\partial t^2}-\varepsilon_1\frac{\partial w_i}{\partial t}=0; \\ \frac{\partial^2 u_i}{\partial x^2}+L_3(w_i,w_i)-\frac{\partial^2 u_i}{\partial t^2}=0; \\ \frac{1}{3}\left[\frac{\partial^2 w_i}{\partial x^2}+\frac{\partial \gamma_{xi}}{\partial x}\right]+\frac{1}{\lambda^2} \\ \left[R_1(w_i,u_i)+R_3(w_i,u_i)+\frac{3}{2}R_2(w_i,w_i)\right]- \\ -(-1)^i K(w_1-w_2-h_k)\Psi+q_i(t)-\frac{\partial^2 w_i}{\partial t^2}-\varepsilon_1\frac{\partial w_i}{\partial t}=0; \\ \frac{\partial^2 u_i}{\partial x^2}+L_4(w_i,w_i)-\frac{\partial^2 u_i}{\partial t^2}=0; \\ \frac{\partial^2 \gamma_{xi}}{\partial x^2}-8\lambda^2\left[\gamma_{xi}+\frac{\partial w_i}{\partial x}\right]-\frac{\partial^2 \gamma_{xi}}{\partial t^2}=0; i=1,2, \end{cases} \quad (1)$$

where: $R_1(w_i,u_i)=\frac{\partial^2 w_i}{\partial x^2}\frac{\partial u_i}{\partial x}$, $R_2(w_i,w_i)=\frac{\partial^2 w_i}{\partial x^2}\left(\frac{\partial w_i}{\partial x}\right)^2$, $R_3(w_i,u_i)=\frac{\partial w_i}{\partial x}\frac{\partial^2 u_i}{\partial x^2}$, $R_4(w_i,w_i)=\frac{\partial w_i}{\partial x}\frac{\partial^2 w_i}{\partial x^2}$, $L_1(u_i,w_i)=\frac{\partial^2 u_i}{\partial x^2}\frac{\partial w_i}{\partial x}+\frac{\partial u_i}{\partial x}\frac{\partial^2 w_i}{\partial x}$, $L_2(w_i,w_i)=\frac{3}{2}\frac{\partial^2 w_i}{\partial x^2}\left(\frac{\partial w_i}{\partial x}\right)^2$, $L_3(w_i,w_i)=\frac{\partial w_i}{\partial x}\frac{\partial^2 w_i}{\partial x^2}$ - are the nonlinear operators, γ_{xi} – is the transverse shear function, w_i, u_i– are the deflection and displacement functions of the beams, respectively, $i=1,2$ - are sequence number of beams.

We must add boundary and initial conditions to the system of differential equations (1). Boundary conditions for case when both ends of the Timoshenko beam are rigidly clamped:

$$w_i(0,t)=w_i(1,t)=u_i(0,t)=u_i(1,t)=\gamma_{xi}(0,t)=\gamma_{xi}(1,t)=0, i=1,2. \quad (2)$$

Initial conditions for Timoshenko beam:

$$w_i(x)_{|_{t=0}}=0, u_i(x)_{|_{t=0}}=0, u_i(x)_{|_{t=0}}=0, \frac{\partial w_i(x)}{\partial t}_{|_{t=0}}=0, \quad (3)$$

$\frac{\partial u_i(x)}{\partial t}_{|t=0} = 0, \frac{\partial \gamma_{xi}(x)}{\partial t}_{|t=0} = 0, i = 1,2.$

Boundary conditions for case when both ends of the Euler-Bernoulli beam are rigidly clamped:

$$w_i(0,t) = w_i(1,t) = u_i(0,t) = u_i(1,t) = \frac{\partial w_i(0,t)}{\partial x} = \frac{\partial w_i(1,t)}{\partial x} = 0, i = 1,2. \quad (4)$$

Initial conditions for beam 2:

$$w_i(x)_{|t=0} = 0, u_i(x)_{|t=0} = 0, \frac{\partial w_i(x)}{\partial t}_{|t=0} = 0, \frac{\partial u_i(x)}{\partial t}_{|t=0} = 0, i = 1,2. \quad (5)$$

If we do not take into account the geometric nonlinearity, we must put non-linear operators equal to zero.

The system of governing PDEs (1) supplemented by boundary (2), (4) and initial conditions (3), (5) is reduced to the counterpart dimensionless form using the following variables (6).

$$\overline{w} = \frac{w}{2h}, \overline{a} = \frac{ua}{(2h)^2}, \overline{x} = \frac{x}{a}, \lambda = \frac{a}{2h}, \overline{q} = q\frac{a^4}{(2h)^4 E}, \quad (6)$$

$$\overline{t} = \frac{t}{\tau}, \tau = \frac{a}{c}, c = \sqrt{\frac{Eg}{\gamma}}, \overline{\varepsilon_1} = \varepsilon_1 \frac{a}{c}, \overline{\gamma_x} = \frac{\gamma_x a}{2h}$$

where: E – is the Young's modulus; g – is the gravity of Earth; γ –is the specific gravity of the beam material, 2h - is the height, a - is the length of beams, respectively.

The clearance between the beams is small. That is, contact between layers occurs even with small deflections of beam 1, $w_i \leq 0.25h$ and these oscillations can be described by linear theory of vibrations, as is usually assumed in theory. The resulting system of nonlinear partial differential equations (1) - (5) reduces to a system of ordinary differential equations by the FDM with approximation $O(c^2)$, where c is a step in the spatial coordinate. The Cauchy problem is solved in time using the Runge-Kutta of the 4th (RK4) and the 2nd (2RK) orders [14], the Runge-Kutta-Fehlberg of the 4th order (rkf45) [15, 16], the Cash-Karp of the 4th order (RKCK) [17], the Runge-Kutta-Prince-Dormand of the 8th order (rk8pd) [18] as well as the implicit Runge-Kutta methods of the 2nd (rk2imp) and the 4th (rk4imp) orders.

On the basis of the described algorithms, the program package has been developed, which allows one to solve the given problem with respect to the control parameters $\{q_0, \omega_p\}$. The main attention has been paid to control and avoid the occurrence of penetration of the structural elements.

The beam 1 is subjected to the uniformly distributed transverse harmonic excitation of the following form:

$$q = q_0 \sin(\omega_p t), \quad (7)$$

where q_0 stands for the amplitude and ω_p for the frequency of excitation.

The paper compares nonlinear dynamics and contact interaction of two types of a beam structure: (i) - beam 1 obeys the Euler-Bernoulli hypothesis, beam 2 - Tymoshenko's hypothesis; (ii) - beam 1 is described by Tymoshenko's hypothesis, and beam 2 by the Euler-Bernoulli hypothesis.

3. Numerical results

The beam 1 is subjected to the transverse harmonic excitation (7). Where $q_0 = 5000$, $\omega_p = 5.1$.The beam clearance equals $h_k = 0.1$.

We give the graphs of signals $w_i(0.5, t)$ for both tasks in Figure 2.

In case (i) – Figure 2 (a – beam 1, b – beam 2), in case (ii) – Figure 2 (b – beam 1, c – beam 2) for n=40; 80; 120; 240; 360; 400, $t \in [500; 506]$. The results were obtained using the 8th order Runge-Kutta method in the modification of Prince-Dormand – Rk8pd.

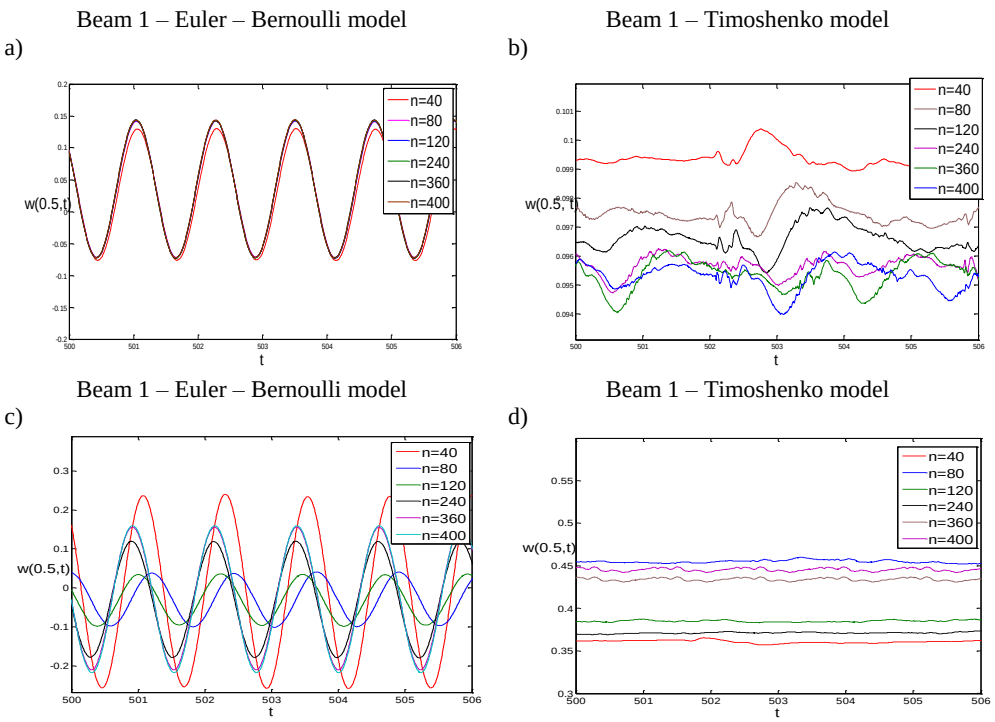

Figure 2. The signals $w_i(0.5, t)$ for n=40; 80; 120; 240; 360; 400, $t \in [500; 506]$. In case (i) - a, b, in case (ii) - b, c.

The kinematic hypothesis taken into account significantly affects on the nonlinear dynamics and contact interaction of the two-layer beam structure. In case (i) (Fig. 2a, b), the convergence of the results for the signal for beam 1 is achieved already at n = 80 (Fig. 2a), for beam 2 there is no

complete convergence, however, the amplitude of oscillations is very small and the waveform coincides (Fig. 2 (b). For problem (ii), the amplitude of the vibrations of the beam 1 (Fig. 2c) differs significantly for different n, and convergence is observed starting from n = 360. For beam 2 (Fig. 2d), the convergence is achieved in the form of vibrations, there are small differences in amplitude. Note that the analysis of oscillations is made with other conditions being equal, but there are differences in the magnitude of the amplitude of the oscillations of the beams, depending on the problem.

Let us analyze the frequency characteristics of beam vibrations using the analysis of the Fourier power spectrum. In Fig. 3 we give the Fourier power spectra for both problems.

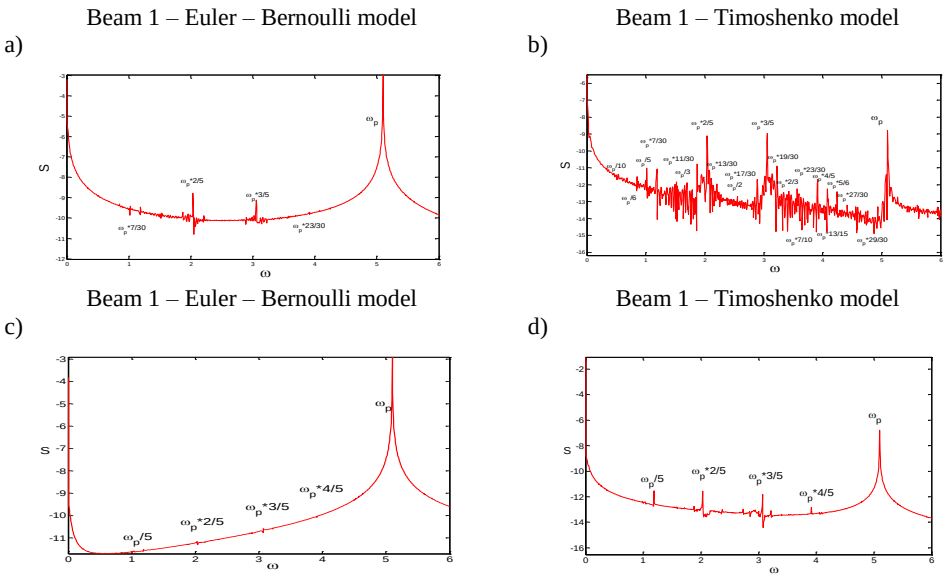

Figure 3. The Fourier power spectrum. For case (i) – a, b; for case (ii) – c, d.

All frequencies reflected on the investigated Fourier power spectra are linearly dependent on the frequency ω_p. If the hypothesis of the normal rotation for beam 1 is taken into account (problem (ii), figure 3 c, d), the structure oscillations occur at five main frequencies: $\omega_p, \frac{\omega_p}{5}, \frac{2}{5}\cdot\omega_p, \frac{3}{5}\cdot\omega_p, \frac{4}{5}\cdot\omega_p$.

There are five main frequencies on the power spectrum. If we take into account the hypothesis of the second approximation for beam 2 (problem (i), figure 3 a, b), then we observe a significant difference in the frequency components of the beam oscillations. The beam oscillations 1 are three-frequency (Figure 3 a), and the beam oscillations 2 (Figure 3 b) are multifrequency, but on the power spectrum the main frequencies are beam 1 - $\omega_p, \frac{2}{5}\cdot\omega_p, \frac{3}{5}\cdot\omega_p$.

For each problem, a comparison of the solution of the Cauchy problem is performed depending on the Runge-Kutta type method. It is established that the eighth order Runge-Kutta method in the

Prince Dormand modification is optimal for both problems. Dynamic characteristics such as phase portraits, the Poincaré map, wavelet spectra for each problem for n=40; 80; 120; 240; 360; 400 and for each Runge-Kutta method are compared.

It was revealed that all dynamic parameters agree with each other and testify to the chaotic vibrations of the structure in both cases. Ensuring the truth of the obtained results is achieved by comparing the values of the largest Lyapunov exponent, calculated with the help of three different algorithms - Wolf [19], Kantz [20] and Rosenstein [21].

All the values of the largest Lyapunov exponent for each problem and for each beam are positive and we can state that the vibrations of the structure are chaotic, regardless of the kinematic hypotheses.

4. Concluding remarks

The paper proves that the vibrations of the investigated two-layer beam structure are truly chaotic, based on ensuring the convergence of the results, depending on the number of beam partitions with respect to the spatial coordinate, in time, on using the method for solving the Cauchy problem.

It was found that taking into account different kinematic hypotheses, when modeling the contact interaction of beams, leads to significant differences in the oscillatory process.

Acknowledgements

This work has been supported by the grants the Russian Science Foundation, RSF 16-19-10290

References

[1] Ren´e Lozi. Can we trust in numerical computations of chaotic solutions of dynamical systems? *World Scientific Series on Nonlinear Science*, World Scientific, 84, (2013), pp.63-98.

[2] Gulick, D. *Encounters with Chaos*, McGraw-Hill, New York, 1992.

[3] Timoshenko, S.P. On the correction for shear of differential equation for transverse vibration of prismatic bar. *Philosophical Magazin* 41 (1921) 744-746.

[4] Euler, L. Sur la force des colones. *Memories de L'Academie de Berlin* 13 (1757) 252 – 282.

[5] Kantor, B.Ya. *Contact Problems of the Nonlinear Theory of Shells of Revolution.* Naukova Dumka, Kiev, 1990 (in Russian).

[6] Hamilton, W. Report of the Fourth Meeting of the British Association for the Advancement of Science, L., 1835, p. 513-518;

[7] Ostrogradsky, M., Mem. de l'Acad, des Sci. de St-Petersbourg, 8(3) (1850) 33-48.

[8] Krysko, A.V., Awrejcewicz, J., Zhigalov, M.V., S.P. Pavlov, Krysko V.A. Nonlinear behaviour of different flexible size-dependent beams models based on the modified couple stress theory. Part 1. Governing equations and static analysis of flexible beams, *International Journal of Non-Linear Mechanics*, 93 (2017) 96-105.

[9] Krysko, A.V., Awrejcewicz, J., Zhigalov, M.V., Pavlov, S.P., Krysko, V.A. Nonlinear behaviour of different flexible size-dependent beams models based on the modified couple

stress theory. Part 2. Chaotic dynamics of flexible beams, *International Journal of Non-Linear Mechanics*, 93 (2017) 106-121.

[10] Awrejcewicz, J., Krysko, V.A., Pavlov, S.P., Zhigalov, M.V. Nonlinear dynamics size-dependent geometrically nonlinear Tymoshenko beams based on a modified moment theory. *Applied Mathematical Sciences*, 11(5) (2017) 237-247.

[11] Krysko, V.A., Pavlov, S.P., Zhigalov, M.V., Dobriyan, V.V. *The study of chaotic dynamics using Lyapunov exponents for functionally graded size dependent beams with transversal shifts*, in Advanced Engineering Research and Applications (AERA), (2017), pp. 163-186.

[12] Krysko, A.V., Awrejcewicz, J., Zhigalov, M.V., Krysko, V.A. On the contact interaction between two rectangular plates, *Nonlinear Dynamic*, 84(4) (2016) 2729-2748.

[13] Awrejcewicz, J., Krysko-jr, V.A., Yakovleva, T.V., Krysko, V.A., Alternating chaos versus synchronized vibrations of interacting plate with beams, *International Journal of Non-Linear Mechanics*, 88 (2017) 21–30.

[14] Süli, E., Mayers, D. *An Introduction to Numerical Analysis*. Cambridge: Cambridge University Press, 2003.

[15] Fehlberg, E. Low-order classical Runge-Kutta formulas with step size control and their application to some heat transfer problems. *NASA Technical Report* 315 (1969).

[16] Fehlberg, E. Klassische Runge-Kutta-Formeln vierter und niedrigerer Ordnung mit Schrittweiten-Kontrolle und ihre Anwendung auf Wärmeleitungsprobleme, *Computing (Arch. Elektron. Rechnen*), 6 (1970) 61–71.

[17] Cash, J.R., Karp A.H. A variable order Runge-Kutta method for initial value problems with rapidly varying right-hand sides. *ACM Transactions on Mathematical Software* 16 (1990) 201-222.

[18] Dormand, J. R., Prince, P. J. A family of embedded Runge-Kutta formulae, *Journal of Computational and Applied Mathematics*, 6(1) (1980), 19–26.

[19] Wolf, A., Swift, J.B., Swinney, H.L., Vastano, J.A. Determining Lyapunov Exponents from a time series. *Physica 16 D* (1985) 285-317.

[20] Kantz, H. A robust method to estimate the maximum Lyapunov exponent of a time series. *Phys. Lett. A*, 185 (1994) 77-87.

[21] Rosenstein, M.T., Collins, J.J., Carlo, J. De Luca A practical method for calculating largest Lyapunov exponents from small data sets. *Neuro Muscular Research Center and Department of Biomedical Engineering, Boston University*, 20, (1992).

Irina V. Papkova, PhD.: Department of Mathematics and Modeling, Saratov State Technical University, Politehnicheskaya 77, 410054 Saratov, RUSSIAN FEDERATION (ikravzova@mail.ru).

Olga A. Saltykova, PhD.: Department of Mathematics and Modeling, Saratov State Technical University, Politehnicheskaya 77, 410054 Saratov, and Cybernetic Institute, National Research Tomsk Polytechnic University, Lenin Avenue, 30, 634050 Tomsk, RUSSIAN FEDERATION (olga_a_saltykova@mail.ru).

Jan Awrejcewicz, Professor: Lodz University of Technology, Faculty of Mechanical Engineering, Department of Automation, Biomechanics and Mechatronics, 1/15 Stefanowski Str., 90-924 Lodz, POLAND (awrejcew@p.lodz.pl). The author gave a presentation of this paper during one of the conference sessions.

Vadim A. Krysko, Professor: Department of Mathematics and Modeling, Saratov State Technical University, Politehnicheskaya 77, 410054 Saratov, RUSSIAN FEDERATION (tak@san.ru).

Theoretical and experimental investigation of nonlinear dynamical features in a MEMS device electrically actuated

Laura Ruzziconi, Nizar Jaber, Lakshmoji Kosuru, Mohammed L. Bellaredj, Stefano Lenci, Mohammad I. Younis

Abstract: We consider a clamped-clamped microbeam electrically actuated. Experimental tests are performed. The microbeam is perfectly straight. The first three experimental natural frequencies are detected and several backward and forward frequency sweeps are acquired. Nonresonant and the resonant branches coexist. They undergo bending toward higher frequencies values, which is a feature not particularly common in MEMS. Experimental behavior charts are obtained where the curves of experimental appearance and/or disappearance of the attractors are reported. After extracting the unknown parameters, a single mode Galerkin reduced-order model is derived. To enhance the computational efficiency, the contribution of the electric force term is computed in advance and stored in a table. Extensive numerical simulations are performed, both from a local and global perspective. The model is observed to catch all the main nonlinear features of the device response and provide a satisfactory agreement with the experimental data. The overall scenario is explored when both the frequency and the electrodynamic voltage are varied.

1. Introduction

Nonlinear phenomena arising in the microelectromechanical systems (MEMS) are receiving increasing attention from the scientific community. Multistability, jump, chaotic motions, snap-through, pull-in and many other complex nonlinear phenomena represent very attractive features for the development of increasingly powerful MEMS systems and new devices deliberately operating in the nonlinear regime are emerging in a variety of different applications [1].

Alsaleem *et al.* [2] experimentally investigate nonlinear dynamic phenomena in a MEMS capacitive accelerometer. Many experimentally measured frequency-response curves are reported, showing the primary resonance, the activation of various superharmonic and subharmonic resonances, the softening-spring behavior with bending towards lower frequency values, the pull-in instability, etc. Focusing on a particular MEMS oscillator, Rhoads *et al.* [3] show that the dynamics may display not only hardening or softening characteristics, but also mixed ones, wherein the principal branches bend toward or away from one another near resonance. The frequency-dynamic voltage behavior chart underlines the complexity of the dynamics, showing Arnold tongues and saddle-node bifurcations and confirming a strong correlation with the experimental data. Mestrom *et al.* [4]

experimentally and theoretically detect both softening and hardening behaviors in a clamped-clamped microbeam-based MEMS resonator. Younis and Alsaleem [5] present an exploratory research on the possibility to make use of the escape and the jump phenomena to realize new concepts for mass sensing and detection and design novel devices of improved characteristics. Krylov *et al.* [6] investigate shallow-arched microbeams electrically actuated. They are fabricated from silicon on insulator (SOI) wafer using deep reactive ion etching and in-plane responses are characterized by means of optical and scanning electron microscopy. Many experimental data and theoretical simulations are developed, highlighting that the microstructure may exhibit numerous non-linear phenomena, as sequential snap-through buckling and pull-in instability. Krylov and Dick [7] further theoretically examine these phenomena, detecting the boundaries of the bistability region and shedding light on the role of generic nonlinearities as well as on the influence of the device parameters. Amazing results are reported in Medina *et al.* [8], where experimental bifurcation maps built in terms of the critical snap-through, release and pull-in deflections of the microbeams are developed, showing the location of the critical points and confirming experimentally the complex nonlinear behavior theoretically predicted. Ouakad and Younis [9] and Younis *et al.* [10] simulate the dynamic behavior of MEMS arched resonators actuated electrically, emphasizing the potential to use them as band-pass filters and low-powered switches. Ruzziconi *et al.* [11, 12] theoretically examine a microbeam-based MEMS device with bistable static configuration. They investigate the possibility to operate the device with several competing attractors with different characteristics, leading to a considerable versatility of behavior, which may have many feasible applications. Ramini *et al.* [13, 14] experimentally examine the rich complex dynamics arising in an in-plane silicon micromachined arch. Optical techniques are used. When the excitation is close to the first resonance frequency, a softening spring behavior is observed. Conversely, when the excitation is close to the third (second symmetric) resonance frequency, a hardening spring behavior arises. Moreover, at the primary resonance with high voltage excitations, dynamic snap-through motion occurs, which exhibits hardening behavior. Hajjaj *et al.* [15] explore the possibility of experimentally tuning the resonance frequencies and their ratios via electrothermal modulation. An electrothermal voltage is applied between the anchors of an arched microbeam generating a current that controls the axial stress caused by thermal expansion. The sensitivity of the frequency values to the variation of the electrothermal load is explored. Ramini *et al.* [16] further develop this experimental investigation, showing that several modal interactions among the vibration modes can be activated. Between the first and third bending modes of vibrations, 2:1 internal resonance, 3:1 internal resonance and mode veering (near crossing) have been observed. This is promising for designing MEMS with higher sensitive and less noisy responses. Ruzziconi *et al.* [17-19] experimentally and theoretically analyze a MEMS device consisting of a clamped-clamped polysilicon microbeam subjected to electrostatic and electrodynamic

actuation. The device has non-negligible imperfections, which are a typical consequence of the microfabrication process. Several nonlinear dynamical phenomena are observed and dynamical integrity investigations are performed to detect the parameter ranges where each dynamical behavior can be actually observed in practice.

In the present work we consider a slender microbeam-based MEMS device electrically actuated, Figure 1. The resonant branch and the non-resonant one are observed to experimentally experience a wide range of bending toward higher frequency values before undergoing dynamic pull-in. This sequence of events is not very common in MEMS. We analyze the multistability in detail, both from an experimental and from a theoretical point of view.

The paper is organized as follows. The experimental investigation is performed (section 2), the problem formulation is introduced (section 3), experimental data are compared with theoretical predictions (section 4), global simulations are developed (section 5), main conclusions are summarized (section 6).

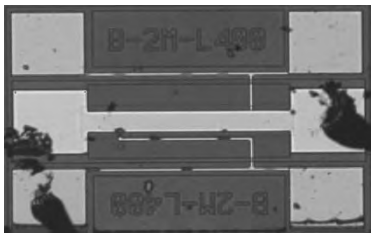

Figure 1. Optical image of the silicon nitride beam.

2. The MEMS device

The MEMS device under consideration is illustrated in Figure 1. It consists of a rectangular microbeam constituted by a layer of Silicon Nitride (Si_3N_4) of thickness h = 1.5 μm, a layer of Chrome (Cr) of 50 nm, and a layer of Gold (Au) of 200 nm. A schematic is illustrated in Fig. 2. The device is fabricated by surface micromachining process [20]. The microbeam has a straight profile, with length L = 400 μm and width w = 50 μm. The separation gap is d = 2.5 μm. The device is actuated electrically, where V_{DC} is the electrostatic voltage excitation and $V_{AC}\cos(\Omega t)$ is the electrodynamic one, with voltage V_{AC} and frequency Ω. When electrically excited, the microbeam oscillates in the out-of-plane direction, i.e. out of the plane of the substrate. The length of the lower electrode is half of the length of the microbeam [21].

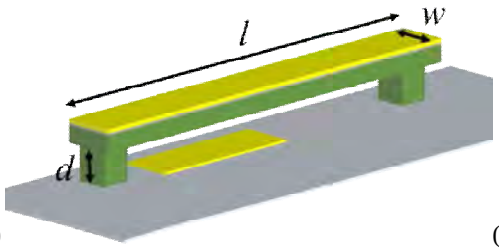

(a)

Color	Material	Thickness
	Silicon Nitride (Si_3N_4)	1.5 μm
	Chrome (Cr)	50 nm
	Gold (Au)	200 nm

(b)

Figure 2. (a) A schematic of the microbeam-based MEMS device. (b) Main dimensions of the microbeam.

The experimentally measured first three natural frequencies and the corresponding RMS amplitude of the experimental mode shapes are reported in Fig. 3. They occur at Ω_1 = 145.2 kHz (first symmetric), Ω_2 = 314.8 kHz (first antisymmetric), Ω_3 = 526.6 kHz (second symmetric).

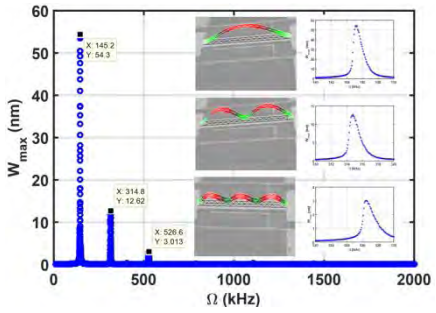

Figure 3. Experimentally measured frequency response and the corresponding RMS amplitude of the experimental mode shapes. The first three natural frequencies occur at Ω_1 = 145.2 kHz (first symmetric), Ω_2 = 314.8 kHz (first antisymmetric), Ω_3 = 526.6 kHz (second symmetric).

In the vicinity of the first symmetric resonance, many experimental frequency sweeps are performed, where the same experimental conditions are adopted. Some of the resulting frequency response curves are reported in the forthcoming Fig. 4, where the blue circles and the red triangles denote forward and backward sweep, respectively. They are acquired by increasing (forward) and/or decreasing (backward) the frequency slowly, while the electrodynamic voltage is kept constant. Both the non-resonant branch (at right) and the resonant one (at left) can be observed, which exhibit bending toward higher frequencies. Increasing the electric voltage excitation, the range of existence of the non-resonant and the resonant branch initially increases, then decreases and finally vanishes, resulting in a range where no one of the attractors exist.

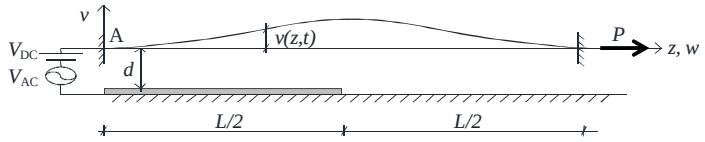

Figure 4. Mechanical model.

3. Problem formulation

The introduced mechanical model consists of a fixed–fixed microbeam with length *L* and constant rectangular cross-section of width *b* and thickness *h*. A constant axial load *P* is supposed, which represents residual stresses. After introducing non-dimensional variables and condensing the axial displacement *w*(*z*, *t*) by a classical procedure [22], so that the elongation of the central line of the microbeam does not depend on *z* but only on *t*, the governing equation is

$$\ddot{v} + \xi\,\dot{v} + v'''' + \left(n - ka\int_0^1 \tfrac{1}{2}(v')^2\,dz\right) v'' = -\gamma\,\frac{(V_{DC}+V_{AC}\cos(\Omega t))^2}{(1-v)^2}\,[U(z_1) - U(z_2)] \tag{1}$$

and the boundary conditions are

$$v(0,t) = 0, v(1,t) = 0, v'(0,t) = 0, v'(1,t) = 0 \tag{2}$$

where $U(z_1)$ and $U(z_2)$ are the unit step functions that define the lower electrode length and position. The non-dimensional variables (denoted with hats, which are dropped in (1)–(2) for convenience) are

$$\tilde{z} = z/L,\ \tilde{v} = v/d,\ \tilde{t} = t/T \tag{3}$$

and the non-dimensional parameters are

$$ka = (EA)d^2/(EJ),\ n = (EA)\,L\,w_B/(EJ),\ \gamma = \tfrac{1}{2}\varepsilon_0\varepsilon_r A_c L^3/(d^3 EJ),$$
$$\xi = c\,L^4/(EJ\,T),\ T = \sqrt{(m\,L^4)/(EJ)},\ \widetilde{\Omega} = \Omega\,T \tag{4}$$

where *EA* is the axial stiffness, *EJ* the bending stiffness, *A* and *J* the area and the moment of inertia of the cross section, *E* the effective Young's modulus, ρ the material density, *d* the gap width, *Ac* = *bL* the area of the microbeam, ε_0 the dielectric constant in the free space, ε_r the relative permittivity of the gap space medium with respect to the free space, *c* the viscous damping coefficient.

The conductive layer of Chromium/Gold applied on top of the microbeam is the upper electrode, whereas the silicon nitride (Si_3N_4) is a dielectric material, whose dielectric constant is $\varepsilon_{r\,Si3N4} = 7$. Accordingly, we consider the equivalent capacitor gap, which is the air gap plus the contribution from the silicon nitride microbeam, which yields:

$$d_{eq} = d + t_{Si3N4}/\varepsilon_{r\,Si3N4} = 2.714\,\mu m \tag{5}$$

The other parameters are extracted in order to have a good matching with the experimental natural frequencies. In particular, neglecting the static deflection due to the electrostatic voltage load,

we obtain the theoretical frequencies Ω_1 = 145.2 kHz (first symmetric), Ω_2 = 315.132 kHz (first antisymmetric), Ω_3 = 526.637 kHz (second symmetric), which are very close to the experimental ones. The associated first symmetric mode is

$$\phi_1(z) = -0.4288cos(3.714z) + 0.4288cosh(12.621z) + 1.4572sin(3.714z) - 0.4288sinh(12.621z) \quad (6)$$

and the associated first antisymmetric mode is

$$\phi_2(z) = 0.6753\,cos(7.2332z) - 0.6753\,cosh(14.0648z) + -1.3131sin(7.2332z) + 0.6753sinh(14.0648z) \quad (7)$$

We derive a single-mode Petrov-Galerkin [23] reduced-order model. Regarding the approximation function, we recall the simple case of a fixed-fixed microbeam with distributed load on half of its length. The static deflection is

$$v_{1_1}(z) = \tfrac{1}{24}z^4 - \tfrac{13}{192}z^3 + \tfrac{11}{384}z^2 \qquad 0 \le z \le 1/2$$
$$v_{1_2}(z) = \tfrac{1}{64}z^3 - \tfrac{1}{96}z^2 - \tfrac{1}{768}z + \tfrac{1}{768} \qquad 1/2 \le z \le 1 \quad (8)$$

We approximate it via a combination of the first symmetric and the first antisymmetric mode, which yields

$$\varphi(z) = \phi_1(z) + \beta\phi_2(z) \quad (9)$$

where $\beta = -0.13623$. We consider $\varphi(z)$ as approximation function in the Petrov-Galerkin method, which allows having a better description for higher voltages, still having a single d.o.f. model.

As weight function, we consider $\phi_1(z)$, to keep the (first) natural frequency. The derived reduced-order model becomes:

$$\ddot{x} + 0.05\dot{x} + 2197.23\,x + 1967.33\,x^3 = 0.08 \cdot (V_{DC} + V_{AC}\cos(\Omega t))^2 \int_0^{1/2} \frac{\phi_1(z)}{(1-\varphi(z)x(t))^2}\,dz \quad (10)$$

Since the integral in the electric force term cannot be solved analytically, we approximate it via the Padé approximation, which yields

$$\ddot{x} + 0.05\dot{x} + 2197.23\,x + 1967.33\,x^3 = (V_{DC} + V_{AC}\cos(\Omega t))^2 \frac{0.016}{(0.691587-x)^2} \quad (11)$$

which is the equation used in the forthcoming simulations.

4. Experimental data vs theoretical predictions

We analyze a neighborhood of the device natural frequency, Figure 5. The experimental frequency response diagrams are overlapped with the theoretical predictions, in order to appreciate similarities and differences. Good matching is achieved with the experimental data. The model is able to detect the value where the natural frequency occurs, to catch the hardening-spring behavior with bending toward higher frequencies arising in a neighborhood of the primary resonance, to properly simulate the separation width between the non-resonant and the resonant branch. Thus, all the main dynamical features are adequately represented. This occurs not only at low electrodynamic excitations, V_{AC} = 4.0 *V* (Fig. 5a), V_{AC} = 6.0 *V* (Fig. 5b), but also at higher values, V_{AC} = 10.0 *V* (Fig. 5c), V_{AC} = 14.4 *V* (Fig. 5d). Note that the theoretical predictions show disappearance of both the non-resonant branch and of the resonant one via saddle-node bifurcation.

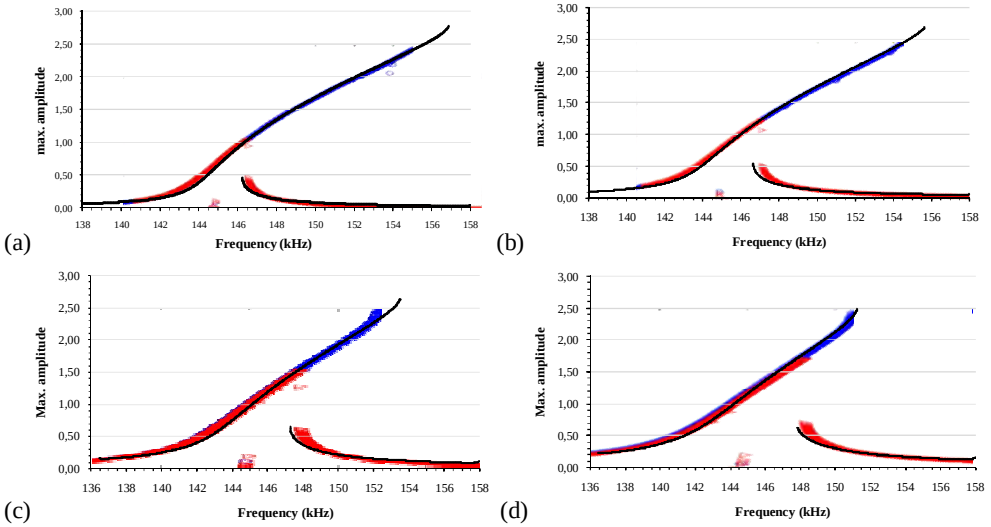

Figure 5. Frequency response diagrams at (a) V_{AC} = 4.0 *V*, (b) V_{AC} = 6.0 *V*, (c) V_{AC} = 10.0 *V*, (d) V_{AC} = 14.4 *V*. Theoretical simulations obtained via the Petrov-Galerkin method are in black solid line; experimental data obtained by forward and backward sweeps are in the blue circles and the red triangles, respectively.

For a comprehensive overview of the main dynamical events, we develop the theoretical behavior chart in Fig. 6, which illustrates the overall scenario when both the electrodynamic voltage and the frequency are varied. The chart describes where a bifurcation occurs and generates an attractor, bounding where each attractor theoretically exists. We can see the range of existence of each branch, the range of coexistence, the escape (dynamic pull-in). The chart confirms that the experimental disappearance of each branch is very close to the theoretical one.

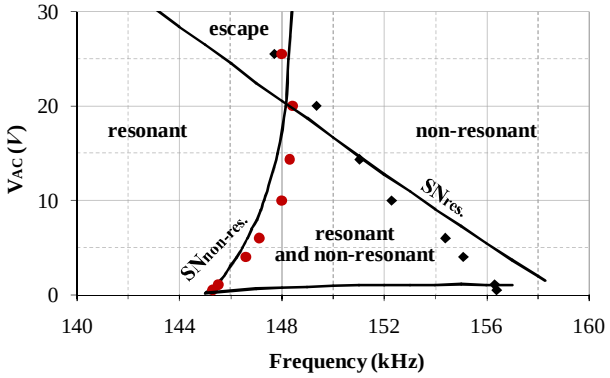

Figure 6. Frequency-dynamic voltage behavior chart. Theoretical appearance and/or disappearance of the attractors is in black solid line; experimental data obtained by forward and backward sweeps are in the red circles and the black diamonds, respectively.

Despite the satisfactory agreement, discrepancies arise in the length of each branch. The experimental curves of disappearance are shifted from the theoretical ones and occur in the region where each attractor is theoretically expected to exist. This mismatching is likely related to the presence of disturbances, which are inevitably encountered under realistic conditions. In fact, disturbances are unavoidable in practice but have not been included in the model. To take disturbances into account, in addition to the local investigations we need to consider the global dynamics and perform a dynamical integrity analysis [24].

5. Practical disappearance of the attractors

An attractor-basins analysis is developed when varying the electrodynamic voltage and frequency. Examples of attractor-basins phase portraits are reported in Fig. 7. The basin of attraction of the non-resonant branch and of the resonant one are orange and green, respectively; the escape is white, which corresponds to the system experiencing dynamic pull-in; the attractors are denoted with a cross.

At V_{AC} = 4 *V* (Fig. 7a-7c), both the non-resonant and the resonant attractor exist and compete in robustness. Approaching the resonance, the basin of the non-resonant attractor becomes wider and wider, at the expense of the resonant one, which gradually shrinks in size, up to vanishing. At this level of voltage, the two basins remain close to each other and form a large and compact safe region. The escape is located outside this safe zone.

At V_{AC} = 8 *V* (Fig. 7d-7f), the escape penetrates inside the central core of the potential well, separating the basins of the two attractors. The two basins settle far from each other, which prevents any safe jump between them.

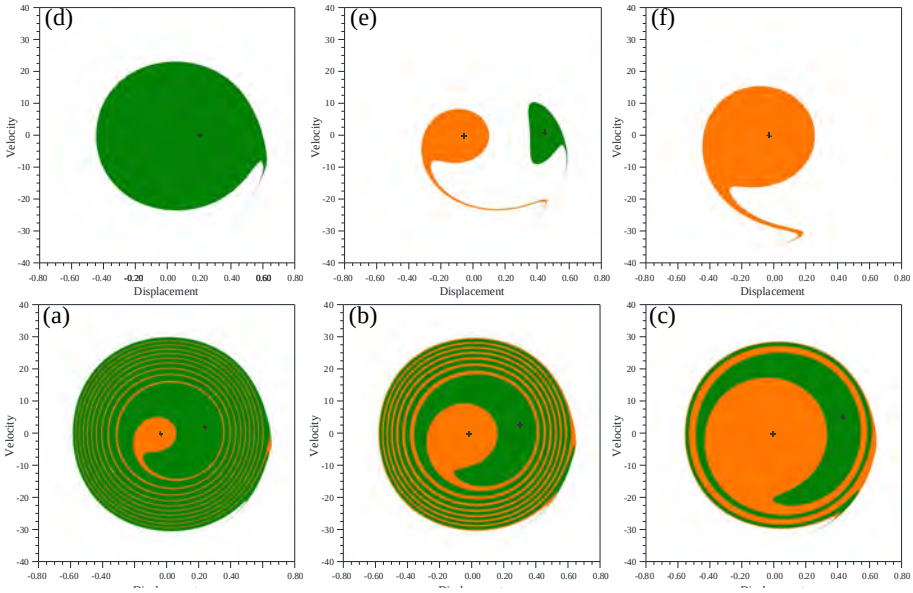

Figure 7. Attractor-basins phase portraits at (from bottom left to top right):
V_{AC} = 4 *V* and (a) Ω = 147 Hz, (b) Ω = 148.5 Hz, (c) Ω = 153 Hz;
V_{AC} = 15 *V* and (d) Ω = 144 Hz, (e) Ω = 150 Hz, (f) Ω = 154 Hz.

We analyze where each attractor may practically (and not theoretically) vanish. As safe basin we consider the own basin of attraction of each attractor, i.e. safe condition are represented by having, at the steady-state dynamics, the motion under consideration, whereas unsafe condition are represented by having other motions (bounded oscillations or escape). As dynamical integrity measure we consider the Local Integrity Measure (LIM), i.e. the radius of the largest circle entirely belonging to the safe basin and centered at the attractor.

We draw the integrity profiles, which describe the loss of dynamical integrity (LIM) when the frequency is varying. We can observe that the experimental disappearance of each attractor occurs exactly when the compact area of its basin of attraction becomes too much reduced. In fact, the smaller integrity enhances the sensitivity of the system to disturbances and makes the attractor vulnerable.

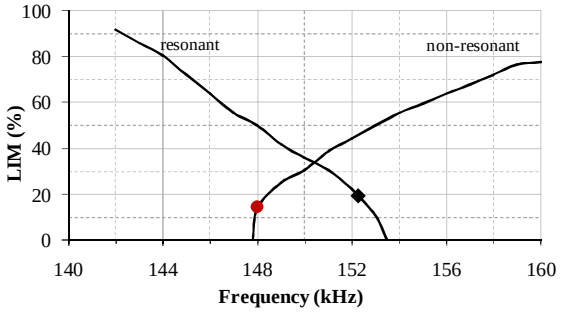

Figure 8. LIM Integrity profile at V_{AC} = 10 *V*.

6. Summary and conclusions

In this study a microbeam-based MEMS device electrically actuated has been experimentally and theoretically investigated. The unknown parameters have been identified and a single mode-reduced order model has been developed via the Petrov-Galerkin technique. Systematic experimental and theoretical investigations have been performed to explore the nonlinear response. The model has been shown to provide valuable information on the MEMS dynamics and catch all the main nonlinear features of the device response. To take into account the presence of disturbances, the loss of dynamical integrity has been examined.

Acknowledgments

This work has been partly developed during Laura Ruzziconi's stay at the King Abdullah University of Science and Technology (KAUST), Saudi Arabia. The kind hospitality is gratefully acknowledged. Laura Ruzziconi would like to thank KAUST for promoting and financially supporting the exchange collaboration.

Mohammad I. Younis acknowledges KAUST funding to support this project.

References

[1] Younis M.I., MEMS Linear and Nonlinear Statics and Dynamics, Springer, New York, 2011.

[2] Alsaleem F. M., Younis M. I., Ruzziconi L., An experimental and theoretical investigation of dynamic pull-in in MEMS resonators actuated electrostatically. *Journal of Microelectromechanical Systems*, 19 (2010), 794-806.

[3] Rhoads J.F., Shaw S.W., Turner K.L., Moehlis J., DeMartini B.E., Generalized parametric resonance in electrostatically actuated microelectromechanical oscillators. *Journal of Sound and Vibration*, 296 (2006), 797–829.

[4] Mestrom, R.M.C., Fey, R.H.B., Phan, K.L. & Nijmeijer, H. Simulations and experiments of hardening and softening resonances in a clamped-clamped beam MEMS resonator. *Sensors and Actuators, A: Physical*, 162 (2010), 225-234.

[5] Younis M.I., Alsaleem F.M., Exploration of new concepts for mass detection in electrostatically-actuated structures based on nonlinear phenomena. *ASME Journal of Computational and Nonlinear Dynamics*, 4 (2009), 021010.

[6] Krylov S., Ilic B.R., Schreiber D., Serentensky S., Craighead H., The pull-in behavior of electrostatically actuated bistable microstructures. *Journal of Micromechanics and Microengineering*, 18 (2008), 055026.

[7] Krylov S., Dick N., Dynamic stability of electrostatically actuated initially curved shallow micro beams, *Continuum Mechanics and Thermodynamics*. 22 (2010), 445–468.

[8] Medina L., Gilat R., Ilic B., Krylov S., Experimental investigation of the snap-through buckling of electrostatically actuated initially curved pre-stressed micro beams. *Sensors and Actuators A: Physical*, 220 (2014), 323-332.

[9] Younis M.I, Ouakad H., Alsaleem F.M., Miles R., Cui W., Nonlinear dynamics of MEMS arches under harmonic electrostatic actuation. *Journal of Microelectromechanical Systems*, 19 (2010), 647-656.

[10] Ouakad H.M., Younis M.I., The dynamic behavior of MEMS arch resonators actuated electrically. *International Journal of Non-Linear Mechanics*, 45 (2010), 704-713.

[11] Ruzziconi L., Younis M. I., Lenci S., An efficient reduced-order model to investigate the behavior of an imperfect microbeam under axial load and electric excitation. *ASME Journal of Computational and Nonlinear Dynamics*, 8 (2012), 011014-1 – 011014-9.

[12] Ruzziconi L., Lenci S., Younis M. I., An imperfect microbeam under an axial load and electric excitation: nonlinear phenomena and dynamical integrity. *International Journal of Bifurcation and Chaos*, 23 (2013), 1350026-1 – 1350026-17.

[13] Ramini A.H., Hennawi Q.M., Younis M.I., Theoretical and experimental investigation of the nonlinear behavior of an electrostatically-actuated in-plane MEMS arch. *Journal of Microelectromechanical Systems*, 25 (2016), 570-578.

[14] Ramini A.H., Bellaredj M.L.F., Al Hafiz M.A., Younis M.I., Experimental investigation of snap-through motion of in-plane MEMS shallow arches under electrostatic excitation. *Journal of Micromechanics and Microengineering*, 26 (2016), 015012.

[15] Hajjaj A.Z., Ramini A.H., Alcheikh N., Younis M.I., Electrothermally tunable arch resonator. *Journal of Microelectromechanical Systems*, 26 (2017), 837 - 845.

[16] Ramini A.H., Hajjaj A.Z., Younis M.I., Tunable resonators for nonlinear modal interactions. *Scientific Report*, 6 (2016), 34717.

[17] Ruzziconi L., Bataineh A. M., Younis M. I., Cui W., Lenci S., Nonlinear dynamics of an electrically actuated imperfect microbeam resonator: experimental investigation and reduced-order modeling. *Journal of Micromechanics and Microengineering*, 23 (2013), 075012-1 – 075012-14.

[18] Ruzziconi L., Younis M. I., Lenci S., Parameter identification of an electrically actuated imperfect microbeam. *International Journal of Nonlinear Mechanics*, 57 (2013), 208–219.

[19] Ruzziconi L., Younis M. I., Lenci S., An electrically actuated imperfect microbeam: dynamical integrity for interpreting and predicting the device response. *Meccanica*, 48 (2013), 1761-1775.

[20] Saghir S., Bellaredj M.L., Ramini A., Younis M.I., Initially curved microplates under electrostatic actuation: theory and experiment. *Journal of Micromechanics and Microengineering* 26 (2016), 095004.

[21] Jaber N., Ramini A., Carreno A.A.A., Younis M.I., Higher order modes excitation of electrostatically actuated clamped–clamped microbeams: experimental and analytical investigation. *Journal of Micromechanics and Microengineering* 26 (2016), 025008.

[22] Villaggio P., *Mathematical Models for Elastic Structures*. Cambridge University Press, Cambridge, 1997.

[23] Reddy J. N., *Energy and Variational Methods in Applied Mechanics, with an Introduction to the Finite Element Method*. Wiley, New York, 1984.

[24] Thompson J.M.T., Stewart H.B., *Nonlinear Dynamics and Chaos*. 2nd edition, Wiley, New York, 2002.

Laura Ruzziconi, Assistant Professor: eCampus University, Faculty of Engineering, 22060 Novedrate, Italy (*laura.ruzziconi@gmail.com*). The author gave a presentation of this paper during one of the conference sessions.

Nizar Jaber, Ph.D.: King Abdullah University of Science and Technology (KAUST), Physical Science and Engineering Division, 23955-6900 Thuwal, Saudi Arabia (*nizar.jaber@kaust.edu.sa*).

Lakshmoji Kosuru, Ph.D.: King Abdullah University of Science and Technology (KAUST), Physical Science and Engineering Division, 23955-6900 Thuwal, Saudi Arabia (*lakshmoji.kosuru@kaust.edu.sa*).

Mohammed L. Bellaredj, Ph.D.: King Abdullah University of Science and Technology (KAUST), Physical Science and Engineering Division, 23955-6900 Thuwal, Saudi Arabia (*bellaredj1_fayal@yahoo.fr*).

Stefano Lenci, Professor: Polytechnic University of Marche, Department of Civil and Building Engineering, and Architecture, via Brecce Bianche, 60131 Ancona, Italy (*lenci@univpm.it*).

Mohammad I. Younis, Associate Professor: King Abdullah University of Science and Technology (KAUST), Physical Science and Engineering Division, 23955-6900 Thuwal, Saudi Arabia (*Mohammad.Younis@kaust.edu.sa*).

Riccati transformation and oscillation of superlinear second order functional differential equations

Abhay Kumar Sethi, Arun Kumar Tripathy

Abstract:

In this work, we establish sufficient conditions for oscillation and asymptotic behavior of solutions of unforced second order nonlinear neutral differential equations with variable delay and variable coefficients for different ranges of neutral coefficient by using Riccati transformation technique. The paper includes the results for various ranges of neutral coefficient depending on two special cases. Also, we have examples to illustrate main results.

1. Introduction

indent Consider a class of nonlinear neutral delay differential equations of the form:

$$(r(t)((x(t)+p(t)x(\tau(t)))')^{\gamma})' + q(t)x^{\gamma}(\sigma(t)) + v(t)x^{\gamma}(\eta(t)) = 0, \tag{1}$$

where $\gamma \geq 1,\ r,\ q,\ v,\ \tau,\ \sigma, \eta \in C(\mathbb{R}_+, \mathbb{R}_+),\ p \in C(\mathbb{R}_+, \mathbb{R}),\ \tau(t) \leq t,\ \sigma(t) \leq t,\ \eta(t) \leq t$ with $\lim_{t\to\infty} \tau(t) = \infty = \lim_{t\to\infty} \sigma(t) = \infty = \lim_{t\to\infty} \eta(t)$. The purpose of this work is to discuss the oscillatory behaviour of solutions of (1) under the assumptions

(H_0) $$\int_0^{\infty} \left(\frac{1}{r(t)}\right)^{\frac{1}{\gamma}} dt = +\infty,$$

and

(H_{00}) $$\int_0^{\infty} \left(\frac{1}{r(t)}\right)^{\frac{1}{\gamma}} dt < +\infty,$$

for various range of $p(t)$ with $|p(t)| < \infty$ and γ is a quotient of odd positive integers.

Consider the following special cases of (1):

$$((x(t)+px(t-\tau))')' + q(t)f(x(t-\sigma)) = 0, \tag{2}$$

$$(r(t)((x(t)+p(t)x(\tau(t)))')^{\gamma})' + q(t)f(x(\sigma(t))) = 0. \tag{3}$$

In [21], the author has discussed the necessary and sufficient conditions for oscillation of all solutions of (2) under the assumptions:
(A_1) $-1 < p \leq 0;\ 0 < \int_c^{\infty} \frac{dy}{f(y)}, \int_{-\infty}^{-c} \frac{dy}{f(y)} < \infty;\ \ 0 < \int_0^c \frac{dy}{f(y)}, \int_{-c}^0 \frac{dy}{f(y)} < \infty,\ \ c > 0.$
However, nothing is known about the oscillatory behaviour of (2) when either $p \in (-\infty, -1] \cup [0, \infty)$ or $p \in C(\mathbb{R}_+, \mathbb{R})$ in [21]. But, the said problem has been discussed in details in the works [19] and [20]. In an another work, Li et al. [12] have studied the oscillatory behaviour of solutions of (3) by means of Riccati transformation using the assumptions:
(A_2) $-1 < p_0 \leq p(t) \leq 0;\ f \in C(\mathbb{R}, \mathbb{R}),\ uf(u) > 0$ *and* $\frac{f(u)}{u^{\gamma}} \geq k$ *for all* $u \neq 0$.
We notice that none of the above works is complete as long as the range of $p(t)$ is concerned.

And the above motivations motivate us to study (1) for various ranges of $p(t)$. Unlike (A_1) and (A_2) an attempt is made here to establish sufficient conditions for oscillation of (1) via Riccati transformation. In this direction we refer the reader to some of the works ([1]-[7],[13]-[18]) and the references cited there in.

As a general reference on Oscillation Theory for neutral differential equations, we refer to Gyori and Ladas [10] and Erbe, Kong and Zhang [9]. The study of oscillatory behaviour of solutions of second order neutral differential equations are of both theoretical and practical interest. In particular, such equations are used in many fields such as vibrating masses attached to an elastic bar, variational problems and to mention a few (see for e.g [11]). As nonneutral differential equations are arising in various problems of physics, biology and economics, and these equations are special cases of neutral differential equations, a special attention has been given to the study of second order neutral differential equations. In spite of the above fact, we find numerous applications of neutral equations in electric networks, where they are frequently used for the study of distributed networks containing lossless transmission lines which arise in high speed computers [11].

By a solution of (1), we mean a continuously differentiable function $x(t)$ which is defined for $t \geq T^* = \min\{\tau(t_0),\ \sigma(t_0),\ \eta(t_0)\}$ such that $x(t)$ satisfies (1) for all $t \geq t_0$. In the sequel, it will always be assumed that the solutions of (1) exist on some half line $[t_1, \infty)$, $t_1 \geq t_0$. A solution of (1) is said to be oscillatory, if it has arbitrarily large zeros; otherwise, it is called non-oscillatory. Equation (1) is called oscillatory, if all its solutions are oscillatory.

2. Oscillation Criteria with (H_0)

This section deals with the sufficient conditions for oscillation of all solutions of (1) under the hypothesis (H_0). Throughout our discussion, we use the notation

$$z(t) = x(t) + p(t)x(\tau(t)). \tag{4}$$

LEMMA 2.1 *[8] Assume that (H_0) holds and $r(t) \in C'[(T_0, \infty), \mathbb{R}]$ such that $r'(t) > 0$. Let $x(t)$ be an eventually positive solution of (1) such that $(r(t)(x'(t))^\gamma)' \leq 0$, for $t \geq t_0$. Then $x'(t) > 0$ and $x''(t) < 0$ for $t \geq t_1 > t_0$, where $\gamma \geq 1$ is a quotient of odd positive integers .*

LEMMA 2.2 *[3] Assume that $A \geq 0, B \geq 0$ and $\lambda \geq 1$. Then*

$$(A + B)^\lambda \leq 2^{\lambda-1}(A^\lambda + B^\lambda). \tag{5}$$

THEOREM 2.3 *Let $0 \leq p(t) \leq a < \infty$. For any large t, suppose that*

(H_1) $\qquad \tau(\sigma(t)) = \sigma(\tau(t)), \tau(\eta(t)) = \eta(\tau(t)), \eta(t) \geq \sigma(t), \sigma(t) \leq \tau(t).$

Assume that (H_0) holds and $r'(t) > 0$, $\sigma'(t) \geq C > 0$ for large t. Furthermore, assume that there exists a positive differentiable function $\rho(t)$ such that

(H_2) $\int_T^\infty \left[\rho(s)\{Q(s) + V(s)\} - \frac{(1+a^\gamma)((\rho'(s))_+)^2(r(\sigma(s)))^\gamma}{2^{(4-2\gamma)}C\gamma\rho(s)(\sigma(s))^{\gamma-1}}\right] ds = \infty,\ T > 0,$

where $Q(t) = min\{q(t), q(\tau(t))\}, V(t) = min\{v(t), v(\tau(t))\}$ and $(\rho'(t))_+ = \max\{\rho'(t), 0\}$. Then every solution of (1) oscillates.

Proof Suppose on the contrary that $x(t)$ is a nonoscillatory solution of (1). Without loss of generality, we may assume that $x(t) > 0$ for $t \geq t_0$. Hence, there exists $t_1 > t_0$ such that $x(t) > 0,\ x(\tau(t)) > 0,\ x(\sigma(t)) > 0$ and $x(\eta(t)) > 0$ for $t \geq t_1$. Using (4), (1) becomes

$$(r(t)(z'(t))^{\gamma})' = -q(t)x^{\gamma}(\sigma(t)) - v(t)x^{\gamma}(\eta(t)) \leq 0,\ \not\equiv 0\ for\ t \geq t_1. \tag{6}$$

So $r(t)(z'(t))^{\gamma}$ is nonincreasing on $[t_1, \infty)$, that is, either $z'(t) > 0$ or $z'(t) < 0$. By Lemma 2.1, it follows that $z'(t) > 0$ for $t \geq t_2$. From (1), it is easy to see that

$$\begin{aligned}(r(t)(z'(t))^{\gamma})' + a^{\gamma}(r(\tau(t))(z'(\tau(t))^{\gamma})' + q(t)x^{\gamma}(\sigma(t)) + a^{\gamma}q(\tau(t))x^{\gamma}(\sigma(\tau(t)) + \\ v(t)x^{\gamma}(\eta(t)) + a^{\gamma}v(\tau(t))x^{\gamma}(\eta(\tau(t)) = 0,\ for\ t \geq t_1.\end{aligned} \tag{7}$$

By using Lemma 2.2, (7) yields that

$$(r(t)(z'(t))^{\gamma})' + a^{\gamma}(r(\tau(t))(z'(\tau(t))^{\gamma})' + 2^{1-\gamma}Q(t)z^{\gamma}(\sigma(t)) + 2^{1-\gamma}V(t)z^{\gamma}(\eta(t)) \leq 0, \tag{8}$$

that is,

$$\frac{(r(t)(z'(t))^{\gamma})'}{z^{\gamma}(\sigma(t))} + \frac{a^{\gamma}(r(\tau(t))(z'(\tau(t)))^{\gamma})'}{z^{\gamma}(\sigma(t))} + 2^{1-\gamma}[Q(t) + V(t)] \leq 0.(\because \eta(t) \geq \sigma(t)) \tag{9}$$

Let $\rho(t)$ be the positive differentiable function and consider the general Riccati substitution

$$w(t) = \rho(t)r(t)\left(\frac{z'(t)}{z(\sigma(t))}\right)^{\gamma} \tag{10}$$

$$u(t) = \rho(t)r(\tau(t))\left(\frac{z'(\tau(t))}{z(\sigma(t))}\right)^{\gamma}. \tag{11}$$

Due to Lemma 2.1, $w(t) > 0$ and $u(t) > 0$ on $[t_1, \infty)$. Indeed,

$$w'(t) = \rho'(t)\left(r(t)\left(\frac{z'(t)}{z(\sigma(t))}\right)^{\gamma}\right) + \rho(t)\left(r(t)\left(\frac{z'(t)}{z(\sigma(t))}\right)^{\gamma}\right)' \tag{12}$$

and

$$u'(t) = \rho'(t)\left(r(\tau(t))\left(\frac{z'(\tau(t))}{z(\sigma(t))}\right)^{\gamma}\right) \qquad + \rho(t)\left(r(\tau(t))\left(\frac{z'(\tau(t))}{z(\sigma(t))}\right)^{\gamma}\right)'. \tag{13}$$

Using (10) and (11)in (12) and (13), we get

$$\begin{aligned}w'(t) + a^{\gamma}u'(t) = \rho'(t)\left[\frac{w(t)}{\rho(t)} + a^{\gamma}\frac{u(t)}{\rho(t)}\right] \\ + \rho(t)\left[\left(r(t)\left(\frac{z'(t)}{z(\sigma(t))}\right)^{\gamma}\right)' + a^{\gamma}\left(r(\tau(t))\left(\frac{z'(\tau(t))}{z(\sigma(t))}\right)^{\gamma}\right)'\right],\end{aligned}$$

that is,

$$\begin{aligned}w'(t) + a^{\gamma}u'(t) = \frac{\rho'(t)}{\rho(t)}\left[w(t) + a^{\gamma}u(t)\right] \\ + \rho(t)\left[\left(r(t)\left(\frac{z'(t)}{z(\sigma(t))}\right)^{\gamma}\right)' + a^{\gamma}\left(r(\tau(t))\left(\frac{z'(\tau(t))}{z(\sigma(t))}\right)^{\gamma}\right)'\right].\end{aligned} \tag{14}$$

Using the fact that

$$\left(r(t)\left(\frac{z'(t)}{z(\sigma(t))}\right)^{\gamma}\right)' = \frac{(r(t)(z'(t))^{\gamma})'}{z^{\gamma}(\sigma(t))} - \frac{r(t)(z'(t))^{\gamma}(z^{\gamma}(\sigma(t)))'}{(z^{\gamma}(\sigma(t)))^2}$$

and

$$\left(r(\tau(t))\left(\frac{z'(\tau(t))}{z(\sigma(t))}\right)^{\gamma}\right)' = \frac{(r(\tau(t))(z'(\tau(t))^{\gamma})'}{z^{\gamma}(\sigma(t))} - \frac{r(\tau(t))(z'(\tau(t))^{\gamma}(z^{\gamma}(\sigma(t))'}{(z^{\gamma}(\sigma(t)))^2},$$

where we have used the fact that $\tau(t) \leq t, z(t)$ nondecreasing on $[t_2, \infty)$ in (14) and then applying (9), we obtain

$$\begin{aligned} w'(t) + a^{\gamma}u'(t) \leq{}& \frac{\rho'(t)}{\rho(t)}[w(t) + a^{\gamma}u(t)] - \rho(t)2^{1-\gamma}\{Q(t) + V(t)\} \\ & - \rho(t)\left[\frac{r(t)(z'(t))^{\gamma}(z^{\gamma}(\sigma(t)))'}{(z^{\gamma}(\sigma(t)))^2} + a^{\gamma}\frac{r(\tau(t))(z'(\tau(t))^{\gamma}(z^{\gamma}(\sigma(t))'}{(z^{\gamma}(\sigma(t))^2}\right]. \end{aligned} \tag{15}$$

Due to Lemma 2.1, we can find a $t_3 \geq 2t_2$ such that

$$z(t) \quad = \quad z(t_2) + \int_{t_2}^{t} z'(s)ds \geq \int_{t_2}^{t} z'(s)ds \geq (t - t_2)z'(t) \geq \frac{t}{2}z'(t)$$

and hence

$$(z^{\gamma}(\sigma(t)))' \geq C\gamma z'(\sigma(t))(z(\sigma(t)))^{\gamma-1} \geq C\gamma\left(\frac{\sigma(t)}{2}\right)^{\gamma-1}(z'(\sigma(t)))^{\gamma} \tag{16}$$

for $t \geq t_3$. Due to (6), $(z'(\sigma(t)))^{\gamma} \geq \frac{(r(t)(z'(t))^{\gamma})}{(r(\sigma(t))^{\gamma}}$ and $\sigma(t) \leq \tau(t)$ implies that

$$(z'(\sigma(t)))^{\gamma} \geq \frac{(r(\tau(t))(z'(\tau(t)))^{\gamma})}{(r(\sigma(t))^{\gamma}}.$$

Therefore, (16) becomes

$$(z^{\gamma}(\sigma(t)))' \geq C\gamma\left(\frac{\sigma(t)}{2}\right)^{\gamma-1}\frac{(r(\tau(t))(z'(\tau(t)))^{\gamma})}{(r(\sigma(t))^{\gamma}}$$

for $t \geq t_3$. Consequently, (15) reduces to

$$\begin{aligned} & w'(t) + a^{\gamma}u'(t) \leq -\rho(t)2^{1-\gamma}\{Q(t) + V(t)\} \\ & + \frac{(\rho'(t))_+}{\rho(t)}w(t) - \frac{C\gamma\left(\frac{\sigma(t)}{2}\right)^{\gamma-1}w^2(t)}{\rho(t)(r(\sigma(t))^{\gamma}} + a^{\gamma}\frac{(\rho'(t))_+}{\rho(t)}u(t) - \frac{C\gamma a^{\gamma}\left(\frac{\sigma(t)}{2}\right)^{\gamma-1}u^2(t)}{\rho(t)(r(\sigma(t))^{\gamma}} \\ & = -\rho(t)2^{1-\gamma}\{Q(t) + V(t)\} + \frac{(\rho'(t))_+}{\rho(t)}\left[w(t) - \frac{C\gamma\left(\frac{\sigma(t)}{2}\right)^{\gamma-1}w^2(t)}{(\rho'(t))_+(r(\sigma(t))^{\gamma}}\right] \\ & \qquad + a^{\gamma}\frac{(\rho'(t))_+}{\rho(t)}\left[u(t) - \frac{C\gamma\left(\frac{\sigma(t)}{2}\right)^{\gamma-1}u^2(t)}{(\rho'(t))_+(r(\sigma(t))^{\gamma}}\right]. \end{aligned} \tag{17}$$

Upon using the relation $x - mx^2 \leq \frac{1}{4m}$, (17) yields

$$w'(t) + a^\gamma u'(t) \leq -2^{1-\gamma}\rho(t)\{Q(t) + V(t)\} + \frac{((\rho'(t))_+)^2(r(\sigma(t))^\gamma}{4C\gamma\rho(t)\left(\frac{\sigma(t)}{2}\right)^{\gamma-1}} + \frac{((\rho'(t))_+)^2 a^\gamma (r(\sigma(t))^\gamma}{4C\gamma\rho(t)\left(\frac{\sigma(t)}{2}\right)^{\gamma-1}}$$

$$\leq -2^{1-\gamma}\rho(t)\{Q(t) + V(t)\} + (1 + a^\gamma)\frac{((\rho'(t))_+)^2(r(\sigma(t))^\gamma}{4C\gamma\rho(t)\left(\frac{\sigma(t)}{2}\right)^{\gamma-1}}.$$

Integrating the preceding inequality from t_3 to t, we get

$$-w(t_3) - a^\gamma u(t_3) < w(t) + a^\gamma u(t) - w(t_3) - a^\gamma u(t_3)$$

$$\leq -\int_{t_3}^{t}\left[2^{1-\gamma}\rho(s)\{Q(s) + V(s)\} - \frac{(1 + a^\gamma)((\rho'(s))_+)^2(r(\sigma(s))^\gamma}{4C\gamma\rho(s)\left(\frac{\sigma(s)}{2}\right)^{\gamma-1}}\right]ds,$$

that is,

$$\int_{t_3}^{t}\left[\rho(s)\{Q(s) + V(s)\} - \frac{(1 + a^\gamma)((\rho'(s))_+)^2(r(\sigma(s))^\gamma}{2^{4-2\gamma}\gamma C\rho(s)(\sigma(s))^{\gamma-1}}\right]ds < \infty,$$

a contradiction to (H_2).

THEOREM 2.4 *Let $0 \leq p(t) \leq a < 1$, $t \in [t_0, \infty)$. Assume that (H_0) holds, and $r'(t) > 0, \eta(t) \geq \sigma(t), \sigma'(t) \geq C$ for any large t. Furthermore, assume that there exists a positive differentiable function $\rho(t)$ such that*

(H_3) $\int_T^\infty \left[\rho(s)\{q(s) + v(s)\} - \frac{((\rho'(s))_+)^2(r(\sigma(s))^\gamma}{(1-a)4C\gamma\rho(s)\left(\frac{\sigma(s)}{2}\right)^{\gamma-1}}\right]ds = \infty,\ T > 0.$

Then every solution of (1) oscillates.

Proof Proceeding as in proof of Theorem 2.3, we get (6) and by Lemma 2.1, $z(t)$ is nondecreasing on $t \in [t_2, \infty)$. Hence, there exists $t_3 > t_2$ such that

$$\begin{aligned} z(t) - p(t)z(\tau(t)) &= x(t) + p(t)x(\tau(t)) - p(t)x(\tau(t)) \\ &- p(t)p(\tau(t))p(\tau(\tau(t))) \\ &= x(t) - p(t)p(\tau(t))p(\tau(\tau(t))) \\ &\leq x(t) \end{aligned}$$

implies that $x(t) \geq (1 - a)z(t)$ on $t \in [t_3, \infty)$. Consequently, (1) reduces to

$$(r(t)(z'(t))^\gamma)' + (1 - a)q(t)z^\gamma(\sigma(t)) + (1 - a)v(t)z^\gamma(\eta(t)) \leq 0$$

for $t \in [t_3, \infty)$. The rest of the proof follows from the proof of Theorem 2.3 except (11) and hence the details are omitted. Thus, the proof of the theorem is complete.

THEOREM 2.5 *Let $-1 < a \leq p(t) \leq 0,\ t \in [t_0, \infty)$. Assume that (H_0), $r'(t) > 0, \eta(t) \geq \sigma(t)$ and $\sigma'(t) \geq C$ hold. Furthermore, assume that there exists a positive differentiable function $\rho(t)$ such that*

(H_4) $\int_T^\infty \left[\rho(s)\{q(s)+v(s)\} - \frac{((\rho'(s))_+)^2 (r(\sigma(s)))^\gamma}{\rho(s) 4C\gamma \left(\frac{\sigma(s)}{2}\right)^{\gamma-1}}\right] ds = \infty,\ T > 0.$

If

(H_5) $\int_{T_1}^\infty \left[\frac{1}{r(\theta)} \int_{t_0}^\theta [q(s)+v(s)]ds\right]^{\frac{1}{\gamma}} d\theta = \infty,\ T_1 > 0$

holds, then every solution of (1) either oscillates or converges to zero as $t \to \infty$.

Proof Proceeding as in the proof of Theorem 2.3 we get (6) for $t \in [t_2, \infty)$. Thus $z(t)$ and $z'(t)$ are monotonic functions on $[t_2, \infty)$. Hence, we have following four possible cases:

$$(i)\ z(t) > 0,\ z'(t) > 0,\ (ii)\ z(t) < 0,\ z'(t) > 0,$$
$$(iii)\ z(t) > 0,\ z'(t) < 0,\ (iv)\ z(t) < 0,\ z'(t) < 0.$$

Case(i) In this case, $z(t) \leq x(t)$ and (1) reduces to

$$(r(t)(z'(t))^\gamma)' + q(t)z^\gamma(\sigma(t)) + v(t)z^\gamma(\eta(t)) \leq 0 \tag{18}$$

for $t \geq t_3 > t_2$. The proof of this case is an immediate consequence of the proof of Theorem 2.3 except (11).

Case(ii) For this case, we claim that $x(t)$ is bounded. Otherwise, there exists a sequence $\{\alpha_n\}$ such that $\alpha_n \to \infty$ as $n \to \infty$ and $x(\alpha_n) = max\{x(t) : t_3 \leq t \leq \alpha_n\}$. Therefore,

$$\begin{aligned} z(\alpha_n) &= x(\alpha_n) + p(\alpha_n)x(\tau(\alpha_n)) \\ &\geq x(\alpha_n) + ax(\tau(\alpha_n)) \geq x(\alpha_n) + ax(\alpha_n) \\ &= (1+a)x(\alpha_n) \to +\infty \ \ as\ n \to \infty\ (\because 1+a > 0) \end{aligned}$$

gives a contradiction to the fact that $\lim_{t\to\infty} z(t)$ exists. Ultimately,

$$\begin{aligned} 0 \geq \lim_{t\to\infty} z(t) &= \limsup_{t\to\infty} z(t) \\ &\geq \limsup_{t\to\infty} (x(t) + ax(\tau(t))) \\ &\geq \limsup_{t\to\infty} x(t) + \liminf_{t\to\infty} (ax(\tau(t))) \\ &= \limsup_{t\to\infty} x(t) + a \limsup_{t\to\infty} x(\tau(t)) \\ &= (1+a) \limsup_{t\to\infty} x(t) \end{aligned}$$

implies that $\limsup_{t\to\infty} x(t) = 0$, that is, $\lim_{t\to\infty} x(t) = 0$.

Case(iii) Let $\lim_{t\to\infty} z(t) = \beta, \beta \in [0, \infty)$. We assert that $\beta = 0$. If not, there exist $t_3 > t_2$ and $l > 0$ such that $z(\sigma(t)) \geq z(t) > l$ and $z(\eta(t)) \geq z(t) > l$ for $t \geq t_3$. Since $z(t) \leq x(t)$, then (18) yields that

$$(r(t)(z'(t))^\gamma)' \leq -l^\gamma\,[q(t)+v(t)]$$

for $t \geq t_3$. Integrating the above inequality from t_3 to t, we get

$$z'(t) < -l\left[\frac{1}{r(t)}\int_{t_3}^{t}[q(s)+v(s)]ds\right]^{\frac{1}{\gamma}},$$

that is,

$$z(t) < z(t_3) - l\int_{t_3}^{t}\left[\frac{1}{r(\theta)}\int_{t_3}^{\theta}[q(s)+v(s)]ds\right]^{\frac{1}{\gamma}}d\theta < 0$$

for large t due to (H_5). Hence $l = 0$. Using the same type of reasoning as in $Case(ii)$, we can show that $x(t)$ is bounded and $\lim_{t\to\infty} x(t) = 0$.

Case(iv) If we assume that $x(t)$ is unbounded, then by $Case(ii)$ we have $z(t) > 0$ for large t which is absurd. So, $x(t)$ is bounded. Consequently, $z(t)$ is bounded and $\lim_{t\to\infty} z(t)$ exists. Because $z(t) < 0$ and nonincreasing, we can find $\beta > 0$ and a $t_3 > t_2$ such that $z(t) < \beta$ for $t \geq t_3$. Proceeding as in $Case(iii)$, it is easy to see that $\lim_{t\to\infty} z(t) = -\infty$ due to (H_5). This contradiction argues against $Case(iv)$. This completes the proof of the theorem.

REMARK 2.6 *In Theorem 2.5, it is learnt that $x(t)$ is bounded when $z(t) < 0$. Also, $x(t)$ is bounded when $z(t) > 0$ in $Case(iii)$. Hence for unbounded $x(t)$, $Cases(ii), (iii)$ and (iv) are not existing ultimately. Therefore, we have proved the following result:*

THEOREM 2.7 *Let $-1 < a \leq p(t) \leq 0$ for $t \in [t_0, \infty)$. Assume that (H_0) and (H_4) hold. Furthermore, assume that $r'(t) > 0, \eta(t) \geq \sigma(t)$ and $\sigma'(t) \geq C$ hold. Then every unbounded solution of (1) oscillates.*

THEOREM 2.8 *Let $-\infty < a \leq p(t) \leq d < -1$, $\tau(\sigma(t)) = \sigma(\tau(t))$ and $\tau(\eta(t)) = \eta(\tau(t))$ be hold for all $t \in [t_0, \infty)$. Assume that all conditions of Theorem 2.5 hold. If*
(H_6) $\int_{t_0}^{\infty}[q(\tau(s)) + v(\tau(s))]\,ds = \infty$,
then every bounded solution of (1) either oscillates or converges to zero as $t \to \infty$.

Proof Let $x(t)$ be a bounded nonoscillatory solution of (1). Proceeding as in the proof of Theorem 2.5, we have four possible cases for $t \in [t_2, \infty)$. Among these cases, $Cases(i), (iii)$ and (iv) are similar. For $Case(ii)$, we claim that $\beta = 0$. Otherwise, there exist $l < 0$ and $t_3 > t_2$ such that $z(\sigma(t)) \leq z(t) < l$, $z(\eta(t)) \leq z(t) < l$ for $t \geq t_3$. From (4), it follows that $z(t) > ax(\tau(t))$ and hence $x(\tau(\sigma(t)) > \frac{1}{a}z(\sigma(t))$, that is, $x(\sigma(\tau(t)) > \left(\frac{l}{a}\right)$ for $t \geq t_3$. Also, $x(\eta(\tau(t)) > \left(\frac{l}{a}\right)$ for $t \geq t_3$. Since (1) can be written as

$$(r(\tau(t))(z'(\tau(t))^{\gamma})' + q(\tau(t))x^{\gamma}(\sigma(\tau(t)) + v(\tau(t))x^{\gamma}(\eta(\tau(t)) = 0,$$

then for $t \geq t_3$, it follows that

$$(r(\tau(t))(z'(\tau(t))^{\gamma})' + \left(\frac{l}{a}\right)^{\gamma}q(\tau(t)) + \left(\frac{l}{a}\right)^{\gamma}v(\tau(t)) \leq 0.$$

Consequently,

$$\left(\frac{l}{a}\right)^{\gamma}\left[\int_{t_3}^{t} q(\tau(s)) + \int_{t_3}^{t} v(\tau(s))\right] ds \leq -\left[(r(\tau(t))(z'(\tau(t))^{\gamma})'\right]_{t_3}^{t}$$
$$< -r(\tau(t))(z'(\tau(t)))^{\gamma} < \infty \; as \; t \to \infty$$

contradicts (H_6). So, our claim holds and

$$\begin{aligned} 0 = \lim_{t\to\infty} z(t) &= \liminf_{t\to\infty} z(t) \\ &\leq \liminf_{t\to\infty}(x(t) + dx(\tau(t))) \\ &\leq \limsup_{t\to\infty} x(t) + \liminf_{t\to\infty}(dx(\tau(t))) \\ &= \limsup_{t\to\infty} x(t) + d\limsup_{t\to\infty} x(\tau(t)) \\ &= (1+d)\limsup_{t\to\infty} x(t) \; (\because (1+d) < 0) \end{aligned}$$

implies that $\limsup_{t\to\infty} x(t) = 0$, that is, $\lim_{t\to\infty} x(t) = 0$. Hence the proof of the theorem is complete.

3. Oscillation Criteria with (H_{00})

In this section, we establish sufficient conditions for oscillation of all solutions of (1) under the hypothesis (H_{00}).

LEMMA 3.1 *[18] Assume that (H_{00}) holds. Let $u(t)$ be an eventually positive continuous function on $[t_0, \infty)$, $t_0 \geq 0$ such that $r(t)u'(t)$ is continuous and differentiable function with $(r(t)u'(t))^{\gamma})' \leq 0, \not\equiv 0$ for large $t \in [t_0, \infty)$, where $r(t)$ is continuous function defined on $[t_0, \infty)$. Then the following statements hold:*
$(i) If\ u'(t) > 0$, then there exists a constant $C > 0$ such that $u(t) > CR(t)$ for large t,
$(ii) If u'(t) < 0$, then $u(t) \geq -(r(t)(u'(t))^{\gamma})^{\frac{1}{\gamma}} R(t)$, where $R(t) = \int_t^{\infty}\left(\frac{1}{r(s)}\right)^{\frac{1}{\gamma}} ds$.

THEOREM 3.2 *Let $0 \leq p(t) \leq a < \infty$ and (H_{00}) hold. Assume that all conditions of Theorem 2.3 hold. If*
(H_7) $\int_T^{\infty} [R^{\gamma}(\sigma(t))Q(t) + R^{\gamma}(\eta(t))V(t)]\, dt = \infty, T > 0$,
then every solution of (1) oscillates.

Proof Proceeding as in the proof of Theorem 2.3, we obtain (6) and (8) for $t \geq t_2$. In what follows, we consider two possible cases $z'(t) > 0$ or $z'(t) < 0$ for $t \geq t_3 > t_2$. The case $z'(t) > 0$ for $t \geq t_3$ follows from Theorem 2.3. Consider $z'(t) < 0$ for $t \geq t_3$. Then there exist $C_1 < 0$ and a $t_4 > t_3$ such that $(r(t)(z'(t))^{\gamma}) \leq (-C_1)^{\gamma}$ for $t \geq t_4$ due to Lemma 3.1(ii). As a result, $z(t) \geq C_1 R(t)$ for $t \geq t_4$. Therefore, (8) implies that

$$\frac{Q(t)}{2^{\gamma-1}} C_1^{\gamma} R^{\gamma}(\sigma(t)) + \frac{V(t)}{2^{\gamma-1}} C_1^{\gamma} R^{\gamma}(\eta(t)) \leq -(r(t)(z'(t))^{\gamma})' - (a^{\gamma} r(\tau(t))(z'(\tau(t)))^{\gamma})' \qquad (19)$$

for $t \geq t_4$. Integrating (19) from t_4 to t, we get

$$\int_{t_4}^{t} \frac{Q(s)}{2^{\gamma-1}} C_1^{\gamma} R^{\gamma}(\sigma(s))ds + \int_{t_4}^{t} \frac{V(s)}{2^{\gamma-1}} C_1^{\gamma} R^{\gamma}(\eta(s))ds < \infty,$$

a contradiction to (H_7). Hence, the theorem is proved.

THEOREM 3.3 *Let $-1 < a \leq p(t) \leq 0$, $t \in [t_0, \infty)$ and (H_{00}) hold. Assume that all conditions of Theorem 2.5 hold. If*
(H_8) $\int_T^{\infty} [R^{\gamma}(\sigma(t))q(t) + R^{\gamma}(\eta(t))v(t)]\, dt = \infty, T > 0$,
then every solution of (1) either oscillates or converges to zero as $t \to \infty$.

Proof The proof of the theorem can be followed from the proofs of Theorem 2.5 and Theorem 3.2. Hence, the details are omitted. This completes the proof of the theorem.

THEOREM 3.4 *Let $-\infty < a \leq p(t) \leq d < -1$, $\tau(\sigma(t)) = \sigma(\tau(t))$ and $\tau(\eta(t)) = \eta(\tau(t))$ be hold for all $t \in [t_0, \infty)$. Assume that all conditions of Theorem 3.3 hold. If (H_6) hold, then every bounded solution of (1) either oscillates or converges to zero as $t \to \infty$*

Proof The proof of the theorem follows from the proofs of Theorem 3.3 and Theorem 2.8 and hence the details are omitted. Thus the theorem is proved.

THEOREM 3.5 *Let $-1 < a \leq p(t) \leq 0$ for $t \in [t_0, \infty)$. Assume that (H_{00}) and (H_4) hold. Furthermore, assume that $r'(t) > 0, \eta(t) \geq \sigma(t)$ and $\sigma'(t) \geq C$ hold. Then every unbounded solution of (1) oscillates.*

Proof The proof of the theorem follows from Remark 2.6. Hence, the details are omitted.

4. Discussion and Examples

EXAMPLE 4.1 *Consider*

$$((t^{\gamma}((x(t) + x(t - 3\pi)))')^{\gamma})' + e^t x^{\gamma}(t - 2\pi) + e^t x^{\gamma}(t - \pi) = 0 \tag{20}$$

on $[3\pi, \infty)$, where $r(t) = t^{\gamma}$, $p(t) = 1$ and $\gamma \geq 1$. If we choose $\rho(t) = 1$, then it is easy to verify all conditions of Theorem 2.3. Hence, (20) is oscillatory. In particular, $x(t) = sint$ is such a solution of (20).

In this work, our objective was to establish the sufficient conditions for oscillation of all solutions of (1). But, our method fails to provide the conclusion in the range $-\infty < a \leq p(t) \leq d < -1$. However, we could manage in Theorems 2.8 and 3.4 with bounded solutions.

EXAMPLE 4.2 *Consider*

$$(e^{\gamma t}((x(t)+x(t-4\pi)))')^{\gamma})' + e^{\gamma t}x^{\gamma}(t-2\pi) + e^{\gamma t}x^{\gamma}(t-\pi) = 0 \tag{21}$$

on $[4\pi,\infty)$*, where* $r(t)=e^{\gamma t}$*,* $p(t)=-1$ *and* $\gamma \geq 1$*. Choose* $\rho(t)=1$*. Clearly,* $(H_4),(H_6)$ *and* (H_8) *are hold true. From* (H_5)*, we have*

$$\begin{aligned}\int_{4\pi}^{\infty}\left[\frac{1}{r(t)}\int_{t_0}^{t}[q(s)+v(s)]ds\right]^{\frac{1}{\gamma}}dt &= \int_{4\pi}^{\infty}\left[\frac{1}{e^{\gamma t}}\int_{t_0}^{t}[2e^{\gamma s}]ds\right]^{\frac{1}{\gamma}}dt \\ &= \left(\frac{2}{\gamma}\right)^{\frac{1}{\gamma}}\int_{4\pi}^{\infty}\left[1-\frac{e^{\gamma t_0}}{e^{\gamma t}}\right]^{\frac{1}{\gamma}}dt.\end{aligned}$$

Since $0 \leq \left[1-\frac{e^{\gamma t_0}}{e^{\gamma t}}\right] \leq 1$ *for any large* t*, then we can find a* $t^* \in [4\pi,\infty)$ *such that* $\left[1-\frac{e^{\gamma t_0}}{e^{\gamma t}}\right] \geq \frac{1}{2}$ *for* $t \geq t^*$*. Consequently,*

$$\begin{aligned}\int_{4\pi}^{\infty}\left[\frac{1}{r(t)}\int_{t_0}^{t}[q(s)+v(s)]ds\right]^{\frac{1}{\gamma}}dt &= \left(\frac{2}{\gamma}\right)^{\frac{1}{\gamma}}\int_{4\pi}^{\infty}\left[1-\frac{e^{\gamma t_0}}{e^{\gamma t}}\right]^{\frac{1}{\gamma}}dt \\ &\geq \left(\frac{2}{\gamma}\right)^{\frac{1}{\gamma}}\int_{t^*}^{\infty}\left[\frac{1}{2}\right]^{\frac{1}{\gamma}}dt = \infty.\end{aligned}$$

All conditions of Theorem 3.4 are satisfied for (21), but we can not apply the theorem due to $p(t)\equiv -1$*. We note that,* $x(t)=sint$ *is an oscillatory solution of (21).*

In the literature, we don't find the discussion concerning the oscillation of neutral equations when $-\infty < p(t) \leq -1$. So, it is interesting to study the oscillation property of neutral equations in this range, and at the same time it would be interesting to see *an all solution oscillatory problem* (may be unlike our method).

Acknowledgments

This work was supported by Rajiv Gandhi National Fellowship(UGC), New Delhi, India, through the letter No. F1-17.1/2013-14/RGNF-2013-14-SC-ORI-42425, dated Feb 6,2014

References

[1] AGARWAL, R. P., BOHNER, M., LI, T., AND ZHANG, C., *Oscillation of second order differential equations with a sublinear neutral term,* Chrpathian. J. Math., 30(2014), 1–6.

[2] ARUL, R., AND SHOBHA, V. S., *Oscillation of second order neutral differential equations with mixed neutral term,* Int. J. Pure and Appl. Math., 104(2015), 181–191.

[3] BACULIKOVA, B., AND DZURINA, J., *Oscillation theorems for second order nonlinear neutral differential equations,* Compu. Math. Appl., 61(2011), 4472–4478.

[4] BACULIKOVA, B., LI, T., AND DZURINA, J., *Oscillation theorems for second order neutral differential equations,* Ele. J. Quali. Theo. Diff. Equs., 74(2011), 1–13.

[5] ZHANG, C., BACULIKOVA, B., DZURINA, J., AND LI, T., *Oscillation results for second order mixed neutral differential equations with distributed devating arguments,* Math. Slovaka, 66(2016)3, 1–12.

[6] DZURINA, J., *Oscillation theorems for second order differential equations with mixed arguments,* J. Math. Anal. Appl., 190(1995), 821-828.

[7] DZURINA, J., *Oscillation of second order advanced neutral differential equations,* Tatra Mt. Math. Pub., 48(2011), 61-71.

[8] DENG, X. H., WANG, Q., AND ZHAN, Z., *Oscillation criteria for second order neutral dynamic equations of Emden-Fowler type with positive and negative coefficients on time scales,* Sci. Chaina Math., 5(2016), 1-24.

[9] ERBE, L. H., KONG, Q., AND ZHANG, B. G., *Oscillation Theory For Functional Differential Equations,* Marcel Dekker, Inc., New York, 1995.

[10] GYORI, I., AND LADAS, G., *Oscillation Theory of Delay Differential Equations: An Introduction with Applications,* Clarendon Press, Oxford, 1991.

[11] HALE, J. K., *Theory of Functional Differential Equations,* Springer-Verlag, New York, 1977.

[12] LI, T., BACULIKOVA, B., AND DZURINA, J., *Oscillation results for second order neutral differential eqquations of mixed type,* Tatra Mt. Math. Pub., 48(2011), 101–116.

[13] YANG, Q., YANG, L., AND ZHU, S., *Interval criteria oscillation of second order nonlinear neutral differential eqquations,* Compu. Math. Appl., 46(2003), 903–918.

[14] HUIZENG, Q., NINA, S., AND YOUMIN, L., *A note on oscillation criteria of second order nonlinear neutral delay differential eqquations,* Compu. Math. App., 56(2008), 2987-2992.

[15] LI, Q., WANG, R., FENG, C., AND LI, T., *Oscillation of second nonlinear neutral delay differential eqquations with nonpositive neutral coefficients,* Advance in Difference Equations, (2015), 2–7.

[16] TAMILVANAN, S., THANDAPANI, E., AND DZURINA, J., *Oscillation of second order nonlinear differential equations with sublinear neutral term,* Diff. Equ. Appl., 9(2017), 29–35.

[17] TRIPATHY, A. K., *Some oscillation results of second order nonlinear dynamic equations of neutral type,* Nonlinear Analysis, 71(2009), e1727–e1735.

[18] TRIPATHY, A. K., AND TENALI, G. B., *Oscillation results for second order neutral delay dynamic equations,* Fun. Diff. Equs., 17(2010), 329-344.

[19] TRIPATHY, A. K., AND SETHI, A. K., *Oscillation of sublinear and superlinear second order neutral differential equations,* Int. J. Pure and Appl. Math., 113(2017), 73–71.

[20] TRIPATHY, A. K., AND SETHI, A. K., *Sufficient condition for oscillation and nonoscillation of a class of second order neutral differential equations* (Communicated).

[21] WONG, J S W., *Necessary and sufficient conditions for oscillation of second order neutral differential equations,*Int. J. Math. Annl and Appl., 252(2000), 342–352.

Abhay Kumar Sethi, Ph.D. Student: Sambalpur University, Jyoti vihar, Burla-768019, India and Department of Mathematics, (*sethiabhaykumar100@gmail.com*).

Corresponding Author- Arun Kumar Tripathy, Ph.D: Sambalpur University, Jyoti vihar, Burla-768019, India and Department of Mathematics, (*arun_tripathy70@rediffmail.com*).

Mathematical modeling of the action of a medium on a conical body

Maxim V. Shamolin

Abstract: We consider a mathematical model of a plane-parallel action of a medium on a rigid body whose surface has a part which is a circular cone. We present a complete system of equations of motion under the quasi-stationarity conditions. The dynamical part of equations of motion form an independent system that possesses an independent second-order subsystem on a two-dimensional cylinder. We obtain an infinite family of phase portraits on the phase cylinder of quasi-velocities corresponding to the presence in the system of only a nonconservative pair of forces.

1. Introduction

In [5, 6], we present a qualitative analysis of plane-parallel and spatial problems on the motion of realistic rigid bodies in a resistive medium. We construct a nonlinear model of the influence of the medium on the rigid body, in which the dependence of the arm of force on the reduced angular velocity of the body is taken into account; in this case, the moment of force is also a function of the angle of attack. Experiments on the motion of homogeneous circular cylinders in water show that these circumstances must be taken into account in modeling. In the study of plane and spatial models of interaction of a rigid body with a medium (both in the presence or absence of an additional tracking force), we find sufficient conditions of stability of one of the key regimes of motion, rectilinear translational motion. We show that under certain conditions, stable or unstable auto-oscillation regimes in the system can appear.

In [7, 8], a mathematical model of the effect of a medium on a homogeneous rigid body whose outer surface includes a circumferential cone is considered. The complete system of equations of motion under quasi-stationarity conditions is given. In the dynamic part forming an independent third-order system, an independent second-order subsystem is distinguished. A new two-parameter family of phase portraits on the phase cylinder of quasi-velocities is obtained.

2. Statement of the Problem

Consider a plane-parallel motion of a homogeneous rigid body of mass m with the cone-shaped front part interacting with a flow of medium under conditions of jet circumfluence of flow-separated circumfluence (see Fig. 1).

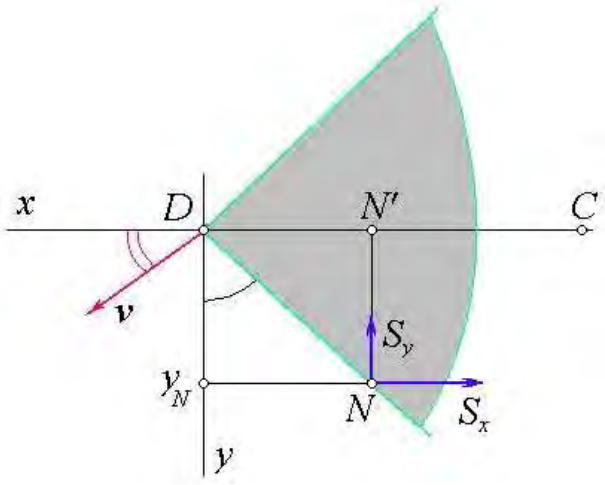

Figure 1. Action of a medium on a rigid body

For simplicity, we assume that the coordinate y_N of the application point N of the action force of the medium is determined by a single parameter, namely, by the angle of attack α, i.e., the angle between the velocity vector of the point D and the symmetry axis Dx:

$$y_N = R(\alpha). \tag{1}$$

We represent the forces of frontal and side resistance (see Fig. 1) as quadratic functions of the speed of the point D:

$$\mathbf{S}_x = -s(\alpha)v^2\mathbf{e}_x,\ \mathbf{S}_y = -b(\alpha)v^2\mathbf{e}_y,\ |\mathbf{v}_D| = v. \tag{2}$$

Thus, we triple of functions $R(\alpha), s(\alpha)$, and $b(\alpha)$ determines the action of a medium on a rigid body under the quasi-stationarity conditions (see [1–3]). In this case, the conical shape of the surface of the body and the hypothesis on the quasi-static action of the medium allow one to determine the complete scheme of forces that contains all characteristics of the system. In the sequel, the analysis of systems constructed is performed by well-known methods of qualitative theory and new methods developed especially for systems with variable dissipation (see [7, 8]).

3. Dynamical Part of Equations of Motion

Taking into account the conditions (1) and (2), we can rewrite the dynamical part of equations of motion in the following form:

$$\dot{v}\cos\alpha - \dot{\alpha}v\sin\alpha + \Omega v\sin\alpha + \sigma\Omega^2 = -\frac{s(\alpha)}{m}v^2, \tag{3}$$

$$\dot{v}\sin\alpha + \dot{\alpha}v\cos\alpha - \Omega v\cos\alpha + \sigma\dot{\Omega} = -\frac{b(\alpha)}{m}v^2, \tag{4}$$

$$I\dot{\Omega} = -F(\alpha)s(\alpha)v^2 + \sigma b(\alpha)v^2 - h\Omega v, \tag{5}$$

where I is the central moment of inertia of the body, m is the mass of a body, $\sigma = CD$, C is the center of mass, $F(\alpha) = R(\alpha)s(\alpha)$, and the coefficient $h > 0$ characterizes an additional moment depending on the angular velocity (see [6]). Note that the the dependence of forces and moments on the angular velocity in such problems is not a priori obvious.

The first two equations are obtained from the theorem on the motion of the center of mass and the third from the theorem on the change of the kinetic moments in the König axes. Similar results without side forces were used earlier in [5].

Since the kinetic energy of the body and generalized forces and moments are independent of the location of the body on the plane, the position coordinates in the system are cyclic. This allow one to consider the system of dynamical equations (3)–(5) as an independent system. The system of kinematic equations

$$\dot{\varphi} = \Omega,\ \dot{x_0} = v\cos(\alpha - \varphi),\ \dot{y_0} = v\sin(\alpha - \varphi),$$

where the variables φ, x_0, and y_0 define the location of the body on the plane, together with the system (3)–(5) for a complete system for the study of the motion in the force field constructed above.

To obtain the form of the functions $R(\alpha), s(\alpha), and b(\alpha)$, one need experimental information about properties of jet circumfluence (see also [8]).

Classes of considered dynamical functions are quite wide: they consist of sufficiently smooths, 2π-periodic functions ($R(\alpha)$ and $b(\alpha)$ are odd and $s(\alpha)$ is even) satisfying the following conditions:

$R(\alpha), b(\alpha) > 0$ for $\alpha \in (0, \pi)$, $R'(0), b'(0) > 0$, $R'(\pi), b'(\pi) < 0$ (class of functions $\{R\}, \{b\}$); $s(\alpha) > 0$ for $\alpha \in (0, \pi/2)$, $s(\alpha) < 0$ for $\alpha \in (\pi/2, \pi)$, $s(0) > 0$, $s'(\pi/2) < 0$ (class of functions $\{s\}$).

The functions R, b, and s change sign if one replace α by $\alpha + \pi$.

In particular, the analytical functions

$$R(\alpha) = A\sin\alpha,\ b(\alpha) = b_1\sin\alpha, \tag{6}$$

$$s(\alpha) = B\cos\alpha;\ A, B, b_1 > 0, \tag{7}$$

are typical representatives of classes described; two of them (namely, R and s) correspond to the functions of action of medium obtained by Chaplygin (see [2]) in the study of a plane-parallel circumfluence of an infinite flat plate by a homogeneous flow.

We explain the necessity of the wide classes of the functions $\{R\}, \{b\}$, and $\{s\}$. Geometric characteristics of cone-shape bodies may be quite different, which allows to classify three dynamical functions into several classes. As was noted above, these functional classes are constrained by sufficiently weak conditions and therefor these classes are sufficiently wide: they contain admissible functions for all bodies and all motions.

Therefore, for the study the circumfluence of a conical body by a medium, we use classes of dynamical systems determined by triples of dynamical functions, which considerably complicates the global nonlinear analysis.

In some cases, without loss of generality (see [2,3,6]), we will consider the representations (6) and (7) for the functions $R(\alpha), s(\alpha)$, and $b(\alpha)$ that determine the action of a medium.

4. Reduction of order

Equations (3)and (4) can be transformed to the form

$$\dot v + \sigma\Omega^2\cos\alpha + \sigma\dot\Omega\sin\alpha = -\frac{s(\alpha)}{m}v^2\cos\alpha - \frac{b(\alpha)}{m}v^2\sin\alpha, \tag{8}$$

$$\dot\alpha v - \Omega v + \sigma\dot\Omega\cos\alpha - \sigma\Omega^2\sin\alpha = -\frac{b(\alpha)}{m}v^2\cos\alpha + \frac{s(\alpha)}{m}v^2\sin\alpha. \tag{9}$$

Introducing the new differentiation by the formula

$$< \cdot >= d/dt = vd/dq = v <'>,$$

where q is the path travelled by the point D, we have $\Omega = \omega v$, $\dot\Omega = v(\omega' v + \omega v')$. Then the dynamical part of the equations of motion takes the following form:

$$v' = v\Psi_1(\alpha, \omega), \tag{10}$$

$$\alpha' = \omega + \frac{\sigma}{I}\psi(\alpha,\omega)\cos\alpha + \sigma\omega^2\sin\alpha + \frac{s(\alpha)}{m}\sin\alpha - \frac{b(\alpha)}{m}\cos\alpha, \tag{11}$$

$$\omega' = -\frac{1}{I}\psi(\alpha,\omega) - \omega\Psi_1(\alpha,\omega), \tag{12}$$

where

$$\psi(\alpha,\omega) = F(\alpha) - \sigma b(\alpha) + h\omega,$$

$$\Psi_1(\alpha,\omega) = \frac{\sigma}{I}\psi(\alpha,\omega)\sin\alpha - \sigma\omega^2\cos\alpha - \frac{s(\alpha)}{m}\cos\alpha - \frac{b(\alpha)}{m}\sin\alpha.$$

We introduce the dimensionless parameters and the differentiation of the form

$$q = Q\sigma,\ \bar{\omega} = \omega\sigma,\ \beta_1 = \frac{\sigma^2 AB}{I},\ \beta_2 = \frac{\sigma^3 b_1}{I},\ \beta_3 = \frac{\sigma h}{I},\ \beta_4 = \frac{B\sigma}{m},\ \beta_5 = \frac{b_1\sigma}{m}.$$

In the sequel, we omit the bar in the notation of the dimensionless variable $\bar{\omega}$ and denote the derivative with respect to the dimensionless variable Q by $'$. In the cases (6) and (7), we can rewrite the system (11), (12) as follows:

$$\alpha' = \omega + \beta_1 \sin\alpha \cos^2\alpha - \beta_2 \sin\alpha\cos\alpha + \beta_3\omega\cos\alpha +$$

$$+\omega^2 \sin\alpha + \beta_4 \sin\alpha\cos\alpha - \beta_5 \sin\alpha\cos\alpha, \tag{13}$$

$$\omega' = -\beta_1 \sin\alpha\cos\alpha + \beta_2 \sin\alpha - \beta_3\omega + \omega^3\cos\alpha - \beta_1\omega\sin^2\alpha\cos\alpha +$$

$$+\beta_2\omega^2\sin\alpha - \beta_3\omega^2\sin\alpha + \beta_4\omega\cos^2\alpha + \beta_5\omega\sin^2\alpha. \tag{14}$$

The dimensionless parameters $\beta_k, k = 1, \ldots, 5$, have the following sense:

β_1 is the parameter of the moment of the frontal resistance force;

β_2 is the parameter of the moment of the lateral force;

β_3 is the parameter of the additional damping moment;

β_4 is the parameter of the frontal resistance force;

β_5 is the parameter of the moment of the lateral force.

Thus, we have a five-parameter family of systems (13), (14) on the two-dimensional phase cylinder

$$\{(\alpha, \omega) \in \mathbf{R}^2 : \alpha \bmod 2\pi\}.$$

5. Regime of Rectilinear Translational Deceleration and Its Stability

Among all possible motions of a body, there exists a key regime — a rectilinear translational deceleration: the body moves translationally with zero attack angle and speeds of all points of the body decrease (see also [6]). The key regime corresponds to the trivial solution of the system (13), (14).

Under the stability of the key regime, we understand the stability of angular oscillations of a body about its longitudinal axis with respect to perturbations of the attack angle and the angular velocity. From the point of view of the theory of stability, this type of stability is treated as the stability with respect to a part of variables.

To examine this stability, we linearize system (13), (14) at the origin:

$$\alpha' = \omega + \beta_1\alpha - \beta_2\alpha + \beta_3\omega + \beta_4\alpha - \beta_5\alpha, \tag{15}$$

$$\omega' = -\beta_1\alpha + \beta_2\alpha - \beta_3\omega + \beta_4\omega. \tag{16}$$

The matrix of this system has the form

$$A = \begin{pmatrix} \beta_1 - \beta_2 + \beta_4 - \beta_5 & 1 + \beta_3 \\ -\beta_1 + \beta_2 & -\beta_3 + \beta_4 \end{pmatrix}, \tag{17}$$

which leads to the characteristic equation

$$\lambda^2 - \mathrm{tr}A \cdot \lambda + \det A = 0, \tag{18}$$

where

$$\mathrm{tr}A = \beta_1 - \beta_2 - \beta_3 + 2\beta_4 - \beta_5. \tag{19}$$

Clearly, the conditions

$$\mathrm{tr}A < 0, \ \det A > 0$$

provide the asymptotic stability of the trivial solution of the system (13), (14).

Relation (19) implies that the presence of a frontal resistance force (and its moment) in the system makes the rectilinear translational deceleration more nonstable. In other words, increasing the coefficients β_1 and β_4 leads to increasing $\mathrm{tr}A$. Conversely, the presence in the system of a lateral resistance force (and its moment) and an additional damping moment makes the rectilinear translational deceleration more stable. In other words, increasing the coefficients β_2, β_3, and β_5 leads to decreasing $\mathrm{tr}A$.

6. Two-parameter Family of Phase Portrait

Consider the case where the system contains two force couples: a couple of frontal resistance forces and a couple of lateral forces (these couples can be added). Namely, we assume that the following conditions hold:

$$\beta_3 = \beta_4 = \beta_5 = 0. \tag{20}$$

In this case, the system (13), (14) becomes

$$\alpha' = \omega + \omega^2 \sin\alpha + \beta_1 \sin\alpha \cos^2\alpha - \beta_2 \sin\alpha \cos\alpha, \tag{21}$$

$$\omega' = -\beta_1 \sin\alpha \cos\alpha + \beta_2 \sin\alpha + \omega^3 \cos\alpha - \beta_1 \omega \sin^2\alpha \cos\alpha +$$

$$+\beta_2 \omega^2 \sin\alpha. \tag{22}$$

Then the system (21), (22) possesses a two-parameter family of phase portraits (see Figs. 2–7, change $\Omega \leftrightarrow \omega$). This family differs from families obtained earlier (see [5]).

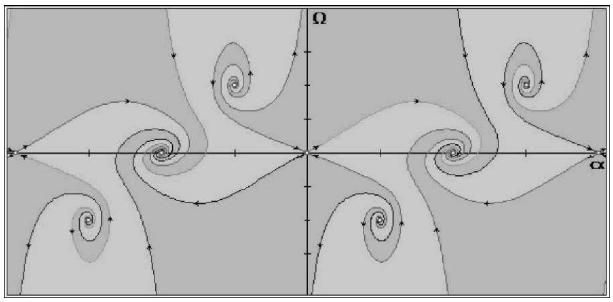

Figure 2.

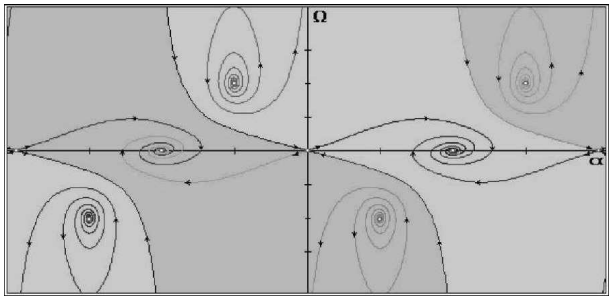

Figure 3.

7. On the Possibility of the Stability of the Key Regime

Under the condition (20), the characteristic equation (18) has the form

$$\lambda^2 + (\beta_2 - \beta_1)\lambda + \beta_1 - \beta_2 = 0; \tag{23}$$

this shows that in the domain of the parameters specified above the stability cannot be achieved. For example, for

$$\beta_1 < \beta_2 \tag{24}$$

the trivial solution of the system is nonstable due to the saddle point. Therefore, by an appropriate choice of the corresponding initial conditions, one can obtain a conditionally stable solution. Indeed, one can take initial conditions near stable separatrices in a neighborhood of the origin and calculate the eigenvectors in the linear approximation.

Another type of nonstability of the trivial solution of the system occurs under the condition

$$\beta_1 > \beta_2. \tag{25}$$

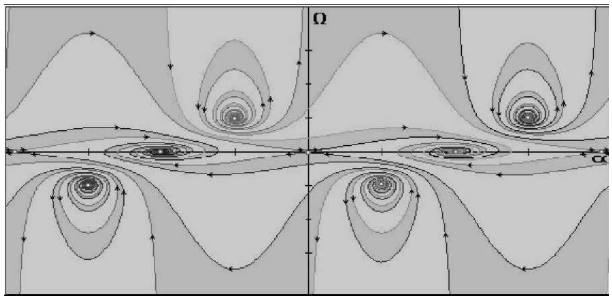

Figure 4.

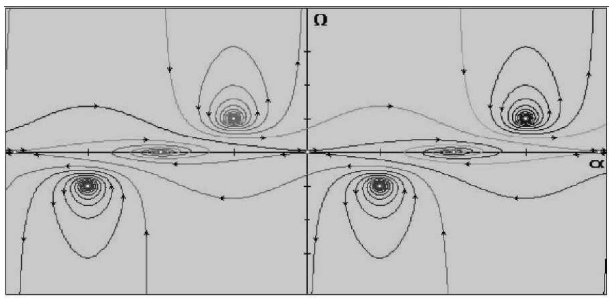

Figure 5.

In this case, the origin is a repelling singular point, and no choice of initial conditions leads to a stable solution.

Families of portraits obtained earlier (see [4,5,8]) deal with the case where the asymptotic stability of the origin can be achieved. The family of portraits obtained in the present paper deals with the case of the conditional stability, which can be achieved by an appropriate choice of initial conditions. In Figs. 2–6, we present the cases corresponding to the inequality (24) (a saddle at the origin), whereas in Fig. 7 the case corresponding to the inequality (25) (a repealing point at the origin) is illustrated.

8. Conclusions

We consider a mathematical model of a plane-parallel action of a medium on a rigid body whose surface has a part which is a circular cone. We present a complete system of equations of motion under the quasi-stationarity conditions. The dynamical part of equations of motion form an independent system that possesses an independent second-order subsystem on a two-dimensional cylinder. We obtain an infinite family of phase portraits on the phase cylinder

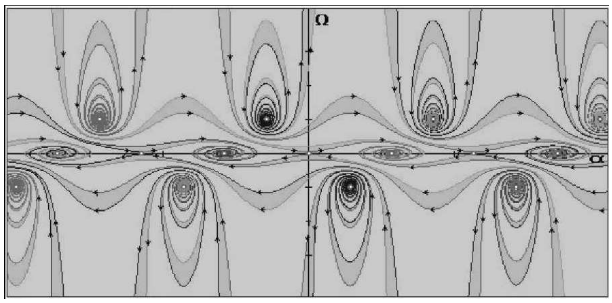

Figure 6.

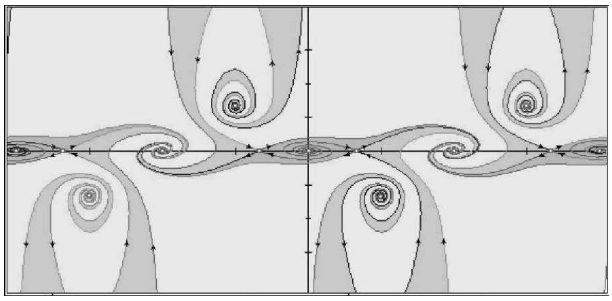

Figure 7.

of quasi-velocities corresponding to the presence in the system only of a nonconservative pair of forces.

Acknowledgments

This work was supported by the Russian Foundation for Basic Research, project no. 15-01-00848-a.

References

[1] Eroshin, V. Model problem of body drag in a resisting medium under streamline flow.

[2] Eroshin, V. Ricochet of a plate from the surface of an ideal incompressible fluid. *Vestn. Mosk. Univ., Ser. Mat. Mekh.*, 6 (1970), 99–104.

[3] Eroshin, V. Immersion of a disk in a compressible fluid at an angle towards the free surface. *Izv. Akad. Nauk SSSR. Mekh. Zhidk. Gaza*, 2 (1983), 142–144.

[4] Eroshin, V. Experimental study of the entrance of an elastic cylinder into water with

high speed. *Izv. Akad. Nauk SSSR. Mekh. Zhidk. Gaza*, 5 (1992), 20–30.

[5] Shamolin, M. New integrable cases and families of portraits in the plane and spatial dynamics of a rigid body interacting with a medium. *J. Math. Sci. 114*, 1 (2003), 919–975.

[6] Shamolin, M. *Methods of Analysis of Variable Dissipation Dynamical Systems in Rigid Body Dynamics*. Ekzamen, Moscow, 2007.

[7] Shamolin, M. Dynamical pendulum-like nonconservative systems. *Applied Non-Linear Dynamical Systems, Springer Proceedings in Mathematics and Statistics 93* (2014), 503–525.

[8] Shamolin, M. Classification of integrable cases in the dynamics of a four-dimensional rigid body in a nonconservative field in the presence of a tracking force. *J. Math. Sci. 204*, 6 (2015), 808–870.

Maxim V. Shamolin, D.Sc. (Full Professor): Lomonosov Moscow State University, Institute of Mechanics, 1 Michurinskii ave., 119192 Moscow, Russian Federation (*shamolin@rambler.ru, shamolin@imec.msu.ru*). The author gave a presentation of this paper during one of the conference sessions.

Deterministic chaos in some pendulum systems with delay

Aleksandr Shvets, Alexander Makaseyev

Abstract: Dynamic system "pendulum - source of limited excitation" with taking into account the various factors of delay is considered. Mathematical model of the system is a system of ordinary differential equations with delay. Three approaches are suggested that allow to reduce the mathematical model of the system to systems of differential equations, into which various delay factors enter as some parameters. Genesis of deterministic chaos is studied in detail. Maps of dynamic regimes, phase-portraits of attractors of systems, phase-parametric characteristics and Lyapunov's characteristic exponents are constructed and analyzed. The scenarios of transition from steady-state regular regimes to chaotic ones are identified. It is shown, that in some cases the delay is the main reason of origination of chaos in the system "pendulum - source of limited excitation".

1. Introduction

In mathematical modeling of oscillatory processes a mathematical model of a relatively simple dynamical system is often used to study the dynamics of much more complex systems. Typical example of this approach is the extensive use of pendulum models to study the dynamics of systems of an entirely different nature. Pendulum mathematical models are widely used to describe the dynamics of various technical constructions, machines and mechanisms, in the study of cardiovascular system, financial markets, etc. Such widespread use of pendulum models makes it relevant to study directly the dynamics of pendulum systems.

Modern development of energy efficient and energy-preserving technologies requires the highest minimization of excitation source power of oscillatory systems. This leads to the fact that the energy of excitation source is comparable to the energy consumed by the oscillating system. Such systems as "source of excitation - oscillating subsystem" are called non-ideal by Zommerfeld-Kononenko [1]. In mathematical modeling of such systems, the limitation of excitation source power must be always taken into account.

Another important factor that significantly affects the change of steady-state regimes of dynamical systems, is the presence of different in their physical substance, factors of delay. The delay factors are always present in rather extended systems due to the limitations of signal transmission speed: stretching, waves of compression, bending, current strength, etc. In some cases, taking into account factors of delay leads only to minor quantitative changes

in dynamical characteristics of pendulum systems. In other cases, taking into account these factors allow to identify qualitative changes in dynamical characteristics [7–9].

The study of the influence of delay factors on the dynamical stability of equilibrium positions of pendulum systems was initiated by Yu. A. Mitropolsky and his scientific school in the 80s of the last century [10]. But only ideal pendulum models were initially considered. In this paper non-ideal pendulum systems of the type "pendulum–electric motor" are considered. Mathematical models of such systems were obtained by A. Yu. Shvets and T. S. Krasnopolskaya. In such systems the existence of chaotic attractors was discovered and proved that the main cause of chaos is limited excitation [5, 6]. The aim of this work is to study the influence of various factors of delay on dynamical behaviour of these system.

2. Mathematical model of the system

In [5] the equations of motion of the system "pendulum - electric motor" in the absence of any delay factors were obtained. They are

$$\begin{cases} \dfrac{dy_1}{d\tau} = Cy_1 - y_2y_3 - \dfrac{1}{8}(y_1^2y_2 + y_2^3); \\ \dfrac{dy_2}{d\tau} = Cy_2 + y_1y_3 + \dfrac{1}{8}(y_1^3 + y_1y_2^2) + 1; \\ \dfrac{dy_3}{d\tau} = Dy_2 + Ey_3 + F; \end{cases} \tag{1}$$

where phase variables y_1y_2 describe the deviation of the pendulum from the vertical and phase variable y_3 is proportional to the rotation speed of the motor shaft. The system parameters are defined by

$$C = -\delta_1\varepsilon^{-2/3}\omega_0^{-1}, D = -\frac{2ml^2}{I}, F = 2\varepsilon^{-2/3}(\frac{N_0}{\omega_0} + E) \tag{2}$$

where m - the pendulum mass, l - the reduced pendulum length, ω_0 - natural frequency of the pendulum, a - the length of the electric motor crank, $\varepsilon = \frac{a}{l}$, δ_1 - damping coefficient of the medium resistance force, I - the electric motor moment of inertia, E, N_0 - constants of the electric motor static characteristics.

Let us consider the following system of equations:

$$\begin{cases} \dfrac{dy_1(\tau)}{d\tau} = Cy_1(\tau-\delta) - y_2(\tau)y_3(\tau-\gamma) - \dfrac{1}{8}(y_1^2(\tau)y_2(\tau) + y_2^3(\tau)); \\ \dfrac{dy_2(\tau)}{d\tau} = Cy_2(\tau-\delta) + y_1(\tau)y_3(\tau-\gamma) + \dfrac{1}{8}(y_1^3(\tau) + y_1(\tau)y_2^2(\tau)) + 1; \\ \dfrac{dy_3(\tau)}{d\tau} = Dy_2(\tau-\gamma) + Ey_3(\tau) + F. \end{cases} \tag{3}$$

This system is a system of equations with constant delay. Positive constant parameter γ was introduced to account the delay effects of electric motor impulse on the pendulum. We assume that the delay of the electric motor response to the impact of the pendulum inertia force is also equal to γ. Taking into account the delay γ conditioned by the fact that the wave velocity perturbations on the elements of the construction has a finite value that depends on the properties of external fields, for instance, the temperature field. In turn, the constant positive parameter δ characterizes the delay of the medium reaction on the dynamical state of the pendulum. This delay is due to the limited sound velocity in that medium.

Let us consider two approaches that allow to reduce the time-delay system (3) to the systems of equations without delay. The first approach is as follows. Assuming a small delay, we can write

$$y_i(\tau-\gamma) = y_i(\tau) - \frac{y_1(\tau)}{d\tau}\gamma + ..., \quad i = 2,3$$

$$y_i(\tau-\delta) = y_i(\tau) - \frac{y_1(\tau)}{d\tau}\delta + ..., \quad i = 1,2$$

Then, if $C\delta \neq -1$, we get the following system of equations:

$$\begin{cases} \dot{y_1} = \dfrac{1}{1+C\delta}\left(Cy_1 - y_2\left[y_3 - \gamma\left(Dy_2 + Ey_3 + F\right)\right] - \dfrac{1}{8}(y_1^2 y_2 + y_2^3)\right); \\ \dot{y_2} = \dfrac{1}{1+C\delta}\left(Cy_2 + y_1 y_3 - y_1\gamma(Dy_2 + Ey_3 + F) + \dfrac{1}{8}(y_1^3 + y_1 y_2^2) + 1\right); \\ \dot{y_3} = (1-C\gamma)Dy_2 - \dfrac{D\gamma}{8}(y_1^3 + y_1 y_2^2 + 8y_1 y_3 + 8) + Ey_3 + F. \end{cases} \tag{4}$$

The obtained system of equations is already a system of ordinary differential equations. Delays are included in this system as additional parameters.

In order to approximate the system (3) another, more precise, method can be used [3]. If $\gamma > 0,\ \delta > 0$ let us divide the segments $[-\gamma;\ 0]$ and $[-\delta;\ 0]$ into m equal parts. We introduce the following notation

$$y_1(\tau - \tfrac{i\delta}{m}) = y_{1i}(\tau),\ y_2(\tau - \tfrac{i\gamma}{m}) = y_{2i}(\tau),\ y_2(\tau - \tfrac{i\delta}{m}) = \tilde{y}_{2i}(\tau),$$

$$y_3(\tau - \tfrac{i\gamma}{m}) = y_{3i}(\tau), i = \overline{0,m}.$$

Then, using difference approximation of derivative [3], [4] we obtain

$$
\begin{cases}
\frac{dy_{10}(\tau)}{d\tau} = Cy_{1m}(\tau) - y_{20}(\tau)y_{3m}(\tau) - \frac{1}{8}(y_{10}^2(\tau)y_{20}(\tau) + y_{20}^3(\tau)); \\
\frac{dy_{20}(\tau)}{d\tau} = C\tilde{y}_{2m}(\tau) + y_{10}(\tau)y_{3m}(\tau) + \frac{1}{8}(y_{10}^3(\tau) + y_{10}(\tau)y_{20}^2(\tau)) + 1; \\
\frac{dy_{30}(\tau)}{d\tau} = Dy_{2m}(\tau) + Ey_{30}(\tau) + F; \\
\frac{dy_{1i}(\tau)}{d\tau} = \frac{m}{\delta}(y_{1\ i-1}(\tau) - y_{1i}(\tau)), \quad i = \overline{1,m}; \\
\frac{dy_{2i}(\tau)}{d\tau} = \frac{m}{\gamma}(y_{2\ i-1}(\tau) - y_{2i}(\tau)), \quad i = \overline{1,m}; \\
\frac{d\tilde{y}_{2i}(\tau)}{d\tau} = \frac{m}{\delta}(\tilde{y}_{2\ i-1}(\tau) - \tilde{y}_{2i}(\tau)), \quad i = \overline{1,m}; \\
\frac{dy_{3i}(\tau)}{d\tau} = \frac{m}{\gamma}(y_{3\ i-1}(\tau) - y_{3i}(\tau)), \quad i = \overline{1,m}.
\end{cases}
\tag{5}
$$

It is a system of ordinary differential equations of $(4m+3)$-th order. In the absence of one of the delays (γ or δ), using the same reasoning, the system (3) can be reduced to the systems of $(2m+3)$-th order. As in the system (4), the delays are included in these systems as additional parameters.

Choosing a sufficiently large m in the system (5), the system (3) will be very well approximated by the system (5) [3]. We note that the solutions y_1, y_2, y_3 of the system (3) are described by the functions y_{10}, y_{20}, y_{30} of the system (5).

Therefore, we obtained three-dimensional (4) and fifteen-dimensional (5) models each describing the system of equations with delay (3). These models are the systems of nonlinear differential equations, so in general the study of steady-state regimes can be carried out only by using numerical methods and algorithms. The methodology of such studies is described in detail in [5].

3. Maps of dynamical regimes

For general analysis of nonlinear dynamical behaviour the maps of dynamical regimes are constructed. Such maps provide a crucial information about the type of steady-state regime of the system depending on its parameters. The construction of dynamical regimes maps is based on analysis and processing of spectrum of Lyapunov characteristic exponents [2, 5]. Where necessary, for more accurate determination of steady-state regime of the system, we study other characteristics of attractors: phase portraits, Poincare sections and maps, Fourier spectrums and distributions of the invariant measure.

Let us consider the behavior of the systems (4) and (5) when the parameters are $C =$

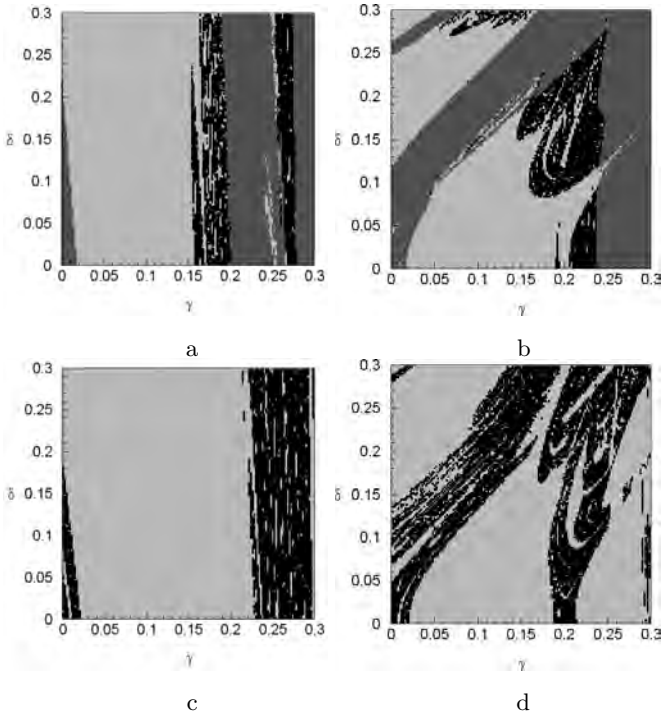

Figure 1. Maps of dynamical regimes

-0.1, $D = -0.53$, $E = -0.59$, $F = -0.4$. The map of dynamical regimes in fig. 1, a was built for three-dimensional model (4) and the map in fig. 1, b was built for fifteen-dimensional model (5). These figures illustrate the effect of the delay of interaction between pendulum and electric motor γ and the delay of the medium δ on changing the type of steady-state regime of the systems. The dark-grey areas of the maps correspond to equilibrium positions of the system. The light-grey areas of the maps correspond to limit cycles of the system. And finally, the black areas of the maps correspond to chaotic attractors.

At small values of the delays both systems have stable equilibrium positions (dark-grey areas in the figures). With an increase of the delay values the region of stable equilibrium positions is replaced by the region of periodic regimes and then by the region of chaotic regimes. With further increase of the delays the alternation of these three types of dynamical regimes takes place.

Let us study the dynamics of the system (4) and (5) at other values of the parameters. The maps of dynamical regimes of three-dimensional system (4) and fifteen-dimensional system (5) at $C = -0.1$, $D = -0.5$, $E = -0.59$, $F = -0.31$ are built respectively in

fig. 1c,d. As seen from the constructed maps, at small values of the delays γ and δ both systems systems have chaotic attractors (black areas in the maps). With an increase of the delay values the region of chaotic regimes is replaced by a large area of periodic steady-state regimes. In the map of dynamical regimes (fig. 1d) of the fifteen-dimensional system (5) in the area of limit cycles there is a sufficiently large region of chaotic regimes. In three-dimensional system (fig. 1d) such region does not exist.

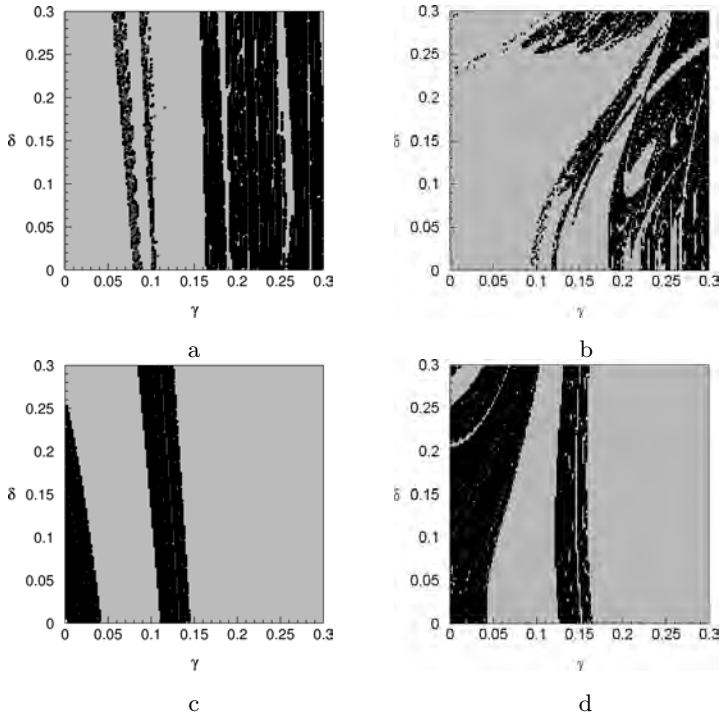

Figure 2. Maps of dynamical regimes

The maps of dynamical regimes of respectively the system (4) and the system (5) at $C = -0.1$, $D = -0.6$, $E = -0.7$, $F = -0.4$ are built in fig. 2a, b. At small values of the delays the steady-state regime of both systems is limit cycle (light-grey areas in the figures). With an increase of the delay values the maps in fig. 2a,b are certainly different. In fig. 2a there are narrow area in which the limit cycle is replaced by an equilibrium position, as well as by a chaotic attractor. Whereas in 2b these narrow area is almost missing. Further in both figures there are a rather wide area of periodic regimes, which with further increase of the delay is replaced by chaos area. Moreover, in this rather wide area of chaos fairly narrow strips of periodic regimes are built in.

In fig. 2c,d the maps of dynamical regimes of respectively the system (4) and the system (5) at $C = -0.1$, $D = -0.53$, $E = -0.6$, $F = 0.19$ are constructed. At small values of the delays both systems have chaotic attractors (black areas in the figures). With an increase of the delay values the region of chaos is replaced by the region of periodic regimes. Then again chaos arises in the system. Further this area is replaced by the area of limit cycles.

As seen from the constructed maps of dynamical regimes, the dynamics of three-dimensional system (4) and fifteen-dimensional system (5) is the same only at small values of the delay γ and δ. With an increase of the delays the dynamical behaviour of these systems is significantly different.

The obtained maps of dynamical regimes allow us to conduct a quick qualitative identification of the type of steady-state regime of the systems (4) and (5). On the basis of constructed maps, more detailed studies of emerging dynamical regimes can be carried out. Particularly we can study the transition from regular to chaotic regimes [6–9].

4. Regular and chaotic dynamics

Let us study the types of regular and chaotic attractors that exist in the systems (4) and (5). We implement a horizontal section of the maps of dynamical regimes in fig.2c,d along the delay γ at $\delta = 0.15$. In other words, let us consider the behavior of the systems (4) and (5) when parameters are $C = -0.1$, $D = -0.53$, $E = -0.6$, $F = 0.19$ and the delays $\delta = 0.15$ and $0 \leq \gamma \leq 0.3$.

In fig. 3a,b the dependence of maximum non-zero Lyapunov's characteristic exponent from γ and phase-parametric characteristic of three-dimensional system (4) are shown respectively. These figures illustrate the influence of the delay of interaction between pendulum and electric motor γ on chaotization of the system (4).

Let us construct the same characteristics at the same values of the parameters for fifteen-dimensional system (5). In fig. 3c,d respectively the dependence of maximum non-zero Lyapunov's characteristic exponent from γ and phase-parametric characteristic are shown.

In fig.3a, 3c we can clearly see the presence of intervals γ in which maximum Lyapunov exponent of the systems is positive. In these intervals the systems have chaotic attractors. The area of existence of chaos is clearly seen in phase-parametric characteristics of the systems. The areas of chaos in the bifurcation trees are densely filled with points. A careful examination of the obtained images allow not only to identify the origin of chaos in the systems, but also to describe the scenario of transition to chaos. So with a decrease of γ there are the transitions to chaos by Feigenbaum scenario (infinite cascade of period-doubling bifurcations of a limit cycle). Bifurcation points for the delay γ are clearly visible in each figures. These points are the points of approaches of the Lyapunov's exponent graph to the

zero line (fig.3a, 3c) and the points of splitting the branches of the bifurcation tree (fig.3b, 3d). In turn, the transition to chaos with an increase of the delay happens under the scenario of Pomeau-Manneville, in a single bifurcation, through intermittency.

A careful analysis of these figures allows to see qualitative similarity of the respective characteristics of the systems (4) and (5). However, with increasing the delay the differences in the dynamics of these systems become very significant.

For instance when the delay of interaction between pendulum and electric motor $\gamma = 0.05$ and the delay of the medium $\delta = 0.15$ the steady-state regime of three-dimensional system (4) is periodic and the attractor is limit cycle. Phase portrait of this attractor is shown in fig.4a. Whereas at this values of the parameters and the delays fifteen-dimensional system (5) has steady-state chaotic dynamical regime. Phase portrait of the chaotic attractor of the

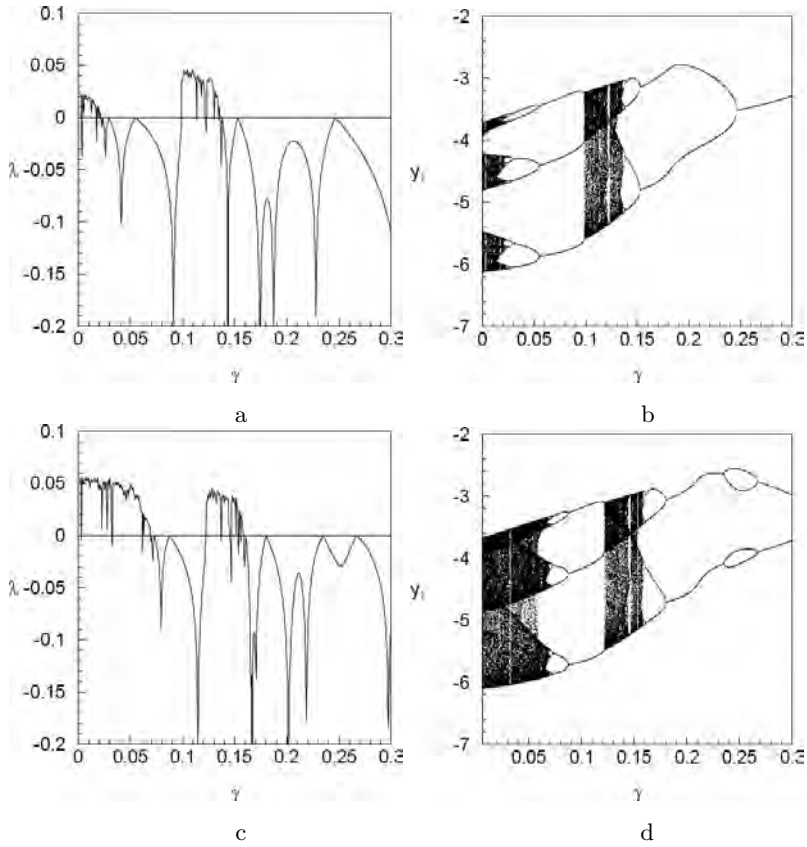

Figure 3. The dependencies of maximal non-zero Lyapunov's characteristic exponent from γ (a,c), phase-parametric characteristics (b ,d)

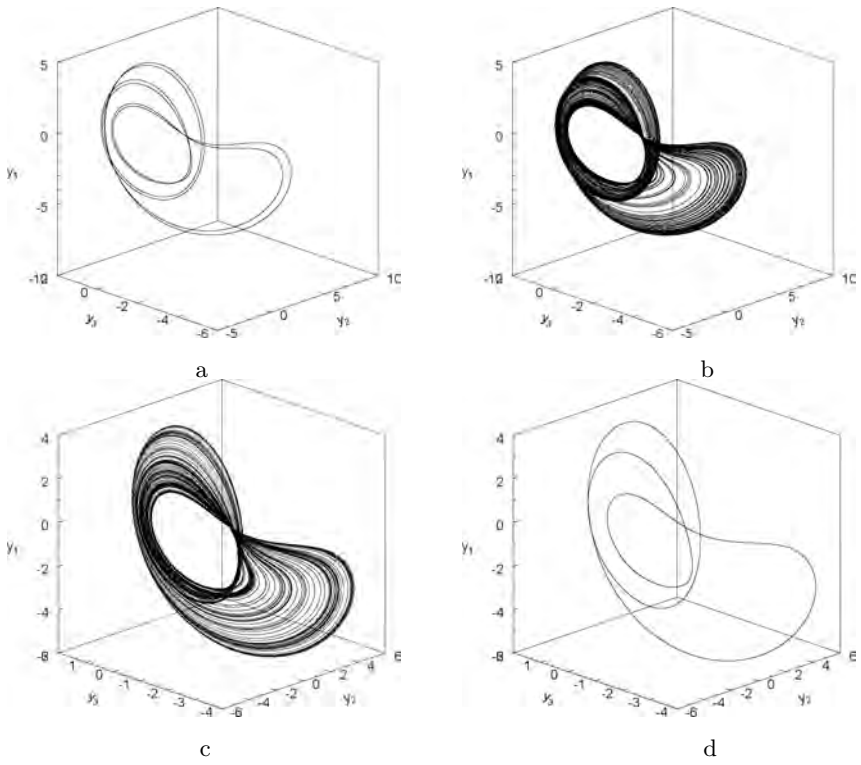

Figure 4. Phase portraits of attractors of the system (4) (a, c) and the system (5) (b, d).

system (5) is built in fig.4b.

It is also possible a different situation. For instance at the delays $\gamma = 0.11, \delta = 0.15$ the system (4) has chaotic steady-state regime of oscillations. Phase portrait of the attractor is shown in fig.4c. Whereas at this values of the delay fifteen-dimensional system (4) has regular periodic dynamical regime and its attractor is limit cycle (fig.4d).

This suggests that three-dimensional system of equations (4) should be used to study the system (3) only at very small values of the delay. With increasing values of the delay to study regular and chaotic oscillations of "pendulum–electric motor" system, fifteen-dimensional system of equations (5) should be used.

5. Conclusion

Taking into account various factors of delay in non-ideal pendulum systems is crucial. The presence of delay in such systems can affect the qualitative change in the dynamical behaviour. It is shown, that in some cases the delay is the main reason of origination as well

as vanishing of chaotic attractors.

It is shown that for small values of the delay it is sufficient to use three-dimensional mathematical model, whereas for relatively high values of the delay the fifteen-dimensional mathematical model should be used.

References

[1] Kononenko, V. O. *Vibrating System with a Limited Power-supply.* Iliffe, London, 1969.

[2] Kouznetsov, S. P. *Dynamic chaos.* Physmatlit, Moscow, 2006.

[3] Magnizkiy, N. A., and Sidorov, S. V. *New methods of chaotic dynamics.* Editorial URSS, 2004.

[4] Samarskiy, A. A., and Gulin, A. V. *Numerical methods.* Nauka, 1989.

[5] Shvets, A. Y., and Krasnopolskaya, T. S. *Regular and chaotical dynamics of systems with limited excitation.* R&C Dynamics, Moscow, 2008.

[6] Shvets, A. Y., and Makaseyev, A. M. Chaotic oscillations of nonideal plane pendulum systems. In *Chaotic Modeling and Simulation (CMSIM) Journal* (2012), no. 1, pp. 195–204.

[7] Shvets, A. Y., and Makaseyev, A. M. The influence of delay factors on regular and chaotic oscillations of plane pendulum. In *Proceedings of Institute of Mathematics of National Academy of Sciences of Ukraine* (Ukraine, 2012), vol. 9, pp. 365–377.

[8] Shvets, A. Y., and Makaseyev, A. M. Mathematical simulation of the influence of delay factors on the oscillations of non-ideal pendulum systems. In *Proceedings of Institute of Mathematics of National Academy of Sciences of Ukraine* (Ukraine, 2014), vol. 11, pp. 269–297.

[9] Shvets, A. Y., and Makasyeyev, O. M. Chaos in pendulum systems with limited excitation in the presence of delay. In *Chaotic Modeling and Simulation (CMSIM) Journal* (2014), no. 3, pp. 233–241.

[10] Shvets, A. Y., and Mitropolsky, Y. A. About influence of delay on a stability of a pendulum with the vibrating suspension point. In *Analytical methods of non-linear oscillations* (Kyiv, 1980), pp. 115–120.

Aleksandr Shvets, Prof., Dr. habil, Ph.D.: National Technical University of Ukraine Igor Sikorsky Kyiv Polytechnic Institute, 37, Pr. Peremohy, Kyiv, Ukraine (*alex.shvets@bigmir.net*). The author gave a presentation of this paper during one of the conference sessions.

Alexander Makaseyev, Ph.D.: National Technical University of Ukraine Igor Sikorsky Kyiv Polytechnic Institute, 37, Pr. Peremohy, Kyiv, Ukraine (*makaseyev@ukr.net*).

The first exit time stochastic theory applied to estimate the life-time of a complicated machine. The case of cars

Christos H Skiadas, Charilaos Skiadas

Abstract: We develop a first exit time methodology to model the life time process of a complicated machine. We assume that the functionality level of a complicated mechanical system follows a stochastic process during time and the end of the functionality of the system comes when the functionality function reaches a zero level. After solving several technical details including the Fokker-Planck equation for the appropriate boundary conditions we estimate the transition probability density function and then the first exit time probability density of the functionality of the system reaching a barrier during time. The formula we arrive is essential for complicated mechanical forms as for several machines. A simpler case has the form called as Inverse Gaussian and was first proposed independently by Schrödinger and Smoluchowsky in the same journal issue (1915) to express the probability density of a simple first exit time process hitting a linear barrier. Applications to the functionality life time of cars are done.

1. Introduction

Several years ago the first exit time or hitting time methodology was used to model the death probability density function for a decaying stochastic process leading to the end of functionality for a machine or of zero health state for an organism. The simpler case was modeled more than 100 years ago independently by Schrödinger [4] and Smoluchowsky [10] in the same journal issue (1915) to express the probability density of a simple first exit time stochastic process hitting a linear barrier. The provided model is the so-called as Inverse Gaussian. Later on the same model was suggested by Siegert [5]. This model was applied to model the death probability density function for the Mediterranean flies (see Weitz and Fraser [12]) whereas Janssen and Skiadas (1995) [1] had provided an expanded first exit time density function to express the human death distribution. More publications are due to Skiadas and Skiadas [6–8] whereas a related book is in the final publication stages by Skiadas and Skiadas [9]. As the mechanical (machines) and electronic (computers) devices developed in nowadays are more and more complicated the methodology used so far for humans and insects could be quite important to apply. In the following we develop the related theory and an application is presented regarding the cars life cycle.

We develop a first exit time methodology to model the life time process of a complicated machine. We assume that the life time $S = S(t)$ of a complicated mechanical system follows a stochastic process of the form:

$$dS(t) = h(t)dt + \sigma(t)dW(t), \tag{1}$$

where $h(t)$ is the drift parameter, $\sigma(t)$ the variance or the diffusion coefficient and $W(t)$ the standard Wiener process. The Wiener process is a standard procedure to reproduce a stochastic process of Brownian motion type that is a random process to account for the random changes of a system functionality or our health state. The last equation is immediately integrable provided that we have selected the appropriate initial conditions as $S(t = 0) = S(0)$.

$$S(t) = S(0) + \int_0^t h(s)ds + \int_0^t \sigma(s)dW(s). \tag{2}$$

This equation form gives a large number of stochastic paths for the health state $S(t)$ of an individual. It should be noted that these paths of a random process with drift are artificial realizations that can not calculated in the real life for a specific device. Instead the mean value of a sufficient large number of stochastic paths can be estimated if we have enough information for the death probability density function. The latter can be found from the number of machines (cars in the specific case explored here) taken out of service at a specific time period.

We set

$$H(t) = \int_0^t h(s)ds, \tag{3}$$

where $H(t)$ stands for the state of functionality of a set of similar mechanical devices or for the health state of a population.

That is important is to find the transition probability density of the stochastic process by solving the associated Fokker-Planck equation for the initial process:

$$\frac{\partial p(S,t)}{\partial t} = -h(t)\frac{\partial [p(S,t)]}{\partial S} + \frac{1}{2}[\sigma(t)]^2 \frac{\partial^2 [p(S,t)]}{\partial S^2}, \tag{4}$$

This partial differential equation for S and t is solved for the following appropriate boundary conditions

$$p(S(t), t_0; S_0, t_0) = \delta(S(t) - S_0), \tag{5}$$

$$\frac{\partial p[S(t), t_0; S_0, t]}{\partial S(t)} \to 0$$
$$\text{as} \tag{6}$$
$$S(t) \to \pm\infty$$

For the solution we use the method of characteristic functions. The characteristic function $\phi(S, t)$ is introduced by the following equation

$$\phi(S, t) = \int_{-\infty}^{+\infty} p(S, t; S_0, t_0) \exp(isS) ds, \tag{7}$$

Integrating by parts and using the Fokker-Plank equation we arrive at

$$\frac{\partial \phi}{\partial t} = ish(t)\phi - \frac{1}{2}[\sigma(t)]^2 s^2 \phi, \tag{8}$$

which with the initial conditions proposed

$$\phi(s, t_0) = \exp(isS_0), \tag{9}$$

is solved providing the following expression for ϕ

$$\phi(s, t_0) = \exp\left[is\left[S_0 + \int_{t_0}^{t} h(t')dt'\right] - \frac{1}{2}s^2 \int_{t_0}^{t} \left[\sigma(t')\right]^2 dt'\right], \tag{10}$$

This is the characteristic function of a Gaussian with mean

$$\left[S_0 + \int_{t_0}^{t} h(t')dt'\right], \tag{11}$$

and variance

$$\left[\sigma(t')\right]^2 dt', \tag{12}$$

After solving several technical details including the Fokker-Planck equation for the appropriate boundary conditions we estimate the transition probability density function

$$p(t) = \frac{1}{[2\pi \int_0^t [\sigma(s)]^2 ds]^{1/2}} \exp\left[-\frac{[H(t)]^2}{2\int_0^t [\sigma(s)]^2 ds}\right], \tag{13}$$

As it is reasonable to assume that the variance could be relatively stable during time, the related transition probability density function for constant σ is of the form:

$$p(t) = \frac{1}{\sigma\sqrt{2\pi t}} \exp\left[-\frac{[H(t)]^2}{2\sigma^2 t}\right]. \tag{14}$$

Then the first exit time probability density function $g(t)$ for the process reaching a barrier (where is the zero functionality level) is given by an approximation proposed by Jennen and Lerche [3] and applied by Skiadas and Skiadas [6–9] of the form

$$g(t) = \frac{|H - tH'|}{t} p(t) = \frac{|H - tH'|}{\sigma\sqrt{2\pi t^3}} \exp\left[-\frac{[H(t)]^2}{2\sigma^2 t}\right]. \tag{15}$$

By using the estimated (for constant σ) Eq. (14) we arrive at the following form for the first exit time probability density function

$$g(t) = \frac{|H - tH'|}{\sigma\sqrt{2\pi t^3}} \exp\left[-\frac{[H(t)]^2}{2\sigma^2 t}\right]. \tag{16}$$

The last formula is coming from a first approximation of the first exit time densities with good results in relatively simpler cases.

For more complicated cases a second approximation was proposed [2]:

$$g(t) = \frac{1}{\sigma\sqrt{2\pi}} \left[\frac{|H - tH'|}{\sqrt{t^3}} + \frac{\sqrt{t^3}H''}{2|H - tH'|^2}\right] \exp\left[-\frac{[H(t)]^2}{2\sigma^2 t}\right]. \tag{17}$$

This is also an approximation and higher order terms are omitted.

For applications in demography an extra parameter k is proposed leading to the following approximation formula providing good fitting to the death data sets of a population (see Skiadas and Skiadas [9])

$$g(t) = \frac{2}{\sigma\sqrt{2\pi}} \left[\frac{|H - tH'|}{\sqrt{t^3}} + \frac{k\sqrt{t^3}H''}{2|H - tH'|}\right] \exp\left[-\frac{[H(t)]^2}{2\sigma^2 t}\right]. \tag{18}$$

Furthermore we can arrive in a very interesting formula by selecting the following form for $H(t)$:

$$H(t) = l - (bt)^c, \tag{19}$$

where l, b, c are parameters. We can easily observe that the system functionality function $H(t)$ as is presented in the last formula is expressing a decay process of time leading to the inevitable fact that it will be a time $T = \frac{l^{1/c}}{b}$ such that $H(t = T) = 0$.

The resulting form is:

$$g(t) = \frac{|l + (c-1)(bt)^c|}{\sigma\sqrt{2\pi t^3}} \exp\left[-\frac{[l - (bt)^c]^2}{2\sigma^2 t}\right]. \tag{20}$$

It should be noted that by setting $c = 1$ in the last formula the well known Inverse Gaussian results

$$g(t) = \frac{|l|}{\sigma\sqrt{2\pi t^3}} \exp\left[-\frac{[l - (bt)]^2}{2\sigma^2 t}\right]. \tag{21}$$

This form was proposed independently by Schrödinger [4] and Smoluchowsky [10] in the same journal issue to express the probability density of simple first exit time process hitting a linear barrier. For complicated mechanical forms as for several machines the parameter c is higher than unity and a convenient form will come from Eq. (18) and Eq. (19).

$$g(t) = \frac{2}{\sigma\sqrt{2\pi}} \left[\frac{|l + (c-1)(bt)^c|}{\sqrt{t^3}} - \frac{k\sqrt{t^3}c(c-1)b^c t^{(c-2)}}{2|l + (c-1)(bt)^c|} \right] \exp\left[-\frac{[l - (bt)^c]^2}{2\sigma^2 t} \right]. \tag{22}$$

Applications to the life time of cars are done

2. Application

For the application we have selected the table for passenger cars taken out of service the year 2007 in Heraklion, Crete, Greece.

We use the following form for the operational state:

$$H(t) = 1 - (bt)^c, \tag{23}$$

We assume that the operational state $H(t)$ of a car is at the maximum level 1 at time zero and then, the operational state gradually declines until a zero level at age $T = 1/b$. Note that the age T is the average of all the stochastic paths hitting the barrier expressed by the axis X. The resulting form for the first exit time probability density function is:

$$g(t) = \frac{|1 + (c-1)(bt)^c|}{\sigma\sqrt{2\pi t^3}} \exp\left[-\frac{[1 - (bt)^c]^2}{2\sigma^2 t} \right]. \tag{24}$$

For the fitting we use a nonlinear regression analysis program, based on a Levenberg-Marquardt algorithm, providing the following values for the parameters: $b = 0.04913, \sigma = 0.06928, c = 1$ with $R^2 = 0.847$. The age at zero operational state is at 20.36 years. The operational state for cars follows a linear declining trend as $c = 1$. Fig. 1 illustrates to death probability density for cars. The data are presented by the dashed line and the fit curve by the continuous line. The maximum death rate is found at 17 years whereas two important age levels are of particular importance that is the age at the left inflection point (11 years) and the age at the right inflection point (21 years) presented by the maximum and minimum points in Fig. 2. Fig. 3 illustrates the linear trend line for the operational state for cars. In the latter case the age at zero operational state is similar to the age at the right inflection point that is 21 years indicating a level at which the car should be taken out of service. Instead the first inflection point (see Fig. 1) corresponding to the maximum in Fig. 2 at 11 years of the car operational age is a good life limit for an average car in the road. A relatively new study in United States by Jack Walsworth [11] found the 11.3 years for the average vehicle in the US roads. Instead for the case of cars in Heraklion, Crete studied the average life was estimated at 18.32 years of operational age.

Figure 1. Death probability density.

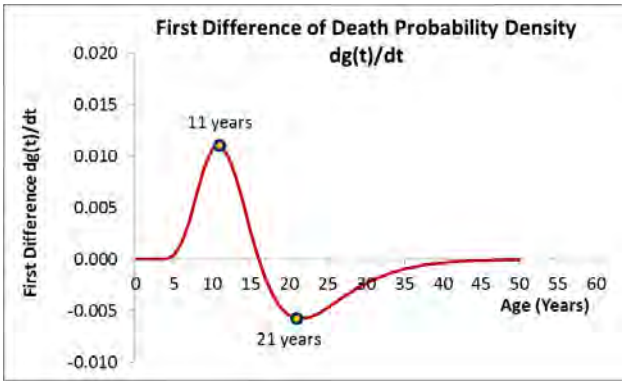

Figure 2. First difference of the first probability density.

3. Conclusions

We have developed a first exit time methodology to model the life time process of a complicated machine. We assume that the functionality level of a complicated mechanical system follows a stochastic process during time and the end of the functionality of the system comes when the functionality function reaches a zero level. We have provided the appropriate functionality functions and the related first exit time probability density functions. The application on cars was very interesting providing adequate information for the development

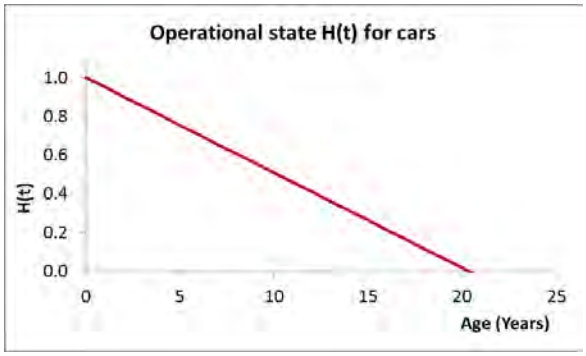

Figure 3. Operational state of cars.

of the operational state of cars over time, the average operational age duration of cars and other statistics related to the maximum and minimum of the rate of change of the operational ability of cars. The very important future of this application on cars functionality level is to establish a concrete method for the evaluation of the cars best circulation age and decide the age at which cars should be taken out of circulation. Applications to other complicated machines and automata are most welcomed.

References

[1] Janssen, J., and Skiadas, C. H. Dynamic modelling of life-table data. *Applied Stochastic Models and Data Analysis 11* (1995), 35–49.

[2] Jennen, C. Second-order approximation for brownian first exit distributions. *Annals of Probability 13* (1985), 126–144.

[3] Jennen, C., and Lerche, H. R. First exit densities of brownian motion through one-sided moving boundaries. *Zeitschrift für Wahrscheinlichkeitstheorie und verwandte Gebiete 55* (1981), 133–148.

[4] Schrödinger, E. Zur theorie der fall- und steigversuche an teilchenn mit brownsche bewegung. *Physikalische Zeitschrift 16* (1915), 289–295.

[5] Siegert, A. J. F. On the first passage time probability problem. *Physical Review 81* (1951), 617–623.

[6] Skiadas, C., and Skiadas, C. H. Development, simulation and application of first exit time densities to life table data. *Communications in Statistics-Theory and Mathods 39* (2010), 444–451.

[7] Skiadas, C., and Skiadas, C. H. The first exit time theory applied to life table data: the health state function of a population and other characteristics. *Communications in Statistics-Theory and Mathods 43* (2014), 1585–1600.

[8] Skiadas, C., and Skiadas, C. H. Exploring the state of a stochastic system via stochastic simulations: An interesting inversion problem and the health state function. *Methodology and Computing in Applied Probability 17* (2015), 973–982.

[9] Skiadas, C. H., and Skiadas, C. *Exploring the Health State of a Population by Dynamic Modeling Methods*. Springer International Publishing, Cham, Switzerland, 2017.

[10] Smoluchowsky, M. V. Notiz ber die berechnung der browschen molekular bewegung bei der ehrenhaft-millikanschen. *Physikalische Zeitschrift 16* (1915), 318–321.

[11] Walsworth, J. Average age of vehicles on road hits 11.6 years. *Automotive News Nov 22* (2016).

[12] Weitz, J. S., and Fraser, H. B. Explaining mortality rate plateaus. *Proceedings of the National Academy of Sciences 98*, 26 (2001), 15383–15386.

Christos H Skiadas, Ph.D.: ManLab Technical University of Crete, Chania, Crete, Greece (*skiadas@cmsim.net*). The author gave a presentation of this paper during one of the conference sessions.

Charilaos Skiadas, Ph.D.: Department of Mathematics and Computer Science, Hanover College, Indiana, USA (*skiadas@hanover.edu*).

A new asymptotic-tolerance model of dynamics of thin uniperiodic cylindrical shells

Barbara Tomczyk, Anna Litawska

Abstract: Thin linearly elastic Kirchhoff-Love-type circular cylindrical shells with a periodically micro-heterogeneous structure in circumferential direction (uniperiodic shells) are analysed. At the same time, the shells have constant structure in axial direction. The aim of this note is to formulate and discuss a new averaged asymptotic-tolerance model for the analysis of dynamic problems for the shells under consideration. This model is derived by applying the combined modelling which includes two techniques: the asymptotic modelling procedure and a certain extended version of the known tolerance non-asymptotic modelling technique based on a new notion of weakly slowly-varying function proposed in [Tomczyk B., Woźniak C., Tolerance models in elastodynamics of certain reinforced thin-walled structures. In: Kołakowski Z. & Kowal-Michalska K. (eds.), Statics, Dynamics and Stability of Structures, vol. 2, Lodz University of Technology Press, Lodz, 123-153, 2012]. Contrary to the exact shell equations with highly oscillating, non-continuous and periodic coefficients, governing equations of the averaged combined model have constant coefficients depending also on a cell size. Hence, this model allows us to investigate the effect of the microstructure size on dynamic behaviour of the shells. An important advantage of the model is that it makes it possible to separate the macroscopic description of some special problems from the microscopic description of these problems.

1. Introduction

Thin linearly elastic Kirchhoff-Love-type circular cylindrical shells with a periodically micro-inhomogeneous structure in circumferential direction (*uniperiodic shells*) are analysed, cf. Fig. 1. Shells of this kind are termed *uniperiodic*. At the same time, the shells under consideration have constant structure in axial direction. Periodic inhomogeneity means here periodically variable shell thickness and/or periodically variable inertial and elastic properties of the shell material.

Dynamic problems of such shells are described by partial differential equations with highly oscillating, periodic and non-continuous coefficients, thus these equations are too complicated to be applied to the investigations of engineering problems. To obtain averaged equations with constant coefficients, various approximate modelling procedures for shells of this kind have been proposed. Periodic cylindrical shells (plates) are usually described using *homogenized models* derived by means of *asymptotic methods*. From the extensive list on this subject we can mention monograph by

Lewiński and Telega [6], where asymptotic modelling of plates, laminates and shells is discussed, book by Andrianov et al. [1], in which a detailed and systematic treatment of asymptotic methods on the theory of plates and shells is presented, monograph by Awrejcewicz et al. [2], which deals with asymptotic approaches to the modelling of statics, dynamics and stability of plates with mixed boundary conditions and in which some modern asymptotic procedures are introduced. Unfortunately, in the models of this kind *the effect of a cell size* (called *the length-scale effect*) on the overall shell behaviour is neglected. This effect can be taken into account using *the tolerance averaging technique* presented and discussed by Woźniak in many monographs, e.g. [12]. This technique based on the concept of *tolerance relations* between points and real numbers related to the accuracy of the performed measurements and calculations. The tolerance relations are determined by *the tolerance parameters*. The second basic concept of this method is *a function slowly-varying within a cell*. It is a function which, together with its derivatives occurring in the problem under consideration, can be treated in the framework of tolerance as constant within every cell. Contrary to starting equations of theories of microheterogeneous structures (partial differential equations with functional, highly oscillating, non-continuous coefficients), *governing equations of the tolerance models have coefficients which are constant or slowly-varying and depend on the period length of inhomogeneity*. Hence, these equations make it possible to analyse the length-scale effect.

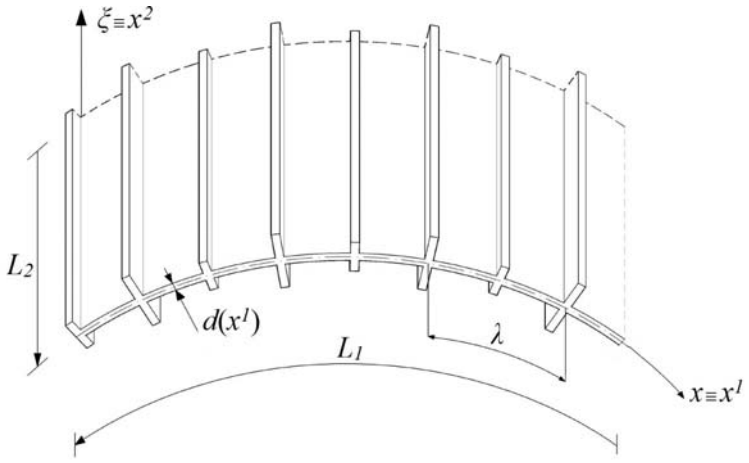

Figure 1. An example of a shell with an uniperiodic microstructure.

Some applications of this method to the modelling of mechanical and thermomechanical problems for various periodic structures are shown in many works. The extended list of publications on this topic can be found in [9, 12]. We mention here monograph by Tomczyk [9], where the length-scale effect in dynamics and stability of periodic cylindrical shells is investigated. In the last years the tolerance modelling was adopted for mechanical and thermomechanical problems of functionally

graded structures, e.g. for heat conduction in longitudinally graded structures by Ostrowski and Michalak [7], for vibrations of functionally graded thin plates by Kaźmierczak and Jędrysiak [5], for dynamics of transversally graded thin cylindrical shells by Tomczyk and Szczerba [11].

A certain extended version of the tolerance modelling technique has been proposed by Tomczyk and Woźniak in [8]. This version is based on a new notion of *weakly slowly-varying functions* which is a certain extension of the well known concept of *slowly-varying functions*, cf. [12]. A new *tolerance model* of dynamic problems for thin uniperiodic cylindrical shells derived by means of the concept of *weakly slowly-varying functions* has been proposed by Tomczyk and Litawska in [10].

The aim of this contribution is to formulate and discuss a new averaged *general combined asymptotic-tolerance model* for the analysis of selected dynamic problems for the uniperiodic shells under consideration. The model will be derived by applying the combined modelling which includes two techniques: *the consistent asymptotic modelling procedure* given by Woźniak [12] and the *extended tolerance non-asymptotic modelling technique* proposed by Tomczyk and Woźniak [8]. Governing equations of *the combined model* have constant coefficients depending also on a cell size. An important advantage of this model is that it makes it possible to study micro-dynamics of periodic shells independently of their macro-dynamics. The differences between *the general combined model* proposed here and the corresponding *known standard combined model* presented by Tomczyk in [9] and derived by means of the more restrictive notion of *slowly-varying functions* will be discussed.

2. Formulation of the problem, starting equations

We assume that x^1 and x^2 are coordinates parametrizing the shell midsurface *M* in circumferential and axial directions, respectively. We denote $x \equiv x^1 \in \Omega \equiv (0, L_1)$ and $\xi \equiv x^2 \in \Xi \equiv (0, L_2)$, where L_1, L_2 are length dimensions of *M*, cf. Fig. 1. Let $O\bar{x}^1\bar{x}^2\bar{x}^3$ stand for a Cartesian orthogonal coordinate system in the physical space R^3 and denote $\bar{\mathbf{x}} \equiv (\bar{x}^1, \bar{x}^2, \bar{x}^3)$. A cylindrical shell midsurface *M* is given by $M \equiv \left\{\bar{\mathbf{x}} \in R^3 : \bar{\mathbf{x}} = \bar{\mathbf{r}}\left(x^1, x^2\right), \left(x^1, x^2\right) \in \Omega \times \Xi\right\}$, where $\bar{\mathbf{r}}(\cdot)$ is the smooth function such that $\partial\bar{\mathbf{r}}/\partial x^1 \cdot \partial\bar{\mathbf{r}}/\partial x^2 = 0$, $\partial\bar{\mathbf{r}}/\partial x^1 \cdot \partial\bar{\mathbf{r}}/\partial x^1 = 1$, $\partial\bar{\mathbf{r}}/\partial x^2 \cdot \partial\bar{\mathbf{r}}/\partial x^2 = 1$. It means that on *M* we have introduced *the orthonormal parametrization.* Sub- and superscripts $\alpha, \beta, \ldots$ run over 1,2 and are related to x^1, x^2, summation convention holds. Partial differentiation related to x^α is represented by ∂_α. Moreover, it is denoted $\partial_{\alpha\ldots\delta} \equiv \partial_\alpha \ldots \partial_\delta$. Let $a^{\alpha\beta}$ stand for the midsurface first metric tensor. Under orthonormal parametrization $a^{\alpha\beta}$ is the unit tensor. The time coordinate is denoted by $t \in \mathrm{I} \equiv [t_0, t_1]$. Let $d(x)$ and r stand for the shell thickness and the midsurface curvature radius, respectively.

The basic cell Δ and an arbitrary cell $\Delta(x)$ with the centre at point $x \in \Omega_\Delta$ are defined by means of: $\Delta \equiv [-\lambda/2, \lambda/2] \in \Omega \equiv (0, L_1)$, $\Delta(x) \equiv x + \Delta$, $x \in \Omega_\Delta$, $\Omega_\Delta \equiv \{x \in \Omega : \Delta(x) \subset \Omega_\Delta\}$, where λ is a cell length dimension in $x \equiv x^1$-direction. *The microstructure length parameter* λ satisfies conditions: $\lambda / d_{\max} >> 1$, $\lambda / r << 1$ and $\lambda / L_1 << 1$.

Setting $z \equiv z^1 \in [-\lambda/2, \lambda/2]$, we assume that the cell Δ has a symmetry axis for $z = 0$. It is also assumed that inside the cell the geometrical, elastic and inertial properties of the shell are described by even functions of argument *z*.

Denote by $u_\alpha = u_\alpha(x, \xi, t)$, $w = w(x, \xi, t)$, $(x, \xi, t) \in \Omega \times \Xi \times \mathrm{I}$, the shell displacements in directions tangent and normal to M, respectively. Elastic properties of the shells are described by shell stiffness tensors $D^{\alpha\beta\gamma\delta}(x)$, $B^{\alpha\beta\gamma\delta}(x)$. Let $\mu(x)$ stand for a shell mass density per midsurface unit area. The external forces will be neglected.

It is assumed that the behaviour of the shell under consideration is described by the action functional determined by Lagrange function *L* being a highly oscillating function with respect to *x* and having the well-known form, cf. [4]

$$L = -\frac{1}{2}(D^{\alpha\beta\gamma\delta}\partial_\beta u_\alpha \partial_\delta u_\gamma + \frac{2}{r} D^{\alpha\beta 11} w \partial_\beta u_\alpha + \frac{1}{r^2} D^{1111} w w + + B^{\alpha\beta\gamma\delta}\partial_{\alpha\beta} w \partial_{\gamma\delta} w + - \mu a^{\alpha\beta} \dot{u}_\alpha \dot{u}_\beta - \mu \dot{w}^2). \tag{1}$$

Applying the principle of stationary action we arrive at the system of Euler-Lagrange equations, which can be written in explicit form as

$$\begin{aligned} &\partial_\beta(D^{\alpha\beta\gamma\delta}\partial_\delta u_\gamma) + r^{-1}\partial_\beta(D^{\alpha\beta 11} w) - \mu a^{\alpha\beta}\ddot{u}_\beta = 0, \\ &r^{-1} D^{\alpha\beta 11}\partial_\beta u_\alpha + \partial_{\alpha\beta}(B^{\alpha\beta\gamma\delta}\partial_{\gamma\delta} w) + r^{-2} D^{1111} w + \mu \ddot{w} = 0. \end{aligned} \tag{2}$$

It can be observed that equations (2) coincide with the well-known governing equations of Kirchhoff-Love theory of thin elastic shells, cf. [4]. For periodic shells, coefficients $D^{\alpha\beta\gamma\delta}(x), B^{\alpha\beta\gamma\delta}(x), \mu(x)$ of equations (2) are highly oscillating, non-continuous and periodic functions in x. Applying the combined asymptotic-tolerance modelling technique to lagrangian (1), we will derive the averaged model equations with constant coefficients depending also on a cell size. The combined modelling under consideration includes two techniques: *the consistent asymptotic modelling procedure* given by Woźniak et al. [12] and *an extended version of the known tolerance non-asymptotic modelling technique* based on a new notion of *weakly slowly-varying function* proposed by Tomczyk and Woźniak [8]. To make the analysis more clear, in the next section we shall

outline the basic concepts and assumptions of the modelling procedure under consideration, following [8, 12].

3. Modelling concepts and assumptions

The fundamental concepts of the extended tolerance modelling procedure under consideration are those of *two tolerance relations between points and real numbers determined by tolerance parameters, weakly slowly-varying functions, tolerance-periodic functions, fluctuation shape functions and the averaging operation.* It has to be emphasized that in the classical approach we deal with not *weakly slowly-varying* but with more restrictive *slowly-varying functions.* Below, the mentioned above concepts and assumptions will be specified with respect to one-dimensional region $\Omega = (0, L_1)$.

Tolerance between points. Let λ be a positive real number. Points x, y belonging to $\Omega = (0, L_1)$ are said to be in tolerance determined by λ, if and only if the distance between points x, y does not exceed λ,

Tolerance between real numbers. Let $\tilde{\delta}$ be a positive real number. Real numbers μ, ν are said to be in tolerance determined by $\tilde{\delta}$, if and only if $|\mu - \nu| \le \tilde{\delta}$.

The above relations are denoted by: $x \overset{\lambda}{\approx} y$, $\mu \overset{\tilde{\delta}}{\approx} \nu$. Positive parameters $\lambda, \tilde{\delta}$ are called *tolerance parameters*.

Let $F(x)$ be a function defined in $\overline{\Omega} = [0, L_1]$, which is continuous, bounded and differentiable in $\overline{\Omega}$ together with their derivatives up to the *R*-th order. Nonnegative integer *R* is assumed to be specified in every problem under consideration. Note, that function *F* can also depend on $\xi \in \overline{\Xi} = [0, L_2]$ and time coordinate *t* as parameters. Let $\delta \equiv (\lambda, \delta_0, \delta_1, .., \delta_R)$ be the set of tolerance parameters. The first of them is related to the distances between points in Ω, the second one is related to the distances between values of function $F(\cdot)$ and the *k*-th one to the distances between values of the *k*-th derivative of $F(\cdot)$, $k = 1, .., R$. A function $F(\cdot)$ is called *weakly slowly-varying of the R-th kind* with respect to cell Δ and tolerance parameters δ, $F \in WSV_{\delta}^{R}(\Omega, \Delta)$, if and only if

$$(\forall (x, y) \in \Omega^2)[(x \overset{\lambda}{\approx} y) \Rightarrow F(x) \overset{\delta_0}{\approx} F(y) \text{ and } \partial_1^k F(x) \overset{\delta_k}{\approx} \partial_1^k F(y), \quad k = 1,2,..., R], \tag{3}$$

where $\partial_1^k F(x)$ stands for the *k*-th derivative of $F(\cdot)$ in Ω. Roughly speaking, *weakly slowly-varying* function $F(\cdot)$ can be treated as constant on an arbitrary cell.

Let us recall that the known *slowly-varying function* $F(x)$, $F \in SV_{\delta}^{R}(\Omega,\Delta) \subset WSV_{\delta}^{R}(\Omega,\Delta)$, satisfies not only condition (3) but also the extra restriction

$$(\forall x \in \Omega)[\lambda\left|\partial_1^k F(x)\right| \overset{\delta_k}{\approx} 0,\ k=1,2,...,R]. \tag{4}$$

An integrable and bounded function $f(x)$ defined in $\overline{\Omega}=[0,L_1]$, which can also depend on $\xi \in \overline{\Xi}$ and time coordinate *t* as parameters, is called *tolerance-periodic* with respect to cell Δ and tolerance parameters $\delta \equiv (\lambda,\delta_0)$, if for every $x \in \Omega_{\Delta}$ there exist Δ-periodic function $\tilde{f}(\cdot)$ such that $f\left|\Delta(x) \cap Dom\, f\right.$ and $\tilde{f}\left|\Delta(x) \cap Dom\, \tilde{f}\right.$ are indiscernible in tolerance determined by $\delta \equiv (\lambda,\delta_0)$. Function $\tilde{f}$ is a Δ*-periodic approximation* of f in $\Delta(x)$. For function $f(\cdot)$ being tolerance periodic together with its derivatives up to the *R*-th order, we shall write $f \in TP_{\delta}^{R}(\Omega,\Delta)$, $\delta \equiv (\lambda,\delta_0,\delta_1,..,\delta_R)$.

Let $f(x)$ be a function defined in $\overline{\Omega}=[0,L_1]$, which is integrable and bounded in every cell $\Delta(x)$, $x \in \Omega_{\Delta}$. By *the averaging of* $f(\cdot)$ we shall mean function $<f>(x)$ defined by

$$<f>(x) \equiv \frac{1}{\lambda}\int_{x-\lambda/2}^{x+\lambda/2} f(z)dz, \quad z \in \Delta(x), \quad x \in \Omega_{\Delta}. \tag{5}$$

If $f(\cdot)$ is a periodic function then $<f>$ is constant.

Let $h(x)$ be a λ-periodic, highly oscillating function defined in $\overline{\Omega}=[0,L_1]$, which is continuous together with derivatives $\partial_1^k h, k=1,...,R-1,$ and has a continuous or piecewise continuous bounded derivative $\partial_1^R h$. Function $h(\cdot)$ will be called *the fluctuation shape function*, $h(\cdot) \in FS^{R}(\Omega,\Delta)$, if it satisfies conditions: $h \in O(\lambda^R)$, $\partial_1^k h \in O(\lambda^{R-k})$, $k=1,2,...,R$, $<\mu h>=0$, where $\mu(x)$ is a shell mass density.

The tolerance modelling is based on two assumptions. The first assumption is called *the tolerance averaging approximation*. The second one is termed *the micro-macro decomposition.*

Let $f(\cdot)$ be an integrable periodic (or tolerance-periodic) function defined in $\overline{\Omega}=[0,L_1]$ and let $F(\cdot) \in WSV_{\delta}^{1}(\Omega,\Delta)$, $G(\cdot) \in WSV_{\delta}^{2}(\Omega,\Delta)$. *The tolerance averaging approximation has the form*

$$\begin{aligned} &<f\,\partial_1^R F>(x) = <f>\partial_1^R F(x) + O(\delta), \quad R=0,1, \quad \partial_1^0 F \equiv F, \\ &<f\,\partial_1^R G>(x) = <f>\partial_1^R G(x) + O(\delta), \quad R=0,1,2, \quad \partial_1^0 G \equiv G. \end{aligned} \tag{6}$$

In the course of modelling, terms $O(\delta)$ will be neglected. Let us observe that the weakly slowly-varying functions can be regarded as invariant under averaging.

We recall that the "classical" *slowly-varying functions* $F(\cdot) \in SV_{\delta}^{1}(\Omega, \Delta)$, $G(\cdot) \in SV_{\delta}^{2}(\Omega, \Delta)$ satisfy not only approximations (6) but also the extra approximate relations

$$\begin{aligned} &< f\, \partial_1(hF) > (x) =< f\, \partial_1 h > (x) F(x) + O(\delta), \quad < f\, \partial_1(gG) > (x) =< f\, \partial_1 g > (x) G(x) + O(\delta), \\ &< f\, \partial_1^2(gG) > (x) =< f\, \partial_1^2 g > (x) G(x) + O(\delta), \end{aligned} \tag{7}$$

where $h(\cdot) \in FS^{1}(\Omega, \Delta)$, $g(\cdot) \in FS^{2}(\Omega, \Delta)$.

The second fundamental assumption, called *the micro-macro decomposition*, states that the displacements fields occurring in the lagrangian under consideration can be decomposed into *unknown averaged* (*macroscopic*) *displacements* being *weakly slowly-varying functions* in $x \in \Omega$ and highly oscillating *fluctuations* represented by the known highly oscillating λ-periodic *fluctuation shape functions* multiplied by unknown *fluctuation amplitudes* (*microscopic variables*) *weakly slowly-varying* in *x*.

On passing from tolerance averaging to *the consistent asymptotic averaging*, we retain only the concept of *fluctuation shape function*. The notion of *weakly slowly-varying function* is not introduced. The fundamental assumption imposed on the starting lagrangian in the framework of the asymptotic approach is called *the consistent asymptotic decomposition.* It states that the displacement fields occurring in the lagrangian have to be replaced by families of fields depending on small parameter $\varepsilon = 1/m$, $m = 1,2,...$ and defined in an arbitrary cell. These families of displacements are decomposed into averaged part independent of ε and highly-oscillating part depending on ε.

4. Combined asymptotic-tolerance model equations

The combined modelling technique under consideration is realized in two steps. The first step is based on *the consistent asymptotic procedure*, cf. [12]. The second one is realized by means of *the extended version of the tolerance non-asymptotic technique*, cf. [8].

4.1. Consistent asymptotic model equations

We start with *the consistent asymptotic averaging of lagrangian L* defined by (1). To this end we have to introduce *the consistent asymptotic decomposition* of displacements $u_{\alpha} = u_{\alpha}(z, \xi, t)$, $w = w(z, \xi, t)$, $z \in \Delta(x)$, $x \in \Omega_{\Delta}$, $(\xi, t) \in \Xi \times \mathrm{I}$, in $\Delta(x) \times \Xi \times \mathrm{I}$

$$\begin{aligned} &u_{\varepsilon\alpha}(z, \xi, t) \equiv u_{\alpha}(z/\varepsilon, \xi, t) = u_{\alpha}^{0}(z, \xi, t) + \varepsilon h_{\varepsilon}(z) U_{\alpha}(z, \xi, t), \\ &w_{\varepsilon}(z, \xi, t) \equiv w(z/\varepsilon, \xi, t) = w^{0}(z, \xi, t) + \varepsilon^{2} g_{\varepsilon}(z) W(z, \xi, t), \end{aligned} \tag{8}$$

where $\varepsilon = 1/m,\ \ m = 1,2,...,\ \ z \in \Delta_\varepsilon(x),\ \ \Delta_\varepsilon \equiv (-\varepsilon\lambda/2, \varepsilon\lambda/2)$ (*scaled cell*), $\Delta_\varepsilon(x) \equiv x + \Delta_\varepsilon$, $x \in \Omega_\Delta$.

Unknown functions u_α^0, U_α in (8) are assumed to be continuous and bounded in Ω together with their first derivatives. Unknown functions w^0, W in (8) are assumed to be continuous and bounded in Ω together with their derivatives up to the second order. Unknowns u_α^0, w^0 and U_α, W are called *macrodisplacements* and *fluctuation amplitudes*, respectively. They are independent of ε.

By $h_\varepsilon(z) \equiv h(z/\varepsilon) \in FS^1(\Omega, \Delta)$ and $g_\varepsilon(z) \equiv g(z/\varepsilon) \in FS^2(\Omega, \Delta)$ in (8) are denoted λ-periodic highly oscillating *fluctuation shape functions* depending on ε. The *fluctuation shape functions* are assumed to be known in every problem under consideration. They have to satisfy conditions: $h \in O(\lambda)$, $\lambda\partial_1 h \in O(\lambda)$, $g \in O(\lambda^2)$, $\lambda\partial_1 g \in O(\lambda^2)$, $\lambda^2\partial_{11} g \in O(\lambda^2)$, $<\mu h> = <\mu g> = 0$.

We introduce decomposition (8) into (1) and take into account that under limit passage $\varepsilon \to 0$, terms depending on ε can be neglected and every continuous and bounded function of argument $z \in \Delta_\varepsilon(x)$ tends to function of argument $x \in \overline{\Omega}$. Moreover, if $\varepsilon \to 0$ then by means of a property of the mean value, cf. [3], the obtained result tends weakly to the following averaged form L_0 of starting lagrangian (1)

$$
\begin{aligned}
&L_0(\partial_\beta u_\alpha^0, U_\alpha, \dot{u}_\alpha^0, \partial_{\alpha\beta} w^0, w^0, W, \dot{w}^0) = <\widetilde{L}(z, \partial_\beta u_\alpha^0, U_\alpha, \dot{u}_\alpha^0, \partial_{\alpha\beta} w^0, w^0, W, \dot{w}^0> = \\
&= -\frac{1}{2}[<D^{\alpha\beta\gamma\delta}> \partial_\beta u_\alpha^0 \partial_\delta u_\gamma^0 + 2<D^{\alpha\beta\gamma 1}\partial_1 h> \partial_\beta u_\alpha^0 U_\gamma + <D^{\alpha 1\gamma 1}(\partial_1 h)^2> U_\gamma U_\alpha + \\
&+ 2r^{-1}(<D^{\alpha\beta 11}> \partial_\beta u_\alpha^0 w^0 + <D^{\alpha 111}\partial_1 h> w^0 U_\alpha) + r^{-2}<D^{1111}> (w^0)^2 + \\
&+ <B^{\alpha\beta\gamma\delta}> \partial_{\alpha\beta} w^0 \partial_{\gamma\delta} w^0 + 2<B^{\alpha\beta 11}\partial_{11} g> \partial_{\alpha\beta} w^0 W + <B^{1111}(\partial_{11} g)^2> W^2 + \\
&- <\mu> a^{\alpha\beta} \dot{u}_\alpha^0 \dot{u}_\beta^0 - <\mu> (\dot{w}^0)^2].
\end{aligned}
\tag{9}
$$

where $\widetilde{L}$ is a periodic approximation of L in $\Delta(x)$ and where averages $<\cdot>$ on the right-hand side of (9) are constant and calculated by means of (5). Then, applying the principle of stationary action we obtain *the governing equations of consistent asymptotic model for the uniperiodic shells under consideration.* These equations consist of partial differential equations for macrodisplacements u_α^0, w^0 coupled with linear algebraic equations for fluctuation amplitudes U_α, W. After eliminating fluctuation amplitudes from the governing equations by means of

$$
U_\gamma = -(G^{-1})_{\gamma\eta}\ [<\partial_1 h D^{1\eta\mu\vartheta}> \partial_\vartheta u_\mu^0 + r^{-1} <\partial_1 h D^{1\eta 11}> w^0],\ W = -E^{-1} <\partial_{11} g B^{11\gamma\delta}> \partial_{\gamma\delta} w^0, \tag{10}
$$

where $G_{\alpha\gamma} = <D^{\alpha 1\gamma 1}(\partial_1 h)^2>$, $E = <B^{1111}(\partial_{11} g)^2>$, we arrive finally at *the asymptotic model equations expressed only in macrodisplacements* u_α, w

$$
\begin{aligned}
&D_h^{\alpha\beta\gamma\delta}\partial_{\beta\delta}u_\gamma^0 + r^{-1}D_h^{\alpha\beta 11}\partial_\beta w^0 - <\mu> a^{\alpha\beta}\ddot{u}_\beta^0 = 0\,,\\
&B_g^{\alpha\beta\gamma\delta}\partial_{\alpha\beta\gamma\delta}w^0 + r^{-1}D_h^{11\gamma\delta}\partial_\delta u_\gamma^0 + r^{-2}D_h^{1111}w^0 + <\mu>\ddot{w}^0 = 0\,,
\end{aligned}
\tag{11}
$$

where $D_h^{\alpha\beta\gamma\delta} \equiv <D^{\alpha\beta\gamma\delta}> - <D^{\alpha\beta\eta 1}\,\partial_1 h>(G^{-1})_{\eta\zeta} <\partial_1 h D^{1\zeta\gamma\delta}>$,

$B_g^{\alpha\beta\gamma\delta} \equiv <B^{\alpha\beta\gamma\delta}> - <B^{\alpha\beta 11}\partial_{11}g> E^{-1} <\partial_{11}gB^{11\gamma\delta}>$.

Coefficients of equations (11) are *constant* but they are *independent of the microstructure cell size*. Hence, this model is not able to describe the length-scale effect on the overall shell dynamics and it will be referred to as *the macroscopic model*. Unknown *macrodisplacements* u_α, w and *fluctuation amplitudes* U_α, W must be continuous and bounded in Ω.

In the first step of combined modelling it is assumed that within the asymptotic model, solutions u_α^0, w^0 to the problem under consideration are known. Hence, there are also known functions $u_{0\alpha} = u_\alpha^0 + hU_\alpha$ and $w_0 = w^0 + gW$, where U_α, W are given by means of (10).

4.2. Superimposed tolerance model equations

The second step is based on *the tolerance averaging* of lagrangian (1) under so-called *superimposed decomposition*.

We introduce *the extra micro-macro decomposition* superimposed on the known solutions $u_{0\alpha}, w_0$ obtained within the macroscopic model

$$
u_{c\alpha}(x,\xi,t) = u_{0\alpha}(x,\xi,t) + c(x)Q_\alpha(x,\xi,t)\,, \quad w_b(x,\xi,t) = w_0(x,\xi,t) + b(x)V(x,\xi,t)\,,
\tag{12}
$$

where *fluctuation amplitudes* Q_α, V are *the new weakly slowly-varying unknowns*, i.e. $Q_\alpha \in WSV_\delta^1(\Omega,\Delta)$, $V \in WSV_\delta^2(\Omega,\Delta)$. Functions $c(x)$ and $b(x)$ are *the new* periodic, continuous and highly-oscillating *fluctuation shape functions* which are assumed to be known in every problem under consideration. These functions have to satisfy conditions: $c \in O(\lambda)$, $\lambda\partial_1 c \in O(\lambda)$, $b \in O(\lambda^2)$, $\lambda\partial_1 b \in O(\lambda^2)$, $\lambda^2\partial_{11}b \in O(\lambda^2)$, $<\mu c> = <\mu b> = 0$.

We substitute the right-hand sides of (12) into (1). The resulting lagrangian is denoted by L_{cb}. Then, we average L_{cb} over cell Δ using averaging formula (5) and applying *the tolerance averaging approximation* (6). As a result we obtain function $<L_{cb}>$ called *the tolerance averaging of starting lagrangian* (1) *in* Δ *under superimposed decomposition* (12)

$$
\begin{aligned}
&< L_{cb} > (\partial_\beta Q_\alpha, Q_\alpha, \dot{Q}_\alpha, \partial_{\alpha\beta} V, \partial_\beta V, V, \dot{V}) = \\
&= -\frac{1}{2}[< D^{\alpha\beta\gamma\delta}\partial_\beta u_{0\alpha}\partial_\delta u_{0\gamma} > +2 < D^{\alpha\beta\gamma 1}\partial_1 c\partial_\beta u_{0\alpha} > Q_\gamma + < D^{\alpha 11\gamma}(\partial_1 c)^2 > Q_\gamma Q_\alpha + \\
&+ \underline{< D^{\alpha\beta\gamma\delta}(c)^2 >}\partial_\beta Q_\alpha \partial_\delta Q_\gamma + 2r^{-1}(< D^{\alpha\beta 11}\partial_\beta u_{0\alpha} w_0 > + < D^{\alpha 111}\partial_1 c\, w_0 > Q_\alpha + \\
&+ \underline{\underline{< D^{\alpha\beta 11} b\,\partial_\beta u_{0\alpha} >}} V + \underline{\underline{< D^{\alpha 111}\partial_1 c\, b >}} Q_\alpha V) + r^{-2}(< D^{1111}(w_0)^2 > + 2\underline{\underline{< D^{1111} b\, w_0 >}} V + \\
&+ \underline{\underline{< D^{1111}(b)^2 >}}(V)^2) + < B^{\alpha\beta\gamma\delta}\partial_{\alpha\beta} w_0 \partial_{\gamma\delta} w_0 > + 2(< B^{\alpha\beta 11}\partial_{11} b\,\partial_{\alpha\beta} w_0 > V + \\
&+ \underline{< B^{\alpha\beta\gamma\delta} b\,\partial_{\alpha\beta} w_0 >}\partial_{\gamma\delta} V + \underline{< B^{11\gamma\delta} b\partial_{11} b >}\partial_{\gamma\delta} V V) + 4\underline{< B^{1\beta 1\delta}(\partial_1 b)^2 >}\partial_\beta V\,\partial_\delta V + \\
&+ < B^{1111}(\partial_{11} b)^2 > (V)^2 + \underline{< B^{\alpha\beta\gamma\delta}(b)^2 >}\partial_{\alpha\beta} V\,\partial_{\gamma\delta} V - < \mu a^{\alpha\beta}\dot{u}_{0\alpha}\dot{u}_{0\beta} > - < \mu(\dot{w}_0)^2 > + \\
&- \underline{< \mu(c)^2 >} a^{\alpha\beta}\dot{Q}_\alpha\dot{Q}_\beta - \underline{< \mu(b)^2 >}(\dot{V})^2] .
\end{aligned}
\tag{13}
$$

The underlined terms in (13) depend on microstructure length parameter λ.

Applying the principle of stationary action, we obtain the system of Euler-Lagrange equations for Q_α, V, which can be written in explicit form as

$$
\begin{aligned}
&\underline{< D^{\alpha\beta\gamma\delta}(c)^2 >}\partial_{\beta\gamma} Q_\delta - < D^{\alpha 11\delta}(\partial_1 c)^2 > Q_\delta - \underline{< \mu(c)^2 >} a^{\alpha\beta}\ddot{Q}_\beta - r^{-1}\underline{\underline{< D^{\alpha 111}\partial_1 c\, b >}} V = \\
&= r^{-1} < D^{\alpha 111}\partial_1 c\, w_0 > + < D^{\alpha\beta\gamma 1}\partial_1 c\,\partial_\beta u_{0\gamma} > ,
\end{aligned}
\tag{14}
$$

$$
\begin{aligned}
&r^{-1}\underline{\underline{< D^{\alpha 111}\partial_1 c\, b >}} Q_\alpha + \underline{< B^{\alpha\beta\gamma\delta}(b)^2 >}\partial_{\alpha\beta\gamma\delta} V + [\underline{2 < B^{\alpha\beta 11} b\partial_{11} b >} - 4\underline{< B^{\alpha 1\beta 1}(\partial_1 b)^2 >}]\partial_{\alpha\beta} V + \\
&+ (\underline{\underline{< D^{1111}(b)^2 >}} + < B^{1111}(\partial_{11} b)^2 >)V + \underline{< \mu(b)^2 >}\ddot{V} = \\
&= - < B^{\alpha\beta 11}\partial_{11} b\,\partial_{\alpha\beta} w_0 > - r^{-1}\underline{\underline{< D^{\alpha\beta 11} b\,\partial_\beta u_{0\alpha} >}} - r^{-2}\underline{\underline{< D^{1111} b\, w_0 >}} .
\end{aligned}
\tag{15}
$$

Equations. (14) and (15) together with *the micro-macro decomposition* (12) constitute *the superimposed microscopic model*. Coefficients of the derived model equations are constant and some of them *depend on a cell size* λ (underlined terms). The right-hand sides of (14) and (15) are known under assumption that $u_{0\alpha}, w_0$ were determined in the first step of modelling. The basic unknowns Q_α, V of the model equations must be *the weakly slowly-varying functions in periodicity direction*, i.e. $Q_\alpha \in WSV_\delta^1(\Omega,\Delta)$, $V \in WSV_\delta^2(\Omega,\Delta)$. This requirement can be verified only *a posteriori and it determines the range of the physical applicability of the model.*

4.3. General combined asymptotic-tolerance model equations

Summarizing results obtained in Subsections 4.1 and 4.2 we conclude that *the combined asymptotic-tolerance model of selected dynamic problems for the uniperiodic shells under consideration* derived here is represented by

a) *Macroscopic model* defined by equations (11) for u_α^0, w^0 with expressions (10) for U_α, W, formulated by means of *the consistent asymptotic modelling* and being independent of the microstructure length. Unknowns of this model must be continuous and bounded functions in *x*.

b) *Superimposed microscopic model equations* (14), (15) derived by means of *an extended version of the tolerance (non-asymptotic) modelling* and having constant coefficients depending also on a cell size λ (underlined terms) as well as combined with the macroscopic model equations under assumption that in the framework of the asymptotic model the solutions to the problem under consideration are known. Unknown fluctuation amplitudes of this model must be *weakly slowly-varying functions* in *x*.

c) Decomposition

$$\begin{aligned} &u_\alpha(x,\xi,t) = u_\alpha^0(x,\xi,t) + h(x)U_\alpha(x,\xi,t) + c(x)Q_\alpha(x,\xi,t), \\ &w(x,\xi,t) = w^0(x,\xi,t) + g(x)W(x,\xi,t) + b(x)V(x,\xi,t), \quad x \in \Omega,\ (\xi,t) \in \Xi \times \mathrm{I}, \end{aligned} \tag{16}$$

where functions $u_\alpha^0, U_\alpha, w^0, W$ have to be obtained in the first step of combined modelling, i.e. in the framework of *the consistent asymptotic modelling.*

Now, let us discuss an important modification of equations (14), (15). It can be shown, cf. [9], that under assumption that fluctuation shape functions $h(x)$, $g(x)$ of macroscopic model coincide with fluctuation shape functions $c(x)$, $b(x)$ of microscopic model and introducing the extra approximation $1 + \lambda / r \approx 1$, we can obtain *microscopic model equations, which are independent of the solutions obtained in the framework of the macroscopic model*

$$\underline{< D^{\alpha\beta\gamma\delta}(h)^2 >} \partial_{\beta\gamma} Q_\delta - < D^{\alpha 11\delta} (\partial_1 h)^2 > Q_\delta - \underline{< \mu(h)^2 >} a^{\alpha\beta} \ddot{Q}_\beta = 0, \tag{17}$$

$$\begin{aligned} &\underline{< B^{\alpha\beta\gamma\delta}(g)^2 >} \partial_{\alpha\beta\gamma\delta} V + [\underline{2 < B^{\alpha\beta 11} g \partial_{11} b >} - 4 \underline{< B^{\alpha 1\beta 1} (\partial_1 g)^2 >}\ ] \partial_{\alpha\beta} V + \\ &+ < B^{1111} (\partial_{11} g)^2 > V + \underline{< \mu(g)^2 >} \ddot{V} = 0. \end{aligned} \tag{18}$$

It means, that an important advantage of the combined model is that it makes *it possible to describe selected problems of the shell micro-dynamics* (e.g. the free micro-vibrations, propagation of waves related to the micro-fluctuation amplitudes) *independently of the shell macro-dynamics*. Moreover, micro-dynamic behaviour of the shell in the axial and circumferential directions can be analysed independently of its micro-dynamic behaviour in direction normal to the shell midsurface.

It can be shown that equations (17), (18) also describe certain *near-initial and near-boundary phenomena* strictly related to the specific form of initial conditions and boundary conditions imposed on fluctuation amplitudes Q_α, V. That is why, equations (17), (18) are referred to as *the boundary*

layer equations, where the term "boundary" is related both to time and space. Note, that the boundary conditions for Q_α, V should be defined on all boundaries, i.e. for $x = 0, L_1$ $\xi = 0, L_2$

4.4. Standard combined asymptotic-tolerance model equations

Let us compare *the general combined model* proposed here with the corresponding known *standard combined model* presented and discussed in [9], which was derived under assumption that the unknown fluctuation amplitudes $Q_\alpha(x,\xi,t), V(x,\xi,t)$ in micro-macro decomposition (12) are *slowly-varying*. We recall that *the slowly-varying functions* being a subclass of *the weakly slowly-varying functions* are defined by means of (3) and (4). For *the slowly-varying functions* approximate relations (6), (7) hold whereas for *the weakly slowly-varying functions* only approximate relations (6) hold. Moreover, the standard combined model shown in [9] was formulated under the additional assumption $1 + \lambda / r \approx 1$.

Following [9], *the standard combined asymptotic-tolerance model* consists of:

a) *Macroscopic model* defined by equations (11) for u_α^0, w^0 with expressions (10) for U_α, W, formulated by means of *the consistent asymptotic modelling* and being independent of the microstructure length. It is assumed that in the framework of this model the solutions to the problem under consideration are known.

b) *Superimposed microscopic model equations* derived by means of *the tolerance (non-asymptotic) modelling* based on the notion of *slowly-varying function*

$$\underline{< D^{\alpha 22\delta}(c)^2 >}\,\partial_{22} Q_\delta - < D^{\alpha 11\delta}(\partial_1 c)^2 > Q_\delta - \underline{< \mu(c)^2 >}\, a^{\alpha\beta}\ddot{Q}_\beta = \\ = r^{-1} < D^{\alpha 111}\partial_1 c\, w_0 > + < D^{\alpha\beta\gamma 1}\partial_1 c\, \partial_\beta u_{0\gamma} >, \tag{19}$$

$$\underline{< B^{2222}(b)^2 >}\,\partial_{2222} V + [\underline{2 < B^{2211} b \partial_{11} b >} - \underline{4 < B^{2121}(\partial_1 b)^2 >}\,]\partial_{22} V < B^{1111}(\partial_{11} b)^2 > V + \\ + \underline{< \mu(b)^2 >}\,\ddot{V} = - < B^{\alpha\beta 11}\partial_{11} b\, \partial_{\alpha\beta} w_0 >. \tag{20}$$

Coefficients of (19), (20) are constant and some of them (underlined terms) depend on a cell size. Unknown fluctuation amplitudes of this model must be *slowly-varying functions* in *x*.

c) Decomposition (16) in which *weakly slowly-varying functions* $Q_\alpha(x,\xi,t) \in WSV_\delta^1(\Omega,\Delta)$, $V(x,\xi,t) \in WSV_\delta^2(\Omega,\Delta)$ are replaced by *slowly-varying functions* $Q_\alpha(x,\xi,t) \in SV_\delta^1(\Omega,\Delta)$, $V(x,\xi,t) \in SV_\delta^2(\Omega,\Delta)$.

From comparison of both the general and the standard combined models it follows that *the general model equations* contain a bigger number of terms depending on the microstructure size then *the standard model equations*. Thus, the general model proposed here makes it possible to investigate

the length-scale effect in more detail. Within the framework of *the general model*, the unknown fluctuation (microscopic) amplitudes Q_α, V are governed by equations (14), (15), which are coupled with each other. Within the framework of *the standard model*, micro-fluctuation amplitudes Q_α are governed by equations (19) (dynamic balance equations in directions tangent to the shell midsurface) which are not conjugated with equation (20) for unknown amplitude V (dynamic balance equation in direction normal to the shell midsurface). The doubly underlined terms in *general microscopic equations* (14), (15), i.e. terms of an order λ / r, do not occur in the corresponding *standard microscopic equations* (19), (20). Absent of these terms in (19), (20) follows from assumption $1 + \lambda / r \approx 1$ introduced into the standard combined modelling. It can be observed that for *the standard model*, the boundary conditions for micro-fluctuation amplitudes Q_α, V should be defined only on boundaries $\xi = 0$, $\xi = L_2$, whereas in the framework of *the general model* the boundary conditions for Q_α, V should be defined on all boundaries of the shell.

5. Final remarks and conclusions

Summing up our considerations, the following remarks and conclusions can be formulated:

- Thin linearly elastic Kirchhoff-Love-type circular cylindrical shells having a periodic microstructure in circumferential direction (*uniperiodic shells*) are objects of consideration, cf. Fig. 1. At the same time, the shells have constant geometrical and material properties in axial direction.
- The aim of this contribution was to formulate and discuss *a new averaged general combined asymptotic-tolerance model for the analysis of selected dynamic problems for the uniperiodic cylindrical shells under consideration.* The governing equations of this model consist of *macroscopic* (*asymptotic*) *model equations* (11) derived by means of *the consistent asymptotic procedure*, cf. [12], and *microscopic* (*non-asymptotic*) *model equations* (14), (15) formulated by applying *an extended version of the tolerance modelling technique*, cf. [8], based on a new notion of *weakly slowly-varying functions.* Macro- and microscopic models are combined together under assumptions that in the framework of the asymptotic model the solutions to the problem under consideration are known.
- Contrary to the well-known governing equations (2) of Kirchhoff-Love theory with highly oscillating, non-continuous and periodic coefficients, *equations of the proposed combined model have constant coefficients depending also on a microstructure size* λ. Hence, this model makes it possible to describe the effect of a length scale on the dynamic shell behaviour. Moreover, *the general combined model equations* formulated in this contribution contain a bigger number of terms depending on a cell size than *the standard combined model equations* presented in [9], which were derived applying "classical" concept of *the slowly-varying functions.* Thus, the general model allow us to investigate the length-scale effect in more detail.

- The main advantage of the combined model is that it makes it possible to separate the macroscopic description of some special dynamic problems from their microscopic description.
- The basic unknowns of the microscopic model equations must be *weakly slowly-varying functions in periodicity direction.* This requirement can be verified only *a posteriori* and it determines the range of the physical applicability of the model.

References

[1] Andrianov, I.V., Awrejcewicz, J. and Manevitch, L. *Asymptotical mechanics of thin-walled structures.* Springer, Berlin, 2004.

[2] Awrejcewicz, A., Andrianov, I.V., Danishevs'kyy, V.V. and Ivankov, A.O. *Asymptotic methods in the theory of plates with mixed boundary conditions.* Wiley, Chichester, 2014.

[3] Jikov, V.V., Kozlov, C.M. and Olejnik, O.A. *Homogenization of differential operators and integral functionals.* Springer Verlag, Berlin-Heidelberg, 1994.

[4] Kaliski, S. (ed.). *Vibrations*. PWN-Elsevir, Warsaw-Amsterdam, 1992.

[5] Kaźmierczak, M. and Jędrysiak, J. Tolerance modelling of vibrations of thin functionally graded plates. *Thin Walled Structures* 49, (2011), 1295-1303.

[6] Lewiński, T. and Telega, J.J. *Plates, laminates and shells*. *Asymptotic analysis and homogenization*. World Scientific Publishing Company, Singapore, 2000.

[7] Ostrowski, P. and Michalak, B. The combined asymptotic-tolerance model of heat conduction in a skeletal microheterogeneous hollow cylinder. *Composite Structures* 134, (2015), 343-352.

[8] Tomczyk, B. and Woźniak. C. Tolerance models in elastodynamics of certain reinforced thin-walled structures. In: Kołakowski, Z. and Kowal-Michalska. K. (eds.). *Statics, dynamics and stability of structural elements and systems.* Lodz University of Technology Press, Lodz, 2012, 123-153.

[9] Tomczyk, B. *Length-scale effect in dynamics and stability of thin periodic cylindrical shells.* Scientific Bulletin of the Lodz University of Technology, No. 1166, series: Scientific Disserations. Lodz University of Technology Press, Lodz, 2013, number of pages: 163.

[10] Tomczyk, B. and Litawska, A. A new tolerance model of vibrations of thin microperiodic cylindrical shells. *Journal of Civil Engineering, Environment and Architecture* 64, (2017), 203-216.

[11] Tomczyk, B., and Szczerba, P. Tolerance and asymptotic modelling of dynamic problems for thin microstructured transversally graded shells. *Composite Structures* 162, (2017), 365-373.

[12] Woźniak, C. et al. (eds). *Mathematical modelling and analysis in continuum mechanics of microstructured media*. Silesian University of Technology Press, Gliwice, 2010.

Barbara Tomczyk, Ph.D., D.Sc.: Lodz University of Technology, Department of Structural Mechanics, Al. Politechniki 6, 90-924 Lodz, Poland (*barbara.tomczyk@p.lodz.pl*).

Anna Litawska, M.Sc. (Ph.D. student): Lodz University of Technology, Department of Structural Mechanics, Al. Politechniki 6, 90-924 Lodz, Poland (*a.litawska@gmail.com*). The author gave a presentation of this paper during one of the conference sessions.

A fractional perspective to the modelling of Lisbon's Public Transportation Network

Duarte Valério, J.A. Tenreiro Machado, António M. Lopes, António Dinis F. Santos

Abstract: In this paper, the public transportation network (PTN) of the city of Lisbon is analysed from 1901 to 2015, employing different mathematical tools. In a first stage, the fractal dimension and the fractional entropy are used to quantify the evolution of the PTN in space and time. These measures prove to be appropriate to quantify the growth of the PTN, as the description is compatible with known historical events. In a second stage, the distance between consecutive stops is analysed, revealing a power-law behaviour, as expected from the fractal geometry of the network.

1. Introduction

Urban growth originates multiscale spatial patterns that are well described by fractal geometry [18]. Such patterns emerge on urban infrastructures, such as built-up spaces, or transportation networks [13]. Several studies on the fractal nature of public transportation networks (PTNs) [4] demonstrated that this concept is capable of describing their complexity and also evolution over time. In this paper, the fractional order entropy is used to analyse this evolution, and the results of both methods are compared. As a case study, the dynamics of Lisbon's PTN and its spatial structure are assessed, and the probabilistic distribution of PTN stops is studied.

The growth of Lisbon's PTN is closely related to the expansion of the city. The increasing need of mobility drives the expansion of the PTN, not only in size but also in complexity. The PTN considered here comprises four means of transportation: bus, subway, tram and train, each with different limitations and attributes. This leads to interesting dynamics within the PTN, as a single trip can involve more than one mode of transport. In addition, distinct types of transports began operating at different years, and were at variate stages of development when introduced. Therefore, there is interest in studying the evolution of the PTN both in time and space.

The geographical scope of this study is the municipality of Lisbon, and the time frame considered is between the years 1901 (year of the first electrified tram line) and 2015 (the last year with available data). Municipalities other than Lisbon, with further public transport operators, are not included.

The information on the available routes in each year was compiled from several sources [1, 6, 9, 15], while their coordinates were obtained in [2].

Lines are constructed by connecting each stop to the following stop by the shortest path between them. While railway, subway and tramway networks are confined to the tracks laid, and their changes are usually the result of extending (or shortening) the routes, bus routes are, on the other hand, much easier to change, and the network often varies differently from the others. Additionally, tramway tracks are cheaper to relocate than railway and subway lines, so this network also undergoes occasional changes other than extensions and cuts. Another difference between the types of transport is that the railway and subway lines do not have to follow some traffic rules and urban geography in the same way trams and buses do. Therefore, while constructing the subway and railway networks in this perspective provides a close approximation of the actual networks, the same cannot be said about the bus and tram networks. The lack of information on transit in the earlier days of the PTN led to this approximation based on more recent configurations of the network, where traffic directions were adapted based on 2015 routes.

The paper is organised as follows. Sections 2 and 3 present results obtained with the box-count fractal dimension and fractional entropy, respectively. Section 4 investigates the distance between stations. Finally, section 5 draws the main conclusions.

2. Box-count Fractal Dimension

While a geometric fractal object can display a pattern repeated at different scales, ranging from infinitely large to infinitely small, a PTN can only show this behaviour at certain scales [11]. For this kind of network, the largest conceivable scale is the size of a continent; the smallest is the distance between two consecutive bus or tram stops. Therefore, within a reasonable limit, a fractal behaviour can be observed and quantified. One such measure is the fractal dimension, which measures the amount of space that a fractal fills as the scale observed goes from the larger to the smaller one. In this sense, it is an indicator of the network compactness.

The fractal dimension has been used together with several networks related to urban questions (see e.g. the tutorial introduction of [11] to both fractals and their application in urban geography). For example, the spatial pattern of built-up areas was studied in [19], demonstrating the usefulness of fractal geometry, not only for characterizing the form, or the landscape, but also for modelling and planning urban realities. In [24] the fractal characteristics of urban surface transit and road networks were analysed for Strasbourg suggesting possible methods for designing road and surface transit networks. Urban boundaries, land use, spatial structure, and allometric relationships between urban area and population

growth were addressed in [3], and more recently in [8], by combining allometric scaling and fractals, as a basis for urban geography.

While there are several definitions for fractal dimension, [16], the one considered in this paper is the box-counting fractal dimension, due to its straightforward numerical implementation. The box counting is similar to other methods, namely grid-counting [10]. However, since the boxes cannot cover perfectly the fractal object, the box counting yields an approximate value of the true fractal dimension. The error is small if we use high resolution images and vary the box size in small steps within a wide range of values. The algorithm adopted herein is structured as follows [21]:

- Repeat
  - cover the fractal object F with a grid composed of equal squares, with size $\epsilon > 0$;
  - count the number of boxes (squares), $N_\epsilon(F) \in \mathbb{N}$, that cover the fractal F;
  - decrease ϵ.
- The fractal dimension $b \in \mathbb{R}$ is the slope of the log-log plot of $N_\epsilon(F)$ vs. ϵ

$$b(F) = -\lim_{\epsilon \to 0^+} \frac{\log N_\epsilon(F)}{\log \epsilon}. \tag{1}$$

  In our case, we consider $\epsilon = 2^k,\ k = 7, 6, \ldots, 2$. Larger values make no sense as they correspond to a square larger than the municipality; smaller values also make no sense because there is not enough resolution.

Equation (1) shows the relationship between the size of the grid and the fractal dimension, such that $N_\epsilon(F)$ corresponds to the number of boxes that cover the fractal object F for a given value of ϵ, with ϵ being the size of the side of each square on the grid. As the PTN only shows a fractal behaviour within a certain scale, a stopping criteria must be introduced to determine the boundaries of ϵ. By plotting the fractal dimension b versus ϵ for a particular year, it is possible to find the interval where ϵ decreases almost linearly with the grid size, and therefore the points obtained with grids outside this interval can be disregarded from the calculation of b.

It can be shown that the fractal dimension b, given by (1), can be estimated as the exponent of a power law [11]:

$$N_\epsilon(F) = a\epsilon^b,\ a, b \in \mathbb{R}^+. \tag{2}$$

In Equation (2), b is related to how the network fills the space, and is a measure of the PTN's compactness, while a is related to the length between the bifurcations of the PTN. This parameter provides additional information regarding the complexity and interconnectivity of the PTN. It can be conversely shown that (2) implies a fractal geometry [10].

To implement this algorithm to the PTN, the following steps are applied, with the parameters adjusted to obtain reliable results:

1. Each map is padded with empty spaces around it in order to create a square image. This is done by adding background pixels around the centered map until the image has a resolution of $2^k \times 2^k$, where $k \in \mathbb{N}$.

   The value of k is chosen so that 2^k is the first power of 2 larger than the largest side of the original map.

2. For every year, the first step of the box-count algorithm is applied. In each iteration, ϵ decreases in powers of base 2, starting at 2^7 and ending at 2^2. Values of $\epsilon \notin [2^2, 2^7]$ do not make sense, since the upper/lower limit to the size a square can have is the size of the image is and the size of the marker of the lines respectively.

3. The results of the previous step are approximated by means of a power law (2) using the least squares method.

The results from this process are presented in Figure 1, for the entire PTN, comprising all means of transportation for the entire municipality of Lisbon.

3. Fractional Entropy

As the PTN evolves, the calculation of the entropy associated with its expansion can give a better understanding of the distribution of the public transportation routes along the years. Using entropy it is possible to assess how the PTN expands in time, and how uniform is the spread of the PTN on the covered region. In the context of information theory, entropy is a measure of information, choice and uncertainty, and its mathematical expression is presented in Equation (3):

$$S = E[I(p_i)] = \sum_i -p_i \ln(p_i), \tag{3}$$

where $E(\cdot)$ denotes the expected value operator, and $I(p_i) = \ln(p_i)$ is the information content of some event having probability p_i of occurring. The expression for Shannon entropy is analogous to the Boltzmann-Gibbs expression for entropy in statistical thermodynamics [17], and it is also refered to as the Boltzmann-Gibbs-Shannon entropy.

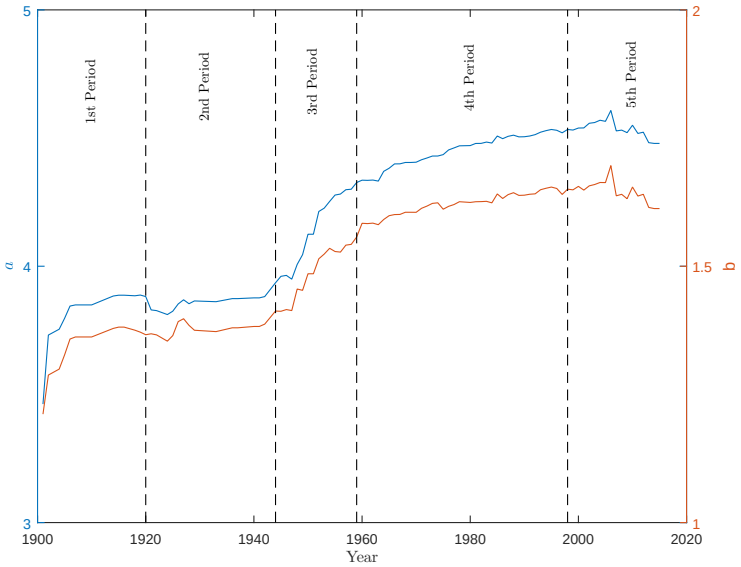

Figure 1. Evolution of the fractal dimension of the PTN of Lisbon from 1901 to 2015.

The usefulness of this measure of uncertainty led to considerable interest in generalizing the Shannon entropy and exploring its applications in other fields, spurring various formulations [20]. One expression that proved to have an higher sensitivity to dynamical phenomena is the entropy of fractional order, S_α [14] given by:

$$S_\alpha = \sum_i \left\{ -\frac{p_i^{-\alpha}}{\Gamma(\alpha+1)} [\ln p_i + \psi(1) - \psi(1-\alpha)] \right\} p_i, \tag{4}$$

where α represents the fractional order, with $-1 \leq \alpha \leq 1$, and $\Gamma(\cdot)$ and $\psi(\cdot)$ are the gamma and digamma functions, respectively. The case $\alpha \to 0$ yields the Shannon entropy. In what follows, both the Shannon entropy and the fractional entropy with order $\alpha = 0.74$ are given; this value of α was taken from previous published work [21], and corresponds to the largest sensitivity of the measure. The computation of S and S_α for the PTN through the years is carried out using the following algorithm:

1. A map for each year is created. These maps are the same as the ones used for the fractal dimension, explained in Section 2, but each line of the PTN is drawn as a succession of equally spaced points, instead of actual lines.

2. A square grid is superimposed over the map. The resolution for the grid is chosen so that the squares on the map are roughly twice the size of the representation of a point.

3. The probabilities are computed as $p_i = \frac{n_i}{N}$, where n_i is the number of points in each square of the grid and N is the total number of points across all squares.

4. Entropy is computed using Equations (3) or (4).

In Figure 2, the periods established in Figure 1 are superimposed over S and S_α, both rescaled to the interval $[0, 1]$ for comparison purposes. The slightly higher sensitivity to the changes in the PTN of the fractional entropy becomes apparent, and thus only its values will be considered below. These results are again for the entire PTN, comprising all means of transportation for the entire municipality of Lisbon.

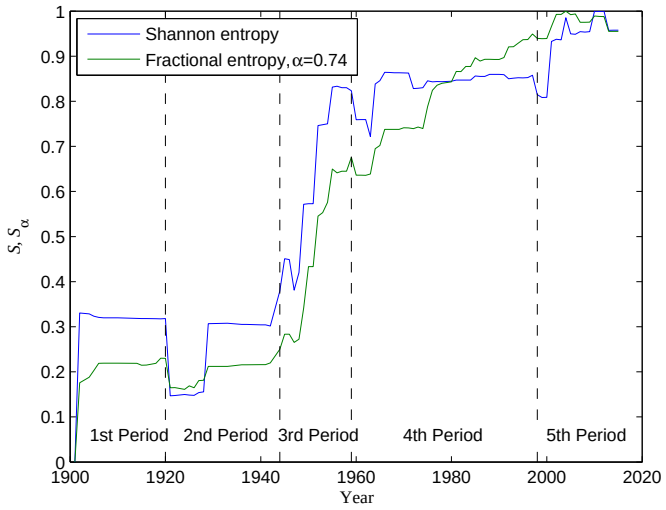

Figure 2. Shannon and fractional order (for $\alpha = 0.74$) entropies of the PTN, rescaled to the interval $[0, 1]$, from 1901 to 2015. The actual ranges are $S \in [4.5, 4.6]$ and $S_\alpha \in [37.9, 201.6]$.

Comparing Figures 1 and 2 provides insight on the evolution of Lisbon PTN:

- 1^{st} Period (1900 – 1920): The evolution of the fractal dimension almost mirrors that of the entropy, growing faster with the inception of the PTN and eventually settling with a near constant value as it approaches 1920.

- 2^{nd} Period (1920 – 1944): After some closings, the PTN remains almost the same till the end of World War II draws near.

- 3^{rd} Period (1944 – 1959): Year 1944 sees the introduction of the bus service in Lisbon. This results in rapid growth of the PTN, as shown by the jump in both the fractal

dimension and the entropy. Finally, in 1959 the subway system is opened, adding even more lines in the centre of the city.

- 4^{th} Period (1959 – 1998): This period begins with a decrease in entropy, once again due to the closing of several tram routes. However, the entropy quickly grows again, as bus routes start to cover the perimeter of Lisbon and reach new locations on the western and north-eastern sides of the municipality. The PTN stagnates by the end of this period, as shown by the slowing of the growth rate for the fractal dimension and the entropy.

- 5^{th} Period (1998 – 2015): The fractal dimension and the entropy increase faster in 1998 due to the growth of the subway network. A big reorganisation of the buses from 2007 onward can be seen. Parameter a is mostly constant, as new intersections are not being created.

4. Inter-Station Distance

The distance between consecutive stations is also a relevant topic in PTN. Ferber and Holovatch [23] studied the fractality within the PTN of Berlin to the distribution of inter-station distances, showing that a Lévy α - stable distribution, $S_L(\alpha_s, \beta, \gamma_s, \delta)$, was an adequate curve fitting, due to the power-law behaviour observed. In a similar line of though, we consider herein the 2015 Lisbon PTN.

The Lévy distribution is a subclass of the family of α–stable distributions, involving the following parameters: $\alpha_s \in [0, 2]$, the characteristic exponent that describes the tail of the distribution; $\beta \in [-1, 1]$, the skewness parameter, specifying if the distribution is either right ($\beta > 0$) or left ($\beta < 0$) skewed; $\gamma_s > 0$, the scale parameter; and $\delta \in \mathbb{R}$, the location parameter [7]. The characteristic function (CF) is shown in Equation (5) for this family of distributions:

$$\phi(t) = \begin{cases} \exp\left(-{\gamma_s}^{\alpha_s} |t|^{\alpha_s} \left[1 - i\beta \operatorname{sgn}(t) \tan\left(\frac{\pi\alpha_s}{2}\right) \right] + i\delta t \right), & \text{for } \alpha_s \neq 1 \\ \exp\left(-\gamma_s |t| \left[1 + i\beta \operatorname{sgn}(t) \frac{2}{\pi} \log(t) \right] + i\delta t \right), & \text{for } \alpha_s = 1 \end{cases}, \tag{5}$$

where $i = \sqrt{-1}$ is the imaginary unit, and $t \in \mathbb{R}$ is the argument of the CF.

Using the CF, it is possible to estimate the parameters of the distribution.

- Plot the right tail of the empirical cumulative distribution function (CFD) on a double logarithmic scale;

- Compute the slope of the linear regression on the linear segment of the CFD plot;
- The slope will be the estimation of α_s.

The downside that this method may reveal is its sensitivity to the sizes of the sample and the set used for the regression [5]. For this reason the estimation based on the CF will also be applied following the tail method estimation. The fit of the CF to the data was processed using the algorithm developed in [22].

Figure 3 (where x is the distance between stations in km) shows that every considered groups of inter-station distances display a power-law decay within a certain interval of values. These intervals correspond to the almost linear segment in the log–log plot.

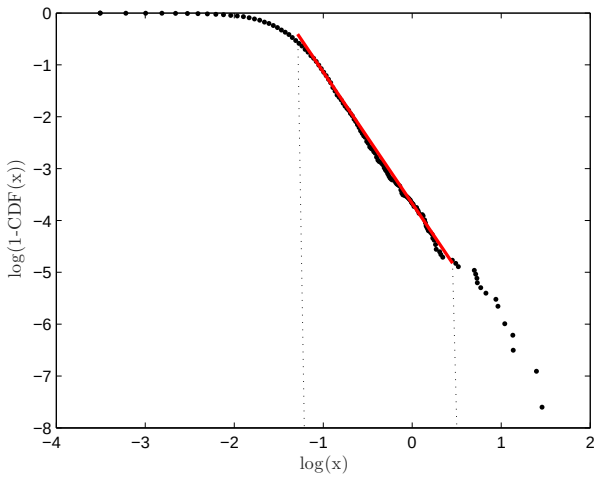

Figure 3. The empirical CDF of inter-station distances, x, in year 2015.

Following the tail exponent method, the slope of this line yields $\hat{\alpha}_s = 2.41$, suggesting that the distribution follows a non-α-stable power-law decay. Table 1 shows the parameters estimated with the CF estimation method. In addition to these, the parameters for the Gaussian, Cauchy and Lévy distributions are also presented for reference.

Based on the estimated parameters presented in Table 1, it is possible to say that the four groups of inter-station distance belong to the α-stable distribution class. Groups $\mathfrak{T}_1$, $\mathfrak{T}_2$ and $\mathfrak{T}_4$ have close values for $\hat{\alpha}_s$ and are all right skewed ($\hat{\beta} = 1$). From these three sets, both groups $\mathfrak{T}_1$ and $\mathfrak{T}_4$ have the same value for $\hat{\gamma}_s$ and very close values for $\hat{\delta}$, while the subway estimated parameters are slightly larger. The results for the subway inter-station distance distribution stand out from the others, as the parameters appear to be more in line

Table 1. Estimated α-stable distribution parameters.

Parameter		$\hat{\alpha}_s$	$\hat{\beta}$	$\hat{\gamma}_s$	$\hat{\delta}$
$\mathfrak{T}_1$	Bus + Tram	1.57	1	0.08	0.35
$\mathfrak{T}_2$	Train	1.67	1	0.14	0.80
$\mathfrak{T}_3$	Subway	1.13	0.27	0.32	1.63
$\mathfrak{T}_4$	All the above	1.42	1	0.08	0.39

Values for distributions which are particular cases:

Parameter	$\hat{\alpha}_s$	$\hat{\beta}$	$\hat{\gamma}_s$	$\hat{\delta}$
Gaussian	2	β	$\frac{\sigma}{\sqrt{2}}$	μ
Cauchy	1	0	γ	δ
Lévy	$\frac{1}{2}$	1	γ	δ

with a Cauchy distribution. A possible reason for this result is that the subway operates underground and thus is not subject to the same restrictions in regards to the location of its stops. Figure 4 shows the probability density function (pdf) for each set of data.

As indicated by the parameter values on Table 1, the pdf for the distribution of inter-station distances for $\mathfrak{T}_1$ (a) takes a similar shape to that for $\mathfrak{T}_4$ of the entire PTN (d). It is also observable the influence of this pair of means of transportation on the entire PTN; however, the complete PTN has more points with larger values for the distance, due to the inclusion of the train set $\mathfrak{T}_2$ (b). Figure 4 (c) also allows to graphically observe the difference between the subway pdf and the others: it is more akin to a Cauchy pdf, as expected based on the parameter values from Table 1.

5. Conclusions

In this paper, both the fractional entropy and the fractal dimension were used to study the evolution of Lisbon's PTN with time, and were found to vary in accordance with its history. To the best of our knowledge, the fractional entropy had not yet been used to this purpose. Its usefulness is confirmed by similar results from the fractal dimension.

The values computed for Lisbon's PTN were in line with what is available in the literature for other cities. Overall, it was concluded that the fractal dimension and the entropy were capable of describing the increase in complexity and extension of the PTN as a whole.

Finally, α-stable probability distributions were found to fit the consecutive inter-station distance dataset. This result suggests that the distribution of the inter-station distance follows a non-trivial power-law, a result compatible with what is found in the literature [7,12,22]. To further continue this work, the following guidelines can be followed in the future:

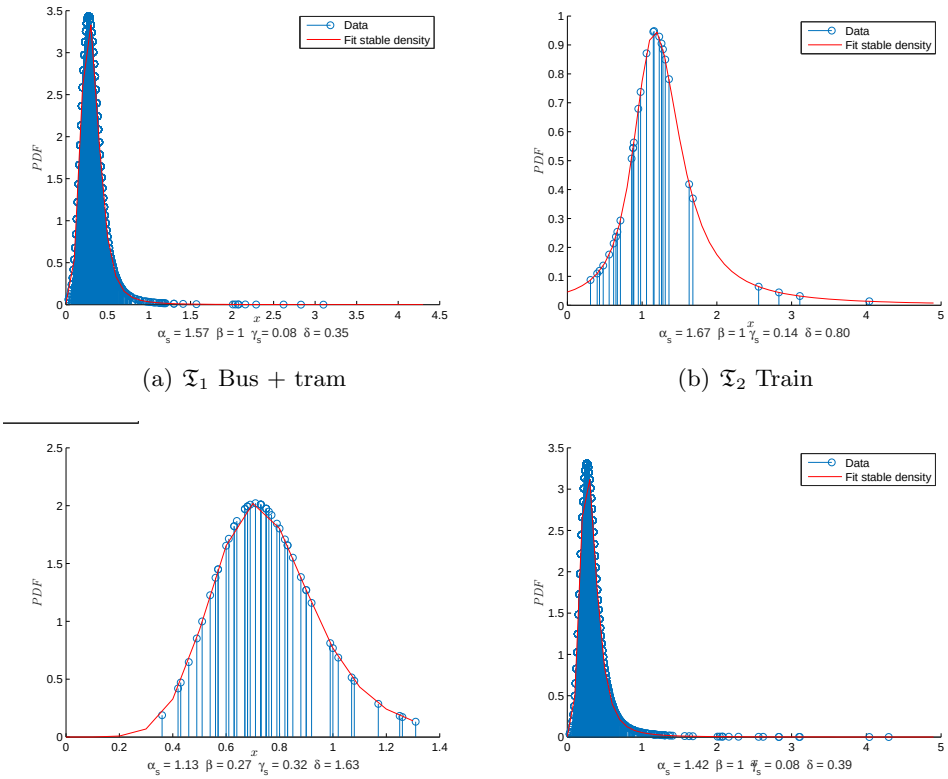

(a) $\mathfrak{T}_1$ Bus + tram

(b) $\mathfrak{T}_2$ Train

(c) $\mathfrak{T}_3$ Subway

(d) $\mathfrak{T}_4$ All the above

Figure 4. Fitted pdf for the inter-station distances in year 2015.

enhance the precision of the network approximation; include more means of transportation from surrounding municipalities that travel to and from Lisbon; apply the multiscaling allometric methods of [8] to confirm the results obtained on the evolution of the PTN with time.

References

[1] Comboios de Portugal. `https://pt.wikipedia.org/wiki/Comboios\_de\_Portugal`, 2016. Accessed in February.

[2] Google Maps. `https://www.google.pt/maps`, 2016. Accessed in February.

[3] Batty, M., and Longley, P. A. *Fractal cities: A geometry of form and function.* Academic Press, London, 1994.

[4] Benguigui, L., and Daoud, M. Is the suburban railway system a fractal? *Geographical Analysis 23*, 4 (1991), 362–368.

[5] Borak, S., Härdle, W., and Weron, R. *Stable Distributions*. Springer Berlin Heidelberg, Berlin, 2005.

[6] Carris. História da Carris. `http://carris.transporteslisboa.pt/pt/historia/`, 2016. Accessed in February.

[7] Chechkin, A. V., Metzler, R., Klafter, J., and Gonchar, V. Y. Introduction to the theory of Lévy flights. In *Anomalous Transport: Foundations and Applications*. Wiley, 2008, pp. 129–162.

[8] Chen, Y. Multi-scaling allometric analysis for urban and regional development. *Physica A: Statistical Mechanics and its Applications 465* (2017), 673–689.

[9] Cruz-Filipe, L. História das carreiras da Carris. `http://historiaccfl.webatu.com/`, 2013. Accessed in February.

[10] Feng, J., and Chen, Y. Spatiotemporal evolution of urban form and land-use structure in Hangzhou, China: Evidence from fractals. *Environment and Planning B: Planning and Design 37*, 5 (2010), 838–856.

[11] Frankhauser, P. Aspects fractals des structures urbaines. *Espace géographique 19*, 1 (1990), 45–69.

[12] Koutrouvelis, I. A. An iterative procedure for the estimation of the parameters of stable laws. *Communication in Statistics — Simulation and Computation 10*, 1 (1981), 17–28.

[13] Lu, Y., and Tang, J. Fractal dimension of a transportation network and its relationship with urban growth: A study of the Dallas-Fort Worth area. *Environment and Planning B: Planning and Design 31*, 6 (2004), 895–911.

[14] Machado, J. A. T. Fractional order generalized information. *Entropy 16*, 4 (2014), 2350–2361.

[15] Metropolitano de Lisboa. Cronologia do Metro. `http://metro.transporteslisboa.pt/empresa/um-pouco-de-historia/cronologia/`, 2016. Accessed in February.

[16] Schroeder, M. *Fractals, chaos, power laws: Minutes from an infinite paradise*. New York, 1991.

[17] Shannon, C. E. A mathematical theory of communication. *Bell Systems Technical Journal 27* (1948), 379–423, 623–656.

[18] Tannier, C., Thomas, I., Vuidel, G., and Frankhauser, P. A fractal approach to identifying urban boundaries. *Geographical Analysis 43*, 2 (2011), 211–227.

[19] Thomas, I., Frankhauser, P., and Biernacki, C. The morphology of built-up landscapes in Wallonia (Belgium): A classification using fractal indices. *Landscape and Urban Planning 84*, 2 (2008), 99–115.

[20] Ubriaco, M. R. Entropies based on fractional calculus. *Physics Letters A 373*, 30 (2009), 2516–2519.

[21] Valério, D., Lopes, A. M., and Machado, J. A. T. Entropy analysis of a railway network complexity. *Entropy 18*, 11 (2016), 388.

[22] Veillette, M. Alpha-stable distributions in MATLAB. `http://math.bu.edu/people/mveillet/html/alphastablepub.html`, 2016. Accessed in August.

[23] von Ferber, C., and Holovatch, Y. Fractal transit networks: Self-avoiding walks and Lévy flights. *The European Physical Journal Special Topics 216*, 1 (2013), 49–55.

[24] Wang, H., Luo, S., and Luo, T. Fractal characteristics of urban surface transit and road networks: Case study of Strasbourg, France. *Advances in Mechanical Engineering 9*, 2 (2017).

Duarte Valério, Ph.D.: IDMEC, Instituto Superior Técnico, Universidade de Lisboa, Av. Rovisco Pais 1, 1049-001 Lisboa, Portugal (*duarte.valerio@tecnico.ulisboa.pt*).

J.A. Tenreiro Machado, Ph.D.: Institute of Engineering, Polytechnic of Porto, Dept. of Electrical Engineering, Rua Dr. António Bernardino de Almeida, 431 4249-015 Porto, Portugal (*jtm@isep.ipp.pt*). The author gave a presentation of this paper during one of the conference sessions.

António M. Lopes, Ph.D.: UISPA - LAETA/INEGI, Faculty of Engineering, University of Porto, Rua Dr. Roberto Frias, 4200-465 Porto, Portugal (*aml@fe.up.pt*).

António Dinis F. Santos, M.Sc.: IDMEC, Instituto Superior Técnico, Universidade de Lisboa, Av. Rovisco Pais 1, 1049-001 Lisboa, Portugal (*antonio.f.santos@tecnico.ulisboa.pt*).

Analytical model of damaged circular membrane using a pseudo torus

Aleksandra Waszczuk-Młyńska, Stanisław Radkowski

Abstract: The presented analytical model shows the vibration analysis of a circular membrane with a damage located in its central part. The damage has a form of a hole. The model uses the general vibration differential equation of circular membrane; however, a torus has been used to describe the investigated object. The flat circular membrane with an opening in the centre was described by the surface of torus intersection with the plane created as a result of a rotation. A vital element is the fact that the radius r describing the torus circumference is a variable from within the range $(0,r_0)$. For a surface created in such a way, the Laplace operator has been computed, and as a result, the vibration equation for a new object. Next, the obtained second-order partial differential equation was computed using the Bessel substitution. To evaluate the damage, changes in natural frequencies were used.

1. Introduction

Vibration phenomena occurring in nature are very interesting because vibrations can be induced in every object and each of them has its intrinsic vibration frequency. This phenomenon can be used in various domains of life; one of the more absorbing applications is energy recovery [1], where a piezoelectric material is placed on the vibrating object. The piezoelectric material also works due to the object vibrations and in such a way, energy can be obtained. An even more interesting application of vibrations in view of this article is damage detection. Damage detection conducted in such a manner can be included among methods of Non-Destructive Testing, whose great advantage consists in obtaining information about the technical state (fit/not fit) in a way that does not interfere with the structure. Due to the damage, stiffness is changed, and therefore, also the modal quantities [2]. One of the parameters is the intrinsic vibration frequency, so observing and monitoring this value can enable damage detection [3,4,5]. Many coefficients help damage detection, e.g. the Damage Location Assurance Criterion (DLAC) [6] makes it possible identifying a single damage. The expansion of this method is the Multiple Damage Location Assurance Criterion (MDLAC) [7], indicating an even greater number of simultaneous damages.

In this article, the analytical model of the element described by the second order equation will be presented: i.e. of a circular membrane with the damage in a form of a hole located in its central part. The model will illustrate changes in the intrinsic vibration frequencies relative to the damage.

2. Analytical model

2.1. Vibrations of the circular membrane

Vibrations of the circular membrane are described by the formula [8]

$$\rho h\frac{\partial^2 w}{\partial t^2} - N\nabla^2 \mathrm{w} = \mathrm{p(x,y,t)} \tag{1}$$

$$w = w(x,y,t) \tag{2}$$

For the circular membrane, operations are performed in polar coordinates

$$w = w(r,\varphi,\mathrm{t}) \tag{3}$$

$$x = rcos\varphi\,,\ \mathrm{y} = \mathrm{r}\sin\varphi \tag{4}$$

Thus, the Laplace operator can be shown as follows

$$\nabla^2 = \frac{\partial^2}{\partial x^2} + \frac{\partial^2}{\partial y^2} = \frac{1}{r}\frac{\partial}{\partial r}r\frac{\partial}{\partial r} + \frac{1}{r^2}\frac{\partial^2}{\partial \varphi^2} = \frac{\partial^2}{\partial r^2} + \frac{1}{r}\frac{\partial}{\partial r} + \frac{1}{r^2}\frac{\partial^2}{\partial \varphi^2} \tag{5}$$

Equation (1) can be also rendered with the help of the formula:

$$\frac{\partial^2 w}{\partial t^2} - a^2\nabla^2 \mathrm{w} = \frac{1}{\rho h}\mathrm{p(r,\varphi,t)} \tag{6}$$

where:

$$a^2 = \frac{N}{\rho h} \tag{7}$$

N – force per circumference length unit, membrane tension

ρ - density

h – thickness

Taking into account the Laplace operator in the polar coordinates (5) allows for obtaining equation (8), the solution to which are the circular membrane intrinsic vibrations

$$\frac{\partial^2 w}{\partial r^2} + \frac{1}{r}\frac{\partial w}{\partial r} + \frac{1}{r^2}\frac{\partial^2 w}{\partial \varphi^2} - \frac{1}{a^2}\frac{\partial^2 w}{\partial t^2} = 0 \tag{8}$$

Under initial conditions

$$w(r_0,\varphi,t) = 0\,, w(0,\varphi,t) < \infty \tag{9}$$

$$w(r,\varphi,t) = w(r,\varphi+2\pi,t) \tag{10}$$

Equation (8) is computed by the method of separated variables – the Fourier method

$$w(r,\varphi,t) = R(r)\Phi(\varphi)T(t) \tag{11}$$

$$\begin{aligned} &\ddot{T}(t) + \omega^2 T(t) = 0 \\ &\Phi''(\varphi) + \mu^2\Phi(\varphi) = 0 \\ &R''(r) + \frac{1}{r}R'(r) + \left(\frac{\omega^2}{a^2} - \frac{\mu^2}{r^2}\right)R(r) = 0 \end{aligned} \tag{12}$$

As a result, two independent solutions are obtained:

$$w^{(1)}(r,\varphi,t) = \sum_{\substack{m=1\\n=0}} w_{mn}^{(1)}(r,\varphi,t) = \sum_{\substack{m=1\\n=0}} (A_{mn}\sin(\omega_{mn}t) + B_{mn}cos(\omega_{mn}t)J_n\left(\frac{\omega_{mn}}{a}r\right)\sin(n\varphi) \tag{13}$$

$$w^{(2)}(r,\varphi,t) = \sum_{\substack{m=1\\n=0}} w_{mn}^{(2)}(r,\varphi,t) = \sum_{\substack{m=1\\n=0}} (C_{mn}\sin(\omega_{mn}t) + D_{mn}cos(\omega_{mn}t)J_n\left(\frac{\omega_{mn}}{a}r\right)\cos(n\varphi) \tag{14}$$

Where: $J_n(x) = \sum_{k=0} \frac{(-1)^k(\frac{x}{2})^{2k+n}}{k!\Gamma(k+n+1)}$ - the Bessel function of the first kind the n-th order

While the intrinsic vibration frequency is described by the formula:

$$\omega_{mn} = \frac{x_{0mn}a}{r_0} = \frac{x_{0mn}}{r_0}\sqrt{\frac{N}{\rho h}} \tag{15}$$

x_{0mn} – zeros of the Bessel function

2.2. Analytical model of the damaged circular membrane

After the introduction to the differential equations of the second order shown above, the equation for the circular membrane with an opening in the centre (Fig.1) will be computed.

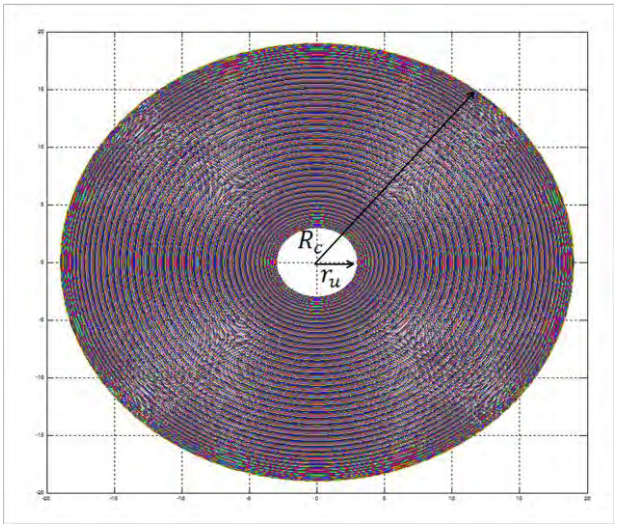

Figure 1. Circular membrane with an opening in the centre

In the considerations below, equation (6) is the starting point, as it was before, the difference consisting in the fact that the answer w = w(, ,r,t) is dependent on four variables, and this is for these new variables that the analytical model will be built. The new membrane model with an opening in the centre is built based on the torus, however, the applied torus is not empty but the radius r

describing the circle, whose rotation creates the torus is the variable $r \in (0, r_0)$, $r \in \mathbb{R}$, this is why the term "pseudo torus" has been used in the article title.

The torus (Fig.2) described by the formula (16), where R_0- is the rotation radius, and r_0 – radius of the circle, which is rotated.

$$\left(\sqrt{x^2 + y^2} - R_0\right)^2 + z^2 = {r_0}^2 \tag{16}$$

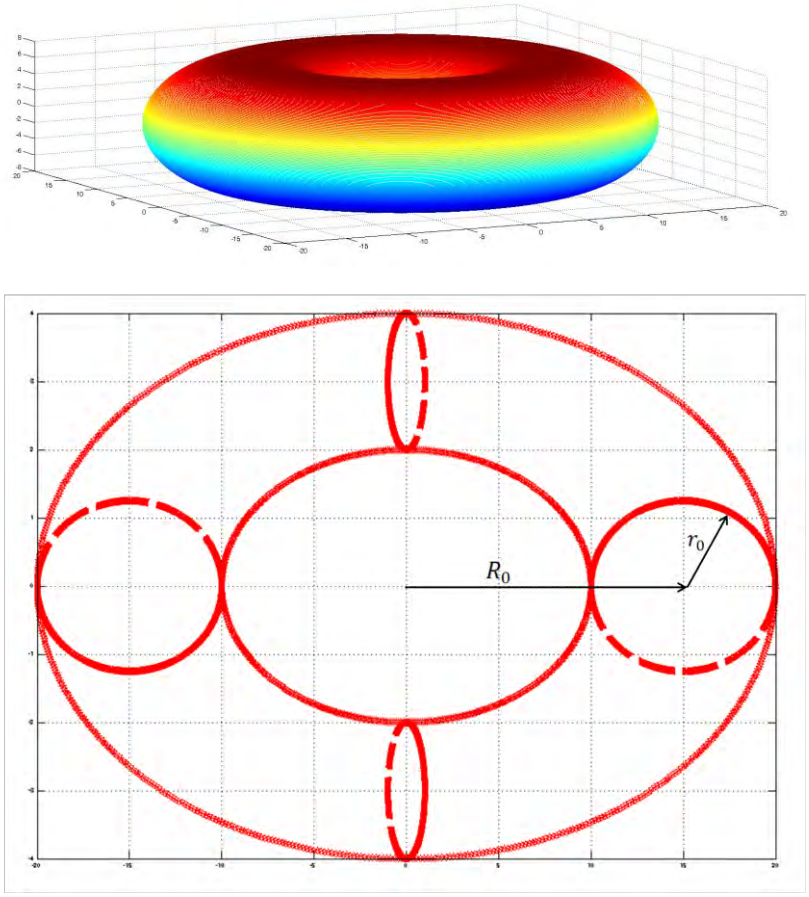

Figure 2. Torus

The tested object is a circular membrane, thus parameterisation of the torus into polar coordinates was conducted

$$\begin{aligned} x &= (R_0 + r cos\alpha) cos\beta \\ y &= (R_0 + r cos\alpha) sin\beta \\ z &= r sin\alpha \end{aligned} \tag{17}$$

For the further computations, the expressions: $r = r(x,y,z)$, $\alpha = \alpha(x,y,z), \beta = \beta(x,y,z)$ will be used, thus, after slight transformations of equations (17):

$$r = \sqrt{\left(\sqrt{x^2+y^2} - R_0\right)^2 + z^2}$$
$$\alpha = arcsin\frac{z}{r} = arcsin\frac{z}{\sqrt{\left(\sqrt{x^2+y^2}-R_0\right)^2+z^2}} \tag{18}$$
$$\beta = arctg\frac{y}{x}$$

The above relationships are differentiated after successive variables: x, y, z:

$$\frac{\partial r}{\partial x} = \frac{x\left(\sqrt{x^2+y^2}-R_0\right)}{\sqrt{x^2+y^2}\sqrt{\left(\sqrt{x^2+y^2}-R_0\right)^2+z^2}} = cos\alpha cos\beta$$
$$\frac{\partial r}{\partial y} = \frac{y\left(\sqrt{x^2+y^2}-R_0\right)}{\sqrt{x^2+y^2}\sqrt{\left(\sqrt{x^2+y^2}-R_0\right)^2+z^2}} = cos\alpha sin\beta$$
$$\frac{\partial r}{\partial z} = \frac{z}{\sqrt{\left(\sqrt{x^2+y^2}-R_0\right)^2+z^2}} = sin\alpha$$
$$\frac{\partial \alpha}{\partial x} = \frac{-x\left(\sqrt{x^2+y^2}-R_0\right)\cdot z}{\sqrt{x^2+y^2}\left(\left(\sqrt{x^2+y^2}-R_0\right)^2+z^2\right)^{\frac{3}{2}}\sqrt{1-\frac{z^2}{\left(\sqrt{x^2+y^2}-R_0\right)^2+z^2}}} = -\frac{sin\alpha cos\beta}{r}$$
$$\frac{\partial \alpha}{\partial y} = \frac{-y\left(\sqrt{x^2+y^2}-R_0\right)\cdot z}{\sqrt{x^2+y^2}\left(\left(\sqrt{x^2+y^2}-R_0\right)^2+z^2\right)^{\frac{3}{2}}\sqrt{1-\frac{z^2}{\left(\sqrt{x^2+y^2}-R_0\right)^2+z^2}}} = -\frac{sin\alpha sin\beta}{r} \tag{19}$$
$$\frac{\partial \alpha}{\partial z} = \frac{\left(\sqrt{x^2+y^2}-R_0\right)^2}{\left(\left(\sqrt{x^2+y^2}-R_0\right)^2+z^2\right)^{\frac{3}{2}}\sqrt{1-\frac{z^2}{\left(\sqrt{x^2+y^2}-R_0\right)^2+z^2}}} = \frac{cos\alpha}{r}$$
$$\frac{\partial \beta}{\partial x} = \frac{-y}{x^2+y^2} = \frac{-sin\beta}{R_0+rsin\alpha}$$
$$\frac{\partial \beta}{\partial y} = \frac{x}{x^2+y^2} = \frac{cos\beta}{R_0+rsin\alpha}$$
$$\frac{\partial \beta}{\partial z} = 0$$

In the Laplace operator formula, there is a sum of second partial derivatives, hence from the formula describing partial derivatives of the complex function, the following can be obtained

$$\frac{\partial f}{\partial x} = \frac{\partial f}{\partial r}\cdot\frac{\partial r}{\partial x} + \frac{\partial f}{\partial \alpha}\cdot\frac{\partial \alpha}{\partial x} + \frac{\partial f}{\partial \beta}\cdot\frac{\partial \beta}{\partial x}$$
$$\frac{\partial^2 f}{\partial x^2} = \frac{\partial}{\partial x}\left(\frac{\partial f}{\partial x}\right) = cos^2\beta\frac{\partial^2 f}{\partial r^2} + \frac{sin^2\beta}{R_0}\frac{\partial f}{\partial r} - 2\frac{sin\beta cos\beta}{R_0}\frac{\partial^2 f}{\partial r\partial\beta} + \frac{sin^2\beta}{R_0^2}\frac{\partial^2 f}{\partial \beta^2} + \frac{sin\beta cos\beta}{R_0^2}\frac{\partial f}{\partial \beta}$$
$$\frac{\partial f}{\partial y} = \frac{\partial f}{\partial r}\cdot\frac{\partial r}{\partial y} + \frac{\partial f}{\partial \alpha}\cdot\frac{\partial \alpha}{\partial y} + \frac{\partial f}{\partial \beta}\cdot\frac{\partial \beta}{\partial y} \tag{20}$$

$$\frac{\partial^2 f}{\partial y^2} = \frac{\partial}{\partial y}\left(\frac{\partial f}{\partial y}\right) = sin^2\beta \frac{\partial^2 f}{\partial r^2} + \frac{cos^2\beta}{R_0}\frac{\partial f}{\partial r} + 2\frac{sin\beta cos\beta}{R_0}\frac{\partial^2 f}{\partial r \partial \beta} + \frac{cos^2\beta}{R_0^2}\frac{\partial^2 f}{\partial \beta^2} - \frac{sin\beta cos\beta}{R_0^2}\frac{\partial f}{\partial \beta}$$

$$\frac{\partial f}{\partial z} = \frac{\partial f}{\partial r}\cdot\frac{\partial r}{\partial z} + \frac{\partial f}{\partial \alpha}\cdot\frac{\partial \alpha}{\partial z} + \frac{\partial f}{\partial \beta}\cdot\frac{\partial \beta}{\partial z}$$

$$\frac{\partial^2 f}{\partial z^2} = \frac{\partial}{\partial z}\left(\frac{\partial f}{\partial z}\right) = \frac{cos^2\alpha}{r}\frac{\partial f}{\partial r}$$

Out of a solid pseudo torus, a fragment is used for computations, and more precisely, it is a surface included within the plane of radius revolution, thus the solution to the task will be the sum of solutions in two cases, when $\alpha = 0$ i $\alpha = \pi$:

1. for $\alpha = 0$ the Laplace operator is expressed as follows:

$$\Delta f = \nabla^2 f = \frac{\partial f^2}{\partial x^2} + \frac{\partial f^2}{\partial y^2} + \frac{\partial f^2}{\partial z^2} = \frac{\partial^2 f}{\partial r^2} + \left(\frac{1}{r} + \frac{1}{R_0}\right)\frac{\partial f}{\partial r} + \frac{1}{R_0^2}\frac{\partial^2 f}{\partial \beta^2} \tag{21}$$

Hence, equation (6) taking the new Laplace operator into account has the form:

$$\frac{\partial^2 w}{\partial r^2} + \left(\frac{1}{r} + \frac{1}{R_0}\right)\frac{\partial w}{\partial r} + \frac{1}{R_0^2}\frac{\partial^2 w}{\partial \beta^2} - \frac{1}{a^2}\frac{\partial^2 w}{\partial t^2} = 0 \tag{22}$$

2. for $\alpha = \pi$

$$\Delta f = \nabla^2 f = \frac{\partial f^2}{\partial x^2} + \frac{\partial f^2}{\partial y^2} + \frac{\partial f^2}{\partial z^2} = \frac{\partial^2 f}{\partial r^2} + \left(\frac{1}{r} - \frac{1}{R_0}\right)\frac{\partial f}{\partial r} + \frac{1}{R_0^2}\frac{\partial^2 f}{\partial \beta^2} \tag{23}$$

Inserting the above Laplace operator (23) into the equation of the membrane motion equation, the following is obtained:

$$\frac{\partial^2 w}{\partial r^2} + \left(\frac{1}{r} - \frac{1}{R_0}\right)\frac{\partial w}{\partial r} + \frac{1}{R_0^2}\frac{\partial^2 w}{\partial \beta^2} - \frac{1}{a^2}\frac{\partial^2 w}{\partial t^2} = 0 \tag{24}$$

Boundary conditions for the circular membrane with an opening in its centre are as follows:

$$w(r_0, \beta, t) = 0 \; dla \; \propto = 0 \tag{25}$$

$$w_{\propto=0}(0, \beta, t) = w_{\propto=\pi}(0, \beta, t) \tag{26}$$

Equations (22) and (24) will be computed by means of the separated variable method, as was performed before

$$w(r, \beta, t) = R(r)B(\beta)T(t)$$

$$\ddot{T}(t) + \omega^2 T(t) = 0 \tag{27}$$

$$B\ (\beta) + \mu^2 B(\beta) = 0 \tag{28}$$

$$R\ (r) + \left(\frac{1}{r} + \frac{1}{R_0}\right)R\ (r) + \left(\frac{\omega^2}{a^2} - \frac{\mu^2}{R_0^2}\right)R(r) = 0 \qquad \text{dla} \propto = 0 \tag{29}$$

$$R\ (r) + \left(\frac{1}{r} + \frac{1}{R_0}\right)R\ (r) + \left(\frac{\omega^2}{a^2} + \frac{\mu^2}{R_0^2}\right)R(r) = 0 \qquad \text{dla} \propto = \pi \tag{30}$$

The solution to the first two equations (27) and (28) is commonly known, this is why the attention will be focused on equation (29) and, for the second case, equation (30).

In the beginning, equation (29) will be solved with the use of the substitution method. For this purpose, the sought integral will be left in the form of a series:

$$R(r) = \sum_{k=0} a_k r^{m+k} \tag{31}$$

This is the Bessel substitution [9].

m – is a temporary unknown

Series (31) is differentiated twice, term after term:

$$R\,(r) = \sum_{k=0} a_k (m+k) r^{m+k-1} \tag{32}$$

$$R\;(r) = \sum_{k=0} a_k (m+k)(m+k-1) r^{m+k-2} \tag{33}$$

Additionally, constants are introduced for the sake of the calculus simplicity:

$$\frac{\omega^2}{a^2} - \frac{\mu^2}{R_0^2} = c = const \tag{34}$$

$$\frac{1}{R_0} = c \; = const \tag{35}$$

As a result of substitution, we obtain:

$$\sum_{k=0} a_k (m+k)(m+k-1) r^{m+k-2} + c \sum_{k=0} a_k (m+k) r^{m+k-1} + \sum_{k=0} a_k (m+k) r^{m+k-2} + c \sum_{k=0} a_k r^{m+k} = 0$$

$$\sum_{k=0} a_k (m+k)^2 r^{m+k-2} + c \sum_{k=1} a_k (m+k) r^{m+k-2} + c \sum_{k=2} a_k r^{m+k-2} = 0$$

Equation is true when the sum of coefficients with the same powers is equal to zero, therefore, the following conditions take place:

$$a_0 m = 0$$

$$a_1 (m+1)^2 + c a_0 (m+1) = 0 \tag{36}$$

$$a_k (m+k)^2 + c a_{k-1} (m+k) + c\, a_{k-2} = 0$$

The first equation results in two possibilities:

1. $a_0 \neq 0\,, m = 0$
2. $a_0 = 0\,,$

Case 1.

$$a_0 \neq 0\,, m = 0$$

$$a_1 = -c a_0 \tag{37}$$

$$a_k = \frac{-cka_{k-1} - c\, a_{k-2}}{k^2}$$

Case 2.

$$a_0 = 0$$

$$a_1 (m+1)^2 = 0$$

$$m = -1 \tag{38}$$

$$a_k (k-1)^2 + c a_{k-1} (k-1) + c\, a_{k-2} = 0$$

$$a_k = \frac{-c(k-1)a_{k-1} - c\, a_{k-2}}{(k-1)^2}$$

In this case, the same solution is obtained as before, with one difference however, that k begins from 1, and not from zero, as in case 1, which does not affect the final result, so consideration of case 1 is sufficient.

Taking into account the above recursion – of equation (37), an attempt was made to compute the coefficient a_k, but unfortunately the final formula was impossible to compute, apart from the first expressions.

$$a_k = (-1)^k \left(\frac{c^k k!}{(k!)^2} - \frac{c^{k-2} c}{(k!)^2} \sum_{i=1}^{k-1} \frac{k! i}{i+1} + \frac{c^{k-4} c^2}{(k!)^2} \sum - \dots \right) a_0 \tag{39}$$

From the boundary conditions of equation (26), the relationship follows

$$a_{0\ for \propto=0} = a_{0\ for \propto=\pi} \tag{40}$$

And from the condition (25) results, that series (41) is converging to zero.

$$\lim_{m\to\infty} \sum_{k=1}^{m} \frac{a_k}{a_0} = \lim_{m\to} \sum_{k=1}^{m} ((-1)^k \left(\frac{c^k k!}{(k!)^2} - \frac{c^{k-2} c}{(k!)^2} \sum_{i=1}^{k-1} \frac{k! i}{i+1} + \frac{c^{k-4} c^2}{(k!)^2} \sum - \dots \right) = 0 \tag{41}$$

By means of equating the series (41) to zero, $c = \frac{\omega^2}{a^2} - \frac{n^2}{R_0^2}$ can be computed for $\propto= 0$ and due to this, ω can be described by the formula:

$$\omega_n = \sqrt{ca^2 + \frac{n^2 a^2}{R_0^2}} \qquad for\ n = 1,2,3, \dots \tag{42}$$

Whereas for $\propto= \pi$, c equals: $c = \frac{\omega^2}{a^2} + \frac{n^2}{R_0^2}$, and as a result:

$$\omega_n = \sqrt{ca^2 - \frac{n^2 a^2}{R_0^2}} \qquad for\ n = 1,2,3, \dots \tag{43}$$

In this case, ω_n is an imaginary number, and for analyses conducted in diagnostics, only the real part is interesting, this is why an example will focus only on computing ω_n for $\propto= 0$.
Further computations will be performed using the Matlab programme.

3. Example

In this part of the article, an example will be discussed illustrating the results of the abovementioned model. Based on the real data, two models of a circular membrane will be compared, one – with the undamaged membrane, the other – with the damage in the central part of the membrane. With an assumption that:

N=50 N/m – force per circumference length unit, membrane tension

$\rho = 850 kg/m^3$ - density

h=0,001 m – membrane thickness

coefficient a=7,67

$R_c = 0.127$ m – membrane radius

The table below shows the frequency relationships for the undamaged membrane and the damaged one, where the damage has the form of a hole in the central part of the membrane.

Tab.1

	Not damaged	Damaged		
		r_u=1mm	r_u=2mm	r_u=5mm
I postać	125,8 Hz	124,9 Hz	124 Hz	121,4 Hz
II postać	244,1 Hz	242,2 Hz	240,4 Hz	235,1 Hz

4. Conclusions

Frequencies in the undamaged membrane are higher than in the membrane with a damage in the form of a circular hole in the middle. The longer the radius of the circular damage, the smaller the frequencies. The reason behind such a state can be the change in the membrane tension, formulas (42) and (7).

Slight variations in the force of the membrane tension change the frequency, thus it is not the best solution to be applied in the diagnostics of such systems because the membrane tension can change over time, even if there is no damage at all.

References

[1] Waszczuk-Młyńska, A., Radkowski, S. *About a certain way of the membrane kinetic energy transformation into electric energy*. Progress in Automation, Robotics and Measuring Techniques Volume 3 Measuring Techniques and Systems / Szewczyk Roman, Zieliński Cezary, Kaliczyńska Małgorzata (*red.*), Advances in Intelligent Systems and Computing, vol. 352, 2015, Springer, ISBN 978-3-319-15834-1, ss. 303-312.

[2] Żółkowski B. *Badanie dynamiki maszyn*, MARKAR, Bydgoszcz 2002

[3] Farrar C.R., Doebling S.W., *An Overview of modal-based damage identification methods*, Proceedeings of DAMAS Conference, Sheffield, UK, June, 1997.

[4] Cawley P., Adams R.D., *The locations of defects in structures from measurements of natural frequencies*, Journal of Strain Analysis, 14 (2),pp.49-57,1979.

[5] Friswell M.I., Penny J.E.T.,Wilson D.A.L*., Using vibration data and statistical measuresto locate damage in structures*, Model Analysis, 9(4),pp.239-254,1994.

[6] Messina A., Jones I.A., Williams E.J., *Damage detection and localization using natural frequency changes*, Proceedings of Conference on Identification in Engineering Systems, Swansea, UK, pp. 56-65, 1996.

[7] Messina A., Williams E.J., Contursi T., *Structural Damage Detection by a Sensitivity and Statistical-Based Method*, Journal of Sound and Vibration, 2016(5), pp.791-808, 1998.

[8] Kaliski S. pod redakcją, *Mechanika Techniczna tom III ,Drgania i fale*, PWN, Warszawa 1986, str.227-235

[9] Żakowski W., Leksiński W., *Matematyka część IV*, Wydawnictwo naukowo-techniczne, Warszawa 1973, str.88-93

Aleksandra Waszczuk-Młyńska, M.Sc. (Ph.D. student): Warsaw University of Technology, Faculty of Automotive and Construction Machinery Engineering, Vehicle Institute, Narbutta St. 84, 02-524, Warsaw, Poland (*awm@simr.pw.edu.pl*).

Stanisław Radkowski, Professor: Warsaw University of Technology, Faculty of Automotive and Construction Machinery Engineering, Vehicle Institute, Narbutta St. 84, 02-524,Warsaw, Poland (*ras@ simr.pw.edu.pl*).

Numerical crash analysis of the cable barrier

Krzysztof Wilde, Dawid Bruski, Stanisław Burzyński, Jacek Chróścielewski, Wojciech Witkowski

Abstract: Safety barriers are used to increase road safety. Their basic task is to prevent the errant vehicle from getting off the road in places which are potentially dangerous for vehicle passengers. Barriers, which are used on European roads, must fulfill the requirements of EN 1317 standards by passing appropriate crash tests. Because of their high cost, numerical simulations are increasingly used to evaluate the properties of safety barriers, especially in the early stages of the barrier design or in the modifications of existing ones. Simulations allow for a detailed insight into the impact mechanism and their cost are much lower compared to real crash tests. Since the crash phenomenon is a dynamic process and the duration of vehicle-barrier contact is short, numerical simulations are performed using explicit dynamics algorithm. The most popular is commercial FEM system LS-DYNA. In this study the numerical simulation of cable barrier crash test using 900 kg vehicle (TB11 test) and 13 000 kg bus (TB51) were carried out. The results of TB51 test were compared with the results obtained from real crash test. Additionally, the influence of friction coefficient value on the results was analyzed.

1. Introduction

The number of vehicles on the road is still increasing. Particular attention should be paid to ensuring the safety of all road users. One of the safety measures are road barriers. They should be located in every place, where leaving the lane by the vehicle is potentially dangerous for passengers. Their main task is to prevent the errant vehicle from getting to the opposite lane of the road (this situation is especially dangerous and is called cross median crashes) or before getting off the road and hitting the obstacle such as trees or bridge abutments. They have to contain and properly redirect vehicles back on vehicle's traveled way. Additionally the barrier must also reduce the negative effects on the occupants and minimalize vehicle's damages. The main types of safety barriers, as far as the construction material is concerned, can be classified as: steel rail barriers, cable barriers and concrete barriers.

Cable barriers are beneficial construction in terms of road safety. Unlike other barriers, they usually provide small decelerations for people inside the vehicle during the collision, preventing them from serious injuries. Cable barriers are relatively inexpensive and easy to install, maintenance and repair after impact. Among the other benefits it should be noted, that they do not impede snow plowing operations [3].

To make sure that barriers provide an appropriate level of protection to road users, they have to undergo full scale crash tests according to EN 1317 standards [6], [7] before they are approved for general use. Nowadays, numerical simulations are increasingly used to evaluate the properties of road barriers, particularly in the early stages of the barrier design or in the modifications of existing ones. Simulations allow for a detailed insight into the impact mechanism and to consider many factors (e.g. change of impact velocity or angle). The great advantage is that their cost are much lower compared to full scale crash tests.

In this work the results of the numerical simulation of cable barrier TB11 test and TB51 test were presented. The TB51 test was compared with the results obtained from real crash test.

2. EN 1317 Standards

Safety barriers, which are used on European roads, must fulfill the requirements of EN 1317 standards [6], [7] by passing appropriate crash tests. Depending on the test, the impact velocity, impact angle, total mass and type of vehicle are varied. Table 1 show impact test criteria.

Table 1. Vehicle impact test descriptions. [7]

Test	Impact speed, km/h	Impact angle, °	Total mass, kg	Type of vehicle
TB11	100	20	900	Car
TB21	80	8	1 300	Car
TB22	80	15	1 300	Car
TB31	80	20	1 500	Car
TB32	110	20	1 500	Car
TB41	70	8	10 000	Rigid HGV
TB42	70	15	10 000	Rigid HGV
TB51	70	20	13 000	Bus
TB61	80	20	16 000	Rigid HGV
TB71	65	20	30 000	Rigid HGV
TB81	65	20	38 000	Articulated HGV

Based on the results of the crash tests, three functional characteristics of safety barrier are determined: containment level, working with and impact severity level. Containment level determines the ability of the barrier to contain impacting vehicle. Four containment levels were defined, as show in table 2. The working with is used to describe barrier's ability to deformation during collision and is defined as the maximum lateral distance between any part of the barrier on the undeformed traffic side and the maximum dynamic position of any part of the barrier or vehicle if vehicle body deforms around

barrier. Impact severity level is used to evaluate impact effects for the vehicle occupants. Two indicators, the acceleration severity index (ASI) and the theoretical head impact velocity (THIV) are needed to injury-risk assessment. It should be noted that the mentioned standards do not specify conditions for barrier's geometry, dimensions or materials.

The acceleration severity index (ASI) is one of the most important parameters which allows for assessment of the injuries of occupants during impact. ASI is a function of time, computed using the following equation

$$\mathrm{ASI}(t) = \sqrt{\left(\frac{\bar{A}_x}{\hat{a}_x}\right)^2 + \left(\frac{\bar{A}_y}{\hat{a}_y}\right)^2 + \left(\frac{\bar{A}_z}{\hat{a}_z}\right)^2} \tag{1}$$

where $\bar{A}_x$, $\bar{A}_y$, $\bar{A}_z$ are the components of the acceleration recorded at the center of gravity of the vehicle which are filtered with a four-pole phaseless Butterworth low-pass digital filter with the cut-off frequency of 13 Hz, $\hat{a}_x$ = 12 g, $\hat{a}_y$ = 9 g, $\hat{a}_z$ = 10 g are limit values for the acceleration components along the body axes *x*, *y* and *z* (g=9,81 m/s^2). The maximum value of the ASI in collision is assumed as a measure of severity. In general, the greater the ASI value, the greater the risk of vehicle occupants injuries. The theoretical head impact velocity (THIV) value is impact speed of the theoretical head with theoretical surfaces inside vehicle during collision. The occupant is considered to be a freely moving theoretical head which has the same speed at the beginning of the impact as the vehicle. Then, the vehicle due to the contact with road restraint system rotates about vertical axis, but the theoretical head continues his move in a straight line until it strikes theoretical surface within the interior of the vehicle.

According to the [8] standard, there is a possibility to evaluate barrier system, which has been modified by computer simulation. This standard defines three categories of modifications of existing barriers systems. In category A (slight change) modifications do not require mechanical changes (e.g. repainting). In category B (moderate change) modifications concern at least one barriers components (e.g. reduced section length between anchorages in cable barrier). For this category, the influence of modifications on the behavior of the barrier may be determined by numerical calculations. For category C (significant change) modifications excess the range of the categories A and B. To obtain certification of the modified product based on numerical simulation, it is necessary to perform the numerical model of the original barrier system, which was certified in real crash test. This model must properly undergo the validation process based on the results obtained from full scale crash test. Afterwards, in this model can be made modifications within the category B and perform numerical calculations on the basis of which the modified product will be certified. This approach reduces the number of expensive crash tests. Calculations where computers models were used should be confirmed by independent third party.

Table 2. Containment levels. [7]

Containment levels		Acceptance test
Low angle containment	T1	TB21
	T2	TB22
	T3	TB41, TB21
Normal containment	N1	TB31
	N2	TB32, TB11
Higher containment	H1	TB42, TB11
	L1	TB42, TB32, TB11
	H2	TB51, TB11
	L2	TB51, TB32, TB11
	H3	TB61, TB11
	L3	TB61, TB32, TB11
Very high containment	H4a	TB71, TB11
	L4a	TB71, TB32, TB11
	H4b	TB81, TB11
	L4b	TB81, TB32, TB11

Table 3. Normalised working width. [7]

Classes of normalized working width levels	Levels of normalized working width, m
W1	$W_N \leq 0.6$
W2	$W_N \leq 0.8$
W3	$W_N \leq 1.0$
W4	$W_N \leq 1.3$
W5	$W_N \leq 1.7$
W6	$W_N \leq 2.1$
W7	$W_N \leq 2.5$
W8	$W_N \leq 3.5$

Table 4. Impact severity [7]

Impact severity levels	ASI, -	THIV, km/h
A	≤ 1.0	≤ 33
B	≤ 1.4	≤ 33
C	≤ 1.9	≤ 33

3. Numerical model of cable barrier impact test

The calculations were performed by using finite element code of LS-DYNA (MPP double precision R8.1.0) on supercomputer Tryton managed by CI TASK in Gdańsk (Poland). Figure 1 shows the time of the calculations, which is needed to perform 0.5 s simulation of the one of TB51 cable barrier crash test, depending on the numbers of 24-core processors. Based on this analysis it was decided that each simulation would be carried out by using 192 threads (eight 24-core processors).

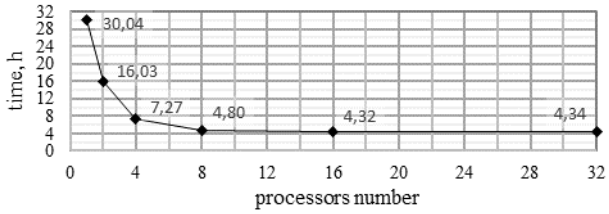

Figure 1. The scalability of 0,5 s TB51 calculations.

To integrate the equations of motion LS-DYNA system uses explicit scheme of special form of central difference method [1] [2]. Nonlinear equation of motion discretized by FEM reads:

$$\boldsymbol{M}\ddot{\boldsymbol{x}}^n = \boldsymbol{r}^n - \boldsymbol{f}^n - \boldsymbol{h}^n \tag{2}$$

where $\boldsymbol{M}$ is the diagonal global mass matrix, $\boldsymbol{r}^n$ is the vector of external loads, $\boldsymbol{f}^n$ is the vector of internal loads and damping and $\boldsymbol{h}^n$ denotes the vector of some kind forces resulting from hourglass control. To update vectors $\dot{\boldsymbol{x}}$ and $\ddot{\boldsymbol{x}}$ the following formulas are used:

$$\ddot{\boldsymbol{x}}^n = \boldsymbol{M}^{-1}(\boldsymbol{r}^n - \boldsymbol{f}^n - \boldsymbol{h}^n), \tag{3}$$

$$\dot{\boldsymbol{x}}^{n+\frac{1}{2}} = \dot{\boldsymbol{x}}^{n-\frac{1}{2}} + \Delta t_n \ddot{\boldsymbol{x}}^n, \tag{4}$$

$$\boldsymbol{x}^{n+1} = \boldsymbol{x}^n + \Delta t_{n+\frac{1}{2}} \dot{\boldsymbol{x}}^{n+\frac{1}{2}}, \tag{5}$$

$$\Delta t_{n+\frac{1}{2}} = \frac{1}{2}(\Delta t_n + \Delta t_{n+1}). \tag{6}$$

In the above formulas the superposed dot represents time derivative.

3.1. Numerical model of cable barrier

Numerical model of road safety barrier (Fig. 2) consists of four 3x7 steel wire ropes (19 mm diameter) mounted on steel posts with slit for wire ropes. Distance between each cable is kept by plastic elements. Between the top ropes (numbers 3 and 4 on Fig. 2) there is a steel clamp. The spacing of the posts is 750 mm. The wire ropes are at a height of 480, 560, 640 and 720 mm above the ground. Length of the barrier is 69 m and it has two 6 m terminals, so the total length of the system is 81 m. The height of the

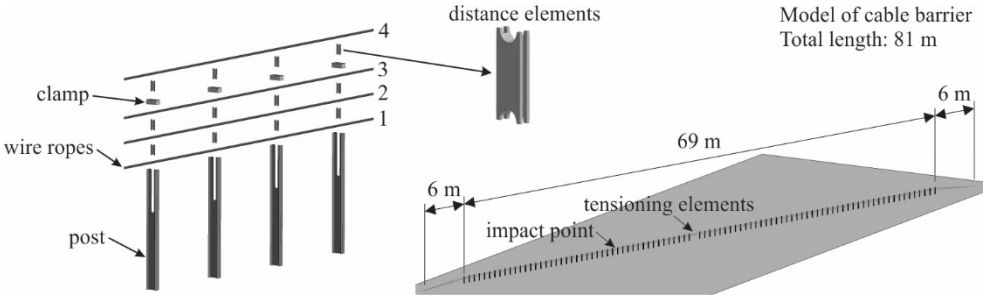

Figure 2. Cable barrier model

barrier is 777.5 mm. Numerical model of the barrier consist of 472 401 nodes and 958 843 finite elements.

To discretize the posts the shell elements of Belytschko-Tsay type are used (formulation ELFORM=2). Posts material is assigned as MAT_PIECEWISE_LINEAR_PLASTICITY. The characteristic dimensions of the elements are 8-10 mm. The plastic elements are represented by solid elements (characteristic dimensions ~4 mm) with material model MAT_ELASTIC. The wire rope model consists of 3 components (Fig. 3): beam elements, shell tube with hexagonal cross section around the beam elements, and CONSTRAINED_NODAL_RIGID_BODY, compare [4] [11]. The beam elements (the length of a single element is 75 mm) are assigned the Belytschko-Schwer formulation (ELFORM 2) and are defined with MAT_MOMENT_CURVATURE_BEAM material. Based on [11] the force-strain, bending moment-bending curvature and torque-rate of twist curves (Fig. 4) are implemented. The shell around the beams is defined with MAT_NULL material and is used only to describe the contact of the wire rope with the remaining parts of the model. The wire ropes in the cable barrier are pretensioned to 20.4 kN like in real crash test. The tensioning element was located in the middle of the barrier, between the posts no. 45 and no. 46. The spacing between these posts is 1500 mm. To perform pretension the beam element with discrete cable formulation and with MAT_CABLE_DISCRETE_BEAM material was defined.

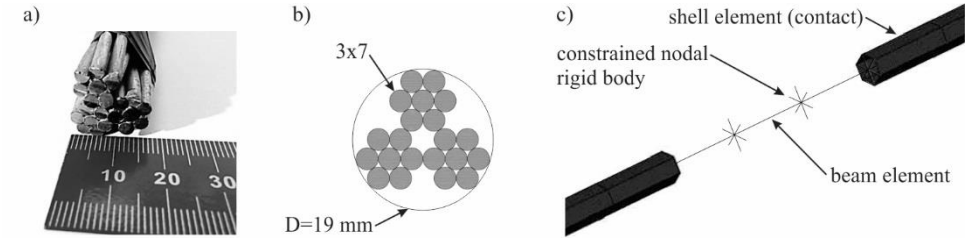

Figure 3. The wire rope: a) photo, b) cross sections, c) numerical model.

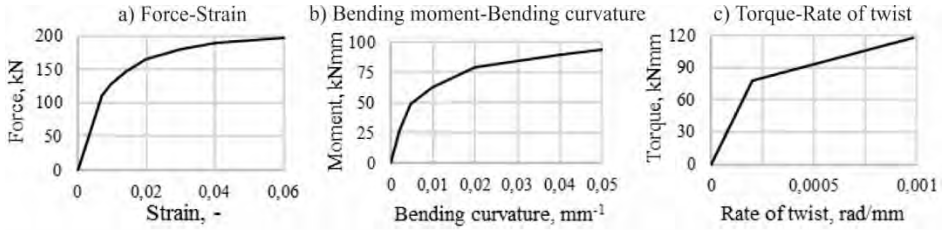

Figure 4. Curves: a) force-strain, b) bending moment-bending curvature, c) torque-rate of twist.

During a collision when the vehicle impacts barrier, the posts are bent towards the ground and the wire ropes should easily detach from them [3]. Since the main task of the posts is to keep the wire ropes on the right height and then easy detach them, simplified way of modeling the ground is used, which was modeled by fixing all degrees of freedom at the base of the posts, 90 mm below ground level.

3.2. Numerical models of vehicles

Numerical model of Bus (Fig. 5b), which was used in TB51 test, consist of 125 327 nodes and 128 485 finite elements and its weight is 12 971.8 kg. In the bus model there are three accelerometers: in front, in the middle (center of gravity) and in the rear of the vehicle. Bus model was developed by Norwegian Public Road Administration (www.vegvesen.no). The use of the model is gratefully acknowledged here.

In the numerical simulations of the TB11 test the Geo Metro (Suzuki Swift) numerical model was used (Fig. 5a). This model was obtained from ROBUST project repository [10] and subjected to minor modifications: improved wheel alignment, some numeric parameters have been modified and discretization has been densified in the important vehicle areas, which contact with the barrier. The weight of the car is 928.7 kg, consist of 20 089 nodes and 16 291 finite elements. The car is equipped with one accelerometer located near the center of gravity.

The accelerometers in these vehicles is realized by using special finite element and ELEMENT_SEATBELT_ACCELEROMETER card. This solution allows to record accelerations and angular velocities in local vehicle coordinate system which are needed to calculate ASI and THIV.

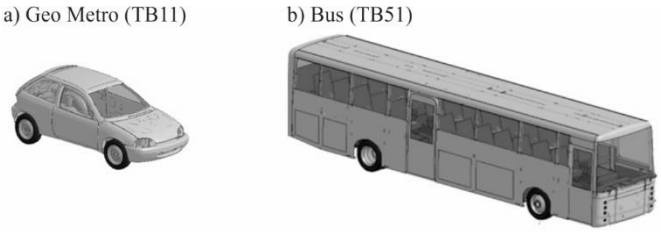

Figure 5. Numerical model of a) Geo Metro (TB11 test), b) Bus (TB51 test).

3.3. Numerical models of impact test

Numerical simulation of collision with the cable barrier with parameters corresponding to TB51 and TB11 standard tests were conducted. The TB51 test consist in total of 597 728 nodes and 1 087 328 elements and TB11 test has 492 490 nodes and 975 134 elements. Ground surface is defined using RIGIDWALL_PLANAR card. The friction coefficient between the tires and the ground is set to 0.3 [12].

To eliminate zero-energy modes the stiffness form of type 2 (Flanagan-Belytschko) in LS-DYNA is used, with value of the hourglass coefficient (QH) set to 0.03.

Contact was defined using the AUTOMATIC_GENERAL and AUTOMATIC_SINGLE_SURFACE cards. In the models one global Columb friction coefficient was used. This approach was used in many works, including [5] [9] [12] [13] [14] [15]. In LS-DYNA [1] the friction coefficient is given by the formula:

$$\mu = \mu_d + (\mu_s - \mu_d)e^{-c|v|} \tag{7}$$

where μ_d is the dynamic coefficient of friction, μ_s is the static coefficient of friction, c denotes a decay constant and $v = \Delta e/\Delta t$, where Δe is the incremental movement of the slave node and Δt is the time step. It is worth to notice, that when c = 0 or $\mu_s = \mu_d$, the equations (7) is reduced to the form:

$$\mu = \mu_s. \tag{8}$$

In publications and in available opensource models, different friction coefficients are used. A short summary of some values is shown in the table 5.

Table 5. Summary of friction coefficients used in publications and models.

Authors and publications	μ_s	μ_d	c
Ren, Z., Vesenjak, M., [9]	0.1	0.05	no data
Vesenjak, M., Ren, Z., [13]	0.1	0.05	no data
Teng T., Liang C., Tran T., [12]	0.15	0.09	$2.66 \cdot 10^{-4}$
Nasution, R. P., Siregar, R. A., Fuad, K., Adom, A. H., [5]	0.1	0.1	no data
File Cable.k, [4]	0.2 (0.4)*	0.1	0.001

* 0,4 in one contact, in others static friction coefficient is 0,2

Two numerical simulations of TB51 test and five TB11 test were conducted. The impact location is the same as in the real crash test, between the posts no. 30 and no. 31. The dynamic friction coefficient μ_d has been assumed as equal to 0.1 and decay constant c as equal to 0.001. The static friction coefficient μ_s was set to 0.1 and 0.3 in TB51 test and from 0.0 to 0.4 every 0.1 in TB11 test. The final values and nomenclatures of the simulation tests are summarized in table 6.

Table 6. Friction coefficients and simulation nomenclatures.

Test	μ_s	μ_d	c	nomenclature
TB51	0.1	0.1	0.001	tb51_01
TB51	0.3	0.1	0.001	tb51_03
TB11	0.0	0.0	0.0	tb11_00
TB11	0.1	0.1	0.001	tb11_01
TB11	0.2	0.1	0.001	tb11_02
TB11	0.3	0.1	0.001	tb11_03
TB11	0.4	0.1	0.001	tb11_04

4. Results of the TB51 numerical test and comparison with real crash test

The full scale crash test was conducted in Inowrocław (Poland) by IBOS (Resears Insitute for Protective Systems, www.ibos.com.pl). During this test bus of 13027.9 kg weight at an angle of 21.37° and with the speed of 74 km/h impact the barrier between posts no. 30 and no. 31. The vehicle was in contact with the barrier at length 35.25 m. Some of the results are shown in Table 7, the crash courses on Fig. 6.

The results from the full scale crash test were compared to the tb51_03 simulation (Tab. 7 and Fig. 6). In the simulation the vehicle struck the barrier into the same place as in real crash test. The front of the bus struck the barrier. The maximum permanent deflection was approximately 1.82 m. The front of the vehicle was redirected and then the second collision occurred, where the rear of the bus impacted the already deformed barrier. This was the decisive factor for the working width (2.18 m). The bus was in contact with the barrier at length 33.89 m and then correctly redirected. The bus trajectory is shown in Fig. 7. The small elements visible on the right side of simulation views on Fig. 6 are the plastic elements and steel clamps. Discrepancies in results of the real crash test and simulation can be attributed to: different bus model and to the differences between the real test velocity and impact angle and those required by standard EN1317.

Table 7. Comparison between full scale crash test and simulation results.

Parameter	Full scale crash test	Simulation tb51_03	Difference
Normalised working width W_N, m	2.4 (W7)	2.2 (W7)	0.2
Length of contact, m	35.25	33.89	1.36
ASI front/rear	0.2/0.2	0.3/0.2	0.1/0.0
THIV front/rear, km/h	10/7	10/6	0/1

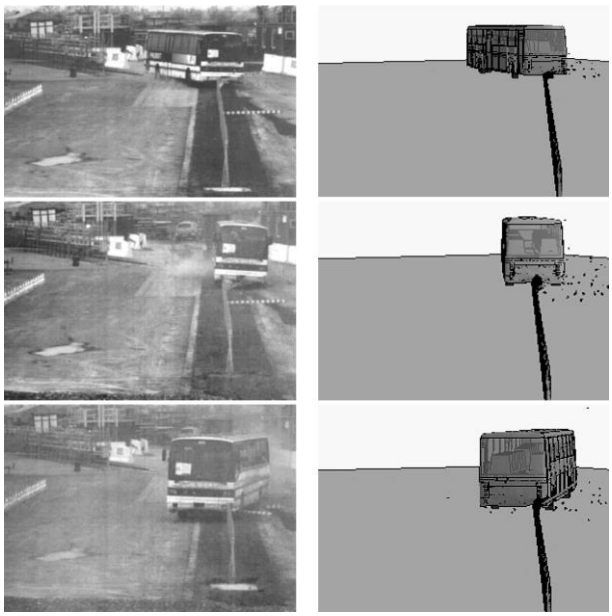

Figure 6. Comparison full scale crash test and simulation (front view).

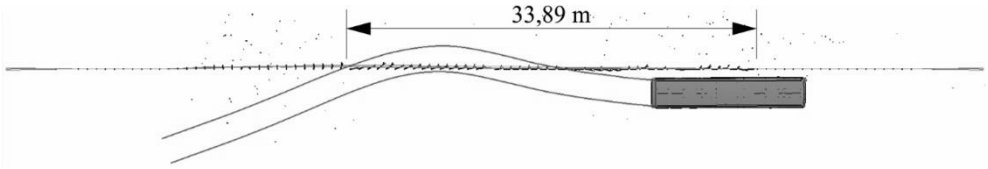

Figure 7. The bus trajectory in numerical simulation.

5. Results of the TB11 and TB51 numerical test and influence of friction coefficient

The tables 8 and 9 show the results of the TB51 and TB11 test simulations. The crash course of TB11 test (tb11_02) is shown in Fig. 6. In the TB51 simulations, low severity indicators ASI and THIV were obtained. ASI measured numerically near to the center of gravity is lower than in the front and rear of the vehicle. Working width is determined by the second impact of the back of the bus.

ASI and THIV obtained from TB11 simulations allows for qualifying barrier to class A. For the analyzed cases of TB11 test, the change of the friction coefficient does not affect the ASI, THIV and working width, which is determined by the first phase of the impact of the front of the car, but increasing friction reduces the length of the vehicle's contact with the barrier. Simulations confirmed the well-known fact that the impact severity is determined by the test with car (ASI and THIV higher for TB11 tests) while the value of working width is assessed from test with heavier vehicles like bus or heavy goods vehicle (HGV).

Table 8. Results from TB51 simulation.

Test	W_N, front/rear impact, m	ASI front/middle/rear, -	THIV front/middle/rear, km/h
tb51_01	1.92 / 2.24 (W7)	0.26 / 0.13 / 0.22	9.0 / 7.5 / 7.2
tb51_03	1.82 / 2.18 (W7)	0.30 / 0.12 / 0.23	9.9 / 9.9 / 6.4

Table 9. Results from TB11 simulation.

Test	ASI, -	THIV, km/h	W_N, m	Contact length, m
tb11_00	0.64	22.5	0.80 (W2)	11.12
tb11_01	0.73	25.0	0.68 (W2)	8.09
tb11_02	0.73	25.3	0.69 (W2)	7.92
tb11_03	0.72	25.7	0.68 (W2)	8.27
tb11_04	0.73	25.1	0.67 (W2)	7.73

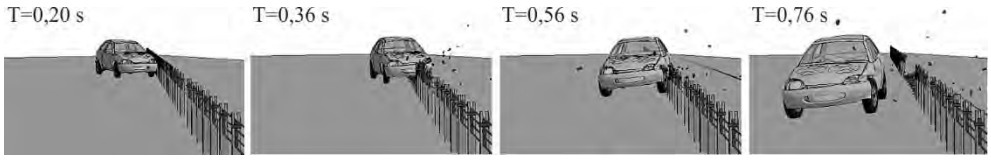

Figure 8. The front views of tb11_02 simulation.

6. Conclusions

In this study the numerical simulation of cable barrier TB11 and TB51 crash test were carried out. The comparison of simulation results with the full scale crash test shows that numerical simulations are a useful and reliable tool for evaluating road restraint systems. The simulations showed that the friction coefficient has an effect on the results.

Acknowledgments

This work was supported by the National Centre for Research and Development (NCBiR) and General Director for National Roads and Motorways (GDDKiA) under the research project "Road Safety Equipment" (contract number DZP/RID-I-67/13/NCBR/2016). Calculations have been carried out at the Academic Computer Center in Gdańsk, Gdańsk University of Technology.

References

[1] Hallquist, J., *Ls-Dyna Theory Manual*, March 2006.

[2] Hughes, T.J.R.: *The Finite Element Method: linear static and dynamics finite element analysis*. Mineola, New York, Dover Publications, Inc., 2000

[3] Mikołajków, L.: Drogowe bariery ochronne linowe, *Magazyn Autostrady*, nr 11, 2006, pp. 36-41.

[4] National Crash Analysis Center, http://www.ncac.gwu.edu/vml/models.html, date of access 10.03.2016.

[5] Nasution, R. P., Siregar, R. A., Fuad, K., Adom, A. H.: The effect of ASI (Acceleration Severity Index) to different crash velocities, *Proceedings of International Conference on Applications and Design in Mechanical Engineering (ICADME)*, Malaysia, 11-13 October 2009, pp. 1-6.

[6] PN-EN 1317-1:2010. Road restraint systems – part 1: Terminology and general criteria for test methods.

[7] PN-EN 1317-2:2010. Road restraint systems – part 2: Performance classes, impact test acceptance criteria and test methods for safety barriers including vehicle parapets.

[8] PN-EN 1317-5+A2:2012. Road restraint systems – part 5: Product requirements and evaluation of conformity for vehicle restraint system.

[9] Ren, Z., Vesenjak, M.: Computational and experimental crash analysis of the road safety barrier, *Engineering Failure Analysis*, 12, 2005, pp. 963-973.

[10] ROBUST project repository, http://www.vegvesen.no/s/robust/, date of access 01.10.2016.

[11] Stolle, S., Reid, J.: Modeling Wire Rope Used in Cable Barrier Systems, *11th International LS-DYNA Users Conference*, Detroit, USA, 2010, s. 1-10.

[12] Teng, T., Liang, C., Tran, T.: Development and validation of finite element model for road safety barrier impact tests, *Simulation: Transactions of the Society for Modeling and Simulation International*, Vol. 92 issue 6, 2016, pp. 565-578

[13] Vasenjak M., Ren Z.: Improving the Roadside Safety with Computational Simulations, *4th European LS-DYNA Users Conference*, Ulm, Germany, 2003, s. 1-10.

[14] Wilde, K., Jamroz, K., Bruski, D., Budzyński, M., Burzyński, S., Chróścielewski, J., Witkowski, W. Curb-to-Barrier Face Distance Variation in a TB51 Bridge Barrier Crash Test Simulation. *Archives of Civil Engineering*, 63, 2017, pp. 187-199.

[15] Wilde, K., Jamroz, K., Bruski, D., Burzyński, S., Chróścielewski, J., Witkowski, W. Numerical simulations of bus crash-test with barrier and truss supporting structure. *Journal of Civil Engineering, Environment and Architecture*, 63, 2016, pp.455–467.

Krzysztof Wilde, Professor: Gdańsk University of Technology, Department of Mechanics of Materials and Structures, Gabriela Narutowicza 11/12, 80-233 Gdańsk, Poland (*krzysztof.wilde@wilis.pg.gda.pl*).

Dawid Bruski, M.Sc. (Ph.D. student): Gdańsk University of Technology, Department of Mechanics of Materials and Structures, Gabriela Narutowicza 11/12, 80-233 Gdańsk, Poland (*dawbrusk@pg.gda.pl*).

Stanisław Burzyński, Assistant Professor: Gdańsk University of Technology, Department of Mechanics of Materials and Structures, Gabriela Narutowicza 11/12, 80-233 Gdańsk, Poland (*stanislaw.burzynski@wilis.pg.gda.pl*).

Jacek Chróścielewski, Professor: Gdańsk University of Technology, Department of Mechanics of Materials and Structures, Gabriela Narutowicza 11/12, 80-233 Gdańsk, Poland (*jacek.chroscielewski@wilis.pg.gda.pl*).

Wojciech Witkowski, Associate Professor: Gdańsk University of Technology, Department of Mechanics of Materials and Structures, Gabriela Narutowicza 11/12, 80-233 Gdańsk, Poland (*wojciech.witkowski@wilis.pg.gda.pl*).

Application of non-linear dynamics to Poland's evolution

Tatyana Y. Yaroshenko, Jan Awrejcewicz, Igor I. Shulga,
Maxim V. Zhigalov, Vadim A. Krysko

Abstraction. The formation and development of states on the one hand is a unique process, but on the other hand there are some general laws of this process. In this article, the authors continue to develop a methodology for studying the historical time series. In this work, the formation and development of the Polish statehood since 960 has been studied up to the present days. For the study, methods of nonlinear dynamics are used: wavelet analysis and the study of the change in the sign of the first Lyapunov exponent. Reliability is achieved by the coincidence of the results of the applied methods with historical events and with each other.

Introduction

In this work we are using the methods of nonlinear dynamics, and we study the development of Poland from 960 until 2004 (see Fig. 4.) Poland is a unique example of a state that throughout its history has ceased existence several times, but then as a phoenix bird rose from the ashes. Currently, Poland occupies a prominent place in the European and world community. Therefore, the study of the development of this state is of undoubted interest. However, mainly in the literature there are historical humanitarian studies of Poland [1, 2]. In work [3] the authors create a mathematical model of the war of the Polish-Lithuanian Commonwealth with Sweden of the 17th century and compare the results with known historical data. In work [4], an analysis of the development of dialects in the southern part of the Pskov region - in the area of Sebezh and Nevel, which once were part of the Commonwealth. In contrast to the above studies, methods of nonlinear dynamics are used in this paper. This allows us to obtain an objective analysis of the historical process and to model both the development of the state as a whole and historical events at individual time intervals. This approach is first used to study the development of Poland. Wavelet analysis, Fourier analysis and the values of the first Lyapunov exponent $\boldsymbol{\lambda_1}$ calculated using neural networks using the Benettin method are employed. When applying the "mathematical microscope" wavelet - analysis, three kinds of wavelets HAAR, MHAT, MEYR are used. In order to choose the most effective of them and compare the results of the research, the Fourier analysis is used to obtain an idea of the historical process under study as a whole. The study of the sign of the first Lyapunov exponent $\boldsymbol{\lambda_1}$ makes it possible to conclude that the historical process is stable or chaotic. This work is a continuation and development of the method proposed in [5, 6]. In work [7], the methods of nonlinear dynamics are applied to mechanical systems. The aim of this study is to follow the development of various states and different epochs and to identi-

fy common patterns of development. This makes it possible to model the development of modern states to prevent crises. The study of historical processes using methods of nonlinear dynamics makes it possible to study the signs of a harmonious and chaotic state development. This results are revealing conditions necessary for the harmonious development of the state. In [5], the methods of nonlinear dynamics study the history of the development of Ancient Rome and the European Union. The analysis showed that the results of studies using the methods of nonlinear dynamics are in good agreement with the processes of changing the internal state of the state (economy, politics, culture, science).

Materials and Methods

1. Wavelet - based analysis of historical series

Wavelet – analysis is a universal method of nonlinear dynamics [7], which can be applied for analysis of time series of any kind from physical to historical issues. For example, in physics, when analyzing the observed data on fluxes of sunlight, the solar wind, the structure of surfaces, galaxies, etc. [8,9]. In this paper, a wavelet transform of a one-dimensional time series is applied, which consists in expanding it by the basis of the wavelet function by means of large-scale transformations and translations. Each function of the basis characterizes the localization in time and frequency ω, which allows us to study the time series simultaneously in time and frequency ω. Frequency and time are independent variables. The wavelet transform is the scalar product of the wavelet and the signal (historical time series), therefore, the wavelet coefficients $W(t,\omega)$ contain information about the signal and the analyzing wavelet. In this paper continuous wavelet analysis of MHAT [10] MEYR [11] and orthogonal wavelet HAAR [12] are used. The time t (years) is the shift parameter. It fixes the point of focus of the wavelet and the scale factor - frequency ω. The "optical quality" of the wavelet, which is a "mathematical microscope", corresponds to the basis wavelet φ. We employ:

Discrete Haar wavelet (HAAR):

$$\varphi(t) = \begin{cases} 1\ ; & if\ \ 0 \le t < 0{,}5 \\ -1\ ; & if\ \ -0{,}5 \le t < 1 \\ 0\ ; & if\ \ t < 0, t \ge 1. \end{cases} \quad (1)$$

Wavelet Mexican hat (MHAT):

$$\psi(t) = (1-t^2)\exp(-\frac{t^2}{2}) \quad (2)$$

Meyer's Wavelet (MEYR):

$$\varphi(\omega) = \begin{cases} \frac{1}{\sqrt{2\pi}}\sin\left(\frac{\pi}{2}\vartheta\left(\frac{3|\omega|}{2\pi}-1\right)\right)e^{j\omega/2}, if\ \ 2\pi/3 < |\omega| < 4\pi/3 \\ \frac{1}{\sqrt{2\pi}}\cos\left(\frac{\pi}{2}\vartheta\left(\frac{3|\omega|}{4\pi}-1\right)\right)e^{j\omega/2}\ , if\ \ 4\pi/3 < |\omega| < 8\pi/3, \\ 0\ \ \ \ \ \ \ \ , otherwise, \end{cases} \quad (3)$$

where $\vartheta(x) = \begin{cases} 0 & if\ x < 0, \\ x & if\ 0 < x < 1, \\ 1 & if\ x > 1. \end{cases}$

The result of the wavelet transform of the time series is the values $W(t,\omega)$ - wavelet coefficients. Since the wavelet transformation is the scalar product of the analyzed signal and the analyzing wavelet, the wavelet coefficients contain information about both the signal itself and the wavelet. The parameter t, here time (years) fixes the wavelet focusing point, since it is the parameter of the shift, ω is the frequency, the scale factor. The "optical quality" of a mathematical microscope is determined by the choice of the basis wavelet, in this article HAAR (see Eq. 1), MHAT (see Eq. 2), MEYR (see Eq. 3).

We use 2D visualization of the spectrum of the wavelet coefficients. With the evolution of the signal, increase in the frequencies correspond to local maxima or minima of the time series. The wavelet spectrum of the historical time series is a surface in the three-dimensional space $W((t,\omega),t,\omega)$. Based on 2D visualization of the spectrum of the wavelet coefficients, one can get an idea of the change in the energy component of the system [5]. The energy of the state is the internal energy of the system. On the other hand the energy of the state is understood as the energy of the signal, i.e. we have

$$E_w = \int_{t_1}^{t_2} |W(t,\omega)|^2\, dt\,, \qquad t_1 < t < t_2. \tag{4}$$

The quantity E_w is the total energy of the system, which consists of the internal energy of the state, and the external energy that is reported to the system as a result of contact with neighboring states. This can be trade, cultural contacts, or military actions.

Applying this notion to historical time series, we can say that those periods when the state undertook new campaigns to escalate military operations in domestic or foreign policy correspond to an increase in the state's energy. Such periods are associated with crises of any nature.

2. Algorithm for the application of an artificial learning neural network for calculating the spectrum of Lyapunov exponents

A single-layer neural network is used [13]. A single-layer unidirectional neural network (see Fig. 1.) uses a layer of n of hidden neurons to perform the next prediction $\hat{x}_k$ on a scalar time series x_k:

$$\hat{X} = \sum_{i=1}^{n} b_i \tanh\left(a_{i0} + \sum_{i=1}^{d} a_{ij} x_{k-i} \right),$$

where a_{ij} are coefficients of the matrix of size $n \times (d+1)$, b_i is a vector of length n. The matrix a_{ij} shows the number of connections at the entrance to the network, the vector b_i is used to determine

the contribution of each neuron at the output from the network. A vector a_{i0} is an offset that facilitates learning on data whose mean is not zero.

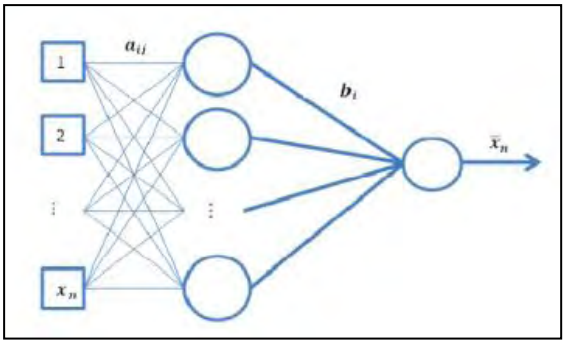

Figure 1. Single-layer neural network of direct propagation

The idea of the method is to calculate, by means of an artificial learning neural network, the divergence of two nearby trajectories in n steps forward. An analog, self-organizing neural network is used, which is represented in the form of real numbers and forms the output space of solutions based on input effects. This is a network with dynamic links, directed strictly from input to output. In the learning process, synaptic connections $dw/dt \neq 0$ are set up, that is, where W are the network weights. To calculate the first Lyapunov exponent $\boldsymbol{\lambda_1}$, a necessary time delay is calculated based on the sample; the dimension of the embedding space is calculated; a pseudo-phase reconstruction of the trajectory by the method of time delays; a neural network is constructed to approximate the time series. The neural network a_{ij} is trained to calculate the next sequence vector of the time series; in the trained neural network, based on the generalized Benettin method [14].

3. Fourier analysis of the time series

The Fourier transform [15] is the integral transformation, defined as follows

$$F(\omega) = \int_{-\infty}^{\infty} f(t)^{i\omega t} dt ,$$

where t is the time, ω is the frequency. If a continuous function $f(t)$ is defined on some interval $[0, T]$ then its vector will be a discrete analogue of the vector $f_n = f(t_n), n = 1, \dots N$. Most often, especially in the numerical definition of the Fourier transform, the sequence $t_n$is equidistant, i.e. it is represented as $t_n = (n-1)\Delta t$, $\Delta t = T/(N-1)$. That is, there are two vectors: a discrete time vector and a vector of values of the function at these points.

Numerical results

The article examines the time series of changes of the territory of Poland since 960 to 2004. The year 960 stands for the beginning of the reign of the first historically reliable prince Meshko I (935 - 992). The Principality of Great Poland, with its center in the city of Gniezno, became the most extensive of the Slavic countries of that time with the strongest and most numerous army. Prince Mieszko accepted the state religion as Catholicism. He pursued the strategic goals to strengthen his power, uniting the ideology of the state and strengthening the position of Poland in the international arena. In fact, this is the time of the birth of the Polish state, whose territory has been steadily expanding. The first Polish coin is introduced into the economy. A state apparatus is created, the head of the state is the prince, in fact the vice-president is the palatine, a treasury with a *skarbnik* at the head and a princely chancellery headed by the chancellor was created. With the expansion of borders, for effective management, the state was divided into 3 regions. At the prince, a council of noblemen and military leaders functioned. Power was inherited by the eldest son. The process of forming the state apparatus, the tax system, building new social relations against the background of often occurring wars. All these processes of forming statehood, building an economic system and creating a state apparatus can be characterized as a time of active change.

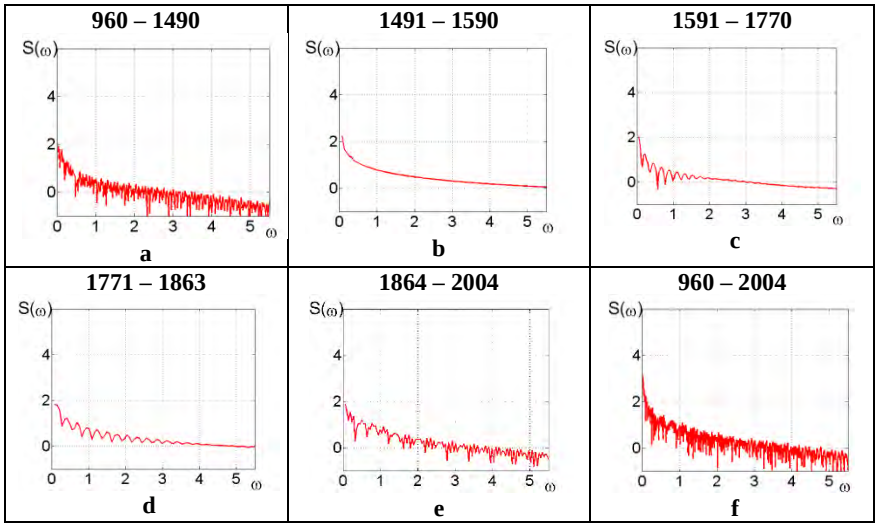

Figure 2. Fourier - analysis of the time series of changes in the territory of Poland, where (a)–time period from 960 to1490; (b)-time period from 1490 to1590; (c)-time period from 1591 to 1770; (d)-time period from 1771 to1863; (e)-time period from 1864 to 2004; (f)–all time period from 960 to 2004.

The system in this period is in an outraged state due to the assimilation and integration of the annexed territories. Therefore, the system is in a chaotic state. Since 960 up to 1490 the Lyapunov exponent $\boldsymbol{\lambda_1}$ has a positive but close to zero value (Table 1). Fourier analysis of this time interval has a solid pedestal of frequencies, which also means chaos (see Fig. 2a). However, with the help of a "mathematical microscope" - wavelet analysis, one can examine the condition of the state at each moment of time. Based on wavelet analysis from 960 on 1100 on the three wavelets, multi-frequency peaks (light areas) are visible, which means a chaotic state (see Fig. 3a, 3b, 3c). This also means an increase in the energy of the state E_w. And indeed, during this period the Polish principality was transformed into a kingdom and after a significant increase in its territory during the reign of Mieszko I and his successor Boleslaw I (967 - 1025). But there were also difficult times when, after the loss of the Milska-Luzhetsk lands, Pomorie and Mazovia, the Polish state was in an economic crisis. The result of this was the recognition of vassal dependence on the Holy Roman Empire in 1038. Then comes the restoration of the Polish state and the period of stability. This is clearly seen also in the dark region on the HAAR wavelet (see Fig. 3a). On the MHAT wavelet (see Fig. 3b), this region is so pronounced. On the MEYR waveguide (see Fig. 3c) this region is absent. The next increase in the frequency spectrum of ω begins with 1300 to 1420. The period of loss of territories and the accession of new lands. The period of strife and attempts to consolidate Polish lands. Great troubles to the Polish kingdom caused the Holy Roman Empire and the Teutonic Order. Therefore, the union of the Polish Kingdom and the Grand Duchy of Lithuania was necessary for both states. By united forces they confronted external enemies. For example, the Great War with the Teutonic Order (1409-1411) which ended with the conclusion of the Torun Peace Treaty with the benefit of Lithuania and the annexation of Samogitia and Prussia. On the background of external wars, internal unrest occurred. They were caused by the movement of the Reformation of Jan Hus in the Czech Republic, which reached the Polish lands. Catholicism was opposed to the Reformation. The feudal disunity of the Kingdom of Poland led to the growing role of the aristocracy. This laid an important political tradition, to limit the power of the king. By the year 1396 on the European arena appears another powerful player - the Ottoman Empire, which will become a constant object of concern and problems for the Kingdom of Poland. The period of increasing frequencies ω (see Fig. 3a, 3b, 3c) falls on the Thirteen-year war (1454 - 1466) with the Teutonic Order. The frequency peak is most clearly expressed on the HAAR wavelet (see Fig. 3a), compared to the wavelets MHAT (see Fig. 3b) and MEYR (see Fig. 3c).

Table 1

time intervals (year) / first Lyapunov exponent λ_1,	**960 – 1491**	**1491 – 1590**	**1591 – 1770**	**1771-1863**	**960 – 2004**
λ_1	**0,001**	**-0. 0023**	**0,004**	**-0,29**	**0.0078**

The period from 1491 to 1590 was marked by the implementation of reforms by King Sigismund I (1467 - 1548). The military reform consisted in the division of the Kingdom of Poland into five districts, from which, each in turn, for five years, carried military service on the eastern border. Another military - financial reform was carried out at the Diet of 1527 was to assess the income from the land and the appointment of salaries to tax collectors. This was to put an end to embezzlement. Also in each district (command), the commissioners choose the gentry suitable for military service and ensure discipline and pay their salaries. But the reforms did not last long because of resistance gentry. Not entirely successful war of the Grand Duchy of Lithuania with the Russian state (1512 - 1522) eventually ended in the loss of Smolensk. After the second war (1534-1537), Sebezh and Zavolochye withdrew to Moscow. Devastating raids were made by the Crimean Tatars. During the flared up contradictions between the aristocracy and the nobility Sigismund I in 1537 recognized the rights of the nobility to the election of the king. Poland waged several wars: the Livonian War (1558 - 1583), the war with Sweden (1561 - 1583). Finally, in 1569, according to the Union of Lublin, a federal state was formed called Polish–Lithuanian Commonwealth, uniting the Kingdom of Poland and the Grand Duchy of Lithuania. A unique experience of state education of that time. The king was elected by the diet, and in some ways depended on him. The Seimas had the right to enact laws, and the law could only be passed unanimously. During this period, on the wavelets HAAR (see Fig. 3a), MHAT (see Fig. 3b) and MEYR (see Fig. 3c), the multifrequency peaks (light areas) are replaced by dark regions, which means that the chaotic state of the state is replaced by periods of stability. The Fourier analysis (see Fig. 2b) of this period shows the stable state of the system. The sign of the highest Lyapunov $\boldsymbol{\lambda_1}$ exponent is negative, which agrees with the Fourier analysis (Table 1). Period 1591 - 1770 years. is the period of the Polish–Lithuanian Commonwealth. The period until the middle of the XVII century was a “golden age” for the “szlachta” and many townspeople who enjoyed the benefits of self-government under the Magdeburg law. In other words, economic activity, property rights, social and political life and the estate status of citizens are regulated by their own system of legal norms. The granted freedoms of the aristocracy and the gentry in the government of the state began to turn into abuses after a while. The tension in the state was caused by national and religious contradictions between Catholics and Orthodox, according to the Gorodel Union of 1413. Catholics had status superiority over the Orthodox. The growth of tension resulted in the rebellion of Bohdan Khmelnitsky in 1648. The Polish army was defeated by the Cossacks and peasants under Korsun. The value of the first Lyapunov exponent $\boldsymbol{\lambda_1}$ is positive but close to zero (Table1). Fourier analysis shows the chaotic state of the system at low frequencies and and a harmonic state at high frequencies (see Fig. 2c). On the HAAR wavelet (see Fig. 3a) during this period, the dark area is replaced by frequency peaks (light area), just coincides with the transition from the "golden age" period to the period of aggravating problems. On the MHAT (see Fig. 3b) and MEYR (see Fig. 3c) wavelets, this transition is practically

invisible. Fourier analysis as a whole characterizes the period as chaotic, without distinguishing between zones of stability and chaotic state. In 1654 in Poland the war with Russia began and a year later with Sweden. However, against the backdrop of these problems, King Jan II Casimir (1609 - 1672) kept the state from disintegration and absorption by neighboring countries. The political might of Poland grew during the period of Jan III Sobieski, who, in particular, put an end to the expansion and Ottoman Empire in Europe due to his victory against the walls of Vienna (1683). During the wars, the state suffered catastrophic demographic losses that predetermined the beginning of the economic crisis. The period 1771 - 1863 years became the decline of Polish–Lithuanian Commonwealth. Internal contradictions against the background of national and religious conflicts led to a protracted economic crisis. And the aggravated religious question gave neighboring states an excuse to interfere in the internal affairs of the state.

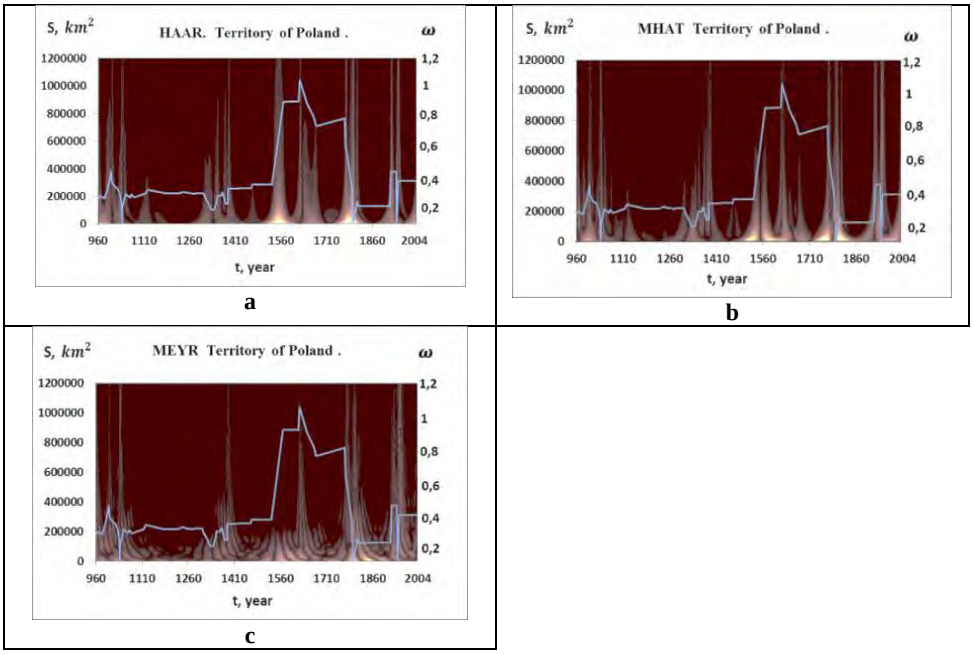

Figure 3. Time series of changes in the territory of Poland from 960 to 2004 - solid line. The time series is superimposed on the 2D interpretation of the wavelets HAAR (a), MHAT (b), MEYR (c).

The result was a series of wars and a threefold division of Poland between Russia, Prussia and Austria in 1772 in 1793 and as a result of the third section of 1795 Polish–Lithuanian Commonwealth ceased to exist as a state. Courland, Lithuania, Western Belorussia and the western part of Volyn fell back to Russia. The genuinely Polish lands were divided between Austria and Prussia. Only in 1807 as a

result of the Tilsit peace between Russia and France, Russia recognized the Grand Duchy of Warsaw. Later in 1815 Poland gained the right to the constitution, the elective diet, its government and its own army. An uneasy situation led to unrest and the Krakow uprising (1846), which was eventually suppressed. The period from 1771 to 1815 on wavelets (see Fig. 3a, 3b, 3c) is characterized by an increase in the frequencies ω. For the period from 1815 to 1863 the territory of the state has not actually changed, and therefore conclusions about the processes that are occurring can be made on the basis of the available historical data. But on the other hand at this time Poland was dependent on Russia, Prussia and Austria and had only partial state freedoms. The state structures functioned under the supervision of this triumvirate, and the independence movement was more likely to be underground or partisan. On the wavelet of HAAR (see Fig. 3a) and MHAT (see Fig. 3b), it corresponds to a dark area, on the MEYR (see Fig. 3c) this region is less pronounced. The sign of the first Lyapunov exponent $\boldsymbol{\lambda_1}$ is negative. Fourier analysis shows the chaotic state of the system at low frequencies (see Fig. 2d).

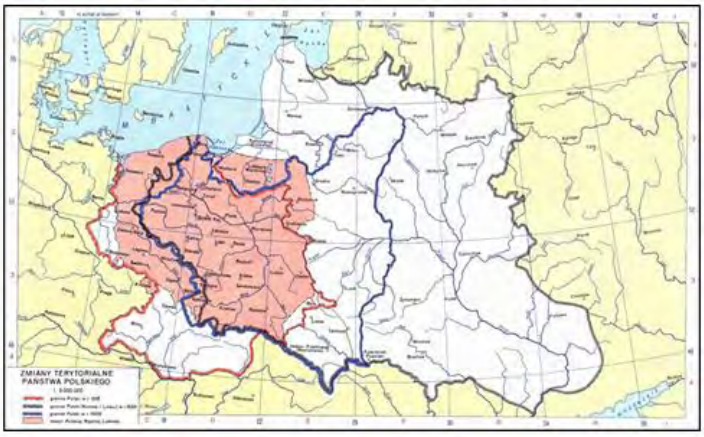

Figure 4. Map of the change of the territory of Poland from 1018 to 1939.

The period from 1863 to 2004 this is the period of the restoration of the state, which passed through two world wars and eventually revived in a new form. The last decades of the XIX century, and the first decade of the XX century in all three parts, Polish society actively resisted assimilation. Secular and religious structures carried out active work to preserve the Polish language and culture. New political parties (National Democratic, Polish Socialist and Peasant) began to form. All this took place against the backdrop of growing tension. As a result, the outbreak of the First World War (1914-1918) gave new opportunities for Poland to gain independence, but in the end, in 1917, after the February Revolution, Russia recognized the independence of Poland. After the restoration of independence, the state restored both the economy and state structures. In Poland, a constitution was

adopted that affirmed the republican system, a bicameral parliament (the Seim and the Senate). During the Second World War (1939 - 1945), Poland was occupied by Germany, but after the termination of Poland, it restored its borders and statehood. In the state there was a change of the system to a socialist one. This process was painful. In 1956 the Poznan uprising against the socialist system took place. During this period, three wavelets (see Fig. 3a, 3b, 3c) have frequency peaks (light areas), which coincides with the turbulent situation in the state. The subsequent developments in the development of the state are such that, at the junction of the 20th century, and the XXI century there was a change in the state system and the reorganization of the state apparatus the establishment of new democratic norms. Before 2004 on the wavelets increases in the frequencies ω are seen. Fourier analysis shows a solid pedestal of frequencies (see Fig. 2e), which means a chaotic state of the system. The results of Fourier analysis (see Fig. 2f) and the change in the sign of the first Lyapunov exponent $\boldsymbol{\lambda_1}$ coincide for the entire time series from 960 to 2004. Fourier analysis shows a solid pedestal of frequencies, the sign of the first Lyapunov exponent $\boldsymbol{\lambda_1}$ is positive. The processes of formation and transformation of the state occur at high energy costs and they can be called chaotic.

Cnclusions

As a result of studies of the historical development of the territory of Poland with the help of wavelets HAAR, MHAT, MEYR, it was revealed that the analysis based on the wavelet of HAAR and, MHAT is the most accurate. The MEYR wavelet can detect only the largest events and crises. Fourier analysis is used to illustrate the benefits of wavelet analysis. Since even a Fourier analysis of individual time intervals allows one to obtain only a representation as a whole, without having a detailed view of the interval studied. Studies have shown good agreement between the results of wavelet analysis, Fourier analysis and change of the sign of the first Lyapunov exponent. These results are in good agreement with historical data and allow us to identify the harmonic and chaotic periods of Poland's development.

Acknowledgments

This work has been supported by the Grant RSF № 16-11-10138

References

[1] Davies, N. *God's Playground. A History of Poland*.1. Oxford: Oxford University Press, New York, 2005.

[2] Davies, N. *God's Playground. A History of Poland.* 2. Oxford: Oxford University Press, New York, 2005.

[3] Waniek, M. Petro: A multi-agent model of historical warfare (Conference Pper*), Proceedings - 2014 IEEE/WIC/ACM International Joint Conference on Web Intelligence and Intelligent Agent Technology - Workshops*, WI-IAT.3. 3, (2014), p. 1407-1408.

[4] Jankowiak, M. The vocabulary of Baltic origin in mixed Belarusian-Russian dialects of the south Pskov region (the area of Sebezh and Nevel). *Acta Baltico-Slavica*, 40, (2016), p 73-92.

[5] Tatyana, Y., Yaroshenko, T. Y., Krysko, D.V., Dobriyan, V., Zhigalov, M. V., Vos, H., Vandenabeele, P., Krysko, V.A. Wavelet modeling and prediction of the stability of states: the Roman Empire and the European Union. *Communications in Nonlinear Science and Numerical Simulation* .26, (2015), p. 1-11.

[6] Krysko, V.A., Vygodchikova, I.Yu., Pleve, Igor R., Yaroshenko, T.Y. Methods of nonlinear dynamics and minimax approximation criterion in the analysis of population dynamics. *Nonlinear world*. 14 (5), (2016), p. 64-73.

[7] Awrejcewicz, J., Krysko, V.A., Papkova, I.V., Krysko, A.V. Routes to chaos in continuous mechanical systems. Part 1*: Mathematical models and solution methods. Chaos, Solitons Fractals*, 45, (2012), p.687–708.

[8] Van den Berg, J. C. *Wavelets in Physics*. Cambridge: Cambridge Univ. Press , New York, 1998.

[9] Bowman, C., Newell, A.C. Natural patterns and wavelets. *Rewiews of Modern Physics*, 70 (1), (1998), p. 289 – 301.

[10] Daubechies, J. Orthogonal bases of compactly supported wavelets. *Comm. Pure. Appl. Math.* 41(7). (1988), p. 906.

[11] Meyer, Y. *Wavelets and operators.* Cambridge University Press, New York, 1992.

[12] Haar, A. Zur theorie der orthogonalen funktionensysteme. *Math Ann*.71, (1911), p. 38–53.

[13] Box, G., Jenkins, G.M., Reinsel, G. *Time Series Analysis.* Forecasting & Control. Prentice Hall. 1994.

[14] Benettin, G., Galgani, L., Strelcyn, J.M. Kolmogorov entropy and numerical experiments. *Phys. Rev.* A14, (1976), p. 2338-2345.

[15] Bracewell, R. N. *The Fourier Transform and Its Applications*. McGraw-Hill, Boston, 2000.

Tatyana Y. Yaroshenko, Associate Professor: Department of Mathematics and Modeling, Saratov State Technical University, Politehnicheskaya 77, 410054 Saratov, RUSSIAN FEDERATION (tyyaroshenko@gmail.com).

Jan Awrejcewicz, Professor: Lodz University of Technology, Faculty of Mechanical Engineering, Department of Automation, Biomechanics and Mechatronics, 1/15 Stefanowski Str., 90-924 Lodz, POLAND (awrejcew@p.lodz.pl).

Igor I. Shulga, Professor: Department History of the Fatherland and Culture, Saratov State Technical University, Politehnicheskaya 77, 410054 Saratov, RUSSIAN FEDERATION (IgorShulga@yandex.ru).

Maxim V. Zhigalov, Professor: Department of Mathematics and Modeling, Saratov State Technical University, Politehnicheskaya 77, 410054 Saratov, RUSSIAN FEDERATION (max.zhigalov@gmail.com).

Vadim A. Krysko, Professor: Department of Mathematics and Modeling, Saratov State Technical University, Politehnicheskaya 77, 410054 Saratov, RUSSIAN FEDERATION (tak@san.ru), the author presented this contribution at the conference.

Understanding of origination, development and the sunset of the Ottoman Empire using wavelets and Lyapunov exponents

Tatyana Y. Yaroshenko, Jan Awrejcewicz, Igor Pelve, Vadim A. Krysko

Abstract. In this work historical time series of change the territory and population of the Ottoman Empire (from 1299 and before the collapse in 1924) is investigated. We apply wavelet analysis (MHAT, HAAR) and changes in the sign of the first Lyapunov exponent. With the help of wavelet analysis the energy of the state is obtained. According to the sign of the first Lyapunov exponent, one can obtain information about the stable or chaotic state of the process. To computate the first Lyapunov exponent the methods of Wolf, Rosenstern, and neural networks are employed.

Keywords: nonlinear dynamics, wavelet analysis, Lyapunov exponent, Haar wavelet, Meyer wavelet, state, Ottoman Empire, time series, territory, population.

1. Introduction

The study of historical processes using methods of non-linear dynamics makes it possible to give an objective assessment for the causes and consequences of prosperity and development crises of the state. The paper studies the development of the Ottoman Empire during the time interval from 1300 until 1924, The empire passed a full cycle of development from education, to disintegration. The origin of the empire can be attributed to 1300 - 1452, rapid growth and flourishing is 1452 - 1617, decline - 1617 - 1757, attempts to reform - 1753 - 1839, the final decline and disintegration - 1757 - 1924 (see maps of Fig. 2). The Ottoman Empire existed for seven centuries. Throughout its existence, it was ruled by a single dynasty named the Osman dynasty. This empire was an important player on the world stage for seven centuries, and it is of interest for research. In work [1] Gündüz draws an analogy of the development of empires with Verhulst or Lotka-Volterra dynamics. He suggests that the development of the empire took place according to a power law. The author takes into account the laws of viscoelasticity and thermodynamics for determining the energy that is allocated when expanding the boundaries of states. This is undoubtedly an interesting approach, which however raises questions about how it is possible to determine the necessary coefficients for determining the energy components and how accurately it is possible to compare the development of a territory with a power law. In references [2] and [3], the authors examine the periods of the last centuries of the existence of the Ottoman Empire. In paper [2] the Gundogdu examines the changes in the socio-

economic and political structures of the Ottoman state, changes in the structures of power, when the vertical of power begins to change and a significant decrease in the authority and authority of the sultans of the ruling dynasty. In work [3], the period of the decline of the empire in the 19th century, which was simultaneously a period of significant state reforms, has been investigated. However, the reforms did not bring the expected results. Unlike the above works, we apply a technique that allows any one to get an idea of the entire time interval of the development of the empire, both in general and at each moment of time. The methods of nonlinear dynamics allow us to make an objective analysis of the development of the state. To study the development of the Ottoman Empire, this approach is applied for the first time. The flowering or decline of states depends on many factors: the quality of the management system, wars, natural conditions, epidemics, etc. The methods of nonlinear dynamics make it possible to produce a qualitative and multi-face analysis of historical events and to give an objective assessment. We have employed the wavelet analysis because of its obvious advantage over Fourier analysis. The Fourier analysis allows one to obtain an estimate of the time series as a whole, whereas wavelet analysis is a "mathematical microscope" and gives an idea of the historical process, and trace its dynamics at each moment of time. The change in the frequencies of the wavelet analysis makes it possible to determine the oscillations of the state energy in time. The change in the sign of the first Lyapunov exponent in time by Wolf's method can reveal periods of stable development and periods of crises. This work is a continuation and development of the methodology proposed earlier in [4,5]. In reference [6], the methods of nonlinear dynamics are applied to mechanical systems.

2. Wavelet - analysis of historical series

Wavelet – analysis is a universal method of nonlinear dynamics [6], which can be applied for analysis of time series of any kind from physical to historical processes. For example, in physics, when analyzing the observed data on fluxes of sunlight, the solar wind, the structure of surfaces, galaxies, etc. [7, 8].

In this paper, a wavelet transform of a one-dimensional time series is applied, which consists in expanding it by the basis of the wavelet function by means of large-scale transformations and translations. Each function of the basis characterizes the localization in time and frequency ω, which allows us to study the time series simultaneously in time and frequency ω. Frequency and time are independent variables. The wavelet transform is the scalar product of the wavelet and the signal (historical time series), therefore, the wavelet coefficients $W(t,\omega)$ contain information about the signal and the analyzing wavelet. In this paper, a continuous wavelet analysis of MHAT [9] and the orthogonal Haar wavelet [10] are used. The time t (years) is the shift parameter. It fixes the point of focus of the wavelet and the scale factor - frequency ω. The "optical quality" of the wavelet, which is a "mathematical microscope", corresponds to the basic wavelet φ. Here, a wavelet transform of a one-

dimensional time series is applied, which consists in expanding it in a basis of the wavelet function by means of scale transformations and translations.

Discrete Haar wavelet (HAAR) is governed by the following formula

$$\varphi(t) = \begin{cases} 1\ ; & if\ \ 0 \le t < 0{,}5, \\ -1\ ; & if\ \ -0{,}5 \le t < 1, \\ 0\ ; & if\ \ t < 0, t \ge 1, \end{cases} \quad (1)$$

Whereas the wavelet Mexican hat (MHAT) is described by the function

$$\psi(t) = (1-t^2)\exp(-\frac{t^2}{2}) \quad (2)$$

The result of the wavelet transform of the time series yields the values $W(t,\omega)$, i.e. wavelet coefficients. Since the wavelet transformation is the scalar product of the analyzed signal and the analyzing wavelet, the wavelet coefficients contain information about both the signal itself and the wavelet. The parameter t is the time (years) fixes the wavelet focusing point, since it is the parameter of the shift, ω is the frequency, the scale factor. The "optical quality" of a mathematical microscope is determined by the choice of the basis wavelet, in this article HAAR (see Eq. 1) and MHAT (see Eq. 2).

The article employes 2D visualization of the spectrum of the wavelet coefficients. With the evolution of the signal, increases in the frequencies correspond to local maxima or minima of the time series. The wavelet spectrum of the historical time series is a surface in the three-dimensional space $W\big((t,\omega),t,\omega\big)$. Based on the 2D visualization of the spectrum of the wavelet coefficients, one can get an idea of the change in the energy component of the system [4]. The energy of the state is the internal energy of the system. The energy of the state is understood as the energy of the signal, that is the value:

$$E_w = \int_{t_1}^{t_2} |W(t,\omega)|^2\, dt \qquad \text{on the interval} \quad t_1 < t < t_2. \quad (3)$$

The quantity E_w is the total energy of the system, which consists of the internal energy of the state, and the external energy that is reported to the system as a result of contact with neighboring states. This can be trade, cultural contacts, or military actions. Applying this notion to historical time series, we can say that those periods, when the state undertook new campaigns to escalate military operations in domestic or foreign policy, correspond to an increase in the state's energy. To such periods can be attributed any periods of crises of any nature.

3. Computation of the highest Lyapunov exponent by the Wolf method

In the process of dynamic development from a regular state, the system can go into chaotic state and vice versa. Lyapunov's characteristic exponents give an idea of the speed at which the system loses information about its initial state, that when it goes into a chaotic state. With the increase of these

changes, the values of Lyapunov's exponents λ_1 increase. The first Lyapunov exponent λ_1 makes it possible to determine the presence of a state of chaos in the process under investigation. If Lyapunov exponent λ_1 is negative, then the system is in a stable state, the positive sign means chaotization of the system. The value of Lyapunov exponent λ_1 allows obtaining a qualitative and quantitative characteristic of its dynamic behavior. In this paper we apply the method proposed by Wolf [11] for the whole time series in general, and the change in the exponent at each moment of time. This is the method for calculating the first Lyapunov exponent λ_1 from a single coordinate, when equations describing the evolution of the system are unknown. The historical time series $s(t)$ is specified, where $(t = 1, \dots, N)$ measurements of one coordinate of the historical process through the same time interval. The delay time τ is determined by the method of mutual information. The dimension of the embedding space m is determined by the method of the nearest false neighbors. A reconstruction is performed, as a result of which we obtain a set of points R^m m in the form of a sequence:

$$s_i = \big(s(i), x(i-\tau), \dots, s(i+(M-1)\tau)\big) = (s_1(i), s_2(i), \dots, s_m(i)). \quad (4)$$

We select the point s_0 from a sequence (see Eq. 4). Then, as a result of the analysis of the sequence, we find the point $\widetilde{s_0}$, for which the following condition is satisfied $\|\widetilde{s_0} - s_0\| = \varepsilon_0 < \varepsilon$, where ε is a fixed quantity that is substantially smaller than the reconstructed attractor. The phase space is a space on which a set of all states of the system is represented in such a way that to each possible state of the system corresponds a point, and the evolution of the system is represented by the displacement of this point. The selected points s_0 and $\widetilde{s_0}$ are separated in time. The evolution of the selected points on the reconstructed attractor is investigated until the distance between them exceeds a certain predetermined value ε_{max}. We introduce new notation: the points s_1 and $\widetilde{s_1}$, the distance between them is ε'_0, the evolution time interval is T_1. Further, again from the sequence (see Eq. 4) a point $\widetilde{s_1}$, close to s_1 is determined, for which the following condition must be fulfilled $\|\widetilde{s_1'} - s_1\| = \varepsilon_1 < \varepsilon$. It is desirable that the vectors $(\widetilde{s_1} - s_1)$ and $(\widetilde{s_1'} - s_1)$ have the same direction. The process is repeated for points s_1 and $\widetilde{s_1}$. As a result of the recurrence of this process, a large number (M) times, the first Lyapunov exponent has the following form

$$\lambda \cong \sum_{k=0}^{M-1} \ln(\varepsilon'_k/\varepsilon_k)/\sum_{k=1}^{M} T_k. \quad (5)$$

4. Computation of the highest Lyapunov exponent by the Rosenstein method

The Rosenstein method [12] is simple to implement and shows a good calculation speed, however, the result of its work is not a numerical value of λ_1, but a function of time:

$$y(i, \Delta t) = \frac{1}{\Delta t}\langle \ln d_j(i)\rangle, d_j(i) = \min_{x_j} \|x_j - x'_j\|, \quad (6)$$

where x_j is the point under consideration, and x_j' is one of its "neighbors". The algorithm is based on the connection d_j and Lyapunov exponents: $d_j(i) \approx e^{\lambda 1(i\Delta t)}$. The closest neighbor of the point under consideration is used for estimation. The higher Lyapunov exponent is proposed to be calculated as the slope angle of its most linear section. Finding such a site turns out to be a nontrivial task, and sometimes such a section can not be specified at all.

5. Algorithm for the application of artificial learning neural network for calculating the spectrum of Lyapunov exponents

A single-layer neural network is used [13]. A single-layer unidirectional neural network (see Fig. 1.) uses the layer n of hidden neurons to perform the next prediction $\hat{x}_k$ on the scalar time series x_k :

$$\hat{X} = \sum_{i=1}^{n} b_i \tanh\left(a_{i0} + \sum_{i=1}^{d} a_{ij} x_{k-i} \right), \tag{7}$$

where a_{ij} are coefficients of the matrix of size $n \times (d+1)$, b_i is a vector of length n. The matrix a_{ij} shows the number of connections at the entrance to the network, the vector b_i is used to determine the contribution of each neuron at the output from the network. A vector a_{i0} is an offset that facilitates learning on data whose mean is not zero. The idea of the method is to calculate, by means of an artificial learning neural network, the divergence of two nearby trajectories in n steps forward. An analog, self-organizing neural network is used, which is represented in the form of real numbers and forms the output space of solutions based on input effects. It is a network with dynamic links directed strictly from input to output. In the learning process, synaptic connections are set up, that is $dw/dt \neq 0$, where W are the network weights. To calculate the highest Lyapunov exponent, a necessary time delay is estimated based on the sample; the dimension of the embedding space is calculated; a pseudo-phase reconstruction of the trajectory by the method of time delays; a neural network is constructed to approximate the time series; The neural network a_{ij} is trained to calculate the next sequence vector of the time series; in the trained neural network, based on the generalized Benettin method [14].

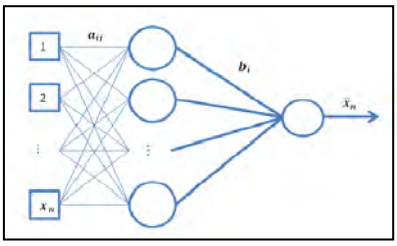

Figure 1. Single-layer neural network of direct propagation

6. Numerical results

We study the dynamics of the development of two time series: changes in time of the territory of the Ottoman Empire and population. These time series are one of the key characteristics of the development of the state. The Ottoman Empire was created by representatives of the Ottoman dynasty. The history of this dynasty begins with Osman I (1281 - 1326) (see Fig. 2A). The favorable location of the Osman Beylik on the border with Byzantium made it possible to make very profitable raids on the border Byzantine territories in order to enrich and simultaneously carry out ideological propaganda. These actions eventually helped him to conquer the rest of the emirates. The values of the first Lyapunov exponent for the time series of the territory change according to the Wolf method $\lambda_1 = 0.06371$, according to Rosenshtein's method $\lambda_1 = 0.01605$, neural networks $\lambda_1 = 0.00612$. For all three methods, the values are positive, but close to zero. This means that the system was in a chaotic state. It is seen in Figs. 3A, 3B, that the time variation graph of the first Lyapunov exponent λ_1 assumes positive values since 1376. This is the time of the beginning of the active expansion of the boundaries by Ottoman I. The dynamic expansion of the territory and the accession of all new states meant the constant allocation of the energy of the Ottoman state for the assimilation of new peoples (see Fig. 2B). The Ottoman Empire was a military-feudal, multiethnic (Turks, Arabs, Jews, Greeks, Armenians, etc.) state with a rigid vertical of power. At the head of this structure was the sultan, on which all structures of the state were closed: administrative - political, financial - tax, judicial - Muslim and judicial - non-Muslim and military.

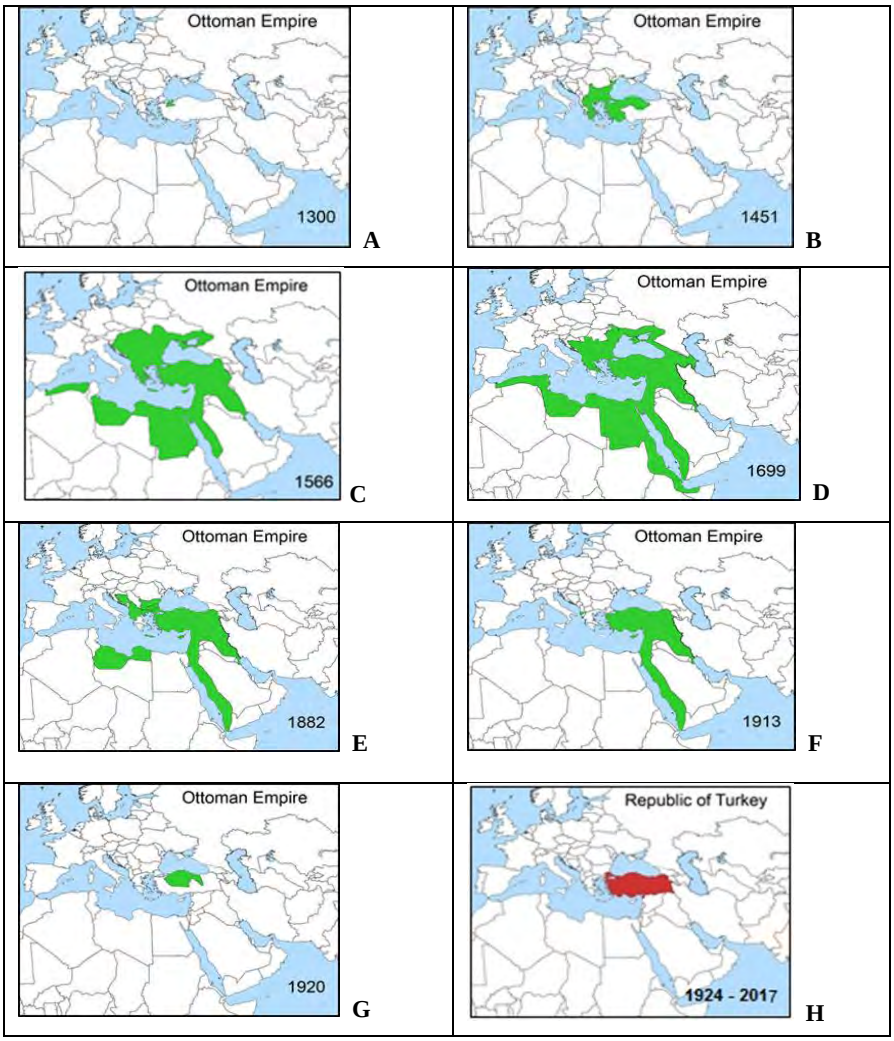

Figure 2. Maps of changes in the territory of the Ottoman Empire superimposed on a geographical map with modern state borders.

The international situation at the time of the formation of the Ottoman Empire was such that around it there were several dynamically developing states like the Holy Roman Empire, Hungary, the Polish-Lithuanian state and, in spite of its problems, Byzantium still existed. Undoubted and long-term dominance in the Mediterranean region, the Ottoman Empire was able to realize at the expense of a well-functioning state apparatus and the introduction of advanced technologies of that era both in the economy and in military structures. For example, the use of gunpowder allowed Mehmed II in 1453 conquer the impregnable Constantinople and make it the capital of a dynamically developing Ottoman state. During this period, the 2D interpretation of the wavelets HAAR and MHAT shows an

increase in the frequency spectrum, hence, of the state's energy. For example, due to the structure of the Treasury and the Chancellery until the XVII century, the Empire was the most progressive among the Muslim and most Christian states of that era. Much attention is paid to education, so in the period from 1463 to 1471 eight madrasahs (religious schools) were built. In 1476 a fundamentally new set of laws was created, detailing the rights and duties of rulers and the supreme clergy, legitimizing a loyal attitude towards the Gentiles and a new administrative division of the state that increased its military effectiveness.

A B

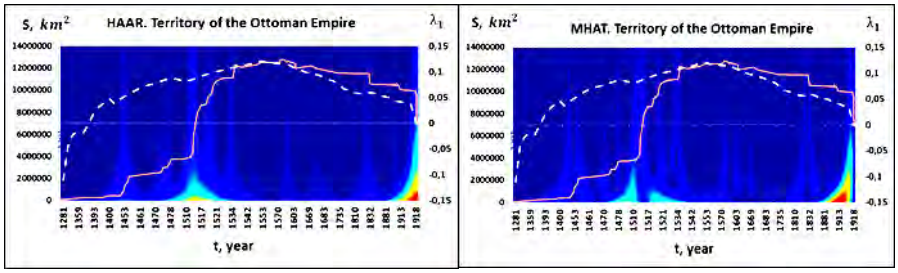

Figure 3. The change in the territory of the Ottoman Empire is a continuous line, the change in the time of the first Lyapunov exponent is a dashed line. The graphs are superimposed on the 2D interpretation of the HAAR (A) and the MHAT (B).

The non-Muslim population, who had a majority in succeeded in handicraft, trading, usurious foreign trade the empire, could not legally make an administrative and military career, but its representatives and economic policy within the empire and towards subordinate neighboring states created an image of just government in the Ottoman Empire in comparison with the aggressive actions of the Catholic leaders of that time. The dark area on 2D wavelets (see Fig. 3A, 3B) corresponds to the period of stability that was due to these reforms. The 2D interpretation of wavelets HAAR and MHAT (see Fig. 3A, 3B) shows that the highest frequencies ω are reached during the peak of the empire, starting from 1514 - the reign of Selim I of Grozny and until 1566, the end of Suleiman I the Magnificent, which means a significant increase in the energy of the state. It was a "golden age" - a period of intense gains and annexations of new territories, reforms of the state system, the creation of a new legislative system, the flowering of construction, architecture, science and art. Sultan Suleiman I controlled much of North Africa, Eastern Europe in 1529 and the troops of Suleiman I reached Vienna), the entire Middle East, the navy of the empire controlled the Mediterranean and Red Seas, the Indian Ocean (see Fig. 2C).This is a period of significant growth in the population of the empire (see Fig. 4A, 4B). The values of the first Lyapunov exponent λ_1 for the time series of population change by the Wolff method over the entire time interval are positive. The average value by the Wolf method $\lambda_1 = 0.17874$. The value calculated with the help of neural networks is negative, but very

close to zero $\lambda_1 = -0.01439$. The 2D interpretation of the wavelets HAAR and MHAT (see Fig. 4A, 4B) shows that the highest frequency values ω are also reached during the peak of the empire under the rule of Suleiman I.

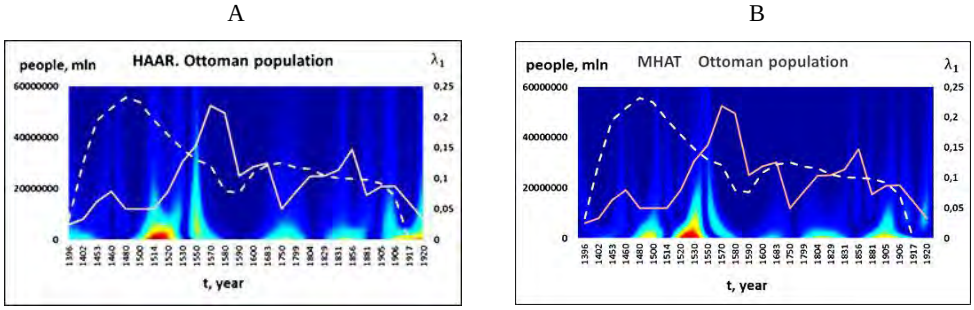

Figure 4. The change in the population of the Ottoman Empire is a continuous line, the change in the time of the first Lyapunov exponent is a dashed line. The graphs are superimposed on the 2D interpretation of the HAAR wavelet (A) and the MHAT (B) wavelet.

Population fluctuations were due to epidemics that covered most of the European and Asian continents. Great losses were suffered by the empire during periods of unsuccessful and constant wars that had occurred since the end of the 17th century. It should be noted that the policy of national and religious tolerance, which was conducted in the Ottoman Empire, made it possible to effectively manage this multinational state. The empire presents a “large building” (see Fig. 4A, 4B). It is clear that by the end of Suleiman I rule, the state energy begins to decrease. That corresponds to the emerging economic problems in the form of tax increases. In many respects this was due to tax benefits. Initially, the feudal possessions were members of the provisional content, which was given to a nobleman for a certain occupation or for lifetime use, but was not hereditary. But over time, the posts began to inherit and with them land. To the landlords from the central power passed the right to collect taxes - tax immunity. This was economically very profitable for the feudal lord and not entirely beneficial for the state. On the other hand, such a tax policy led to the fact that part of the Christian feudal lords (from Bulgarians and Serbs) accepted Islam and became military-feudal nobility in order to preserve their possessions and receive tax benefits. While feudal lords, Christians who recognized themselves as vassals of the Sultan had to pay taxes. The presence of several multifrequency peaks ω means that despite the large number of successful military campaigns, from which a fifth of the extraction was allocated by the law, nevertheless the funds in the treasury start to be catastrophically short. The growth of former taxes and the emergence of new ones begin. Such changes are always precursors of the approaching economic crises, since the internal energy of the state during the Magnificent Age period decreased noticeably (see Fig. 3A, 3B). In the empire, in many respects, the vertical of management was correlated with a strong leader, and the strict

regulation of all spheres of the state led to the fact that even the reforms that were being implemented did not keep peace with the new needs for the development of the empire. The entire infrastructure was programmed for war and conquest. This led to an overstrain of his forces (see Fig. 2D). After a succession of unsuccessful boards of weak sultans, disruption of state mechanisms, growth of corruption, taxes, and a slowdown in the expansion of imperial borders, there has been a decline and a significant decrease in state energy E_w (see Fig. 3A, 3B). For the period of the end of the XVI century. and the beginning of the XVII century there were political and economic crises, which correspond to the wavelet 2D analysis (see Fig. 3A, 3B). There is an increase in the frequency spectrum ω. At the end of the XVI century, before the Ottoman Empire, the world wave of the "price revolution" came, provoking a rapidly growing budget deficit and a financial crisis. The price revolution arose in Europe and on closely connected lands and meant an increase in trade prices of 2.5 - 4 times. The positions of the bureaucratic apparatus and the trade and usurious class have strengthened strongly, taxes continued to grow. The power structures practically could not keep under control the development of events, the political and socio-economic crisis broke out in the empire. A state that has little energy is unable to function steadily, which is confirmed by a series of riots by the non-Muslim population, which was most dangerous, i.e. the janissary corps is the elite military corps of sultans. All this greatly weakened the empire and undermined its international authority, and the Ottomans could not perceive the next stage of the military revolution. The values of the first λ_1 indicator are positive, that is, the state of the state system remains chaotic, the reforms did not help stabilize it. Period from the beginning of the XVIII century has a moderate increase in frequency ω. On the one hand, the frequency spectrum has increased, but with a different number of frequencies is not as large as in the previous multifrequency peaks. In the same period, the energy value of the state E_w does not increase. This is the period when the state apparatus worked ineffectively, and most of the collected as a result of taxes did not fall into the state treasury. Corruption practically paralyzed the work of the state machine. The empire increasingly became both economically and politically dependent on the more developed European states. At the end of the XVIII century and early XIX century. Reform attempts were periodically made and the situation was temporarily stabilized. This observation is consistent with the dark area on 2D wavelets (see Fig. 3A, 3B). For example, the reforms of Mustafa III (1757 - 1774), when the first public library was created in Constantinople, several hospitals and schools were built. Reform of Selim III (1789 - 1807), at the beginning of the XIX century the value of E_w increases significantly (see Fig. 3A, 3B). There is a disintegration of the military system of the state and a deep social crisis begun. A series of military defeats and the loss of significant territories only aggravate the problems. At the end of the XVIII century and early XIX century, there were several wars between the Ottoman Empire and the Russian Empire, the Egyptian expedition of Napoleon, the Crimean War of 1853-1856. As a result of the defeat in these wars, the

Ottoman Empire lost vast territories of Crimea, almost all of Serbia, Moldavia, Wallachia, Greece, Greece, the eastern coast of the Black Sea (see Fig. 2I). Throughout the XIX century and early XX century, the empire continues to lose territory (see Fig. 2E). Attempts are being made to transform and reform, which bring temporary and more local solutions to problems, which corresponds to a decrease in the frequency peaks ω (see Fig. 3A, 3B). In particular, the progressive state elite of the state carried out reforms on the Europeanization of the governance system and the legislative system of the state, but it met the aggressive resistance of the radical Muslim population and led to a new surge of unrest. After the end of the First World War, which ended in the defeat of Germany where the Ottoman Empire allied with it, large territories were diverted from the empire and troops of Atlanta were present in almost every province (see Fig. 2F). In the spring of 1920, the Great National Assembly was convened on which the patriotic forces of the empire were united and for two years the foreign troops were expelled. At the end of 1922 the sultanate was abolished. In place of the empire, a republic was formed (see Fig. 2J), which positively affected the values of the first Lyapunov index λ_1, which became zero.

7. Conclusions

As a result of the study of time series of changes in the territory and population of the Ottoman Empire, the Haar wavelet and the Mexican hat were chosen from a variety of options. These wavelets made it possible to localize the energy values of the state and clearly revealed the periods of its increase. For the first time to study the development of the Ottoman Empire, methods of nonlinear dynamics were applied and the notion of state energy was introduced. This provided an opportunity to analyze the social and economic development of the Ottoman Empire. The calculation of the Lyapunov exponent in three ways made it possible to obtain the reliability of the results. The results of wavelet analysis of historical time series and changes in the values of the first Lyapunov exponent λ_1 are in good agreement with each other.

Acknowledgments

This work has been supported by the Grant RSF № 16-11-10138

References

[1] Gündüz, G., The dynamics of the rise and fall of empires. *International Journal of Modern Physics C.* 27(10) (2016) 1650123.

[2] Gundogdu, B., Political and economic transition of ottoman sovereignty from a sole monarch to numerous ottoman elites, 1683-1750s. *Acta Orientalia* 70(1) (2017) 49-90.

[3] Ak, G., Reform efforts in the ottoman-Turkish maritime history: The case of 'mushaver pasha' adolphus slade [Osmanli-Türk denizcilik tarihi'nde reform çabalari ve 'müsavir pasa' adolphus slade]. *Amme Idaresi Dergisi* 49(4) (2016) 117-140.

[4] Tatyana, Y., Yaroshenko, T.Y., Krysko, D.V., Dobriyan, V., Zhigalov, M.V., Vos H., Vandenabeele, P., Krysko, V.A., Wavelet modeling and prediction of the stability of states: the Roman Empire and the European Union. *Communications in Nonlinear Science and Numerical Simulation* 26 (2015) 1-11.

[5] Krysko, V.A., Vygodchikova, I.Yu., Pleve, I.R., Yaroshenko, T.Y., Methods of nonlinear dynamics and minimax approximation criterion in the analysis of population dynamics. *Nonlinear World* 14(5) (2016) 64-73.

[6] Awrejcewicz, J, Krysko, V.A., Papkova, I.V., Krysko, A.V., Routes to chaos in continuous mechanical systems. Part 1*: Mathematical models and solution methods. Chaos, Solitons Fractals* 45 (2012) 687–708.

[7] Van den Berg, J.C., *Wavelets in Physics*. Cambridge: Cambridge Univ. Press, New York, 1998.

[8] Bowman, C., Newell, A.C., Natural patterns and wavelets. *Rewiews of Modern Physics*, 70(1) (1998) 289 – 301.

[9] Daubechies, J., Orthogonal bases of compactly supported wavelets. *Comm. Pure. Appl. Math.* 41(7) (1988) 906.

[10] Haar, A., Zur theorie der orthogonalen funktionensysteme. *Math Ann*. 71 (1911) 38–53.

[11] Wolf, A., Swift, J.B., Swinney, H.L., Vastano, J.A., Determining Lyapunov exponents from a time series. *Physica* D 16 (1985) 285-317.

[12] Rosenstein, M.T., Collins, J.J., De Luca, C.J., F practical method for calculatinglargest Lyapunov exponents from small data sets. *Physica D* 65 (1993) 117-134.

[13] Box, G., Jenkins, G.M., Reinsel, G., Time Series Analysis: Forecasting & Control. Prentice Hall, 1994.

[14] Benettin, G., Galgani, L., Strelcyn ,J.M., Kolmogorov entropy and numerical experiments. *Phys. Rev*. A 14 (1976) 2338-2345.

Tatyana Y. Yaroshenko, Associate Professor: Department of Mathematics and Modeling, Saratov State Technical University, Politehnicheskaya 77, 410054 Saratov, RUSSIAN FEDERATION (tyyaroshenko@gmail.com).

Jan Awrejcewicz, Professor: Lodz University of Technology, Faculty of Mechanical Engineering,Department of Automation, Biomechanics and Mechatronics, 1/15 Stefanowskego Str., 90-924 Lodz, POLAND (jan.awrejcewicz@p.lodz.pl).

Igor Pelve, Professor: Saratov State Technical University, Politehnicheskaya 77, 410054 Saratov, RUSSIAN FEDERATION (rectorat@sstu.ru).

Vadim A. Krysko, Professor: Department of Mathematics and Modeling, Saratov State Technical University, Politehnicheskaya 77, 410054 Saratov, RUSSIAN FEDERATION (tak@san.ru). the author presented this contribution at the conference.

Optimal thrust programming along the brachistochronic trajectory with drag

Alena Zarodnyuk, Oleg Cherkasov

Abstract: The problem of maximization of the horizontal coordinate of mass-point moving in the vertical plane driven by gravity, viscous drag, and thrust is considered. The slope angle and the thrust are considered as a control variables. The problem is related to the modified brachistochrone problem. Principle maximum procedure allows to reduce the optimal control problem to the boundary value problem for a system of two nonlinear differential equations. The qualitative analysis of the trajectories of this system is performed, and the robust properties of the optimal solutions are determined. Optimal controls depending on the state variables are designed. Characteristic features of the designed controls allow to construct quasi-optimal solutions for the more complex systems, where phase plane method is not applicable.

1. Introduction

The motion of a material point by a mass m in the vertical plane in a homogeneous field of gravity and in a homogeneous, resisting medium is considered. The slope angle and the thrust are considered as a control variables. The aim of the control is to maximize the horizontal range (terminal term in the functional) and minimize energy costs (integral term) at a given time of the process. Along with the problem of maximizing the range, we consider the brachistochrone problem - the problem of choosing the shape of a trajectory connecting two given points on a vertical plane, the time of travel along which is minimal, and the total control efforts should be also minimized. It is assumed that the dependence of the maximum range on time is monotonic. Then the problem of brachistochrone and the problem of maximizing the range in a given time are interrelated in the following sense. Let us take the maximum distance value obtained as a result of solving the problem with fixed time as a given final condition for the brachistochrone problem. Then the minimum time, obtained as a result of the solution of the latter, coincides with the time that was fixed when solving the problem of maximizing the range. Trajectories also coincide.

Various generalizations of the brachistochrone problem have not only methodological interest, but also have applications. Examples include the problem of optimizing the trajectories of aircraft, for which it is possible to control the lift force without changing the resistance force, the problem of optimal pursuit of a rectilinearly moving aircraft. The problem is relevant for the design of the

optimal drill and casing pipe drill profile in wells with given initial and final points, for determining the shape of trays for various bulk materials, for constructing the profile of rail sorting slides, for choosing the form of evacuation gangways, amusement rides like "roller coaster" etc. [1]. Generalizations of the classical problem of brachistochrone with the accelerating force were considered in [2-7]. In [2], the results of modeling for the case of an acceleration force proportional to the velocity were presented, and in [3] the same problem was solved using the genetic algorithm. In the dissertation [4] the problem of a brachistochrone with a constant accelerating force was considered. In [5] the problem was studied in the presence of a constant accelerating force and the force of linear viscous friction. In [6], the case of a quasi-constant acceleration force was investigated. In this case, the special class of optimal trajectories was considered, for which the transit time of each of its interior points is minimal for this point. In [7], the properties of trajectories with a quasi-constant acceleration force without friction are investigated analytically.

In this paper two control variables are considered: the thrust and the slope angle. The results obtained could be considered as some generalization of the papers, mentioned above.

2. Problem formulation

Equations of motion of the particle with constant mass in dimensionless variables are as follows:

$$\begin{cases} \dot{x} = v\cos\theta, \\ \dot{y} = v\sin\theta, \\ \dot{v} = p - v - \sin\theta. \end{cases} \tag{1}$$

Here x, y are the horizontal distance and vertical altitude respectively; v is the module of the velocity; θ is the slope angle, considered as a control variable; p is the thrust, another control variable subjected to inequality $-\overline{p} \le p(t) \le \overline{p}$, where $\overline{p}$ is positive constant; both controls are piecewise continuous function. The dot over symbols indicates the differentiation with respect to a dimensionless time. Initial conditions for the system (1) are as follows:

$$x(0) = x_0,\ y(0) = y_0,\ v(0) = v_0, \tag{2}$$

final conditions for variables v, y are free.

Goal function is

$$J = -x(T) + \int_0^T p^2(t)dt \to \min_{\theta, p}. \tag{3}$$

Let introduce new variable ξ by formula $\xi(t) = \int_0^t p^2(\tau)d\tau,$ and reduce the problem (1)-(3) to the following Mayer's optimal control problem for the system:

$$\begin{cases} \dot{x} = v\cos\theta, \\ \dot{y} = v\sin\theta, \\ \dot{v} = p - v - \sin\theta, \\ \dot{\xi}(t) = p^2, \end{cases} \tag{4}$$

with initial conditions

$$x(0) = x_0,\ y(0) = y_0,\ v(0) = v_0,\ \xi(0) = 0, \tag{5}$$

and the following goal function:

$$J = -x(T) + \xi(T) \to \min_{\theta,\ p}, \tag{6}$$

3. Problem analysis

The Hamiltonian of the problem (4)-(6) has a form:

$$H = \psi_x v\cos\theta + \psi_y v\sin\theta + \psi_v(p - v - \sin\theta) + \psi_\xi p^2 = C,$$

where C is unknown constant. Equations for co-state variables are written as follows:

$$\dot{\psi}_x = 0, \dot{\psi}_y = 0, \dot{\psi}_\xi = 0, \dot{\psi}_v = -\cos\theta + \psi_v. \tag{7}$$

From the transversality conditions it follows that

$$\psi_x(t) = 1,\ \psi_y(t) = 0,\ \psi_\xi(t) = -1,\ t \in [0, T],\ \psi_v(T) = 0.$$

The conditions for the maximum of the function H with respect to control θ are written in the form

$$\frac{\partial H}{\partial\theta} = -v\sin\theta - \psi_v\cos\theta = 0,\ \frac{\partial^2 H}{\partial\theta^2} = -\frac{v}{\cos\theta} < 0. \tag{8}$$

From the transversality conditions and the relations (8) it follows:

$$\psi_v = -vtg\theta,\ \theta(T) = 0,\ \cos\theta > 0.$$

The conditions for the maximum of the function H with respect to control p are written in the form

$$\frac{\partial H}{\partial p} = \psi_v - 2p,\ \frac{\partial^2 H}{\partial p^2} = -2 < 0.$$

Since the inequality

$$H''_{\theta\theta} \cdot H''_{pp} - (H''_{p\theta})^2 = 2v\cos\theta > 0$$

is fulfilled, the extremum exists, moreover, function H reaches its maximum. The extremal thrust control could be calculated from formula

$$p = -\psi_v / 2 = -(vtg\theta) / 2.$$

Taking into account restriction for the thrust $-\bar{p} \le p(t) \le \bar{p}$ we get the following control logic:

$p(t)=\bar{p}$, if $vtg\theta<-2\bar{p}$, $p(t)=-\dfrac{vtg\theta}{2}$, if $-2\bar{p}\le vtg\theta\le 2\bar{p}$, $p(t)=-\bar{p}$, if $vtg\theta>2\bar{p}$.

By differentiating ψ_v with respect to time according the systems (4), (7) the expression for the value of $\dot{\theta}$ could be found. Thus, the optimal control problem (4)-(6) is reduced to the following boundary-value problems:

$$vtg\theta<-2\bar{p},\quad p(t)=\bar{p}\qquad \begin{cases}\dot{v}=\bar{p}-v-\sin\theta, & v(0)=v_0\\ \dot{\theta}=\dfrac{\cos\theta}{v}\left(1+\left(2v-\bar{p}\right)\sin\theta\right), & \theta(T)=0,\end{cases} \tag{9}$$

$$vtg\theta>2\bar{p},\quad p(t)=-\bar{p}\qquad \begin{cases}\dot{v}=-\bar{p}-v-\sin\theta, & v(0)=v_0\\ \dot{\theta}=\dfrac{\cos\theta}{v}\left(1+\left(2v+\bar{p}\right)\sin\theta\right), & \theta(T)=0.\end{cases} \tag{10}$$

$$-2p\le vtg\theta\le 2\bar{p},\quad p(t)=-(vtg\theta)/2\qquad \begin{cases}\dot{v}=p-v-\sin\theta, & v(0)=v_0\\ \dot{\theta}=\dfrac{\cos\theta}{v}\left(1+v\left(2+\dfrac{tg\theta}{2}\right)\sin\theta\right), & \theta(T)=0,\end{cases} \tag{11}$$

Following to the presented logic, one can divide the plane into domains where the thrust takes boundary values, and where the value of the thrust belongs to internal range of the set of admissible values (see Fig.1). The system (9) has two states of equilibrium (θ_1, v_1) and (θ_2, v_2) for $\bar{p}\in[0;1]$, first of them is stable proper node, and the second is saddle-type point.

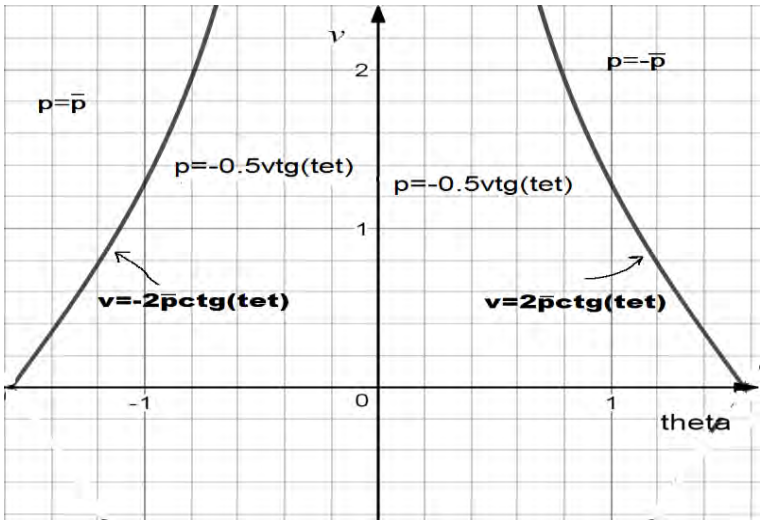

Figure 1. The domains of the motion with intermediate and boundary thrust.

For $\overline{p} > 1$ one more stationary solutions (θ_3, v_3) appears, it also presents the stable proper node. Corresponding phase portraits are presented in Fig.2 and Fig.3. The phase portrait makes it possible to analyze the qualitative properties of the solutions to the boundary value problem (9). It is seen that, at fixed value of $v(0)$, the initial value of $\theta(0)$ must be chosen between the separatrices entering the saddle point and the coordinate axis to ensure that at the time when the process is terminated the trajectory is on the straight line $\theta(T) = 0$. The set of possible initial conditions is shaded in Fig.2, 3.

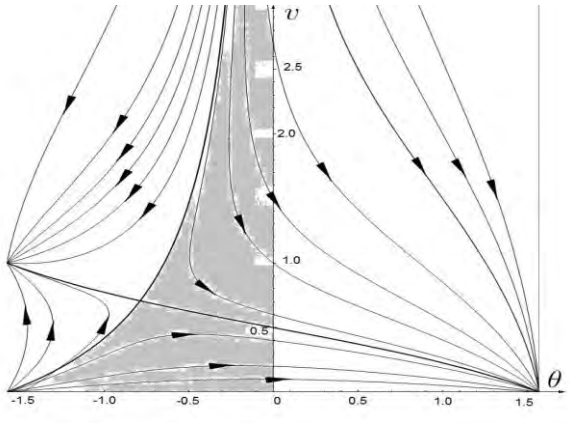

Figure 2. Phase portrait of the system (9) for $\overline{p} \in [0; 1]$.

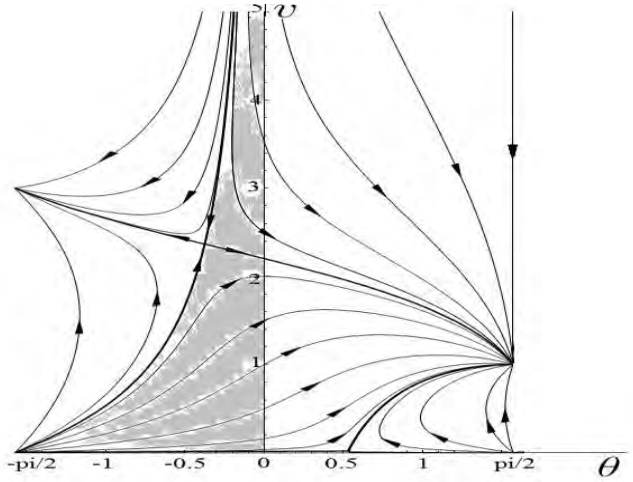

Figure 3. Phase portrait of the system (9) for $\overline{p} > 1$.

Consider system (10). The motion with control $p = -\overline{p}$ is acceptable in the domain $vtg\theta > 2\overline{p}$. It is easy to check, that in this mode the trajectory doesn't leave the domain. Thus, the motion under control $p = -\overline{p}$ doesn't include in the optimal trajectory.

Consider system (11). When intermediate thrust is applied, the system has single state of equilibrium, the saddle point with following coordinates:

$$\theta^* = arctg\left(\frac{1-\sqrt{17}}{4}\right), v^* = -\frac{2\sin\theta^*}{tg(\theta^*)+2}.$$

Corresponding phase portrait is presented in Fig.4.

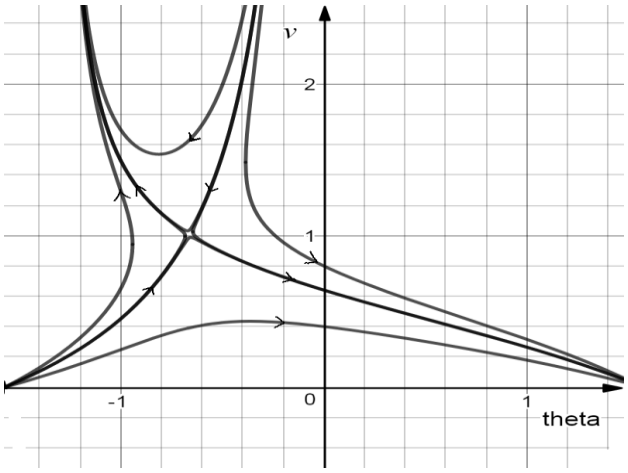

Figure 4. Phase portrait of the system (11).

Thus, the extremal synthesis of the thrust is designed. Extremal trajectory of the problem (4)-(6) consists either of single arc with intermediate thrust control or two arcs, starting with $p = \overline{p}$ and ending with the intermediate thrust.

In Fig.5 the extremal control, depending on time is presented. Corresponding trajectory in the plane (x, y) is shown in Fig.6.

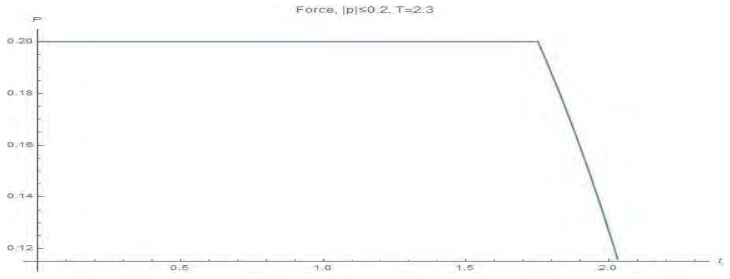

Figure 5. Extremal thrust along the trajectory, $\overline{p} = 0,2, T = 2,3$.

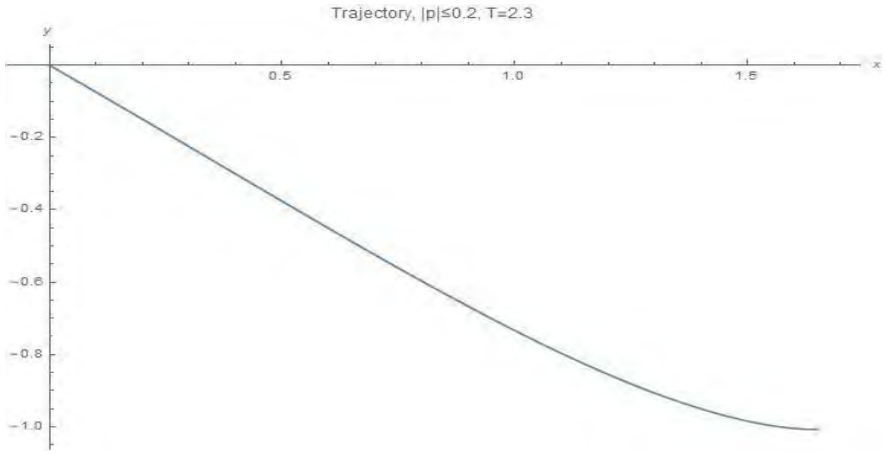

Figure 6. Trajectory in the plane (x, y), $\bar{p} = 0,2, T = 2,3$.

It is a characteristic feature that the type of the stationary solution corresponding to the inclined motion does not change when using various models of viscous friction, and also when taking into account the accelerating force. The existence of a saddle point is an illustration of the stability and unstability of the initial and conjugate systems. This point represents an asymptotic line of extremal motion. Its presence is a qualitative and "rough" property of boundary value problems, to which the optimal control problems are reduced if the trajectory spends excess time in a limited region of the subspace of states.

At sufficiently large values of the time T, the optimal trajectory consists of three parts. The first part corresponds to the rapid motion from the initial point to the neighborhood of the saddle point; the second part corresponds to the slow "drift" in the neighborhood of the saddle point; and the third part corresponds to the rapid motion from the neighborhood of the saddle point to the terminal point on the coordinate axis. The drift of the phase trajectory in the neighborhood of the saddle point in the plane (x, y) is associated with the almost straight part of the optimal trajectory.

1. Conclusions

The qualitative analysis of the brachistochrone problem with two control variables, the slope angle and the thrust allows to substantiate the simulation results presented in [2, 3, 5] and elaborate the properties of the analytical solutions obtained in [6,7].

Acknowledgments

This work was supported by RFBR according to the research projects №16-31-00204, 17-08-01366.

References

[1] Zarodnyuk, A.V., Cherkasov O.Yu. On the Maximization of the Horizontal Range and the Brachistochrone with an Accelerating Force and Viscous Friction. *Journal of Computer and Systems Sciences International* 56, 4 (2017), 553-560.

[2] Vratanar, B., Saje, M. On the Analytical Solution of the Brachistochrone Problem in a Non-conservative Field. *Int. J. Non-Linear Mechanics* 33, 3 (1998), 489-505.

[3] Chen D., Liao, G., Wang J. The Solution of Brachistochrone Problem Based on the Genetic Algorithm. *International Journal of Mechanics Research* 4, 4 (2015), 76-88.

[4] Thomas V. *The use of variational techniques in the optimization of flight trajectories.* Ph.D. thesis, University of Arizona, 1963, Parks, E.K.

[5] Drummond J.E., Downes, G.L. The Brachistochrone with Acceleration: A Running Track. *Journal of Optimization Theory and Applications* 7, 6 (1971), 444-449.

[6] Vondrukhov A.S., Golubev Yu.F. Brachistochrone with an Accelerating Force. *Journal of Computer and Systems Sciences International* 53, 6 (2014), 824-838.

[7] Vondrukhov A.S., Golubev Yu.F. Brachistochrone with an Accelerating Force. *Journal of Computer and Systems Sciences International* 54, 4 (2015), 514-524.

Oleg Cherkasov, Ph.D.: Lomonosov Moscow State University and Department of Mechanics and Mathematics, Leninskie Gory, 119991 Moscow, Russia (*oyuche@yandex.ru*). The author gave a presentation of this paper during one of the conference sessions.

Alena Zarodnyuk, Ph.D. student: Lomonosov Moscow State University and Department of Mechanics and Mathematics, Leninskie Gory, 119991 Moscow, Russia (*alenaz_90@inbox.ru*).

A remark on point coordinates in multibody dynamics formulations

Ulrike Zwiers

Abstract: This paper shows that condensed point-coordinate models of rigid bodies depend greatly on the method used to generate the governing set of equations. Referring to planar multibody systems, four different methods to formulate dynamically equivalent two-point models of arbitrarily shaped rigid bodies are presented, namely, reduction of three-point models, transformation of body-coordinate models in both centroidal and non-centroidal formulation, and a direct modeling approach. The numerical analysis of a physical pendulum serving as a benchmark example reveals that the resulting two-point models partially lack characteristics common to mechanical systems such as a symmetric, positive-definite mass matrix. However, despite their remarkable differences in inertia and inertial coupling, all models are proved to be capable to predict the pendulum's motion and the reactions at the pivot point correctly.

1. Introduction

In the point-coordinate formulation of multibody systems, also known as natural or fully Cartesian coordinates formulation, the rigid bodies are represented as a collection of mass points connected by massless links. The kinematic constraints of such models derive in two ways, from the assumption of rigidity of the bodies and from the joints or kinematic pairs. While the former leads to quadratic polynomials forcing constant distances between the points associated with a body, the latter is covered by simple algebraic equations that – as no angular coordinates are used – never involve trigonometric functions. Anyway, if the bodies are allowed to share some of their points, most kinematic joints do not cause any additional constraint equations in the formulation.

Thus, point-coordinate models can be expected to require less coordinates as body-coordinate models, but – in general – to be not as dense as joint-coordinate models. However, as the constraint equations occurring in point-coordinate models are significantly simpler as those formulated in either body or joint coordinates, their use might be advantageously in some cases.

From a didactic perspective, point coordinates allow to focus on the fundamental concepts of multibody dynamics without the need to distinguish between global and local coordinates, to work with rotary matrices, to pay special attention to closed kinematic chains, and so on. Especially when restricted to planar models, the point-coordinate formulation

enables – after a brief introduction – even undergraduate students to build quickly multibody models as basis for numerical simulations.

In this regard, the textbook [2] by Parviz E. Nikravesh is an excellent reference apart from giving the misleading impression that three points are required to represent a rigid body of arbitrary geometry in the plane[1]. Using actually three points to represent each body of a planar multibody system results in unnecessary large models, which motivates the formulation of condenced point-coordinate models as studied in this paper.

A generally applicable two-point representation of a planar rigid body can be derived in different ways. It should be noted, however, that the chosen approach determines the structure of the resulting model, which – after a concise account of the point-coordinate formulation – is shown by means of four methods that yield dynamically equivalent, but significantly different point-coordinate models.

2. Fundamentals of Point Coordinates

Properly formulated point-coordinate models preserve the kinematics and inertial characteristics of a system such that no approximations are involved. A general description of this formulation can be found in [1], while [2] refers exclusively to planar models. The notation used in this section is mainly adopted from [2].

2.1. Kinematics

A point in the plane is uniquely defined by its two Cartesian coordinates. If these coordinates are constant, the point is referred to as a *stationary point*, whereas a point with at least one variable coordinate that appears explicitly in the constraint equations is denoted as a *primary point*. In contrast to stationary points which can be defined arbitrarily without increasing the computational cost, the number of primary points is directly related to the model size and, thus, should be kept to a minimum.

The position, velocity, and acceleration of a point i are defined by the x-y components of $\boldsymbol{r}_i$, $\dot{\boldsymbol{r}}_i$, and $\ddot{\boldsymbol{r}}_i$, respectively. As most constraints occurring in point-coordinate models describe a condition on a vector that connects two points, such a vector between point i and point j is introduced first as $\boldsymbol{d}_{ij} = \boldsymbol{r}_j - \boldsymbol{r}_i$. Two points defined on a rigid body must keep their distance constant, which can be expressed as

$$\Phi = \frac{1}{2}\left(\boldsymbol{d}_{ij}^{\mathsf{T}}\boldsymbol{d}_{ij} - \ell_{ij}^2\right) = 0 \,, \tag{1}$$

[1]Only for the special case of a rod-like body, i. e., a body with a dominant axis along which its center of mass as well as all other points are located, a two-point representation is provided.

with ℓ_{ij} denoting the distance between the two points.

Taking the partial derivative of the kth constraint equation of the form (1) with respect to the array of coordinates yields one row in the Jacobian matrix whose non-zero entries read as

$$\boldsymbol{J}_k = \left[\cdots - \boldsymbol{d}_{ij}^{\mathsf{T}} \ldots \boldsymbol{d}_{ij}^{\mathsf{T}} \ldots \right] . \tag{2}$$

The negative product of the time derivative of the Jacobian matrix and the array of velocities constitutes the right-hand side array of the constraint equations at the acceleration level, which in case of the constant-length constraint assumes the form

$$\boldsymbol{\gamma}_k = -\dot{\boldsymbol{d}}_{ij}^{\mathsf{T}} \dot{\boldsymbol{d}}_{ij} . \tag{3}$$

Since only the constant-length constraint is of interest in the course of this study, other types of constraints occurring in point-coordinate formulations are not considered here.

2.2. Exact Mass Distribution

While a force whose point of application coincides with one of the particles representing a body of a point-coordinate model can be applied directly to that particle, general loads, such as torques and distributed loadings, must be distributed properly to the individual particles. This also holds for inertial characteristics, i. e., the masses of the particles must be specified in such a way that they behave dynamically just like the bodies they are representing. The following three conditions must be fulfilled in order to obtain an exact mass distribution:

1. The sum of the masses of the particles representing a single body must be equal to the overall mass of that body.

2. The mass center of the system of particles must coincide with the mass center of the body.

3. The moment of inertia of the system of particles about an arbitrary point must be the same as the moment of inertia of the body about that point.

As the second condition defines actually a vector equation, i. e., two algebraic equations for a body in the plane, these three conditions together lead to a total of four equations defining four unknown masses. With point S denoting the center of mass, these equations may be expressed in expanded form as

$$\begin{bmatrix} 1 & 1 & 1 & 1 \\ \xi_{\mathsf{A}} & \xi_{\mathsf{B}} & \xi_{\mathsf{C}} & 0 \\ \eta_{\mathsf{A}} & \eta_{\mathsf{B}} & \eta_{\mathsf{C}} & 0 \\ \boldsymbol{s}_{\mathsf{A}}^{\mathsf{T}} \boldsymbol{s}_{\mathsf{A}} & \boldsymbol{s}_{\mathsf{B}}^{\mathsf{T}} \boldsymbol{s}_{\mathsf{B}} & \boldsymbol{s}_{\mathsf{C}}^{\mathsf{T}} \boldsymbol{s}_{\mathsf{C}} & 0 \end{bmatrix} \begin{bmatrix} m_{\mathsf{A}} \\ m_{\mathsf{B}} \\ m_{\mathsf{C}} \\ m_{\mathsf{S}} \end{bmatrix} = \begin{bmatrix} m \\ 0 \\ 0 \\ \Theta_{\mathsf{S}} \end{bmatrix} , \tag{4}$$

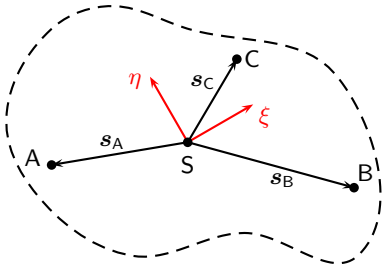

Figure 1. Point-coordinate representation of a planar body

with the positions of the other three points A, B, C being specified with respect to the ξ-η coordinate system located at the center of mass S, as shown in Figure 1.

Solving the system of equations (4) allows to construct the corresponding 8×8 diagonal mass matrix as[2]

$$\boldsymbol{M}_{4\mathsf{p}} = \begin{bmatrix} m_{\mathsf{A}}\boldsymbol{I} & \boldsymbol{0} & \boldsymbol{0} & \boldsymbol{0} \\ \boldsymbol{0} & m_{\mathsf{B}}\boldsymbol{I} & \boldsymbol{0} & \boldsymbol{0} \\ \boldsymbol{0} & \boldsymbol{0} & m_{\mathsf{C}}\boldsymbol{I} & \boldsymbol{0} \\ \boldsymbol{0} & \boldsymbol{0} & \boldsymbol{0} & m_{\mathsf{S}}\boldsymbol{I} \end{bmatrix} . \tag{5}$$

If a planar rigid body is modeled by four points, i. e., by eight Cartesian coordinates, five constraint equations of the form (1) must be established to end up with three degrees of freedom. It is, however, not necessary to use actually four points to model a rigid body in the plane as the coordinates of point S, the center of mass, can be expressed as functions of the coordinates of the other three particles[3]:

$$\boldsymbol{r}_{\mathsf{S}} = \frac{m_{\mathsf{A}}\boldsymbol{r}_{\mathsf{A}} + m_{\mathsf{B}}\boldsymbol{r}_{\mathsf{B}} + m_{\mathsf{C}}\boldsymbol{r}_{\mathsf{C}}}{m_{\mathsf{A}} + m_{\mathsf{B}} + m_{\mathsf{C}}}$$

[2] As for the special case of a rigid body with a dominant axis along which its center of mass as well as the other particles are located (*rod-like body*), one of the equations in (4) becomes redundant such that the exact mass distribution is obtained by only three points.

[3] In case of a rod-like body, the coordinates of point S may be expressed accordingly as functions of the coordinates of the other two particles.

Thus, the vector of coordinates can be transformed as

$$\begin{bmatrix} \boldsymbol{r}_{\mathsf{A}} \\ \boldsymbol{r}_{\mathsf{B}} \\ \boldsymbol{r}_{\mathsf{C}} \\ \boldsymbol{r}_{\mathsf{S}} \end{bmatrix} = \underbrace{\begin{bmatrix} \boldsymbol{I} & \boldsymbol{0} & \boldsymbol{0} \\ \boldsymbol{0} & \boldsymbol{I} & \boldsymbol{0} \\ \boldsymbol{0} & \boldsymbol{0} & \boldsymbol{I} \\ \mu_{\mathsf{A}}\boldsymbol{I} & \mu_{\mathsf{B}}\boldsymbol{I} & \mu_{\mathsf{C}}\boldsymbol{I} \end{bmatrix}}_{\boldsymbol{B}} \begin{bmatrix} \boldsymbol{r}_{\mathsf{A}} \\ \boldsymbol{r}_{\mathsf{B}} \\ \boldsymbol{r}_{\mathsf{C}} \end{bmatrix} ,$$

with the mass ratios

$$\mu_i = \frac{m_i}{m_{\mathsf{A}} + m_{\mathsf{B}} + m_{\mathsf{C}}} , \quad i = \mathsf{A}, \mathsf{B}, \mathsf{C} .$$

Now, using the 8×6 transformation matrix $\boldsymbol{B}$, the 8×8 mass matrix (5) can be reduced to the 6×6 mass matrix $\boldsymbol{M}_{3\mathsf{p}} = \boldsymbol{B}^{\mathsf{T}} \boldsymbol{M}_{4\mathsf{p}} \boldsymbol{B}$ representing a planar body by only three points:

$$\boldsymbol{M}_{3\mathsf{p}} = \begin{bmatrix} (m_{\mathsf{A}} + \mu_{\mathsf{A}}^2 m_{\mathsf{S}})\boldsymbol{I} & \mu_{\mathsf{A}}\mu_{\mathsf{B}} m_{\mathsf{S}} \boldsymbol{I} & \mu_{\mathsf{A}}\mu_{\mathsf{C}} m_{\mathsf{S}} \boldsymbol{I} \\ \mu_{\mathsf{B}}\mu_{\mathsf{A}} m_{\mathsf{S}} \boldsymbol{I} & (m_{\mathsf{B}} + \mu_{\mathsf{B}}^2 m_{\mathsf{S}})\boldsymbol{I} & \mu_{\mathsf{B}}\mu_{\mathsf{C}} m_{\mathsf{S}} \boldsymbol{I} \\ \mu_{\mathsf{C}}\mu_{\mathsf{A}} m_{\mathsf{S}} \boldsymbol{I} & \mu_{\mathsf{C}}\mu_{\mathsf{B}} m_{\mathsf{S}} \boldsymbol{I} & (m_{\mathsf{C}} + \mu_{\mathsf{C}}^2 m_{\mathsf{S}})\boldsymbol{I} \end{bmatrix} \tag{6}$$

Even though the coordinates of point S are eliminated from the model, its contribution to the mass matrix is obviously kept. The resulting mass matrix of the three-point model is still time-invariant and symmetric, but no longer diagonal.

Assuming a rigid body which is only subject to the gravitational force, the load vector associated with the four-point model reads as

$$\boldsymbol{g}_{4\mathsf{p}} = \begin{bmatrix} \boldsymbol{F}_{g,\mathsf{A}} \\ \boldsymbol{F}_{g,\mathsf{B}} \\ \boldsymbol{F}_{g,\mathsf{C}} \\ \boldsymbol{F}_{g,\mathsf{S}} \end{bmatrix} \quad \text{with} \quad \boldsymbol{F}_{g,j} = \begin{bmatrix} 0 \\ -m_j g \end{bmatrix} , \quad j = \mathsf{A}, \mathsf{B}, \mathsf{C}, \mathsf{S}. \tag{7}$$

Transforming the load vector to the three-point model according to $\boldsymbol{g}_{3\mathsf{p}} = \boldsymbol{B}^{\mathsf{T}} \boldsymbol{g}_{4\mathsf{p}}$ yields the reduced load vector

$$\boldsymbol{g}_{3\mathsf{p}} = \begin{bmatrix} \boldsymbol{F}_{g,\mathsf{A}} + \mu_{\mathsf{A}} \boldsymbol{F}_{g,\mathsf{S}} \\ \boldsymbol{F}_{g,\mathsf{B}} + \mu_{\mathsf{B}} \boldsymbol{F}_{g,\mathsf{S}} \\ \boldsymbol{F}_{g,\mathsf{C}} + \mu_{\mathsf{C}} \boldsymbol{F}_{g,\mathsf{S}} \end{bmatrix} . \tag{8}$$

Thus, for each of the remaining three points, an effective mass can be defined as

$$m_i^* = m_i + \mu_i \, m_{\mathsf{S}} \quad , \quad i = \mathsf{A}, \mathsf{B}, \mathsf{C} , \tag{9}$$

which equals the sum of the corresponding rows or columns, respectively, of the mass matrix given by (6).

Anyway, the three-point model of a planar body given by (6) and (9) together with three constraints of the type (1) can be further reduced as shown in the next section.

3. Two-point representation of planar bodies

There are actually various ways to end up with a two-point model of a planar body. This study considers four of them: reduction of the three-point model (*model I*), transformation of the body-coordinate model in centroidal formulation (*model II*), transformation of the body-coordinate model in non-centroidal formulation (*model III*) and a direct modeling approach (*model IV*). Even though the process of transforming an existing model is straight forward, it possesses the disadvantage of obscuring the underlying mechanical concepts, which motivates the attempt to formulate the model in a direct manner. Furthermore, as each method leads to a different, yet equivalent model, this study might provide additional insight into inertia coupling.

All models, however, lead to a differential equation of the general form

$$\boldsymbol{M}_k \begin{bmatrix} \ddot{\boldsymbol{r}}_{\mathsf{A}} \\ \ddot{\boldsymbol{r}}_{\mathsf{B}} \end{bmatrix} + \boldsymbol{J}^{\mathsf{T}} \lambda = \boldsymbol{g}_k \quad , \quad k = \mathsf{I}, \mathsf{II}, \mathsf{III}, \mathsf{IV}, \tag{10}$$

in which the mass matrix $\boldsymbol{M}_k$ and the load vector $\boldsymbol{g}_k$ depend on the method applied for derivation. As a two-point model is formulated in four Cartesian coordinates, only one constraint of the form (1) is required anymore. Consequently, the Jacobian reduces to a vector given by (2).

3.1. Reduction of the three-point model

In the first instance, the three-point model introduced above is simply reduced by eliminating one particle and its corresponding constraints from the equations of motion.

Referring to Figure 2, the position of one particle of the three-point model of a planar body can be expressed as function of the coordinates of the two other particles, e. g.,

$$\boldsymbol{r}_{\mathsf{C}} = \boldsymbol{r}_{\mathsf{A}} + \frac{p}{\ell}(\boldsymbol{r}_{\mathsf{B}} - \boldsymbol{r}_{\mathsf{A}}) + \frac{q}{\ell}\boldsymbol{D}(\boldsymbol{r}_{\mathsf{B}} - \boldsymbol{r}_{\mathsf{A}}) \, , \tag{11}$$

where $\boldsymbol{D}$ is the matrix that rotates a vector in the plane counter-clockwise by 90°, i. e.,

$$\boldsymbol{D} = \begin{bmatrix} 0 & -1 \\ 1 & 0 \end{bmatrix} .$$

By means of the transformation expression

$$\begin{bmatrix} \boldsymbol{r}_{\mathsf{A}} \\ \boldsymbol{r}_{\mathsf{B}} \\ \boldsymbol{r}_{\mathsf{C}} \end{bmatrix} = \underbrace{\begin{bmatrix} \boldsymbol{I} & \boldsymbol{0} \\ \boldsymbol{0} & \boldsymbol{I} \\ \left(1 - \frac{p}{\ell}\right)\boldsymbol{I} - \frac{q}{\ell}\boldsymbol{D} & \frac{p}{\ell}\boldsymbol{I} + \frac{q}{\ell}\boldsymbol{D} \end{bmatrix}}_{\boldsymbol{T}_{\mathsf{I}}} \begin{bmatrix} \boldsymbol{r}_{\mathsf{A}} \\ \boldsymbol{r}_{\mathsf{B}} \end{bmatrix} ,$$

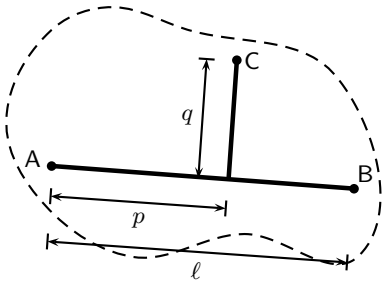

Figure 2. Geometry of the three-point model

one may construct the reduced 4×4 mass matrix as

$$\boldsymbol{M}_{\mathsf{I}} = \boldsymbol{T}_{\mathsf{I}}^{\mathsf{T}} \boldsymbol{M}_{\mathsf{3p}} \boldsymbol{T}_{\mathsf{I}} = \begin{bmatrix} \boldsymbol{M}_{\mathsf{I,AA}} & \boldsymbol{M}_{\mathsf{I,AB}} \\ \boldsymbol{M}_{\mathsf{I,BA}} & \boldsymbol{M}_{\mathsf{I,BB}} \end{bmatrix} , \tag{12}$$

which is a time-invariant, symmetric matrix whose block matrices $\boldsymbol{M}_{\mathsf{I,AA}}$ and $\boldsymbol{M}_{\mathsf{I,BB}}$ are diagonal each with identical non-zero entries, while the other two block matrices are dense with identical diagonal and off-diagonal entries, and it holds that $\boldsymbol{M}_{\mathsf{I,AB}} = \boldsymbol{M}_{\mathsf{I,BA}}^{\mathsf{T}}$.

The reduced load vector of this first two-point model is also time-invariant. It is constructed as follows

$$\boldsymbol{g}_{\mathsf{I}} = \boldsymbol{T}_{\mathsf{I}}^{\mathsf{T}} \boldsymbol{g}_{\mathsf{3p}} = \begin{bmatrix} F_{g,\mathsf{A}}^{*} + F_{g,\mathsf{C}}^{*} - \left(\dfrac{p}{\ell} \boldsymbol{I} - \dfrac{q}{\ell} \boldsymbol{D} \right) F_{g,\mathsf{C}}^{*} \\ F_{g,\mathsf{B}}^{*} + \left(\dfrac{p}{\ell} \boldsymbol{I} - \dfrac{q}{\ell} \boldsymbol{D} \right) F_{g,\mathsf{C}}^{*} \end{bmatrix} , \tag{13}$$

where $F_{g,i}^{*}$, $i = \mathsf{A}, \mathsf{B}, \mathsf{C}$, are the effective gravitational forces with the masses given by (9).

3.2. Transformation of body-coordinate models

In a body-coordinate model of a planar multibody system, three coordinates are introduced for each body, namely two Cartesian coordinates defining the position of a point of the body and one angular coordinate describing the orientation of the body, regardless of the constraints that may couple some of the coordinates.

Referring to Figure 2, the lengths p and q are replaced by α and β, respectively, to specify the position of the center of mass, denoted with S, in an analogous manner as the position of point C given by (11), i. e.,

$$\boldsymbol{r}_{\mathsf{S}} = \boldsymbol{r}_{\mathsf{A}} + \frac{\alpha}{\ell} (\boldsymbol{r}_{\mathsf{B}} - \boldsymbol{r}_{\mathsf{A}}) + \frac{\beta}{\ell} \boldsymbol{D} (\boldsymbol{r}_{\mathsf{B}} - \boldsymbol{r}_{\mathsf{A}}) \, . \tag{14}$$

3.2.1. Centroidal formulation

If the local, body-fixed ξ-η coordinate system is defined at the center of mass, the equations of motion of a single, unconstrained body read as

$$\underbrace{\begin{bmatrix} m\boldsymbol{I} & \boldsymbol{0} \\ \boldsymbol{0}^{\mathsf{T}} & \Theta_{\mathsf{S}} \end{bmatrix}}_{\boldsymbol{M}_{\mathsf{S}}} \begin{bmatrix} \ddot{\boldsymbol{r}}_{\mathsf{S}} \\ \ddot{\phi} \end{bmatrix} = \begin{bmatrix} \boldsymbol{F}_g \\ 0 \end{bmatrix} . \tag{15}$$

As before, the body is assumed to be only subject to the gravitational force.

By means of the transformation expression

$$\begin{bmatrix} \ddot{\boldsymbol{r}}_{\mathsf{S}} \\ \ddot{\phi} \end{bmatrix} = \underbrace{\frac{1}{\ell^2} \begin{bmatrix} (\ell - \alpha)\,\ell\boldsymbol{I} - \beta\ell\boldsymbol{D} & \alpha\ell\boldsymbol{I} + \beta\ell\boldsymbol{D} \\ -\left(\boldsymbol{D}(\boldsymbol{r}_{\mathsf{B}} - \boldsymbol{r}_{\mathsf{A}})\right)^{\mathsf{T}} & \left(\boldsymbol{D}(\boldsymbol{r}_{\mathsf{B}} - \boldsymbol{r}_{\mathsf{A}})\right)^{\mathsf{T}} \end{bmatrix}}_{\boldsymbol{T}_{\mathsf{II}}} \begin{bmatrix} \ddot{\boldsymbol{r}}_{\mathsf{A}} \\ \ddot{\boldsymbol{r}}_{\mathsf{B}} \end{bmatrix}$$

formulated at the acceleration level, one may construct the reduced 4×4 mass matrix of the second model as $\boldsymbol{M}_{\mathsf{II}} = \boldsymbol{T}_{\mathsf{II}}^{\mathsf{T}} \boldsymbol{M}_{\mathsf{S}} \boldsymbol{T}_{\mathsf{II}}$ which is a time-variant, symmetric, but singular matrix of rank three as the transformation introduces a redundant coordinate. However, the governing differential-algebraic system of equations built of the differential equation (10) and the algebraic constraint equation (1) is well defined.

It can be shown that the reduced load vector of this second model is identical to the one of the first model, i. e., $\boldsymbol{g}_{\mathsf{II}} = \boldsymbol{g}_{\mathsf{I}}$ as given by (13).

3.2.2. Non-centroidal formulation

If the local ξ-η coordinate system is defined at an arbitrary point A, the inertia matrix is no longer diagonal and time-invariant. Furthermore, the load vector must account for the centrifugal force and the moment now caused by the gravitational force. Thus, the equations of motion assume the form

$$\underbrace{\begin{bmatrix} m\boldsymbol{I} & m\boldsymbol{D}\boldsymbol{s}_{\mathsf{AS}} \\ m(\boldsymbol{D}\boldsymbol{s}_{\mathsf{AS}})^{\mathsf{T}} & \Theta_{\mathsf{A}} \end{bmatrix}}_{\boldsymbol{M}_{\mathsf{A}}} \begin{bmatrix} \ddot{\boldsymbol{r}}_{\mathsf{A}} \\ \ddot{\phi} \end{bmatrix} = \underbrace{\begin{bmatrix} \boldsymbol{F}_g + m\dot{\phi}^2 \boldsymbol{s}_{\mathsf{AS}} \\ (\boldsymbol{D}\boldsymbol{s}_{\mathsf{AS}})^{\mathsf{T}} \boldsymbol{F}_{\mathsf{g}} \end{bmatrix}}_{\boldsymbol{g}_{\mathsf{A}}} . \tag{16}$$

By means of the transformation expression

$$\begin{bmatrix} \ddot{\boldsymbol{r}}_{\mathsf{A}} \\ \ddot{\phi} \end{bmatrix} = \underbrace{\frac{1}{\ell^2} \begin{bmatrix} \ell^2\boldsymbol{I} & \boldsymbol{0} \\ -\left(\boldsymbol{D}(\boldsymbol{r}_{\mathsf{B}} - \boldsymbol{r}_{\mathsf{A}})\right)^{\mathsf{T}} & \left(\boldsymbol{D}(\boldsymbol{r}_{\mathsf{B}} - \boldsymbol{r}_{\mathsf{A}})\right)^{\mathsf{T}} \end{bmatrix}}_{\boldsymbol{T}_{\mathsf{III}}} \begin{bmatrix} \ddot{\boldsymbol{r}}_{\mathsf{A}} \\ \ddot{\boldsymbol{r}}_{\mathsf{B}} \end{bmatrix}$$

one may construct the reduced 4×4 mass matrix of the third model as $\boldsymbol{M}_{\mathsf{III}} = \boldsymbol{T}_{\mathsf{III}}^{\mathsf{T}} \boldsymbol{M}_{\mathsf{A}} \boldsymbol{T}_{\mathsf{III}}$ which is – just like the one of the second model – a time-variant, symmetric matrix of rank three.

As for the reduced load vector, one obtains a time-variant vector due to the time dependency of the right-hand side of (16), $\boldsymbol{g}_{\mathsf{III}} = \boldsymbol{T}_{\mathsf{III}}^{\mathsf{T}} \boldsymbol{g}_{\mathsf{A}}$, where the angular velocity can be expressed as

$$\dot{\phi} = \frac{1}{\ell^2} \left(\dot{\boldsymbol{r}}_{\mathsf{B}} - \dot{\boldsymbol{r}}_{\mathsf{A}} \right)^{\mathsf{T}} \boldsymbol{D} \left(\boldsymbol{r}_{\mathsf{B}} - \boldsymbol{r}_{\mathsf{A}} \right) \ .$$

3.3. Direct Modeling

Another approach of deriving a two-point model of a planar rigid body consists of expressing its kinetic energy instead of

$$T = \frac{1}{2} m v_{\mathsf{S}}^2 + \frac{1}{2} \Theta_{\mathsf{S}} \dot{\phi}^2 \tag{17}$$

in terms of the velocities of the two points A and B

$$T = \frac{1}{2} \begin{bmatrix} \dot{\boldsymbol{r}}_{\mathsf{A}}^{\mathsf{T}} & \dot{\boldsymbol{r}}_{\mathsf{B}}^{\mathsf{T}} \end{bmatrix} \boldsymbol{M}_{\mathsf{IV}} \begin{bmatrix} \dot{\boldsymbol{r}}_{\mathsf{A}} \\ \dot{\boldsymbol{r}}_{\mathsf{B}} \end{bmatrix} \ . \tag{18}$$

This quadratic form allows to identify directly the elements of the mass matrix $\boldsymbol{M}_{\mathsf{IV}}$.

The velocity of the center of mass may be expressed as

$$\boldsymbol{v}_{\mathsf{S}} = \frac{1}{\ell} \begin{bmatrix} (\ell - \alpha) \boldsymbol{I} - \beta \boldsymbol{D} & \alpha \boldsymbol{I} + \beta \boldsymbol{D} \end{bmatrix} \begin{bmatrix} \dot{\boldsymbol{r}}_{\mathsf{A}} \\ \dot{\boldsymbol{r}}_{\mathsf{B}} \end{bmatrix} \tag{19}$$

which leads to

$$v_{\mathsf{S}}^2 = \frac{1}{\ell^2} \begin{bmatrix} \dot{\boldsymbol{r}}_{\mathsf{A}} & \dot{\boldsymbol{r}}_{\mathsf{B}} \end{bmatrix} \begin{bmatrix} \left((\ell - \alpha)^2 + \beta^2 \right) \boldsymbol{I} & \left((\ell - \alpha)\alpha - \beta^2 \right) \boldsymbol{I} + \beta \ell \boldsymbol{D} \\ \left((\ell - \alpha)\alpha - \beta^2 \right) \boldsymbol{I} - \beta \ell \boldsymbol{D} & (\alpha^2 + \beta^2) \boldsymbol{I} \end{bmatrix} \begin{bmatrix} \dot{\boldsymbol{r}}_{\mathsf{A}} \\ \dot{\boldsymbol{r}}_{\mathsf{B}} \end{bmatrix} \ .$$

In an analogous manner, the squared angular velocity may be expressed as

$$\dot{\phi}^2 = \frac{1}{\ell^2} \begin{bmatrix} \dot{\boldsymbol{r}}_{\mathsf{A}} & \dot{\boldsymbol{r}}_{\mathsf{B}} \end{bmatrix} \begin{bmatrix} \boldsymbol{I} & -\boldsymbol{I} \\ -\boldsymbol{I} & \boldsymbol{I} \end{bmatrix} \begin{bmatrix} \dot{\boldsymbol{r}}_{\mathsf{A}} \\ \dot{\boldsymbol{r}}_{\mathsf{B}} \end{bmatrix} \ ,$$

such that the mass matrix assumes the form

$$\boldsymbol{M}_{\mathsf{IV}} = \frac{m}{\ell^2} \begin{bmatrix} \left((\ell - \alpha)^2 + \beta^2 + k_{\mathsf{S}}^2 \right) \boldsymbol{I} & \left((\ell - \alpha)\alpha - \beta^2 - k_{\mathsf{S}}^2 \right) \boldsymbol{I} + \beta \ell \boldsymbol{D} \\ \left((\ell - \alpha)\alpha - \beta^2 - k_{\mathsf{S}}^2 \right) \boldsymbol{I} - \beta \ell \boldsymbol{D} & (\alpha^2 + \beta^2 + k_{\mathsf{S}}^2) \boldsymbol{I} \end{bmatrix} \tag{20}$$

where k_{S} is the radius of inertia according to $\Theta_{\mathsf{S}} = m k_{\mathsf{S}}^2$.

The load vector can be constructed in different ways. For example, the gravitational force may be split onto both points such that the load vector assumes the form

$$\boldsymbol{g}_{\mathsf{IV}} = \begin{bmatrix} F^*_{g,\mathsf{A}} + F_{n,\mathsf{A}} \\ F^*_{g,\mathsf{B}} + F_{n,\mathsf{B}} \end{bmatrix} , \tag{21}$$

with the effective gravitational forces $F^*_{g,i}$, $i = \mathsf{A}, \mathsf{B}$ whose effective masses are obtained by summing up the respective entries in the columns or rows of the mass matrix:

$$\begin{aligned} m^*_{\mathsf{A}} &= (\ell - \alpha + \beta)\,\frac{m}{\ell} \\ m^*_{\mathsf{B}} &= (\alpha - \beta)\,\frac{m}{\ell} \end{aligned}$$

The forces $F_{n,\mathsf{A}}$ and $F_{n,\mathsf{B}}$ appearing in (21) form a force couple, i. e., $F_{n,\mathsf{A}} = -F_{n,\mathsf{B}}$, acting perpendicularly on the axis of the two-point model:

$$F_{n,\mathsf{B}} = \frac{n}{\ell^2}\boldsymbol{D}\boldsymbol{s}_{\mathsf{AB}} , \tag{22}$$

where n is the displacement moment of the gravitational force. Taking the moment with respect to point A, it reads as

$$n = (\boldsymbol{D}\boldsymbol{s}_{\mathsf{AS}})^{\mathsf{T}}\boldsymbol{F}_g - (\boldsymbol{D}\boldsymbol{s}_{\mathsf{AB}})^{\mathsf{T}}\boldsymbol{F}_{g,\mathsf{B}} .$$

Obviously, the load vector of this fourth model as given by (21) is time-variant.

4. Example: Physical Pendulum

In order to compare the four different two-point models derived above, numerical simulations of the physical pendulum depicted in Figure 3 are carried out. Starting from the configuration in which the ξ-η coordinate system is oriented horizontally without initial velocity, the

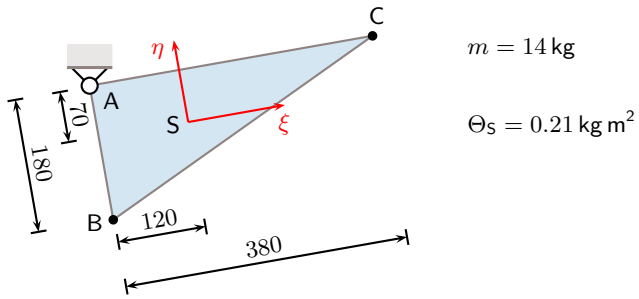

Figure 3. Geometry and inertia of the physical pendulum

	$t = 0$	$t = 4\,\mathsf{s}$
$\boldsymbol{M}_{\mathsf{I}}$	$\begin{bmatrix} 14.821 & 0.000 & -9.377 & 9.333 \\ 0.000 & 14.821 & 9.333 & -9.377 \\ -9.377 & 9.333 & 17.932 & 0.000 \\ -9.333 & -9.377 & 0.000 & 17.932 \end{bmatrix}$	$\cdots$
$\boldsymbol{M}_{\mathsf{II}}$	$\begin{bmatrix} 14.821 & 0.000 & -9.377 & -9.333 \\ 0.000 & 8.340 & 9.333 & -2.895 \\ -9.377 & 9.333 & 17.932 & 0.000 \\ -9.333 & -2.895 & 0.000 & 11.451 \end{bmatrix}$	$\begin{bmatrix} 12.245 & -3.172 & -6.800 & -6.161 \\ -3.172 & 10.916 & 12.505 & -5.471 \\ -6.800 & 12.505 & 15.356 & -3.172 \\ -6.161 & -5.471 & -3.172 & 14.027 \end{bmatrix}$
$\boldsymbol{M}_{\mathsf{III}}$	$\begin{bmatrix} 14.821 & -9.333 & -9.377 & 0.000 \\ -9.333 & 14.000 & 9.333 & 0.000 \\ -9.377 & 9.333 & 17.932 & 0.000 \\ 0.000 & 0.000 & 0.000 & 0.000 \end{bmatrix}$	$\begin{bmatrix} 5.502 & -2.814 & -1.395 & 1.070 \\ -2.814 & 23.319 & 10.404 & -7.981 \\ -1.395 & 10.404 & 11.288 & -8.660 \\ 1.070 & -7.981 & -8.660 & 6.644 \end{bmatrix}$
$\boldsymbol{M}_{\mathsf{IV}}$	$\begin{bmatrix} 14.821 & 0.000 & -9.377 & -9.333 \\ 0.000 & 14.821 & 9.333 & -9.377 \\ -9.377 & 9.333 & 17.932 & 0.000 \\ -9.333 & -9.377 & 0.000 & 17.932 \end{bmatrix}$	$\cdots$

Figure 4. Entries of the mass matrices

temporal development of both the swing angle and the reaction forces at the pivot point are verified to assure the dynamical equivalence of the four models.

Figures 4 and 5 document the entries of the mass matrices and load vectors of the four models at the initial state and at an arbitrary instant of time, namely after four seconds. It can be seen that the first and the fourth model yield the same time-invariant, symmetric mass matrix, but different load vectors. While the load vector of the first model is time-

	$t = 0$	$t = 4\,\mathsf{s}$
$\boldsymbol{g}_{\mathsf{I}}$	$\begin{bmatrix} 91.56 \\ -53.41 \\ -91.56 \\ -83.93 \end{bmatrix}$	$\cdots$
$\boldsymbol{g}_{\mathsf{II}}$	$\begin{bmatrix} 91.56 \\ -53.41 \\ -91.56 \\ -83.93 \end{bmatrix}$	$\cdots$
$\boldsymbol{g}_{\mathsf{III}}$	$\begin{bmatrix} 91.56 \\ -137.34 \\ -91.56 \\ 0.00 \end{bmatrix}$	$\begin{bmatrix} 26.512 \\ -203.854 \\ -17.103 \\ 13.121 \end{bmatrix}$
$\boldsymbol{g}_{\mathsf{IV}}$	$\begin{bmatrix} 91.56 \\ -144.97 \\ -91.56 \\ 7.63 \end{bmatrix}$	$\begin{bmatrix} 11.508 \\ -154.117 \\ -11.508 \\ 16.778 \end{bmatrix}$

Figure 5. Entries of the load vectors

invariant, the load vector of the fourth model depends on time and differs even at the initial state. On the other hand, the load vector of the second model is identical to the one of the first model, but the mass matrix differs. The mass matrices of the second and third model feature different, time-varying diagonal entries related to the inertia of the corresponding coordinates.

5. Conclusion

Referring to planar systems, the two-point representation of rigid bodies is outlined in a systematic manner applying four different methods. Even though the resulting models are dynamically equivalent, they differ significantly, which is exemplified numerically by means of simulations of a physical pendulum.

Using a two-point model to describe the planar motion of a rigid body appears to be a promising approach to gain further insight into the role of mass matrices and load vectors in the analysis of mechanical systems. It is expected that the presented models help to interpret properly the diagonal and off-diagonal terms of mass matrices and to understand related concepts such as inertial coupling, effective mass and dynamic isotropy.

References

[1] Nikravesh, P. E. An overview of several formulations for multibody dynamics. *Product Engineering: Eco-Design, Technologies and Green Energy* (2005), 189–226.

[2] Nikravesh, P. E. *Planar Multibody Dynamics.* CRC Press, 2007.

Ulrike Zwiers, Professor: Hochschule Bochum University of Applied Sciences, Faculty of Mechatronics and Mechanical Engineering, Lennershofstr. 140, 44801 Bochum, Germany (*ulrike.zwiers@hs-bochum.de*). The author gave a presentation of this paper during one of the conference sessions.

Modelling of high frequency dynamic responses of engineering structures

Arkadiusz Żak, Marek Krawczuk, Grzegorz Redlarski, Wiktor Waszkowiak

Abstract: Modelling of high frequency dynamic responses of engineering structures, especially those related to wave propagation, is a real numerical challenge. Nowadays most of numerical models, used for that purpose, are based on the application of various finite element techniques. However, finite element discrete models may also be considered as possessing certain periodic structures, which may manifest themselves in particular scenarios. The source of their periodicity comes from the discontinuity of the stress/strain field between adjacent finite elements, which usually are ignored by modellers as having no influence on numerical results. Indeed, their influence remains unnoticeable, when low frequency dynamics is investigated. On the other hand at high frequency regimes its influence may be strong enough to dominate calculated structural dynamic responses distorting or even falsifying them completely. In this paper certain issues of modelling of high frequency dynamic responses by finite element techniques are discussed by the authors. In this discussion the authors focus their interest on exemplary problems related to modal analysis as well as wave propagation, with a special attention paid to the periodicity of numerical finite element models. The authors also present and discuss certain methods to minimise, or avoid, the numerical issues mentioned.

1. Introduction

The Finite Element Method (FEM), as well as its many available variants, including the Spectral Finite Element Method (SFEM), still remain one of the most popular computational methods used to analyse the behaviour of engineering structures [4]. As a very robust numerical tool the FEM is employed not only for that purpose, but it also enables researchers to carry out numerical investigations of various physical phenomena in domains of very complex geometries [10]. Beside static or classical dynamic investigations, one of many fields of its applications is modelling and analysis of wave propagation phenomena, especially for the purpose of structural health monitoring (SHM) [3], where sophisticated damage detection algorithms can be tested numerically before their practical implementation [9].

However, discrete numerical models produced by the FEM or SFEM poses certain numerical properties that can be a source of significant numerical errors in particular computational scenarios. The source of these errors come from the stress/strain field discontinuity

between adjacent finite elements (FEs) and it strongest influence manifests itself at high frequency regimes, when high frequency dynamic responses are investigated. For this very reason discrete numerical models may be also considered as periodic structures, which periodicities result in the appearance of certain forbidden frequency band gaps in their natural frequency spectra, in a very similar manner as it is observed in nano-scale in the case of periodic electromagnetic or acoustic metamaterials [7]. Since structural dynamic responses of engineering structures may be considered as a superposition of natural vibration modes of certain amplitudes, the presence of frequency band gaps may have a profound impact on the dynamic responses calculated. This can be very well observed in the case of wave propagation problems [8], therefore the knowledge about this kind of numerical behaviour, resulting from the properties of discrete numerical models, should be always taken into account.

The aim of this paper is to demonstrate the influence of the structural periodicity of discrete numerical models on calculated dynamic responses. The analysis carried out by the authors begins from simple one-dimensional (1-D) engineering structures as rods and beams and further on its results are generalised onto more complex two-dimensional (2-D) as well as three-dimensional (3-D) cases. Based on this analysis certain practical conclusions are formulated and presented by the authors.

2. Periodic properties of FE models

The immanent property of the classical (displacement) formulation of the FEM is the discontinuity of the stress/strain field between adjacent FEs. Because of this, regardless their finite dimensions and various types of boundary conditions or mesh densities, FE models may be considered as representing structures of properties typical to periodic structures. This can be well observed for 1-D structures, however, for 2-D or 3-D structures the same kind of behaviour may be found. Periodic properties of FE models may manifest themselves particularly strong in the case of problems related to propagation of elastic waves, in various elements of engineering structures, especially in the case of 1-D problems. This is a direct consequence of the fact that this particular type of analysis require very dense and regular FE meshes [3].

2.1. Bloch theorem and its consequences

The Bloch theorem in a analytical tool that enables researchers the investigation of the properties and behaviour of periodic structures [1] in nano-, micro- as well as in macro-scales. Most commonly it is used to study the behaviour of electrons in various crystals, however, its application is much more general. The Bloch theorem can be employed to study wave propagation phenomena in periodic media or structures. For example, in periodic

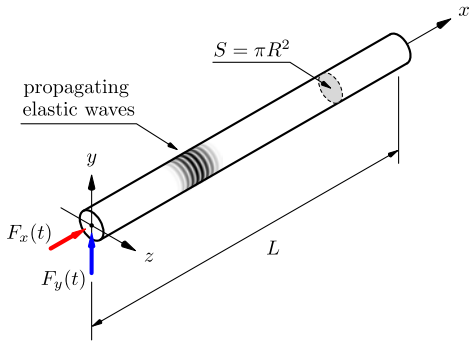

Figure 1. Geometry of an isotropic bar.

dielectric materials the Bloch theorem is used to analyse photonic crystals or in periodic media to analyse phononic crystals [2].

The application of the Bloch theorem is demonstrated by the authors in the case of longitudinal vibrations of 1-D periodic aluminium bar presented in Fig. 1. For this analysis it was assumed that the bar under investigation, of periodic boundary conditions, has the following dimensions: length $L = 2000$ mm and radius $R = 20$ mm, as well as the following material properties: elastic modulus $E = 67.5$ GPa, Poisson's ratio $\nu = 0.33$ and mass density $\rho = 2700$ kg/m^3.

In this simple case it was also assumed that the bar consists of $M = 100$ periodic cells of length $a = 20$ mm characterised by two different wave propagation phase velocities: $c_1 = 5$ km/s over the cell length $l_1 = 16$ mm and $c_2 = 2.5$ km/s over the cell length $l_2 = 4$ mm. The results of analytical calculations obtained by the application of the Bloch theorem are presented in Fig. 2, together with corresponding results of numerical calculations obtained

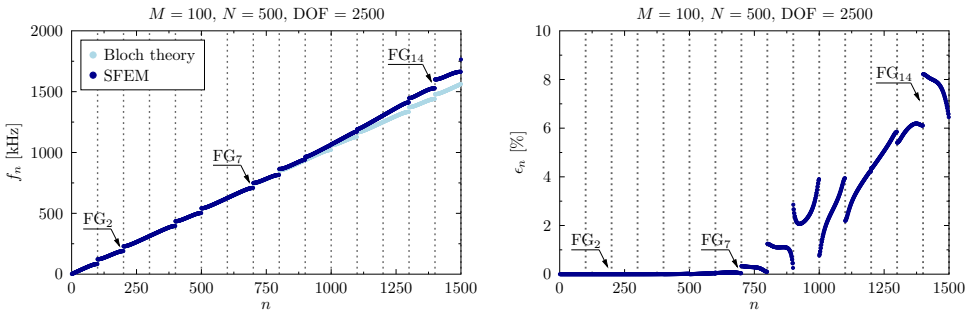

Figure 2. Spectrum of longitudinal natural frequencies f_n (left) and natural frequency relative errors ϵ_n (right) of a periodic bar consisting of $M = 100$ cells.

by the application of the SFEM. In this case $N = 500$ SFEs were applied. They were defined according to elementary theory of longitudinal vibrations of rods [5], for $p = 5$ degree of approximation polynomials, and Chebyshev node distribution [3]. The total number of nodes, i.e. degrees of freedom (DOF), of the numerical model was DOF = 2500. It can be clearly seen that periodic properties of the bar results in the presence of frequency band gaps in the spectrum of natural frequencies. Their widths are closely correlated with the intensity of periodicity, which in the current case is dependent on the ratio c_1/c_2 as well as l_1/l_2. On the other hand the number of these frequency band gaps is dependent on the number of cells M. Moreover, it is evident that the natural frequency f_n calculated numerically agree very well with the analytical ones and the increasing modelling error ϵ_n has its source in the periodicity of the numerical model itself.

This phenomenon is demonstrated by the results of numerical calculations presented in Fig. 3, which are related to the same bar, but having no periodic properties. In this case the bar of fixed ends was modelled by $N = 100$ SFEs of $p = 5$ degree of approximation polynomials and Chebyshev node distribution. As before, the analysis carried out was related to the natural frequencies of the bar and the relative modelling error.

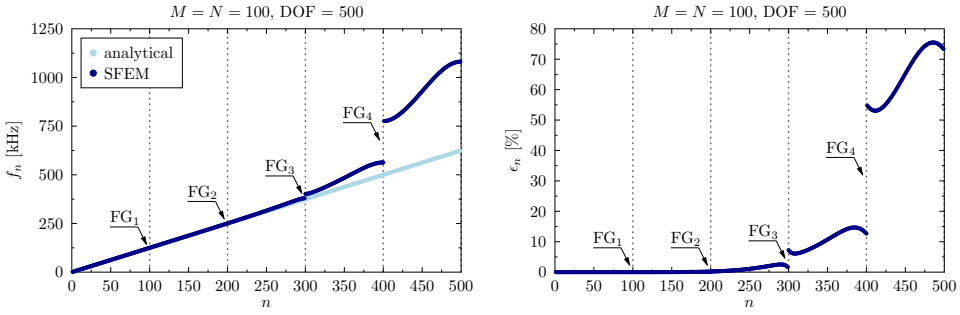

Figure 3. Spectrum of longitudinal natural frequencies f_n (left) and natural frequency relative errors ϵ_k (right) of a non-periodic aluminium bar of fixed ends, calculated for $N = 100$ SFEs of $p = 5$ degree of approximation polynomials and Chebyshev node distribution.

Indeed, the results presented in Fig. 3 confirm that the numerical model of SFEs used in this analysis has properties of periodic nature. It turns out that the resulting model periodicity is equal to the number of SFEs used. As a consequence of that the calculated spectrum of natural frequencies of the bar is divided into $p = 5$ parts separated by $p - 1$ frequency band gaps. It can be also seen that the frequency band gaps associated with high natural frequency numbers n lead to quite significant numerical errors, however, those from the lower part of the natural frequency spectrum can also play a significant role in the problems related to wave propagation.

3. Natural frequency spectra and wave propagation problems

3.1. Longitudinal behaviour of one-dimensional structures

The presence of unnoticeable frequency band gaps in the spectrum of natural frequencies of the bar under consideration has profound effects in the case of wave propagation analysis, as shown in Fig. 4. These results were obtained for the same numerical model of the bar and its dynamic responses in the time domain were calculated by the application of the central difference method. The total time of analysis $T = 0.8$ ms was divided into 2^{14} time steps and chosen so, that the signal propagating within the bar as a longitudinal wave could fully reflect from both free ends of the bar. The final position of the signal at the end of the analysis, calculated analytically, was denoted as λ_m.

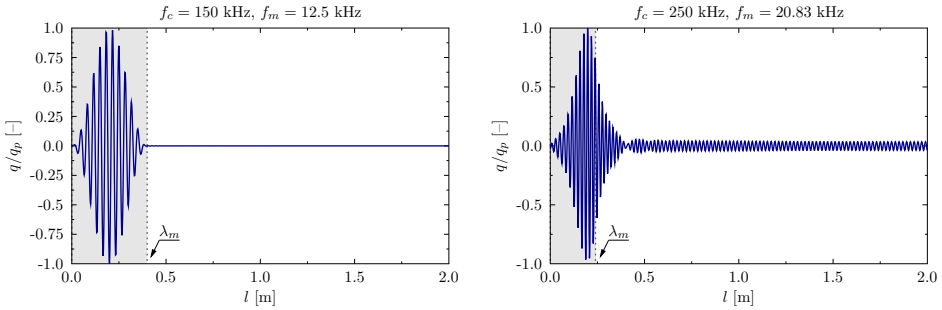

Figure 4. Non-dimensional patterns of longitudinal waves in a non-periodic aluminium bar of free ends, for two different excitation frequencies $f_c = 150$ kHz (left) and $f_c = 250$ kHz (right), calculated for $N = 100$ SFEs of $p = 5$ degree of approximation polynomials and Chebyshev node distribution.

According to the applied theory of rods the phase and group wave propagation velocities in the bar are the same $c_p = c_g = 5$ km/s, which means no signal dispersion should be observed during the analysis. As an excitation a force signal $F_x(t)$ was chosen in the form of sine wave of 12 pulses and amplitude 1 N modulated by the Hann window. Two different excitation frequencies were selected as $f_c = 150$ kHz as well as $f_c = 250$ kHz, with corresponding modulation frequencies $f_m = 12.5$ kHz and $f_m = 20.83$ kHz. For clarity the results obtained in Fig. 4 are presented in a non-dimensional form as related to its peak value q_p, where q denotes the displacement response at the excitation point $x = 0$.

It is clear from Fig. 4 that the dynamic responses of the bar calculated for the excitation frequency $f_c = 150$ kHz (left) are clear of any undesirable behaviour. Contrary to that the dynamic responses of the bar calculated for the excitation frequency $f_c = 250$ kHz (right) reveal some undesired behaviour manifesting in strong signal distortion and some dispersion,

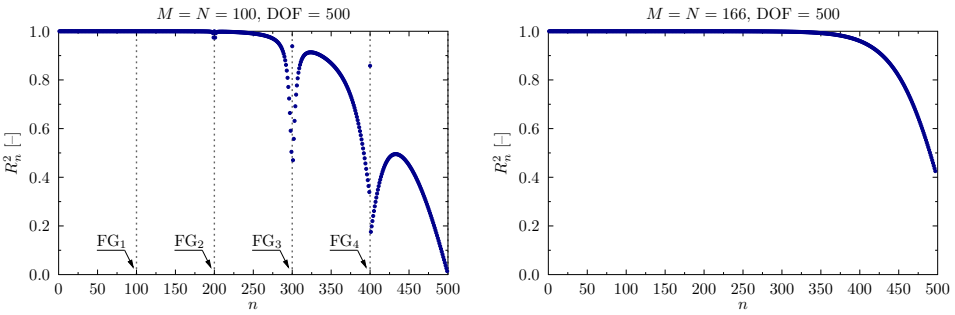

Figure 5. Coefficient of determination R_n^2 for longitudinal modes of natural vibrations of a non-periodic aluminium bar of fixed ends, calculated for $N = 100$ SFEs of $p = 5$ degree of approximation polynomials and Chebyshev node distribution (left) and for $N = 166$ spline-based FEs of $p = 3$ degree of approximation polynomials (right) and developed by the authors.

which has its origin in the periodicity of the numerical model applied. However, it should be also noted that according to the results presented in Fig. 3, up to frequency gap FG_2, no significant modelling errors in the natural frequency spectrum are seen. It turns out the observed behaviour is closely related to the model inability to recover properly the modes on natural vibrations within the frequency range of interest.

Additionally, it can be seen from Fig. 5 that this inability is much more sensible to the periodicity of numerical model than the natural frequency spectrum. The results presented in Fig. 5 refer to the coefficient of determination R_n^2 based on analytically and numerically calculated modes of longitudinal natural vibrations of the bar. They were obtained for a

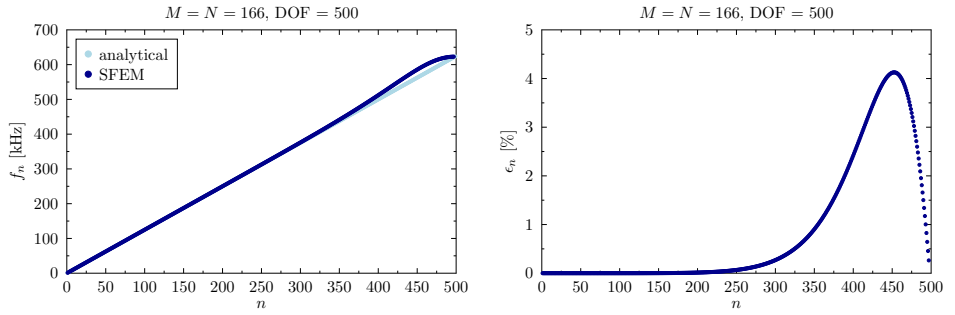

Figure 6. Spectrum of longitudinal natural frequencies f_n (left) and natural frequency relative errors ϵ_n (right) of a non-periodic aluminium bar of fixed ends, calculated for $N = 166$ spline-based FEs of $p = 3$ degree of approximation polynomials and developed by the authors.

numerical model based on $N = 100$ SFEs of $p = 5$ degree of approximation polynomials and Chebyshev node distribution (left), and a numerical model of $N = 166$ spline-based FEs of $p = 3$ degree of approximation polynomials (right) and developed by the authors.

It is interesting to note that the coefficient of determination R_n^2 calculated in the case of the spline-based FEs reveals no frequency band gaps in the entire natural frequency spectrum. This is due to the assumed, on the FE level, continuity of the strain/stress field between adjacent FEs, which eliminates numerical model periodicity. It can be also added that the results presented in Fig. 5 (left) fully explain the source of the undesired numerical behaviour of the numerical model, for which results are presented in Fig. 4, despite the fact that for the natural frequency of interest no significant band gaps are visible, but their influence is strong on the modes of natural vibrations.

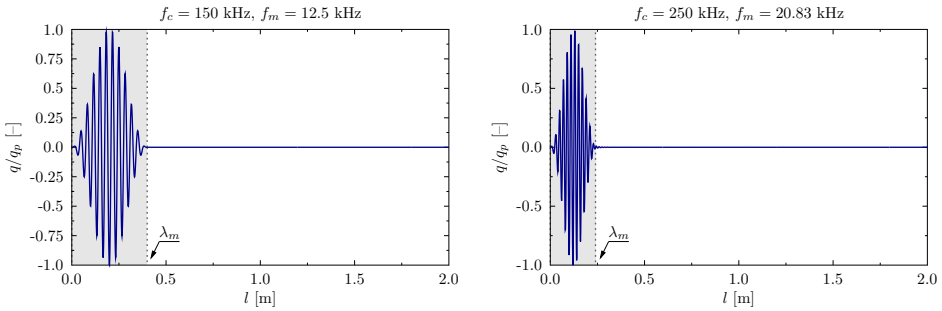

Figure 7. Non-dimensional patterns of longitudinal waves in a non-periodic aluminium bar of free ends, for two different excitation frequencies $f_c = 150$ kHz (left) and $f_c = 250$ kHz (right), calculated for $N = 166$ spline-based FEs of $p = 3$ degree of approximation polynomials and developed by the authors.

In order to supplement the results discussed above also the natural frequencies f_n as well as natural frequency relative errors ϵ_n of the bar under investigation are presented in Fig. 6, calculated in the case of $N = 166$ spline-based FEs of $p = 3$ degree of approximation polynomials and developed by the authors. Additionally, corresponding wave propagation patters are presented in Fig. 7.

3.2. Flexural behaviour of one-dimensional structures

The results shown in Fig. 8 are related to flexural behaviour of the aluminium bar under investigation, according to the classical beam theory [6]. Taking into account the result presented and discussed previously, the authors decided to focus their attention on the coefficient of determination R_n^2 for two different types of FEs used. In the first case a classical approach was used, for which the approximation polynomials in the form of Hermite poly-

nomials of $p = 3$ degree were employed. These polynomial provide the continuity of the unknown displacement functions and their first derivatives. In the second case as the approximation polynomials Hermite polynomials of $p = 5$ degree were employed, which provide the continuity not only for the unknown displacement functions and their first derivatives, but also their second derivatives.

However, it should be noted that despite the fact of the continuity of the displacement functions and their derivatives the coefficient of determination R_n^2 calculated based on analytically and numerically calculated modes of flexural natural vibrations of the bar indicate the presence of frequency band gaps. Again, as before, the presence of the frequency band gaps has a strong influence on calculated dynamic responses of the bar, which may significantly distort wave propagation patterns observed.

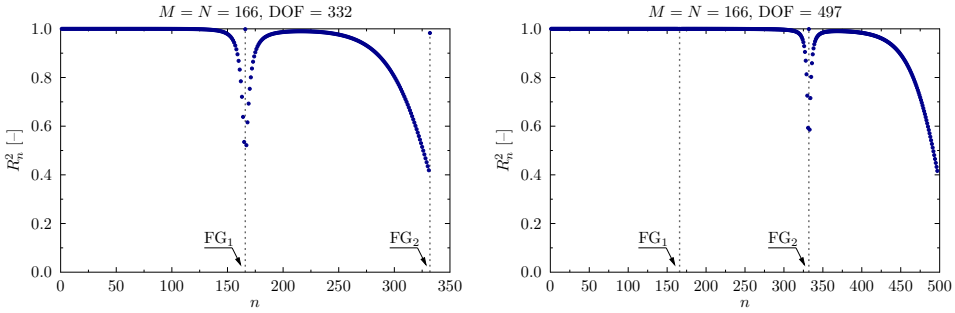

Figure 8. Coefficient of determination R_n^2 for flexural modes of natural vibrations of a non-periodic aluminium bar of simply-supported ends, calculated for $N = 166$ FEs of $p = 3$ degree of Hermite approximation polynomials (left) and $p = 5$ degree of Hermite approximation polynomials (right).

3.3. Flexural behaviour of two-dimensional structures

It can be expected that to some degree the influence of the periodicity of numerical FE models in the case of 2-D engineering structures must correspond to the observations made in the case of 1-D problems. Indeed, this can be confirmed through careful numerical investigations, however, due to 2-D nature of the problems and complexity of the analysis, the methodology employed for this purpose is much more complicated.

A typical spectrum of flexural natural frequencies obtained in the case of a non-periodic aluminium plate in the case of periodic boundary conditions is shown in Fig. 9. It was assumed in this case that the plate under investigation had the following dimensions: length $L = 2000$ mm, width $B = 2000$ mm and thickness $h = 10$ mm. The same material properties were used here. The results presented in Fig. 9 are related to the case, when for modelling the

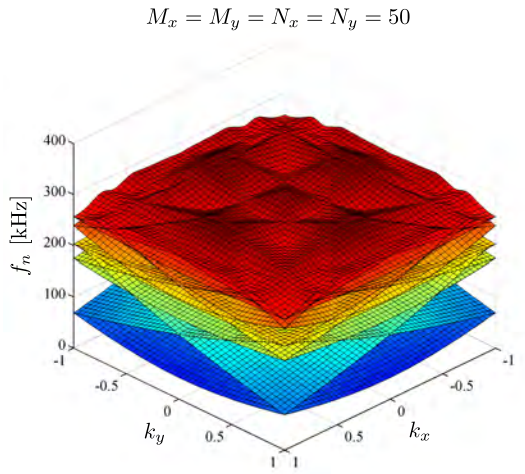

Figure 9. Spectrum of flexural natural frequencies f_n of a non-periodic aluminium plate in the case of periodic boundary conditions in the reciprocal lattice, as a function of non-dimensional wave vectors k_x and k_y, calculated for a regular mesh of 2500 SFEs and $p = 4$ degree of approximation polynomials and Chebyshev node distribution.

plate a regular mesh of 2500 SFEs was used forming a grid $N_x \times N_y$, where $N_x = N_y = 50$.

Numerical calculations were carried out for $p = 4$ degree of approximation polynomials and Chebyshev node distribution. The total number of model degrees of freedom was DOF = 120 000. In Fig. 9 calculated surfaces of flexural natural frequencies of the plate are

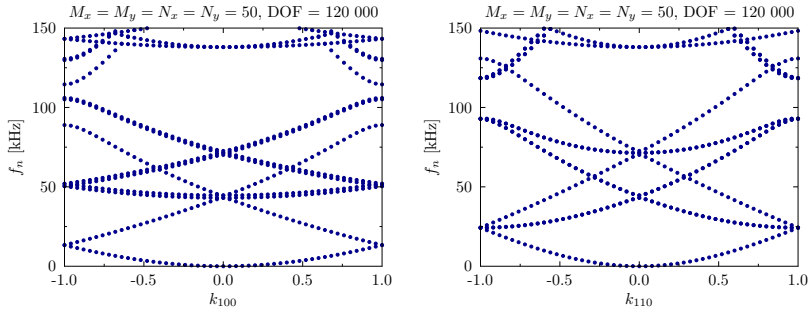

Figure 10. Spectrum of flexural natural frequencies f_n of a non-periodic aluminium plate in the case of periodic boundary conditions as a function of non-dimensional wave vectors k_{100}(left) and k_{110} (right) of the reciprocal lattice, calculated for a regular mesh of 2500 SFEs and $p = 4$ degree of approximation polynomials and Chebyshev node distribution.

expressed as dependent on non-dimensional wave vectors k_x and k_y of the reciprocal lattice.

Observation of any existing frequency band gaps becomes much easier if the analysis is taking place in two particular directions associated with the reciprocal lattice, these being k_{100} and k_{110}, as presented in Fig. 10.

It can be clearly seen that the results presented in Fig. 10 indicate on no observable frequency band gaps in both reciprocal lattice directions. However, in the case of the reciprocal lattice direction k_{100} a frequency band gap just above 100 kHz can be found. This indicates that a mesh of FEs used in the analysis of wave propagation related problems, considered as a numerical periodic structure, has directional properties and as a consequence may influence results of numerical calculations related with wave propagation patters by introducing some artificial model anisotropy. Moreover, it can be demonstrated that in the case of problems related with low frequency behaviour this anisotropy can be, in computational practice, neglected, but in the realm of high frequency excitation signals must be carefully taken into account. This is clearly seen by the results of numerical calculations presented in Fig. 11.

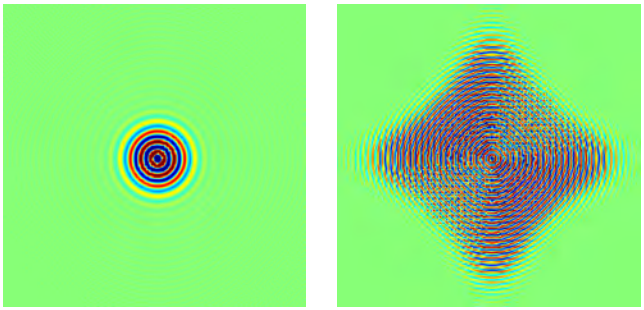

Figure 11. Wave propagation patterns of flexural waves in a non-periodic aluminium plate of free edges for the excitation frequency $f_c = 10$ kHz (left) and $f_c = 44$ kHz (right) at time instance $t = 3$ ms, calculated for a regular mesh of 2500 SFEs and $p = 4$ degree of approximation polynomials and Chebyshev node distribution.

In the case under investigation the total calculation time $T = 15$ ms was divided into 8000 equal time steps and, as before, in order to solve equations of motions the central difference method was employed. The characteristic of the force excitation $F_z(t)$, acting transversally at the plate centre, remained the same as in the case of the aluminium bar.

4. Conclusions

Based on the results of numerical investigations carried out by the authors certain general constitutions can be formulated:

- FE discrete models of engineering structures can poses certain periodic properties.
- The source of these periodic properties comes form the discontinuities of the stress/strain fields between adjacent FEs.
- These discontinuities result in the presence of so-called frequency band gaps in the natural frequency spectra thus influencing calculated dynamic responses of the structures under investigation at high frequency regimes.
- At low frequency regimes the presence of frequency band gaps may remain unnoticed.
- More profoundly frequency band gaps influence the inability of FE numerical models to represent correctly modes of natural vibrations, on which structural dynamic responses are built, even in the frequency regions where no apparent frequency band gaps can be found in the frequency spectrum.
- The number of frequency band gaps is closely correlated with the density of FE mesh: in one-dimensional cases directly with the total number of FEs, while in two- or three-dimensional cases with the FE mesh size in particular directions.
- Analysis of periodic properties of FE discrete models in two- or three-dimensional cases requires the application of very sophisticated analytical and numerical tools in order to reveal any periodic properties of these models.
- The influence of periodic properties of FE discrete models may be reduced or removed by the application of special spline-based FEs, which provide full continuity of the stress/strain fields between adjacent FEs.

Acknowledgments

The authors of this work would like to gratefully acknowledge the support for their research provided by the National Science Centre via project UMO-2012/07/B/ST8/03741 *Wave propagation in periodic structures.* All results presented in this paper have been obtained by the use of the software available at the Academic Computer Centre in Gdansk in the frame of a computational project.

References

[1] Brillouin, L. *Wave propagation in periodic structures, electric filters and crystal laticies.* Dover Publications, Inc., New York, 1946.

[2] Kittel, C. *Introduction to solid state physics.* John Wiley & Sons, Inc, New York, 2005.

[3] Ostachowicz, W., Kudela, P., Krawczuk, M., and Żak, A. *Guided Waves in Structures for SHM. The Time-domain Spectral Element Method*. John Wiley & Sons Ltd., Singapore, 2012.

[4] Rao, S. S. *The Finite Element Method in Engineering*. Pergamon Press, Oxford, 1981.

[5] Żak, A., and Krawczuk, M. Assessment of rod behaviour theories used in spectral finite element modelling. *Journal of Sound and Vibration 329*, 11 (2010), 2099–2113.

[6] Żak, A., and Krawczuk, M. Assessment of flexural beam behaviour theories used for dynamics and wave propagation problems. *Journal of Sound and Vibration 331* (2012), 5715–5731.

[7] Żak, A., Krawczuk, M., and Palacz, M. Periodic properties of 1D FE discrete models in high frequency dynamics. *Mathematical Problems in Engineering 2016* (2016), doi:10.1155/2016/9651430.

[8] Żak, A., Krawczuk, M., Palcz, M., Doliński, Ł., and Waszkowiak, W. High frequency dynamics of an isotropic timoshenko periodic beam by the use of the time-domain spectral finite element method. *Journal of Sound and Vibration 409*, 3 (2017), 318–335.

[9] Żak, A., Krawczuk, M., Radzieński, M., and Ostachowicz, W. Damage detection strategies based on propagation of guided elastic waves. *Smart Materials and Structures 21* (2012), 035024.

[10] Zienkiewicz, O. C. *The Finite Element Method*. McGraw-Hill Book Company, London, 1989.

Arkadiusz Żak, Assoc. Prof.: Gdańsk University of Technology, Faculty of Electrical and Control Engineering, Department of Mechatronics and High Voltage Engineering, ul. Narutowicza 11/12, 80-233, Gdańsk, Poland (*arkadiusz.zak@pg.edu.pl*). The author gave a presentation of this paper during one of the conference sessions.

Marek Krawczuk, Full Prof.: Gdańsk University of Technology, Faculty of Electrical and Control Engineering, Department of Mechatronics and High Voltage Engineering, ul. Narutowicza 11/12, 80-233, Gdańsk, Poland (*marek.krawczuk@pg.edu.pl*).

Grzegorz Redlarski, Assoc. Prof.: Gdańsk University of Technology, Faculty of Electrical and Control Engineering, Department of Mechatronics and High Voltage Engineering, ul. Narutowicza 11/12, 80-233, Gdańsk, Poland (*grzegorz.redlarski@pg.edu.pl*).

Wiktor Waszkowiak, M.Sc. (Ph.D. student): Gdańsk University of Technology, Faculty of Electrical and Control Engineering, Department of Mechatronics and High Voltage Engineering, ul. Narutowicza 11/12, 80-233, Gdańsk, Poland (*wiktor.waszkowiak@pg.edu.pl*).

INDEX OF AUTHORS

Auciello Nicola Maria **9**
Awrejcewicz Jan **31**, **19**, **289, 301, 311**, **449**, **459**, **567**, **579**
Bartoszewicz Andrzej **39**
Beda Peter B. **49**
Bellaredj Mohammed L. **467**
Bencsik László **405**
Benner Peter **59**
Birnir Björn **67**
Birs Isabela **395**
Borisov Alexey **87**
Breunung Thomas **101**
Bruski Dawid **555**
Burzyński Stanisław **555**
Buyadzhi Vasily **205**
Cherkasov Oleg **591**
Chróścielewski Jacek **555**
Chwastek Stefan **109**
Ciechanowicz Ewa **119**
Clerkin Eoin **131**
Cveticanin Livija **143**
Danik Yulia **155**
Demiyanushko Irina **165**
De Keyser Robin **395**
De Rosa Maria Anna **9**
Dmitriev Mikhail **155**
Dubrovskaya Yuliya **205**
Fabro Adriano **323**
Fečkan Michal **449**
Filipuk Galina **175**, **185**
Giesl Peter **193**
Glushkov Alexander **205**
Gupta Sayan **215**
Hafstein Sigurdur **229**
Haller George **101**

Hedrih (Stevanovic) Katica **241**
Herisanu Nicolae **335**
Insperger Tamás **405**
Ionescu Clara **395**
Jaber Nizar **467**
Kalashnikova Margarita **253**
Karavaev Yury **87**
Karpov Ilya **165**
Kecker Thomas **185**
Khalij Leila **323**
Komarova Ekaterina **155**
Komorski Paweł **437**
Kosuru Lakshmoji **467**
Kovacic Ivana **265**
Krawczuk Marek **611**
Krot Alexander **277**
Kruzhilin Vadim S. **31**
Krylova Ekaterina Y. **19**
Krysko Vadim A. **31**, **289, 301, 459**, **567**, **579**
Krysko - jr. Vadim A. **19**, **289, 301**
Kumar Pankaj **215**
Kurina Galina **253**
Kurpa Lidiya **311**
Lenci Stefano **467**
Lippiello Maria **9**
Litawska Anna **519**
Lopes António **533**
Machado Marcela **323**
Makarov Dmitry **155**
Makaseyev Alexander **501**
Marinca Vasile **335**
Martowicz Adam **345**, **357**
Matevossian Hovik **369**
Metelski Marek **425**

Mitskevich Svetlana A. **31**
Mirosław Tomasz **381**
Muresan Cristina **395**
Nagy Dalma **405**
Narayanan Sadagopan **215**
Nikabadze Mikhail **369**, **413**
Nowak Andrzej **425**
Nowak Paweł **425**
Nowakowski Tomasz **437**
Olejnik Paweł **449**
Papkova Irina V. **289, 301, 459**
Pelve Igor **579**
Radkowski Stanisław **545**
Redlarski Grzegorz **611**
Ruzzene Massimo **345**, **357**
Ruzziconi Laura **467**
Saltykova Olga A., ... **459**
Sampaio Rubens **131**
Santos Antonio **533**
Seidel-Morgenstern Andreas **59**
Sethi Abhay Kumar **479**
Shamolin Maxim V. **491**
Shmatko Tetyana **311**
Shulga Igor I. **567**
Shvets Aleksandr **501**
Sinichkina Anastasiya O. **19**
Skiadas Charilaos **511**
Skiadas Christos **511**
Staszewski Wieslaw J. **345**, **357**
Szymański Grzegorz Marek **437**
Tavshavadze Beka **165**
Tenreiro Machado José **533**
Ternovsky Eugeny **205**
Tomasiello Stefania **9**

Tomaszewski Franciszek **437**
Tomczyk Barbara **519**
Tripathy Arun Kumar **479**
Uhl Tadeusz **345**, **357**
Ulukhanian Armine **369**
Valério Duarte **533**
Valfells Asgeir **229**
Waszczuk-Młyńska Aleksandra **545**
Waszkowiak Wiktor **611**
Wilde Krzysztof **555**
Witkowski Wojciech **555**
Yakovleva Tatyana V. **31**, **19**
Yaroshenko Tatyana Y. **579**, **567**
Younis Mohammad **467**
Zarodnyuk Alena **591**
Zhigalov Maxim V. **567**
Zuyev Alexander **59**
Zwiers Ulrike **599**
Żak Arkadiusz **611**